Lecture Notes in Electrical Engineering 245

Jiadong Sun · Wenhai Jiao
Haitao Wu · Chuang Shi
Editors

China Satellite Navigation Conference (CSNC) 2013 Proceedings

Precise Orbit Determination & Positioning • Atomic Clock Technique & Time-Frequency System • Integrated Navigation & New Methods

Springer

Lecture Notes in Electrical Engineering

Volume 245

For further volumes:
http://www.springer.com/series/7818

Jiadong Sun · Wenhai Jiao
Haitao Wu · Chuang Shi
Editors

China Satellite Navigation Conference (CSNC) 2013 Proceedings

Precise Orbit Determination & Positioning • Atomic Clock Technique & Time–Frequency System • Integrated Navigation & New Methods

Springer

Editors
Jiadong Sun
China Aerospace Science and Technology Corporation
Chinese Academy of Sciences
Beijing
People's Republic of China

Wenhai Jiao
China Satellite Navigation Office
Beijing
People's Republic of China

Haitao Wu
Navigation Headquarters
Chinese Academy of Sciences
Beijing
People's Republic of China

Chuang Shi
Wuhan University
Wuhan
People's Republic of China

ISSN 1876-1100 ISSN 1876-1119 (electronic)
ISBN 978-3-642-37406-7 ISBN 978-3-642-37407-4 (eBook)
DOI 10.1007/978-3-642-37407-4
Springer Heidelberg New York Dordrecht London

Library of Congress Control Number: 2013938171

Printed on acid-free paper

Springer is part of Springer Science+Business Media (www.springer.com)

Preface

China's BeiDou Navigation Satellite System (BDS) has been independently developed, which is similar in principle to global positioning system (GPS) and compatible with other global satellite navigation systems (GNSS). The BeiDou will provide highly reliable and precise positioning, navigation, and timing (PNT) services as well as short-message communication for all users under all-weather, all-time, and worldwide conditions.

Since BeiDou Navigation Satellite System provided the test run services on December 27, 2011, more than 6 satellites have been successfully launched in 4 times with large improvements in system coverage, constellation robustness and positioning accuracy. Currently, all in-orbit satellites and ground systems run well, which meet the design requirements through the testing and evaluation of various user terminals. After the news conference announced the Full Operational Capability (FOC) of BeiDou Navigation Satellite System for China and surrounding area on December 27, 2012, the BeiDou Navigation Satellite System officially starts to provide continuous passive positioning, navigation and timing services as well as active positioning, two-way timing and short message communication services.

China Satellite Navigation Conference (CSNC) is an open platform for academic exchanges in the field of satellite navigation. It aims to encourage technological innovation, accelerate GNSS engineering and boost the development of the satellite navigation industry in China and in the world.

The 4th China Satellite Navigation Conference (CSNC 2013) is held on May 13–17, 2013, Wuhan, China. The theme of CSNC 2013 is BeiDou Application—Opportunities and Challenges, which covers a wide range of activities, including technical seminars, academic exchange, forum, exhibition, lectures as well as ION panel. The main topics are as:

1. BeiDou/GNSS Navigation Applications
2. Satellite Navigation Signal System, Compatibility and Interoperability
3. Precise Orbit Determination and Positioning
4. Atomic Clock Technique and Time–Frequency System

5. Satellite Navigation Augmentation and Integrity Monitoring
6. BeiDou/GNSS Test and Assessment Technology
7. BeiDou/GNSS User Terminal Technology
8. Satellite Navigation Models and Methods
9. Integrated Navigation and New Methods

The proceedings have 181 papers in nine topics of the conference, which were selected through a strict peer-review process from 627 papers presented at CSNC 2013.

We thank the contribution of each author and extend our gratitude to over 100 referees and 36 session chairmen who are listed as members of editorial board. The assistance of CSNC 2013's organizing committees and the Springer editorial office is highly appreciated.

Jiadong Sun
Chair of CSNC 2013

Editorial Board

The 4th China Satellite Navigation Conference (CSNC 2013)

Scientific Committee

Chairman:
Jiadong Sun, China Aerospace Science and Technology Corporation

Vice-Chairman:
Rongjun Shen, China
Jisheng Li, China
Qisheng Sui, China
Zuhong Li, China Academy of Space Technology
Shusen Tan, Beijing Satellite Navigation Center, China

Executive Chairman:
Jingnan Liu, Wuhan University
Yuanxi Yang, China National Administration of GNSS and Applications
Shiwei Fan, China

Committee Members (By Surnames Stroke Order):
Xiancheng Ding, China Electronics Technology Group Corporation
Qingjun Bu, China
Liheng Wang, China Aerospace Science and Technology Corporation
Yuzhu Wang, Shanghai Institute of Optics and Fine Mechanics, Chinese Academy of Sciences
Guoxiang Ai, National Astronomical Observatories, Chinese Academy of Sciences
Shuhua Ye, Shanghai Astronomical Observatories, Chinese Academy of Sciences
Zhaowen Zhuang, National University of Defense Technology
Qifeng Xu, PLA Information Engineering University
Houze Xu, Institute of Geodesy and Geophysics, Chinese Academy of Sciences
Guirong Min, China Academy of Space Technology
Xixiang Zhang, China Electronics Technology Group Corporation
Lvqian Zhang, China Aerospace Science and Technology Corporation

Junyong Chen, National Administration of Surveying, Mapping and Geoinformation
Benyao Fan, China Academy of Space Technology
Dongjin Luo, China
Guohong Xia, China Aerospace Science and Industry Corporation
Chong Cao, China Research Institute of Radio Wave Propagation (CETC 22)
Faren Qi, China Academy of Space Technology
Sili Liang, China Aerospace Science and Technology Corporation
Shancheng Tu, China Academy of Space Technology
Rongsheng Su, China
Zhipeng Tong, China Electronics Technology Group Corporation
Ziqing Wei, Xi′an Institute of Surveying and Mapping

Organizing Committee

Secretary General:
Haitao Wu, Navigation Headquarters, Chinese Academy of Sciences

Vice-Secretary General:
Wenhai Jiao, China Satellite Navigation Office
Tao Peng, Academy of Satellite Application, China Aerospace Science and Technology Corporation
Wenjun Zhao, Beijing Satellite Navigation Center
Chuang Shi, Wuhan University
Weina Hao, Navigation Headquarters, Chinese Academy of Sciences

Committee Members (By Surnames Stroke Order):
Qun Ding, Xi'an Institute of Navigation Technology
Miao Yu, Beijing Institute of Space Science and Technology Information
Yinhu Ma, Navigation Satellite Systems Engineering Center, China Academy of Aerospace Electronics Technology
Xiuwan Chen, Institute of Digital China, Peking University
Mingquan Lu, Tsinghua University
Guangzhou Ouyang, Academy of Opto-Electronics, Chinese Academy of Sciences
Shuanggen Jin, Shanghai Astronomical Observatory, Chinese Academy of Sciences
Xiang'an Zhao, China Defense Science and Technology Information Center
Hong Yuan, Navigation Headquarters, Chinese Academy of Sciences
Yamin Dang, Chinese Academy of Surveying and Mapping
Zhong Dou, National Time Service Center, Chinese Academy of Sciences

Contents

Part II Atomic Clock Technique and Time-Frequency System

Part I
Precise Orbit Determination and Positioning

Chapter 1
A Satellite Selection Algorithm for Achieving High Reliability of Ambiguity Resolution with GPS and Beidou Constellations

Jun Wang and Yanming Feng

Abstract Reliability of carrier phase ambiguity resolution (AR) of an integer least-squares (ILS) problem depends on ambiguity success rate (ASR), which in practice can be well approximated by the success probability of integer bootstrapping solutions. With the current GPS constellation, sufficiently high ASR of geometry-based model can only be achievable at certain percentage of time. As a result, high reliability of AR cannot be assured by the single constellation. In the event of dual constellations system (DCS), for example, GPS and Beidou, which provide more satellites in view, users can expect significant performance benefits such as AR reliability and high precision positioning solutions. Simply using all the satellites in view for AR and positioning is a straightforward solution, but does not necessarily lead to high reliability as it is hoped. The paper presents an alternative approach that selects a subset of the visible satellites to achieve a higher reliability performance of the AR solutions in a multi-GNSS environment, instead of using all the satellites. Traditionally, satellite selection algorithms are mostly based on the position dilution of precision (PDOP) in order to meet accuracy requirements. In this contribution, some reliability criteria are introduced for GNSS satellite selection, and a novel satellite selection algorithm for reliable ambiguity resolution (SARA) is developed. The SARA algorithm allows receivers to select a subset of satellites for achieving high ASR such as above 0.99. Numerical results from a simulated dual constellation cases show that with the SARA procedure, the percentages of ASR values in excess of 0.99 and the percentages of ratio-test values passing the threshold 3 are both higher than those directly using all satellites in view, particularly in the case of dual-constellation, the percentages of ASRs (>0.99) and ratio-test values (>3) could be as high as 98.0 and 98.5 % respectively, compared to 18.1 and 25.0 % without satellite selection process. It is also worth noting that the implementation of SARA is simple and the computation time is low, which can be applied in most real-time data processing applications.

J. Wang (✉) · Y. Feng
Queensland University of Technology, Brisbane, Australia
e-mail: jun.wang@connect.qut.edu.au

J. Sun et al. (eds.), *China Satellite Navigation Conference (CSNC) 2013 Proceedings*, Lecture Notes in Electrical Engineering 245,
DOI: 10.1007/978-3-642-37407-4_1,

Keywords Satellite selection algorithm · Ambiguity success rate · Reliability · Dual-GNSS signals · Ambiguity resolution

1.1 Introduction

Global Navigation Satellite Systems (GNSSs) is the generic term for all jurisdictional satellite navigation systems including the United States Global Position System (GPS), Russia's GLONASS, European Space Agency's Galileo, China's Beidou, Japan's Quasi Zenith Satellite System (QZSS) and India's Indian Regional Navigation Satellite Systems (IRNSS) [1]. In the very future, there will be 25–45 satellites in view depending on users' locations. Australia is one of many countries eventually receiving maximum numbers of satellite signals from all six systems simultaneously. O'Keefe et al. have investigated and demonstrated that a combined GNSS system provides significantly improved availability for navigation in obstructed areas, where navigation with GPS alone is currently difficult [2]. Yang et al. have defined and analysed three types of generalised dilution of precision (G-DOP) among different GNSS systems based on robust estimation. However, these performance benefits do not come without cost [3]. Benefits that multi-GNSS and multi-frequency signals can bring to users may be maximized by selective use of satellite systems, or signals, or subset of visible satellites from different systems in order to achieve required positioning performance at affordable costs. This is certainly the case for real-time kinematic positioning or other precise positioning based on successful resolutions of carrier phase ambiguities of satellite signals. This research work will prove that it is possible to select a subset of satellites from two constellations in order to achieve higher reliability of carrier phase ambiguity resolutions, thus assuring the reliability and accuracy of the RTK solutions.

For integer least-squares (ILS) solutions of a linear system with integer parameters, the ambiguity dilution of precision (ADOP) and the ambiguity success rate (ASR) have been introduced to capture and analyze the precision and reliability characteristics of the ambiguities [4–6]. Theoretically only when the ASR is very close to 1, the integer ambiguities can be considered deterministic, thus guaranteeing the precision of fixed solution better that the float solution [7]. Since incorrect ambiguity fixing can lead to largely biased positioning solutions, so it is always worthwhile to have an AR solution with the high ASR. An approach to achieve the high ASR is to apply the concept of partial ambiguity resolution (PAR), which is a technique for fixing a subset of the ambiguities with a higher ASR of resolving them correctly [8]. This study is focused on the geometry-free model; however the success rate of the geometry-based model cannot guaranteed to be increased with less satellites imposed because of the poor geometry. Cao et al. has also numerically demonstrated that the ASR decreases as the number of ambiguities increases and a combination of constellations can achieve a higher ASR in shorter observation periods compared to a single constellation used

independently [9]. Wang and Feng have clearly demonstrated that only when the computed success rate is very high, the AR validation can provide the decisions about the correctness of AR close to real world with both low AR risk and false alarm rate [10]. The results from that work also indicate that an advantage of using multi-GNSS signals for PAR is that actually only part of satellites or signals are needed to archive a very high-success rate instead of using all satellites. This is how high reliability of PAR can be achieved with multi-GNSS signals.

In terms of satellite selection algorithms, there are quite a few methods to obtain the minimum DOP with limited satellites which aim at low-cost receivers and meter-level pseudorange positioning. One early contribution was the maximum volume algorithm [11]. The four-step satellites selection algorithm is developed to select four satellites to form near optimal geometry [12]. Park proposed the quasi-optimal satellite selection algorithm for GPS receivers used in low earth orbit (LEO) application, which can select any required number of satellites [13]. A heuristic method combining the maximum volume algorithm and the redundancy technique is developed to mitigate computational burdens while maintaining benefits of the combined navigation satellite systems and called multi-constellations satellite selection algorithm [14]. However, to the best of our knowledge there is no method for selecting a subset of the satellites towards achieving a high reliability of a positioning system. On the other hand, once the number of selected satellite reaches certain numbers, such as more than ten, the variation rate of PDOP values is no longer evident. The improvement of ASR is still remarkable, thus deserving more investigation. Figure 1.1 shows the PDOP, ADOP and ASR of four different ten-satellite subsets from overall fifteen satellites. It is clear that the PDOP values are fluctuating between 0.9 and 1.5, while the ADOP values and the ASR values are portioned into four separate layers. The hierarchical structure of the ASR is more obvious than that of the ADOP. Moreover, it is interesting to see that in some samples, ASR values are very close to 1, which indicates their integer ambiguities will be reliable. This implies that it is possible to find a subset of satellites which maintains both the low PDOP and the high ASR when the total visible satellite number is large enough. This research effort develops and tests a satellite selection strategy that allows high reliability of AR to be achieved with multi-constellations. Results from numerical analysis will confirm that this satellite selection method can result in better ASR outcomes without loss of positioning accuracy.

The remainder of this paper is organized as follows. In Sect. 1.2, the measures of least squares solution reliability are described, which are related to the ADOP and the ASR. Section 1.3 describes the Satellite-selection Algorithm for Reliable Ambiguity-resolution (SARA). In Sect. 1.4, numerical experiment results for different constellations are provided to demonstrate the advantage of this proposed algorithm over other satellite selection algorithms and contribution to high reliability of ambiguity resolutions comparing no satellite selection. Finally, the main research findings from this work are summarized.

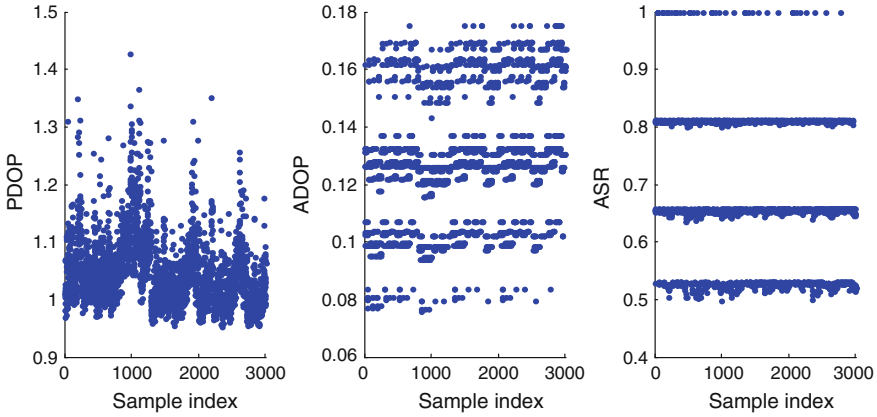

Fig. 1.1 PDOP, ADOP and ASR of different ten satellites from fifteen satellites

1.2 Reliability Criteria for Ambiguity Resolution

Traditionally, reliability is the measure of the capability of a system to detect blunders or biases in the measurements and to estimate the effects that undetected blunders may have on a solution. Redundancy number is an important factor in reliability theory which refers to the contribution of the ith observation of the linear observation system to the degree of freedom (DOF). There are two measures of reliability: internal reliability represented by the minimum detectable bias (MDB) and external reliability quantified by the effect of undetectable bias in the observation [15, 16]. Internal reliability and external reliability are used to characterize the least squares solutions of unknown parameters. The reliability criteria are referred to the parameters to be used in selection of satellites for achieving reliable ambiguity solution in processing GNSS carrier phase measurements. The criteria include concepts of internal and external reliability from the traditional real-value least-squares estimation and the concepts of the ADOP and the ASR that is directly related to the ILS solutions' reliability. This section will introduce the internal and external reliability concept first, followed by the ADOP and success rate computations and numerical analysis regarding the reliability criteria.

1.2.1 Internal Reliability and External Reliability

A linear observational model is defined by

$$\mathbf{y} = \mathbf{A}\mathbf{x} + \mathbf{e},\ \mathbf{e} \sim \left(0,\ \sigma_0^2\mathbf{Q}\right) \tag{1.1}$$

where $\mathbf{y}$ is the observation vector, $\mathbf{x}$ is the unknown parameter vector, $\mathbf{e}$ is the random error vector, σ_0^2 is the variance of the unit-weight measurements and $\mathbf{Q}$ is the cofactor matrix. We have the weight matrix $\mathbf{P} = \mathbf{Q}^{-1}$.

The redundancy number r_i is given as

$$r_i = (\mathbf{Q}_{vv}\mathbf{P})_{ii} \tag{1.2}$$

with a normal equation matrix

$$\mathbf{N} = \mathbf{A}^T\mathbf{P}\mathbf{A} \tag{1.3}$$

and a cofactor matrix for residuals

$$\mathbf{Q}_{vv} = \mathbf{Q} - \mathbf{A}\mathbf{N}^{-1}\mathbf{A}^T \tag{1.4}$$

The internal reliability measure is represented by the minimal detectable bias (MDB) as [15, 16]

$$|\nabla_{0i}| = \frac{\delta}{\sqrt{r_i}}\sigma_i \tag{1.5}$$

where σ_i is the standard deviation of the ith observation, which is a function of the diagonal element of $\mathbf{Q_{vv}}$ and σ_0^2; δ is the non-centrality parameter depending on the level of significance $\alpha$and the power of the test β.

The external reliability is the influence of each of the MDBs on the estimated parameters. The effect of the blunder or the bias ∇_i in ith observation is

$$\nabla_{\mathbf{x}} = \mathbf{N}^{-1}\mathbf{A}^T\mathbf{P}\mathbf{c}_i\nabla_i \tag{1.6}$$

where the c-vector takes the form $(0, \ldots, 1, \ldots, 0)^T$, with the 1 as the ith entry of $\mathbf{c}$. Consequently, the impact of the MDB ∇_{0i} is given as

$$\nabla_{\mathbf{x}_{0i}} = \mathbf{N}^{-1}\mathbf{A}^T\mathbf{P}\mathbf{c}_i\nabla_{0i} \tag{1.7}$$

Baarda suggested the follow alternative expression:

$$\lambda_{0i}^2 = \frac{\nabla_{\mathbf{x}_{0i}}^T\mathbf{N}\nabla_{\mathbf{x}_{0i}}}{\sigma_0^2} \tag{1.8}$$

The value λ_{0i}^2 is considered to be a measure of global external reliability. When the external reliability becomes large, the global falsification caused by a blunder or bias can be significant [17].

1.2.2 Adop

Like the PDOP measure commonly used to describe the impact of receiver-satellite geometry on the positioning precision, the concept of the ADOP is introduced to measure the intrinsic precision characteristics of the ambiguities [4]. It is defined as

$$\mathrm{ADOP} = \sqrt{\left|\mathbf{Q}_{\hat{\mathrm{N}}}\right|^{\frac{1}{m}}} \text{ (cycle)} \tag{1.9}$$

where $\mathbf{Q}_{\hat{\mathrm{N}}}$ is the variance–covariance (vc-) matrix of the m-dimensional float ambiguities.

Smaller ADOP values imply more precise estimation of the float ambiguities and higher possibility of successful ambiguity validation. It is suggested that for successful AR the ADOP should be smaller than 0.15 cycles [18]. For a short observation time span, the approximation of the ADOP can be expressed as [19]

$$\mathrm{ADOP} \approx m^{\frac{1}{2(m-1)}} \cdot \left(\frac{\sigma_\phi^2}{\sigma_p^2}\right)^{\frac{m-4}{4(m-1)}} \cdot \left(\frac{\sigma_\phi \sigma_p}{k\lambda_1\lambda_2}\right)^{\frac{1}{2}} \text{ (cycle)} \tag{1.10}$$

where σ_p^2 denotes the variance of code, σ_ϕ^2 denotes the variance of phase, λ_1 and λ_2 denote the wavelengths of L1 and L2, and k denotes the number of epochs.

1.2.3 Success Rate

The success rate P_S is defined as follows [5, 20]

$$P_S = P\left(\breve{\mathbf{N}} = \mathbf{N}\right) = \int_R f_{\hat{N}}(x)dX \tag{1.11}$$

where R and $f_{\hat{N}}(x)$ denote the ILS pull-in region and the probability density function of the float ambiguities $\hat{\mathbf{N}}$ respectively. In general, we assume the float ambiguity is normally distributed, e.g., $N\left(\mathbf{N}, \sigma_0^2\mathbf{Q}_{\hat{N}}\right)$. Therefore, the success rate can be expressed as

$$\begin{aligned} P_S &= \int_R N\left(\mathbf{N}, \sigma_0^2\mathbf{Q}_{\hat{N}}\right)dX \\ &= \int_R \frac{1}{(2\pi)^{\frac{1}{m}}\left|\sigma_0^2\mathbf{Q}_{\hat{N}}\right|^{1/2}} \exp\left[-\frac{1}{2\sigma_0^2}(\mathbf{X}-\mathbf{N})^{\mathbf{T}}\mathbf{Q}_{\hat{Z}}^{-1}(\mathbf{X}-\mathbf{N})\right]dX \end{aligned} \tag{1.12}$$

Nevertheless, construction of the ILS pull-in region or Voronoi cell can be complex, the real-time computation of AR success rate is considered difficult and impractical [5, 20]. Fortunately the success rate of bootstrapping estimator has been proved to be a sharp lower bound and good approximations of the actual success rate, expressed as [5, 21]

$$P\left(\breve{\mathbf{N}} = \mathbf{N}\right) \geq P_{boot} = \prod_{i=1}^{m}\left[2\Phi\left(\frac{1}{2\sigma_{\hat{N}_i|I}}\right) - 1\right] \tag{1.13}$$

with

$$\Phi(t) = \int_{-\infty}^{t} \frac{1}{\sqrt{2\pi}} \exp\left(-\frac{1}{2}x^2\right) dx. \tag{1.14}$$

The invariant ADOP can be used to obtain an upper bound for the bootstrapped ASR as [22]

$$P_{boot} = \prod_{i=1}^{m}\left[2\Phi\left(\frac{1}{2\sigma_{\hat{N}_i|I}}\right) - 1\right] \leq \left[2\Phi\left(\frac{1}{2\mathrm{ADOP}}\right) - 1\right]^m. \tag{1.15}$$

1.2.4 Reliability Criteria for Satellite Selection

Figure 1.2 shows the redundancy numbers (RNUM), the MDBs and the external global reliabilities (EXTR) of a dual-constellation design matrix for 1,000 samples that can be generated from the experiment data in Sect. 1.4. It is interesting to note that those relevant reliability values are grouped into two separate Clusters. To be specific, the values of RNUM are either close *1* or below 0.9 while the MDB values are either around 0.02 or below 0.2 and the EXTR are either around 0.3 or around 2.5. Besides, Fig. 1.2 also shows the selected satellites with extreme values in terms of RNUM (>0.9), MDB (>0.15) and EXTR (<0.4) are the same. Taking a sample with 10 satellites as an example, the redundancy numbers, the MDBs and the external global reliabilities are listed in Table 1.1. It is shown that the maximum redundancy number and MDB and the minimum external global reliability can be easily identified. The question naturally is whether the removal of the measurements with extreme values from the observation system can sufficiently assure the higher success rate of AR in the ILS solutions. Alternatively, the question is if the high AR success rates necessarily require the removal of the extreme measurements. These questions are not easily answered theoretically. However, Sect. 1.4 will seek the answers to the questions numerically.

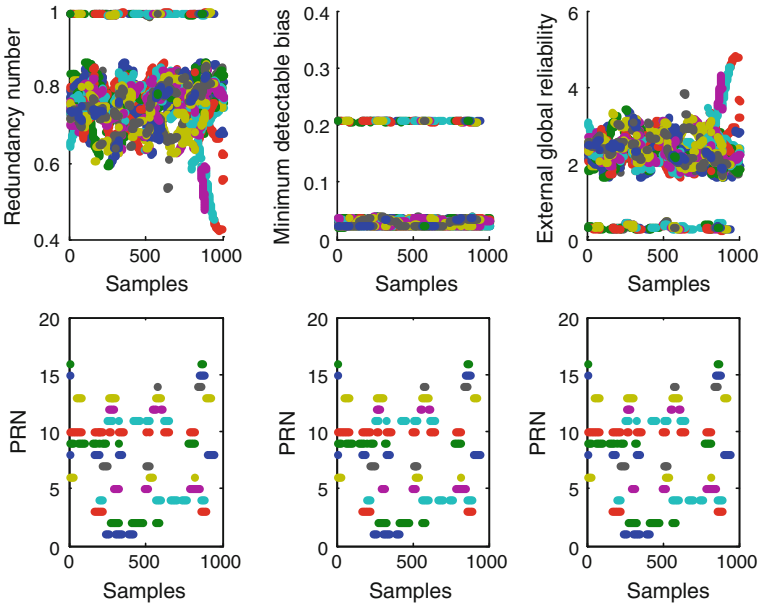

Fig. 1.2 The redundancy number, minimum detectable bias and external global reliability of a dual-constellation design matrix for 1,000 samples

Table 1.1 The extreme values of RNUM, MDB and EXTR

PRN	1	2	3	4	5	**6**	7	8	9	10
RNUM	0.77	0.83	0.79	0.67	0.69	**0.99**	0.77	0.77	0.73	0.73
MDB	0.02	0.02	0.03	0.02	0.02	**0.20**	0.03	0.03	0.03	0.03
EXTR	2.21	1.83	2.10	2.85	2.71	**0.32**	2.21	2.21	2.46	2.46

1.3 Satellite-Selection Algorithm for Reliable Ambiguity-Resolution

Based on the given reliability criteria in the previous section, this section presents a satellite- selection algorithm for reliable ambiguity-resolution (SARA), which searches for a subset of satellites with a high ASR and low computational burden. In addition, this algorithm assumes that there are adequate satellites, for instance, in the case of multiple constellations where the PDOP requirement is easy to satisfy. The purpose or the advantage of SARA is to improve the ASR compared to other satellite selection algorithms, whereas, the computation load of SARA is maintained at a low level.

In fact, it is simple to implement the SARA algorithm which only consists of the following four steps.

Step 1. Create a list of visible satellites and form the design matrix A of un-differenced model with all the satellites.
Step 2. Calculate the reliability parameters mentioned in Sect. 1.2.1.
Step 3. Remove the satellite with extreme values.
Step 4. Select the remaining satellites.

Unlike the existing pseudorange-based algorithms, there is no need for a pre-defined number of selected satellites for SARA, because SARA can make the decision with its own reliability characteristics. As shown in Fig. 1.3 and Table 1.1, the criteria for the extreme redundancy number, the MDB and the external global reliability give the equivalent results. The criterion of selecting the subset of satellites can be based on any of the three parameters. In Step 3, usually there are two options: Option 1 is to remove all the satellites with the extreme RNUM, or MDBs or EXTR values; Option 2 is to remove the satellite with the most extreme value and return to Step 2. Figure 1.3 gives the flowchart of Option 1 and Option 2. Obviously, the second scheme is more complicated. Figure 1.4 shows the ASR difference between these two options based on SARA. It is shown that the ASR performances of these two options are just the same in most samples in spite of having some ignorable difference, smaller than 0.1 % in other samples. Therefore, the SARA algorithm adopts the first option that removes the high redundant satellites at once. The fourteen satellites selected by SARA from eighteen satellites are plotted in Fig. 1.5. Considering inter constellation biases, the different reference satellites are used in their corresponding system respectively.

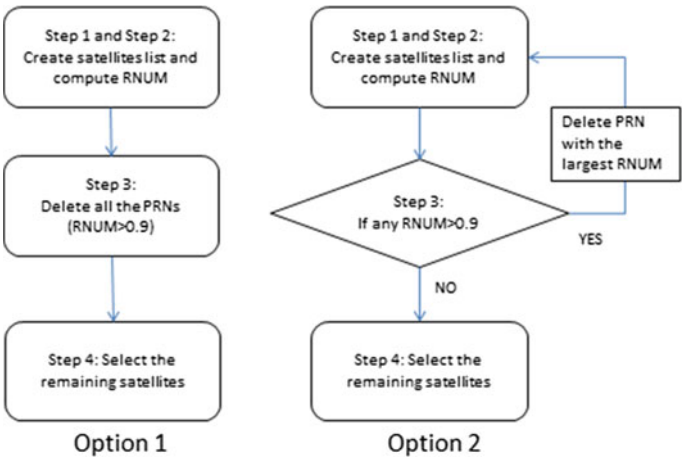

Fig. 1.3 The two options of SARA algorithm

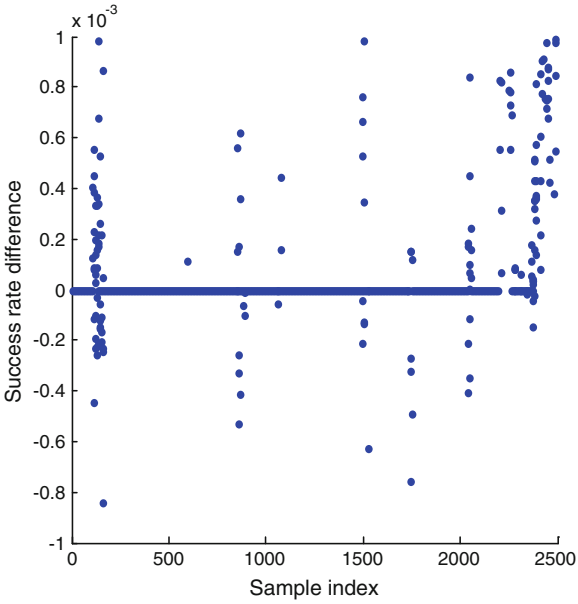

Fig. 1.4 The ASR difference between option 1 and option 2 in SARA algorithm

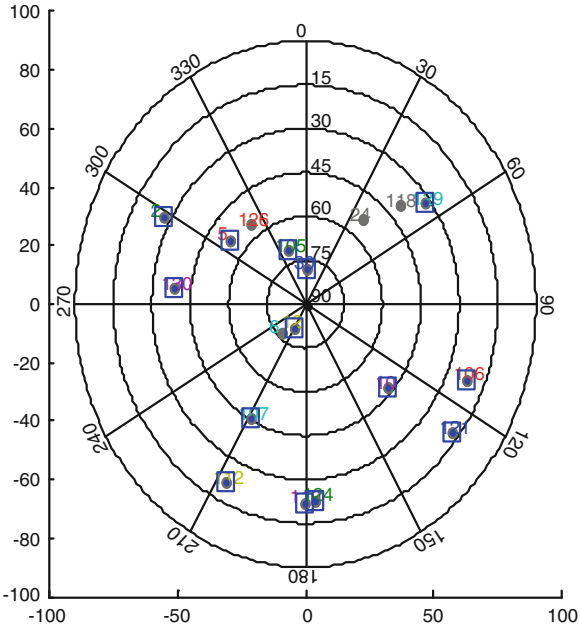

Fig. 1.5 The sky plot of selected 14 visible satellites as an example from 18 visible satellites by SARA, □ denotes the selected satellite

1.4 Experiments and Analysis

To demonstrate the efficiency of SARA, results from the simulated dual-constellation system (DCS) are analyzed. A total of 2,500 epochs of dual-frequency (L1 and L2) data set collected at the interval of 30 s on 1 January 2007 about a 21 km baseline was processed for analysis. A typical elevation cut-off angle of 15° is used. Prior variance settings for code and phase measurements are given as 30 and 0.5 cm^2 respectively. The geometry-based model and the LAMBDA method are used in this experiment and the solutions are resolved epoch-by-epoch in kinematic mode. Similar to the virtual Galileo constellation (VGC) method [23], the virtual Beidou navigation and observation data is generated by the real GPS data with time-latency of 300 epochs. In this work, the SARA uses the extreme redundancy number (RNUM > 0.9) as the criterion to remove all the corresponding satellites as the concept of redundancy number is more familiar and simple too. For ambiguity validation purposes, the ratio-test is applied and the critical values of t are chosen as 1.5, 2 or 3 [24–26]. Moreover, the concept of ambiguity validation decision matrix is utilized to analyse the AR performance of SARA [10]. Particularly, we pay more attention to the probability of false alarm, which means while the integer ambiguity is fixed correctly, but the ratio-test is rejected.

To demonstrate the performance of SARA, especially the improvement of ASR, we calculate and compare different AR factors of using all the visible satellites with those of applying SARA scheme. Figure 1.6 shows the satellite numbers of original dual constellations and those with satellite selection algorithms. SARA can detect and delete more satellites with the increasing of satellites number. It is shown that the maximum deleted satellites number of dual-constellation is 6 and SARA still keeps the minimum satellites number more than 10 in this experiment. Figure 1.7 illustrates the PDOP values from the two cases. As we can see, DCS scheme results in smaller PDOPs, however, the PDOPs of SARA is still good enough with the values from 0.8 to 1.2 due to the enough visible satellites as shown in Fig. 1.6. The PDOPs difference between the two cases is not significant; nevertheless, it is clearly shown that the ADOPs with SARA algorithm are smaller than the DCS in Fig. 1.8. All the epochs with SARA can meet the ADOP 0.15 cycles requirement [18]. Figure 1.9 illustrates the ASR results. A remarkable phenomenon is that the ASR values with SARA are larger than those of DCS. More specifically, most ASR values over the 2,500 samples are over than 90 % and very close to 100 %, whereas the ASR values from the DCS scheme is fluctuated between 0 and 1.

For the sake of conciseness, only the results of redundancy numbers are given as Fig. 1.10. Obviously, SARA removes all the observations with the redundancy number of 0.9 or higher. In contrast, the result from the DCS illustrates two distinct structural patterns involving extremely large redundancy numbers.

Figure 1.11 gives the histograms of AR ratio-test values obtained from DCS and SARA cases. Obviously, compared to DCS, SARA has more numbers of

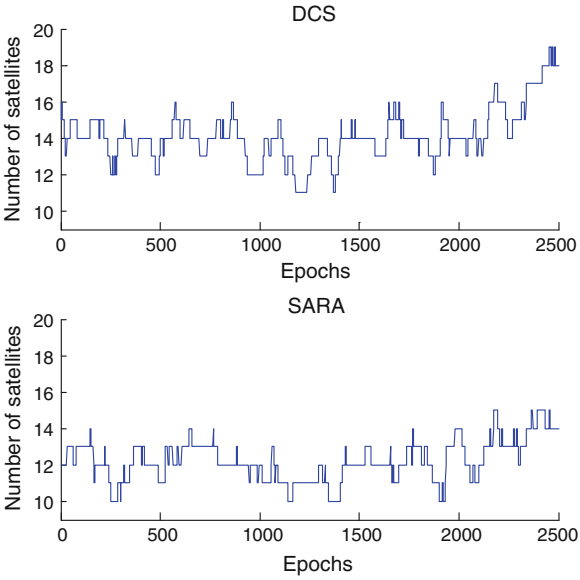

Fig. 1.6 Satellite numbers computed with all visible satellites and SARA

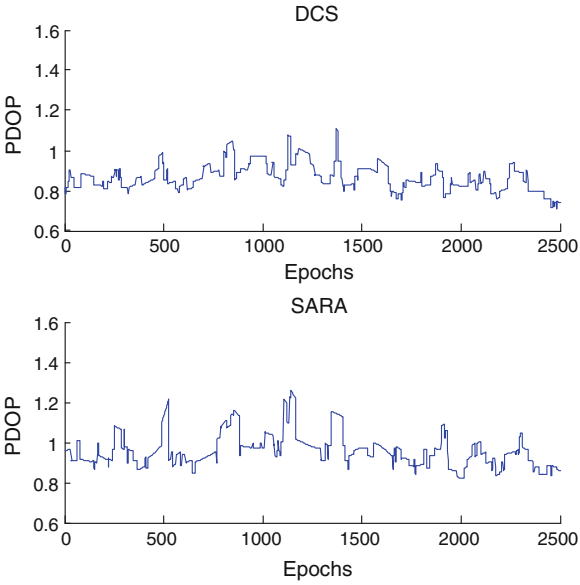

Fig. 1.7 PDOPs computed with all visible satellites and SARA

larger ratio-test values. In fact, the real AR probabilities of correct fix (PCF) in DCS and SARA are 100 % in this experiment. However, due to the smaller ratio-test values in DCS, the false alarm rate is higher than that of SARA; hence a lot of correct integer ambiguities are unfortunately rejected by ratio-test. As a result,

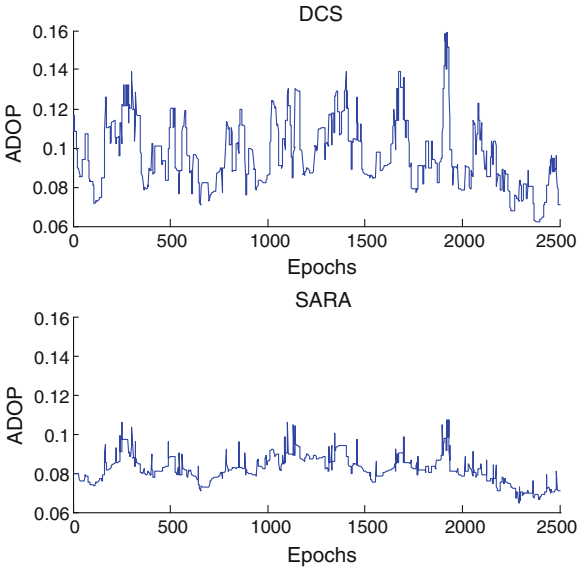

Fig. 1.8 ADOPs computed with all visible satellites and SARA

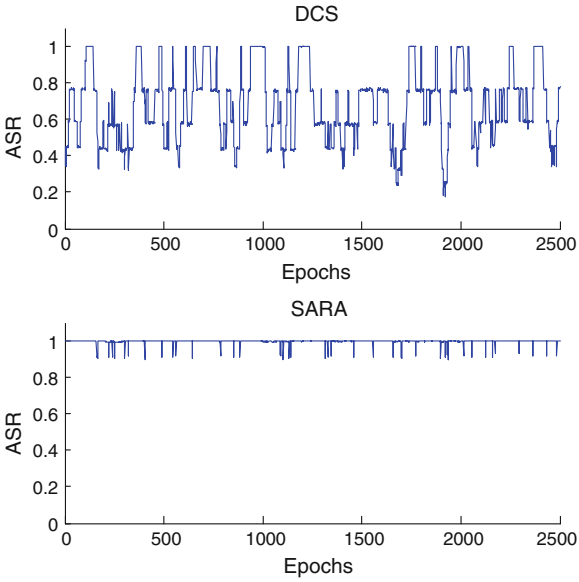

Fig. 1.9 ASRs computed with all visible satellites and SARA

Fig. 1.12 shows that the positioning performance of DCS is much worse than that of SARA.

Table 1.2 summarizes the percentages of samples whose ratio-test values exceed the given ratio-test critical values (1.5, 2, and 3) and the percentages of samples whose ASR values exceed the given thresholds (0.90, 0.95 and 0.99) in the two cases. These percentages given under different t thresholds (rows 2, 3 and

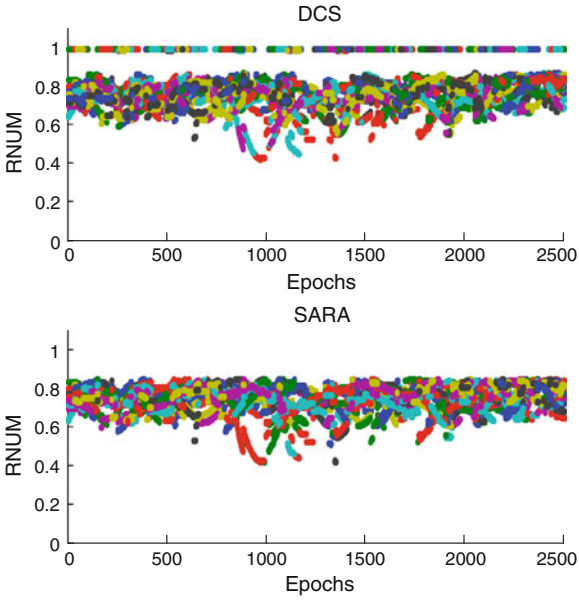

Fig. 1.10 Redundancy numbers computed with all visible satellites and SARA

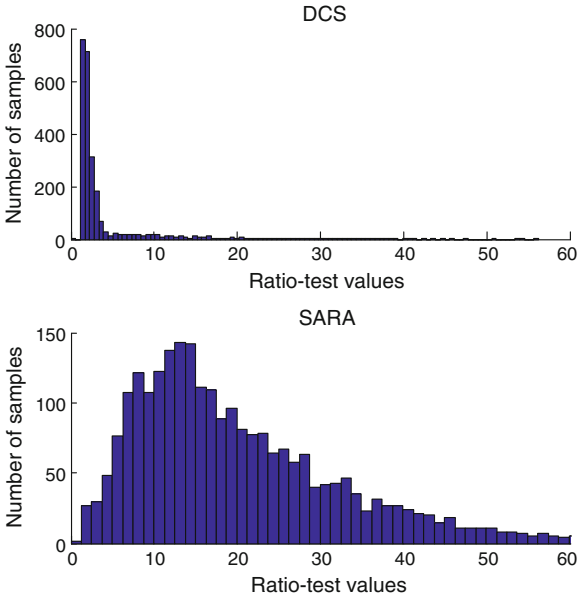

Fig. 1.11 Ratio-test values computed with all visible satellites and SARA

4) and ASR thresholds (columns 5, 6 and 7) actually indicate, to large extend, the acceptance rates of correct integer solutions and the reliability of AR. From the above figures and Table 1.2, it can be concluded that SARA process gives much higher ASR percentages than these obtained from all the visible. As a specific

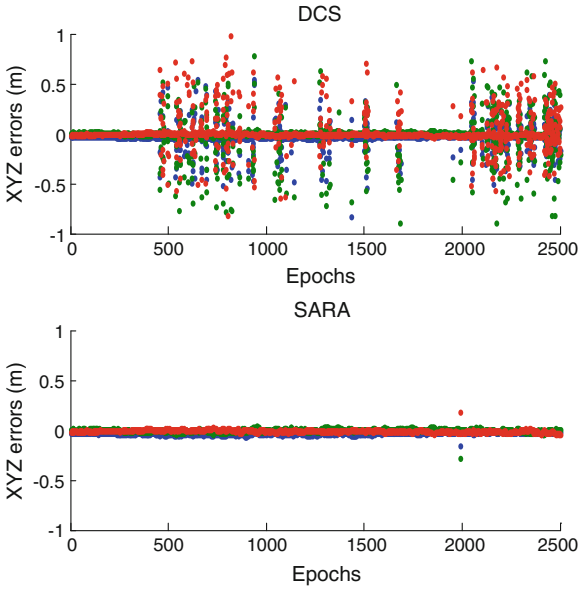

Fig. 1.12 *XYZ* positioning errors computed with all visible satellites and SARA, t > 1.5

Table 1.2 The percentages of samples number for ratio-test and ASR with given critical values

	DCS (%)	SARA (%)
t > 1.5	82.9	99.9
t > 2	50.5	99.6
t > 3	25.0	98.5
ASR > 0.9	18.9	99.9
ASR > 0.95	18.1	98.0
SR > 0.99	18.1	98.0

example shown in Table 1.2, only 82.9, 50.5 and 25.0 % of samples passed the ratio tests using all the satellites in view when the critical value is 1.5, 2 and 3, respectively. These percentage turn out to be 100, 99.7 and 98.6 % if the SARA procedure is applied. In terms of ASR values, it is clearly demonstrated that the SARA process increases those samples with ASR values larger than 0.99 from 18.1 to 98.0 %. This result may vary when different data sets or periods are used, but the distinctive difference indeed shows the significant advantages of the SARA method with respect to the scheme of without adopting satellite selection strategy. Considering the fact that the real PCF in the two cases are 100 %, those events that fail to pass the ratio-test happens to be the corresponding false alarm. Table 1.3 shows the false alarm rates in DCS are larger than those with SARA algorithm. It is easy to understand that when the ratio-test threshold value increases, the false alarm rate is also getting larger. The false alarm rate of DCS increase from 17.1 to 75 % with $t = 1.5$ and $t = 3$ respectively, while the case with SARA algorithm still limits the false alarm rate as 1.5 % even $t = 3$.

Table 1.3 The percentages of samples number for ratio-test and ASR with given critical values

False alarm rate	DCS (%)	SARA (%)
t > 1.5	17.1	0.1
t > 2	49.5	0.4
t > 3	75.0	1.5

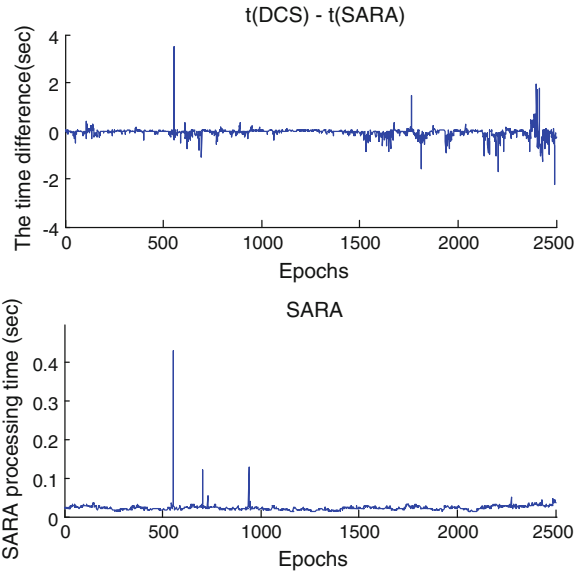

Fig. 1.13 Time cost computed with all visible satellites and SARA

In addition to the performance of reliability and accuracy, computation time is also an important factor in real-time applications. Figure 1.13 shows the time cost difference between the two cases as well as the SARA implementation time consuming. It is seen that there is no major difference between these two cases. SARA is expected to spend less time because the dimensions of ambiguities are reduced. However, since the AR reliability is improved by SARA, which also potentially expands larger ambiguity search space. That's why we have larger ratio-test values. This disadvantage can be overcome by changing the prior search space size with fixed ratio-test value [27]. The computational speed is still a challenging problem for AR with high dimensions [28], but this disadvantage is not caused by SARA itself.

1.5 Conclusions and Future Work

Benefits from multi-GNSS and multi-frequency signals could be significant, but do not come without cost. Simply using measurements from all satellites in view does not necessarily lead to higher quality solutions, because various biases in different

systems. For real time kinematic positioning users, the major benefits of multi-GNSS and multi-frequency signals may be the option for the selective use of satellite systems, or signals, or subsets of visible satellites from different systems to assure the required reliability and accuracy of the RTK solutions.

The paper has developed a new satellite selection algorithm for reliable ambiguity resolution, namely SARA, which can select a subset of visible satellites from a single or multiple constellations based on reliability criteria while giving low PDOP values as well. The purpose is to achieve high ambiguity resolution success rate and reliable position solutions. The principle behind SARA strategy is to remove those satellites with extreme large redundancy number or MDB, or with extremely small external global reliability parameters. Experimental analysis has demonstrated that SARA process gives much higher acceptance rate of correct integer solutions and much higher ASR percentages than these obtained from all the visible satellites in both single and dual constellation cases.

Though the SARA algorithm can select satellite to achieve much higher ASR in a dual-constellation system, there are still some epochs where ASR values are not high enough to assure AR reliability. A possible future research effort may combine the SARA with the partial ambiguity resolution (PAR) algorithm to further improve AR reliability. Ultimately, the proposed algorithms and theory have to pass verification using a large number of real time multi-GNSS data sets, which however are not available yet.

References

1. Hofmann-Wellenhof B, Lichtenegger H, Wasle E (2008) GNSS—global navigation satellite systems: GPS, GLONASS, Galileo, and more. Springer, New York
2. O'Keefe K, Ryan S, Lachapelle G (2002) Global availability and reliability assessment of the GPS and Galileo global navigation satellite systems. Can Aeronaut Space J 48:123–132
3. Yang Y, Li J, Xu J, Tang J (2011) Generalised DOPs with consideration of the influence function of signal-in-space errors. J Navig 64:S3–S18
4. Teunissen PJG, Odijk D (1997) Ambiguity dilution of precision: definition, properties and application. In: Proceedings of the 10th international technical meeting of the satellite division of the institute of navigation, Kansas City, MO, 16–19 Sep 1997, pp 891–899
5. Teunissen PJG (1998) Success probability of integer GPS ambiguity rounding and bootstrapping. J Geod 72(10):606–612
6. Teunissen PJG, Joosten P, Odijk D (1999) The reliability of GPS ambiguity resolution. GPS Solut 2(3):63–69
7. Verhagen S (2005b) On the reliability of integer ambiguity resolution. Navigation (Washington, DC) 52(2):99–110
8. Teunissen PJG, Joosten P, Tiberius C (1999) Geometry-free ambiguity success rates in case of partial fixing. In: Proceedings of the 1999 national technical meeting of the institute of navigation, San Diego, CA, 25–27 Jan 1999, pp 201–207
9. Cao W, O'Keefe K, Cannon M (2007) Partial ambiguity fixing within multiple frequencies and systems. In: Proceedings of ION GNSS07, the satellite division of the institute of navigation 20th international technical meeting, Fort Worth, TX, 2007 Sep 25–28, pp 312–323

10. Wang J, Feng Y (2012a) Reliability of partial ambiguity fixing with multiple GNSS constellations. J Geodesy (in press). doi 10.1007/s00190-012-0573-4
11. Kihara M, Okada T (1984) A satellite selection method and accuracy for the global positioning system. Navigation 31(1):8–20
12. Li J, Ndili A, Ward L, Buchman S (1999) GPS receiver satellite/antenna selection algorithm for the Stanford gravity probe B relativity mission. In: institute of navigation, national technical meeting 'Vision 2010: Present and Future', San Diego, CA, 1999 Jan 25–27, pp 541–550
13. Park C-W (2001) Precise relative navigation using augmented CDGPS. Ph.D. Dissertation, Stanford University, United States
14. Roongpiboonsopit D, Karimi HA (2009) A multi-constellations satellite selection algorithm for integrated global navigation satellite systems. J Intell Transp Sys Technol Plann Oper 13(3):127–141
15. Baarda W (1968) A testing procedure for use in geodetic networks. Delft, Kanaalweg 4, Rijkscommissie voor Geodesie
16. Cross P, Hawksbee D, Nicolai R (1994) Quality measures for differential GPS positioning. Hydrogr J 72:17–22
17. Verhagen S (2005a) The GNSS Integer Ambiguities: Estimation And Validation. Technische Universiteit Delft, The Netherlands
18. Verhagen S, Odijk D, Teunissen PJG, Huisman L (2010) Performance improvement with low-cost multi-GNSS receivers. In: Satellite navigation technologies and european workshop on GNSS signals and signal processing (NAVITEC), 5th ESA Workshop on, 8–10 Dec 2010, pp 1–8
19. Takac F, Walford J (2006) Leica system 1200: high performance GNSS technology for RTK applications. In: Proceedings of ION GNSS 2006, Fort Worth, Texas, 2006 Sep 26–29, pp. 217–225
20. Hassibi A, Boyd S (1998) Integer parameter estimation in linear models with applications to GPS. IEEE Trans Signal Process 46(11):2938–2952
21. Feng Y, Wang J (2011) Computed success rates of various carrier phase integer estimation solutions and their comparison with statistical success rates. J Geod 85(2):93–103. doi:10.1007/s00190-010-0418-y
22. Teunissen PJG (2003) An invariant upperbound for the GNSS bootstrapped ambiguity success rate. J GPS 2(1):13–17
23. Feng Y (2005) Future GNSS performance predictions using GPS with a virtual Galileo constellation. GPS World 16(3):46–52
24. Han S, Rizos C (1996) Integrated method for instantaneous ambiguity resolution using new generation GPS receivers. In: Position location and navigation symposium, IEEE 1996, 22–26 Apr 1996, pp 254–261
25. Wei M, Schwarz KP (1995) Fast ambiguity resolution using an integer nonlinear programming method. In: Proceedings of the 8th international technical meeting of the satellite division of the institute of navigation (ION GPS 1995), Palm Springs, CA, pp. 1101–1110
26. Leick A (2004) GPS satellite surveying, 3rd edn. Wiley, New York
27. Wang J, Feng Y (2012b) Orthogonality defect and reduced search-space size for solving integer least-squares problems. GPS Solutions (in press). doi:10.1007/s10291-012-0276-6
28. Chang XW, Yang X, Zhou T (2005) MLAMBDA: a modified LAMBDA method for integer least-squares estimation. J Geod 79(9):552–565

Chapter 2
Ocean Tidal Loading Effects to Displacements at GNSS Sites

Dejun Zhao, Xinqiang Xu, Jing Li, Jinmei Duan and Liang Yu

Abstract Ocean tidal loading (OTL) effects to displacements should be considered during GNSS precise positioning. Especially, along with the shift of geodesy from mainland to ocean, the OTL corrections to displacements play more and more important roles in precise positioning. The approaches to resolve OTL effects in precise GNSS data processing software GAMIT are that, either directly reading out the amplitudes and phases of several main tidal constituents (also called tidal coefficients) at site from file station.oct, or interpolating the site's tidal coefficients from global grid file grid.oct. It's not ideal to modify the OTL effects in China mainland (especially in coast areas, islands and reefs) using GAMIT directly, because of tidal coefficients' errors or the limitations of tracking stations' distribution. This paper detailed describes the OTL effects theories to displacements based on convolution integration approach about OTL and Green's functions. Numerical integration of OTL is performed using the Gauss quadrature method and the integration areas are separated to inner zone and outer zone. A newest $2' \times 2'$ resolutions local ocean tidal model of the East China Sea and South China Sea was adopted for inner zone, and a global model TPXO7.2 for the outer zone. Some OTL corrections to displacements at coast GNSS sites were computed, and which were applied to the GNSS data processing. The estimation of amplitudes and phases for the main tidal constituent M2 were acquired at some sites, variation functions changed with time for displacement were constructed. Numerical tests show that, the displacements at coast sites are bigger than those at inland sites, amplitudes of local loading on displacements reach the order of centimetre. If the amplitudes and phases of tidal constituents calculated by this method are appended into the station.oct file, the baselines' accuracies will be improved greatly for GAMIT software. Not only the OTL corrections but also suitable ocean tidal models and tide constituents should be taken into account in GNSS data analyses.

D. Zhao (✉) · X. Xu · J. Li · J. Duan · L. Yu
Xian Division of Surveying and Mapping, Xian, China
e-mail: xiaosanzhi@163.com

J. Sun et al. (eds.), *China Satellite Navigation Conference (CSNC) 2013 Proceedings*, Lecture Notes in Electrical Engineering 245,
DOI: 10.1007/978-3-642-37407-4_2,

Keywords GNSS · Ocean tidal loading · OTL · Ocean tide model · Green's functions

2.1 Introduction

Researches indicated that the ocean tidal loading effects to displacements can be up to several centimetre in magnitude, even to dm in some parts of our Earth and during some periods, especially in rapidly changing ocean [1–6]. With the developments of national surveying and mapping projects of islands and reefs, China's geodetic measurements are being extended from inlands to oceans, thus the OTL effects can't be ignored.

With the developments of satellites altimetry technologies, so many ocean tidal models were released one after another, such as CRS3.0, CRS4.0, AG95, GOT, NAO, FES2004, and TPXO7 et al. [4, 5]. The GAMIT software used for precise positioning corrects OTL displacements by means of using OTL grid file created by Swedish Onsala Space Observatory (OSO), which was based on global fundamental GNSS stations. OTL grid file created by National Astronomical Observatory of Japan (NAO) was also added to GAMIT for candidate from ver. 10.2 then on. Ocean tidal model FES2004 was selected to correct OTL displacements from GAMIT ver. 10.3 then on, which was released by French Tidal Group (FTG) and was established on the formula of tidal hydrokinetics and the technologies of data fusion. The approaches to resolve OTL effects in GAMIT are that, either directly reading out the amplitudes and phases of several main tidal constituents (also called tidal coefficients) at sites from file station.oct, or interpolating the site's tidal coefficients from grid file grid.oct. The file station.oct comprises lots of tidal coefficients at global 465 tracking stations (including GPS, SLR and VLBI). If the distance between the unknown site and a tracking station is less than 10 km, then the tidal coefficients for the tracking stations are used for this unknown site, otherwise by the mean of interpolating from grid.oct file. It's not ideal to modify the OTL effects in China mainland (especially in oceans) because of tidal coefficients' errors and the limitations of interpolations methods.

2.2 Theories and Computation of Loading Effects

OTL effects to displacements at GNSS sites are usually calculated by the convolution integrals of tidal heights and mass loading Green's functions [1, 7–9]:

$$L(\theta, \lambda, t) = \rho R^2 \iint H(\theta', \lambda', t) G(\psi, A) ds \tag{2.1}$$

where, θ and λ are colatitude and longitude for computing point, θ' and λ' are colatitude and longitude for loading point, ρ is the average density of sea water (1.03 g cm^{-3}), R is the average Earth radius, $L(\theta, \lambda, t)$ is the OTL effects, $H(\theta', \lambda', t)$ is the tidal height of loading point, A is the azimuth from computing point to loading point, ψ is the spherical distance between computing point and loading point, which can be calculated from below equation.

$$\cos\psi = \sin\theta\sin\theta' + \cos\theta\cos\theta'\cos(\lambda - \lambda')$$

$G(\theta, A)$ is mass loading Green's functions, which come from the Earth model parameters. $ds = \sin\theta' d\theta' d\lambda'$ stands for surface element. Instantaneous tidal height $H(\theta', \lambda', t)$ can be described as a sum of harmonic oscillations:

$$\begin{aligned} H(\theta', \lambda', t) &= \sum_{p=1}^{N} \zeta_p(\theta', \lambda') \cos\left(\varpi_p t + \chi_p - \delta_p\right) \\ &= \sum_{p=1}^{N} \left[H_{cp}(\theta', \lambda') \cos\left(\varpi_p t + \chi_p\right) + H_{sp}(\theta', \lambda') \sin\left(\varpi_p t + \chi_p\right)\right] \end{aligned} \tag{2.2}$$

where,

$$\begin{aligned} H_{cp}(\theta', \lambda') &= \zeta_p(\theta', \lambda') \cos\delta_p \\ H_{sp}(\theta', \lambda') &= \zeta_p(\theta', \lambda') \sin\delta_p \end{aligned}$$

ζ_p, δ_p, χ_p and ϖ_p is the amplitude, initial phase, astronomical argument and angular velocity of the pth tidal constituent at loading point, respectively. t is UT, N is the count of tidal constituent. Submit Eqs. (2.2) to (2.1):

$$\begin{aligned} L &= \sum_{p=1}^{N} \left[LC_p(\theta, \lambda) \cos\left(\varpi_p t + \chi_p\right) + LS_p(\theta, \lambda) \sin\left(\varpi_p t + \chi_p\right)\right] \\ &= \sum_{p=1}^{N} \left[L_p(\theta, \lambda) \cos\left(\varpi_p t + \chi_p - \beta_p\right)\right] \end{aligned} \tag{2.3}$$

where [10],

$$\begin{aligned} LC_p(\theta, \lambda) &= \rho R^2 \iint H_{cp}(\theta', \lambda') G(\psi, A) \sin\theta' d\theta' d\lambda \\ LS_p(\theta, \lambda) &= \rho R^2 \iint H_{sp}(\theta', \lambda') G(\psi, A) \sin\theta' d\theta' d\lambda' \end{aligned} \tag{2.4}$$

and that,

$$\begin{aligned} L_p(\theta, \lambda) &= \sqrt{LC_p^2 + LS_p^2} \\ \tan\beta_p &= LS_p / LC_p \end{aligned} \tag{2.5}$$

Thus, the key question to OTL effects lies in the integrations of Eq. (2.4), through which the amplitudes L_p and phases β_p who describe the loading response for the chosen site can be worked out. There exists four different open sources programs including CONMODB, GOTIC2, NLOADF and OLFG/OLMPP in the world at present, which can complete the convolution integrals of Eq. (2.4) successfully, and the difference between the four results from these programs is not more than 5 % [8]. Agnew [11] developed a method and its corresponding program for calculating loading tides named after NLOADF, which is based on the Green's functions by Farrell [7], and is capable of combining regional ocean tide model with a global ocean tide model, so that users can use more accurate coastal models to improve the loading tide results.

Now, only two unkown parameters including angular velocity ϖ_p and astronomical argument χ_p are left in Eq. (2.3). Conventionally, the tide is decomposed into a series of harmonics which frequencies lie in semidiurnal, diurnal and long-period three bands, including the semidiurnal waves M2, S2, N2, K2, the diurnal waves K1, O1, P1, Q1 and the long-period waves Mf, Mm and Ssa. More than 95 % of the tidal signal is characterized by these 11 tidal constituents, whose angular velocities are listed in Table 2.1 [10].

The argument χ_p is the linear combination of astronomical argument, which can be computed from below equation [10].

$$\begin{aligned}
\chi_{M2} &= 2h - 2s \\
\chi_{S2} &= 0 \\
\chi_{N2} &= 2h - 3s + q \\
\chi_{k2} &= 2h \\
\chi_{K1} &= h + 90^\circ \\
\chi_{O1} &= h - 2s - 90^\circ \\
\chi_{P1} &= -h - 90^\circ \\
\chi_{Q1} &= h - 3s + q - 90^\circ \\
\chi_{MF} &= 2s \\
\chi_{MM} &= s - q \\
\chi_{SSA} &= 2h
\end{aligned}$$

where, h, s and q respectively stands for mean longitude of sun, mean longitude of moon and mean longitude of lunar perigee at beginning of a day, which can be detailed deduced from reference [10].

Table 2.1 Angular velocities of main tidal constituents

Tidal constituent	Angular velocity (°/h)
M2	28.984
S2	30.000
N2	28.439
K2	30.082
K1	15.041
O1	13.942
P1	14.958
Q1	13.405
Mf	1.098
Mm	0.544
Ssa	0.082

2.3 Tests and Computing

2.3.1 Choice of Global and Local Tidal Models

In the numerical integration Eq. (2.4), the total OTL effects are the sum of inner zone and outer zone effects. The inner zone effect uses a refined grid of tidal heights and the outer zone uses a coarse grid. Ideally, tidal heights for the inner zone should be from a local tidal model and those for the outer zone should be from a global tidal model. In this paper, we chose osu.chinasea.2010 tidal model for inner zone which resolution was $2' \times 2'$ and comprised these 11 main constituents listed in Table 2.1, and TPXO7.2 tidal model for the outer zone which was the newest one at present and resolution reached $15' \times 15'$. M2 tidal constituent's amplitudes and phases in China East Sea and South Sea are shown in Fig. 2.1, where real lines stand for amplitudes (unit is centimetre) and broken line stand for phases (unit is degree).

2.3.2 OTL Effects to Displacements

The standard "Gutenberg-Bullen A" Earth mean model was adopted to determine the OTL displacements effects at some sites. These results are compared to those from WU et al. [12], which only simply adopted NAO99b global tidal model. The displacements' amplitudes and phases in three directions [stands for Westward, Southward and Upward, separately, which is positive direction according to Eq. (2.1)] due to M2 and S2 tidal constituents are listed in Table 2.2, where two typical IGS stations are selected, including SHAO which is adjacent to coast and URUM which is far from sea. From Table 2.2, we obtain that the amplitudes of OTL displacements in the areas of nearby sea is obviously bigger than these far

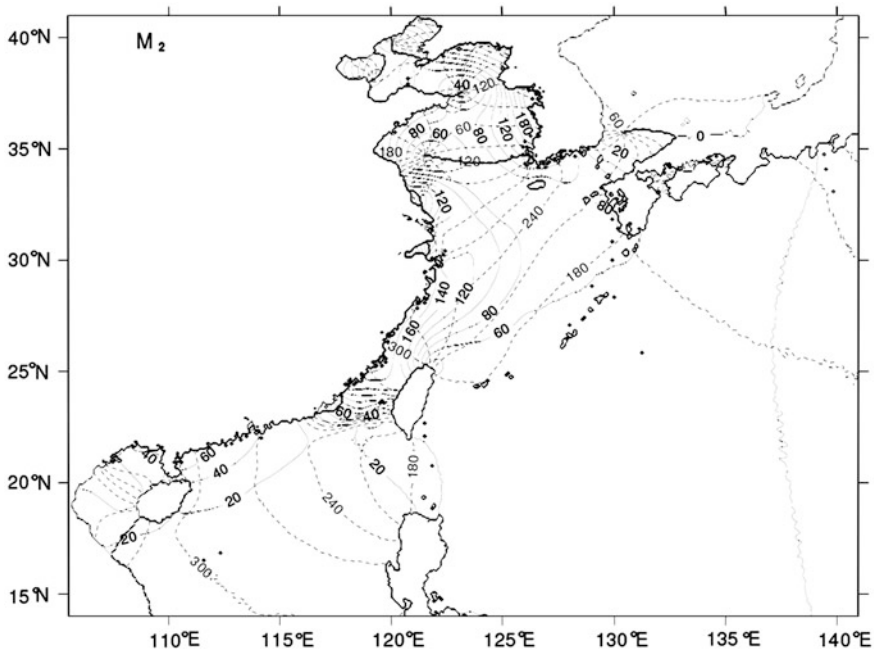

Fig. 2.1 M2 tidal constituents' amplitudes and phases in East China Sea and South China

away from sea. So, we must take into account the OTL effects when precision positioning projects are carried out nearby the coast.

The time series of total OTL corrections to displacements at SHAO station are shown in Fig. 2.2. The time is from August 1st to 31st in 2010. Figure 2.2 indicates that the effects in upward is obviously bigger than these in northward and eastward, which are up to 22 mm.

Table 2.2 The effects to station displacements of M2 and S2 tidal constituent

Station	Comp.	M2				S2			
		Ampl. (mm)		Phase (°)		Ampl. (mm)		Phase (°)	
		This	WU	This	WU	This	WU	This	WU
SHAO	W	2.81	2.60	−158.87	−160.20	0.88	0.86	−125.13	−114.5
	S	3.42	3.98	−25.20	−31.70	1.43	1.62	−4.23	−7.5
	U	8.56	8.16	−133.91	−146.40	2.86	2.99	−93.41	−95.0
URUM	W	0.68	0.70	−153.2	−156.5	0.23	0.26	−156.7	−161.9
	S	0.49	0.44	145.3	141.1	0.16	0.13	−136.2	132.5
	U	0.39	0.23	−2.7	−2.9	0.43	0.45	35.8	40.4

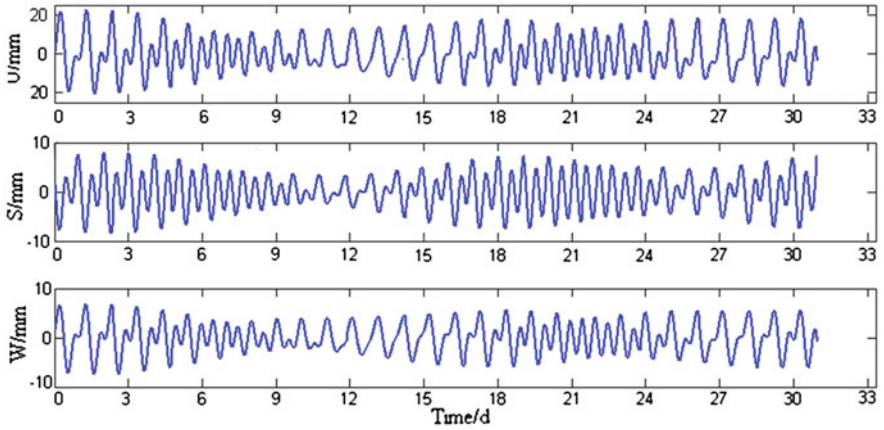

Fig. 2.2 Time series of total OTL effects to displacements at SHAO

2.3.3 Coordinates Computing

There was a grade B GNSS network, which consists of sites located in either near coast or islands and reefs, and the GNSS data from Crustal Movements Observation Network of China were used for known values. Following are two schemes:

Scheme 1 Directly adopt FES2004 global tidal modelstation.oct file and grid.oct file from GAMIT software to determine OTL corrections

Scheme 2 First determine the OTL displacements' amplitudes and phases of every site by numerical integral using East China Sea local tidal model for inner zone and TPXO7.2 global tidal model for outer zone. Then, append these amplitudes and phases to station.oct file in GAMIT software

A statistics about adjustment results from above two schemes were listed in Table 2.3. After corrections of scheme 2, accuracies of baselines are improved greatly, and both standard deviations of coordinates and overlaps with baselines are obviously decreased, and the overlaps with baselines in upward are bigger than those in horizontal directions, which disclaim that OTL corrections do bigger contribution to improving the accuracies in radial direction.

Table 2.3 A statistics about adjustment results to coordinates at GNSS sites

	Avg Std (cm)			Max Std (cm)			Baseline Accu. (mm + ppb)		
	N	E	U	N	E	U	N	E	U
Sch. 1	0.22	0.55	1.26	0.37	0.89	2.27	0.4 + 0.6	0.3 + 0.6	0.2 + 0.8
Sch. 2	0.18	0.41	0.83	0.31	0.73	1.82	0.3 + 0.5	0.3 + 0.5	0.2 + 0.5

2.4 Conclusions

The OTL displacements corrections are computed by means of Green's functions convolution integral. Some conclusions are drawed through theory analyses and numerical tests:

1. The OTL displacements effects are bigger near coast, even reach several centimeter in magnitude, however, it is up to only several mm in inland. So, in order to improve GNSS positioning accuracy, the OTL effects at sites near coastlines must be considered using various global ocean tidal models and numerical algorithms.
2. Employ higher accuracy and higher resolution ocean tidal model to determine the displacements' amplitude and phase at sites, which will be applied to OTL corrections computing. For GAMIT users, what needed to do is only appending the amplitudes and phases into stations.oct file.
3. Even if the newest ocean tidal model also can't describe the tidal movement characters in our nearby seas, because the continental shelf and geologic structures are very complicated. So, it's better to employ the observed tidal data from gauge during the course of accuracy positioning.

Acknowledgments This research is supported by National Natural Science Foundation of China (Grant no: 41104047). Professor Agnew is very much thanked for making the program NLOADF freely available to the public.

References

1. Penna NT, Bos MS, Baker TF (2008) Assessing the accuracy of predicted ocean tide loading displacement values. J Geod 82:893–907. doi:10.1007/s00190-008-0220-2
2. Shfaqat AK, Hans GS (2003) The M2 ocean tide loading wave in Alaska: vertical and horizontal displacements, modelled and observed. J Geod 77:117–127. doi:10.1007/s00190-003-0312-y
3. Stavros A, Melachroinos R, Biancale M et al (2008) Ocean tide loading (OTL) displacements from global and local grids: comparisons to GPS estimates over the shelf of Brittany, France. J Geod 82:357–371. doi:10.1007/s00190-007-0185-6
4. Fu Y, Freymueller JT (2012) The effect of using inconsistent ocean tidal loading models on GPS coordinates solutions. J Geod 86:409–421. doi:10.1007/s00190-011-0528-1
5. Yuan LG, Ding XL, Zhong P et al (2009) Estimates of ocean tide loading displacements and its impact on position time series in Hong Kong using a dense continuous GPS network. J Geod 83:999–1015. doi:10.1007/s00190-009-0319-0
6. Thomas DI, King MA, Clarke PJ (2006) A comparison of GPS, VLBI and model estimates of ocean tide loading displacements. J Geod 81:359–368. doi:10.1007/s00190-006-0118-9
7. Farrell WE (1972) Deformation of earth by surface loads. Rev Geophys Space Phys 10(3):761–797
8. Bos MS, Baker TF (2005) An estimate of the errors in gravity ocean tide loading computations. J Geod 79:50–63. doi:10.1007/s00190-005-0442-5

9. Zahran KH, Jentzsch G, Seeber G (2005) World-wide synthetic tide parameters for gravity and vertical and horizontal displacements. J Geod 79:293–299. doi:10.1007/s00190-005-0460-3
10. Institute of Geodesy and Geophysics, Chinese Academy of Sciences (IGG) (1988) Earth tide proceedings. Survey and Mapping Press, Beijing
11. Agnew DC (1997) NLOADF: a program for computing ocean tide loading. J Geophys Res 102(B3):5109–5110
12. WU J, WANG J, GU G (2003) Ocean tidal displacement corrections in GPS precision positioning. Geomatics Inform Sci Wuhan Univ 28:405–408

Chapter 3
A Study on the Beidou IGSO/MEO Satellite Orbit Determination and Prediction of the Different Yaw Control Mode

Wei Wang, Gucang Chen, Shuren Guo, Xiaoyong Song and Qile Zhao

Abstract During the conversion between yaw steering and orbit normal mode of the Beidou IGSO and MEO satellite, the dynamic model changes. As a result, the accuracy of the orbit determination and prediction decrease. As the yaw control mode changes, the variation of the dynamic model has been studied. Based on the empirical and analytical solar radiation pressure models, one piecewise model and one linear model have been proposed. The two models were tested with the actual Beidou satellites' on-orbit data. The results showed that the two models which are raised in this paper can improve the accuracy of the Beidou IGSO/MEO orbit determination and prediction.

Keywords Yaw steering · Orbit normal · Precise orbit determination · Parameter variation · Solar radiation pressure

3.1 Introduction

To complete the specific applications, the satellites must maintain corresponding orbits and attitudes. Compared with other kinds of satellites, GNSS IGSO and MEO satellites adopt the inclination circular orbits with the 55°, who need a

W. Wang (✉) · S. Guo
Beijing Institute of Tracking and Telecommunication Technology, Beijing 100094, China
e-mail: wwishere@163.com

G. Chen
China Satellite navigation Office, Beijing 100034, China

X. Song
Xi'an Research Institiute of Surveying and Mapping, Xi'an 710054, China

Q. Zhao
Wuhan University, Wuhan 430079, China

J. Sun et al. (eds.), *China Satellite Navigation Conference (CSNC) 2013 Proceedings*, Lecture Notes in Electrical Engineering 245,
DOI: 10.1007/978-3-642-37407-4_3,

specific attitude control method of the yaw angle to keep the angle between the Sun and the satellite's body XOZ surface small, so that the solar panels can orient to the sun in order to get enough energy.

A MEO GNSS satellite such as a GPS satellite, applies a yaw steering attitude control mode. The satellite's z-axis (yaw) points towards the center of the Earth, and the y-axis points towards the solar panels, perpendicular to the Sun. In this way the solar panels' is controlled to keep itself facing the Sun. However, when the Sun's Elevation angle of the satellite orbital plane is small and the satellite moves toward the collinear approximation to the Sun and the Earth, the satellite's yaw manoeuvring rate will greatly increase. Due to the limit of the control capacity constraints, the attitude control law changes. This leads to the error incensement of the orbit determination and prediction. In the 1990s, for the GPS BLOCK II A satellite, foreign scholars [1–3] proposed a variety of improved models to increase the orbit determination accuracy. But the problem that the accuracy of the orbit determination and prediction of BLOCK II A satellites decline when they just go out of the earth shadow so far is not well solved. The GPS BLOCK II R satellite then is improved on the satellite attitude control scheme.

The control method of the Beidou IGSO/MEO satellites is quite different from the GPS satellites. When the sun elevation angle of the orbit plane is large, it also uses the yaw steering method. When the sun elevation angle is small enough, it uses the orbit normal method, in which the yaw angle is always kept to zero. Taking into account that the GNSS satellites' orbit and attitude are highly coupled, the dynamic model of the solar pressure model makes a significant change when the attitude control mode change occurred, which makes a greater impact on orbit determination and orbit prediction. So it is needed to establish the appropriate precision orbit determination methods. This paper studies the attitude mode control law of the GPS/GLONASS navigation satellite, especially the Beidou navigation satellites when they are in the earth's shadow, and analyses the dynamic characteristics when the Beidou satellite attitude control mode changes, as well as the reasons of the decrease of the orbit determination and prediction accuracy. Then the variable parameter methods for both empirical model and analytical model of the solar radiation pressure are established. And further discussions of the thermal radiation effects modifications and the phase center of antenna corrections are approached. The actual measured data shows that the proposed model effectively improves the precision of orbit determination and orbit prediction of the Beidou navigation satellite when yaw control mode changes.

3.2 The Attitude Control Method of the Beidou Satellites

The attitude of a Navigation satellite should satisfied two requirements: First, it should keep the +Z axis which installed navigation antenna towards to the earth; secondly, it should control the yaw angle making solar panels facing the sun,

which eventually makes solar panels receive enough sunlight and get enough energy. The IGSO/MEO satellites have the inclination of 55°. When the sun elevation angle is large, to get enough energy, the satellite's yaw angle is controlled to be a non-zero value, which is called the Yaw Steering Mode.

In the Yaw Steering Mode, the yaw angle is in accordance with the following formula:

$$\psi_n = ATAN2(-\tan\beta, \sin\mu) \tag{3.1}$$

In this formula, β is the Sun's elevation angle of satellite orbit plane, and μ is geometry angle between the satellite and the midnight of the orbit, as shown in Fig. 3.1.

The nominal yaw rate can be easily obtained:

$$\dot{\psi}_n = \dot{\mu}\tan\beta\cos\mu/(\sin^2\mu + \tan^2\beta) \tag{3.2}$$

As can be seen by Formula (3.2), the rate of yaw angle get the maximum when $\mu = 0°$ or 180°. And its value is:

$$\dot{\psi}_n = \dot{\mu}/\tan\beta \tag{3.3}$$

The Beidou satellite uses the momentum wheel to control the attitude, rather than using the jet propelling in case of changing the satellite's orbit. Given the momentum wheel adjustment rate limit R, the critical value of the Sun's elevation angle of the satellite's orbital planes at noon and midnight can obtained:

$$\beta_0 = \tan^{-1}(\dot{\mu}/R) \tag{3.4}$$

The Sun rotation speed to the orbit plane is about 1 degree per day. The sun's elevation angle of the orbital plane is gradually changed. When the Sun elevation angle β is greater than β_0, the Yaw steering mode proceed. When the sun elevation angle β is smaller than β_0, the Yaw steering mode cannot proceed around $\mu = 0°$ or 180°. So the dynamic model is changed.

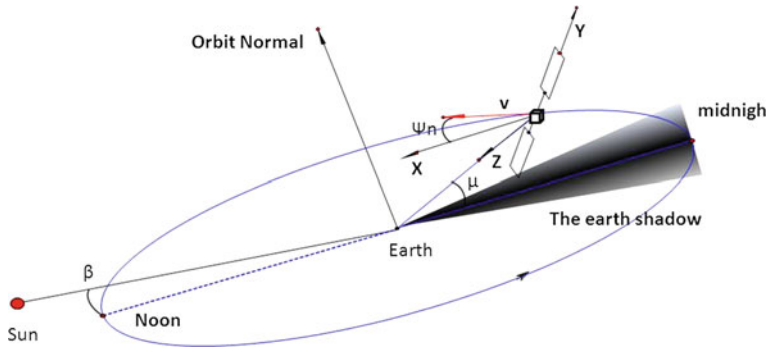

Fig. 3.1 Yaw control diagram

Table 3.1 Various navigation satellite yaw control mode

	GPS II/IIA	GPSIIR	GLONASS-M
Max yaw rate°/s	0.10–0.13	0.2	0.25
Noon maneuver	$\|ß\| < 3.6/4.9°$, using max yaw rate	$\|ß\| < 2.4°$,using max yaw rate	$\|ß\| < 2°$,using max yaw rate
Shadow crossing	Using max yaw rate, all time in the shadow	Using mean yaw rate, stops when the satellite moves out of the shadow	Using max yaw rate, stops at the theoretical control amount
Post-shadow maneuver	Yes	No	No

For GPS BLOCK IIA satellite, the yaw attitude of a GPS satellite can be divided into four regimes: nominal attitude, shadow crossing, post-shadow maneuver and noon maneuver. In the post-shadow maneuver regime, the satellite's yaw angle and solar panel's corner cannot be well calculated. So the orbit precise prediction is affected. Some better orbit determination and prediction model such as GYM95 is used to get better results [2, 3].

For GPS BLOCK IIR, IIF, and GLONASS-M satellites attitude control strategy take some adjustment [4–6] based on BLOCK IIA. In the earth's shadow midnight maneuver, Calculation of the theoretical control amount is calculated. The satellite uses the average speed or the maximum speed to get the theoretical amount. So the post-shadow maneuver is avoided.

A yaw control mode of the various types of navigation satellites are shown in the following table (Table 3.1):

Unlike GPS and GLONASS, the Beidou IGSO/MEO Navigation Satellite use the Orbit Normal Mode when β is smaller than β_0, in which the satellite's Z-axis always points to the ground, and the X-axis always points to the direction of the velocity. So the yaw angle is:

$$\psi_n = 0 \tag{3.5}$$

The advantage of using the orbit normal mode is that the rapid mobility of the yaw angle is avoid. And the Sun's elevation angle is small; the solar panel can get enough energy.

However, for the Beidou IGSO/MEO high-orbiting satellites, geometric observations is weak, and the dynamic model of the accuracy can be better than 1.0E-8 m/s^2 acceleration, which is significantly better than the geometric observation accuracy. So GNSS precision orbit determination is usually using long arcs (3 days or more) to achieve precise orbit of the dynamic model. In this way once the dynamic model of the satellite is changed, orbit accuracy would be significantly reduced, even 1.0E-9 in magnitude, can also produce the meter-amount error.

The Beidou Navigation Satellite's dynamic model has a change which must be adaptive to establish the corresponding orbit determination strategy. The corresponding orbit determination strategy must be established to cope with the dynamic model change of the Beidou Navigation Satellite's. Otherwise, the accuracy will be greatly decreased.

3.3 Dynamic Modeling of the Yaw-Steering and Orbit-Normal Mode

For the Beidou the IGSO/MEO Satellite, the most important perturbation forces are the J2 Perturbation, the solar radiation and the Sun/moon gravitational perturbation. The main factor of the change of the dynamic model is the change of the solar radiation model. At the same time, the changes of the thermal radiation model and the changes of the satellite antenna phase center correction should be considered.

3.3.1 Dynamic Analysis

In the Yaw Steering model, the Satellite body's X panels and solar panel are always perpendicular to the Sun. In one orbit period, the composition of the tangent component of the solar radiation force is zero, while the radial component and the normal force component is not, which causes five classical orbital elements long periodic perturbation except the semi-major axis.

In the orbit normal mode, as shown in Fig. 3.1, the solar radiation pressure is totally different. In one orbital period, the satellite body's +X,−X, +Z, −Z panels face the sun in turns. And the solar panel is not perpendicular to the sun but has a β bevel. Because the satellite body panels' property cannot be exactly the same, in one orbit period the composition of the tangent component of the solar radiation force is not zero so the semi-major axis changes.

Because the Sun's elevation angle β is varying all the time, the pressure of the solar radiation is varying, too.

As can be seen from Table 3.2, the Beidou IGSO/MEO satellite solar radiation pressure dynamic model in the yaw steering mode, compared with the orbit normal mode, has two variations. The First is that the body's shined area is changed with the orbit period and the second is that the solar panel shined area is changed with the Sun's elevation angle. Ultimate solar radiation pressure change is the superposition of these two changes.

Table 3.2 The differences between the yaw steering and the orbit normal mode

Mode	Yaw	Satellite body	Satellite solar panel
Yaw steering	Varing all the time	The area of surface stay nearly constantly Body's +X panel is vertically shined +Z, −Z panel are inclined shined in turn −X, +Y, −Y panel are s nearly not shined	Vertically shined
Orbit normal	Keeping to be zero	The area of surface stay changes all the time +X, +Z, −X, −Z panel are shined in turn +Y, −Y are shined half in a period	Not vertically shined, with β bevel

3.3.2 Solar Radiation Pressure Model Establishment

According to the solar radiation pressure variation, it is possible to establish the analytical model and empirical model of the solar radiation pressure model which are adapted for the Beidou IGSO/MEO satellite.

Analytical solar radiation pressure model, based on the satellite stellar structure, optical properties and satellite attitude to model the pressure of sunlight on the satellite as exactly as possible, has a clear physical meaning. GPS BLOCK I and the BLOCK II satellite manufacturers Rockwell International and released ROCK 4 (S10) and ROCK 42 (S20) solar radiation pressure model. In this model satellite astral plane and cylinder combination to simulate, but the model does not consider the satellite stars and the heat radiation of the panel, so Fliegel made ROCK model T10 and T20 model, subsequently for Block IIR satellite T30 model. T20 solar radiation pressure model is as follows:

$$\vec{F} = S\begin{bmatrix} F_x \\ 0 \\ F_z \end{bmatrix} + \begin{bmatrix} 0 \\ y_{bias} \\ 0 \end{bmatrix} + \begin{bmatrix} \mathrm{CORcos}\mu + SIR\sin\mu \\ \mathrm{COTcos}\mu + \mathrm{SIT}\sin\mu \\ \mathrm{CONcos}\mu + \mathrm{SIN}\sin\mu \end{bmatrix}$$

$$F_x = -8.96\sin\alpha + 0.16\sin 3\alpha - 0.10\sin 5\alpha - 0.07\sin 7\alpha$$

$$F_z = -8.43\cos\alpha \tag{3.6}$$

In the equation, F_x is the component force on the X axis, F_z is the component force on the Z axis, α is the angle between the sun and the Z-axis positive direction, S is the factor of scale.

The scale of factor S reflects the satellite surface-mass ratio changes. Solar Wings is little changed in yaw steering mode, the scale factor can be considered constant.

Considering in the orbit normal mode, the solar radiation pressure changes over a period, the scale of factor S will change by time. We treat it as a linear variable. Let S_1, the S_2, …, S_{n+1} be a linear factor in period T_1, T_2, …,T_{n+1}. The linear factor S can be expressed as:

$$\mathrm{S}_i = \phi[S_1, S_2, \ldots S_{n+1}] \tag{3.7}$$

Therefore, simply solving S_1, the S_2, …, S_{n+1}, the j-th linear factor S of can be obtained:

$$\mathrm{S}(t) = S_j + \frac{S_{j+1} - S_k}{t_{k+1} - t_k}(t - t_j) \tag{3.8}$$

The empirical model, without understanding the satellite stellar structure and optical properties, is based on long-term and large number of in-orbit data fitting. But the model has no actual physical meaning and is not suitable for the new navigation satellite. The CODE model in DYB framework can effectively reaction pressure of solar radiation. Springer developed the ECOM solar radiation pressure

model, the model is establish in DYB coordinates, and widely used in GPS Precise Orbit determination. Using The ECOM model, the respective parameters are treated as changing parameters and calculated in several hours periodically.

3.3.3 Changes in the Thermal Radiation Model

For navigation satellites, the thermal radiation force is expressed as:

$$F_i = \frac{2\sigma \cdot \varepsilon_i(T_i) \cdot A_i \cdot T_i^4}{3c} \tag{3.9}$$

In this Formula, c is the speed of light; σ is Boltzman's constant; $\varepsilon_i(T_i)$ is the radiation rate; A is the area of surface; T is the temperature.

When a satellite is in a conversion from the yaw steering to the orbit normal mode, the satellite's area of surface is changed from the +X panel individually exposed to the +Z, +X, −Z, −X four panels exposed in turn. Meantime, the +Y, −Y two panels are exposed in orbit normal mode to contribute to a radiation pressure for the cross-plane direction. Therefore, the thermal radiation model should be considered.

3.3.4 Correction of Antenna Phase Center

In general, there is a small deviation from the satellite center of mass to the antenna phase center. And this deviation changes with the change of satellite elevation angle and azimuth, which should be considered when the attitude control mode is changed from the yaw steering to the orbit normal mode.

Suppose [x, y, z] is the position of the satellite in the J2000.0 coordinates frame, and $[x_b, y_b, z_b]$ is the position of the center of phase in the satellite body coordinates. Then the position of the satellite antenna phase center $[x_s, y_s, z_s]$ after corrections is as follows:

$$[x_s, y_s, z_s]^T = [x, y, z]^T - R_{io} R_Z(\psi)[x_b, y_b, z_b]^T \tag{3.10}$$

R_{io} is the transformation matrix from the orbit coordinate frame to the inertial frame. $R_Z(\psi)$ is the transformation matrix from the body coordinate frame to the orbit frame.

3.4 Results

For a Beidou IGSO satellite, it is considered that a 12 order Earth's gravitational field model, the sun and the moon gravity, tide, pole tide perturbation. A constant variable solar radiation pressure model is used. Solar radiation pressure mode use

combined empirical model compensation method with a priori model. The empirical model is the T20 model, estimated force parameters including solar radiation pressure scale factor, Y deviation parameters as well as the orbital period of the empirical force parameters. In the orbit determination and prediction, we used the data of five stations in Xi'an, Changchun, Kunming, Kashgar, Urumqi. And we get a result as follows (Fig. 3.2).

As can be seen, the orbit determination error at the radial overlap dropped to 7.5 m, at the positions overlap dropped down to 10 m. The main error is in the tangential direction. It shows that the X-direction component of solar radiation pressure model is not accurate.

Using the piecewise linear solar radiation pressure model parameters, the orbital overlap arc accuracy greatly improved, as shown in the Fig. 3.3.

The solutions of the scale of factor *S*before and after the transverse of the yaw steering and the orbit normal mode are different, as shown below. It proof that the transverse of the yaw steering and the orbit normal mode did lead to a change of the solar radiation pressure perturbation (Table 3.3).

Using the Segmentation ECOM solar radiation pressure model, with the same arc IGSO satellite data, we get results as follows (Fig. 3.4).

Therefore, using of piecewise linear light pressure solution algorithm and the Segmentation ECOM solar radiation pressure model strategy, we can solve the precise orbit determination and prediction problem of the attitude control mode conversion from the yaw steering to orbit normal.

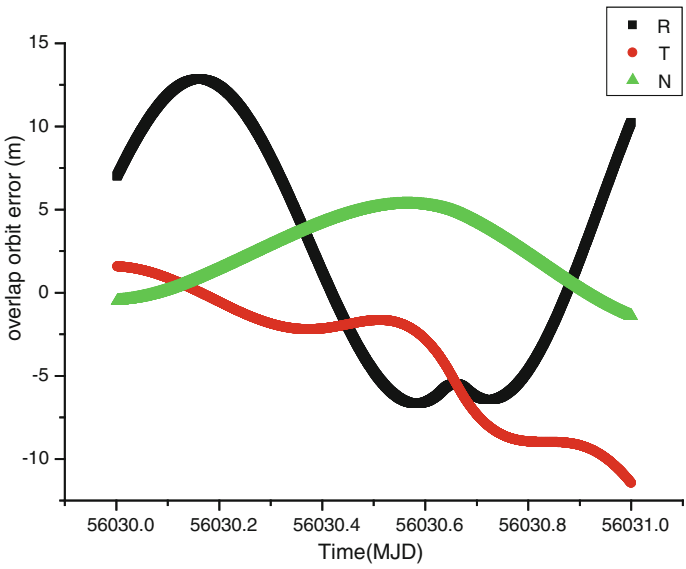

Fig. 3.2 Results of the normal T20 model

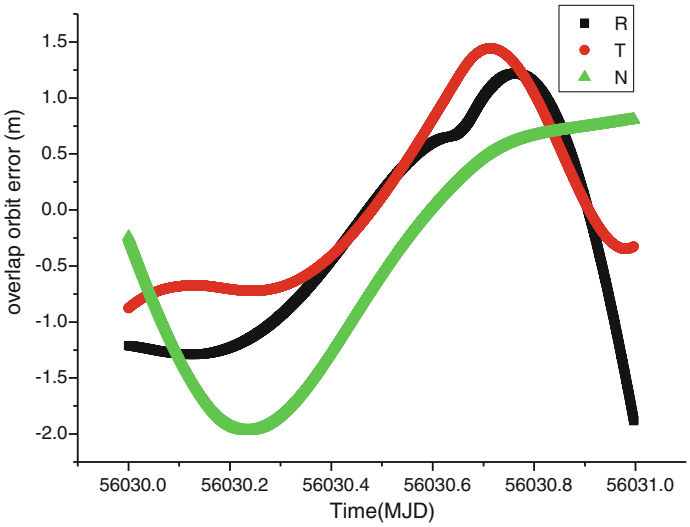

Fig. 3.3 Results of the piecewise linear parameters T20 model

Table 3.3 scale of factor *S* in yaws-steering and orbit normal mode

Scale of factor *S*	Yaw steering	Middle	Orbit normal
X component	2.550	3.073	2.618
Y-Bias	−0.108E-07	0.256E-08	−0.313E-07
Z component	2.944	2.288	1.885

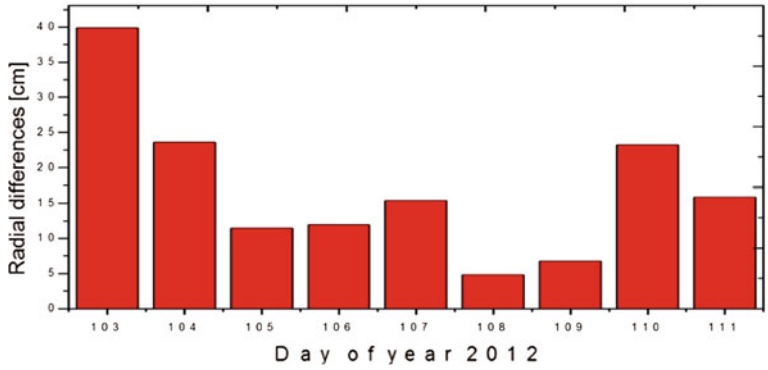

Fig. 3.4 Results of segmentation ECOM solar radiation pressure model

Since these two methods introduced more fitting parameters, they need enough measurement data for fitting parameters. They can get a considerable orbit determination and prediction accuracy within a few hours. The long time forecast accuracy is not convergence.

3.5 Conclusions

The Beidou MEO/IGSO satellite makes a change from the yaw steering mode to the orbit normal mode. The dynamic model is divided into two separate processes. During the conversion, if we do not distinguish them, the orbit determination precision will be significantly reduced.

The parameters of the solar radiation pressure model are linear and periodical changing in the orbit normal mode. To use of linear parameter solar radiation pressure algorithm, orbit determination is not significantly reduced when the attitude control mode is changed.

However, due to the change of the linear parameters of the solar radiation pressure are very not easy to fit, the orbit determination and predication accuracy is declined slightly. Therefore, the methods to build a property model have yet to be studied further.

References

1. Zhang BC, Ou JK, Yuan YB et al (2010) Yaw attitude of eclipsing GPS satellites and its impact on solutions from precise point positioning. Chin Sci Bull 55(32):3687–3693
2. Bar-Sever YE (1996) A new model for GPS yaw-attitude. J Geodesy 70:714–723
3. Kouba J (2009) A simplified yaw-attitude model for eclipsing GPS satellites. GPS Solution 13:1–12
4. Dilssner F, Springer T, Gienger G, Dow J (2010) The GLONASS-M satellite yaw-attitude model. Adv Space Res 47:160–171. doi:10.1016/j.asr.2010.09.007
5. Dow JM, Neilan RE, Gendt G (2005) The international GPS service (IGS): celebrating the 10th anniversary and looking to the next decade. Adv Space Res 36:320–326
6. Dilssner F, Springer T, Gienger G (2011) Dancing in the dark: how GNSS satellites cross the earth's shadow. Eur Space Oper Centre Rep
7. Kogure S The orbit and clock estimation result of GPS, GLONASS and QZSS by MADOCA. 4th Asia Oceania regional workshop on GNSS

Chapter 4
Precise Orbit Determination for COMPASS IGSO Satellites During Yaw Maneuvers

Jing Guo, Qile Zhao, Tao Geng, Xing Su and Jingnan Liu

Abstract Contrary to GPS and GLONASS, the COMPASS IGSO satellites use two different attitude modes depending on the Sun's elevation angle with respect to the orbital plane, namely yaw-steering regime and yaw-fixed regime. However, transition of attitude modes will cause the significant degradation of the orbit accuracy. We present two approaches to improve the orbit accuracy based on Extended CODE Orbit Model (ECOM) and Adjustable box-wing model. The differences of overlapping orbits and SLR validation indicate that the orbit accuracy could increase to better than 30 cm from several meters level during yaw maneuvers. Furthermore, we investigate the possible reasons of orbit accuracy degradation with telemetry data, and the reasons are likely the variations of non-gravitational forces in along- and cross-track directions caused by attitude mode switches, temperature variations of −X bus and some devices on −X surface which result in non-systematic geometry of −X and +X bus.

Keywords COMPASS/BeiDou-2 · IGSO · Yaw attitude · Precise orbit determination

4.1 Introduction

The proper model of the satellites' yaw attitude is extremely essential for high-precision Global Navigation Satellite System (GNSS) positioning and its other geodetic applications. Generally, the nominal attitude of the GNSS satellites is constrained by two conditions at the same time. First, the navigation antenna needs to be pointed toward the earth and second, solar panels have to be orientated

J. Guo (✉) · Q. Zhao · T. Geng · X. Su · J. Liu
GNSS Research Center, Wuhan University, Luoyu Road No. 129, Wuhan 430079, China
e-mail: jingguo@whu.edu.cn

J. Sun et al. (eds.), *China Satellite Navigation Conference (CSNC) 2013 Proceedings*, Lecture Notes in Electrical Engineering 245,
DOI: 10.1007/978-3-642-37407-4_4,

perpendicular to the satellite-Sun direction. These requirements necessitate that the satellites constantly rotate (yaw) along the antenna axis, which points toward the Earth and is defined as the Z-axis of body-fixed frame (BF). The Y-axis of BF is the rotation axis of solar panel and perpendicular to the satellite-Sun direction usually, and the X-axis points either towards the Sun for GPS BLOCK II/IIA, IIF and GLONASS-M or away from it for GPS BLOCK IIR satellites, and it completes the right-handed coordinate system [1–4].

However, the GNSS satellites could not maintain the normal yaw attitude when they cross the Earth shadow and the satellite-Sun as well as satellite-Earth vectors are nearly collinear. Hence, the GNSS satellites experience shadow-crossing maneuvers and noon-turn as well as midnight-turn maneuvers. The shadow-crossing maneuvers are caused by that the Sun sensors of the attitude control system cannot follow the Sun during the eclipsing period. The noon-turn and midnight-turn maneuvers are caused by limitation of the maximum hardware yaw rates. Knowing the satellite attitude is quite important for three reasons, firstly for the precise orbit determination (POD) in order to model the non-gravitational forces, such as solar radiation pressure (SRP), thermal re-radiation (TRR) and earth radiation. Secondly, to correct the so called 'phase wind-up'. Thirdly, to correct the navigation antenna phase center offset. Currently, several dedicated attitude models for different GNSS satellites provide the yaw angle during the maneuvers. Hence, the last two attitude-related errors could be eliminated correctly or reduced significantly with attitude models. But the orbital one still have non-ignorable influence on orbit and clock solutions.

According to analysis descriptions (see ftp://igs.org/igscb/center/analysis/), several International GNSS Service (IGS) Analysis Centers (ACs) ignore yaw attitude maneuvers, whilst Jet Propulsion Laboratory(JPL), Geoforschungszentrum, Germany (GFZ), Natural Resources Canada (EMR), Scripps Orbit and Permanent Array Center (SIO), and GRG (GRGS-CNES/CLS) ACs include the yaw models in their processing strategies. Furthermore, only JPL, GFZ, and EMR estimate the satellite-dependent yaw rates among all ACs. In order to absorb unmodelled force errors, especially for eclipsing satellite, constrained noon velocity breaks are introduced by several ACs (e.g., CODE, GFZ, and SIO). Although the 'long-arc' approach used by IGS to assess the orbit accuracy is often overly pessimistic [5], it could clearly show the degradation of orbit accuracy during Sun and Luna eclipse seasons. Similar as GPS and GLONASS, COMPASS IGSO satellites also experience yaw maneuvers, but the orbit accuracy of COMPASS IGSO satellites degrades dramatically during these periods (see Fig. 4.1).

In this contribution, we present two approaches that could significantly increase the orbit accuracy for COMPASS IGSO satellites during yaw maneuvers. In Sect. 4.2, the COMPASS IGSO yaw attitude profile is introduced briefly. After then, the methods are presented in Sect. 4.3 and their performances are assessed by overlapping orbit comparison and Satellite Laser Ranging (SLR) validation in Sect. 4.4 following by discussion and analysis in Sect. 4.5. The final section concludes this contribution.

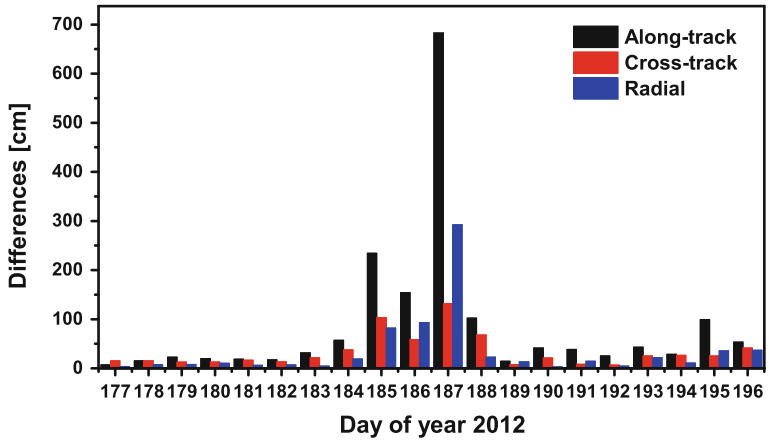

Fig. 4.1 Overlapping orbit differences in along-, cross-track and radial direction for COMPASS I3

4.2 Yaw Attitude Profile for COMPASS IGSO Satellites

Same as other navigation satellites, COMPASS IGSO satellites are also oriented to keep the navigation antenna pointed toward the Earth and simultaneously rotate around the yaw axis to maximize the power absorbed by the solar array. These two conditions constrain that the BF of COMPASS IGSO satellites are same as the aforementioned for GPS BLOCK II/IIA. Figure 4.2 illustrates COMPASS IGSO satellite and its BF. Contrary to GPS and GLONASS, COMPASS IGSO satellite does not experience the noon-turn and midnight-turn maneuvers as well as shadow-crossing maneuvers, but uses two different attitude modes depending on the Sun's elevation angle above the orbital plane, namely yaw-steering regime and yaw-fixed regime. In yaw-fixed regime, the satellite switches to orbit-normal orientation, in which the solar panel axis is oriented normally to the orbital plane and the body-fixed Z-axis points toward the earth. The transitions from fixed to steering yaw, and vice versa, are denoted as ramp-up and ramp-down. Using different attitude modes could avoid rotating the spacecraft with high yaw rates in the vicinity of noon as well as midnight turn points and using much more complicate yaw attitude control approaches. The Japanese Quasi Zenith Satellite System (QZSS) also use the similar yaw attitude profile, but it switches from yaw-steering regime to yaw-fixed regime once the Sun's elevation is at approximately 20.59° [6]. However, there are no any publications showing orbit accuracy degradation for QZSS during yaw maneuvers currently.

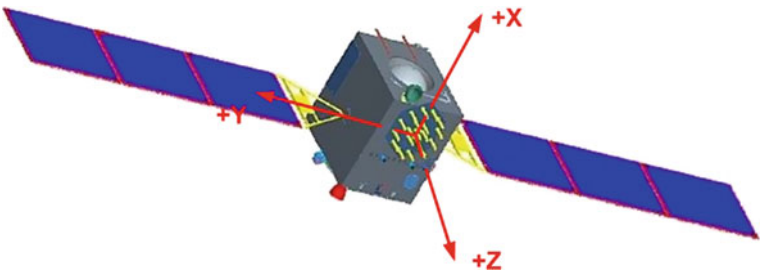

Fig. 4.2 COMPASS IGSO satellite and its body-fixed frame

4.3 POD Strategies

The data collected by COMPASS Experimental Tracking Network (CETN) are used in this paper. This network is operated by GNSS Research Center, Wuhan University. Currently, the CETN comprises 15 stations totally equipped with the dual-frequency COMPASS/GPS receivers, but the actual number of available stations for each POD arc is no more than 12.

The strategy of COMPASS IGSO orbit and clock determination is similar as that used in [7] for POD of GIOVE-B. The approach consists of two steps. The collected GPS data are firstly used to estimate receiver clocks, station coordinates, and zenith troposphere delays (ZTD) by Precise Point Positioning (PPP) technique. Afterwards, these estimates are fixed as known for COMPASS IGSO orbit and clock determination. For POD, 3-day solution is employed for orbit and clock determination in order to improve the solution strength. Only the orbital parameters of COMPASS IGSO satellites, their clock offsets, float ambiguities, and one combined inter-system/inter-frequency bias for each receiver are estimated. Because the yaw attitude profile and state-of-art measurement corrections are used in data processing, the performance of POD products mainly is affected by dynamical models, especially the SRP model.

Traditionally, the Extended CODE Orbit Model (ECOM) is used for GNSS satellites POD by adjusting 5 or 9 SRP parameters [8]. For COMPASS IGSO satellite in yaw-steering regime, the high accuracy orbit solutions could be produced with this model, but it is unsuitable for POD in yaw-fixed and other regimes. We have found one more constant parameter in along-track direction should be adjusted together with 5 SRP parameters in yaw-fixed regime, but it is still not valid for POD in ramp-down regime. Fortunately, the dimensions and optical properties of COMPASS IGSO satellites were kindly provided by satellite manufacture. With these data, we could model SRP based on the bow-wing model. Recently, Rodriguez-Solano et al. [9] presents the more physical adjustable box-wing model (BOXW) and 9 parameters are adjusted, namely solar panel scaling factor, solar panel rotation lag, Y-bias acceleration, absorption plus diffusion and

reflection coefficients for +X and ±Z bus, respectively. And among these parameters, the solar panel rotation lag is a key factor for POD. However, as to our tests, the reflection coefficients have little impact on the POD results for COMPASS IGSO satellites, so they are removed. Furthermore, the solar panel rotation lag could be replaced by the empirical 1-CPR (cycle-per-revolution) sine and cosine parameters in B direction. We identify that the Y-bias acceleration is necessity for I1 and I4. In addition, the 1-CPR parameters in B direction are the key factor for COMPASS IGSO POD. However, contrary to different strategies used in yaw-steering and yaw-fixed regime by the approach based on ECOM model, the POD strategy of BOXW approach is also valid in yaw-fixed regime.

Compared with the several meters level degradation of orbit accuracy for COMPASS IGSO in ramp-down regime, the degradation in ramp-up regime is not remarkable (see Fig. 4.1). Hence, we do not pay special attention on it, and use the same POD strategy as that used for yaw-fixed regime. However, the POD for ramp-down regime should be handled separately. In the ECOM approach, we adjust the constant parameters in Y and B directions per 6 h, whereas one more constant parameter in along-track direction is introduced and adjusted per 12 h together with Y-bias acceleration for BOXW approach.

4.4 Results and Validation

The precise orbits were determined for all IGSO satellites for the period from January 2012 to September 2012 based on the approaches presented in Sect. 4.3. Figure 4.3 illustrates the definition of orbit arcs for different attitude regimes. The 3-day arcs containing the epoch at which the −X bus starts to expose to Sun radiation are termed as ‘ramp-down arcs’, and the reason will be given in Sect. 4.5. In addition, we use the terms ‘yaw-steering arcs’ and ‘yaw-fixed arcs’ in this paper to refer to those 3-day arcs at which COMPASS IGSO satellites orbit the Earth in yaw-steering regime or yaw-fixed regime, respectively. Similarly, the term ‘ramp-up arcs’ is given to those arcs containing the epoch of attitude mode switches from yaw-fixed to yaw-steering. In this section, only the POD results of I3 in July 2012 and I5 in August 2012 are assessed due to the following two reasons: (1) there are SLR data available for I3 and I5 during these periods for us to make objective assessment on the performance of the proposed two approaches; (2) Although the telemetry data of I3 and I5 during these periods could not be accessed, we have the telemetry data during January for I3 and February for I5, respectively. Those will be used to analyze the possible reasons for orbit accuracy degradation during yaw maneuvers in Sect. 4.5. Furthermore, Table 4.1 lists the Day of Year (DOY) of attitude mode switch for I3 and I5 in 2012.

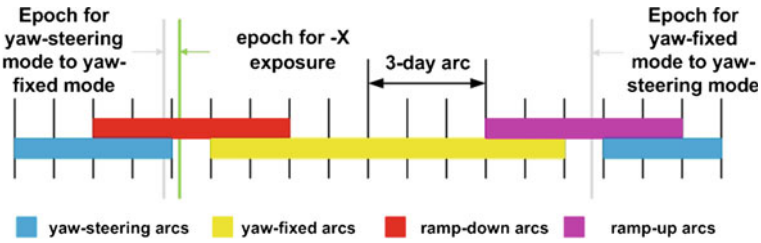

Fig. 4.3 Orbit arc definition and orbit overlap comparison

Table 4.1 DOY of attitude mode switches for I3 and I5 in 2012

SVN	Day of yaw-steering to yaw-fixed mode	Day of yaw-fixed to yaw-steering mode
I3	DOY 4	DOY 13
	DOY 185	DOY 195
I5	DOY 33	DOY 47
	DOY 215	DOY 229

4.4.1 Overlap Comparison

As an internal validation of orbit accuracy, the direct comparison of the consecutive orbit solutions is commonly used. For any two adjacent 3-day solutions shifted by one day, there are 48 h overlapping orbits. There is also 24 h overlap for any two 3-day solutions with a time-lag of two days. We use the later to evaluate the internal consistency of orbit solutions.

Figure 4.4 shows the daily RMS values of 24 h overlap in along-, cross-track and radial direction for I3 with ECOM and BOXW from DOY 177 to DOY 196 2012, respectively. In general, the differences in the along-track direction are largest, and the radial are the smallest. The following similar behaviors for these two solutions are observed: the overlap differences for yaw-steering arcs are smallest, whereas that of ramp-down arcs are largest; the differences of ramp-up arcs are almost at the same level of that of ramp-down arcs; yaw-fixed arcs show the intermediate performance. For GNSS satellites, the radial accuracy is essential for navigation and positioning among the three directions. The averaged RMS of radial orbit differences is below 10 cm for yaw-steering arcs, whereas better than 20 cm is achieved for yaw-fixed arcs. However, the radial orbit differences degrade to about 40 cm for ramp-up and ramp-down arcs with exception of DOY 187.

In addition, Fig. 4.5 shows the overlap differences for I5 from DOY 209 to DOY 231 2012 with the two approaches. The similar behaviors as I3 are observed. However, the performance of ramp-down arcs is better that of I3, whereas differences of ramp-up arcs are inferior to that of I3, especially in along-track direction, where the orbit differences could reach above 2 m.

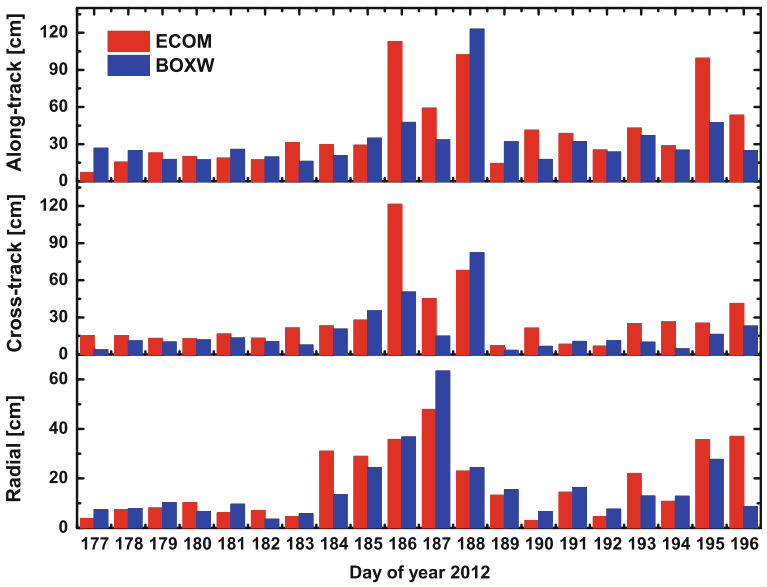

Fig. 4.4 Orbit overlap differences in along-, cross-track and radial direction for I3 in July 2012

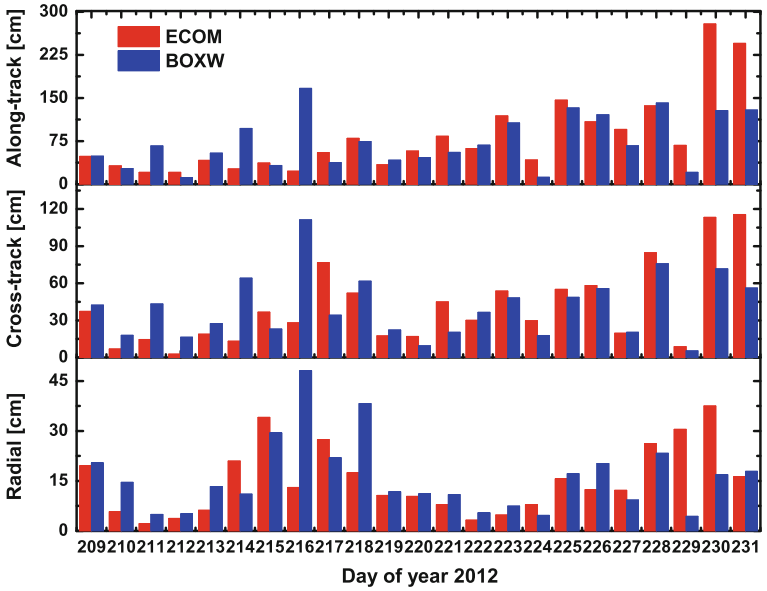

Fig. 4.5 Orbit overlap differences in along-, cross-track and radial direction for I5 in August 2012

In general, the overlap comparison indicates that the two approaches have the similar performance, although the results of ECOM model seem a little better than that of BOXW for yaw-steering arcs. However, the BOXW seems superior to the ECOM for yaw-fixed arcs and ramp-up arcs, especially in along- and cross-track direction. In addition, as a reminder, the same strategy is used not only for yaw-steering arcs but also for yaw-fixed arcs for BOXW, whereas an additional constant parameter is introduced in ECOM. We think this could be explained by that ECOM developed initially for GPS POD in the yaw-steering regime is not appropriate for POD in yaw-fixed regime, but BOXW could adapt to the attitude mode transition. Comparison with the overlap differences in Fig. 4.1, it clearly show that the orbit accuracy increases dramatically by these two approaches.

4.4.2 SLR Validation

The SLR is a powerful technique which allows for an independent validation of satellite orbits. All of COMPASS IGSO satellites are equipped with laser retro-reflector arrays, but only I3 and I5 have been being observed by the SLR tracking stations since April and July 2012, respectively. Most SLR data are provided by Yarragadee, Mt Stromlo, Changchun, and Beijing SLR stations, which are located in Australia and China, respectively. These SLR observations are corrected using retro-reflector offsets provided by ILRS. Gross errors in SLR observations are detected and not used.

Figures 4.6 and 4.7 show the daily RMS of Observed minus Computed (O–C) residuals of the middle day of the 3-day solutions for satellite I3 and I5, respectively. In general, the averaged RMS for yaw-steering arcs is better than 10 cm for I3 and I5, whereas better than 15 cm is achieved for yaw-fixed arcs. However, the degradation of SLR RMS could still be observed for ramp-down and ramp-up arcs. The daily SLR RMSs are almost less than 30 cm with exception of DOY 185 by BOXW. As to I3, the performance of BOXW is inferior to ECOM model for the yaw-steering, ramp-up and ramp-down arcs. But the SLR validation of orbits with BOXW approach is better than that of ECOM for yaw-fixed arcs. However, the behavior is different for the results of I5. It seems that the orbits based on BOXW are superior to that of ECOM for the whole four different types of arcs only with a few exceptions, or at least the same performance is achieved for these two approaches. Hence, the further investigation on the differences between ECOM and BOXW is needed.

4.5 Analysis and Discussion

The transition of satellite attitude modes could cause the change of exposure surfaces, further resulting in variations of non-gravitational forces, such as SRP and TRR. Figure 4.8 illustrates the change of exposure surfaces during attitude

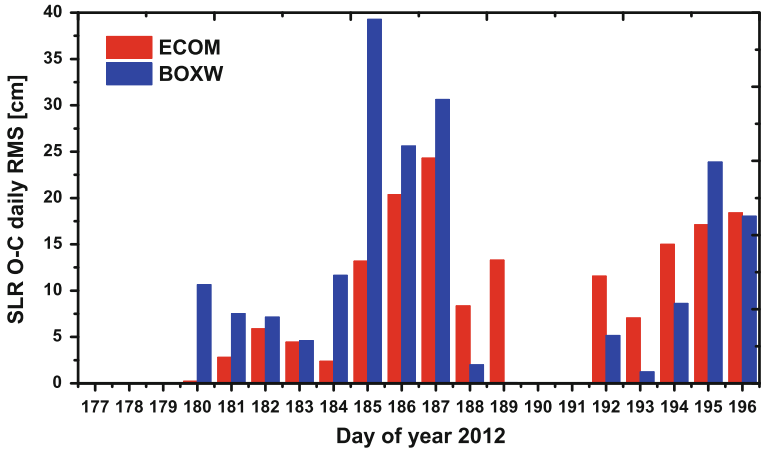

Fig. 4.6 Daily SLR RMS for I3 in July 2012

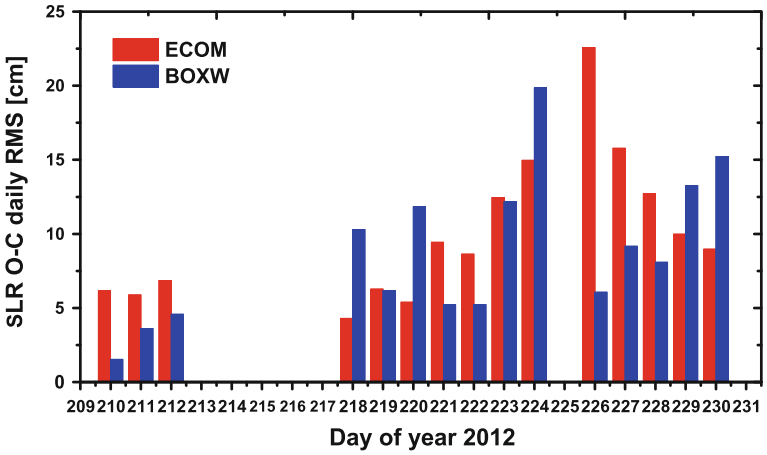

Fig. 4.7 Daily SLR RMS for I5 in August 2012

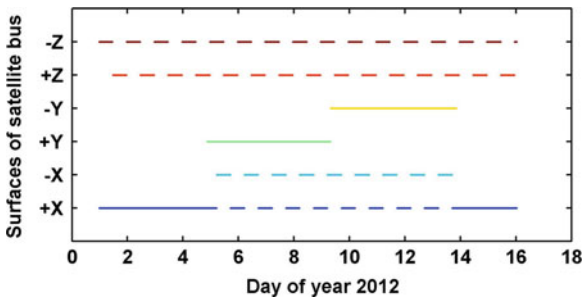

Fig. 4.8 Change for exposure surfaces of I3 in January 2012

transition periods, e.g., yaw-steering to yaw-fixed mode, and vice versa. When satellite orbits the Earth in yaw-steering regime, the +X surface is always exposed to Sun radiation, meanwhile the +Z and −Z surface are exposed alternatively. However, once the yaw attitude switches to yaw-fixed mode, additional ±Y and −X surfaces are Sun-lit. In yaw-steering regime, the +X-surface always points to the hemisphere containing the Sun, whereas it coincides with along-track direction, pointing toward or backward the satellite-Sun direction in yaw-fixed regime. Furthermore, the Y-axis is oriented normally to the orbital plane in yaw-fixed regime, resulting in a small angle between satellite-Sun direction and normal direction of solar panel, and the angle equals to the Sun's elevation with respect to the orbital plane. In addition, the +Y and −Y surface take turn to expose to Sun radiation following the variation of Sun's elevation from positive to negative or vice versa in yaw-fixed regime.

Figure 4.9 shows the differences of SRP accelerations in cross-track direction with nominal and actual attitude for I3 from DOY 2 to DOY 15, 2012. The SRP accelerations are computed based on box-wing model as following. First, the SPR scale was adjusted together with Y-bias by fitting the observations for one-month yaw-steering arcs. Afterwards, the average scale value was fixed as known to compute the SRP accelerations with different attitude profiles. We had found the variation of estimated solar scale parameters could be as large as 10 %, which indicated the model error may be at that level. It could be seen that the SRP differences show half-day periodic behavior, and the amplitudes change according to the Sun's elevation. Once the attitude mode switches, the rapidly jumps appear, and the magnitudes could be as large as about 1.3×10^{-9} m/s^2. Considering the 10 % SRP model error as well as the errors induced by SRP scale only estimated using yaw-steering arcs, the actual SRP variations caused by attitude switch may be up to 1.5×10^{-9} m/s^2 in cross-track direction. And the SPR differences in radial and along-track direction are less than one in ten of that in cross-track direction. The SRP acceleration variations in cross-track direction could explain why the constant parameter in Y direction should be adjusted per 6 or 12 h, but it is hard to explain why a constant parameter in along-track direction should be introduced.

Figure 4.10 demonstrates the actual SRP accelerations for I3 during January 2012. The accelerations were computed by orbit integration with dynamical parameters estimated by fitting the observations based on ECOM approach. It could be seen the SRP accelerations are quite stable until the abnormal accelerations appears after several hours when the attitude mode switches to yaw-fixed. We found the actual SRP accelerations of other IGSO satellites showed the similar pattern, but with different magnitude. This phenomenon indicates the orbit accuracy degradation is not simply contributed to the variations of SRP caused by attitude transition. Indeed, the abnormal forces may be responsible for that. In order to explore the reason, we investigated the telemetry data, but no orbit maneuvers and abnormal behaviors were founded with exception of the temperature of −X bus (see Fig. 4.11).

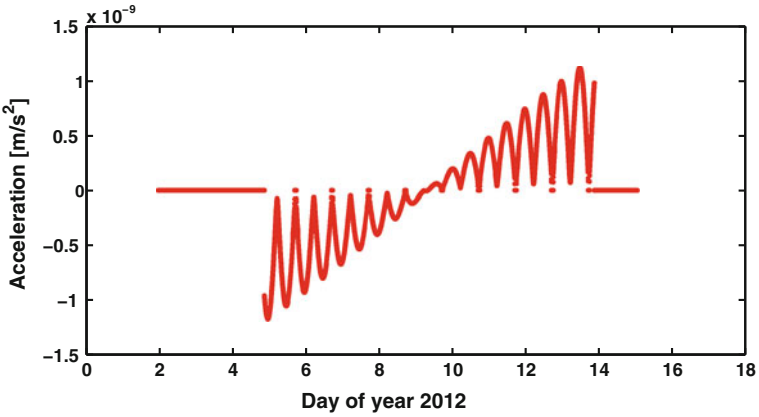

Fig. 4.9 Differences of SRP accelerations in cross-track direction for I3 in different attitude modes

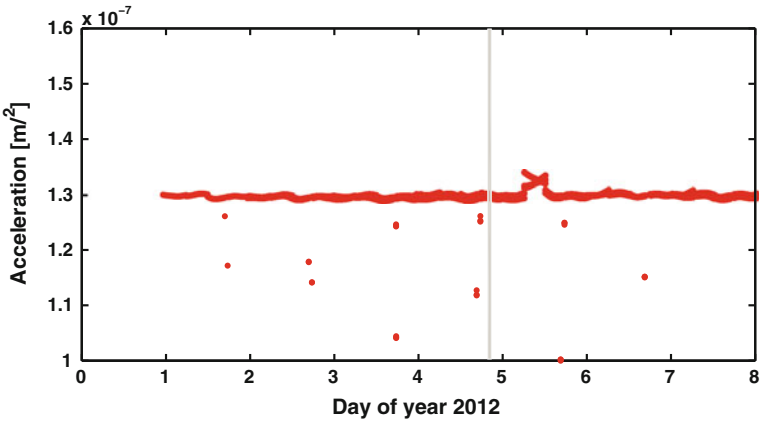

Fig. 4.10 Actual SRP accelerations computed by ECOM for I3 in January 2012

Figure 4.11 illustrates the temperature of −X bus for I3 in January 2012, which varies dramatically once attitude mode switches. The temperature variation from peak to peak is more than 25 °C for −X surface, whereas it is less than 6 °C for +X bus (not shown). The phenomenon is mainly due to that the −X bus is exposed to Sun radiation in yaw-fixed regime, but not in yaw-steering regime. The exposure causes variations of surface's temperature and further results in the TRR acceleration variations, which are mainly in along-track direction due to that X-axis coincides with the along-track direction in the yaw-fixed regime. That is why the const parameter in along-track direction should be introduced for the two presented approaches. Furthermore, we tried to model the TRR with satellite's telemetry data and determined the precise orbits, but unfortunately no improvements had been obtained. One reason is that the emissivity coefficients of the

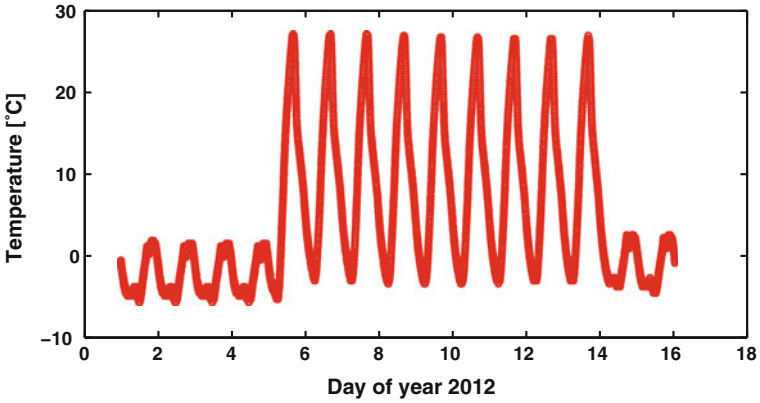

Fig. 4.11 Temperature variations of −X bus for I3 in January 2012

satellite surfaces are unavailable. And the other is that the telemetry temperature only presents a region of the surface, but is not valid for the whole. We estimated that the accelerations caused by TRR are less than 1.0×10^{-9} m/s^2, so the abnormal acceleration in Fig. 4.10 could not be explained by TRR. However, the phenomenon that the abnormal accelerations appears once the −X surface is exposed to Sun radiation (see Figs. 4.8, 4.10) indicates the accuracy degradation must have relation with −X surface. Investigation on the satellite bus, we have found there are several devices on −X surface, but not on +X (see Fig. 4.2). Hence, we speculate that the abnormal acceleration may be caused by this, but further investigations are needed.

4.6 Conclusion

For COMPASS IGSO satellites, the orbit accuracy degrades dramatically once attitude mode switches. We present two approaches to improve the orbit accuracy based on ECOM and BOXW model. The differences of orbit overlap and SLR validation indicate that the orbit accuracy could increase to better than 30 cm from several meters level.

On basis of dimensions and optical properties of COMPASS IGSO satellites, we investigate SRP acceleration variations caused by different attitude profiles. The largest variations are mainly in cross-track direction and the magnitudes are no more than 1.5×10^{-9} m/s^2 according to our analysis. Further investigation on telemetry data, we have found the significant temperature variations of −X bus before and after attitude transition could introduce acceleration variations in along-track direction. However, all of the aforementioned force variations could not explain the abnormal accelerations for all IGSO satellites, which appear once the −X surface is exposed to Sun radiation. However, several devices on −X surface may be responsible for that.

This is a very preliminary achievement we have accomplished. We are looking forward to results from the other colleagues for improving our models and strategies. Anyway, further studies will be conducted in order to validate new strategies and approaches. We believe that with more data and proper POD strategies, the problem could be solved in the near future. And maybe the COMPASS specific SRP model should be needed.

Acknowledgment This work is partially supported by the National Nature Science Foundation of China (Projects 41231174, 41274049), the Open Fund of Key Laboratory of Precision Navigation and Technology, National Time Service Center (Grant No. 2012PNTT06), and the fundamental research funds for the central universities (Grand No. 2012618020201). We would also like to thank Mr. Xiaotao Li for managing data of the CETN stations.

References

1. Bar-Sever Y (1996) A new model for GPS yaw attitude. J Geod 70:714–723. doi:10.1007/BF00867149
2. Kouba J (2009) A simplified yaw-attitude model for eclipsing GPS satellites. GPS Sol 13:1–12. doi:10.1007/s10291-008-0092-1
3. Dilssner F (2010) GPS IIF-1 satellite antenna phase center and attitude modeling. In: Inside GNSS. Gibbons Media and Research, LLC, Eugene, Orefon, U.S.A, pp 59–64
4. Dilssner F, Springer T, Gienger G, Dow J (2011) The GLONASS-M satellite yaw-attitude model. Adv Space Res 47:160–171. doi:10.1016/j.asr.2010.09.007
5. Griffiths J, Ray J (2009) On the precision and accuracy of IGS orbits. J Geod 83:277–287. doi:10.1007/s00190-008-0237-6
6. Hauschild A, Steigenberger P, Rodriguez-Solano C (2012) Signal, orbit and attitude analysis of Japan's first QZSS satellite Michibiki. GPS Sol 16:127–133. doi:10.1007/s10291-011-0245-5
7. Steigenberger P, Hugentobler U, Montenbruck O, Hauschild A (2011) Precise orbit determination of GIOVE-B based on the CONGO network. J Geod 85:357–365. doi:10.1007/s00190-011-0443-5
8. Springer TA, Beutler G, Rothacher M (1999) A new solar radiation pressure model for GPS satellites. GPS Sol 2:50–62. doi:10.1007/PL00012757
9. Rodriguez-Solano CJ, Hugentobler U, Steigenberger P (2012) Adjustable box-wing model for solar radiation pressure impacting GPS satellites. Adv Space Res 49:1113–1128. doi:10.1016/j.asr.2012.01.016

Chapter 5
Application of Thrust Force Model in GEO's Orbit Determination in Case of Maneuvers

Jun-Li Zhang, Hong-Xing Qiu, Yong Yang and Wen-Ge Guo

Abstract GEO satellites play a significant role in COMPASS satellite navigation system. The GEO's orbit must be maneuvered periodically for station-keeping. The method of the maneuvering orbit determination and prediction must be studied for advancing the COMPASS navigation system service precision. In the paper, the continuous constant thrust maneuver model is established. And based on the measurement from C transponder, the COMPASS-GEO orbit determination is analyzed with maneuver arc. It realized the continuous orbit determination and prediction crossing the orbit maneuver.

Keywords GEO · Maneuver · Orbit determination · Orbit prediction

5.1 Introduction

China's COMPASS navigation system adopts constellation configuration combined by GEO+IGSO+MEO, and the GEO satellite plays a particularly important role in the COMPASS satellite navigation [1]. In order to maintain its special position, the GEO satellite must be maneuvered periodically for station-keeping [2]. In case satellite maneuver occurs, prediction will be soon unusable. Therefore, how to decrease the influence of GEO satellites maneuver, and realize the precise maneuver orbit determination and prediction for improving the navigation ephemeris usability is the question to be solved.

Aiming at the method of the maneuvering orbit determination, the continuous constant thrust maneuver model considering changing attitude is put forward. And the partial differential equation is given which realized the continuous orbit

J.-L. Zhang (✉) · H.-X. Qiu · Y. Yang · W.-G. Guo
Beijing Space Information Relay and Transmission Technology Research Center, Beijing, China
e-mail: lindallyy@tom.com

J. Sun et al. (eds.), *China Satellite Navigation Conference (CSNC) 2013 Proceedings*, Lecture Notes in Electrical Engineering 245,
DOI: 10.1007/978-3-642-37407-4_5,

determination and prediction crossing orbit maneuver. At last, GEO satellite maneuver orbit prediction test considering control parameters and orbit determination and prediction crossing maneuver are realized. The orbit measurement data of 3 days former and after maneuver is obtained from the "CAPS" system established by national time service center, Chinese Academy of Sciences.

5.2 Thrust Force Model

5.2.1 Dynamic Model

There are many thrust force models, such as piecewise constant experience force model, pulse thrust model, pulse experience force model and so on [3–5]. A continuous acceleration function is set up to describe equivalently the magnitude and direction of the thrust force. The average thrust force only exists during the period of maneuver. Compared with piecewise constant experience force model, it does not require a restart process at the thrust force acceleration node during orbit control. The border of thrust force doesn't process especially if the magnitude and direction of thrust force are estimated. The effects of the thrust on orbit can be considered as the continuous uniformly increase or decrease.

The satellite velocity vector (v_x, v_y, v_z) in J2000.0 coordinates system is selected as the reference direction. Then the pitch angle (α) and yaw angle (β) are described by the angle between the direction thrust force and velocity.

The transformation from J2000 coordinates to RTN coordinates may be written as

$$\begin{bmatrix} v_r \\ v_t \\ v_n \end{bmatrix} = RTN \begin{bmatrix} v_x \\ v_y \\ v_z \end{bmatrix} \tag{5.1}$$

The thrust force vector is set up by rotating around the N axis angle α and R axis angle β respectively, and then switched to the J2000.0 coordinates. The thrust force model in maneuver interval can be built up as:

$$\bar{P}_{thrust} = F \cdot AT \cdot RTN \begin{bmatrix} v_x \\ v_y \\ v_z \end{bmatrix} \tag{5.2}$$

$$\begin{aligned} AT &= RTN^T R_Z(\beta) R_X(\alpha) \\ &= RTN^T \begin{bmatrix} 1 & 0 & 0 \\ 0 & \cos\beta & -\sin\beta \\ 0 & \sin\beta & \cos\beta \end{bmatrix} \begin{bmatrix} \cos\alpha & -\sin\alpha & 0 \\ \sin\alpha & \cos\alpha & 0 \\ 0 & 0 & 1 \end{bmatrix} \end{aligned} \tag{5.3}$$

The magnitude F and the pitch angle α, yaw angle β are evaluated as orbit determination crossing maneuver, which may calibrate the efficiency of engine thrusters.

Furthermore, the thrust force information calculated before maneuver may be regarded as prior value to predict the in and after control orbit.

5.2.2 Partial Derivatives of the Acceleration

$\vec{a}$ is the thrust force acceleration, and m is the mass of satellite, then

$$\vec{a} = \bar{P}_{thrust}/m \tag{5.4}$$

The partial derivatives of the acceleration with respect to the state are given by

$$\frac{\partial \vec{a}}{\partial \vec{r}} = \frac{F}{m}\begin{pmatrix} \frac{\partial RTN^T}{\partial \vec{r}} R_Z(\beta)R_X(\alpha)RTN \begin{bmatrix} v_r \\ v_t \\ v_n \end{bmatrix} \\ +RTN^T R_Z(\beta)R_X(\alpha)\frac{\partial RTN}{\partial \vec{r}} \begin{bmatrix} v_r \\ v_t \\ v_n \end{bmatrix} \end{pmatrix} \tag{5.5}$$

$$\frac{\partial \vec{a}}{\partial \vec{v}} = \frac{F}{m}\begin{pmatrix} \frac{\partial RTN^T}{\partial \vec{v}} R_Z(\beta)R_X(\alpha)RTN \begin{bmatrix} v_r \\ v_t \\ v_n \end{bmatrix} \\ +RTN^T R_Z(\beta)R_X(\alpha)\frac{\partial RTN}{\partial \vec{v}} \begin{bmatrix} v_r \\ v_t \\ v_n \end{bmatrix} \\ +RTN^T R_Z(\beta)R_X(\alpha)RTN \end{pmatrix} \tag{5.6}$$

Likewise

$$\frac{\partial \vec{a}}{\partial \alpha} = \frac{F}{m} RTN^T \begin{bmatrix} 1 & 0 & 0 \\ 0 & \cos\beta & -\sin\beta \\ 0 & \sin\beta & \cos\beta \end{bmatrix} \begin{bmatrix} -\sin\alpha & -\cos\alpha & 0 \\ \cos\alpha & -\sin\alpha & 0 \\ 0 & 0 & 1 \end{bmatrix} RTN \begin{bmatrix} v_x \\ v_y \\ v_z \end{bmatrix} \tag{5.7}$$

$$\frac{\partial \vec{a}}{\partial \beta} = \frac{F}{m} RTN^T \begin{bmatrix} 1 & 0 & 0 \\ 0 & -\sin\beta & -\cos\beta \\ 0 & \cos\beta & -\sin\beta \end{bmatrix} \begin{bmatrix} \cos\alpha & -\sin\alpha & 0 \\ \sin\alpha & \cos\alpha & 0 \\ 0 & 0 & 1 \end{bmatrix} RTN \begin{bmatrix} v_x \\ v_y \\ v_z \end{bmatrix} \tag{5.8}$$

are the partial derivatives of the acceleration with respect to the angle α and β.

5.3 Data and Orbit Parameters

Two COMPASS-GEO satellites' observing data during East–West station-keeping has been obtained through the transponder ranging system. The system can provide high precise and sampling rate data [6, 7]. Four stations are located at Beijing, Sanya, Kashi and Chengdu. The measurement data span is from April 13 to April 20, 2012 and April 30 to May 5, 2012. Thrusters burned time and thrust force magnitude calculated before maneuver are as follows (Table 5.1):

The dynamic models for orbit determination are [8, 9]:

(1) the earth non-spherical gravitational model: JGM3 (20 × 20);
(2) the third-body forces of the Sun and the Moon perturbations (DE200);
(3) solar radiation pressure perturbation fixing ratio of area to mass;
(4) tidal perturbation: Solid earth tides and Ocean tides;
(5) relativity perturbation;
(6) periodic experience force perturbation.

The SAASTAMOINEN atmospheric refraction model is used to correct troposphere delay. The relativistic correction, station antenna phase correction, earth deformation and tidal displacements are considered in data processing.

Based on the thrust model, orbit determination and prediction crossing maneuver and orbit prediction tests are performed as follows.

The tests results are quantified through orbit residuals and comparison with reference orbit respectively. The comparison presents mean square errors of RTN

Table 5.1 Orbit maneuver parameters calculated before station-keeping

Maneuver parameters	Satellite A	Satellite B
Burn time	9:04 April 4 2012	10:52 May 2 2012
Duration	696 s	952 s
Thrust force	14.532 N	15.158 N
Thrust efficiency	0.93	0.94
Thrust acceleration	9.954 e–5 N/m	1.0513 e–4 N/m

orbit position on orbit plane. The reference orbit is the precise orbit determination results with former and after maneuver long arc that its radial residual is better than 0.7 m evaluated by laser data. The arc length of reference orbit is 3 days.

5.4 Analysis of Orbit Prediction Prison Considering Maneuver Parameters

In this section, the precise orbit determination test solves the satellite position and velocity, a solar pressure coefficient, a set of T direction experience acceleration with 1 day's data before maneuver. Making use of the result and the thrust force calculated before station-keeping, and setting the angle between thrust force and velocity 0°, 2/4 h satellite ephemeris is predicted. Comparing with the reference ephemeris, position error is shown in the table below (Fig. 5.1) (Table 5.2):

From the above, 2 h prediction accuracy is better than 60 m, and 4 h prediction is better than 100 m.

Because the main navigation precision error is the satellite ephemeris error on the direction between satellite and station, O–C method can evaluate the prediction precision during maneuver that is the deviation between the measurement and prediction. Table 5.3 and Fig. 5.2 present the comparison of the station residuals whether considering maneuver parameters.

As it can be seen from the graph, the predicted station residuals in maneuver decrease by orbit determination considering the thrust model with 1 day's arc. Especially satellite B, the station residuals is less than 1 m. Therefore, this thrust model is benefit for in and after maneuvers orbit prediction before station-keeping. However, the residuals of satellite A also indicate that the model deviation which is likely to be caused by the calculated maneuver time is not consistent with the actual thrusters firing time.

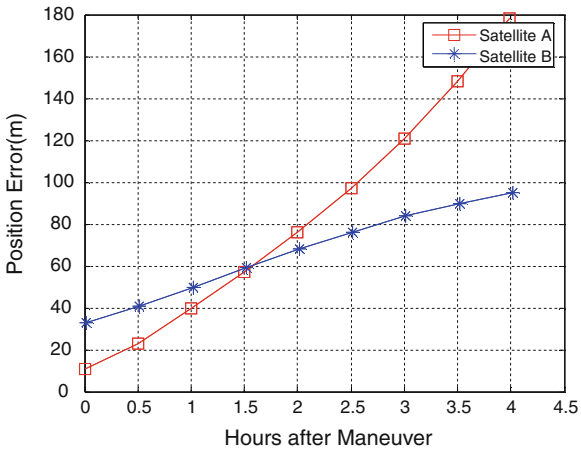

Fig. 5.1 Prediction accuracy with maneuver parameters calculated

Table 5.2 Prediction accuracy with maneuver parameters calculated (RMS: m)

Satellite	2 h Ephemeris predicted				4 h Ephemeris predicted			
	Radial	Transverse	Normal	Position	Radial	Transverse	Normal	Position
A	38.5	6.3	22.7	45.2	85.4	24.4	33.8	95.0
B	6.2	30.8	49.2	58.4	7.7	32.5	61.1	69.6

Table 5.3 Residuals chart during maneuver (RMS: m)

Satellite	Do not consider maneuver parameters				Considering maneuver parameters			
	Beijing	Sanya	Kashi	Chengdu	Beijing	Sanya	Kashi	Chengdu
A	1.56	/	2.11	1.47	1.48	/	1.97	1.39
B	2.09	2.95	/	2.41	0.18	0.15	/	0.87

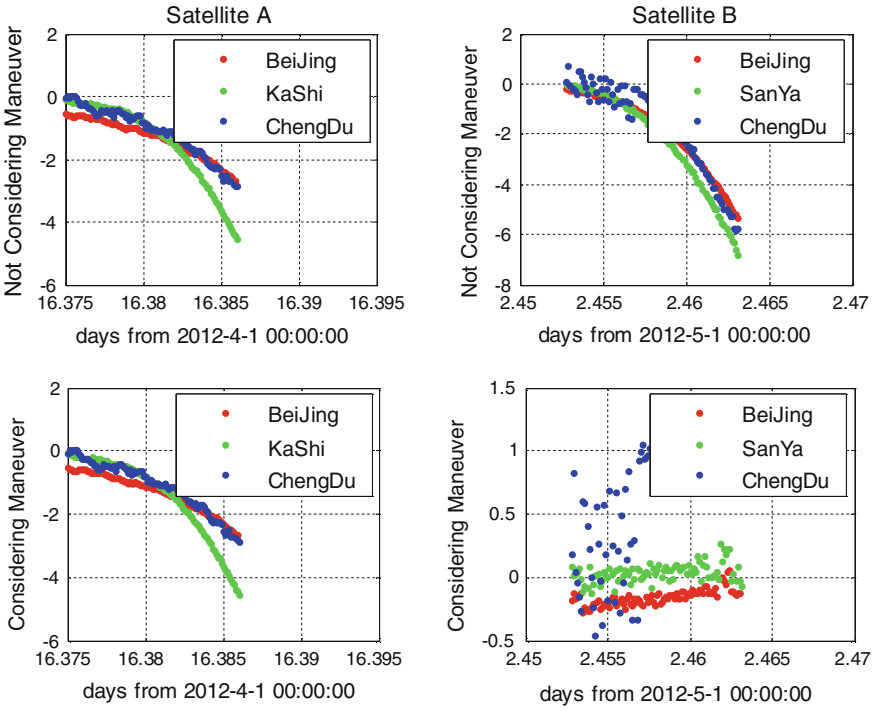

Fig. 5.2 Residuals chart during maneuver (RMS: m)

5.5 Analysis of POD and Prediction Accuracy Across Maneuver Arc

5.5.1 POD with Long Segmental Arc

With 6 days of long segmental arc crossing the maneuver, the orbit determination estimates the satellite position and velocity, the thrust force, pitch angle, yaw angle, a solar pressure coefficient and a set of T direction experience acceleration per 6 h. Meanwhile, the satellite transponder time delay is also solved and each station range system error is iteratively eliminated. Orbit residuals are shown as Fig. 3.

The graph shows that the maneuver arc residuals have the same lever as non-maneuver arc. But the residuals distribution implied that the thrust model exists certain error while the maneuver arc residuals are larger.

The thrust acceleration of satellite A calculated is 0.000116158 m/s^2, and pitch angle is 4.608°, and yaw Angle is 3.321°. While, the thrust acceleration of satellite B calculated is 0. 000109691 m/s^2, and pitch angle is −0.244°, and yaw Angle is 4.886°.

The results can be used to calibrate the thruster efficiency. Satellite A thrust engine efficiency is 91.2 %, and satellite B thrust engine's efficiency is 98 %. Therefore, the results also validate the previous conclusion that the orbit prediction accuracy of satellite B considering maneuver parameters calculated beforehand is higher.

Comparing with the reference orbit, the average position error crossing maneuver is less than 10 m (Fig. 5.4). Given the time of satellite station-keeping, the orbit determination that solves thrust parameters gains better data fitting effect with 3 days' former and after maneuver arc.

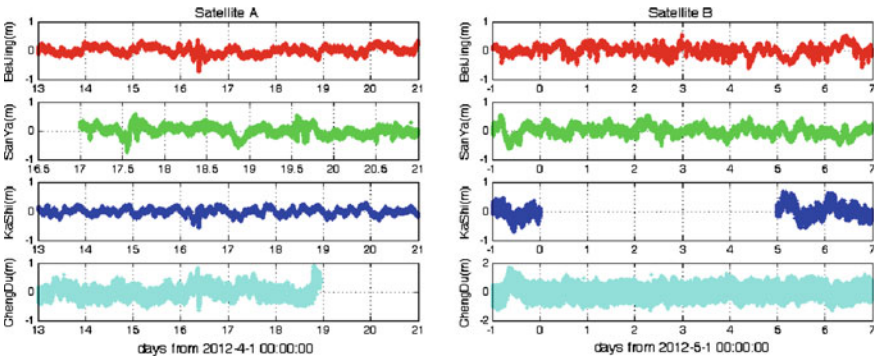

Fig. 5.3 Residuals chart with long arc

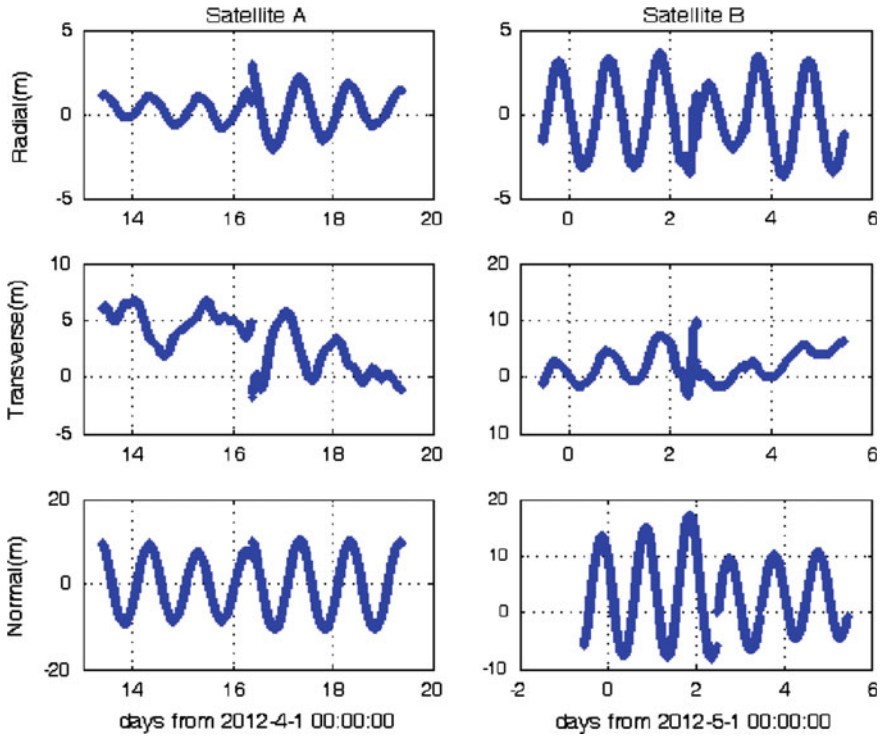

Fig. 5.4 POD accuracy with long arc

5.5.2 POD with Short Segmental Arc

Aiming at shorting the satellite ephemeris recovery time, the orbit determination tests are carried out with 1 day's former-maneuver data, maneuver data and 2/4 h after-maneuver data. The 2/4 h ephemeris predicted is compared. The satellite transponder time delay and every station range system error are fixed. And the satellite position and velocity thrust force, pitch angle, yaw angle, a solar pressure coefficient and a set of T direction experience acceleration are estimated. The residuals and the calculated parameters are shown as follows (Fig. 5.5):

The residuals chart shows that each station of residuals of satellite A and B has basically the same time series. Because of the short arc after maneuver, the thrust model solved can not be better constrained. And the actual thrust time is may be inconsistent with the computation that results in the difference of reflecting the orbit change.

The thrust acceleration of satellite A calculated is 0.000116568 m/s^2, and pitch angle is 4.466°, and yaw angle is 2.454°. While, the thrust acceleration satellite B calculated is 0. 000107983/s^2, and pitch angle is −0.283°, and yaw Angle is 4.208°.

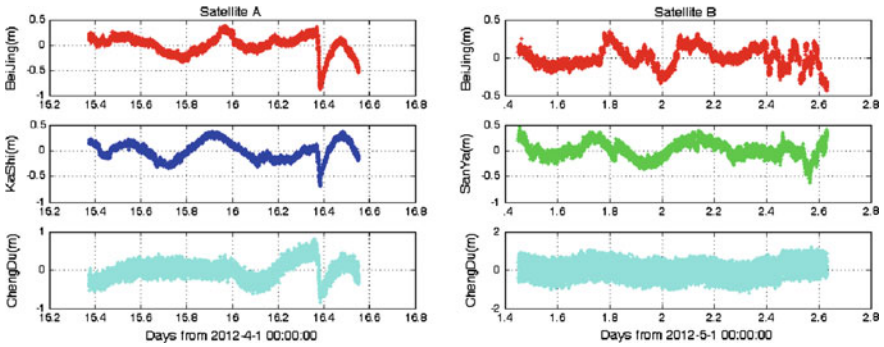

Fig. 5.5 Residuals chart with short arc

With one day former-maneuver arc and 2 h after-maneuver arc, the orbit determination accuracy is 15 m, and the radial error is 2.5 m. The 4 h orbit prediction accuracy is 20 m, and the radial error is 3 m which realized precise orbit recovery. With one day former-maneuver arc and 4 h after-maneuver arc, the orbit determination accuracy is 20 m, and the radial error is 2 m (Fig. 5.6) (Table 5.4).

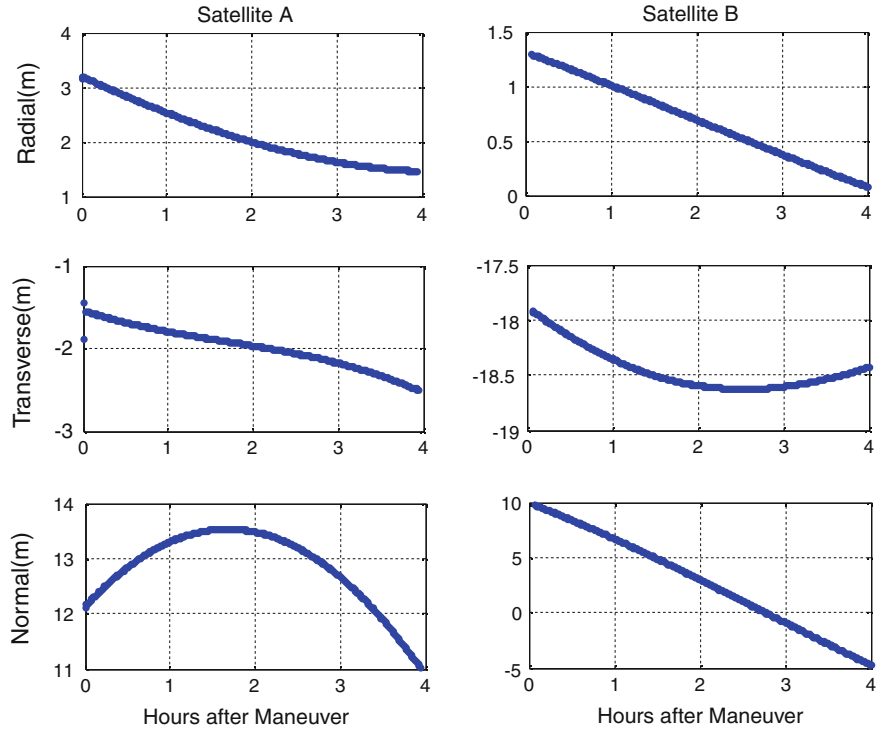

Fig. 5.6 POD and prediction accuracy with short arc

Table 5.4 POD and prediction accuracy with short arc (unit: m)

Time		Satellite A				Satellite B			
		Radial	Transverse	Normal	Position	Radial	Transverse	Normal	Position
2h POD	2 h recovery	2.5	2.6	9.7	10.3	2.2	2.0	12.9	13.2
	4 h recovery	3.2	1.9	7.3	8.2	2.6	1.8	13.1	13.5
4h POD	2 h recovery	2.6	1.8	13.1	13.5	0.8	18.5	5.1	19.2
	4 h recovery	2.2	2.0	12.8	13.2	1.0	18.3	6.8	19.6

Position error mainly reflected on transverse and normal direction. For satellite navigation system user, satellite radial position accuracy affects more than the other direction. Thereby, the precise radial position is benefiting for the navigation application.

5.6 Conclusions

The maneuver orbit determination question is studied in the paper. With high precise and sampling rate ranging measurement by CAPS, the maneuver orbit determination of two COMPASS-GEO satellites is analyzed. How to build up and utilize the thrust model in precise orbit determination and prediction with the maneuver parameters calculated beforehand is emphasized. The tests show that:

(1) The thrust model describes the maneuver by means of thrust force and satellite attitude information that gets good orbit fitting and precise orbit prediction.
(2) Based on the maneuver information predicted, the 4 h after-maneuver orbit prediction accuracy is better than 100 m and every station measurements residuals is less than 3 m.
(3) Only given the control time, the position accuracy is better than 10 m with long tracking arc crossing maneuver. And the thrust magnitude and direction are estimated which verify the thrust engine efficiency.
(4) With one day former-maneuver arc and 2 h after-maneuver arc, the orbit determination accuracy is 15 m, and the radial error is 2.5 m. The 4 h orbit prediction accuracy is 20 m, and the radial error is 3 m. With one day former-maneuver arc and 4 h after-maneuver arc, the orbit determination accuracy is 20 m, and the radial error is 2 m which realized precise orbit recovery.

The conclusion has significant reference for continuous seamless orbit determination of the navigation system.

References

1. Zhang JL, Dong KF, Qiu HX, Zhu ZM (2008) Analysis of orbit determination of COMPASS-MEO navigation satellite with pseudorange. J Spacecraft TTC Technol 27(06):60–64
2. Li HN, Li JS, Huang YX (2010) On-line orbit determinative method for satellites with continuous thrust acceleration. Syst Eng Electron 32(9):1957–1961
3. Song XY, Mao Y, Jia XL, Wu XB (2010) Analysis on the applicability of several thrust force models for maneuver orbit. Geomantic Sci Eng 30(2):15–19
4. LI H (2010) Geostationary satellite orbital analysis and collocation strategies. National Defense Industry Press, Beijing
5. Huang Y, Hu XG, Huang C, Yang QW, Jiao WH (2008) Geo satellite orbit determination during maneuver with ranging data from CAPS. Sci China Ser G Phys Mech Astron 38(12):1750–1758

6. Li ZG, Yang XH, Shi HL, Ai GX, Feng CG (2008) A new orbit measuring technique of transponder satellite. Sci China Ser G Phys Mech Astron 38(12):1711–1722
7. Hua AH, Yang XH, Wang XH (2007) A method to monitor geostationary satellite maneuver based on orbit measuring system with transponder. J Time Freq 30(2):118–124
8. Li JS (1995) Satellite precision orbit determination. PLA Press, Beijing
9. Montentruck O, Gill E (2000) Satellite orbits models, methods, and applications. Springer, Berlin

Chapter 6
Study of Determination Orbit of COMPASS-GEO After Maneuvers with Short Segmental Arc

Jun-Li Zhang, Hong-Xing Qiu, Yong Yang and Wen-Ge Guo

Abstract The GEO satellite must be maneuvered periodically for station-keeping due to its particular orbit. How to realize rapid orbit determination and prediction after orbit maneuver of GEO and shorten the orbit recovery time must be studied for COMPASS navigation system. With high sampling rate measurement from C transponder by TWSTFT, the precision of COMPASS-GEO orbit determination and prediction in non-maneuver period is analyzed. Then, the strategy of orbit determination with short segmental arc is discussed in detail. Base on transcendental information including dynamic model and observation model of former maneuver arc, only six orbit elements are computed for improving the precision of prediction. It is tested that the transponder time delay and bias of station are the key factor in short arc determination. With 15 min tracking arc, the 2 h prediction accuracy is better than 15 m, and the radial accuracy is better than 2.5 m. With 1 h tracking arc, the 4 h prediction accuracy is better than 20 m, and the radial accuracy is better than 2.0 m.

Keywords COMPASS-GEO · Short segmental arc · Orbit maneuver · Orbit determination · Orbit prediction

6.1 Introduction

GEO satellite plays important role in COMPASS navigation system and its ephemeris precision directly restricts the service performance of navigation system [1]. Due to GEO satellite's particular position, it must be maneuvered periodically for station-keeping. How to realize rapid orbit determination and prediction after

J.-L. Zhang (✉) · H.-X. Qiu · Y. Yang · W.-G. Guo
Beijing Space Information Relay and Transmission Technology Research Center, Beijing, China
e-mail: lindallyy@tom.com

J. Sun et al. (eds.), *China Satellite Navigation Conference (CSNC) 2013 Proceedings*, Lecture Notes in Electrical Engineering 245,
DOI: 10.1007/978-3-642-37407-4_6, © Springer-Verlag Berlin Heidelberg 2013

orbit maneuver and shorten the orbit recovery time must be studied for COMPASS navigation system [2].

As for short segmental arc observation data, the satellite position is determined with geometric method such as single point positioning, and the velocity is gained by fitting and smoothing the sequence position. This method gets so poor precision of determination with decimeter velocity and prediction that the result can not reflect the movement of the satellite and unable to meet the demand of high precision orbit determination. Aiming at this question, Guo Rui proposed the short-arc kinematic orbit determination approach based on 9-parameter ephemeris parameter fitting. The satellite ephemeris is fitted with the position by single point positioning that describes the satellite movement in short arc. It is confirmed that with 10 min tracking arc data the position accuracy is better than 19 m and the 10 min orbit prediction accuracy was 18.168 m. But the approach is precise orbit determination of two body problem, only for short arc orbit determination and the short time predication [3].

However, with dynamic orbit determination method for short segmental arc, the precise orbit prediction is provided after the maneuver of GEO quickly [4]. Based on high sampling rate measurement from C transponder by TWSTFT, the accuracy of COMPASS-GEO orbit determination and prediction in non-maneuver period is discussed. The strategy of orbit determination with short segmental arc is studied in detail. With transcendental information including dynamic model and observation model of former maneuver arc, only six orbit elements are evaluated for improving the accuracy of prediction. It is tested that with 15 min tracking arc the 2 h prediction position accuracy is better than 15 m, and the radial accuracy is better than 2.5 m. With 1 h tracking arc the 4 h prediction position accuracy is better than 20 m, and the radial accuracy is better than 2.0 m.

6.2 Dynamics Orbit Determination

Dynamics orbit determination method has high precision which relies on not only the precision measurement data, but also the high precision dynamic model. Actually, the dynamics and observation model parameters need to be estimated in precise orbit determination process with long segmental arc. As the observation segment is special short, the solution of dynamics model and observation model will lead to the equation of determination algorithm seriously sick, while the constraint is required [5].

Orbit measurement data is used from the “CAPS” system established by national time service center, Chinese Academy of Sciences. The system can provide the high precision, all-weather and high sampling rate measurement data for GEO satellites [6].

The dynamic models for orbit determination are [7, 8]:

1. the earth non-spherical gravitational model: JGM3 (20 * 20);

2. the third-body forces of the Sun and the Moon perturbations (DE200);
3. solar radiation pressure perturbation fixing ratio of area with mass;
4. tidal perturbation: Solid earth tides and Ocean tides;
5. relativity perturbation;
6. periodic experience force perturbation.

The SAASTAMOINEN atmospheric refraction model is used to correct troposphere delay. The relativistic correction, station antenna phase correction, earth deformation and tidal displacements are considered in data processing.

For a single COMPASS-GEO satellite as an example, its orbit determination and prediction accuracy is performed with long segmental arc in non-maneuver period. The solved parameters in precise orbit determination are as follows:

1. The position and velocity of the satellite in inertial system;
2. The solar pressure reflection coefficient per 6 h;
3. A set of T direction experience acceleration per 6 h;
4. Satellite transponder time delay;
5. Stations ranging system error is eliminated literately.

Figure 6.1 shows the orbit residuals chart with continuous 3 days data, and total station residuals is 13.9 cm.

Table 6.1 lists the satellite transponder time delay and each station range system error of per day's solution results. From this table, we can see that the system error solution is relatively stable.

Solving a solar pressure reflection coefficient and a set of T direction experience acceleration, orbit is determined and predicted with one day's arc. 12 h prediction error compared is shown in Table 6.2.

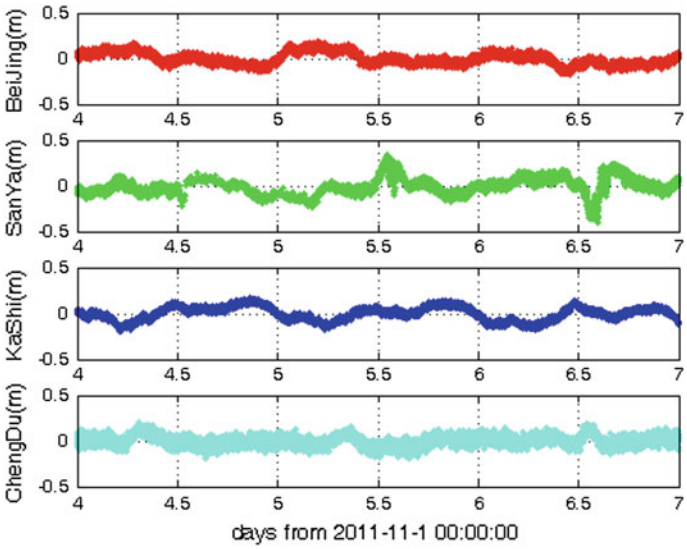

Fig. 6.1 Residuals chart of 3 days' segmental arc

Table 6.1 System error solved with 1 day's segmental arc (unit : m)

Date	Station 1	Station 2	Station 3	Station 4	Transponder time delay
2011-11-4	0.35	0.50	0.21	−0.96	30.33
2011-11-5	0.36	0.54	0.22	−1.00	30.35
2011-11-6	0.25	0.61	0.21	−0.96	30.21
2011-11-8	0.13	0.64	0.22	−0.99	30.63
2011-11-9	0.16	0.59	0.22	−0.96	30.49
2011-11-10	0.13	0.54	0.19	−0.87	30.29

Table 6.2 Prediction accuracy of 12 h (unit : m)

Date	Radial	Transverse	Normal	Position
2011-11-4	1.43	2.29	2.21	3.49
2011-11-5	1.12	2.63	1.94	3.45
2011-11-8	1.05	2.19	0.78	2.55
2011-11-9	1.19	3.63	1.10	3.98

Compared with 3 day's orbit determination result, the 12 h prediction accuracy is better than 5 m, and the radial position is better than 1.5 m. Therefore, COMPASS-GEO satellite orbit determination and prediction accuracy is better than 10 m with the high precise transponder data.

6.3 Orbit Determinations with Short Arc

6.3.1 Analysis of Short Arc Orbit Determination Strategy

For the short arc orbit determination, the less estimate parameters are benefit for the orbit parameter estimation. Based on the results of COMPASS-GEO satellite orbit determination and prediction during non-maneuvering, we can conclude that the range system error is relatively stable and the prediction accuracy is relatively high with 1 day's segmental arc.

Making use of its characteristic and fixing satellite transponder time delay, the station range system error and the dynamic parameters such as solar pressure coefficient and experience acceleration that all estimated with 1 day's segmental arc before maneuver, the dynamic orbit determination with dense short arc is realized which only 6 orbit elements are solved. This method reduces the solved parameters to improve the prediction accuracy which realized satellite ephemeris short recovery.

As the transponder time delay and the rang system error calibration are the key factor of GEO satellite orbit determination, the system error solved with 3 and 1 day's arc before orbit maneuver is used to test different determination precision. The short arc orbit determination strategy is shown in Table 6.3.

Table 6.3 Determination strategy with short arc

Parameters	Strategy 1		Strategy 2	
	POD with 1 day's former-maneuver arc	POD with short arc	POD with 1 day's former-maneuver arc	POD with short arc
POS&VEL	Solved	Solved	Solved	Solved
System error	Fixing transponder time delay and the rang system error solved with 3 days' former-maneuver arc	Fixing transponder delay and the rang system error solved with 3 days' former-maneuver arc	Solving transponder delay and the rang system error	Fixing transponder delay and the rang system error solved with 1 day's former-maneuver arc
Dynamic parameters	Solving solar pressure coefficient and a set of T direction experience acceleration	Fixing solar pressure coefficient and a set of T direction experience acceleration solved with 1 days' former-maneuver arc	Solving solar pressure coefficient and a set of T direction experience acceleration	Fixing solar pressure coefficient and a set of T direction experience acceleration solved with 1 days' former-maneuver arc

Table 6.4 Statistical results of POD accuracy with laser data (unit : m)

Arc number	Mean	Std	Min	Max
1	0.682	0.101	0.270	0.849
2	−0.299	0.195	−0.552	0.363
3	1.157	0.073	1.038	1.388

To verify the short arc orbit determination precision, this paper performs two COMPASS-GEO satellites' three orbit recovery tests after East–West station-keeping in October 2011, April 2012 and May 2012. Four C band transponder measuring stations are located at Beijing, Sanya, Kashi and Chengdu.

6.3.2 Reference Orbit

With the 3 days' long segmental arc, precise orbit determination result is the reference orbit to quantify the short arc orbit prediction precision. The reference orbit is evaluated by laser data. Table 6.4 gives the evaluation statistics.

As we can see above, the first two reference orbit radial residuals are better than the 0.7 m, and the third segment is about 1 m. Therefore, the orbit determination results with long arc can be used as the reference standard.

6.3.3 Analysis of the Orbit Determination Precision

Three batches short arc after the E-W station-keeping are set to segment 1–3. The satellite transponder time delay and the range system error are determined as shown in the following table with different strategy listed in Table 6.3 (Table 6.5).

Table 6.5 System err used in short arc determination (unit : m)

Arc number	Measurement data used	Beijing	Sanya	Kashi	Chengdu	Transponder delay
1	Long former-maneuver arc	0.32	0.56	0.21	−0.98	29.50
	Long after-maneuver arc	0.15	0.60	0.21	−0.96	29.61
	1 day's former-maneuver arc	0.25	0.61	0.21	−0.96	30.24
2	Long former-maneuver arc	0.15	/	0.17	−1.43	57.51
	Long after-maneuver arc	0.15	0.56	0.18	−1.49	57.43
	1 day's former-maneuver arc	0.25	/	0.20	−1.55	55.97
3	Long former-maneuver arc	0.15	−0.51	−0.27	0.38	56.61
	Long after-maneuver arc	0.05	−0.30	−0.58	0.38	57.35
	1 day's former-maneuver arc	0.01	−0.25	/	0.24	59.67

Table 6.6 POD and prediction accuracy with 15 min arc (unit : m)

Arc		Strategy 1				Strategy 2			
		Radial	Transverse	Normal	Position	Radial	Transverse	Normal	Position
1	2 h prediction	1.4	3.2	1.3	3.7	2.5	3.8	3.2	5.5
	4 h prediction	2.6	3.4	1.5	4.6	3.9	3.8	2.4	5.9
2	2 h prediction	2.3	3.7	11.1	11.9	2.5	3.6	11.4	12.2
	4 h prediction	8.9	4.5	28.5	30.2	7.1	4.5	26.6	27.9
3	2 h prediction	1.0	7.5	3.3	8.2	1.6	9.5	4.2	10.5
	4 h prediction	7.7	13.6	8.3	17.7	8.8	14.3	9.6	19.3

Due to the absence of one station, the transponder time delay and station range system error calculated have little discrepancy between long arc determination and 1 day's determination.

The short arc determination tests are performed with 15, 30 min and 1 h segmental arc respectively. The POD and 2/4 h prediction precision is measured by reference orbit (Table 6.6) (Fig. 6.2).

With 15 min tracking arc, the 2 h prediction position accuracy is better than 15 m, and the radial accuracy is better than 2.5 m (Table 6.7) (Fig. 6.3).

With 30 min tracking arc, the 2 h prediction position accuracy is better than 10 m, and the radial accuracy is better than 2 m (Table 6.8) (Fig. 6.4).

With a 1 h tracking arc, the 4 h prediction position accuracy is better than 20 m, and the radial accuracy is better than 2.0 m.

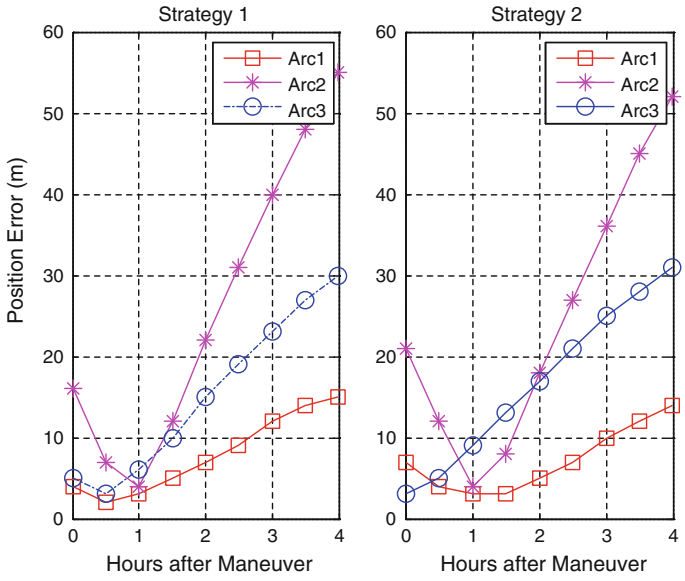

Fig. 6.2 POD and prediction accuracy with 15 min arc

Table 6.7 POD and prediction accuracy with 30 min arc (unit : m)

Arc		Strategy 1				Strategy 2			
		Radial	Transverse	Radial	Position	Radial	Transverse	Radial	Position
1	2 h prediction	1.2	3.2	2.0	4.0	2.2	3.7	2.5	5.0
	4 h prediction	1.9	3.6	5.2	6.6	3.0	3.8	4.6	6.7
2	2 h prediction	1.9	2.4	9.9	10.4	2.6	2.4	11.3	11.9
	4 h prediction	5.9	2.8	24.7	25.6	4.8	3.1	23.6	24.3
3	2 h prediction	0.4	3.3	4.2	5.4	0.9	4.9	4.9	7.0
	4 h prediction	3.9	7.6	10.5	13.6	4.7	7.9	11.7	14.9

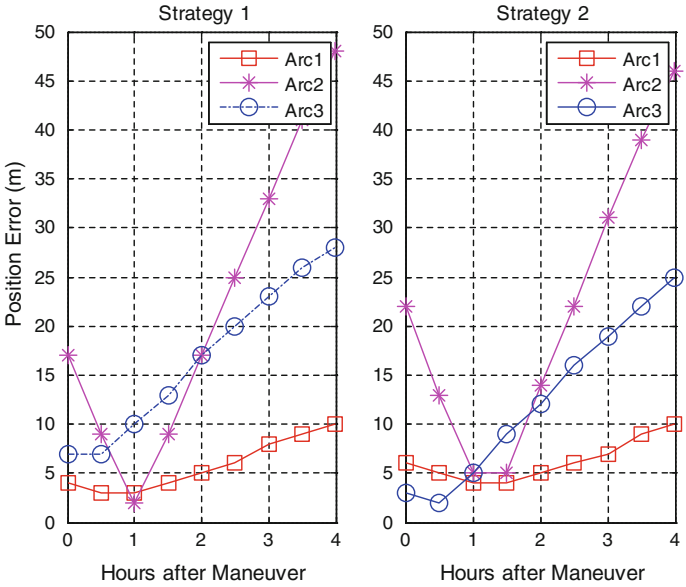

Fig. 6.3 POD and prediction accuracy with 30 min arc

Table 6.8 POD and prediction accuracy with 1 h arc (unit : m)

Arc		Strategy 1				Strategy 2			
		Radial	Transverse	Radial	Position	Radial	Transverse	Radial	Position
1	2 h prediction	1.0	2.8	2.5	3.8	1.9	3.3	2.7	4.6
	4 h prediction	0.7	2.7	6.3	6.9	1.6	2.9	5.7	6.6
2	2 h prediction	2.3	0.8	10.0	10.3	3.5	1.0	14.5	14.9
	4 h prediction	1.7	1.4	7.4	7.7	2.9	1.9	10.7	11.2
3	2 h prediction	0.7	1.5	9.0	9.1	0.7	4.5	8.0	9.2
	4 h prediction	0.5	1.3	21.2	21.3	1.0	3.4	20.1	20.4

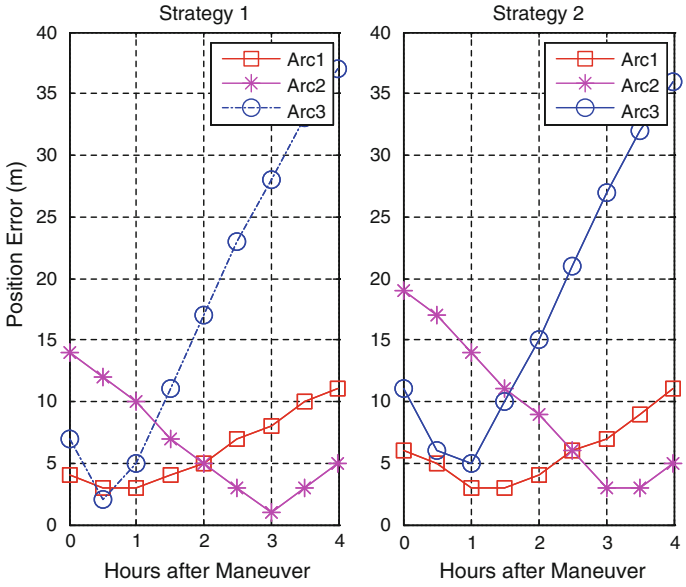

Fig. 6.4 POD and prediction accuracy with 1 h arc

By comparison, the first strategy is better that utilizes the system error solved with long arc before maneuver mainly due to its stability. Therefore, with the 15 min GEO satellite's dense and stable observational data, 2 h prediction position accuracy is better than 15 m using a short arc dynamics method. However, short arc orbit determination has poor stability.

6.4 Conclusions

The paper analyses and optimizes the short arc orbit determination strategy and explores the orbit recovery time limit after maneuver. The result is verified by the measurement from C band transponder by TWSTFT.

In conclusion, the short arc orbit determination uses the dynamic method can provide quickly the precise orbit prediction after GEO satellite maneuver by fixing satellite priori dynamics model and observation model information. With 15 min tracking arc, 2 h prediction position accuracy is better than 15 m, and the radial accuracy is better than 2.5 m.

However, short arc dynamics determination depends strongly the observation data. Because of the short time span of data, the higher precision and dense measuring are necessary. Meanwhile, system errors can not have suddenly deviation which means the whole system must have high stability.

It is only the preliminary result of short arc orbit determination. The stability of short arc orbit determination needs to be studied further aiming at shorting the recovery time of navigation satellite.

References

1. Zhang JL, Dong KF, Qiu HX, Zhu ZM (2008) Analysis of orbit determination of COMPASS-MEO navigation satellite with pseudorang. J Spacecraft TTC Technol 27(06):60–64
2. Huang Y, Hu XG, Huang C, Yang QW, Jiao WH (2008) Geo satellite orbit determination during maneuver with ranging data from CAPS. Sci China Ser G Phys Mech Astron 38(12):1750–1758
3. Guo R, Hu XG, Huang Y, He F (2010) Short-arc kinematic orbit determination based on ephemeris fitting. J Astronautics 31(2):416–422
4. Yin DM, Zhao Y, Li ZG (2007) Determination orbit of synchronous satellite with short segmental arc. AcASn 48(2):248–255
5. Yang XH, Li ZG, Feng CG, Guo J, Shi HL, Ai GX, Wu FL, Qiao RC (2008) Study the method of GEO satellite ephemeris recovery. Sci China Ser G Phys Mech Astron 38(12):1759–1765
6. Li ZG, Yang XH, Shi HL, Ai GX, Feng CG (2008) A new orbit measuring technique of transponder satellite. Sci China Ser G Phys Mech Astron 38(12):1711–1722
7. Li JS (1995) Satellite precision orbit determination. PLA Press, Beijing
8. Montentruck O, Gill E (2000) Satellite orbits models, methods, and applications. Springer, Berlin

Chapter 7
Precise Orbit Determination of BeiDou Regional Navigation Satellite System Via Double-Difference Observations

Jun Zhu, Jiasong Wang, Guang Zeng, Jie Li and Junshou Chen

Abstract The precise orbit determination (POD) for BeiDou satellites mainly relies on a regional tracking network distributed in China area at the present time. The multi-satellite POD for BeiDou regional navigation satellite system via double-difference observations is presented. First, the double-difference phase measurements are modeled on ionosphere-free combination of B1 and B2 signals. The POD strategies are detailed, followed by a brief data-processing flow. Then, the POD tests based on regional network of domestic monitoring stations are developed, and the orbit quality assessed by arc overlaps and Satellite Laser Ranging (SLR) residuals shows an accuracy of about 20 cm in radial direction. Finally, contributions of the overseas monitoring stations to the POD accuracy of BeiDou satellites are investigated by introducing several IGS Multi-GNSS Experiment (IGS M-GEX) monitoring stations with BeiDou tracking capability into the multi-satellite POD test. The improved orbit accuracy indicates that more BeiDou observing sites should be established worldwide in future.

Keywords Precise orbit determination (POD) · BeiDou regional navigation satellite system · Double-difference observation · Multi-GNSS experiment (M-GEX)

Foundation item: National Natural Science Foundation of China (41274018).

J. Zhu (✉) · J. Wang
State Key Laboratory of Astronautic Dynamics, Xian 710043, China
e-mail: zhujun9306@126.com

J. Zhu · J. Wang · G. Zeng · J. Li · J. Chen
Xi'an Satellite Control Center, Xian 710043, China

J. Sun et al. (eds.), *China Satellite Navigation Conference (CSNC) 2013 Proceedings*, Lecture Notes in Electrical Engineering 245,
DOI: 10.1007/978-3-642-37407-4_7,

7.1 Introduction

The Compass/Beidou Navigation Satellite System is a global navigation satellite system (GNSS), which is independently developed, deployed, and operated by China. This system is still in progress, and is designed to provide global coverage around 2020. At present, only the Beidou regional navigation satellite system has been built up, which can provide coverage in the Asia–Pacific region with Positioning, Navigation, Timing (PNT), and short-message communication service capabilities [1, 2].

The PNT performance of GNSS is directly related to the satellite orbit accuracy. The precise orbit determination (POD) for BeiDou satellites can reach a radial accuracy of decimeter level currently, which is limited in tracking hour and geometric strength of regional configuration of ground-tracks observing in China area [3–5]. The POD performance can be improved by adopting some appropriate data processing techniques, such as differenced data processing. Differences of the original observations allow to eliminate or to reduce some biases, such as clock offset of satellites and receivers. The single-difference is simply defined as determining the relative differences between a pair of receivers measuring satellite simultaneously, and the double-difference means differencing between a pair of receivers and a pair of satellites [6].

In this paper a multi-satellite POD approach of processing double difference observations of phase and pseudorange observations for BeiDou regional navigation satellite system is presented, and the orbit accuracy assessment is performed by the overlapping difference and post fit of satellite laser ranging (SLR) residuals. In addition, to investigate the contribution of the configuration of ground-tracks geometry to the POD accuracy, measurements from several IGS Multi-GNSS Experiment (IGS M-GEX) monitoring stations with BeiDou tracking capability are processed. And some initially results are obtained.

7.2 Observation Modeling

The BeiDou satellites transmit navigation signals in Quadrature Phase-Shift Keying (QPSK) modulation on a total of three frequency bands (B1, B2, B3) [1, 7], which can form many high-quality combinations for navigation data process. Refer to paper [8], the Beidou pseudorange at high elevation can reach an accuracy of 20 $\sim$ 40 cm, and the accuracy of phase at high elevation is about 3 mm.

7.2.1 Double-Difference Observations Modeling

Beidou navigation system's original phase observations can be modeled as

$$\begin{aligned}\phi_r^s(t) = & f\rho(t_s,t_r)/c - f\delta t_s + f\delta t_r + \Delta\phi_{\text{trop}} - \Delta\phi_{\text{iono}} \\ & + \Delta\phi_{\text{rel}} + \Delta\phi_{\text{mult}} + N_r^s + \varepsilon(t)\end{aligned} \tag{7.1}$$

where, ϕ_r^s is the phase observation from satellite s to receiver r, t is the observation epoch, $f\,(=\text{B1},\ \text{B2},\ \text{B3})$ is the signal frequency, $\rho(t_s,t_r)$ is the geometric distance from satellite to receiver, c is velocity of light, δt_s is the satellite clock offset, δt_r is the receiver clock offset, $\Delta\phi_{\text{trop}}$ is tropospheric delay error, $\Delta\phi_{\text{iono}}$ is ionospheric delay error, $\Delta\phi_{\text{rel}}$ is relativistic effects error, $\Delta\phi_{\text{mult}}$ is multipath effects error, N_r^s is integer ambiguity, and $\varepsilon(t)$ is measurement noise.

The double-difference phase between stations and satellites is defined as the difference between satellites of the single-difference, and the single-difference can be got by 2 stations $(m,\ n)$ observing the same satellite in the same epoch. The double-difference phase is given by

$$\text{DD}(m,n,j,k) = (\phi_{mj} - \phi_{nj}) - (\phi_{mk} - \phi_{nk}) \tag{7.2}$$

The best feature of double-difference observation is the clock offset error was completely eliminated. Relativistic effects and multipath effects error also was significantly weakened. If the 2 stations in double-difference observation are close to each other, the tropospheric and ionospheric effects could be weakened. Substituting Eq. (7.1) into (7.2), we get

$$\begin{aligned}\text{DD}(m,n,j,k) = & f\left(\rho_m^j - \rho_n^j - \rho_m^k + \rho_n^k\right)/c + \left(\Delta\phi_{\text{trop}}^{mj} - \Delta\phi_{\text{trop}}^{nj} - \Delta\phi_{\text{trop}}^{mk} + \Delta\phi_{\text{trop}}^{nk}\right) \\ & - \left(\Delta\phi_{\text{iono}}^{mj} - \Delta\phi_{\text{iono}}^{nj} - \Delta\phi_{\text{iono}}^{mk} + \Delta\phi_{\text{iono}}^{nk}\right) + N_m^j - N_n^j - N_m^k + N_n^k + \text{dd}(\varepsilon)\end{aligned}$$

Where $\text{dd}(\varepsilon)$ is the measurement noise of combined observations. The noise's variance is magnified after combination, and the noise contains the residual multipath error.

7.2.2 Ionospheric-Free Combination

Ionospheric delay error is the maximum error in Beidou navigation system observation, if the clock offset error could be eliminated. It depends on the total electron content (TEC) in ionosphere. The first order term of ionospheric delay error is the main part, and can be eliminated by dual-frequency data combination, which is

$$\text{IF}(\phi_1,\phi_2) = \frac{1}{f_1^2 - f_2^2}\left(f_1^2\phi_1 - f_2^2\phi_2\right) \tag{7.3}$$

The second order term is only about 0.1 % of the first, and can be eliminated by triple-frequency data combination. That is

$$\begin{aligned}\mathrm{DIF}(\phi_1,\ \phi_2,\ \phi_3) &= \mathrm{IF}(\phi_1,\ \phi_2)\ -\ \mathrm{IF}(\phi_2,\ \phi_3)\\ &= \left(\frac{f_1^2}{f_1^2\ -\ f_2^2}\ -\ \frac{f_1^2}{f_1^2\ -\ f_3^2}\right)\cdot\phi_1\ -\ \left(\frac{f_2^2}{f_1^2\ -\ f_2^2}\right)\cdot\phi_2\ +\ \left(\frac{f_3^2}{f_1^2\ -\ f_3^2}\right)\phi_3\end{aligned} \tag{7.4}$$

7.2.3 Tropospheric Delay Modelling

The zenith path delay (ZPD) due to tropospheric refraction is of the order of 2.3 m (or about 8 ns) for a station at sea level and standard atmospheric conditions, and can reach 20 m when elevation angle less than 10° [6]. Tropospheric delay contains two parts, the dry component and the wet component. We can calculate the tropospheric zenith delay by a priori model, and convert to the other directions using the mapping function. The dry component accounts for more than 90 % in tropospheric zenith delay. It could be almost completely corrected by using typical models, such as Hopfield model [9] or Saastamoinen model [10]. However, an uniform effective wet component correction model is difficult to build, due to the regional and seasonal changing characteristics of atmospheric humidity. In precise orbit determination, the wet component of tropospheric zenith delay is usually taken as a solve-for parameter in calculation. The whole tropospheric delay model can be written as

$$\Delta\rho_r^s(t,\ z)\ =\ \Delta\rho_{\mathrm{apr},\,k}\left(z_r^s\right)\ +\ \Delta\rho_k(t)f\left(z_r^s\right) \tag{7.5}$$

where, $\Delta\rho_r^s$ is the tropospheric path delay from receiver r to satellite s, z is the elevation of the observation scenario, $\Delta\rho_{\mathrm{apr},\,k}\left(z_r^s\right)$ is the slant delay according to an a priori model, $\Delta\rho_k(t)$ is the solve-for zenith path delay parameter, and $f\left(z_r^s\right)$ is the mapping function of $\Delta\rho_k(t)$.

7.2.4 Data Weighting

In satellite orbit determination, the numerical process method of code pseudorange and carrier phase measurements is weighting fusion. A typical prior weight is inversely proportional to measurement noise, and the measurement noise can be written as

$$\frac{\sigma_c}{\sigma_p}\ =\ 100 \tag{7.6}$$

where, σ_c is the measurement noise of code pseudorange, and σ_p is the measurement noise of carrier phase.

Table 7.1 System resulting data of standard experiment

Reference frame	
Station coordinate	ITRF2000 [15]
Data time tags	BDT
Solid tide	Wahr 1981 [16]
Ocean tide	GOT00 [12]
EOP	IERS C04
Precession/nutation	IAU2000 [17]
Planetary ephemeris	DE200
Gravity	JGM3 (12 × 12)
Satellite surface force and attitude	
Solar radiation	ECOM [13] + Box-Wing (pre-launch)
Thermo-radiation	Non-considered
Attitude	Nominal attitude
Data and parameterization	
Data using	Pseudorange and phase on frequency bands (B1, B2)
Data sampling and weighting	30s, elevation-dependent
Receiver and satellite clocks	Eliminated by double-differences
Troposphere model	Saastamoinen/Niell [14]
Antenna offset	Pre-launch
Phase windup	Wu (1993) [18]
Parameterization	Keplerian elements + CODE 9 parameters + ambiguities + zenith tropospheric delays

Observations at low elevations are generally much more susceptible to tropospheric refraction and multipath effects than those at high elevations. The unmodeled systematic errors decrease the quality of results. Using low-elevation observations, however, may also improve the estimation of tropospheric zenith delays and, consequently, the vertical component of station positions [11]. In order to optimize the use of low-elevation observations, there is an elevation-dependent weighting of observations, which is

$$w(\mathrm{z}) = \cos^2(\mathrm{z}) \tag{7.7}$$

7.3 POD Strategies

We apply the dynamic method to determine BeiDou satellites' orbit. The arc length is defined as 3 days. The ionospheric-free combination observations are used to form the double-difference observation equations. And the baselines are selected according to the criterion: the two stations have the maximum common-view satellites. The Least-Squares method is adopted for parameter estimation. The POD strategies are detailed in Table 7.1.

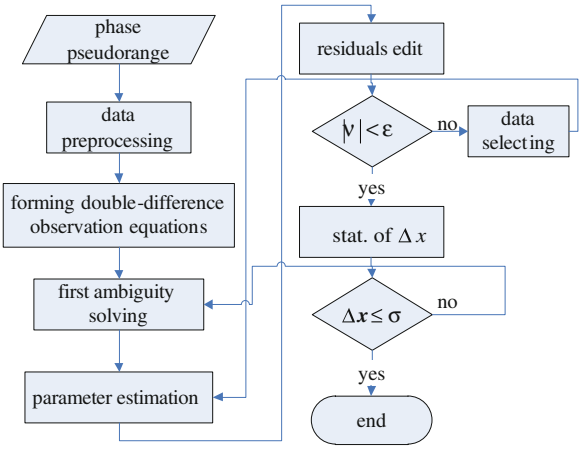

Fig. 7.1 A brief flow of data processing

A brief flow of data processing is showed as follows (Fig. 7.1).

7.4 POD Test Based on Regional Tracking Net

7.4.1 Overlapping Difference

A group of data from 07/17/2012 to 07/27/2012, domestic observation network data for 11 days, is selected for analysis. The orbit determination strategy is proposed in Part 3, determining a set of orbits with every 3 days observations (9 sets of orbits in total). So there is orbital overlap for 1 day between the set D the set D + 2. According to statistics orbit determination principle, the two sets of orbit, set D and D + 2, are mutually independence under ideal conditions. Therefore the consistency of the overlapping arcs orbits can be an index of the orbital accuracy in some way. Figure 7.2 shows the orbital overlapping differences of the Beidou operating satellites (C03, C05, C07, C10) in radial direction, and Fig. 7.3 shows the statistics of the three-dimensional orbital overlapping differences.

The results in Figs. 7.2 and 7.3 demonstrate the orbital differences in radial direction are about 20 cm, and about 1 m of three-dimensional position.

7.4.2 Independent SLR Residuals

Another method to estimate the precision of orbit determination is utilizing high-precision Satellite Laser Ranging (SLR) data for external checking on the results of the orbit determination. Independent SLR residuals directly reflect the precision

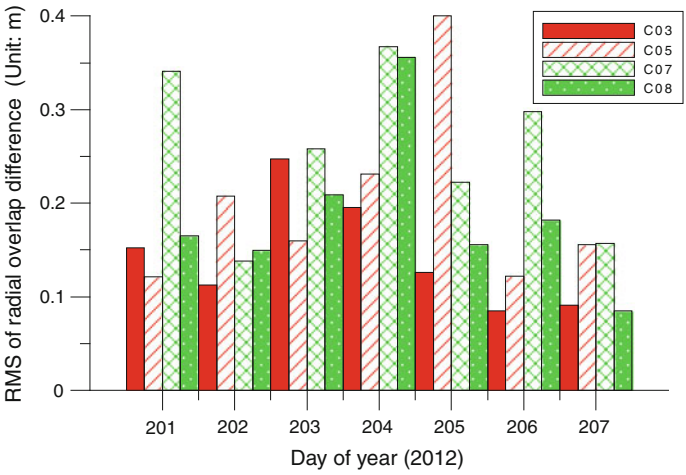

Fig. 7.2 Radial overlapping difference of BeiDou satellites

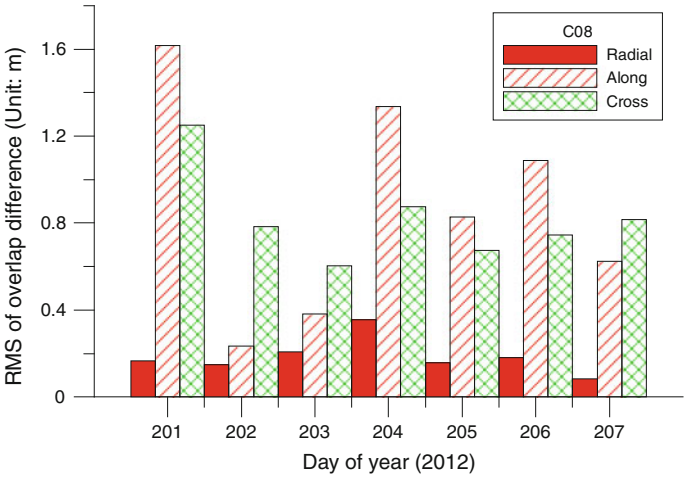

Fig. 7.3 Overlapping difference of BeiDou C08

of orbit determination. Supposing we get the SLR observation ρ_o at the time t, it can be expressed as

$$\Delta\rho = \rho_o - (\rho_c + \Delta\rho_{\text{stides}} + \Delta\rho_{\text{oloading}} + \Delta\rho_{\text{atm}} + \Delta\rho_{\text{rel}} + \Delta\rho_{\text{ec}} + \Delta\rho_{\text{st}} + \varepsilon \tag{7.8}$$

where, ρ_c is the distance from satellite to stations calculated by the POD results, $\Delta\rho_{\text{stides}}$ and $\Delta\rho_{\text{oloading}}$ are the influence of earth tides and sea tides to stations respectively, $\Delta\rho_{\text{atm}}$ is the atmospheric delay error which can be determined by

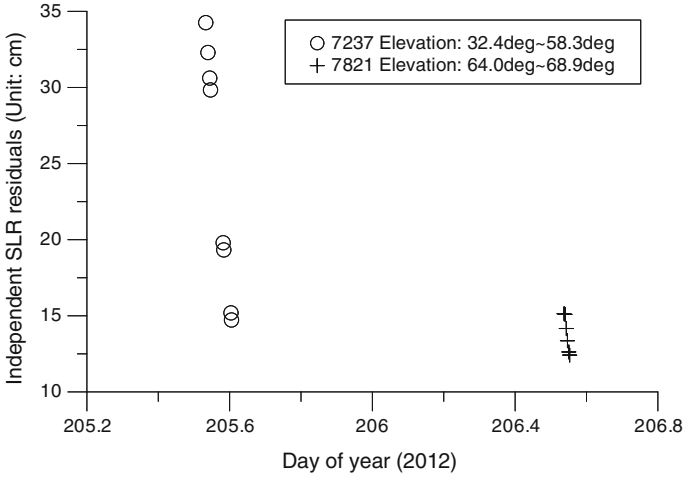

Fig. 7.4 Independent SLR residuals of BeiDou C08

Marini/Murray Model, $\Delta\rho_{rel}$ is the general relativity effects error, $\Delta\rho_{ec}$ and $\Delta\rho_{st}$ are the eccentric corrections and the displacement of observation stations respectively, ε is measurement error.

The SLR data we can get is relatively few. In the POD arcs mentioned in Part 4.1, we only have a small amount of data in July 23 (Station 7237) and July 24 (Station 7821). The post fit of SLR residuals were shown in Fig. 7.4. They indicate that the SLR residuals of Station 7821 are all less than 15 cm, while the SLR residuals of Station 7821 vary in 13 $\sim$ 35 cm. One possible reason is the elevation angles of Station 7821 are relatively lower.

7.5 IGS Multi-GNSS Experiment

In 2011, IGS initiated and organized an experiment utilize more than one navigation systems navigation, named IGS M-GEX. They tracked and monitored several GNSS signals at the same time in daily operations to analysis the performance and signal characteristics of the GNSS constellations emerging in recent years. Dozens of GNSS multimode tracking stations have been established in this experiment. Part of these stations can track Beidou Satellites, and they are shown in Table 7.2.

An analysis of Beidou satellite tracking data from these stations was presented in Ref. [8], and it preliminarily assessed the performance of Beidou regional navigation system. The results using orbit overlap method indicated that the precision of Beidou satellite orbits in three-dimensional position is 1 $\sim$ 10 m.

The M-GEX experiment provided valuable observations, which can be applied to study the influence of the layout of the station on the Beidou satellites POD

Table 7.2 M-GEX monitoring stations with BeiDou tracking capability

Name	Site	Lat	Long
CUT0	Bentley	−32.00	115.32
DLF1	Delft	51.59	4.23
KIR8	Kiruna	67.51	20.58
MAR7	Maartsbo	60.35	17.16
ONS1	Onsala	57.24	11.56
UNB3	Fredericton	45.57	293.21

precision. First, we analyzed the visibility of the satellite for tracking stations listed in Table 7.2. In the 6 stations listed in Table 7.2, all the stations except Station CUT0 are in the high latitudes. Actually, their tracking range for Beidou satellite is smaller, and there is low elevation observation data in almost all visible arcs. Figures 7.5 and 7.6 depicts the visibility of Beidou satellites to Station CUT0 and Station KIR8 for one day (Cut-off Elevation = 10°), respectively.

As illustrated in Fig. 7.5, the station CUT0 can observe two BeiDou GEOstationary (GEO) satellites (C03, C05), as well as all BeiDou Inclining Geostationary Synchronized Orbit (IGSO) satellites. Because it is located in southern hemisphere, this observing site should quietly enhance the geometric strength of the domestic regional tracking net. However, KIR8 has poor BeiDou tracking capability (Fig. 7.6). Almost no GEO satellite can be seen at this station. And most of the IGSO satellites are at low elevation. Obviously, measurements of KIR8 have limited contribution to POD of BeiDou satellites.

When integrating the observations obtained from M-GEX stations and observations from the domestic regional tracking net to carry out the POD test at the

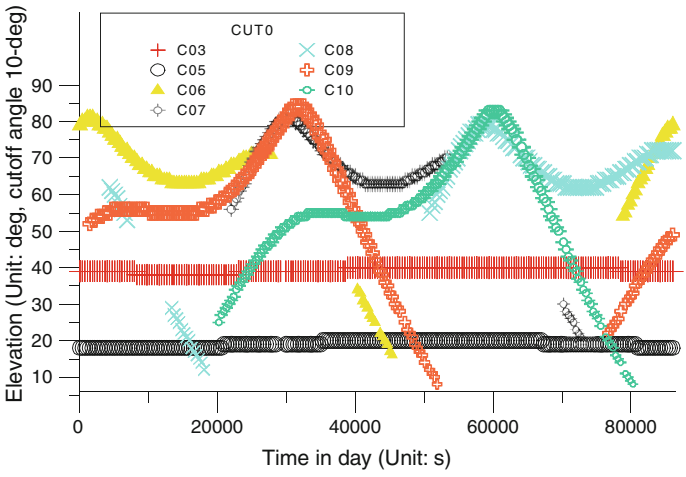

Fig. 7.5 Visibility of BeiDou satellites at station CUT0

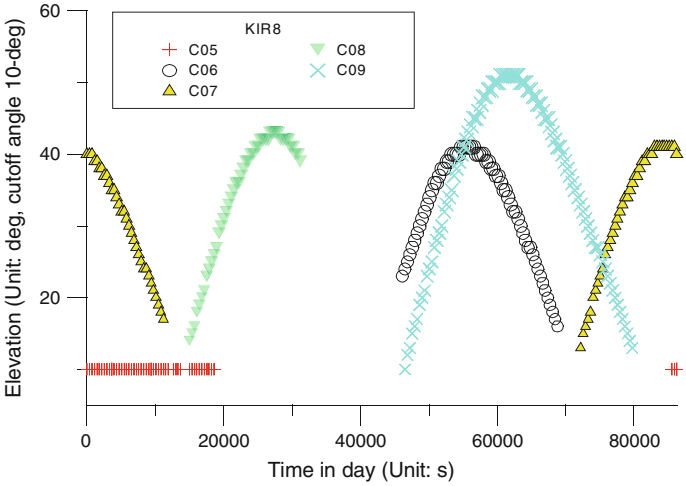

Fig. 7.6 Visibility of BeiDou satellites at station KIR8

same data period of time defined in Sect. 7.4, we can obtain a new result (Figs. 7.7 and 7.8).

In this two figures (Figs. 7.7 and 7.8), most of the radial overlapping differences of BeiDou satellites have decreased within 20 cm, and 3-D position differences have fall within 1 m, according to Figs. 7.2 and 7.3. As a result, though most of the IGS M-GEX monitoring stations have limited tracking capability for BeiDou satellites, they have improved the orbit accuracy a lot, compared to the orbit

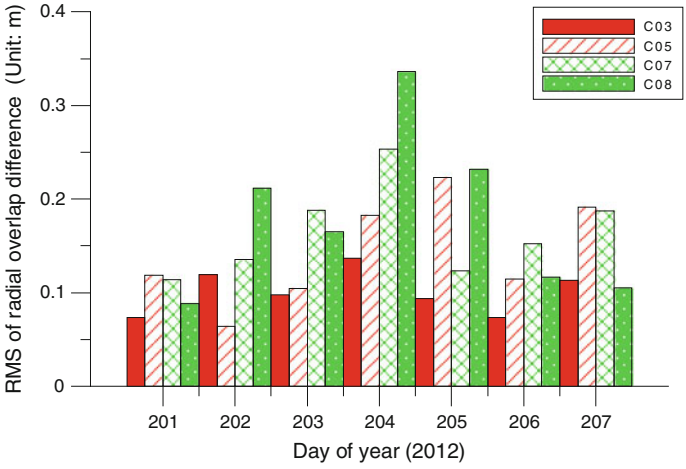

Fig. 7.7 Radial overlapping difference of BeiDou satellites, supported by IGS M-GEX monitoring stations

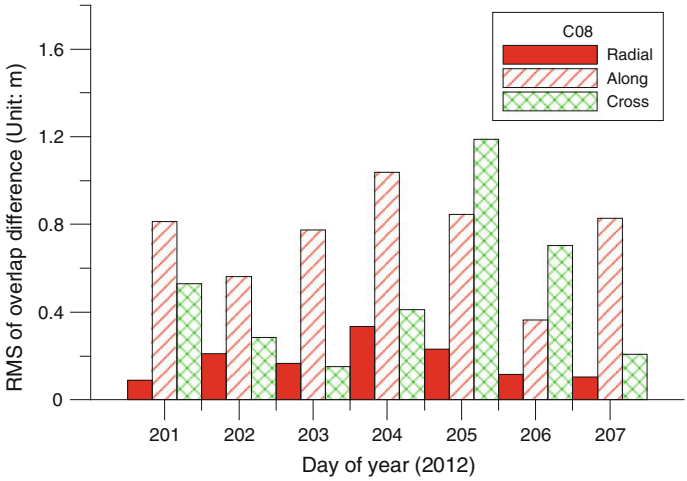

Fig. 7.8 Overlapping difference of BeiDou C08, supported by IGS M-GEX monitoring stations

derived from domestic tracking data only. The benefit of offshore monitoring stations is exhibited here preliminarily.

7.6 Summary and Conclusions

The multi-satellite POD for BeiDou regional navigation satellite system based on double-difference observation processing is discussed in this paper. Tests using overlapping differences and SLR residuals suggest the double-difference solutions of BeiDou regional ground-tracks net have achieved 20 cm radial accuracy, which can satisfy the needs of our domestic navigation users in the near future. With several IGS M-GEX monitoring stations observing BeiDou satellites supplied, the higher orbital accuracy can be obtained. Therefore, to improve the PNT service capability, it is of critical strategic significance to build up more BeiDou monitoring stations in the global region.

References

1. CSNO (2011) BeiDou navigation satellite system signal in space interface control document (Test Version), China satellite navigation office, December 2011. URL http://www.beidou.gov.cn/
2. Yang YX, Li JL, Xu JY et al (2011) Contribution of the compass satellite navigation system to global PNT users. Chinese Sci Bull 56(21):P1734–P1740
3. Wen Y, Liu Q, Zhu J et al (2007) The effect of TT and C deployment on the regional satellite navigation system, J Nat Univ Defense Technol, 29(1):P1–P6

4. Jianhua Z, LiuCheng C, XiaoGong H et al (2010) The precise orbit determination of GEO navigation satellite with multi-types observation, Scientia Sinica Phys.Mech and Astron, 40(5):P520–52
5. Geng T, Zhao Q (2009). Determining orbit of COMPASS-M1 Using international laser ranging data. Geomatics and information science of Wuhan University, 34(11):P1290–1292
6. Kaplan ED, Hegarty CJ (2006) Understanding GPS: principles and applications (Second edn). Norwood, MA 02062: ARTECH HOUSE
7. Han C, Yang Y, Cai Z (2011) BeiDou navigation satellite system and its timescales. Metrologia 48:P213–P218
8. Montenbruck O, Hauschild A, Steigenberger P et al (2012) Initial assessment of the COMPASS/BeiDou-2 regional navigation satellite system, Springer GPS Solut
9. Goad CC, Goodman L (1974) A modified hopfield tropospheric refraction correction model, In: Proceedings of the fall annual meeting of the american geophysical union, San Francisco, California, December 12–17
10. Saastamoinen II (1973) Contribution to the theory of atmospheric refraction[J]. Bulletin Geodesique 107:P13–P34
11. Meindl M, Schaer S, Hugentobler U et al (2004) Tropospheric gradient estimation at CODE: results from global solutions, in applications of GPS remote sensing to meteorology and related fields. J Meteor Soc Japan, 82(1B), P331–338, Meteorological Society of Japan
12. Ray RD (1999) A global ocean tide model from TOPEX/Poseidon altimetry: GOT99.2. NASA TM-1999-209478, NASA Goddard Space Flight Center, September
13. Springer TA, Beutler G, Rothacher M (1999) A new solar radiation pressure model for the GPS Satellites. GPS Solutions 3(2):P50–P62
14. Niell AE (1996) Global mapping functions for the atmosphere delay of radio wavelengths. J Geophys Res 101:P3227–P3246
15. Altamimi Z, Sillard P, Boucher C (2002) ITRF2000: A new release of the International Terrestrial Reference Frame for Earth science applications. J Geophys Res 107(B10):19
16. Wahr JM (1981) The forced nutation of an elliptical, rotating, elastic and oceanless Earth. Geophys J R astr Soc 64:705–727
17. McCarthy DD, Petit G (2004) IERS Conventions (2003) IERS Technical Note No. 32, 33–56
18. Wu JT, Wu C, Hajj GA, Bertiger WI, Lichten SM (1993) Effects of antenna orientation on GPS carrier phase. Manuscripta Geodaetica 18:91–98

Chapter 8
Accuracy Analyses of Precise Orbit Determination and Timing for COMPASS/Beidou-2 4GEO/ 5IGSO/4MEO Constellation

Shanshi Zhou, Xiaogong Hu, Jianhua Zhou, Junping Chen, Xiuqiang Gong, Chengpan Tang, Bin Wu, Li Liu, Rui Guo, Feng He, Xiaojie Li and Hongli Tan

Abstract Up to the end of October 2012, 14 COMPASS/Beidou-2 regional satellite navigation satellites are fully operational. Different with Global Positioning System (GPS), the space segment of COMPASS consists of Geostationary Earth Orbit (GEO) satellites, Inclined Geosynchronous Satellite Orbit (IGSO) satellites and Medium Earth Orbit (MEO) satellites, and navigation information is provided by monitoring stations limited in regional area. Besides, attitude control mode is different for each type of satellites. The predictability of satellite attitude will make broadcast ephemeris precisely predicted. In this study, satellite telemetry data are compared with nominal attitude to assess the accuracy of satellite attitude prediction. Experiments show that the accuracy is different for each type satellites, and overall prediction accuracy is better than 1°. The analyses of pseudo-range multipath noise for receivers from different manufacturers show that the random noise characteristics is significantly for the US and European manufacturers' receivers, and the magnitude is larger than domestic manufacturers', but strong daily repeatability of multipath noise characteristics is displayed for domestic receivers. The accuracy of precision orbit determination (OD) for COMPASS using regional and global monitoring stations data are compared to evaluate the impact of monitoring stations' distribution on the accuracy of satellite OD. Satellite Leaser Range (SLR) residuals are adopted to assess the satellite orbit accuracy in station line-of-sight direction. The results show that the accuracy of satellite orbit overlap is about 0.2, 1.2 and 0.6 m in R/T/N direction for regional monitor network, the accuracy for MEO overlap is slightly worse than two other type satellites, and the SLR residual is better than 1 m. The two-way satellite time

S. Zhou (✉) · X. Hu · J. Chen · X. Gong · C. Tang · B. Wu
Shanghai Astronomical Observatory, Chinese Academy of Sciences,
Shanghai 200030, China
e-mail: sszhou@shao.ac.cn

J. Zhou · L. Liu · R. Guo · F. He · X. Li · H. Tan
Beijing satellite navigation center, Beijing 100094, China

J. Sun et al. (eds.), *China Satellite Navigation Conference (CSNC) 2013 Proceedings*, Lecture Notes in Electrical Engineering 245,
DOI: 10.1007/978-3-642-37407-4_8,

frequency transfer (TWSTFT) observations are adopted to evaluate the accuracy of satellite clock error estimations. Experiments show that the standard deviation of satellite clock estimations solved by OD is about 1.4 ns. Global monitoring stations can increase the depth of coverage for MEO satellites, and the accuracy of clock estimations may be improved by about 0.6 ns. The observations from multi-constellation GNSS receiver are adopted to realize the system timing service. The results show that the stability of time system for COMPASS is consistent with GPS, the standard deviation of comparison for COMPASS and GPS precise timing is about 1.5 ns, the real time timing is about 3 ns.

Keywords COMPASS/Beidou-2 · Satellite attitude · Multi-path noise · POD · Timing

8.1 Introduction

As of October 25, 2012, a total of 16 Chinese COMPASS/Beidou-2 regional navigation system satellites has been launched [1]. Now 14 satellites are fully operational except 2 test satellites. Similar with other Global Navigation Satellite Systems (GNSS), COMPASS transmits L-band ranging signal and provides real-time broadcast ephemeris information to global area to provide real-time navigation positioning and timing (PNT) services.

Different with other GNSS, the space segment consists of GEO, IGSO and MEO satellites. The existent of GEO satellites increase correlation of orbit determination (OD) estimations, which may decrease the OD accuracy and stability. Since the monitoring stations limited to the territory of China area, and all stations located in the same side of the GEO satellite orbital plane, we rise to the challenge of mix constellation precise orbit determination. Furthermore, MEO satellite orbit can't be covered by regional tracking network. The coverage of MEO is less than 50 %, which may decrease the accuracy of MEO orbit estimations. Last, different attitude control modes are applied to each type COMPASS satellites. The satellite antenna phase center correction mode should be established accordingly in OD, positioning and timing processing.

Currently, many researchers had carried out studies for COMPASS OD and positioning. Reference [2] analyzed the code and carrier phase noise and satellite clock character for 4GEO/5IGSO constellation. The baseline vector is recovered with an accuracy of 2, 4, and 9 mm in the east, north, and up directions relative to the mean value of a GPS-based solution. Considering the highly correlation between orbital and satellite clock estimations, Ref. [3] proposed a new method for orbit accuracy assessment by two-way satellite time frequency transfer (TWSTFT) measurements. Reference [4] found that solve empirical acceleration estimations may increase the correlation of solar radiation pressure estimations and decrease orbit accuracy for 2GEO/1IGSO constellation. Reference [5] adopting regional tracking network assessed orbit accuracy and post-time and real-time positioning

error. Precise Point Positioning (PPP) accuracy is about 5 and 10 cm in horizontal and vertical direction. Within Chinese regional area, three-dimensional accuracy for open and authorized service positioning is about 5 and 3 m in terms of Root-Mean-Square (RMS). Reference [6] achieved precise OD and Real-time kinematic (RTK) positioning for 2GEO/3IGSO constellation using Beidou Experimental Tracking Stations (BETS) which lay in the Asia–Pacific region and established by Wuhan University since early 2011. The overlap accuracy is 10 cm in orbital radial direction. The static PPP accuracy is about centimeter-level, relative positioning accuracy is about millimeter-level for short baseline and RTK accuracy is about 4 m.

This study assesses the prediction accuracy of satellite nominal attitude comparing with satellite telemetry data, and provides satellite antenna phase center correction model for each type satellites. The pseudo-range noise characteristics of different manufacturers' receiver are compared. Tracking network distribution impact on OD accuracy is assessed for 4GEO/5IGSO/4MEO constellation. Satellite Laser Ranging data are adopted to evaluate orbit accuracy and verified the feasibility of orbit accuracy assessment method proposed in Ref. [3]. Multi-constellation GNSS receiver data are adopted to compare COMPASS precise and real-time timing accuracy with GPS timing service.

8.2 Algorithms

8.2.1 Satellite Attitude

Satellite attitude describes the relationship between satellite body-fix coordinate system and satellite orbit coordinate system. Define satellite mass center as the origin, satellite motion direction as X-axis, orbital plane normal direction as Y-axis, and Z-axis orthogonal to the XOY plane. The attitude angle of rotation about the X/Y/Z axis is called roll, pitch and yaw angle respectively.

Different attitude control modes are utilized for COMPASS satellites. Orbit-normal mode is applied to GEO satellites, which define satellite to center of the earth direction as Z-axis, the direction orthogonal to satellite position and velocity plan as Y-axis, and X-axis orthogonal to YOZ plane. Yaw-steering mode is applied to IGSO/MEO satellites, which define the same Z-axis as orbit-normal mode, Y-axis perpendicular to the plane of sun-earth-satellite, and X-axis orthogonal to YOZ plane. Accordingly, satellite antenna phase center should be established for each type satellite in OD processing [7]. COMPASS provides the satellite telemetry measurements. We compare it with nominal attitude prediction to evaluate the accuracy of attitude prediction. Figure 8.1 shows the yaw angel prediction errors time series for each type satellite. Since yaw angle is zero for GEO, only yaw angle measurements are figured out in first row. The bottom left two sub graphs show IGSO/MEO yaw angle time series, and the right two graphs

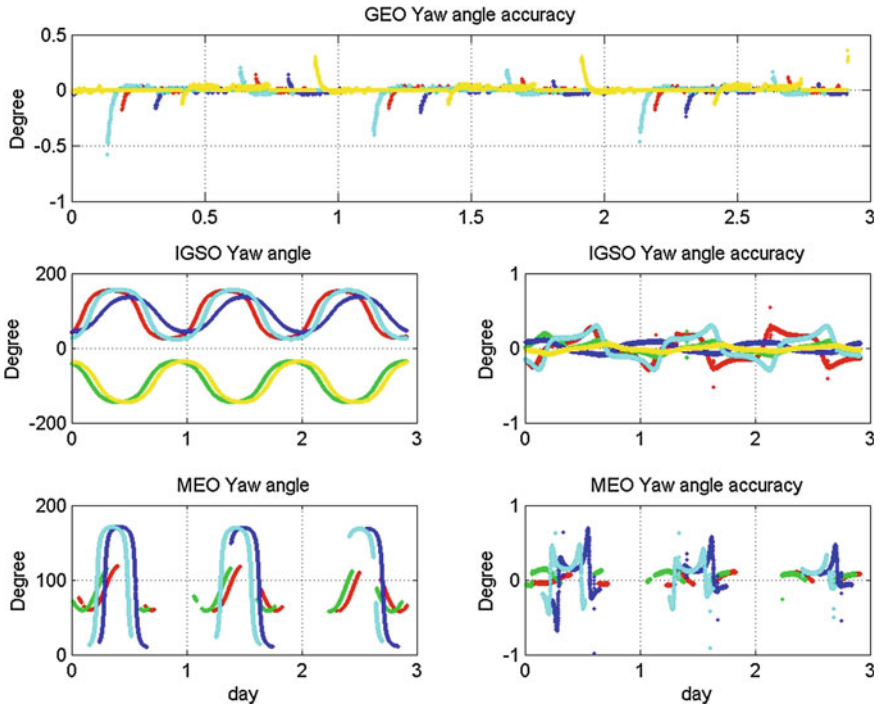

Fig. 8.1 Satellite yaw angle prediction errors time series. Different colors represent different satellites. The *top* row satellite yaw angle prediction errors. The *bottom left* two sub graphs show IGSO/MEO yaw angle time series, the *right* two graphs show IGSO/MEO yaw angle prediction errors. Unit is angle degree

show IGSO/MEO yaw angle prediction errors. Different colors represent different satellites.

Figure 8.1 shows that the accuracy of yaw angle prediction are better than 0.5°, 0.5° and 1° for GEO/IGSO/MEO respectively. As shown in telemetry measurements, roll and pitch angle are close to zero, which are in accord with nominal attitude. Consequently, only yaw angle should be considered in satellite antenna phase center correction model. The expression can be written as:

$$\begin{pmatrix} X \\ Y \\ Z \end{pmatrix} = R_{ciscts} \cdot \begin{pmatrix} \bar{e}_x & \bar{e}_y & \bar{e}_z \end{pmatrix} \cdot \begin{pmatrix} x_{phs} \\ y_{phs} \\ z_{phs} \end{pmatrix}, \quad d\rho_{phs} = \begin{pmatrix} X \\ Y \\ Z \end{pmatrix}^T \cdot \frac{\bar{r}_{sta} - \bar{r}}{|\bar{r}_{sta} - \bar{r}|} \tag{8.1}$$

where R_{ciscts} is rotation matrix between Conventional inertial system (CIS) and Conventional inertial system (CTS), $\bar{r}_{sta}$ is location of receiver, $d\rho_{phs}$ is satellite antenna center phase correction in line-of-sight direction.

For GEO satellites:

$$\bar{e}_z = -\frac{\bar{r}}{|\bar{r}|},\ \bar{e}_y = \bar{e}_z \times \frac{\bar{v}}{|\bar{v}|},\ \bar{e}_x = \bar{e}_y \times \bar{e}_z \tag{8.2}$$

For IGSO/MEO satellites:

$$\bar{e}_z = -\frac{\bar{r}}{|\bar{r}|},\ \bar{e}_y = \bar{e}_z \times \frac{\bar{r}_{sun} - \bar{r}}{|\bar{r}_{sun} - \bar{r}|},\ \bar{e}_x = \bar{e}_y \times \bar{e}_z \tag{8.3}$$

Where $\bar{r}$, $\bar{v}$ and $\bar{r}_{sun}$ are satellite position, velocity and sun position vector in CIS respectively.

Antenna phase center of COMPASS satellites relative to the mass center is mainly in Z direction, the direction from satellite to earth center. The phase center correction is meter level for ground receiver, while the nominal attitude prediction error impact on antenna correction is less 1 mm. So the nominal attitude could be used in antenna phase center correction model. Due to length limitation, corrections for are not listed.

8.2.2 Orbit Determination and Timing

In this paper, the multi-satellite orbit determination (MPOD) strategy is adopted. The estimations are orbital parameters (initial orbital elements, solar radiation pressure parameters and empirical acceleration parameters) for all satellites, receiver zenith delay and satellite and receiver clock errors for each epoch. Limited by the regional monitoring network distribution, 3 day arc with 60 s sampling pseudo-range and carrier phase ionospheric free combinations are adopted. See Ref. [2, 5] for details.

Known satellite orbit and clock errors information, receiver location and clock errors could be estimated, and simultaneously system positioning and timing service is realized. Positioning accuracy is discussed in Ref. [5], only timing accuracy is shown in this study.

Considering the correlation of receiver position and clock errors estimation, we fix receiver position and get receiver clock errors by averaging ranging residual of all visible satellite. Receiver clock errors can be written as:

$$Clk_{sta}(i) = \frac{1}{n}\sum\nolimits_1^n oc_{sta}^j(i) \tag{8.4}$$

Where $Clk_{sta}(i)$ is the receiver clock in epoch i, $oc_{sta}^j(i)$ is ranging residual from satellite j to receiver in epoch i, which can be calculated using satellite and receiver position, satellite clock error and systemic error correction models [8], n is the number of visible satellite.

Depending on the accuracy of ephemeris, system timing could be divided into precise and real-time service. Post-processing precise orbit and precise satellite clock errors are used for precise timing, and broadcast ephemeris for real-time service. Multi-constellation GNSS receiver observations are adopted to get

receiver clock errors in GPS and COMPASS system. Comparing COMPASS precise receiver clock errors with GPS precise clock errors to evaluate COMPASS precise timing accuracy, and comparing real-time clock errors estimations for real-time timing accuracy.

8.3 Results

8.3.1 Observation Noise

Reference [9] shows that pseudo-range measurements are seriously affected by multi-path noise for COMPASS, especially for GEO satellites. To analyze pseudo-range multipath noise, differences between pseudo-range and carrier phase B1I/B2I ionospheric free combinations (PC-LC) are figured out. These differences include carrier phase ambiguity, dual-frequency pseudo-range and carrier phase observation noise and multi-path noise. 7 receiver made by domestic manufacturers which are located within China territory and 12 receiver made by US and European manufacturers which are located abroad are compared in this study. Foreign manufacturers' receiver and antenna type are listed in Table 8.1.

PC-LC time series for Beijing and Curtin are shown in Fig. 8.2. The noise of Beijing (domestic manufacturer) shows multi-path characteristic obviously. The daily repeatability feature is significant for GEO satellites. IGSO/MEO also show daily repeatability and observation white noise decrease when satellites are tracked by receiver. Curtin receiver (TRIMBLE NETR9) shows white noise characteristic, and the magnitude of noise is larger than Beijing receiver. It should be noted that both PC-LC time series are combined by original observation. GEO PC-LC RMS for Beijing is 0.3 m, while for Curtin is 1.3 m. The average of 3 day arc PC-LC RMS for domestic receivers is about 0.7, 0.7 and 0.8 m for GEO/IGSO/MEO satellites respectively, and 1.1, 1.5 and 1.4 m for other receiver.

Draw PC-LC series for IGSO/MEO satellites with observation elevation angle in Fig. 8.3. The left four sub graphs represent domestic manufacturer receivers, the right represent foreign receiver. Different colors represent different located receiver. Comparing low elevation noise in the two columns, both type receivers show the noise about 10 m. With elevation angle increase, the PC-LC noise

Table 8.1 Foreign manufacturers' receiver and antenna type

Site ID	Receiver type	Antenna type	Site ID	Receiver type	Antenna type
BRST	TRIMBLE NETR9	TRM57971.00	MAR7	TRIMBLE NETR9	LEIAR25.R3
CUT0	TRIMBLE NETR9	TRM59800.00	ONS1	TRIMBLE NETR9	LEIAR25.R3
DLF1	TRIMBLE NETR9	LEIAR25.R3	REUN	TRIMBLE NETR9	TRM55971.00
GRAC	TRIMBLE NETR9	TRM55971.00	UNB3	TRIMBLE NETR9	TRM57971.00
KIR8	TRIMBLE NETR9	LEIAR25.R3	UNBS	SEPT POLARXS	TRM55971.00
LMMF	TRIMBLE NETR9	TRM55971.00	USN4	SEPT POLARX4TR	AOAD/M_T

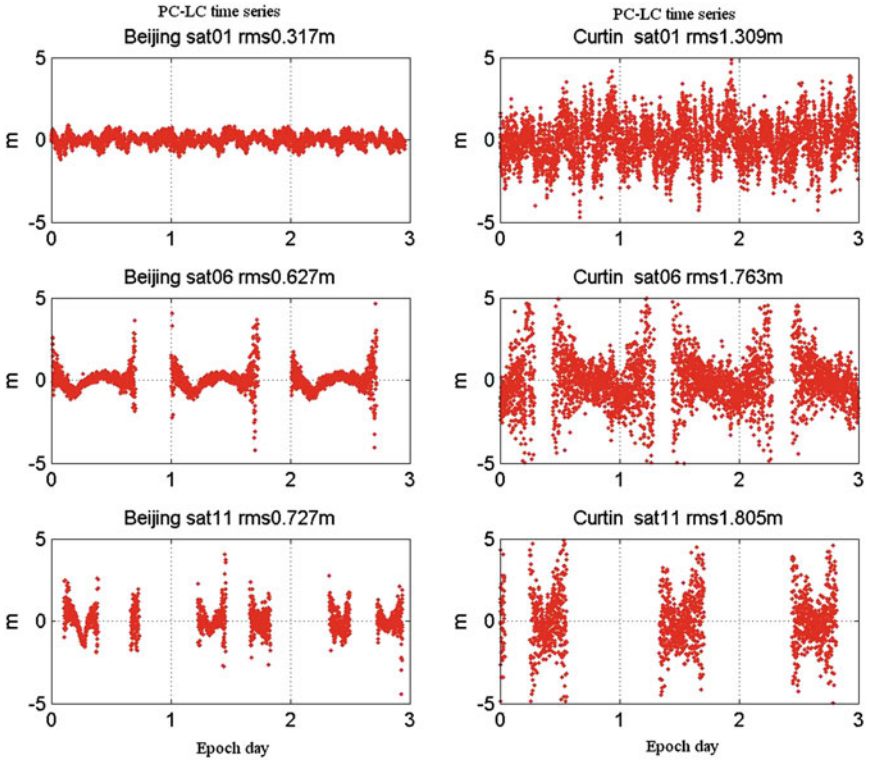

Fig. 8.2 PC-LC time series for Beijing and Curtin receiver. The *top*/*middle*/*bottom* rows represent GEO/IGSO/MEO respectively. *Left* three sub graphs represent PC-LC for Beijing and *right* for Curtin station

decrease dramatically for domestic manufacturer receiver, while slowly for foreign receivers.

8.3.2 Orbit Accuracy

Adopting regional monitor network dataset from Nov. 13th 2012 to 19th, 4GEO/5IGSO/4MEO constellation satellite orbital parameters are determined. Table 8.2 shows MPOD residual and 24 h overlap RMS in orbital radial (R), along-track (T) and orbital normal (N) direction. SAT01-05 are GEO, 06-10 are IGSO and 11–14 are MEO satellites. Pseudo-range residual is about 80 cm, and carrier phase is about 0.8 cm. The residuals differ for each type satellites, GEO residual is slightly larger than two other type satellites. Compare two 3 day arc with 24 h overlapped, three-dimension error is about meter level, GEO orbital R/T/N error are 0.2, 1.8 and 0.3 m respectively. IGSO orbital error in T direction is less than GEO, and

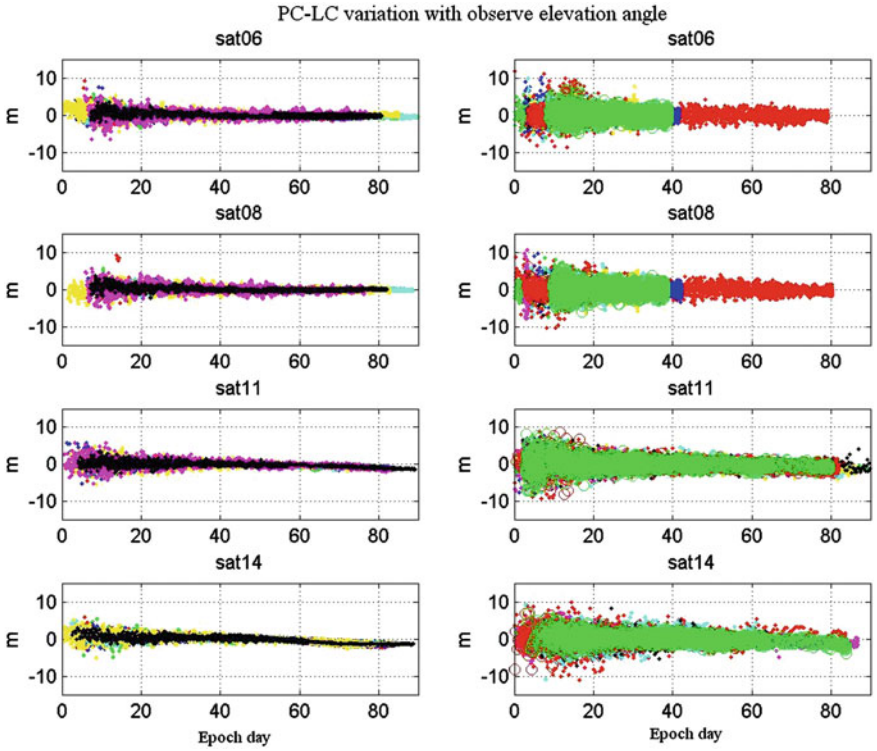

Fig. 8.3 PC-LC variation with observe elevation angle. The *top* two rows represent IGSO, *bottom* two represent MEO, *left* sub graphs are domestic and *right* are foreign receivers. *X-axis* is elevation (unit: degree), *Y-axis* is PC-LC (unit: m). Different colors represent different receivers

Table 8.2 MPOD overlap error and MPOD residual

SATID	dR/m	dT/m	dN/m	PC/cm	LC/cm
01	0.101	2.305	0.230	96.14	0.57
03	0.123	1.245	0.311	66.90	0.59
04	0.214	3.550	0.100	85.35	0.61
05	0.348	0.338	0.689	92.24	0.76
06	0.129	0.763	0.527	63.22	0.68
07	0.262	0.889	0.951	66.30	0.69
08	0.124	0.571	0.459	57.08	0.70
09	0.147	0.807	0.487	58.15	0.63
10	0.264	1.266	1.009	58.65	0.62
11	0.313	0.656	0.970	78.11	0.88
12	0.305	1.035	0.848	85.84	0.79
13	0.493	1.435	0.397	76.37	0.85
14	0.232	1.110	0.364	87.47	0.87

about 0.2, 0.8 and 0.7 m in three directions. MEO orbital error in R direction is larger than GEO and IGSO, about 0.3 m. T/N errors are 1 and 0.6 m.

SLR data are adopted to evaluate the orbit accuracy in station line-of-sight direction. Nov. 13th to 15th residual RMS is about 0.2 m for SAT08, and 0.9 m for SAT10.

8.3.3 Satellite Clock Errors Accuracy

According to Ref. [5], TWSTFT measurements can be used to assess orbital errors. Table 8.3 shows the RMS of satellite clock difference between MPOD estimations and the TWSTFT measurements. Except SAT04 whose RMS is about 3 ns, other three GEO RMS is about 1 ns, IGSO/MEO accuracy is about 1.4 ns.

Comparing SLR residual and clock errors difference obtained above in Fig. 8.4. The red lines represent clock errors difference and blue lines represent SLR residual. Three rows mean three arcs. Figure 8.4 shows that the two time series have similar variation trend.

Comparing orbital overlap time series with clock estimations obtained by two MPOD, shown in Fig. 8.5. Orbital difference in R/T/N direction is shown as red, green and blue line, and clock difference as light blue line. Three rows represent three type satellites. Figure 8.5 shows that the clock difference is highly correlated with orbital difference in R direction, especially for GEO and IGSO satellites. Beside, the differences in T/N direction impact the average of clock difference. Considering the high correlation between satellite orbital error in R direction and clock error estimations, we could assess orbit accuracy by comparing satellite clock estimations with TWSTFT observations.

8.3.4 Tracking Network Distribution Impact on OD Accuracy

As analysis in Sect. 8.3.2, regional tracking network can not cover MEO orbit arc, orbital overlap error for MEO is less than GEO/IGSO. To assess network

Table 8.3 Satellite clock errors difference RMS (Unit : ns)

SATID	RMS	SATID	RMS
01	1.385	09	1.555
03	1.090	10	1.799
04	2.965	11	1.021
05	0.903	12	0.842
06	1.196	13	1.887
07	1.491	14	1.265
08	1.192		

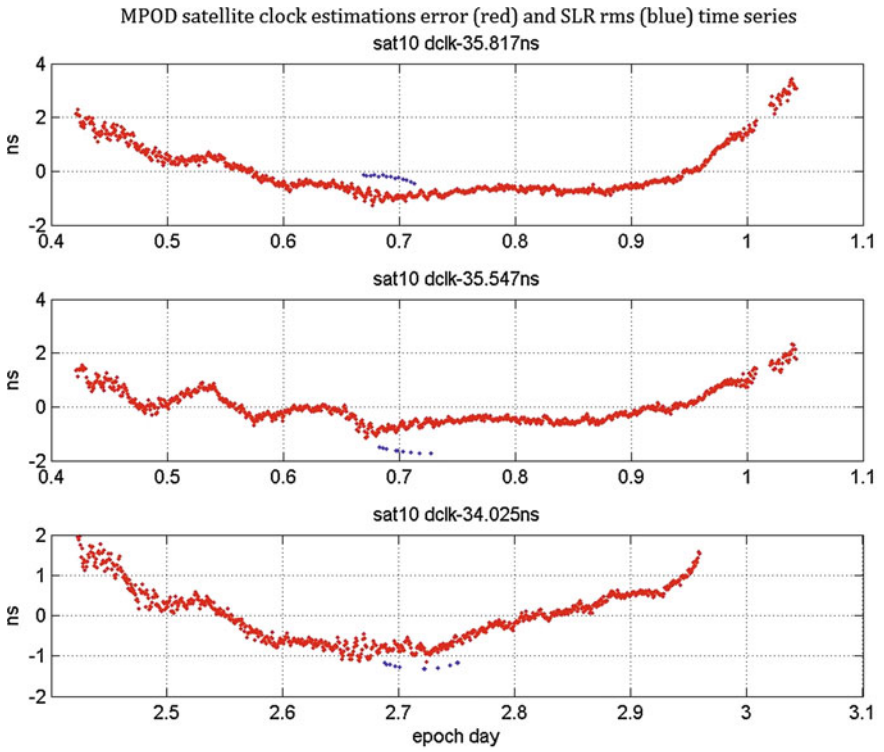

Fig. 8.4 SLR residual and clock errors difference time series. The *red lines* represent clock errors difference and *blue lines* represent SLR residual

distribution impact on OD accuracy, 12 IGS multi-constellation GNSS receiver are adopted. These receivers are distributed in Europe, American and Australia and listed in Table 8.1. Figure 8.6 shows the depth of coverage (DOC) with abroad stations. It's obviously that these stations could increase DOC for IGSO and MEO satellites.

Table 8.4 shows the orbital overlap and clock accuracy of MPOD adopting abroad stations data. Comparing with Table 8.2, orbital overlap accuracy for IGSO is the same as regional tracking network, while R/T/N accuracy increase 0.1 m respectively for MEO satellites. Comparing clock accuracy in Table 8.4 with Table 8.3, it has been improved 0.7 and 0.4 ns for IGSO and MEO. The improvements indicate that adopting abroad station may enhance the DOC for IGSO and MEO. The reason of different improvements for IGSO and MEO is that adding abroad stations, MEO orbital arc is still not completely covered, and continuity of abroad stations observation is worse than China regional network. Hence, the clock accuracy improvement for MEO is less than IGSO satellites.

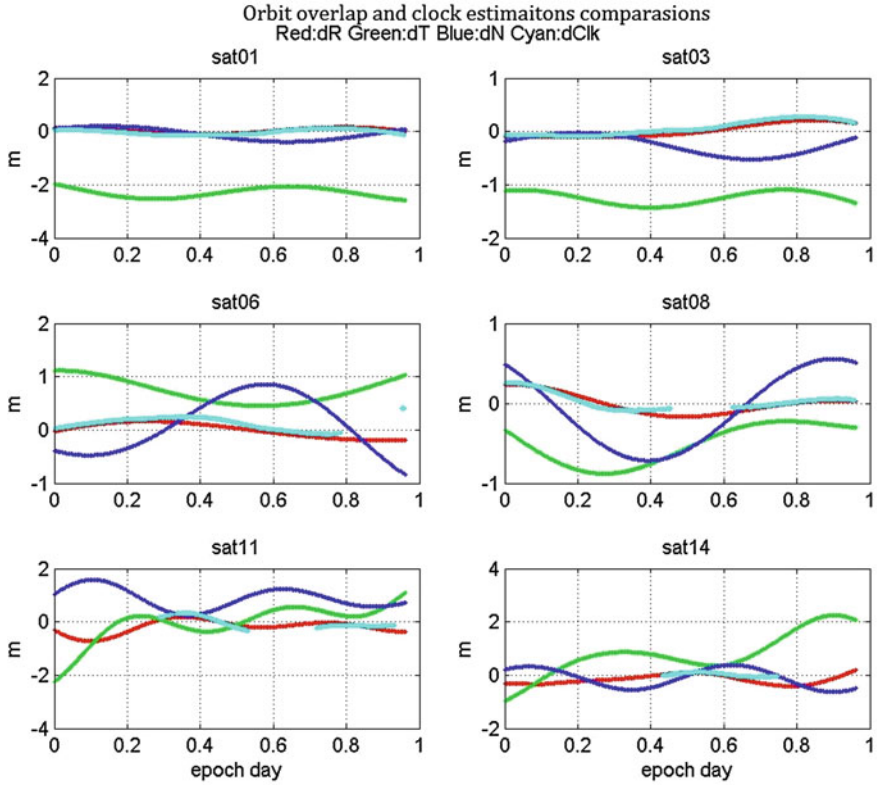

Fig. 8.5 Orbital difference in R/T/N directions and clock errors difference time series. Orbital difference in R/T/N direction is shown as *red*, *green* and *blue line*, and clock difference as light *blue line*. Three rows represent GEO/IGSO/MEO satellites. Two different satellites are drawn in the same line

8.3.5 Timing Accuracy

System timing service can be achieved by satellite orbit and clock error information. Depending on the accuracy of the ephemeris, system timing can be divided into precise and real-time service. Precise orbit and clock realize the precise timing service, and broadcast ephemeris achieves real-time service.

This study realizes system timing by precise and broadcast ephemeris respectively. In precise timing processing, PPP strategy is adopted, in which station clock errors are estimated with position parameter [5]. In real-time processing, station position is fixed and station clock errors are the average of all visible satellite UERE in each epoch, see Eq. (8.4). This strategy may reduce the impact of constellation DOP to timing accuracy.

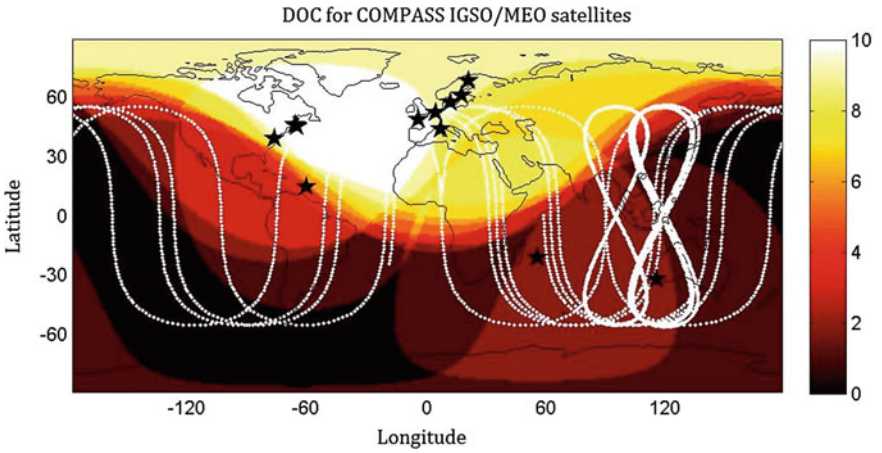

Fig. 8.6 Depth of coverage of abroad station for COMPASS IGSO/MEO. Black stars represent abroad stations, white points represent footprints of satellites. Different colors mean DOC value

Table 8.4 Orbital overlap and clock accuracy wit domestic and abroad stations

SATID	dR (m)	dT (m)	dN (m)	Clock (ns)
06	0.116	1.080	0.778	0.652
07	0.329	0.885	0.571	0.512
08	0.121	0.732	0.898	0.936
09	0.378	1.147	0.916	0.781
10	0.289	1.321	0.630	0.869
11	0.100	0.296	0.938	0.650
12	0.166	0.577	0.492	0.669
13	0.373	1.290	0.741	0.740
14	0.196	1.373	0.769	1.059

The multi-constellation GNSS station can receive navigation information from each system simultaneously. The difference of station clock error estimations by different system ephemeris include difference of time system, receiver equipment delay the orbit and clock errors of difference system and random noise. Considering the complexity of system error for station clock estimations in different navigation system, we only discuss the stability of timing service.

Figure 8.7 shows the comparison time series of station clock estimations between COMPASS and GPS in precise and real-time mode. The two rows represents the real-time and precise mode respectively, the standard deviation is about 2.5 and 1.5 ns. It indicates that both post and real-time ephemeris can realize system timing service, and are consistent with GPS results. Except the constant bias, there is no other systemic relative variation between two navigation systems (linear or higher degree). Consequently, it illustrates that the stability of two systems is consistent with each other.

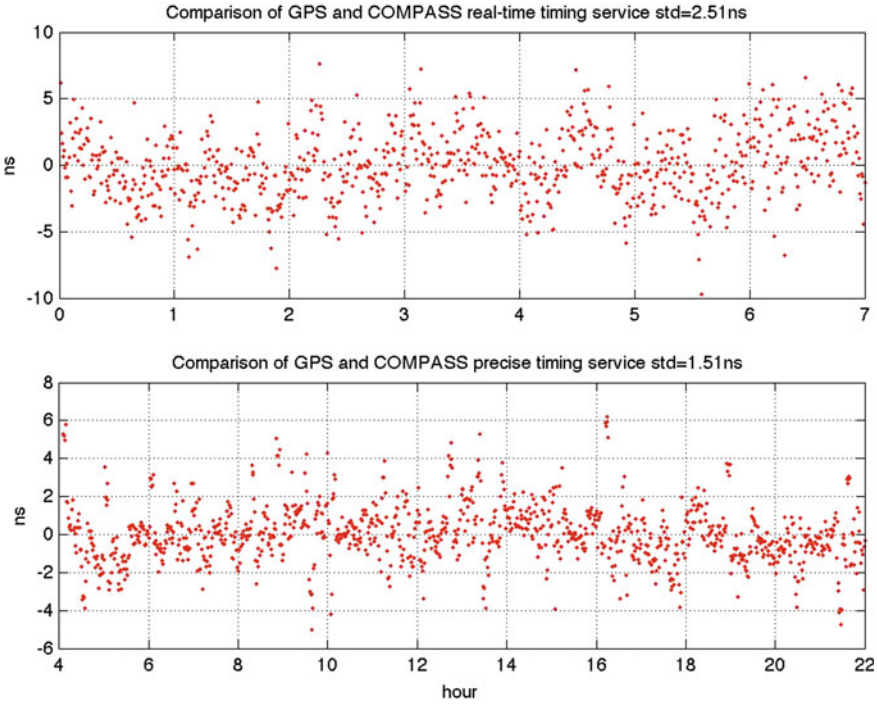

Fig. 8.7 Comparison of COMPASS and GPS timing. The *top* row is real-time results and the *bottom* is post results

8.4 Conclusions

In this study, the accuracy of satellite nominal attitude prediction is assessed, COMPASS satellite orbit parameters are determined adopting regional and global tracking network datasets, the accuracy of satellite orbit is evaluated by orbital overlap, SLR residual and TWSTFT, the accuracy of system timing service are also discussed. Conclusions are as followed:

1. Different attitude control modes are applied to GEO and IGSO/MEO satellites. It's necessary to establish satellite antenna phase center correction model for each type satellites in OD processing. The overall accuracy of nominal attitude prediction is better than 1° which can be used to establish antenna phase center correction model.
2. The characteristics of pseudo-range noise for domestic and foreign manufacturer receivers are quite different. It shows multipath characteristics for domestic receivers, while shows white noise for foreign receiver and the magnitude is larger than domestic receiver.
3. The pseudo-range and carrier phase RMS for 4GEO/5IGSO/4MEO constellation MPOD is about 80 and 0.8 cm. Since the regional tracking network can't

cover all MEO orbital arc, the overlap accuracy for MEO is slight less than GEO and IGSO satellites.
4. Adding abroad stations can increase depth of coverage for IGSO and MEO satellites, and both of overlap and satellite clock errors accuracy can be improved. Satellite clock errors accuracy increases 0.7 and 0.4 ns for IGSO and MEO respectively.
5. System timing service can be realized by precise or real-time ephemeris. The stability of COMPASS is consistent with GPS, the standard deviation of comparison for COMPASS and GPS precise timing is about 1.5 ns, the real time timing is about 3 ns.

Acknowledgments We would like to thank Beijing Global Information Application and Development Center for providing the observations of COMPASS and navigation messages. The differential and integrity information have also kindly been made available from them. The authors would gratefully acknowledge the support of all individuals and institutions that have supported this study. This paper is supported by the Natural Sciences Foundation of China (Grant No. 11103064), the Shanghai Committee of Science and Technology, China (Grant No. 11ZR1443500), the National High Technology Research and Development Program of China (Grant No. 2013AA122402) and China Satellite Navigation Conference (Grant No. CSNC2011-QY-01).

References

1. www.beidou.gov.cn/xtjs.html
2. Zhou SS, Hu XG, Wu B et al (2011) Orbit determination and time synchronization for a GEO/IGSO satellite navigation constellation with regional tracking network. Sci China Phys Mech Astron 54(6):1089–1097
3. Mao Y, Du Y, Song XY et al (2011) GEO and IGSO joint precise orbit determination. Sci China Phys Mech Astron 54(6):1009–1013
4. Zhou SS, Cao YL, Zhou JH et al (2012) Positioning accuracy assessment for the 4GEO/5IGSO/2MEO constellation of COMPASS. Sci China-Phys Mech Astron 55:1–10. doi:10.1007/s11433-012-4942-z
5. Shi C, Zhao QL, Li M et al (2012) Precise orbit determination of Beidou Satellites with precise positioning. Sci China Earth Sci 55:1079–1086. doi:10.1007/s11430-012-4446-8
6. Montenbruck O (2012) ANTEX Considerations for Multi-GNSS Work, Antenna WG Metting. IGS Workshop 2012
7. Montenbruck O, Hauschild A et al (2012) Initial assessment of the COMPASS/BeiDou-2 regional navigation satellite system. GPS Solution. doi:10.1007/s10291-012-0272-x
8. Wang JX (1997) GPS precise orbit determination and positioning (in Chinese). Tongji University, Shanghai
9. Cao YL, Hu XG et al (2012) The wide-area difference system for the regional satellite navigation system of COMPASS. Sci China Phys Mech Astron 55(7):1307–1315

Chapter 9
Improving Efficiency of Data Analysis for Huge GNSS Network

Junping Chen, Yize Zhang, Yibing Xie, Xuhua Zhou, Xiao Pei, Wei Yu and Bin Wu

Abstract The development of GNSS system and its applications is accompanied by the fast development of the ground tracking networks. The expansion of tracking network could contribute to the improvement of precision of satellite orbits, clocks, ERPs and so on. However, the increase of number of tracking stations causes non-linear gain of computing time, especially in the case of data processing based on the Zero-difference (ZD) strategy. Parameter elimination is one of the most used methods to fasten ZD data processing, nevertheless it involves matrix transformation and inversion at each epoch and the computing time is still very long in case of huge network and Multi-GNSS combined solutions. The first part of the paper presents the current status of ZD data processing in case of huge networks and Multi-GNSS data processing. Using 110 GPS/GLONASS stations from the IGS network, we perform classical IGR-like data processing with different data sampling ranging from 5, 6, 7….. till 15 min. Estimated parameters including orbits, clocks, ZTDs, coordinates, ERPs etc. Comparison of the products using different sampling data shows: precision of orbit and clock somehow linearly increases with sampling rate changing from 5 to 15 min, and ERP precision is not influenced by the change of sampling rate. To analyze the impacts of products based on different data sampling on positioning applications, we perform PPP for 22 globally distributed IGS stations using 4 weeks' data and kinematic precise orbit determination for GRACE satellites. Results show that the coordinates/orbits precision is at the same level: precision of PPP coordinate is of 2.3, 3.8, 8.8 mm in NEU directions using products based on

J. Chen (✉) · Y. Zhang · Y. Xie · X. Zhou · XiaoPei · W. Yu · B. Wu
Shanghai Astronomical Observatory, Chinese Academy of Science, Shanghai, People's Republic of China
e-mail: junping@shao.ac.cn

Y. Zhang · Y. Xie · XiaoPei · W. Yu
College of Surveying and Geo-Informatics, Tongji University, Shanghai, People's Republic of China

J. Sun et al. (eds.), *China Satellite Navigation Conference (CSNC) 2013 Proceedings*, Lecture Notes in Electrical Engineering 245,
DOI: 10.1007/978-3-642-37407-4_9,

5 min sampling data, and of 2.5, 4.3, 8.6 mm in case of using 15 min sampling data.

Keywords GNSS · SHA · Analysis center · Precise orbit determination · Efficiency

9.1 Introduction

GNSS (Global Navigation Satellite System) tracking network expands with the developing/upgrading of GNSS stations. Currently, there are about 380 GNSS tracking stations within IGS (International GNSS Service) global network, including about 150 GPS/GLONASS stations [1]. Additionally, there are many other regional GNSS networks, e.g. the CMONOC (Crustal Movement Observation Network of China) consisting of 260 reference stations and more than 2,000 campaign stations [2]. With more stations adding to the network and contributing to data analysis, GNSS products like orbits, clocks and Earth Rotation Parameter (ERPs) etc. could be improved. The combined GPS/GLONASS data analysis may improve the accuracy of reference frame and other station-dependent parameters as well. However, including more stations and satellites into data analysis results in more parameters to be estimated and more computation time. Taking the current daily data analysis using GPS/GLONASS constellation with 32 GPS satellites and 24 GLONASS satellite as example, Table 9.1 summarize the number of parameters for GPS only and GPS/GLONASS combined daily data analysis. In Table 9.1, we assume there are 2 ambiguity parameters for each station/satellite pair and 1 ISB (inter system bias) parameter for each station/GLONASS satellite pair. Additionally there are 12 ZTD parameters for each station, 15 orbit parameters for each satellite, 3 coordinates for each station and 6 ERP parameters. The epoch-wise clock parameters are eliminated during data analysis. From Table 9.1, we clearly see that the dramatic non-linear increase of parameter numbers with the growth of number of tracking stations. Consequently, this may cause problems in data analysis using huge GNSS networks.

Currently, there are two strategies to handle this problem: the first is to use the double-difference observations to remove clock parameters and reduce number of ambiguities [3]; and the second is applied in Zero-difference solutions, it

Table 9.1 Growth of the number of parameters versus the increase in the number of stations tracking GPS and GPS + GLONASS (G + G) constellation

Number of stations	Ambiguity		Others		ISB (G + G)	Total number of parameter	
	GPS	G + G	GPS	G + G		GPS	G + G
50	3,200	5,600	1,236	1,686	1,200	4,436	8,486
100	6,400	11,200	1,986	2,436	2,400	8,386	16,036
150	9,600	16,800	2,736	3,186	3,600	12,336	23,586
200	2,800	22,400	3,486	3,936	4,800	16,286	31,136

eliminates epoch-wise parameters and non-active parameters at each epoch [4]. Using the double-difference strategy, clock parameters no longer exist by definition and thus special procedure is needed to recovery them, which makes the procedure of data analysis more complicated [5]. On the other hand, using the parameter elimination strategy in Zero-difference solution cannot really solve the problem when the number of stations and satellites increases to more than 200. Taking the routine daily IGR analysis at Shanghai Astronomical Observatory for example, GPS-only Zero-difference analysis needs 2 min for one iteration using around 100 stations and it takes around 20 min to finish the entire solution. While in case of GPS-only analysis using 300 stations, it takes more than 40 min for one iteration and the entire daily analysis takes more than 10 h on the same computer. As for the combined GPS/GLONASS data analysis, it needs 10 min for one iteration, which is almost 5 times of the GPS-only solution. Based on this analysis, the computation time is extremely long for the combined GPS/GLONASS solution using more than 200 stations. The reason that Zero-difference solution is time-consuming is because parameter elimination has to be carried out at each epoch, which actually involves a lot of matrix inversion and multiplication between big matrixes. The matrix dimension at each epoch is at the same level as we stated in Table 9.1.

Parameter eliminate is performed at each epoch, therefore the computation time depends on the total number of epochs. Reducing the number of processing epochs could in genera reduce computation time. However, decrease of observations could result in the decrease of precision of estimated parameters. This impact could be marginable for daily constant parameters, e.g. orbit, coordinates, ERPs and ISB etc. For other parameters like clocks and ZTDs this impact could be noticeable. In order to find the optimal setting of Zero-difference data analysis to improve efficiency and to keep the highest precision, we analysis the impacts on processing time and product precision by changing data sampling. Four week data of around 110 stations from the IGS global network is used in this paper. Data analyses are performed under different scenarios with different data sampling.

9.2 Data and Analysis Settings

Data analysis is based on the iGPOS (integrated Geodetic Platform of SHAO) system, which is the platform of the GNSS data analysis center SHAO (SHA) [6, 7]. iGPOS is based on the traditional least-square estimator. It implements Zero-difference strategy, its correction models follow IERS and IGS conventions [8]. Routine parameters include: orbits (15 parameters for each satellite), coordinates (3 parameters for each station), ERP (6 parameters for each day), clocks (epoch-wise parameter for each satellite and station), ZTD (1 parameter each hour for each station) and ambiguities. After the generation of all parameters, we densify the GNSS clocks from original sampling (normally 5 min) to 30 s [9]. Comparisons between the products of SHA and IGS analysis centers show: GPS orbit precision

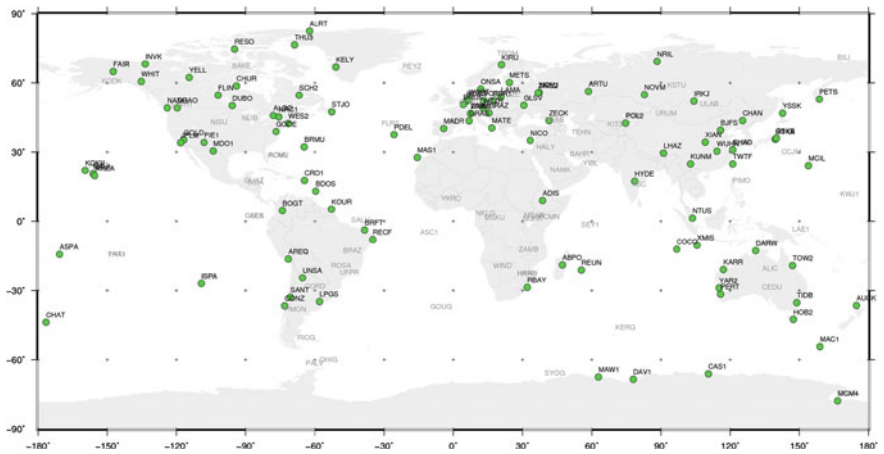

Fig. 9.1 Ground tracking network processed at SHA

of SHA is around 1.5 cm and GLONASS orbit precision is of 3.2 cm; precision of GPS clocks is of 40 ps and it is around 100 ps for GLONASS clocks [6]. To analysis the impact of data sampling on computation time and product precision, data of around 110 stations from the IGS global network spanning from GPS week 1686 to 1689 is used. Figure 9.1 shows the IGS network used in this paper, which include around 65 stations providing GPS/GLONASS combined observations. Data analyses follow the setting of daily routine analysis of SHA.

9.3 Impacts on Computation Time and Product Precision

9.3.1 Impacts on Computation Time

Computation efficiency is one of the important issues for GNSS data analysis centers. For the analysis of computation time, data processing is performed on a normal desktop (CPU: Intel Core i7-2600, 3.4 GHz; RAM: 8 * 2.0G = 16.0G). Data processing is carried out in different scenario with data sampling set to 300 s (5 min), 360 s (6 min), …, till 900 s (15 min). All together there are 308 (11 * 28) daily solutions. Figure 9.2 illustrates mean computation time for daily analysis under different data sampling. As it is shown in Fig. 9.2, the computation time is linearly decreased with the sampling changes from 5 to 15 min. Comparing the mean computation time under 5 and 15 min sampling, we notice that: the time for GPS-only solution changes from 40 to 23 min (decreased by 42 %); the time for GPS/GLONASS combined solution changes from 114 to 55 min (decreased by 52 %). Additionally, test of the CMONOC GNSS data analysis center at SHAO [10] shows: time for daily routine with 5 min data sampling using 270 GPS stations is about 727 min, and it takes 475 min when data sampling changes to

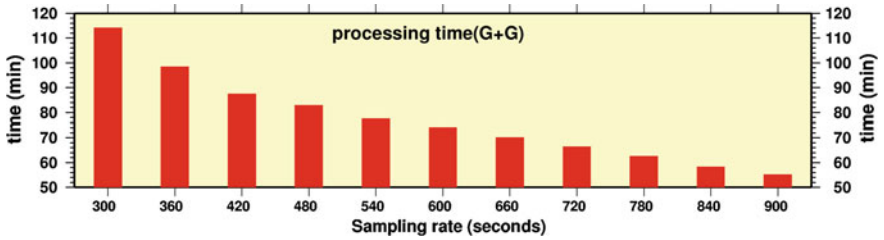

Fig. 9.2 Mean processing time using data of different sampling of GPS + GLONASS combined solution

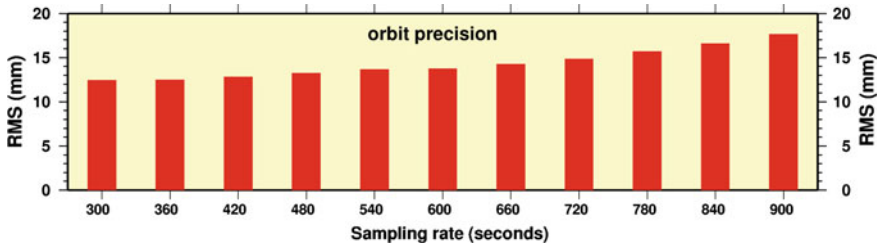

Fig. 9.3 Mean precision of orbits using data of different sampling, comparing to the IGS final orbits

15 min, which is decrease by more than 30 %. All the tests show that the efficiency of data analysis could be greatly improved by changing data sampling.

9.3.2 Impacts on Product Precision

Besides efficiency, product precision is another important issue for GNSS data analysis centers. Currently GNSS orbits/clocks and other products from IGS analysis centers are the most accurate products providing to world-wide users. Product precision should not be sacrificed while improving efficiency.

9.3.2.1 Orbits

Figure 9.3 shows the comparisons between IGS orbits and the derived GPS orbits under different data sampling. The RMS values range from 13 to 18 mm, which, in general, is in the range of the current IGS orbit precision. And it could be explained that there are enough tracking stations to ensure that satellites are simultaneously tracked by many stations at each sampling epoch. And the accurate orbit dynamic models ensure the overall orbit precision. Also, we notice that orbit precision is better than 14 mm when sampling is smaller than 10 min, and it gradually degrades when the sampling is bigger than 10 min. Based on the results

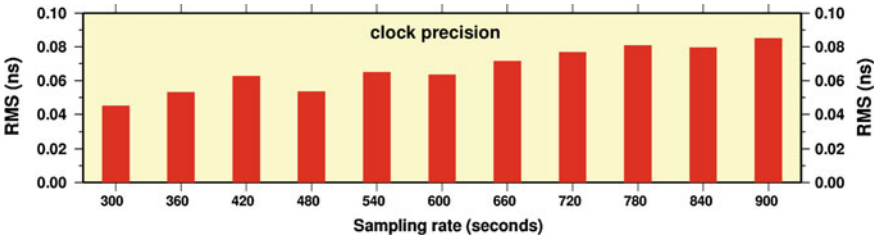

Fig. 9.4 Mean precision of satellite clocks using data of different sampling, comparing to the IGS final clocks

of orbit comparison, we could reduce the data sampling to 10 min. By doing this, the precision remains unaffected while computation time is largely reduced.

9.3.2.2 Satellite Clocks

Figure 9.4 shows the comparisons between IGS satellite clocks and the derived GPS clocks under different data sampling. The RMS values range from 0.04 to 0.08 ns, which, in general, is in the range of the current IGS clock precision. As clocks have to be estimated at each epoch, the errors introduced by changing data sampling could be absorbed by epoch-wise clocks. We notice that clock precision is better than 0.06 ns when sampling is smaller than 10 min, and it gradually degrades when the sampling is bigger than 10 min. Results based on data sampling of 15 min have the worst precision of 0.085 ns ($\sim$2.6 cm). Based on the results of clock comparison, we could reduce the data sampling to 10 min. By doing this, the precision remains almost unaffected while computation time is largely reduced.

9.3.2.3 Earth Rotation Parameters

ERP parameters are defined as daily constants therefore the impact from difference data sampling should be marginal. Figure 9.5 shows the comparisons between IGS

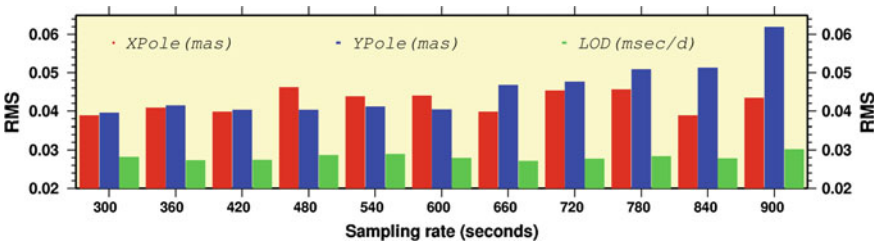

Fig. 9.5 Precision of pole parameters using data of different sampling, comparing to the IGS final ERP parameters

ERPs and the derived ERPs under different data sampling. The RMS values range from 0.04 to 0.08 mas for pole parameters and are around 0.025 ms per day for LOD parameter. We notice that ERP precision is better than 0.04 mas when sampling is smaller than 10 min, and it gradually degrades when the sampling is bigger than 10 min. Meanwhile, LOD parameters are almost unaffected by the difference of data sampling.

9.3.2.4 Reference Frame

Reference frame is defined by satellite orbits and station coordinates. To reflect the impact on reference frame using different data sampling, we make Helmert transformation between estimated orbits and IGS final orbits to derive Helmert parameters [11]. Results show: the change of mean scale parameter is small than 0.01 ppb, change of mean translation parameters are less than 0.4 mm. The daily variation of these parameters shows random property with values much smaller than its precision. Figure 9.6 shows the mean rotation parameters for each sampling scenario. We notice that the rotation parameters changes randomly in the range smaller than 0.02 mas for the direction of Y and Z, while the mean rotation parameter in X-axis becomes gradually bigger along with the increase of data sampling. One possible explanation is related to the tracking network. As there are fewer stations along the longitude of ± 90 (Y-axis), the coordinates/orbits along the Y-axis could be more affected by number of observations. According to the mapping function, larger values are required in X-axis in order to introduce such impact.

9.4 Impacts on User Applications

To further assess the influence of data sampling, we apply the products derived from different scenario (named 5 min-Prod, 6 min-Prod, …, 15 min-Prod) in static and kinematic PPP (Precise Point Positioning). For the static PPP, data of 22 IGS

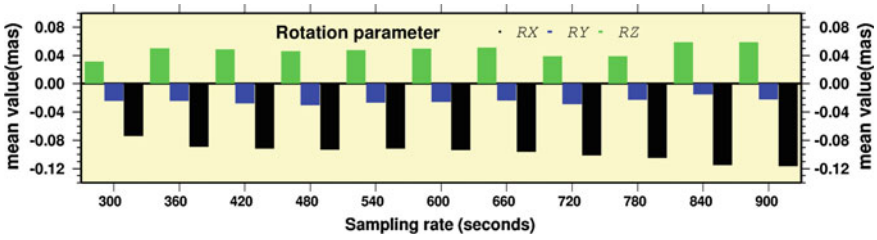

Fig. 9.6 Mean rotation parameters of Helmert transformation between GPS orbits under different data sampling and the IGS final orbits

stations, which are not used in product generation step, spanning the whole 4 weeks are used; and data of GRACE satellites spanning from Doy (Day of year) 94–100, 2010 are used in kinematic PPP.

9.4.1 Static PPP

Station used including: ALGO, AMC2, BRAZ, DRAO, GUAM, GUAO, HOB2, IISC, ISPA, KARR, KELY, KOKB, KUNM, MAS1, MDVJ, OHI2, RAMO, SCH2, SYOG, TIXI, TSKB, WUHN, YELL. BERNESE 5.0 [12] software is used for static PPP. In the first step, daily coordinates are firstly estimated with data sampling set to 30 s. Coordinate repeatability is derived for each station in weekly combination. As we use 4 weeks data, there are 4 repeatability values for each station, and mean values are used for comparison. Figure 9.7 shows the mean repeatability of all stations using different products, which shows that the impacts on the static PPP coordinates is less than 2 mm in horizontal and less than 6 mm in vertical directions.

9.4.2 Kinematic Orbits of Low Earth Orbiters

Kinematic coordinates are most sensitive to the errors in orbits/clocks and other input products. To reflect the impact of different products on kinematic PPP, data of GRACE-A and GRACE-B satellites are processed using the in-house developed LEO orbit determination software [13]. The kinematic orbits are compared to the precise PSO orbits from JPL for precision assessment. Figure 9.8 shows the RMS for results using products under different scenario. The precision in 3D changes from 8 to 10 cm. Considering the accuracy of kinematic PPP, we could conclude that the kinematic PPP is marginally affected by the data sampling in products generation. Comparing the GRACE-A kinematic orbit on Doy 98 based on 5 min-Prod and 15 min-Prod, results show: the mean coordinate difference is of (0.1, 0.2, 0.5) cm and RMS is of (3.4, 3.6, 3.6) cm in the R, T, N directions, respectively.

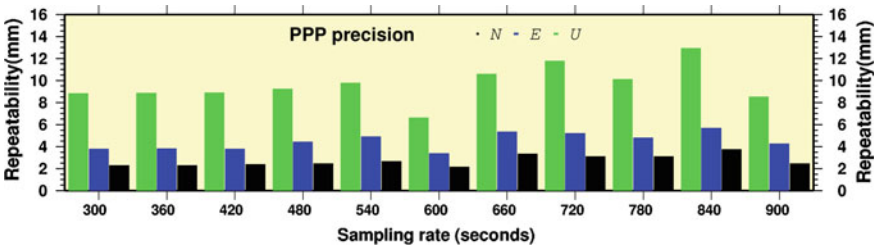

Fig. 9.7 Median coordinates precision of static PPP of 22 stations, using different GPS orbits/clocks from different scenario

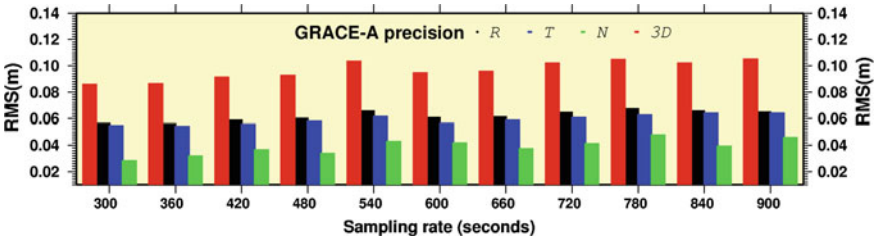

Fig. 9.8 Kinematic orbit precision of GRACE-A, using different GPS orbits/clocks from different scenario

9.5 Conclusions

Data analysis using Zero-difference strategy is widely used, because it could estimate most satellite and station related parameters. However, its computation efficiency has become a bottleneck with the development of the observing network and inclusion of multi-GNSS systems. We discuss the impacts of changing data sampling on product precision and user application. Using the GNSS data analysis platform of SHAO, big amount of data from the 110 IGS globally distributed stations are analyzed. Results show:(1) Computation time linearly decreases with the data sampling change from 5 to 15 min; and this trend is more obvious when processing more stations and satellites; Computation efficiency could be improved by more than 50 % by changing data sampling from 5 to 15 min; (2) The change of data sampling has not too much impact on the derived orbits, clocks, ERPs and reference frame; And the impact could be ignored when data sampling is between 5 and 10 min; (3) PPP using products based on different data sampling shows the user kinematic and static positioning are almost not influenced by the input products.

Acknowledgments This paper is supported by the 100 Talents Programme of The Chinese Academy of Sciences, the National High Technology Research and Development Program of China (Grant No. 2013AA122402), and the National Natural Science Foundation of China (NSFC) (Grant No. 40974018 and 11273046).

References

1. Weber R, Hugentobler U, Neilan R (2011) IGS M-GEX: the IGS Multi-GNSS global experiment
2. CMONOC: http://www.lssf.cas.cn/lsyg/lsygk/201001/t20100116_2728038.html
3. Dach R, Hugentobler U, Fridez P, Meindl M (eds) (2007) Bernese GPS software version 5.0. Astronomical Institute, University of Bern, Bern
4. Ge M, Gendt G, Dick G, Zhang FP, Rothacher M (2006) A new data processing strategy for huge GNSS global networks. J Goed 80:199–203. doi:10.1007/s00190-006-044-x6
5. Bock H, Dach R, Jaggi A, Beutler G (2009) High-rate GPS clock corrections from CODE: support of 1 Hz applications. J Geod 83:1083–1094. doi:10.1007/s009190-009-0326-1

6. Chen J, Wu B, Hu X, Li H (2012) SHA: the GNSS analysis center at SHAO, In: Lecture Notes in Electrical Engineering, vol 160 LNEE, pp 213–221
7. GNSS data analysis center: www.shao.ac.cn/shao_gnss_ac
8. McCarthy D, Petit G (2004) IERS conventions (2003). IERS Technical Note 32, Bundesamt für Kartographie und Geodäsie, Frankfurt am Main
9. Chen J, Zhang Y, Zhou X, Pei X, Wang J, Wu B (2012) GNSS clock corrections densification at SHAO: from 5 minutes to 30 seconds, submitted to Science China
10. Chen J, Wu B, Hu X, Li H (2012) CMONOC data analysis center at SHAO. In: Electronic proceeding of China satellite navigation conference (CSNC) (in Chinese)
11. IGS ACC: http://ac.igs.org
12. Dach R, Hugentobler U, Fridez P, Meindl M (eds) (2007) Bernese GPS software version 5.0. Astronomical Institute, University of Bern, Bern
13. Peng D, Wu B (2011) Kinematic Precise Orbit Determination for LEO Satellites Using Space-borne Dual-frequency GPS Measurements. Acta Astronomica Sinica 52(6):495–509 (in Chinese)

Chapter 10
Ionospheric Grid Modeling of Regional Satellite Navigation System with Spherical Harmonics

Jiachen Fan, Xiaoli Wu, Enqiang Dong, He Zhao, Haibo Kan and Jinshi Xie

Abstract As an important component of differential navigation service, ionospheric grid can greatly improve the accuracy of single frequency users. Wide-Area Augmentation System (WAAS) broadcasts a set of ionospheric grids data for authorized single frequency GPS users every 300 s. WAAS uses inverse distance weighting (IDW) algorithm to calculate the vertical total electron content (VTEC) at those ionosphere grid points (IGP). IDW algorithm has good correction accuracy, but has low availability in the area with few ionosphere pierce points (IPP). The availability and accuracy of ionospheric grid by IDW algorithm depend on the distribution of monitoring stations and the constellation of navigation system. As the constellation of regional satellite navigation system consists mainly of geostationary earth orbits (GEO) satellites and inclined geosynchronous orbits (IGSO) satellites, the IPPs have a concentrating distribution. Considering that the distribution of monitoring stations are all in China, using IDW algorithm to calculate ionospheric grid will not have good availability. This paper proposes a practical algorithm to calculate the regional ionospheric grid based on spherical harmonics (SH) model and International Reference Ionosphere (IRI-2012) model. Compared with IDW algorithm, the simulation data analysis indicates that the SH algorithm can greatly improve the availability from 82.62 to 99.83 % for mainland China and from 34.66 to 94.25 % for all grids, but the average correction RMS of ionospheric grid increases from 2.60TECU to 3.33TECU.

Keywords Regional satellite navigation system · Ionospheric grid · Spherical harmonics · Inverse distance weighting

J. Fan (✉) · X. Wu · E. Dong · H. Zhao · H. Kan · J. Xie
Beijing Satellite Navigation Center, Beijing 100094, China
e-mail: cfan89@gmail.com

J. Sun et al. (eds.), *China Satellite Navigation Conference (CSNC) 2013 Proceedings*, Lecture Notes in Electrical Engineering 245,
DOI: 10.1007/978-3-642-37407-4_10,

10.1 Introduction

As one of the error sources for navigation calculation, ionospheric delay seriously affects the positioning accuracy of the users. Dual-frequency users can remove ionospheric delay by linear ionosphere-free combination ignoring the higher-order term. Single-frequency users can calculate the ionospheric delay of IPP by the broadcasted parameters of ionosphere model. GPS broadcasts 8 parameters Klobuchar model on geomagnetic coordinate, and the correction accuracy is about 60 % [1, 2]; Galileo uses Nequick model, the designed correction accuracy is about 70 %. The error of ionosphere model becomes the most important factor determining single-frequency users' positioning accuracy.

To meet the needs of advanced users, especially the aviation users, institutions in different countries begin to build augmentation system, such as WAAS of America, EGNOS of European and the GAGAN of Indian. Each system has a similar principle to calculate the ionospheric grid: several monitoring stations and a center station are distributed in service area. Each monitoring station equipped with dual-frequency receivers collects the observation of all visible satellites, and calculates the IPP's coordinates and the ionospheric delays. Data mentioned above transmits to the center station every second through the network. Then ionospheric grid delay can be solved by the center station, and broadcasted by GEO satellites for the authorized single-frequency users.

WAAS broadcasts 5° × 5° ionospheric grid corrections by GEO satellites and correction accuracy is about 80 % [3, 4]. Regional satellite navigation system provides differential services for authorized users, the service area covers from 7.5° to 55° north latitude, 70° to 145° east longitude, and using its GEOs to broadcast the ionospheric grid correction.

As regional satellite navigation system constellation consists mainly of high orbit satellites, the distribution of IPPs has a relative concentration. The availability of ionospheric grid by IDW algorithm greatly depends on the distribution of monitoring stations. IGP has low availability in case that there are few IPPs nearby.

To solve this problem, this paper will propose a spherical harmonics (SH) algorithm combined with regional satellite navigation system observation data and the IRI-2012 model to calculate the ionospheric grid. Real data and simulation analysis shows that this algorithm has a great increase in availability of grid points, and loss little accuracy compared with the ionospheric grid by the IDW algorithm.

10.2 IDW Algorithm

The IDW algorithm is wildly used to calculate the ionospheric grid. It relies on the IPPs near the IGP. The algorithm is simple but has good accuracy at the available IGP. However, as the algorithm seriously relies on the distribution of IPPs,

it shows bad accuracy at IGP with not enough IPPs nearby. IDW algorithm is introduced as below.

According to global navigation satellite system (GNSS) observation equation, the dual-frequency linear geometry-free combination P_4 is:

$$P_4 = P_1 - P_2 \tag{10.1}$$

where P_1, P_2 are the P-code observations on B1, B2 frequency. Linear geometry-free combination eliminates all errors related to geometry, and the remaining factors are ionosphere delay, differential code bias (DCB) of satellite and receiver, multipath error and ranging noise. Ignoring the multi-path and measuring error,

$$P_4 = -(\frac{f_1^2 - f_2^2}{f_2^2})F(z) \cdot I + c \cdot \Delta b^s + c \cdot \Delta b_r \tag{10.2}$$

where f_1, f_2 are the frequencies of B1, B2. Δb^s is the TGD of satellite s; Δb_r is the IFB of receiver r; c is the speed of light; I is the ionosphere delay from receiver r to the satellite s:

$$I = \frac{40.28}{f_1^2} \cdot VTEC \tag{10.3}$$

$F(\cdot)$ is the ionospheric mapping function depending on the zenith distance z.

$$F(z) = \frac{1}{\cos(z)}, \sin(z) = \frac{R}{R+H}\sin(z' + \frac{\pi}{2}) \tag{10.4}$$

where z' is the zenith distance at the IPP; $R = 6371$ km is the mean earth radius; $H = 375$ km is the ionospheric single layer height. As Δb^s and Δb_r are already known, VTEC of every epoch at every IPP can be got by Eq. (10.2).

For every IGP, IDW algorithm uses the VTEC of IPPs in the four adjacent grids to calculate the VTEC of IGP.

$$I_{IGP_i} = \sum_{j=1}^{n} I_{IPP_j} P_{ij} / \sum_{j=1}^{n} P_{ij} \tag{10.5}$$

where I_{IGP_i} is the VTEC of ith IGP; n is the number of IPPs in the four adjacent grids; I_{IPP_j} is VTEC of IPPs; P_{ij} is the weight of jth IPP to the IGP. Here we take P_{ij} as the inverse distance from jth IPP to ith IGP.

10.3 Solution Method of Ionospheric Grid Based on Spherical Harmonics

The SH algorithm uses all VTEC of IPPs to fit the ionosphere of whole area, but this algorithm is relatively complex.

Assume there are N IPPs during some time, $IPP_i(i = 1, \cdots, N)$ is the IPP at the position of $(lat_i,\ lon_i)$ at t_i, and its VTEC is $VTEC_i$. Using the SH to fit VTEC.

$$VTEC = \sum_{n=0}^{n_{max}} \sum_{m=0}^{n} P_{nm}(\sin\beta)(C_{nm}\cos(ms) + S_{nm}\sin(ms)) \tag{10.6}$$

where β is the latitude of IPP; $s = sod + lon/15$ is the local time of IPP; $n_{\max}$ is the maximum degree of SH expansion; P_{nm} is the normalized Legendre function; C_{nm}, S_{nm} are the unknown SH coefficients. According to the SH function above, we can solve C_{nm} and S_{nm} using the least squares. Then we can calculate the ionospheric grid VTEC by the SH coefficients.

As regional satellite navigation system has less monitoring stations in western and northern China, there are less IPPs in those areas. However, the SH algorithm relies on the distribution of IPPs, better results are presented in IPPs covered areas, and SH function diverges rapidly out of boundary. The greater degree of SH function, the more seriously the SH function diverges. In order to decrease the divergency of SH function in area out of China with no IPP, we use the IRI-2012 model to forecast the exact boundary of ionospheric grid service area.

IRI-2012 model is an experimental model based on observation data of satellites and receivers, aiming to describe the ionosphere in a peaceful geomagnetic condition. Yayukevich showed that given the geomagnetic planetary index Kp under 7, IRI-2007 model has an accuracy of 30 % relative to measurement data from satellite altimeters, and the amplitude of the absolute error is about 11TECU in the abnormal areas [5].

Figure 10.1a is the VTEC map only using IPPs of navigation system by 6° SH functions for day 300 of 2012 at 21:00 (UT), and we use pseudo-color to present the VTEC value. It is assumed that the reasonable ionosphere delay is between 0TECU and 150TECU, we make the VTEC value equals 0TECU when it is out of the interval above. From the figure, it is obvious that SH algorithm has a normal condition in China, but diverges rapidly at high latitudes and low latitudes. Figure 10.1b is the VTEC map using both IPPs of navigation system and boundary IPPs of IRI-2012 model at the same time. In the same circumstance, SH algorithm covers all area at high latitudes and most area at low latitudes.

Figure 10.2 is the VTEC map using the SH algorithm at the daily peak of ionosphere. The SH function diverges at low latitudes. It is probably because IRI-2012 model has low accuracy at low latitudes, then the additional IPPs of ionospheric grid boundary lack of enough data supporting. So the SH algorithm has a bad performance in those areas.

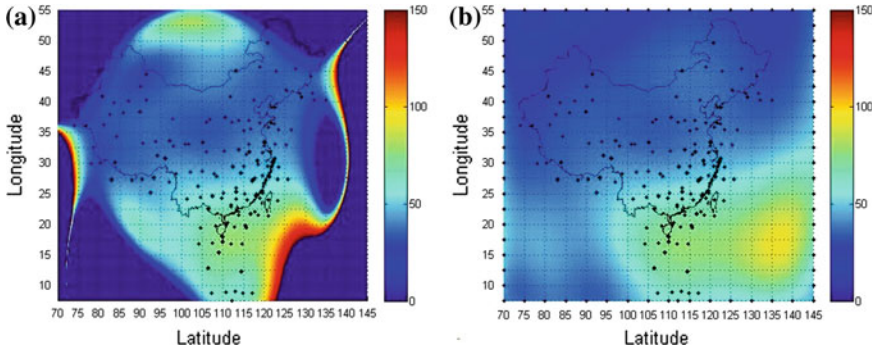

Fig. 10.1 Example of VTEC map using different IPPs, for day 300 of 2012, at 21:00 UT, unit TECU. **a** Using IPPs of navigation system receivers. **b** Using IPPs of navigation system receivers and boundary IPPS from IRI-2012

Fig. 10.2 Example of VTEC map using IPPs of navigation system receivers and boundary IPPs from IRI-2012, for day 300 of 2012, at 7:00 UT, unit TECU

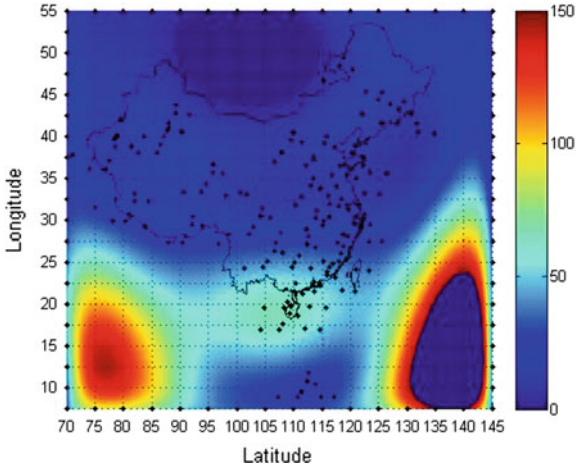

10.4 Interpolation Algorithm of IGPs

As the user receives the VTEC data of IGPs, interpolation algorithm is needed to calculate the VTEC at an IPP. There are many interpolation algorithms. Here we introduce a simple algorithm for the accuracy analysis of different ionospheric grid algorithms in the next section.

As shown in Fig. 10.3, the IPP P is located in the grid ABCD. We can calculate the VTEC of IPP with weighted VTEC of four IGPs. The weight of each IGP takes the way of inverse distance weighted.

$$Q_A = \omega_x \omega_y \tag{10.7}$$

$$Q_B = (1 - \omega_x)\omega_y \tag{10.8}$$

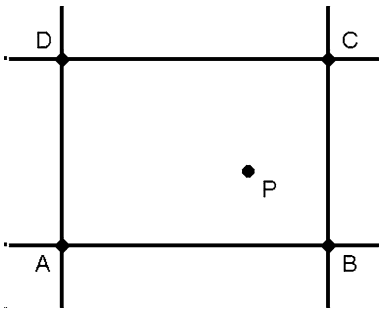

Fig. 10.3 Example of IPP and IGPs

$$Q_C = (1 - \omega_x)(1 - \omega_y) \tag{10.9}$$

$$Q_D = \omega_x(1 - \omega_y) \tag{10.10}$$

where

$$\omega_x = \frac{x_p - x_A}{\delta_x} \tag{10.11}$$

$$\omega_y = \frac{y_P - y_A}{\delta_y} \tag{10.12}$$

δ_x is the grid interval of longitude; δ_y is the grid interval of latitude. The VTEC of IPP P is:

$$I_P = \frac{Q_A I_A + Q_B I_B + Q_C I_C + Q_D I_D}{Q_A + Q_B + Q_C + Q_D} \tag{10.13}$$

10.5 Numerical Experiments

In three sections above, we introduce the IDW algorithm, SH algorithm and interpolation algorithm. This section will evaluate the performance of two ionospheric grid algorithms in both availability and accuracy.

We assume that 23 cities distributed in China include Nansha and Xisha islands have monitoring stations. Coordinates of IPPs at every epoch can be achieved by the coordinates of monitoring stations and broadcast ephemeris of navigation satellites. VTEC of every IPP can be got by global ionosphere map of IGS. Then we can use the VTEC of IPP to do simulation experiment and numerical analysis of IDW algorithm and SH algorithm.

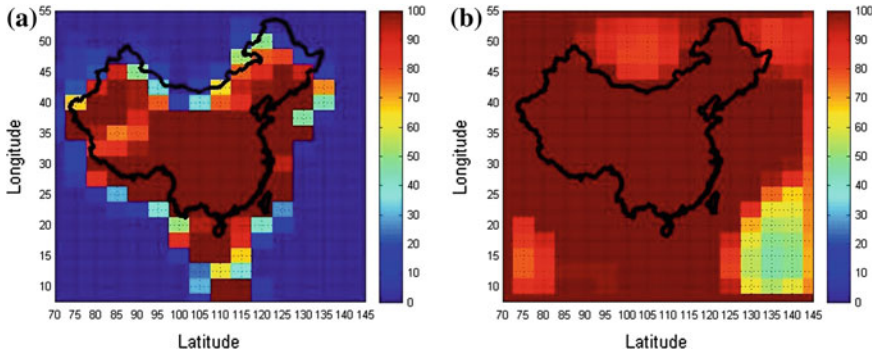

Fig. 10.4 Availability of two algorithms ionospheric grid, for day 300 of 2012, unit %. **a** Availability of IDW grid. **b** Availability of SH grid

10.5.1 Availability Analysis

If VTEC of a IGP can't be calculated, we set this IGP unavailable. The number and distribution of unavailable IGPs have a bad influence on differential service. Define the daily availability of a IGP ρ:

$$\rho = \frac{t}{86400} \tag{10.14}$$

where t is the time span in which this IGP is available for one day, units second. We define the areal availability as the average of daily availabilities of all IGPs in the area.

Figure 10.4a shows the availability of ionospheric grid by IDW algorithm for day 300 of 2012. Pseudo colors represent the availability. Dark red stands for the availability of 100 %. It is obvious that most area in China has good availability, however, the availability is quite low in northwestern China such as Inner Mongolia, Xinjiang and Tibet. The area out of China is almost unavailable in all daytime.

Figure 10.4b shows the availability of ionospheric grid by SH algorithm for day 300 of 2012. It is 100 % available in most China. The availability out of China is improved by a large margin, and there is no IGP unavailable.

Table 10.1 Availability of two algorithms ionospheric grid in different areas

	IDW algorithm (%)	SH algorithm (%)
Low latitudes	16.85	88.86
Mid-latitudes	60.04	97.23
High latitudes	18.62	95.65
Mainland China	82.62	99.83
All grids	34.66	94.25

Table 10.1 shows the availability in different areas. IDW algorithm has low availability (less than 20 %) at low latitudes and high latitudes, and the availability is 60.04 % at mid-latitudes. The availability of SH algorithm improved greatly, all latitudes are more than 88 %. The availability increased from 82.62 to 99.83 % in mainland China, and from 34.66 to 94.25 % in all service area. SH algorithm can not only improve the availability of mainland China, but also can greatly improve the availability of area out of China.

10.5.2 Accuracy Analysis

To comprehensively compare the effectiveness of IDW algorithm and SH algorithm, this part analyses the accuracy of two algorithms. Since GEO satellite has geostationary characteristics, it can be a good method to monitor ionosphere delay at a specific point. In mainland China, we take dual-frequency COMPASS receivers' real observations to calculate the VTEC of IPP. We take this VTEC as the reference. Ionospheric grid of IDW algorithm and SH algorithm are used to calculate the VTEC of IPP by the interpolating algorithm in Sect. 10.4, compared to the VTEC of dual-frequency observation can evaluate the accuracy of two algorithms.

The top graph in Fig. 10.5 describes VTECs calculated by three methods above, the bottom graph is the difference between VTECs of two grid algorithms and VTECs of dual-frequency observations. It is shown that SH algorithm and IDW

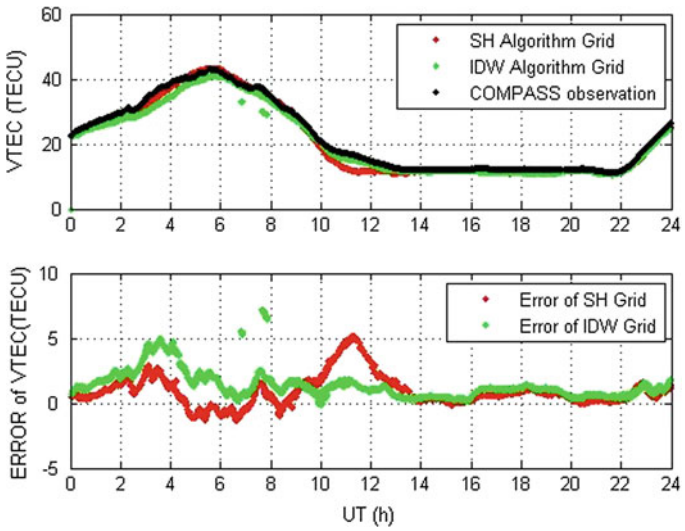

Fig. 10.5 VTEC of three methods, and the differences between two ionospheric grids and COMPASS observation, for day 300 of 2012

Table 10.2 Two kinds of ionospheric grid RMS in different regions, for day 300 of 2012, unit TECU

	IDW algorithm	SH algorithm
San Ya	4.81	6.74
Cheng Du	2.89	4.43
Ka Shi	2.75	2.06
Zheng Zhou	1.33	0.74
La Sa	1.96	3.97
Nan Jing	1.84	2.04

Table 10.3 RMS and correction accuracy of three grids solved by SH algorithm compared with IGS map, for day 300 of 2012, unit TECU

IGP	RMS	Correction accuracy (%)
(20°, 90°)	14.92	71.65
(35°, 135°)	11.21	76.86
(50°, 80°)	8.18	65.95

algorithm have almost same correction accuracy, and their RMS are 1.25TECU and 1.14TECU.

Table 10.2 is RMS of ionospheric grid by two algorithms in different areas. Chengdu and Sanya are ionosphere abnormal areas, but RMS has little difference by two algorithms. The difference of RMS in all areas is less than 2TECU (0.33 m of B1).

As there is no COMPASS receiver, global ionosphere map of IGS is used to evaluate the accuracy of IGPs out of China. We take three IGPs (20°, 90°), (35°, 135°) and (50°, 80°) as an example, which are all unavailable by IDW algorithm.

Table 10.3 shows RMS and correction accuracy of three IGPs by SH algorithm. RMS is small at high latitudes for 8.18TECU, with over 10TECU RMS at low latitudes. As large ionosphere delay at low latitudes, it has a big RMS but good correction accuracy. However, since ionosphere delay is small at high latitudes, it has a small RMS but bad correction accuracy.

10.6 Conclusions

The theoretical analysis and numerical analysis above shows that the availability in mainland China of IDW algorithm is 82.62 %, and almost unavailable out of China, but has good accuracy at available IGPs. Mean of daily RMS in different areas is 2.60TECU. The availability of SH algorithm improves greatly: all IGPs are 100 % available in mainland China, the availability is 95.65 % at high latitudes, and the availability is 88.86 % at low latitudes. SH algorithm and IDW algorithm have almost same correction accuracy in mainland China. The difference is less than 2TECU. Average RMS of SH algorithm in different areas is 3.33TECU. In conclusion, two algorithms both have advantages and

disadvantages. Compared with IDW algorithm, SH algorithm shows better availability and slightly lower accuracy. As for differential single-frequency users, availability is an important factor to ensure their navigation and positioning service. Under the circumstance of sacrificing accuracy in small rang, it is very meaningful that SH algorithm can greatly improve the availability.

References

1. Zhang HP (2006) Study on GPS based China regional ionosphere monitoring and ionospheric delay correction. Ph.D. Dissertation, Shanghai Astronomical Observatory, Chinese Academy of Sciences, May 2006, Shanghai China
2. Klobuchar J, John A (1987) Ionospheric time-delay algorithm for single-frequency GPS users. IEEE Trans Aerosp Electron Syst 3:325–331
3. MOPS WAAS (1999) Minimum operational performance standards for global positioning system/wide area augmentation system airborne equipment. RTCA Inc. Documentation No. RTCA/DO-229B, 6
4. Van Graas F (2004) Wide area augmentation system research and development. Final Report, Prepared under Federal Aviation Administration Research Grant
5. Yasyukevich YV, Afraimoich EL, Palamartchouk KS, Tatarinov PV (2010) Cross testing of ionosphere models IRI-2001 and IRI-2012, data from satellite altimeters (Topex/Poseidon and Jason-1) and global ionosphere maps. Adv Space Res 46(8):990–1007

Chapter 11
Lunar Satellite Orbit Measurement Based on Visual/Radio Fusion

Yanlong Bu, Geshi Tang, Jianfeng Cao, Songjie Hu, Lue Chen and Baofeng Wang

Abstract A set of new orbit Measurement method was proposed based on the integration of high-resolution lunar surface imaging and ground-based radio measurement. Through the method, the advantage of stable tracking by radio measurements and the advantage of short-range measurement by onboard camera are expect to be fully integrated. The basic idea of the method is as following. First, combined with orbit constraints of a lunar high resolution imaging satellite, relying on optical imaging information and available reference images on the lunar surface, and based on the visual related theory of multi-view geometry and photogrammetry, the accurate location information of the satellite platform in a moment was calculated. Then, the location information was fused reasonably with satellite speed, range and angle by ground radio measurements. Thereby, a more flexible lunar orbiter orbit determination method than the existing methods was established. Currently, based on real data of "Chang'E II" satellite, visual/radio fusion-based orbit determination model were studied. Transfer relationship of the position and attitude between the satellite and imaging points on lunar surface was derived. Typical aspects of information fusion-based orbit determination were analyzed. Preliminary experimental results verify the feasibility of the proposed method. After parameter calibration, the partial positioning accuracy of "Chang'E II" is better than 100 m, variance limits at 30 m.

Supported by NSFC (No.41204026); DPFC (No.9140A24060712KG13290).

Y. Bu (✉) · G. Tang · J. Cao · S. Hu · L. Chen · B. Wang
National Key Laboratory of Science and Technology on Aerospace Flight Dynamics, Beijing, China
e-mail: byl_nudt@yahoo.com.cn

Y. Bu
Beijing Aerospace Control Center, Beijing, China

J. Sun et al. (eds.), *China Satellite Navigation Conference (CSNC) 2013 Proceedings*, Lecture Notes in Electrical Engineering 245,
DOI: 10.1007/978-3-642-37407-4_11,

Keywords Lunar orbiter · Orbit measure and determination · Photogrammetry · Radio measurement · Information fusion · "Chang'e II" satellite

11.1 Introduction

Under the current lunar and deep space TT&C system, the orbit measurement of the lunar satellite and other orbiter relies mainly on the earth based radio method, including the unified microwave system and the radio interferometry system [1]. In this way the accuracy of measurement is affected by the long distance between the earth based measurement station and the orbiter, also it's limited by the earth based observational arc. The visual/radio fusion positioning, with its flexibility and immediacy, has been well used in the UAV and the cruise missile. As the development of satellite borne high resolution imaging technology, the research of the orbiter positioning method with the information of the high resolution images started.

A typical case is the terrain relative navigation (TRN) technology, proposed by and given priority to the development by NASA. With this technology, when the orbiter is at its nearest approach to the astronomical body, the camera load takes photos for the characteristic area on the astronomical body, and the real time matching is executed between the observed images and the pre-built map and characteristic data base, so that the position and attitude of the orbiter can be decided [2, 3]. John Hopkins Lab (JHAPL) and JPL have verified TRN method with images from the moon and other solar system objects. Besides, the visual photography measurement and positioning technology used by ESA, for the Mars precise mapping, is based on the bundle adjustment [4–6]. Although the final goal is to precisely calibrate coordinates of all pixels in the Mars image, the solving of the camera platform position and attitude is an important step. This method is by its nature a from-coarse-to-fine iteration process. With the success of "Chang'E I" and "Chang'E II" lunar exploration missions, China owns the technology of deep space exploration. At the same time, a big amount of lunar surface images [7] and elevation data [8] have been acquired, which provide a good condition for us to develop visual fusion based orbit measurement and determination technology for deep space orbiters.

Based on the "Chang'E II" satellite measured data, visual/radio fusion based orbit measurement for a lunar satellite was studied in this paper. The primary position and attitude transfer model from the satellite to lunar surface was established. The typical implementation aspects were analyzed. Also the visual-only based lunar satellite positioning method and the visual/radio fusion based satellite orbit measurements have been preliminarily implemented.

11.2 Fundamentals

The main idea of the visual/radio fusion based lunar satellite orbit measurement is to solve the accurate position information of the lunar satellite platform at a certain moment, by using the multi-view geometry theory and photogrammetry technology, based on satellite imaging information and all kinds of available lunar base map, and taking into consideration the operating constraints of the satellite. At the same time, fuse the solved position information and the speed, distance and angle information from earth based radio stations, to come to a more flexible and complementary orbit measurement result, compared to results by current methods. The fundamental is shown in Fig. 11.1.

11.3 Lunar Satellite Position Transfer Relation Model

11.3.1 Major Coordinate Systems

The lunar satellite position transmission based on visual methods involves four major coordinate systems, which respectively are the lunar fixed coordinate system, the camera coordinate system, the image coordinate system and the satellite orbit coordinate system. The lunar fixed coordinate system is a coordinate system that describes the position of a certain space point relative to the moon. The camera coordinate system describes the position of a certain point relative to the

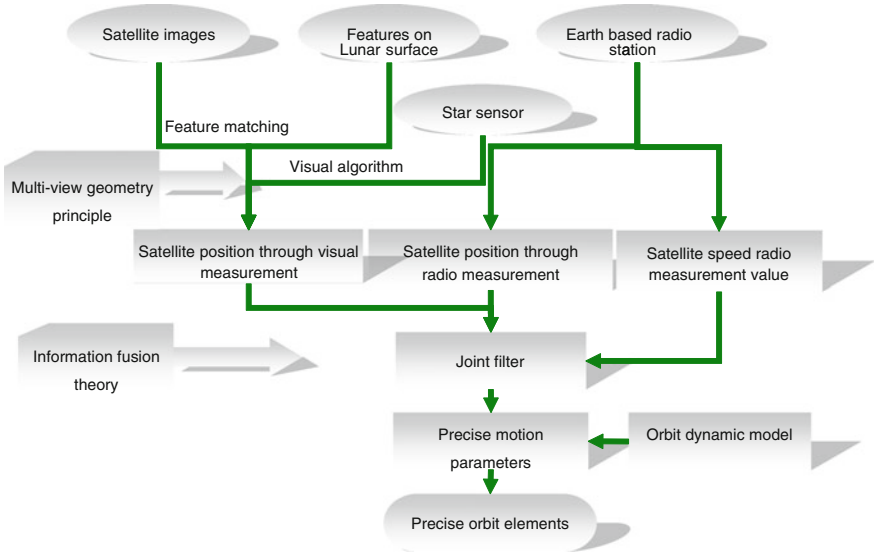

Fig. 11.1 Visual/radio fusion based satellite orbit measurement process

camera centre. It is fixedly connected to the satellite orbit, only with a fixed offset and angle relationship. The origin of the camera coordinate system is at the position (X_0, Y_0, Z_0) in the lunar fixed coordinate system, the rotation Euler angles between the two coordinate systems are φ, ω, κ. The image coordinate system is a two dimensional projected coordinate system located in the imaging plane of the camera. The origin is the corrected coordinate of the principal point (x_0, y_0, c) where x_0, y_0 are relative to the camera coordinate system, while c is the camera focus length 0. The orbit coordinate system is a transient coordinate system which can be used to be an intermediate coordinate system between the camera coordinate system and the lunar fixed coordinate system.

11.3.2 Colinearity Equation Constrains

According to the photogrammetry theory, for any point in the image coordinate system, there is a fixed colinearity equation constraint relation between its lunar fixed system coordinate (X, Y, Z) and its image system coordinate (x, y), as in Eq. (11.1). M and D are the rotation matrixes, λ is the scale factor, $\Delta x, \Delta y, \Delta z, \Delta\varphi, \Delta\omega, \Delta\kappa$ are the conversion parameters, and $X_0, Y_0, Z_0, \varphi, \omega, \kappa$ can be presented as a function of the camera image scanning lines [9].

$$\begin{pmatrix} x - x_0 \\ y - y_0 \\ -c \end{pmatrix} = \lambda M^T(\Delta\varphi, \Delta\omega, \Delta\kappa) D^T(\varphi, \omega, \kappa) \left[\begin{pmatrix} X \\ Y \\ Z \end{pmatrix} - \begin{pmatrix} X_0 + \Delta X_0 \\ Y_0 + \Delta Y_0 \\ Z_0 + \Delta Z_0 \end{pmatrix} \right] \tag{11.1}$$

$$\begin{pmatrix} \Delta X_0 \\ \Delta Y_0 \\ \Delta Z_0 \end{pmatrix} = D(\varphi, \omega, \kappa) \begin{pmatrix} \Delta x \\ \Delta y \\ \Delta z \end{pmatrix} \tag{11.2}$$

11.3.3 Lunar Satellite Space Position Transfer

In Eq. (11.1), $\Delta x, \Delta y, \Delta z, \Delta\varphi, \Delta\omega, \Delta\kappa$ can be taken as constants after correction, φ, ω, κ can be measured by star sensors. The coordinate of the principal point (x_0, y_0, c) can take the pre-defined value. The image points (x, y) can take the corresponding points, which are acquired via matching of the satellite observed image and the base map. Thus, for each image point, the camera center coordinate, namely the origin coordinate (X_0, Y_0, Z_0) of the camera system under the lunar fixed system, can be acquired by solving the colinearity equation. Because there is only a small fixed bias between the camera center and the lunar satellite platform center, when camera center positions are acquired in a time sequence, the satellite positions can be acquired at the same time. Furthermore, since there is a big

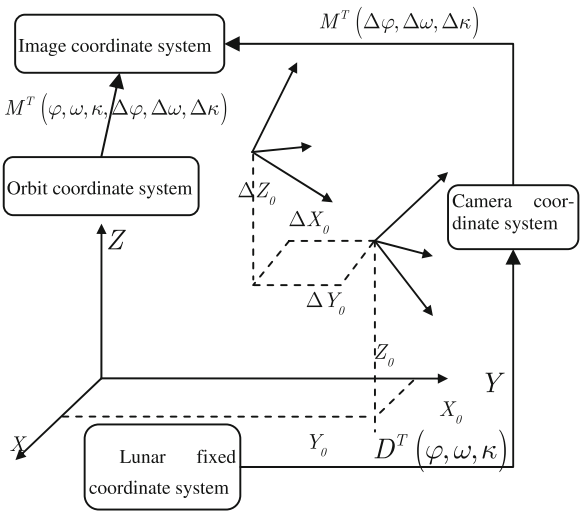

Fig. 11.2 Coordinate conversion diagram of satellite position and lunar surface match points

amount of corresponding points, the satellite attitude can be more sufficiently compensated. Figure 11.2 shows the lunar satellite platform center position transfer relationship based on the colinearity equation.

11.4 Visual Fusion Measurement Implementation Process

According to the principle of visual/radio fusion based lunar satellite orbit measurement, the implementation process can be divided into five basic modules. They are the radio data preprocessing module, the lunar surface image block array matching module, the fusion based parameter optimization module, the satellite position visual solving module and the fusion based satellite orbit computing module. Presented in Fig. 11.3 are the sequence of different modules and the key processing chains.

11.5 Experiment Results and Analysis

11.5.1 Base Map Preparation and Observed Image Calibration

The WAC global mosaic is of the best positioning accuracy among all existing global lunar surface base maps. This mosaic is made from the LROC (carried by US LRO) wide range camera images. Its resolution and positioning accuracy both reach 100 m. Based on the LROC-WAC lunar surface global base map,

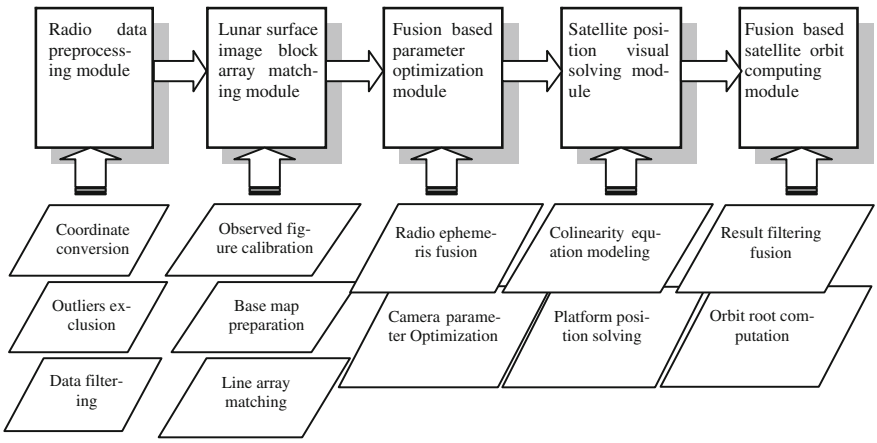

Fig. 11.3 Fusion based orbit determination implementation process modularization

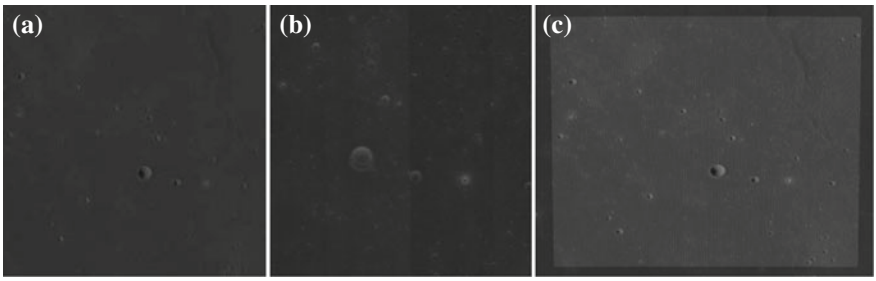

Fig. 11.4 Local base map preparation and observation image calibration. **a** A prepared local base map. **b** "Chang'e II" calibrated image. **c** The corresponding position in WAC

considering the actual operation situation of "Chang'E II" satellite and its constraint conditions, local base maps can be made. Figure 11.4a is a local base map of 20 × 20 km in size at lunar surface position (309.001°, 33.3°), with a pixel size of 200 × 200 pix. Figure 11.4b is the geometry calibration result of the "Chang'E II" satellite observation image on the corresponding area. As a comparison, the shadow part in Fig. 11.4c is the corresponding area of the local base map in the WAC original map [10].

11.5.2 Image Blocks Array Match in Wide Range

According to the operation characteristic of "Chang'E II" satellite and the imaging characteristic of the twin-line array CCD camera, local base map block

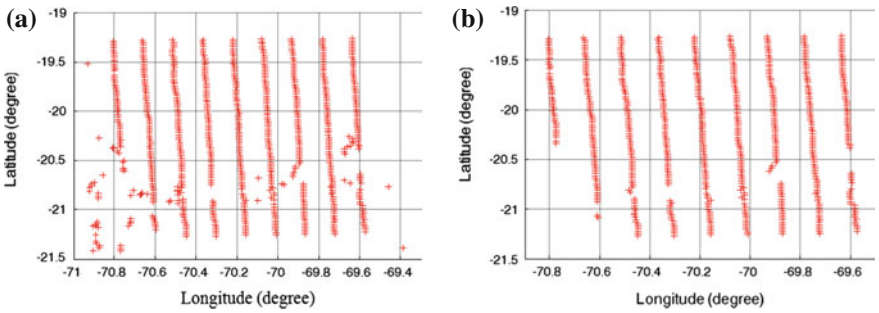

Fig. 11.5 Array match and correction. **a** Original match result. **b** RANSA corrected result

arrays and the observation image block arrays in wide range are made respectively, matching between array image blocks is achieved, and the RANSAC model is built to remove the wrong match points. Figure 11.5 shows the array match result and the correction result between the latitude of $-20.3 \pm 1.0°$. After correction, the math rate increases to 99 % from 95 %.

11.5.3 Position Solving Independent by Visual Method

Let the satellite attitude be fixed, no radio measurement information needed, the lunar satellite position can be solved via the colinearity constraint equation. Thus the lunar satellite independent visual positioning is achieved. But it is found that there exist biggish deviations in longitude, latitude and height, based on the exterior coincidence evaluation with the radio precise ephemeris, while the factional variances are minor. This provides beneficial conditions for the fusion based orbit measurement, as shown in Fig. 11.6.

11.5.4 Visual/radio Fusion Positioning

Because of high precision in the height direction by the earth based radio measurement, the weight of radio measurements in the height direction should be increased when information fusion. Also it can be taken as the constraints when building the object function to correct the satellite attitude. In Table 11.1, the correction results of four imaging areas in the 620th orbit are listed. Based on the attitude correction, visual based position solving can be carried out again. Compared to the radio precise ephemeris, the deviation in longitude, latitude and height can be largely reduced. As shown in Fig. 11.7, in the longitude and latitude

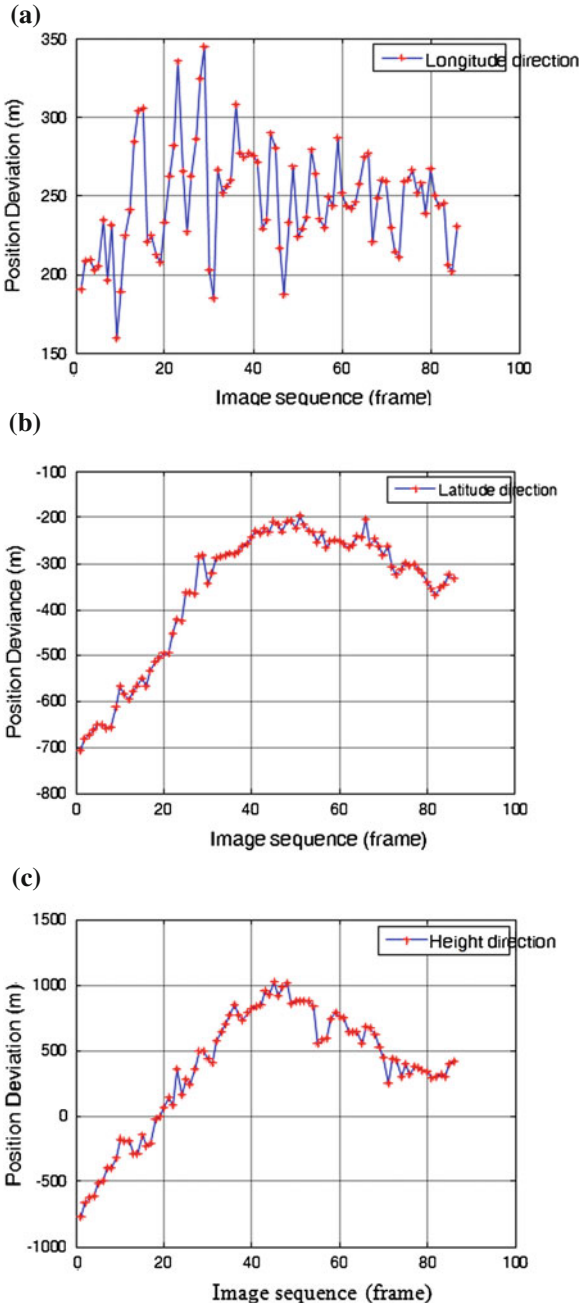

Fig. 11.6 Independent position solving result by visual method. **a** Deviation in longitude direction. **b** Deviation in latitude direction. **c** Deviation in height direction

Table 11.1 Height fused satellite attitude parameter correction

Orbit round	Sections	Pitch angle (radian)	Yaw angle (radian)	Roll angle (radian)
620	50	−0.007	0.002	0.002
	20	−0.006	0.002	0.004
	−20	0.001	0.001	0.003
	−50	0.001	−0.001	0.004

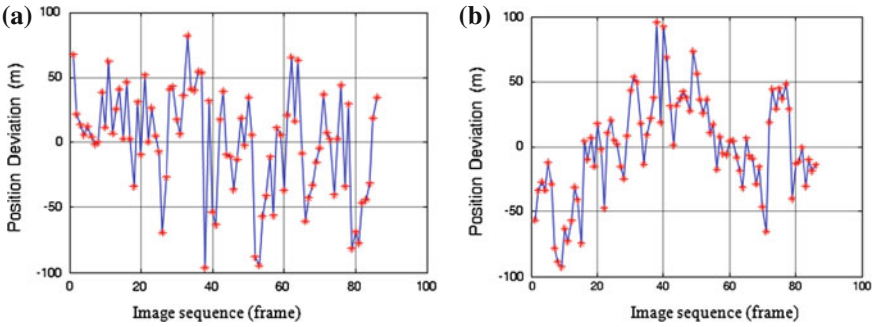

Fig. 11.7 Positioning results based on visual/radio fusion. **a** Deviation in longitude direction. **b** Deviation in latitude direction

direction, the precision of exterior coincidence between the visual/radio fusion based positioning result and the radio precise ephemeris is smaller than 100 m, and the variance is less than 30 m.

11.6 Conclusion

Aiming at high precision orbit measurement for deep space orbiter, a visual/radio fusion based lunar satellite orbit measurement model is build. A fusion measurement procedure is implemented combining with the "Chang'E II" satellite images, radio ephemeris and the related measurement and control constraints. After the parameter correction with the precise ephemeris, a precision of exterior coincidence of less than 100 m, with 30 m variance is achieved, which primarily prove the feasibility of the mentioned model. During the research, many error factors are found to affect the model precision. Further, the exact error source will be studied, and a deeper theoretical analysis will be performed, through which the visual/radio fusion base orbit measurement model is expected to be perfected.

Acknowledgments Thank Academician Yu Qifeng, Professor Liu Lin and Dr. Li Xiang for their beneficial help in the course of the study of this article.

References

1. Jian NC, Shang K, Zhang SJ et al (2009) A digital open-loop Doppler processing prototype for deep-space navigation. Sci China Ser G: Phys, Mech Astron 52(12):1849–1857
2. Johnson AE, Montgomery JF (2008) Overview of terrain relative navigation approaches for precise lunar landing. IEEE aerospace conference, pp 1–10
3. Johnson AE, Adnan Ansar, Larry H. Matthies (2007) A general approach to terrain relative navigation for planetary landing. In: Proceedings of the AIAA infotech and aerospace conference, AIAA 2007, p 2854
4. Schmidt R, Brand R (2003) Automatic determination of tie points for HRSC on Mars express. ISPRS workshop high resolution mapping from space 2003, Hannover
5. Heipke C, Ebner H, Schmidt R et al (2004) Camera orientation of Mars express using DTM information. Pattern Recogn Lect Notes Comput Sci 3175:544–552
6. Ebner H, Spiegel M, Baumgartner A et al (2004) Improving the exterior orientation of Mars express HRSC imagery. Int Arch Photogrammetry Remote Sens 35(B4):852–857
7. Li CL, Liu JJ, Ren X et al (2010) The global image of the Moon by the Chang'E-1: data processing and lunar cartography. Sci China Earth Sci 40(3):294–306
8. Ping J, Huang Q, Yan J et al (2008) Lunar terrain model CLTM-s01 based on ChangE-1 laser elevate data. Sci China 38(11):1601–1612
9. Yu QF, Shang Y (2009) Videometrics: principles and researches. Science Press, Beijing
10. Bu Y, Tang G, Wang M (2012) Local base map preparation for lunar orbiter scene matching aided navigation. Opt Precis Eng 20(8):1838–1845

Chapter 12
Performance Analysis of Single-Epoch Dual-Frequency RTK by BeiDou Navigation Satellite System

Jinlong Li, Yuanxi Yang, Junyi Xu, Haibo He, Hairong Guo and Aibing Wang

Abstract The initial performance of the BeiDou single-epoch dual-frequency RTK is evaluated. The success rate and reliability of single-epoch dual-frequency ambiguity resolution (AR) by BeiDou or BeiDou/GPS are analyzed, which are also compared with those by GPS alone. The results show that the BeiDou-only dual-frequency RTK is already feasible, whose single-epoch AR performance and positioning accuracy are compared to those of GPS alone. Furthermore, the success rate and reliability of BeiDou/GPS single-epoch AR are improved when compared to GPS, in particular under high cut-off elevation situations. It is also observed that the improvement of positioning accuracy reach to 31 % for the very short baseline of 4.2 m and is 2.9 % for the short baseline of 8.2 km.

Keywords BeiDou navigation satellite system · BeiDou/GPS · RTK · Single-epoch · Ambiguity resolution · Positioning accuracy

12.1 Introduction

In early 1980s, China began to study the navigation satellite system consistent with China's conditions. In 1994, China started the construction of BeiDou Navigation Satellite Demonstration System. In 2000, two BeiDou experimental satellites were launched, and the BeiDou Navigation Satellite Demonstration System was basically established. The third BeiDou experimental satellite was launched in 2003,

J. Li (✉) · J. Xu
Information Engineering University, Zhengzhou 450052, China
e-mail: along0730@163.com

Y. Yang
National Key Laboratory of Geo-Information Engineering, Xi'an 710054, China

H. He · H. Guo · A. Wang
Beijing Satellite Navigation Center, Beijing 100094, China

J. Sun et al. (eds.), *China Satellite Navigation Conference (CSNC) 2013 Proceedings*, Lecture Notes in Electrical Engineering 245,
DOI: 10.1007/978-3-642-37407-4_12,

further enhancing the performance of the BeiDou Navigation Satellite Demonstration System, and then it was officially brought into services [1]. In 2004 China started construction of BeiDou Navigation Satellite System (BDS) [2], and the first Medium Earth Orbit (MEO) satellite was launched in 2007. By the end of 2012, the BeiDou system will consist of 14 satellites, including 5 Geostationary Orbit (GEO) satellites, 5 Inclined Geosynchronous Orbit (IGSO) satellites (two in-orbit spares), and 4 MEO satellites. BeiDou Navigation Satellite System with global coverage will be completely established by 2020 [1]. BeiDou Navigation Satellite System retains the active positioning and short message services from BeiDou Navigation Satellite Demonstration System, and has provided initial operational services to China and most parts of its surrounding areas from December 27, 2011, including continuous passive positioning, navigation and timing services. Up to October 25, 2012, 16 BeiDou navigation satellites have been launched successfully, excepting that 3 satellites launched in September 19 and October 25, 2012 are testing in orbit, of which 11 satellites (4 GEO, 5 IGSO and 2 MEO) are in operation normally in the period considered for this paper (September 2012), which enables initial evaluation of the BeiDou-only RTK positioning. Shi et al. [3] assessed the accuracy of BeiDou/GPS dual-frequency precise relative positioning over very short baseline under the BeiDou "3 GEO + 3 IGSO" constellation. Montenbruck et al. [4] analyzed the success rate of BeiDou triple-frequency geometry-free AR and the accuracy of epoch-wise relative positioning by BeiDou carrier phase measurements over very short baseline. In this contribution, we evaluate the performance of the BeiDou single-epoch dual-frequency RTK over short baseline; the success rate and reliability of single-epoch AR and the accuracy of RTK positioning for BeiDou or BeiDou/GPS are demonstrated by BeiDou/GPS dual-frequency data collected in Beijing; the improvements of adding the BeiDou data to the GPS data in AR and positioning accuracy are also analyzed.

12.2 Short-Baseline BeiDou/GPS RTK Model

Because there are no common frequencies between BeiDou B1/B2 (1,561.098 MHz/1,207.14 MHz) and GPS L1/L2 carrier frequency, the respective reference satellites were selected for BeiDou and GPS system when constructing the Double-Differenced (DD) observation equation, in order to retain the integer property of the DD ambiguities [5, 6]. For simultaneous measurements over short baselines, the receiver and satellite related errors (the clock error, hardware delay and the initial phase offsets etc.) are completely eliminated, while the DD troposphere and ionosphere errors can also be neglected. As a result, the DD observation equation from the receivers r and b and the satellites s and k can be written as:

$$P_{br,j}^{ks} = \rho_{br}^{ks} + e_{br,j}^{ks} \tag{12.1}$$

$$L_{br,j}^{ks} = \rho_{br}^{ks} + \lambda_j N_{br,j}^{ks} + \varepsilon_{br,j}^{ks} \tag{12.2}$$

where the symbol $(\cdot)_{br}^{ks} = (\cdot)_r^s - (\cdot)_r^k - \left((\cdot)_b^s - (\cdot)_b^k\right)$ indicates the DD operator, P and L is the code and phase observations. The subscript j denotes B1, B2, L1 or L2, ρ the geometric distance between receiver and satellite, λ the wavelength, N the ambiguity, e and ε the code and phase measurement errors include unmodelled errors. It is well known that the satellites orbit errors and base receiver position errors will have no significant influence on the short baseline (<10 km) [7]. Thus, the linearized DD code and phase observation equations can be written as:

$$P_{br,j}^{ks} = \bar{\rho}_{br}^{ks} - \left(\mathbf{u}_r^s - \mathbf{u}_r^k\right)^{\mathrm{T}} \Delta\mathbf{r}_{br} + e_{br,j}^{ks} \tag{12.3}$$

$$L_{br,j}^{ks} = \bar{\rho}_{br}^{ks} - \left(\mathbf{u}_r^s - \mathbf{u}_r^k\right)^{\mathrm{T}} \Delta\mathbf{r}_{br} + N_{br,j}^{ks}\lambda_j + \varepsilon_{br,j}^{ks} \tag{12.4}$$

where the symbol $\bar{\rho}_{br}^{ks}$ denotes the approximate geometric distance between receiver and satellite, $\mathbf{u}_r^s = (\bar{\mathbf{r}}^s - \bar{\mathbf{r}}_r)\|\bar{\mathbf{r}}^s - \bar{\mathbf{r}}_r\|^{-1}$ is the unit line-of-sight vector from receiver to satellite. The baseline increment vector is $\Delta\mathbf{r}_{br}$, and the satellite and receiver approximate position vector are $\bar{\mathbf{r}}^s$ and $\bar{\mathbf{r}}_r$. As a result, the parameters to be estimated are the baseline increment vector and the DD integer ambiguities. After the real-valued ambiguities and its covariance matrix were obtained, the well-known LAMBDA algorithm [8] was applied to solve ambiguities to their integers, and the solved integer ambiguities were validated by the ratio test [9]. If the ratio test was passed, the corresponding integer ambiguities were fixed, and then the fixed solutions of the baseline vector were computed.

12.3 Inter-System Time and Coordinate System Differences

BeiDou and GPS both use their own time scales, in addition, which are connected to different realizations of UTC. The BeiDou system time is the BeiDou Time (BDT), which is connected to the UTC maintained by Nation Time Service Center ($\mathrm{UTC_{NTSC}}$), Chinese Academy of Sciences. The GPS system Time (GPST) is connected to the UTC kept by the US Naval Observatory ($\mathrm{UTC_{USNO}}$). Both GPST and BDT are continuous uniform time scale, which differ from UTC by leap seconds. GPST was started on January 6, 1980 UTC, and BDT was started on January 1, 2006 UTC [1], when the number of leap seconds is 14 s. As a result, the difference between GPST and BDT is 14 s, and further difference τ (modulo one second) arises from the fact that GPST and BDT are kept by different master clocks, namely, BDT = GPST − 14 s + τ. From the Eqs. (12.3) and (12.4), it is known that the clock errors related to difference time system are eliminated, and

thus the inter-system time system difference has no influence on the DD observations. The main influence of the time system difference reflects on the determination of the signal transmission time which will be used for satellite position calculation by using the navigation message. The time in the GPS and BeiDou navigation message belongs to their own time system respectively. Assuming that the receiver time of reception of the signal is in GPST, the signal transmission time t_s (in GPST for GPS satellites or BDT for BeiDou satellites) can be computed by the following formulas:

$$t_s^{\mathrm{GPS}} = t_r^{\mathrm{GPS}} - \frac{P^{\mathrm{GPS}}}{c} + dt^{\mathrm{GPS}} \quad t_s^{\mathrm{BDS}} = t_r^{\mathrm{GPS}} - 14 - \frac{P^{\mathrm{BDS}}}{c} + dt^{\mathrm{BDS}} \tag{12.5}$$

where the symbol t_r denotes the reception time at receiver (in GPS Time), and BDS denotes BeiDou system, *dt* satellite clock error. It should be pointed out that the difference between the GPST and BDT (modulo one second) is included in the code observations.

The coordinate reference system of the BeiDou system is China Geodetic Coordinate System 2000 (CGCS2000) [2], and that of GPS is World Geodetic System 1984 (WGS84). The definitions of the origin, scale, orientation and time evolution of the orientation for CGCS2000 and WGS84 are identical [10, 11]. Their realization is also consistent, and they can be treated as the same coordinate system at the level of a few centimeters. It should be pointed out that the baseline increment vector $\Delta\mathbf{r}_{br}$ in the Eqs. (12.3) and (12.4) respectively belong to CGCS2000 for BeiDou observations and WGS84 for GPS observations, namely, in nature that it is different in BeiDou and GPS satellite observation equations. However, the influence of the cm-level inter-coordinate system difference on the calculation of the baseline vector can be neglected for the short baseline. Namely, it can be treated as the common parameter of GPS and BeiDou observations, while the BeiDou and GPS DD observations are related to each other just by the common parameter.

12.4 Computations and Analysis

Three static stations (zz03, zz01 and gs01) data in Beijing were collected on September 5, 2012 by the UB240-CORS-II BD2/GPS dual-system quad-frequency (B1/B2 + L1/L2) receivers produced by Beijing Unicore Communications Incorporation. The time span is 24 h, and the sampling rate is 1 s. All data have been processed in a simulated single-epoch RTK mode and the success rate and failure rate of single-epoch AR and the positioning accuracy were analyzed. The success rate of AR was determined as the proportion between the ambiguity-fixed epochs and the total epochs, which denoted the availability of the RTK positioning, and the failure rate of AR was the proportion between the epochs that the integer ambiguity was fixed incorrectly and the ambiguity-fixed epochs, which

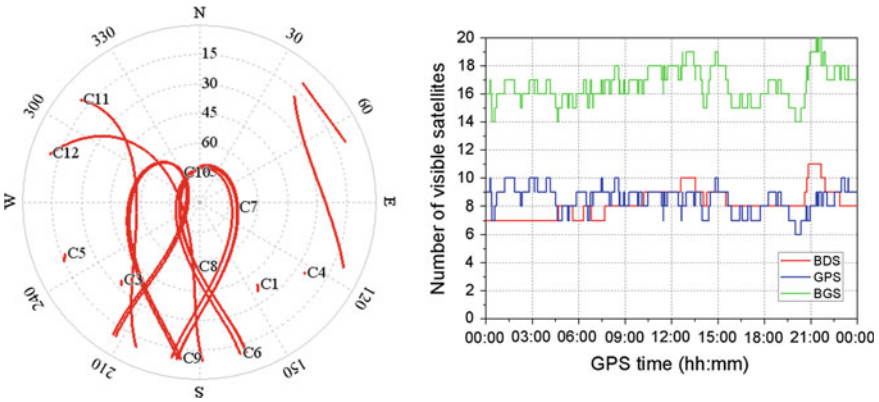

Fig. 12.1 Sky plot of BeiDou satellites in Beijing (*left*) and the number of visible satellites (*right*)

denoted the reliability of the RTK positioning. The sky plot of BeiDou satellites in Beijing is shown in Fig. 12.1 (left).

The number of visible satellites, EDOP, NDOP and UDOP of BeiDou, GPS and BeiDou/GPS with the cut-off elevation of 10° are depicted in Figs. 12.1 (right) and 12.2. In the following text, we name BeiDou/GPS as BGS in the figures and tables for brevity.

From Fig. 12.1 (right), it is known that the number of visible satellites is 6–10 for GPS, 7–11 for BeiDou, and 14–20 for BeiDou/GPS. The number of visible satellites for BeiDou/GPS is about the double of that for GPS. It is can be clearly seen in Fig. 12.2 that the EDOP of BeiDou is almost comparable to that of GPS and even it is smoother, while the NDOP and UDOP of BeiDou are larger than those of GPS. The averaged EDOP, NDOP and UDOP are 0.73, 1.46 and 2.06 for BeiDou, 0.66, 0.82 and 1.64 for GPS, and 0.45, 0.57 and 1.11 for BeiDou/GPS. Compared to those of GPS, the improvements of these DOPs of BeiDou/GPS are 32, 30 and 32 % respectively. Therefore, it is expectable that the BeiDou/GPS single-epoch AR will be significantly enhance, due to the increased number of visible satellites in combination with the stronger model.

12.4.1 Experiment over Very Short Baseline

A very short baseline of 4.2 m was formed from two stations zz03 and zz01. The total number of epochs is 86,383, but only one epoch the ratio of BeiDou single-epoch AR is smaller than the threshold of ratio test (ratio = 1.5). Both the success rates for GPS and BeiDou/GPS are 100 %. While the failure rates are 0 for BeiDou, GPS and BeiDou/GPS. The ratio values of single-epoch AR for BeiDou, GPS and BeiDou/GPS are shown in Fig. 12.3.

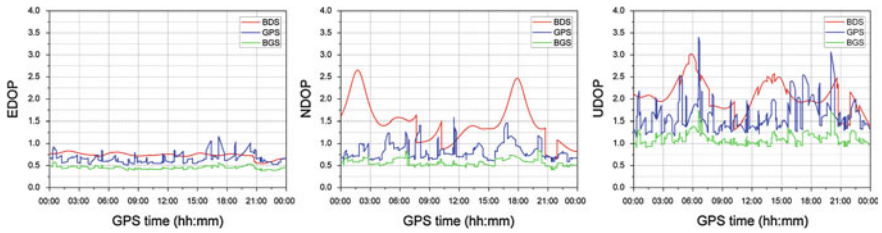

Fig. 12.2 DOP values (*left* EDOP; *middle* NDOP; *right* UDOP)

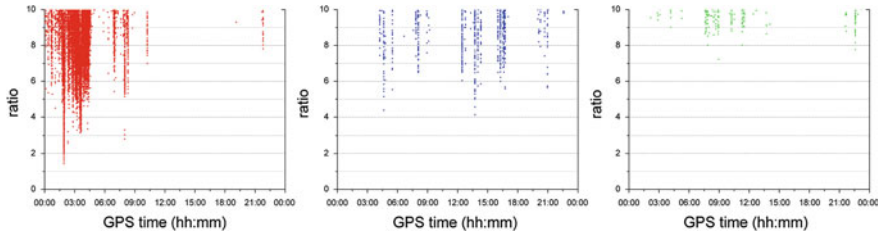

Fig. 12.3 Ratio values (*left* BDS; *middle* GPS; *right* BGS)

From Fig. 12.3, it is seen that the ratio values of BeiDou single-epoch AR is smaller than 2 only a few epochs. The ratio values of single-epoch AR are larger than 4 for GPS and 7 for BeiDou/GPS. The ratio-test tests the closeness of the float solution to its nearest integer vector [12], the larger it is, the closer the float solution to its nearest integer vector, and the reliability of the integer solution is higher.

The static baseline fixed solution of GPS dual-frequency narrow-lane combination (Ln) by Trimble Total Control 2.71 is used as "true" position. The horizontal scatters and vertical time series of single-epoch RTK fixed solution for BeiDou, GPS and BeiDou/GPS are depicted in Figs. 12.4 and 12.5. The STD and BIAS in the east, north and up direction are given in Table 12.1.

From Fig. 12.4, it can be clearly seen that the scatter in the east direction is evidently smaller than that in the north direction for BeiDou (the left graph), of which scatter plot is analogously oval, while the scatter plots of GPS (the middle graph) or BeiDou/GPS (the right graph) is almost circular. From Fig. 12.5, we can see that the fluctuating of vertical time series of BeiDou/GPS RTK positioning is smaller than those of BeiDou or GPS. The STD of BeiDou RTK positioning in the east direction is 0.88 mm even smaller than that of GPS, whose STD is 1.36 mm, see Table 12.1. Though the STDs of BeiDou RTK positioning in the north and up direction are only 2.45 and 4.85 mm, they are still larger than those of GPS, of which the STDs are 1.65 and 3.65 mm. The STDs of BeiDou/GPS RTK positioning in the east, north and up are 0.85, 1.18 and 2.68 mm respectively, and the corresponding improvements are about 37.5, 28.5 and 26.6 % when compared to GPS. Furthermore, the BAISs of BeiDou RTK positioning are only 0.09, −1.63

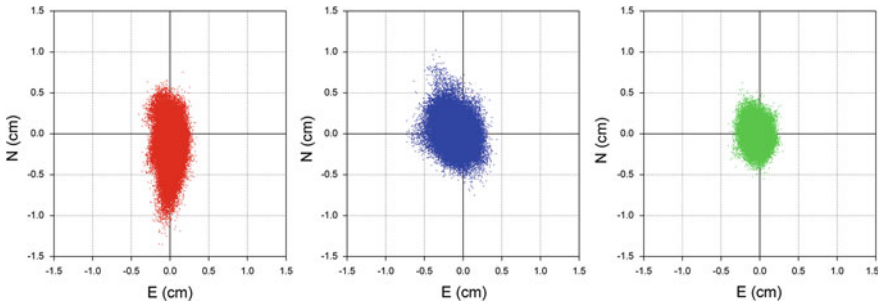

Fig. 12.4 Horizontal error of RTK positioning (*left* BDS; *middle* GPS; *right* BGS)

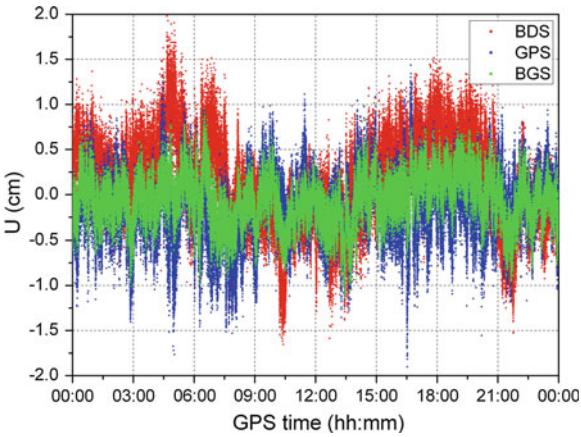

Fig. 12.5 Vertical errors of RTK positioning

Table 12.1 RTK positioning accuracy for very short baseline of 4.2 m (unit: mm)

	STD			Improvement (%)	BIAS		
	BDS	GPS	BGS		BDS	GPS	BGS
E	0.88	1.36	0.85	37.5	0.09	−0.93	−0.41
N	2.45	1.65	1.18	28.5	−1.63	0.24	−0.11
U	4.85	3.65	2.68	26.6	1.51	−1.53	−0.69

and 1.51 mm in the east, north and up direction, which means there is no evident bias exist between the BeiDou RTK solution and the "true" position obtained by GPS data. The BIASs of BeiDou/GPS RTK positioning in the east, north and up direction are −0.41, −0.11 and −0.69 mm and also smaller than those of GPS. As a whole, the 3D RMSs of BeiDou, GPS and BeiDou/GPS RTK positioning are 5.94, 4.60 and 3.16 mm respectively, and the improvement of adding the BeiDou data to the GPS data achieve 31.3 %, which is very exciting.

12.4.2 Experiment over Short Baseline

A short baseline of 8.2 km was formed from two stations zz03 and gs01. In order to evaluate the performance of BeiDou and BeiDou/GPS RTK under some challenging circumstances, the success rate and failure rate of single-epoch AR are counted under different cut-off elevations of 10°–40° and the consequent results are shown in Table 12.2.

From Table 12.2, we can see that the success rates of single-epoch AR are larger than 94 % for BeiDou and 96 % for GPS with the cut-off elevations of 10°–25°, and the failure rates are smaller than 0.7 % for BeiDou or GPS. Therefore, it is evident that the availability and reliability of the BeiDou single-epoch RTK are comparable to those of GPS at least in the open-sky conditions. When the cut-off elevation is higher than 30°, the success rates of BeiDou are smaller than those of GPS, and its failure rates are also larger than those of GPS. This may be related to the special configuration of BeiDou constellation. It can be seen in Fig. 12.1 (left) that two GEO satellites (C04 and C05) will be shielded when the cut-off elevation reach to 30°, which reduces the number of visible satellite. The success rates of BeiDou/GPS single-epoch AR are larger than those of GPS. The success rates are 100 % when the cut-off elevation is 20° and 25°. Besides, the improvement becomes more evident with higher the cut-off elevations. The failure rates of BeiDou/GPS single-epoch AR are smaller than those of GPS except for the cut off elevation of 40° situation. When the cut-off elevations are smaller than 30°, their failure rates is 0 %. Therefore, the availability and reliability of BeiDou/GPS are obviously superior to those of GPS.

The static baseline fixed solution of GPS dual-frequency ionosphere-free combination (Lc) by Trimble Total Control 2.71 is used as "true" position. The horizontal scatters and vertical time series of single-epoch RTK fixed solution for BeiDou, GPS and BeiDou/GPS with cut-off elevation of 10° are depicted in Figs. 12.6 and 12.7 (left). The STD and BIAS in the east, north and up direction are given in Table 12.3.

From Fig. 12.6, it is seen that the solution of BeiDou, GPS and BeiDou/GPS RTK positioning are offset from the "true" position in the west–north direction. The BIASs of BeiDou, GPS and BeiDou/GPS solution are about −1, 1 and

Table 12.2 Success rate and failure rate of single-epoch AR (ratio = 1.5)

Cut-off elevation (°)	BDS		GPS		BGS	
	Success	Failure	Success	Failure	Success	Failure
10	94.29	0.11	96.93	0.03	98.43	0.00
15	94.74	0.15	98.36	0.16	99.997	0.00
20	94.61	0.45	98.00	0.20	100.00	0.00
25	94.09	0.63	96.77	0.17	100.00	0.00
30	75.66	2.31	92.00	0.67	99.81	0.00
35	46.00	12.39	77.22	1.02	98.94	0.05
40	10.52	9.00	54.62	0.93	91.66	1.84

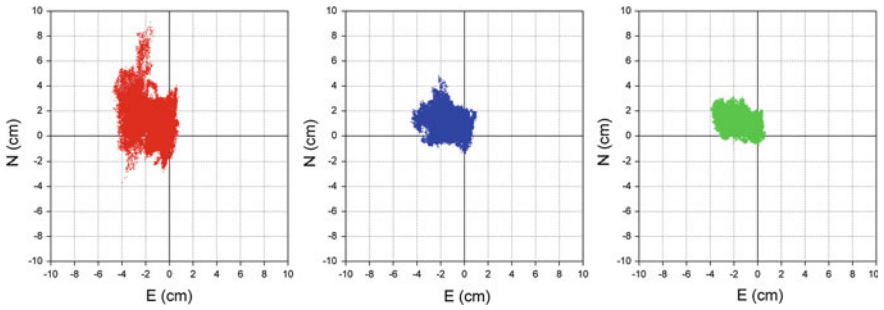

Fig. 12.6 Horizontal error of RTK positioning (*left* BDS; *middle* GPS; *right* BGS)

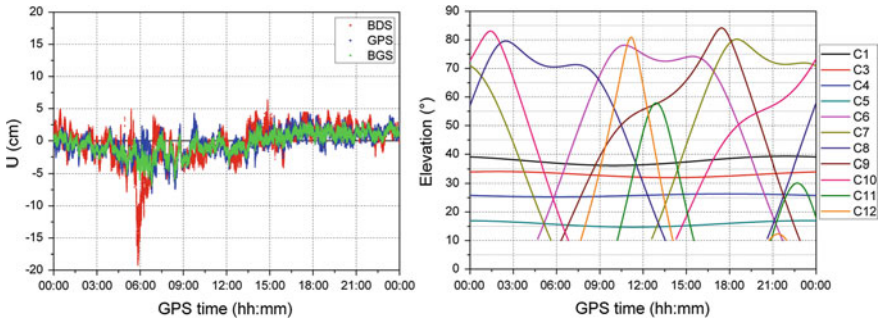

Fig. 12.7 Vertical error of RTK positioning (*left*) and the elevation of BeiDou satellites (*right*)

Table 12.3 RTK positioning accuracy over short baseline of 8.2 km (unit: cm)

	STD			Improvement (%)	BIAS		
	BDS	GPS	BGS		BDS	GPS	BGS
E	1.16	0.94	0.97	−3.2	−1.24	−1.03	−1.10
N	1.29	0.72	0.63	12.5	0.96	0.96	0.97
U	2.77	1.80	1.66	7.8	−0.32	−0.33	−0.34

−0.3 cm in the east, north and up direction respectively, see Table 12.3. The similar BIAS between the BeiDou and GPS solutions suggest that there are strong correlative errors exist between the BeiDou and GPS DD observations. It is easily concluded that they should be the DD ionosphere remainder because the ionosphere delay is not processed in this study while the "true" position is computed by the GPS ionosphere-free combinations. As a result, the STD improvements brought by the adding BeiDou measurements are only −3.2, 12.5 and 7.8 % in the east, north and up directions when compared to GPS-only. As a whole, the 3D RMSs of BeiDou, GPS and BeiDou/GPS RTK positioning are 3.64, 2.60 and 2.52 cm respectively, and the improvement of adding the BieDou data to the GPS data is only 2.9 % and marginal. Therefore, in order to take full advantage of the

adding BeiDou data, it may be necessary to minutely deal with the DD ionosphere remainder, though it has no significant influence on AR over short baselines. However, though the ionosphere delay is not processed, the 3D RMS of BeiDou RTK positioning is only 3.64 cm. From Fig. 12.7 (left), we can see that there is a large jump of near 20 cm at 6:00 in the vertical time series of BeiDou RTK positioning. The may be caused by the large DD ionosphere remainder due to the large satellite elevation differences (see Fig. 12.7) and the large UDOP value (see Fig. 12.2).

12.5 Conclusions

BeiDou Navigation Satellite System has accomplished the deployment of "5 GEO + 5 IGSO + 4 MEO" region constellation, and will officially provide the full services at least in the Asia–Pacific area by the end of 2012. In the present initial services phase, we evaluated the performance of BeiDou single-epoch dual-frequency RTK with real data collected in Beijing, and the following conclusions can be drawn:

- The availability and reliability of BeiDou single-epoch dual-frequency RTK AR are almost comparable to those of GPS, and those of BeiDou/GPS are higher than those of GPS. Furthermore, the advantage is more remarkable with the higher cut-off elevations.
- As a whole, the accuracy of BeiDou RTK positioning is slightly worse than that of GPS at present, but it has reach to mm–cm level over very short and short baselines in this contribution. The accuracy of BeiDou RTK positioning in the east direction is even better than that of GPS over very short baseline.
- The accuracy improvement of adding the BeiDou data to the GPS data reach to 31.3 % for the very short baseline of 4.2 m, but the improvement is only marginal (2.9 %) for the short baseline of 8.2 km, which imply that the strong correlative errors is exist between BeiDou and GPS DD observations, likely due to the DD ionosphere remain errors which is not dealt with in this study.
- The high availability and reliability of BeiDou/GPS single-epoch AR under the cut-off elevations of 30°–40° is promising to relieve the embarrassment of GPS RTK positioning in the urban canyon.
- With a completed BeiDou constellation or in the low latitude area of Asia–Pacific area, the number of BeiDou visible satellites will further increase [13]. Thus, it is expectable that the availability and reliability of BeiDou single-epoch RTK positioning will be improved consequently and those of BeiDou/GPS will be much better than at present based on GPS-only.

Acknowledgments This work is supported by the National Natural Science Funds of China (Grant Nos. 41020144004; 41104022), the National ''863 Program'' of China (Grant No: 2013AA122501) and the 2nd and 3rd China Satellite Navigation Conference (Grant Nos. CSNC2011-QY-13; CSNC2012-QY-3).

References

1. China Satellite Navigation Office (2012) Report on the development of BeiDou navigation satellite system (Version 2.0). May 2012
2. Yang Y (2010) Progress, contribution and challenges of Compass/Beidou satellite navigation system. Acta Geodaetica et Cartographica Sinica 39(1):1–6
3. Shi C, Zhao Q, Hu Z, Liu J (2012) Precise relative positioning using real tracking data from COMPASS GEO and IGSO satellites. GPS Solut, Published online: 19 May 2012, doi: 10.1007/s10291-012-0264-x
4. Montenbruck O, Hauschild A, Steigenberger P, Hugentobler U, Teunissen P, Nakamura S (2012) Initial assessment of the COMPASS/BeiDou-2 regional navigation satellite system. GPS Solut, Published online: 12 June 2012, doi: 10.1007/s10291-012-0272-x
5. Alves P (2001) The effect of Galileo on carrier phase ambiguity resolution. In: ION GPS 2001, 11–14 Sept 2001, Salt Lake City, UT, pp 2086–2095
6. Julien O, Cannon ME, Alves P, Lachapelle G (2004) Triple frequency ambiguity resolution using GPS/Galileo. Eur J Navig 2(2):51–56
7. Kleusberg A, Teunissen PJG (eds) (1996) GPS for geodesy. Springer, Berlin
8. Teunissen PJG (1995) The least-squares ambiguity decorrelation adjustment: a method for fast GPS integer ambiguity estimation. J Geod 70(1–2):65–82. doi:10.1007/BF00863419
9. Verhagen S (2004) Integer ambiguity validation: an open problem? GPS Solut 8:36–43. doi:10.1007/s10291-004-0087-5
10. Ziqing W (2008) China geodetic coordinate system 2000 and its comparison with WGS84. J Geodesy Geodyn 28(5):1–5
11. Yang YX (2009) Chinese geodetic coordinate system 2000. Chin Sci Bull 54:2714–2721. doi:10.1007/s11434-009-0342-9
12. Teunissen PJG, Verhagen S (2009) The GNSS ambiguity ratio-test revisited: a better way of using it. Surv Rev 41(312):138–151
13. Yang Y, Li J, Xu J, Tang J, Guo H, He H (2011) Contribution of the COMPASS satellite navigation system to global PNT users. Chin Sci Bull 56(26):2813–2819. doi:10.1007/s11434-011-4627-4

Chapter 13
Research on Receiver Clock Jump Detection and Processing in Precise Point Positioning

Rui Zhang, Yibin Yao, Runan Wu and Weiwei Song

Abstract The Melbourne-Wubbena (*MW*) and Geometry-Free (*GF*) combinations of observations are generally used to detect cycle slips in Precise Point Positioning (PPP). This article describes the GNSS receiver clock jump phenomenon, and analyzes its impact on *MW* and *GF* combined observations from the observation model. The experiment confirms that receiver clock jump will not affect *GF* combination observations, but will lead to a misjudgment of *MW* cycle slip detection; and changes are same for all satellites. This essay proposes a new method that uses satellite differenced *MW* together with the undifferenced *MW* and *GF* combinations to detect the clock jump in PPP; in the processing, clock jump is estimated with the coordinate parameters together. The experimental results show that this method can detect and estimate receiver clock jump, avoid unnecessary re-initialization and help to improve the positioning accuracy, effectively.

Keywords GNSS receiver · PPP · Clock jump · Cycle slip

13.1 Introduction

Using Single GNSS receiver's observation data, the users can achieve high accuracy positioning both real time and afterwards with precise satellite ephemeris and clock correction product at any position of the global scope, which is called

R. Zhang (✉) · Y. Yao
School of Geodesy and Geomatics, Wuhan University, Wuhan, China
e-mail: zhangrui_sgg@126.com

R. Wu
State Key Laboratory of Information Engineering in Surveying, Mapping and Remote Sensing, Wuhan University, Wuhan, China

W. Song
Research Center of GNSS, Wuhan University, Wuhan, China

J. Sun et al. (eds.), *China Satellite Navigation Conference (CSNC) 2013 Proceedings*, Lecture Notes in Electrical Engineering 245,
DOI: 10.1007/978-3-642-37407-4_13,

the precise point positioning (PPP). PPP has more advantages compared with relative positioning mode, such as: supply more available observations and preserve the original observation information; get the receive station coordinates directly, at the same time, estimated coordinates of each station are uncorrelated, which is easy for quality control [1]. After the satellite signal is captured by GNSS receiver, as long as the tracking is not interrupted, the receiver will automatically give the carrier phase changes during tracking. High-precision positioning results will be obtained using continuous phase observations. Therefore, in PPP solution, it is very necessary to pretreat the observations before coordinate estimated. The quality of pretreatment will directly determine the positioning accuracy and reliability. A lot of methods have been proposed for cycle slip and gross error detection up till now, such as: differential method, Doppler frequency shift method, Kalman filtering method and so on [2]. Among all these, the turbo-edit algorithm proposed by Blewitt is most widely used in PPP, which uses the *MW* and *GF* combined observations to detect cycle slip [3].

Generally, GNSS receiver's internal time scale takes quartz clock, whose day frequency stability is around 10^{-11}. In the start of GNSS observation, the receiver is set to synchronize with the GNSS time, but the synchronization is not so rigorous due to the limit of quartz clock's accuracy. Moreover, with the measurement carried out, the receiver clock will shift gradually [4]. In order to maintain sync with the GNSS time, most receivers will insert periodically clock jump to control the receiver clock keeping within a certain range of accuracy. Receiver clock jump has an effect on observations similar to cycle slip. At present, the receiver clock jump is usually detected and repaired PPP data processing. This essay proposes a new method that uses satellite differenced *MW* together with the undifferenced *MW* and *GF* combinations to detect the clock jump in PPP; in the processing, clock jump is estimated with the coordinate parameters together.

13.2 GNSS Receiver Clock Jump

There are mainly two kinds of receiver clock jumps: millisecond jump and every second jump. Millisecond jump is to correct the receiver by inserting 1 ms clock correction periodically; while every second jump is to correct the receiver clock every second, and the correction is very small (usually superior to the microsecond range). Generally speaking, millisecond jump has little influence on GNSS observation, so milliseconds jump is mostly considered during clock jump detection [5]. The clock jump will lead to pseudorange or phase observations jumping at all frequencies for all observed satellites which are similar to cycle slip. However the two kinds of data step is different essentially, because the clock jump will not change satellite ambiguity but cause a systematic bias for all satellites. Data step caused by clock jump can roughly divided into two categories: The phase step from clock jump divided into two classes roughly: one is that

pseudorange and phase jump together; the other is pseudorange jumps and phase keeps continuation [6].

MW is phase position Wide-lane and pseudorange Narrow lane combined:

$$M_w = L_w - P_n,\ P_n = \frac{f_1 P_1 + f_2 P_2}{f_1 + f_2} \tag{13.1}$$

GF combination is L_1L_2 combination:

$$L_I = L_1 - L_2,\ N_I = N_1 - N_2 = \frac{\lambda_1\lambda_2}{\lambda_m\lambda_n}(N_w - N_c) \tag{13.2}$$

where f_k represents the frequency of k wave range; λ_k represents the wavelength; L_k is phase observation, P_k is pseudorange observation and N_k is ambiguity; λ_w is wide-lane wavelength, λ_n is narrow lane wavelength.

From the above equations, it can be seen that *MW* combination can reflect the variety of wide-lane integer ambiguity well, but it can't detect the cycles slip when there are same cycles slips at both frequencies, and *GF* combination is sensitive to cycle slip, but not useful for some specific cycle slip combination. Priori information such as satellite orbits or station coordinates are not needed when using the two combinations to detect cycle slip, at the same time, there is no need to do any difference between the stations or the satellites; so it can be used for any length of baseline, especially suitable for PPP [3].

When the clock jump happens both for pseudorange and phase observations, the *MW* and *GF* combination will not be influenced, and the systematic bias caused by clock jump can be absorbed in receiver clock in parameter estimation, which will not affect the positioning solver results. However, when the clock jump just happens for pseudorange observations, it will not affect the *GF* combination, but will influence the *MW* combination badly. When this happens, the clock jump is easy to be mistaken for cycle slip. This may lead to ambiguity resetting of all satellites and reinitialize of PPP solution. The solving accuracy and continuity will be seriously affected [6].

13.3 Detect and Processing of Receiver Clock Jump in PPP

The clock jump happens just for pseudorange observations will cause misjudgment of *MW* combination and appear an illusion that there are cycle slips for all satellites. So when detecting cycle slips, the interference of the receiver clock must be excluded. Because the interference of clock jump is the same for all satellites, it can be eliminated by inter-satellite differential. The single differential combination observation between satellite i and satellite j is:

$$\Delta M_w^{ij} = \left(L_w^i - L_w^j\right) - \left(P_n^i - P_n^j\right) \tag{13.3}$$

The single differential *MW* combination can eliminate the impact of receiver clock jump on pseudorange observation, and avoid the misjudgment of cycle slip detecting. But only using the single differential *MW* combination may cause some other weak points as follows: (1) the processing can be complicated when reference satellite changes; (2) when cycle slip happens, it is needed to judge whether it happens at the reference satellite or the no reference satellite, which may lead to misjudgment. In this paper, we propose a new method: single differential *MW* is used to assist the undifferenced *MW* and *GF* combinations to detect the cycle slip in PPP. The procedure is as follows: (Fig. 13.1).

After detecting the clock jump, the general processing approach is to correct it on the observations directly. However this method not only changes the original observations, but also when the value of receiver clock jump changes (not completely 1 ms), it may cause the positioning results appear deviation. The mathematical model of PPP is as follows [1]:

$$\begin{cases} P_i^j = \rho^j - cdt + dI^j - dT^j + \varepsilon_{i,P}^j \\ \lambda_i \Phi_i^j = \rho^j - cdt - N_i^j \lambda_i - dI^j - dT^j + \varepsilon_{i,\varphi}^j \end{cases} \tag{13.4}$$

where P, Φ represent the code and phase measurements of the receiver transmitter, respectively; ρ, c, dt, dI, dT are the corresponding distance, light speed receiver and transmitter clock errors, slant total electron content (STEC), and slant tropospheric delay, respectively; λ represents the wavelength of carrier observations, and N represents carrier phase ambiguity in cycles.

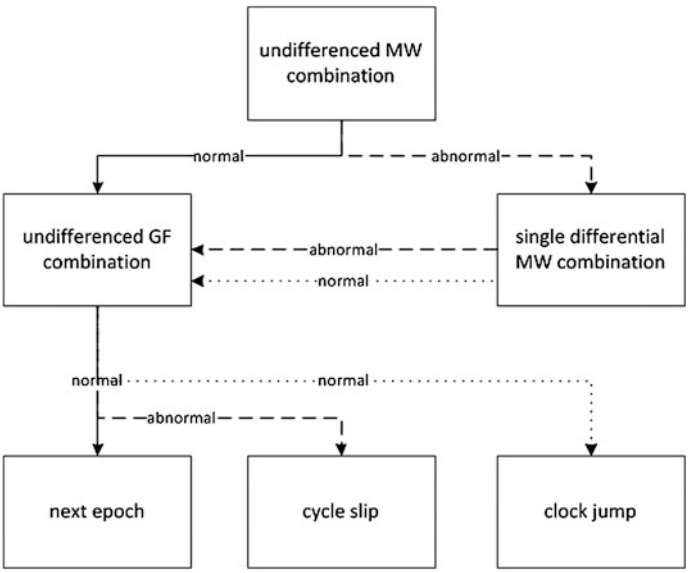

Fig. 13.1 Cycle slip and clock jump detection flowchart

Because the receiver clock jump is the same for pseudorange observations of all satellites, we can add a clock jump parameter for the pseudorange equation, and then the mathematical model turns to be:

$$\begin{cases} P_i^j = \rho^j - cdt + J_{clk} + dI^j - dT^j + \varepsilon_{i,P}^j \\ \lambda_i \Phi_i^j = \rho^j - cdt - N_i^j \lambda_i - dI^j - dT^j + \varepsilon_{i,\varphi}^j \end{cases} \tag{13.5}$$

where J_{clk} represent receiver clock jump. When receiver clock jump is detected, the parameter is reset, or it will be estimated as a same parameter between the epochs.

13.4 Experimental and Analysis

In this experiment, observation data used are from BeiDou Experimental Tracking Stations (BETS) network [7]. The network is built from early 2011 by Wuhan University, and the reference stations mostly lay in Asia-Pacific region. The BETS tracking network is equipped with receiver named UR240-CORS. The kind of receiver is independently developed by China, and can capture dual-band BeiDou/GPS signal, but the data appear frequently clock jump phenomenon. Because temporary no public institutions can provide precise ephemeris and clock products for BeiDou satellites, only GPS data are used in PPP processing and the precision ephemeris and clock products for GPS satellites are provided by IGS. Data processing is based on Passion software which is developed by the author. Figure 13.2 shows the positioning results of lasa station at DOY126, 2012. The data is simulation dynamic and processed by two different algorithms: the new clock jump parameter model and the traditional PPP model.

It can be seen from Fig. 13.3: the receiver clock jump often occurs, and the frequency is approximately 1 h. The traditional PPP algorithm always mistaken clock jump for cycle slip, and reinitialize. This causes poor positioning results; the 3D deviation RMS of full arcs is 0.309, 0.435 and 1.142 m for N, E, and U directions, respectively. The PPP model considering the clock jump parameters can effectively detect, estimated the clock jump, so that the clock jump does not have a negative impact on the positioning results. The 3D deviation RMS of full arcs is 0.038, 0.075, 0.089 m, and the statistical results after the convergence is 0.015, 0.018 and 0.047 m, respectively (Fig. 13.4).

13.5 Summary

This essay proposes a new method that uses satellite differenced *MW* together with the undifferenced *MW* and *GF* combinations to detect the clock jump in PPP; in the processing, clock jump is estimated with the coordinate parameters together.

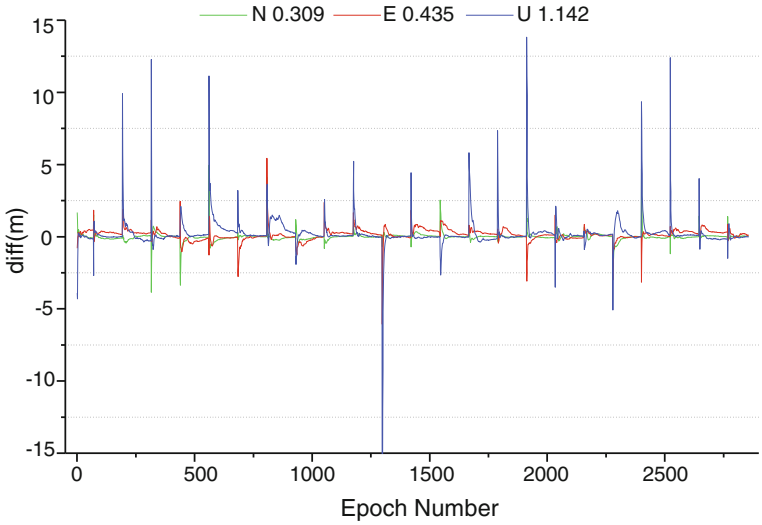

Fig. 13.2 Traditional algorithm solving results

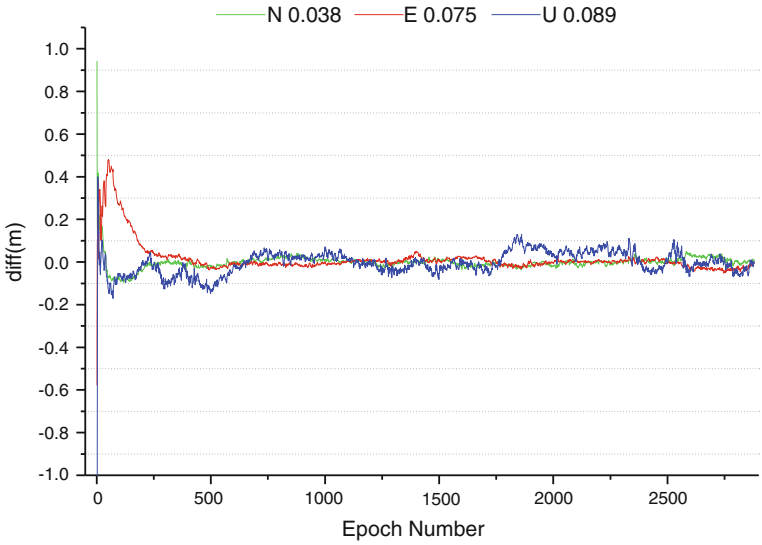

Fig. 13.3 New algorithm solving results

The new algorithm is validated analysis by measured data of lasa station which is equipped with UR240-CORS receiver. The experimental results show that this method can detect and estimate receiver clock jump, avoid unnecessary reinitialize

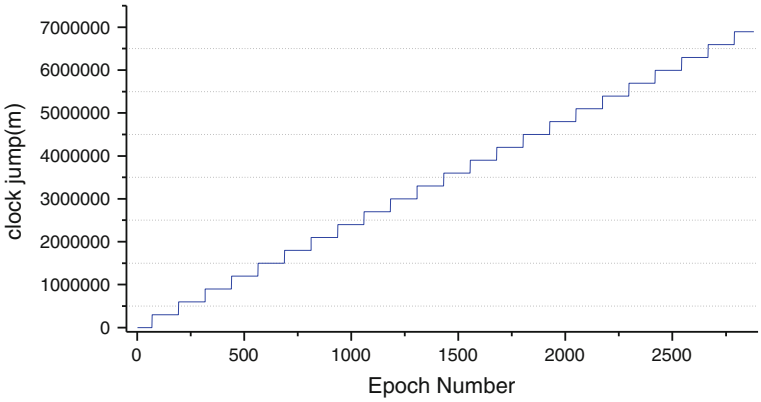

Fig. 13.4 Estimated receiver clock parameter

and help to improve the positioning accuracy effectively. The positioning accuracy is increased from 3D RMS 0.309, 0.435 and 1.142 m to 0.038, 0.075, 0.089 m for N, E, and U directions, respectively.

References

1. Ye S (2002) The theory and implementation of GPS undifferenced phase position point positioning. Wuhan University
2. Li Z, Zhang X (2009) The new GNSS technology and high precision data processing method. Wuhan University Press
3. Blewitt G (1990) An automatic editing algorithm for GPS data. Geophys Res Lett 17(3):199–202
4. Zhang Q, Li J (2005) Principle and application of GPS measurement. Science Press, Beijing
5. Zhang C, Jia X (2009) The influence and detection method of receiver clock jumps on GPS positioning. Bull Surv Mapp 12
6. Zhang X, Guo F, Li P, Zuo X (2012) Real time quality controlling for GNSS precise point positioning. J Wuhan Univ (Inf Sci Edn) 8:940–943
7. Shi C, Zhao Q, Li M et al (2012) Precision orbit determination and positioning research on BeiDou satellite navigation system. Chin Sci: Earth sci 06

Chapter 14
Positioning Error Research and Analysis Based on Comprehensive RDSS Method

Ji Dong Cao, Ran Ran Su, Wei Jie Sun and Xin Shi

Abstract Comprehensive RDSS positioning method is a combined positioning method, using the pseudo range difference between a RDSS repeater satellite and any other two navigation satellites to calculate the position information of the users. This method has become an important research direction of global satellite navigation to improve the ratio of cost and efficiency, reduce the user machine complexity and improve the positioning accuracy. In this paper, combined positioning accuracy error source, including satellite constellation, measurement error and multi-path effects is analyzed by the comprehensive RDSS method. On the same time, the method to eliminate and weaken the influence of errors on the positioning precision is also proposed.

Keywords Satellite navigation system · Comprehensive RDSS · Error analysis

14.1 Introduction

In recent years, along with the construction of the COMPASS regional satellite navigation system and GALILEO system, global navigation satellite system (GNSS) development will enter a new period. The compatibility and sharing of the GPS, GLONASS, GALILEO and COMPASS four global systems is formed [1]. Because information development impetus is swift and violent, personal location services sharing business needs grow with each passing day. The traditional position and communication position report mode has been unable to meet the wide needs of the industrial applications; there is an urgent need for a new positioning integration mode.

J. D. Cao (✉) · R. R. Su · W. J. Sun · X. Shi
Beijing Satellite Navigation Center, Beijing, China
e-mail: jncs313@139.com

J. Sun et al. (eds.), *China Satellite Navigation Conference (CSNC) 2013 Proceedings*, Lecture Notes in Electrical Engineering 245,
DOI: 10.1007/978-3-642-37407-4_14,

China's COMPASS regional satellite navigation system has abilities of Radio Determination Satellite Service, satellite services (RDSS) and Radio Navigation Satellite Service, satellite radio navigation service (RNSS) service, which has already preliminarily realized the new mode of integrating positioning and position report. But because its RDSS service ability is extended on the basis of COMPASS satellite navigation test system and has no comprehensive treatment with RNSS business services, it is different in the constellation selection, error control, and the positioning accuracy is 20 m. The independent RNSS system need at least 4 satellites to complete the navigation and positioning services, positioning accuracy is 10 m, and cannot realize the communication and position report function. Therefore, the further research should study a new service mode with RNSS system and RDSS system integration. In this service mode, the positioning can be realized without visible 4 satellites on the condition of high shielding angle, which can meet the user communication and location reporting function to realize the user fast and precise positioning.

14.2 Comprehensive RDSS Positioning Principle

14.2.1 Comprehensive RDSS Concept

Comprehensive Comprehensive Radio Determination Satellite Service, Comprehensive satellite services (RDSS) is the basic concept: completing the distance measurement between the master control center (MCC) to the users through back and a measure of distance through a transmitting RDSS satellite with two-way shuttle ranging function; The user complete the pseudo-range measurement with any other two navigation satellites; Through the calculation and processing of MCC, the user location determination and the location report to MCC can be realized. Laying two RDSS transmitting satellites on geostationary orbit (GEO) can complete the personal location services of the global land and the 70 % sea coverage area, the location services of 85 % satellite coverage area [2].

Compared with GPS position reports by positioning and communication means, the Comprehensive RDSS cost-effectiveness ratio significantly increased and the traditional navigation service of at least 4 satellites can descend to 3 satellites. In the same condition of the constellation satellites number, it is possible to select a lower DOP value and improve the positioning accuracy. Another great advantage is decreasing the additional communication equipment and reducing the user cost and burden. So the Comprehensive RDSS can realize higher positioning precision, more flexible user information sharing, the sharing of navigation system resources,

which is a new application model of the system on the basis of comprehensively use present existing global navigation satellite systems, taking the COMPASS system as the main body [3].

14.2.2 Comprehensive RDSS Positioning Method

Comprehensive RDSS system is in fact a radio positioning system with multiple reference stations distance measurement, which geometric principle is shown as Fig. 14.1.

Its working principle is as follows: in the measuring station MCC (or at a user location) the distance between the user U and the reference station S_i is obtained, then the user position is the three spherical intersection, which takes the three reference stations S_i as the center and the distance to users r_s^ias the radius. The matrix equation expressed by user vector is as follows.

$$\bar{R} = \bar{R}_S^i - \bar{R}_{Su}^i \qquad i = 3 \tag{14.1}$$

$\bar{R}_s^i$ is the satellite vector, $\bar{R}_{Su}^i$ is a vector between satellite to the user.

Its observation equation is:

$$r_s^i = \left[\sum_{i=1}^{3}\left(x_j^i - x_j\right)^2\right]^{\frac{1}{2}} \tag{14.2}$$

r_s^i is the observation distance between the reference station i to the user;
x_j^i is the three-dimensional (i = 3) coordinates of the reference station I;
x_j is three-dimensional (j = 3) coordinates of the user.

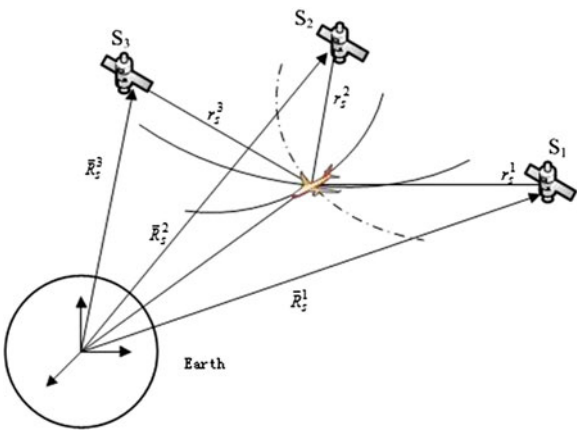

Fig. 14.1 Comprehensive RDSS positioning principle

When i = 3, it is a typical distance measurement of RDSS radio positioning service. When the reference station is satellite, it is typical distance measurement of RDSS satellite radio positioning service. Equation (14.1) is a common expression of the Comprehensive RDSS satellite radio positioning, include all the circumstances of taking the user or the known points outside the user as the measuring and locating center, which is the prototype expression of Comprehensive RDSS [2].

In the multiple reference station distance measurement radio positioning system shown as Fig. 14.1, the distance r_u^i between the user u and the satellite S can not only be completed by the user, but also be completed by the center control system outside the user. When it is completed by the user u, RNSS is constituted; when it is completed by the MCC outside the user, the practical RDSS system is constituted. So the Comprehensive RDSS business is the organic integration of RNSS service and RDSS service, which integrates double-satellites RDSS, three-satellite RDSS and four-satellite RNSS business, according to the different users' needs, to realize positioning and location reporting function. Figure 14.2 is the system structure of the Comprehensive RDSS function implementation, which is made up of a ground measurement and control center MCC, three navigation satellites (S_{G1}, S_{G2}, S_I) and a user. S_{G1} and S_{G2} are working in a geostationary orbit. S_I can work in an inclined orbit. Its working process is as follows.

A measurement and control center MCC is established on the ground of known position. The three satellites constitute two-way distance measurement link from MCC to user u as the transponder mode. The MCC launches the ranging signals; the user u sends response signals to the three satellite transponder after it receives the launch signal from any satellites; MCC receives the response signal return from the three satellites to obtain round trip distance D_u^i between the MCC and the user u through the three satellites. Because the position of the three satellites S_{G1}, S_{G2}, S_I is known, the distance between the three satellites and the user can be calculated. MCC can use Eq. (14.2) to complete the user position calculation.

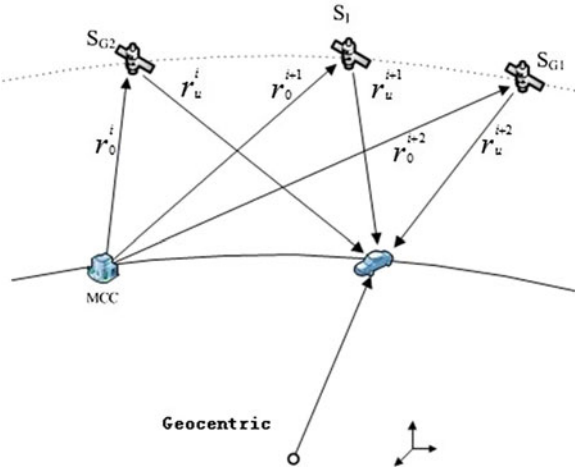

Fig. 14.2 Comprehensive RDSS system

In which:

$$r_u^i = \frac{1}{2} D_u^i - r_0^i \tag{14.3}$$

D_u^i is distance measured MCC
r_0^i is the calculated distance between the known satellite position and MCC.

The positioning equation is:

$$r_u^i = \left[\sum_{i=1}^{3} \left(x_j^i - x_j \right)^2 \right]^{\frac{1}{2}} \tag{14.4}$$

x_j^i is the three-dimensional position coordinates of the satellite i in user coordinate system, which is the known parameters
x_j is the user three-dimensional position coordinates, which is the unknown solved parameters
r_u^i is the distance between the satellite i to the user, which is a measurement.

Solving user coordinate three unknowns, the Comprehensive RDSS requires at least three satellites to form three observation equations. In order to satisfy certain geometric shapes, two of the three satellites are geostationary satellites, and an inclined geosynchronous orbit (IGSO) satellite or circular orbit (MEO) satellite.

From the Comprehensive RDSS positioning principle knowable, navigation parameter measuring and user position calculation is completed by the MCC, the user terminal only needs to transmit a response signal to complete the orientation and position report [2].

Advantage generalized RDSS positioning:

1. Due to the increase in non-GEO satellite observations, MCC solver position is no longer dependent on the limitations of the digital elevation database;
2. Use RDSS positioning function at the same time, be able to get the RNSS timing, the timing accuracy better than RDSS timing accuracy.

14.3 Comprehensive RDSS Positioning Precision Analysis

Comprehensive RDSS positioning accuracy is affected mainly by satellite constellation geometry, satellite clock, ephemeris, propagation path, the user machine and so on.

14.3.1 Satellite Constellation Selection

Constellation selection depends entirely on the position of geometrical attenuation factor PDOP, PDOP value is smaller, and the navigation system positioning accuracy is higher [4]. Satellites selection design conditions include:

1. Provide the best DOP value

Observed satellites can be selected in the 2–3 constellation systems, taking into account that it can make HDOP $\leq$ 1.5 and VDOP $\leq$ 1.5 in any place of the service area. When using the two composite satellite constellation with 24 satellites, the DOP value is greater than the probability of 90 %.

2. Elevation angle of the selected satellite

All users in the best DOP satellite observation angle is greater than 15 degrees in order to avoid as much as possible multi-path effect.

3. Integrity of the selected satellite navigation signal.

The selected satellite should meet the integrity requirements totally. There is no signal distortion and navigation parameters failure. Through the clock error, trajectory correction, the clock error and tracking error can meet the accuracy requirements.

2 GEO satellites +1 MEO satellite within a period of time, the average PDOP values are shown in Table 14.1.

Table 14.1 2 GEO + 1 MEO satellites PDOP value

B	L						
	75°	85°	95°	105°	115°	125°	135°
55°	4.782	5.249	5.184	5.419	5.204	5.161	4.806
50°	5.201	5.261	5.260	5.220	5.119	5.218	5.192
45°	5.265	5.403	5.414	5.291	5.261	5.298	5.425
40°	5.467	5.529	5.234	5.114	4.995	5.108	5.208
35°	5.213	5.184	5.050	5.088	5.126	5.026	5.333
30°	5.244	5.125	5.005	4.885	4.948	5.031	5.151
25°	5.269	5.027	5.138	4.975	5.136	5.053	5.064
20°	5.274	5.129	5.022	5.083	5.075	4.933	5.033
15°	5.174	5.028	5.056	4.941	4.784	4.851	4.948
10°	5.096	4.977	4.765	4.819	4.813	4.883	4.910
5°	5.129	4.896	4.803	4.775	4.884	4.839	4.952

14.3.2 Error Sources Analysis

14.3.2.1 Observation Equipment Error Analysis

Pseudo range measurement error is derived from the observation equipment and its observation error caused by the environment in the observation process, which is the main error source. This error includes three parts.

1. Equipment time delay error, including the channel time delay and time delay of the signals' going into the observation receiving device.
2. Time accuracy of the measurements, especially the pseudo range measurement time accuracy.
3. The influence of multipath effects in the observation error, using only the multipath antenna case, even for high elevation observation satellites, there is about 1.0 m multipath error. In the high dynamic user, difficulties to further suppress are the main error sources to improve the dynamic precision.

14.3.2.2 Single Point Positioning Error Analysis

Standard single point positioning error sources and estimation is shown in Table 14.2.

According to the analysis result, single point positioning is affected by various error factors, which can only meet the low dynamic and normal user demand.

14.3.2.3 Single Reference Station GPS Differential Positioning Error Analysis

Single reference station pseudo-range differential positioning error sources and estimation is shown in Table 14.3 (suitable for the situation that the distance between the user to baseline station distance is 100 km).

Table 14.2 Standard single point positioning error table (unit: m)

Error sources	Error name	Single point positioning
Satellite	Clock error	3.0
	Orbit error radial	1.0
MCC	Ephemeris prediction error	4.0
	Star clock forecast error	1.0
Propagation path	Ionospheric error	5.0
	Tropospheric	1.5
User machine error	Noise	0.3
	Multipath	1.0
The total errors of user distances (RMS)		7.4
User position error 2DRMS, DOP $\leq$ 1.5		26.4

Table 14.3 Single reference station pseudorange differential positioning error table (unit: m)

Error sources	Error name	Single point positioning
Satellite	Clock error	0.0
	Orbit error radial	0.0
MCC	Ephemeris prediction error	0.0
	Star clock forecast error	1.0
Propagation path	Ionospheric error	0.0
	Tropospheric	0.0
User machine error	Noise	0.3
	Multipath	1.0
The total errors of user distances (RMS)		1.45
User position error 2DRMS, DOP $\leq$ 1.5		4.33(H)
		4.33(V)

The basic conclusions can be drawn by the analysis:

1. The differential orientation method can eliminate most of positioning accuracy influence of the satellite clock and track error.
2. Differential positioning method can significantly weaken the influence of the transmission error on positioning accuracy.
3. Satellite clock error and the multipath error is the main error source of precision positioning. Realization of m to submeter precision is very difficult.

The simulation used 2 GEO satellites and 1 MEO satellites, according to UERE = 1.5 m, adding random white noise on the simulation measurements, which mean is 0 and RMS is 1.5 m, then made a count on the positioning error of 14 days, which specific results is shown in Table 14.4.

14.3.2.4 The Datum Network Pseudo Range Differential Positioning Error Analysis

Single reference station pseudo range differential positioning accuracy reduces with the growth of the distance between stations. When the distance between stations is greater than 500 km, the relativities between the base station and users get worse. Ionosphere, troposphere propagation error cannot be completely eliminated. The propagation delay error increases by $\pm$0.0216 m/Km. When the distance between stations is 600 km, the transmission error is $\pm$2.16 m, position error increases $\pm$6.48 m [5].

Using reference station network (wide area differential) can overcome the shortcoming of single pseudo-range differential accuracy's change with the distance between stations. The correction value is composed of multiple reference station observations for ionosphere correction parameter separation, tropospheric correction parameters, satellite clock correction, and satellite orbit correction

Table 14.4 2 GEO + 1 MEO RMS satellite positioning value (unit: m)

B	L						
	75°	85°	95°	105°	115°	125°	135°
55°	5.792	6.205	6.102	6.033	5.974	5.921	5.881
50°	6.228	6.215	6.101	6.033	5.971	5.922	5.886
45°	6.304	6.224	6.112	6.034	5.977	5.924	5.893
40°	6.329	6.239	6.113	6.029	5.972	5.925	5.899
35°	6.308	6.240	6.102	6.026	5.970	5.919	5.902
30°	6.302	6.225	6.094	6.017	5.964	5.917	5.902
25°	6.309	6.211	6.094	6.017	5.957	5.910	5.899
20°	6.284	6.197	6.074	6.010	5.950	5.908	5.892
15°	6.242	6.163	6.058	6.002	5.946	5.905	5.890
10°	6.222	6.126	6.037	5.988	5.930	5.895	5.885
5°	6.195	6.103	6.018	5.974	5.917	5.885	5.878

parameters, noted in a different component representation in the message format. A typical WASS error estimation is shown in Table 14.5.

Wide area differential GPS, base station uses dual-frequency monitoring receiver to calculate ionosphere delay correction individually. But the three-dimensional ephemeris error, satellite clock error and base station monitoring receiver local clock error has a combined treatment using pseudo-range system by MCC. Because of the error types, the involved factors are complex, the error correlation after separation is weak, so the accuracy is still limited.

14.3.2.5 Comprehensive RDSS Single Reference Station Carrier Phase Differential Positioning Error Analysis

Due to the high accuracy of the carrier phase measurements, closing to the 1/4 carrier wave, the observation accuracy is better than 5–6 cm when the carrier frequency is between 1200 and 1575 MHz. The multipath effect has significant inhibiting effect. From the measurement method, carrier phase recovers. Adopting more narrow processing bandwidth and scale compared with PN code phase

Table 14.5 WASS pseudo range differential positioning error table (unit: m)

Error sources	Error name	Single point positioning
Satellite	Clock error	0.1
MCC	Ephemeris prediction error	0.1
Propagation path	Ionospheric error	0.2
	Tropospheric	0.1
User machine error	Noise	0.1
	Multipath (carrier phase processing)	0.2
The total errors of user distances (RMS)		0.35
User position error 2DRMS, DOP $\leq$ 1.5		1.04

recovery, random measurement error is 2 orders of magnitude higher than the pseudo code phase. Therefore, to ensure the continuous observation of the carrier phase can make the multipath effect weaken to obtain higher positioning accuracy. Due to the propagation error varies with the increasing distance between stations, to get distance measurements of cm grade accuracy in order to get m grade positioning accuracy should increase the density of base station as the cost.

However, due to the two-way data communication function of the GEO satellite RDSS loads L/S channel, it create the conditions for the transmission differential correction parameters. In this two-way data exchange process, because the station's S and L beam signal has strict time synchronization, the round-trip distance measurements from the user to MCC can eliminate the cycle slip, reduce the total number of satellites for difference positioning. So the function and advantage of the RDSS business involvement is more obvious, compared with the simple RNSS service and communication service [3].

14.4 The Ending

Comprehensive RDSS positioning is a deep coupling positioning method combining RDSS and RNSS characteristics and their positioning mode, which has advantages including high positioning accuracy, less desired satellite number, rapid first positioning speed and the simple user machine. The Comprehensive RDSS positioning method research is the important technical measures not only of creating a good competition with the service quality level, but also of independent innovation support, national navigation industry development, major body of the COMPASS system, service model opening and value-added services value creation. It is also the new thinking and new scheme of highlighting the user application demands, enlarging the application scale, promoting the traditional services to the on-demand advanced service stage, to realize the implementation of satellite navigation industry [3].

References

1. Shu-sen TAN (2010) The engineering of satellite navigation and positioning. National Defense Industry Press, Beijing. ISBN 978-7-118-06711-8
2. Shu-sen TAN (2011) The comprehensive RDSS global position and report system. National Defense Industry Press, Beijing. ISBN 978-7-118-06869-6
3. Shu-sen TAN (2009) Theory and application of comprehensive RDSS position and report. Acta Geodaetica et Cartographlca Sinica 38(1):1–5
4. Guo JJ, Wang L, Zhang P (2008) The application and expectation of CORS in international and China [J]. GNSS World Chin 34(1):20–25
5. Huang ZG et a1 (2007) Radio navigation theory and system [M]. Beijing University of Aeronautics and Astronautics Press, Beijing

Chapter 15
Research on Technique of Single-Satellite Orbit Determination for GEO Satellite of Partial Subsatellite Point

Xiao Jie Li, Jian Hua Zhou, Li Liu, Ji Dong Cao, Rui Guo, Feng He, Shan Wu and Hua Huang

Abstract Regional satellite navigation system contains geostationary satellites (GEO) of partial subsatellite point, subsatellite points of these satellites are away from ground tracking network. These satellites are important to improve the geometric dilution of precision (GDOP) for positioning and time service in sevice area. Comparing with geostationary satellite (GEO) of other subsatellite point, ground tracking geometry condition of GEO of partial subsatellite point is worse, precision of orbit determination of this kind of satellites is not stable and easier to be affected by systemic error. In this paper the principle of POD based on time synchronization mode was proposed particularly and thoroughly. Integrative orbit determination of all satellites could provide precise clock offsets of all satellites and all stations, precise orbit determination (POD) were realized using pseudorange data without clock offset. The technique of single-satellite orbit determination could use all stations which participated in integrative orbit determination, ground tracking geometry condition was improved greatly, at the same time, it could achieve integrative solution of systemic error, POD of this kind of GEO was realized, which could get rid of the restriction of satellite laser ranging data (SLR). Precision of orbit determination were analyzed based on four orbit determination strategies, including solving solar radiation pressure parameters, empirical force parameters and common systemic error, solving solar radiation pressure parameters and common systemic error, solving solar radiation pressure parameters, empirical force parameters and fixing up common systemic error, solving solar radiation pressure parameters and fixing up common systemic error. The experiment based on ground data results indicated that precision of orbit determination based on the strategies of solving solar radiation pressure parameters and fixing up

X. J. Li (✉)
China Beijing Satellite Navigation Center, 5136 Rail Box in Beijing city, Beijing 100094, China
e-mail: lxjant1984@126.com

J. H. Zhou · L. Liu · J. D. Cao · R. Guo · F. He · S. Wu · H. Huang
Shanghai Astronomical Observatory, Chinese Academy of Sciences, Shanghai 200030, China

J. Sun et al. (eds.), *China Satellite Navigation Conference (CSNC) 2013 Proceedings*, Lecture Notes in Electrical Engineering 245,
DOI: 10.1007/978-3-642-37407-4_15,

common systemic error was highest. The orbit accuracy in radial component was better than 1 m, which was evaluated with SLR data, the 2 h orbital prediction errors were 1 m, the precision was stable, POD of GEO of partial subsatellite point was come true.

Keywords Geostationary satellite (GEO) · Precise orbit determination (POD) · Systemic error · Solar radiation pressure · Empirical force · Clock offset · Satellite laser ranging (SLR)

15.1 Introduction

With the constraints of geostationary orbit, geostationary satellite (GEO) satellite is adopted extensively in satellite navigation area. Especially GEO satellite of partial subsatellite point, it not only can communicate information, but also can boost up the geometric dilution of precision (GDOP), it is an indispensable component in regional navigation system (COMPASS). Because of partial subsatellite point, POD for this kind of GEO become the hotspot and difficulty. The main factors affected the orbit precision are as follows: one hand, ground tracking geometry condition of GEO satellite is nearly unchanged due to regional tracking network, and certain stations can't observe this kind of GEO. The dynamic restriction of stations for GEO satellite is very weak. The other hand, the current measurement technique for GEO satellite contains distinct systematic error or ranging biases. So, the precise orbit determination of this kind of GEO need to be studied deeply.

Three conventional GEO tracking techniques are the pseudoranging, C-band transfer ranging and satellite laser ranging (SLR). The transfer ranging is a two-way ranging mode. The C-band ranging signal from a ground station is transmitted by a transfer onboard GEO satellites designed for communication, and is also received by the station, without clock corrections in the ranging data, its precision is high. The precision of SLR is high, and doesn't contain obvious systematic error, but can't get observation in whole day. The L-band downlink navigation signal is received by the receiver and the pseudorange is observed with clock corrections of both the satellite and the receiver, it is easy to come true and spread [1–3].

As to the orbit determination based on pseudorange, overseas satellite navigation system currently adopts the uniting estimation method of orbit and clock offset. But Compass regional satellite navigation system adopt the stations in China, with the constraints of geostationary orbit, orbit parameters and clock parameters can't be effectively separated, the strong correlation of clock parameters and other parameters results in the morbidity of normal equation, we can't effectively estimate the satellite and station combination clock offset. The radio comparison method is widely employed in the satellite navigation system for the satellite-station time synchronization, which is an independent technique. The clock offset is deducted from pseudorange in order to separate the orbit and clock,

then only estimate the orbit parameters, which is the best method to determine the orbit for GEO satellite of partial subsatellite point in COMPASS system.

At present, the conventional technique is POD based on time synchronization mode, its principle is that adopting satellite-earth wireless two-way method and C wave band satellite two-way method to get high precise satellite clock and station clock, which are deducted from pseudorange, then determine the orbit. In this method, systematic error is the key ingredient to restrict the orbit precision [4]. We need SLR data to demarcate the equipment time delay, so this technique strongly relies on SLR. At the same time, the tracking geometric condition is restricted the distribution and number of time synchronization stations. As a result, an absolute orbit determination method is needed to get rid of the time synchronization stations and SLR.

As to the POD for GEO satellite of partial subsatellite point, this paper brings forward a single-satellite POD method based on multi-satellite orbit determination. Its principle is as follows: the satellite clock is obtained from satellite-earth wireless two-way method, the station clock is obtained from the multi-satellite orbit determination, which are deducted from pseudorange in order to reduce the estimated parameters. The systematic error parameter with other parameters are estimated synchronously in orbit determination. Based on this method, we can use anyone station without restriction of time synchronization stations and SLR data. SLR is adopted to evaluate the orbit precision. This method is good for improve the single-satellite orbit precision and stability.

15.2 Orbit Determination Method and Estimated Strategy

In the dynamical POD, both the quality of dynamical models and the parameter estimation are the two main factors that influence the POD precision. According to the feature, we may divide the force acting on the satellite into three groups: the center gravity from the Earth and the satellite, the conservative acceleration and non-conservative acceleration. The conservative acceleration includes the non-spherical perturbation acceleration, the tidal perturbation acceleration, including the solid earth tide, the ocean tide and the atmospheric tide, the rotational deformation acceleration due to polar motion, the relativistic perturbation acceleration, non-conservative acceleration includes the solar radiation pressure perturbation, the Earth radiation pressure perturbation, the satellite thermal radiator perturbation. JGM-3 Earth gravitation model truncated to 10 by 10° and order, JPL DE403 planetary ephemeris, IAU80 nutation model, Box-Wing solar radiation pressure model, and IERS96 solid tide model are employed in the POD.

With orbital pre-processing, measurement errors are corrected. Firstly, the antenna phase offset errors of tracking stations are corrected, secondly reductions of satellite antenna phase center to satellite mass center are made, and finally propagation errors are corrected. The tropospheric errors are corrected by using the Saastamoinen model, and the ionospheric errors are corrected by using global

precise ionosphere delay model provided by CODE. The satellite-earth wireless two-way method is adopted to get high precise satellite clock and multi-satellite orbit determination method is adopted to get high precise station clock, whose precision all are better than 2 ns [5, 6].

The concrete strategy of POD method based on multi-satellite orbit determination is as follows: pseudorange is smoothed by phase data. The estimated parameters include initial orbit, solar radiation pressure parameter, common systemic error, sine and cosine value of T orientation empirical force.

The labor of all parameters is as follows: firstly, the common systematic error is designed to absorb the error of inconsistent benchmark between satellite clock and station clock. The benchmark of satellite clock is time of communication antenna's 1 pps port, that of station clock is the time of receiver.

Secondly, in single-satellite orbit determination, the solar radiation pressure model is simple ball model, whose precision can't satisfy the demand of orbit precision for regional satellite. The most potential of the solar radiation pressure is as follows:

$$R = \beta r[A\cos f + B\cos f] \tag{15.1}$$

Thereinto, β is correlative with reflectance, A, B is correlative with directional parameters of orbit plane. From formula (15.1), the solar radiation pressure is correlative with orbit period. The empirical force can be adopted to absorb the error of the solar radiation pressure. At the same time, if R, T, N empirical forces are synchronously estimated, overfull parameters can result in the strong correlation among parameters and serious morbidity of normal equation. The extent of T orientation is larger, so only the sine and cosine value of T orientation empirical force are estimated. The T orientation empirical force is as follows:

$$T = a\cos(f + \omega) + b\sin(f + \omega) \tag{15.2}$$

a, b is the estimated parameters.

15.3 Analysis of Orbit Determination Precision

15.3.1 Orbit Determination Based on Multi-Satellite Orbit Determination

We make experiments on GEO on 160° E. The five stations include Beijing, a certain station in Hainan, a certain station in Sichuan, a certain station in Northeast, a certain station in Southeast. The arc is 24 h. Table 15.1 represents the residual error and the orbit accuracy in radial component and the 2 h orbital prediction errors, which was evaluated with SLR data.

Table 15.1 Residual error and the orbit accuracy in radial component (Unit: m)

Time	Stations num	Residual error	Num of SLR	Orbit accuracy evaluated with SLR data	
				Orbit accuracy	2 h prediction
1 Mar 2011	5	0.618	6931	0.870	1.051
4 Sept 2011	5	0.546	878	1.547	2.162
22 Sept 2011	5	0.765	1254	1.478	1.978

Table 15.1 indicates that:

1. This method gets rid of the restriction of time synchronization stations, so we can choose more stations. The problem is that what distribution of stations can make the orbit precision highest.
2. The orbit accuracy evaluated with SLR data is better than 1 m only in 1 Mar 2011. Those in other two days are larger than 1 m. The orbit precision isn't stable, why? How to eliminate this phenomenon?

As to above problems, we make experiments as follows.

15.3.2 Influence of Stations Distribution to Orbit Precision

Because the orbit precision is high in 1 Mar 2011. The stations are Beijing, a certain station in Hainan, a certain station in Sichuan, a certain station in Northeast, a certain station in Southeast, the distribution is symmetrical in China. We adopt GDOP and orbit precision to evaluate the stations distribution. Table 15.2 represents the GDOP and orbit precision for a certain GEO in 1 Mar 2011.

Table 15.2 indicates that:

1. PDOP of five stations is least, according to the sort order of PDOP, the stations combination is five stations except a certain station in Sichuan, a certain station in Beijing, a certain station in Southeast, a certain station in Hainan, a certain station in Northeast.

Table 15.2 1 Mar 2011 orbit precision based on different stations (Unit: m)

Station	PDOP	Orbit accuracy evaluated with SLR	
		Orbit accuracy	2 h prediction
Hainan, Sichuan, Northeast, Southeast	57.3	0.952	0.916
Beijing, Sichuan, Northeast, Southeast	66.5	2.658	2.600
Beijing, Hainan, Northeast, Southeast	52.0	0.318	0.310
Beijing, Hainan, Sichuan, Southeast	67.9	2.658	2.880
Beijing, Hainan, Sichuan, Northeast	60.7	1.537	1.504
Five stations	51.4	0.870	1.051

2. Using the five stations respectively except Beijing, a certain station in Hainan, a certain station in Sichuan, a certain station in Northeast, a certain station in Southeast, the orbit precision is 0.952, 2.658, 0.318, 2.658, and 1.537 m. We can find that the closer the station away the subsatellite point of GEO, the stronger the restriction for GEO. We should choose the more stations, at least 4 stations close to the subsatellite point of GEO.

15.3.3 Decorrelationship Method Based on Priori Restriction

From above analysis we can find that the orbit precision isn't stable based on multi-satellite orbit determination, we make experiments to improve this phenomenon. The definition of correlationship is as follows [7]:

As to X, Y, when $D(X) > 0$, $D(Y) > 0$, $E(X^*, Y^*)$ is correlationship of X, Y, namely $\rho(X, Y)$.

$$\rho(X, Y) = E\left[\frac{X - E(X)}{\sqrt{D(X)}} \cdot \frac{Y - E(Y)}{\sqrt{D(Y)}}\right] = \frac{\mathrm{cov}(X, Y)}{\sqrt{D(X) \cdot D(Y)}} \tag{15.3}$$

When $\rho(X, Y) = \pm 1$, linearity correlationship exists in X and Y. When $\rho(X, Y) = 1$, positive 1 correlationship, when $\rho(X, Y) = -1$, negative 1 correlationship. Namely, non-zero constant k, c exists to make the relationship:

$$Y = kX + c \tag{15.4}$$

When we use the least squares prediction method, the normal equation is as follows:

$$\begin{bmatrix} X_1 \\ \vdots \\ X_n \end{bmatrix} = \begin{bmatrix} Na_{1,1} & \cdots & Na_{1,n} \\ \vdots & \vdots & \vdots \\ Na_{n,1} & \cdots & Na_{n,n} \end{bmatrix} \cdot \begin{bmatrix} U_1 \\ \vdots \\ U_n \end{bmatrix} = \begin{bmatrix} Q_{1,1} & \cdots & Q_{1,n} \\ \vdots & \vdots & \vdots \\ Q_{n,1} & \cdots & Q_{n,n} \end{bmatrix} \cdot \begin{bmatrix} U_1 \\ \vdots \\ U_n \end{bmatrix} \tag{15.5}$$

The relativity of parameters is as follows:

$$\rho(X_m, Y_n) = \frac{\mathrm{cov}(X, Y)}{\sqrt{D(X) \cdot D(Y)}} = \frac{Q_{m,n}}{\sqrt{Q_{m,m} \cdot Q_{n,n}}} \tag{15.6}$$

The estimated parameters must be independent. If the linearity correlationship exists in parameters, the normal equation will be rank-defect; the solution isn't alone, which affect the orbit precision and stability.

The orbit precision isn't stable, which represents that the correlationship of parameters is strong. We should choose the parameters of weak correlationship. Table 15.3 represents the correlation parameters matrix in 4 Sept 2011 (which is diagonal matrices). Cr is solar radiation pressure reflectance, dCr is the ratio of Cr,

Table 15.3 Correlation parameters matrix in 4 Sept 2011

	X	Y	Z	Vx	Vy	Vz	Cr	dCr	T-c	T-s	Bias0
X	1										
Y	0.898	1									
Z	−0.734	−0.918	1								
Vx	−0.949	−0.964	0.867	1							
Vy	0.994	0.854	−0.681	−0.866	1						
Vz	0.233	0.558	−0.617	−0.917	−0.266	1					
Cr	−0.847	−0.904	0.930	−0.450	0.155	−0.597	1				
dCr	−0.321	−0.244	0.115	0.970	−0.798	0.132	0.139	1			
T−c	−0.862	−0.967	0.927	0.227	−0.294	−0.578	0.999	0.162	1		
T−s	0.853	0.958	−0.930	0.966	−0.814	0.590	−0.999	−0.168	−0.999	1	
Bias0	−0.992	−0.633	0.445	−0.972	0.802	0.151	0.570	0.396	0.595	−0.579	1

T-c, T-s is the cosine and sine parameter of T orientation empirical force, Bias0 is the common systematic error.

Table 15.3 indicates that: there are relativity in different extent among T orientation empirical force, common systematic error, orbit parameters and solar radiation pressure parameters. If we reduce the estimated parameters, depress the relativity, can the orbit precision be stable? We bring forward the decorrelationship method based on priori restriction, through fixupping the best Bias0 based on the UERE, making orbit determination again. If all the orbit precision is lower, we can recalculate the accurate Bias0 through UERE. The calculating method is as follows: accurate Bias0 = calculative Bias0—the value of UERE. If the value of UERE is 3 m, the calculative Bias0 is 3.5 m, the accurate Bias0 should be 1.5 m. The relativity of parameters is depressed, the orbit precision should be stable.

At the same time, we analyze the influence of empirical force in orbit determination, four strategies are constituted:

First strategy: the estimated parameters are initial orbit, solar radiation pressure parameter, common systemic error, sine and cosine value of T orientation empirical force.

Second strategy: the estimated parameters are initial orbit, solar radiation pressure parameter, common systemic error.

Third strategy: the estimated parameters are initial orbit, solar radiation pressure parameter, sine and cosine value of T orientation empirical force.

Fourth strategy: the estimated parameters are initial orbit, solar radiation pressure parameter.

Figures 15.1 and 15.2 represent the orbit accuracy evaluated with SLR data in 4 and 22 Sept 2011. 1 represents 1 h from the ending time of observation data to the starting time of SLR, 1 represents 1 h from the ending time of SLR a to the ending time of observation data.

Figures 15.1 and 15.2 indicate that:

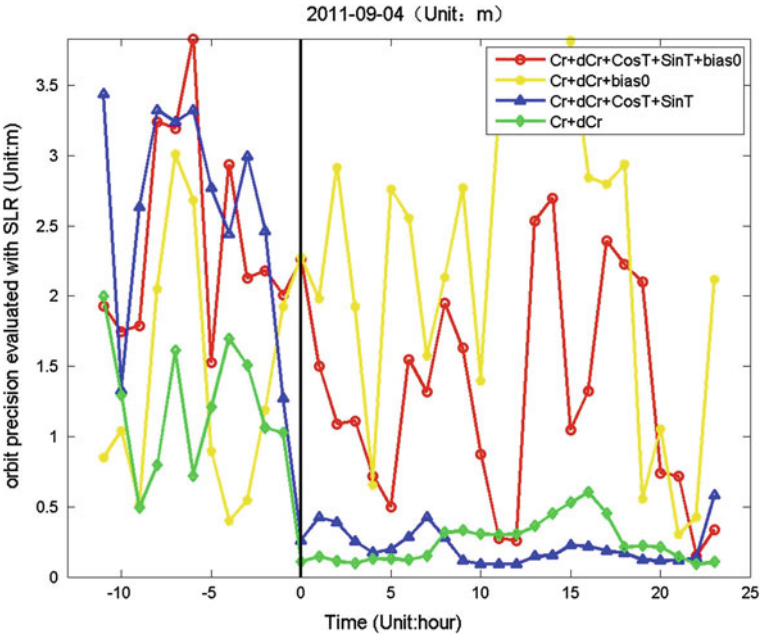

Fig. 15.1 Orbit accuracy evaluated with SLR data in 4 Sept 2011 (*black beeline* represents the starting time of SLR)

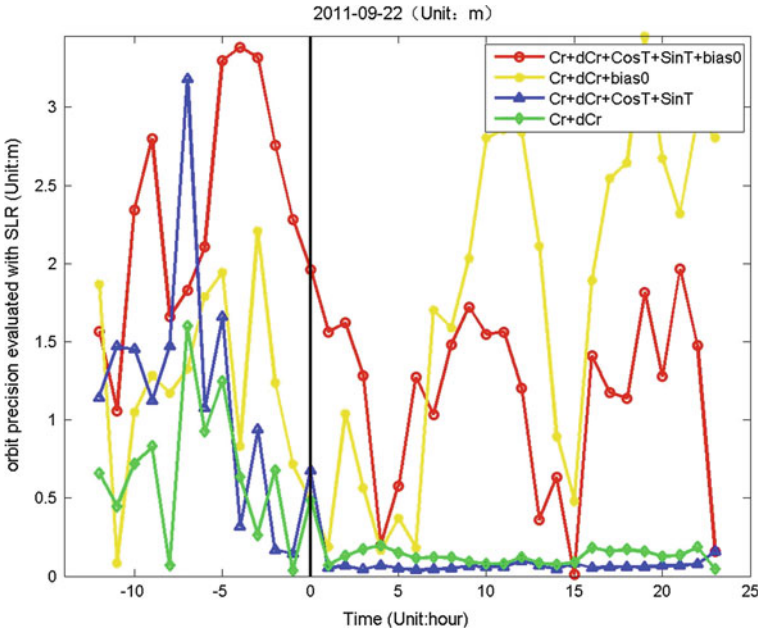

Fig. 15.2 Orbit accuracy evaluated with SLR data in 22 Sept 2011

1. The orbit precision based on first strategy isn't stable, orbit precision some times is better than 1 m, some times is larger than 2 m, the 2 h orbital prediction error is about 2 m.
2. The orbit precision based on second strategy is high and stable, but the orbital prediction error is larger with the time, so when we estimate the empirical force parameters in orbit determination, the orbital prediction will be low.
3. Bias0 coming from the results of first strategy is adopted in third strategy and fourth strategy. The orbit precision based on fourth strategy is highest and stablest. The orbit precision and the 2 h orbital prediction all are better than 1 m.

15.4 Conclusion

This paper analyzed the orbit determination of GEO satellite of partial subsatellite point. The orbit determination method based on multi-satellite orbit determination is systematically analyzed. The advantage of this method is as follows: firstly, this method doesn't rely on the number and distribution of stations, secondly, we can estimate systematic error and other parameters in orbit determination, then get the exactest value of systematic error based on UERE evaluation, which make this method get rid of the restriction of SLR. In this paper, systematic error, distribution of stations, orbit determination strategy, correlation of parameters are analyzed detailedly. The decorrelationship method based on priori restriction is brought forward. The main conclusions are as follows:

1. The orbit precision based on time synchronization mode relies on the equipment systematic error, which relies on SLR data. If the systematic error isn't be adjusted for a long time, the orbit precision will be decayed; this method is in the restriction of number and distribution of time synchronization stations, whose number is little, if trouble of a certain station occurs, the number is less than 3, the orbit determination can't carry through.
2. We should choose the stations near to the subsatellite point of GEO in order to endure the lesser PDOP and geometric condition.
3. The decorrelationship method based on priori restriction can make the orbit prediction stable, the experiment results show that the orbit precision and the 2 h orbital prediction all are better than 1 m.

References

1. Guo R, Hu XG et al (2010) Precise orbit determination for geostationary satellites with multiple tracking techniques. Chinese Sci Bull 55:428–434
2. Li ZG, Yang XH, Ai GX et al (2008) A new method for determination of satellite orbits by transfer. Sci China Ser G: Phys Mech Astron 38(12):1711–1722

3. Zhou SS, Hu XG, Wu B et al (2011) Orbit determination and time synchronization for a GEO/IGSO satellite navigation constellation with regional tracking network. Sci Chin Phys, Mech Astron 54(6):1089–1097
4. Song XY, Jia X, Mao Y (2009) Single-satellite orbit determination based on time synchronization stations [J]. Surveying Mapp Sci 34(5):8–10
5. Liu L, Zhu LF, Han CH (2009) Satellite-earth wireless two-way method and experiment analysis. Acta Astron Sin [J] 50(2): 189–196
6. Liu L, Han CH (2004) Satellite-earth wireless two-way method and error analysis. Acta Astron Sin [J] 22(3):219–226
7. Zhou SS (2011) Studies on precise orbit determination theory and application for satellite navigation system with regional tracking network [D].Shanghai Astron Observatory 6:39–46

Chapter 16
BeiDou Regional Navigation System Network Solution and Precision Analysis

Yang Liu, Yidong Lou, Chuang Shi, Fu Zheng and Qianqian Yin

Abstract In this paper, BeiDou post-mission high precision orbit determination and positioning in network solution mode are researched and implemented under current BeiDou regional navigation system conditions. We made an in-depth analysis of the influence factors, such as ambiguity resolution, orbit precision, reference station selection, inter-station distance, on precision of BeiDou network solution. We analysed the different ambiguity resolution strategy among GEO, IGSO and MEO, and its impact on precision orbit determination and network solution positioning. We conducted an experimental comparison of BeiDou network solution with BeiDou precise point positioning (PPP). With long-term continuous measurement data from Wuhan University BeiDou Experimental Tracking Stations processed, the results show that ambiguity resolution improves all the GEO, IGSO and MEO orbit precision, especially for the along direction and 3D RMS of GEO, IGSO and MEO is 155, 33 and 28 cm respectively, the radial precision is basically better than 10 cm. BeiDou one-day network solution positioning precision is better than 1 cm in horizontal and better than 2 cm in vertical, which is slightly better than BeiDou PPP precision.

Keywords BeiDou · Network solution · PPP · Ambiguity resolution · Precision analysis

16.1 Introduction

BeiDou Navigation Satellite System began test service at the end of 2011, and has now completed a constellation comprising four Geostationary Earth Orbit (GEO) satellites, five Inclined Geosynchronous Satellite Orbit (IGSO) satellites and four

Y. Liu · Y. Lou (✉) · C. Shi · F. Zheng · Q. Yin
GNSS Research Center, Wuhan University, Wuhan, China
e-mail: ydlou@whu.edu.cn

J. Sun et al. (eds.), *China Satellite Navigation Conference (CSNC) 2013 Proceedings*, Lecture Notes in Electrical Engineering 245,
DOI: 10.1007/978-3-642-37407-4_16,

Medium Earth Orbit (MEO) satellites in operation, and will provide official service for most parts of the Asia–Pacific in early 2013. In order to explore the application of BeiDou regional navigation system in high precision positioning, we need to analyse the precision of orbit determination and positioning it can reach. Some scholars have conducted a series of studies on this issue. In BeiDou precise orbit determination, Mao et al. [1] conducted GEO and IGSO joint orbit determination, the overlap orbit accuracy reaches a few meters with additional custom acceleration, and radial accuracy is better than 10 cm assessed using satellite laser ranging; Zhou et al. [2] achieved the GEO/IGSO orbit determination under a regional monitoring network and used independent time synchronization system of BeiDou and SLR to assess the accuracy of orbit and clock; Montenbruck et al. [3] analysed the signal characteristics of the BeiDou regional navigation system, the 3D orbit overlapping accuracy of BeiDou satellite is 1–10 m; Shi et al. [4] used joint orbit determination of GPS and BeiDou, where the coordinate of station, receiver clock error and tropospheric parameters are firstly calculated using GPS precise ephemeris, and then the above parameters are fixed in BeiDou orbit determination to make the radial overlapping accuracy of BeiDou GEO and IGSO to 10 cm level; Ge et al. [5] analysed independent orbit determination of BeiDou system, where post-mission data is used to simulate real-time orbit determination, and the 3D overlapping accuracy of GEO and IGSO respectively reaches 330 and 51 cm. In BeiDou precise positioning, Shi et al. [4, 6] used dual-frequency data, Montenbruck et al. [3] used triple-frequency data, to analyse the relative positioning of BeiDou, and the precision can reach cm-level, but they are limited to short baselines, e.g., a few hundred meters. Shi et al. [4] analysed BeiDou static precise point positioning, with the accuracy reaching 2 cm in horizontal and 5 cm in vertical; Ge et al. [5] conducted simulated BeiDou real-time kinematic precise point positioning, with the accuracy reaching 10–20 cm.

The papers above have rarely discussed the ambiguity resolution which is an important factor in BeiDou precise orbit determination and positioning; and the BeiDou relative positioning is limited to the ultra-short or short baseline,while long baseline positioning and the whole network solution have not been researched. On the basis of the above analysis, and under current BeiDou regional system conditions, with long-term continuous measurement data from Wuhan University BeiDou Experimental Tracking Stations, we adopt GPS and BeiDou joint network solution to discuss the effect of ambiguity resolution on BeiDou precise orbit determination and analyse some factors in BeiDou network positioning, such as ambiguity resolution, the selection of reference stations and interstation distance. The precision of BeiDou orbit determination and positioning is analyse by checking BeiDou orbit overlapping differences, and by comparison of differences between BeiDou network solution and precise point positioning.

16.2 BeiDou Precise Orbit Determination and Precision Analysis

16.2.1 Orbit Determination

GNSS multi-system joint precise orbit determination can obtain unified adjustment of the observations and geophysical parameters in the strict sense. Based on this idea, CODE realized joint orbit determination of GPS and GLONASS in 2003. In order to gain high precision BeiDou orbit, we adopt joint orbit determination of GPS and BeiDou, mainly based on the following two points: firstly, taking advantage of GPS observations and mature refined error models, to obtain joint adjustment results in a unified time and space frame and improve the precision of BeiDou satellite orbit; secondly, using the GPS orbit and clock obtained from joint solution of dual-system as an external check, where possible errors in joint solution can be detected by comparison with IGS post-mission precise orbit and clock, and the factors which affect both GPS and BeiDou orbit determination can be analyzed. Inter-system bias exists in receivers with dual-system capability in joint processing. Taking receiver clock error of GPS signal as reference, inter-system bias between GPS and BeiDou can be set as a parameter to be estimated in joint orbit determination.

To analyze the accuracy of BeiDou orbit in joint orbit determination, we use data from Wuhan University BeiDou Experimental Tracking Stations which is between DOY 196 and DOY 205 in 2012, and distribution of BeiDou satellites and stations is shown in Fig. 16.1. During this time, BeiDou satellite constellation consists of four GEOs, five IGSOs and two MEOs, of which C04 and C08 have a few unhealthy cases, leading to anomaly in some stations' observation of them. The stations used in orbit determination consist of six stations (HRBN, NTSC, XIAN, CENT, CHDU, HKTU) in China and two stations abroad (XILA in Greece

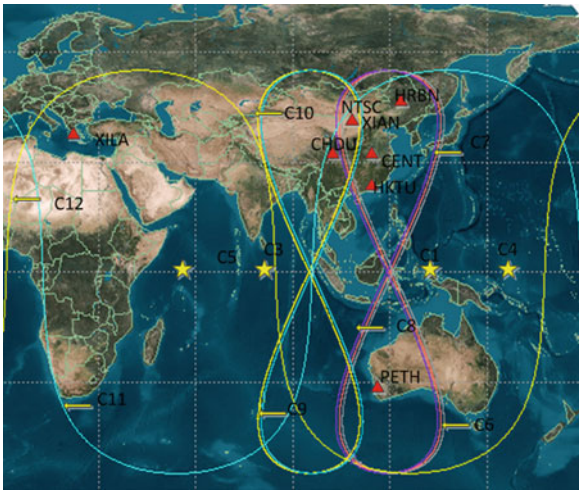

Fig. 16.1 BeiDou satellite and station schematic diagram

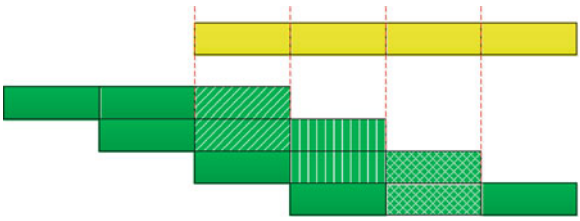

Fig. 16.2 Overlapping arcs diagram

and PETH in Australia), all of which are equipped with dual frequency GPS and BeiDou receiver UR240 [7].

Firstly, all stations' precise coordinates are obtained by GPS PPP using IGS post-mission precise products. During the test time, one-day static PPP standard deviation is better than 1 cm, and we takes the average value and fix it in the joint orbit determination of GPS and BeiDou. Since the observation geometry of the regional monitoring network is weaker than global one, observation arc of three days is employed to improve the strength of solution. The accuracy of GPS orbit can be validated by comparison with IGS precise ephemeris, while the accuracy of BeiDou orbit can be validated by checking the orbit differences of the overlapped time span between two adjacent three-day solutions, as shown in Fig. 16.2, comparison between the orbit of the last day of a three-day solution and the orbit of the middle day of the next one.

Observation and force models used in three-day joint orbit determination in this paper are listed as below (Table 16.1).

Table 16.1 Observation and force models and parameters used in the processing

Parameters	Model	Constraint
Observation	Un-differenced LC and PC	0.02 cycle, 1.0 m
Interval	300 s	
Cutoff elevation	7°	
Weight	Elevation	1 for E > 30°, otherwise 2 × sin(E)
PCV	GPS: IGS absolute correction	
	BeiDou: only PCO	
	Station: not supplied	
Phase wind up	Applied	
Tropospheric delay	Saastamoinen model	Initial value 20 cm, random walk
	GMF mapping function	$1\text{cm}/\sqrt{hour}$
Satellite clock error	White noise	500 m
Receiver clock error	White noise	500 m
ISB	White noise	900 m
Tide displacement	Solid tide, sea tide, pole tide	
Relativity effect	Corrected	
Earth gravity	EIGEN_GL04 12	
EOP	Fixed IERS EOPC	
N-body gravitation	Sun, moon and other planet	
Atmospheric drag	Not considered	
Solar radiation	Bern 5 parameter $(D_0, Y_0, B_0, B_C, B_S)$	Parameter estimation

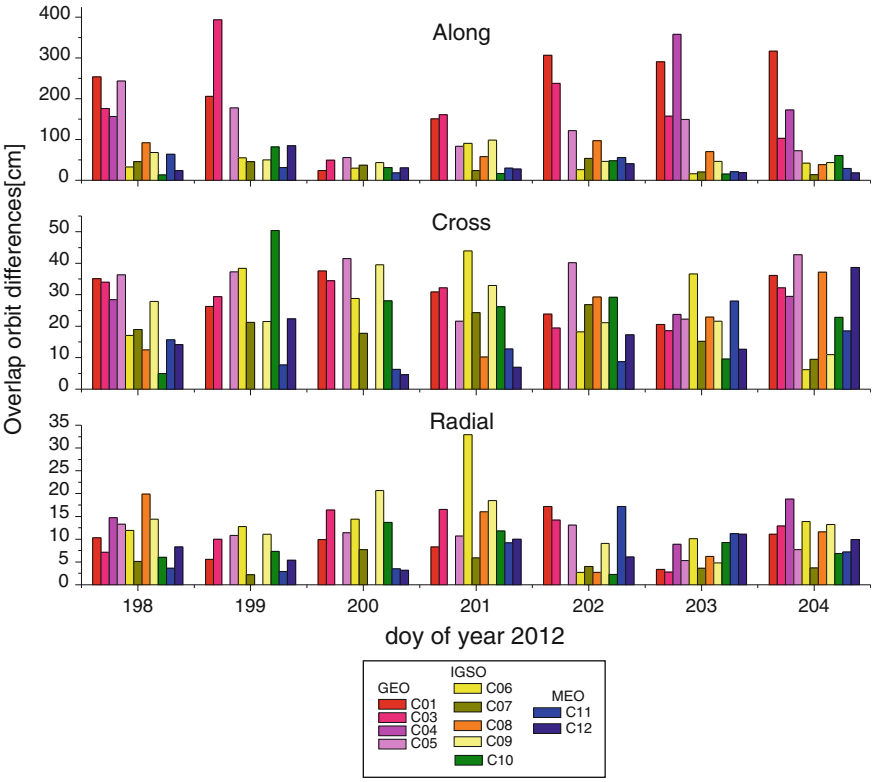

Fig. 16.3 Overlap orbit difference without ambiguity resolution

The joint orbit determination without ambiguity resolution is carried out and then a week of the RMS of BeiDou overlapping arcs in along, cross and radial direction are presented in Fig. 16.3. It can be seen that BeiDou orbit, the same as GPS, has its accuracy in along direction worse than in cross and radial direction. Due to the geostationary property of GEO, there exists a big bias in its along direction, whereas the three direction's accuracy of IGSO and MEO are obviously better than GEO, because of their movement relative to ground stations.

16.2.2 Ambiguity Resolution

Ambiguity resolution is an efficient mean to improve the precision of orbit and positioning as it can reduce the strong correlations between ambiguity and other parameters, such as orbit and station coordinate. The un-differenced ambiguity doesn't have the integer property because of the influence of the UPD at the satellites and receivers which can be removed by double difference between

satellites and receivers. Many scholars have researched ambiguity fixing in GPS network solution and the precision of orbit and positioning have been improved [8–11]. As the method in [10] considers the factors that affect ambiguity fixing in actual data processing and chooses independent ambiguity based on the possibility of fixing, we adopt it in GPS and BeiDou joint processing. As the error models are still not refined in BeiDou system, strict and conservative criteria are adopted in ambiguity fixing. The basic procedure is as following.

1. Choose the double difference ambiguity with certain common-view time (at least 20 min) and baseline length(at most 4,000 km in this paper), divide undifferenced ionosphere-free ambiguities at baseline and network level according to the possibility of ambiguity fixing, and choose the ambiguities above to form independent double difference ambiguities.
2. Use MW combination to get the estimate and variance of the wide lane ambiguities and then make decision whether the wide lane double difference ambiguities can be fixed according to the probability function, whose formula is [8]:

$$P_0 = 1 - \sum_{n=1}^{\infty} \left[erfc\left(\frac{n-(b-I)}{\sqrt{2}\sigma}\right) - erfc\left(\frac{n+(b-I)}{\sqrt{2}\sigma}\right)\right] \tag{16.1}$$

where

$$erfc(x) = \frac{2}{\sqrt{\pi}} \int_x^{\infty} e^{-t^2} dt \tag{16.2}$$

b and σ is the estimate and standard deviation of ambiguity, and I is the closest integer to b. We take the confidence level α of ambiguity fixing as 0.1 %, i.e., when P_0 is bigger than $1 - \alpha$, fix b to I, otherwise not.

3. Get the estimate and variance of the narrow lane ambiguities with the fixed wide lane ambiguities and ionosphere-free combination ambiguities and then make decision whether the ambiguities can be fixed according to the probability function in the same way.
4. Obtain the fixed ionosphere-free double difference ambiguities using the fixed wide and narrow lane ambiguities.
5. Introduce the fixed ionosphere-free double difference ambiguities into the normal equation by way of adding virtual observation equation to improve the estimation precision of other parameters (including the ambiguities still not fixed). Fixing one double difference ambiguity is equivalent to put four undifferenced ambiguities to integer constraints.

$$v_b = Dx - b_c^{-d} \; P_b \tag{16.3}$$

where D is the ambiguity projection matrix, b_c^{-d} is the fixed ionosphere-free double difference ambiguity, P_b is the weight of virtual observation which should be large enough to ensure strong constraint to un-differenced ambiguities.

Repeat the procedure (1) to (5) until there are no more ambiguities to fix. It must be pointed out that BeiDou GEO satellite ambiguity parameters are not easy to be separated from other parameters because of the geostationary property and error terms that are not refined. Ge et al. [5] find that in GEO orbit determination there's a systematic error in the along direction and its influence to carrier phase can be absorbed by the ambiguity parameter, and its influence to pseudorange can be dealt with by reducing its weight. Based on the two points above, fixing BeiDou IGSO and MEO ambiguities to improve the orbit determination and positioning precision is adopted in this paper.

In order to evaluate the effect of ambiguity fixing on BeiDou orbit determination, the STD of satellites' initial state parameters (position, velocity and solar radiation pressure) and the RMS of the overlap difference before and after ambiguity fixing are analysed. Taking the three-day solution of the DOY of 197, 198 and 199 as an example, Figure 16.4 shows the percentage of improvement of the STD of satellites' initial state parameters after ambiguity fixing. It can be seen that STD of initial state of both IGSO and MEO are reduced greatly where IGSO by about 50 % and MEO by about 20 %. The difference between IGSO and MEO may be related to the observation length, i.e., IGSO can be observed by the regional monitoring stations the whole 3-day arc so that there are more ambiguities

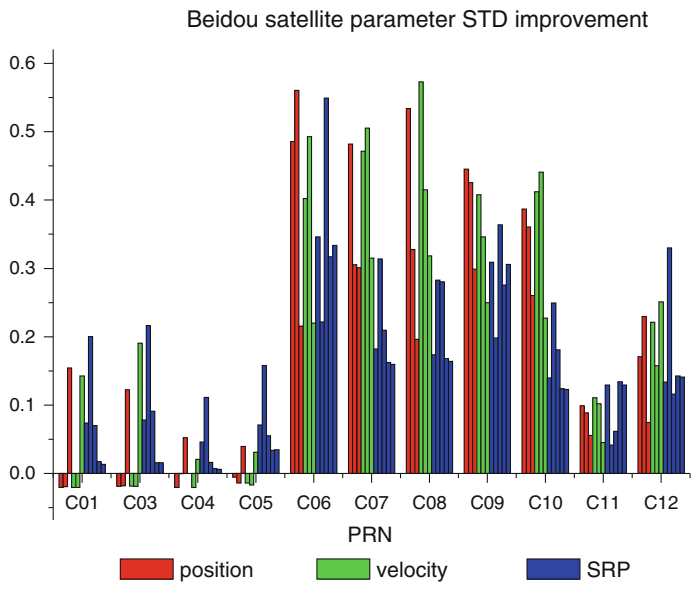

Fig. 16.4 Percent of STD improvement of initial state of BeiDou satellite after ambiguity fixing

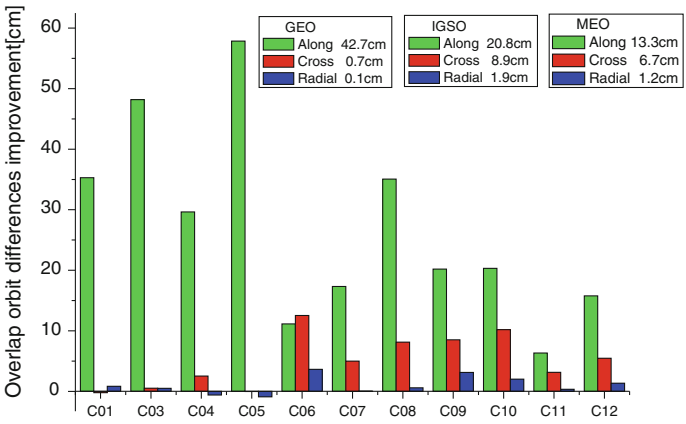

Fig. 16.5 Improvement of orbit accuracy after ambiguity fixing

to be fixed than MEO, which can't be observed at some part of the 3-day arc. After ambiguity fixing of IGSO and MEO, the precision of GEO solar radiation pressure parameters is improved and so do the initial position and velocity in some cases. It shows that improvement of estimation of GEO parameters by fixing ambiguities of IGSO and MEO is feasible.

Figure 16.5 is the average improvement of BeiDou satellite orbit accuracy in a week by making statistics of RMS of overlap differences before and after ambiguity fixing, which shows that after ambiguity fixing, the improvement of accuracy in along direction is most significant, with 43, 21 and 13 cm for GEO, IGSO and MEO respectively; the improvement in cross direction reaches 9 and 7 cm for IGSO and MEO respectively; and the improvement in radial direction is not significant, about 1 cm. A week of the RMS of BeiDou overlapping arcs after ambiguity fixing is presented in Fig. 16.6.

Statistics of average orbit accuracy in a week is shown in Fig. 16.7. It shows that using six domestic stations and two foreign stations, the 3D-RMS of the GEOs, IGSOs and MEOs is 155, 33 and 28 cm, respectively, the accuracy of radial direction is basically better than 10 cm, the accuracy of GEO in along direction is much worse than IGSO and MEO, although with improvement after ambiguity fixing. It can be expected that with the increase of stations, improvement of distribution and refined models, the accuracy of BeiDou orbit determination will be improved further.

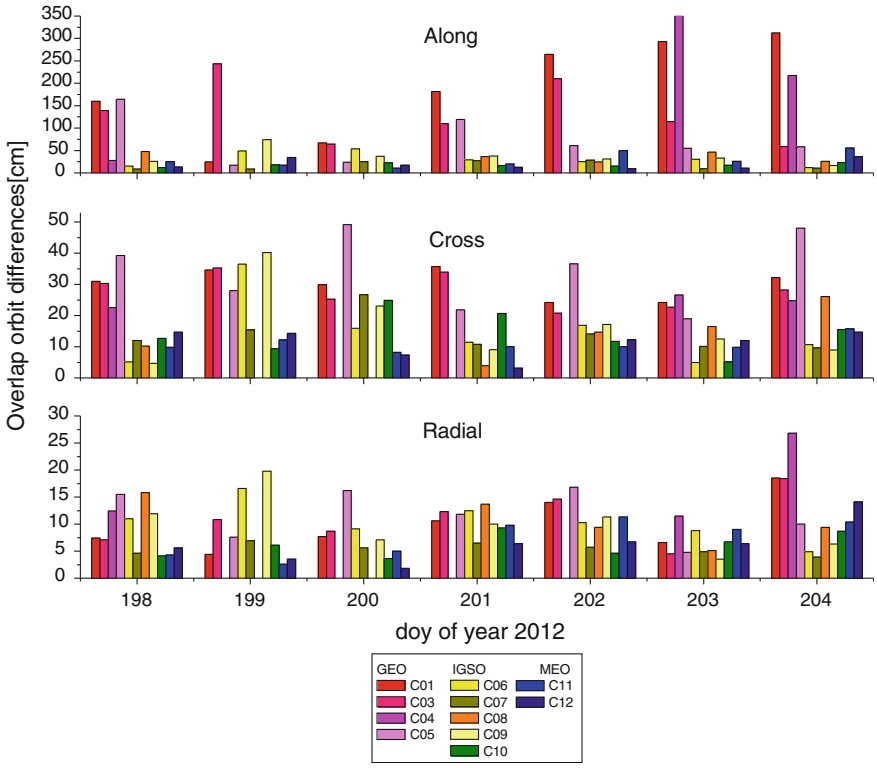

Fig. 16.6 Overlap orbit difference with ambiguity resolution

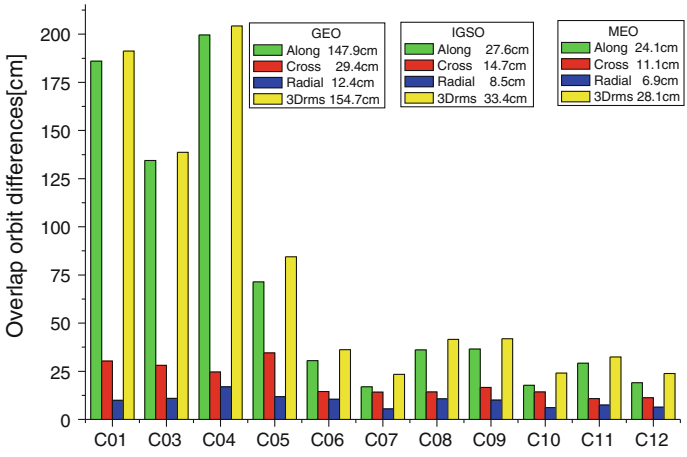

Fig. 16.7 Average accuracy of orbit after ambiguity fix

16.3 BeiDou Network Solution Positioning and Precision Analysis

16.3.1 BeiDou Network Solution Positioning

To analyse the precision of BeiDou relative positioning, network solution is conducted using orbit from the joint GPS and BeiDou orbit determination in previous section. The distribution of stations in network solution is shown in Fig. 16.8, where red triangle is the reference stations of fixed coordinates, blue circle is the rover stations, all of which are in Asia–Pacific service area of BeiDou regional system. We select three reference stations (HRBN, CENT, HKTU), and among all the stations the shortest baseline is about 30 km and the longest one is about 6000 km. In double difference ambiguity fixing, we select the same mode as in orbit determination, i.e., fixing the ambiguities of IGSOs and MEOs of BeiDou and keep float ambiguity of GEO.

Using GPS one-day static PPP coordinates as reference true value, the results of BeiDou network solution before and after ambiguity fixing is shown in Figs. 16.9 and 16.10. From the statistics, ambiguity fixing mainly improves the repeatability and accuracy in east direction. For all domestic stations, the average accuracy improves from 7.7 to 5.7 mm in east direction and from 8.9 to 7.8 mm in

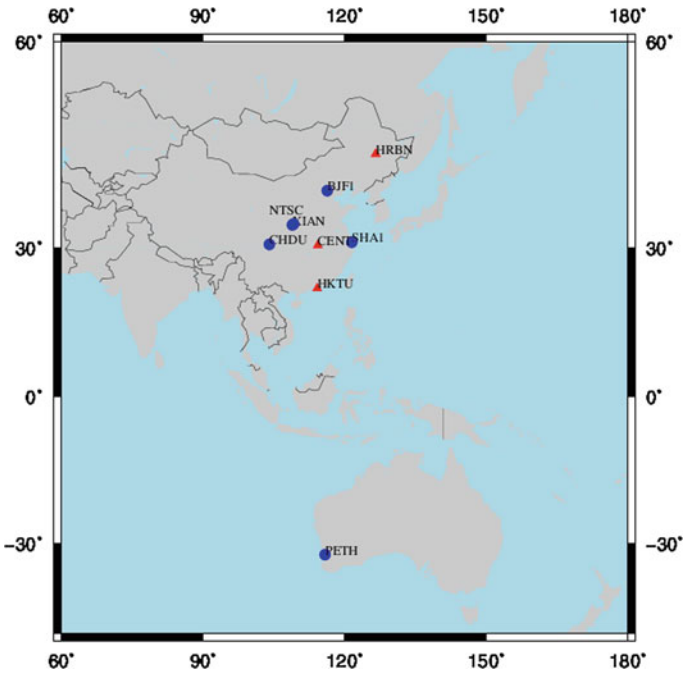

Fig. 16.8 Distribution of network solution stations

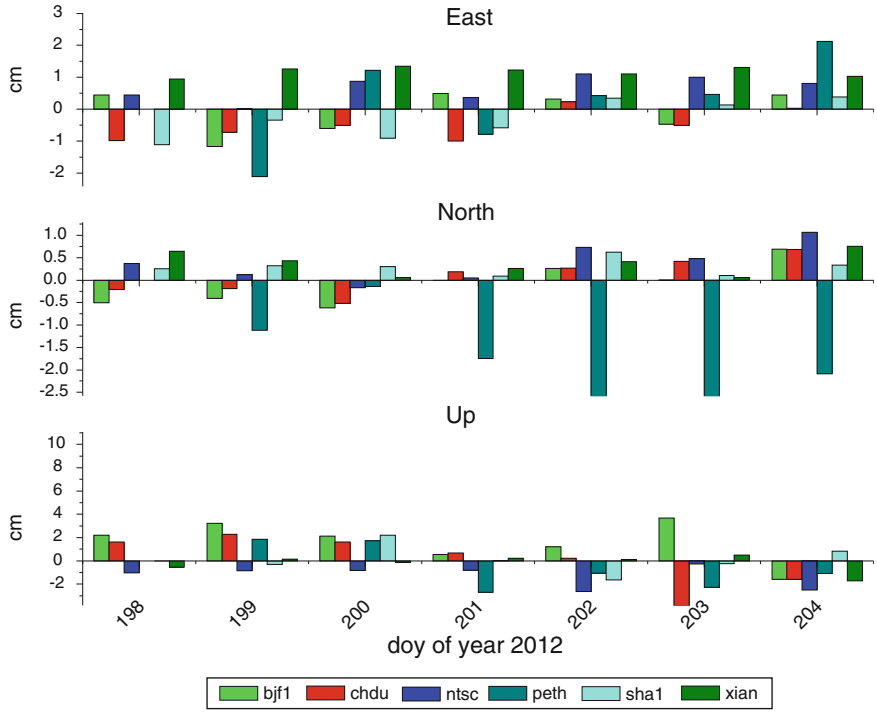

Fig. 16.9 Network solution positioning before ambiguity fixing

horizontal after ambiguity resolution. The accuracy in horizontal and vertical is basically better than 1 and 2 cm, respectively. For foreign station PETH, which is about 6000 km from the nearest reference station HKTU, accuracy of about 1.5 cm in horizontal and about 1.9 cm in vertical can be achieved.

16.3.2 Comparison with BeiDou PPP

In order to compare BeiDou network solution positioning and BeiDou PPP, we conduct one-day static PPP to all stations in Asia–Pacific region, using BeiDou orbit and clock obtained from previous section and the result is shown in Fig. 16.11. From the statistics, the average accuracy in horizontal and vertical is 8.8 and 19.2 mm, respectively. The accuracy in horizontal and vertical is basically better than 1.4 and 3.0 cm, respectively, which is slightly worse than BeiDou network solution, but basically at the same level.

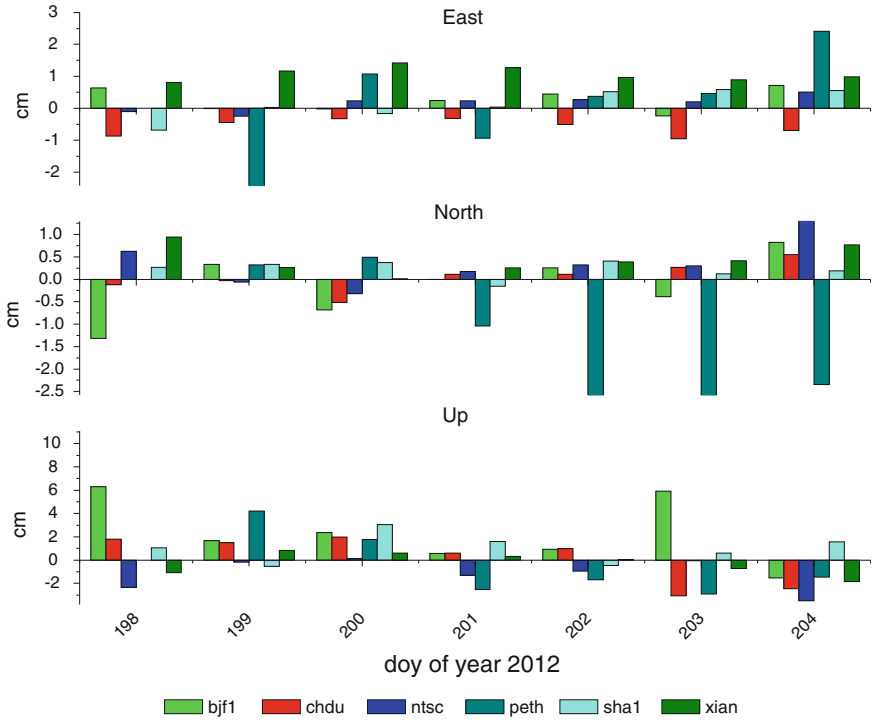

Fig. 16.10 Network solution positioning after ambiguity fixing

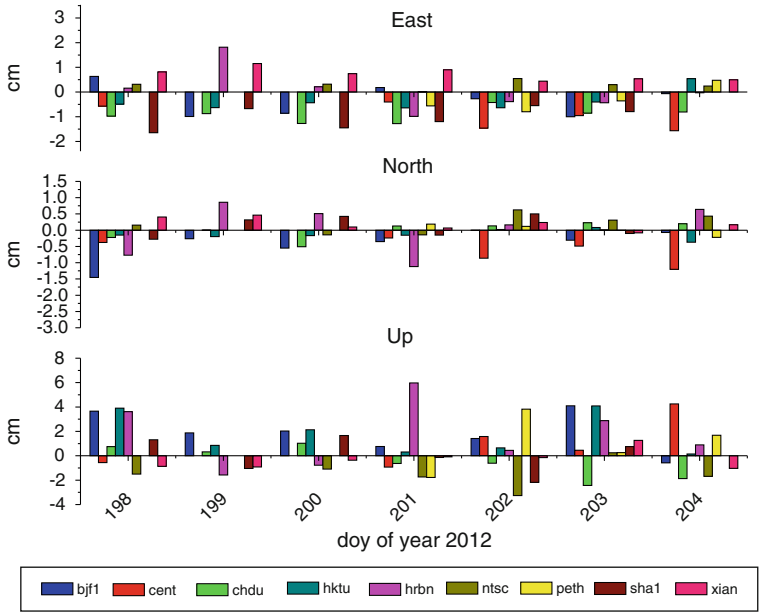

Fig. 16.11 BeiDou one-day static PPP

16.4 Conclusion and Discussion

In this paper, GPS and BeiDou joint orbit determination is implemented and the influence of ambiguity fixing on the precision of BeiDou orbit is analysed. Using regional monitoring network consisting of six stations in China and two stations abroad, the results show that the orbit precision of all GEO, IGSO and MEO satellites of BeiDou is improved by ambiguity fixing, especially in the along direction. The overlapping 3D RMS of the GEO, IGSO and MEO satellites of BeiDou is 155, 33 and 28 cm, respectively, and the precision in radial direction is basically better than 10 cm. The application of BeiDou regional navigation system in precise positioning is analysed and discussed. In BeiDou single system network solution, the result shows that the ambiguity fixing mainly improve the positioning precision in the east direction. BeiDou network solution can achieve horizontal accuracy of better than 1 cm and vertical accuracy of better than 2 cm, and for long baseline about 6000 km, the horizontal accuracy of 1.5 cm and vertical accuracy of 1.9 cm can be achieved. At last, the difference of BeiDou network solution and BeiDou PPP is compared and the result shows that BeiDou static PPP solution can achieve horizontal accuracy better than 1.4 cm and vertical accuracy better than 3 cm, which is a little worse than BeiDou network solution, but basically at the same level. The positioning result of BeiDou network solution and PPP indicates the application of BeiDou regional system in precise positioning can achieve the precision level close to GPS.

The sequential ambiguity fixing is used in ambiguity resolution in this paper, and it has resulted in the improvement of the accuracy of BeiDou orbit determination and positioning. Other ambiguity resolution methods based on searching algorithm can also be employed, such as LAMDA [12]. SLR is another effective technique to examine BeiDou orbit accuracy, and after ambiguity resolution the SLR data residual of BeiDou satellite is about 10 cm, which will be discussed in another paper. BeiDou system is still at an early stage, but with the development of data processing techniques, the refinement of satellite attitude control and force model, the elimination or reduction of various error terms, the addition of data from more stations with more evenly distribution, the orbit determination and positioning accuracy of BeiDou system will be further improved and the application in precise positioning field will be better.

Acknowledgments This study is supported by the '863 Project' of China (No. 2012AA12A202). We are grateful to three anonymous reviewers for their valuable comments and suggestions.

References

1. Mao Y, Du Y, Song XY et al (2011) GEO and IGSO joint precise orbit determination. Sci China Phys, Mech Astron 54:1009–1013
2. Zhou S, Hu X, Wu B et al (2011) Orbit determination and time synchronization for a GEO/IGSO satellite navigation constellation with regional tracking network, Sci China Phys, Mech Astron 54(6):1089–1097

3. Montenbruck O, Hauschild A et al (2012) Initial assessment of the COMPASS/BeiDou-2 regional navigation satellite system. GPS Solut 6:1–12
4. Shi C, Zhao QL, Li M et al (2012) Precise orbit determination of BeiDou satellites with precise positioning. Sci China Earth Sci 55:1079–1086
5. Ge M, Zhang H, Jia X, Song S, Wickert J (2012) What is achievable with the current compass constellation. ION-GNSS
6. Shi C, Zhao QL, Hu ZG, Liu JN (2012) Precise relative positioning using real tracking data from COMPASS GEO and IGSO satellites. GPS Solut 17(1):103–119
7. Unicore (2010) Installation and operation user manual: UB240-CORS BeiDou/GPS dual-system dual-frequency high precision receiver
8. Blewitt G (1989) Carrier phase ambiguity resolution for the global positioning system applied to geodetic baselines up to 2000 km. J Geophys Res 94:10187–10203
9. Dong D, Bock Y (1989) Global positioning system network analysis with phase ambiguity resolution applied to crustal deformation studies in California. J Geophys Res 94:3949–3966
10. Ge M, Gendt G, Dick G, Zhang FP (2005) Improving carrier-phase ambiguity resolution in global GPS network solutions. J Geod 79(1–3):103–110
11. Mervart L (1995) Ambiguity resolution techniques in geodetic and geodynamic applications of the global positioning system. PhD Thesis, University of Berne
12. Teunissen (1995) The least-squares ambiguity decorrelation adjustment: a method for fast GPS integer ambiguity estimation. J Geod 70:65-82

Chapter 17
A Method Based on the Orbital Error Correction of the Wide Area Differential Positioning Algorithm

Ranran Su, Nan Xing, Lei Zhang, Li Liu, Guifen Tang, Guangming Hu and Min Ma

Abstract Satellite navigation service using GEO satellite provides positioning service to local users. Continuous services ask for kinetic method to determine orbit during the GEO satellite orbital maneuver phase. However, kinetic method brings larger orbital error so that the positioning accuracy will drop. This paper presents a method based on the orbital error correction of the wide area differential positioning algorithm. Based on analysis of the GEO satellite orbit maneuver characteristics and other factors that affect positioning accuracy, an improved algorithm is designed, which can enhance the positioning accuracy during orbit maneuver.

Keywords Satellite navigation service · Orbital maneuver · Orbit error correction · Wide-area differential positioning

17.1 Introduction

Satellite navigation and positioning system can provide users with real-time, continuous, under all-weather condition, precise positioning, navigation and timing services. GPS of the United States and GLONASS of Russia are the main passive positioning systems actually putting into use at present. RNSS, a passive positioning system of China, is developed to serve the regional user.

R. Su (✉) · L. Zhang · L. Liu · G. Tang · G. Hu · M. Ma
Beijing Satellite Navigation Center, Beijing, China
e-mail: shuyy_2003@yahoo.com.cn

N. Xing
Chinese Academy of Sciences, Shanghai Astronomical Observatory, 200030 Shanghai, China

J. Sun et al. (eds.), *China Satellite Navigation Conference (CSNC) 2013 Proceedings*, Lecture Notes in Electrical Engineering 245,
DOI: 10.1007/978-3-642-37407-4_17,

Unlike passive positioning mode of RNSS, active positioning system only using geostationary orbit (GEO) satellites provides a 24/7 positioning service. Since only GEO satellites have the ability of transmitting the outbound and inbound signal, with the constraint of the elevation, the main error source of active positioning is GEO satellite orbital error. In coasting phase, GEO satellite orbit accuracy broadcasted in RNSS navigation message is better than 10 m, the radial precision better than 2 m [1]. But in order to maintain the ascending node longitude, GEO satellite maneuvers frequently in east–west and north–south direction. During the orbit maneuver phase, perturbation model needed by the conventional dynamic orbit determination method is not clear so that orbit precision given by navigation message will drop quickly. The kinetic orbit determination method, therefore, is needed to maintain the continuity of the real-time positioning service [2].

Positioning precision is a vital indicator to measure the performance of a navigation system. Although kinetic method can supplement the gap brought by orbital maneuver, the positioning precision is a little lower than that when dynamic method is used. Considering all above factors and the pseudorange correction in wide area differential GPS positioning algorithm, we proposed one new positioning algorithm, which is based on the orbit precision correction in wide area differential, in order to, increase positioning accuracy. Applying such method to the observation data, we find that our algorithm can indeed enhance the positioning accuracy by 10 %.

17.2 Principle of Active Positioning Based on GEO Satellite

Principle of active positioning based on GEO satellite is on the basis of user receiver that can respond to positioning inquiry signal sent from the Main Control Center (MCC) and sent a request back to MCC. MCC can calculate the distance between the satellite and the user and determine the position of the user and report the result to the user [3]. The most simple system comprises a MCC, the two GEO satellites with signal transponder, and a certain amount of difference reference station [4]. The position of the user can be obtained according to intersection of three spheres whose cores are two GEO satellites and geometric center of the earth [5]. Since the distances between the user and the satellites have been measured, once we know the distance between the user and the center of the earth, the position of the user is uniquely determined, as shown in Fig. 17.1.

The measurement equation is shown as follows:

$$\begin{cases} O_1 = 2S_1 + 2\rho_1 \\ O_2 = S_1 + S_2 + \rho_1 + \rho_2 \\ O_3 = H \end{cases} \tag{17.1}$$

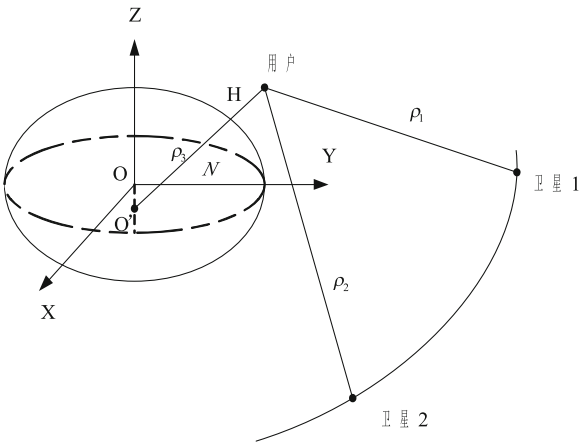

Fig. 17.1 Principle of active positioning

where O_1 is the observation that MCC received from the first satellite, S_1 is the distance between MCC and the first satellite, ρ_1 is the distance between the satellite and user. O_2 is the observation that MCC received from the second satellite, S_2 is the distance between MCC and the second satellite, ρ_2 is the distance between the second satellite and user. O_3 is the elevation constraint, H is the elevation retrieved from the elevation database. By solving the Eq. (17.1), coordinate of user position can be derived.

17.3 The Method of Wide Area Differential Correction Calculation

In order to improve the positioning precision of the user, we design a wide area differential method based on the pseudorange corrections. Using reference station within the scope of China, the method solves the differential corrections of each satellite and applies corrections to calculation of the user position. Specific methods are as follows.

In RNSS positioning and navigation service, after user correcting their real-time observation with information broadcasted in navigation messages, there still are several sources of errors remaining, such as ionospheric delay, satellite clock error, the receiver clock error, orbital error, multi-path error. Using the monitoring stations located in known high accuracy position coordinates and distributed uniformly in the service area within China, satellite orbital error and clock error, called wide area differential correction, can be estimated and predicted.

Observation equation is as followed:

$$v + \rho_i^j = \left|R^j - R_i\right| + \Delta t_i - \Delta t^j - \Delta t'^j + \Delta t_{ion} + b - B + \Delta t_{rel} + \Delta t_{trop} \tag{17.2}$$

where, i and j specify the station and the satellite, v is the residual, R_j is the satellite coordinates, R_i is the receiver coordinates, Δt_i is the parameters for the receiver clock error, Δt^j is the parameters for satellite wide area differential correction, $\Delta t'^j$ is the satellite broadcast ephemeris clock error correction, Δt_{ion} is the ionospheric correction, Δt_{rel} is the relativistic correction, b and B specify hardware time delay bias corresponding to each frequency of satellite and receiver respectively, Δt_{trop} is the tropospheric correction.

Using the satellite orbital error, clock error, ionospheric correction model and satellite time delay parameter given by the navigation message, the relevant error of the observation in Eq. (17.2) can be corrected. Consider that the prediction error in navigation message, including the orbital error, clock error, ionospheric model error, will accumulate with time. Therefore, the measurements of reference station provide a effective tool to calculate differential correction and improve the positioning accuracy [6].

The public delay of the system is corrected with models. Ionospheric delay is eliminated by dual frequency observation. The receiver clock error and hardware time delay are unknown. With the monitoring receiver whose coordinates are precisely measured, using multi-satellite observation, wide area differential correction and monitoring receiver clock error at the same time can be calculated together, as shown in Eq. (17.3).

$$pcor + (\Delta t_{rcvclk} + \tau_{IFB}) = \frac{f_1^2 P_1 - f_2^2 P_2}{f_1^2 - f_2^2} - \frac{f_1^2 \tau_{tgd1} - f_2^2 \tau_{tgd2}}{f_1^2 - f_2^2} - \left|X^{sat} - X_{rcv}\right| - \Delta t_{satclk} - \Delta t_{cor} - \delta t_{mp} - \delta\varepsilon \tag{17.3}$$

Using the data set of all the stations and satellites, a set of equations can be list and solved with least-squares method.

17.4 GEO Satellite Error Analysis During Orbit Maneuver

During coasting phase, RNSS navigation and positioning system determine the satellites orbit with multi-satellite combined orbit determination method based on days of the orbit arc data. And orbit precision, estimated with the laser measurement, proved to be within 1 m in radial direction. Therefore, we can use the orbit mentioned above as reference, and analyze the orbit precision of GEO satellite determined with kinetic method. As shown in Fig. 17.2, radial, tangential, normal orbital errors in July 12, 2012 when two methods are both used to compare.

The figure indicates that kinetic method introduces radial error of 6–8 m, tangential error of 150 m and normal error of 20 m. And the total error is

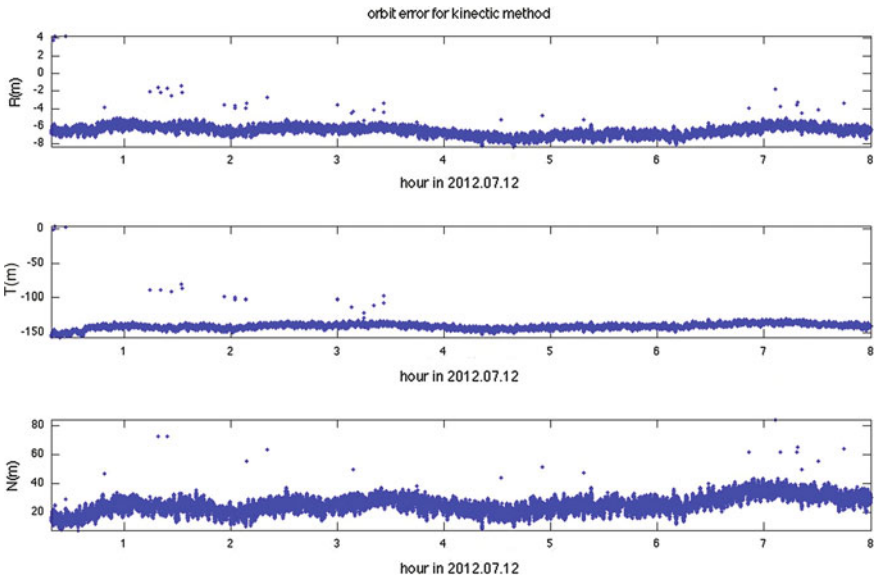

Fig. 17.2 Orbit accuracy assessment during GEO satellite maneuver

$$\sqrt{8^2 + 150^2 + 20^2} = 151 \text{ m}$$

In GEO satellite coasting phase, GEO satellite orbit precision given by RNSS navigation message is higher than maneuver phase and O–C residuals of all stations are almost the same. The differences between the residuals are less than 0.1 m. So a wide area differential correction scalar can apply to all stations for orbital error correction. But during the orbit maneuver phase, orbit error is up to 150 m and differences between the residuals are remarkable. Since different satellite in orbit maneuver phase has different orbital error, in order to analyze how such facts effects the O–C residuals, we manually assumed three orbital error conditions, i.e., 50, 100 and 500 m, and list the results in Table 17.1. We chose 6 imaginary receivers placed in Beijing, Hainan, Xinjiang, Heilongjiang, Neimeng and Guangdong and calculate their O–C residuals. The differences between the residuals are 1.24, 3.53 and 5.41 m when orbital error are 50, 100 and 500 m respectively. Because the differences for the stations are larger than in coasting phase, only wide area differential correction scalar cannot offset the projection of orbital error into line-in-sight direction of all user within the service area. The positioning precision after corrected by wide area differential correction will drop.

From the above table, it can be seen that, during orbit maneuver, when orbital error is 500 m, O–C residual of each station is 5.41 m in maximum.

Table 17.1 Different conditions of station error under different orbit error table

Station	Orbit error		
	50 m	100 m	500 m
BeiJing	5.72	33.60	67.20
HaiNan	6.83	34.18	69.36
XinJiang	6.96	35.80	72.60
HeiLongJiang	5.65	32.27	67.54
NeiMeng	6.85	34.26	70.53
GuangDong	5.76	33.82	69.64
Max	1.24	3.53	5.41

17.5 An Orbit Error Correction Method Based on the Wide Area Differential Algorithm

During orbit maneuver, orbital error is large and wide area differential correction precision drops. Therefore, we design a new method based on orbit correction calculated with the wide area differential GPS algorithm. The correction is decomposed into X, Y, Z three components and apply directly to the orbit correction. Specific methods are as follows:

Based on distance correction of the wide area differential active positioning observation equations:

$$\tau^{ij} = |\mathbf{S}_i - \mathbf{C}| + |\mathbf{S}_i - \mathbf{U}| + \left|\mathbf{S}_j - \mathbf{U}\right| + \left|\mathbf{S}_j - \mathbf{C}\right| + \Delta\tau^{ij} \tag{17.4}$$

where, τ^{ij} is the concept of measurement, $\mathbf{C}$ is the ground station position, $\mathbf{U}$ representative of the need for solution of user location, $\mathbf{S}_i$ is ($i = 1, 5$) the satellite ephemeris position, $\mathbf{S}_j$ is the ($j = 1, 5$) forwarding user response signal of the satellite ephemeris location, $\Delta\tau^{ij}$ is the error based service system from the observed data by removing the error. In the formula, calculation $\mathbf{S}_i$ and $\mathbf{S}_j$ error correction for the orbit after the satellite ephemeris position, the wide area differential correction decomposition to X, Y, Z three components of the specific implementation method as shown below.

Based on GEO satellite active positioning method, we can use the wide area differential corrections to correct orbit error.

$$\begin{aligned}\rho = \left|\vec{R}_{sat} - \vec{R}_{sta}\right| &= \left|\widetilde{\vec{R}}_{sat} + \Delta\vec{R} - \vec{R}_{sta}\right| \\ &= \left|\widetilde{\vec{R}}_{sat} - \vec{R}_{sta}\right| + \frac{\left(\widetilde{\vec{R}}_{sat} - \vec{R}_{sta}\right)\cdot\Delta\vec{R}}{\left|\widetilde{\vec{R}}_{sat} - \vec{R}_{sta}\right|}\end{aligned} \tag{17.5}$$

The wide area differential correction is as followed:

$$\Delta\rho = \frac{\left(\widetilde{\vec{R}}_{sat} - \vec{R}_{sta}\right) \cdot \Delta\vec{R}}{\left|\widetilde{\vec{R}}_{sat} - \vec{R}_{sta}\right|} \tag{17.6}$$

However, one need to consider the self-consistency of wide area differential correction calculation and GEO satellite active positioning calculation. Both of the calculation are needed when using the same orbit data. Wide area differential correction can be used during satellite maneuver phase.

17.6 Results

We analyzed observation data from two GEO satellites during their maneuver phase on July 12, 2012 and July 18, 2012 respectively. Positioning results are as follows:

1. July 12, 2012:

Figure 17.3 shows positioning results in Beijing area when GEO satellite is during maneuver phase on July 12, 2012. In the figure, black stars are for primary positioning results from geometry method, dark gray plus denotes when only correcting the orbit of satellite in maneuver phase while the remaining satellite

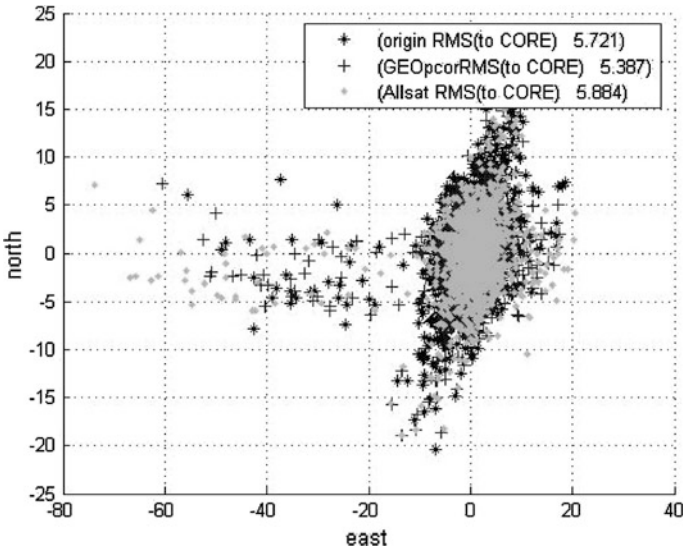

Fig. 17.3 Positioning results of GEO satellite maneuver phase on July 12, 2012

using geometric method, light gray dots denotes that all satellite orbit errors are corrected using all the orbit positioning results.

2. July 18, 2012:

Figure 17.4 shows the results for July 18, 2012 data. All the captions are the same with Fig. 17.3.

From the above figures, we can see that positioning results from three methods have some common properties: error box shape of positioning results are all ellipse and long axis of the ellipse is close to the north–south direction, while short axis close to the east–west direction. Such formation should be composed of GEO constellation characteristics. The constellation configuration to the north of the NDOP value is greater than the east to EDOP. The major axis of the ellipse and the north and south direction angle may be associated with the inbound satellite relative user angularly related. Scattered points on the southwest direction corresponds to the satellite number less than 4, since when the satellite number is reduced, EDOP obviously increased so that the east–west direction errors increased significantly.

Comparing the three methods, we find that results of only correcting the orbit of satellite in maneuver phase are better than primary positioning results from geometry method, however it is worse than results that orbits of all satellites are corrected. Note that the North–South error effect is more obvious since orbit correction values are in radial direction of GEO satellite orbit.

We also collect the statistical results as shown in the figures in Table 17.2, we find:

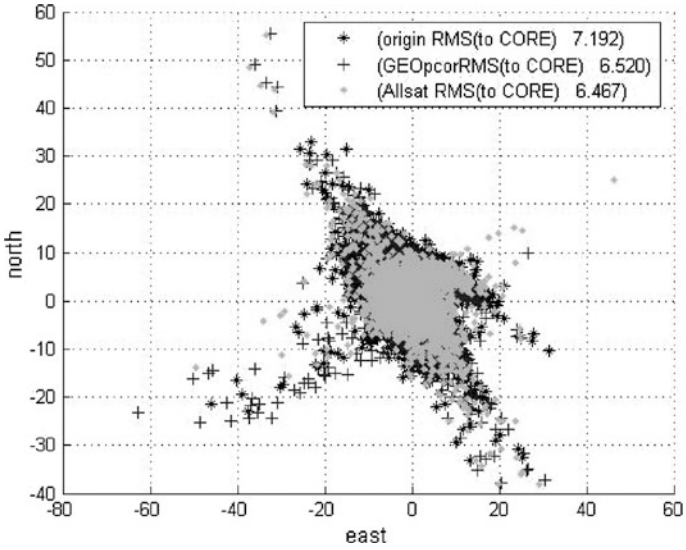

Fig. 17.4 Positioning results of GEO satellite maneuver phase on July 18, 2012

Table 17.2 Positioning results

Positioning method	Date	
	7.12	7.18
Primary positioning results from geometry method	4.950	6.475
Only correcting the orbit of satellite in maneuver phase	4.462	5.835
Correcting all satellites	4.393	5.779

1. when different satellite is in orbit maneuver phase, geometric orbit determination precision is different, resulting in slightly different positioning accuracy.
2. applying error correction to all satellites could improve positioning precision by 10 %, comparing with the primary positioning results from geometry method.

17.7 Conclusion

Orbit precision is one of the key factors to guarantee satellite navigation system operation, In this paper, based on wide area differential GPS positioning and in-depth analysis, we proposed to use the wide area differential correction correcting orbit error, in order to achieve high positioning precision. The simulation results show that with initial precision positioning, this method can effectively enhance the positioning accuracy by more than 10 %.

References

1. Guo Rui, Hu X et al (2010) Precise orbit determination for geostationary satellites with multiple tracking techniques. Sci China Bull 55(8):687–692
2. Tang J, Wang L (1989) The application of augmentation technology in quick position communication system. Chin J Space Sci
3. Wu T, Li G (1998) The earth synchronization satellite position. The PLA Publishing company, Beijing
4. Gerard.O'neill GK (2005) A multi purpose satellite system to serve civil aviation needs. LCAO Bull
5. Tan S (1997) The satellite navigation engineering. The PLA Publishing company, Beijing
6. Cao YL, Hu XG et al (2012) The wide-area difference system for the regional satellite navigation system of COMPASS. Sci China Phys Mech Astron 55:1307–1315

Chapter 18
Realization of High-Precision Relative Positioning Using Beidou Regional Navigation Satellite System

Laiping Feng, Wei Zhou and Xianbing Wu

Abstract Based on Beidou regional navigation satellite system in the phase of 4GEO + 5IGSO constellation, systematic research on Beidou high-precision relative positioning has been carried out by sufficient measured data from Beidou test network. A comparison scheme with Beidou/GPS dual-mode data is designed, and feasibility and attainable precision of Beidou relative positioning have been verified effectively. As shown in results: coordinate accuracy realized by Beidou relative positioning has achieved centimeter level, and baseline repeatability has reached millimeter level, which are equivalent to GPS high-precision relative positioning level. For short baseline, coordinate repeatability in the North, East and Up direction is respectively better than 0.5, 1.3 and 2.9 mm, and absolute error of coordinate is respectively better than 0.2, 0.6 and 1.7 mm by comparison with GPS; for medium/long baseline, the coordinate repeatability in the NEU direction is respectively better than 2.1, 5.9 and 7.3 mm, and absolute error of coordinate is respectively better than 1.6, 1.3 and 2.2 mm; for long baseline over 1000 m, NEU coordinate repeatability is respectively better than 8.4, 14.6 and 21.3 mm, and absolute error is respectively better than 1.5, 1.5 and 14.5 mm, and baseline repeatability is approximately 0.003 ppm. The conclusion

L. Feng (✉)
College of Geographic Space Information, Information Engineering University, ZhengZhou, People's Republic of China
e-mail: fenglaiping@163.com

L. Feng
National Key Laboratory of Geographic Information Engineering, Xi'an, People's Republic of China

L. Feng
Xi'an Research Institute of Surveying and Mapping, Xi'an, People's Republic of China

W. Zhou
College of Navigation and Aerospace Engineering, Information Engineering University, ZhengZhou, People's Republic of China

X. Wu
College of Geological Engineering and Surying, Chang'an University, Xi'an, People's Republic of China

J. Sun et al. (eds.), *China Satellite Navigation Conference (CSNC) 2013 Proceedings*, Lecture Notes in Electrical Engineering 245,
DOI: 10.1007/978-3-642-37407-4_18,

from the article provides technical criteria for widespread use of Beidou in the high precision application fields, and makes sense for promotion of application prospect and enhancement of usage confidence with Beidou.

Keywords Beidou navigation system · Relative positioning · Ambiguity · Baseline · Repeatability · ppm

18.1 Forewords

The relative positioning technology based on carrier phase observable is an important mode in GNSS application, therefore, the precision of relative positioning has become an major indicator used to evaluate performance of navigation satellite system. In 1984, Dr B.W. Remondi had proposed mathematical model and processing method of high precision relative positioning by the carrier phase observables form two GPS receivers synchronously, conducted initial verification by baseline with the length of 100 m, and achieved the precision of mm level by relative positioning [1]. In the GPS test campaign in 1993, measuring accuracy can be achieved 0.001 ppm order of magnitude for baseline of 3,000 km by GPS relative positioning technology [2]. The development of IGS has tremendously propelled the application of GPS, at present, the technologies of network RTK and virtual reference station based on the prototype of relative positioning have been gradually mature, and realized real-time, high precision, and dynamic positioning [3]. The relative positioning technology has become one of the most important work mode, and plays an important role in fundamental research of high-precision surveying and mapping, atmospheric science, geosciences and so on. After several decades of development, GPS has dominated high-precision GNSS application market both at home and abroad [4–6].

Whole Beidou constellation had been completed in October 2012, which symbolizes that the construction of China independent navigation satellite system has entered a new development phase. As a strategic national infrastructure, the promotion in application field of Beidou satellite navigation system in key fields of national economy of China plays an important strategic role [7]. There are differences between Beidou regional navigation satellite system and GPS in terms of constellation distribution, character of signal, satellite orbit precision and observation data quality [8], so it is essential to research feasibility and precision of high-precision relative positioning using Beidou regional navigation satellite system.

Based on actual measured data form Beidou test network, large scope of Beidou relative positioning test has carried out, systematic research under condition of short, medium and long baseline. The results show that coordinate precision realized by Beidou relative positioning has reached centimeter level, and baseline repeatability has reached millimeter level, which are equivalent to GPS level of high-precision relative positioning precision.

18.2 Relative Positioning Strategy of Beidou

In this section, we first give the selection of model and parameter estimation, and then perform data processing procedure in detail.

18.2.1 Ambiguity Fixing Strategy

Determination of integer cycle ambiguity is a critical technology of relative positioning, after determination of ambiguity, observed value of phase will be transformed as precise range observation. Therefore, ambiguity fixing plays an important role for enhancement of positioning precision and positioning efficiency [9]. Determination of ambiguity is divided into two steps: firstly calculate the float solution of ambiguity, and then restrict float ambiguity to fixed one by covariance information [10, 11]. Under the condition of poor pseudo-range precision of dual-frequency, QIF method can be used for long baseline ambiguity resolving, and good result have been achieved in Bernese software [12], and it applies to long baseline data processing. For detailed algorithm about QIF, please refer to the literature 12.

18.2.2 Parameter Estimation Strategy

The important details on selection of parameter and model adopted in paper such as ionosphere and troposphere involved in resolution are listed in Table 18.1.

Table 18.1 Strategy of model selection and parameter estimation in baseline processing

Parameter	Selection of parameter and model
Basic observables	Ionosphere-free combination
Satellite ephemeris	Post-processed Satellite orbit
Difference strategy	Maximum of observation time
Ionosphere model	TEC model of China region
Troposphere model	Niell model (moisture content per hour) [11]
Troposphere mapping function	Gradient is LINEAR
Ambiguity resolution method	QIF
Network solution strategy	Fixing constraint of one station
Tide model	Hans-Georg Scherneck
Earth rotation parameter	IGS ERP
Earth gravity field	JGM3
Reference framework	IGS 05

18.2.3 Data Processing Procedure

Detailed processing procedure of Beidou relative positioning is as follows: (1) pre-processing of original data: firstly, by performing pre-processing of zero-difference data, clean phase observation value is acquired through detection of gross error and cycle slip of phase observables, cycle slip detection of zero-difference observables adopts Blewitt method [13]; (2) time synchronization and formation of single-difference: using pseudo range observables for single epoch positioning, receiver clock error is obtained, then we acquire single-difference observables with zero-difference observables in observation network as certain rules and algorithm, takes observables maximization as rules this article; (3) data pre-processing in the triple-difference mode: adopt triple-difference observables combination to get certain precise station coordinate, perform further cycle slip detection through assumption inspection method of ionosphere-free combination residual error; (4) residual error editing: under condition of mandatory constraint of prior coordinate, we get positioning residual error by using phase ionosphere-free combination, proceed with residual error editing, and further eliminate the gross error of observation data, therefore pre-processing of observation data is completed; (5) getting the first network solution using observation data after residual error editing, meanwhile, the troposphere parameter is estimate; (6) ambiguity fixing: using ionosphere model as prior constraint, to get the estimated value of wide-lane ambiguity, use ionosphere-free combination to get and save the estimated value of narrow-lane ambiguity with QIF method; (7) final result estimation: introduce the fixed double-difference ambiguity into ionosphere-free combination observables, so as to enhance precision of estimated parameter and get the fixed solution of observation network. The processing procedure is shown in Fig. 18.1.

There are two schemes to detect the precision of Beidou relative positioning, one is to use the precise coordinate acquired through GPS as reference, the other is to use repeatability of multiple single-day solutions as evaluation index.

18.3 Processing Scheme of Beidou Relative Positioning

18.3.1 Design of Comparison Scheme

In order to verify relative positioning precision of Beidou reasonably, a detailed schemes are designed, and flow chart is showed in Fig. 18.2. Firstly, we estimate station coordinate with confederative GPS data from both Beidou/GPS dual-mode receiver and IGS core stations (see yellow parts in Fig. 18.2), fix one IGS core station for constrained adjustment, and unify reference framework to IGS05.

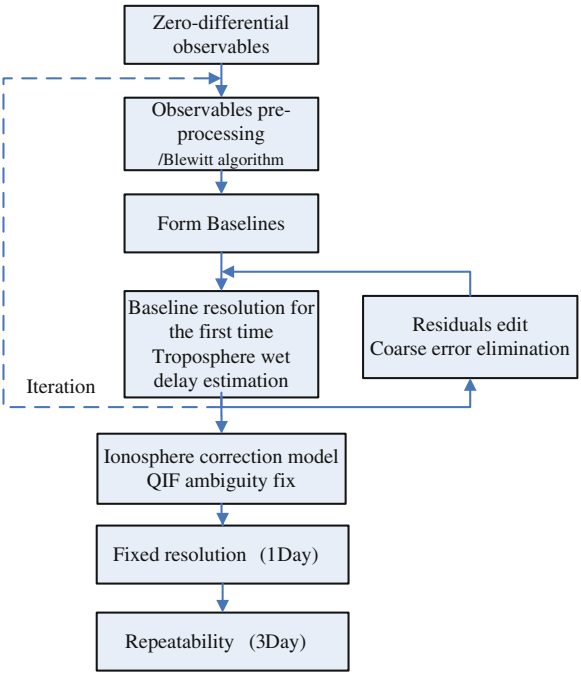

Fig. 18.1 Flow chart of data processing with Beidou

In this way, precision coordinates of dual-mode station may be gotten, and then they are used to reference for testing the precision of Beidou relative positioning which are estimated with only Beidou data (see grey parts in Fig. 18.2). So coordinates that come from different navigation system may be compared to evaluate performance of Beidou.

18.3.2 Observation Data

The actual measurement data between June 18 2012 and June 20 (day of year 170–172) are processed, all stations are equip with Beidou/GPS dual-mode receivers which can receive of Beidou and GPS data simultaneously. The data sampling interval is 30 s, B1I and B2I carrier phase data are selected. The on-orbit satellites of Beidou during the period of time are 4GEO + 5IGSO constellation (C01, C3, C04, C5, C06, C07, C08, C09 and C10). Distances between each stations are showed in Table 18.2.

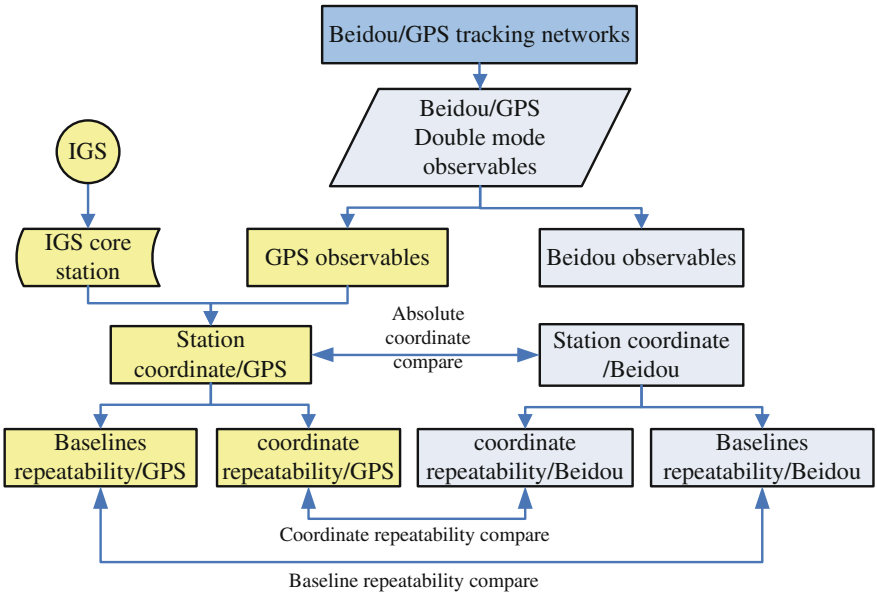

Fig. 18.2 Data processing scheme

Table 18.2 Distance between stations (unit : km)

	CENT	SHA1	XIAN	CHDU	HRBN	NTSC	WUHN	SHAO
BGLD	652	1225	0.786	605	1958	28	652	1196
	CENT	687	652	987	1986	643	0.43	657
		SHA1	1225	1663	1679	1205	687	30
			XIAN	604	1959	30	652	1197
				CHDU	2551	633	987	1634
					HRBN	1931	1986	1686
						NTSC	643	1177
							WUHN	657

18.4 Processing Results and Discussion

18.4.1 GPS Relative Positioning Test of Beidou/GPS Dual-Mode Receiver

The purpose of this test is to acquire GPS relative positioning criterion, so as to get precise coordinate of dual-mode receiver for comparison with Beidou positioning results later. The GPS data form three IGS core stations including BJFS, WUHN and from seven Beidou/GPS trace SHAO of IGS are selected, and form including CENT, SHA1, XIAN, CHDU, HRBN, NTSC and BGLD of are together process,

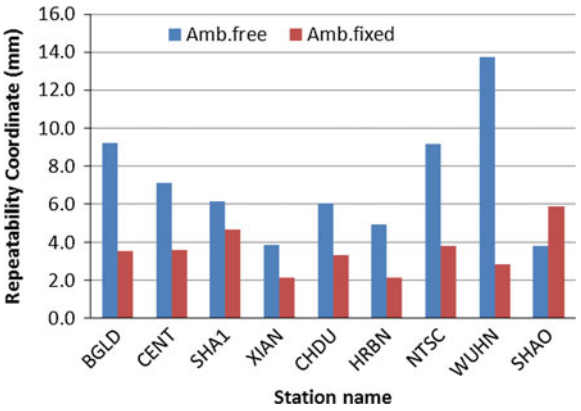

Fig. 18.3 Coordiante repeatability with GPS data

processing strategy in Sect. 18.3 is adopted, and BJFS is deemed as fixed station constraint, coordinate repeatability of the other stations are shown in Fig. 18.3. As shown in results, with the exception of slightly large statistics value of WUHN, coordinate floating solution repeatability of all stations are better than 1.0 cm, and fixed solutions are better than 6 mm.

Altogether 28 independent baselines have been formed from observation data of 3 days, and 2998 ambiguity parameters have been estimated, and 2318 parameters have been successfully fixed, the average success rate is 77.3 %, as the statistics characteristics of wide-lane and narrow-lane ambiguity, the residual error should comply with normal distribution [14]. Figure 18.4 shows that wide-lane ambiguity statistics in scope of 0.5 cycle, which complies with normal distribution well.

Analysing relative positioning residual error, Fig. 18.5 shows time series of baseline of BJFS-SHA1 in one day, and Fig. 18.6 shows statistics of all double difference observable. The result shows that GPS relative positioning residual error is approximately 0.0015 m.

Relative positioning mainly measures coordinate difference between two stations, therefore baseline repeatability is especially important, for the sake of

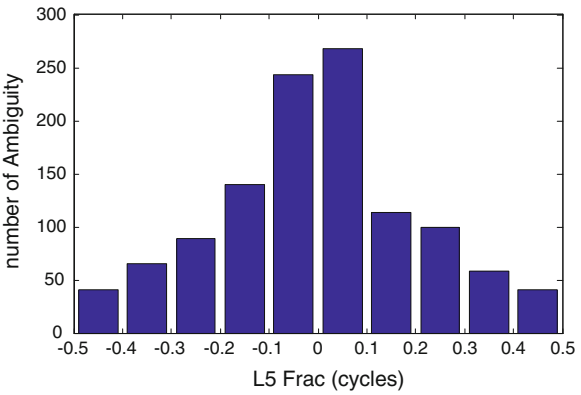

Fig. 18.4 Distribution of fractional part of GPS wide-lane ambiguity

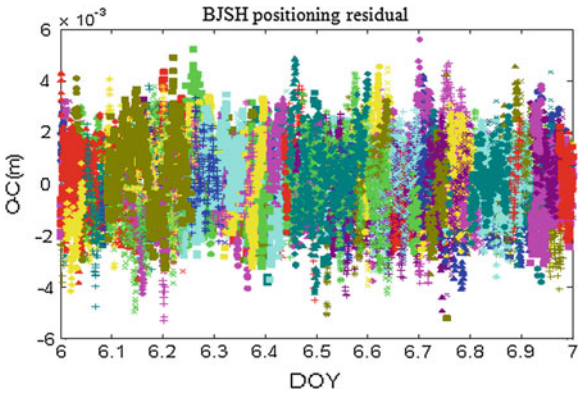

Fig. 18.5 Time series of relative positioning residual error with GPS

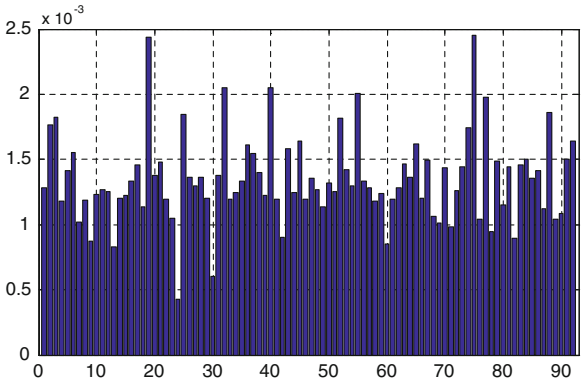

Fig. 18.6 Statistics of relative positioning residual error with GPS (unit : m)

correspondence with comparison with Beidou baseline repeatability later, 9 among 28 baselines are selected to analyze repeatability of three-days solution, as shows in Table 18.3, baseline repeatability is related to baseline length, for long baseline up to one thousand kilometres, the repeatability of GPS baseline is approximately 0.001 ppm.

18.4.2 Beidou Relative Positioning Test of Beidou/GPS Dual-Mode Receiver

Scheme II realized relative positioning by Beidou observational data acquired from dual-mode receiver, configuration of parameter is identical with scheme I, CENT station is the restriction of fixed station. Figure 18.7 shows coordinate repeatability of BGLD, SHA1, XIAN, CHDU and NTSC involved in positioning resolution, as shown in the results, coordinate repeatability of five stations are

Table 18.3 Repeatability of baselines by GPS

Baseline	Baseline length/m	D(LGT)	D(LGT) (ppm)
BGLD-SHA1	1225216.7	0.0006	0.001
BGLD-CHDU	605095.4	0.0010	0.002
BGLD-NTSC	28481.5	0.0010	0.035
SHA1-XIAN	1225641.0	0.0002	0.001
SHA1-CHDU	1663819.5	0.0004	0.001
SHA1-NTSC	1205323.7	0.0006	0.001
XIAN-CHDU	604313.9	0.0006	0.001
XIAN-NTSC	29250.1	0.0008	0.028
CHDU-NTSC	633341.0	0.0010	0.002

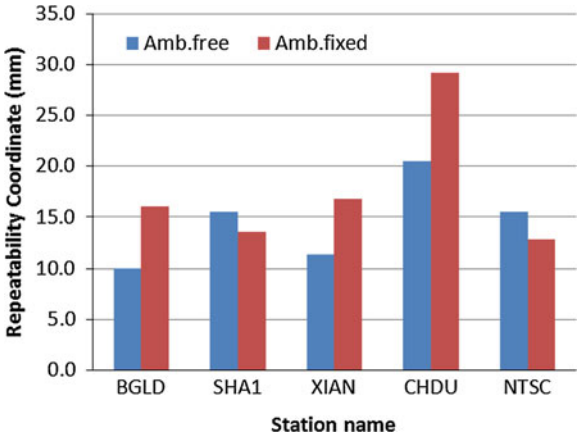

Fig. 18.7 Repeatability of 3D position with Beidou

better than 2 cm, and the accuracy of coordinate is not improved dramatically after ambiguity fixing.

Due to the fact that the number of Beidou satellite is fewer than GPS, furthermore, GEO satellite in Beidou constellation is always visible to observation station and IGSO satellite regression cycle is one day, the number of satellite rises and falls is fewer, so the number of ambiguities during three-day observation period is relatively small, altogether there are 658 ambiguity parameters resolved, 326 parameters are successfully fixed and success rate is 55.0 %. The residual error of wide lane ambiguity is shown in Fig. 18.8.

The observation residuals are analysed, the time serie of residual error of CENT-SHA1 baseline is shown in Fig. 18.9, and the statistics results is given in Fig.18.10 according to different baselines of Beidou, as seen from the above results, most residual error of baselines are smaller than 0.0015 mm, and the longer the baseline, the greater the residual.

Similarly, Repeatability of the nine baselines of Beidou is given, and the results are shown in Table 18.4. Compared with the results in Table 18.3 obtained from

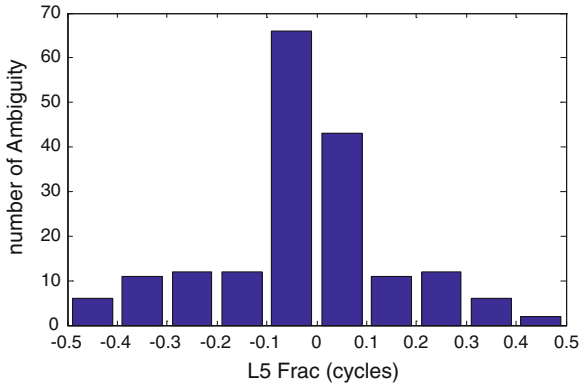

Fig. 18.8 Distribution of fractional part of Beidou wide-lane ambiguity

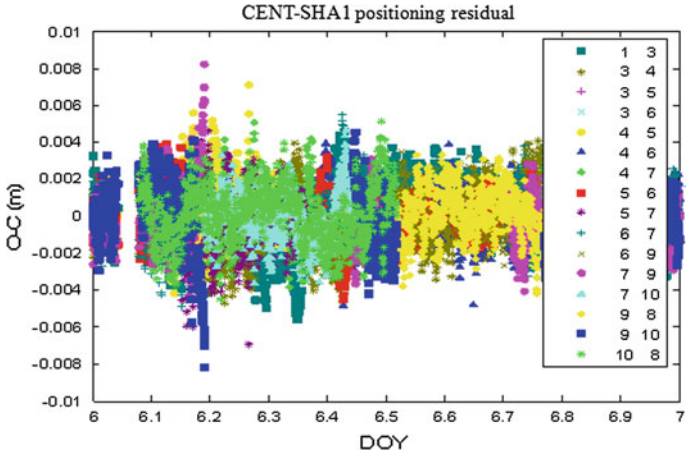

Fig. 18.9 Time series of Beidou relative positioning residual error

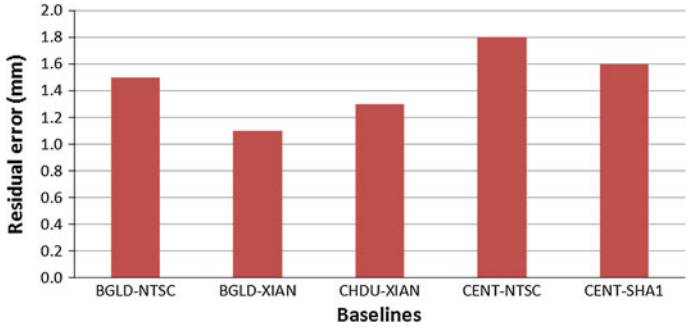

Fig. 18.10 Statistics of relative positioning residual error according to baselines with Beidou

Table 18.4 Repeatability of baselines by Beidou

Baseline	Baseline length/m	D(LGT)	D(LGT) (ppm)
BGLD-SHA1	1225216.7	0.0039	0.003
BGLD-CHDU	605095.4	0.0026	0.004
BGLD-NTSC	28481.5	0.0025	0.087
SHA1-XIAN	1225641.0	0.0049	0.004
SHA1-CHDU	1663819.5	0.0053	0.003
SHA1-NTSC	1205323.7	0.0045	0.004
XIAN-CHDU	604313.9	0.0056	0.009
XIAN-NTSC	29250.1	0.0007	0.025
CHDU-NTSC	633341.0	0.0047	0.007

the GPS, The results show that the repeatability of Beidou is an order of magnitude with GPS, but the accuracy is slightly lower.

18.4.3 Analysis of Relative Positioning Precision of Beidou Individual Baseline

In order to further verify precision of Beidou relative positioning, three individual baselines with different length, take BGLD as fixed station, and the other three stations are XIAN, NTSC and SHA1, the formed baseline length are respectively 0.78, 28 and 1225 km, which covering short, medium and long baseline, the coordinate repeatability of all baseline for 3 days are calculated (Fig. 18.11). By comparing the coordinate of 3 days with ones by using GPS, the results are shown in Table18.5. For short baseline, coordinate repeatability in the North, East and Up direction is respectively better than 0.5, 1.3 and 2.9 mm, and absolute error of

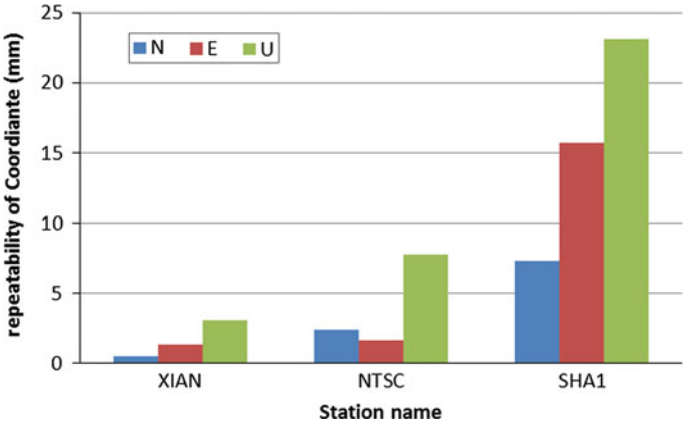

Fig. 18.11 Coordinate repeatability with different length

Table 18.5 Comparisons of coordinates between Beidou and GPS (mm)

Station	Direction	170 day	171 day	172 day
XIAN	N	0.3	0.0	−0.2
786 m	E	0.7	0.0	−0.6
	U	−1.2	0.5	1.7
NTSC	N	0.5	−1.6	0.5
28 km	E	−5.3	−1.3	0.4
	U	−5.5	2.2	−2.1
SHA1	N	−1.5	−10.9	−7.3
1225 km	E	1.5	−6.3	−4.0
	U	−14.5	8.5	−7.9

Table 18.6 Repeatability of single baseline (mm)

Baselines	Baseline length/km	D(LGT) (ppm)
BGLD-XIAN	0.786	1.627
BGLD-NTSC	28.0	0.062
BGLD-SHA1	1225.0	0.003

coordinate is respectively better than 0.2, 0.6 and 1.7 mm by comparison with GPS; for medium/long baseline, NEU direction coordinate repeatability is respectively better than 2.1, 5.9 and 7.3 mm, and absolute error of coordinate is respectively better than 1.6, 1.3 and 2.2 mm; for baseline over 1,000 m, NEU direction coordinate repeatability is respectively better than 8.4, 14.6 and 21.3 mm, and absolute error is respectively better than 1.5, 1.5 and 14.5 mm.

Baseline repeatability is related to baseline length, Table 18.6 shows repeatability results of short, medium and long baseline, short baseline BGLD-XIAN is approximately 1.627 ppm, medium baseline BGLD-NTSC is approximately 0.062 ppm and short baseline BGLD-SHA1 is approximately 0.003 ppm. It can be seen from comparison between the baseline repeatability Beidou and GPS in Table 18.3 that Beidou is at a magnitude same with GPS baseline repeatability, with slightly lower precision, the potential reason may be no precise calibration of correction of antenna phase center, furthermore, the conclusion of this article are drawn when Beidou is in the phase of incomplete 4GEO+5IGSO constellation.

18.5 Summary

Utilizing the 4GEO/5IGSO constellation during initial operation phase of Beidou regional navigation satellite system, The method is systematically researched on Beidou relative positioning, and then a large scope adjustment of Beidou control network is carried out firstly, and the precision of short, medium and long baseline based on Beidou are verified, as shown in the research results, coordinate accuracy

of Beidou regional satellite navigation system has reached centimeter level, baseline repeatability has reached millimeter level, and can be widely used in scientific research and engineering application.

The conclusions obtained in this study provide the technical basis for the use of Beidou in the field of high precision applications fields. Although the accuracy of current Beidou relative positioning is slightly lower than GPS, it has room for further improvement. We should continue to strive to improve the Beidou orbital accuracy, calibrate antenna phase center of the satellite and receiver. In addition, the results of this paper is confined to incomplete 4GEO/5IGSO constellation, when the constellation is completed, the relative positioning accuracy could be further enhanced necessarily.

References

1. Remondi BW (1985) Global positioning system carrier phase: description and use. J Geodesy 59(4):361–377
2. Beutler G (1993) Epoch'92 and the IGS PILOT service: an overview. In: Proceedings of the 1993 IGS workshop, Bern, pp 3–9
3. Heo Y, Li B, Lim S, Rizos C (2009) Development of a network real-time kinematic processing platform. In: Proceedings of 22nd international meeting of the satellite division of the Institute of Navigation, Savannah, GA
4. Cheng P, Yang Y, Li J, Sun H, Bi J (2007) The latest advances in geodesy and GPS technique in China. Bull Surv Mapp 2:01–04
5. Yang Y, Zha M, Song L et al (2005) Combined adjustment project of national astronomical geodetic networks and 2000' national GPS control network. Prog Natl Sci 15(4):435–441
6. Wei Z (2008) CHINA geodetic coordinate system 2000 and its comparison with WGS84. J Geodesy Geodyn 25(5):01–05
7. Yang Y, Li J, Xu J (2011) Contribution of the compass satellite navigation system to global PNT users. Chin Sci Bull 56(5):1734–1740
8. Dong C, Wang J, Zhang X (2012) Analysis on use project for frequency and orbit resources of satellite navigation system. Scientific Research Publishing, USA, pp 1–5
9. Wei Z, Ge M (1998) Mathematical model of GPS relative positioning. Surveying and mapping press, Beijing
10. Zhou Z, Yi J (1997) Principle and application of satellite positioning. Surveying and mapping press, Beijing
11. Liu J, Li Z, Wang Y, Sang J (1999) The principle and application of GPS. Surveying and mapping press, Beijing
12. Hugentobler U, Dach R (2007) Bernese GPS software version 5.0. Draft, University of Bern
13. Blewitt G (2000) Carrier phase ambiguity resolution for the global positioning system applied to geodetic baselines up to 2000 km. J Geophys Res 94(B8):10–187
14. Teunissen PJG (2000) Probabilistic properties of GNSS integer ambiguity estimation. Earth Planet Space 52:19–25

Chapter 19
GOCE Precise Orbit Determination Using Pure Dynamic Method and Reduced Dynamic Method

Tianhe Xu, Min Li and Kangkang Chen

Abstract The basic principles and mathematical models for pure dynamic orbit determination and reduced dynamic orbit determination are reviewed briefly. The GOCE orbit determination accuracies of pure dynamic method (PDM) and reduced dynamic method (RDM) are compared using different gravity field model with different degree and order (d/o). The computational results show that the orbit accuracies of the two methods using GOCO02S is obviously higher than those of EIGEN-5C and a little superior to those of ITG-GRACE2010S with the same d/o. The orbit determination accuracies of PDM and RDM using gravity field model with 150 and 180 d/o are greatly higher than those with 120 d/o. The SST observation, common-mode acceleration and attitude quaternion from 16/11/2009 to 18/11/2009 are used for GOCE orbit determination. The results show that the orbit accuracy of using PDM is about 11 cm, which can meet the accuracy requirement of GOCE rapid science orbit (RSO). The orbit accuracy of using RDM is about 2.2 cm, which is very close to the accuracy requirement of GOCE precise science orbit (PSO). There is still space of accuracy improvement since the GOCE satellite antenna phase center variation (PCV) is not estimated and considered in PDM and RDM.

Keywords GOCE · Precise orbit determination · Pure dynamic method · Reduced dynamic method

T. Xu (✉)
State Key Laboratory of Geo-information Engineering, Xi'an, China
e-mail: thxugfz@163.com

T. Xu
State Key Laboratory of Geodesy and Earth's Dynamics, Wuhan, China

M. Li · K. Chen
School of Geology Engineering and Surveying, Chang'an University, Xi'an, China

T. Xu
Xian Research Institute of Surveying and Mapping, Xi'an, China

J. Sun et al. (eds.), *China Satellite Navigation Conference (CSNC) 2013 Proceedings*, Lecture Notes in Electrical Engineering 245,
DOI: 10.1007/978-3-642-37407-4_19,

19.1 Introduction

The GOCE (Gravity Field and Steady-state Ocean Circulation Explorer) satellite was successfully launched on 17 March 2009. It is the first mission using gradiometry measurement to recover the Earth gravity field model (EGM) at least up to 240° and order (d/o) [1]. Due to the limitation of measuring bandwidth of GOCE satellite gradiometer, the ability to recover the low frequency information of EGM is poor. The GPS SST observations of GOCE satellite or GRACE data are used to determine the low-degree information of EGM. There are two types of GOCE orbits, kinematic orbits and reduced dynamic orbits released by ESA, whose accuracy is about 1–2 cm [2]. From the point of time latency, they can be classified into two types, rapid science orbit (RSO) and precise science orbit (PSO). RSO is usually used for the preprocessing of gradiometer data, quick-look of GOCE gravity field and the primary quality checking for GOCE data. It is provided by orbit determination workgroup of ESA just for interior use without released. The time latency of RSO is one day and the accuracy is about 10 cm far better than the specified accuracy of 0.5 m [3]. The kinematic orbit and reduced dynamic orbit belong to the PSO products. The time latency of reduce dynamic orbit provided by ESA is usually 7–10 days, and its accuracy is about 1–2 cm [2].

The pure dynamic and reduced dynamic orbit determination strategies are best-known strategies for LEO precise orbit determination (POD) based on GPS tracking data. The latter has been successfully applied in T/P, CHAMP, GRACE and GOCE satellite POD [4–8]. The model errors resulted in systematic errors limit the pure dynamic strategies. The key element of reduced dynamic strategies is to introduce empirical parameters, e.g., one-per-revolution parameters or stochastic pulses, in the parameter estimation. A lot of Chinese scholars have also performed the reduced dynamic orbit determination for CHAMP and GRACE [9–12], but few of them focus on the GOCE POD. GOCE satellite has high-precision onboard accelerometer for measuring the non-conservative accelerations. It provides the possibility of using pure dynamic orbit determination for GOCE RSO computation. In this paper, the computations and comparisons are conduced for GOCE pure dynamic method (PDM) and reduced dynamic method (RDM). Emphases of the influence of different EGM with different d/o on the orbit accuracy of PDM and RDM are analyzed. By comparing with the official released GOCE PSO, the ability and level of GOCE POD from our research team can be tested and evaluated.

19.2 GOCE POD Using PDM and RDM

The movement equation of GOCE satellite can be expressed as [7]:

$$\ddot{\vec{r}} = -\mu \frac{\vec{r}}{r^3} + \vec{F}_\alpha(\vec{r}, \dot{\vec{r}}, t, \alpha) \tag{19.1}$$

where $\vec{r}$ and $\dot{\vec{r}}$ are position and velocity vector respectively, $\mu = GM_e$ the gravitational constant, t the time, α the dynamic model parameter vector. There are two parts in the right side of Eq. (19.1), where the first one is the acceleration vector caused by two-body central gravitation and the second one $\vec{F}_\alpha$ is the disturbing acceleration vector. The disturbing forces acting on satellite can be classified into two types, conservative and non-conservative forces measured by GOCE common-mode accelerometer.

For GOCE POD using GPS tracking data, ionosphere free linear combination is usually used. After linearization, the error equations for the code and carrier phase observations of the ionosphere free combination can be expressed as

$$V_{PC} = AX + c \cdot dt_i - c \cdot dT^j + d^j_{i,trop} + \phi_{nm} + \varepsilon_{pc} \tag{2}$$

$$V_{LC} = AX + c \cdot dt_i - c \cdot dT^j + d^j_{i,trop} + \lambda B^j_i + \phi_{nm} + \varepsilon_{lc} \tag{3}$$

where V_{PC} and V_{LC} are residual vector of ionosphere free combination of code and carrier phase respectively. c is the light speed. dt_i and dT^j are receiver clock offset and satellite clock offset respectively. $d^j_{i,trop}$ is the tropospheric refraction; λB^j is the ambiguity parameter of ionosphere free combination. ε_{PC} and ε_{LC} are code and carrier phase noise respectively. X *is* the position correction vector. A *is* the design matrix for position parameters. ϕ_{nm} includes non-modeling corrections such as multipath errors, GPS orbit errors and atmospheric errors. GOCE POD can be performed using least square batch strategy, which can be seen in a lot of literature such as [5, 13].

Pure dynamic orbit determination makes use of known physical models of the spacecraft motion to constrain the resulting position estimates. It allows an averaging of measurement from different epochs and the satellite trajectory can even be propagated across data gaps. However, the dynamics of real-world LEO spacecraft are hardly known to a level that matches the accuracy of GPS pseudorange and carrier phase measurements. Fortunately, there is onboard accelerometer for measuring non-conservative forces on gravity satellites such as CHAMP, GRACE and GOCE, which can realize the POD using PDM for these satellites.

Due to the accuracy limitations of PDM, the concept of reduced dynamic orbit determination has been introduced since 1994. There are two different reduced dynamic POD approaches, empirical acceleration-based RDM and pseudo-stochastic pulse-based RDM. The first approach considers empirical accelerations in radial, along-track and cross-track direction to compensate for any modeling deficiencies in the employed spacecraft dynamics [5, 10]. The second approach defines the process noise as pseudo-stochastic pulse by introducing the velocity change as pseudo observation [6, 7]. Usually, the onboard accelerometer data are

not used in reduced dynamic orbit determination because of the strong correlation between pseudo-stochastic pulses and the accelerometer data. According to the experience of GOCE POD strategy by ESA, we adopt the first approach, namely empirical acceleration-based RDM to perform GOCE orbit determination.

19.3 Computations and Comparisons

The GOCE data including SST observation, common-mode acceleration and attitude quaternion from 16/11/2009 to 18/11/2009 provided by ESA are used in this paper. The reduced dynamic orbit (RDO) from ESA with accuracy of 1-2 cm are used as true orbits for comparison. In PDM, two biases are estimated in radial (R), along-track (T) and normal (N) directions per revolution and one scale factor in R and N directions per day. Piece-wise constant accelerations are estimated per 6 min according to the suggested strategy in GOCE orbit determination using RDM [2]. The GPS orbits and clock offsets are adopted from CODE final products.

19.3.1 Influence Analysis of Earth's Gravity Field Model

In order to analyze the influence of different EGM with different d/o in orbit determination of PDM and RDM, three representative EGMs EIGEN-5C [14], ITG-GRACE2010S [15] and GOCO02S [16] with 120, 150 and 180 d/o are adopted. The GOCE data of 16/11/2009 is used to perform the examination. For

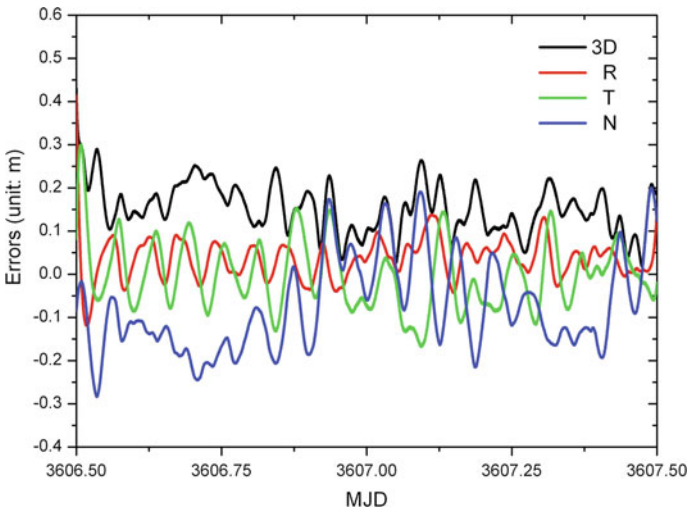

Fig. 19.1 Orbit errors of PDM using EIGEN-5C with 120 d/o

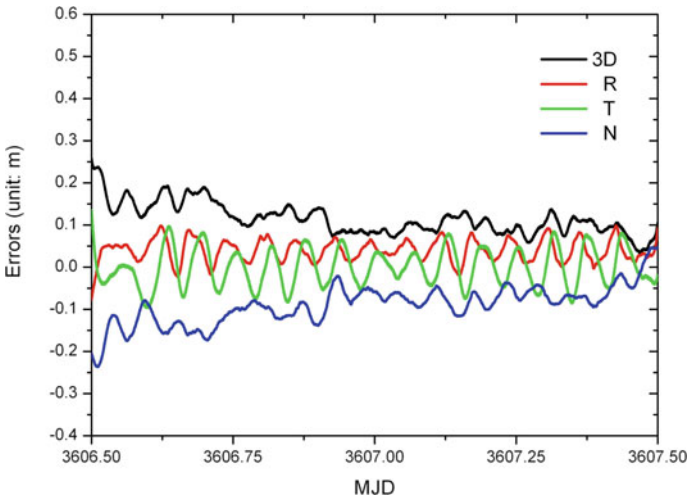

Fig. 19.2 Orbit errors of PDM using GOCO02S with 180 d/o

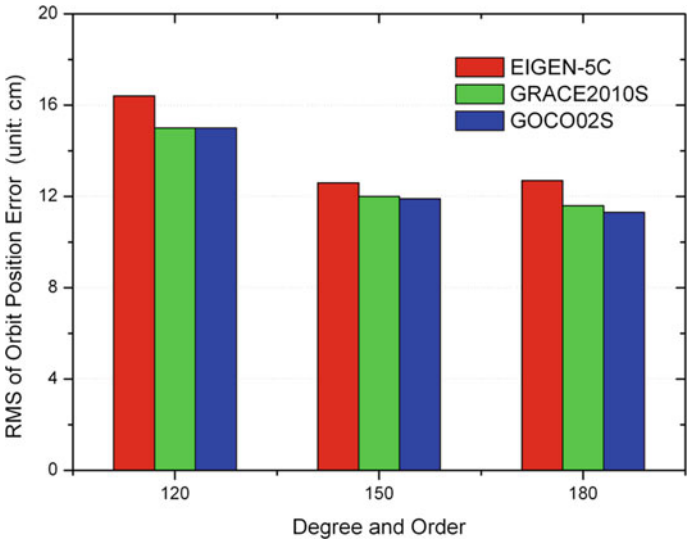

Fig. 19.3 RMS of orbit errors of PDM using different EGM with different d/o

the limitation of length, only the graphs of orbit errors using EIGEN-5C with 120 d/o and GOCO02S with 180 d/o are shown (seen from Figs. 19.1, 19.2, 19.3, 19.4, 19.5, and 19.6). All the statistical results of orbit errors can be seen in Tables 19.1, 19.2, Figs. 19.3, 19.6.

The following conclusions can be drawn from the computational results. The orbit accuracies of PDM and RDM using GOCO02S are obviously higher than

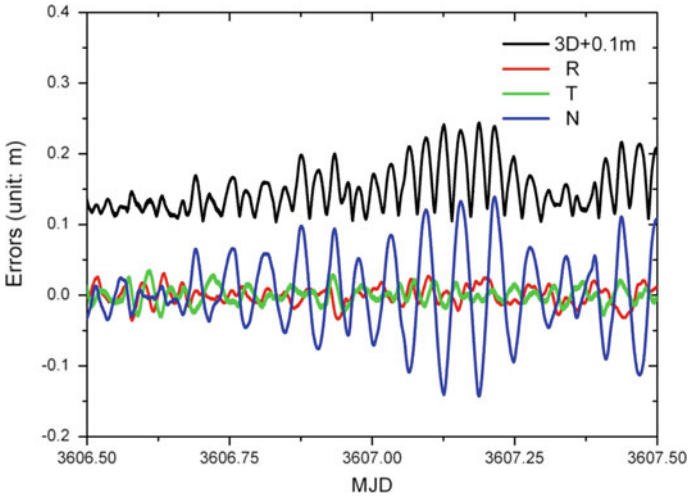

Fig. 19.4 Orbit errors of RDM using EIGEN-5C with 120 d/o

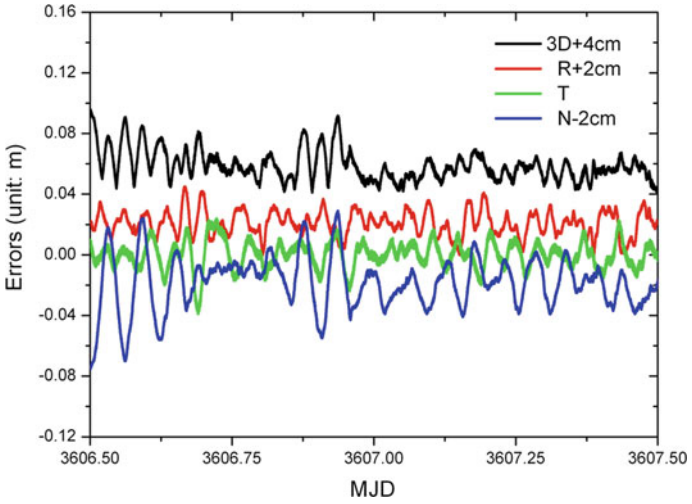

Fig. 19.5 Orbit errors of RDM using GOCO02S with 180 d/o

those of EIGEN-5C and a little superior to those of ITG-GRACE2010S with the same d/o. The orbit accuracy of PDM and RDM using EGM with 150 and 180 d/o is greatly higher than those with 120 d/o. It can be improved from 16.4 to 11.3 cm using PDM and from 6.5 to 2.2 cm using RDM when changing the EGM from EIGEN-5C with 120 d/o to GOCO02S with 180 d/o. It is suggested that the newest released gravity field model including GOCE data such as GOCO02S up to at least 150 d/o should be chosen in GOCE PDM and RDM.

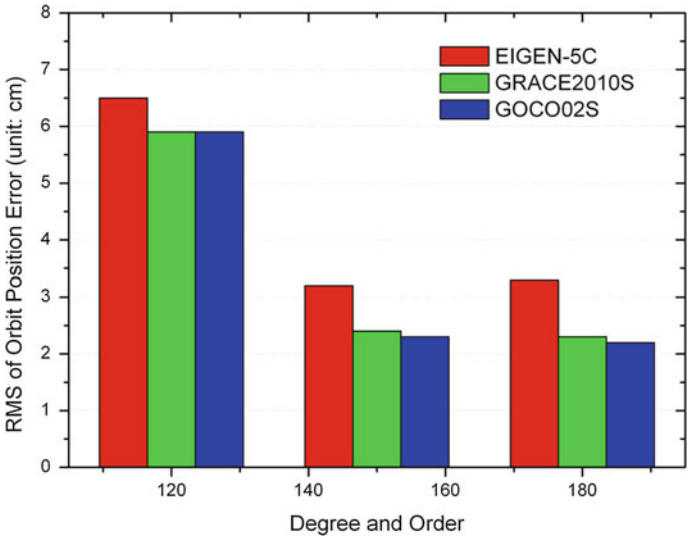

Fig. 19.6 RMS of orbit errors of RDM using different EGM with different d/o

19.3.2 Comparisons Between PDM and RDM

The 3-day' GOCE data from 16/11/2009 to 18/11/2009 is used to test and compare the orbit accuracies of using PDM and RDM. According to the above conclusions, GOCO02S with 180 d/o are chosen in GOCE orbit determination of PDM and RDM. Orbit errors are shown in Figs. 19.7, 19.8, and the statistical results are listed in Tables 19.3, 19.4.

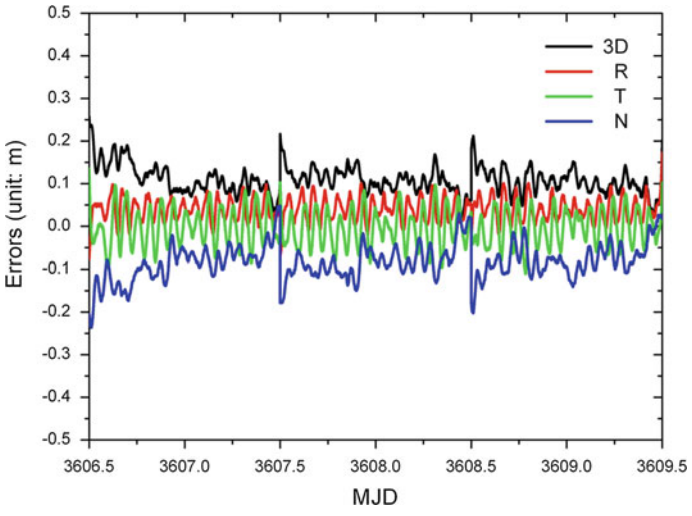

Fig. 19.7 The orbit errors of PDM

Table 19.1 Statistical results of PDM using different EGM with different d/o (unit: cm)

EGM		EIGEN-5C	GRACE2010S	GOCO02S
120 d/o	R	5.8	5.3	5.2
	T	7.9	7.0	6.8
	N	13.1	12.2	12.3
	3D	16.4	15.0	15.0
150 d/o	R	5.1	4.8	4.8
	T	5.6	4.7	4.7
	N	10.1	10.0	9.8
	3D	12.6	12.0	11.9
180 d/o	R	5.0	4.7	4.7
	T	5.4	4.4	4.5
	N	10.3	9.6	9.3
	3D	12.7	11.6	11.3

Table 19.2 Statistical results of RDM using different EGM with different d/o (unit: cm)

EGM		EIGEN-5C	GRACE2010S	GOCO02S
120 d/o	R	1.4	1.4	1.3
	T	1.2	1.2	1.1
	N	6.2	5.6	5.6
	3D	6.5	5.9	5.9
150 d/o	R	0.9	1.0	0.9
	T	1.3	1.2	1.2
	N	2.9	1.8	1.8
	3D	3.3	2.4	2.3
180 d/o	R	0.9	1.0	0.8
	T	1.1	1.1	1.1
	N	3.0	1.8	1.7
	3D	3.3	2.3	2.2

The above results show that the orbit accuracies of R, T and N directions are 4.7, 4.5 and 9.1 cm respectively and position accuracy is about 11.2 cm when using PDM. The N direction has poor accuracy because of uncompleted or inaccurate force models. It can meet the accuracy requirement of GOCE RSO. There is obvious orbit jump between the day's borders, which is a usual phenomena since 24 h data length are used for orbit determination. The orbit accuracies are great improved when using RDM with orbit accuracies of 0.9, 1.0 and 1.7 cm respectively in R, T and N directions and position accuracy of 2.2 cm. It is very close to the accuracy requirement of GOCE PSO. There is still space of further improvement since the GOCE satellite antenna phase center variation (PCV) is not estimated and considered in orbit determination.

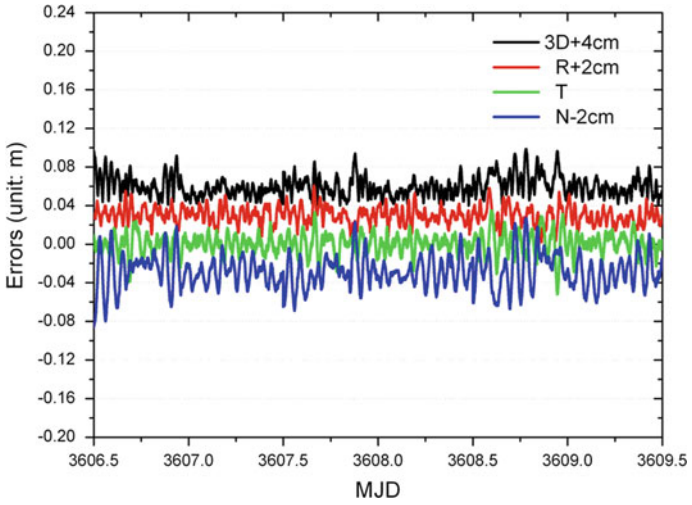

Fig. 19.8 The orbit errors of RDM

Table 19.3 The statistical results of PDM (unit: cm)

Statistics	Max	Min	RMS
R	17.3	−7.7	4.7
Tv	13.5	−11.1	4.5
N	4.8	−23.7	9.1
3D	25.7	1.4	11.2

Table 19.4 The statistical results of RDM (unit: cm)

Statistics	Max	Min	RMS
R	3.1	−2.8	0.9
T	3.5	−5.2	1.0
N	5.7	−5.5	1.7
3D	5.9	0.2	2.2

19.4 Conclusion

There is high-precision accelerometer on GOCE satellite for measuring the non-conservative accelerations, which provides the possibility of using PDM for GOCE RSO computation. The GOCE PSO products with the highest accuracy up to now is still relied on RDM. In this paper, the comparisons between PDM and RDM using different EGM with different d/o are conducted. The results show that he newest released gravity field model including GOCE data such as GOCO02S up to at least 150 d/o should be chosen in GOCE pure dynamic or reduced dynamic orbit determination. Orbit accuracies of 11 cm and 2.2 cm can be obtained when

using PDM and RDM respectively. One way to further improve the orbit accuracy is to estimate the GOCE satellite PCV using long-term observations which can be feedback to GOCE POD.

Acknowledgments This work was supported by Natural Science Foundation of China (41174008), the Open Foundation of State Key Laboratory of Geodesy and Earth's Dynamics (SKLGED2013-4-2-EZ) and the Foundation for the Author of National Excellent Doctoral Dissertation of China (2007B51). The authors are grateful to the ESA for providing the GOCE SST observations, reduced dynamic orbits, accelerometer and attitude data.

References

1. European GOCE Gravity Consortium (EGG-C) (2010) GOCE standards. GO-TN-HPF-GS-0111, Issue 3.0
2. Bock H, Jaggi A, Meyer U (2011) GOCE precise science orbit. Presented at the 2011 general assembly of the European Geosciences Union, Vienna, Austria, April 3–8
3. IJssel J, Visser P, Helleputte T (2010) GOCE rapid science orbit determination: achieving sub-dim orbit precision with minimal latency. COSPAR 38th scientific assembly 18–25 July, Bremen
4. Yunck TP, Bertiger WI, Wu SC et al (1994) First assessment of GPS-based reduced dynamic orbit determination on TOPEX/POSEIDON. Geophys Res Lett 21:541–544
5. Qile Z (2004) Research on theory and software of GPS navigation constellation and low earth orbiter. Wuhan University, Wuhan (Ch.)
6. Beutler G (2005) Methods of celestial mechanics. Springer, Berlin, Heidelberg, New York
7. Svehla D, Rothacher M (2002) Kinematic and reduced-dynamic precise orbit determination of low earth orbiters. Paper presented at EGU 2002, Nice, France
8. Montenbruck O, Gill E (2000) Satellite orbits: models, methods and applications. Springer, Heidelberg
9. Han BM (2007) Studies on reduced dynamic orbit determination based on zero-difference GPS observation of LEO. J Nanjin Aviat Space Univ 39(2):50–54 (Ch.)
10. Bock H (2003) Efficient methods for determining precise orbits of low earth orbiters using the global positioning system. Ph.D. dissertation, Astronomical Institute of University of Berne, Berne
11. Forste C et al (2008) EIGEN-GL05C—a new global combined high-resolution GRACE-based gravity field model of the GFZ-GRGS cooperation. Presented at the 2008 general assembly of the European Geosciences Union, vol 10. EGU2008-A-03426
12. Mayer-Gurr T, Kurtenbach E, Eicker A (2010) ITG-GRACE2010S gravity field model. www.igg.unibonn.de/aprmg/index.php?id=itg-grace2010s
13. Goiginger H et al (2011) The satellite-only global gravity field model GOCO02S. Presented at the 2011 general assembly of the European Geosciences Union, Vienna, Austria, April 3–8
14. Beulter G, Jaggi A, Mervart L et al (2010) The celestial mechanics approach—theoretical foundations. J Geodesy 84(10):605–624
15. Peng D, Wu B (2007) Explosions of non-differential and single-difference LEO using GPS precise orbit determination. Sci Bull 52(6):715–719 (Ch.)
16. Xianping Qin (2009) Research on precision orbit determination theory and method of low earth orbiter based on GPS technique. Information Engineering University, Zhengzhou, Henan (Ch.)

Chapter 20
Precise Orbit Determination of BeiDou Satellites Using Satellite Laser Ranging

Gang Zhao, Shanshi Zhou, Xuhua Zhou and Bin Wu

Abstract As a highly accurate technique of satellite orbit tracking, a precise determination method of satellite orbit, and an independent way of external validation on the orbits obtained by other satellite precise orbit determination (POD) means, satellite laser ranging (SLR) has been applied in many international and Chinese satellite projects. In China's BeiDou (Compass) Navigation Satellite System, as the cooperative targets of international SLR monitoring, multiple satellites have been equipped with on-board laser retro-reflector array, and high-quality observation data have been obtained from around 20 tracking stations distributed all over the world. In this work, we summarized the SLR tracking status on BeiDou satellites and determined the proper SLR dynamic POD strategy. Using SLR tracking data, we determined orbits of four BeiDou satellites, assessed SLR orbits' accuracies by orbit overlap and orbit comparison with precise ephemeris produced from radio navigation bands, and analyzed characters and possible causes of orbit errors. The results demonstrated that SLR-derived orbits on BeiDou satellites are on the level of meter, and the precisions along radial direction can achieved decimeter level. For current BeiDou satellites in different types of orbits, and in the future construction and improvement of BeiDou Navigation Satellite System, SLR has already and will continue to play an important role in the process of POD and orbit validation.

Keywords Satellite navigation · Satellite laser ranging · Precise orbit determination

G. Zhao (✉) · S. Zhou · X. Zhou · B. Wu
Shanghai Astronomical Observatory, Chinese Academy of Sciences, Shanghai, China
e-mail: zhaogang@shao.ac.cn

G. Zhao
University of Chinese Academy of Sciences, Beijing, China

J. Sun et al. (eds.), *China Satellite Navigation Conference (CSNC) 2013 Proceedings*, Lecture Notes in Electrical Engineering 245,
DOI: 10.1007/978-3-642-37407-4_20,

20.1 Introduction

BeiDou (Compass) Satellite Navigation System is an independent-development, independent-operation global satellite navigation system being implemented in China. With the successful launching of the 16th BeiDou satellite on Oct 25, 2012, the construction of China's regional satellite navigation system has been completed, and will provide passive location, navigation and time service freely in recent future. The space segment adopted in such regional system is a hybrid constellation. In the current 16 satellites, 6 are Geostationary Earth Orbit (GEO) satellites, 5 are Inclined Geo-Synchronous Orbit (IGSO) satellites and 5 are Medium Earth Orbit (MEO) satellites. Several precise orbit determination (POD) strategies have been carried out and validated in practice. For example, GEO single-satellite POD method combined with satellite laser ranging (SLR) and C-band transfer ranging is able to obtain fitting root mean squares (RMS) 0.205 m and 3-D position precision is better than 5 m [1–3]. Using IGSO/MEO multi-satellite POD method based on L-band multi-frequency pseudorange and carrier-phase data, the fitting RMS is around 1 m, and the carrier phase post-fit RMS is about 1 cm [4]. Furthermore, with the combination of GPS parameter solution, more precise orbit of BeiDou satellites can be obtained, and their radial precision can be better than 10 cm [5].

In the process of multi-satellite hybrid-constellation POD using L-band data, errors introduced in orbit estimation are inevitable, no matter clock offset be taken as estimated parameter or be fit with polynomials. And for MEO satellites, orbit coverage is restricted by regional tracking network. These problems lead to some difficulties in POD based on L-band data.

Alternatively, SLR observation is insensitive to satellite's or receiver's clock offset. For MEO satellites, tracking data by global SLR network can be achieved. SLR measures the round-trip propagation time of laser pulse between ground station and satellite, and its accuracy is basically independent from the station-satellite distance. Currently, the absolute cm-level even sub-cm-level station-satellite distance can be derived from single-shot SLR measurement. As an independent POD method, or as an auxiliary with other POD methods, SLR can improve the precision and reliability of satellite POD. The SLR-derived station-satellite distance can also validate orbits derived from other methods externally. SLR has been exploited as POD and validation method in many satellite projects. In this work, based on the current SLR tracking data from global SLR network, we studied SLR dynamic POD method specified to BeiDou satellites, determined their precise orbits and assessed the orbit precision in different ways.

20.2 SLR Tracking Performance

As the cooperative targets of international SLR monitoring, multiple satellites in BeiDou navigation system have been equipped with on-board laser retro-reflector array. At present, tracking data of 4 BeiDou satellites, including 1 GEO, 2 IGSO and 1 MEO satellites, have been obtained from the global SLR network. The basic information of these 4 satellites is summarized in Table 20.1. (Another 1 IGSO BeiDou satellite has been tracked only on Oct 14 and 15, 2012 and obtained few observations, so it has been excluded from the discussion in this paper.)

The sub-satellite point of BeiDou-G1 is almost fixed, and the ground tracks of BeiDou-I3 and -I5 are narrow 8-shaped curves and north–south symmetrical relatively to Earth equator approximately. Generally, each of these 3 satellites can only be tracked by the SLR stations located in the Earth's hemisphere which is east–west symmetrical to its corresponding orbital central longitude. Relatively to that of BeiDou-I5, the orbits of BeiDou-G1 and -I3 are more eastward, and such spatial configurations are inconvenient for the tracking by European SLR stations which play important roles in global SLR network, so the volume of the measurement data of BeiDou-G1 and -I3 are smaller than that of BeiDou-I5. BeiDou-M3 belongs to 12-hour satellite, and can be tracked globally. From the time of SLR tracking beginning to the end of Oct, 2012, BeiDou-G1 has been tracked by 6 stations, which distributed as circles in Fig. 20.1. For BeiDou-I3 and -I5, 7 and 12 stations have carried out observations respectively. BeiDou-M3 has been tracked by 20 stations, which geographical distribution is shown as stars in Fig. 20.1.

As the echo amplitude of SLR is inversely proportional to the 4th power of distance, and additionally, the meteorological condition will effect the SLR observation greatly, the tracking on these 4 satellites is fairly difficult. As a consequence, the quantities of SLR tracking data are limited and distributed unevenly. In Fig. 20.2, temporal distributions of SLR normal points per day during 4 months from Jul to Oct, 2012 are shown. The vertical lines in figure divide the time span by month. It is obvious that observation on BeiDou-G1 and -I3 are relatively sparse, with the daily mean of normal points are only 9 and 7 respectively. The situations of BeiDou-I5 and -M3 stand a little better, and their daily means are slightly more than 14.

Table 20.1 Overview of BeiDou navigation satellites tracked by SLR

Satellite Name	-G1	-I3	-I5	-M3
Orbit type	GEO	IGSO	IGSO	MEO
Altitude	35793 km	35790 km	35790 km	21528 km
Inclination	1.53°	55.6°	55.6°	55.0°
Longitude of central sub-satellite point	140°E	120°E	95°E	——
Launch date	2010-01-17	2011-04-10	2011-12-01	2012-04-29
First SLR tracking date	2012-04-28	2012-04-27	2012-07-06	2012-07-11

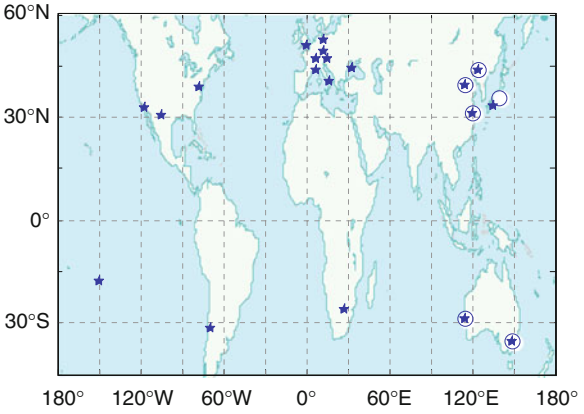

Fig. 20.1 Geographical distributions of SLR stations which tracked BeiDou-G1 (*circles*) and BeiDou-M3 (*stars*)

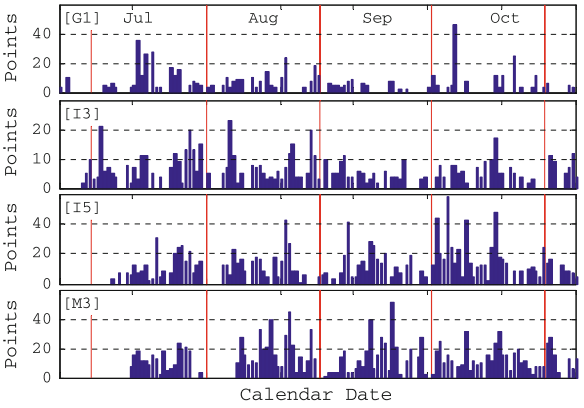

Fig. 20.2 Temporal distributions of BeiDou satellites' SLR normal points (from Jul to Oct, 2012)

20.3 SLR POD Strategy

In general, attitude control for BeiDou GEO satellites belongs to "orbit normal" mode in which Z axis is towards nadir, Y axis is perpendicular to the instantaneous orbital plane, and X axis is orthogonal with Y and Z axis. While for BeiDou IGSO or MEO satellites, "yaw-steering" mode are adopted, in which Z axis is towards nadir, Y axis is perpendicular to the sun-earth-satellite plane, and X axis is orthogonal with Y and Z axis [6].

For the motion of these 4 medium and high satellites, the drag of Earth atmosphere can be safely neglected, the rather low order/degree geopotential can be used, and the solar radiation pressure must be adopted properly. For absorbing perturbations which cannot be modeled precisely, empirical acceleration should be taken into account. Considering the quantity of SLR tracking data, too much estimated parameters should not be introduced.

In this work, the whole SLR single-satellite dynamic POD strategy is [7]:

1. measurement models: satellite center-of-mass correction, tropospheric delay, general relativistic propagation delay, station eccentricity correction, solid tide correction, ocean tide loading correction, tectonic displacement;
2. force models: Earth central gravitation, Earth nonspherical perturbation (GGM02C model, 15 order/degree for BeiDou-M3 and 10 order/degree for the other 3), N-body perturbation (JPL DE405 ephemeris, including effects of sun, moon and planets), solar radiation pressure (Box-Wing model), additional Y-bias, solid tide and ocean tide perturbation, general relativity perturbation, RTN empirical acceleration;
3. reference systems: J2000.0 inertial system, ITRF2000 coordinate system;
4. estimated parameters: satellite's initial state vector (3-D position and velocity), solar radiation pressure coefficient, Y-bias coefficient, harmonic T/N empirical acceleration coefficients. All parameters are estimated globally.

20.4 Evaluation of Orbit Precision

After enough trials, we conclude that 7-day arc length is suitable for the 4 satellites' SLR orbit determination and can get the best precision. Only the 7-day orbit arc which hasn't crossed the time of maneuver is considered. The time interval of two adjacent sequenced normal points should be no more than 2 days so as to determine the orbit rationally. Too short arcs lead to difficulty in parameter estimation, while too long arcs lead to orbit deviation because of inaccuracy of force models, which would degenerate the precision of orbit determination. The 7-day orbit arc starts from UTC (Universal Time Coordinated) 00:00 in each day. It is demonstrated that for BeiDou-G1, -I3 and -I5, orbit residual RMS of SLR POD are generally better than 1 cm. For BeiDou-M3, residual RMS is around 2 cm. The utilization ratios of SLR tracking data in POD processes are above 80 %. Table 20.2 shows the statistics of SLR internal fitting during Jul to Oct, 2012. Besides internal accuracy, we assess SLR results comprehensively from multi-aspects, including orbit overlap analysis, comparison between independent orbits, and SLR station-satellite distance validation.

Table 20.2 SLR internal accuracies of BeiDou satellites (from Jul to Oct, 2012)

Satellite name	-G1	-I3	-I5	-M3
Number of orbit arc	53	80	65	77
Mean fitting RMS	0.55 cm	0.40 cm	0.80 cm	1.83 cm
Utilization ratio of observation	87.0 %	90.9 %	82.0 %	85.3 %

20.4.1 Orbit Overlap Analysis

Every pair of 7-day orbit arcs with 5-day difference in their initial epochs holds a 2-day overlap period. Although SLR observation data in this 2-day period are just the same, the pair of 7-day orbit arcs is estimated independently from each other. Thus we can take the two estimated orbits within the overlap period as uncorrelated. The orbit agreement in this 2-day period is one of the indications of the POD quality.

Two samples of differences in 2-day overlap period are shown in Fig. 20.3. In each panel of Fig. 20.3, the horizontal axis represents the time and the vertical axis represents the difference along R/T/N direction in meter unit. For the overlap of BeiDou-I5 in Sep 6 and 7, 2012 (in top panel), the radial RMS is 0.43 m, the RMS in T and N directions are 1.46 and 1.42 m respectively, and the 3-D RMS is 2.08 m. For the overlap of BeiDou-M3 in Sep 12 and 13, 2012 (in bottom panel), the radial RMS is 0.11 m, the RMS in T and N directions are 0.22 and 0.66 m respectively, and the 3-D RMS is 0.71 m. These results are in the same order of magnitude as calculated before based on the overlap of BeiDou-M1 [8]. For BeiDou-G1 and -I3, similar results can be derived, the 3-D position precisions are on the level of few meters, and the precisions in radial direction are on the level of decimeters.

20.4.2 Comparison with L-Band Precise Orbits

At present, BeiDou Navigation System broadcasts positioning and navigation signals in three frequency channels of L band. Using L-band multi-frequency pseudorange and carrier-phase data obtained from 7 ground stations in China, based on multi-satellite POD strategy, orbits of BeiDou satellites can be derived.

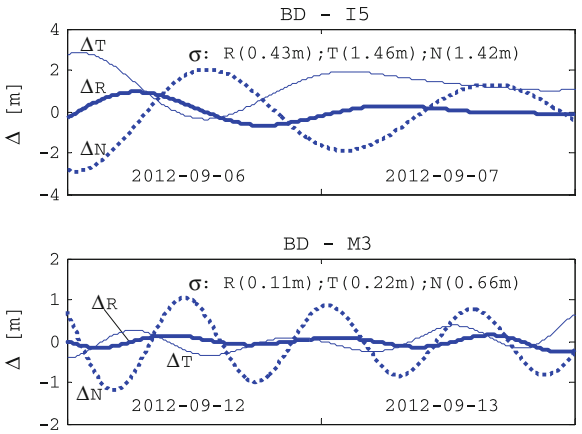

Fig. 20.3 Overlap errors of SLR orbits for BeiDou-I5 (*top*, from Sep 6 to 7, 2012) and -M3 (*bottom*, from Sep 12 to 13, 2012)

L-band derived orbits and SLR derived orbits are independent from each other, so the position differences between them are important reflection of orbit precisions.

Nodes of BeiDou time system used in L-band orbits and UTC time system used in SLR orbits are unified by 9th-order Chebyshev polynomial interpolation. Taking L-band orbit as reference orbit, the difference between them can be calculated. Such differences are shown in Figs. 20.4 and 20.5. It can be seen that the agreement degree of BeiDou-G1 (from Jul 13 to 19, 2012, in top panel of Fig. 20.4) is the lowest, in which radial RMS is 0.63 m, T/N RMS are 1.16 and 2.40 m respectively, and the 3-D position RMS is 2.74 m. The agreement degrees of BeiDou-I3 (from Oct 4 to 10, 2012, in top panel of Fig. 20.5) and BeiDou-I5 (from Oct 18 to 24, 2012, in bottom panel of Fig. 20.5) are moderate, in which 3-D position RMS are 1.91 and 1.65 m, radial RMS are 0.43 and 0.61 m respectively, and T/N RMS are both around 1 m. For BeiDou-M3 (from Sep 27 to Oct 3, 012, in bottom panel of Fig. 20.4), the agreement degrees between two orbits are the highest, in which radial RMS is 0.16 m, T/N RMS are 0.57 and 0.74 m respectively, and 3-D position RMS is 0.94 m. These results consist with those of orbit overlap analysis in the previous section. In general, radial differences RMS are smallest, which can be on the level of decimeter for BeiDou-M3, and on the level of several decimeters for the other 3. The differences along N direction are greater than those along T direction in some cases, which might be attributed to the rather poor geometric configuration of spatial distribution of SLR data. No significant biases exit between these two kinds of orbits. The errors relevant to the satellites' orbital periods are demonstrated in the orbit differences.

Since the SLR orbit is derived every 7 days with global estimation, it can be taken as continuous trajectory. While the 7-day L-band orbit adopted here is the consequence of certain connection which means the head of one 3-day orbit is connected with the tail of another 3-day orbit according to the time sequence. The time nodes when sudden jumps appear in Figs. 20.4 and 20.5 just locate in the connection time nodes of 3-day L-band orbits, so the amplitudes of such jump reflect essentially the precisions of L-band orbits in connection time nodes.

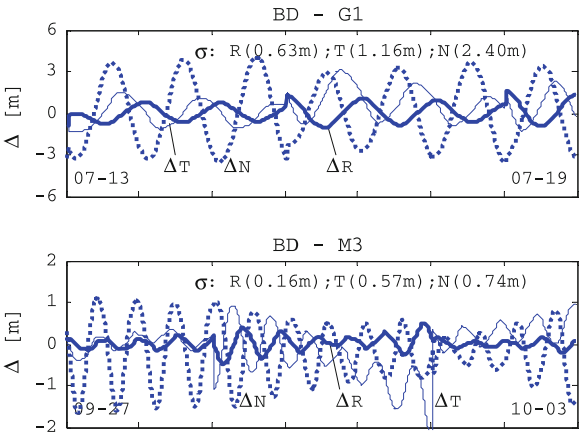

Fig. 20.4 Differences between SLR orbits and L-band orbits for BeiDou-G1 (*top*, from Jul 13 to 19, 2012) and -M3 (*bottom*, from Sep 27 to Oct 13, 2012)

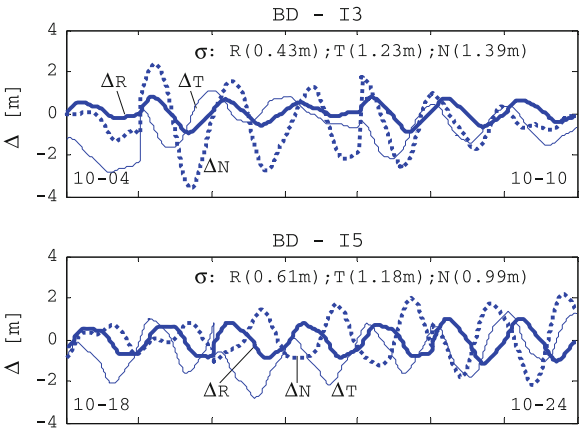

Fig. 20.5 Differences between SLR orbits and L-band orbits for BeiDou-I3 (*top*, from Oct 4 to 10, 2012) and -I5 (*bottom*, from Oct 18 to 24, 2012)

The consistency at orbit connection point is also a commonly used index assessed orbit precision. In this aspect, the precision of L-band orbits are also on the level of meter.

20.4.3 SLR Validation

SLR measures the time difference between the emission and reception of laser pulse in the ground station, and then the geometric distance from station to satellite can be derived. As the frequency of laser is very high, the accuracy of media delay along the propagation path can be up to cm level. SLR can be treated as a useful verification tool on the orbit precision along the line of laser "sight". Even during the period within which too few SLR tracking data obtained so that SLR POD cannot be carried out successfully, SLR distance verification can also be taken to evaluate the quality of L-band orbit.

In the process of SLR validation, "theoretical" station-satellite distance is derived after the effects of solid tide, ocean tide loading, tectonic motion, station eccentricity, tropospheric delay, general relativity correction and center-of-mass correction have been taken off from SLR measurement. The corresponding L-band distance can be derived by 9th Chebyshev interpolation and coordinate system transformation from L-band orbit. The difference of "theoretical" distance and L-band derived distance at the same time point is the SLR validation residual. The performances of L-band orbits verified by SLR distance during the period from Oct 18 to 24, 2012 are demonstrated in Table 20.3. It shows that the residual RMS of BeiDou-G1, -I3 and -I5 are on the level of several decimeters, and the RMS of -M3 is around 0.2 m, which is close to the orbit difference RMS along radial directions.

Table 20.3 SLR distance validation on L-band orbits of BeiDou satellites (from Oct 18 to 24, 2012)

Satellite name	-G1	-I3	-I5	-M3
Quality of SLR normal points	52	39	102	126
Distance residual RMS	0.69 cm	0.42 cm	0.52 cm	0.18 cm

20.5 Summary

In this work, we summarized the status of monitoring carried out to BeiDou navigation satellites by global SLR network. The analyses in this work show that SLR orbit determination precisions of BeiDou-G1, -I3, -I5 and -M3 are on the level of meter or few meters, the radial precisions are on or near decimeter level. SLR can be taken as effective POD method and orbit precision evaluation tool on BeiDou satellites. In the progress of China's Navigation Satellite System, as an independent or auxiliary method of POD, SLR will play an important role continuously in orbit precision and reliability improvement.

Acknowledgments The authors thank ILRS for providing BeiDou SLR tracking data. This paper is supported by the Natural Sciences Foundation of China (Grant No. 11103064), the Shanghai Committee of Science and Technology, China (Grant No. 11ZR1443500), the National High Technology Research and Development Program of China (Grant No. 2013AA122402) and China Satellite Navigation Conference (Grant No. CSNC2011-QY-01).

References

1. Huang Y, Huang C et al (2008) Precise orbit determination of a maneuvered GEO satellite using CAPS ranging data. Sci China Ser G-Phys Mech Astron 52:346–352
2. Li Z, Xuhai Y, Huli S et al (2009) A new method for determination of satellite orbits by transfer. Sci China Ser G-Phys Mech Astron 52:P384–P392
3. Guo R, Hu X, Tang B et al (2010) Precise orbit determination for geostationary satellites with multiple tracking techniques. Chin Sci Bull 55:687–692
4. Zhou S, Hu X, Wu B et al. (2011) Orbit determination and time synchronization for a GEO/IGSO satellite navigation constellation with regional tracking network. Sci China Ser G-Phys Mech Astron, 54:1089-1097
5. Shi C, Zhao Q, Li M et al (2012) Precise orbit determination of Beidou satellites with precise positioning. Sci China Earth Sci 55:1079–1086
6. Montenbruck O (2012) ANTEX considerations for Multi-GNSS work. Antenna WG Meeting, IGS Workshop
7. Huang C, Feng C (2003) SLR data processing and its software implementation (in Chinese). Shanghai astronomical observatory
8. Hauschild A, Montenbruck O, Sleewaegen J-M et al (2012) Characterization of BeiDou M-1 Signal. GPS Solut 16:117–126

Chapter 21
Prediction of UT1-UTC Based on Combination of Weighted Least-Squares and Multivariate Autoregressive

Zhang-zhen Sun and Tian-he Xu

Abstract High accurate prediction of UT1-UTC is very important for high-precision aircraft navigation and positioning. In this paper, the weighted least-squares (WLS) combined with multivariate autoregressive (MAR) is proposed to predict UT1-UTC with different span. The new method can efficiently consider the influence of time-varying for the cycle and trend terms of UT1-UTC, which is closely related to atmospheric angular momentum (AAM). The numerical example shows that the prediction accuracy of WLS + MAR method is better than that of LS + MAR method as well as LS + AR method. The results prove that the WLS + MAR model can effectively improve the prediction accuracy of UT1-UTC.

Keywords UT1-UTC · Weighted least-squares · Atmospheric angular momentum · Multivariate autoregressive

21.1 Introduction

The Earth's rotation movement characterizes the situation of the whole earth movement, as well as the interaction between the Earths's various spheres of the Earth's core, mantle, crust and atmosphere, it can be described by Earth Orientation

Z. Sun (✉)
School of Geology Engineering and Surveying, Chang'an University, Xi'an, Shanxi, China
e-mail: sunzhangzhen@126.com

T. Xu
State Key Laboratory of Geo-information Engineering, Xi'an, Shanxi, China

T. Xu
Xian Research Institute of Surveying and Mapping, Xi'an, Shanxi, China

T. Xu
State Key Laboratory of Geodesy and Earth's Dynamics, Wuhan, China

J. Sun et al. (eds.), *China Satellite Navigation Conference (CSNC) 2013 Proceedings*, Lecture Notes in Electrical Engineering 245,
DOI: 10.1007/978-3-642-37407-4_21,

Parameters (EOP) [1]. EOP include the Nutation-precession parameters, the Polar Motion (PM) parameters, the Length of day (LOD) and the Universal Time (UT1-UTC) or the Earth's rotation variation. The PM, UT1-UTC and LOD are also called as Earth Rotation Parameters (ERP). EOP are the necessary parameters to achieve mutual conversion of the celestial reference frame and earth reference frame, and are very important for high-precision space navigation and positioning. Modern measurement techniques (such as VLBI, SLR, GPS and DORIS) can provide users with high precision, high spatial and temporal resolution of EOP [2]. However, due to the complexity of data processing, it is difficult to access to these parameters in real-time. In order to meet the needs of the space navigation and positioning, high-precision prediction for EOP is urgent. The prediction of UT1-UTC is very difficult, because it is impact by the Earth's zonal harmonic tidal and strongly correlated with the atmospheric angular momentum (AAM). AAM changes frequently, and makes UT1-UTC more unstable and hard to be predicted.

At present, the prediction methods of UT1-UTC include: least square extrapolation (LS), combination of least square extrapolation and auto-regressive (LS + AR) [3–6], combination of least square extrapolation and auto-covariance (LS + AC) [7], Artificial Neural Network (ANN) (Schuh et al. [8]), (Wang [9]). Due to the strong correlation between UT1-UTC and AAM, more than 80 % of the UT1-UTC variation can be explained by the changes in the AAM on the scale of a few hours to a few years [9]. Many scholars used this important information to predict them and achieved good results [10]. Least square used in the above methods should be performed based on the deterministic cycle and trend terms. In fact, these terms have the characteristic of time-varying in the observational data of the UT1-UTC [11, 12]. The closer the observational data is near to the prediction point, the greater the impact on the prediction accuracy is. Based on the above idea, the combination of the weighted least-square (WLS) and the multivariate autoregressive (MAR) is proposed. The procedure of the new method follows two steps: Firstly, WLS is applied to fit the UT1-UTC data and the AAM data, and generate the fitting residuals of UT1-UTC and AAM. Secondly, the multivariate autoregressive (MAR) technique is applied to generate prediction value of residuals and the final forecast UT1-UTC is obtained by adding the WLS extrapolation value.

21.2 Data Description

In this paper, the UT1-UTC time series EOP 05C04 provided by the IERS is used for calculation and analysis (http://hpiers.obspm.fr/eoppc/eop/). The time span from 1980.01.01 to 2012.04.16 is select as the experimental data with sampling interval of one day. The variation of UT1-UTC for this period is shown in Fig. 21.1. Atmospheric angular momentum (AAM) consists with 3 main components: equatorial component χ_1, χ_2 and axial component χ_3, each component can be divided into pressure terms χ^p and wind terms χ^w. The first two components are

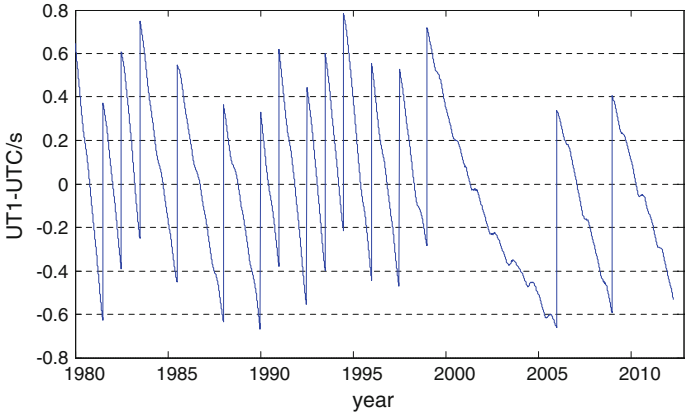

Fig. 21.1 The variation of UT1-UTC

associated with the excitation of polar motion, whereas the third one is responsible for the excitation of UT1-UTC. AAM can be obtained from the National Centers for Environmental Prediction (NCEP). Here we analyses the pressure terms χ_3^p modified by inverse barometer correction and wind terms χ_3^w are computed by integrating winds from the Earth surface to 10 hPa. The following data sets: aamf.ncep.reanalysis.1948.2009, aamf.ncep.reanalysis.2010, aamf.ncep.reanalysis.2011 and aamf.ncep.reanalysis.2012 are provided by NCEP. The sampling interval of these data is 6 h. In order to use them to predict UT1-UTC by WLS + MAR technique, the data should be selected with 1 day sampling interval. The time span of 1980.01.01 to 2012.04.16 is select to calculate as the experimental data in this paper.

The UT1-UTC is discontinuous according to Fig. 21.1. Thus, before the prediction of UT1-UTC, the leap second should be removed from UT1-UTC first to get UT1-TAI based on IERS Convention 2003 [13], and then the Earth's zonal harmonic tidal be removed from UT1-TAI to generate the series of UT1R-TAI. The equation of tidal correction can be expressed as:

$$\delta \mathrm{UT1} = \sum_{i=1}^{62} B_i \sin \xi_i + C_i \cos \xi_i \tag{21.1}$$

The meanings of symbols in Eq. (21.1) can refer to IERS Convention 2003.

The weighted least-square is applied to fit the UT1-UTC data and the AAM χ_3 data in order to get residuals of these time series. Then the multivariate autoregressive (MAR) technique is used to generate prediction value added with WLS extrapolation. The specific prediction process is showed in Fig. 21.2.

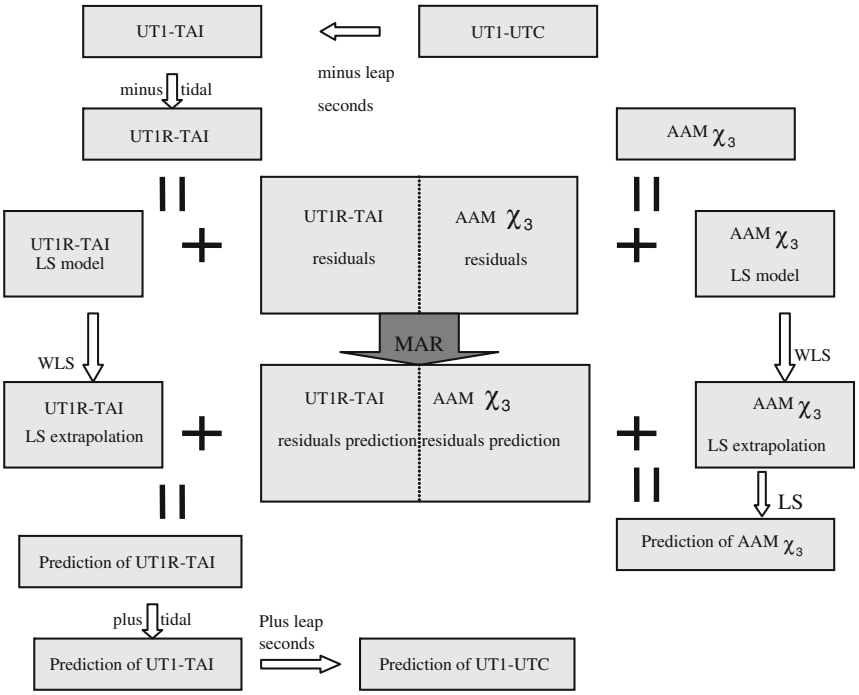

Fig. 21.2 Algorithm for UT1-UTC by combination of WLS and MAR prediction

21.2.1 WLS + MAR Model

21.2.1.1 WLS Model

The fitting equation of LS model for UT1R-TAI can be expressed as:

$$\begin{aligned} f_{ut}(t) = a_0 + a_1 t + B_1 \cos\left(\frac{2\pi t}{R_1}\right) + B_2 \sin\left(\frac{2\pi t}{R_1}\right) + C_1 \cos\left(\frac{2\pi t}{R_2}\right) \\ + C_2 \sin\left(\frac{2\pi t}{R_2}\right) + D_1 \cos\left(\frac{2\pi t}{R_3}\right) + D_2 \sin\left(\frac{2\pi t}{R_3}\right) + \cdots \end{aligned} \tag{21.2}$$

where a_0 is the constant term, a_1 is the linear term, B_1, B_2, C_1, C_2, D_1, D_2⋯are the coefficients for periodic terms, R_1, R_2, R_3⋯are the corresponding periodic for UT1R-TAI including long-term of 18.6 years and 9.3 years, annual and semi-annual, **t** is the time of UTC.

The fitting equation of LS model for AAM can be expressed as:

$$f_{AAM}(t) = \alpha_0 + \beta_1 \cos\left(\frac{2\pi t}{\phi_1}\right) + \beta_2 \sin\left(\frac{2\pi t}{\phi_1}\right) + \gamma_1 \cos\left(\frac{2\pi t}{\phi_2}\right) + \gamma_2 \sin\left(\frac{2\pi t}{\phi_2}\right) \tag{21.3}$$

where α_0 is the constant term, β_1, β_2, γ_1, γ_2 are the coefficients for periodic terms, ϕ_1, ϕ_2 are the corresponding periodic for AAM has annual and semi-annual, **t** is the time of UTC.

The estimator by using the WLS for parameter solution can be written as:

$$X = (B^T PB)^{-1} B^T PL \tag{21.4}$$

where X is the estimated parameter vector; B is the coefficient matrix; L is observation vector; P is the weight matrix and a diagonal matrix is considered in this paper.

For UT1R-TAI:

$$X = [\ a_0 \quad a_1 \quad B_1 \quad B_2 \quad C_1 \quad C_2 \quad D_1 \quad D_2 \quad \cdots\ ] \tag{21.5}$$

$$B = \begin{bmatrix} 1 & t_1 & \cos\left(\frac{2\pi t_1}{R_1}\right) & \sin\left(\frac{2\pi t_1}{R_1}\right) & \cdots \\ \vdots & \vdots & \vdots & \vdots & \vdots \\ 1 & t_n & \cos\left(\frac{2\pi t_n}{R_1}\right) & \sin\left(\frac{2\pi t_n}{R_1}\right) & \cdots \end{bmatrix} \tag{21.6}$$

For AAM:

$$X = [\ \alpha_0 \quad \beta_1 \quad \beta_2 \quad \gamma_1 \quad \gamma_2\ ] \tag{21.7}$$

$$B = \begin{bmatrix} 1 & \cos\left(\frac{2\pi t_1}{\phi_1}\right) & \sin\left(\frac{2\pi t_1}{\phi_1}\right) & \cdots \\ \vdots & \vdots & \vdots & \vdots \\ 1 & \cos\left(\frac{2\pi t_n}{\phi_1}\right) & \sin\left(\frac{2\pi t_n}{\phi_1}\right) & \cdots \end{bmatrix} \tag{21.8}$$

The WLS model is mainly used to generate UT1-UTC residuals Y_t^1 and AAM residuals Y_t^2, which can be denoted by bivariate residual vector $Y_t = (Y_t^1, Y_t^2)^T$.

21.2.1.2 Determination of the Weight Elements

The main principle for the choice of weight matrix is that the closer the data is near to the predicted value, the greater the weight is. In this paper, 2 schemes are designed to choose weight according to this principle [14].

Scheme 1: divide the basic observation sequence to 3 equal parts and each part has different weight matrix, that is:

$$P = \begin{bmatrix} P_1 & & \\ & P_2 & \\ & & P_3 \end{bmatrix}^e \tag{21.9}$$

where P_1, P_2 and P_3 are the diagonal matrix with diagonal elements as $\frac{1}{3}$, $\frac{1}{2}$ and 1 respectively, and e is the power.

Scheme 2: divide the basic of observation sequence to 10 equal parts, that is:

$$P = \begin{bmatrix} P_1 & & & \\ & P_2 & & \\ & & \ddots & \\ & & & P_{10} \end{bmatrix}^e \tag{21.10}$$

where: $P_1, P_2 \cdots$ and P_{10} are the diagonal matrix with diagonal elements as $\frac{1}{10}, \frac{1}{9} \cdots$ and 1 respectively.

21.2.1.3 Multivariate Autoregressive

Multivariate autoregressive (MAR) model is similar to univariate autoregressive model, which can be expressed as:

$$Y_t = A_1 Y_{t-1} + \cdots + A_p Y_{t-p} + E \tag{21.11}$$

where $Y_t = (Y_t^1, Y_t^2)^T$ is a random vector of residuals at time t, $A_i (A_i \in R^{2\times 2})$ are the matrices of autoregressive coefficients $(i = 1, 2, \cdots, p)$. **E** is the multivariate white noise vector with zero mean and covariance matrix **C**. The above equation usually denoted by MAR (p) is well-known as the multivariate autoregressive model of the order p.

The order p of MAR model can be determined according to the Schwarz Bayesian criterion (SBC), which can be process by:

$$SBC(p) = \frac{l_p}{2} - \left(1 - \frac{2p+1}{n-p}\right) \log(n-p) \tag{21.12}$$

where $l_p = \log \det((n - 3p - 1)\hat{C})$, $\hat{C}$ is the estimate of the residual covariance matrix C, n is the data number.

21.2.1.4 Error Analysis

In order to evaluate the prediction accuracy, we use the mean absolute error (MAE) standards. It can be expressed as following:

$$E_i = P_i - O_i \tag{21.13}$$

$$MAE_j = \frac{1}{n} \sum_{i=1}^{n} (|E_i|) \tag{21.14}$$

where P_i is the predicted value of the i-th prediction, O_i is the corresponding observation value, E_i is real error (Assumed the observation value as true value), n is the total prediction number.

21.2.2 Calculation and Analysis

The description of the data used in this paper can be seen in Sect. 21.2. In order to verify the validation of the proposed WLS + MAR model, 4 cases are conducted as following:

Case 1: Application of the LS + AR model to predict the UT1-UTC;
Case 2: Application of the LS + MAR model to predict the UT1-UTC;
Case 3: Application of the WLS + MAR model to predict the UT1-UTC, choose the weighted scheme 1;
Case 4: Application of the WLS + MAR model to predict the UT1-UTC, choose the weighted scheme 2.

The power e is determined according to the principle of minimize the prediction error. The steps in detail are the following. The weight power e is chosen in the range of 0–10 with 0.5 interval, the number that the highest of prediction accuracy is selected as the best one. The absolute error of 4 cases shown in Fig. 21.3 and the comparisons for them is shown in Fig. 21.4. Table 21.1 shows each span prediction accuracy values of UT1-UTC under 4 schemes. It can be seen from the Figs. 21.3, 21.4 and Table 21.1 show that the prediction accuracy of case 2 is higher than that of case 1, since there are strongly correlation between UT1-UTC and AAM. The prediction accuracy of UT1-UTC can be improved if AAM can be taken into account. The prediction accuracies of case 3 and case 4 are higher than of case 2 in the whole, especially in recent years. The prediction accuracy of case 3 is a little better than that of case 4, which means different weighting scheme has a

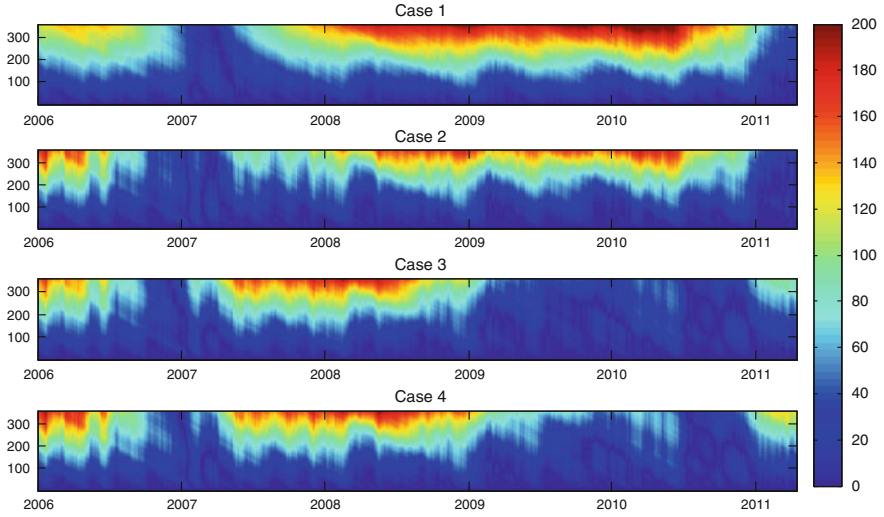

Fig. 21.3 :Absolute prediction errors (in ms) for 4 schemes

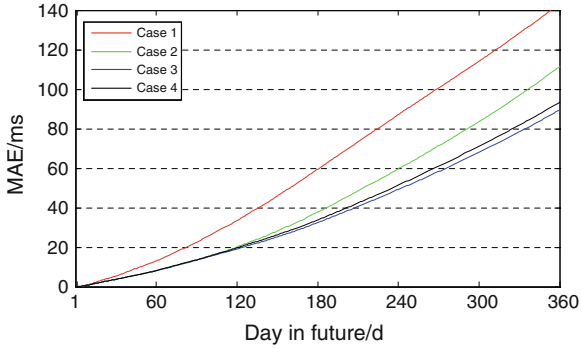

Fig. 21.4 Comparison of prediction accuracy of UT1-UTC under 4 schemes

Table 21.1 Comparison of prediction accuracy under 4 schemes

Day in future	Case 1 ms	Case 2 ms	Case 3 ms	Case 4 ms
1	0.0296	0.0272	0.0267	0.0269
5	0.4294	0.3552	0.3428	0.3480
10	1.2690	0.9929	0.9565	0.9664
20	3.3607	2.4611	2.4200	2.4179
30	5.4372	3.7475	3.7751	3.7288
60	13.0714	8.0541	8.2544	8.1569
90	22.5952	13.5016	13.5568	13.6616
120	33.5244	20.1686	19.1311	19.7094
180	59.4820	37.7832	32.4750	33.8374
240	87.1792	59.6874	49.3033	51.4981
300	114.2647	83.6285	68.0697	71.1483
360	143.1541	111.4165	89.4790	93.3763

little influence on prediction accuracy. All these prove that the proposed method WLS + MAR in this paper, can improve the prediction accuracy of UT1-UTC effectively.

21.3 Conclusions

Due to the cycle and trend terms have the characteristic of time-varying in the observational data of the UT1-UTC, the closer the observational data is near to the prediction point, the greater the impact on the prediction is. It is also strongly correlated with the atmospheric angular momentum (AAM), and more than 80 % of the UT1-UTC can be explained by the changes in the AAM on the scale of a few hours to a few years. Based on the above reason, the weighted least-squares and multivariate autoregressive (WLS + MAR) is developed to predict UT1-UTC

with different time span in this paper. Two kinds of weighted methods have been proposed. The results show that the UT1-UTC prediction accuracy of WLS + MAR model is obviously higher than LS + AR and LS + MAR.A optimal weighted method should be studied in further work.

Acknowledgments This work was supported by the Foundation for the Author of National Excellent Doctoral Dissertation of China (2007B51), the Open Foundation of State Key Laboratory of Geodesy and Earth's Dynamics (SKLGED2013-4-2-EZ) and Natural Science Foundation of China (41174008).

References

1. Zheng DW, Yu NH (1996) Earth rotation and it's relations to geophysical phenomena: the changes of length of the day. Adv Geophys 11(2):81–101 (In Chinese)
2. Kosek W et al. (2004) Comparison of polar motion prediction results supplied by the IERS sub-bureau for rapid service and predictions and results of other prediction methods [A]. Astronomy Russian Academy Sciences
3. McCarthy DD, Luzum BJ (1991) Prediction of Earth orientation. J Geodesy, 65:18–21
4. Kosek W, Kalarus M, Niedzielski T (2008) Forecasting of the Earth orientation parameters—comparison of different algorithms. In: Capitaine N (ed) Proceedings of the journèes 2007, systèmes de référence spatio-temporels The celestial reference frame for the future. Observatoire de Paris Systèmes de Référence Temps-Espace UMR8630/CNRS, Paris, France, pp 155–158
5. Kosek W (2010a) Future improvements in EOP prediction. In: Proceedings of the IAG 2009, Geodesy for planet earth, August 31–September 4, 2009, Buenos Aires, Argentina
6. Xu XQ, Zhou YH (2010) High precision prediction method of earth orientation. Parameters 29(2):70–76 (In Chinese)
7. Kosek W, McCarthy DD, Luzum BJ (1998) Possible improvement of Earth orientation forecast using autocovariance prediction procedures. J Geodesy 72:189–199
8. Schuh H, Ulrich M, Egger D et al (2002) Prediction of Earth orientation parameters by artificial neural networks. J Geodesy 76:247–258
9. Wang QJ (2007) Studies on the prediction of Earth's variable rotation by artificial neural networks [D]. Shanghai Astronomical observatory, Chinese Academy of Sciences. Shanghai, China (In Chinese)
10. Niedzielski T, Kosek W (2008) Prediction of UT1-UTC,LOD and AAM $\chi_3$by combination of least-squares and multivariate stochastic methods. J Geodesy, 82:83–92
11. Kosek W, McCarthy DD, Luzum BJ (2010) Studia geoph. Et geod 45:347
12. Zhang H, Wang Qj, Zhu JJ et al. (2011) Joint model of weighted least-squares and AR in prediction of polar motion 29(3):343–352 (In Chinese)
13. McCarthy DD, Petit G (2003) IERS conventions (2003) [S]. America
14. Sun ZZ, Xu TH(2012) Prediction of Earth rotation parameters based on an improved weighted least-squares and AR model. Geodesy and Geodynamics, 3(3):57–64

Chapter 22
Precise Point Positioning Using Combined Beidou and GPS Observations

Lizhong Qu, Qile Zhao, Min Li, Jing Guo, Xing Su and Jingnan Liu

Abstract By the end of year 2012, China has launched 16 Beidou-2/Compass-2 navigation satellites that include 6 GEO, 5IGSO and 5 MEO. Initial navigation and precise pointing services ability has formed in the Asian-Pacific regions. In order to know the navigation and positioning performance of Beidou-2 system, Wuhan University has built up a Beidou Experimental Tracking Stations over the world and extents the PANDA software to determine the orbits of Beidou satellites, that supplies the Beidou satellites' precise orbit and satellite clock offset for the users needing high accuracy positioning services. This article uses the Beidou/GPS observations of the Beidou Experimental Tracking Stations to realize the Beidou and Beidou/GPS static and kinematic precise point positioning (PPP). The result indicates that the precision of Beidou static and kinematic PPP reaches centimeter level, the precision of combined Beidou/GPS static and kinematic PPP improves than that of both only-Beidou and only-GPS and the convergence time is less than that of both only-Beidou and only-GPS.

Keywords Beidou satellite navigation system · Beidou experimental tracking stations · PNADA · Beidou/GPS · Precise point positioning (PPP)

22.1 Introduction

On Oct. 25 of year 2012, the 16th Beidou-2 navigation satellite is launched successfully, indicating that the Beidou region navigation satellite system has been initially built up and the preliminary ability of navigation and high accuracy positioning services has formed in Asian-Pacific regions. The scholars both at home and

L. Qu (✉) · Q. Zhao · M. Li · J. Guo · X. Su · J. Liu
GNSS Center, Wuhan University, 129 Luoyu Road, Wuhan 430079, China
e-mail: qulizhong@whu.edu.cn

J. Sun et al. (eds.), *China Satellite Navigation Conference (CSNC) 2013 Proceedings*, Lecture Notes in Electrical Engineering 245,
DOI: 10.1007/978-3-642-37407-4_22,

abroad have a large of researches on the precise orbit determination and the static precise positioning. Shi et al. [1] have researched on the precise orbit determination of Beidou satellites and the Beidou PPP by using the precise orbit and satellites clock error productions. The observations come from the Beidou Experimental Tracking Stations and the software platform is PANDA while the constellation of Beidou system had just 6 satellites at that time. The RMS of the difference in the radial components are smaller than 10 cm and the static daily PPP COMPASS solutions show an accuracy of 2 cm in horizontal and 7 cm in vertical. Hauschild et al. [2] used the Satellite Laser Ranging (SLR) tracking data to determine the orbit of Beidou M01 with 7 days arc length. The RMS of the 3-D overlap error varies from 11 to 50 cm in the selected periods. Montenbruck et al. [3] researched on the Beidou PPP and the errors in the horizontal and vertical position components of static PPP can reach up to 12 cm, that due to the fewer tracking stations resulting in the lower precision of Beidou orbit and clock error. Shi et al. [1, 4] also researched on the static and kinematic precise relative positioning and the accuracy of static solutions reached millimeter level and the kinematic solutions reached to centimeter level.

The precision of navigation and positioning of satellites system mainly depends on the numbers of satellites observed by users, the geometry structure of satellites distribution and the precision of space signals containing the precision of the precise orbit and the satellite clock error. The multi-systems data processing can increase the numbers of satellites observed effectively, improve the geometry structure of space distribution and improve the accuracy, continuity and reliability of positioning [1, 5]. Nowadays the data processing of multi-systems focuses on the combination of GPS and GLONASS [5–8]. So the researches on the Beidou positioning and combined Beidou/GPS positioning will benefit the application and popularisation of Beidou system. This article adopts the PANDA (Position And Navigation Data Analysist Software) researched and developed by Wuhan University independently and process the data of Beidou Experimental Tracking Stations in the modes of Beidou static and kinematic PPP, GPS static and kinematic PPP and combined Beidou/GPS static and kinematic PPP [9–11].

22.2 Precise Point Positioning Strategy for Beidou System

22.2.1 Data Acquisition

Beidou Experimental Tracking Stations (BETS) has 9 stations at home and 6 stations abroad. All the stations have equipped UR240-CORS receivers made by the Beijing Unicore Communication Company. The receiver can receive both the phase and pseudo-range observations on the dual frequencies. During the research of this article, we have adopt 11 satellites operating well containing 4 GEO including C01, C03, C04 and C05, 5IGSO including C06–C10, and 2MEO

including C11, C12. The Fig. 22.1 displays the distribution of "BETS" over the world and the tracks of sub-satellite points of Beidou system. As Fig. 22.1 shows, 5IGSO operates in the southern hemisphere and the northern hemisphere in the shape "8", the difference of longitude of each IGSO satellite is about 30° and the eastern and western parts of China and adjoining regions can be covered effectively. 4GEO distribute in the Indian and Pacific oceans over the equator as the supplements for the IGSO satellites to ensure users in Asian-Pacific regions to observe enough satellites. Meanwhile, 2MEO operates over the world and their periods are about 12 h.

22.2.2 Precise Point Positioning Strategy

The observation equations of Beidou satellite j are:

$$B_i{}^j = \rho_0^j + c \cdot dt_R - c \cdot dt^j + \rho_{orb}^j + \rho_{trop} + \rho_{iono/\Phi_i}^j + b_{B_i}^j + \rho_{mul/B_i}^j + \varepsilon_{B_i} \quad (22.1)$$

$$\Phi_i{}^j = \rho_0^j + c \cdot dt_R - c \cdot dt^j - \lambda_i N_i^j + \rho_{orb}^j + \rho_{trop} - \rho_{iono/\Phi_i}^j + b_{\Phi_i}^j + \rho_{mul/\Phi_i}^j + \varepsilon_{\Phi_i} \quad (22.2)$$

Where B_i, Φ_i, $i = 1, 2$ are the pseudo-range and phase observations, ρ_0^j is the geometry distance between satellite and station, dt_R is the receiver clock offset, dt^j is the satellite clock offset, ρ_{orb}, ρ_{trop}, ρ_{iono} and ρ_{mul} is the satellite orbit error, the troposphere delay error, the ionosphere error and the multipath error, respectively, ε

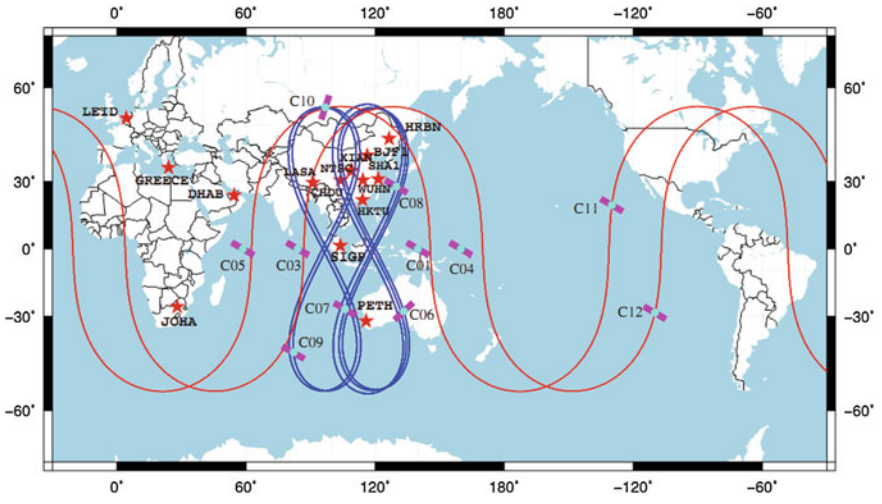

Fig. 22.1 The distribution of Beidou Experimental Stations over the world and the sub-satellite points of Beidou 4GEO, 5IGSO and 2MEO

is the observation noise, N_i^j is integer ambiguity that is not an integer because of the introduction of the initial phase biases, $b_{B_i}^j$, $b_{\Phi_i}^j$ is the hardware delay of the pseudo-range and phase observations respectively containing both the hardware delay in the satellites and receivers that is always expressed in the way below [7]. However, the hardware delays of GPS satellites have been included in the IGS satellites precise clock product so there are just the hardware delays of receivers [8, 9].

$$b_{B_i}^j = b_{B_i}^{avg} + db_{B_i}^j \tag{22.3}$$

$$b_{\Phi_i}^j = b_{\Phi_i}^{avg} + db_{\Phi_i}^j = b_{B_i}^{avg} + d\tilde{b}_{\Phi_i}^j \tag{22.4}$$

Where $b_{B_i}^{avg}$, $b_{\Phi_i}^{avg}$ is the mean hardware delay offset, $db_{B_i}^j$, $db_{\Phi_i}^j$ is the delay offset between the channels. $d\tilde{b}_{\Phi_i}^j = b_{B_i}^{avg} - b_{\Phi_i}^{avg} + db_{\Phi_i}^j$ is always stable and always absorbed by the integer ambiguity, while the delay offset between pseudo-range channels is included by the pseudo-range noise, then we put Eq. (22.3) and (22.4) into Eq. (22.1) and (22.2):

$$\begin{aligned} B_i^j =& \rho_0^j + (c \cdot dt_R + b_{B_i}^{avg}) - c \cdot dt^j + \rho_{orb}^j + \rho_{trop} + \rho_{iono/\Phi_i}^j + \rho_{mul/B_i}^j \\ &+ (\varepsilon_{B_i} + db_{B_i}^j) \end{aligned} \tag{22.5}$$

$$\begin{aligned} \Phi_i^j =& \rho_0^j + (c \cdot dt_R + b_{B_i}^{avg}) - c \cdot dt^j - (\lambda_i N_i^j + d\tilde{b}_{\Phi_i}^j) + \rho_{orb}^j + \rho_{trop} - \rho_{iono/\Phi_i}^j \\ &+ \rho_{mul/\Phi_i}^j + \varepsilon_{\Phi_i} \end{aligned} \tag{22.6}$$

When applying the precise orbit and clock offset correction and put the multipath error and observation noise into the noise together, the ionosphere-free pseudo-range and phase observation equations can be written as:

$$B_{IF}^j = \rho_0^j + c \cdot d\tilde{t}_R + \rho_{trop} + \tilde{\varepsilon}_{B_{IF}} \tag{22.7}$$

$$\Phi_{IF}^j = \rho_0^j + c \cdot d\tilde{t}_R - \lambda_{IF}^b \tilde{N}_{IF}^j + \rho_{trop} + \tilde{\varepsilon}_{\Phi_{IF}} \tag{22.8}$$

where $c \cdot d\tilde{t}_R = c \cdot dt_R + b_{B_{IF}}^{avg}$, $\lambda_{IF}\tilde{N}_{IF}^j = \lambda_{IF}N_{IF}^j + d\tilde{b}_{\Phi_{IF}}^j$, λ_{IF}^b is the Beidou ionosphere free combination phase wavelength, $\tilde{N}_{IF}^j$ the Beidou ionosphere free combination phase integer ambiguity, meanwhile, the ionosphere free combination observation equations for GPS satellite k can be written as:

$$P_{IF}^k = \rho_0^k + c \cdot \widehat{dt}_R + \rho_{trop} + \widehat{\varepsilon}_{P_{IF}} \tag{22.9}$$

$$L_{IF}^k = \rho_0^k + c \cdot \widehat{dt}_R - \lambda_{IF}^g \widehat{N}_{IF}^k + \rho_{trop} + \widehat{\varepsilon}_{L_{IF}} \tag{22.10}$$

λ_{IF}^g is the GPS ionosphere free combination phase wavelength, $\widehat{N}_{IF}^k$ is the GPS ionosphere free combination phase integer ambiguity. From Eq. (22.7) to (22.10),

we need to introduce an system time bias between GPS and Beidou system like the Eq. (22.11) because of the different hardware delay for GPS and Beidou system.

$$dt_{sys} = d\tilde{t}_R - d\hat{t}_R \tag{22.11}$$

The combined Beidou/GPS PPP observation equations can be written as:

$$B_{IF}^j = \rho_0^j + c \cdot (d\hat{t}_R + dt_{sys}) + \rho_{trop}^j + \tilde{\varepsilon}_{B_{IF}} \tag{22.12}$$

$$\Phi_{IF}^j = \rho_0^j + c \cdot (d\hat{t}_R + dt_{sys}) - \lambda_{IF}\tilde{N}_{IF}^j + \rho_{trop}^j + \tilde{\varepsilon}_{\Phi_{IF}} \tag{22.13}$$

$$P_{IF}^k = \rho_0^k + c \cdot d\hat{t}_R + \rho_{trop}^k + \hat{\varepsilon}_{P_{IF}} \tag{22.14}$$

$$L_{IF}^k = \rho_0^k + c \cdot d\hat{t}_R - \lambda_{IF}\hat{N}_{IF}^k + \rho_{trop}^k + \hat{\varepsilon}_{L_{IF}} \tag{22.15}$$

Equations above are the function model for Beidou PPP and combined Beidou/GPS PPP. After turning Eqs. (22.11–22.15) into the error equations, we adopt the recursive least square adjustment method to process data. The prior variances of Beidou and GPS phase observations are $\sigma_{pbd} = 2\,mm$, $\sigma_{pgps} = 2\,mm$ respectively, the prior variances of Beidou and GPS pseudo-range observations are $\sigma_{rbd} = 0.2\,m$, $\sigma_{rgps} = 0.2\,m$. We also use the elevation to decide the weighting of observations.

We consider the errors relating with the satellites (i.e. the default satellite antenna phase offset from the satellite manufacturer), the errors relating with the propagation path (i.e. the zenith tropospheric delay, the phase wind up), the errors relating with the ground stations (i.e. the solid earth tide, the ocean loading) as shown in Table 22.1 and do not consider the variation between the mean antenna phase center and the mass center of satellite, the phase center offset between the mean phase center of the receiver antenna and the receiver antenna reference point and the variation between the instantaneous phase center of the receiver antenna and the mean phase center of the receiver antenna because their values are unknown.

22.3 Results and Analysis

Basing on the methods shown above, we process data of 7 days from September 4 to 10 in 2012 (day of year from 248 to 254) by using the PANDA software package in the modes of Beidou, GPS, Beidou/GPS static PPP and kinematic PPP and analysis the precisions of the positioning results. The stations referred below contain 11 stations of "BETS" and in order to produce the independent solutions, other 3 stations including WDKJ, CWKJ and GDCH are not used for orbit and clock determination. WDKJ and CWKJ are in the City of Wuhan and GDCH is in the City of Guangzhou.

Table 22.1 The measurement model and parameters estimation on for Beidou PPP

Measurement model	
Observations	Undifferenced ionosphere-free linear combination PC and LC
Cutoff elevations angular	7°
Sampling rate	30 s
Precise obit	IGS Final ephemeris
	PANDA Beidou final ephemeris
Precise clock offset	IGS precise satellite clock offset 30 s
	PANDA Beidou precise satellite clock offset 30 s
Satellite antenna PCO	Default value
Satellite antenna PCV	Unknown
Receiver antenna PCO and PCV	Unknown
Troposphere	Saastamoinen model for wet and dry hydrostatic delay with global mapping function
Ionosphere	1st order effect eliminated by forming Ionosphere-free linear combination
Solid earth tide, ocean tide loading and pole tide	IERS conventions 2003
Parameters estimation	
Coordination	Static: constant
	Kinematic: random walk for each epoch
Receiver clock offset	Random walk process for each epoch
Troposphere	Piece-wise constant
Integer ambiguity	As a constant for each ambiguity arc
System time difference	Random walk process for each epoch

22.3.1 Static PPP

Table 22.2 is the bias in the east, north and up components of the results of the Beidou, GPS, Beidou/GPS static PPP to the "ground true value" that is the mean value of the GPS static PPP coordination from September 4 to 10 in 2012. And interval of data processing is 300 s. From the table, we can see that:

1. The biases of the north components of almost all the stations are less than 1 cm except LEID and GREECE, nearly all the biases of east components are less than 2 cm except JOHA, LEID and GREECE and the biases of the up components are less than 3 cm except CHDU, that may dues to the differences of geometry structures of the satellites space distribution and the observations environments between stations. The RMS of east, north and up components are less than 2, 1 and 2 cm respectively;
2. The biases of east, north and up components of Beidou/GPS static PPP against the "ground true value" are nearly less than 1 cm and the RMS of the biases of the Beidou/GPS static PPP solutions are less than that of GPS static PPP solutions in the north and up components but the east components, which dues

Table 22.2 The biases of the results of the Beidou, GPS and Beidou/GPS static PPP of the "BETS" against the "ground true value" in the east, north, up components in Sep 4 of year 2012 (Day of year is 248)

	BD			GPS			BD/GPS		
	East (cm)	North (cm)	Up (cm)	East (cm)	North (cm)	Up (cm)	East (cm)	North (cm)	Up (cm)
BJF1	−1.12	0.58	−1.4	−0.08	−0.18	1.04	−0.52	0.23	−0.11
WUHN	−1.21	−0.18	0.19	0.23	−0.27	−1.49	−0.32	−0.15	−0.83
CHDU	0.19	−0.05	3.71	−0.26	−0.27	0.15	−0.12	0.01	1.48
HKTU	0.08	−0.12	−2.16	0.44	−0.55	−2.02	0.64	−0.22	−1.71
HRBN	−0.07	−0.02	0.52	0.69	−0.07	−0.82	0.44	−0.03	−0.66
LASA	0.62	0.26	−2.51	−0.23	−0.29	−0.12	0.01	−0.09	−0.9
WDKJ	−0.48	0.12	−1.79	0.22	−0.07	−0.42	−0.29	0.06	−0.99
CWKJ	−1.27	0.02	−0.24	0.31	−0.3	−0.19	−0.25	−0.02	−0.54
GDCH	−0.05	0.15	0.69	−0.28	−0.19	−0.75	0.05	0.13	0.25
XIAN	−0.75	0.37	−0.32	0.21	−0.15	0.94	−0.14	0.16	0.53
JOHA	4.82	−0.71	−1.48	−0.38	0.11	2.05	−0.3	−0.06	−1.48
LEID	−2.45	−2.17	0.81	0.51	−0.22	−0.01	0.15	−0.01	0.07
PETH	−1.02	0.01	0.77	−0.55	−0.39	−0.81	−0.82	−0.27	0.01
GREECE	−1.66	−1.46	2.65	−0.28	0.02	−0.06	−0.82	−0.02	0.68
RMS	1.66	0.75	1.72	0.37	0.26	1.02	0.43	0.14	0.89

to that the "ground true value" is the mean value of GPS solutions and when the weightings of GPS and Beidou observations are the same, the unknown PCO and PCV of the receiver and PCV of the satellites may result in that, which needs more researches.

Figure 22.2 is the RMS of the biases of the results of the Beidou, GPS and Beidou/GPS static PPP of the "BETS" against the "ground true value" in the east, north, up components from September 4 to 10 in 2012. It can be seen that:

1. The RMS of the biases of the east, north and up components of Beidou static PPP against the "ground true value" are less than 1, 1 and 3 cm in the Asian-Pacific region while that of station JOHA, LEID and GREECE are less than 4, 4 and 5 cm because the fewer Beidou satellites observed as shown in Fig. 22.1 and the poor geometry structure of satellites distribution there. The mean value of the RMS of the east, north and up components of all the stations are 1.11, 0.66 and 2.43 cm;
2. The RMS of the biases of the east, north and up components of combined Beidou/GPS static PPP against the "ground true value" are all less than 1 cm and the mean values of the RMS of the east, north components are 0.44, 0.23 that are less than the values of GPS that are 0.47, 0.28 cm respectively while the mean value of the biases of the up component of Beidou/GPS static PPP is 0.98 cm that is close to that of GPS that is 0.93 cm. The reason why the up component of the Beidou/GPS static PPP is worse than that of GPS may due to

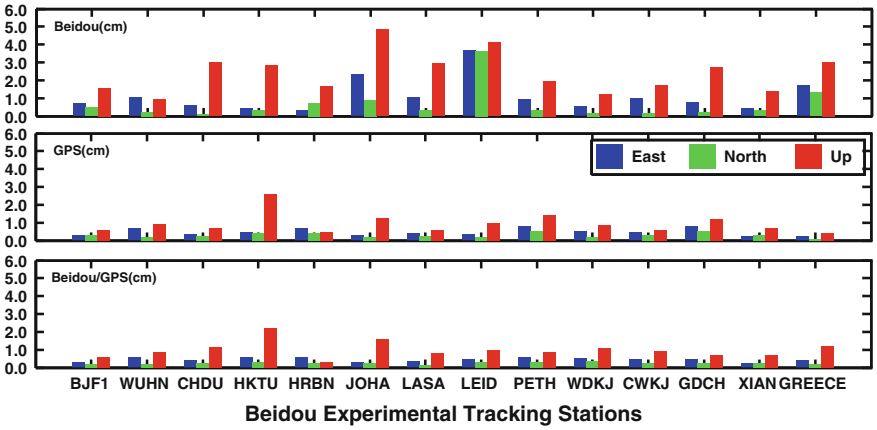

Fig. 22.2 The RMS of the biases of the results of the Beidou, GPS, Beidou/GPS static PPP of the "BETS" against the "ground true value" in the east, north, up components from Sep 4 to 10 in 2012 (Day of year from 248 to 254)

that the source of "ground true value", the unknown PCV and PCO correction of the receivers and the differences of the positioning results of different stations influencing the final mean values.

22.3.2 Kinematic PPP

Figure 22.3 is the time series of the biases of the results of the Beidou, GPS, Beidou/GPS kinematic PPP in CWKJ against the "ground true value" in the East, North, Up components with the satellites numbers and the PDOP variation of Sep 4 in 2012. Table 22.3 is the RMS of the biases of the east, north and up components of CWKJ, HRBN, XIAN and PETH. And interval of data processing is 30 s. It can be seen that:

1. The east and north components of the Beidou kinematic solutions are within ±10 cm while the up components are within ± 20 cm after convergence (when the absolute value of the bias is below 10 cm). And the east component has the quickest convergence time while that of the up component is the slowest. The mean RMS of the east, north and up components for the four stations are 1.5, 2.0 and 9.0 cm;
2. The east, north and up components of the Beidou/GPS kinematic solutions are within ±10 cm after convergence and the convergence time also becomes less in the north and up components. The mean RMS of east, north and up components of the Beidou/GPS kinematic solutions for the four stations 1.3,1.8 and 3.8 cm and that of GPS are 3.5, 3.8 and 8.3 cm. That the precision and the

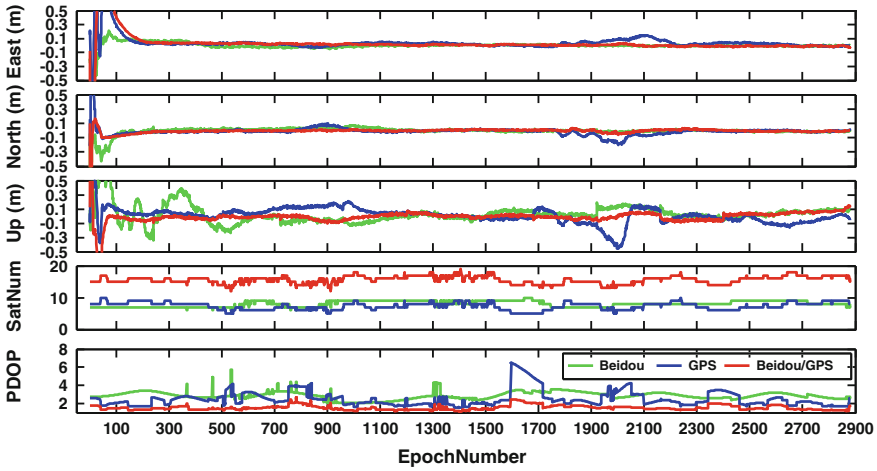

Fig. 22.3 The biases of the results of the Beidou, GPS, Beidou/GPS kinematic PPP in CWKJ against the "ground true value" in the East, North, Up components with the satellites numbers and the PDOP variation of September 4 in 2012 (Day of year is 248)

Table 22.3 The RMS of the biases of the results of the Beidou, GPS, Beidou/GPS kinematic PPP in CWKJ, HRBN, XIAN and PETH against the "ground true value" in the East, North, Up components of Sep 4 in 2012 (Day of year is 248)

	BD			GPS			BD/GPS		
	East (m)	North (m)	Up (m)	East (m)	North (m)	Up (m)	East (m)	North (m)	Up (m)
CWKJ	0.01	0.01	0.08	0.02	0.01	0.04	0.01	0.02	0.03
HRBN	0.03	0.03	0.12	0.04	0.06	0.08	0.01	0.03	0.04
XIAN	0.01	0.02	0.07	0.04	0.04	0.11	0.02	0.01	0.04
PETH	0.01	0.02	0.09	0.04	0.04	0.10	0.01	0.01	0.04

convergence time improve more than both that of GPS and Beidou dues to the numbers of satellites observed increasing to 15 at least and the PDOP decreasing obviously than that of the single system.

The reason why the kinematic results of Beidou PPP look better than that of GPS may be that the numbers of Beidou satellites observed are less changeable and more than that of GPS in Asian-Pacific region resulting in the stable changes of PDOP and some satellites also may be deleted in the process of the residual edit.

22.3.3 The Time Difference Between GPS and Beidou

Figure 22.4 are the system time biases of Beidou/GPS static PPP of the station CWKJ, HRBN, XIAN and PETH of September 4 in 2012 and Table 22.4 are the

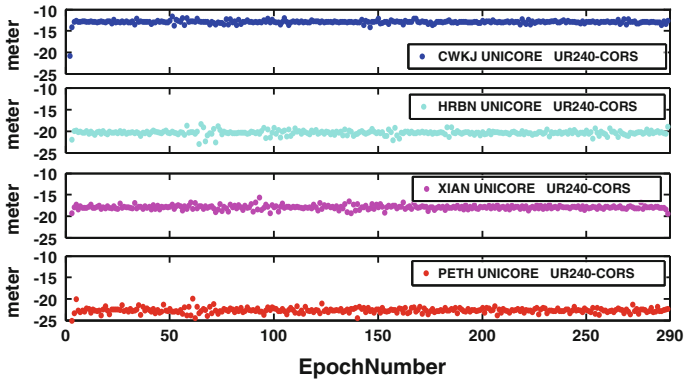

Fig. 22.4 The system time biases [Eq. (22.11)] of Beidou/GPS static PPP in CWKJ, HRBN, XIAN and PETH of Sep 4 in 2012 (Day of year is 248)

Table 22.4 The mean value of biases of Beidou/GPS PPP in CWKJ, HRBN, XIAN and PETH of Sep 4 in 2012 (Day of year is 248)

STATION	MEAN (m)
CWKJ	−12.89
HRBN	−20.36
XIAN	−17.91
PETH	−22.66

mean values of the biases. We adopt the random walk process to estimate the values in every epoch. The biases are mainly the differences of the average hardware delays of GPS and Beidou signals channel. It can be seen that the biases are different for different stations but within −10 and −25 m, that implies that the hardware delays of the same type receivers may be close.

22.3.4 Residuals Analysis

The residuals usually contain the observations' noise, the multipath error, the orbit error and the unmodelled error (i.e. the receiver PCV and PCO). The residuals are usually used as an important index of the positioning precision. Figure 22.5 are the residuals of Beidou satellites ionosphere-free pseudo-range combination (PC) and phase combination (LC) in CWKJ, HRBN, XIAN and PETH of Sep 4 in 2012 (Day of year is 248) and Fig. 22.6 are the RMS of the residuals from September 4 to 9 in 2012. It can be seen that:

1. The LC residuals of all the satellites are within ±2 cm and the PC residuals are within ±4 cm while the LC RMS of all the satellites are less than 1.5 cm and the PC RMS are less than 2.5 cm;

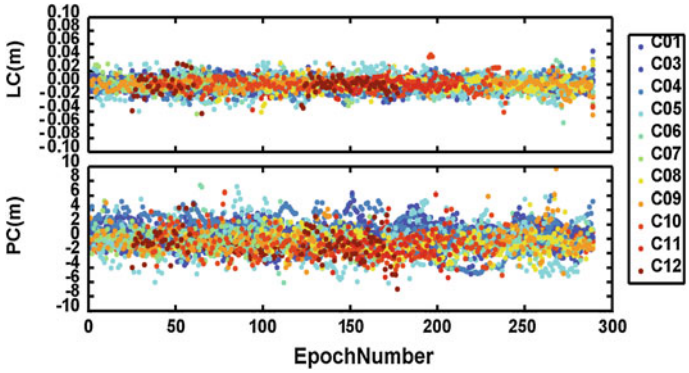

Fig. 22.5 The residuals of Beidou satellites ionosphere-free pseudo-range combination (*PC*) and phase combination (*LC*) in CWKJ, HRBN, XIAN and PETH of Sep 4 in 2012 (Day of year is 248)

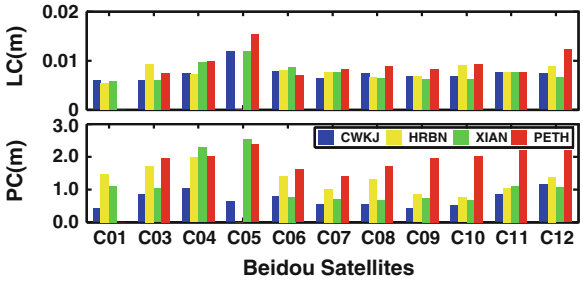

Fig. 22.6 The RMS of residuals of Beidou satellites ionosphere-free pseudo-range combination (*PC*) and phase combination (*LC*) in CWKJ, HRBN, XIAN and PETH of Sep 4–9 in 2012 (Day of year is 248–254)

2. That the LC and PC residuals of PETH are larger than that of other stations may dues to the different orbit error between the northern hemisphere and the southern hemisphere because of the different stations distribution shown in Fig. 22.1 and the residuals are also influenced by the multipath effect determined by the local environments;
3. That the LC residuals of C04 and C05 are larger than that of other satellites dues to that the positions of GEO have less changes than that of MEO or IGSO and the four stations distribution also may result in the nearly unchangeable and lower elevations so that the observations noise become larger.

22.4 Summary and Discussion

PANDA software is used to process the Beidou/GPS data from the Beidou Experimental Tracking Stations in the modes of Beidou, GPS and combined Beidou/GPS static and kinematic PPP. The Beidou PPP model and Beidou/GPS

PPP model are developed. A system time difference between Beidou and GPS is introduced into the integration of Beidou and GPS observations. The strategy of Beidou PPP and combined Beidou/GPS PPP is demonstrated in this article. The results of Beidou and Beidou/GPS static and kinematic PPP are compared with the "ground true value" from the mean value of the GPS static PPP. The measured data indicated that the accuracies of Beidou static and kinematic PPP have reached centimeter level; the results of combined Beidou and GPS static PPP have significant improvement than that of both only-Beidou and only-GPS and the convergence time of combined Beidou and GPS also improved than that of both only-Beidou and only-GPS. With the improvement of the orbit precision for the increasing and the proper distribution of the ground tracking stations and with the deploying of the other Beidou satellites, the precision of Beidou positioning may have significant improvement in the future. The determination of the PCV of the satellites' antennas and the PCO and PCV of the receivers may also benefit the positioning of Beidou system.

References

1. Shi C, Zhao Q, Li M et al. (2011) Precise orbit determination of Beidou Satellites with precise positioning. China Scie: Earth Sci, 42(6):854–861
2. Hauschild A, Montenbruck O, Sleewaegen JM, Huisman L, Teunissen P (2012) Characterization of Compass M-1 signals. GPS Solut 16(1):117–126. doi:10.1007/s10291-011-0210-3
3. Montenbruck O, Hauschild A, Steigenberger P, Hugentobler U, Teunissen P, Nakamura S (2012) Initial assessment of the COMPASS/Beidou-2 regional navigation satellite system. GPS Solut. doi:10.1007/s10291-012-0272-x
4. Shi C, Zhao Q, Hu Z, Liu J (2012) Precise relative positioning using real tracking data from COMPASS GEO and IGSO satellites. GPS Solut. doi:10.1007/s10291-012-0264-x
5. Changsheng Cai, Yang Gao (2007) Precise point positioning using combined GPS and GLONASS Observations. J Glob Positioning Syst 6:13–22
6. Xiangguang M, Guo J The Research on Combined GPS and GLONASS Precise Po-int Positioning. J Wuhan Univ·Inf sci edn, 2010, 35(12):1409–1413
7. Cai C, Gao Y (2012) Modeling and assessment of combined GPS/GLONASS precise point positioning. GPS Solut. doi:10.1007/s10291-012-0273-9
8. Defraigne P, Baire Q (2011) Combining GPS and GLONASS for time and frequency transfer. Adv Space Res 47(2):265–275. doi:10.1016/j.asr.2010.07.003
9. Liu J, Ge M (2003) PANDA software and its preliminary result of positioning and orbit determination. Wuhan Univ J Nat Sci 8:603–609
10. Zhao Q (2004) Research on precise orbit determination theory and software of both GPS navigation constellation and LEO satellites. PhD dissertation in Chinese with an abstract in English, School of Geodesy and Geomatics, Wuhan University, Wuhan, China
11. Shi C, Zhao Q, Geng J et al. (2008) Recent development of PANDA software in GNSS data processing. In: Proceedings of the society of photographic instrumentation engineers, 7285: 72851S, doi: 10.1117/12.816261

Chapter 23
The Establishment and Precision Analysis of Global Ionospheric Model of COMPASS System

Xiuqiang Gong, Nan Xing, Shanshi Zhou, Yueling Cao, Xiaogong Hu and Bin Wu

Abstract Ionospheric delay is one of the main error sources affecting the positioning and timing precision of satellite navigation system for single frequency users. China's regional satellite navigation system uses ionospheric puncture point data of monitoring stations to fit the 8 parameters of klobuchar model in geographic coordinate system,and broadcasts them to users through the navigation message which is valid for 2 h. Long-term monitoring shows that this model can correct the ionospheric delay up to 74 % in service area around China. Due to the lack of ionospheric measured data in the southern hemisphere and high latitudes of the northern hemisphere, this model can not guarantee the correction accuracy in equatorial belt and high latitudes. This paper improves the klobuchar model expressed in the form of 9 parameters. Not only this model can keep the ionospheric double-peak characteristic but also ensure global fitting precision. In order to obtain real-time ionospheric data outside regional monitoring network, this paper examines the precision of forecasting model based on ionosphere spherical harmonic coefficient. According to the results of comparison,the model in this paper can correct the ionospheric delay for the next 24 h up to 72 % in China. Globally, the correction accuracy reaches 70 % in the north hemisphere, while 69 % in the south hemisphere. As a result, the correction precision of the model is better than the model broadcasted by GPS.

Keywords COMPASS · Ionosphere · Klobuchar · Amplitude · Spherical harmonics · Magnetic symmetry

X. Gong (✉) · N. Xing · S. Zhou · Y. Cao · XiaogongHu · B. Wu
Shanghai Astronomical Observatory, Chinese Academy of Sciences, Shanghai 200030, China
e-mail: xqgong@shao.ac.cn

J. Sun et al. (eds.), *China Satellite Navigation Conference (CSNC) 2013 Proceedings*, Lecture Notes in Electrical Engineering 245,
DOI: 10.1007/978-3-642-37407-4_23,

23.1 Introduction

Ionosphere is usually instable and described by some empirical models, such as klobuchar, IRI and NeQuick, etc. IRI [1] model is built on large number of ionospheric sounding data, integration of multiple atmospheric modes and introduction of solar activity parameters and geomagnetic activity index. NeQuick model is based on the DGR profile proposed by Di Giovanni [2] and Radicella [2], and now it serves for Galileo's single frequency users after modification and optimization. IRI and NeQuick model can both describe the three-dimensional ionospheric image, simulate the ionosphere's double-peak structure [3] located on both sides of the equator. However, klobuchar model considers all of the free electrons concentrated on one spherical surface about 350–450 km height. Klobuchar model is especially suitable for mid-latitude zone. It is adopted for GPS and the precision is lower than NeQuick model.

Regional satellite navigation system also adopts klobuchar 8-parameter model for ionospheric delay. Domestic Hongping Zhang [4, 5], Jinsong Ping [4, 6] and Xiaoli Wu [4, 6] detail this model and analyze its correction precision in service area around China. Different from klobuchar model GPS use: this model is based under geographic coordinate system, and the ionospheric data fitting the model is from monitoring stations. In addition, when using this model in the southern hemisphere, the latitude should be taken absolute value. In order to view the accuracy of this model, the ionospheric delay calculated by this model is compared with the Global Ionospheric Maps (GIM) [7] data in UTC3 on November 3, 2012. Then draw the difference as shown in Fig. 23.1. The horizontal axis and vertical axis respectively represent the longitude and latitude with degree as unit. Color depth expresses vertical total electron content with TECU as unit. From Fig. 23.1, average error around China's region is below 10 TECU [6], correction precision around the equator is low and in the northern hemisphere is better than in the southern hemisphere.

This paper first introduces regional system's klobuchar 8-parameter model and analyses its disadvantages, then designs four models to discuss the optimum fitting method of global klobuchar model. It had better to examine the forecasting

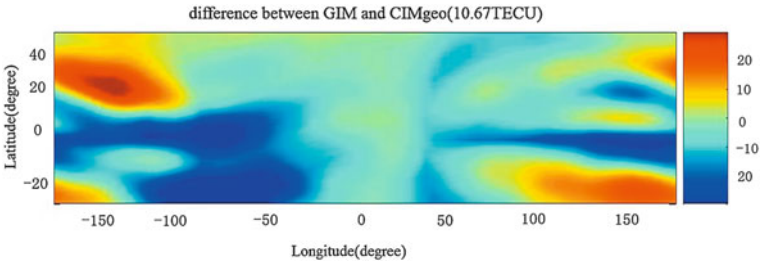

Fig. 23.1 Difference of ionospheric delay computed between COMPASS model and GIM. The *horizontal axis* represents longitude and the *vertical axis* represents the latitude in degrees

precision of ionospheric model if we want to obtain real-time ionospheric data outside China's region. Subsequently the improved klobuchar model is fitted using measured data of monitoring stations and forecasting ionospheric data. At last, the ionospheric delay calculated by this model is compared with GIM and dual-frequency measured data to give out the model's correction precision around China's region as well as in the globe. In addition, some conclusions are given to provide reference for China's global navigation satellite system.

23.2 The Klobuchar 8-Parameter Model of Regional Satellite Navigation System

23.2.1 Model Formula

Klobuchar model consider the ionospheric delay in the same latitude can be expressed by trigonometric cosine function as below.

$$I_z(t) = \begin{cases} A_1 + A_2 \cos\left(\dfrac{2\pi(t - A_3)}{A_4}\right), & |t - A_3| < \dfrac{A_4}{4} \\ A_1 \quad , & \text{others} \end{cases} \tag{23.1}$$

where I_z is the ionospheric delay in seconds, t represents the local time in seconds. For regional navigation system, flat-field A_1 and initial phase A_3 has the same value with GPS's model, usually set 5 ns and 50400 s. The remaining two parameters amplitude A_2 and period A_4 are usually described by 3-order polynomial on the latitude, see Eqs. (23.2, 23.3).

$$A_2 = \begin{cases} \sum\limits_{n=0}^{3} \alpha_n |\phi_g|^n, & A_2 \geq 0 \\ 0 \quad , & A_2 < 0 \end{cases} \tag{23.2}$$

$$A_4 = \begin{cases} \sum\limits_{n=0}^{3} \beta_n |\phi_g|^n, & A_2 \geq 72,000 \\ 72,000, & A_2 < 72,000 \end{cases} \tag{23.3}$$

where α_n, β_n(n = 1, 2, 3, 4) is third-order polynomial coefficients of amplitude and period, ϕ_g represents geographic latitude of puncture points.

23.2.2 Model Analysis

There are two steps to generate klobuchar model for regional navigation system. Firstly, according to Eq. (23.1), calculate amplitude and period for each latitude by

fixing flat field and initial phase. By the way it is necessary to compress the ionospheric puncture point data every three latitudes. Then fit all the amplitude and period by three-order polynomial on the latitude. In order to analyze the reason why klobuchar model's accuracy loses, we realize the above two steps using measured data from monitoring stations on November 3, 2012. Select 30° latitude to analyze, see Fig. 23.2. The horizontal axis represents the local time with hour as unit, and the vertical axis represents the vertical ionospheric electron content, with TECU as unit. Yellow dots are the measured data of puncture points. The black curve is drawn using 4 parameters calculated from the first step, meanwhile the red curve using 8 parameters from the second step. It is clear to see the black curve can basically express the yellow area, that is to say, the fitting of 4 parameters has high accuracy. However great deviation between red curve and black curve has taken place in the fitting of three-order polynomial of amplitude.

In order to view the three-order polynomial fitting more clearly, draw the amplitude of each latitude in Fig. 23.3. The horizontal axis represents latitude with degree as unit, and the vertical axis represents the value of amplitude with TECU as unit. The blue '*' are calculated using ionospheric puncture point data of monitoring stations, then fit the blue curve using three-order polynomial on the latitude. For comparative analysis, it is helpful to draw the amplitude fitted using false puncture points interpolated from GIM data. See symbol 'o' in Fig. 23.3.

As you can see from Fig. 23.3, the fitting mode being used by regional navigation system has high accuracy in middle and low latitude, the blue curve basically agrees with the read circles. But when providing global service, it will bring great error, since the blue dotted curve deviates a lot from the read circles in the southern hemisphere and the high latitudes of the northern hemisphere.

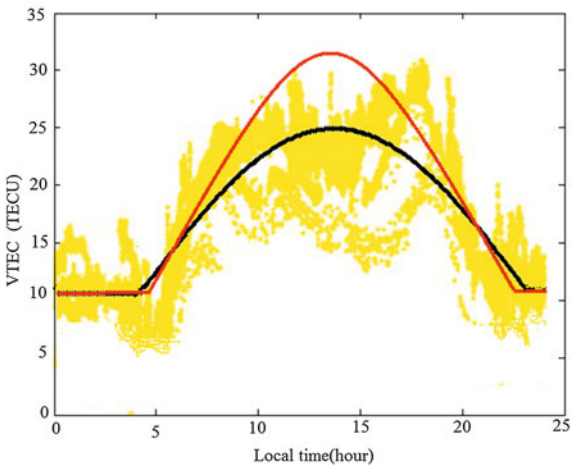

Fig. 23.2 Ionospheric measurement data,4-para and 8-para curve in 30° of the northern hemisphere

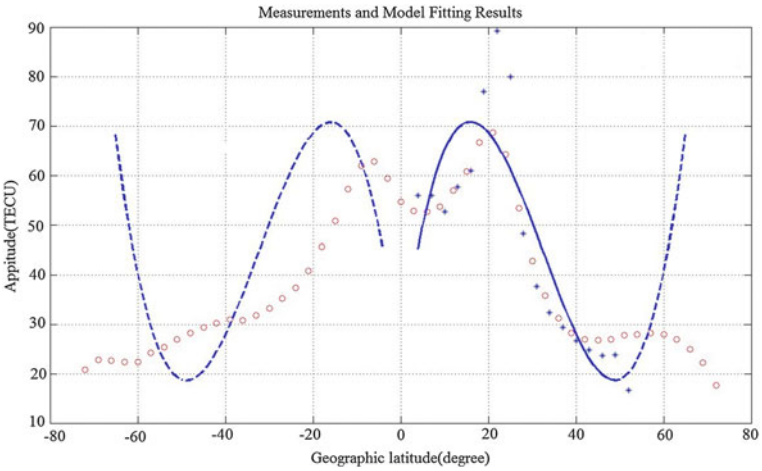

Fig. 23.3 Cubic polynomial fitting of each latitude's amplitude

23.3 The Global Ionospheric Klobuchar Model

23.3.1 Selection of the Global Klobuchar Model's Parameters

Considering ionospheric anomalies in the two polar regions, the global scope in this paper refers to negative 75°–75° of latitude. In order to find the best fitting method of amplitude, four kinds of models are designed in geomagnetic coordinate system as shown in Table 23.1, the ionospheric data is interpolated from GIM data on November 3, 2012.

Model 1 is a global average model similar to klobuchar model GPS use, unable to describe the double-peak structure on both sides of equator, see the blue curve in Fig. 23.4. Mode 2, 3 and 4 only fit the model in the northern hemisphere, therefore the ionospheric delay in the southern hemisphere is symmetric about the equator. Comparing model 2 (pink curve) with model 3 (red curve), find that three-order polynomial cannot accurately express the peak of amplitude, thus it is necessary to use four-order polynomial. In addition, the amplitude of north hemisphere is not

Table 23.1 Methods of modeling for klobuchar's parameters

Model	Detail
Model 1	Using data of the globe, three-order polynomial
Model 2	Using data of the north hemisphere, three-order polynomial
Model 3	Using data of the north hemisphere, four-order polynomial
Model 4	Using data of the north hemisphere and symmetry from the south hemisphere, four-order polynomial

Table 23.2 RMS of different fitting methods

	Model 1	Model 2	Model 3	Model 4
RMS	7.8	5.3	3.4	2.9

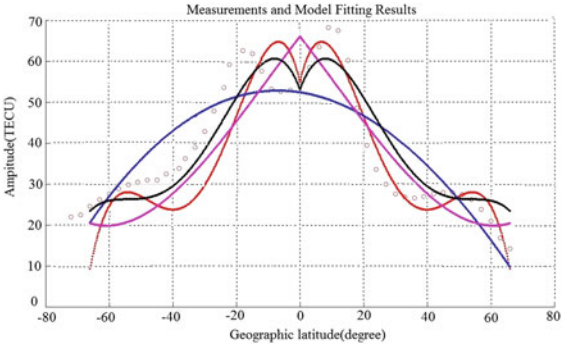

Fig. 23.4 Polynomial fitting of global klobuchar model's each amplitude. The *horizontal axis* indicates geographic latitude in degree, the *vertical axis* represents the amplitude in TECU

completely symmetric with that of south hemisphere. In order to achieve global optimal fitting result, model 4 is designed. First set the ionospheric data of the southern hemisphere symmetric to the northern hemisphere, then fit this model using four-order polynomial, as black curve shows, this method can ensure the precision of both north and south hemisphere. At this time, the Eq. (23.2) is modified to Eq. (23.4). From Table 23.2, we also can see that this model's RMS is less that the others.

$$A_2 = \begin{cases} \sum_{n=0}^{4} \alpha_n |\phi_g|^n, & \text{当} A_2 \geq 0 \\ 0, & \text{当} A_2 < 0 \end{cases} \tag{23.4}$$

23.3.2 Data Acquisition Outside China

The regional navigation system cannot obtain real-time global ionospheric observations. It is a good choice to use the ionosphere background field to generate false ionospheric puncture point data outside China. This section examines the precision of forecasting model based on ionosphere spherical harmonic coefficients, and compared with IRI and GIM.

The ionospheric delay calculated by IRI model, forecasting model based on the spherical harmonic coefficients and GIM in every day of 2011 are drawn in Fig. 23.5. The horizontal axis represents day of year, the vertical axis represents the total electron concentration in TECU. This paper's forecasting value (green)

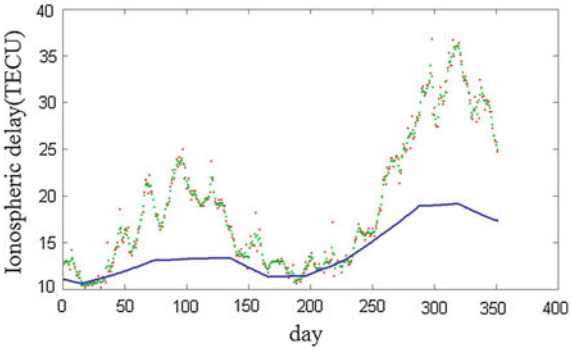

Fig. 23.5 The ionospheric delay calculated by IRI model, forecasting model based on the spherical harmonic coefficients and GIM

and GIM data (red) are in good agreement, the precision of IRI model is not so high. Statistics of difference from GIM indicates that the accuracy of this paper's foresting model is up 85 %, meanwhile IRI model is only 62 %.

23.4 Analysis of the Ionospheric Model's Correction Accuracy

Integrated monitoring stations' data with the forecasting ionospheric data, referring to Eqs. (23.1), (23.3) and (23.4), the klobuchar model can be fitted. Then use this model to calculate ionospheric delay of any place at anytime. This section designs two paths to verify the accuracy of the model. One is comparison with GIM data provided by IGS, the other is comparison with measured data of IGS stations around the world.

23.4.1 Comparison with GIM

Mode 1 in the second section is similar to fitting model GPS uses, so it is retained as a reference. With GIM data as benchmark,compare the ionospheric delay correction precision of regional navigation system, model 1 and model 4. The statistical method is as below.

First the globle is divided into 5° × 5° grid,then calculate ionospheric delay of grid points using each model at 12 Clock of Beijing time on january 3, 2012. $Model_k$ is ionospheric delay calculated by each model, while Tec_k is that calculated by GIM, with unit in TECU. So ionospheric correction accuracy *CorrectRatio* and average correction error *CorrectError* of each mode can be calculated by Eqs. (23.5) and (23.6) respectively.

Table 23.3 Mean correction precision of different ionospheric models in China

Latitudes	COMPASS (%)	Model 1 (%)	Model 4 (%)
0°–20°	67.5	64.8	68.6
20°–35°	76.4	69.2	71.9
35°–50°	78.2	69.7	77.6
Mean	74.0	66.9	72.3

Table 23.4 Mean correction error of different ionospheric models in China (TECU)

Latitudes	COMPASS	Model 1	Model 4
0°–20°	12.2	12.7	12.1
20°–35°	7.8	8.5	8.8
35°–50°	4.5	8.4	5.1
Mean	8.1	9.8	8.6

$$CorrectRatio = \sum_{k=1}^{n} \left(1 - \frac{|Model_k - Tec_k|}{Tec_k}\right) \Big/ n \tag{23.5}$$

$$CorrectError = \sum_{k=1}^{n} \frac{|Model_k - Tec_k|}{n} \tag{23.6}$$

where n represents total number of puncture points.

Tables 23.3, 23.4 give the Ionospheric average correction accuracy and Correction error of three model in Chinese area. From Table 23.3 in can see, using this model in China could reach 72 % of the correction accuracy. And regional COMPASS system equivalent accuracy. But the use of class GPS8 parameters, accuracy is only 66.9 % in China region.

Tables 23.4, 23.5 give the Ionospheric average correction accuracy and Correction error of three model in the globle. Globally, the correcting accuracy reaches 70 % in the north hemisphere, while 69 % in the south hemisphere. As a

Table 23.5 Mean correction precision of different ionospheric models globally

Latitudes	COMPASS (%)	Model 1 (%)	Model 4 (%)
50° to 75°	15.9	60.5	68.2
0° to 50°	73.5	64.4	72.3
−30° to 0°	62.8	65.4	69.6
−30° to 50°	67.5	64.7	71.4
−75° to −50°	31.6	59.3	66.8
均值	50.4	62.8	69.6

Table 23.6 Mean correction error of different ionospheric models globally (TECU)

Latitudes	COMPASS	Model 1	Model 4
50° to 75°	97.0	9.2	5.3
0° to 50°	7.4	10.5	9.2
−30° to 0°	12.9	9.7	12.5
−30° to 50°	8.8	12.6	10.2
−75° to −50°	48.4	14.5	11.4
Mean	34.9	11.3	9.7

result, the precision of the model is better than the model broadcasted by GPS (Table 23.6).

23.4.2 Comparison with Measured Data of IGS Stations

Dual-frequency measured data discounted hardware delay can actually express the ionospheric delay, thus comparison with delay calculated by other models can directly reflect the ionospheric correction accuracy. So select 8 IGS stations around the world as follows:

scor (70.8 N, 21.9 W), opmt (48.8 N, 2.3 E), pdel (37.7 N, 154.2 W), nklg (1.2 N, 9.6 E)
brft (3.8 S, 21.5 W), kouc (20.5 S, 164.2 E), kerg (49.3 S, 70.2 E), maw1 (67.6 S, 62.8 E)

The value in the brackets are in degrees, S and N is separately on behalf of the north and south hemisphere, while E, W behalves the east and west hemisphere.

Calculate ionospheric delay of puncture points at every epoch on January 3, 2012. There are four models used: dual-frequency measured data, GPS's model, regional system's model and this paper's model.

In order to visually reflect ionospheric delay correction situation of each model, draw ionospheric puncture points' data of different latitudes. As shown in the following four illustrations: the horizontal axis represents time in hours, and the vertical axis is ionospheric delay in meters. Yellow, red, green and blue dots respectively describe ionospheric delay calculated using dual-frequency data, this paper's model, GPS's model, and regional system's model.

Figure 23.6 shows that in the mid-latitudes of the southern hemisphere, the correction accuracy of regional system's model is a little lower, while this paper's model and GPS model are more suitable. From Figs. 23.7, 23.9, we can see in the equatorial region, the correction effect of this paper's model model is better than the GPS model. As shown in Fig. 23.8, the accuracy of regional system's model is equivalent to this paper's model in service area around China.

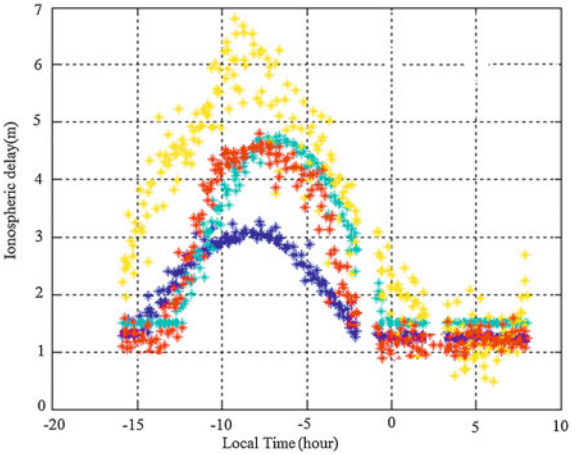

Fig. 23.6 The middle latitudes in the southern hemisphere

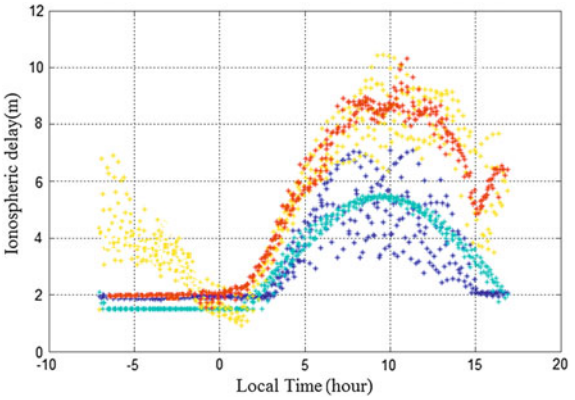

Fig. 23.7 The low latitude in the northern hemisphere

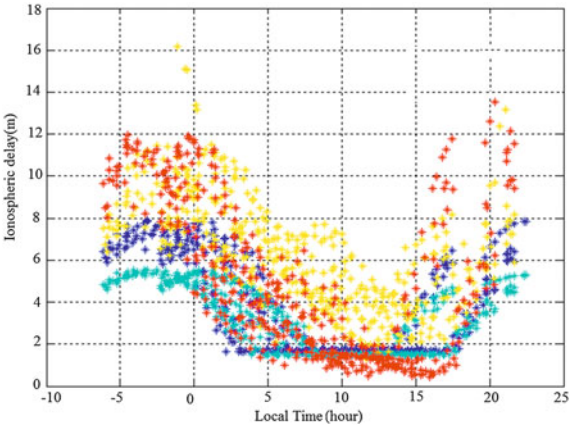

Fig. 23.8 The middle latitudes in the northern hemisphere

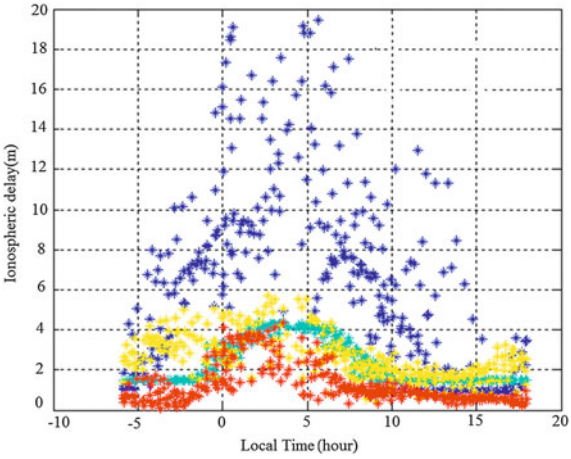

Fig. 23.9 The higher latitudes of the southern hemisphere

23.5 Conclusions

Regional navigation system corrects ionospheric delay using klobuchar 8-parameter model, and long-term monitoring shows that the correction accuracy of this model around China is up to 74 % [8] and the mean error of this model is about 12 TECU in China's service area.

When broadcasting global ionospheric model, COMPASS system should ensure the precision index across the globe including zones of high latitudes and near the equator. Analysis of klobuchar model's parameters shows that: third-order polynomial is unable to reflect changes of amplitude correctly, and can not describe the double-peak characteristic of the day-time ionosphere. As a result, the precision of fitting global klobuchar model is lost. Based on the above analysis, this paper presents klobuchar 9-parameter model. It uses 4-order polynomial on the latitude to fit the amplitude and 3-order polynomial to fit the period, the ionospheric delay in the southern hemisphere would be calculated through taking absolute value of the latitude.

Using both measured data of monitoring stations and forecasting ionospheric data, the method in this paper can correct the ionospheric delay for the next 24 h up to 72 % in China. Globally, the correcting accuracy reaches 70 % in the north hemisphere, while 69 % in the south hemisphere. As a result, the precision of the model is better than the model broadcasted by GPS. In other words, comparing with the model of regional system, this method can ensure correction accuracy within the service area,while significantly improves correction accuracy in high latitudes and in the equatorial region. Thus, the global correction accuracy index can be achieved. Of course, this method also needs long-term verification in the system.

Acknowledgments This paper is supported by the Natural Sciences Foundation of China (Grant No. 11103064), the Shanghai Committee of Science and Technology, China (Grant No. 11ZR1443500), the National High Technology Research and Development Program of China (Grant No. 2013AA122402) and China Satellite Navigation Conference (Grant No. CSNC2011-QY-01).

References

1. Jodogne JC, Nebdi H, Warnant R (2004) GPS TEC and ITRC from digisonde data compared with NEQICK model. Adv Space Res 2:269–273
2. Klobuchar J (1987) Ionospheric Time-Delay algorithm for single-frequency gps users [J]. IEEE Trans Aerosp Electron Syst (ISSN 0018-9251) AES-23: 325–331
3. Fang HX, Weng LB, Yang SG, et al (2012) The research of IRI, NeQuick and Klobuchar model. Progress Geophys 27(l):0001–0007
4. Zhang HP, Ping JS, Zhu WY et al (2006) Brief review of the ionospheric delay models. Progress Astron 24(1):16–26
5. HongPing Z (2006) Study on GPS based China regional ionosphere monitoring and ionospheric delay correction [D]. Ph.D. Dissertation, Shanghai Astronomical Observatory, Chinese Academy of Sciences, Shanghai China
6. WU XL, PING JS, LIU L et al (2011) Hardware delay solution of regional satellite navigation system. Geomatics and information science of Wuhan University 36(10)
7. Schaer S,Gurtner W,Feltens J (1998) IONEX: The IONosphere MaP Exchange Format Vesion 1[C]. In: Proceedings of the 1998 IGS Analysis Centers Workshop 1 ESOC, Darmstadt, Germany, February, 1998, pp 9–11
8. Cao YL, Hu XG et al (2012) The wide-area difference system for the regional satellite navigation system of COMPASS. Sci China Phys Mech Astron 55(7):1307–1315

Chapter 24
Analysis of Effect About On-Orbit Satellite Properties to Pseudo-Range Measurement

Hui Yang, Meihong Li and Hong Mi

Abstract Pseudo-range measurement is effected with on-orbit satellite properties. By the analysis and compares with the experimentation and on-orbit data, it gets the satellite factors which influence the pseudo-range, including the satellite orbit motion, attitude motion, temperature variation, antenna phase center variation, and time-delay's stability of channel. It also analyzes the effects mechanism and magnitude of these factors, which has the significances to improve the correction precision of pseudo-range measurement.

Keywords On-orbit satellite properties · Pseudo-range · Orbit · Attitude

24.1 Introduction

The navigation principle of satellite is based on Pseudo-range measurement. The precision of the navigation is directly decided by the precision of Pseudo-range measurement when the GDOP value is given [1, 2]. The factor influencing precision of pseudo-range measurement is from three parts: on-orbit satellite property, space segment influences, the receive equipment and the influence of the environment. We just analyze on-orbit satellite property aiming to roundly find the correlative factors which influence the precision of pseudo-range measurement, then analyze the effects mechanism and magnitude of these factors and try our best to compare the data from ground test with that on-orbit test.

H. Yang · M. Li (✉) · H. Mi
China Academy of Space Technology, Beijing, People's Republic of China
e-mail: meihong_li@163.com

H. Yang
e-mail: 2008yanghuiling@sina.com

J. Sun et al. (eds.), *China Satellite Navigation Conference (CSNC) 2013 Proceedings*, Lecture Notes in Electrical Engineering 245,
DOI: 10.1007/978-3-642-37407-4_24,

24.2 The Properties of Pseudo-Range

Using the ground monitoring receivers to observe on-orbit satellite multifrequency each branch consecutively [3], after processing data, we find that the difference between pseudo-range and carrier range presents many kinds of change laws, mainly including fast change and slow change, which presents strongly day-periodic repeat, as shown in Fig. 24.1.

24.3 The On-Orbit Parameters Affecting Pseudo-Range Measurement

We learn pseudo-range fluctuation is periodic from the property of pseudo-range measurement. First of all we pay attention to the generation of navigation information and the transiting path in satellite. During flying time, satellite searches and catches the uplink signals from ground, according to satellite time information and orbit information, and the phase of preset code. Navigation mission processor receives the uplink injection signals and range code information, and then completes the formatting arrange of downlink navigation information.

During the flying segment, whether injection or not, downlink receives the navigation data information from navigation mission processor, six spread

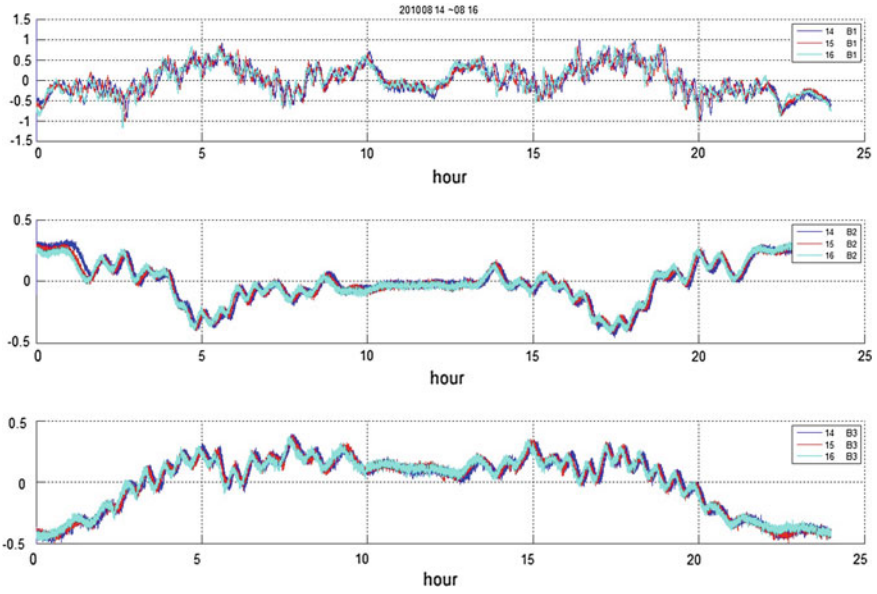

Fig. 24.1 *Curve* pseudo-range fluctuation for 3 days

spectrum synchronization modulates B1, B2, B3 tri-frequency orthogonal microwave, and sends the signals to emission antenna through power amplifier. Ground devices receive the signal from satellites, then measure the distance between the satellite antenna phase center and the ground antenna phase center, named pseudo-range.

The factors arising pseudo-range fluctuation stems from satellite system, space segment, and ground segment. The factors related to satellite system include orbit motion and antenna phase center change along with satellite attitude variation, multipath disturbance related to Satellite configuration, satellite payload channel time-delay fluctuation,channel time-delay variation because of satellite temperature changing, and multipath disturbance inside navigation antenna (different frequency signals note). The following sections analyze every factor one by one, considering the periodic property of pseudo-range fluctuation.

24.3.1 Pseudo-Range Fluctuation Caused by Orbit Movement

Satellite's orbit changes due to perturbation of the Earth, Sun and Moon [4]. Figure 24.2 shows the change of semi-axis during 1 year.

The perturbation has relationship with satellite shape, optical character, antenna phase center disagree with mass center, attitude control. Figure 24.2 is just a special example. Generally, perturbation is predictable with the aid of engineer parameters. In practice, the knowledge of satellite attitude scheme and attitude control on orbit is a key problem to the use of engineer parameters.

The jet of engine will change satellite orbit, and the satellite engineers set a rule that the number of engine jet is as little as possible (Generally, one jet can cause the several meters change on semi-axis), and the jet control is plan-able. Such as, the use of momentum wheel can avoid the random jet, and the orbit correction and momentum wheel unloading are predictable and plan-able. The design can avoid the break due to the momentum wheel unloading.

The orbit change due to perturbation and attitude control is not day-period.

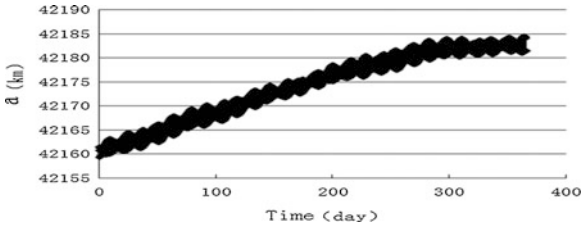

Fig. 24.2 *Curve* IGSO's semi-major axis for 1 year

24.3.2 Antenna Phase Center Variation Lead to Pseudo-Range Variation Caused by Satellite Attitude Movement

If the antenna phase center is not at the center of mass, satellite's attitude variation will cause the change of pseudo-range. The mechanism of pseudo-range variation caused by roll, pitch and yaw attitude change are the same. Consider the changes of real roll and pitch attitudes in orbit are usually small, it is only necessary to illuminate the change of yaw attitude. The antenna phase center variation lead to pseudo-range variation caused by satellite yaw attitude change is shown in Fig. 24.3.

As shown in Fig. 24.3, if the ground station is at the sub-satellite point, when the yaw attitude changes, the pseudo-range is invariable; when the ground station is not at the sub-satellite point, the pseudo-range will change with the variation of yaw attitude. Suppose the coordinate of antenna phase center is $(x_1, y_1, z_1)^T$ in the satellite body coordinate system, the orbit oriental elements are (i, Ω_λ, w, f), the coordinate of the ground station in the earth-fixed coordinate system is $(x_{2G}, y_{2G}, z_{2G})^T$, the roll angle is R, the pitch angle is P, the yaw angle is Y, the pseudo-range from the antenna phase center and the ground station can be calculated as follows:

1. Transform the ground station coordinate from the earth-fixed coordinate system to the satellite body coordinate system.

$$u = w + f \tag{24.1}$$

$$\begin{aligned} M\_GtoB = {} & R1\_TRAN(-90) * R3\_TRAN(90) * R3\_TRAN(u) \\ & * R1\_TRAN(i) * R3\_TRAN(\Omega_\lambda) \end{aligned} \tag{24.2}$$

$$M\_OtoB = R2\_TRAN(P) * R1\_TRAN(R) * R3\_TRAN(Y) \tag{24.3}$$

$$M\_GtoB = M\_OtoB * M\_GtoO \tag{24.4}$$

where, R3_TRAN (u) denotes the angle u rotate around Z axis, R1_TRAN (i) denotes the angle i rotate around X axis, R3_TRAN ($\Omega\lambda$) denotes the angle $\Omega\lambda$ rotate around Z axis;

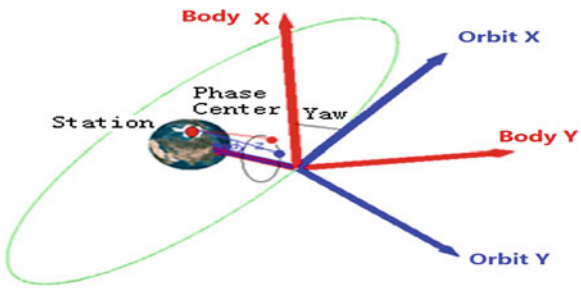

Fig. 24.3 Pseudo-range variation caused by satellite yaw attitude change

$$(x_{2B}y_{2B}z_{2B})^{T} = M\_GtoB * (x_{2G}y_{2G}z_{2G})^{T} \quad (24.5)$$

2. In the satellite body coordinate system, calculate the distance between the ground station and the antenna phase center.

$$d = ||(x_1y_1z_1)^{T} - (x_{2B}y_{2B}z_{2B})^{T}|| \quad (24.6)$$

The designed attitude error index of the three-axis stable satellite is usually within 0.2°. However, the actual attitude error data in orbit are better than the demand index. The following table shows the pseudo-range variation to satellite's attitude with some typical satellite engineering parameters and some given ground station such as Beijing. Select different time points, the value of pseudo-range variation will be different; however, the numerical quantity level is basically the same.

From the Table 24.1, GEO satellite attitude wave cause little effect on the pseudo-range variation, the pseudo-range wave $\leq$0.3 mm, the contribution to the observation of pseudo-range $\leq$1 ps. As for the IGSO satellite the yaw axis is controlled to let the X axis point to the sun direction, the IGSO satellite attitude wave cause greater effect on the pseudo-range variation, the pseudo-range wave <40 mm, the contribution to the observation of pseudo-range <0.14 ns. There are no period change rules of the roll and pitch, the affect of the pseudo-range is relatively small. The yaw angle wave is changed in daily period rule, these changes can be modified by the ground under the condition of the attitude angle can be real time obtainable.

24.3.3 The Mass Center Change Caused by the Consumption of Propellant

With the consumption of the propellant of the in orbit satellite, the mass center of the satellite will be changed. As mentioned before the change of the mass is the change of the satellite antenna phase center. The attitude error will affect the

Table 24.1 Pseudo-range variation due to satellite's attitude

No.	The variation range of three axis attitudes	Pseudo-range variation (mm)
GEO1	Roll: −0.01° ~ 0.01°	Beam 1: 0.24
	Pitch: −0.01° ~ 0.01°	Beam 2: 0.24
	Yaw: −0.14° ~ 0.02°	Beam 3: 0.24
GEO2	Roll: −0.01° ~ 0.02°	Beam 1: 0.27
	Pitch: 3.18° ~ 3.21°	Beam 2: 0.27
	Yaw: −0.14° ~ 0.04°	Beam 3: 0.28
IGSO1	Roll: −0.01° ~ 0.01°	Beam 1: 38.45
	Pitch: −0.01° ~ 0.01°	Beam 2: 38.54
	Yaw: 42.7° ~ 136.8°	Beam 3: 38.34

measure value of pseudo-range variation. Take the GEO satellite for example, this type of satellite consumes relatively more propellant in orbit, and the change of the mass center is a lot. The following Fig. 24.4 shows the change of the mass center with the consumption of the propellant.

As showing above, when satellite works in orbit, the fuel consumption is planed without random state, fuel consumption of every orbit maneuver or uninstall is foreseeable beforehand and measurable afterwards, the influence of measurement error to center of mass is very little.

When satellite works in orbit, to master the centroid changing rule along with fuel consumption is useful to improve distance measurement error. The changing of centroid influences the torque of solar pressure to satellite, which is reflected to the attitude change of satellite. As showing above, this influence is of millimeter or centimeter.

24.3.4 Pseudo-Range Fluctuation Caused by Multipath Effects from Layout

Pseudo-range measurement will be affected while outer equipment is in shadow of satellite. For this reason, it is one of the important constrains of the satellite design that the antenna beam should not be shadowed by the outer equipment. With example of one kind navigation satellite construction design, we analyses the multipath effects caused by outer equipment. For the electromagnetic field reciprocity principle, the receive antenna beam will be analyzed, as shown in Fig. 24.5.

Assume the view field of navigation satellite antenna is about ±10°, the first side lobe of the antenna is at ±30° and 20 dB below the main lobe. So, the side lobe will not form interference to the main lobe. In the design of equipments layout, interference between beams is already considered. Other items onboard should not shadow the view field of antenna. Large area equipments should be laid

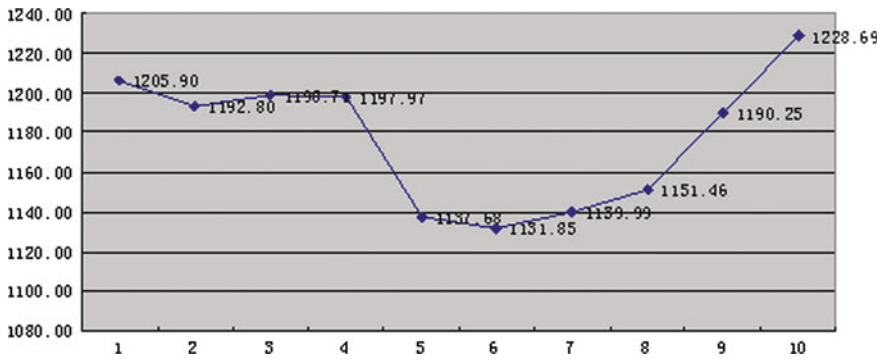

Fig. 24.4 *Curve* satellite's mass center to the propellant consumption

on back lobes of antenna, such as solar arrays, far from the view field of antenna. Through the geometrical reflection and antenna beam coverage analysis, multipath interference which causes pseudo-range fluctuation wouldn't exist.

24.3.5 Pseudo-Range Fluctuation Caused by the Channel Delay Fluctuation of the Satellite Payload

Under the condition of constant exterior environment temperature, the channel delay of the satellite payload is fluctuant caused by the excursion of the circuit parameters. The delay fluctuation is less than 0.1 ns in the long-term field test on the ground, consequently affects the measured pseudo-orange fluctuation by mm level. The error is random and not periodically.

24.3.6 Channel Delay Fluctuation Caused by Satellite's Temperature Variation

When the temperature is constant, the influence made by the delay has been talked in Sect. 24.3.5, however, the temperature in the satellite is changing, we will analyse the delay error made by temperature. Now we will analyze the law of the temperate changing of the typical orbit of stationary satellite and synchronous satellite.

The temperate change from internal to external of the satellite is made by solar location. The solar will illuminate the different face of the three-axis stable satellite in different time. Because of the difference of the orbit of the solar and the orbit of the satellite, the faces of the three-axis stable satellite illuminated are different in different season, which makes heat flow change notably. To the lean-obit satellite, the satellite will be illuminated by the solar in a fix face, so the heat flow change little. When the solar run in the plane of the orbit, the heat flow outside of the three-axis stable satellite is invariant, the same as it in the Spring Equinox. Because the solar rise from the east, the southern and northern face of the satellite will not be illuminate.

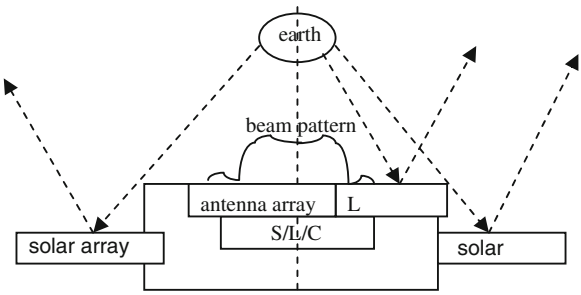

Fig. 24.5 Antenna receiving wave

To sum up, the external heat flux of satellites fluctuates periodically. A day or a year is a cycle. Satellites on different orbits present different fluctuation of external heat flux. The thermal design of satellite should be done according to the fluctuation of external heat flux, so as to ensure the onboard equipments working in a relatively stable temperature.

Different satellites have the same requirements on temperature tolerance for onboard equipments. For general electronic equipments, it's $-5° \sim 55°$. According to this range of temperature variation, the range of delay variation is $0.35 \sim 1.9$ ns, as field test results. However, the results of satellites' thermal design are much better than the requirements for onboard equipments. For GEO, the range of environment temperature for onboard equipments is below 8 °C for a day and $10 \sim 20$ °C for a year. For IGSO, the range of environment temperature for onboard equipments is about 6 °C for a day and shows no annual variation. Typical measurement data for temperature is as shown in Figs. 24.6, 24.7.

The above variables are stable as the on-orbit measurement data. For on-orbit environment temperature, the pseudo-range variation caused by satellite's downlink channel delay fluctuation is below 0.25 ns.

24.3.7 Multipath Inherence in Antenna

The Pseudo-range instability of SVN49 which is one of the GPS IIR-M satellites is introduced, in order to understand the inner-design of typical satellite antenna.

24.3.7.1 Pseudo-Range Fluctuation Analysis on GPSIIRM SVN49

The payload of this satellite has an additional signal channel compared with the other GPS satellites. The antenna system of the satellite consist feed network plus

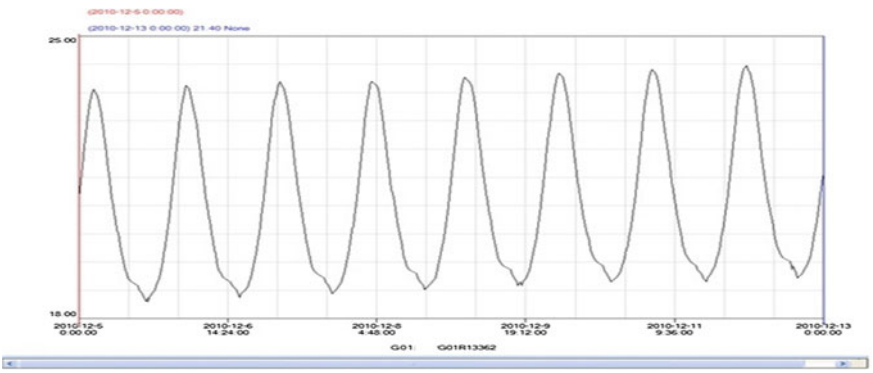

Fig. 24.6 *Curve* type temperature of GEO satellite

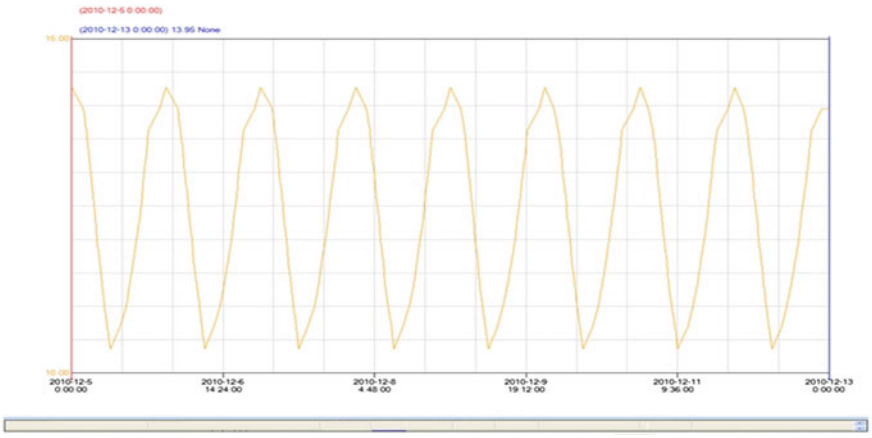

Fig. 24.7 *Curve* type temperature of IGSO satellite

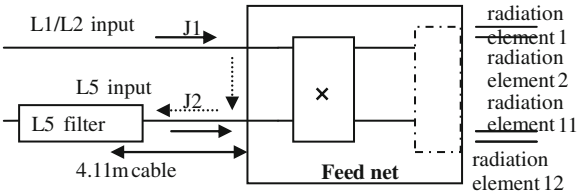

Fig. 24.8 Navigation antenna of GPS/SVN-49

antenna array. The navigation signal is broadcast by antenna array through feed network, which is illustrated by Fig. 24.8.

The array comprises 12 units, and feed module is a "one in 12 out" feed networks, which make the power pattern is like a saddle. The feed module has two inputs (J1, J2), one input (J1) feed in L1/L2 signals, which is adopted by the other satellites. Another input (J2) feeds in L5 signal. J1 and J2 are insulated, and the other satellites have no L5 signal, and J2 is put load and matched.

SVN49 feeds the L5 signal into the feed network through isolation part and radiated by antenna. The L5 antenna beam is actually narrow beam, for the range-phase relationship is changed by isolation part.

Pseudo-range instability of SVN49 is founded in orbit. The reason is the L1/L2 signal goes into the input of L5 channel, which is feed back when reach to the L5 signal filter, and go into the L5 channel again. The feedback signal added by the L1/L2 signal, and form the Multipath interferes, which is the major reason of Pseudo-range instability.

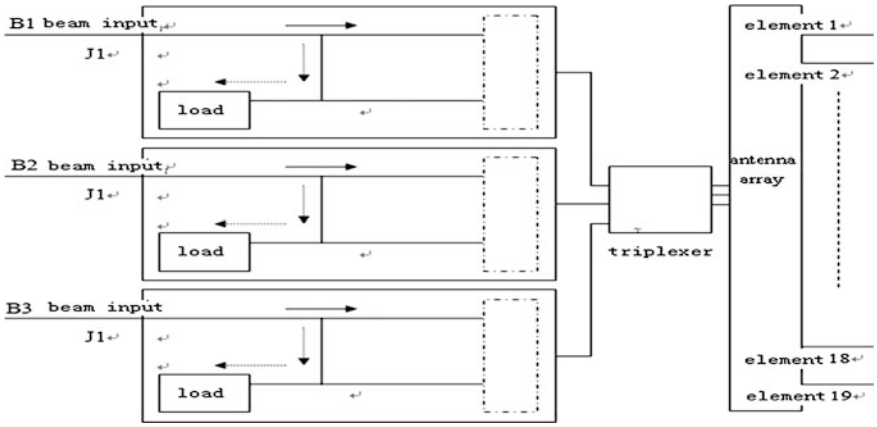

Fig. 24.9 Navigation satellite antenna

24.3.7.2 Inside Design of Antenna

The antenna feed network of GPS, which has a lower isolation between J1 and J2 than a narrowband designed antenna feed network normally, is designed for a broad band including L1, L2 and L5. The antenna feed network is designed for a narrow band. As shown in Fig. 24.9, signals broadcast through a triplexer before broadcasted by antenna array, the isolation requirement between any two beams is more than 25 dB, and the isolation in field test is better than 40 dB. Therefore, we can conclude that the isolation between RF channels can not cause a multipath effect on pseudo-range fluctuation.

The antenna feed network of use a matched load connect with the isolation end, which is different from the GPS SVN49 design that use the isolation end for L5 signal feed.

The antenna feed network of GEO satellite and IGSO satellite is all the same. Through theory analysis, the multipath effect inside satellite is not periodical, and it can also be avoided by considering the isolation between RF channels when the satellite is designing.

24.4 Conclusion

By the analysis above, it has follow conclusions:

1. Generally, the factors of on-orbit satellite properties affect the Pseudo-range measurement, including the satellite orbit motion, antenna phase center variation with attitude motion, multipath effects from layout, channel delay fluctuation of the satellite payload, Channel delay fluctuation caused by satellite

temperature variation and Multipath inherence in antenna (different frequency signals note).
2. The typical navigation satellites analyzed above avoid "Pseudo-range fluctuation caused by multipath effects from layout" and "Multipath inherence in antenna" for special design.
3. The typical navigation satellites analyzed above have follow characteristics:

   a. "Orbit movement". The perturbation is predictable with the aid of engineer parameters. Satellite automatism control is plan-able and predictable. The orbit change due to perturbation and attitude control is not day-period.
   b. "Antenna phase center variation with attitude motion". GEO attitude wave cause the observation of pseudo-range variation $\leq$1 ps. IGSO attitude wave cause the observation of pseudo-range variation <0.14 ns. These changes can be modified by the ground under the condition of the attitude angle can be real time obtainable.
   c. "Centroid changing brought by fuel consumption". The changing of centroid influences the torque of solar pressure to satellite, which is reflected to the attitude change of satellite without periodic characteristic.
   d. "The channel delay fluctuation of the satellite payload". The delay fluctuation is less than 0.1 ns in the long-term field test on the ground, consequently affects the measured pseudo-range fluctuation by mm level. The error is random and not periodically.
   e. "The channel delay variation caused by temperature variation". Under the on-orbit temperature condition, the periodic variation (with period of 24 h) of the delay fluctuation of the satellite downlink channel is less than 0.25 ns, the period of which is one day.

References

1. Han C, Liu L, Zhao J (2009) Conception, definition and evaluation of pseudo-range measurement. J Astronaut 30(6):2421–2425
2. Xu Q (2001) Space Geodesy-satellite navigation and precision positioning [M]. PLA Press, Beijing
3. Wu X, Zhou S, Hu X, Liu L, Feng X, Dong E (2011). Fluctuation analysis of regional navigation system. In: The 2nd China Satellite Navigation Conference
4. Renwei Z (1998) Satellite orbit & attitude dynamics and control [M]. Beijing University of Aeronautics and Astronautics Press, Beijing

Chapter 25
Towards a Precise Multi-GNSS Positioning System Enhanced for the Asia–Pacific Region

Xiaoming Chen, Herbert Landau, Feipeng Zhang, Markus Nitschke, Markus Glocker, Adrian Kipka, Ulrich Weinbach and Dagoberto Salazar

Abstract In June 2011, Trimble introduced the CenterPoint RTX service providing a real-time global centimeter level GNSS positioning service. The correction data stream is generated from the precise GNSS orbit and clock information derived from the Trimble world-wide CenterPoint RTX tracking network and delivered through L-band satellite links and Internet to support high precision real time applications in a number of high accuracy markets like precision agriculture, survey and construction. While the system initially was introduced supporting GPS and GLONASS satellites, developments have led to the inclusion of the QZSS satellite in early 2012. The paper describes the current status of the Trimble CenterPoint RTX system, its setup and its current performance. Special emphasis is put on the evaluation of the possibility to include BeiDou/Compass satellites. The authors have started to research the ability to integrate BeiDou/Compass into the RTX system. First results on the achievable orbit and clock quality for BeiDou/Compass satellites are presented when using the Trimble NetR9 receivers in the CenterPoint RTX tracking network.

Keywords BeiDou · CenterPoint RTX · Multi GNSS · Real-time PPP

25.1 Introduction

Mid of 2011 Trimble introduced the CenterPoint RTX service providing centimeter-accurate positions for real-time applications in static or kinematic applications. The CenterPoint RTX service broadcasts satellite orbit and clock corrections via multiple media to the client receivers, which carries out a PPP-like positioning

X. Chen (✉) · H. Landau · F. Zhang · M. Nitschke · M. Glocker · A. Kipka · U. Weinbach · D. Salazar
Trimble TerraSat GmbH, Haringstr. 19, Hoehenkirchen 85635, Germany
e-mail: Xiaoming_Chen@Trimble.com

J. Sun et al. (eds.), *China Satellite Navigation Conference (CSNC) 2013 Proceedings*, Lecture Notes in Electrical Engineering 245,
DOI: 10.1007/978-3-642-37407-4_25,

Fig. 25.1 Trimble CenterPoint RTX L-Band coverage using six geostationary satellites

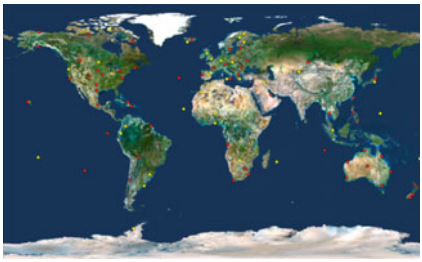

Fig. 25.2 Trimble CenterPoint RTX tracking network with NetR9 (*red*) and NetR5/8 (*yellow*) receivers

computation without assistance of other ground reference stations. Trimble CenterPoint RTX corrections are available from six geostationary satellites via L-band signals covering most of the main continents, as shown on Fig. 25.1.

In addition to the L-band transmission the RTX corrections are globally available for Trimble customers via NTRIP protocol and can be used for real-time applications. Trimble also offers a post-processing service based on CenterPoint RTX, which is available via a web interface www.TrimbleRTX.com [1].

After its introduction, the Trimble CenterPoint RTX service has been well accepted by customers in precision agriculture due to its high accuracy, high reliability, easy access and fast convergence. Trimble CenterPoint RTX has been also prepared for other precision applications like survey, GIS, construction, mining, natural hazard monitoring, etc. Products to monitor the reference station positions for infrastructure solutions and for other types of monitoring applications have been introduced by Trimble in 2012. This includes the support of RTX Positioning in Trimble NetR9 receivers resulting in centimetre accurate absolute positions in ITRF2008. Early 2012 the CenterPoint RTX service has been further enhanced by adding QZSS support. The inclusion of the QZSS satellite in the system has demonstrated around 20 % reductions in convergence time in the Asia Pacific region [2]. Further improvements are expected once the BeiDou/Compass system is added to the service.

25.2 Trimble CenterPoint RTX Global Tracking Network

One of the most important infrastructures of the CenterPoint RTX system is the global tracking network. The tracking network consists of ~100 Trimble receivers as illustrated in Fig. 25.2. Only Trimble NetR5, NetR8 and NetR9 receivers are used. In order to be future-proof, the NetR5 and NetR8 receivers (yellow circles in Fig. 25.2) are being replaced with modern Trimble NetR9 receivers (red circles, 57 receivers in early 2013). The Trimble NetR9 receiver

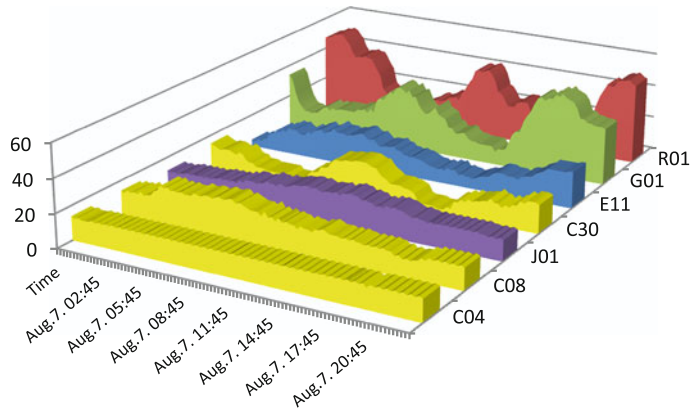

Fig. 25.3 Number of tracking stations observing different satellites during a day

uses 440 channels and is capable of tracking the GPS, GLONASS, Galileo, BeiDou/Compass and QZSS satellites. Due to the geographic distribution of stations and satellites, different satellites are tracked by a different number of stations as can be seen in Fig. 25.3. GPS and GLONASS satellites can be tracked by all receivers in the network; the other satellite systems can only be tracked by the NetR9 receivers. As an example for medium earth orbit (MEO) satellites, E11, G01 and R01 have been chosen and are shown in Fig. 25.3. They show a typical pattern, which reflects the density of the network in Europe and North America. BeiDou/Compass satellite C08 and QZSS satellite J01 represent the group of satellites in inclined geosynchronous orbits (IGSO) and BeiDou/Compass satellite C04 shows the almost constant graph of a satellite on a geostationary orbit (GEO).

Stations with good Internet connection are required to keep the latency of correction generation as low as possible. Precise station coordinates are determined in the ITRF2008 coordinate frame via weekly PPP solutions and the coordinate changes are monitored via daily PPP solutions [1]. In addition, the station positions are monitored continuously with real-time RTX positioning resulting in 1 Hz position estimates. If necessary, the station coordinates used in the RTX system are intermittently updated based on the weekly PPP solutions. This might happen in cases of earthquakes, antenna movements or other effects influencing the station positions.

25.3 Trimble CenterPoint RTX Performance

The service specification for Trimble CenterPoint RTX is currently described as 3.8 cm horizontal accuracy (95 %) after a convergence time of typically less than 30 min. This is achieved and has been demonstrated in dynamic scenarios like precision agriculture. In an ideal situation of a low multipath fixed reference

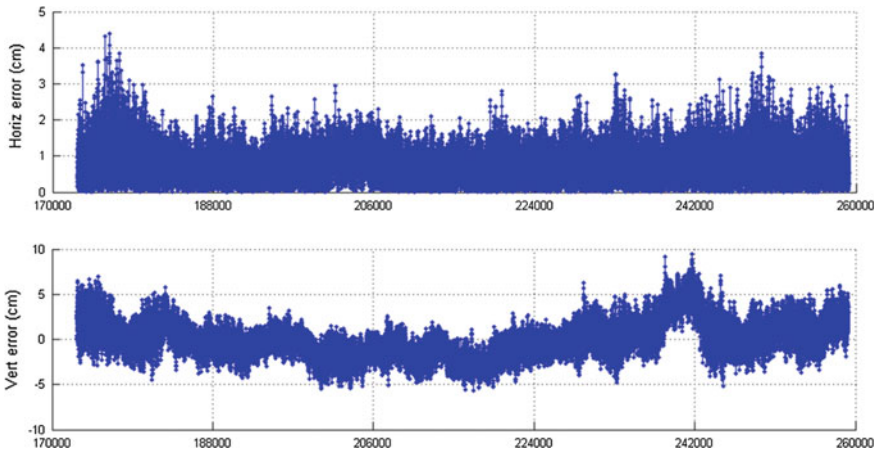

Fig. 25.4 CenterPoint RTX position errors on a fixed monitoring station, 24 h (time in seconds of week), horizontal RMS: 9 mm, vertical RMS: 19 mm

station with geodetic antenna we achieve better accuracies. An example for an ideally located, low multipath monitoring station is given in Fig. 25.4.

The convergence of CenterPoint RTX was derived by using 85 globally distributed monitoring stations for a time period of two weeks in December 2012 and resetting the RTX positioning engines every hour (Fig. 25.5). Again, the situation on these fixed stations is optimum compared to a typical dynamic positioning environment. Still it gives an idea on the status and the potential of the system.

25.4 Specifics of Different GNSS Systems

While GPS and GLONASS are currently globally available satellite systems, QZSS is a purely regional system, Galileo has four GNSS satellites in orbit for an In-Orbit-Validation (IOV), BeiDou/Compass is a satellite system with a focus on the Asia–Pacific region but targeting a global coverage in the next deployment phase until 2020. Recently, the BeiDou Interface Control Document (ICD) V1.0 [3] was released.

The US-American, Russian and European systems have their satellites in medium earth orbits. The GPS satellite system is fully operational since many years with up to 32 operational satellites. The GLONASS system is fully operational too with up to 24 MEO satellites. Due to the higher inclination of the satellites ($\sim 64°$ instead of $\sim 55°$), the GLONASS satellites reach higher latitudes than GPS satellites. QZSS has currently only one satellite in orbit. The orbital shape is optimized in a way that the QZSS satellite is nearly in the zenith over Japan.

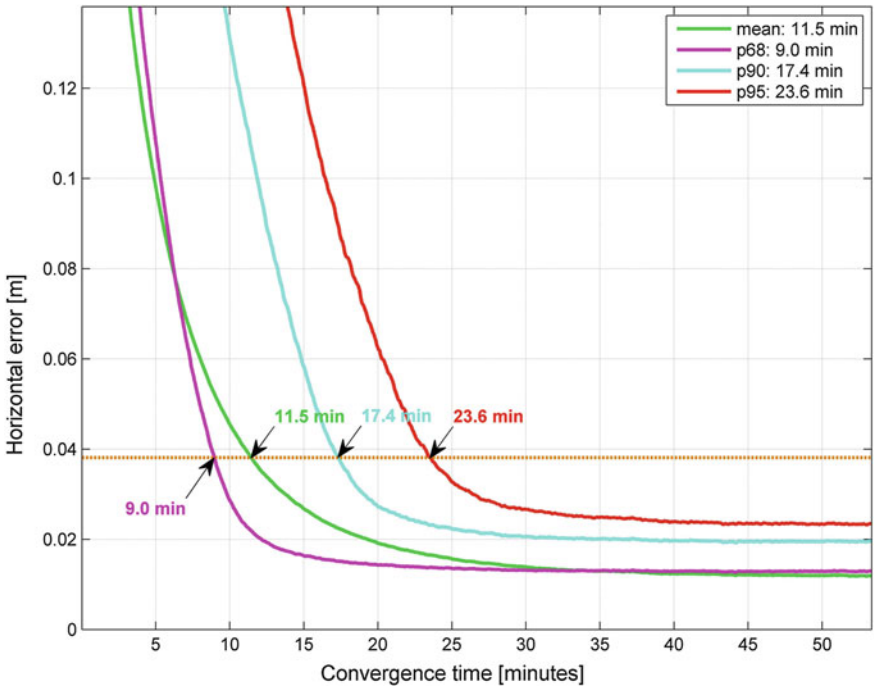

Fig. 25.5 Trimble CenterPoint RTX convergence on fixed reference stations

The Chinese BeiDou/Compass satellite system consists of satellites in medium earth, inclined geosynchronous and geostationary orbits. Hence it combines the benefits and drawbacks of all kind of orbit types. The MEO satellites have a large geometric change relative to a tracking station on the ground. The change in geometry is especially helpful in orbit determination to achieve fast convergence and highly accurate orbits. This benefit is much smaller for IGSO's and almost completely lost for GEO's. On the other hand the IGSO's and GEO's can sometimes be tracked by a station for several days without any loss of lock and the estimation process can benefit from a fixed ambiguity for a long time.

To date only GPS and GLONASS are in full operation. QZSS is predicted to be in full operation by 2018 with three IGSO and one GEO satellite. Galileo uses four satellites in orbit and is going through an IOV phase before the next satellites are launched. At the time of preparation of this paper the Galileo satellites did not transmit useful navigation data. This is why we decided to concentrate on GPS, GLONASS and QZSS only for the Trimble CenterPoint RTX correction service. However, orbit and clock processing for Galileo satellites will be very similar to GPS processing and we expect similar or even better orbit and clock quality for Galileo as for GPS, due to the fact that Galileo uses more modern signals. Besides the geostationary satellites, BeiDou/Compass is comparable to a combined GPS plus QZSS processing. Due to the high altitude of the QZSS satellite and its IGSO

shape, the modeling of the QZSS orbit was undergoing an optimization procedure. At present, the possibility to include BeiDou/Compass in the CenterPoint RTX system is under investigation.

As an example a current user of Trimble CenterPoint RTX in Hong Kong will find that he is able to track up to 19 GPS&GLONASS satellites simultaneously above 10° elevation angle plus the QZSS satellite. This already provides good convergence and accuracy. However, BeiDou/Compass will increase the number of visible GNSS satellites on that location to up to 35 when also considering the 4 Galileo IOV satellites. In an earlier publication [2] we have demonstrated that by adding the QZSS satellite to the Trimble CenterPoint RTX system we were able to reduce the convergence time by approximately 20 % and the vertical error by a similar percentage amount. This is why we seriously believe that adding BeiDou/Compass to the Trimble GNSS positioning systems will make a considerable difference in performance.

25.5 BeiDou and QZSS Pseudorange Observation Quality

The quality of pseudoranges for the different satellite systems was analyzed using the MP1 and MP2 multipath combinations. A typical MP1/MP2 plot for BeiDou/Compass GEO satellite C01 for station Bangkok is shown in Fig. 25.6.

The IGSO satellites exhibit a different behavior. As an example Fig. 25.7 shows the multipath combination MP1/MP2 and elevation angle for the BeiDou/Compass

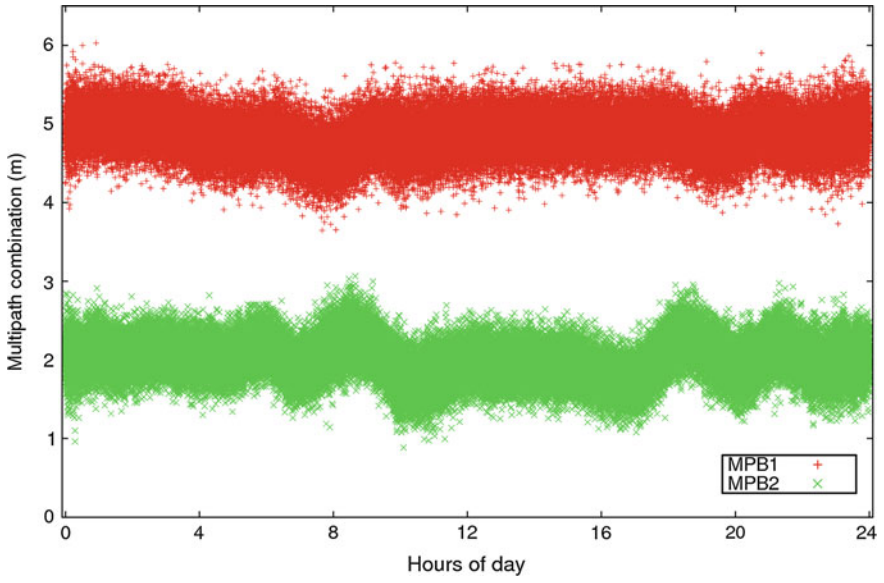

Fig. 25.6 MP1/MP2 for station Bangkok and BeiDou/Compass satellite C01

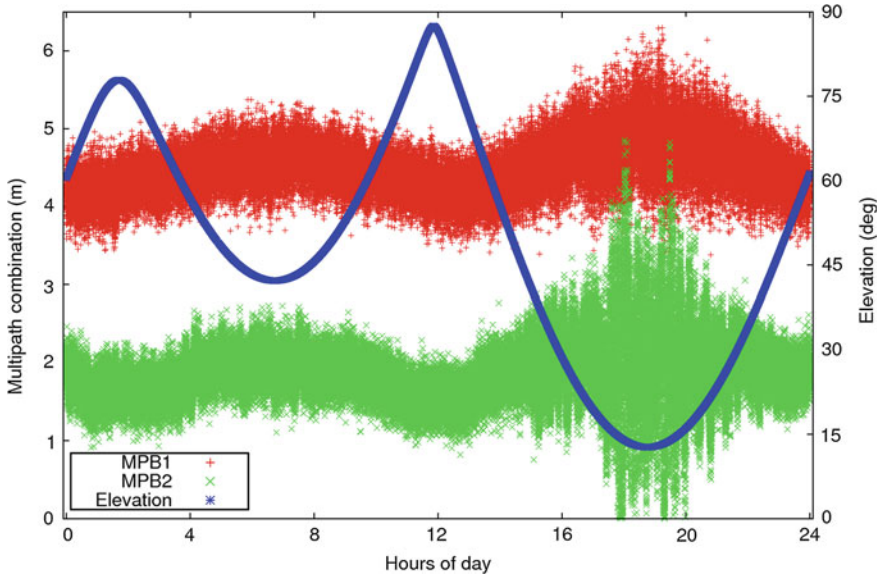

Fig. 25.7 MP1/MP2 and elevation for station Bangkok and Beidou/Compass satellite C09

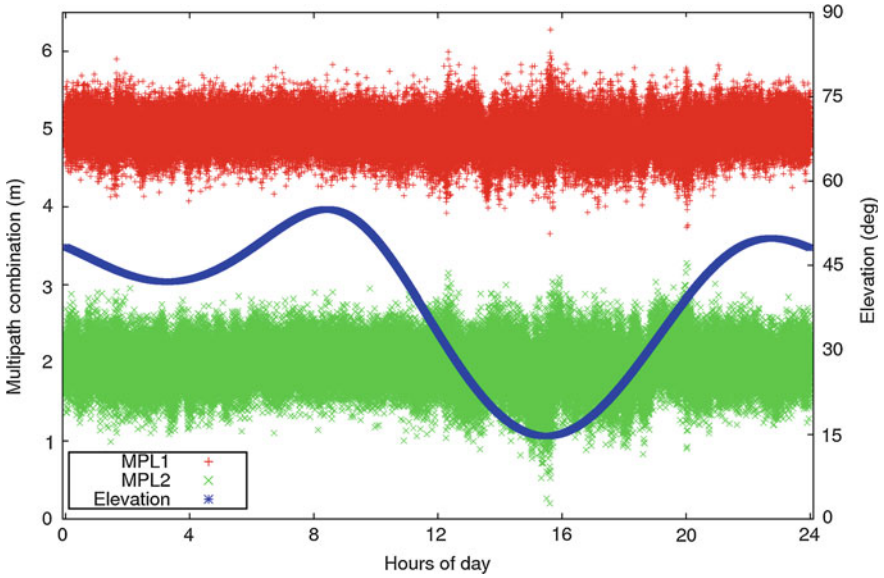

Fig. 25.8 MP1/MP2 and elevation for station Bangkok and IGSO QZSS satellite

satellite C09 observed from station Bangkok. The larger noise occurs when the satellite is observed at a low elevation angle of $\sim 10°$ as shown in the figure. For comparison we can look at the MP1 and MP2 values of the QZSS satellite for the

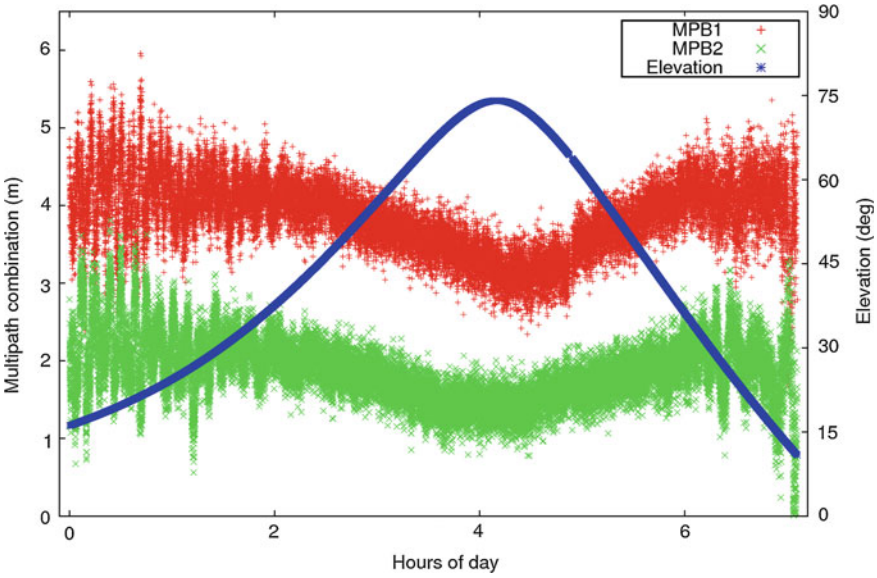

Fig. 25.9 MP1 for station Bangkok and IGSO BeiDou/Compass satellite C12

same station Bangkok (Fig. 25.8). The elevation angle of the QZSS satellite varies between 15 and 55°.

The MP1/MP2 values for the MEO satellite C12 shows the following behavior in station Bangkok (Fig. 25.9). Again the higher noise/multipath occurs for lower elevation angles.

BeiDou/Compass ionosphere-free B1/B2 pseudorange combination residuals were analyzed from the satellite orbit/clock estimation process and plotted with respect to the elevation angles (Fig. 25.10). 46 tracking stations during the time period December 18–20, 2012 were used to derive the statistics shown in the following figure. Satellite C01 was not computed during this time period and thus is missing. All satellites except the GEO C02 are showing consistent error behavior. C02 had shown some larger outliers at lower elevation angles during the analyzed time period.

25.6 Orbit Estimation

In Trimble CenterPoint RTX we routinely estimate the satellite orbit for GPS, QZSS and GLONASS in real-time. The accuracy we achieve on a regular basis is of the order of a couple of centimeters when comparing with IGS/CODE final and rapid orbits for GPS and GLONASS [4]. The achievable orbit accuracy for QZSS and BeiDou/Compass is more difficult to judge since we currently have no good reference orbit to compare with. Therefore our analyses so far are based on judging

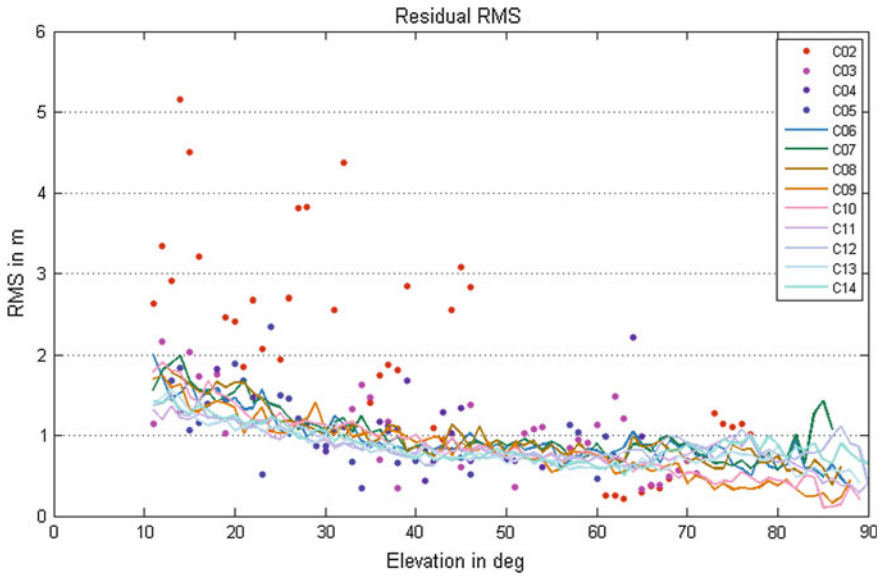

Fig. 25.10 Pseudorange RMS with respect to elevation angle (December 18–20, 2012)

the overlap periods of different satellite arcs computed in a post-processing approach. The scheme we are using for this first analysis is based on RMS values computed from a 24 h overlap time period of two arcs in three days. The tangential (along track), normal (cross track) and radial discrepancies of the overlap time

Table 25.1 RMS of orbit overlap RMS of the BeiDou/QZSS satellites (unit: meters)

	Radial [m]	Along-track (m)	Cross-track (m)
C01	0.062	7.485	0.055
C02	0.046	16.308	0.087
C03	0.031	22.111	0.055
C04	0.045	19.121	0.025
C05	0.076	2.250	0.050
C06	0.056	0.716	0.100
C07	0.031	0.328	0.080
C08	0.037	0.448	0.087
C09	0.052	0.553	0.079
C10	0.034	0.382	0.084
C11	0.016	0.225	0.056
C12	0.036	0.285	0.067
C13	0.039	0.352	0.088
C14	0.026	0.212	0.055
J01	0.026	0.168	0.101

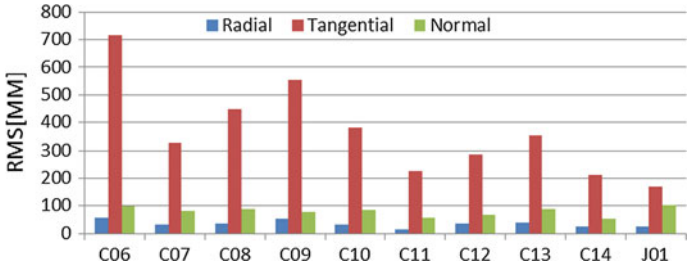

Fig. 25.11 Overlap RMS for BeiDou (IGSO and MEO) and QZSS satellites

period are computed for a time period of three months from October to December 2012.

The overlap analysis results of BeiDou/Compass satellites and the QZSS satellite are summarized in Table 25.1. The results for BeiDou/Compass IGSO, MEO satellites and the QZSS satellite are shown in Fig. 25.11. The radial repeatability is in the order of a few centimeters for all BeiDou/Compass satellites and the QZSS satellite. As expected, the geostationary satellites show much larger along track errors than the other satellites.

In comparison, the RMS values for GPS and GLONASS satellites were computed too. The GPS and GLONASS satellites benefit a lot from the more complete tracking network (all CenterPoint RTX tracking stations track GPS and GLONASS satellites). This results in very small overlap differences, which are just in the mm-range for the radial component. Figures 25.12 and 25.13 show the overlap RMS in radial, tangential, normal direction for GPS and GLONASS satellites respectively.

The carrier phase residuals in the orbit estimation process look similar to what we typically get for GPS, there are also no significant differences between GEOs, IGSOs, and MEOs. Figure 25.14 shows phase residuals for three selected satellites, different stations are shown by using different colors.

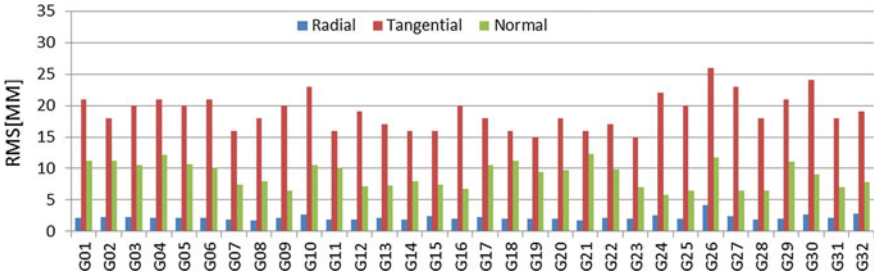

Fig. 25.12 Overlap RMS for GPS satellites

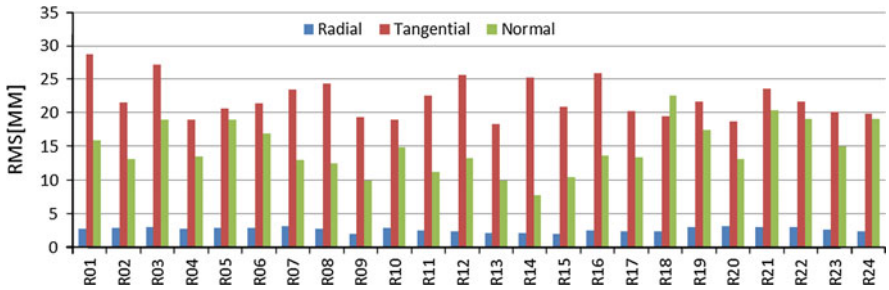

Fig. 25.13 Overlap RMS for GLONASS satellites

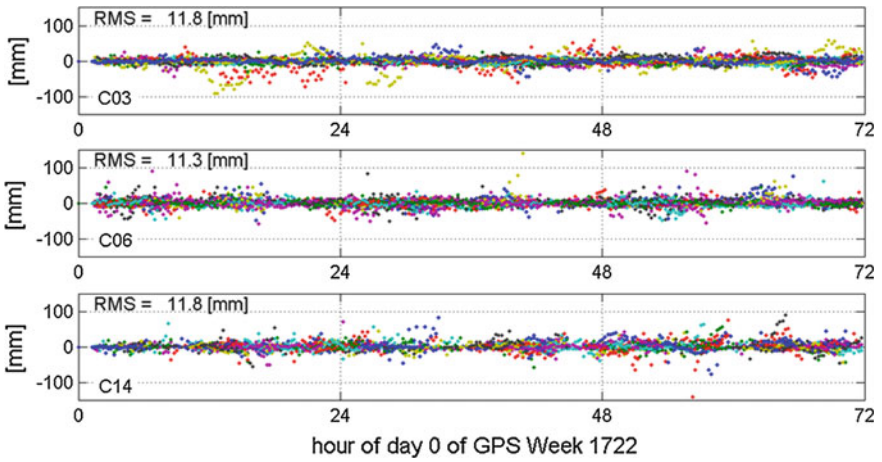

Fig. 25.14 Carrier phase residuals for selected BeiDou/Compass satellites during the days from January 6–8, 2013 (stations indicated by different colors)

25.7 Satellite Clock Stability

The satellite clock stability is an important factor for precise dynamic GNSS positioning techniques like RTK, RTX, and PPP. Therefore we studied the frequency stability of the different satellite clocks using the Allan deviation [5]. The following results are based on clock estimates computed by the Trimble CenterPoint RTX system.

Figure 25.15 shows the Allan deviation of the GPS constellation on November 29, 2012. The superior performance of the new generation of rubidium clocks on board of the GPS IIF satellites is evident. However, the Allan deviation of the IIF satellite clocks is affected by the reference timescale of the clock errors which is based on the average of all GPS clocks. The actual performance of these clocks should therefore be significantly better. The first QZSS satellite J01 is equipped with the same high-performance Rubidium (Rb) oscillator that is used in the GPS

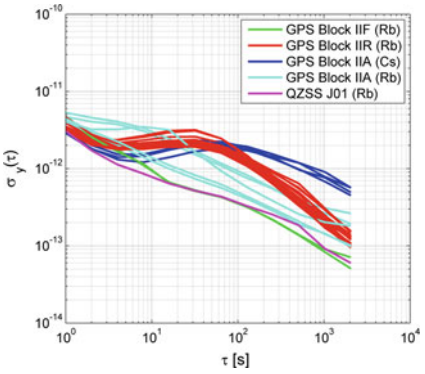

Fig. 25.15 Allan deviations for the GPS satellite clocks and the QZSS satellite J01 on November 29, 2012

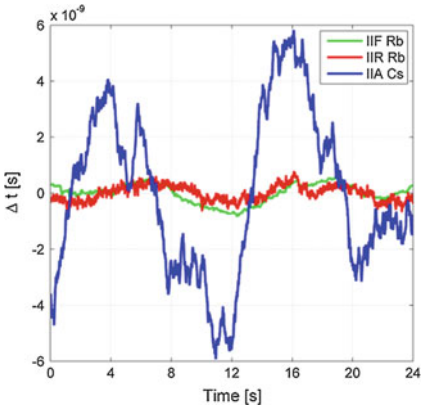

Fig. 25.16 Exemplary time series for different generations of GPS satellite clocks (trend removed)

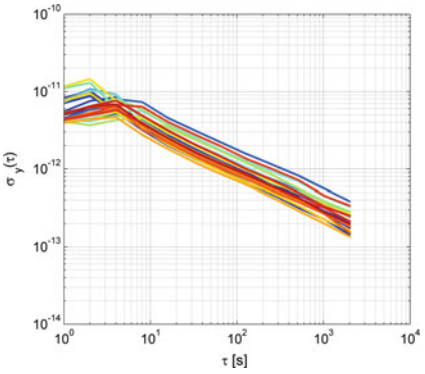

Fig. 25.17 Allan deviations for the GLONASS satellite clocks on November 29, 2012

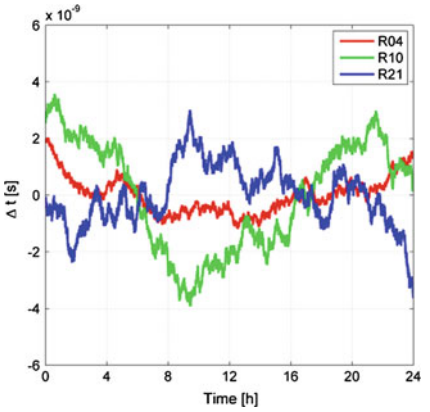

Fig. 25.18 Example time series for three different GLONASS satellite clocks (trend removed)

Block IIF satellites. As expected the Allan deviation of the J01 clock errors, also shown in Fig. 25.15, is at a similar level as the GPS Block IIF satellites. Exemplary GPS satellite clock time series are shown in Fig. 25.16. A linear trend was removed from each of the time series.

The frequency stabilities of the GLONASS satellite clocks are summarized in Fig. 25.17. They show consistent values for the different satellites. Overall, the Allan deviations for the GLONASS satellite clocks are not as good as for the newer GPS satellites but better than the GPS IIA satellite clocks. Example time

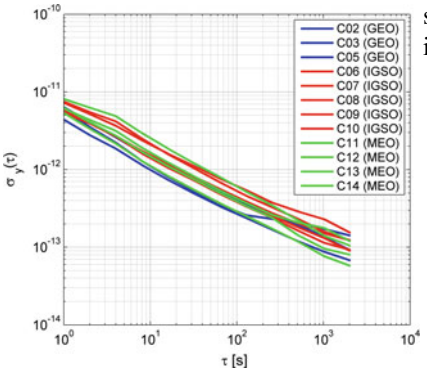

Fig. 25.19 Allan deviation for the BeiDou/Compass satellites on December 19, 2012

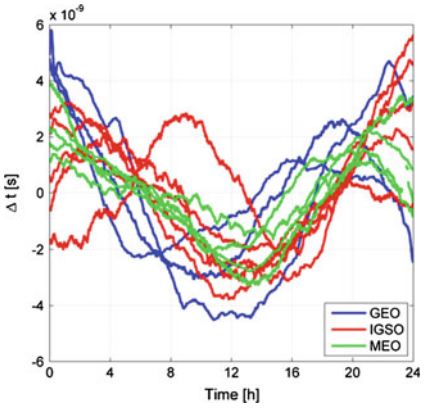

Fig. 25.20 Example time series for the BeiDou/Compass satellite clocks (trend removed)

(Fig. 25.18) for the GLONASS satellite clocks show larger variations than for the newer GPS satellites, but better performance than for the GPS IIA satellite clocks.

The Allan deviations of the BeiDou/Compass satellite clock errors are shown in Fig. 25.19. No significant differences in terms of frequency stability can be observed for GEO, IGSO and MEO satellites. The average frequency stability of the BeiDou/Compass satellite clocks is significantly better than that of the GLONASS clocks but does not reach the stability of the latest GPS frequency standards (Fig. 25.20).

25.8 Summary and Outlook

Currently (early January 2013) the Trimble CenterPoint RTX service supports the GPS, GLONASS and QZSS allowing a fast convergence of less than 30 min (95 %) and a horizontal accuracy of better than 4 cm (2D, 95 %). Applications in precision agriculture, infrastructure and monitoring solutions are supported in PC software and receiver hardware implementations. The system is continuously extended and improved by increasing the number of tracking stations, improving the orbit modeling and the satellite clock estimation process.

Currently the potential use of BeiDou/Compass signals is being investigated. BeiDou/Compass satellite orbits are computed with first post-processing batch solutions with promising consistency numbers between satellite arcs of a few centimeters in radial direction. The addition of these currently 14 Chinese satellites to the Trimble CenterPoint RTX system is expected to provide significant performance improvements with respect to RTX convergence, especially for the Asia–Pacific region.

References

1. Doucet K et al. (2012) Introducing ambiguity resolution in web-hosted global multi-GNSS precise positioning with trimble RTX-PP. Paper presented at ION-GNSS-2012, Nashville, TN, USA, 17–21 Sept 2012
2. Landau H, Glocker M, Kipka A, Leandro R, Nitschke M, Stolz R, Zhang F (2012) Aspects of using the QZSS satellite in the trimble centerpoint^{TM} RTX^{TM} service: QZSS orbit and clock accuracy, RTX positioning performance improvements. Paper presented at ION-GNSS-2012, Nashville, TN, USA, Sept 17–21 2012
3. BeiDou navigation satellite system signal in space interface control document open service signal B1I (version 1.0). China Satellite Navigation Office, Dec 2012
4. Glocker M, Landau H, Leandro R, Nitschke M (2012) Global precise multi-GNSS positioning with trimble centerpoint RTX, NAVITEC 2012—European workshop on GNSS signals and signal processing, 5–7 Dec 2012
5. David WA (1966) Statistics of atomic frequency standards. Proc. IEEE, vol. 54, pp 221–230

Chapter 26
Cycle Slip Detection and Repair with Different Sampling Interval Based on Compass Triple-Frequency

Kai Xie, Hongzhou Chai, Min Wang and Zongpeng Pan

Abstract On the basis of the multiple-frequency observation combination theory, the triple-frequency MW and Geometry-free combination and the triple-frequency pseudorange/carrier phase combination cycle-slip detection model have been deduced respectively. Using the Compass triple-frequency observation data, under the circumstances of different sampling intervals, the detection effects of the two methods have been studied in cases of cycle slip occurring on a single frequency and multiple frequencies. The results have shown that when the sampling interval is 1 s, both the two methods have good results; when sampling interval is 10 s, the MW and Geometry-free combination is better; when the sampling interval is 30 s, both the two methods are affected in some extent. Then we have the conclusion, in the process of observation, the sampling interval should be set smaller than 10 s which is beneficial for cycle slip detection and repair. And in most cases, the MW and Geometry-free combination is more effective.

Keywords: Sampling interval · Cycle Slip detection and repair · MW and geometry-free combination · Pseudorange/carrier phase combination

26.1 Introduction

As a result of self-fault of GPS signal receiver or unexpected interrupt of the signal, the phase-lock loop momentarily loses lock, which causes a momentary break in the Doppler count. The phenomenon of this break is called cycle slip [1]. Since cycle slip detection and repair is a necessary part of preprocessing, many scholars have put forward various methods in solving this problem. Remondi [2]

K. Xie (✉) · H. Chai · M. Wang · Z. Pan
Geospatial Information Institute, Information Engineering University, Zhengzhou 450052, People's Republic of China
e-mail: nicholas_kevin2003@yahoo.com.cn

J. Sun et al. (eds.), *China Satellite Navigation Conference (CSNC) 2013 Proceedings*, Lecture Notes in Electrical Engineering 245,
DOI: 10.1007/978-3-642-37407-4_26,

suggested using differential method to conduct cycle slip detection. Goad introduced using the ionospheric residual of dual-frequency carrier phase observation for cycle slip detection. Chen appropriately modified the detection model introduced by Canon and then put forward polynomial method [3]. But all these methods are based on single or dual-frequency observation, triple-frequency signal can provide more observation information and more combinations with good properties such as long wavelength and low observation noise. With the development of triple frequency technology, Dai [4] put forward triple-frequency Geometry-free combination. Fan [5] put forward MW and Geometry-free combination which is suit for the automatic detection and repair of cycle slip in the case of undifferenced triple-frequency data. Xiong [6] put forward triple-frequency pseudorange/carrier phase combination on the basis of the traditional method.

In the context of that Compass-II will send signals in three different frequencies, using Compass observation data, with different sampling interval, the effectiveness of triple-frequency MW and Geometry-free combination and triple-frequency Pseudorange/Carrier Phase combination are compared when cycle slip occurs on a single frequency and multiple frequencies respectively. The condition for these methods and the optimal sampling interval are analyzed.

26.2 MW & Geometry-Free Combination

26.2.1 MW Combination

MW (wide phase minus narrow pseudo range) combination uses the difference of wide-lane carrier phase and narrow-lane pseudo range to consist the combination observation. The triple-frequency MW combination can be expressed as follows:

$$N_{ij} = \frac{f_i - f_j}{f_i + f_j}\left(\frac{P_i}{\lambda_i} + \frac{P_j}{\lambda_j}\right) - (\phi_i - \phi_j) \tag{26.1}$$

Where: $N_{ij} = N_i - N_j (i = 1, 2, 3; j = 1, 2, 3; i \neq j)$
Wavelength of combination is $\lambda_{wij} = 1/\lambda_i - 1/\lambda_j (i = 1, 2, 3; j = 1, 2, 3; i \neq j)$

26.2.2 Geometry-Free Combination

The Geometry-free combination is as follows

$$\begin{aligned} L_{\alpha,\beta,\gamma} &= \alpha L_1 + \beta L_2 + \gamma L_3 \\ &= \alpha\lambda_1 N_1 + \beta\lambda_2 N_2 + \gamma\lambda_3 N_3 - \left(\alpha + \beta\frac{f_1^2}{f_2^2} + \gamma\frac{f_1^2}{f_3^2}\right) I + \alpha\varepsilon_1 + \beta\varepsilon_2 + \gamma\varepsilon_3 \end{aligned} \tag{26.2}$$

to eliminate the distance,set $\alpha + \beta + \gamma = 0$

Make a difference of the above formula between epochs. Then the cycle slip of geometry-free combination after eliminating the ionospheric error and observation noise is

$$\Delta N_{\alpha,\beta,\gamma} = \frac{[L_{\alpha,\beta,\gamma}(t) - L_{\alpha,\beta,\gamma}(t-1)]}{\alpha\lambda_1} = \Delta N_1(t) + (\frac{\beta\lambda_2}{\alpha\lambda_1})\Delta N_2(t) + (\frac{\gamma\lambda_3}{\alpha\lambda_1})\Delta N_3(t) \ (\alpha \neq 0) \quad (26.3)$$

where: $\Delta N_i(t) = N_i(t) - N_i(t-1) \quad (i = 1, 2, 3)$

26.2.3 The Combination of MW and Geometry-Free Methods

After analyzing the combination error, we can get the referenced standard in selecting the observation value [7]: long wavelength, small ionospheric effect and small observation noise.

Then combinations of $N_{(-1,1,0)}$ $N_{(-1,0,1)}$ N_{w32} are selected. The cycle slip detection equations are as follows,

$$\left.\begin{array}{l} \Delta N_1 - \frac{\lambda_2}{\lambda_1}\Delta N_2 = n_1 \\ \Delta N_1 - \frac{\lambda_3}{\lambda_1}\Delta N_3 = n_2 \\ -\Delta N_2 + \Delta N_3 = n_3 \end{array}\right\} \quad (26.4)$$

where $\Delta N_1, \Delta N_2, \Delta N_3$ are the cycle slip values on three frequencies, n_1, n_2, n_3 are the cycle slip detection values of three combinations.

26.3 Multiple-Frequency Pseudorange/Carrier Phase Combination

The cycle slip detection formula of Multiple-frequency Pseudorange/Carrier Phase Combination is

$$\begin{aligned} \Delta N_c &= N_c(t_2) - N_c(t_1) \\ &= \phi_c(t_2) - \phi_c(t_1) - \frac{R(t_2) - R(t_1)}{\lambda_c} \end{aligned} \quad (26.5)$$

a. Wavelength of Combination Observation

$$\lambda_C = \lambda_1\lambda_2\lambda_3/(i\lambda_2\lambda_3 + j\lambda_1\lambda_3 + k\lambda_1\lambda_2) \quad (26.6)$$

where i, j, k are the combination coefficients.

b. Ionospheric delay coefficient

α_{ion} is the specific value of dividing the ionospheric error by wavelength after combination and dividing the ionospheric error by wavelength of L_1.

$$\alpha_{ion} = \frac{I_c/\lambda}{I/\lambda_1} = (i + j\frac{\lambda_2}{\lambda_1} + k\frac{\lambda_3}{\lambda_1}) \tag{26.7}$$

The smaller α_{ion} is, the smaller distance error of ionosphere is.

c. Observation Noise

Set $\sigma_{L_1} = \sigma_{L_2} = \sigma_{L_3} = \sigma_L$, then the variance of observation noise after combination is

$$\sigma_{L_{i,j,k}} = \sqrt{(i\lambda/\lambda_1)^2 + (j\lambda/\lambda_2)^2 + (k\lambda/\lambda_3)^2}\sigma_L \tag{26.8}$$

According to the above three referenced standards, go through -10 to 10 for i, j, k, then three coefficient combinations can be obtained after filter (Table 26.1).

Therefore the combination cycle slip value n_1, n_2, n_3 of three combinations can be expressed as follows

$$\begin{aligned} n_1 &= -\Delta N_1 - 5\Delta N_2 + 6\Delta N_3 \\ n_2 &= \Delta N_1 + 4\Delta N_2 - 5\Delta N_3 \\ n_3 &= -4\Delta N_1 + \Delta N_2 + 4\Delta N_3 \end{aligned} \tag{26.9}$$

26.4 Example Analysis

A range of "clean" data collected by a Compass receiver in Beijing on Nov.16th 2012 is used to conduct the experiment. The effectiveness of MW & Geometry-free combination and Pseudorange/Carrier Phase combination are compared when the sampling interval is 1, 10 and 30 s respectively.

The three frequencies of Compass signal are shown in the chart below Table 26.2

Table 26.1 Combination observation property

Combination	f/MHz	λ/m	α_{ion}	σ_c/m
(−1, −5, 6)	14.322	20.932	−8.963	1.374
(1, 4, −5)	47.058	6.371	0.652	0.345
(−4, 1, 4)	36.828	8.140	93.925	0.442

Table 26.2 The carrier phase frequency and wavelength of Compass system signals

Signal	Carrier frequency/MHz	Wavelength/m
B1	1561.098	0.192
B2	1207.14	0.248
B3	1268.52	0.236

26.4.1 Cycle-Slip on a Single Frequency

In the cases of different sampling intervals, add −1, −5, −10 cycle slip to L_1 in epoch 20, 50, 80 respectively. Then in theory, adopting the MW and Geometry-free combination, the cycle slip value of combination $N_{(-1,1,0)}$ is 1, 5, 10 respectively in corresponding epoch and 1, 5, 10 respectively for combination $N_{(-1,0,1)}$, while for combination N_{w32}, the cycle slip is 0 in each epoch. Adopting the Pseudorange/Carrier Phase combination, the cycle slip value of combination (−1, −5, 6) is −1, 1, −4 respectively in corresponding epoch. The cycle slip value of combination (1, 4, −5) is −5, 5, −20 respectively in corresponding epoch. And the cycle slip value of combination (−4, 1, 4) is −10, 10, −40 respectively in corresponding epoch.

1. **The sampling interval is 1 s**

After analyzing Figs. 26.1, 26.2, we can come to the conclusion. When the sampling interval is 1 s, both the two methods can accurately detect the epoch where cycle slip occurs. The difference between the detected cycle slip value and the true value is smaller than 0.1 cycle. Therefore in the case of cycle slip occurring on a single frequency, when the sampling interval is 1 s, both the two methods can accurately detect and repair cycle slip.

2. **The sampling interval is 10 s**

After analyzing Figs. 26.3, 26.4, we can come to the conclusion. When the sampling interval is 10 s, adopting the Pseudorange/Carrier Phase combination, the difference between the detected cycle slip and the true value is smaller than 0.5 cycle while it's bigger than 0.5 cycle for N_{w32} combination of MW & Geometry-free combination. Therefore in the case of cycle slip occurring on a single frequency, when the sampling interval is 10 s, adopting the Pseudorange/Carrier Phase combination can detect and repair the cycle slip more accurately.

3. **The sampling interval is 30 s**

After analyzing Figs. 26.5, 26.6, we can come to the conclusion. When the sampling interval is 30 s, the detection precision of both the two methods are greatly affected. When adopting the Pseudorange/Carrier Phase combination, the difference between the detected cycle slip and the true value is bigger than 1 cycle, making it unable to accurately repair the cycle slip, while it's smaller than 0.5

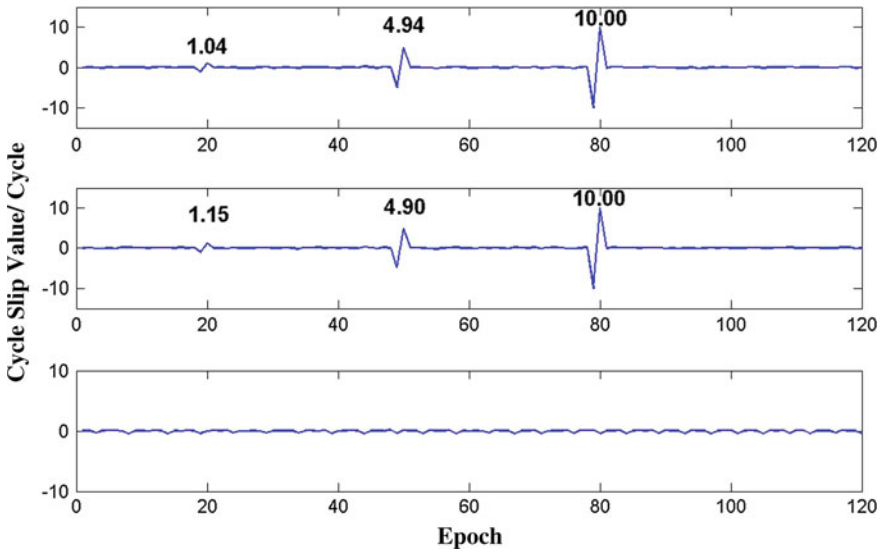

Fig. 26.1 Detection result of MW and Geometry-free combination

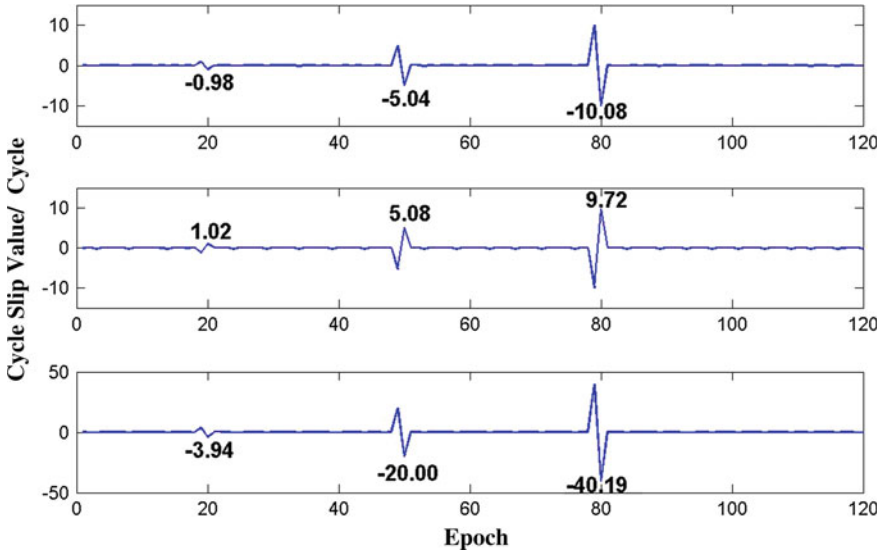

Fig. 26.2 Detection result of pseudorange/carrier phase combination

cycle for $N_{(-1,1,0)}$ and $N_{(-1,0,1)}$ combination of MW and Geometry-free combination. Therefore in the case of cycle slip occurring on a single frequency, when the sampling interval is 30 s, both the two methods cannot reach a relatively high precision in detecting and repairing the cycle slip. In contrast, the MW & Geometry-free combination is better.

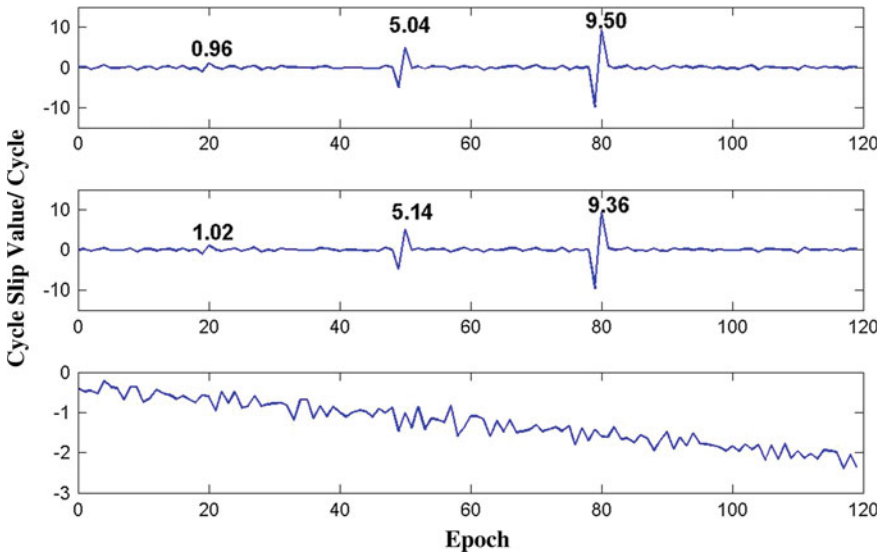

Fig. 26.3 Detection result of MW and geometry-free combination

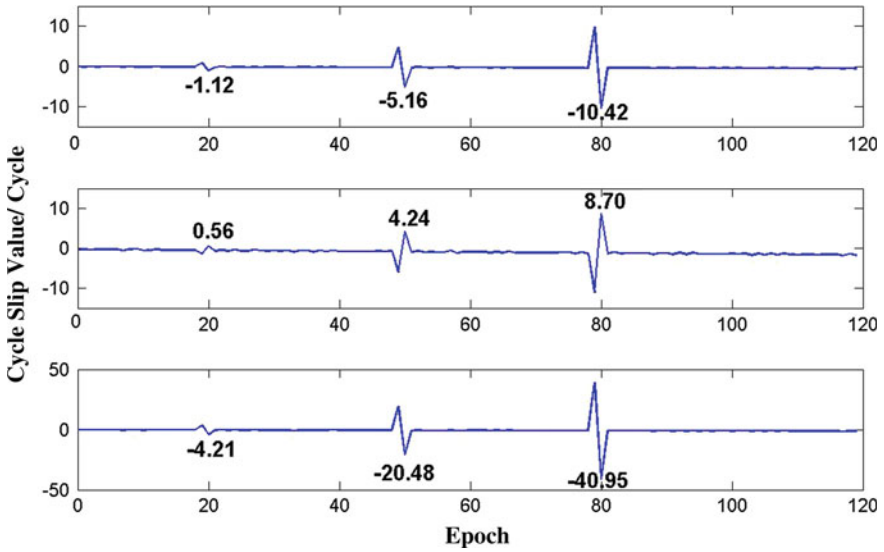

Fig. 26.4 Detection result of pseudorange/carrier phase combination

26.4.2 Cycle-Slip on Multiple Frequencies

In the cases of different sampling intervals, add 1, 2, 3 cycle slip to L_1, L_2, L_3 in epoch 30 respectively. Then in theory, adopting the MW & Geometry-free

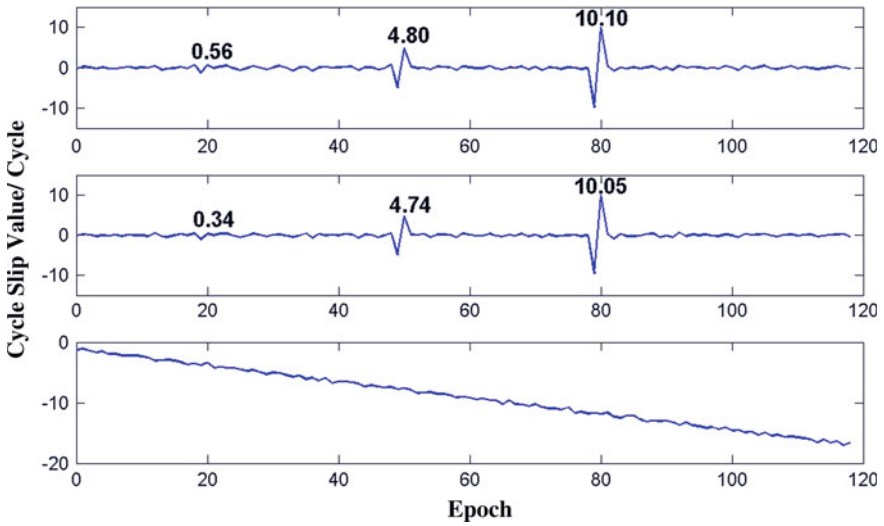

Fig. 26.5 Detection result of MW & Geometry-free combination

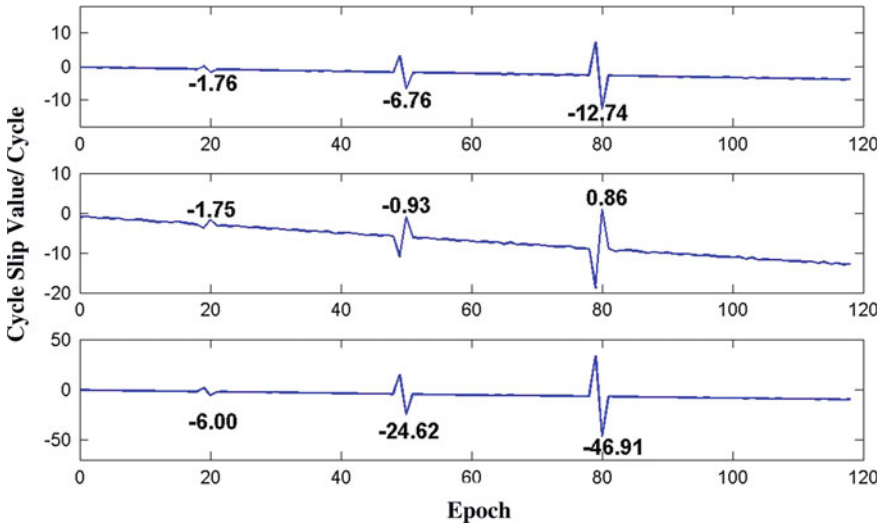

Fig. 26.6 Detection result of Pseudorange/Carrier Phase combination

combination, the cycle slip value is 1.58 for combination $N_{(-1,1,0)}$, 2.69 for combination $N_{(-1,0,1)}$, and -1 for combination N_{w32}. Adopting the Pseudorange/Carrier Phase combination, the cycle slip value is -7 for combination (-1,-5, 6), 6 for combination (1, 4, -5), and -10 for combination (-4, 1, 4).

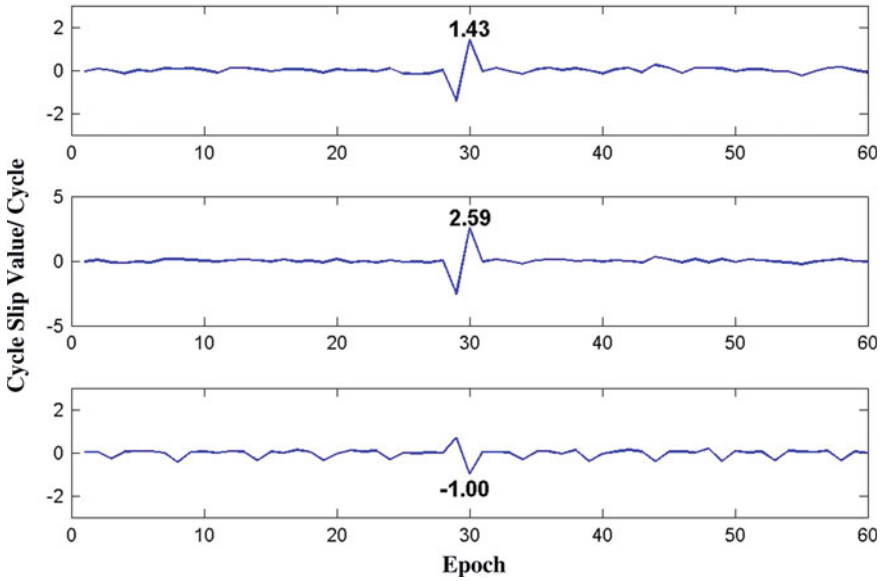

Fig. 26.7 Detection result of MW and Geometry-free combination

(1) **The sampling interval is 1 s**

After analyzing Figs. 26.7, 26.8, we can come to the conclusion. When the sampling interval is 1 s, both the two methods can accurately detect the epoch where cycle slip occurs. The difference between the detected cycle slip value and the true value is smaller than 0.1 cycle. Therefore in the case of cycle slip occurring on multiple frequencies, when the sampling interval is 1 s, both the two methods can accurately detect and repair cycle slip.

(2) **The sampling interval is 10 s**

After analyzing Figs. 26.9, 26.10, we can come to the conclusion. When the sampling interval is 10 s, adopting the MW and Geometry-free combination, the difference between the detected cycle slip is smaller than 0.2, while it reaches to 0.5 for combination (1, 4, −5) and (−4, 1, 4) of Pseudorange/Carrier Phase combination. Therefore in the case of cycle slip occurring on multiple frequencies, when the sampling interval is 10 s, adopting the MW and Geometry-free combination can detect and repair the cycle slip more accurately.

(3) **The sampling interval is 30 s**

After analyzing Figs. 26.11, 26.12, we can come to the conclusion. When the sampling interval is 30 s, the detection precision of both the two methods are greatly affected. When adopting the pseudorange/Carrier Phase combination, the difference between the detected cycle slip and the true value is bigger than 1 cycle,

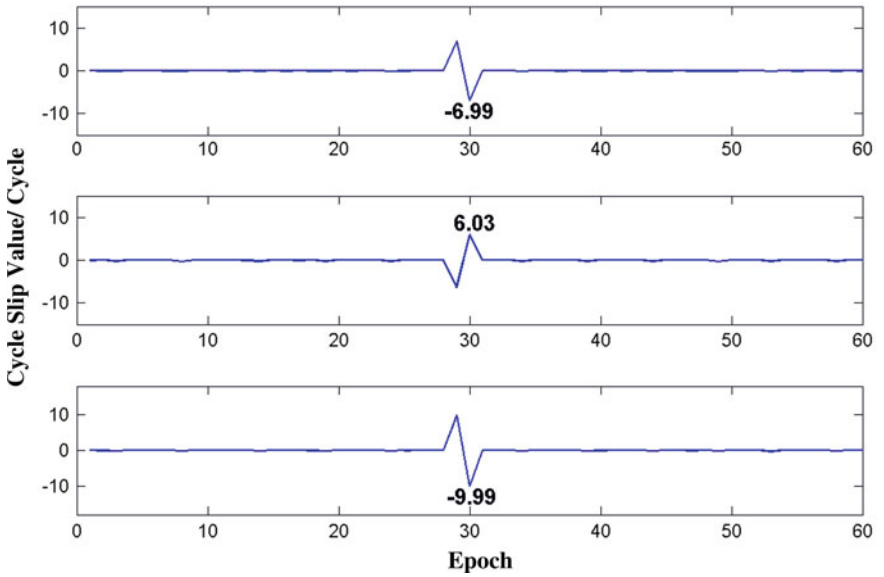

Fig. 26.8 Detection result of Pseudorange/Carrier Phase combination

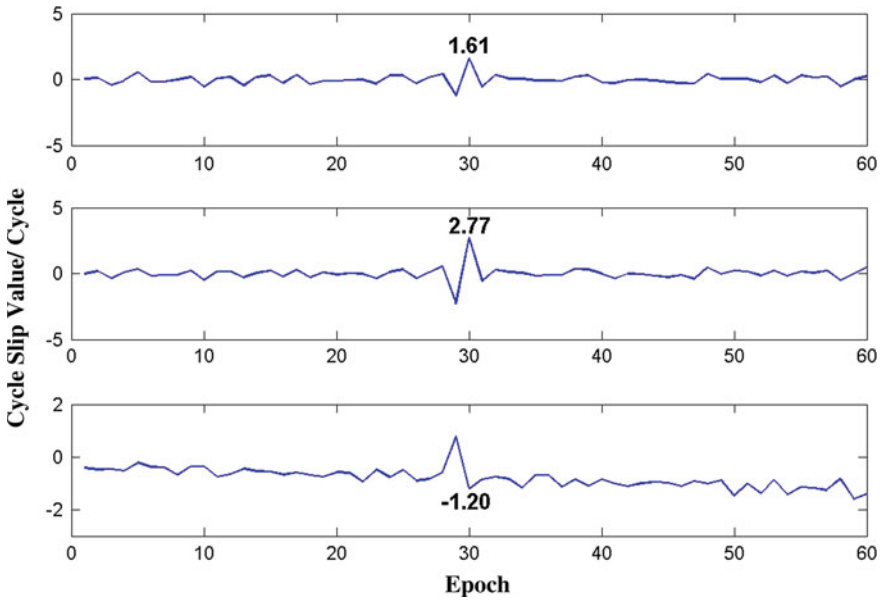

Fig. 26.9 Detection result of MW and Geometry-free combination

making it unable to accurately repair the cycle slip, while it's smaller than 0.2 cycle for $N_{(-1,1,0)}$ and $N_{(-1,0,1)}$ combination of MW & Geometry-free

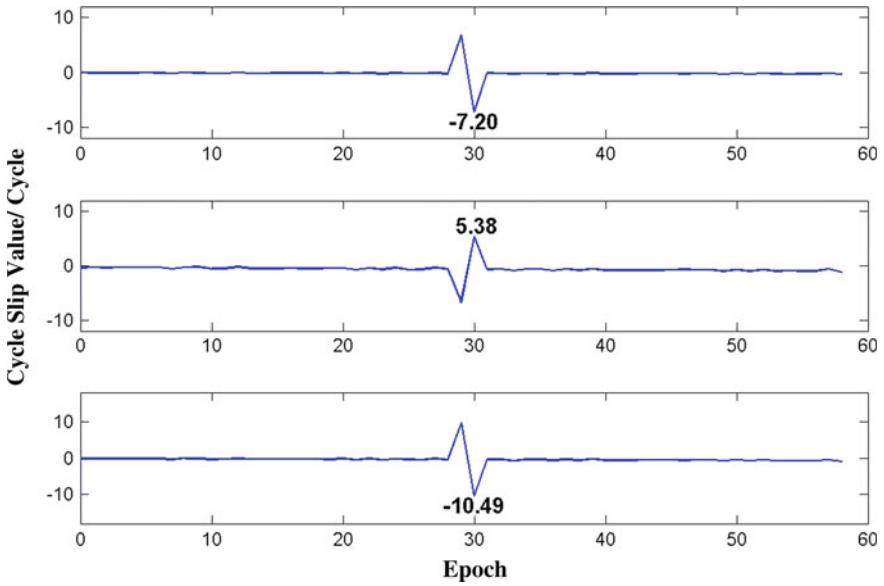

Fig. 26.10 Detection result of Pseudorange/Carrier Phase combination

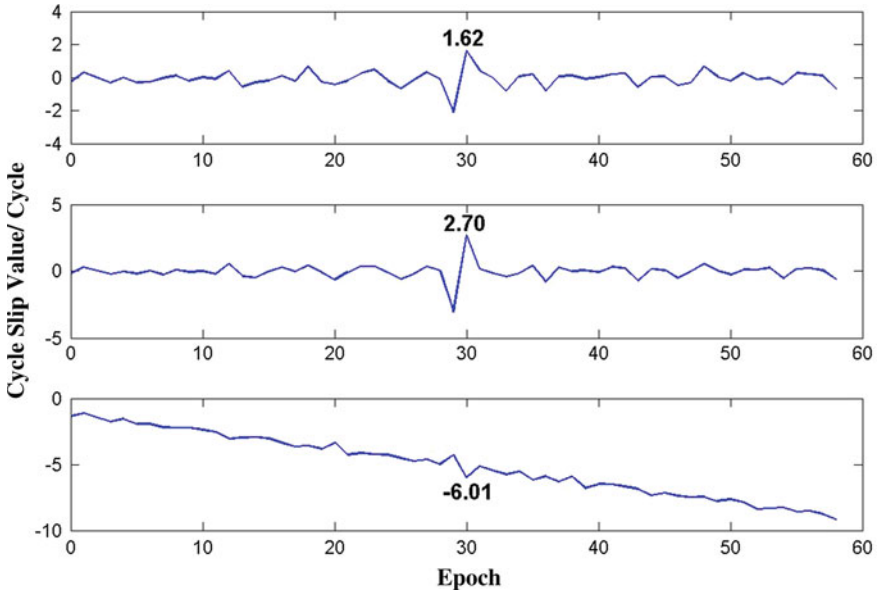

Fig. 26.11 Detection result of MW and Geometry-free combination

combination. Therefore in the case of cycle slip occurring on multiple frequencies, when the sampling interval is 30 s, both the two methods cannot reach a relatively

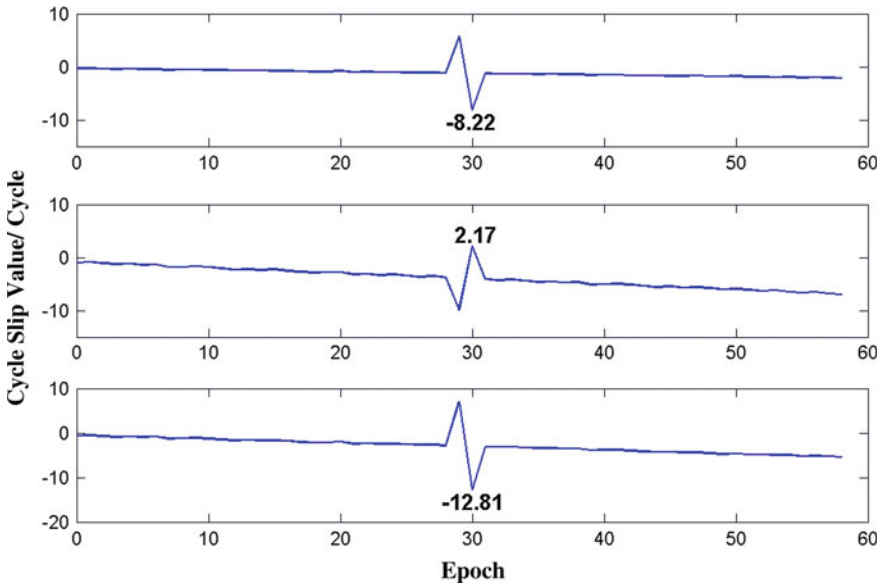

Fig. 26.12 Detection result of pseudorange/carrier phase combination

high precision in detecting and repairing the cycle slip. In contrast, the MW & Geometry-free combination is better.

26.5 Conclusion

Adopting the Compass triple-frequency data, the effectiveness of MW & Geometry-free combination and Pseudorange/Carrier Phase combination is analyzed in detecting and repairing cycle slips in cases of different sampling intervals. The results can be concluded as follows. When the sampling interval is 1 s, both the two methods have good results when cycle slip occurs both on a single frequency and multiple frequencies; when sampling interval is 10 s, the Pseudorange/Carrier Phase combination is better in case of cycle slip occurring on a single frequency while the MW & Geometry-free combination is better in case of cycle slip occurring on multiple frequencies; when the sampling interval is 30 s, although both the two methods are affected in great extent, the MW and Geometry-free combination is relatively more effective in detecting and repairing cycle slips.

In a word, in cases of different sampling intervals, the MW-Geometry-free combination is more effective in detecting and repairing cycle slips. In addition, with the increase of sampling interval, the detecting result is affected in some extent. Therefore, the sampling interval should be set smaller than 10 s in order to obtain precise data.

Since the data adopted in this paper is relatively ideal, the multi-path effect of G satellite, the noise of I/M satellite when elevation angle is small and the inconsistency of pseudo range and carrier phase are neglected in cycle slip detection and repair. Due to the limit of the experimental conditions, the paper has only adopted sampling intervals of 1, 10, and 30 s to conduct the experiment. For the next step, more sampling intervals will be tested to find the optimal sampling interval.

References

1. Huangetal. GPS-Method and realization[M]. Chengdu: South-west University Press. 2006: 84
2. Remondi BW (1985) Performing centimeters relative surveying in seconds using GPS Carrier Phase [J]. J Inst Navig 32(4):386–400
3. Liu J (2003) GPS satellite concept and methods [M]. Sicence Press, Beijing, pp 337–343
4. Dai Z,Knedlik S,Loffeld O (2008) Real-time cycle-slip detection and determination for multiple frequency GNSS[C].In:Proceedings of the 5th workshop on positioning, navigation and communication, Hannover, Germany, pp 37–43
5. Fan J, Wang F (2007) A Study of GNSS triple-frequency ambiguity resolution based on geometry-free model [J]. J Astronaut 28(6):1593–1599
6. Xiong W (2007) Multiple frequency combination in cycle-slip detection and repair[J]. Wuhan Univ J 32(4):319–322
7. Ziqing W (1998) GPS relative positioning model [M]. Surveying and Mapping Press, Beijing, pp 130–137

Part II
Atomic Clock Technique and Time-Frequency System

Chapter 27
Progress Towards a Microwave Atomic Clock Based on the Laser-Cooled Cadmium Ions

Jianwei Zhang, Shiguang Wang, Kai Miao, Zhengbo Wang and Lijun Wang

Abstract In the past decades, many groups in the world were engaged in building the microwave or optical frequency standards based on different trapped ions and achieved great improvements. A project aimed at a microwave atomic clock based on the laser-cooled $^{113}Cd^{+}$ ions has been carried out since 2010 in our laboratory. The cadmium ion clock, a transportable clock with excellent frequency stability, is suitable in the comparison between the clocks located in different places, for example, to compare the time systems at different stations of BeiDou Navigation Satellite System, or to examine the general relativity. A linear quadruple ion trap and the technique of laser cooling are applied in this clock. Meanwhile, the cadmium clock can be designed to be transportable which requires only one laser to accomplish the laser cooling, optical pump and optical detection. In this paper, we will report the detailed progress of this clock.

Keywords Microwave frequency standard · Ion trap · Cadmium ion · Laser cooling

J. Zhang (✉) · S. Wang · K. Miao · Z. Wang · L. Wang
NIM-THU Joint Institute for Measurement Science (JMI), Tsinghua University, Beijing 100084, People's Republic of China
e-mail: zhangjw@tsinghua.edu.cn

J. Zhang · K. Miao · Z. Wang · L. Wang
Department of Precision Instrument, Tsinghua University, Beijing 100084, People's Republic of China

S. Wang · L. Wang
Department of Physics, Tsinghua University, Beijing 100084, People's Republic of China

J. Sun et al. (eds.), *China Satellite Navigation Conference (CSNC) 2013 Proceedings*, Lecture Notes in Electrical Engineering 245,
DOI: 10.1007/978-3-642-37407-4_27,

27.1 Introduction

The optical lattice and ion trap are successfully applied in the field of precision frequency metrology taking the advantages of the narrow spectrum linewidth due to the long interaction time between the radiation field and the trapped atoms or ions. Meanwhile, the technique of laser cooling is also applied to cool down the temperature of the atoms to greatly reduce the Doppler effect. The state of the art of the ion clocks is the optical clock based on Al^+ [1], which keeps the record of the most precision atomic clock in the world to 8.6×10^{-18}. Recently, an optical clock based on a single $^{88}Sr^+$ with the frequency uncertainty of 2×10^{-17} has been reported [2]. These optical clocks outperform the current realization of SI second, the caesium fountains. This makes it possible to redefine the unit of time in the future.

Although the optical clocks are extremely accurate, they have to be operated only in laboratory condition, at least until now, because of their complexity and big volumes. In some special application fields, for example, the frequency comparison between the different atomic clocks located in different laboratories, the comparison between the frequency and time systems at the different ground stations of BeiDou Navigation Satellite System, not only the precision, but also the transportability of clocks is required. At LNE-SYTRE in France, a transportable caesium fountain clock has been developed [3]. In China, the National Institute of Metrology (NIM) is the one who builds and operates the best caesium fountain clocks [4] so far.

The hyperfine splitting of the ground state of the $^{113}Cd^+$ ions is a promising choice as a clock transition for a microwave atomic clock, which has been proposed by the groups in Japan and the USA [5, 6]. In the previous works, the buffer gas is applied to cool the ions, which makes the temperature of ions to be slightly higher than the room temperature. The fractional frequency shift due to the second order Doppler effect is one of the factors limiting the final performance. In this paper, a laser-cooled cadmium ion clock is reported, in which the temperature of the ions can be cooled to be less than 1 K and the second order Doppler frequency shift is greatly reduced. In the same time, the simple energy level structure of the cadmium ions opens the way to build a transportable atomic clock.

27.2 Principles of the Cadmium Ions Clock

Figure 27.1 shows the energy levels of the $^{113}Cd^+$ ions. The transition of $|F = 0, m_F = 0> \rightarrow |F = 1, m_F = 0>$ of the ground state is the clock transition with the frequency of 15 199 862 854.96(12) Hz [7]. The cycling transition of $|S_{1/2}, F = 1, m_F = 1> \rightarrow |P_{3/2}, F = 2, m_F = 2>$ is used to laser cool the ions and to excite the fluorescence signal for detection. Meanwhile, the ions can be optically pumped to the state of $|S_{1/2}, F = 0, m_F = 0>$ via the transition of $|S_{1/2}, F = 1> \rightarrow |P_{3/2}, F = 1>$.

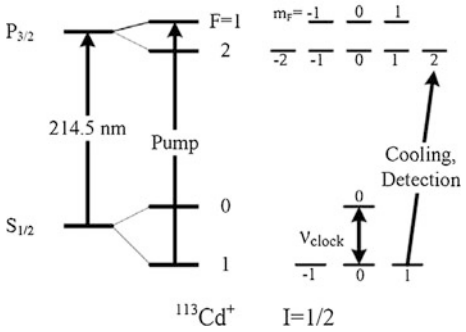

Fig. 27.1 Energy levels of $^{113}Cd^{+}$ ions. (Not to scale)

After the ions are loaded, firstly, the cooling laser is unblocked to cool the ions to below 1 K. Secondly, the cooling laser is blocked after cooling phase, and the pump laser is unblocked to pump the ions to the state of $|S_{1/2}, F = 0, m_F = 0>$. Thirdly, all of the lasers are blocked, and two successive microwave pulses with the Ramsey interval time of T are applied for interrogation. Last, the cooling laser is unblocked again, and the fluorescence signal excited by the laser is detected to obtain the transition probability of the ions in the detuning microwave field.

For the atomic clock based on the laser-cooled $^{113}Cd^{+}$ ions, the cooling laser and the detection laser can be the same one. There is a frequency difference of about 800 MHz between the cooling laser and the pump laser, corresponding to the hyperfine splitting of the $P_{3/2}$ state, which can be realized by using an acoustic-optic modulator. Consequently, only one laser is need for all of the laser cooling, optical pump and detection. To our knowledge, in all of the atomic clocks based on laser-cooled ions, the microwave $^{113}Cd^{+}$ ion clock is the only one that needs only one laser.

Since the design of the ion trap has been well described elsewhere [7, 8], only a brief introduction is given here. A linear quadrupole trap is used for trapping ions. The four electrodes of the trap are made of oxygen-free copper, and the dimension of the trap is optimized. The diameter of the electrodes is 14.22 mm and the minimum radial distance from the center of the trap to the surface of the electrodes is 6.2 mm. Every electrode is cut into three segments. On the outer segments of each electrode, a dc voltage is applied as endcap voltage to confine the ions in the axial direction. And on the inner segments of the diagonal electrodes, a radio frequency voltage with the frequency of 1.25 MHz and the amplitude of 300 V is applied to confine the ions in the radial direction. Small dc voltages are added on the inner segments of the electrodes to compensate the scattering electric fields. The ion trap is installed in an ultrahigh vacuum chamber with a pressure of 5×10^{-8} Pa.

The used laser system for the cadmium ions clock is a TA-FHG pro from Topitca Inc., a frequency-quadrupled diode laser system. An external cavity diode laser, a DL pro operating at 858 nm, used as the seed laser, is boosted by a tapered amplifier, a TA pro. The amplified laser is frequency-quadrupled to 214.5 nm by two cascade doubling cavity.

For laser cooling, pumping and detection, the frequency of the laser must be stabilized to MHz level. Normally the precision control of the laser frequency can be achieved by directly locking the uv laser to the cadmium ion transition line, but this method is not appropriate in our case because of the limited power output of the laser system. Therefore, the seed laser of 858 nm is stabilized to MHz level by comparing the frequency with an 852 nm laser stabilized to the cesium lines via a transfer cavity [9].

27.3 Progress

To load ions, we heat the cadmium oven pointing the center of the trap and switch on the electron gun on the opposite direction of the oven. The cadmium vapor from the oven is ionized by the electron bombardment and some of these ions can be trapped. The fluorescence signal of the trapped ions is induced by a resonant laser and detected by a photomultiplier tube (PMT). Meanwhile, the appearance of the ion cloud is captured by a electron multiplying charge coupled device (EMCCD), as shown in Fig. 27.2.

By the technique of laser cooling, the ions can be cooled down to crystallization state, i.e. the ions are confined in so small space that a crystal lattice structure is formed by the Coulomb repulsion interaction among the ions. Usually, the more the ions in the trap, the more difficult to cool the ions because many ions are out of the nodal line of the trap, and they could be heated by the applied radio frequency field. In our experiments, approximately 10^4 ions are cooled to 16 mK by laser cooling [10].

After the trapped ions are cooled, the ions are optically pumped to the state of $|S_{1/2}, F = 0, m_F = 0>$ by a laser pulse. Then the transition probability of the ions in the detuning microwave field is measured by detecting the fluorescence intensity with the Ramsey's separated oscillation fields technique, in our experiment the pulse width is t and the interval separation is T. Figure 27.3 shows a typical measured Ramsey fringe. In the experiment, the separation between the two microwave pulse is T = 2 s. Consequently, the FWHM of the center fringe is 0.25 Hz.

Although the clock transition of the cadmium ions clock is insensitive to the magnetic field, the quadratic Zeeman shift still exists, and it is one of the main factors affecting the performance of the clock. To insure high precision of the clock, one has to measure the frequency of the clock transition in zero magnetic

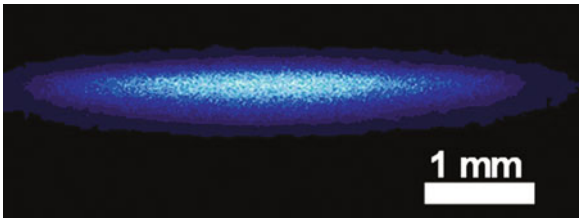

Fig. 27.2 The $^{113}Cd^+$ ions cloud photograph. (Exposure time is 0.2 s)

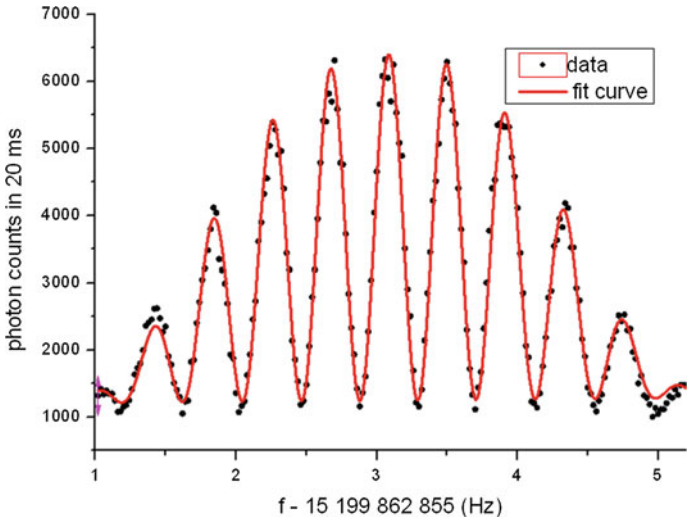

Fig. 27.3 The Ramsey fringe of the clock transition. The solid circle is the photon counts of the fluorescence with a gate time of 20 ms, and the curve is the fit to the measured data

field. In our experiment, the frequencies of the clock transition in different magnetic fields are measured and the frequency in zero field is extrapolated. During the measurement, the frequency reference is a commercial cesium clock (Symmetricom 5071). The measurement results of two isotopes of $^{113}Cd^{+}$ and $^{111}Cd^{+}$ are

$$^{113}\nu_0 = \ 15\ 199\ 862\ 854.96(12)\ \text{Hz} \tag{27.1}$$

and

$$^{111}\nu_0 = \ 14\ 530\ 507\ 349.9\ (1.1)\ \text{Hz}, \tag{27.2}$$

respectively [7]. The result of $^{113}Cd^{+}$ agrees with other's report very well [6] and the precision of the $^{111}Cd^{+}$ is improved by seven orders than previously reported data [11].

The performance of the clock is measured further by the close-loop operation of the atomic clock. According to the formula of Allan variance

$$\sigma_y^2(\tau) = \left(T_{cycle}/\tau\right)/(2\pi\, Q\ SNR)^2, \tag{27.3}$$

where τ is the sampling time, T_{cycle} the cycling time to obtain an error data, Q the quality factor of the clock transition line and SNR the signal-to-noise ratio of the clock transition signal. In the experiment, $T_{cycle} = 9$ s, $Q = 6.1 \times 10^{10}$, SNR $\approx$ 30, hence the frequency stability of the experimental setup should be approximately $\sigma_y = 3 \times 10^{-13}\ \tau^{-1/2}$. In our laboratory, the best frequency reference is an ultra-stable quartz oscillator (Symmetricom 4145B) with phase locked

to a commercial cesium clock, which is not sufficient to measure the frequency stability of the cadmium ion clock.

In order to obtain the preliminary stability performance of the experimental setup, we measured the frequency stability in open-loop operation mode. The cadmium ion is used to interrogate the microwave signal synthesized from the frequency reference 4145B. This measurement result is a combination of the stability of the frequency reference and the cadmium ions clock. Analyzing the data measured in a time duration of 1.5 h, we find that the obtained frequency stability is consistent with the specification of the 4145B. Consequently, the frequency stability of the clock is limited by the reference in the measurement.

A technique for the precise and continuous time and frequency synchronization based on fibers has been developed in our lab recently [12]. It has been demonstrated that a precision frequency signal can be transmitted by about 90 km with the residual frequency instability at the 10^{-19} level for 1-day sampling time. Now, an experiment has been planned to be carried out, in which the ultra-precise standard frequency signal from NIM, who keeps the primary time standard of China, will be used as the frequency reference. Further measurement result will be reported once the experiment is accomplished.

27.4 Summary

The atomic clocks based on the trapped ions with outstanding performances have been developed thanks to the successful application of techniques of ion trapping and laser cooling. The microwave atomic clock based on laser-cooled $^{113}Cd^{+}$ ions seems to be of great performance potential, and can be design to be transportable due to the simple energy level structure of the cadmium ions. This clock is promising to be applied in the field of precise comparison of atomic clocks. In this paper, we reported the principle and the design of the clock under development. In the experiments, the laser-cooled ions cloud is obtained and the ground state hyperfine splitting of the cadmium ions is measured precisely. These progresses make it possible for us to build a transportable microwave atomic clock with high performance in near future.

Acknowledgments This work was supported by the National "973" Program of China (No. 2010CB922901) and the Tsinghua University Scientific Research Initiative Program (No. 20131080063).

References

1. Chou C, Hume D, Koelemeij J et al (2010) Frequency comparison of two high-accuracy Al^{+} optical clocks. Phys Rev Lett 104:070802

2. Madej A, Dube P, Zhou Z et al (2012) 88Sr + 445-THz single-ion reference at the 10–17 level via control and cancellation of systematic uncertainties and its measurement against the SI second. Phys Rev Lett 109:203002
3. Guéna J, Abgrall M, Rovera D et al (2012) Progress in atomic fountains at LNE-SYRTE. IEEE Ttrans. Ultrason., Ferroelect., Freq. Cont. 59, 391
4. Li T, Lin P, Li M et al (2009) The transportable cesium fountain clock NIM5: its construction and performance. Front Phys China 4:155
5. Tanaka U, Imajo H, Hayasaka K et al (1996) Determination of the ground-state hyperfine splitting of trapped $^{113}Cd^{+}$ ions. Phys Rev A 53:3982
6. Jelenkovic B, Chung S, Prestage J et al (2006) High-resolution microwave-optical double-resonance spectroscopy of hyperfine splitting of trapped $^{113}Cd^{+}$ ions. Phys Rev A 74:022505
7. Zhang J, Wang Z, Wang S et al (2012) High-resolution laser microwave double-resonance spectroscopy of hyperfine splitting of trapped $^{113}Cd^{+}$ and $^{111}Cd^{+}$ ions. Phys Rev A 86:022523
8. Zhang J, Wang Z, Wang S et al (2012) Progress towards a microwave frequency standard based on the laser cooled $^{113}Cd+$ ions. 2012 IEEE international frequency control symposium (IFCS), Baltimore, MD, USA
9. Wang S, Zhang J, Wang Z et al Frequency stabilization of 214.5 nm ultraviolet laser. Chin Opt Lett (in press)
10. Wand S, Zhang J, Miao K et al Cooling and crystallization of trapped $^{113}Cd^{+}$ Ions for atomic clock. Chin. Phys Lett (in press)
11. Brimicombe MSWM, Stacey DN, Stacey V, Huhnermann H, Menzel N (1976) Proc. R. Soc. London, Ser.A 352, 141
12. Wang B, Gao C, Chen W et al (2012) Precise and continuous time and frequency synchronisation at the 5×10^{-19} accuracy level. Sci Rep 2:556

Chapter 28
The Electronic System of ^{87}Rb CPT Maser Atomic Clock

Wenyu Zhao, Xin Wang, Xiaofeng Li, Jie Liu, Kan Zhao and Shougang Zhang

Abstract We present the electronic system, together with the physical package, of the ^{87}Rb CPT maser atomic clock, which is related to the coherent population trapping phenomenon. Moreover, frequency locking of our experimental apparatus was also developed based on this system. Our results show that the measured short-term frequency stability (Allan deviation) is better than $2 \times 10^{-12}\ \tau^{-1/2}$ from 1 to 100 s.

Keywords CPT maser · Atomic clock · Microwave synthesizer

28.1 Introduction

Since the pioneering experimental observation of coherent population trapping (CPT) phenomenon in 1976 [1], it raise the possibility of potential applications in many fields, such as atom cooling [2], magnetometry [3], lasing without inversion [4] and atomic frequency standard [4–6]. In recent years, its application in atomic frequency standards has extensively drawn much attention [7–10]. The CPT atomic clock is especially suitable for atomic clocks of small size and low power consumption, and it has been widely used in measurement, navigation, communication, etc.

W. Zhao (✉) · X. Wang · X. Li · J. Liu · K. Zhao · S. Zhang
National Time Service Centre. Chinese Academy of Sciences, Xi'an 710600, China
e-mail: zhaowy@ntsc.ac.cn

W. Zhao
Key Laboratory of Time and Frequency Primary Standards. Chinese Academy of Sciences, Xi'an 710600, China

W. Zhao
Graduate University of Chinese Academy of Sciences, Beijing 100049, China

J. Sun et al. (eds.), *China Satellite Navigation Conference (CSNC) 2013 Proceedings*, Lecture Notes in Electrical Engineering 245,
DOI: 10.1007/978-3-642-37407-4_28,

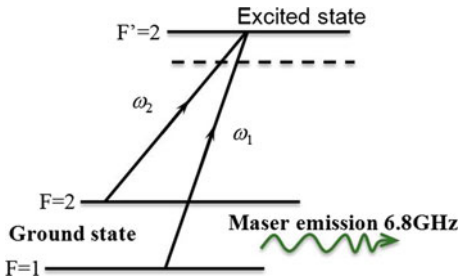

Fig. 28.1 Three-level lambda atomic system

In this paper, we first present the electronic system and the physical package of the ^{87}Rb CPT maser atomic clock. Then, we give a detailed description of the subsystems, including the microwave synthesis chain, the detection apparatus, the digital servo system, the circuits of temperature control, and the C-field. Based on the designs, a CPT maser with ^{87}Rb as the atomic medium has been built. Our results show that the measured short-term frequency stability (Allan deviation) is better than $2 \times 10^{-12}\ \tau^{-1/2}$ from 1 to 100 s.

We illustrate the CPT effect using a three-level Λ-system, where alkali metal atoms are interacting with a pair of coherent radiation laser fields (as shown in Fig. 28.1). When the atoms are placed in an electromagnetic cavity, this magnetization is responsible for a coherent microwave emission, namely, the so-called CPT maser [11].

28.2 CPT Maser Experimental Setup

Figure 28.2 shows the CPT Maser experimental setup. The setup is composed of optical sub-system (including laser, electro-optic modulator, fiber couplers etc.), physical package (including microwave cavity, absorption cell, C-field coils, magnetic shields), and electronic package [12, 13] (including microwave synthesis chain, heterodyne Rb-maser receiver, and servo electronic system). Then we give a detailed description of such system as follows:

Within our model, the quartz cell where ^{87}Rb atoms, together with buffer gas, are loaded, and the cavity are the most important ingredients of the physical package. The coupling between CPT maser and the cavity is detected by the heterodyne Rb-maser receiver. A double magnetic shield is used to reduce environment magnetic field fluctuations, and the microwave synthesis chain is used to modulate the phase of the laser carrier by driving the electro-optic modulator (EOM), which modulates the laser with two frequencies according to the Λ scheme. When the laser carrier is modulated at 3,417 MHz, which is half of the hyperfine splitting, the first two modulation sidebands of the laser spectrum separated by 6,834 MHz, allowing the excitation of the atomic transition through the CPT phenomenon. Finally, the servo electronic locks the quartz oscillator to the atomic transition.

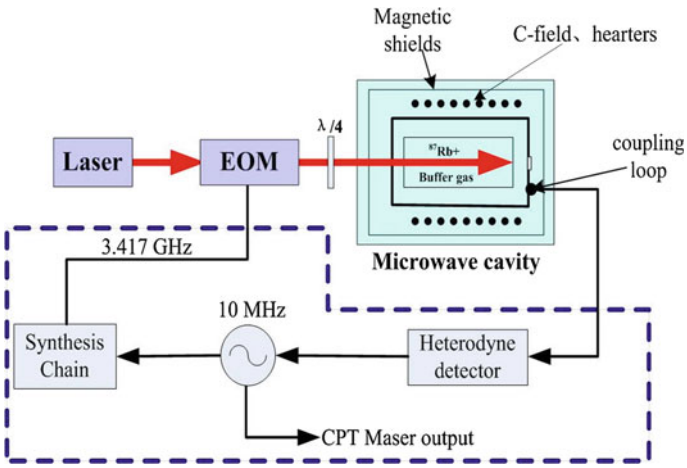

Fig. 28.2 CPT maser prototype

28.3 Electronics

Next we describe the prototype of a CPT maser with emphasis on the electronic setup in laboratory. With regard to main blocks, it can be realized by following three parts.

28.3.1 The Microwave Synthesis Chain

The microwave synthesis chain requires low phase noise and adjustable fractional frequency. Therefore, we use phase locked loop and direct digital synthesis (DDS). The former compares the phase of the interrogate signal with the phase of the signal derived from local oscillator, and adjusts the dielectrically stabilized microwave oscillator (DRO) to keeping the phases matched. The latter provides much better frequency agility, phase noise, and can be used to precise controlling the phase of output. In the following subsections, our detailed design is described.

In the microwave synthesis chain, a 10 MHz low-phase noise Oven-Controlled Crystal Oscillator (OCXO) is used as the local reference. The short-term stability of OCXO is 10^{-13}, satisfying the requirement of CPT maser short-term stability up to 10^{-12}. The range of the OCXO frequency control must be suitable for a lifetime of 10 years. At the same time, it should keep the control range as narrow as possible to minimize the frequency instability effects coming from the amplitude noise.

The initial frequency multiplication stages are designed to multiply the 10 MHz signal to 100 MHz. First, 10 MHz signal is multiplied 5 times to 50 MHz. Its power is split into two parts. One is mixed with 100 MHz with a mixer, the other is phase detected with the output of the pre-mixer. The output of the phase detector is

fed back to control the OCXO through a loop filter. The 100 MHz oscillator is locked with similar method. The frequency of 100 MHz is fed to a varactor-based comb generator exploiting the nonlinear behavior of a varactor diode junction to step-up the signal to 3,200 MHz (×32). The required components at 3,200 MHz are filtered out by a band-pass filter. The signal of 3,200 MHz is power split into two parts. One is doubled to 6400 MHz and used in the maser receiver. The other is mixed to 217 MHz with the signal of the 3,417 MHz, which is output by dielectrically stabilized microwave oscillator (DRO). The signal of 217 MHz is down converted again with the signal of 200 MHz which is doubled from the output by 100 MHz oscillator. This signal can be phase-compared with the 17 MHz component. The 17 MHz is produced by a commercially available 48-bit DDS chip, which is clocked by 200 MHz obtained by double frequency of 100 MHz oscillator. The output of the DDS is controlled by an 8-bit microcontroller. Then the DRO is phase-locked to the appropriate component of the comb generator (as shown in Fig. 28.3).

The phase noise of CPT synthesis chain at 3,417 MHz is measured to 3 kHz by using a FSUP26 phase noise measurement system (Fig. 28.4). The result of the phase noise measurement is close to theoretical value calculated by the deteriorating formula of 20lgN (dB) with N being the multiple times.

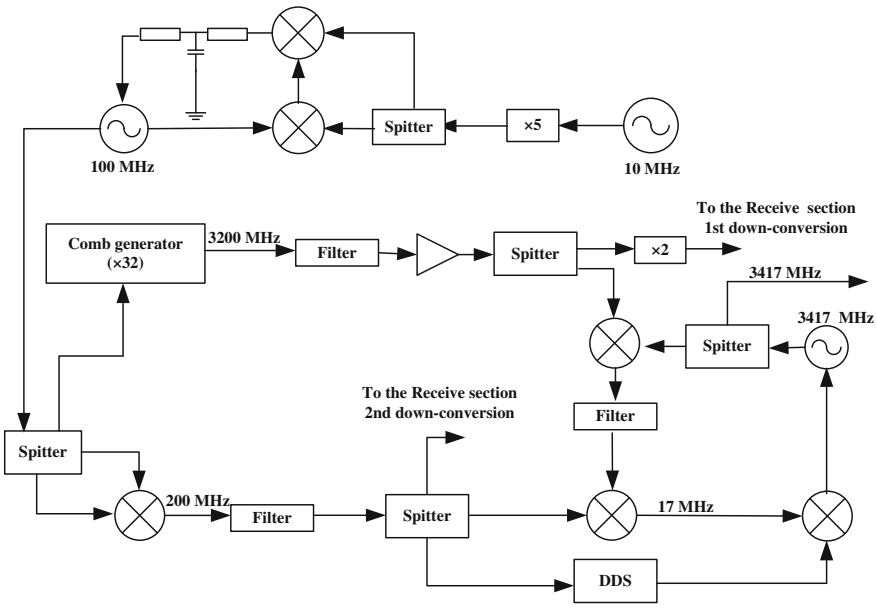

Fig. 28.3 Block scheme of the synthesis chain

According to Eq. (28.1) [14], the calculated contribution of the synthesiser to the clock frequency stability is 2×10^{-13} at 1 s, which is the most important factor in the electronic system.

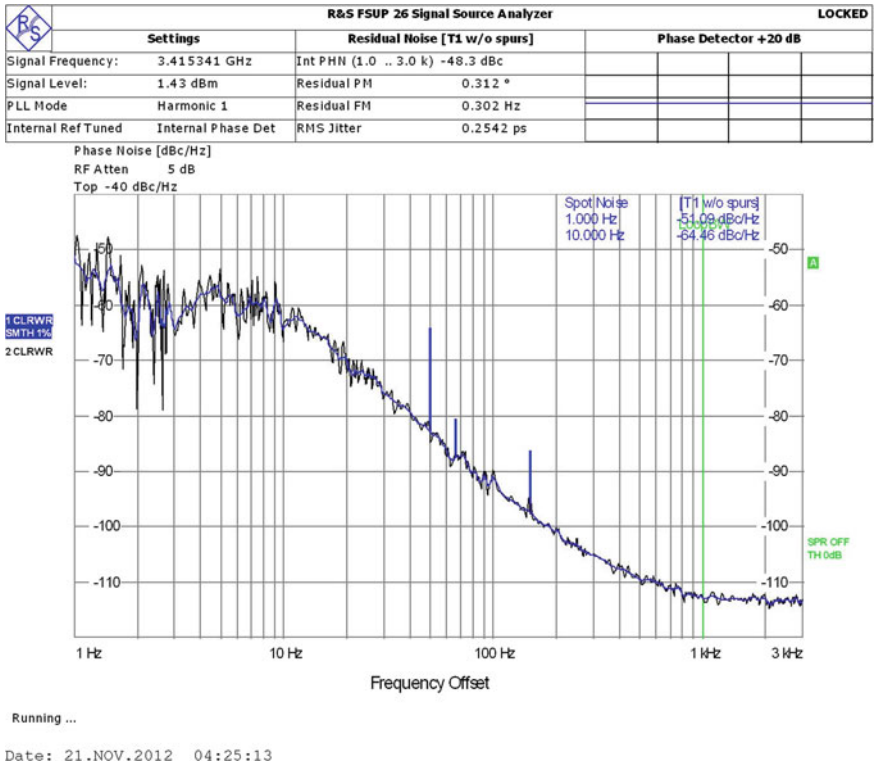

Fig. 28.4 Phase noise of CPT synthesizer at 3,417 MHz

$$\sigma_y(\tau) = 0.45\, S_y(2f_M)^{1/2} \cdot \tau^{-1/2} \tag{28.1}$$

where f_M is modulation frequency, $S_y(f)$ is phase noise of the synthesizer.

28.3.2 The Rb-Maser Receiver

Another functional block is the Rb-maser receiver (Fig. 28.5). It is a classical super-heterodyne architecture with a double down-conversion in our scheme, which offers superior sensitivity, frequency stability and selectivity. When the laser is modulated in the cavity by the 3,417 MHz microwave signal exported from the microwave synthesiser centered on the atomic resonance, it results in the resonance interrogation. The CPT maser signal is detected by a coupling loop. The function of Rb-maser receiver is detecting the power of this signal. The frequency of the CPT maser signal is 6,834 MHz, and about −100 dBm in level actually measured. It is fed to a low-noise amplifier (LNA) first with gain of 25 dB. The

double down-conversion transforms the input signal to IF frequency of 434 and 34 MHz. One of the local oscillators (LO) is 6,400 MHz doubled to the output of the comb generator. And the other is 400 MHz doubled to 200 MHz from the microwave synthesis chain. The gain of double down-conversion is 30 and 40 dB separately. Finally, there is a voltage that is direct proportion to the power of CPT maser signal converted through a power detector. The sensitivity of the receiver is about −110 dBm approved in practice.

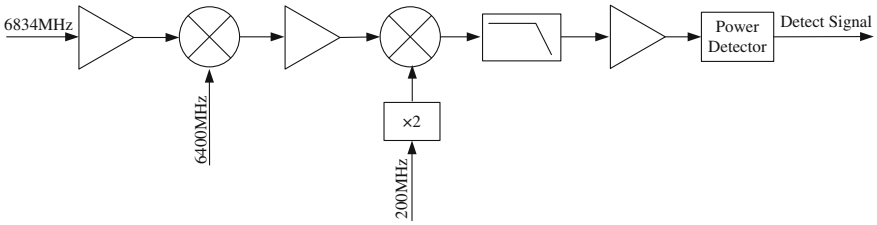

Fig. 28.5 Block scheme of the Rb-maser receiver

28.3.3 The Servo System

We built a digital quartz servo system (shown in Fig. 28.6). The output signal of the heterodyne receiver is transformed by an analog to digital converter (ADC). Then it is processed by a programmable microcontroller (MCU) that implements the Lock-in and PI calculating blocks. The loop gain and the loop bandwidth can be adjusted by changing a multiplicative constant. All the parameters are set via the communication port of computer.

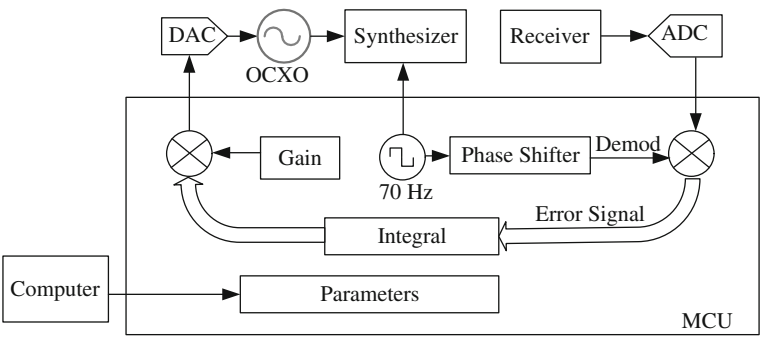

Fig. 28.6 Digital servo system

The stability of CPT maser is influenced by the temperature stability of the physics package. There are several effects causing frequency shifts through temperature, such as the collisions of Rb atoms with the buffer gas atoms contained in

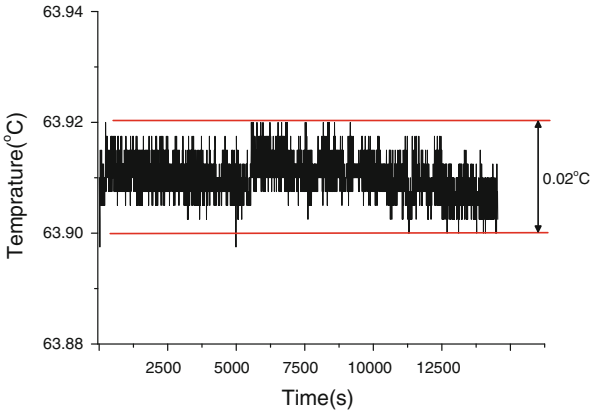

Fig. 28.7 Temperature stability of cavity

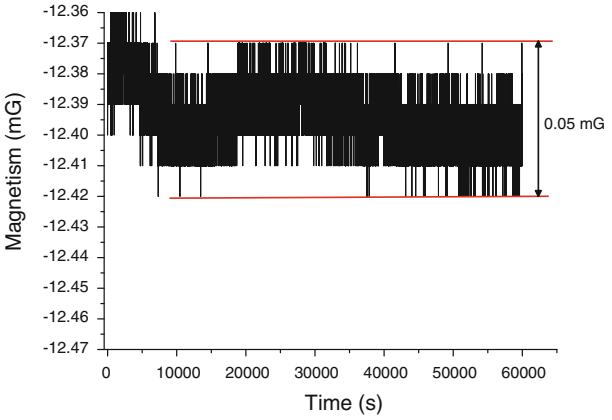

Fig. 28.8 C-field magnetic stability

the cell, the cavity pulling, the atomic density and the light shift. The temperature of the microwave cavity in the physics package is set about 60 °C. The temperature control circuit is designed with analog technic. The temperature has a long-term stability of about 20 mK for average times of 10,000 s (shown in Fig. 28.7). And the C-field produced by a current source is measured, which has a long-term stability of about 0.05 mG a day (shown in Fig. 28.8).

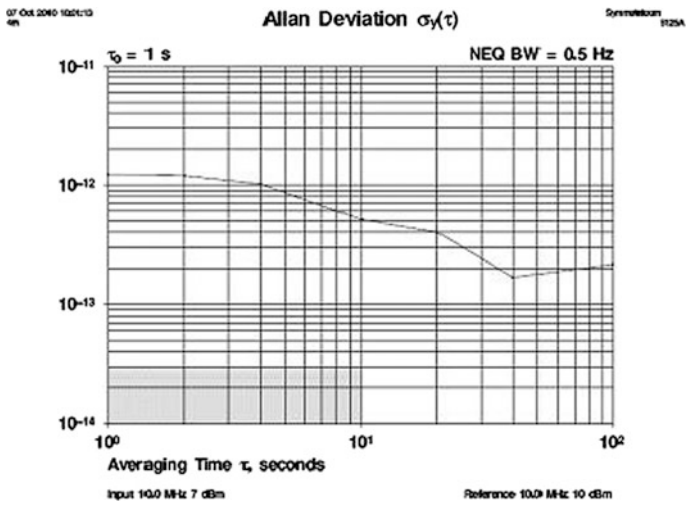

Fig. 28.9 CPT maser frequency stability

28.4 Conclusion

In conclusion, the scheme of the electronic system for CPT maser was introduced. With the system, the clock stability is measured (shown in Fig. 28.9). The electronic system we realized does not limit the performance of the CPT maser prototype. The stability of CPT reaches a level of $2 \times 10^{-12}\ \tau^{-1/2}$ from 1 to 100 s.

Acknowledgments This study is supported by the National Science Fund for Distinguished Young Scholars of China (Grant No.61025023).

References

1. Alzetta G, Gozzini A, Moi L, Orriols G (1976) An experimental method for the observation of r.f. transitions and laser beat resonances in oriented Na vapour. Nuovo Cimento Soc. Ital Fis B 36(1):5–20
2. Aspect A, Arimondo E, Kaiser R, Vansteenkiste N, Cohen-Tannoudji C (1989) Laser cooling below the one-photon recoil energy by velocity-selective coherent population trapping: theoretical analysis. J Opt Soc Am B 6(11):2112–2124
3. Scullt MO, Fleischauer M (1992) High-sensitivity magnetometer based on index-enhanced media. Phys Rev Lett 69:1360–1363
4. Scullt MO (1992) lasers and masers to phaseonium and phasers. Phy Rep 219:191
5. Cyr N, Tetu M, Breton M (1993) All-optical microwave frequency standard: a proposal. IEEE Trans Instrum Meas 42:640–649
6. Arimondo E Progress in optics (1996) V Coherent Population Trapping in Laser Spectroscopy. Progress in Optics 35:257–354
7. Knappe S, Schwindt PDD, Shah V et al. (2005) A chip-scale atomic clock based on ^{87}Rb with improved frequency stability. Optics express 13(4):1249–1253

8. Vanier JLevine M, Janssen D (2003) The coherent population trapping passive frequency standard [Rb example]. IEEE 52(2):258–262
9. Levi F, Godone A, Micalizio S, Calosso C (2003) maser clock evaluation for Galileo. 34th Annual precise time and time interval (PTTI) meeting
10. Knappe S, Wynanda RW, Kitching J (2001) Characterization of coherent population-trapping resonances as atomic frequency references. J Opt Soc Am B 18(11):1545–1553
11. Vanier J, Godone A, Levi F (1998) Coherent population trapping in cesium: Dark lines and coherent microwave emission. Phy Rev A 62 58(3):2345–2358
12. Calosso CE, Levi F, Bertacco EK, Godone A, Micalizio S (2005) Low-noise electronic design for the 87Rb coherent population trapping maser. IEEE Transactions on ultrasonics, ferroelectrics, and frequency control 52(11):1923–1930
13. Levi F, Micalizio S, Godone A, Calosso CE, Bertacco EK et al. (2003) Realization of a CPT Rb maser prototype for Galileo. IEEE international frequency control symposium and PDA exhibition jointly with the 17th European frequency and time forum, pp 22–26
14. Barillet R, Giordano V, Viennet J, Audoin C (1993) Limitation of the clock frequency stability by the interrogation frequency noise: experimental results. IEEE transactions on instrumentation and measurement 42(2):276–280

Chapter 29
Research of Satellite Clock Error Prediction Based on RBF Neural Network and ARMA Model

Xiaoyu Li, Xurong Dong, Kun Zheng and Yatao Liu

Abstract As the main error sources of the observation data, the precision of prediction model has a direct effect on the performance of navigation system. Considering that the clock error was composed of trend part and random component, an integrated model was proposed, which was based on RBF neural network and ARMA. The trend was modeled using the RBF neural network, while the random part by the ARMA model, and last added them to the predicted results. The simulation results validate the feasibility and the better performance of the integrated method through an example by using the precise IGS clock data.

Keywords Clock error prediction · RBF neural network · ARMA · Integrated model

29.1 Introduction

The satellite clock error is one of the main error sources in precise navigation satellite positioning. Taking GNSS for example, the accuracy of ex-post clock error provided by IGS can be up to 75 ps, which fully meet the requirement of centimeter-level orbit determination, but with a 13-days delay. It is difficult to establish the accurate atomic clocks errors model for that the atomic clock frequency fluctuation is a linear superposition of several different noises [1]. Clock errors prediction has a great effect on the accuracy of navigation, which helps to improve the reliability and accuracy of parameters forecast [2].

Traditional clock error prediction models include linear model, quadratic terms model and gray model. Linear model and quadratic terms model are simple and

X. Li (✉) · X. Dong · K. Zheng · Y. Liu
Academy of Equipment, Beijing 101416, China
e-mail: li1999xiaoyu@163.com

J. Sun et al. (eds.), *China Satellite Navigation Conference (CSNC) 2013 Proceedings*, Lecture Notes in Electrical Engineering 245,
DOI: 10.1007/978-3-642-37407-4_29,

suitable for short-term prediction, but errors accumulate seriously with the increase of the prediction time; gray model has the advantages of less sample data and strong anti-interference ability, while the model requires that the original function is smooth and exponentially changes which affect the prediction accuracy and length [3]. All these models consider the trend item of the clock errors, but ignore the random part.

Combining the Radial Basis Function (RBF) neural network which has better nonlinear prediction ability with the ARMA model that highlights random items modeling, the paper builds up an integrated model to forecast the clock errors. In order to verify the effectiveness and feasibility of the model, precise clock errors offered by IGS are used to simulate and analyze.

29.2 Clock Error Prediction Models

29.2.1 RBF Neural Network Model

Radial Basis Function (RBF) neural network proposed by Powell in 1985 is a two-layer forward-feed network with the single hidden-layer. It simulates the neural network structure of human brain that can adjust partially, overwrite each accepted domain and approximate overall performance [4]. The basic RBF neural network structure is shown in Fig. 29.1.

RBF neural network is a feedforward neural network that uses the radial basis function as the hidden-layer, including the three-layer structure of the input-layer, hidden-layer and output-layer. From the input-layer to the hidden-layer is nonlinear, while it is linear between the hidden-layer and the output-layer. Transformation function of the hidden layer adopts radial basis function which is a local distribution center radially symmetric attenuation non-negative non-linear function [5]. Gaussian function is used as the basis function generally.

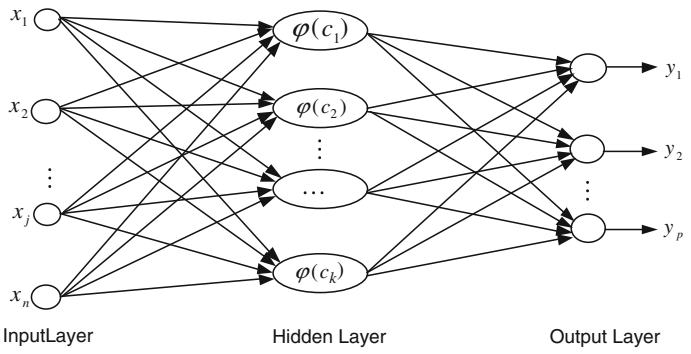

Fig. 29.1 RBF neural network structure

Gaussian function can be expressed as Eq. (29.1)

$$G(X_k) = \exp\left(-\frac{\|X_k i - C_i\|^2}{r^2}\right) \tag{29.1}$$

where X_k is a set of input variables, C_i is the center of each cluster, r represents the width of the radial basis function. Shown in Eq. (29.2), process between the hidden-layer and output-layer is linearly-adding [6].

$$y_k = \sum_{i=1}^{m} w_1 G_1(X_k) \tag{29.2}$$

29.2.2 ARMA Model

To a time series $\{X_i\}$, the Auto Regressive Moving Average (ARMA) can be expressed as ARIMA (p, d, q), where p, q are the orders of the model, and d is the number of differencing.

The basic form of autoregressive moving average model ARMA (p, q) can be expressed as Eq. (29.3)

$$x_t = \phi_1 x_{t-1} + \ldots + \phi_p x_{t-p} + \varepsilon_t - \theta_1 \varepsilon_{t-1} - \ldots - \theta_q \varepsilon_{t-q} \tag{29.3}$$

To determine the order of ARMA model and estimate the parameters, we need to calculate autocorrelation function and partial correlation function of the series [7].

The autocorrelation and partial correlation calculated plot can roughly determine the order of the ARMA model, and the BIC criteria is given to decide the precise model order as follows [8].

$$BIC(p) = N \ln \sigma_x^2 + P \ln N \tag{29.4}$$

where P is the order of the model, σ_x^2 is the variance of the residuals and N is length of the series.

After the model determine, the regression method is used to estimate the model parameters. Firstly, establish the AR model of observational data, define the upper bound of the regression order to $P = [\sqrt{N}]$, and then adopt the BIC criteria to calculate the estimates of the regression coefficients $\left(a'_1, a'_2, \cdots a'_{p'}\right)$, calculate residuals as Eq. (29.5).

$$\varepsilon'_t = x_t - \sum_{i=1}^{p'} a'_i x_{t-i} \tag{29.5}$$

where $t = p' + 1, p' + 2, \cdots, N$. And the approximate ARMA (p, q) model can be expressed as follow.

$$x_t = \sum_{i=1}^{p} a_i x_{t-i} + \varepsilon'_t + \sum_{j=1}^{q} b_j \varepsilon'_{t-j} \tag{29.6}$$

where $t = L+1, L+2, \cdots, N$, $L = \max(p', \mathrm{p}, \mathrm{q})$, a and b are the undetermined parameters.

Using the least squares estimation method to solve the undetermined parameters.

Assumed that,

$$X = \begin{bmatrix} x_L & x_{L-1} & \cdots & x_{L-P+1} \\ x_{L+1} & x_L & \cdots & x_{L-P+2} \\ \vdots & \vdots & \vdots & \vdots \\ x_{N-1} & x_{N-2} & \cdots & x_{N-P} \end{bmatrix}, \; Y = \begin{bmatrix} x_{L+1} \\ x_{L+2} \\ \vdots \\ x_N \end{bmatrix},$$

$$\varepsilon = \begin{bmatrix} \varepsilon'_L & \varepsilon'_{L-1} & \cdots & \varepsilon'_{L-q+1} \\ \varepsilon'_{L+1} & \varepsilon'_L & \cdots & \varepsilon'_{L-q+2} \\ \vdots & \vdots & \vdots & \vdots \\ \varepsilon'_{N-1} & \varepsilon'_{N-2} & \cdots & \varepsilon'_{N-P} \end{bmatrix} \text{ and } \beta = [a, b]^T.$$

Least squares estimation of parameters can be solved as:

$$\beta = \begin{bmatrix} X^T X & X^T \varepsilon \\ \varepsilon^T X & \varepsilon^T \varepsilon \end{bmatrix}^{-1} \begin{bmatrix} X^T Y \\ \varepsilon^T Y \end{bmatrix}. \tag{29.7}$$

29.3 Integrated Model

Clock error sequence can be considered as the superposition of two parts of the trend part and the random component. The paper proposes an integrated model based on RBF neural network and ARMA model, which is the combination of a trend part and random part. The integrated model clock error prediction process is shown in Fig. 29.2.

1. Clock error data preprocessing. To detect outliers, non-data segment, data transition and so on, and correct them in order to achieve better results. As to outliers and non-data segment, the interpolation method is used to interpolate these points and the non-data segment after removing outliers. To deal with the data transition a moving window method is given to detect the transition. The clock error prediction model can be built up after the preprocessing;

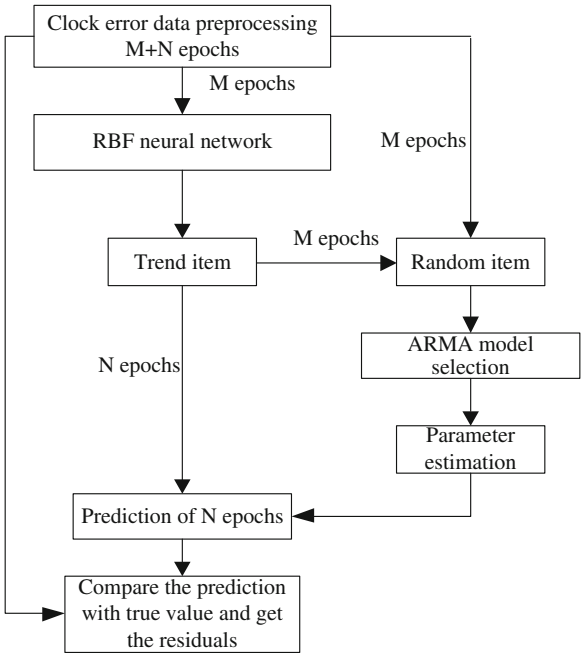

Fig. 29.2 Clock error prediction with integrated model

2. Use the RBF neural network model to predict clock error of M epochs, extract trend items and random items, and establish random items prediction model based on ARMA model;
3. To the following N epochs RBF neural network is adopted to predict the trend part and ARMA model is utilized to the random items, and then add both results to the predict the clock error.

29.4 Testing and Simulation

Use IGS precise clock product to analyze the real data of spaceborne atomic clocks between 0:00 on January 1st, 2011 and 23:55 on July 30, 2011 with 5 min interval. The results are evaluated by the maximum (MAX), minimum (MIN), standard deviation (STD) and the mean square error (RMS) of the result.

29.4.1 Experiments Design

Case I: Research on model sampling interval and the input vector dimension. Different dimensions and different intervals are used to improve the RBF model on

the satellite clock error prediction. Compare the simulation results to obtain the optimal parameters that are suitable in clock error prediction, and taking the PRN14 as an example.

Case II: Utilizing the optimal sampling interval and the input vector dimension that obtained from Case I, the clock errors for PRN3 and PRN14t were predicted for 1 and 30 days respectively, and compared with the RBF neural network model at the same time. A cesium clock and a rubidium clock are onboard PRN3 and PRN14, respectively.

29.4.2 Results Analysis

29.4.2.1 The Result of Case I

1. The influence of the sample interval

The test samples are used to predict with RBF neural network model. Figure 29.3 and Table 29.1 show the results that when the input dimension is set to 500 and training sample interval is set to 5, 10 and 15 min respectively.

As we can see from Fig. 29.3 and Table 29.1, with sample interval increases the prediction accuracy gradually decreases The reason is that with the increase of sample interval training samples become more sparse, leading to ignore serious short-term and the model can't accurately predict the characteristics of the sample.

2. The influence of the input vector dimension

Figure 29.4 and Table 29.2 show the RBF neural network prediction results when the sample interval is 5 min and the input vector dimensions are 100, 200 and 500.

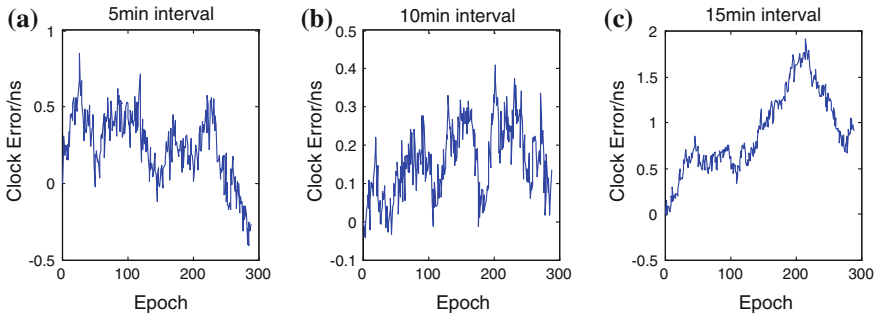

Fig. 29.3 Clock error prediction with different interval

Table 29.1 Error result with different interval

Interval (min)	Clock error (ns)	
	STD	RMS
5	0.291	0.429
10	0.319	0.470
15	0.880	0.202

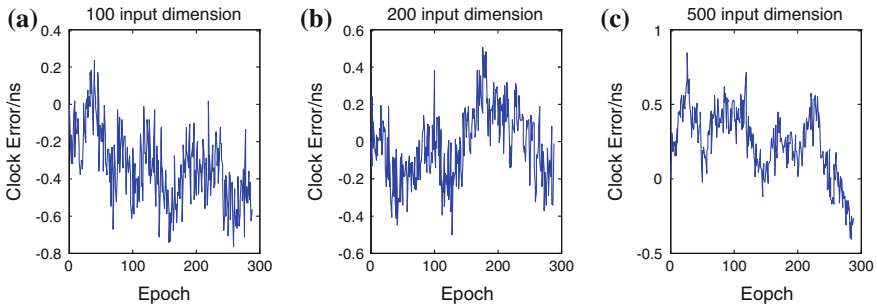

Fig. 29.4 Clock error prediction with different dimension

Table 29.2 Error result with different dimension

Dimension	Clock error (ns)	
	STD	RMS
100	0.294	0.386
200	0.289	0.291
500	0.291	0.429

As shown in the table, the input vector dimension of 200 gets the best results, and the input vector dimension that is too large or too small will reduce the accuracy of the model, which indicates that the current output is related with the past 200 epochs input vector to cover most of the features and can well be generalized. When the input is too small, it can't accurately reflect the regularity of clock error of sample, while excessive input dimension will lead to the interference term and affect the accuracy of result.

29.4.2.2 The Result of Case II

Firstly, the prediction for 1 day is given by the model of RBF neural network and ARMA based on the result obtained from the case I. The results are shown in Fig. 29.5 and Table 29.3.

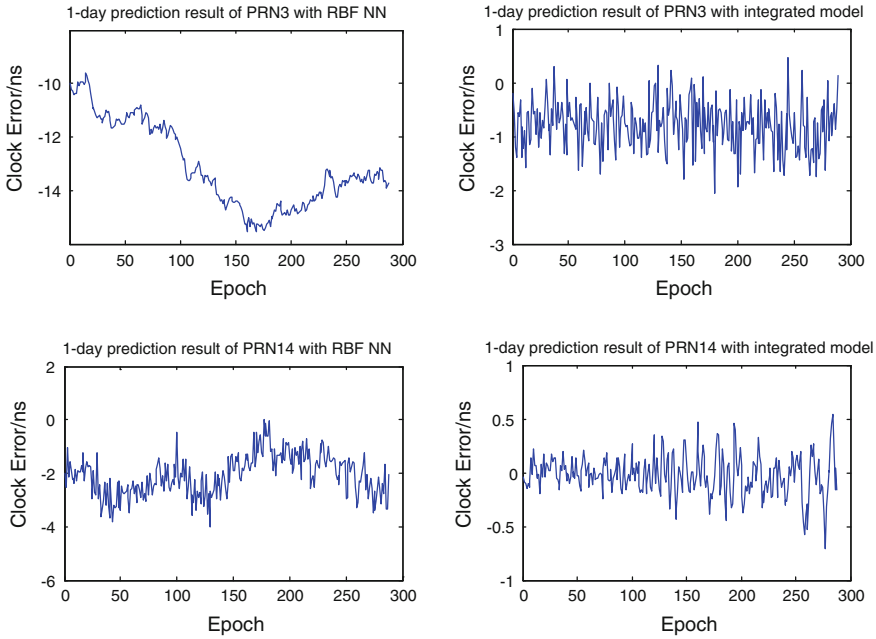

Fig. 29.5 Prediction results for 1 day

Table 29.3 Results for 1 day

Prediction model	Clock error (ns)			
	MIN	MAX	STD	RMS
PRN3 RBF NN	−15.21	0.532	7.282	8.134
PRN3 integrated model	−1.069	0.4604	1.307	1.311
PRN14 RBF NN	−4.087	0.106	0.289	0.291
PRN14 integrated model	−0.706	0.546	0.127	0.128

As we can see from the results, the accuracy of the integrated model can reach ns level, which is higher than the traditional RBF neural network model. Comparing the prediction result of PRN3 satellite with that of PRN14 satellite, PRN14 satellite is better.

Secondly, the prediction of 30-days is given and the results are shown in Fig. 29.6 and Table 29.4.

From the conclusion of 30-days prediction results, it is easy to conclude that the integrated model is better than the traditional RBF neural network model and the accuracy is better than 100 ns. Unlike the 1-day result, the long-term clock error prediction result of PRN14 satellite is worse than that of PRN3 satellite. The reason is that RBF neural network prediction model of the PRN14 satellite can't

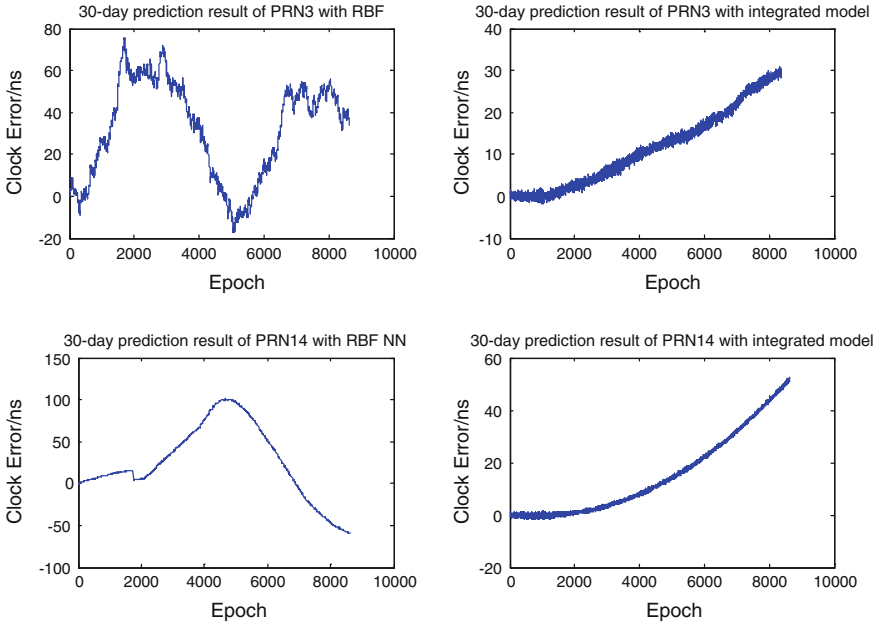

Fig. 29.6 Prediction results for 30-days

Table 29.4 Results for 30-days

Prediction model	Clock error (ns)			
	MIN	MAX	STD	RMS
PRN3 RBF NN	−17.48	75.66	25.38	28.69
PRN3 integrated model	−1.777	30.94	8.439	10.02
PRN14 RBF NN	−59.76	100.9	43.99	51.08
PRN14 integrated model	−1.855	52.62	13.44	15.45

give better results, which then influence the random part extracting and ARMA modeling.

29.5 Conclusion

Considering that the clock error is composed of trend part and random component, an integrated model is proposed based on RBF neural network and ARMA model. Simulation results verify the feasibility and effectiveness of the model. However, the long-term prediction is not ideal, for the reason that in the long-term forecast for network training structure learning is inefficiency, easy to fall into local

minimum point. Improvement of the neural network can be studied in the next step to overcome this problem.

References

1. Mishra A, Shenyblat L (2007) Multipath and satellite clock bias error minimization in DGPS based radiolocation[C]. EUROCOMM 2000. Information systems for enhanced public safety and security. IEEE/AFCEA, 3:95–99
2. Guo CJ, Teng YL (2011) Application of neural network in satellite clock bias short-term prediction. Sci Surv Mapp 36(4):198–201
3. Wang Y, Xu B (2011) Improving prediction precision of navigation satellite clocks with functional network[J]. 2011 3rd World Congress on Nature and Biologically Inspired Computing, NaBIC, 119–124
4. Gotoh T (2005) Improvement GPS time link in Asia with all in view[C]. 2005 Joint IEEE International Frequency Control Symposium (FCS) and Precise Time and Time Interval (PTTI) Systems and Applications Meeting, 2005
5. Radulovic JJ, Rankovic VM (2009) Application of RBF neural network and ANFIS for electromagnetic field prediction around the power lines[C]. 9th International Conference on Telecommunications in Modern Satellite, Cable, and Broadcasting Services, Oct 2009
6. Xu J, Zeng A (2009) Application of ARIMA (0, 2, q) model to prediction of satellite clock error. J Geodesy Geodyn 29(5):116–120
7. Zheng Z, Lu X (2008) Comparison and precision analysis of several GPS satellite clock bias prediction methods[J]. J Shandong Univ Sci Technol (Natural Sci) 27(4):6–11
8. Zhang Q, Sui L, Mu Z (2010) A GPS precise clock errors prediction model based on wavelet and ARMA[J]. J Geodesy Geodyn 30(6):100–104

Chapter 30
Progress on Linear Ion Trap Mercury-Ion Frequency Standard

Hao Liu, Yuna Yang, Yuehong He, Haixia Li, Zhihui Yang, Yihe Chen, Lei She and Jiaomei Li

Abstract Mercury-ion microwave frequency standard could achieve excellent stability and insensitivity to environment perturbations, due to its large atomic mass and Q value of clock transition spectrum line. These performances make it attractive for both ground-based and space applications. After the closed-loop operation on hyperboloid trap, we developed the mercury microwave frequency standard based on linear ion trap. Buffer gas cooling and ^{202}Hg isotope discharged lamp are used for microwave-optical double resonance experiment. The detection of clock transition signal and $^{199}Hg^{+}$ ground-state Zeeman spectrum has been preliminarily realized. All these work provide the foundation for the accomplishment of linear trap mercury-ion microwave frequency standards.

Keywords Mercury-ion frequency standard · Linear ion trap · Space atomic clock

30.1 Introduction

Frequency stability is the one of the most significant performance for atomic frequency standards [1], not only for ground based timekeeping but also space-flight applications. And it is related to the quality factor ($Q = \nu_0/\Delta\nu$) and Signal to Noise Ratio (SNR) of clock transition line [2]. Improving the line Q value and signal-to-noise ratio (SNR) are the effective ways for higher frequency stability. $^{199}Hg^{+}$ has a much larger ground-state hyperfine splitting (about 40.5 GHz) comparing the hydrogen (1.4 GHz), rubidium (6.8 GHz) and cesium (9.19 GHz). In ion trapping system, owing to the absence of wall collision and ignorable first

H. Liu · Y. Yang · Y. He · H. Li · Z. Yang · Y. Chen · L. She · J. Li (✉)
Key Laboratory of Atomic Frequency Standard, CAS, Wuhan Institute of Physics and Mathematics, CAS, WuHan, China
e-mail: jmlee@wipm.ac.cn

J. Sun et al. (eds.), *China Satellite Navigation Conference (CSNC) 2013 Proceedings*, Lecture Notes in Electrical Engineering 245,
DOI: 10.1007/978-3-642-37407-4_30,

order Doppler shift, a very narrow clock transition linewidth can be obtained [3], which means very high line Q and excellent frequency stability. The Jet Propulsion Laboratory (JPL) mercury clocks have realized a record line Q of 5×10^{12} [4], a short-term stability of $4 \times 10^{-14}\tau^{1/2}$ [5] and long-term stability beyond 2×10^{-16} [6, 7].

Due to the large atomic mass and line Q value, mercury-ion microwave frequency standard are more immune to environmental changes than other microwave standards. For 10^{-15} frequency stability, H-masers require 10^{-4} °C active temperature regulation while $^{199}Hg^{+}$ microwave frequency standards just need to control in 0.1 °C temperature range [8]. These provide a very suitable capability for continuously operating. There are three Hewlett Packard $^{199}Hg^{+}$ frequency standards maintained in U.S. Naval Observatory (USNO) for nearly a decennium [9]. And Buffer gas for cooling and ^{202}Hg isotope discharged lamp for state preparation make it suitable for space applications. The JPL compact engineering prototype based on multi-pole linear ion trap standard (LITS) has demonstrated excellent long-term stability for 10^{-15} order of magnitudes, but only in 2 liters [7]. And the National Aeronautics and Space Administration (NASA) has planned to fly and validate the miniaturized mercury clock in Technology Demonstration Missions [10].

Increasing the number of trapped ions can enhance the SNR of mercury-ion frequency standards. The linear ion trap permits storage of a string of ions close to the center axis [11]. Theoretical calculation shows that this trap should store about 20 times the number of ions as a conventional RF trap without increasing the second-order Doppler shift [11, 12].

With the closed-loop operation on hyperboloid trap, we developed the linear trap mercury-ion frequency standards. Buffer gas cooling and ^{202}Hg isotope discharged lamp are currently used for microwave-optical double resonance experiment, and the clock transition signal detection and ground-state Zeeman spectrum of $^{199}Hg^{+}$ has been preliminarily realized. All these work provide the foundation for the accomplishment of linear trap mercury-ion microwave frequency standards.

30.2 Experimental Setup

The experimental setup is shown in Fig. 30.1. Our linear trap is composed of four parallel cylindrical rods, each in diameter 4 mm, equally located on a circumference with a diameter 20 mm, and two pins as end electrode on the each end. The trap is set in an ultrahigh vacuum chamber with a background pressure of 5×10^{-8} Pa. The RF potential for radial confinement $V_0\cos(\Omega t)$ is applied on one pair of the opposing rods with the other pair grounded, with $V_0 = 1{,}000$ V and $\Omega/2\pi = 800$ kHz respectively. The DC voltage $U_0 = 200$ V on each end electrode generates the axial confinement. A pair of Helmholtz coils is used to supply an adjustable magnetic field along the nodal line of the trap.

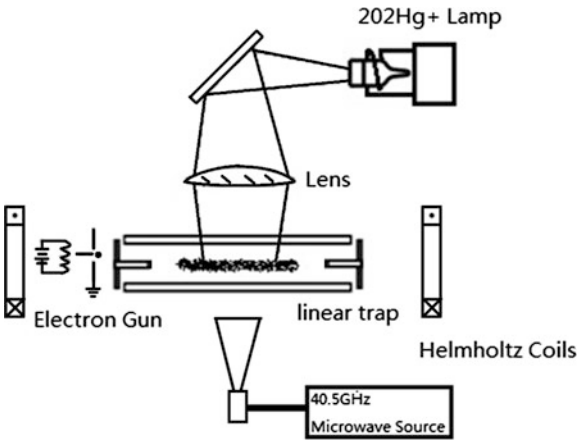

Fig. 30.1 Schematic of the experimental setup

In our experiment, $^{199}Hg^{+}$ ions are created inside the trap by electron bombardment of the ^{199}Hg neutral vapor with an electron beam along the trap axis. The mercury vapor is obtained by heating the oven of HgO powder (^{199}Hg isotopic purity $\sim$90 %) to about 260 °C. A cold-cathode electron gun with LaB_6 filament is adopted to for reducing fringing light. The trapped ions are cooled to near room temperature by collision with the helium buffer gas injected into the vacuum chamber via a helium leak. The ultraviolet radiation (UV) of wavelength 194.2 nm, emitted by the ^{202}Hg discharge lamp, is focused to a oval spot by the lens to overlap the ion cloud as much as possible after a reflection on the surface of a 45° filter, which could get rid of the noise contribution of the pumping light. Microwave radiation interrogation is in the opposite direction of the UV pumping light, and the detection of ions fluorescence produced by pumping light is on the direction perpendicular to this pumping light.

30.3 Present Operation and Result

The process of the $^{199}Hg^{+}$ state preparation is shown as Fig. 30.2. The ions are excited into $^{2}P_{1/2}$ state from the ground-state $^{2}S_{1/2}$ (F = 1) by absorption of the 194.2 nm light, and they will decay to ground-state $^{2}S_{1/2}$ (F = 1) and $^{2}S_{1/2}$ (F = 0) with a certain probability. The absorption of pumping light will depopulate the state $^{2}S_{1/2}$ (F = 1), and the ion population will be accumulated onto the state $^{2}S_{1/2}$ (F = 0) which will not be affected by pumping light. The 40.5 GHz microwave interrogation will drive the $^{2}S_{1/2}$ (F = 0) to $^{2}S_{1/2}$ (F = 1) hyperfine transition and then ions absorbed the 194.2 nm light will jump to state $^{2}P_{1/2}$ again. Those are the namely microwave-optical double resonance. With the cycling of this process, continuous fluorescence signal could be detected by the photomultipliertube (PMT).

Scanning the frequency of microwave source nearby 40.5 GHz with an H-maser as the external reference, the hyperfine structure Zeeman spectrum of $^{2}S_{1/}$

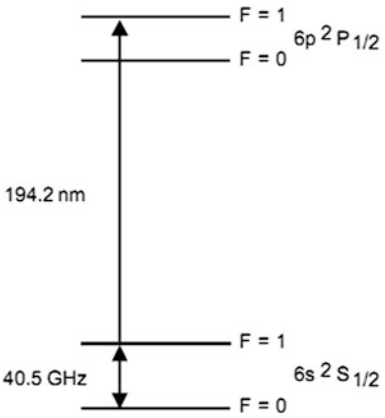

Fig. 30.2 Simplified schematic of the $^{199}Hg^{+}$ hyperfine structure

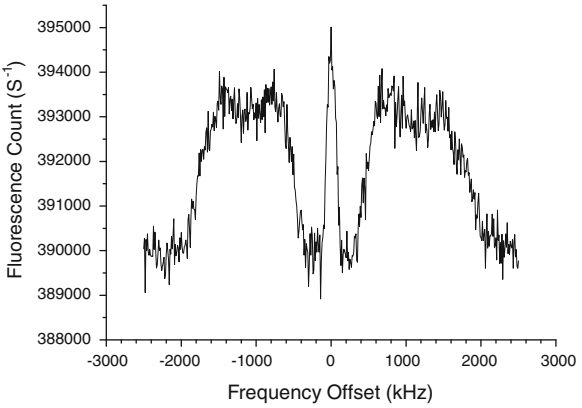

Fig. 30.3 The hyperfine Zeeman spectrum of ground-state $^{2}S_{1/2}$ (F = 1). The three *peaks* corresponding the three Zeeman sublevels, $m_F = -1$, 0, +1. The sweep range is ±2.5 MHz, and *centre* frequency 40.507347997 GHz

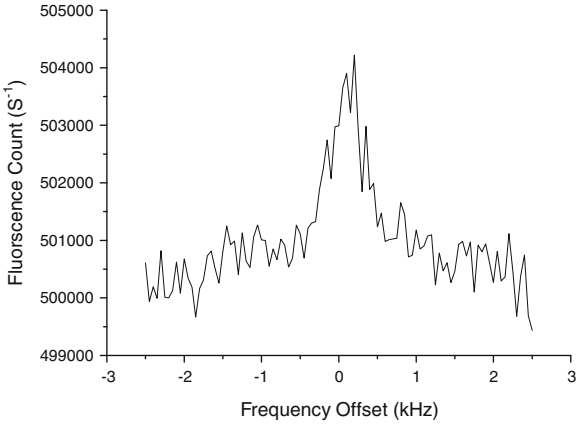

Fig. 30.4 The clock transition line of $^{199}Hg^{+}$

$_2$(F = 1) (See Fig. 30.3) could be depicted. Changing the C field by adjusting current intensity of Helmholtz coils, frequency shift of the two Zeeman sidebands is observed, nearly 600 kHz per 0.4 Gauss, which approximately correspond to the theoretical calculation [13]. By decreasing the scanning range and the steps, clock transition line appears, and the line width is about 600 Hz (Fig. 30.4).

30.4 Conclusion and Summary

The microwave-optical double resonance experiment on linear ion trap has been demonstrated. The detection of clock transition signal and ground-state Zeeman spectrum of $^{199}Hg^+$ has been preliminarily realized by sweeping the microwave frequency. Optimization of the optical system to restrain the stray light for better signal-to-noise ratio and installation of magnetic shielding system for narrowing line width are the mainly improvement before the closed-loop for achieving a microwave frequency standard based on linear ion trap mercury hyperfine transition signal in the near future.

References

1. Wang YQ, Wang Q, Fu J, Dong T (1986) The principle of quantum frequency standard. Science Press, Beijing, p 236 (Ch)
2. Glaude A, Bernard G (2001) The measurement of time, time, frequency and the atomic clock, Cambridge University Press, Cambridge, p 65
3. Prestage JD, Dick GJ, Maleki L (1987a) Proc. 41st Annual Frequency Control Symp. pp 20–4
4. Burt EA, Diener WA Tjoelker RL, (2008) A compensated multi-pole linear ion trap mercury frequency standard for ultra-stable timekeeping. IEEE Trans Ultrason Ferroelectrics Freq Control 55(12):2586–2585. http://ieeexplore.ieee.org/xpl/articleDetails.jsp?tp=&arnumber=4683467&contentType=Journals+%26+Magazines&queryText%3DA+compensated+multi-pole+linear+ion+trap+mercury
5. Eric AB, Robert LT (2006) IPN Progress Report 42-166, Jet Propulsion Laboratory, Pasadena, California, 15 Aug 2006
6. Tjoelker RL, Prestage JD, Koppang P, Swanson T (2003) Joint Meeting EFTF and IEEE IFCS (Tampa 5–8 May 2003) p 21
7. Prestage JD, Chung S, Le T, Lim L, Maleki L (2005) Liter sized ion clock with 10–15 stability. Frequency Control Symposium and Exposition. In: Proceedings of the 2005 IEEE International (Vancouver 29–31 Aug 2005) p 472. http://ieeexplore.ieee.org/xpl/articleDetails.jsp?tp=&arnumber=1573976&contentType=Conference+Publications&queryText%3DLiter+sized+ion+clock+with+10%E2%80%9315
8. Prestage JD, Maleki L (1994) Space flyable Hg^+ frequency standards. IEEE International Frequency Control Symposium, p 747
9. Matsakis DN, Kubik AJ, DeYoung J A, Giffard RP, Cutler LS (1995) IEEE International Frequency Control Symposium. In: Proceedings of the 1995 IEEE International (31 May–2 Jun 1995) pp 86–109
10. NASA Picks Three Proposals for Flight Demonstration. http://www.jpl.nasa.gov/news/news.cfm?release=2011-261. 22 Aug 2011

11. Prestage JD, Dick GJ, Maleki L (1989) New ion trap for frequency standard applications. J Appl Phys 66(3):1013–1017
12. Prestage JD, Janik GR, Dick GJ, Tucker TK, Maleki L (1989) Linear ion trap for second order doppler shift reduction in frequency standard applications. 43rd Annual Symposium on Frequency Control, p 135
13. Huang X, Yang YN, Liu H, Gao KL, She L, Li JM (2011) Zeeman spectrum and magnetic effect of trapped $^{199}Hg^{+}$ ions[J]. Chin J Quantum Electron 28(1):19–24

Chapter 31
The Research of Miniaturization CPT Rb Atomic Clocks

Shuangyou Zhang, Zhong Wang and Jianye Zhao

Abstract Based on current situation of the study in this area, our work will introduce a miniature CPT atomic clock system with small physical size, high stability and lower power consumption. The use of our original innovational technology to fabricate small cells can avoid the complexity and difficulty of the anodic bonding technology. By this technology, we could accomplish the objective to minimize the occupied volume of the physical part of the system to 1 cm^3. The single FPGA chip is the main part of the control circuit to accomplish the slower start-up of the laser, two necessary locking loops to make the system work, and the temperature control logic. Our 3.035 GHz RF signal is generated from a TCXO via the technology of DDS. Our prototype is a significant progress to realize CSAC with the use of the single FPGA chip. We demonstrate our CPT clock prototype with the volume less than 100 cm^3. This prototype has frequency instability of 1×10^{-10} for 1 s and 3×10^{-11} for 1000 s.

Keywords CPT · CSAC · FPGA · Rb · Instability

31.1 Introduction

Because of the atomic clocks based on Coherent Population Trapping (CPT) without use of the centimetre-scale microwave cavity, they have been a hot topic in chip-scale atomic clocks (CSAC) research for sometimes. With the

S. Zhang · Z. Wang · J. Zhao (✉)
School of Electronics Engineering and Computer Science, Peking University, Beijing, China
e-mail: zhaojianye@pku.deu.cn

S. Zhang
e-mail: shyzhang@pku.deu.cn

Z. Wang
e-mail: zw@pku.deu.cn

J. Sun et al. (eds.), *China Satellite Navigation Conference (CSNC) 2013 Proceedings*, Lecture Notes in Electrical Engineering 245,
DOI: 10.1007/978-3-642-37407-4_31,

development of micro-fabrication and semiconductor laser technologies, micro-fabricated atomic clocks with their low power consumption, miniaturization and high stability, are expected to provide the precise timing for GPS receivers, network communication and data processing devices [1], will be much competitive in the field of atomic frequency standard. Foreign research organizations on micro-fabricated atomic clocks mainly concentrate on US, France and Italy, like National Institute of Standards and Technology (NIST), Symmetricom Company and FEMTO-ST Institute. Symmetricom Company has launched a miniature CPT atomic clock in 2009, but compared with conventional atomic clocks, it has no obvious advantage, and its market share is not high. Emerging Chip-Scale Atomic Clocks (CSAC) should meet the requirement of our country's second generation of satellite navigation technology.

31.2 Coherent Population Trapping

Taking ^{85}Rb as an example, when the two ground-state hyperfine levels (F = 3, F = 2) of Λ configuration are coupled to a common excited state ($5^2P_{1/2}$) by means of two coherent laser fields, a phenomenon has been called coherent population trapping takes place. This leads to a reduction of fluorescence intensity from the vapor and an increase of the amount of light passing through the atoms. This phenomenon was firstly observed by Alzetta et al. [2] in 1976. The atomic clocks based on CPT are all-optically pumped, and do not need large components like rubidium lamp and microwave cavity, so they have been an important research direction of CSAC. Figure 31.1 shows the Λ three-level system involved in ^{85}Rb D1 line, and Fig. 31.2 shows the experimental setup of CPT phenomenon. The $\lambda/4$-plate and Polarizing Beam Splitter (PBS) convert the beam from laser into linearly polarization.

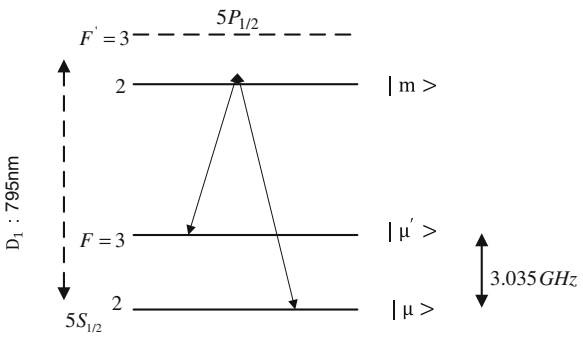

Fig. 31.1 Typical schematic of a Λ three-level system involved in ^{85}Rb D1 line

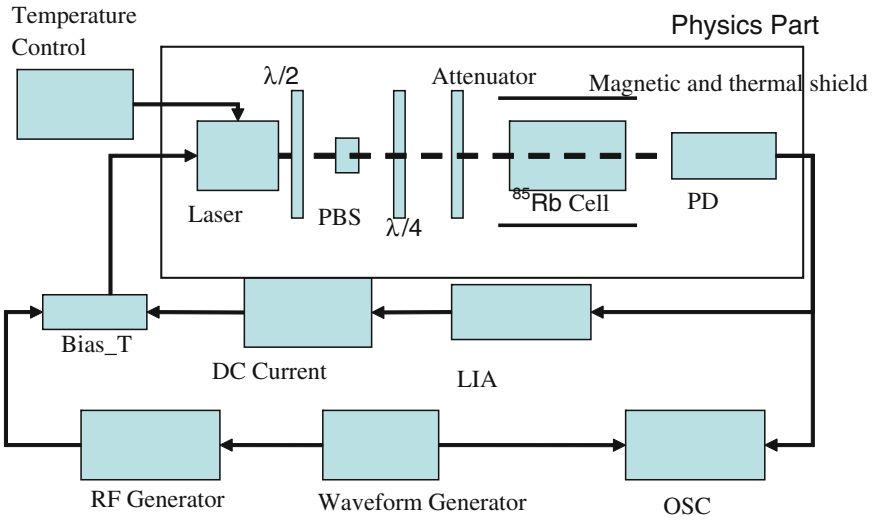

Fig. 31.2 Experimental setup of CPT phenomenon

31.3 Physics Part

This paper has achieved further improvement on the volume and power consumption of the physics part of CPT Rb atomic clocks. An important milestone toward realizing CSAC is the development of methods to fabricate highly miniaturized atomic vapor cells, which determine the linewidth and height of CPT resonances. This paper also has some improvement on the physics package.

31.3.1 Microfabricated Vapour Cell

In this article, we have developed an original innovational technology to fabricate millimeter-sized rubidium cells filled with rubidium atoms and buffer gas mixture. The use of this innovational technology not only can figure out the flatness of transmitted surface, but also can avoid the complexity and difficulty of the anodic bonding technology. Using silicon micromachining and anodic bonding techniques cannot guarantee the accurate pressure ratio of different buffer gases and the excellent sealing performance [3]. Our cells can share the same reliability and working life with the cells by traditional glass-blowing techniques.

The distance between two windows is 2.5 mm. The two windows are designed to be convex mirrors that are better for the effective use of light beam. The volume is 24 mm^3. By this technology, we successfully introduce rubidium and a mixture buffer gas in optimized pressure and ratio to the microfabricated vapor cell [4]. We have developed a new method to fabricate the cells for the miniature CPT atomic clocks.

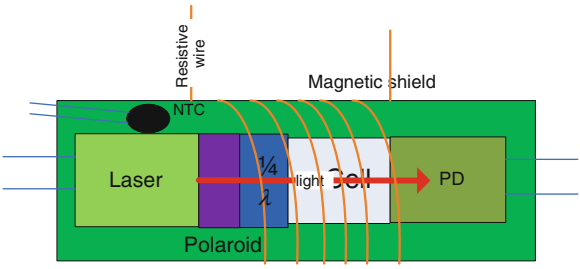

Fig. 31.3 Schematic view of physics components

31.3.2 Physics Package

Figure 31.3 shows the physics package components employed for this paper by the method of CPT, it consists of VCSEL laser, polaroid, $\lambda/4$-plate, rubidium cell, temperature controlling element, photodiode (PD) and magnetic shield. The key parts of physics part are the laser and the rubidium cell, which decide the linewidth and signal-to-noise ratio (SNR) of CPT resonances and shift of frequency reference. The output from VCSEL is allowed to propagate through the polaroid and $\lambda/4$-plate before it enters into the cell. A quarter-wave polarization retarder ($\lambda/4$) converts the linearly polarized laser beam into circular polarization that passes through the rubidium vapor. The photodiode converts the light into electronic signal which is processed by servo circuits. The temperature controller consists of NTC and resistive wire. Because the operating temperature of cell and VCSEL is much higher than the operating ambient, we use resistive wire to make sure that the temperature is stabilized to within 0.01 K, and to make sure that the output of VCSEL is 795 nm. The ensemble is magnetically shielded with permalloy metal in order to reduce spurious environmental magnetic fields. Based on the existing mechanical process, we remove the defect of the traditional glass-blowing techniques, and we can easily minimize the occupied size of the physical part of the system to 1 cubic centimeter. Figure 31.4 shows the optical absorption signal and CPT resonance signal.

Fig. 31.4 Typical optical absorption signal (*left*, *blue*) and CPT resonances (*right*, *blue*) of microfabricated cells

31.4 Circuit Part

The function of circuit part is locking the microwave frequency to the rubidium atomic ground state hyperfine splitting, and then the output frequency shares the same stability with the atomic ground state hyperfine splitting. In order to minimize the volume of atomic clock, we use the algorithm in digital chip to take place of analog functions as many as possible. The Field Programmable Gate Array (FPGA) chip is the key component of circuit part. With the use of FPGA, we can minimize the component count, power consumption and size. Compared with the microprocessor employed in traditional atomic clock architecture, FPGA chip is the base of application specific integrated circuit (ASIC) for our late design.

Most functions are realized in FPGA, including the slower start-up of the laser, two necessary locking loops to make the system work, power-off and power-up protection. In addition to the physics package, the system consists principally of DC current for laser, analog signal conditioning, temperature controlling and the microwave synthesizer. A block diagram of the miniature atomic clock is shown in Fig. 31.5. The signal from PD is amplified and filtered in order to avoid the mutual interference from two feed-back loops before converted into digital signal by AD. Because we use full band modulation (FBM), in which the laser is modulated with a frequency equal to the atomic ground-state hyperfine splitting [5], the microwave frequency is 3.035 GHz.

31.4.1 Laser DC Current

The current input of the VCSEL includes several components: DC bias, AC modulation, and the 3.035 GHz RF. The DC current source for VCSEL is provided by the summation of coarse tuning from a DA which is controlled by the FPGA chip. The pulse current will cause the permanent damage of the VCSEL, especially

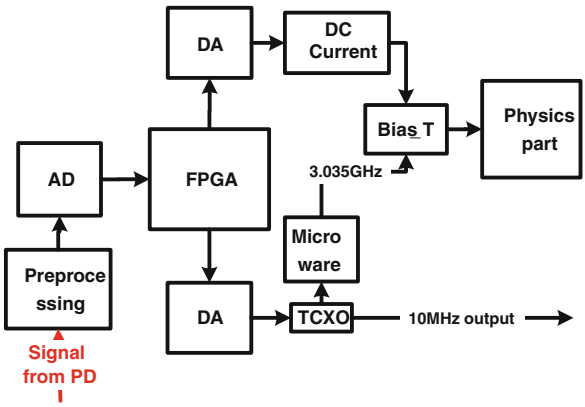

Fig. 31.5 Schematic of the microfabricated atomic clock circuit

when power-on and power-off, so we design the slow-start and power-off step for protecting the laser. The noise of current source will cause the output of laser with noise that will impact on the short-term frequency stability. Therefore, we should keep the circuit low-noise and low temperature drift. Besides, a lock-frequency-amplify (LFA) is employed in order to lock the laser to the ^{85}Rb absorption maximums, that is, we superpose an AC modulation and the feed-back error signal from PD on the DC injection current to adjust and lock the center frequency.

31.4.2 Lock-Frequency-Amplify Loop

As mentioned above, there are two locking loops in the CPT atomic clocks; one lock-in at 3 kHz is used to lock the laser to the ^{85}Rb D1 absorption, the other is used to lock the microwave frequency at the CPT resonance frequency by control the TCXO output frequency. The LFA is employed in both of two loops. They have the same architecture, but different operating frequencies in order to estimate the mutual interference. Taking the first one as an example, the laser is operated with a DC injection current which is superposed with AC modulation at 3 kHz. The AC current modulation produces a corresponding laser frequency modulation which results in amplitude modulation after the detection of PD. The signal from PD is amplified by an operational amplifier and filtered by an analog filter at 3 kHz. The signal is rapidly digitized by the AD and the error signals are implemented in FPGA chip. The DC current and RF error signals are integrated in FPGA and applied to two DACs, which control the laser DC bias and TCXO tuning respectively.

31.4.3 Microwave Synthesizer

The CSAC has three requirements for microwave synthesizer: frequency stability, power consumption and tuning sensitivity [6, 7]. The long-term stability of CSAC can be improved by locking the temperature-compensated quartz oscillator (TCXO) frequency to the rubidium atomic ground state hyperfine splitting, but the short-term stability depends on the free-running stability of TCXO. Considering the low power consumption, small volume and stability, we chose TCXO to generate 3.035 GHz signal. The microwave synthesizer (Fig. 31.6), made up of the TCXO, DDS and an integer-N phase-locked loop (PLL) and a microwave VCO. The PLL and VCO are implemented in the multiplier chip. The output of TCXO is direct digital synthesized to 10.11911 MHz, and then multiplied to 3.035 GHz.

Fig. 31.6 Schematic of the microwave synthesizer

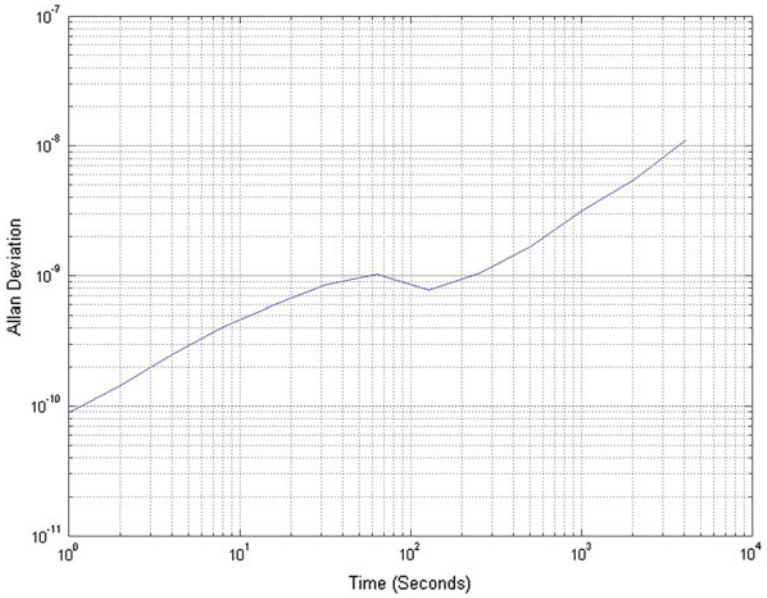

Fig. 31.7 Measured instability of the free-running TCXO

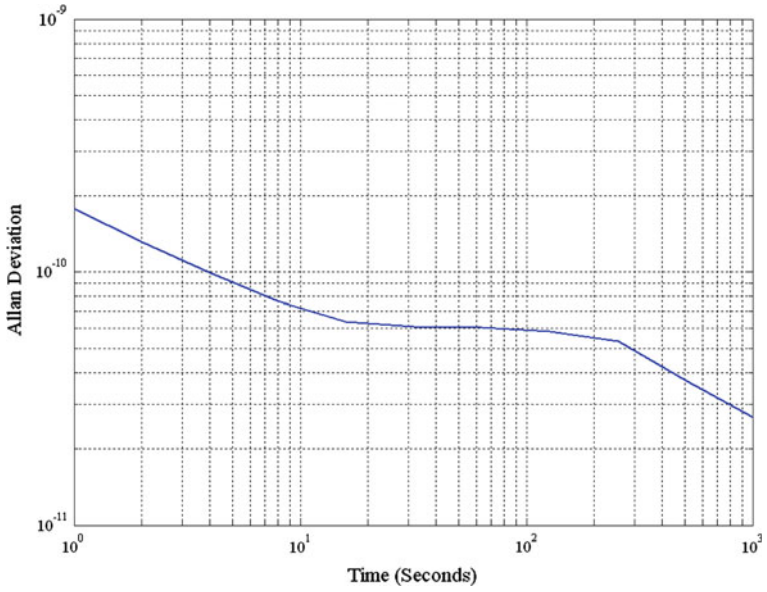

Fig. 31.8 Measured instability of the TCXO locked to the physics package

In this paper, we also have researched other microwave schemes. One scheme uses dielectric resonator oscillator (DRO) to generate the 3.035 GHz signal, but its short-term instability can just reach10^{-9}. The short-term instability by using TCXO can reach 10^{-10} and by using OCXO can reach 10^{-11}. From the view of power consumption, the scheme by using DRO is the best with a power consumption of 5 mW. The power consumption of using OCXO is more than 3 W, so this scheme is not suit for CSAC. The microwave synthesizer with the use of TCXO can be realized by DDS, and this part is implemented in FPGA, which does not need much power consumption. Figure 31.7 shows the instability of TCXO while free-running. Figure 31.8 shows the instability of TCXO while locked to the atomic CPT resonance of the integrated physics package.

31.5 Conclusions

Based on our previous work, we have continued to evolve the CSAC electronics and physics part. We demonstrate our CPT clock prototype with the whole volume less than 100 cm^3 and the physics part occupied volume about 1 cm^3. This prototype has frequency instability of 1×10^{-10} for 1 s and 3×10^{-11} for 1000 s.

Acknowledgments The authors acknowledge the organizing committee of satellite navigation for giving us the opportunity to share our research, and we also gratefully acknowledge valuable advice and help from the students of Circuits and Systems Laboratory, Peking University. We hope that our country's second generation of satellite navigation undertaking will be developed vigorously in the near future.

References

1. Svenja K, Vishal S, Peter DDS, Leo H, John K et al (2004) A microfabricated atomic clock. Appl Phys Lett 85:1460
2. Alzetta G, Gozzini A, Moi M, Orriols G (1976) An experimental method for the observation of rf transitions and laser beat resonances in oriented Na vapour. Nuovo Cimento B 36:5
3. Liew LA, Knappe S, Moreland J, Kitching J et al (2004) Microfabricated alkali atom vapor cells. Appl Phys Lett 84:2694
4. Deng K, Guo T, Liu X, Chen X, Wang Z (2008) Effect of buffer gas ratios on the relationship between cell temperature and frequency shifts of the coherent population trapping resonance. Appl Phys Lett 92:211104
5. Deng K, Guo T, Juan S, Guo D, Liu X, Liu L, Chen X, Wang Z (2009) Full hyperfine frequency modulation in the implementation of coherent population trapping atomic clocks. Phys Lett A 373:1130
6. Ke D, Xuzong C, Zhong W (2010) A ^{85}Rb coherent population trapping atomic clock. In: Proceedings of 2010 IEEE International Frequency Control
7. Brannon A et al (2006) A local oscillator for chip-scale atomic clocks at NIST. IEEE Int Freq Control Symp 443–447

Chapter 32
Fiber Based Time and Frequency Synchronization System

Bo Wang, Chao Gao, Weiliang Chen, Yu Bai, Jing Miao, Xi Zhu, Tianchu Li and Lijun Wang

Abstract We build up a time and frequency synchronization system via the 80 km urban fiber link between Tsinghua University and the National Institute of Metrology in Changping city. Using the system, we demonstrate simultaneous time and RF signal distribution via optical fibers. The measured frequency dissemination stability of a 9.1 GHz RF signal is 7×10^{-15}/s, 5×10^{-19}/day, and the measured time synchronization accuracy is 50 ps. Relevant results were published on the Scientific Reports of Nature Publishing Group. To further build up a regional time and frequency network, integrated-designed modules are needed. Its long term continuous running stability and commonality should be tested. In this paper, we introduce the design of the frequency dissemination modules. After 135 days' continuously running, we get the million-second frequency dissemination stability of $8 \times 10^{-19}/10^6$ s. We also introduce our multiple-access download module, which improves the frequency dissemination scheme from the traditional point to point protocol to be a tree structure protocol, and greatly improves its applicability. Using it, the stability of the receiving frequency signal at arbitrary accessing point is almost 4 orders of magnitude better than that using directly accessing method. All of these modules will be applied to build up the regional time and frequency network.

B. Wang (✉) · C. Gao · Y. Bai · J. Miao · X. Zhu · T. Li · L. Wang
Joint Institute for Measurement Science, Tsinghua University, Beijing 100084, China
e-mail: bo.wang@tsinghua.edu.cn

B. Wang · L. Wang
The state key lab of precision Measurement Technology and Instrument,
Department of Precision Instruments, Tsinghua University, Beijing 100084, China

C. Gao · Y. Bai · J. Miao · X. Zhu · L. Wang
Department of Physics, Tsinghua University, Beijing 100084, China

W. Chen · T. Li · L. Wang
National Institute of Metrology, Beijing 100013, China

J. Sun et al. (eds.), *China Satellite Navigation Conference (CSNC) 2013 Proceedings*, Lecture Notes in Electrical Engineering 245,
DOI: 10.1007/978-3-642-37407-4_32,

Keywords Time · Frequency · Dissemination · Synchronization · Stability · Multiple-access

32.1 Introduction

With the definition of second changing from astronomical second to atomic second, in order to measure and further improve the accuracy of atomic second, a regular time and frequency comparisons between atomic clocks located in different locations are required. These requirements give birth to a new research directions-precise time and frequency synchronization [1]. More importantly, precise time and frequency synchronization has important applications in navigation systems. In the satellite based global positioning systems (such as COMPASS, GPS, and GLONASS), the entire system shares one common clock frequency and one common highly synchronized system time. The entire system's time is often synchronized at the nanosecond accuracy level.

At present, the time and frequency synchronization between different atomic clocks is mainly realized via the satellite link. Using the two-way satellite time and frequency transfer (TWSTFT) [2] or GPS common view (CV) [3] method, the frequency transfer stability at 10^{-15}/day level and the time synchronization accuracy at nanosecond level can be realized [4, 5]. With significant progress of the precise atomic clock, the oscillator with frequency stability of 10^{-16}/s [6] and the optical clock with fractional frequency uncertainty of 10^{-18} [7] have been realized. The conventional frequency dissemination methods can no longer satisfy the requirement of measurement and comparison below 10^{-16}/day. Due to its prosperities of low attenuation, high reliability, and continuous availability, the ubiquitous fiber network has become an attractive option for long-distance dissemination of time and frequency signals. Recently, the transfer of ultrastable optical [8–13], microwave [14–21], and even frequency comb signals [22, 23] via fiber link have been demonstrated.

The Joint Institute of Measurement Science (JMI) is co-established by Tsinghua University (THU) and the National Institute of Metrology (NIM). There are regular requirements of the time and frequency comparisons between THU and NIM. We build up a time and frequency synchronization system via the 80 km urban fiber link between THU and NIM in Changping city, and demonstrate simultaneous time and RF signal distribution via the optical fibers. The measured frequency dissemination stability of a 9.1 GHz RF signal is 7×10^{-15}/s, 5×10^{-19}/day, and the time synchronizing accuracy is 50 ps [14]. Next step, since we will build up the regional time and frequency network together with other research institutions in Beijing area, integrated-designed modules are needed and its long term continuous running stability and commonality should be tested. In this paper, we introduce the designs of the frequency transmitting module and the receiving module, respectively. We also test their 135 days continuously running stability, and a million-second frequency dissemination stability of $8 \times 10^{-19}/10^6$ s has been

demonstrated. Although frequency transfer via fiber link has higher stability than that of using conventional satellite links, the latter still occupies the dominant position in practical time and frequency dissemination. One of the main drawbacks of the fiber link is its limited accessibility of the dissemination frequency signal. For satellite link, it can disseminate frequency signals to cover essentially the entire globe, while for fiber link, one can only reproduce the disseminated frequency signal at specific locations using all current schemes. To realize a branching time and frequency network, we design a multiple-access download module [20]. Using it, the download frequency signal is about 4 orders of magnitude in improvement on the relative frequency stability compared to those of directly download signals.

32.2 The Frequency Transmitting, Receiving, and Download Module

32.2.1 The Frequency Transmitting Module

The fiber based frequency dissemination system is composed by the frequency transmitting module, receiving module and the multiple-access download module. Figure 32.1a gives the schematic diagram of the frequency transmitting module. It needs a 100 MHz frequency signal (V_{ref}) working as the reference of the whole system. The 100 MHz signal may come from a Hydrogen Maser. To achieve a higher signal-to-noise ratio error signal for compensation, V_{ref} is boosted to 9.1 GHz. There are also two oscillators phase locked to V_{ref} with oscillation frequency of 9.0 GHz (V_1) and 9.2 GHz (V_2), respectively. They work as two assistant frequency references which is used to generate the error signal. A stable oscillator containing a voltage-controlled crystal oscillator (VCXO) and a phase-locked dielectric resonant oscillator (PDRO) generates a 9.1 GHz frequency signal V_0. The phase of V_0 can be controlled by the PLL. In this way, the phase noise induced by fiber dissemination can be compensated. V_0 is amplified by AMP and used to modulate the amplitude of the 1,550 nm laser light. After passing through a polarization scrambler and EDFA1, the modulated laser carrier is split into two parts. One part is detected by FPD1, and the generated signal V'_0 used to detect and compensate the phase noise of the out-of-loop devices [16]. The other part, passing through an optical circulator, couples into the fiber link. After the round-trip transfer in the fiber link, the feedback light (see Sect. 32.2.2) carries the round-trip phase noise of the fiber link and returns to the transmitting module again through the optical circulator. The returned feedback light is amplified by EDFA2 and detected by FPD2 (generate signal V_4). We mix down the signal V_1 and V'_0 to obtain V_{e1}, and mix down the signal V_2 and V_4 to obtain V_{e2}. Then, by mixing the signal V_{e1} and V_{e2}, we get the error signal V_e. Passing through a PLL, the error signal V_e is fed to VCXO. In order to reduce the influence of temperature

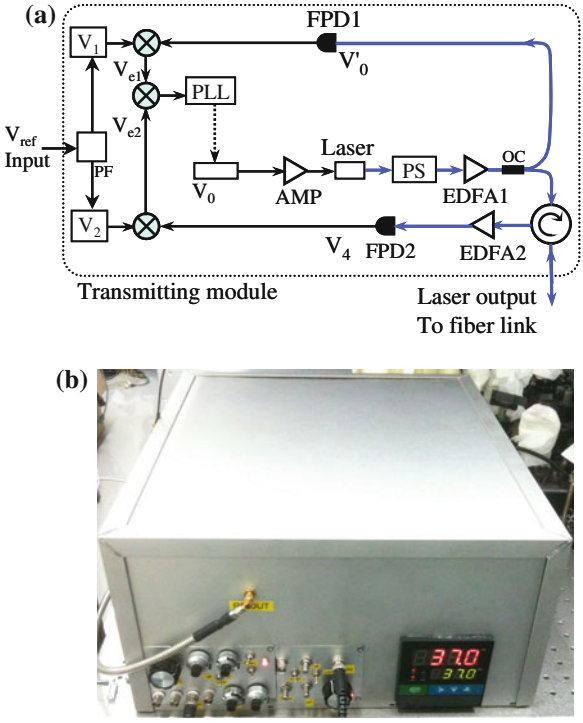

Fig. 32.1 The frequency transmitting module. **a** The schematic diagram of the module, where *PF* RF power splitter, *PLL* phase lock loop, *AMP* RF power amplifier, *PS* polarization scrambler, *EDFA* erbium-doped fiber amplifier, *OC* fiber coupler, *FPD* fast photo detector. **b** The photo of the transmitting module

fluctuation on the frequency dissemination stability, the optical parts (blue link in Fig. 32.1a) inside the module is temperature controlled. Figure 32.1b is the photo of the temperature-controlled transmitting module.

32.2.2 The Frequency Receiving Module

At the receiving site, the disseminated frequency is reproduced by the receiving module. Figure 32.2a gives the schematic diagram of the module. The disseminated 1,550 nm laser carrier is coupled into the module by an optical circulator, and is split into two parts. One part is amplified by EDFA3 and transferred back to the transmitting module along the same fiber link. The other part is detected by FPD3 to reproduce the 9.1 GHz frequency signal V_3 which is phase locked to the reference frequency signal V_r at the transmitting site. As the locking bandwidth of the fiber noise compensation system is limited by the length of the fiber link, normally, it is below 1 kHz. In other words, if the phase noise of the single-sideband was greater than 1 kHz of the reproduced frequency signal V_3, it could not be kept at the normal scale. To solve this problem, at the receiving site, a 9.1 GHz oscillator (V_5) should be phase locked to V_3 using a narrow-band locking loop. Consequently, the SSB noise of V_5 below 1 kHz is follow that of V_r, and the

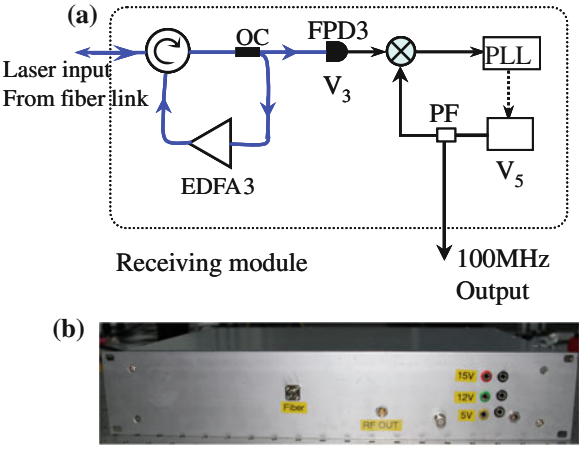

Fig. 32.2 The frequency receiving module. **a** The schematic diagram of the module, where *PF* RF power splitter, *PLL* phase lock loop, *EDFA* erbium-doped fiber amplifier, *OC* fiber coupler, *FPD* fast photo detector. **b** The photo of the receiving module

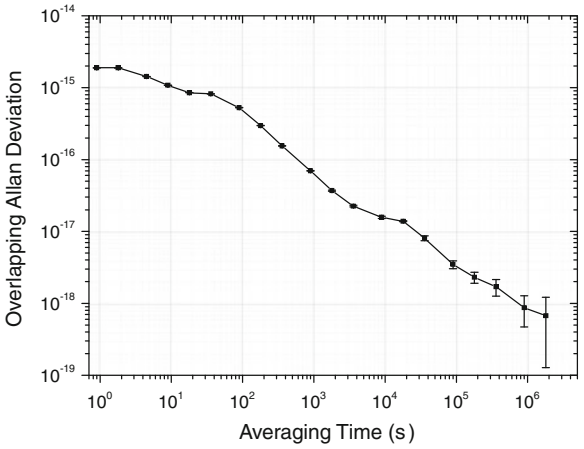

Fig. 32.3 The measured frequency dissemination stability of the 135 day continuous running via the 50 km fiber spool

SSB noise of V_5 above 1 kHz is kept as its own character. Figure 32.2b is the photo of the receiving module.

To test the long term continuously running stability of the fiber based frequency dissemination module, using a 50 km fiber spool, we measure its 135 days continuous frequency dissemination stability. The results are shown in Fig. 32.3, and the frequency dissemination stability is 1.9×10^{-15}/s, and $8 \times 10^{-19}/10^6$.

32.2.3 Multiple-Access Download Module

Figure 32.4 is the schematic diagram of the multiple-access frequency download module. Using a 2×2 fiber coupler, the module can be connected with the existing main fiber link. The laser carriers transferring forward and backward in

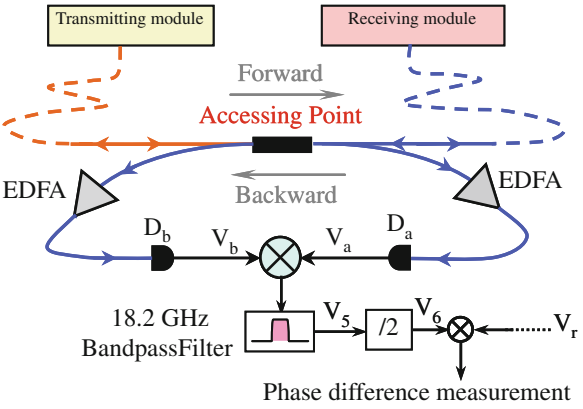

Fig. 32.4 The schematic diagram of the multiple-access frequency download module, where D_a and D_b fast photo detector, *EDFA* erbium-doped fiber amplifier, ϕ_a: the phase noise induced by the fiber link between accessing point and the transmitting site, ϕ_b: the phase noise induced by the fiber link between accessing point and the receiving site

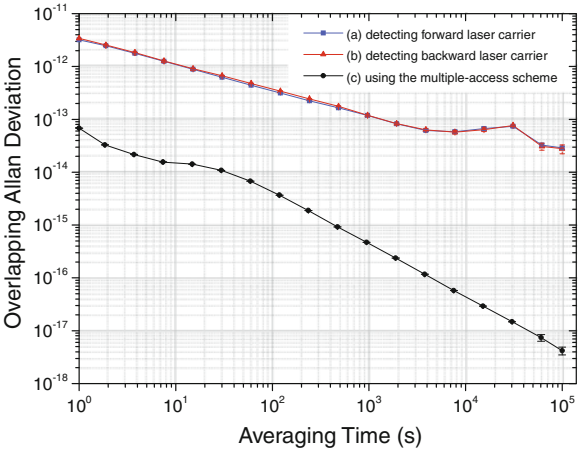

Fig. 32.5 Measured relative frequency stability of the reproduced frequency signal at the accessing point 3 km away from the transmitting site

the main fiber link can be coupled out. The frequency signal modulated on the laser carriers can be detected and reproduced by two fast photo-detectors D_a and D_b. The reproduced signal V_a and V_b are mixed by a frequency mixer and filtered by an 18.2 GHz bandpass filter. Using a divide-by-2 prescaling frequency divider, a 9.1 GHz frequency signal V_6 phase-locked to V_r at the transmitting site can be reproduced.

As a performance test, via the 80 km round trip fiber link between THU and NIM, we reproduce the disseminated 9.1 GHz signal at a location 3 km away from the transmitting site and demonstrate the relative stability of the reproduced frequency signal. The measurement results are shown is Fig. 32.5. For the directly

download signal V_a and V_b, they show very similar stabilities of 3.5×10^{-12}/s and 3×10^{-14}/day. While for the frequency signal reproduced by the multiple-access download module, relative frequency stability of 7×10^{-14}/s and 5×10^{-18}/day is obtained. It is almost 4 orders of magnitude better than that using directly accessing method.

32.3 Conclusions

Based on the THU-NIM precise time and frequency dissemination system, the integrated frequency transmitting module, receiving module, and the multiple-access download module are designed and demonstrated. For the transmitting and the receiving module, we demonstrate their 135 days continuous running stability, and get the million-second frequency dissemination stability of $8 \times 10^{-19}/10^6$ s. Using the multiple-access frequency download module we designed, the stability of the receiving frequency signal at arbitrary accessing point is almost 4 orders of magnitude better than that using directly accessing method. All of these modules will be applied to build up the regional time and frequency network.

Acknowledgments The authors acknowledge funding support from the Major State Basic Research Development Program of China (No. 2010CB922901) and the Tsinghua University Scientific Research Initiative Program (No. 20131080063).

References

1. Warrington B (2012) Two atomic clocks ticking as one. Science 336:421–422
2. Michito I, Mizuhiko H, Kuniyasu I et al (2001) Two-way satellite time and frequency transfer networks in pacific region. IEEE 5:2
3. Allan DW, Weiss MA (1980) Accurate time and frequency transfer during common-view of a GPS satellite. In: Proceedings of 34th annual frequency control symposium, USAERADCOM, Ft. Monmouth, NJ 07703, May 1980
4. Bauch A, Achkar J, Bize S et al (2006) Comparison between frequency standards in Europe and USA at the 10–15 uncertainty level. Metrologia 43:109–120
5. Levine J (2008) A review of time and frequency transfer methods. Metrologia 45:162–174
6. Jiang YY, Ludlow AD, Lemke ND et al (2011) Making optical atomic clocks more stable with 10–16 level laser stabilization. Nat Photon 5:158–161
7. Chou CW, Hume DB, Koelemeij JCJ et al (2010) Frequency comparison of two high-accuracy Al^+ optical clocks. Phys Rev Lett 104:070802
8. Predehl K, Grosche G, Raupach SMF et al (2012) A 920-kilometer optical fiber link for frequency metrology at the 19th decimal place. Science 336:441–444
9. Foreman SM, Ludlow AD, Miranda MHG et al (2007) Coherent optical phase transfer over a 32-km fiber with 1 s instability at 10–17. Phys Rev Lett 99:153601
10. Williams PA, Swann WC, Newbury NR (2008) High-stability transfer of an optical frequency over long fiber-optic links. J Opt Soc Am B 25:1284–1293
11. Jiang H, Kéfélian F, Crane S et al (2008) Long-distance frequency transfer over an urban fiber link using optical phase stabilization. J Opt Soc Am B 25:2029–2035

12. Grosche G, Terra O, Predehl K et al (2009) Optical frequency transfer via 146 km fiber link with 10–19 relative accuracy. Opt Lett 34:2270–2272
13. Musha M, Hong FL, Nakagawa K et al (2008) Coherent optical frequency transfer over 50-km physical distance using a 120-km-long installed telecom fiber network. Opt Express 16:16459–16466
14. Wang B, Gao C, Chen WL et al (2012) Precise and continuous time and frequency synchronisation at the 5×10^{-19} accuracy level. Sci Rep 2:556
15. Wang B, Gao C, Chen WL et al (2012) Fiber-based time and frequency dissemination between THU and NIM. In: IFCS: 2012 (IEEE, Baltimore), p 179
16. Wang B, Gao C, Chen WL et al (2012) A 10-18/day fiber-based RF frequency dissemination Chain. In: CLEO: 2012 (Optical Society of America, Washington, DC), CTh4A.3
17. Wang B, Gao C, Chen WL et al (2012) Precise time and frequency synchronization at the 5×10^{-19} level. In: ISCAP-V (International symposium on cold atom physics, The Three Gorges), p 57
18. Wang B, Gao C, Chen WL et al (2011) Stable atomic time transfer and comparison. In: China time and frequency symposium (China time and frequency symposium, Beijing, 2011), p 381. 王波,高超,陈伟亮等. 原子时信号的高稳定度传输与比对. 2011全国时间频率学术会议, P381
19. Gao C, Wang B, Chen WL et al (2012) Fiber-based multiple-access ultrastable frequency dissemination. Opt Lett 37:4690–4692
20. Fujieda M, Kumagai M, Gotoh T et al (2009) Ultrastable frequency dissemination via optical fiber an NICT. IEEE Trans Instrum Meas 58:1223–1228
21. Lopez O, Amy-Klein A, Lours M et al (2010) High-resolution microwave frequency dissemination on an 86-km urban optical link. Appl Phys B 98:723–727
22. Marra G, Margolis HS, Lea SN et al (2011) High-stability microwave frequency transfer by propagation of an optical frequency comb over 50 km of optical fiber. Opt Lett 35:1025–1027
23. Hou D, Li P, Liu C et al (2010) Long-term stable frequency transfer over an urban fiber link using microwave phase stabilization. Opt. Express 19:P506–P511

Chapter 33
Progress on Sapphire Hydrogen Maser for Beidou Navigation System

Tiezhong Zhou, Qiong Wu, Jian Huang and Lianshan Gao

Abstract Active hydrogen maser is one of the most important equipments for the Beidou Navigation system. The stability of active hydrogen maser does influence the synchronize accuracy of time and frequency between the satellites and the ground devices. In order to improve the stability of Sapphire Hydrogen Maser, we had done several improvements on the physical package and electrical package, which include magnetic shield improvements, developing a method to probe the hydrogen atom beam, getter pump improvement and cavity auto-turning system researching. The factor of magnetic shield has been improved to above 10^5. We had researched several kinds of getter materials which can improve the lifetime of physical package. We had designed a new form of getter pump, which make the volume of physical package smaller than ever. The stability of the maser after improvement can get 3.1×10^{-13} @ 1 s, 2.9×10^{-15} @ 1 day.

Keywords Hydrogen maser · Magnetic shield · Improvement · Beam controlling · Frequency stability

33.1 Introduction

To ensure normal operation of the Beidou Compass Navigation Satellite System [1] of China which is under construction, the ground stations must conduct continual detection and control over the space satellite system. In order to maintain Beidou time system, master control station, injection station and monitoring

T. Zhou (✉)
Beijing University of Aeronautics and Astronautics, Beijing 100191, China
e-mail: Falcon@ee.buaa.edu.cn

T. Zhou · Q. Wu · J. Huang · L. Gao
Beijing Institute of Radio Metrology and Measurement, Beijing 100854, China

J. Sun et al. (eds.), *China Satellite Navigation Conference (CSNC) 2013 Proceedings*, Lecture Notes in Electrical Engineering 245,
DOI: 10.1007/978-3-642-37407-4_33,

station jointly track Beidou Satellite to calculate data such as satellite ephemeris, satellite clock stability, and drifting, input navigation message and control instruction, detect and control over the "health" status of the satellite. The accomplishment of above tasks is based on the accurate atomic clock system on the ground. During the synchronizing process between ground clock and satellite clock, the system time base on central control station is regarded as the ideal clock, and it has to be made up of large amount of reliable hydrogen clocks and caesium clocks. Moreover, the strict synchronization between local ground stations for orbit calculation and ground stations for time synchronization also rely heavily on the highly stable and reliable hydrogen clocks and caesium clocks on the ground. Therefore, highly reliable and stable active hydrogen maser is basic equipment of ground time frequency system of Beidou System and its performance indicators determines the generation and maintenance of the time of Beidou System, and directly affects the timing accuracy and navigation positioning accuracy of Beidou System.

Beijing Institute of Radio Metrology and Measurement has been working on the research of sapphire active hydrogen maser frequency standard for many years. So far sapphire hydrogen maser frequency standard technology has been mature, and sapphire hydrogen clocks in many regions of China, such as the systems of China Mainland Tectonic Environment Monitoring Network (CMTEMN) in Changchun, Shanghai, Lhasa, and Kunming, as well as Navy Changhe Navigation System, have been put into operation. The sapphire hydrogen clocks in operation are stabile and reliable, and their breakdown maintenance rate is zero. According to a recent report, the sapphire active hydrogen clock has been "fully qualified" to be used in "Beidou" time keeping system.

In order to further improve the performances of sapphire active hydrogen maser frequency standard, and to meet the requirements of ground time frequency system of Beidou Navigation System on atomic clock, we have made significant technological improvement on the physical package and electrical circuit system based on the current status of sapphire active hydrogen atomic clock. The indicators of the improved sapphire active hydrogen maser frequency standard could reach 3.3×10^{-13} @ 1 s, 2.9×10^{-15} @ 1 day.

33.2 Major Improvement

Structure of the sapphire active hydrogen maser is illustrated in the Fig. 33.1. During the development of the device, we have found that shielding factor of magnetic shielding system of sapphire active hydrogen maser is relatively small in the process of long-term use, only about 60,000, which is difficult to meet the requirement that the frequency fluctuation of maser frequency output is less than 1×10^{-15}; the stability of the hydrogen atom beam of physical system is an important factor to affect the long-term stability of maser, and it is necessary to develop flowmeter to control atom beams; in terms of vacuum maintenance

system, previous method used small cartridge getter, small titanium pump was placed in an equal position with getter pump, and the change of the pumping speed of getter pump had certain impact on the long-term stability of the overall device; in addition, the current automatic servo system used for microwave cavity has potential to be further optimized.

33.2.1 Improvement of Magnetic Shielding System

In order to reduce the impact of change of external magnetic field on the frequency of maser output, four layers of magnetic shielding have been installed outside the microwave cavity. Magnetic shielding is directional, and usually shielding factors of the magnetic shielding are divided into longitudinal shielding factors and lateral shielding factors. For multilayer straight cartridge magnetic shielding, the lateral

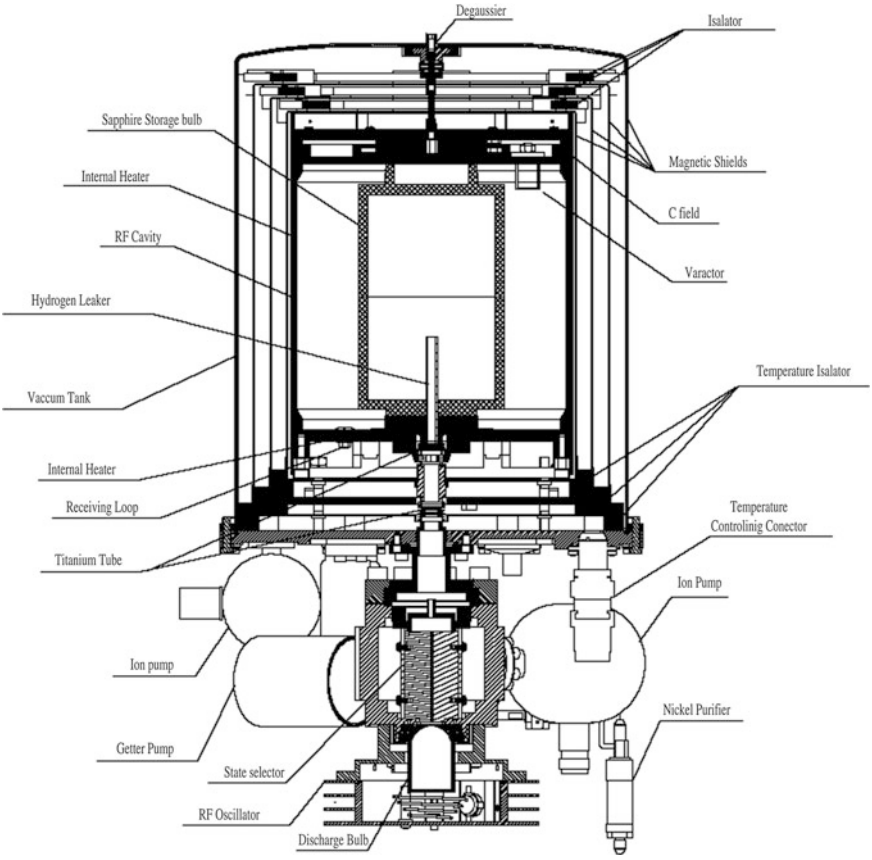

Fig. 33.1 Structure of sapphire active hydrogen maser frequency standard before improvement

shielding factors are usually two magnitudes larger than longitudinal shielding factors. Therefore, we use longitudinal shielding factors S_l to define the shielding ability of magnetic shielding. Assuming that change of the magnetic field of atomic working area is caused by the change of external magnetic field. The variation of output frequency of hydrogen atomic transition frequency along with the internal magnetic field $\Delta\upsilon_m$ is expressed in the following formula [2]:

$$\Delta\upsilon_m/\upsilon_0 = 3.875 \times 10^2 B_z(\Delta B_{ext}/S_l) \tag{33.1}$$

Usually internal magnetic field of maser operation $B_z = 100\,nT$, and we can get relation between maser frequency fluctuation and shielding factor. If we require the fluctuation of the output frequency of physical section less than 1×10^{-15} and external magnetic field fluctuation less than 10 % of the geomagnetism, namely 5 μT, then the shielding factor of the magnetic shielding must be larger than 2×10^5.

During the development of sapphire active hydrogen maser frequency standard, we found that the structures and the processing methods of existing shielding system have many problems, and there are only several ten thousand shielding factors in overall shielding system, which is difficult to meet the technical requirements of high performance hydrogen atomic clocks. Three layers of magnetic shielding cartridges inside the sapphire hydrogen maser frequency standard are fixed on chassis in an extruding approach. Since magnetic shielding material is thick, with weak rigidity, and easy to deform, this method of fixation is easy to cause the defective tightness between magnetic shielding cartridge and the side joint of the chassis. Partial joints are not surface contact, but just the line contact, even virtual contact. Under condition of poor contact between cartridge and chassis, the additional magnetic field of the uniform area is increased by the magnetic leakage from the joints, which undermine the uniformity of magnetic field of the uniform area. We have found that the defective tightness in the joint between magnetic shielding cartridge and the chassis may lead to the problem of magnetic leakage. To deal with this problem, we filled Perm alloy into the joint between magnetic shielding cartridge and the chassis of the first and second layers. The testing method is illustrated in Fig. 33.2a. We can calculate the remaining magnetic field of the place by measuring the magnetic field within the magnetic shielding of two directions at different places. The measurement results are illustrated in the Fig. 33.2b.

Above experiment result shows that, there is crevice in the joint between shielding cartridge and the back cover of the magnetic shielding system and it affects the shielding effect. In addition, we found that, the short circuit may occur between four magnetic shielding layers during the long-term operation of the clock, and it leads to the change of the performance of the clock. In summary, it is necessary to conduct the research on the optimization of the structure of magnetic shielding, to improve the shielding effect, and to ensure the stability of the overall system.

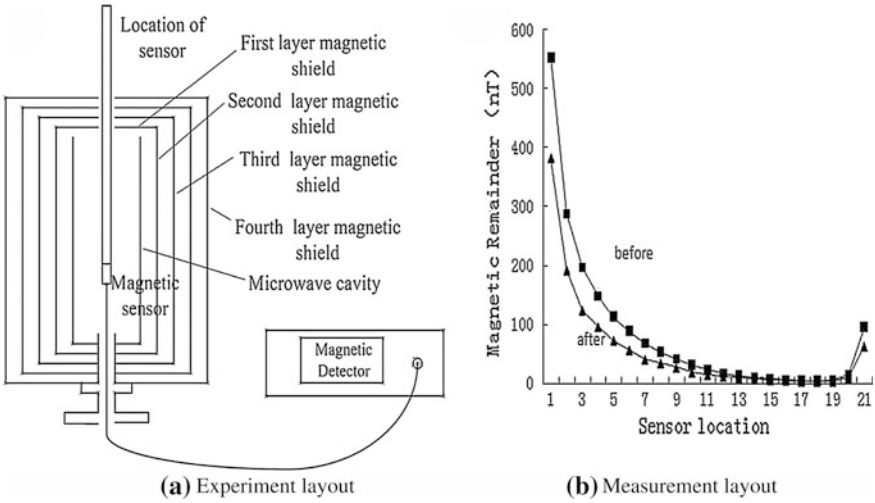

Fig. 33.2 Measurement of the performances of magnetic shielding, and comparison of remaining magnetic fields before and after adding the shielding seal

From above experiment, we have made improvement on the structure which illustrated in Fig. 33.3 and processing method of magnetic shielding system. Non-metals vacuum materials are filled into the spaces between the magnetic shielding layers to improve the shielding effect and reliability of the magnetic shielding system.

In order to calculate the shielding coefficient of magnetic shielding, we measured the magnetic shielding after improvement, and the residual magnetism of the internal magnetic shielding system was measured by changing the magnitude of external magnetic field. The measurement results are illustrated in the Table 33.1. The table gives the magnitudes of internal magnetic fields at different locations. It can be seen from the table, the shielding coefficients at different locations of the

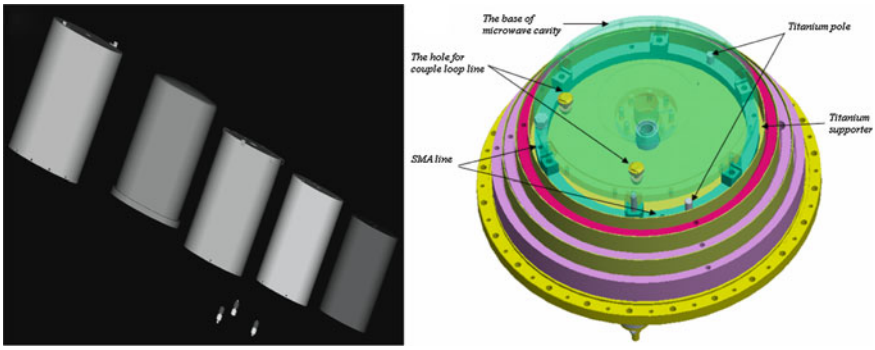

Fig. 33.3 Magnetic shielding structures after improvement

Table 33.1 Comparison of the residual magnetism of magnetic shielding system before and after oscillation

Measurement location	External magnetic field is zero Residual magnetism (nT)	External magnetic field is 5Gs Residual magnetism(nT)	Shielding factor
1	1.5	7.5	83,333.33
2	0.5	2.5	250,000
3	0	2	250,000
4	0.5	2.5	250,000
5	0	2	250,000
6	0	2	250,000
7	0	2	250,000
8	0	2	250,000
9	0	2	250,000
10	0.5	1	100,000
11	0	1	500,000
12	0.5	1	500,000
13	0	1	500,000
14	0.5	1.5	500,000
15	0	1	500,000
16	0.5	1	500,000
17	0.5	1.5	500,000
18	0	1	333,333.3
19	0	1	333,333.3
20	1.5	2.5	500,000
21	2.5	2.5	500,000

magnetic shielding are above 2×10^5, which satisfies the requirement on magnetic field for ensuring the maser frequency being maintained at 1×10^{-15}.

33.2.2 Control of Hydrogen Atom Beams

The stability of the hydrogen atom beams has great impact on the long-term stability of frequency of the clock. In most other countries, flowmeters are used on hydrogen atomic clocks to control the stability of hydrogen atom beams. Since the consumption of hydrogen on Sapphire hydrogen clock is very small, 1 mol hydrogen could be used for three years, and the hydrogen flow rate is 2.37×10^{-10} Pa · m^3/s, it is difficult to measure it accurately, and it is necessary to develop highly accurate and stable hydrogen flowmeter.

The experiment is shown in the Fig. 33.4. After hydrogen passes nickel purifier and is purified, the hydrogen flow rate could be controlled by the electric current of the purifier. Purifier is a device for providing high purity hydrogen to physical section, and its structure is shown in the Fig. 33.3. Two ends of electrodes in the purifier are connected by small nickel tubes. The nickel tube outlets are connected with vacuum system, and the internal end of nickel tube is connected with

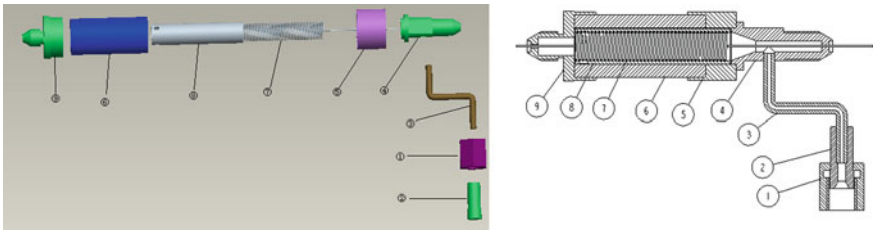

Fig. 33.4 Nickel purifier

hydrogen source. When electric current passes the nickel tube, the temperature of nickel tube increases; when the temperature exceeds 500 °C, the metal lattice of nickel material will inflate to the size larger than the hydrogen molecular, and the hydrogen molecular could enter into vacuum through tube wall.

Figure 33.5 is flowmeter experimental layout and the experiment result. Vacuum detection section of the flowmeter has two thermistors. One R_{T1} is placed in the hydrogen passageway and used for sensing the impact of gas flow to thermistors temperature. We use another thermistor R_{T2} to sense the change of environmental temperature, and R_{T2} are placed far away from the gas passageway. The impact of error caused by the change of the external environmental temperature could be eliminated by detecting the differences of temperature change of above two circumstances. The change of flow rate of the gas could be calculated by measuring the change of the voltage difference between A and B. In the experiment, experimental device is connected with mass spectrometer (can measure a variety of gas compositions). We record the electric current of nickel purifier, change of vacuum degree of the system, the leakage rate change of mass spectrometer, and the voltage

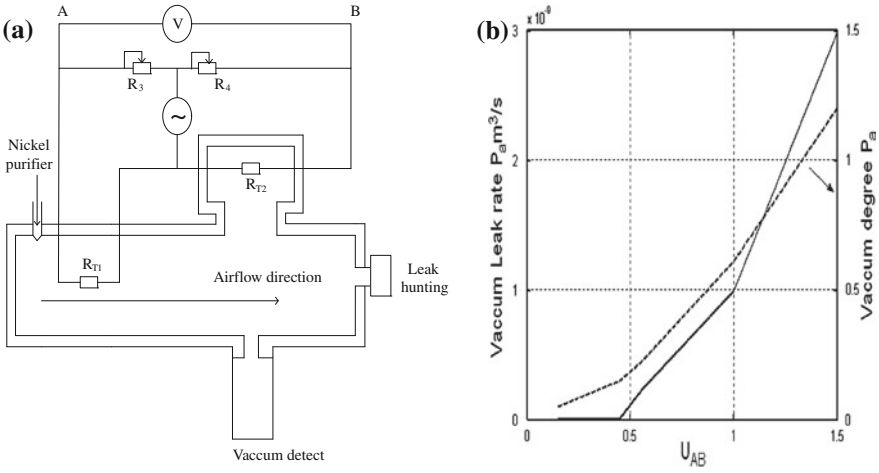

Fig. 33.5 Experiment on flow rate measurement. **a** Experimental layout. **b** The principle of circuits and relationship between flow rate U_{AB} and system vacuum degree and leakage rate

difference between A and B. The data recorded are listed in the Fig. 33.5b. It can be see that, the leakage rate of the system, the change of vacuum degree, and the voltage difference between A and B of the flowmeter are nearly linear.

33.2.3 Improvement of Vacuum Maintenance System

Highly reliable and long-life internal vacuum maintenance system is a precondition for the long lifespan and high performance of a physical system. Previously, the vacuum maintenance system of sapphire hydrogen clock of our institute was equipped with one sputtering ion pump and 4 getter pump, which has the main drawback of short 2 years lifespan of ion pump. When the speed of ion pump decay, the total speed of the whole system will be changed, which will influence the performance the maser. It could not meet the requirement of hydrogen maser frequency standard products on long lifespan. In addition, it requires long-time power connection, which limits the usage scope of the products and requires higher requirement on maintenance.

Through experiment and analysis of the pumping effect of titanium wire getter of other countries, we developed usable getter with the reference to foreign products. During the experiment and development, we have developed production, processing and activation technologies for getter. The pumping effect is tested after processing titanium wire getter, and the test result is shown in the Fig. 33.6. The test result shows that, the pumping effect of this kind of titanium wire getter has been close to the pumping effect of the getter of other countries.

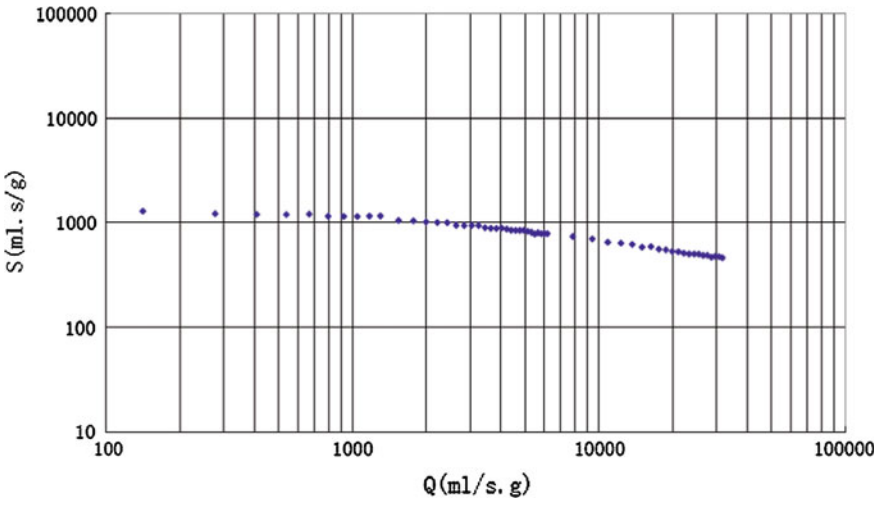

Fig. 33.6 Relationship between four-hour domestic titanium getter rate and getter capacity

After the getter materials test, we design a new form of getter pump, which make the volume of physical package smaller than ever. Moreover the new form of getter pump has a very attractive advantage than ever, the pumping speed of ion pump have nothing impact on the long-term stability of the overall device. The contrast of new scheme and old one is shown in the Fig. 33.7.

33.2.4 Automatic Tuning of Microwave Cavity

The temperature coefficient of the sapphire loading microwave cavity is −50 kHz/°C, given temperature precision of microwave cavity is 1 ‰ °C. Formula (33.2) is cavity pulling formula [3]. In the formula, v_C is the resonance frequency of microwave cavity TE_{011} model; v_0 is base frequency; Q_C is unloaded quality factor of microwave cavity; Q_a is the quality factor of output maser signal. If output frequency fluctuation of physical system is required to be less than 1×10^{-15}

$$\frac{\Delta v_C}{v} = \frac{Q_C}{Q_a} \times \frac{(v_C - v_0)}{v_0} \tag{33.2}$$

Q_C Typical value is 40,000; Q_a typical value is 1×10^9; v_0 is 1,420.405751 MHz; then it can be calculated that the fluctuation of v_C should be less than 0.1 Hz, namely, the resonant frequency of microwave cavity should be controlled within the scope of 1,420.405751 ± 0.1 Hz. However, it could not be realized only be relying on temperature control system. Therefore, it is necessary to use servo circuit to control the frequency of microwave cavity.

Current servo system in cavity servo phase locked circuit has three schemes: microwave detecting cavity scheme [4], low frequency modulation detecting cavity scheme, and electromagnetic field phase detecting cavity scheme [5–10].

Microwave detecting cavity scheme is a traditional approach, and its major principle is to input two detecting signals in the two sides of the central frequency (1,420.405751xxx MHz) of maser output signal with the interval of 20 kHz in the microwave cavity. If the microwave cavity frequency is not aligned with maser transition signal, there will be a difference in the ranges of two jumping

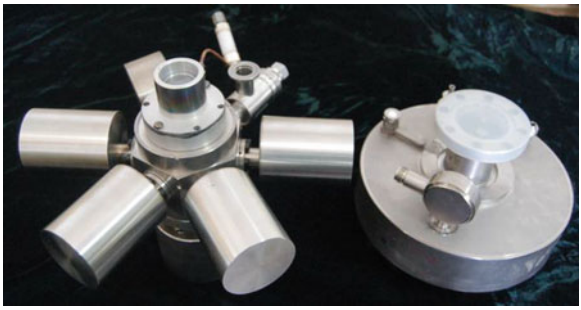

Fig. 33.7 Two kinds of Getter pump contrast

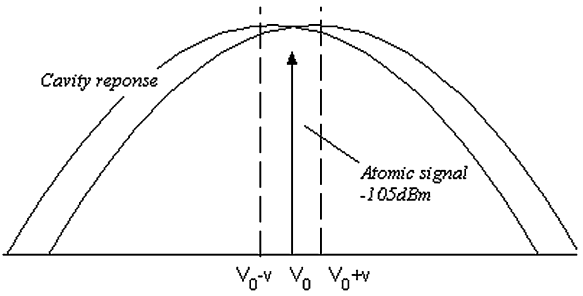

Fig. 33.8 Schematic diagram of low frequency modulation scheme

frequencies. After passing the follow-up detecting circuit, the error signal of microwave cavity could be calculated. Microwave detecting scheme is relative mature. However, this scheme needs to input microwave signal to microwave cavity, which may have impact on the maser oscillation signals, to further impact the short term stability of the whole device. After inputting microwave cavity detecting signal, the stability of maser signal frequency at 1 s and 10 s will deteriorate 30 %.

Low frequency modulation scheme is a microwave cavity servo scheme used by international advanced active atomic clock. In this scheme, the frequency of microwave cavity is modulated through adding square-wave modulating signal into the variable capacitance diode in microwave cavity. After the frequency of microwave cavity TE_{011} model is modulated, the maser output signal contains modulated information of microwave cavity. Meanwhile, since the TE_{011} model

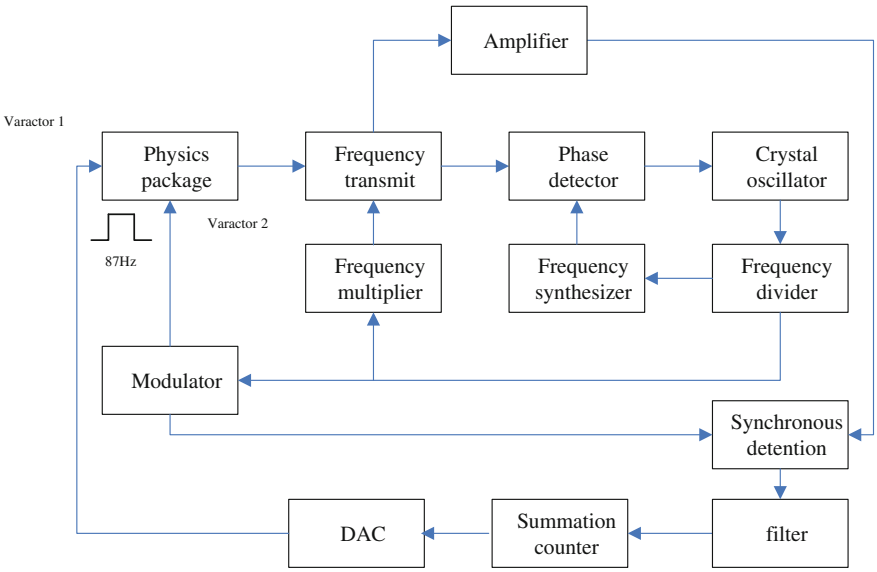

Fig. 33.9 Implementation diagram of low frequency modulation scheme

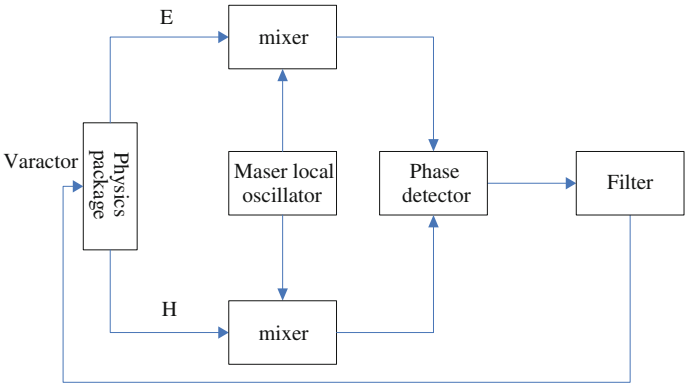

Fig. 33.10 Electromagnetic field phase detecting scheme

frequency response is featured with symmetry, when maser output signal amplitude no longer changes, we could regard the frequency of microwave cavity has been aligned. Its principle is illustrated in the Fig. 33.8. Figure 33.9 is implementation diagram. The advantage of this scheme is that it reduces the interference

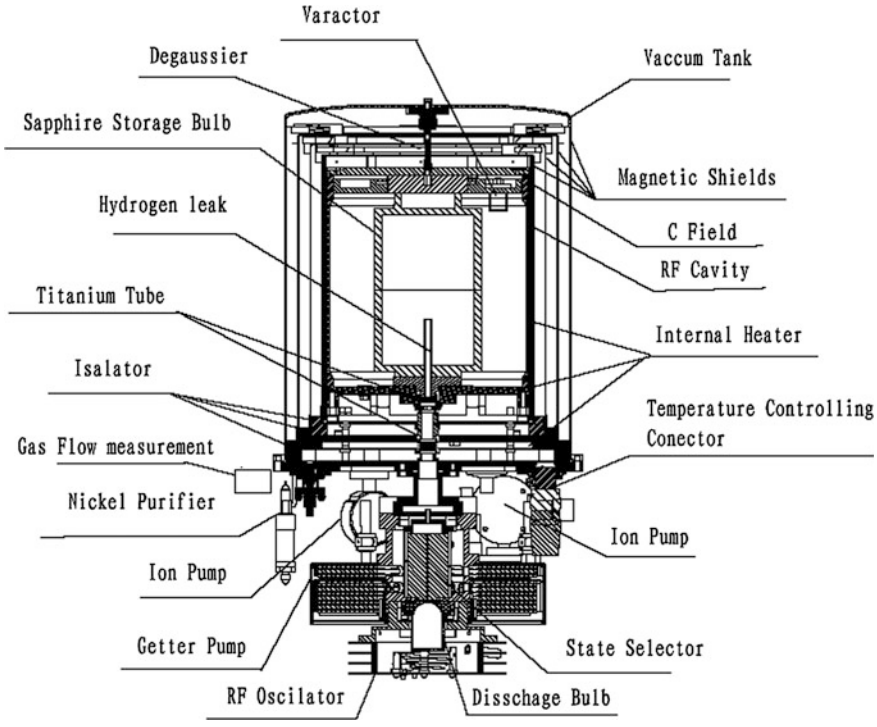

Fig. 33.11 Physical system of sapphire hydrogen clock after improvement

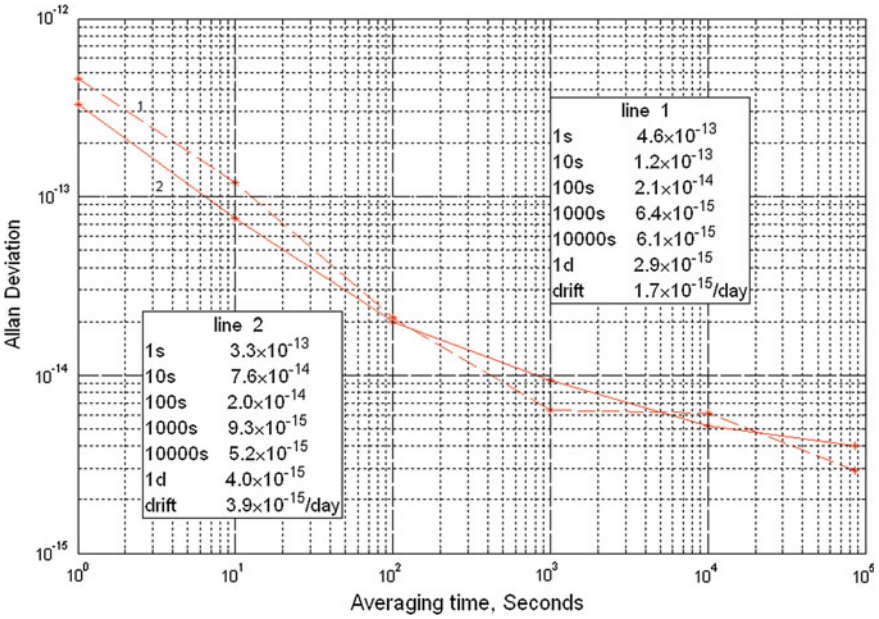

Fig. 33.12 Frequency stability of the two sets of improved sapphire active hydrogen maser frequency standards (measured by the Chinese National Institutive of Metrology)

generated by the maser oscillation caused by external signal, but this scheme has relative high requirement on the indexes of time constant of the components such as variable capacitance diode.

The main principle of electromagnetic field phase detecting cavity is that the microwave signal released by hydrogen atoms in the storage bubble oscillates in the microwave cavity in TE_{011} model. both of above two schemes are the coupling of magnetic field energy of microwave field, but electric field energy in the microwave cavity also contains the stability and accuracy of maser transition, and the phase difference information between electric field signal and magnetic field signal contains frequency information of microwave cavity. Therefore, by coupling the electric field energy and magnetic field energy of microwave field at the same time, the phase information of two fields could be detected and thus the resonance frequency information of microwave cavity TE_{011} model could also be worked out. Figure 33.10 is the specific implementation diagram of this concept.

We have made specific experiments on above methods. From experiments, we found that microwave detecting cavity scheme is a mature technology to realize the joint alignment of overall device; low frequency modulation scheme has relatively higher requirement on the performance of components, and its experiment is underway; the electromagnetic field phase detecting cavity scheme has realized the detection of probe field of the physical system, and the overall device joint alignment is underway.

33.3 Design Validation

Based on the improvements discussed above, we developed two sets of improved sapphire active hydrogen maser frequency standards, and their servo systems still use microwave detecting cavity scheme. Figure 33.11 illustrates the structure of the physical system of hydrogen maser frequency standard after improvements. Frequency stability of the hydrogen maser frequency standards has been tested, and the testing result is illustrated in the Fig. 33.12, which were measured by the Chinese National Institutive of Metrology.

33.4 Conclusion

The research has made improvement on the key areas of magnetic shielding, flowmeter, and servo system of microwave cavity of sapphire active hydrogen maser frequency standards, and developed two sets of improved sapphire active hydrogen maser frequency standards. The tests on two sets of devices have been conducted and the test results show that, the optimal stability of sapphire active hydrogen maser frequency standards could reach 3.3×10^{-13}/s, 2.9×10^{-15}/day. Two newly developed devices uses microwave detecting cavity scheme as their servo schemes. The stability of the sapphire hydrogen maser could be further improved by the next step works of realizing the low frequency modulation detecting cavity scheme and electromagnetic field phase detecting cavity scheme.

References

1. Haiyan (2001) Beidou Navigation System in China, China Acad J Electron Publishing House 12: 22
2. Gubser DU, Wolf SA, Cox JE (1979) Shielding of longitudinal magnetic fields with thin, closely spaced, concentric cylinders of high permeability material. Rev Sci Insreum 50(6):751–756
3. Qiang C, Jihong Z, Guohui S, LianshanG (2009) Analysis of the characteristic of the nickel purifier in hydrogen maser, IGNSS Conference
4. Vanier J, Audoin C (1989) The quantum physics of atomic frequency standards. Adam Hilger, Bristol
5. Li J (2004) Study on hydrogen maser frequency standard cavity servo. J Astronaut Metrol Meas 24(1):43–45
6. Kleppner D, Goldenberg HM, Ramsey NF (1962) Theory of the hydrogen maser, Phys Rev 126: 603
7. Audoin C (1981) Fast cavity auto-tuning systems for hydrogen maser, Revue Phys Appl 16: 125
8. Wang H, To M (1980) Proceedings of 34th Annual symposium on frequency control, Philadelphia, p 364
9. Peters HE (1982) Proceedings of 36th Annual symposium on frequency control, Philadelphia, p 240
10. Sydnor RL, Maleki L (1983) Proceedings of 37th Annual symposium on frequency control, Philadelphia, p 621

Chapter 34
High-Resolution Frequency Measurement of the Ground-State Hyperfine Splitting of $^{113}Cd^{+}$ Ions

Shiguang Wang, Jianwei Zhang, Kai Miao, Zhengbo Wang and Lijun Wang

Abstract Time-keeping clock is one of the most important parts in COMPASS global navigation satellite system (GNSS) of China and the synchronization of these time-keeping clocks is the basis of GNSS. Recently, we have engaged in developing a transportable atomic clock based on $^{113}Cd^{+}$ ions, which is potentially applied in the comparison of atomic clocks in different locations, including the time-keeping clocks at the ground stations of the COMPASS system. To operate a high precision microwave atomic clock, one has to measure its clock transition frequency precisely at zero external magnetic field. In this paper, the progress of the precision measurement of the ground-state hyperfine splitting of laser-cooled $^{113}Cd^{+}$ ions is reported. In the previous experiment, the hyperfine splitting was measured to be 15,199,862,854.96(12) Hz, using Ramsey's separated oscillation fields technique. Recently, by upgrading the ion trap apparatus, the control time sequence, and the magnetic field stabilization, we obtained a preliminary improved result of 15,199,862,855.013 Hz. This value is nearly one order of magnitude more accurate than the results obtained before.

Keywords Microwave atomic clock · Ion trap · Hyperfine splitting · $^{113}Cd^{+}$ ions

S. Wang (✉) · J. Zhang · K. Miao · Z. Wang · L. Wang
Joint Institute for Measurement Science, Tsinghua University, Beijing 100084, China
e-mail: wangsg08@mails.tsinghua.edu.cn

S. Wang · L. Wang
Department of Physics, Tsinghua University, Beijing 100084, China

J. Zhang · K. Miao · Z. Wang · L. Wang
The state key lab of precision Measurement Technology and Instrument, Department of Precision Instruments, Tsinghua University, Beijing 100084, China

J. Sun et al. (eds.), *China Satellite Navigation Conference (CSNC) 2013 Proceedings*, Lecture Notes in Electrical Engineering 245,
DOI: 10.1007/978-3-642-37407-4_34,

34.1 Introduction

As an almost unperturbed atomic system, the trapped ion has been widely used in atomic frequency standards. Trapped ions can provide frequency references in both of the microwave and optical regions. The optical frequency standard based on Al^+ [1] is the most precise clock so far. And those microwave frequency standards based on $^{199}Hg^+$, $^{137}Ba^+$, and $^{171}Yb^+$ [2–4] were also investigated in the past decades. Recently, we begun a program to develop a transportable microwave frequency standard based on $^{113}Cd^+$ ions with high precision, which has potential application in the comparison of the time-keeping clocks at different ground stations of the COMPASS system. One of the main features of the $^{113}Cd^+$ ion frequency standard is that only one laser is needed to realize laser cooling, optical pump, and probing due to its simple energy level structure compared to the $^{199}Hg^+$, $^{137}Ba^+$ and $^{171}Yb^+$ ions.

High-precision measurement of the clock transition line at zero external magnetic field is a key step toward developing a frequency standard. In this paper, we report the measurement of the ground-state hyperfine splitting of $^{113}Cd^+$ ion by using Ramsey's separated oscillation fields technique. Compared with the results of 15,240(200) MHz obtained by Hamel and Vienne [5], 15,199,862,858(2) Hz obtained by Tanaka et al. [6], and 15,199,862,855.0(2) Hz obtained by Jelenkovic et al. [7], our result is consistent with the recent one very well and the precision improved. In order to further improve the measurement accuracy of the clock transition, we upgraded the experimental setup and obtained a preliminary result which precision is improved by nearly one order.

34.2 Experimental Setup

34.2.1 The Ion Trap

Figure 34.1a is a photograph of the linear quadrupole Paul trap used in experiment, which is installed inside a vacuum chamber with the pressure of approximately 5×10^{-10} mbar. In the chamber, a homemade cadmium oven and an e-gun are installed. The cadmium atoms evaporated from the heated oven are ionized by electron bombardment. As shown in Fig. 34.1b, to confine the ions in radial direction, the potential of both diagonal pairs of electrodes is alternated periodically. The alternating radio frequency (rf) voltage is 300 V with a frequency of 971 kHz. For the axial direction confinement, a dc potential of approximately 30 V is applied on the ring endcaps. Compensating voltages are applied on the electrodes to compensate the scattering electric fields. The radius of the four rod electrodes R is 3 mm, the minimum distance from the center of the trap to the electrode surface r_0 is 8.5 mm. The length of the trap is 49.5 mm. Outside the vacuum chamber, there are three orthogonal pairs of Helmholtz coils. One of them

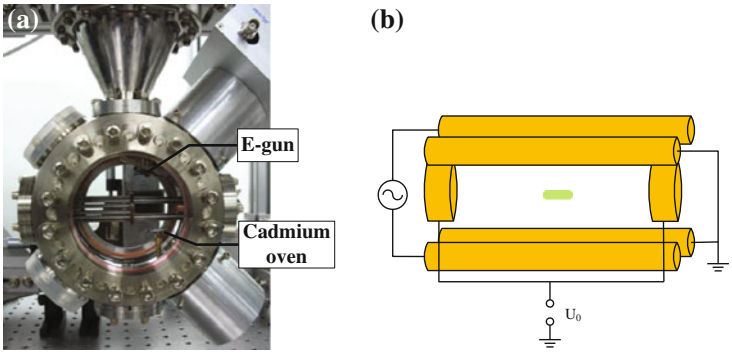

Fig. 34.1 **a** A photograph of the linear Paul trap installed inside the vacuum chamber. **b** The schematic diagram of the linear quadrupole Paul trap with four rod electrodes and two ring endcaps

is used to create the static magnetic field parallel to the electrodes of the trap, and the other two are used to compensate ambient magnetic fields.

34.2.2 State Preparation and Laser System

The energy level of $^{113}Cd^{+}$ is shown in Fig. 34.2. The ions can be laser cooled and detected by a laser using the cycling transition of $^{2}S_{1/2}\,|F=1> \leftrightarrow {}^{2}P_{3/2}\,|F=2>$. During the cooling process, the ions can be trapped in the dark state of $^{2}S_{1/2}\,|F=0>$ since the hyperfine splitting of the $^{2}P_{3/2}$ state is only 800 MHz. To avoid the circumstance, a microwave radiation field resonant with the hyperfine transition of $^{2}S_{1/2}\,|F=1> \leftrightarrow {}^{2}S_{1/2}\,|F=0>$ is applied to repump the ions back to the cycling transition. The same laser is also used to pump the ions to the state of $^{2}S_{1/2}\,|F=0>$

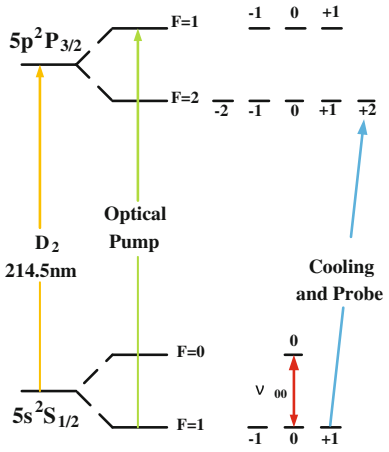

Fig. 34.2 Energy levels of the $^{113}Cd^{+}$ ion

after the laser frequency is blue shifted 800 MHz by an acousto-optic modulator (AOM) to reach the $^2P_{3/2}|F = 1>$ state. Hence, only a single laser is needed for laser cooling, pumping and detection in the experiment.

The laser system in the experiment is a frequency-quadrupled, tunable diode laser system (TA-FHG Pro, Toptica), oscillating at 214.5 nm. The output power of the laser is about 5 mW, and the frequency is stabilized to the megahertz level by employing a Fabry–Perot optical spectrum analyzer as a transfer cavity [8]. The ultra-violet (uv) laser beam is split into two parts. One of them is used to cool and probe ions, which is circularly polarized via a quarter-wave plate. The other is used to pump ions after its frequency is blueshifted by an AOM. Two optical shutters are inserted in the light paths of these two beams to switch the laser on or off during measurement, which are remotely controlled by a computer. The fluorescence signal from the ions is detected by a uv photomultiplier tube (PMT) in the Geiger mode. The microwave is generated by a signal generator referenced to a cesium clock and fed to the ions via a horn antenna.

34.3 Experimental Results

In the experiment, we measured the ground-state hyperfine splitting of $^{113}Cd^+$ ions using Ramsey's separated oscillation fields technique. Figure 34.3 shows a Ramsey fringe obtained in the experiment. Every data point is obtained according to the sequence of cooling, pumping, the first microwave interaction, free precession, the second microwave interaction and detection. For cooling, the uv laser is tuned to the red side of the $^2S_{1/2}|F = 1, m_F = 1 > \leftrightarrow {}^2P_{3/2}|F = 2, m_F = 2 >$ transition, and the microwave radiation resonant with the ground-state hyperfine splitting is switched on to repump the ions back to the $^2S_{1/2}|F = 1, m_F = 0 >$ state. After that, the cooling laser is switched off by an optical shutter, and the repumping microwave radiation is also switched off. Then the pump laser beam resonant with the $^2S_{1/2}|F = 1 > \leftrightarrow {}^2P_{3/2}|F = 1 >$ transition is switched on to pump all the ions into the $^2S_{1/2}|F = 1, m_F = 0 >$ state. After the state preparation, a microwave pulse of $\tau = 5$ ms at the frequency ν is applied after all lasers are blocked. After a free

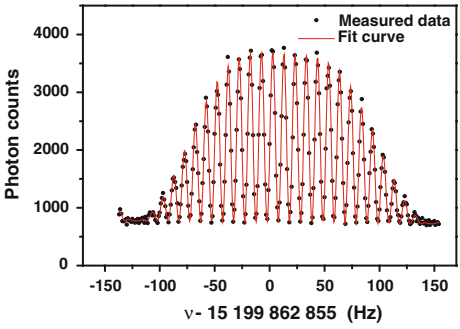

Fig. 34.3 Ramsey spectroscopy of $^{113}Cd^+$ obtained with a period of 0.1 s free precession between two microwave pulses of 5 ms. The gate time of photon counting is set at 28 ms

precession with a period time of $T = 0.1$ s, the second phase-coherent microwave pulses of $\tau = 5$ ms is applied. After one Ramsey interrogation, the cooling laser is unblocked and the fluorescence signal is detected by the PMT. The Ramsey fringes as shown in Fig. 34.3 are fitted to the following equation [9],

$$P_{Ramsey}(2\pi v) = \frac{4b^2}{\Omega^2}\sin^2\frac{\Omega}{2}\tau\left(\cos\frac{\Omega}{2}\tau\cos\frac{\Omega_0}{2}T - \frac{\Omega_0}{\Omega}\sin\frac{\Omega}{2}\tau\sin\frac{\Omega_0}{2}T\right)^2 \quad (34.1)$$

with

$$\Omega = \sqrt{(2\pi v - 2\pi v_0)^2 + b^2}, \quad (34.2)$$

where b is the Rabi angular frequency, v is the frequency of the microwave, v_0 is the center frequency of the transition spectrum, $\Omega_0 = 2\pi(v - v_0)$, τ is the duration of the microwave pulse, and T is the free procession time between two microwave pulses. The statistical error of the center frequency during the curve fitting is less than 0.02 Hz for $^{113}Cd^+$.

According to the Rabi-Breit formula

$$v_{0,0}(B) = v_{HFS} + K_0 B^2, \quad (34.3)$$

where B is the static magnetic field, $v_{0,0}$ (B) is the transition frequency in the B static magnetic field, v_{HFS} is the ground state hyperfine splitting at $B = 0$ and K_0 is 257.5 Hz/G^2 for $^{113}Cd^+$ [10]. Since the magnetic field is generated by a Helmholtz coil pair, the magnetic flux density at the midpoint of the Paul trap is proportional to the current in the coil. Hence v_{HFS} can be obtained by measuring a series of $v_{0,0}$ (B) at different magnetic field intensities, namely at different coil currents. By fitting the experimental data according to the Eq. (34.3), we obtain the ground-state hyperfine splitting of $v_{HFS} = 15{,}199{,}862{,}854.96(11)$ Hz for $^{113}Cd^+$. The errors are the statistical errors from extrapolating.

In estimating the measurement errors, the light shift can be neglected because during microwave interrogations all of the laser beams are blocked. The temperature of the ions is measured to be approximately 1 K, hence the second order Doppler shift is at the level of 10^{-14}. The frequency reference of the microwave in the measurement is a commercial cesium clock which frequency accuracy is 5×10^{-13}, calibrated by the National Institute of Metrology of China (NIM). The variation of the magnetic field is the main limit of our measurement. After compensating the magnetic field in the orthogonal directions, the residual magnetic field in the orthogonal directions is estimated to be less than 10 mG. Hence, the error of the second-order Zeeman shift is less than 0.03 Hz. Therefore, the ground-state hyperfine splitting of $^{113}Cd^+$ is

$$v_{HFS} = 15,199,862,854.96(12)\,\text{Hz},$$

where the main error is the combination of the statistical errors from the extrapolation according to the Rabi-Breit formula, and the second-order Zeeman shift.

34.4 Improvement

In order to further improve the accuracy of the measurement of the clock transition, we upgraded the experimental setup, including the ion trap apparatus, the control time sequence, and the magnetic field stabilization.

For the ion trap part, the ratio of R/r_0 is optimized to be 1.1468, and the optimum ratio formation can reduce the rf heating effect. In this new trap, we measured the temperature of $^{113}Cd^+$ ions to be approximately 16 ± 3 mK [11]. Hence, the second-order Doppler frequency shift is less than 1×10^{-16}. Since there is no magnetic shield outside the physical package, in order to stabilize the magnetic field, we use a magnetometer with a nano-Tesla resolution close to the vacuum chamber to measure the temporal variation of the magnetic field in three dimensions. The magnetic field is stabilized via the feedback to the current of the pair of the Helmholtz coils parallel to the electrodes, and the final fluctuation of the magnetic field is controlled at the tens of nano-Tesla level. Furthermore, for Rabi and Ramsey interrogation, the measurement sequence is controlled by a microprocessor, and the time control precision is improved to microsecond level. All of these improvements offer us a better signal-to-noise ratio (SNR) of the spectroscopy and a more precise measurement result of the clock transition than before.

According to the Rabi-Breit formula, the 0–0 ground state hyperfine frequency $\nu_{0,0}$ at a given magnetic field can be expressed as

$$\nu_{0,0}(B) = \nu_{HFS} + \frac{1}{2}\left(\frac{g_J - g_I}{g_J + g_I}\right)^2 \frac{(\nu_{0,1} - \nu_{0,-1})^2}{\nu_{HFS}}, \tag{34.4}$$

where $\nu_{0,1}$ and $\nu_{0,-1}$ are the $^2S_{1/2}\,|F = 0, m_F = 0> \leftrightarrow {}^2S_{1/2}\,|F = 1, m_F = 1>$, and $^2S_{1/2}\,|F = 0, m_F = 0> \leftrightarrow {}^2S_{1/2}\,|F = 1, m_F = -1>$ transition frequencies at a given magnetic field, g_J and g_I are constants. So we can obtain the ν_{HFS} by fitting the experimental data of $\nu_{0,0}$, $\nu_{0,1} - \nu_{0,-1}$ at different static magnetic fields. In the experiment, $\nu_{0,1}$ and $\nu_{0,-1}$ are measured with Rabi interrogation technique since it is difficult to be measured with Ramsey's method due to the $\Delta F = 1$, $\Delta m_F = \pm 1$ Zeeman lines are magnetic field sensitive. The clock transition is measured also with Ramsey interrogation technique. In the upgraded experiment system, the pulse duration τ is 400 ms, and the free precession period T between two pulses can be up to 2 s. Figure 34.4 shows one example of measured Ramsey spectroscopy of the clock transition at a given magnetic field. The statistical error of the center frequency of the Ramsey spectra is less than 0.006 Hz, improved nearly one order compared to the results obtained before. By fitting the experimental data according to the Eq. (34.4), we obtain the ground state hyperfine splitting of $^{113}Cd^+$ $\nu_{HFS} = 15{,}199{,}862{,}855.013$ Hz.

This result consistent with previous ones very well. And the detailed error analysis of this result is still under study. By the improved experimental setup, the measurement precision of the ground-state hyperfine splitting of $^{113}Cd^+$ is expected to be improved about one order of magnitude than the results obtained before.

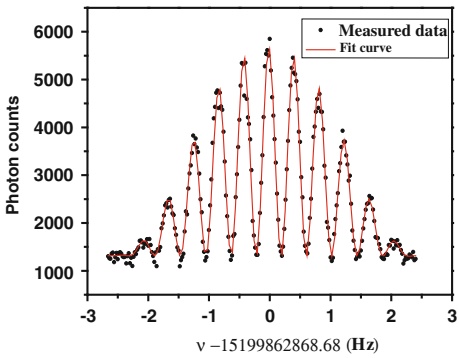

Fig. 34.4 Ramsey spectroscopy of $^{113}Cd^{+}$ obtained with a period of 2 s free precession between two microwave pulses of 400 ms. The gate time of photon counting is set at 15 ms

34.5 Conclusion

We have reported the ground-state hyperfine splitting measurement of $^{113}Cd^{+}$ ions trapped in a linear quadrupole Paul trap by Ramsey's separated oscillation fields technique. In the previous experimental setup, the values of $^{113}Cd^{+}$ ground-state hyperfine splitting is measured to be 15,199,862,54.96(12) Hz. This result consistent with the other's measurements very well. In order to improve the measurement accuracy, we upgraded the experimental setup. In the upgraded setup, we have obtained 15,199,862,855.013 Hz for the ground-state hyperfine splitting of $^{113}Cd^{+}$. Although the detailed measurement error analysis is still under study, the frequency precision is expected to improve by one order. These measurements are significant for the development of the microwave frequency standard based on trapped $^{113}Cd^{+}$ ions, which is potentially applied to the comparison of atomic clock in different locations.

Acknowledgments We acknowledge funding supports from the Major State Basic Research Development Program of China (973 Program) (No.2010CB922901) and the Tsinghua University Scientific Research Initiative Program (No. 20131080063).

References

1. Chou CW, Hume DB, Koelemeij JCJ, Wineland DJ, Rosenband T (2010) Frequency comparison of two high-accuracy Al^{+} optical clocks. Phys Rev Lett 104:070802
2. Prestage JD, Dick GJ, Maleki L (1991) Linear ion trap based atomic frequency standard. IEEE Trans Instrum Meas 40:132–136
3. Knab H, Niebling K-D, Werth G (1985) Ion trap as a frequency standard measurement of Ba+ HFS frequency fluctuations. IEEE Trans Instrum Meas 34:242–245
4. Park SJ, Manson PJ, Wouters MJ, Warrington RB, Lawn MA, Fisk PTH (2007) $^{171}Yb^{+}$ microwave frequency standard proceedings of the 2007 joint meeting EFTF-IEEE IFCS, pp 613–616
5. Hamel J, Vienne JF (1973) Optical pumping measurement of the hyperfine structure of cadmium ion ground state. Opt Commun 7:83–85

6. Tanaka U, Imajo H, Hayasaka K, Ohmukai R, Watanabe M, Urabe S (1996) Determination of the ground-state hyperfine splitting of trapped $^{113}Cd^{+}$ ions. Phys Rev A 53:3982
7. Jelenkovic BM, Chung S, Prestage JD, Maleki L (2006) High-resolution microwave-optical double-resonance spectroscopy of hyperfine splitting of trapped $^{113}Cd^{+}$ ions. Phys Rev A 74: 022505-5
8. Wang S, Zhang J, Wang Z, Wang B, Liu W, Zhao Y, Wang L (2013) Frequency stabilization of a 214.5 nm ultra-violet laser. Chin Opt Lett 11(3):031401
9. Vanier J, Audoin C (1989) The quantum physics of atomic frequency standards Adam Hilger Bristol, Bailey A (ed), vol 2, Chap 5, p 628
10. Vanier J, Audoin C (1989) The quantum physics of atomic frequency standards Adam Hilger Bristol, Bailey A (ed), vol 1, Chap 1, p 37
11. Shi-Guang W, Jian-Wei Z, Kai M, Zheng-Bo W, Li-jun W (2013) Crystallization and crystallization of trapped $^{113}Cd^{+}$ ions for atomic clock. Chin Phys. Lett 30(1):013703

Chapter 35
Development of New-Generation Space-Borne Rubidium Clock

Chunjing Li, Tongmin Yang, Liang Zhai and Li Ma

Abstract Beijing Institute of Radio Metrology and Measurement began to develop space-borne rubidium clocks from 2000. As one of the manufacturers of space-borne rubidium clocks, the institute had delivered more than 10 products to a satellite system of China until 2011, greatly supporting the construction of the satellite system. This paper summarizes the design features and performances of its previous products. The institute started to develop the new-generation space-borne rubidium clock in 2011. By using a series of new techniques, a prototype has been built. Compared to the previous products, the performance of the prototype is greatly improved. This paper also discusses the main differences between the previous and current products, both in design and in performance.

Keywords Space rubidium clock · New generation · Prototype

35.1 Background

Beijing Institute of Radio Metrology and Measurement began to develop space-borne rubidium clocks from 2000. Our work includes the design of the whole clock and the circuit system, the physics package, is supplied by another domestic unit. We have produced space-borne rubidium atomic clocks, and the products have been applied to more than 10 satellites. Recently, based on our previous experience, we are developing a new-generation space-borne rubidium clock, aiming at improving the key performances of our products.

C. Li (✉) · T. Yang · L. Zhai · L. Ma
Beijing Institute of Radio Metrology and Measurement, Beijing, China
e-mail: Casic2035@163.com

J. Sun et al. (eds.), *China Satellite Navigation Conference (CSNC) 2013 Proceedings*, Lecture Notes in Electrical Engineering 245,
DOI: 10.1007/978-3-642-37407-4_35,

35.2 Technical Features of Existing Space-Borne Rubidium Clock

Our previous product is a 10 MHz output rubidium clock, see Fig. 35.1. Only one 10 MHz OCXO is employed inside the whole rubidium clock. The 10 MHz signal is sent to a RF low-order frequency multiplier with 135 Hz modulation for 9× frequency multiplication to obtain a 90 MHz signal. Then the signal is frequency multiplied by a 76× high-order frequency multiplier, and synthesized with the 5.3125 MHz signal generated by the frequency synthesizer to produce a 6,834.6875 MHz signal required for the physics package. The output discriminator signal of the physics package is then subject to AC amplification, synchronous detection and integral amplification, and is finally sent to the voltage control terminal of the OCXO, so as to lock the 10 MHz frequency of the OCXO to the transition frequency of rubidium atoms.

This design scheme is mature and reliable, in which the localization rate of parts and components reaches 100 %. The advantages and disadvantages of the design are as follows.

- The typical integrated filter mode was used. This design is simple and reliable, but has a large microwave power frequency drift.
- A nonlinear transistor frequency multiplier was used. The 90 MHz signal with a square wave FM modulation is sent to a four-transistor push–pull amplifier. The merit is that few components are needed, and all the transistors work at low power, not more than 300 mW. The demerit is that the microwave signal has large temperature coefficient, and is difficult to be adjusted.

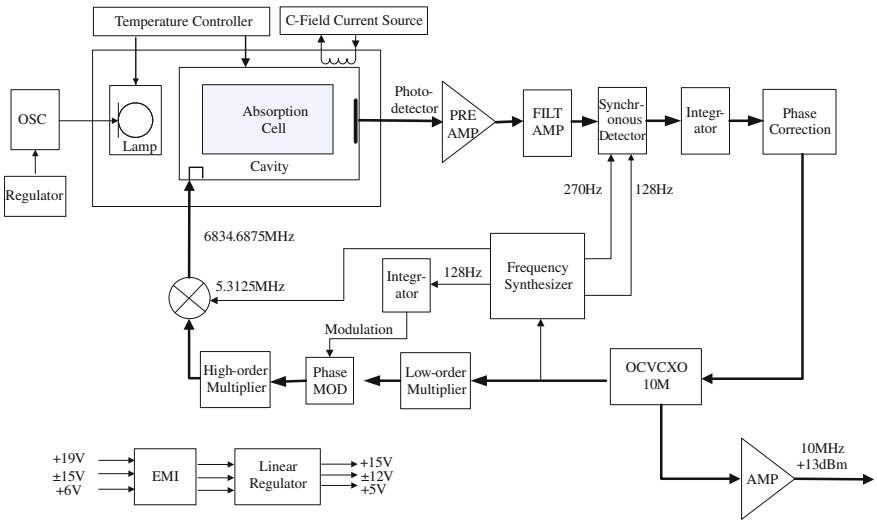

Fig. 35.1 Space-borne rubidium clock (old version)

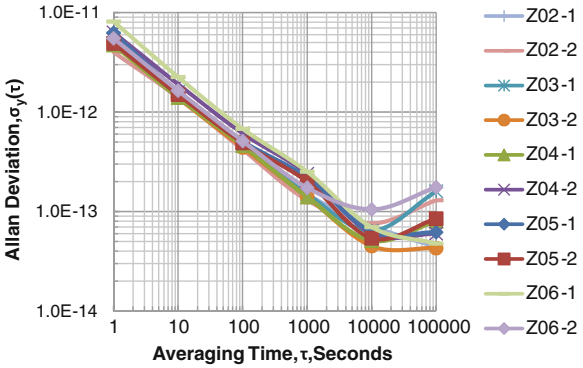

Fig. 35.2 Space-borne rubidium clock composite stability plot (old version)

- The amplifier, synchronous detector and integrator for the discriminator signal are composed of operational amplifiers and analog switches, no notch filter and lock acquisition circuit are used.
- The extra cavity step recovery diode (SRD) multiplication technique was used, the 6,834.6875 MHz microwave signal is is sent to the cavity-cell assembly. The signal adjustment is convenient, but the circuit structure is complicated.
- A glass sealed crystal resonator is employed for the 10 MHz oscillator. The resonator is of demerit of large size.
- The mass of the whole set is up to 5.8 kg, excluding the secondary power supply.

This kind of space-borne rubidium clock is of frequency stability of $5 \times 10^{-12}/\tau^{1/2}$ ($\tau = 1 \sim 10{,}000$ s), and frequency drift of less than 3×10^{-13}/d. Figure 35.2 shows the test performances of 10 products.

35.3 Technical Features of New-Generation Space-Borne Rubidium Clock

In recent two years, we summarized main features of our previous products and developed a new-generation space-borne rubidium clock with better overall performance.

35.3.1 Conceptual Design

The system design scheme of the new-generation space-borne rubidium clock is shown in Fig. 35.3. Key improvement is in the RF chain, which omits the mixer and uses a 12.6568287 MHz SC cut OCXO. Its output signal is amplified to 20 dBm and then sent to the high-order frequency multiplier and cavity filter to

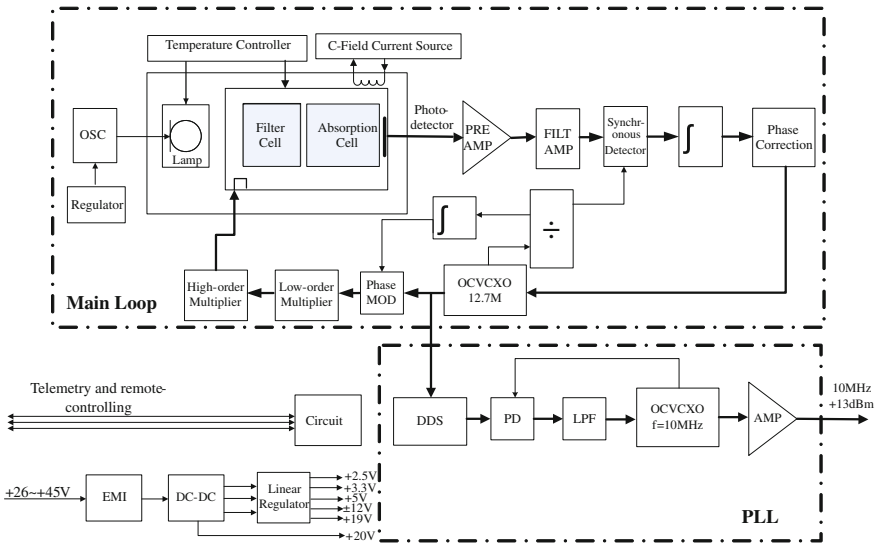

Fig. 35.3 Space-borne rubidium clock (new version)

obtain a microwave signal with power of $-40 \sim -30$ dBm, and frequency of 6,834.6875 MHz. The signal is sent to the physics package for discrimination. The discriminator signal is subject to AC amplification, synchronous detection and integration and then controls the 12.7 MHz crystal oscillator to obtain a stable 12.7 MHz sine wave signal.

For purpose of finally acquiring the 10 MHz signal with low phase noise and good short-term stability, a 10 MHz SC cut OCXO locked to the 12.7 MHz signal with superior phase noise and short-term stability is added.

The physics package adopts separate filter technique to improve the S/N ratio of the discriminator signal.

35.3.2 Structure Design

The new design requires that the secondary power supply and on–off command response units are integrated inside the rubidium clock, and the mass of the whole set should be reduced to below 5 kg. In order to meet the above design requirements, we adjust the layout of components inside the rubidium clock, see Fig. 35.4.

Two OCXOs and all circuits except for the power supply are all integrated in a box shield, and installed parallel to the physics package in order to reduce the mass and to facilitate assembly/disassembly operation and overall adjustment. The circuit box and physics package are mounted on a base plate. Optimized thermal conduction between the base plate and the chassis is realized. Through adjusting

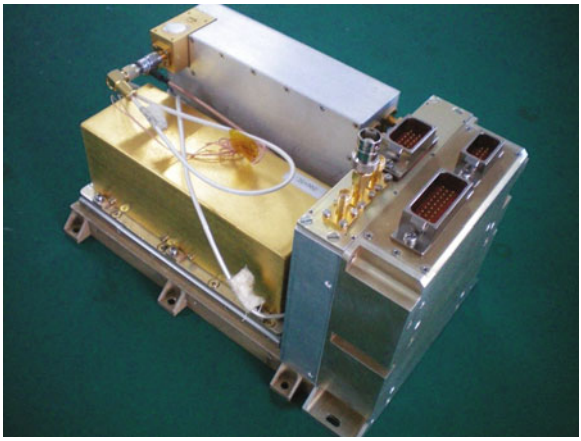

Fig. 35.4 Photograph of new rubidium clock inner structure

the thermal conductivity and properly setting temperature point, the temperature control system for the base plate can work smoothly within the whole temperature range determined by the satellite environment, and the temperature stability for the rubidium clock is satisfactory.

The secondary power supply and linear voltage-stabilizing part of the rubidium clock are installed in a single metal box. There is no temperature control for the box. This closed structure can prevent the internal RF signal from radiating to external space, improving electromagnetic compatibility of the clock.

The mass of the whole set is about 4.2 kg when the secondary power supply is added. Compared to our previous product, the mass is reduced remarkably.

35.3.3 Circuit Design

The RF chain omits the mixer. To convert the 12.6568287 MHz signal to a low-distortion modulated 6,834.6875 MHz microwave signal, a square wave frequency modulator, a 4× low-order frequency multiplier and a 135× high-order frequency multiplier are used. The low-order frequency multiplier employs a current switch frequency multiplier acting at the zero crossings to reduce AM-PM conversion effect. Meanwhile, an amplitude limiter with optimized parameters is employed to improve clutters so as to improve microwave spectrum purity. The high-order frequency multiplier still adopts the extra cavity SRD multiplication technique. Compared with the previous product, the temperature coefficient is reduced by one magnitude order due to redesign and optimization of the frequency multipliers.

The servo amplifier for the discriminator signal adopts substantially the old scheme, in which the discriminator signal is AC amplified by the operational amplifier, and passes through the synchronous detection, integration and phase correction network to obtain a voltage controlled signal for the 12.7 MHz crystal

oscillator. Different from the previous product, in order to reduce the risk of residual amplitude modulation and synchronous detector saturation, a high-Q notch filter is added before the synchronous detector to reduce the amplitude of the 2nd harmonic (256 Hz) of the discriminator signal. Because of the narrower absorption linewidth of the physics package, lock acquisition function is added in the circuit to prevent unlocking. A new synchronous detector is designed, in which the fundamental synchronous detection, lock detection and lock acquisition circuits share one analog switch chip.

In order to convert the 12.7 MHz signal into the 10 MHz signal, an analog PLL circuit integrated with a DDS is employed. By using the DDS the frequency accuracy of the whole set can be precisely adjusted with the controlled voltage of the 10 MHz crystal oscillator in the reasonable range, which means that there is no more requirement of frequency accuracy of atomic transition line for the physics package. There is an accelerated lock circuit in the PLL, realizing rapid lock and reducing the risk of unlocking and accidental off-locking.

In the secondary power supply (DC–DC) module integrated inside the rubidium clock, the power supply voltage +26 $\sim$ +45 V is converted into +20, $\pm$16 and +6 V for the first step, and the voltages are further converted into the required +19, $\pm$12, +5, +3.3 and +2.5 V by using the linear voltage regulator. The switch power supply module is a purchased component, the linear voltage-stabilized part is a specially designed one. No integrated voltage regulator is employed in the special design to guarantee low temperature coefficient, low noise and better stability.

35.3.4 Design of Temperature Control System

For the purpose to reduce the temperature coefficient and therefore to guarantee the long-term frequency stability of the clock, the base plate temperature control system is redesigned. In the new design, all the circuits and the physics package except for the power supply are under temperature control. The temperature stability of the power supply is guaranteed by special circuit design. The temperature point of the base plate is set to +40 $\sim$ +45 °C. The working parameters of the temperature control part are optimized.

Generally, the extra cavity SRD multiplier has a large temperature coefficient. In the previous deign, the SRD multiplier has a secondary temperature control to meet the requirement of low temperature coefficient. But the newly designed SRD multiplier is of low temperature sensitivity, so the secondary temperature control is removed.

The structure of base plate temperature control is similar to that of the previous product. Analog circuits are employed for temperature acquisition and control. The temperature control is realized by controlling heat exchange rate between the temperature controlled part and environment. Based on the our previous experience, measures as follows are taken: (1) To enhance further the temperature control gain, and (2) A nonmetallic plate, instead of metal parts as before, is used

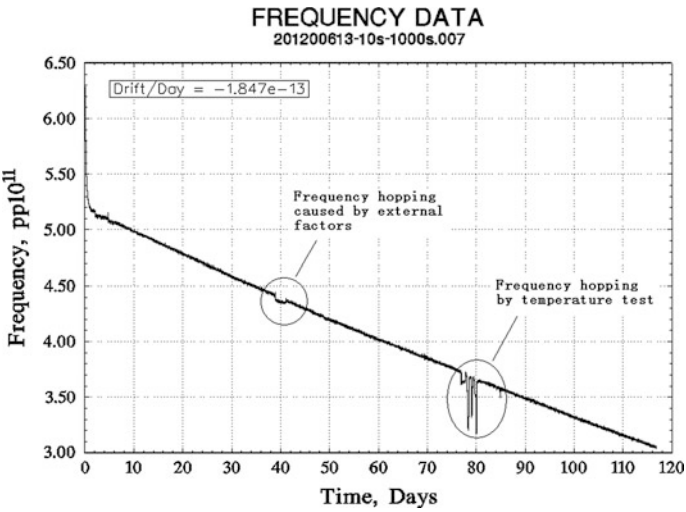

Fig. 35.5 New space-borne rubidium clock frequency plot

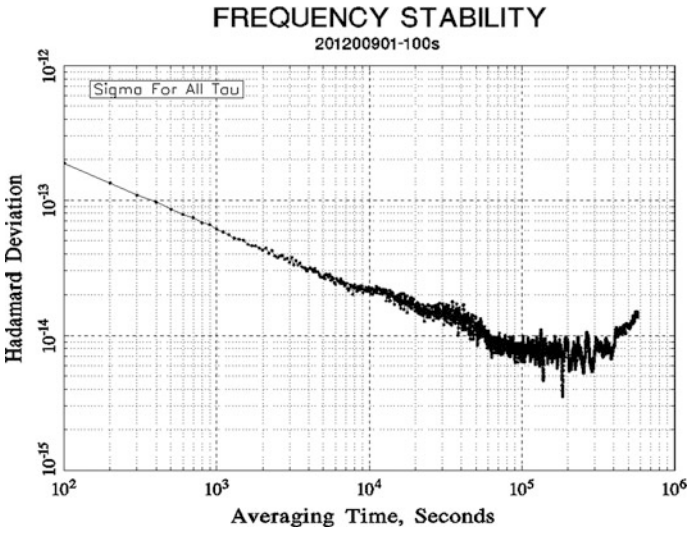

Fig. 35.6 New space-borne rubidium clock stability plot

as the heat conducting part, to make the temperature distribution more uniform. These measures avoid poor local temperature control in areas where the metal parts are located.

35.3.5 Frequency Stability Test Results

The principle prototype has been tested for about 4 months, its frequency curve is shown in Fig. 35.5. Except for two frequency hopping, one is caused by external factors and the other one by temperature test, the frequency curve is smooth and stable, but aging drift is still large, which is of -1.8×10^{-13}/d. The frequency stability is improved by a factor of about 5 compared with that of our previous product, as shown in Fig. 35.6. The frequency stability (Hadamard deviation) in $6 \times 10^4 \sim 4 \times 10^5$ s sampling time region of the prototype is in the 10^{-15} level.

The following work will focus on further reduction of aging. For this purpose rubidium gas cell produce process and circuit element aging parameters will be further optimized.

Chapter 36
Novel Scheme for Chip-Scale CPT Atomic Clock

Yi Zhang and Sihong Gu

Abstract In the presently prevailing CPT atomic clock the CPT state is prepared with either a pure left (or right) circularly polarized light, which pumps certain atoms into spin-polarized dark states thus degrading the quality of the CPT signal. The contrast (the CPT signal intensity divided by the background intensity) is normally only 4 % with this scheme. The paper presents our recently developed scheme in which laser beam is twice utilized by means of polarization reflection and the so obtained coaxial left and right circularly polarized lights simultaneously resonate with atoms, which eliminates spin-polarized dark state and stronger CPT resonance can be achieved with resonance interference enhancement. The contrast higher than 12 % of CPT signal has been obtained and the experimental result also reveals that the scheme especially suits for achieving atomic clock with good long-term behavior. Moreover, our scheme is suitable for integration, which makes it a promising candidate for both small-size and chip-scale CPT atomic clock.

Keywords Coherent population trapping · Atomic clock · Miniature · CSAC

36.1 Introduction

Coherent Population Trapping (CPT) phenomenon has been applied in atomic clocks, atomic magnetometers, quantum computing, and other areas. CPT atomic clock can be made of chip scale and is expected to be utilized in wide fields. In the

Y. Zhang · S. Gu (✉)
Key Laboratory of Atomic Frequency Standards, Wuhan Institute of Physics and Mathematics, Chinese Academy of Sciences, Wuhan 430071, People's Republic of China
e-mail: shgu@wipm.ac.cn

Y. Zhang
e-mail: zhangyi@wipm.ac.cn

J. Sun et al. (eds.), *China Satellite Navigation Conference (CSNC) 2013 Proceedings*, Lecture Notes in Electrical Engineering 245,
DOI: 10.1007/978-3-642-37407-4_36,

presently prevailing CPT atomic clock, CPT resonance is prepared with either a pure left (or right) circularly polarized light [1]. This scheme gives rise to the polarized dark state, which degrades the quality of the CPT signal. And the contrast (the CPT signal intensity divided by the background intensity) is normally only 4 % with the scheme [2]. For the purpose of improving the quality of CPT signal, new schemes, such as vertically linear polarization [3], parallel linear polarization [4], PUSH–PULL pumping [5], σ^{-}–σ^{+} light [6, 7], have been developed. All of those can eliminate polarized dark states and enhance the contrast of CPT signal. Among them, the σ^{-}–σ^{+} light scheme utilizes both left circularly polarized (σ^{-}) light and right circularly polarized (σ^{+}) light to resonate with atoms simultaneously, that makes constructive interference between the two CPT resonances generated by σ^{-} light and σ^{+} light and eliminates the polarized dark state thus more atoms participate in CPT resonance.

We have developed a Left-and-Right-Circularly-Polarized-Lasers (LRCPL) CPT state preparation scheme [7]. In LRCPL CPT scheme, a dichromatic light in σ^{-} form first interacts with atoms, then it is translated into a dichromatic σ^{+} light by a space delay and polarization rotation and reflection system and interacts with atoms again. As a result, CPT resonance interference enhancement can be achieved by properly adjusting the distance of space delay. Meanwhile, polarized dark state is eliminated by the interaction between σ^{-}, σ^{+} light and atoms. Here, we give the studied results of LRCPL CPT scheme.

36.2 Theories

Figure 36.1 shows a simplified four-levels system of ^{87}Rb associated in LRCPL CPT scheme. The $5P_{1/2}$, $F' = 2$, $m_F = -1$, 1 are excited state levels. The $5S_{1/2}$, $F = 2$, $m_F = 0$ and $5S_{1/2}$, $F = 1$, $m_F = 0$ are ground state levels. The four levels are respectively represented by |e1>, |e2>, |g1> and |g2> in the figure. Ei represents energy of |i>. The ω_1 and ω_2 are angular frequency of dichromatic pumping light. The k_1, k_2 are magnitude of wave vector of the corresponding light. The Rabi frequency corresponding to the four light components are respectively Ω_1^{+}, Ω_2^{+}, Ω_1^{-} and Ω_2^{-}. Here we assume σ^{+}, σ^{-} light is homologous. The wave front of σ^{-}, σ^{+}

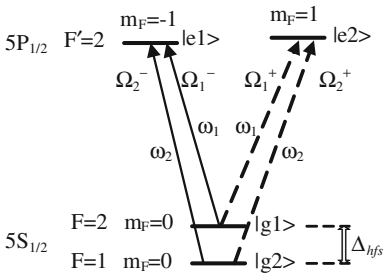

Fig. 36.1 Simplified interaction between dichromatic σ^{+}, σ^{-} light and 87Rb

light is z^-, z^+ in the light transmission direction. Ee1 could be regarded equally to Ee2 for the studied system. In the experiment, we set $\Omega_1^+ = -\Omega_2^+ = \Omega^+$, $\Omega_1^- = \Omega_2^- = \Omega^-$.

Define Light-atoms interaction Hamiltonian according to σ^+ and σ^- light as H_I^+ and H_I^-, then we get

$$H_I^+ = \frac{1}{2}\hbar\Omega^+ e^{-i\omega_1 t} e^{ik_1 z^+} |e2\rangle\langle g1| - \frac{1}{2}\hbar\Omega^+ e^{-i\omega_2 t} e^{ik_2 z^+} |e2\rangle\langle g2| + h.c.$$
$$H_I^- = \frac{1}{2}\hbar\Omega^- e^{-i\omega_1 t} e^{ik_1 z^-} |e1\rangle\langle g1| + \frac{1}{2}\hbar\Omega^- e^{-i\omega_2 t} e^{ik_2 z^-} |e1\rangle\langle g2| + h.c.$$

Assuming atoms are in dark state, which satisfies <e|H_I|dark state> = 0, then we obtain

$$|\text{dark state}^+\rangle = \Omega^+ e^{i\omega_1 t} e^{-ik_1 z^+} |g1\rangle - \Omega^+ e^{i\omega_2 t} e^{-ik_2 z^+} |g2\rangle$$
$$|\text{dark state}^-\rangle = \Omega^- e^{i\omega_1 t} e^{-ik_1 z^-} |g1\rangle + \Omega^- e^{i\omega_2 t} e^{-ik_2 z^-} |g2\rangle$$

Where $|\text{dark state}^- >$, $|\text{dark state}^+ >$ are CPT states prepared by σ^- and σ^+ light.

When dichromatic σ^-, σ^+ light interact with atoms at the same time, There would be quantum interference between $|\text{dark state}^- >$ and $|\text{dark state}^+ >$. The interference maximum is achieved while $|\text{dark state}^- > = |\text{dark state}^+ >$, to which we have

$$\frac{e^{-ik_2 z^+}}{e^{-ik_1 z^+}} = \frac{-e^{-ik_2 z^-}}{e^{-ik_1 z^-}} \Leftrightarrow e^{i(k_1 - k_2)(z^+ - z^-)} = -1$$
$$\Leftrightarrow z^+ - Z^- = (n - 1/2)\lambda_{00}, n = 1, 2, \mathrm{L}, \lambda_{00} = 2\pi\hbar c/(\mathrm{Eg1} - \mathrm{Eg2})$$

The above equation reveals that the interference maximum is achieved, that is to say, the two CPT resonance phases are equal, when the wave front difference between dichromatic σ^- and σ^+ light equals to half-integer times of microwave wavelength corresponding to hyperfine separation frequency of atomic ground state levels.

36.3 Experimental Setup

The experimental setup is as shown in Fig. 36.2. The vapor cell (length = 8 mm, diameter = 25 mm) is filled with ^{87}Rb atoms accompanied by a mixture buffer gas of N_2 and CH_4 at pressure of 28.2 Torr. The cell temperature is controlled at 75 °C to produce certain ^{87}Rb atomic vapor. Outside the cell, a solenoid produces a uniform magnetic field B, which is shielded from the environmental magnet by a permalloy shell. A Vertical Cavity Surface Emitting Laser (VCSEL) is used to provide about 794.7 nm-wavelength 100 MHz-bandwidth linearly polarized laser

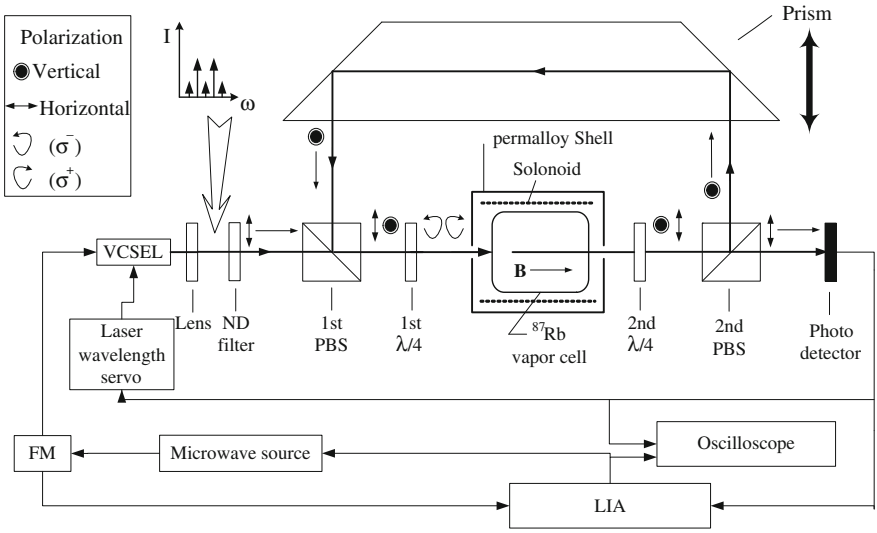

Fig. 36.2 Experimental setup for LRCPL scheme

beam. The VCSEL is frequency modulated by coupling a microwave signal at frequency of $\Delta_{hfs}/2 \approx 3.417$ GHz into the injection DC current. Therefore, the VCSEL outputs a frequency-modulated monochromatic light. In experiment, the $\pm$1st order sidebands of light serves as CPT-generation frequency, whose power meets the self maximum by tuning the microwave power.

The divergent laser beam emitted by the VCSEL is focused into a 1 mm diameter parallel one by a lens system. A ND filter is arranged to adjust light intensity. The first PBS (PBS1) selects out the horizontal linearly polarized component of the light, which is converted into σ^- light for interacting with ^{87}Rb in the vapor cell by the first $\lambda/4$ waveplate (1st $\lambda/4$). The polarization of transmitting part of the σ^- light is then translated into a vertical one by the second $\lambda/4$ waveplate (2nd $\lambda/4$). The vertically polarized light is then reflected by the second PBS (PBS2) and the prism in turn, and overlaps with the horizontal linearly polarized one at PBS1. The vertically polarized component of the overlapped light goes through 1st $\lambda/4$ and is transformed into σ^+ light to interact with ^{87}Rb atoms one more time. After the second interaction, the component is turned horizontal by means of the 2nd $\lambda/4$, which consequently passes through PBS2 and reaches the photo detector to be detected.

By twice applications of laser beam, simultaneous interaction of σ^- and σ^+ light with atoms is achieved in the scheme. In the experimental setup, the prism is fixed on a one-axis platform, so that the wave front difference between σ^- light and σ^+ light can be adjusted in certain range. With the experiment setup, if we rotate the 2nd $\lambda/4$ by 90°, the transmitting σ^- light after the first interaction can be converted into a horizontal one which will pass through PBS2 and be detected like that of the prevailing scheme. Thus, through rotation of the 2nd $\lambda/4$, it is allowed to

experimentally compare LRCPL with the prevailing scheme under the same experimental conditions.

In order to stabilize laser frequency, Doppler-broadened atoms-laser absorption spectrum is adopted to discriminate laser frequency in the scheme. Laser wavelength servo in Fig. 36.2 is arranged for processing discrimination signal, producing frequency correction signal and mixing it into injection DC current of VCSEL to realize negative feedback control. CPT resonance spectrum is adopted to discriminate microwave frequency. The microwave frequency stabilization loop includes a microwave source, a homemade frequency modulation (FM) module and a Lock-In Amplifier (LIA). The output of the microwave source is 500 Hz frequency modulated with the modulation depth of 80 Hz by the FM module. The LIA synchronously phase-sensitive demodulates the 500 Hz signal in the output of photo detector. The demodulation result, i.e., the differential signal of CPT resonance spectrum, serves as frequency correction signal to stabilize microwave frequency in CPT atomic clock. In the experiment, the oscilloscope in Fig. 36.2 simultaneously monitors and records photo detector output signal and differential signal of CPT resonance spectrum.

36.4 Experimental Process and Results

36.4.1 Contrast

We have experimentally observed periodical variation of CPT signal amplitude original from interference effect when changing wave front difference between σ^- and σ^+ light by adjusting platform in the marked direction in Fig. 36.2. Figure 36.3 shows a recorded maximum LRCPL CPT signal by fixing the platform at a proper position. The CPT signal in prevailing CPT scheme has also been

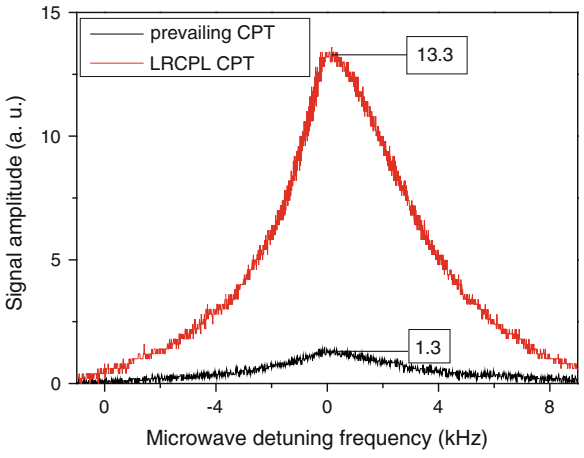

Fig. 36.3 Photo detector signal versus microwave detuning frequency for LRCPL CPT scheme and prevailing CPT scheme. The background light signal is removed

recorded by rotating the 2nd $\lambda/4$ by 90° under the same conditions. The CPT signal amplitude in prevailing CPT scheme is 1.3 while that in LRCPL CPT scheme is 13.3 with enhancement of more than 10 times. Signal contrast is one of key quantity to evaluate the performance of CPT atomic clock. We have studied the dependence of CPT signal contrast on light intensity in certain range for LRCPL CPT scheme. As it is shown in Fig. 36.4, for LRCPL CPT scheme the contrast increases linearly along with the increase of light intensity within 20 $\mu W/mm^2$, after that it increases slower and then appears saturate. However it is seen that the contrast increases along with light intensity in the whole experimental range of light intensity, which is much different from that for prevailing CPT scheme [1], where the contrast reaches the maximum value then decreases sharply.

Long-term light intensity aging is common for VCSELs. As a result, CPT signal contrast changes in prevailing CPT atomic clock, which degrades long-term working stabilization. However, for LRCPL CPT atomic clock, if light intensity more than 30 $\mu W/mm^2$ in Fig. 36.4 is chosen, more stable long-term performance can be developed thanks to the less dependence of contrast drift on light intensity aging.

36.4.2 Line Width

Signal line width is another key quantity related to performance of the atomic clock. The CPT signal line width increases linearly with light intensity for prevailing CPT atomic clock [1]. Figure 36.5 indicates the linear dependence of signal line width on light intensity for LRCPL CPT scheme in agreement with that of prevailing CPT scheme. That implies the two schemes have the same line width broadening mechanism related to light intensity.

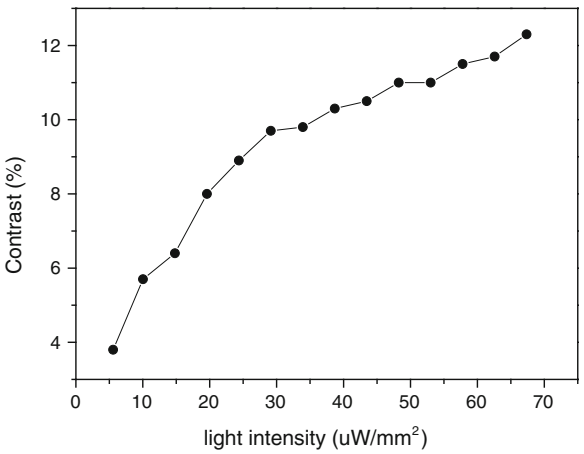

Fig. 36.4 CPT signal contrast versus light intensity for LRCPL CPT scheme

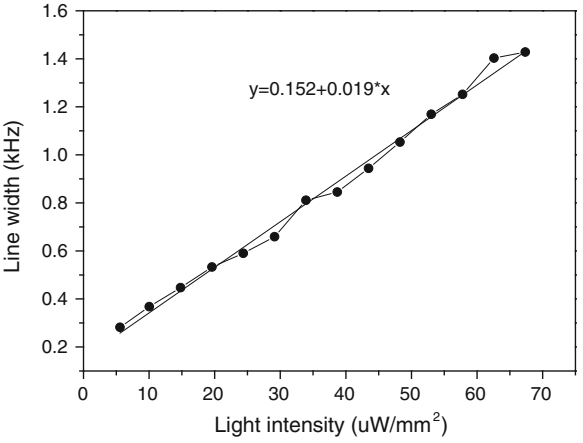

Fig. 36.5 CPT resonance line width as a function of light intensity

36.5 Miniaturization Prospect

Miniaturization is important for application of CPT atomic clock. In comparison to the prevailing scheme CPT atomic clock, the new scheme needs more optical components while the added components can all be miniaturized. For ^{87}Rb atoms in our experiment, the minimum reflection delay length is 22 mm, while for ^{133}Cs atoms maybe used in experiment, the minimum reflection delay length is 16 mm. Within the given size, it is not difficult to integrate the all components including the additional components, such as optical path accurately set mirror (or prism) [8] into a miniature physics package. Figure 36.6 illustrates our designed scheme of chip-scale physics package for CPT atomic clock [9]. CPT signal is generally weak in Chip-Scale Atomic Clock (CSAC), While it can be considerably improved by application of LRCPL CPT scheme. Moreover, the deterioration of CPT signal

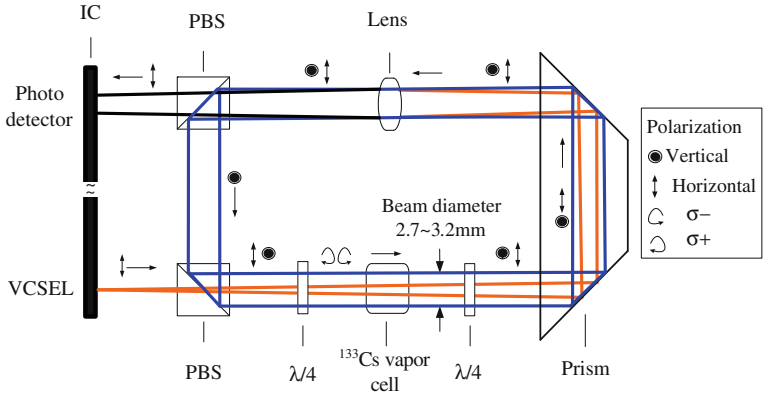

Fig. 36.6 A type of chip-scale physics package based on LRCPL CPT scheme

quality owing to laser polarization fluctuations [10] can be depressed and the less sensitive dependence of CPT signal contrast on laser intensity can be achieved, all of those make the LRCPL CPT scheme atomic clock a better performance one. Therefore, the LRCPL CPT atomic clock is a promise candidate for new generation CSAC.

36.6 Conclusions

In the presently prevailing CPT atomic clock the CPT state is prepared with either a pure left (or right) circularly polarized light. For the scheme, CPT signal contrast is normally limited in 4 %. We have developed and studied LRCPL CPT scheme, with which laser beam is twice utilized by means of polarization reflection and the so obtained simultaneous resonances of left and right circularly polarized lights with atoms. Therefore, spin-polarized dark states are eliminated and atoms are utilized more efficiently. A contrast of more than 12 % has been measured in the experiment. The dependence of CPT signal contrast on the VCSEL light intensity is monotonous, and near the saturation range the contrast is insensitive to light intensity in a wide range. When the working light intensity close to the saturation range is chosen, a more stable long-term performance can be developed in comparison to the prevailing scheme CPT atomic clock. LRCPL CPT atomic clock can also be micro-fabricated into chip scale, we have presented our designed LRCPL CSAC scheme.

References

1. Vanier J, Godone A, Levi F, Micalizio S (2003) Atomic clocks based on coherent population trapping: basic theoretical models and frequency stability. In: Frequency control symposium and PDA exhibition jointly with the 17th European frequency and time forum
2. Vanier J, Levine MW, Janssen D, Delaney M (2003) Contrast and linewidth of the coherent population trapping transmission hyperfine resonance line in 87Rb effect of optical pumping. Phys Rev A 67:065801
3. Zanon T, Guerandel S, de Clercq E, Holleville D, Dimarcq N, Clairon A (2005) High contrast ramsey fringes with coherent-population-trapping pulses in a double lambda atomic system. Phys Rev Lett 94:193002
4. Zibrov SA, Velichansky VL, Zibrov AS, Taichenachev AV, Yudin VI (2005) Experimental investigation of the dark pseudoresonance on the D1 line of the 87Rb atom excited by a linearly polarized field. JETP Lett 82(8):477–481
5. Jau Y-Y, Miron E, Post AB, Kuzma NN, Happer W (2004) Push–pull optical pumping of pure superposition states. Phys Rev Lett 93:160802
6. Kargapoltsev SV, Kitching J, Hollberg L, Taichenachev AV, Velichansky VL, Yudin VI (2004) High-contrast dark resonance in σ^+–σ^- optical field. Laser Phys Lett 1(10):495–499
7. Zhang Y, Qu S, Gu S (2012) Spin-polarized dark state free CPT state preparation with co-propagating left and right circularly polarized lasers. Opt Express 20(6):6400–6405

8. Knappe SA, Robinson HG, Hollberg L (2007) Microfabricated saturated absorption laser spectrometer. Opt Express 15(10):6293–6299
9. Chinese invention patent pending, Wuhan Institute of Physics and Math, China Academy of Sciences, Wuhan, China
10. Camparo J, Huang M, Coffer J (2007) Laser polarization noise & CPT atomic clock signals. In: Frequency control symposium 2007 joint with the 21st European frequency and time forum, IEEE International

Chapter 37
An On-Board Clock Integrity Monitoring Algorithm for Detecting Weak Anomaly Bias

Xinming Huang, Hang Gong, Wenke Yang, Xiangwei Zhu and Gang Ou

Abstract As a core part of satellite payload, on-board clock has a direct influence on GNSS service performance. Therefore, it is necessary to monitor its integrity. In this paper, real-time on-board clock phase residuals are obtained by sequential least squares estimation, and a novel sum test statistic based on residuals is constructed. An integrity monitoring algorithm for on-board clock based on this test statistic is proposed. Performance of the new algorithm is analyzed and verified by simulation. The results show that the new algorithm has a perfect performance of detecting weak on-board clock anomaly bias. The integrity monitoring algorithm for on-board clock proposed in this paper is helpful to GNSS on-board clock autonomous integrity monitoring.

Keywords On-board clock · Weak anomaly bias · Sum test statistic · Integrity monitoring

37.1 Introduction

As the frequency and time reference of space satellites, on-board clock has a direct influence on GNSS service performance. Therefore, it is necessary to monitor its integrity. Reference [1] for the first time proposes the idea of satellite autonomous on-board clock monitoring, and related algorithms are given, including the dynamic ADEV and moving average filtering. However, performances of these methods are analyzed unspecific. Reference [2] presents a frequency jump detector for space clocks, which can detect the satellite clock frequency jump, but it is not real-time. Clearly, an algorithm for on-board clock autonomous integrity monitoring is useful.

X. Huang (✉) · H. Gong · W. Yang · X. Zhu · G. Ou
Satellite Navigation R&D Center, National University of Defense Technology, Changsha 410073, China
e-mail: huangxinming_2007@163.com

J. Sun et al. (eds.), *China Satellite Navigation Conference (CSNC) 2013 Proceedings*, Lecture Notes in Electrical Engineering 245,
DOI: 10.1007/978-3-642-37407-4_37,

Reference [3] provides a useful method to detect phase and frequency anomaly using predicted errors. It is useful to detect obvious anomaly bias, but not very effective for weak anomaly, especially under gradual change.

In this paper, real-time on-board clock phase residuals are obtained by sequential least squares estimation, and a novel sum test statistic based on residuals is constructed. An integrity monitoring algorithm for on-board clock based on this statistic is proposed. Performance of the new algorithm is analyzed and verified by simulation. The results show that the new algorithm has a perfect performance of detecting weak on-board clock anomaly bias.

37.2 Statistic Characteristic Analysis of Sequential Least Square Estimation Residuals

It can be known that the on-board clock model can be expressed as a quadratic model [4], which is computed as following

$$x(t) = a_0 + a_1 \cdot t + a_2 \cdot t^2 + \varepsilon_x(t) \tag{37.1}$$

where a_0 is initial atomic clock phase deviation, a_1 is initial frequency deviation, a_2 is initial frequency drift of atomic clocks; $\varepsilon_x(t)$ is atomic clock phase noise. Equation (37.1) can be also expressed as following

$$X = HA + \varepsilon \tag{37.2}$$

where

$$H = \begin{bmatrix} h[0] \\ \vdots \\ h[n] \end{bmatrix} = \begin{bmatrix} 1 & t_1 - t_0 & (t_1 - t_0)^2 \\ \vdots & \vdots & \vdots \\ 1 & t_n - t_0 & (t_n - t_0)^2 \end{bmatrix}, A = \begin{bmatrix} a_0 \\ a_1 \\ a_2 \end{bmatrix}, X = \begin{bmatrix} x_1 \\ \vdots \\ x_n \end{bmatrix}, \varepsilon = \begin{bmatrix} \varepsilon_1 \\ \vdots \\ \varepsilon_n \end{bmatrix}.$$

In order to achieve real-time detection of phase anomaly, sequential least squares estimation method is adapted to estimate parameters of on-board clock, and estimation residuals are obtained by taking difference between the measured and estimated phase offsets, which will be used to construct weak anomaly detection test statistic.

Satellite clock parameters at time of t_n can be computed as following

$$\hat{A}[n] = \begin{bmatrix} \hat{a}_0[n] \\ \hat{a}_1[n] \\ \hat{a}_2[n] \end{bmatrix} = (H^T[n]C^{-1}[n]H[n])^{-1}H^T[n]X[n] \tag{37.3}$$

The measurement updates as following

$$\hat{A}[n] = \hat{A}[n-1] + K[n] \cdot (x[n] - h^T[n] \cdot \hat{A}[n-1]) \tag{37.4}$$

Where

$$K[n] = \frac{\Sigma[n-1] \cdot h[n]}{\sigma_n^2 + h[n] \cdot \Sigma[n-1] \cdot h[n]} \tag{37.5}$$

Covariance updates as

$$\Sigma[n] = (I - K[n] \cdot h^T[n]) \cdot \Sigma[n-1] \tag{37.6}$$

The one-step estimation residual is given as

$$z(n+1) = x_{n+1} - \hat{x}_{n+1} = x_{n+1} - h^T[n+1] \cdot \hat{A}[n+1] \tag{37.7}$$

We shall construct the new weak anomaly test statistic by discussing the Probability Density Function (PDF) of $z(n+1) = x_{n+1} - \hat{x}_{n+1}$.

Under normal circumstances, the on-board clock measurements acquired each time is independent and identically distributed. Statistical properties of RLS residuals remain same as phase residuals of satellite clock after removal of the trend term, which vary with sampling time interval. The statistical property of satellite clock random items is often denoted as Allan variance. The relationship between the sampling intervals τ and Allan variance is shown in Fig. 37.1.

As the sampling interval is generally 1 s for on board satellite clock measurement, random items of measurements mainly contain the phase modulation white noise and white measurement noise.

Statistic characteristic of measurement noise can be get from measurements, white phase noise can be obtained through the Allan variance, and specific compute method can refer to Ref. [5].

Therefore, it can be concluded that residuals of RLS follow a Gaussian distribution. Its mean and variance are computed as following

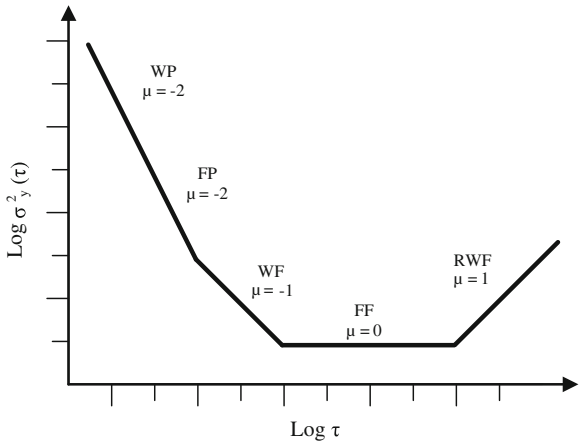

Fig. 37.1 Relationship between the sampling intervals τ and Allan variance

$$\begin{aligned} E(z) &= E(x_{n+1} - \hat{x}_{n+1}) \\ &= E((h^T[n+1]A + \varepsilon_{n+1} - h^T[n+1](H^TH)^{-1}H^T(HA+\varepsilon)) = 0 \end{aligned} \tag{37.8}$$

$$\begin{aligned} \mathrm{var}(z) &= E((x_{n+1} - \hat{x}_{n+1})(x_{n+1} - \hat{x}_{n+1})^T) \\ &= (1 + h^T[n+1](H^TH)^{-1}h^T[n+1]^T) \cdot \sigma^2 \end{aligned} \tag{37.9}$$

Therefore, $z \sim N(0, (1 + h^T[n+1](H^TH)^{-1}h[n+1])\sigma^2)$

With the recursive computation, statistic characteristic of residuals tend to be consistent with characteristic of satellite clock.

37.3 Integrity Monitoring Method for Weak Anomaly

In practical applications, the satellite clocks will appear minor deviation due to space radiation, temperature change and other factors. Such deviation is at the same level of satellite clock noise standard deviation or measurement noise standard deviation, and changes slowly, often in the drift. Such anomaly is collectively referred to weak anomaly in this paper.

In case of weak anomaly, the abnormal value is small, and often in the drift, which will lead to a larger satellite clock deviation after a period of time, directly affecting the positioning results. To this end, a new Integrity monitoring algorithm for weak anomaly is proposed, whose processing flow is shown below (Fig. 37.2).

Measurement residuals are acquired by sequential least squares estimation, which is used to update the data within the sliding window, guarantying sliding window containing the latest measurement information. New sum test statistic is constructed based on the residuals in the sliding window, which is used to anomaly detecting. With a given probability of false alarm, we can get detection threshold, if it fails, which decides detection performance.

37.3.1 New Test Statistic

In order to improve detection performance, residuals are accumulated. The new test statistic can be expressed as following

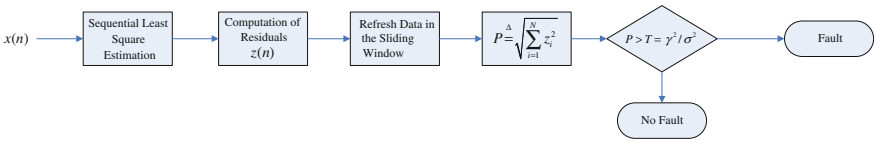

Fig. 37.2 Architecture of on-board clock integrity monitoring algorithm

$$P = \sqrt{\sum_{i=1}^{n} z_i^2} \tag{37.10}$$

It can be known from Sect. 37.1 that least square estimation residuals z follow a Gaussian distribution, so we can conclude that test statistic P follow a generalized Rayleigh distribution, which will be named as square root test statistic. Statistic P will follow a generalized Racine distribution when anomaly exists.

Assume length of sliding window is n, PDF of square root test statistic P can be expressed as following

$$p(x) = \begin{cases} \dfrac{x^{n-1}}{2^{(n-2)/2}\sigma^n \Gamma\left(\frac{1}{2}n\right)} e^{-\dfrac{x^2}{2\sigma^2}}, x > 0 \\ 0, x < 0 \end{cases} \tag{37.11}$$

When anomaly exists, PDF of square root test statistic P can be expressed as following

$$p(x) = \begin{cases} \dfrac{x^{n/2}}{s^{(n-2)/2}\sigma^2} e^{-\dfrac{x^2+s^2}{2\sigma^2}} I_{n/2-1}\left(\dfrac{rs}{\sigma^2}\right), x > 0 \\ 0, x < 0 \end{cases} \tag{37.12}$$

37.3.2 Detection Performance

In order to detect anomaly, we view the anomaly detection problem as an attempt to distinguish between the hypotheses

$$\begin{aligned} H_0 &: z(n) = w(n) \\ H_1 &: z(n) = l_n + w(n) \end{aligned} \tag{37.13}$$

Test statistics in the hypotheses can be expressed as following

$$\begin{aligned} H_0 &: p = \sqrt{\sum_{i=1}^{N} w^2(i)} \\ H_1 &: p = \sqrt{\sum_{i=1}^{N} (w(i) + l_i)^2} \end{aligned} \tag{37.14}$$

Square root test statistic P follows a generalized Rayleigh distribution under H_0, while follows a generalized Racine distribution under H_1.

Assume the probability of false alarm is P_f, and the probability of detection is P_d, the detection threshold can be confirmed by false alarm as following [6]

$$P_f = \int_{T(P_f)}^{\infty} \frac{x^{n-1}}{2^{(n-2)/2}\sigma^n \Gamma\left(\frac{1}{2}n\right)} e^{-\frac{x^2}{2\sigma^2}} dx \tag{37.15}$$

The probability of detection is given as

$$P_d = \int_{T(P_f)}^{\infty} \frac{x^{n/2}}{s^{(n-2)/2}\sigma^2} e^{-\frac{x^2+s^2}{2\sigma^2}} I_{n/2-1}\left(\frac{rs}{\sigma^2}\right) dx \tag{37.16}$$

Where $s^2 = \sum_{i=1}^{N} l_i^2$

Detection performance is only related to parameter s for a given probability of false alarm. In order to improve the detection performance, an effective way is to increase Value of parameter s.

Performance of sum test statistic can be obtained for a given probability of false alarm detection according to formula (37.15) and (37.16).

Square root test statistic proposed is constructed by sliding accumulation of the residuals within the entire sliding window, and detection performance varies with accumulation number of anomaly measurement at each moment. Detection performance of the sum statistic increases gradually with the accumulation of residuals within the sliding window.

Square root test statistic P follows a generalized Rayleigh distribution under normal circumstance, while it follows a generalized Racine distribution when there have anomaly measurements in the sliding window. The detection performance is decided by parameter s^2, which is sum of abnormal bias. If there is only one abnormal measurement, then s^2 is equal to l^2. And the detection performance of the test statistic of current time can be confirmed when the probability of false alarm is constant. If there are two abnormal measurements, then s^2 is equal to $l_1^2 + l_2^2$. It is obvious that parameter s^2 increase gradually with the accumulation of abnormal measurements. Therefore, the detection performance has been improved with the accumulation of abnormal measurements. Weak anomaly will be detected by selecting the appropriate window length.

37.4 Algorithm Verification

The detection performance of the new method is derived in the previous section. Detection probability of the CFAR conditions under weak anomaly can be expressed as formula (37.16). Conclusions of previous section are further analyzed and validated by simulation means as following.

Assume the measurement time interval is taken for 1 s, observation noise standard deviation is taken as 0.1 ns, and second stability of satellite clock is about 10^{-12}, so sequential least squares estimation residuals of the standard deviation

can be regarded as 0.1 ns. Therefore, standard deviation of the residuals can be taken as 0.1 ns; probability of the false alarm is 10^{-6}.

In order to verify the correctness of the fault detection probability in the statistics, and analyze the relationship between the probability of detection and the abnormal deviation in conditions of CFAR, numerical and Mont-Carlo simulation are verified. Numerical calculation results of fault detection probability according to formula (37.16) are compared with simulation results of repeat 10,000 Mont-Carlo (MC) simulations, the results are shown below.

The number of accumulated residuals is 10 for prescribing square root test statistic within a sliding window, while the number of accumulated abnormal residuals is also 10 (Fig. 37.3).

It can be seen from simulation results that Mont-Carlo (MC) simulation results are highly consistent with results of the calculation formula, which illustrates the correctness of the calculation formula of detection probability. It is also obvious that detection performance of new test statistic is better than that of one-step test statistic.

As we can see that detection performance of prescribing square root test statistic is related the number of observed accumulated residuals, as well as that of accumulated abnormal residuals within the sliding window. Simulation is adopted in order to analyze detection performance of square root test statistic under conditions of different observation residuals and accumulated abnormal residuals within the sliding window. The results are shown in Figs. 37.4 and 37.5.

Simulation results of Fig. 37.4 shows the relationship between detection performance of square root test statistic and accumulated abnormal residuals within

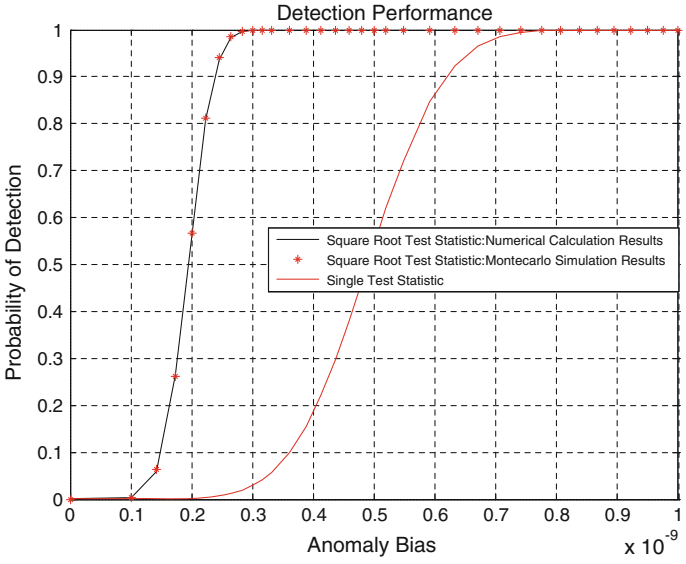

Fig. 37.3 Simulation results of detection performance

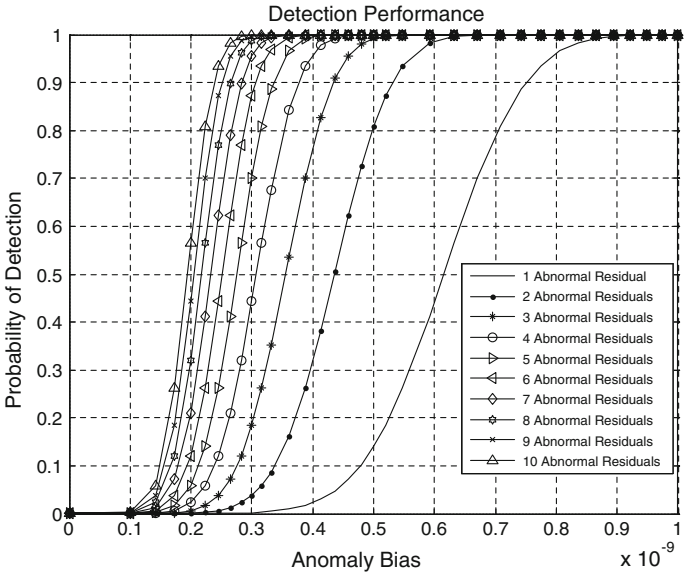

Fig. 37.4 Relationship between detection performance of square root test statistic and accumulated abnormal residuals within the sliding window under conditions of fix observation residuals

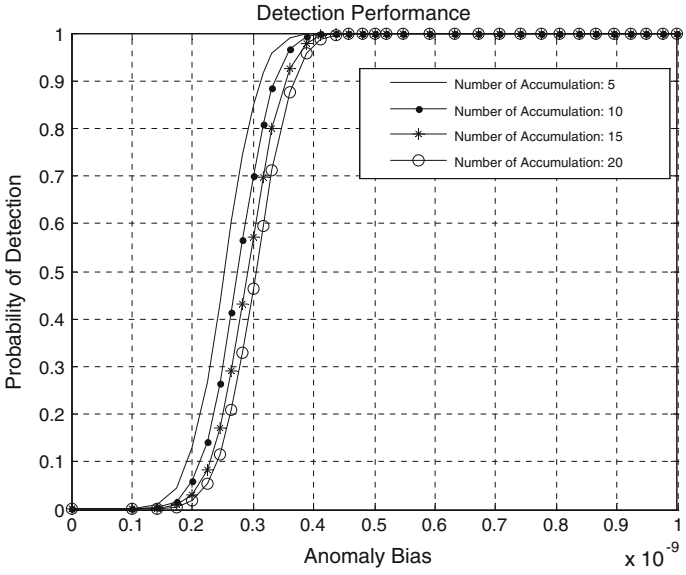

Fig. 37.5 Relationship between detection performance of square root test statistic and observation residuals under conditions of accumulated abnormal residuals within the sliding window

the sliding window under conditions of fix observation residuals. Length of the sliding window is taken as 10 sampling intervals. It can be seen that detection performance improves gradually with accumulation of the abnormal residuals in the window, but it also means that the detection delay is bigger. Assume that the number of accumulated residuals is 10 in order to meet the detection performance, and then detection lag delay is 10 sampling intervals. Therefore, the maximum lag delay that can be tolerated and the detection performance that need to meet should be comprehensively considered to select the length of the sliding window.

Simulation results of Fig. 37.5 shows the relationship between detection performance of square root test statistic and observation residuals under conditions of accumulated abnormal residuals within the sliding window. The maximum lag delay that can be tolerated is fixed as 5 sampling intervals. Length of the sliding window is taken as 5 sampling intervals, 10 sampling intervals, 15 sampling intervals, and 20 sampling intervals respectively. It can be seen that detection performance fades gradually with growth of length of the sliding window when length of the sliding window exceeds the maximum lag delay that can be tolerated. Therefore, the length of the sliding window should not the maximum lag delay that can be tolerated and the detection performance that needs to meet should be comprehensively considered to select the length of the sliding window.

37.5 Conclusion

In this paper, real-time on-board clock phase residuals are obtained by sequential least squares estimation, and a novel sum test statistic based on residuals is constructed. An integrity monitoring algorithm for on-board clock based on this test statistic is proposed. Performance of the new algorithm is analyzed and verified by simulation. The results show that the new algorithm has a perfect performance of detecting weak on-board clock anomaly bias. The integrity monitoring algorithm for on-board clock proposed in this paper is helpful to GNSS satellite clock autonomous integrity monitoring.

References

1. Rodríguez I, García C, Catalán C, et al. (2009) Satellite autonomous integrity monitoring (SAIM) for GNSS systems. In: ION GNSS 2009, Sept 2009
2. Galleani L, Tavella P (2010) An algorithm for the detection of frequency jumps in space clocks. In: Proceedings of the 42th annual precise time and time interval (PTTI) applications and planning meeting 2010
3. Huang X, Gong H, Yanf W, Zhu X, Ou G (2012) An integrity monitoring algorithm for satellite clock based on test statistics. In: Proceedings of the 3th China satellite navigation conference 2012

4. Guo H (2006) Study on the analysis theories and algorithms of the time and frequency characterization for atomic clocks of navigation satellites. Information Engineering University 2006
5. Allan DW (1987) Time and frequency (time-domain) characterization, estimation and prediction of precision clocks and oscillators. IEEE Trans Ultrason Ferroelectrics Freq Control (UFFC) 34(6):647–654
6. Liu W, Li Z, Wang F (2010) A New RAIM method for detecting and correcting weak pseudo-range bias under gradual change. J Astronaut 31(4):1024–1029

Chapter 38
Non-Reciprocity Correction Using Broadcast Ephemeris in Two-Way Satellite Time and Frequency Transfer (TWSTFT)

Wenke Yang, Hang Gong, Xiangwei Zhu and Guangfu Sun

Abstract Two-way satellite time and frequency transfer (TWSTFT) is applied in BeiDou Navigation Satellite System for time synchronization of the ground stations. In fact, the geostationary (GEO) satellites have periodic motions around their planned orbits instead of being stationary to the ground stations, which results in periodic fluctuations of Sagnac correction and signal path geometry correction in TWSTFT. Precise TWSTFT is relaying on the non-reciprocity corrections. An analysis method with broadcast ephemeris of GEO satellite for Sagnac correction and signal path geometry correction is introduced in this paper. With this method, TWSTFT experiment result using BeiDou GEO satellite at 140°E of three links between Beijing and three different sites is analyzed and the periodic fluctuation of Sagnac correction and signal path geometry correction are presented in detail. The fluctuation range of Sagnac correction is from 0.04 to 0.16 ns and that of signal path geometry correction is from 0.01 to 0.53 ns for the three links, which shows that Sagnac correction and signal path geometry correction can not be ignored in time transfer requiring sub-nanosecond precision generally for the three links.

Keywords TWSTFT · Non-reciprocity corrections · Sagnac correction · Signal path geometry correction · Broadcast ephemeris

38.1 Introduction

TWSTFT is applied in BeiDou Navigation Satellite System for time synchronization of the ground stations [1]. Precise TWSTFT is relaying on the non-reciprocity corrections, where the signal delay difference in the transmitter and

W. Yang (✉) · H. Gong · X. Zhu · G. Sun
School of Electronic Science and Engineering, National University of Defense Technology, Changsha, Hunan 410073, China
e-mail: ywk@nudt.edu.cn

J. Sun et al. (eds.), *China Satellite Navigation Conference (CSNC) 2013 Proceedings*, Lecture Notes in Electrical Engineering 245,
DOI: 10.1007/978-3-642-37407-4_38,

receiver of ground stations, the path difference of the geostationary (GEO) satellite transponder in both directions can be calibrated [2, 3], the troposphere correction can be ignored with the error of less than 10 ps and the ionosphere correction can be obtained with the total electron content (TEC) along the signal path [2]. The Sagnac correction considering the motion of GEO satellite have been analysed in [4] with the satellite relative velocity and in [5, 6] with orbit data of GEO satellite. But it is not introduced in detail on the exact use of orbit data of GEO satellite in the literatures. For the signal path geometry correction, there are literatures on the analysis with the satellite relative velocity [7], but it is lack of detail description on the calculation process. In this paper, we will introduce an analysis method with broadcast ephemeris for Sagnac correction and signal path geometry correction in detail.

38.2 Non-Reciprocity Corrections of TWSTFT

As demonstrated in Fig. 38.1, TWSTFT is working as below: each ground station transmits a radio frequency signal modulated by pseudorandom noise (PRN) codes at the beginning of every second according to its own clock to GEO satellite through one transmitter, which is called upward link. The transmitted signal is retransmitted by GEO satellite using another radio frequency back to the earth, which is called downward link. Each ground station receives the transmitted signals from the other station (downward real line in Fig. 38.1) and its own (for round-trip ranging, downward dashed line in Fig. 38.1). At both sites, the received PRN code is correlated with the shifted local reproduced PRN and the one-way measurement is given by the shifted phase of the local reproduced PRN referring to the local clock when the correlation is above the threshold designed by the receiver. Since the distances of the satellite from the two sites are different, the signal transmitted by the two sites at the same time will reach the satellite at different time [8], as is also demonstrated in Fig. 38.1.

The clock difference of station 1 relative to station 2, described as $T_1 - T_2$, is determined as follows.

The one-way measurement PR_{21} at station 1 is,

$$T_1 - T_2 + \tau_{T2} + \tau_{U2}|_{Sat} + \tau_{U2}|_{Ion} + \tau_{U2}|_{Trop} + \tau_{SCU2} + \tau_{S21} + \tau_{D1}|_{Sat} + \tau_{D1}|_{Ion} + \tau_{D1}|_{Trop} + \tau_{SCD1} + \tau_{R1} = PR_{21} \tag{38.1}$$

and the one-way measurement PR_{12} at station 2 is,

$$T_2 - T_1 + \tau_{T1} + \tau_{U1}|_{Sat} + \tau_{U1}|_{Ion} + \tau_{U1}|_{Trop} + \tau_{SCU1} + \tau_{S12} + \tau_{D2}|_{Sat} + \tau_{D2}|_{Ion} + \tau_{D2}|_{Trop} + \tau_{SCD2} + \tau_{R2} = PR_{12} \tag{38.2}$$

Thus, the clock difference measured of site 1 and site 2 can be obtained as

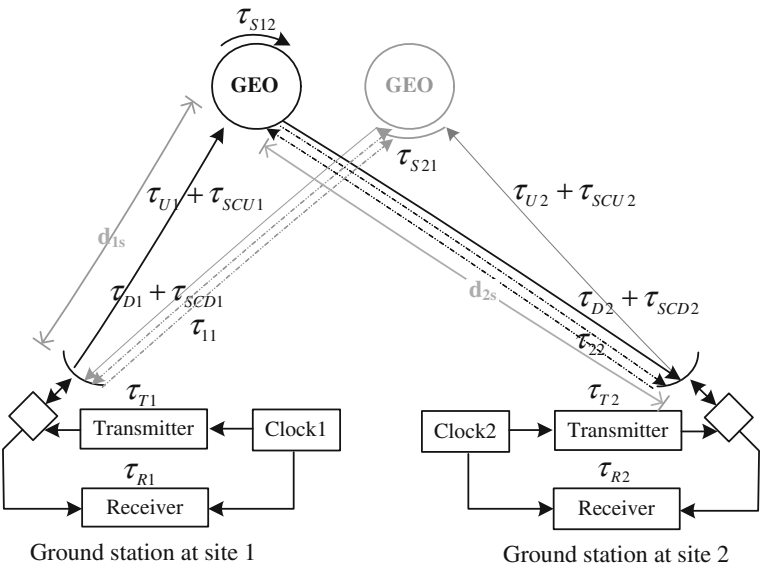

Fig. 38.1 Two-way time and frequency transfer system

$$\begin{aligned} T_1 - T_2 = {} & 0.5(PR_{21} - PR_{12}) \\ & + 0.5((\tau_{T1} - \tau_{R1}) - (\tau_{T2} - \tau_{R2})) \\ & + 0.5(\tau_{S12} - \tau_{S21}) \\ & + 0.5((\tau_{U1} - \tau_{D1})|_{Ion} - (\tau_{U2} - \tau_{D2})|_{Ion}) \\ & + 0.5((\tau_{U1} - \tau_{D1})|_{Trop} - (\tau_{U2} - \tau_{D2})|_{Trop}) \\ & + 0.5((\tau_{SCU1} - \tau_{SCD1}) - (\tau_{SCU2} - \tau_{SCD2})) \\ & + 0.5((\tau_{U1} - \tau_{D1})|_{Sat} - (\tau_{U2} - \tau_{D2})|_{Sat}) \end{aligned} \tag{38.3}$$

The symbols despite of $T_1 - T_2$, PR_{21} and PR_{12} in Eqs. 38.1 and 38.2, and the symbols in Fig. 38.1 are listed in Table 38.1.

In Eq. 38.3, $0.5((\tau_{T1} - \tau_{R1})\text{-}(\tau_{T2} - \tau_{R2}))$ is half of difference of the difference of the transmit and receive delay of both stations, and $0.5(\tau_{S12} - \tau_{S21})$ is half of difference of the satellite transfer delay in both directions, both of which can be obtained by calibration [2, 3]. And $0.5((\tau_{U1} - \tau_{D1})\ |_{Ion} - (\tau_{U2} - \tau_{D2})\ |_{Ion})$ is ionosphere correction, which can be obtained with the total electron content (TEC) along the signal path [2]. And $0.5((\tau_{U1} - \tau_{D1})\ |_{Trop} - (\tau_{U2} - \tau_{D2})\ |_{Trop})$ is troposphere correction and can be ignored with the error of less than 10 ps [2]. The above four terms are out of the scope of this paper.

In addition, $0.5((\tau_{SCU1} - \tau_{SCD1}) - (\tau_{SCU2} - \tau_{SCD2}))$ is Sagnac correction and represented as

$$\tau_{SC} = 0.5((\tau_{SCU1} - \tau_{SCD1}) - (\tau_{SCU2} - \tau_{SCD2})) \tag{38.4}$$

Table 38.1 The symbol list

Symbol	Explainations
τ_{Ti}	Signal delay in the transmit path of the ground station i
$\tau_{Ui}\|_{Sat}$	Signal delay caused by geometry path from ground station i upward to GEO satellite
$\tau_{Ui}\|_{Ion}$	Signal delay caused by ionosphere from ground station i upward to GEO satellite
$\tau_{Ui}\|_{Trop}$	Signal delay caused by troposphere from ground station i upward to GEO satellite
τ_{SCUi}	Sagnac correction of the signal path from ground station i upward to GEO satellite
τ_{Sij}	Signal delay in satellite transfer path with the direction from ground station i to ground station j
$\tau_{Di}\|_{Sat}$	Signal delay caused by geometry path from GEO satellite downward to ground station i
$\tau_{Di}\|_{Ion}$	Signal delay caused by ionosphere from GEO satellite downward to ground station i
$\tau_{Di}\|_{Trop}$	Signal delay caused by troposphere from GEO satellite downward to ground station i
τ_{SCDi}	Sagnac correction of the signal path from GEO satellite downward to ground station i
τ_{Ri}	Signal delay in the receive path of the ground station i
d_{is}	Distance between ground station i and GEO satellite
τ_{Ui}	$\tau_{Ui}\|_{Sat} + \tau_{Ui}\|_{Ion} + \tau_{Ui}\|_{Trop}$
τ_{Di}	$\tau_{Di}\|_{Sat} + \tau_{Di}\|_{Ion} + \tau_{Di}\|_{Trop}$

And $0.5((\tau_{U1} - \tau_{D1})\,|_{Sat} - (\tau_{U2} - \tau_{D2})\,|_{Sat})$ is the signal path geometry correction and represented as

$$\tau_{UD,Sat} = 0.5((\tau_{U1} - \tau_{D1})|_{Sat} - (\tau_{U2} - \tau_{D2})|_{Sat}) \tag{38.5}$$

We will focus on the last two non-reciprocity terms in the following sections.

38.3 Sagnac Correction

Sagnac correction for upward (downward) signal path is the difference of the signal paths from the ground station (GEO satellite) to the GEO satellite (ground station) with the consideration of the earth rotation and without, which are illustrated in Figs. 38.2 and 38.3 for the Sagnac effect of the upward signal and the downward signal respectively.

In Fig. 38.2, when the signal is transmitted from the ground station at location A, the GEO satellite is located at S. For the rotation of the GEO satellite along with the earth, the GEO satellite receives the signal at location S'. The Sagnac correction of the upward signal path is as $\tau_{SCU} = AS' - AS$. In Fig. 38.3, the GEO satellite transmits the signal at location S, and at the same time, the ground station is at location A. When the ground station receives the signal, it rotates with the earth to the location A'. The Sagnac correction of the downward signal path is $\tau_{SCD} = SA' - SA$.

The equations for the Sagnac correction of the upward signal path is [9, 10]

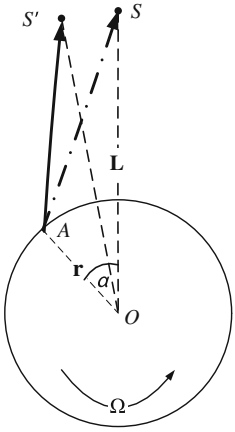

Fig. 38.2 Sagnac effect of the upward signal path

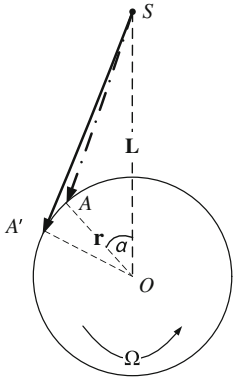

Fig. 38.3 Sagnac effect of the downward signal path

$$\begin{aligned}\tau_{SCU} &= -\Omega/c^2 \cdot \frac{1}{2} rL \sin\alpha \\ &= -\Omega/c^2 (r + ALT(s))(r + ALT(k)) \cos(LA(s)) \cos(LA(k)) \sin((LO(k) - LO(s))\end{aligned} \tag{38.6}$$

And the one for the downward signal path is [9, 10]

$$\begin{aligned}\tau_{SCD} &= \Omega/c^2 \cdot \frac{1}{2} rL \sin\alpha \\ &= \Omega/c^2 (r + ALT(s))(r + ALT(k)) \cos(LA(s)) \cos(LA(k)) \sin((LO(k) - LO(s))\end{aligned} \tag{38.7}$$

Where Ω is earth rotation rate, c is the speed of light, r is earth radius, L is Distance from the earth mass centre to the mapped point of GEO satellite on the Earth's equatorial plane, α is the difference of the longitude of the ground station and the GEO satellite, $ALT\ (s)$ and $ALT\ (k)$ are the altitude of GEO satellite and

ground station k respectively, $LA(s)$ and $LA(k)$ are the latitude of the track of sub-satellite points of GEO satellite and ground station k respectively, $LO(s)$ and $LO(k)$ are the longitude of the track of sub-satellite points of GEO satellite and ground station k respectively.

When considering the motion of GEO satellite, the broadcast ephemeris is interpolated to the proper epochs to calculate the GEO satellite locations to obtain the Sagnac correction for the upward signal path and the downward signal path respectively. According to Eq. (38.6), the Sagnac correction of the upward signal path τ_{SCU} is decided by the GEO satellite's location at the epoch when it receives the signal from the ground station. While according to Eq. (38.7), Sagnac correction of the downward signal path τ_{SCD} should be calculated by the GEO satellite's location at the epoch when it retransmits signal back to the ground station.

38.4 Signal Path Geometry Correction

To take the one way signal path from ground station 1 to GEO to station 2 as an example, we demonstrate a method to estimate the up and down signal path distance respectively.

Thanks to the round-trip ranging link from the ground station to the satellite and back working simultaneously with the TWSTFT, the one way ranging delay can be estimated as the half of the round-trip delay measured by the ranging link, as τ_{11} for ground station 1 and τ_{22} for ground station 2 in Fig. 38.1.

The epoch of the arrival of the transmitted signal from station 1 referring to the local clock at station 2 is known as t_{12}, and the round-trip delay measured at station 2 at the same epoch as τ_{22}. Supposing that the stations has no clock bias referring to the navigation system time, the epoch of the signal transmitted by ground station 1 arriving at the satellite can be obtained as

$$t_{1,Sat} = t_{12} - \frac{1}{2}\tau_{22} \tag{38.8}$$

Then, the location of the satellite $\vec{S}_{1,Sat}$ at the epoch of signal retransmitting can be calculated from the broadcast ephemeris by interpolation. If we define that the locations of ground station 1 and ground station 2 are $\vec{A}_1$ and $\vec{A}_2$ respectively, then the signal path geometry distance (expressed as the signal transfer time with the speed of light) from ground station 1 to GEO satellite of the uplink is as below.

$$\tau_{U1}|_{\mathrm{Sat}} = |\vec{S}_{1,Sat} - \vec{A}_1|/c \tag{38.9}$$

The signal path geometry distance (expressed as the signal transfer time with the speed of light) from GEO satellite to ground station 2 of the downlink is as below.

$$\tau_{D2}|_{\mathrm{Sat}} = |\vec{S}_{1,Sat} - \vec{A}_2|/c \tag{38.10}$$

Similarly, $\tau_{U2}|_{\mathrm{Sat}}$ and $\tau_{D1}|_{\mathrm{Sat}}$ can be obtained. Then, $\tau_{UD}|_{\mathrm{Sat}}$ can be obtained from Eq. (38.5).

38.5 Experiment Results

TWSTFT with BeiDou GEO satellite at 140°E experiments have been conducted among stations at Beijing and other three sites. These three sites are at the southwest, south and west of China respectively, which are named as 'SWest', 'South' and 'West' accordingly afterwards. The measurement data for two days of the three links between Beijing and SWest, Beijing and South, Beijing and West simultaneously collected in 2012 with sampling interval of 1 s without averaging are analyzed in this section.

The motion of the GEO satellite is shown in Fig. 38.4 with the altitude subtracted by 35,784.504 km for the sake of clarity, and the latitude and longitude of the track of the sub-satellite points of the GEO satellite obtained from the broadcast ephemeris are shown in Figs. 38.5 and 38.6 respectively. All of them show periodic fluctuations of 24 h around the nominal value. And the track of the sub-satellite points of the GEO satellite is shown in Fig. 38.7, which shows an '8' style with a big head.

The Sagnac correction and signal path geometry correction for the three links are shown in Figs. 38.8 and 38.9 respectively. In addition, the distance difference between d_{1s} and $d_{2s,}$ which is shown in Fig. 38.1 with Beijing set as site 1 and SWest, South and West set as site 2 for links of Beijing-SWest, Beijing-South and Beijing-West respectively, are demonstrated in Fig. 38.10.

The period and the amplitude of the motion of GEO satellite is listed in Table 38.2.

The period and amplitude of the non-reciprocity corrections are listed in Table 38.3. The mean values of $|d_{1s} - d_{2s}|$ are listed in Table 38.4.

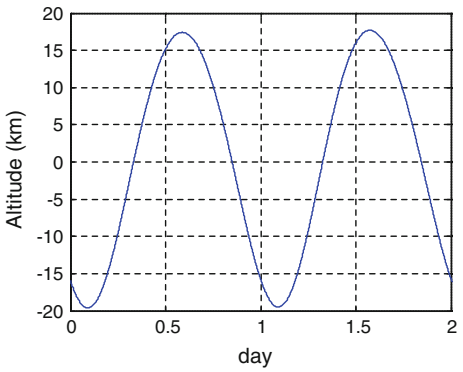

Fig. 38.4 The altitude of GEO satellite obtained from the broadcast ephemeris (with an offset of 35,784.504 km)

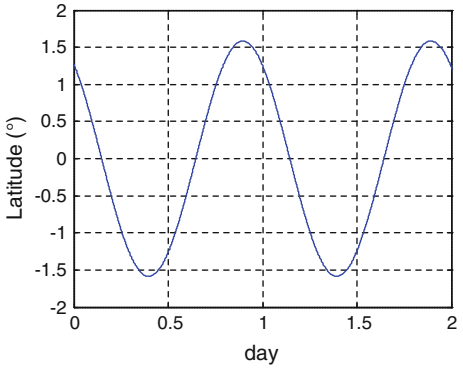

Fig. 38.5 The latitude of the track of the sub-satellite points of the GEO satellite obtained from the broadcast ephemeris

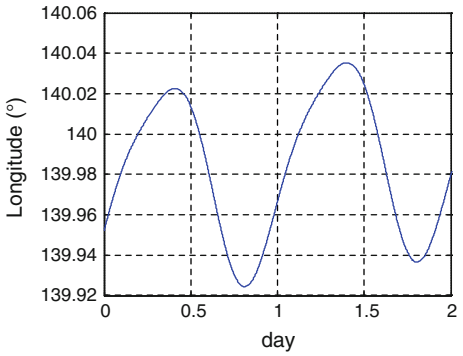

Fig. 38.6 The longitude of the track of the sub-satellite points of the GEO satellite obtained from the broadcast ephemeris

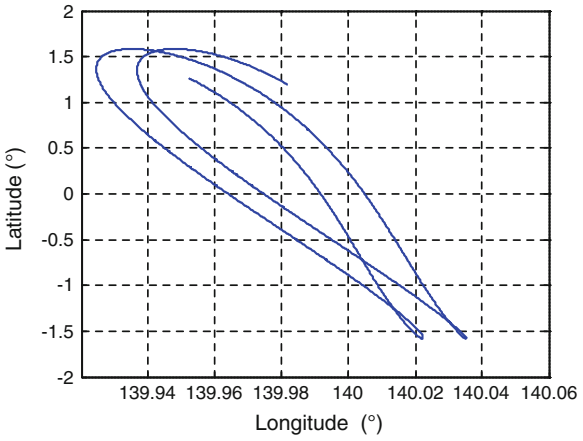

Fig. 38.7 The track of the sub-satellite points of the GEO satellite obtained from the broadcast ephemeris

From Table 38.3 it can be seen that the fluctuation amplitude of Sagnac correction is from 0.04 to 0.16 ns for the three links, and signal path geometry correction is from 0.01 to 0.53 ns for the three links. For time transfer with subnanosecond precision, both of non-reciprocity corrections can not be ignored as to

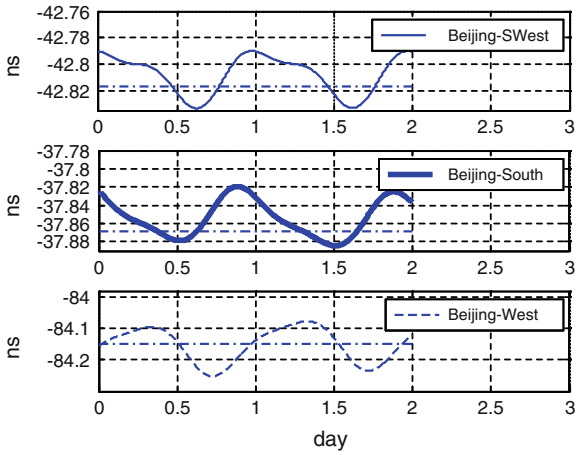

Fig. 38.8 The sagnac correction considering the motion GEO satellite against to the sagnac correction as GEO satellite at the planned location as a straight dash-dot line for each link

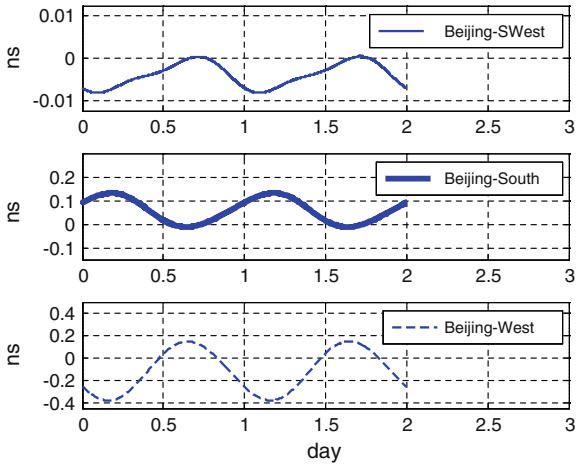

Fig. 38.9 The signal path geometry correction for links of Beijing-SWest, Beijing-South and Beijing-West

the three links, except signal path geometry correction of Beijing-SWest link. Especially for Beijing-West link, the fluctuation amplitude of signal path geometry correction is larger than 0.5 ns. And it can be seen from Table 38.4 that Beijing-West link has worse geometry non- reciprocity for the two ground stations respect to the GEO satellite than the other two links, which is possibly the reason for the large signal path geometry correction.

In addition, Sagnac correction and signal path geometry correction of the three links have the same fluctuation period as that of the GEO satellite motion.

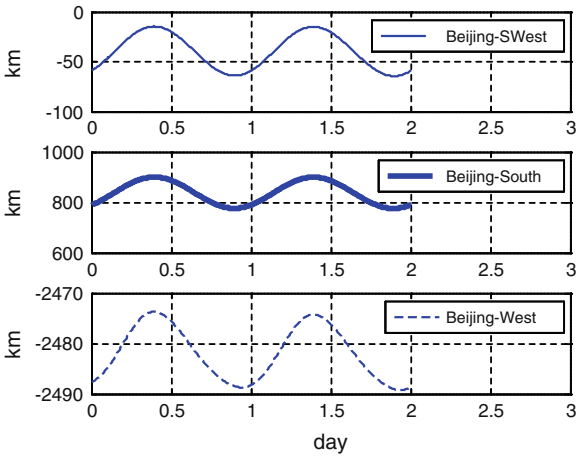

Fig. 38.10 The distance difference $d_{1s} - d_{2s}$ for links of Beijing-SWest, Beijing-South and Beijing-West

Table 38.2 The period and amplitude of GEO satellite motion

Symbol	Period (h)	Amplitude
ALT	24	37.11 km
LA	24	3.18°
LO	24	0.09°

Table 38.3 The period and amplitude of the non-reciprocity corrections

Symbol	Period (h)	Links	Amplitude (ns)
τ_{SC}	24	Beijing-SWest	0.04
	24	Beijing-South	0.06
	24	Beijing-West	0.16
$\tau_{UD,Sat}$	24	Beijing-SWest	0.01
	24	Beijing-South	0.14
	24	Beijing-West	0.53

Table 38.4 The mean value of $|d_{1s} - d_{2s}|$

Symbol	Links	Mean value (km)
$\lvert d_{1s} - d_{2s} \rvert$	Beijing-SWest	39.53
	Beijing-South	838.01
	Beijing-West	2481.84

38.6 Conclusions

In this paper, we have introduced an analysis method of non-reciprocity correction for TWSTFT concerning Sagnac correction, the signal path geometry correction considering the GEO satellite motion with broadcast ephemeris. For Sagnac correction considering GEO satellite motion, it is pointed out that the Sagnac correction of the upward signal path is decided by the GEO satellite's location at the

epoch when the ground station transmits signal, while the Sagnac correction of the downward signal path should be calculated by the GEO satellite's location at the epoch when it retransmits signal back to the ground station. For signal path geometry correction, the analysis method introduced in this paper is easy to apply.

With this method, TWSTFT experiment result using BeiDou GEO satellite at 140°E of three links between Beijing and other three sites, which distribute from southwest to south and west of China, is analyzed and the periodic fluctuation of Sagnac correction and signal path geometry correction are presented in detail. Sagnac correction and signal path geometry correction of the three links have the same fluctuation period as that of the GEO satellite motion. The fluctuation amplitude of Sagnac correction is from 0.04 to 0.16 ns and that of signal path geometry correction is from 0.01 to 0.53 ns for the three links. For time transfer with sub-nanosecond precision, both of non-reciprocity corrections can not be ignored as to the three links, except signal path geometry correction of Beijing-SWest link. Especially for Beijing-West link, the fluctuation amplitude of signal path geometry correction is larger than 0.5 ns, which is possibly suffered from the bad geometry non-reciprocity for the two ground stations respect to the GEO satellite.

More investigations can be done to the signal path geometry correction considering the clock bias of the ground stations referring to the navigation system time.

References

1. Han C, Yang Y, Cai Z (2011) BeiDou navigation satellite system and its time scales. Metrologia. doi:10.1088/0026-1394/4/S13
2. Bauch A, Piester D, Fujieda M, Lewandowski W (2011) Directive for operational use and data handling in two-way satellite time and frequency transfer (TWSTFT). Bureau International des Poids et Mesures, Rapport BIPM-2011/01
3. Li X, Geng S, Li Y (2011) Research of equipment delay calibration technique in two-way time synchronization system (in Chinese). In: China satellite navigation conference, Shanghai, China
4. Tseng W, Feng K, Lin S et al (2011) Sagnac effect and diurnal correction on two-way satellite time transfer. IEEE Trans Instrum Meas. doi:10.1109/TIM.2010.2095542
5. Piester D, Bauch A, Fujieda M et al. (2007) Studies on instabilities in long-baseline two-way satellite time and frequency transfer (TWSTFT) including a troposphere delay model. In: 39th annual precise time and time interval systems and applications meeting, Long Beach, USA
6. Wu W, Li Z, Yang X et al (2012) Sagnac effect on two-way satellite time and frequency transfer (in Chinese). J Astron. doi:10.3873/j.issn.1000-1328.2012.07.012
7. Zhou B, Fang B, You W (2011) Study on satellite motion error of TWSTFT (in Chinese). In: 2nd China satellite navigation conference, Shanghai, China
8. Hongwei S, Imae M, Gotoh T (2003) Impact of satellite motion on two-way satellite time and frequency transfer. Electron Lett 39:452–463. doi:10.1049/el:20030291
9. Kirchner D (1999) Two-way satellite time and frequency transfer (TWSTFT): principle, implementation, and current performance. Review of Radio Sciences
10. Wang X, Yang X (2006) Calculation of sagnac effect in two way satellite time and frequency transfer (in Chinese). Chin J. Sci Instrum. doi:10.3321/j.issn:0254-3087.2006.z1.244

Chapter 39
Progress of the Portable Rubidium Atomic Fountain Clock in SIOM

Yuanbo Du, Rong Wei, Richang Dong and Yuzhu Wang

Abstract A portable ^{87}Rb atomic fountain clock has been constructed and researched in Shanghai Institute of Optics and Fine Mechanics, and some improvements have been made recently. So far, comparison data with the H-maser shows that, the Allan deviation of the relative frequency stability of this fountain clock is $5.0 \times 10^{-13}\tau^{-1/2}$, which reaches 2.6×10^{-15} at the average time of 40000 s, and degenerates for longer time due to the frequency drift of the H-maser. The relative frequency uncertainty has been evaluated with the value of 2.4×10^{-15}. In addition, some characteristics technique has been realized on this fountain clock, including "local-oscillator-locking" which gives the error signal back to the local oscillator directly and offers the standard frequency output whose stabilities arrive at the limit determined by the Dick effect, "health safeguard", an improvement used to increase the continuous running time, and suppress the possible faults caused by frequency unlocking and power fluctuation of the laser, and "self comparing", a simple and effective way for the frequency uncertainty evaluation, which is used to evaluate the distributed cavity phase shift, collision shift, and light shift.

Keyword Fountain clock · Rubidium · Frequency stability · Local-oscillator-locking · Health safeguard · Self comparing

Y. Du · R. Wei (✉) · R. Dong · Y. Wang
Key Laboratory for Quantum Optics, Shanghai Institute of Optics and Fine Mechanics, Chinese Academy of Sciences, Shanghai 201800, China
e-mail: weirong@siom.ac.cn

Y. Du · R. Wei · R. Dong · Y. Wang
Center for Cold Atom Physics, Chinese Academy of Sciences, Shanghai 201800, China

J. Sun et al. (eds.), *China Satellite Navigation Conference (CSNC) 2013 Proceedings*, Lecture Notes in Electrical Engineering 245,
DOI: 10.1007/978-3-642-37407-4_39,

39.1 Introduction

Atomic fountain clocks (AFC) are the most accurate atomic clocks participating in the UTC and TAI [1], which have been or are being built in most important timing laboratories all over the world. For example, seven rubidium atomic fountain clocks are being constructed to upgrade the timekeeping system in USNO [2]. A portable ^{87}Rb AFC device has been made and researched in Shanghai Institute of Optics and Fine Mechanics since 2003, and early works were reported in the CSNC in 2011 [3]. Since then, a new microwave synthesizer with lower phase noise for a better stability of AFC has been set up and certificated, and the local oscillator locking (LOL) technology is adopted to lock the microwave frequency, namely, error signal given back to the servo local oscillator instead of the DDS in the microwave synthesizer. In addition, certain characteristics technique such as "health safeguard"(HS) is applied to increase the continuous running time and suppress the possible faults caused by frequency unlocking and power fluctuation of the laser in the AFC. "Self comparing" technology is proposed and applies to type B evaluation of frequency uncertainties such as distributed cavity phase, collision shift, light shift and so on.

39.2 Experimental Scheme

39.2.1 The LOL and Evaluation of the Frequency Stability of the Fountain

The difference between our device and usual AFCs is the locking mode. In usual AFCs, error signal is given back to the DDS in the microwave synthesizer, and in the meantime, the clock does not output standard frequency signal, as shown in Fig. 39.1a. In contrast our device is working in LOL mode, and the scheme is plotted in Fig. 39.1b. In LOL mode, feedback of error signal is directly transmitted to the local oscillator, an oven controlled crystal oscillator (BVA 8607 option 10, OSA comp.) for our device, with the capability of outputting standard signal with good frequency stability.

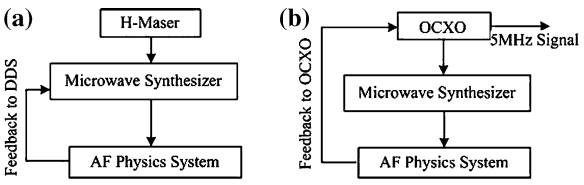

Fig. 39.1 **a** Scheme of the locking mode in which the error signal is given back to the DDS. **b** Scheme of the locking mode in which the error signal is given back to the OCXO

The frequency stability of output signal is limited by phase noise of the OCXO and microwave synthesizer adopted, and Dick effect of AFC which works in periodic mode. For realization of better stability, a new set of microwave synthesizer has been built with the help of professor Giorgio of Paris Observatory. Measured single sideband power spectrum of this microwave synthesizer is as illustrated in Fig. 39.2.

Dick proved in 1987 that in the periodical atomic clock, frequency stability of atomic clocks would degenerate due to the down conversion of the phase noise of the local oscillator adopted [4], which is addressed as Dick effect. The limit of the frequency stability is shown as in Eq. (39.1) [5].

$$\sigma_y^2(\tau) = \frac{1}{\tau}\sum_{m=1}^{\infty}\left(\frac{g_m^{c2}}{g_0^2} + \frac{g_m^{s2}}{g_0^2}\right) S_y^f(m/T_c) \tag{39.1}$$

Here g_m^s and g_m^c are defined in Eq. (39.2).

$$\begin{pmatrix} g_m^s \\ g_m^c \end{pmatrix} = \frac{1}{T_c}\int_0^{T_c} g(\xi)\begin{pmatrix} \sin 2\pi m\xi/T_c \\ \cos 2\pi m\xi/T_c \end{pmatrix} d\xi \tag{39.2}$$

g(t) is sensitivity function. According to the characteristic of time sequence in our AFC, and the single sideband power spectrum of the microwave synthesizer, we could obtain the limit of the frequency stability determined by the Dick effect which is $4.9 \times 10^{-13}\tau^{-1/2}$, which is better than $8 \times 10^{-13}\tau^{-1/2}$, our previous result reported in Ref. [3].

One difficulty for LOL is obtaining a high resolution through the low noise value-controlling circuit of OCXO. Compared with frequency resolution of less than 1μHz, or fractional resolution of less than 1×10^{-16} for DDS, it is required that value resolution is less than 10nV at value data in the vicinity of 5 V. We design and realize a circuit with value resolution of 15 μV or fractional frequency resolution of 1.5×10^{-13}. It's obvious that the resolution of OCXO is far lower

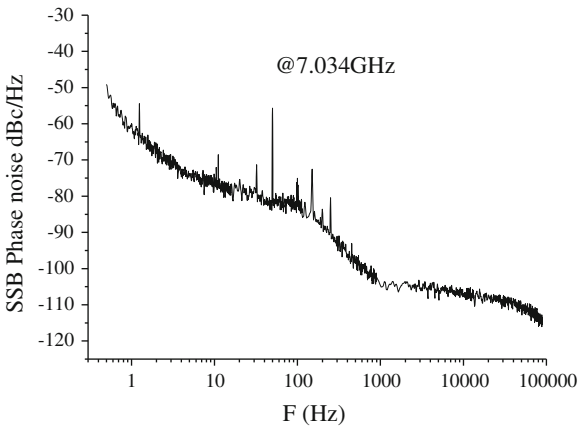

Fig. 39.2 Single sideband power spectrum of the microwave synthesizer @7.034 GHz

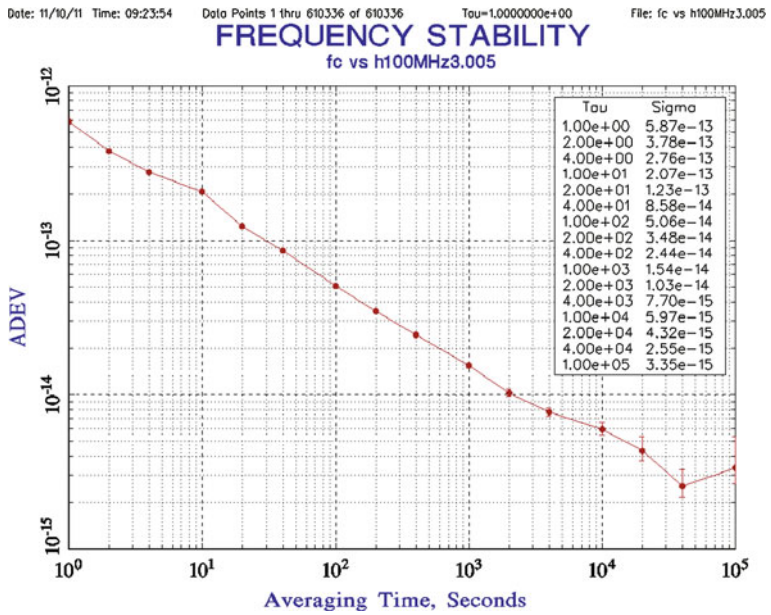

Fig. 39.3 The frequency stability of the atomic fountain compared with the H-maser

than that of DDS, but it can basically fit the requirement of short-term stability of the AFC, and thus is enough for it. The comparison data of the frequency stability of the AFC with the H-maser is as shown in Fig. 39.3, whose fitting curve is $5.0 \times 10^{-13}\tau^{-1/2}$, and it reaches 2.6×10^{-15} at the average time of 40,000 s, which almost arrives at the frequency limit of the H-maser, but data of longer average time degenerates limited by the H-maser, for there are some faults on the oven temperature-controlling module of this device. In all, the result is coincident with calculated data above, so it's considered that the frequency stability of the AFC in LOL mode arrives at the limit determined by the Dick effect.

39.2.2 Evaluation of Type-B Uncertainties

By now, evaluation of certain type B uncertainties has been made, including the 2nd Zeeman shift, collision shift, blackbody radiation shift, microwave power-related shift, cavity pulling, gravity redshift, Majorana transitions, Rabi & Ramsey pulling, light shift and frequency error due to OCXO drift. The evaluated data is as illustrated in Table 39.1. Here we propose and experimentally realize a novel evaluating method named as "self comparing", which enables AFC to alternately work in two states, one locking and one unlocking state respectively. By analyzing the frequency difference between two states, the effect of corresponding parameters on frequency will be obtained, and the uncertainty could be evaluated. The

Table 39.1 Evaluated data of frequency drift and uncertainties, and experiment methods of evaluation

Cause of frequency shift	Drift (10^{-15})	Uncertainty (10^{-15})	Experiment methods
2nd Zeeman effect	140.0	0.6	Magnetic intensity map
Collision shift	−0.1	0.03	Measure Density of cold cloud
Blackbody radiation shift	−17.3	0.2	Measure temperature map
Microwave power-related shift	0	<2	Directly measure distributed cavity phase, need improving
Cavity pulling	0	0.08	Measure temperature of Ramsey cavity
Gravity redshift	0.9	0.1	Measure height above sea level
Majorana transitions	<0.001	<0.001	Measure magnetic intensity map
Rabi & Ramsey pulling	<0.001	<0.001	Measure split and population of sub-levels
Light shift	0	<0.1	Direct measurement
Error due to OCXO drift	0.2	0.3	Direct measurement
Total	123.7	2.4	

method has been used to evaluate the uncertainty due to distributed cavity phase, and the detail will be shown in following paper of our group.

In conclusion, the evaluation result of the total frequency shift is 1.237×10^{-13}, while the total frequency uncertainty is 2.4×10^{-15}.

39.2.3 The Health Safeguard of the Fountain

Though performance of AFCs is much better than that of traditional thermal atomic clocks [6], the failure rate (FR) is still a shortage for AFCs, and by now there exists no AFC satisfying the requirement of continuous work with FR of less than one time per year. Thus an idea is proposed to decrease the FR, make AFC robust and reliable enough, which is named health safeguard (HS) here. If there exist several elements affecting FR, we could monitor the corresponding parameters of these elements. Only if they exceed a data range (named health range) which is still far from failure, we could adjust them to normal value, as illustrated in Fig. 39.4. After several improvements to increase reliability of AFC, we observe that frequency unlocking and power fluctuation of the laser are main elements leading to failures of AFC. Thus HS is used to decrease the failures, through which a subprogram is running to monitor the control voltage of the laser head and total power of the laser, together with the locking program. If the values of the monitoring parameters are beyond the health range, the system will alarm, and message will be sent to alert members of the laboratory to such a situation. The improvements increase continuous time of AFC from about 10 day to several months.

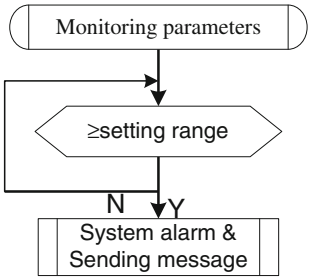

Fig. 39.4 Schematic diagram of health safeguard

39.3 Conclusion

There have been several improvements in our ^{87}Rb AFC. Better stability data has been obtained by improving the microwave synthesizer and other corresponding work, with $5.0 \times 10^{-13}\tau^{-1/2}$ from 3.5 to 40,000 s, and 2.4×10^{-15} at 40,000 s. And primary type-B uncertainty evaluating tasks have been done, with fractional frequency error of shift of 1.237×10^{-13}, uncertainty of 2.4×10^{-15}. Besides, optimizing and improving works are being launched for better data. Several characteristic works have been proposed and realized, such as LOL is used to obtain an independent clock, self comparing for simplifying uncertainty evaluation, and health safeguard for lower FR.

This work was supported by national natural science fund of China (Grant No. 10974215 and 1302121).

References

1. Petit G (2009) Atomic time scales tai and Tt (BIPM): present status and prospects. In: Frequency standards and metrology 2009, 1:475–482
2. Peil S, et al. (2011) Measurements with multiple operational fountain clocks. In: Frequency control and the european frequency and time forum (FCS) 2011 joint conference of the IEEE international
3. Shi CY, Wei R, Li T et al (2011) Working for a mobile high accuracy (10–15) rubidium atomic fountain clock (in Chinese). Sci Sin Phys Mech Astron 41:611–619
4. Dick GJ (1987) Local oscillator induced instabilities in trapped ion frequency standards. DTIC Document
5. Santarelli G et al (1998) Frequency stability degradation of an oscillator slaved to a periodically interrogated atomic resonator. IEEE Trans Ultrason Ferroelectrics Freq Control 45(4):887–894
6. Wynands R, Weyers S (2005) Atomic fountain clocks. Metrologia 42(3):S64

Chapter 40
Precision Analysis of RDSS Two-Way Timing

Bingcheng Liu, Jianghua Qu, Hong Yuan, Lijuan Xu and Ting Liu

Abstract RDSS system of Compass provides the service of two-way timing. In this paper, the factors which may affect the precision of system are analyzed according to the theory of RDSS two-way timing. Through the experimental data in Sanya, each of the factors is calculated and analyzed. The results show that the ionospheric error and multipath error have some impact on the RDSS two-way timing error, but the impact is small, while the approximation error which is caused by ignoring satellite motion and the RDSS two-way timing error is fairly close in magnitude, so the approximation error may be the main factor which causes the error of RDSS two-way timing.

Keywords RDSS · Two-way timing · Time

40.1 Introduction

Compass satellite navigation system which is constructed by ourselves is a new-type, all-weather, high-precision, regional satellite navigation and positioning system. It has three functions, which are quick positioning (navigation), two-way short message communication and timing [1]. One of the ways to achieve timing function of Compass is RDSS two-way timing.

In this paper, two-way timing service of Compass RDSS system is discussed. Through the theory of two-way timing, the factors which may affect the precision of two-way timing are analyzed. With the experimental data, the impact of various factors on the precision is discussed.

B. Liu (✉) · J. Qu · H. Yuan · L. Xu · T. Liu
Academy of Opto-electronics, Chinese Academy of Sciences, Beijing 100094, China
e-mail: bcliu@aoe.ac.cn

J. Sun et al. (eds.), *China Satellite Navigation Conference (CSNC) 2013 Proceedings*, Lecture Notes in Electrical Engineering 245,
DOI: 10.1007/978-3-642-37407-4_40,

40.2 Theoretical Analysis

40.2.1 The Theory of Two-Way Timing

The theory of RDSS two-way timing is: under the control of local time reference, a time frame interrogation signal is transmitted from the central station to satellite with regular time via satellite transponder, and finally received by the two-way timing terminal. The time difference between the local clock 1 PPS signal and the interrogation signal is measured by the terminal. At the same time, a response signal is transmitted from the timing terminal to satellite via satellite transponder, and finally received by the central station. The round-trip time delay between sending the interrogation signal and receiving the response signal is measured by the central station. The forward propagation delay, which refers to the transmission time of the interrogation signal conveying from the central station to timing terminal, is calculated and then sent to the terminal as delay correction value. Finally, based on the measured time difference and the received delay correction value, the clock error between user clock and system time is calculated by the two-way timing terminal [2–4].

The basic theory of the two-way timing is shown in Fig. 40.1. According to the above-mentioned basic theory, for any user i, specific formula of two-way timing is as follows:

$$\Delta T_i = 1 - n\Delta t - R_i - \tau_{oi} \tag{40.1}$$

Wherein, $\Delta T_i \equiv T_i(t) - t$ stands for clock error between the user local clock and the system time clock, t stands for the system time, $T_i(t)$ stands for the clock time of user i when the system time is t, R_i stands for time delay measured by user i, Δt stands for the time span of each frame of interrogation signal, $n\Delta t$ stands for the system time corresponding to the nth frame, τ_{oi} stands for the forward propagation delay from central station to the user i. And the unit of the formula is second (s).

In actual system, τ_{oi} is calculated as follows:

$$\tau_{oi} = \frac{1}{2}\left[R_{oio} + (\tau_{oi}^{air} - \tau_{io}^{air}) - \tau_i^{equ2}\right] + \tau_i^{equ1} \tag{40.2}$$

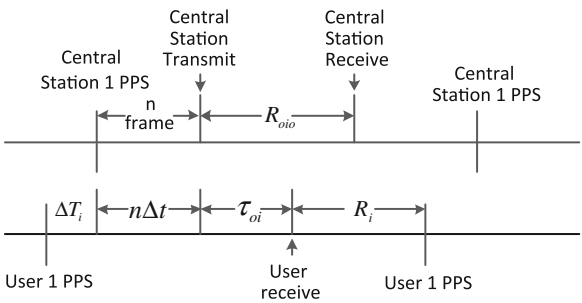

Fig. 40.1 Theory of two-way timing

In formula (40.2), τ_i^{equ1} stands for the one-way total device delay in forward propagation process from central station to the user, τ_i^{equ2} stands for the two-way total device delay in forward and backward propagation process between central station and the user; τ_{oi}^{air} and τ_{io}^{air} respectively stand for atmospheric delay in forward propagation process and in backward propagation process; R_{oio} stands for time delay measured in forward and backward propagation process between central station and the user i by central station.

After inserting formula (40.2) to formula (40.1), formula (40.3) can be obtained as:

$$\Delta T_i = 1 - n\Delta t - R_i - \frac{1}{2}\left[R_{oio} + (\tau_{oi}^{air} - \tau_{io}^{air}) - \tau_i^{equ2}\right] - \tau_i^{equ1} \tag{40.3}$$

40.2.2 Analysis of Influencing Factors

The factors which mainly affect the precision of RDSS two-way timing could be obtained from formula (40.3). $1 - n\Delta t$ contains second signal error. R_i and R_{oio} contain measurement error which composed of multipath error and random error. τ_{oi}^{air} and τ_{io}^{air} contain atmospheric delay error, τ_i^{equ1} and τ_i^{equ2} contain device delay error. Consequently, some factors which would affect the precision contain measurement error, device delay error, atmospheric delay error, second signal error and so on. In addition, the relativistic effect error, which is caused by the motion of central station, user and the satellite with the transmission of signal, should be considered.

Meanwhile, it should be noted that formula (40.3) is just approximation. As the satellite is kinetic with the signal transmission, the satellite position is different at each transponding time. Therefore, $R_{oio}/2$ in formula (40.3) is an approximation which contains an approximation error.

In conclusion, as shown in Fig. 40.2 the factors which affect the precision of RDSS two-way timing include the following six aspects: (1) Measurement error; (2) Device delay error; (3) Atmospheric delay error; (4) Second signal error; (5). Approximation error; (6). Relativistic effect error.

40.2.2.1 Measurement Error

Measurement error mainly comes from multipath error and random error measured in user device and central station. Normally, in RDSS two-way timing system, the measurement random errors of both user device and central station are about a few nanoseconds, which have little effect on the precision of RDSS two-way timing.

Multipath error has large fluctuation range with the changes of environment. So it may be the main factor affecting the precision of RDSS two-way timing and it will be analyzed in this paper.

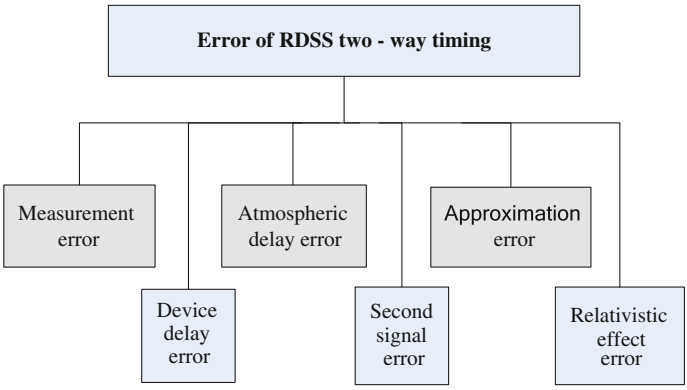

Fig. 40.2 Analysis of RDSS two-way timing error

40.2.2.2 Device Delay Error

In RDSS two-way timing system, both one-way and two-way device delays are prior calibrated and stored in the central station as constants. Although the actual device delay does not necessarily remain constant at all times, and may change with the influences of temperature and other conditions with small magnitude. The device delay could be regarded as a constant within a short time, which has little effect on the precision of RDSS two-way timing. Therefore, the device delay error would not be analyzed in this paper.

40.2.2.3 Atmospheric Delay Error

Atmospheric delay error, comprised of ionospheric error and tropospheric error, includes forward and backward propagation processes. Atmospheric delay error has obvious daily-cycle property.

Although the tropospheric delay changes with the atmosphere, temperature, barometric pressure, it could be modified well with accurate model. The residual tropospheric error based on the model modification is small. So the tropospheric error has little effect on the precision of RDSS two-way timing and would not be analyzed in this paper.

Because the ionospheric delay is large and the influencing factors are quite complex, the residual ionospheric error of current model modification is large. So the ionospheric delay may be the main factor affecting the precision of RDSS two-way timing and would be analyzed in this paper.

40.2.2.4 Second Signal Error

Second signal error is caused by the instability of atomic clock and the second signal error of central station is negligible. Normally, the second signal error of user has little effect on the precision of RDSS two-way timing, which would not be analyzed in this paper.

40.2.2.5 Relativistic Effect Error

The relativistic effect error is due to the motion of central station, user and satellite caused by the earth rotation. With the correction of earth rotation, the relativistic effect error has little effect on the precision of RDSS two-way timing, and would not be analyzed in this paper.

40.2.2.6 Approximation Error

GEO satellite owns daily-cycle property. The relative velocity between GEO satellite and the earth is small. But since GEO satellite is far away from the earth and it moves quickly, the position of satellite is quite different between the two times when the central station transmits signal to timing terminal. So if the approximation error is ignored on the timing terminal, it would affect the precision of RDSS two-way timing. Meanwhile, the approximation error has significant daily-cycle property which would be analyzed in this paper.

In conclusion, multipath error, ionospheric delay error and approximation error, which are considered as main factors affecting the precision of RDSS two-way timing, would be analyzed in this paper.

40.3 Experimental Results and Analysis

In order to analyze the factors above, a time reference was established in Sanya. Based on historical data, the time synchronization accuracy between the time reference and Compass time is less than 10 ns and aperiodic. On that basis, a two-way timing test was carried out based on the two-way timing terminal. The data was collected for nearly 3 days, and it was analyzed as follows.

40.3.1 Magnitude Analysis of Two-Way Timing Error

The distance, from the central station to user via satellite transponder and then from user to the central station via satellite transponder, is calculated with both satellite ephemeris and user approximate coordinates. The distance is subtracted

from the original pseudo-range, getting the original O–C. As the user's precise location is unknown, the result contains certain systematic error. Comparing the two-way timing error with O–C (without systematic error), the result is shown in Fig. 40.3.

As can be seen in the figure above, two-way timing error is daily-cycle and the change of peak-to-peak is approximately 80 ns.

40.3.2 Analysis of Multipath Error

Two two-way timing terminals were placed in short distance. As the terminals were near, the effects of ionosphere, troposphere and satellite motion are almost the same for the two terminals. However, multipath environment of both terminals were quite different. The residual error is mainly caused by multipath error. The result is shown in Fig. 40.4.

As can be seen in the figure above, the error fluctuates around 15 ns (peak-to-peak) which is significantly lower than the two-way timing error. Therefore, the multipath error would not be the main factor which affects the precision of RDSS two-way timing.

40.3.3 Analysis of Ionospheric Error

The ionospheric delay, from the central station to user via satellite transponder and then from user to the central station via satellite transponder, was calculated with grid ionospheric data. Comparing the ionospheric delay with O–C (without systematic error), the result is shown in Fig. 40.5.

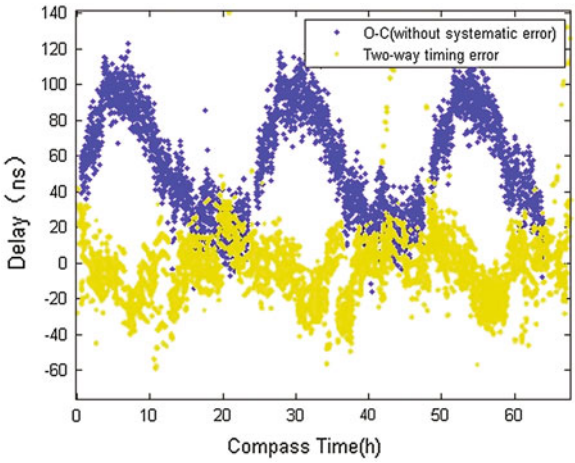

Fig. 40.3 Comparison of two-way timing error and O–C (without systematic error)

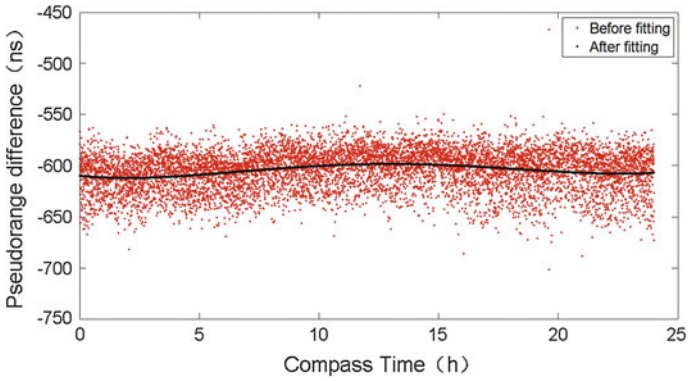

Fig. 40.4 Effect of multipath error

Taking the O–C (without systematic error) as reference (that is with accurate zero-correction), the ionospheric delay error across the entire path was calculated. In case of the accurate zero-correction, the residual ionospheric error is within 25 ns with current grid ionosphere model. For delay correction process of the two-way timing, the delay correction is one half of the ionospheric delay across the entire path, and the ionosphere impact factor is about −1/5 of total delay. So in case of the accurate zero-correction, the residual ionospheric correction error is within 5 ns with current grid ionospheric model correction. The result is shown in Fig. 40.6.

Comparing the residual ionospheric correction error with two-way timing error, the result is shown in Fig. 40.7.

As can be seen in the figure above, the residual ionospheric correction error has significant daily-cycle property, and its effect on two-way timing is significantly smaller than the two-way timing error. So the ionospheric error would not be the main factor which affects the precision of RDSS two-way timing.

Fig. 40.5 Comparison of ionospheric error and O–C (without systematic error)

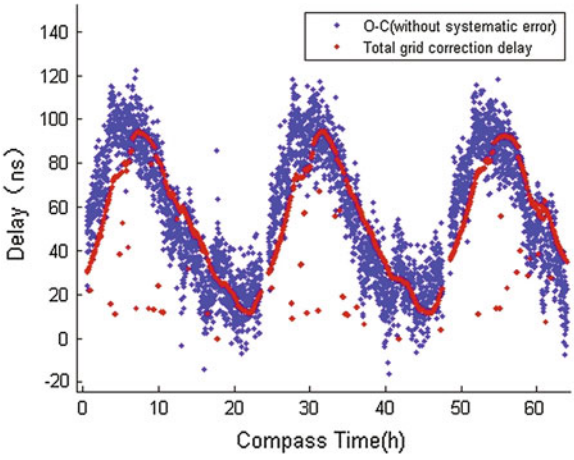

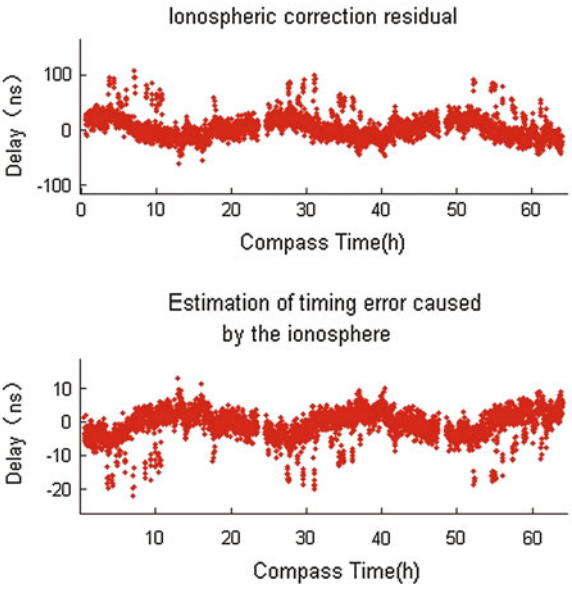

Fig. 40.6 Effect of ionospheric error

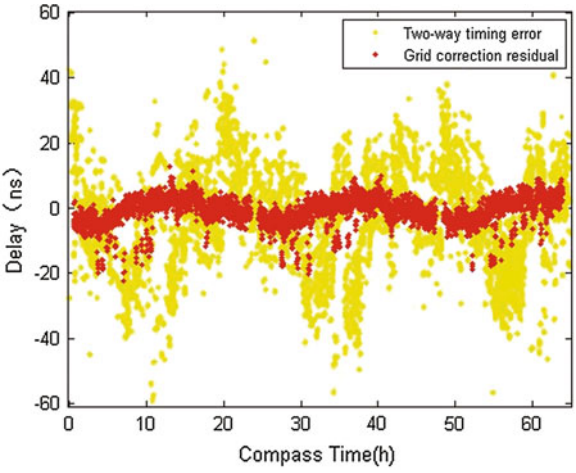

Fig. 40.7 Comparison of ionospheric correction residual and two-way timing error

40.3.4 Analysis of Approximation Error

Two distances were calculated based on the satellite ephemeris and user approximate coordinates. One distance is from the central station to user via satellite transponder for the first time when the interrogation signal is sent out. Another distance is from the central station to user via satellite transponder for the second time when the delay correction value is sent to user. Subtracting one distance from

another and calculating the distance of satellite position at the two times when the signal is outbound from the central station, the results are shown in Fig. 40.8.

As the satellite position changes greatly at the two different times, the distance from the central station to user via satellite transponder changes greatly. Comparing the difference of distance with the two-way timing error, the result is shown in Fig. 40.9.

As can be seen in the figure above, if the approximation error due to the changes of satellite position is ignored in user, the error is equivalent to the two-way timing error in magnitude. So the approximation error may be the main factor which affects the precision of RDSS two-way timing.

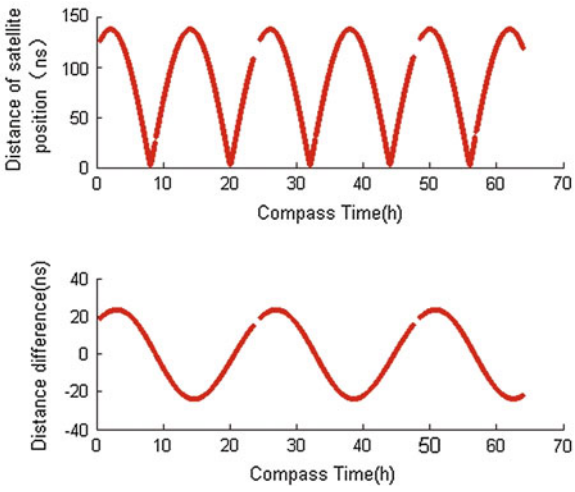

Fig. 40.8 Effect of approximation error

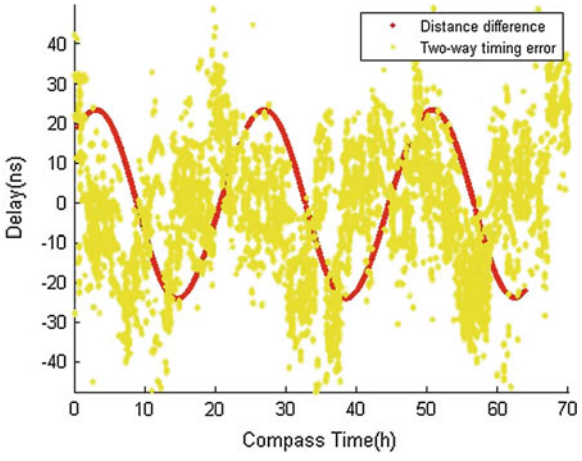

Fig. 40.9 Comparison of approximation error and two-way timing error

40.4 Conclusion

The factors affecting the precision of RDSS two-way timing mainly include multipath error, ionospheric error and approximation error. As the discussion shown above, the ionospheric error and multipath error have little effect on the precision of RDSS two-way timing and would not be the main factors, while the approximation error due to ignoring satellite motion is equivalent to the two-way timing error in magnitude. Therefore, the approximation error may be the main factor causing RDSS two-way timing error.

Acknowledgments This work is supported by the National Natural Science Foundation of China (Grant No.41204031) and Open Fund of Key Laboratory of Precision Navigation and Timing Technology, Chinese Academy of Sciences (2012PNTT16).

References

1. Wu Y, Li G (1992) Geostationary satellite positioning .PLA Publishing House, Beijing
2. Liu L, Han C, Tang B (2005) Analysis of Geosynchronous satellite two-way timing. Navigation Conference Proceedings, Hangzhou
3. Li B, Liu L, Ju X, Shi X, Zhu L (2010) Precision analysis of satellite two-way timing. J Time Freq
4. Liu L, Han C, Tang B (2007) Approximate daily error analysis of two-way time determination. Progress In Astronomy

Chapter 41
Demonstration of a Physics Package with High SNR for Rubidium Atomic Frequency Standards

Wenbing Li, Songbai Kang, Gang Ming, Feng Zhao, Feng Qi, Fang Wang, Shaofeng An, Da Zhong and Ganghua Mei

Abstract The frequency stability of a rubidium atomic frequency standard (RAFS) depends mainly on the signal to noise ratio (SNR) of atomic discrimination signal provided by the physics package. In order to improve further the frequency stability of our RAFS, a new physics package with high SNR was designed recently. The physics package was designed based on an improved slotted tube cavity. Compared with our previous design, the new cavity has more uniform magnetic line distribution and larger size, so that a larger resonance cell can be used. In the design the separated filter technique (SFT) was used. A Helmholtz coil was substituted for a solenoid one to create a more uniform C field. At present a prototype of the physics package has been made. A preliminary test has been performed, and a short term frequency stability of $6 \times 10^{-13}/1$ s was achieved. This result indicates that the SNR of the physics package could meet the requirement for building a RAFS with frequency stability better than $1 \times 10^{-12}/\tau^{1/2}$.

Keywords Rubidium atomic frequency standard · Signal to noise ratio · Physics package · Separated filter technique · Slotted tube cavity

W. Li (✉) · S. Kang · G. Ming · F. Zhao · F. Qi · FangWang · S. An · D. Zhong · G. Mei
Key Laboratory of Atomic Frequency Standards of Chinese Academy of Sciences, Wuhan Institute of Physics and Mathematics, Wuhan 430071, China
e-mail: leeyu04@163.com

G. Mei
e-mail: mei@wipm.ac.cn

W. Li
University of Chinese Academy of Sciences, Beijing 100049, China

J. Sun et al. (eds.), *China Satellite Navigation Conference (CSNC) 2013 Proceedings*, Lecture Notes in Electrical Engineering 245,
DOI: 10.1007/978-3-642-37407-4_41,

41.1 Introduction

The on-board atomic frequency standard is a key part of a Global Navigation Satellite System (GNSS), and its frequency stability has great influence on the positioning accuracy of the GNSS. Up to now the on-board atomic frequency standards used in the GNSS are the rubidium atomic frequency standard (RAFS), the passive hydrogen atomic frequency standard and the cesium beam frequency standard. The RAFS has always been the first choice for the GNSS satellites due to its small volume, low power consumption, high reliability and satisfactory performance. Motivated by the GNSS application, the performance of the RAFS has been largely improved in recent decades. The newly launched GPS IIF satellites used the so called "enhanced RAFS" produced by the PerkinElmer. The RAFS is of frequency stability better than $1 \times 10^{-12}/\tau^{1/2}$ [1], which is recognized as the best performance for the RAFS in the world.

We have been engaged in developing high performance RAFS for a long time. The short-term frequency stability of our RAFS products was better than $3 \times 10^{-12}/\tau^{1/2}$ [2]. The frequency stability of the RAFS is mainly determined by the signal to noise ratio (SNR) of the physics package. In order to improve further the frequency stability of our RAFS, a modified physics package with higher SNR has been designed. A preliminary test indicated that the SNR of the physics package could meet the requirement for building a RAFS with frequency stability better than $1 \times 10^{-12}/\tau^{1/2}$. In this paper we report the main design features and the test result of the physics package.

41.2 Structure of the Physics Package

Figure 41.1 shows the structure of the RAFS new physics package. The system is mainly composed of a rubidium spectral lamp, a filter cell and a cavity-cell assembly. The physics package was designed by using the separated filter technique (SFT). The light beam from the ^{87}Rb spectral lamp is collimated by a lens, then passes the filter cell containing ^{85}Rb vapor for isotope light filtering. The filtered light beam enters the cavity-cell assembly to pump ^{87}Rb vapor atoms in the absorption cell. The absorption cell and the filter cell temperatures are controlled separately. The cavity-cell assembly is composed of a slotted tube cavity [3] and the absorption cell. The key part of the cavity is the slotted tube, which determines the resonance frequency and the microwave mode of the cavity. A dielectric ring located between the slotted tube and the cavity body was used to minimize the volume of the cavity and to finely adjust the cavity's resonance frequency. A Helmholtz coil outside the cavity body creates a weak and static magnetic field, defining the quantum axis for clock transition. The coupling loop is used to feed microwave signal into the cavity, and the photocell is used as a light detector. A two-layer magnetic shielding is used to minimize the influence of environmental magnetic field on the atomic transition frequency.

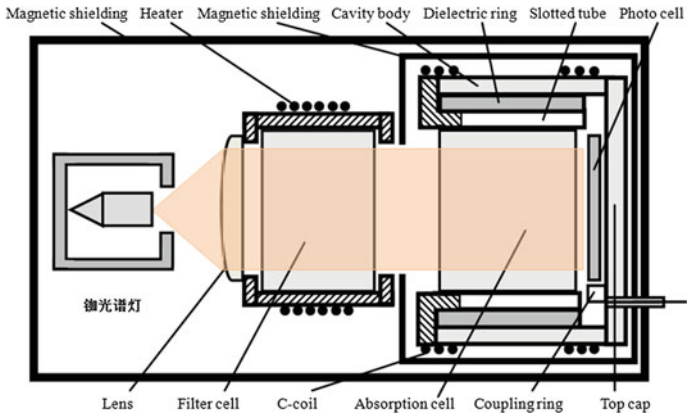

Fig. 41.1 Structure of the physics package

Compared to the structure of our previous one, the physics package has many improvements. Firstly, a lens is used to collimate the pumping light beam, improving its spatial uniformity. Secondly, the filter cell is moved out of the cavity, therefore higher filtering and pumping efficiencies could be expected by independently adjusting the temperatures of the filter cell and the absorption cell. Thirdly, the uniformity of the microwave field distribution inside the cavity is obviously improved so as to increase atom utilization ratio. Fourthly, the inner diameter of the slotted tube is increased from 14 to 20 mm, so that an absorption cell with larger size could be used. Finally, a Helmholtz coil was substituted for a solenoid one to create a more uniform C field. All the improvements are aimed at increasing the number of atoms participating in atomic transition.

41.3 Characteristic of the Slotted Tube Cavity

The microwave resonance mode inside the cavity has great influence on the discrimination signal of a RAFS. According to quantum mechanics theory, only those magnetic lines with component parallel with quantum axis defined by C field are useful to excite the rubidium atomic clock transition, i.e. the transition between the two ground state hyperfine Zeeman levels ($F = 2$, $m_F = 0$) and ($F = 1$, $m_F = 0$). To obtain a strong clock transition signal, the microwave magnetic lines are required to be uniformly and densely distributed in the cavity, and to be in parallel with the direction of the C field as much as possible. While for our current slotted tube cavity, it was found that the microwave magnetic field in the axis area inside the cavity is weak [4, 5], similar to the standard TE_{111} mode. This means that the atoms in the axis area can't be used efficiently. Besides, the inner diameter of the current slotted tube is 14 mm, restricting the size of the absorption cell used.

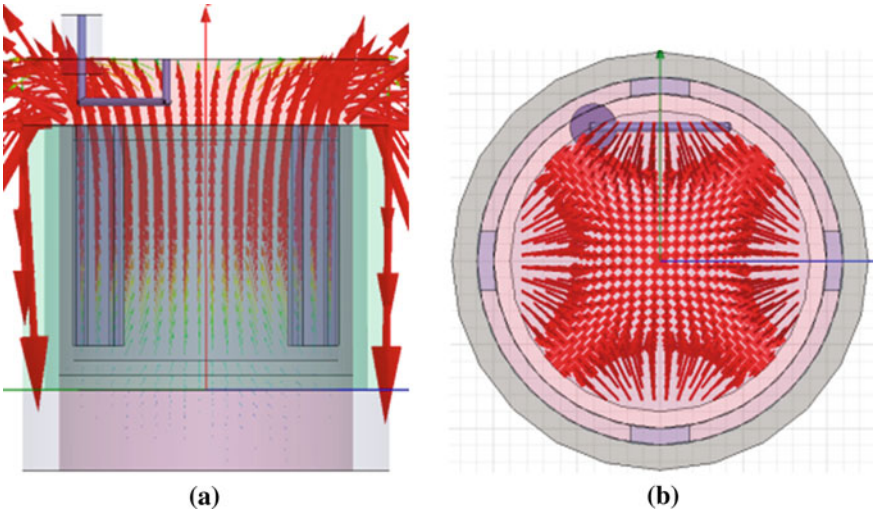

Fig. 41.2 Distribution of magnetic field lines in the slotted tube cavity. **a** and **b** show the distribution in a *side view* section and in a *top view* section respectively

Considering these disadvantages, we developed a microwave cavity with more uniform microwave field distribution and larger size by changing the structural parameters of the slotted tube. The simulation result of the microwave filed distribution inside the cavity is shown in Fig. 41.2.

As shown in Fig. 41.2, the magnetic lines of the microwave field are densely and uniformly distributed in most area inside the slotted tube, and have a dominant orientation parallel with the axis of the cavity. The microwave mode is similar to that of the standard TE_{011} cavity. This means that the atoms in center area can be used efficiently. The inner diameter of the slotted tube is increased to 20 mm from 14 mm, enabling to use an absorption cell with diameter of 20 mm. The microwave distribution in the area near to the inner wall of the slotted tube is slightly inhomogeneous, but if the 1 mm wall thickness of the absorption cell is taken into account, the effect of the field inhomogeneity can be neglected. With this modification in cavity size, the SNR of the atomic transition signal could be enhanced by a factor of nearly $2^{1/2}$, since the cross section of the absorption cell has been increased by a factor of nearly 2. This would lead to a considerable enhancement in SNR.

41.4 Characteristic of the C Filed

Since the modified cavity has a bigger diameter and a shorter length than our previous one, the uniformity of C filed distribution may be a problem if a solenoid coil is still used as before. To ensure a uniform C field inside the cavity,

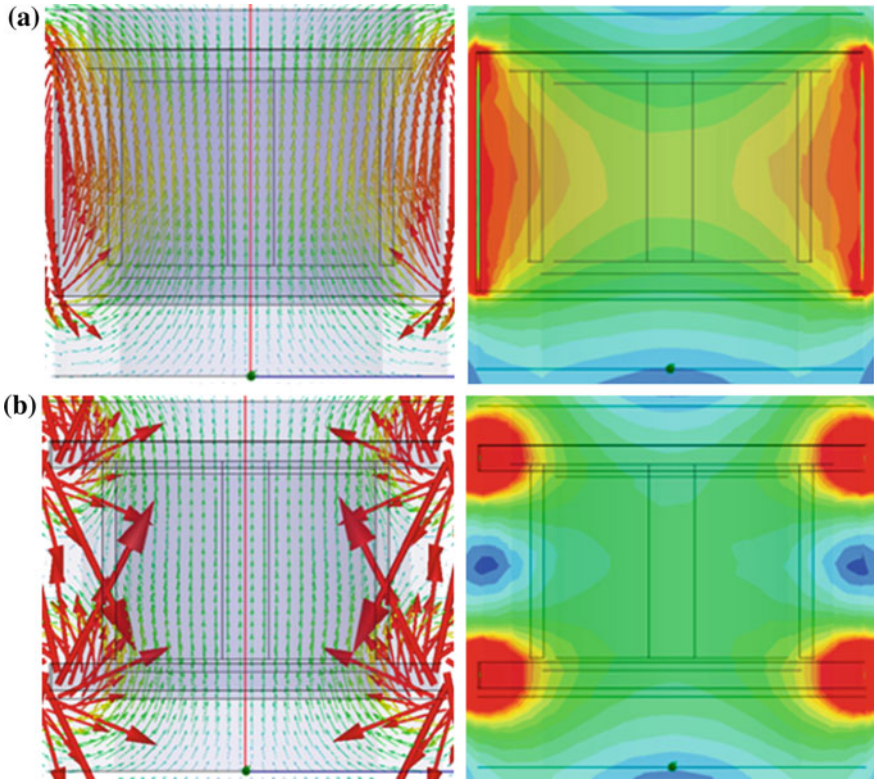

Fig. 41.3 Simulation results of magnetic fields produced by a solenoid coil (**a**) and a Helmholtz coil (**b**). The *left* and the *right* two figures correspond to the victor and the scalar simulation results respectively

using a Helmholtz coil to create the C field maybe a better choice. To make it clear, we simulated the static magnetic fields created by the two kinds of coils. The results are shown in Fig. 41.3. The left two pictures show the magnetic lines, with arrows standing for the orientation of the magnetic field. The right two figures show the field intensity distributions, with red color representing "strong", and the blue one representing "weak". Comparing Fig. 41.3a and b, we see that both orientation and uniformity of the C field will be improved if a Helmholtz coil is used instead of solenoid one. The quantitative calculation showed that there is an about 25 % increase in field uniformity if the Helmholtz coil is used. This is the reason why a Helmholtz coil is used to create C field in the physics package shown in Fig. 41.1.

41.5 Optimization of Operation Temperatures of the Filter Cell and the Absorption Cell

The filter cell and absorption cell are temperature controlled separately, as shown in Fig. 41.1. The higher isotope filter efficiency and a higher SNR of the physics package could be expected by independently adjusting operation temperatures of the filter cell and the absorption cell.

We studied the relationship between the SNR of the physics package and the cells temperatures through a table system of RAFS consisting of the physics package and the relevant electronics. For simplicity the locking signal of the system, whose peak to peak amplitude (V_{PP}) is proportional to the atomic discrimination slope of the system, was taken to measure the SNR of the physics package. The experimentally obtained V_{PP} as a function of the filter cell temperature (T_F) for three absorption cell temperatures (T_A) 66, 68.1 and 70.1 °C is shown in Fig. 41.4.

As shown in Fig. 41.4, for a fixed absorption cell temperature, the SNR of the system increases and then decreases with arising of the filter cell temperature, being of a maximum value. This behavior is reasonable since the filtering efficiency of the filter cell has a maximum value for an appropriate cell temperature [6]. The SNR of the physics package is also influenced by the absorption cell temperature. When the cell temperature is low, the atomic transition signal will increase as the cell temperature increases, since when the ^{87}Rb density inside the absorption cell will increase (see Fig. 41.6). But the cell temperature can't be taken too high, since in this case the atomic transition signal will reduce due to the self-filtering effect of ^{87}Rb atomic vapor, resulting that many atoms can't be

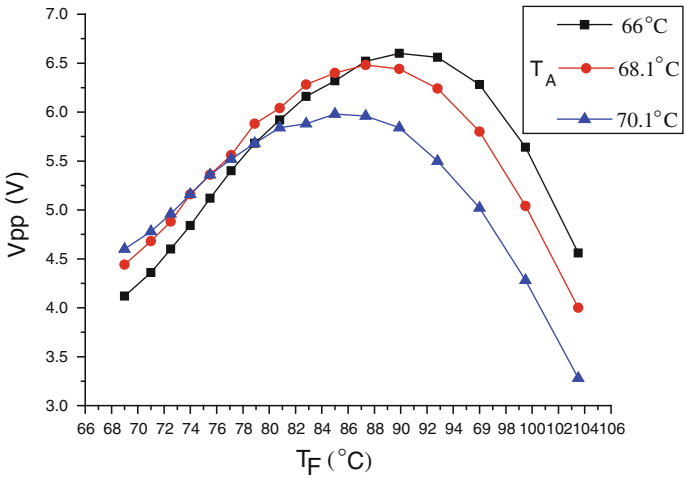

Fig. 41.4 Locking signal amplitude (V_{PP}) as the function of the filter cell temperature (T_F) and the absorption cell temperature (T_A)

efficiently pumped. Therefore to obtain a high SNR of the physics package, both the filter cell temperature and the absorption cell temperature should be optimized. As shown in Fig. 41.4, the maximum SNR is achieved when the absorption cell temperature is set at 66 °C and the filter cell temperature is set around 90 °C. In our previous design of physics package, both the filter cell and the absorption cell were located inside the cavity, sharing the same temperature of 68 °C. As seen in Fig. 41.4, if both temperatures are still set at 68 °C, the SNR will be reduced by more than 50 %. Obviously, it is advantageous for improving the SNR of physics package to control the temperature of the two cells separately.

Figure 41.5 shows the fractional frequency (δF/F) of the RAFS system as a function of the filter cell temperature when the absorption cell temperature is set at 66, 68.1 and 70.1 °C respectively. As shown in Fig. 41.5, the fractional frequency decreases and then increases as the filter cell temperature rises, no matter what temperature is chosen for the absorption cell. The output frequency of the RAFS system is no sensitive to the filter cell temperature if the filter cell temperature is around 90 °C. This temperature dependent behavior of output frequency will be useful to minimize the temperature coefficient of the RAFS. From Fig. 41.4 we know that the highest SNR occurs also at 90 °C of the filter cell temperature, so 90 °C of the filer temperature should be a good choice for both temperature sensitivity suppression and SNR enhancement of the RAFS.

To investigate further the relationship between characteristic of the physics package and the absorption cell temperature, we obtained the dependence of the locking signal amplitude and the fractional frequency of the system on the absorption cell temperature. The results are shown in Figs. 41.6 and 41.7. In both experiments the filter cell temperature is fixed at 90 °C.

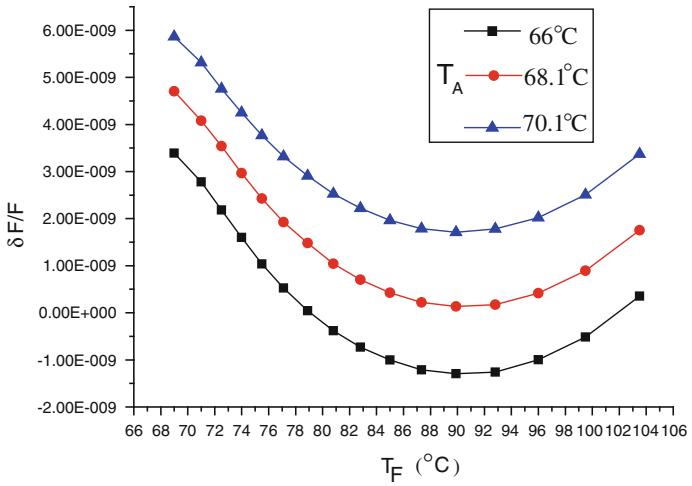

Fig. 41.5 Fractional frequency (δF/F) as the function of the filter cell temperature (T_F) and the absorption cell temperature (T_A)

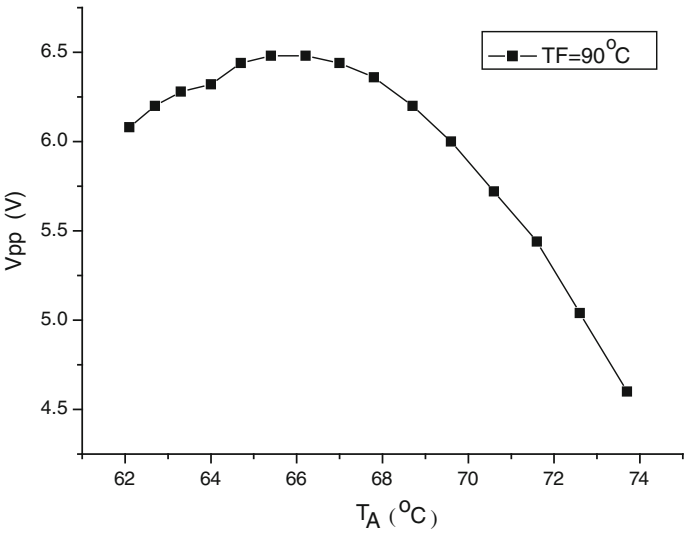

Fig. 41.6 Locking signal amplitude (V_{PP}) as the function of the absorption cell temperature (T_A). The filter cell temperature is fixed at 90 °C

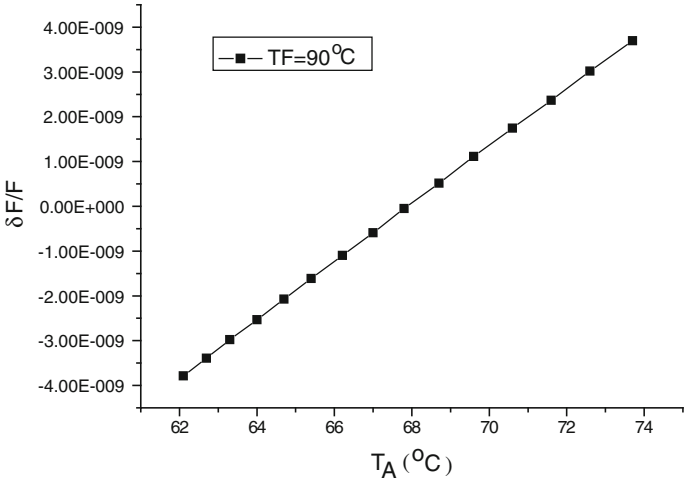

Fig. 41.7 Fractional frequency ($\delta F/F$) as the function of the absorption cell temperature (T_A). The filter cell temperature is fixed at 90 °C

As shown in Fig. 41.6, the SNR increases and then decreases with the absorption cell temperature arises. The maximum SNR occurs at the absorption cell temperature of 66 °C. The reason for the behavior has been analyzed in above text. From Fig. 41.7 we see that the fractional frequency increases linearly as the absorption cell temperature increases, and the temperature coefficient is 6.46×10^{-10}/°C. The temperature coefficient with this value is acceptable. On

one hand, the absorption cell temperature could be strongly controlled by a high gain temperature controller. On the other band, the positive temperature coefficient of the absorption cell could be partly compensated by the negative temperature coefficient of the filter cell if the cell temperature is set at a value slightly lower than 90 °C (see Fig. 41.5). In this case we don't think that the SNR of the physics package will be affected so much.

Through the optimization above, the operation temperatures of the absorption cell and the filter cell were finally chosen to be at 66 and 90 °C respectively.

41.6 Short-Term Frequency Stability Test and Discussion

A short-term frequency stability test of the RAFS has been performed. The reference frequency source was the OCXO 8607 produced by the O.S.A, which has frequency stability of 2×10^{-13}/1 s and 8×10^{-14}/10 s. The stability test was performed by using the Frequency and Phase Difference Meter modeled A7-MX from the QUARTZlock. The test result is 5.57×10^{-13}/1 s, 2.53×10^{-13}/10 s and 8.40×10^{-14}/100 s (Fig. 41.8). This result indicates that the SNR of the physics package meets the requirement for building a RAFS with frequency stability better than $1 \times 10^{-12}/\tau^{1/2}$. It should be pointed out that the obtained result may be restricted to some extent by the performance of the frequency source and the noise of the electronics of the RAFS system, especially when the sampling time is longer than 10 s. Therefore the actual performance of the physics package may be better than the obtained. The relevant work is still in progress.

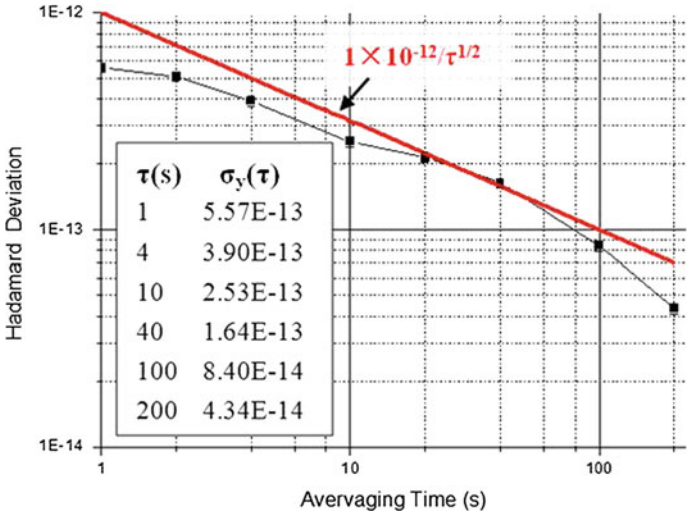

Fig. 41.8 Test result of short term frequency stability of the RAFS system containing the physics package

References

1. Vannicla F, Beard R, White J et al (2009) GPS Block IIF rubidium frequency standard lift test. In: 41st annual precise time and time interval (PTTI) meeting
2. Xia B, Zhong D, An S, Mei (2006) Characteristics of a novel kind of miniaturized cavity-cell assembly for rubidium frequency standards. IEEE Trans Instrum Meas 55(3):1000–1005
3. Mei G, Zhong D, An S, Liu J, Huang X (2001) Miniaturized microwave cavity for atomic frequency standard, U.S. Patent, No. 6 225 870 B1, 1 May, 2001
4. Kang S, Li W, Zhong D, Mei G (2012) Preliminary study of the slotted tube cavity's field distribution. Chin J Magn Reson, 01 2012 (in Chinese)
5. Li W, Kang S, Ming G, Mei G (2011) Optimization of the slotted tube cavity's field distribution. J Astronautic Metrology Meas 31(5) (in Chinese)
6. Mei G, Chen X, Zhu X, Xian Y, Deng J (1987) Isotope filtering experiment on rubidium spectral lamp. Spectrosc Spectral Anal 8(1) (in Chinese)

Chapter 42
Realization and Performance Analysis of Time and Frequency Remote Calibration System

Tao He, Huijun Zhang, Xiaohui Li and Zhixiong Zhao

Abstract On the basis of traditional GPS common-view, Continuous Comparison Technique of Time and Frequency (CCTTF) had been put forward by National Time Service Center (NTSC). With this method, Time and Frequency Remote Calibration System (TFRCS) has been designed and realized to achieve time and frequency calibration as well as traceability for remote users. The design idea and framework of TFRCS are described in this paper, and the data processing of near real-time common-view is presented. Moreover, the experiments of short baseline comparison and long baseline comparison are designed to calibrate the measurement system and test the performance of TFRCS; meanwhile, the measurement uncertainty has been analyzed. The experimental results show that high-precision comparison of time and frequency has been realized by TFRCS, which can be used to establish traceability to UTC (NTSC) for remote users. Time is measured with a combined expanded uncertainty of less than 14 ns, and the frequency is measured with a combined expanded uncertainty of less than 1.5×10^{-13} after 1 day of averaging.

Keywords Time and frequency · Remote calibration · GPS · Common-view · Uncertainty

T. He (✉) · H. Zhang · X. Li · Z. Zhao
National Time Service Center, Chinese Academy of Sciences, Xi'an 710600, China
e-mail: hetao10@mails.ucas.ac.cn

T. He · H. Zhang · X. Li · Z. Zhao
Key Laboratory of Precision Navigation Positioning and Timing, Chinese Academy of Sciences, Xi'an 710600, China

T. He · Z. Zhao
University of Chinese Academy of Sciences, Beijing 100039, China

J. Sun et al. (eds.), *China Satellite Navigation Conference (CSNC) 2013 Proceedings*, Lecture Notes in Electrical Engineering 245,
DOI: 10.1007/978-3-642-37407-4_42,

42.1 Introduction

The requirement of time and frequency is increasingly extensive with the development of science and engineering technology. Crystal oscillator and atomic clock are generally used as the signal source of time and frequency in modern measurement of time and frequency [1]. However, local time and frequency reference standard should be traceable to national standard or international standard before used as the measuring standard of time interval or the synchronizing resource of another timing system.

GPS common-view is a method of remote high-precision time transfer. Common time transfer yields a great reduction in the effect of the ephemeris or position error of a satellite between two stations [2], and achieves high-precision time comparison; if common-view data are exchanged between difference client stations, the comparisons can be realized between these stations.

The Coordinated Universal Time (UTC) maintained at National Time Service Center (NTSC) of Chinese Academy of Science (CAS), known as UTC (NTSC), can be used as a resource to achieve time and frequency calibration as well as traceability for remote users. On the basis of traditional common-view method, Continuous Comparison Technology of Time and Frequency (CCTTF) has been put forward by NTSC. With this technology, TFRCS is developed to establish time and frequency traceability to UTC (NTSC) for remote users.

The design idea and framework of TFRCS are described in the paper, and the data processing of near real-time common-view is also presented. Moreover, the experiments of short baseline comparison and long baseline comparison are designed to calibrate the measurement system and test the performance of TFRCS. Finally, the time uncertainty and frequency uncertainty are analyzed.

42.2 General Designs of TFRCS

42.2.1 Design Idea and Structure of TFRCS

With traditional GPS common-view, 16 min are regarded as an observation cycle. 2 min are used to track satellites by GPS receiver, the following 13 min are used to record the visible satellites data during a series of scheduled tracks, and the last 1 min is the tracking gap [2, 3]. So there is the dead time lasting for 3 min in each observation cycle.

On the basis of traditional GPS common-view, CCTTF had been put forward by NTSC. 10 min rather than 16 min are regarded as an observation cycle for GPS satellites tracking with CCTTF. Furthermore, the measurement of time difference between local reference time and GPS system time (GPST), and data processing proceed simultaneously in the client stations and master station by measurement

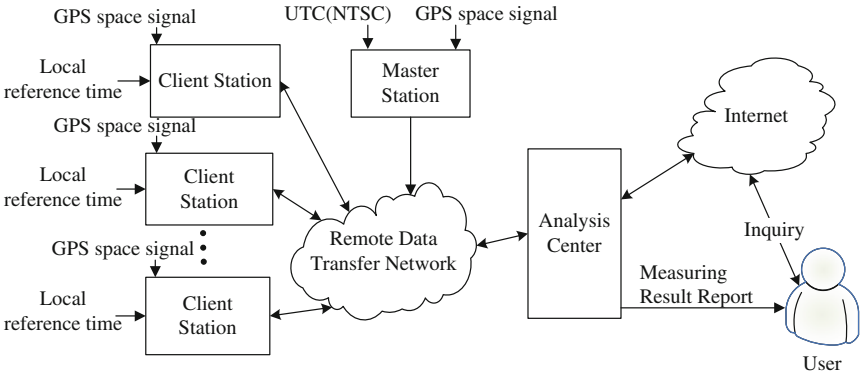

Fig. 42.1 Framework of time and frequency remote calibration system

system. If the former observation cycle is over, a new observation cycle will proceed at once. So the dead time in the observation cycle has been removed with CCTTF.

According to this design idea, TFRCS, shown as Fig. 42.1, has been developed.

TFRCS consists of three parts, including multiple client stations, a master station and a data analysis center. The time difference between local reference time and GPST (REFGPS) is measured by measurement system in client stations once a second. The data processing and GPS satellite tracking proceed simultaneously. When an observation cycle is over, the REFGPS data collected in the observation cycle are fitted with linear least squares and the results are sent to analysis center by remote data transfer network (RDTN). After receiving the fitted REFGPS data of client stations and master station, the software in analysis center will calculate the time difference between UTC (NTSC) and local reference time of each client station, and send them back to each client station and published them on the Internet web. The measuring result reports also can be provided according to user' request.

42.2.2 Improvements on Traditional GPS Common-View System

CCTTF instead of International Bureau of Weights and Measures (BIPM) tracking schedule is required in TFRCS, and 144 segments tracking data will represent the REFGPS at 1 day in measurement system. Generally speaking, eight GPS satellites are being tracked at any time of 1 day. Subsequently, 11,520 min (144 cycles × 10 min × 8 satellites) data can be collected in 1 day. Compared to 9,360 min (90 cycles × 13 min × 8 satellites) data collected with traditional GPS multi-channel common-view, tracking data collected with CCTTF have increased by 23 %.

On the aspect of data transmission, RDTN has been used in TFRCS, and it makes possible that users can view their time difference with respect to UTC(NTSC) from measurement system or Internet web in near real-time. As traditional common view system, Global Time Service (GTS) system served for original remote time calibration service, the users of which only can view the result by monthly report in the mail [4]. So it is convenient for users of TFRCS to view the measurement results as soon as possible.

In 2005, near real-time common-view systems had been implemented in the SIM region [5], but they are still the exception rather the rule now. In addition, data transmission by means of wireless network instead of wire network in RDTN is also a great improvement on traditional common-view system.

42.3 Data Processing of Near Real-Time Common-View

42.3.1 Calculation of REFGPS

The travel time of GPS satellite signal can be divided into two parts [6], the one is the propagation time required by the geometrical distance between satellite and GPS receiver; the other is the time delay caused by atmospheric refraction in the proceeding of signal transmission, including the ionospheric delay and the tropospheric delay. So the total travel time of GPS signal can be calculated by the equation:

$$\tau = r/c + I + T \tag{42.1}$$

where in Eq. (42.1), τ is the total travel time of GPS signal, r is the geometrical distance between GPS satellite and antenna of GPS receiver, c is the speed of light traveling though a vacuum, I is the time delay caused by ionosphere, and T is the time delay caused by troposphere.

Generally speaking, the GPS receiver time and GPST are asynchronous, and the time difference between them is recorded as δt_{u}. Likewise, the time of every satellite clock are also asynchronous, the time difference between GPST and time of a satellite clock is recorded as $\delta t^{(\mathrm{s})}$. The time difference between GPS receiver time and GPST will be calculated with pseudorange as Eq. (42.2).

$$\delta t_{\mathrm{u}} = t_{\mathrm{u}} - t_{GPS} = (\rho - r)/c - I - T + \delta t^{(\mathrm{s})} \tag{42.2}$$

In Eq. (42.2), t_u is the receiver time, ρ is the pseudorange for measurement system in client station.

The relationship between local reference time and GPS receiver time is presented as Eq. (42.3).

$$t_{tic} = t_{ref} - t_u \tag{42.3}$$

where, t_{tic} is the time-interval measurement result from time interval counter, t_{ref} is the local reference time of remote user.

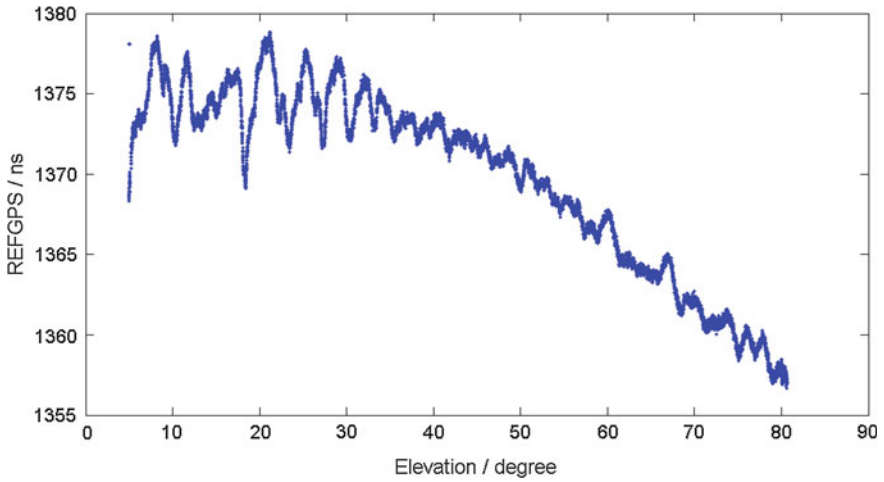

Fig. 42.2 The relationship between REFGPS and elevation of a GPS satellite

The equipment delay should be taken into account during data processing, which include receiver delay, expressed as τ_{rec}, and delay of local reference time, expressed as τ_{ref}. Accordingly, the REFGPS, expressed as t_{REFGPS}, can be calculated with Eq. (42.4).

$$t_{REFGPS} = t\left(_{ref} + \tau_{ref}\right) - \left(t_{GPS} + \tau_{rec}\right) = t_{ref} - t_{GPS} + \tau_{ref} - \tau_{rec} \tag{42.4}$$

Combined of Eqs. (42.2–42.4), t_{REFGPS} can be calculated as Eq. (42.5).

$$t_{REFGPS} = (\rho - r)/c - I - T + \delta t^{(s)} + t_{tic} + \tau_{ref} - \tau_{rec} \tag{42.5}$$

The relationship between REFGPS and elevation of a GPS satellite is showed in Fig. 42.2. Ionosphere and troposphere have an important impact on the GPS signal in the proceeding of signal transmission when a satellite is at low elevation angles, and the REFGPS data is with high uncertainty [7]. So the REFGPS data from the GPS satellite, the elevation of which is below 30°, should be abandoned during data processing.

42.3.2 Least Square Linear Fitting

Six hundred REFGPS data are collected in an observation cycle by tracking a GPS satellite in measurement system, and these data should be smoothed by least square linear fitting to remove the measurement noise.

As is shown in Fig. 42.3, 600 REFGPS data, collected in an observation, have been smoothed with least square linear fitting. Finally, the midpoint of the fitting line is selected as the final measurement result and sent to analysis center.

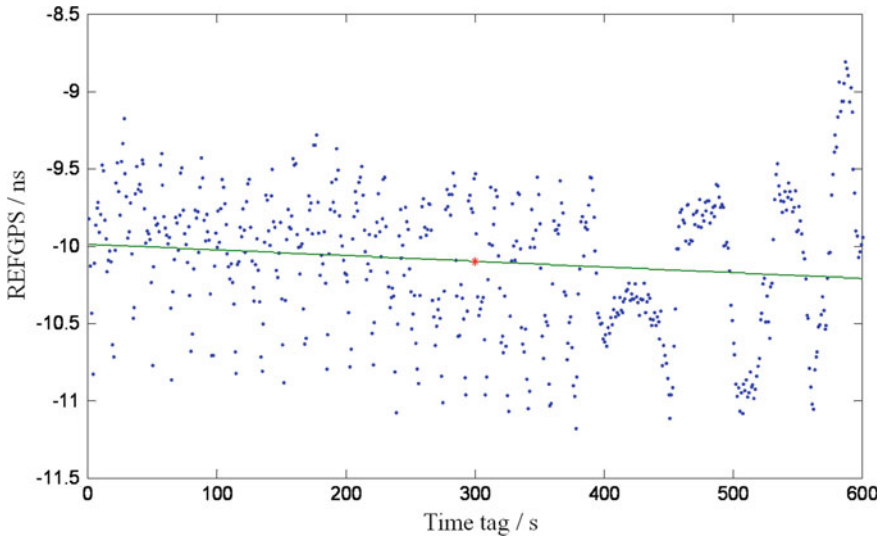

Fig. 42.3 The time difference data and the directed line after filtering

42.3.3 Time Difference Between Local Reference Time and UTC(NTSC)

After receiving the smoothed REFGPS data from the measurement system, software in analysis center will calculate the time difference between local reference time of remote user and UTC(NTSC) for an observation cycle with Eq. (42.6).

$$T = \frac{\sum_{i=1}^{n} (SatUser_i - SatMaster_i)}{n} \tag{42.6}$$

Where, T is the time difference for an observation cycle, $SatUser_i$ is the series of individual satellite tracks recorded by measurement system at client station, $SatMaster_i$ is the series of individual satellite tracks recorded in NTSC, n is the number of satellites tracked by both station.

42.4 Experimental Design and Performance Analysis

42.4.1 Experiment of Short Baseline Comparison

42.4.1.1 Experimental Design

The measurement system should be calibrated with the experimental results of short baseline before being shipped to client station for remote time and frequency

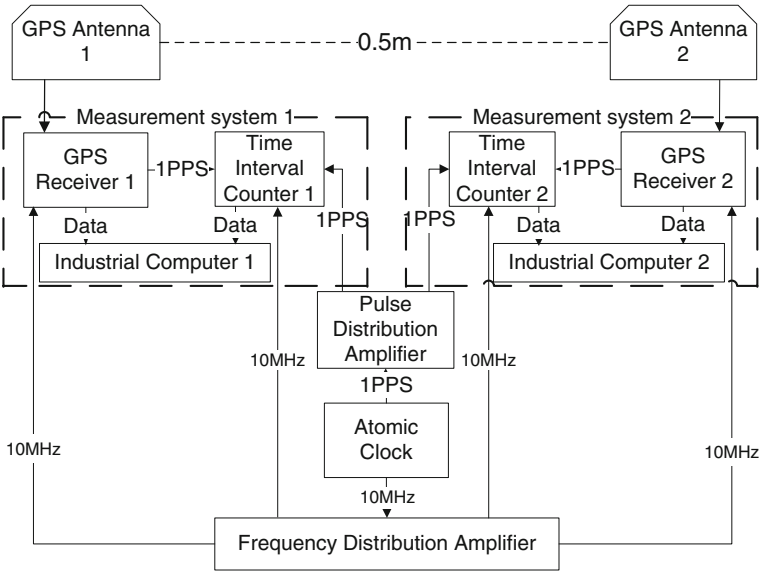

Fig. 42.4 Experiment of short baseline comparison

calibration. In the experiment of short baseline comparison, relative errors can be removed as much as possible, because the same time signal is used in both measurement systems. The comparison results are just impacted by the time delay of measurement system and observation noise [8].

As is shown in Fig. 42.4, the same 10 MHz frequency standard has been connected to GPS receivers and time interval counters. The distance between two GPS antennas is about 0.5 m, and their coordinates has been measured accurately.

42.4.1.2 Analysis of Experiment Results

The experiment of short baseline comparison lasts for about 5 days, and 650 REFGPS data has been selected in each measurement system to calculate the relative time delay between two measurement systems.

Figure 42.5 shows that the peak-to-peak variation of experimental results is less than 5 ns, the average time delay is −33.68 ns, and the standard deviation is 0.64 ns. However, if the experiment of short base line comparison is continued for several months or longer, the average result of 5 day will vary by several nanoseconds due to the environment factor, so the uncertainty of delay calibration is estimated as 5 ns.

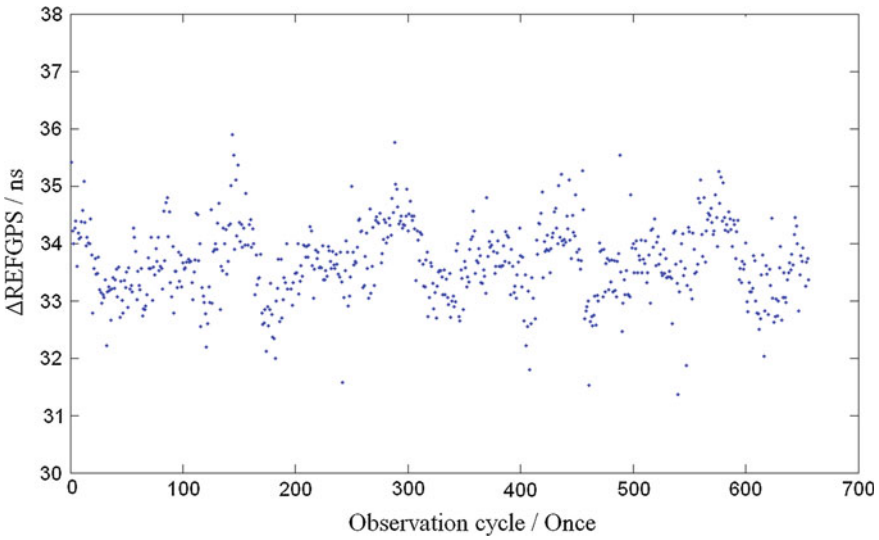

Fig. 42.5 Experimental results of short baseline comparison

42.4.2 Experiment of Long Baseline Comparison

42.4.2.1 Experimental Design

As is shown in Fig. 42.6, the framework of long baseline comparison is presented. The master station locates in NTSC (Xi'an), and the client station locates in Changchun Satellite Observation Station (Changchun). The baseline is about 1,800 km, the time and frequency standard used in Changchun is cesium clock, and the data transmission is achieved by RDTN. The experiment of long baseline comparison lasts for nearly 30 days, and the relative frequency deviation, frequency drift rate, time stability as well as the frequency stability will be calculated.

42.4.2.2 Analysis of the Experiment Results

Figure 42.7 shows the experimental results. It indicates that the measurement of the time difference between two stations for a long distance can be realized by TFRCS. The relative frequency deviation can be calculated with the time difference data obtained in the experiment, the time stability and frequency stability of cesium clock in Changchun Satellite Observation Station also can be measured by TFRCS.

Table 42.1 shows the experimental results of long baseline comparison: the time stability at 1 day is less than 3.5 ns, the frequency stability at 1 day is less than 7×10^{-14}, and the frequency drift rate at 1 day is -5.25×10^{-15}.

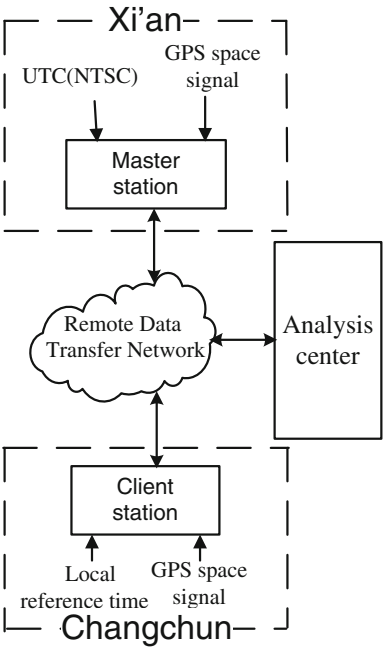

Fig. 42.6 Design framework of long baseline experiment of time and frequency remote calibration system

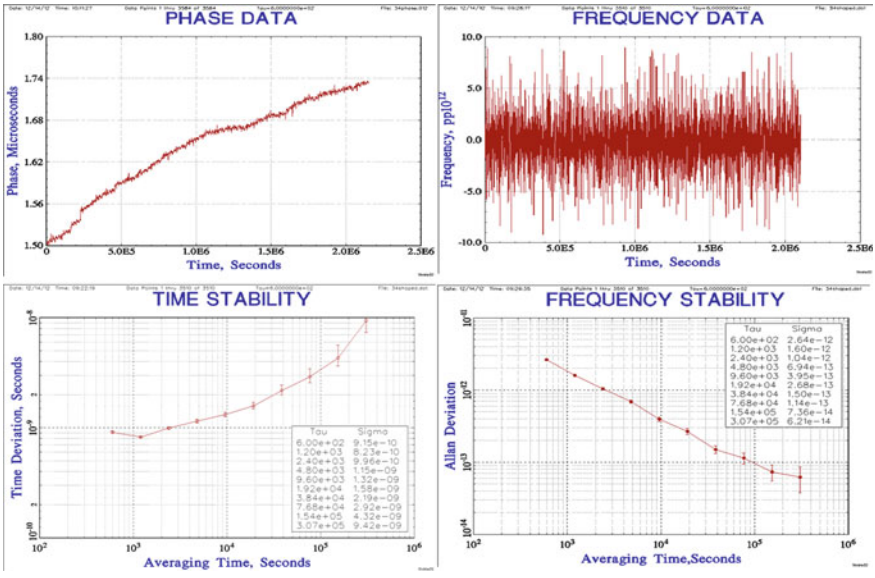

Fig. 42.7 Experimental results of long baseline comparison

According to the statistic, the measurement system in Chang Chun receives the responding time difference from analysis center within 13 s after sending REFGPS data. It means that remote user can obtain their time difference with respect to UTC (NTSC) within 13 s when an observation cycle is over.

The experiment of long baseline experiment indicated that TFRCS has a well performance on the time difference measurement as well as analysis of time and frequency standard stability. Moreover, it has a good real-time performance.

42.5 Uncertainty Analysis

42.5.1 Analysis of Time Uncertainty

The time uncertainty analysis of TFRCS is divided into two parts, the one is Type A uncertainty, U_{A}, and the other is Type B uncertainty, U_B. The time stability of 1 day time average is used to evaluate the Type A uncertainty, as presented in Table 42.1, $U_{\mathrm{A}} = \sigma_x = 3.45$ ns.

It is difficult to evaluate the Type B uncertainty, because more components which can potentially introduce systematic errors should be considered. As is described in Table 42.2, eight components are taken into account in Type B uncertainty evaluation.

Accord to Table 42.2, the combined Type B uncertainty is 6.01 ns. The combined expanded uncertainty, U_{C}, is calculated by Eq. (42.7).

$$U_{\mathrm{C}} = k\sqrt{U_A^2 + U_B^2} \tag{42.7}$$

Where, k is the coverage factor. If $k = 2$, the combined expanded uncertainty is 13.86 ns, and the confidence probability is 0.95.

However, the time uncertainty would become less as the decrease of baseline length between client station and NTSC. So it is expected that the time uncertainty is less than 14 ns for all the client stations with the distance less than 1,800 km from NTSC. Although the combined uncertainty may change as the change of temperature or humid in the laboratory, the errors in any condition have been contained by using the coverage factor of $k = 2$.

Table 42.1 Experimental results of long baseline comparison of TFRCS

Time stability σ_x (1 day)	Frequency stability σ_y (1 day)	Frequency drift rate (1 day)
3.45 ns	6.92×10^{-14}	-5.25×10^{-15}

Table 42.2 Analysis of type B time uncertainty of TFRCS

Uncertainty component	Analysis of errors	Estimated uncertainty (ns)
Ionospheric delay errors	The ionospheric delay is acquired from broadcast ephemeris with large uncertainty	3
Measurement system calibration errors	Refer to Sect. 42.4.1	5
Time interval counter	Multiple measurements accuracy of self-developed time interval counter is less than 0.4 ns	0.4
Antenna coordinate error	The errors of antenna coordinate is less than 0.2 m	0.7
Equipment delay change because of environmental factors	A sudden temperature change in laboratory may cause the equipment delay to change	1
Travel time change of GPS signal because of multiple path	The reflection of GPS signal beside the antenna is subject to the errors about 0.5 ns	0.5
Error of cable delay measurement	The cable delay represented the time delay from local time standard to the measurement system, and is measured with SR620	0.5
Resolution uncertainty of software	The software limits the resolution of the entering value, including calibration value of measurement system and cable delay	0.1

42.5.2 Analysis of Frequency Uncertainty

The frequency stability at 1 day, σ_y, is used to evaluate the Type A frequency uncertainty of TFRCS as Eq. (42.8).

$$U_a = k\sigma_y = 2\sigma_y = 1.38 \times 10^{-13} \tag{42.8}$$

In Eq. (42.8), k is the coverage factor.

There is no critical Type B component for frequency measurement, so the combined expanded uncertainty U_c is equal to U_a.

42.5.3 Uncertainty Comparison Between TMSA and TFRCS

Time Measurement and Analysis Service (TMSA) developed by National Institute of Standard and Technology (NIST) assist laboratories that maintain an accurate local time standard just like TFRCS. We compare the time uncertainty and frequency uncertainty of TMSA and TFRCS in Table 42.3.

Table 42.3 Uncertainty comparison between TMSA and TFRCS

	Time uncertainty (ns)	Frequency uncertainty
TMSA (NIST)	13.70	Less than 1×10^{-13}
TFRCS (NTSC)	13.86	1.38×10^{-13}

Table 42.3 shows that the time uncertainty and frequency uncertainty of TMSA is better than that of TFRCS. Now, we prepare to search for a method to smooth the pseudorange with carrier phase and remove the measurement noise to decrease uncertainty of TFRCS.

42.6 Conclusion

The method of CCTTF has a great improvement on the traditional GPS common view, and TFRCS has been realized with this method. Time is measured with a combined expanded uncertainty of less than 14 ns, and the frequency is measured with a combined expanded uncertainty of less than 1.5×10^{-13} after 1 day of averaging.

The performance test and analysis indicated that TFRCS can achieve remote time and frequency comparison with high precision and good performance in real-time, it can be used to establish traceability to UTC (NTSC) for remote users.

Acknowledgments This paper is supported by the State Key Program of National Natural Science Foundation of China (11033004) and the Western Light Training Project of Chinese Academy of Sciences (Y109YR2701).

References

1. Wu H, Li X, Lu X, Yu H, Yang XH (2011) Fundamentals of satellite navigation system time. Science Press, Beijing, p 15 (Ch)
2. David A,Marc W (1980) Accurate time and frequency transfer during common-view of a GPS satellite. In: Proceedings of 34th frequency control symposium, p 334
3. Qi G (2006) Fundamentals of time science. Higher Education Press, Beijing, p 115(Ch)
4. Lombardi MA, Novick AN (2006) Remote time calibration via the NIST time measurement and analysis service. In: Proceeding of the 2006 NCSLI conference, pp 51–59
5. Lombardi MA, Novick AN, Boulanger JS, Pelletier R et al (2005) The Inter-American metrology system (SIM) common-view GPS comparison network. In: Proceeding of the 2005 IEEE frequency control symposium, pp 691–698
6. Xie G (2009) GPS principles and receiver design. Publishing House of Electronic Industry, Beijing, p 78(Ch)
7. Zhang H, Li X, Xu L, Xue Y (2011) Research on method of clock difference correcting for GNSS time difference monitoring receiver. Chinese second navigation academic symposium, p 836 (Ch)
8. Yuping G, Sujuan Q (2008) Performance test of GPS/GLONASS time transfer receiver NTSCGNSS-2. J Time Freq 31(1):3

Chapter 43
Use of the Global Navigation Satellite Systems for the Construction of the International Time Reference UTC

Z. Jiang and E. F. Arias

Abstract The International Bureau of Weights and Measures (BIPM) has the mandate to generate and distribute the international time scales Coordinated Universal Time (UTC) and International Atomic Time (TAI). About 400 atomic clocks belonging to national timing laboratories world-wide are used to generate UTC/TAI at the BIPM. Clock comparison is the key issue in the generation of any international time scale based on individual clock readings. Considering that in the case of UTC the clocks are located in remote laboratories, the use of time and frequency transfer techniques is necessary. Time transfer by Global Navigation Satellite System (GNSS), at present consisting mainly of the American GPS and the Russian GLONASS, constitutes the major technique used in the computation of UTC/TAI. To enable higher accuracy and robustness, a multi-system strategy is indispensable. Combined GPS and GLONASS time transfer has already been implemented at the BIPM with excellent results. In the near future it will be desirable to incorporate the Chinese BeiDou and the European Galileo systems in the computation of UTC/TAI. The GNSS time and frequency transfer is completed with another spatial technique, the Two-Way Satellite Time and Frequency Transfer (TWSTFT), that is completely independent of GNSS. In this paper, we present the applications of GNSS to accurate time and frequency transfer; we describe new data processing techniques such All in View (AV), Precise Point Positioning (PPP) and combined multi-system solutions; we analyze the corresponding uncertainties and introduce the BIPM's new projects.

Keywords UTC · TAI · Time and frequency transfer · GNSS · GPS · GLONASS

Z. Jiang (✉) · E. F. Arias
International Bureau of Weights and Measures (BIPM), Pavillon de Breteuil,
Sèvres Cedex F-92312, France
e-mail: zjiang@bipm.org

J. Sun et al. (eds.), *China Satellite Navigation Conference (CSNC) 2013 Proceedings*, Lecture Notes in Electrical Engineering 245,
DOI: 10.1007/978-3-642-37407-4_43,

43.1 Introduction

A practical time scale has two essential elements: a realization of the unit of time and a continuous temporal reference. The time scale that provides the international reference is Coordinated Universal Time (UTC) maintained at the International Bureau of Weights and Measures (BIPM) using data from about four hundred atomic clocks [1] (Fig. 43.1) and a dozen primary frequency standards (PFS) installed and maintained by over seventy national laboratories (Figs. 43.2, 43.5 and 43.7).

The continuous atomic time is in fact International Atomic Time TAI; since it does not keep in step with the slightly irregular rotation of the Earth, UTC was defined in 1972 as a time scale which is identical to TAI except that from time to time a leap second is inserted to ensure that, when averaged over a year, the Sun crosses the Greenwich meridian at noon UTC to within 0.9 s. The dates of application of the leap second are decided by the International Earth Rotation and Reference Systems Service (IERS). While TAI can only provide a reference for frequency, UTC is the reference for world-wide time coordination. The metrological characteristics of UTC and TAI are identical.

The stability of TAI is assured by a judicious way of weighting the participating clocks and by an adequate model for predicting their frequencies. The scale unit of TAI is kept as close as possible to the SI (the International System of Units) second by using primary frequency standards data [1] (PFS, Figs. 43.2 and 43.3).

Fig. 43.1 Industrial Cs tube clock (*left*) and H-maser clock (*right*) with the stabilities respectively 10^{-14} and 10^{-15} in frequency or correspondingly 1 and 0.1 ns in time in one day

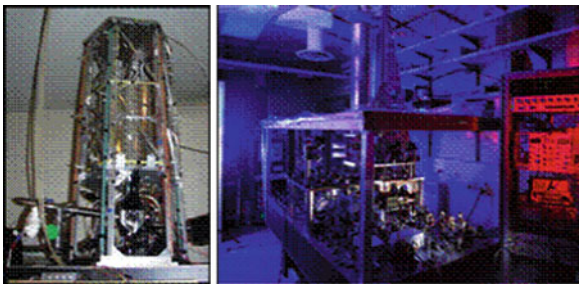

Fig. 43.2 Cs fountains at LNE-SYRTE in France (*left*) and NIST in USA (*right*) with the stabilities respectively 10^{-16} per 10-day in frequency or correspondingly 10 ps in time in one day

Standard	Period of Estimation		d	uA	uB	ul/Lab	ul/Tai	u	Ref(uB)	uB(Ref)	Note
PTB-CS1	56229	56259	-3.03	6.00	8.00	0.00	0.07	10.00	T148	8.	(1)
PTB-CS2	56229	56259	-8.62	3.00	12.00	0.00	0.07	12.37	T148	12.	(1)
NIST-F1	56229	56254	0.01	0.32	0.31	0.21	0.23	0.54	T214	0.35	(2)
NPL-CsF2	56224	56254	-0.36	0.20	0.23	0.04	0.20	0.36	T284	0.23	(3)
SYRTE-FO1	56229	56259	-0.17	0.30	0.43	0.11	0.20	0.57	T227	0.72	(4)
SYRTE-FO2	56234	56259	-0.52	0.40	0.33	0.12	0.23	0.58	T227	0.65	(4)
PTB-CSF1	56224	56244	0.04	0.14	0.74	0.10	0.09	0.77	T162	1.40	(5)

Notes:
(1) Continuously operating as a clock participating to TAI
(2) Report 27 NOV. 2012 by NIST
(3) Report 23 NOV. 2012 by NPL
(4) Report 03 DEC. 2012 by LNE-SYRTE
(5) Report 03 DEC. 2012 by PTB

Fig. 43.3 Example of the primary frequency standard comparison for improving the accuracy of TAI in Sect. 43.4 of BIPM *Circular T 299*, with data from November 2012. Here *d* is the difference of a particular PFS to the weighted mean value

UTC is published monthly in BIPM *Circular T*, in which UTC is represented by the values of the differences [*UTC–UTC*(*k*)] (Fig. 43.4) [1]. UTC(*k*) is the local realization of UTC at laboratory *k*.

The BIPM is mandated to compute the international time scales UTC/TAI. The differences between clock readings are the basis of the construction of any composite time scale. In the case of UTC it consists on comparing clocks located at remote sites and developing strategies for accurate time transfer is one of the major tasks at the BIPM. These comparisons are implemented by using various techniques and methods of time and frequency transfer. In time metrology, the result of the comparison of clocks over the baseline between two remote laboratories is referred to as a "link". The progress in time and frequency transfer technology allows today to use different methods and techniques that in many cases provide

CIRCULAR T 299 ISSN 1143-1393
2012 DECEMBER 10, 15h UTC

BUREAU INTERNATIONAL DES POIDS ET MESURES
ORGANISATION INTERGOUVERNEMENTALE DE LA CONVENTION DU METRE
PAVILLON DE BRETEUIL F-92312 SEVRES CEDEX TEL. +33 1 45 07 70 70 FAX. +33 1 45 34 20 21 tai@bipm.org

1 - Coordinated Universal Time UTC and its local realizations UTC(k). Computed values of [UTC-UTC(k)] and uncertainties valid for the period of this Circular.
From 2012 July 1, 0h UTC, TAI-UTC = 35 s.

Date 2012 0h UTC / MJD / Laboratory k	OCT 29 56229	NOV 3 56234	NOV 8 56239	NOV 13 56244	NOV 18 56249	NOV 23 56254	NOV 28 56259	Uncertainty/ns uA	uB	u	Notes
				[UTC-UTC(k)]/ns							
AOS (Borowiec)	-2.3	-3.5	-5.0	-5.0	-5.1	-5.8	-6.5	0.3	5.3	5.3	
APL (Laurel)	-143.4	-358.2	-57.0	-7.9	-23.0	-19.2	-15.8	0.3	5.3	5.3	
AUS (Sydney)	423.5	424.8	437.0	425.8	420.7	418.1	422.6	0.3	5.2	5.2	
BEV (Wien)	26.7	28.7	27.3	25.3	31.6	33.0	35.9	0.3	3.4	3.4	
BIM (Sofiya)	1728.6	1738.2	1742.7	1754.6	1764.5	1784.5	1788.5	1.5	7.2	7.3	
BIRM (Beijing)	248.1	245.0	241.4	236.3	240.9	239.9	242.3	1.5	20.1	20.1	
BY (Minsk)	35.0	24.1	15.5	11.1	6.2	-1.2	-6.7	1.5	7.2	7.3	
CAO (Cagliari)	-	-	-	-	-	-	-				
CH (Bern)	-4.5	-0.1	4.5	6.1	9.4	12.7	4.6	0.3	1.9	1.9	

Fig. 43.4 Excerpt of the table containing values of [*UTC–UTC*(*k*)] in Sect. 43.1 of the BIPM *Circular T 299*, with data from November 2012

redundant results over a baseline. Examples of this are laboratories that have multi-GNSS reception, enabling the calculation of the time link by GPS and GLONASS and in the future also by Galileo and BeiDou.

GNSS clock comparison is re-enforced by the use of two-way satellite time and frequency transfer (TWSTFT). This is an independent technique that allows remote clock comparisons through a telecommunication satellite.

The BIPM organizes and maintains the international network of time links, see Fig. 43.5. By the end of year 2012, 72 national time and frequency (T/F) laboratories contribute to the maintenance of UTC. All the contributing laboratories are linked to a unique pivot for clock comparison; it is the Physikalisch-Technische Bundesanstalt (PTB) in Germany. This single pivot comparison structure has been in use since 2006 when the Consultative Committee for Time and Frequency (CCTF) approved to change from GPS Common View (CV) [2] to GPS All-in-View (AV) time comparisons [3].

In the following sections, we describe the evolution of GNSS T/F comparisons during the last 15 years, their role and the uncertainty that characterizes the time links used for the generation of UTC. We conclude by a brief overview of promising T/F transfer techniques.

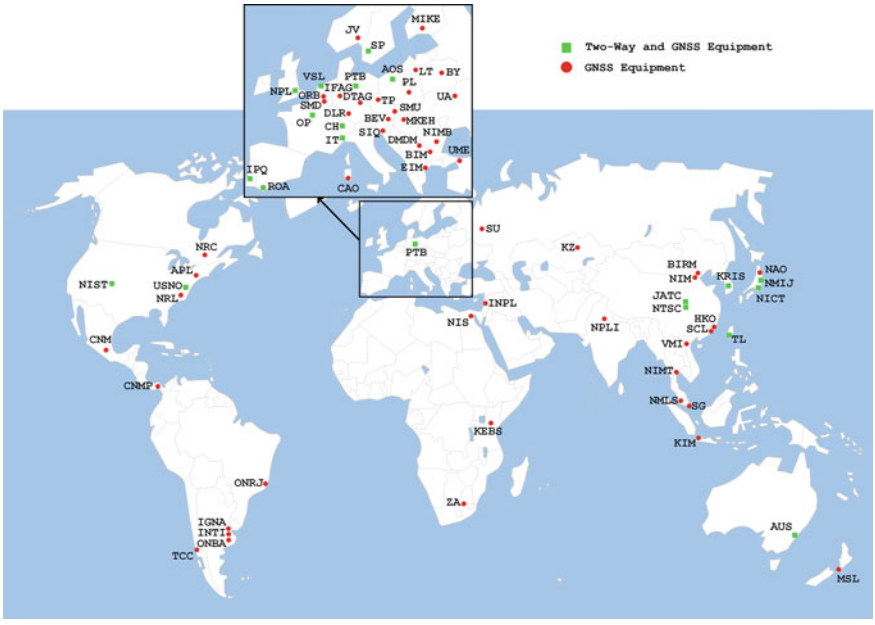

Fig. 43.5 Geographical distribution of the 72 national time laboratories that contribute to UTC

43.2 GNSS Techniques Used in the Generation of UTC

During the past three decades, GNSS has been used in modern timing metrology and is still the most used technique. The GPS constellation was the only in use for time comparisons over more than twenty years. Only since 2009 GLONASS observations were incorporated to clock comparisons for UTC, and finally a combination of both GPS and GLONASS links proved to give satisfactory results. In 2009 and 2011 respectively the GPS PPP method (Precise Point Positioning) [4] and a combination of GPS and TWSTFT were introduced in *Circular T* [5].

The GNSS observables cover the C/A (GPS) and L1C (GLN) codes, the precise P3 codes [6] and the carrier phase (CP). The type A (statistical) uncertainty (u_A) of the time links has decreased more than one order of magnitude from 3–5 ns in 2000 to 0.3 ns in 2009, cf. Fig. 43.8, 43.9 and [1]. This improvement was achieved in successive steps due to different causes; before Selective Availability (SA) in the broadcast GPS time (GPST) was switched off in May 2000, the noise in the intermediate system time was greater than 30 ns. Considerable improvement became possible thanks to the products provided by the International GNSS Service (IGS); the IGST (IGS time, a more stable realization of the GPST) replaced the GPST as the common reference for all-in-view clock comparison. Table 43.1 shows the evolution of the impact of the progressive improvements in the system times during the last one and half decades.

An important step in the generation of UTC was the change from GPS common view (CV) [2] to GPS All-in-View (AV) [3], see Fig. 43.6. Until 2006, CV was used in all the GPS links (note that only GPS was in use at that epoch). CV requires simultaneous observation of a satellite from two remote laboratories on the Earth so as to cancel the common errors in the GNSS signals, which were the dominant error sources in the past. For a very long distance baseline, one or even two intermediate laboratories are needed to establish a comparison, as illustrated in the left plot of Fig. 43.6. For the very long baseline between AUS (in Australia) and PTB (in Germany), NICT (in Tokyo region) served as a bridge. In consequence extra error sources were added into the total link uncertainty. Therefore, the quality of the final link also depends on the intermediate measurements. Since the beginning of the 21st century, dual frequency multi-channel receivers have been in widespread use to allow the ionosphere delay to be measured. Meanwhile IGS provides precise GNSS satellite ephemeredes and clock corrections. The most

Table 43.1 Impact on GPST and IGST due to selective availability (SA) and measurement noise

Circular T #	Year/month	σ/ns	Note
T 97	1996 January	30–55	GPST/SA on
T 150	2000 May 3	6	GPST/SA off
T 199	2004 July	1.8	IGST/CA
T 299	2012 December	0.7	IGST/P3
T 299	2012 December	0.3	IGST/PPP

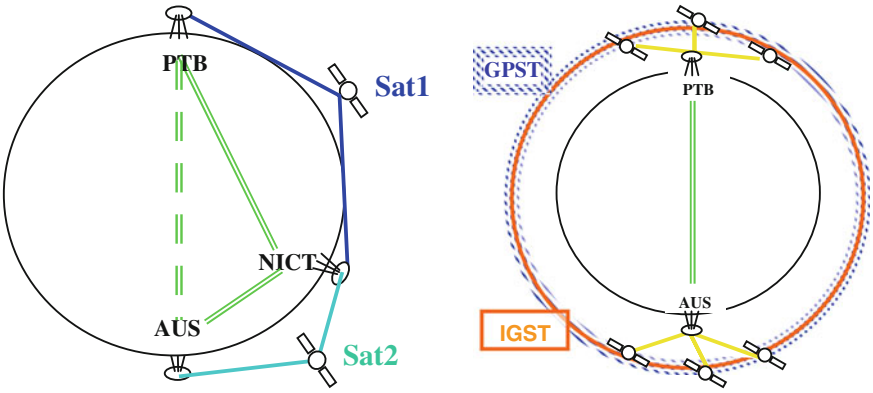

Fig. 43.6 Illustration of time and frequency transfer between the AUS in Australia and the PTB in Germany using the CV (*left* bridged by the NICT in Japan) and the AV (*right* direct without bridging)

important error sources disturbing the GNSS links are hence greatly reduced and CV has lost its advantages. AV does not require the geometric conditions required by CV. In AV the local reference is compared directly to the precise IGST using all the available satellites in view (right plot in Fig. 43.6). Compared with CV, the advantages of AV are obvious, especially for long distances. T/F transfer can be performed directly between any two remote laboratories on the Earth and the stabilities in the links are therefore considerably improved. Intermediate bridges are no longer necessary and the network becomes a single pivot system.

GNSS PPP is a natural extension of the AV code links where the carrier phase (CP) data are used. The CP measurements are two orders of magnitude more precise than the code data, much less sensitive to multi-path, and allow a better estimate of the atmospheric effects. By fully using CP, precise satellite orbits and clock corrections evaluated by IGS, we can obtain the differences between a ground clock and the IGST reference with utmost precision. Combining the precise CP and accurate code measurements provides very good short- and long–term stabilities. GPS PPP has been used in *Circular T* computation since September 2009. The Time Deviations of the best PPP links may achieve 100 ps or lower within hours, heralding a new era of precise UTC clock comparisons.

On the other hand, GLONASS has been developed in parallel with GPS. The first GLONASS satellite was launched in 1982 and the system became operational several years afterwards. Efforts to introduce this system into the generation of UTC began in the early 1990s [7, 8]. In 2005, the BIPM proposed an operational method to enable GLONASS to be used for UTC generation [9]. In 2009, the GLONASS satellite constellation was complete and the more GLONASS multi-channel timing receivers were available. The CCTF recommended the use of multi-techniques in time transfer to ensure precision, accuracy and robustness in UTC. To complement existing GPS and TW links, the first two GLONASS time links were introduced into the UTC time link network in November 2009 [9]. As in

January 2013 six GLONASS time links are used in UTC computation. This is a benchmark of the beginning of the era of multi-GNSS time transfer in the history of UTC. The use of GLONASS PPP is currently under investigation.

Until the end of 2010, a unique technique of time transfer was used for the computation of *Circular T*. The choice was made following the order of priority imposed by the quality of a link; TW first, followed by GPS PPP, GPS P3, GPS C/A or GLN L1C codes. Many of the laboratories contributing to UTC operate more than one time transfer technique, resulting in a rich redundancy in the UTC time link. All the major laboratories support practically all three main satellite systems: TW, GPS and GLONASS. How to profit from this redundancy for UTC generation was a challenge. The studies in [9] and [5] proved the advantage of combining different techniques. Two kinds of combination, GPS + GLN code and TW + GPS PPP code and phase combination are applicable. Since *Circular T* 277 in January 2011, combined links have been used in the UTC regular computation [1, 5, 9]. At present there are 16 combined links which account for nearly a quarter of the total UTC links, which in turn support more than two thirds of the clock weight and all the primary frequency standards (Figs. 43.4 and 43.7). The main advantages of the combined links are: (1) to provide better robustness due to the independence between GPS, GLONASS and TW; (2) to repair the disruptions in the raw measurement data, such as gaps, jumps, discontinuities and drift in the links; (3) in the case of the TW + GPS PPP to keep accurate TW calibration and precise GNSS CP short-term stability and still reduce the diurnal signal present in TW links; (4) to fully use the existing redundancy. Briefly, the multi-technique combination has proven to be an effective strategy to improve UTC and the BIPM will continue to use it.

An estimation of the short-term stability or of the measurement precision of the links can be obtained in different ways: by smoothing residual analysis, through the Time Deviations and by comparisons of the different links. We present in Table 43.2 statistical results of different links on the baseline OP-PTB (Paris-Braunschweig). Comparisons between the links obtained using the different techniques over the common-clock baselines allow a better understanding of the uncertainty and the advantages of the combinations of the different links without the influence of clock noise.

The values of the u_A uncertainties of the time links are updated in *Circular T* individually whenever necessary. However, a new estimation of the u_A was carried

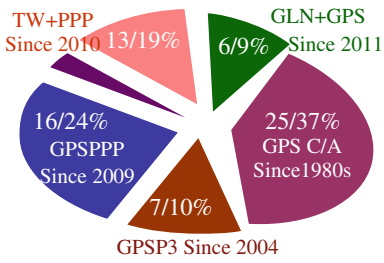

Fig. 43.7 Status of time comparisons for UTC (end of 2012)

Table 43.2 Statistics of all link types and the link differences (dL = Lk2-Lk2 corresponding to the non-diagonal elements) on baseline OP-PTB (over 15 months between July 2010 and September 2011. u_A is the type A uncertainty; u_A': standard uncertainty of the dL; σ: standard deviation of the dL; σ: standard deviation of the Vondrak smoothing residuals of a link; TDev/τ': time deviation corresponding to the averaging time τ' indicating the flicker PM segment)

Lk1 \ Lk2	1 TW		2 TW+PPP		3 GPS+GLN		4 C/A		5 P3		6 PPP		7 GLN	
TW u_A σ TDev/τ	1	/ns 0.5 0.710 0.40/2h												
TW+PPP u_A/u_A σ/σ TDev/τ	2	0.6 0.664	/ns 0.3 0.429 0.25/2h											
GPS+GLN u_A/u_A σ/σ TDev/τ	3	1.3 1.078	1.3 0.852	/ns 1.2 1.066 0.81/10h										
C/A u_A/u_A σ/σ TDev/τ	4	1.6 1.253	1.6 1.109	2.0 0.117	/ns 1.5 1.154 0.95/10h									
P3 u_A/u_A σ/σ TDev/τ	5	0.9 0.886	0.8 0.669	1.4 1.077	1.7-2.6 0.605	/ns 0.7 0.744 0.7/10h								
PPP u_A/u_A σ/σ TDev/τ	6	0.7 0.756	0.5 0.705	1.3 1.161	1.6-2.6 1.042	0.8 0.566	/ns 0.3 0.176 0.31/2h							
GLN u_A/u_A σ/σ TDev/τ	7	1.6 1.135	1.6 0.968	2.0 0.186	2.2 0.277	1.7 0.897	1.6 1.027	/ns 1.5 1.180 0.94/10h						

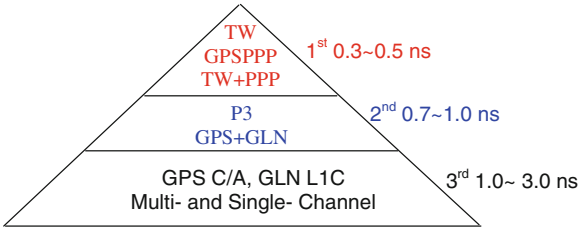

Fig. 43.8 The three groups resulting from the 2011 re-evaluation of the u_A values

out globally, for all time links at the end of 2011 and introduced in BIPM *Circular T*. The UTC links can be roughly divided into three groups depending on the values of u_A: the u_A of the first group is between 0.3–0.5 ns; the second 0.7–1 ns and the third 1–3 ns, see Fig. 43.8.

The type B uncertainty (u_B) is represented by the calibration uncertainty. Until present, the calibration of GNSS receiving equipment has been organized by the BIPM. We have established four categories depending on the values of u_B (cf. Fig. 43.9): the first is $u_B = 1$ ns for certain TW links. These are calibrated by employing the transportable TW calibration station performed by a commercial company; the second is $u_B = 5$ ns for some GNSS receivers, with relative calibrations performed by using the BIPM traveling standard receivers; the third is $u_B = 7$ ns also for GNSS where the calibrations are made by the receiver manufacturer and the fourth $u_B = 20$ ns when the relevant receiver has not been

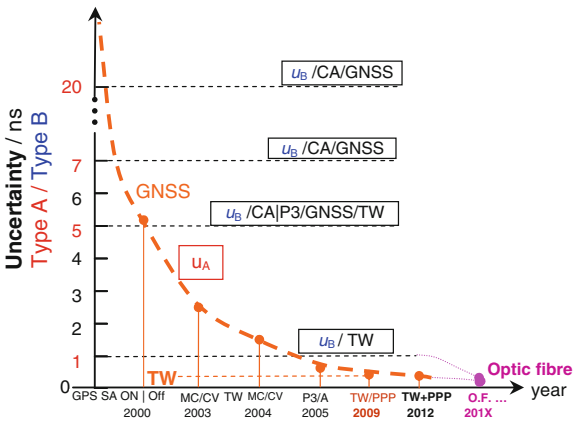

Fig. 43.9 Evolution of the Type A uncertainty and the present Type B uncertainty

calibrated. A BIPM pilot study currently underway aims to reduce the u_B to lower than 2 ns for the UTC time links.

43.3 Future Outlook

Accurate and precise time and frequency transfer have been ceaselessly developed due to the introduction of new techniques. It is anticipated that in the near future the Chinese BeiDou and the European Galileo GNSS will be used in the computation of UTC/TAI. Both are basically similar to GPS and GLONASS. Hopefully, their data will be used directly in the UTC/TAI computation as soon as the relevant receivers are available to output the measurement data in the standard formats, i.e., CCTF CGGTTS or IGS RINEX conventions. New frequency, new CP and code observables supported by new and more satellites suggest significant amelioration in T/F transfers: a few parts of 10^{-16} in days in frequency and subnanosecond in time are predicted.

Using telecommunication satellites and CP plus code data, TW potentially allows T/F transfer of a few parts of 10^{-16} in one day in frequency and 0.1 ns in time.

A promising technique which is progressing very quickly is the optical fibre link. Some successful experiments, up to 900 km in distance, have demonstrated encouraging results: 10^{-18} in frequency within one day. Type B uncertainty below 100 ps was reported in some experiments.

The European Space Agency (ESA) mission Atomic Clock Ensemble in Space (ACES) onboard the International Space Station which is programmed to be launched in 2016 [10] will allow the next generation of TW T/F transfers. It is expected to achieve a stability of 1 ps with an accuracy of 0.1 ns in time and a corresponding stability of 10^{-17} in frequency in one day.

43.4 Summary

Seventy two national time and frequency (T/F) laboratories located world-wide contribute to the generation of the UTC/TAI using data from around four hundred atomic clocks and a dozen primary frequency standards.

GNSS is the major tool for clock comparison and contributes to all the T/F links. As can be seen in the Fig. 43.9, during the last decade, the type A uncertainty reduced significantly from 3–5 ns to 0.3 ns, thanks to the new methods introduced. The present strategy consists in enhancing clock comparison for UTC/TAI by using all available techniques, including also the combinations of the different techniques. A major challenge to further improve the accuracy of UTC is in reducing the uncertainty of the GNSS calibrations.

In addition to GPS and GLONASS, the Chinese BeiDou and the European Galileo systems are the most promising techniques and are forecast to make indispensable contributions to UTC/TAI generation in future years.

Optical fibre links will also contribute significantly to T/F transfers for comparison of optical clocks.

Finally, complementing the monthly *Circular T*, the BIPM Time Department supplies other products. To view these products visit the BIPM web page: http://www.bipm.org/jsp/en/TimeFtp.jsp, cf. also [11] for more information about UTC/TAI time links and the link comparisons.

References

1. BIPM *Circular T* 299 Dec (2012) ftp://ftp2.bipm.org/pub/tai/publication/cirt.299
2. Allan D, Weiss MM (1980) Accurate time and frequency transfer during common-view of a GPS satellite. In: Proceedings of 1980 frequency control symposium, Philadelphia, pp 334–356
3. Jiang Z, Petit G (2005) Time transfer with GPS all in view. In: Proceedings Asia-Pacific workshop on time and frequency, pp 236–243
4. Petit G, Jiang Z (2008) Precise point positioning for TAI computation. Int J Navig Obs, Article ID 562878:8
5. Jiang Z, Petit G (2009) Combination of TWSTFT and GNSS for UTC time transfer. Metrologia 46:305–314
6. Peng H, Liao C (2004) GPS smoothed P3 code for time transfer. In: Proceedings of EFTF 2004, pp 137–141
7. Daly P, Koshelyaevsly NB, Lewandowski W, Petit G, Thomas C (1993) Comparison of GLONASS and GPS time transfer. Metrologia 30:89–94
8. Lewandowski W, Azoubib J, Klepczynski WJ (1999) GPS: primary tool for time transfer. Proc IEEE 87(1):163–172
9. Jiang Z, Lewandowski W (2011) Use of GLONASS for UTC time transfer. Metrologia 49:57–61. doi:10.1088/0026-1394/49/1/009
10. ESA mission ACES (2011) http://www.esa.int/Our_Activities/Human_Spaceflight/Human_Spaceflight_Research/Atomic_Clock_Ensemble_in_Space_ACES
11. Arias EF et al (2005) BIPM Comparison of time transfer techniques. In: Proceedings of FCS/PTTI 2005

Part III
Integrated Navigation and New Methods

Chapter 44
Research and Implementation of Ambiguity Resolution for Combined GPS/GLONASS/COMPASS Positioning

Xiaoyu Shi, Benyin Yuan and Zhixiong Bao

Abstract As GLONASS and COMPASS systems are approaching their full constellations, and more Galileo satellites are to be launched, the need of combined positioning is increasing quickly. For high precise applications, data preprocessing and ambiguity resolution are the most important parts. Because Code Division Multiple Access technology is applied by both GPS and COMPASS, so the current data processing methods are also suitable for combined GPS/COMPASS positioning, but for GLONASS the cycle slip detecting and ambiguity resolution will biased by satellite wavelength differences because the Frequency Division Multiple Access technology. To solve this problem, a single difference phase observable differenced in time is proposed in this paper. With a majority voting procedure using the observable residuals from all the satellites we can detect and mark satellites obviously suffering from a cycle slip and "clean" satellites, then fixed the cycle slip using the receiver clock term computed by "clean" satellite. Iterative search approach is applied in ambiguity resolution. One double differenced ambiguity is fixed to integer according to the specified criteria in each iteration until all double differenced ambiguities are fixed. The data experiment shows that even one cycle of slip can be detected and fixed and ambiguities can be resolved correctly.

Keywords GPS · GLONASS · COMPASS · Combined positioning · Difference in time · Cycle slip · Ambiguity

X. Shi (✉) · B. Yuan · Z. Bao
Hi-Target Surveying Instruments Co. Ltd, GuangZhou, China
e-mail: sweetrain2008@163.com

J. Sun et al. (eds.), *China Satellite Navigation Conference (CSNC) 2013 Proceedings*, Lecture Notes in Electrical Engineering 245,
DOI: 10.1007/978-3-642-37407-4_44,

44.1 Introduction

With the 16th COMPASS satellite launched on October 2012, the COMPASS system network in the Asia–Pacific region has been completed, at the same time GLONASS system reached full constellation, experimental Galileo satellite has been lifted off, it is widely known that the combination of multiple GNSS constellations for positioning will be a future trend. Compared to a single system, multi-system positioning has efficiency advantages in terms of continuity, availability, reliability, accuracy, can greatly improve the usability, precise integrity and reliability of the user by the advantage of wealthy navigation information [1].

Although the combination of multi-system positioning make satellite positioning and navigation applications more widely, it also faces a number of challenges: the COMPASS system with GPS system using code division multiple access technology, the GPS processing technology is equally applicable to the GPS/COMPASS combination positioning; but the GLONASS system uses frequency division multiple access system, each satellite has different carrier frequency, so original cycle slip detection methods (such as triple differential method) and ambiguity resolution would be effected by the wavelength difference between the satellites. Therefore, how to weaken or eliminate the impact of the wavelength differences between GLONASS satellites is the key point in the relative positioning with the combined GPS/GLONASS/COMPASS constellations. The data preprocessing especially ambiguity resolution of GPS/GLONASS/COMPASS is studied and a data processing method suitable for multi-system applications is proposed in this paper, through the implementation of the new method into our commercial software. The corresponding results are obtained and presented here.

44.2 Cycle-Slip Detection and Repair

44.2.1 Triple Difference Cycle-Slip Detection

In GPS relative positioning, the triple difference carrier phase observations are commonly used to the detection and repair of cycle slip. Triple difference observations eliminate the initial ambiguity and avoid constant value for the integer cycles after slip occurs and almost eliminate the clock error and common error terms of two stations. The ionospheric delay, tropospheric delay and multipath error are also considerably weakened after differencing for shorter baseline. So the triple difference model can be used to obtain the initial position to fix the ambiguities and cycle slip detection. Through examine the triple difference observation residuals based on initial baseline solution after adjustment, we can use the triple difference observation residuals changes to detect and repair cycle slips.

Triple difference observation model can be expressed as:

$$\begin{aligned}\nabla\Delta\varphi_{ij}^{pq}(t_1,t_2) &= \nabla\Delta\varphi_{ij}^{pq}(t_2) - \nabla\Delta\varphi_{ij}^{pq}(t_1) \\ &= \nabla\Delta\rho_{ij}^{pq}(t_1,t_2) + \lambda^p b^p - \lambda^q b^q\end{aligned} \tag{44.1}$$

with:

$$\begin{aligned}b^p &= N_{ij}^p(t_2) - N_{ij}^p(t_1) \\ b^q &= N_{ij}^q(t_2) - N_{ij}^q(t_1)\end{aligned}$$

Residual can be expressed:

$$\delta\nabla\Delta r = \lambda^p b^p - \lambda^q b^q \tag{44.2}$$

For data without cycle slip, $\delta\nabla\Delta r$ should be a small value, but if the observation exists cycle slips, residual will result in great changes. We can think observations exist cycle slips when this change large than a certain limit. But for same cycle slip occurs both on base station and rover station, this method also can't accurate detecting.

For GPS, $\lambda^p = \lambda^q$, the only requirement is the double difference phase observations without cycle slip effect, we do not need to determine which satellite suffers cycle slip; but for GLONASS as different satellite has different signal wavelength, so after the cycle slip detection, we can eliminate its influence only if the satellite can be indicated exactly, so triple difference method can't detect and repair GLONASS satellites cycle slips [2].

44.2.2 Single Difference Phase Observable Differenced in Time

We form a new type of difference starting from the single difference phase observable:

$$\Delta\varphi_{ij}^p(t_1,t_2) = \Delta\rho_{ij}^p(t_1,t_2) + c\cdot\Delta t_{ij}(t_1,t_2) \tag{44.3}$$

with:

$$\begin{aligned}\Delta\varphi_{ij}^p(t_1,t_2) &= \Delta\varphi_{ij}^p(t_2) - \Delta\varphi_{ij}^p(t_1) \\ \Delta\rho_{ij}^p(t_1,t_2) &= \Delta\rho_{ij}^p(t_2) - \Delta\rho_{ij}^p(t_1) \\ \Delta t_{ij}(t_1,t_2) &= \Delta t_{ij}(t_2) - \Delta t_{ij}(t_1)\end{aligned}$$

called a single difference phase observable "differenced in time". The residuals derived from the observation type (44.3) may be interpreted as sum of a possible cycle slip and the change of the receiver clock in the time interval, neglecting other error sources. We may thus write:

$$\Delta r_{ij}^p(t_1,t_2) = \lambda^p\cdot b^p + c\cdot\Delta t_{ij}(t_1,t_2) \tag{44.4}$$

This residual can be expressed in cycles of satellite i and shows the integer nature of the cycle slip, but it is biased by the receiver clock change. If the receiver clock change would be known to a few cm, Eq. (44.4) could be used directly to detect cycle slips. The receiver clock term derived from code measurements (single point positioning) shows an error of a few nanoseconds or some tens of cycles (a few 0.1 μs or some hundreds of cycles) and is certainly not good enough.

44.2.3 Cycle Slip Detection Algorithm

We have seen in Sect. 44.2.1 that the triple difference cannot be used to detect all possible cycle slips and to correct them on the single difference level. However, the single difference residuals "differenced in time" (44.4) may be used to detect a cycle slip on the single difference level by computing:

$$b^p = \frac{\Delta r_{ij}^p(t_1, t_2) - c \cdot \Delta t_{ij}(t_1, t_2)}{\lambda^p} \tag{44.5}$$

But it requires the receiver clock change is known exactly. In order to keep the receiver clock term smaller than 0.1 cycles, the receiver clock change has to be determined with a precision of 6×10^{-11} s (or a few cm in units of length). In order to achieve this purpose, we first calculated all satellite single difference phase observable "differenced in time" of each epoch, then use a majority vote procedure we detect and mark satellites obviously suffering from a cycle slip and "clean" satellites and then calculate the receiver clock change using clean satellite:

$$\Delta\bar{t}_{ij}(t_1, t_2) = \frac{\sum_{i=1}^{n} \Delta r_{ij}^p(t_1, t_2)}{n \cdot c} \tag{44.6}$$

New ambiguities for all satellites are introduced if the number n of "clean" satellites is lower than two. Using Eq. (44.5) for each satellite with the receiver clock estimate $\Delta\bar{t}_{ij}(t_1, t_2)$ the cycle slip is:

$$b^p = \frac{\Delta r_{ij}^p(t_1, t_2) - c \cdot \Delta\bar{t}_{ij}(t_1, t_2)}{\lambda^p} \tag{44.7}$$

The data measurement proved this method can detect and repair more than one cycle slip, and at the same time, this method can be used for GPS and COMPASS and GPS/GLONASS/COMPASS combination observations.

44.3 Ambiguity Resolution

44.3.1 Mathematical Model

Traditional double difference observation model can be expressed as:

$$\begin{aligned}\nabla\Delta\varphi_{ij}^{pq} &= \nabla\Delta\rho_{ij}^{pq} + \lambda^p N_{ij}^p - \lambda^q N_{ij}^q \\ &= \nabla\Delta\rho_{ij}^{pq} + \lambda^p N_{ij}^{pq} + (\lambda^q - \lambda^p) N_{ij}^q\end{aligned} \tag{44.8}$$

For GPS and COMPASS system, since the code division multiple access technology is adopt, satellite wavelength equal for every satellite, the last term in Eq. (44.8) can eliminate, and the site the initial position and ambiguity floating solution can be acquired using the least square principle. Finally, with a certain ambiguity resolution methods (such as FARA, LAMBDA, etc.) to get the integer ambiguity, and then accurate three-dimensional site coordinates can be resolved [3].

Frequency division multiple access technology make the GLONASS satellite signals emitted at a different wavelength, when forming double difference observation equation a new single differential bias term $b_{SD} = (\lambda^q - \lambda^p)N_{ij}^q$ can't be eliminated. The single difference ambiguity and double difference ambiguity cannot be separated, the normal equation become singular. One solution is to use other information such as pseudorange to obtain single difference ambiguity:

$$N_{ij}^q = \frac{1}{\lambda_q}(R_{ij}^q - \lambda_q \varphi_{ij}^q) \tag{44.9}$$

With R_{ij}^q is the single differential pseudorange observation value. If we want to make the double difference ambiguity well fixed, its precision must be less than 0.1 cycles, the requirements of single difference ambiguity for different GLONASS satellites combination is showed on Table 44.1.

It is easy to see from the previous discussion that properly estimation of the Ambiguity greatly depends on the precision pseudorange observations. In many practical situation, however, pseudorange may be seriously biased by multipath and hardware delay. For example, a 5 m error in pseudorange can lead to an error of 26 cycles in single difference ambiguity. These errors can be negligible for the smaller wavelength difference satellite combination, but for the satellites combination with large wavelength difference the pseudorange accuracy will greatly affect the ambiguity resolution.

Table 44.1 GLONASS wavelength differences in cycles and maximum bias allowed for the single differences ambiguities

Satellite pare	Wavelength difference (cycle)	Maximum bias allowed
Min	0.000351	285
Max	0.00810	12

44.3.2 Ambiguity Resolution Algorithm

In view of that the single difference ambiguity has smaller effect on satellite combination with small wavelength difference, an iterative solution of the double difference ambiguity is adopted, one double ambiguity in each iteration step. A specific algorithm is as follows:

1. For n satellites n single difference ambiguities are set up as unknown parameters in the normal equation system, assuming that there are no breaks or problems in the data forcing us to set up additional ambiguities.
2. After introducing code observations to remove the singularity of normal equation system, single difference can be estimated as real values.
3. Using the estimated single difference ambiguities and their covariance matrix, all possible double difference ambiguities are computed with the corresponding formal errors.
4. After the computation of all possible double difference ambiguities and their formal errors, a first double difference ambiguity parameter with the smallest wavelength difference is fixed to an integer number, according to specified resolution criteria (such as FARA, LAMBDA, etc.) [4].
5. After fixing the first double difference ambiguity, one of the two single difference ambiguities involved in the double difference ambiguity may be eliminated from the normal equation system and go to the next iteration until n−1 double ambiguities is fixed to integer.
6. In the final solution the unresolved single difference ambiguities and the baseline components are estimated at the same time using the fixed double ambiguities.

Theories prove the above method is applicable to GLONASS and combined GPS/GLONASS/COMPASS solution applies to both the original and a combination of carrier phase observations [5].

44.4 Applications and Results

44.4.1 Software Implementation

According to the model, the author added and modified a number of modules on the basis of Guangzhou Hi-Target Survey Instruments Co. Ltd new version data processing software HGO (Hi-Target Geomatics Office), including cycle slip detection and repair, GPS/GLONASS/COMPASS ambiguity resolution, developed a software oriented multi-system data integration and processing. When processing the data, you can set a certain kind of system separately or set using a variety of systems integration to conduct relative positioning. The following testing and analysis of the measured data is based on new HGO software.

44.4.2 Results

As there is no multi-system baseline data, GPS/GLONASS and GPS/COMPASS experiments are implemented separately. The measured data is acquired by Hi-target Vnet6 and Vnet8 receiver. Vnet6 and VNet8 is CORS reference station receivers of GPS/GLONASS and GPS/COMPASS systems. GPS/GLONASS data collected in Hainan in November 13, 2012 and GPS/COMPASS data collected in Guangzhou in March 21, 2012 is adapted for example, the baseline length is 34.4 and 20.1 km, observation time span is two hours, the interval is 5 s, the total COMPASS satellites is 11 and average observed number is 8 during observing period. The baseline fixed solution reference value is the previous day's single-day solution results.

In order to fully evaluate the combination of relative positioning performance, two different programs is used based on the observation environment. The first program is the ideal observing environment, more than four satellites and geometry strength is good; the second program is the non-ideal observation environment, the number of observation satellites is few. In each program, three ways including independent positioning and combined positioning is used for data processing.

44.4.2.1 Ideal Environment Results

In ideal environment, Hainan and Guangzhou baselines processing results shown in Tables 44.2 and 44.3.

From Tables 44.2 and 44.3, we can see:

1. Independent positioning accuracy of GLONASS system is poor due to defects in the design and cannot meet the demand of relative positioning.
2. Under ideal conditions, the GPS/GLONASS combined positioning ratio value is lower than GPS, but the positioning accuracy is better than the standalone GPS, which is due to an increase in the number of satellites, space geometric distribution conditions improved.
3. COMPASS system has met the need of independent relative positioning and positioning accuracy is comparable with GPS. Under ideal conditions, as separate system has meet the requirements, positioning accuracy of combination of GPS/COMPASS is not significant improved, the advantage is not obvious.

Table 44.2 Comparison of relative positioning results in good environment in Hainan

System	Satellite number	Precision (mm)			Ratio	RMS (mm)
		X	Y	Z		
GPS	9	2.0	15.9	6.6	39.7	7.4
GLONASS	6	19.4	−37.1	−9.8	2.5	9.9
GPS/GLONASS	15	5.0	1.7	4.0	2.1	11.5

Table 44.3 Comparison of relative positioning results in good environment in Guangzhou

System	Satellite number	Precision (mm)			Ratio	RMS (mm)
		X	Y	Z		
GPS	8	0.7	−2.5	−2.2	26.4	10.9
COMPASS	8	−1.4	2.0	2.6	56.6	8.9
GPS/COMPASS	16	0.8	−1.6	−3.0	22.7	9.8

44.4.2.2 Non-ideal Environment Results

In many observations case, the user cannot guarantee continuously tracking many GNSS satellites, such as in urban areas with dense buildings or serious occlusion area, sometimes the number of satellites is too insufficient to positioning. In order to artificially simulate the harsh environment of observations, part of the GPS satellite and part of the COMPASS satellite as well as GLONASS satellite is disabled in HGO software respectively, only remaining four satellites to solve, and the results are shown in the following Tables. 44.4 and 44.5.

We can see that in the case of less simultaneous observing satellites the positioning accuracy of the single system descend sharply, especially GLONASS and COMPASS system. This may be because the satellite number is few, space geometric distribution is poor, wrong ambiguity resolution is likely to appear in this regard. In combined relative positioning the positioning accuracy is declined but still within the allowable range due to the large number of synchronous satellite, we can see the advantage of combination of GPS/GLONASS/COMPASS positioning performs well in non-ideal observing conditions.

Table 44.4 Comparison of relative positioning results in bad environment in Hainan

System	Satellite number	Precision (mm)			Ratio	RMS (mm)
		X	Y	Z		
GPS	4	−4.7	20.1	11.6	23.6	7.6
GLONASS	4	−23.5	62.3	13.9	1.9	9.6
GPS/GLONASS	8	2.2	16.3	10.4	6.3	9.6

Table 44.5 Comparison of relative positioning results in bad environment in Guangzhou

System	Satellite number	Precision (mm)			Ratio	RMS (mm)
		X	Y	Z		
GPS	4	10.1	−7.1	7.7	3.5	10.6
COMPASS	4	−13.8	20.4	10.1	1.6	8.3
GPS/COMPASS	8	−0.6	2.5	−3.5	26.3	9.9

44.5 Conclusions

The correctness and feasibility of the proposed relative positioning algorithm for combined GPS/GLONASS/COMPASS constellations have been demonstrated by our experimental results. The COMPASS system has been used to carry out relative positioning independently, but the latest COMPASS positioning results are not yet as good as the results from the GPS system because the low number of satellites and weak constellation distribution. In addition, independent GLONASS positioning is not an easy task. GPS/GLONASS and GPS/COMPASS combination for relative positioning have no obvious advantages compared to a single system under ideal observing conditions, but in non-ideal observing conditions the combined positioning approach can well enhance observing satellite geometry strength, thus improving reliability and accuracy significantly.

As the lack of multi-system baseline data, the multi-system data experiment didn't take in this article, so the effect of multi-system positioning accuracy still needs further discussion.

References

1. Yang YX (2010) Progress, contribution and challenges of Compass/Beidou satellite navigation system. Acta Geodaetica et Cartographica Sinica
2. Zhang Y, Xu S, Wang Z, Zhang X (2001) Ambiguity processing approach in combined GPS/GLONASS positioning. Editorial Board of Geomatics and Information Science of Wuhan University
3. Rolf D, Urs H, Pierre F, Michael M (1996) Bernese GPS software version 5.0. Astronomical Institute University of Berne
4. Teunissen PJG, Verhagen S (2004) On the foundation of the popular ratio test for GNSS ambiguity resolution. In: Proceedings of ION GNSS-2004, The Institute of Navigation, Fairfax, VA, pp 2529–2540
5. Habrich H (1999) Geodetic applications of the global navigation satellite system (GLONASS) and of GLONASS/GPS combinations. Astronomical Institute, University of Berne, Switzerland

Chapter 45
A New Celestial Positioning Model Based on Robust Estimation

Chonghui Li, Yong Zheng, Zhuyang Li, Liang Yu and Yonghai Wang

Abstract A large field of vision (FOV) star sensor can be used to image multiple celestial bodies at the same time, and then through center extraction of the star point and star patterns matching to realize navigation and positioning. The FOV based method has gradually become the main way of celestial navigation. However, in the process of center extraction, mistakenly identifying image noise as the star point and encountering some abnormal coordinate errors are inevitable. Meanwhile, in the process of star patterns matching, wrong matches are always encountered too. To solve these problems, this paper introduces the Robust Estimation for the first time, and based on it a celestial positioning model is established. The experiment shows that the model can effectively exclude the impact of noise and wrong patching, limit the abnormal observations, and take full advantage of high-precision observation information, by which positioning accuracy is increased from 4.05″ to 1.15″.

Keywords Robust estimation · Celestial navigation · Equal weights · Positioning

Assistance Information: Nature science funds (41174025, 41174026), Shanghais Aerospace Navigation and Positioning Technology Key Laboratory Open Fund (0901), Accuracy PNT Key Laboratory Open Fund (2012PNTT07), Zhengzhou Institute of Surveying and Mapping Fund (Y1101).

C. Li (✉) · Y. Zheng · Z. Li · Y. Wang
Zhengzhou Institute of Surveying and Mapping, HeNan 450052, China
e-mail: lichonghui6501@126.com

L. Yu
Zhengzhou Institute of Surveying and Mapping, 61363 Troops,, Xi an 710054, China

J. Sun et al. (eds.), *China Satellite Navigation Conference (CSNC) 2013 Proceedings*, Lecture Notes in Electrical Engineering 245,
DOI: 10.1007/978-3-642-37407-4_45,

45.1 Introduction

Celestial navigation is a kind of technique and method which uses sun, moon, stars and other natural objects as navigation beacons. Taking the celestial horizon coordinates (azimuth or height) of such objects as observations, it could finally determine the geographical position (or space position) and orientation of the station [1, 2]. It has the advantages of simple equipment, not easy to be disturbed, and the positioning error doesn't accumulate over time. So it is an important way of autonomous navigation. Early celestial navigation mainly used in sailing, which utilize the sextant for manual observation, and the International Maritime Organization (IMO) also explicitly provides that mariners must have the ability to use celestial bodies to determine the ship's position in "STCW78/95 Convention" [3, 4]. Celestial navigation equipment has gradually developed into a star sensor with large field of vision, which can image multiply celestial body at the same time, and then realize navigation and positioning through solve integrated information of the image coordinates of celestial bodies, the imaging time and the theoretical position of celestial bodies. Correspondingly, the application range of celestial navigation was extended from sailing to land, aerospace and other fields [3].

The image acquired from the large FOV star sensor generally contains dozens of stars or even hundreds of stars. When use it to realize positioning, first need to extract the star point in the image by the star point extracting algorithm, to calculate the coordinates of star center by gradation weighting or other algorithm. Secondly, need to match the stars in image with the known stars in star catalogue according their image coordinates, to identify their star series number and calculate their theoretical apparent position depending on location. Finally, celestial navigation and positioning could be realized by comprehensive utilization of the coordinates of the center of the star point and the corresponding theoretical apparent position. However, such circumstance like mistakenly identify image noise as a star and too large abnormal coordinates errors are widely exist when extract the center of the star point. Meanwhile, wrong match is also frequently occurs in the star matching process. Unfortunately, those existing algorithms cannot effectively solve these problems. The paper introduces robust estimation for the first time, which will assigning zero weights to the wrong match stars and noise observations, carried down the weights for those large error observations, and will take full advantage of the high-precision observation information to improve navigation and positioning accuracy.

45.2 Robust Estimation

45.2.1 Fundamental

Robust Estimation stems from the concept of statistical robustness, it is proposed for least squares estimation which does not have the characteristic of the anti-interference. Its principle is to take full advantage of effective information, limit the use of useful information and exclude harmful information, to obtain a more reliable, effective and meaningful parameter estimates under the assumed model, it is a estimation which can both relief the affect of outlier and has a high efficiency [5–9]. Set error equation as:

$$V = A\hat{X} - L \tag{45.1}$$

where, V is a $n \times 1$ residual vector, A is a $n \times t$ design matrix, $\hat{X}$ is a $t \times 1$ estimate parameter vector, L is a $n \times 1$ observations vector. Assuming the observations are independent, the priori weight matrix is diagonal. In order to eliminate or reduce the impact of outliers and large deviation observations on estimates, set $\bar{P}$ as equivalent weight matrix and its diagonal element is $\bar{p}_i$, Then we arrive at

$$A^T\bar{P}A\hat{X} - A^T\bar{P}L = 0 \tag{45.2}$$

The robust M estimation of unknown parameters is as follows.

$$\hat{X} = \left(A^T\bar{P}A\right)^{-1}A^T\bar{P}L \tag{45.3}$$

The posterior covariance matrix of $\hat{X}$

$$\sum_{\hat{X}} = \sigma_0^2\left(A^T\bar{P}A\right)^{-1}A^T\bar{P}P^{-1}\bar{P}A\left(A^T\bar{P}A\right)^{-1} \tag{45.4}$$

To get the solution we generally use iterative method, the $k+1$ times iterative solution is as follow.

$$\hat{X}^{k+1} = \left(A^T\bar{P}^kA\right)^{-1}A^T\bar{P}^kL \tag{45.5}$$

The element of $\bar{P}^k$ is

$$p_i^k = p_i\omega_i^k, \omega_i^k = \frac{\psi\left(v_i^k\right)}{v_i^k} \tag{45.6}$$

v_i^k is the residual component of k time iterative solution.

45.2.2 Equivalent Rights

From the robust M estimation principle we can see, a kind of ρ function is corresponding to a kind of M estimation, at present, many scholars have put forward various equivalent weight functions [10, 11]. Equivalent weight function assigns outlier zero weight, decreases doubtful observation's weight, a common equivalent weight function is IGG3 scheme.

$$\psi(\tilde{v}_i) = \begin{cases} \tilde{v}_i & |\tilde{v}_i| \le k_0 \\ k_0 \left(\frac{k_1 - |\tilde{v}_i|}{k_1 - k_0}\right)^2 & k_0 \le |\tilde{v}_i| \le k_1 \\ 0 & k_1 \le |\tilde{v}_i| \end{cases} \tag{45.7}$$

As for independent observation situation, equivalent weight function is:

$$\bar{p}(\tilde{v}_i) = \begin{cases} 1 & |\tilde{v}_i| \le k_0 \\ \frac{k_0}{|\tilde{v}_i|} \left(\frac{k_1 - |\tilde{v}_i|}{k_1 - k_0}\right)^2 & k_0 \le |\tilde{v}_i| \le k_1 \\ 0 & k_1 \le |\tilde{v}_i| \end{cases} \tag{45.8}$$

In Eq. (45.8), the value of k_0 and k_1 is respectively 1.5 and 3.0, $\tilde{v}_i$ is for standardization residual, which is

$$\tilde{v}_i = \frac{v_i}{m_{v_i}} \tag{45.9}$$

In Eq. (45.9), v_i is observation residual, m_{v_i} is mean error to v_i, m_{v_i} is calculated by followed equation.

$$m_{v_i} = \sigma_0 \sqrt{\frac{1}{p_i} - A_i (A^T P A)^{-1} A_i^T} \tag{45.10}$$

In Eq. (45.10), σ_0 is unit weight of error, we can use theoretical or empirical value; p_i is the weight of observations, A_i is the i line of the matrix A, and it is the i error equation coefficient vector [12].

45.3 Robust Celestial Positioning Model

45.3.1 Error Equation

In the celestial sphere, north celestial pole, zenith and stars can constitute a positioning triangle [13, 14], as is shown in Fig. 45.1.

In Fig. 45.1, P is the north celestial pole, Z is the zenith, W is the west point, WMQ is the horizon circle, WNQ' is celestial equator, σ is a star in celestial sphere. According to the spherical triangle cosine formula, we can get zenith Angle z,

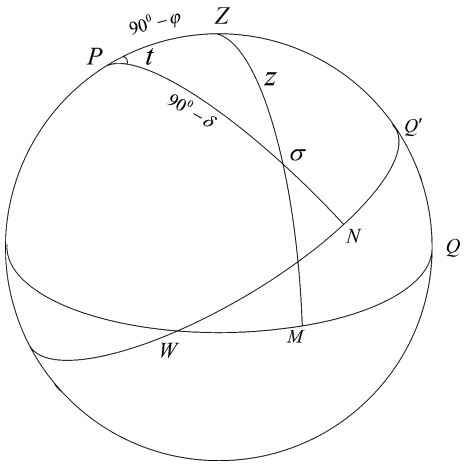

Fig. 45.1 Positioning triangle

station astronomical latitude φ, longitude λ, and star right ascension α and declination Angle δ, the connection with t is shown as Eq. (45.11).

$$\cos z = \sin\varphi \sin\delta + \cos\varphi \cos\delta \cos t \tag{45.11}$$

Among them

$$t = S - \alpha + \lambda \tag{45.12}$$

S is the Greenwich true sidereal time when observe, it can be obtained through observation time *UTC* instant of time T. First of all, according to the time bulletin A of IERS, *UTC* time T plus time difference between UT_1 and *UTC* is UT_1 time T', then transform it into mean sidereal time, then add nutation Δu ($\Delta u = \Delta\psi \cos\varepsilon$, $\Delta\psi$ is nutation of ecliptic longitude, ε is obliquity of the ecliptic), we can transform it into true sidereal time S. Star's right ascension α and declination δ can be obtained through apparent position calculation program. Zenith distance z and time T (or T') can be obtained through observation. Therefore, only φ and λ remains unknown, observe 2 stars is enough to get the survey station's astronomical longitude and latitude. But as a result of astronomical measurements atmospheric refraction correction is not complete, the zenith Angle obtained is not precise, a tiny amount Δz should be introduced, then the observation of the zenith Angle should be as $z + \Delta z$, therefore, at least 3 stars is needed to calculate the three parameters [13].

45.3.2 Robust Positioning Model

Some stars are observed, the equations can be written as:

$$\cos(z_i + \Delta z + v_i) = \sin(\varphi_0 + \Delta\varphi)\sin\delta_i + \cos(\varphi_0 + \Delta\varphi)\cos\delta_i\cos(S_i - \alpha_i + \lambda_0 + \Delta\lambda) \tag{45.13}$$

In Eq. (45.13), $\Delta\varphi$ is the difference between station latitude φ and its initial value φ_0.

$$\Delta\varphi = \varphi - \varphi_0 \tag{45.14}$$

$\Delta\lambda$ is the difference between the station's longitude and its initial value λ_0.

$$\Delta\lambda = \lambda - \lambda_0 \tag{45.15}$$

Therefore, the equation only needs to calculate three parameters, $\Delta\varphi$, $\Delta\lambda$ and Δz. Suppose

$$t_i = S_i - \alpha_i + \lambda_0 \tag{45.16}$$

Eq. (45.13) is transformed into

$$\cos(z_i + \Delta z + v_i) = \sin(\varphi_0 + \Delta\varphi)\sin\delta_i + \cos(\varphi_0 + \Delta\varphi)\cos\delta_i\cos(t_i + \Delta\lambda) \tag{45.17}$$

Suppose

$$P_i = \sin(\varphi_0 + \Delta\varphi)\sin\delta_i + \cos(\varphi_0 + \Delta\varphi)\cos\delta_i\cos(t_i + \Delta\lambda) \tag{45.18}$$

Eq. (45.17) is transformed into

$$v_i = \arccos P_i - z_i - \Delta z \tag{45.19}$$

Put $\arccos P_i$ in place by Taylor series expansion at P_{i0}, then

$$\begin{aligned}\arccos P_i &= \arccos P_{i0} + (_i)' \\ &= \arccos P_{i0} - \frac{1}{\sqrt{1 - P_{i0}^2}}[(\cos\varphi_0\sin\delta_i - \sin\varphi_0\cos\delta_i\cos t_i)\Delta\varphi \\ &\quad - \cos\varphi_0\cos\delta_i\sin t_i\Delta\lambda\end{aligned}$$

Among them:

$$P_{i0} = \cos\varphi_0\sin\delta_i + \cos\varphi_0\cos\delta_i\cos t_i \tag{45.21}$$

P_{i0} is the zenith Angle cosine value calculated by approximate latitude and longitude at the station, the error equation is

$$v_i = -\frac{\cos\varphi_0\sin\delta_i - \sin\varphi_0\cos\delta_i\cos t_i}{\sqrt{1 - P_{i0}^2}}\Delta\varphi + \frac{\cos\varphi_0\cos\delta_i\sin t_i}{\sqrt{1 - P_{i0}^2}}\Delta\lambda + \Delta z + (\arccos P_{i0} - z_i) \tag{45.22}$$

Suppose

$$a_i = \frac{\cos\varphi_0 \sin\delta_i - \sin\varphi_0 \cos\delta_i \cos t_i}{\sqrt{1 - P_{i0}^2}} \tag{45.23}$$

$$b_i = \frac{-\cos\varphi_0 \cos\delta_i \sin t_i}{\sqrt{1 - P_{i0}^2}} \tag{45.24}$$

$$l_i = \arccos P_{i0} - z_i \tag{45.25}$$

So, Eq. (45.22) is transformed into

$$v_i = a_i \Delta\varphi + b_i \Delta\lambda + \Delta z + l_i \tag{45.26}$$

Many scholars have pointed out that the success of the robust estimation mainly depends on the robust property of the initial parameters. Because every star's center coordinates calculation precision is different from each other, and always contain matching errors, therefore the parameters' least squares estimates of is not suitable as a robust estimation's initial value, first set L_1 norm which has strong selection properties minimum as criterion to calculate initial parameter [15]. In the extreme function suppose

$$\rho(v_i) = v_i \tag{45.27}$$

Then

$$\omega_i = \frac{\psi(v_i)}{v_i} = \frac{1}{v_i} \tag{45.28}$$

$$\bar{p}_i = p_i \omega_i = \frac{p_i}{v_i} \tag{45.29}$$

Put the equivalent weight function into Eq. (45.3), we can get much more accurate initial parameter, according to type Eqs. (45.9) and (45.10), we can obtain every observation's standardized residual. Among them, the coefficient matrix A and estimating parameter vector $X$is shown as Eq. (45.30)

$$A = \begin{bmatrix} a_1 & b_1 & 1 \\ a_2 & b_2 & 1 \\ \cdots & \cdots & \cdots \\ a_n & b_n & 1 \end{bmatrix} \hat{X} = \begin{bmatrix} \Delta\varphi \\ \Delta\lambda \\ \Delta z \end{bmatrix} \tag{45.30}$$

Error equation's free item L and residual vector V is shown as Eq. (45.31):

$$L = \begin{bmatrix} L_1 \\ L_2 \\ \cdots \\ L_n \end{bmatrix} V = \begin{bmatrix} v_1 \\ v_2 \\ \cdots \\ v_n \end{bmatrix} \tag{45.31}$$

Put the standard residual into Eq. (45.8),we can get equivalent weight function, and according to Eq. (45.3), we can get preliminary parameters robust solution, after Eq. (45.5) iteration, we can get final robust valuation about $\hat{X}$, take advantage of Eqs. (45.15) and (45.15), station longitude λ and latitude φ are obtained.

45.4 Measured Data Analysis

The experimental data collected from the star sensor on October 31, 2012 were used in this analysis. Through star point extraction, star center coordinates calculation, star map matching, 127 stars were identified from the star map, the zenith Angle error of the stars is shown in Fig. 45.2.

From Fig. 45.2, most of the stars' zenith Angle errors are within the range of $\pm 100''$, the observation accuracy is relatively higher; a few errors lie within the range of $\pm 100''$ to $\pm 200''$, the observation accuracy is relatively lower; individual errors may be larger than $\pm 300''$, which can be recognized as observation outliers. Two types of schemes were used to process on the experimental data, the first scheme uses the least squares estimate to obtain the parameters' estimates and its observation residuals, and set 2 times of mean square error as limit to eliminate the outlier, and once again use the least squares estimate. The second scheme uses robust estimation, among them robust initial value is obtained through the criterion whose L_1 norm is minimum, equivalent weight uses IGG3 model, mean square error of unit weight uses the mean square error of unit weight of initial the least square adjustment. The differences between two schemes' results and station's real coordinates are shown in Table 45.1.

The first scheme set 2 times of mean square error as limit and eliminate 8 observations as outliers, point error is $4.05''$, the second scheme assumed 4 observations as outliers and were given zero weight, while 13 observations were

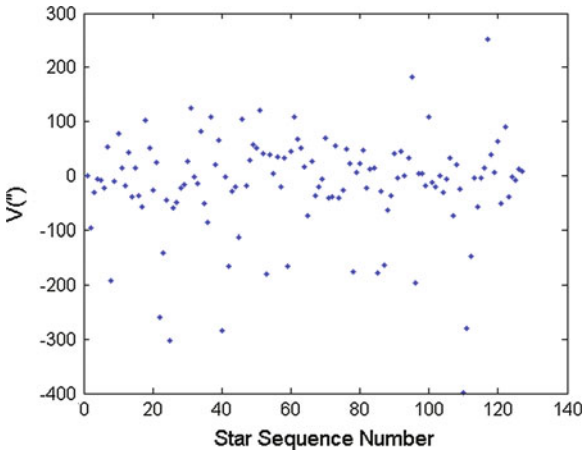

Fig. 45.2 Zenith angle error

Table 45.1 Two schemes error comparison

Scheme	Longitude error	Latitude error	Station error
1	3.26″	3.06″	4.05″
2	0.14″	1.14″	1.15″

treated as abnormal and their weights were reduced. Then, the data processing made full use of another 110 high-precision observations for calculating. The position error is 1.15″. From Table 45.1 it is noted that, based on the robust estimation, the celestial positioning model can effectively eliminate the influence of noise and wrong matching, limit the use of observations whose center coordinate errors are relatively bigger, make full use of high-precision observation information, effectively improve the navigation and positioning accuracy.

References

1. Ji B, Huilan F (1998) How to develop of astronomical navigation across to the 21st century. Navigation Technology Analecta of the Turn of Century. Chinese Institute of Electronics Navigation Branch, Xi'an, pp 30–38 (Ch)
2. Anguo W (2007) Modern celestial navigation and its key technologies. J Electron 12:2347–2348 (Ch)
3. Fang J, Ning X (2006) The theory and application of celestial navigation. Beijing University of Aeronautics & Astronautics Press, Beijing (Ch)
4. Hu W, Wu G, Huang L (2002) Research on marine electronics sextant angle sensor systerm. J Shanghai Marit Univ 23(3):17–20 (Ch)
5. Yang Y (1994) Survey adjustment model robust least squares solution and its influence function. J Inst Surveying Mapp 11(2):77–82
6. Yang Y (1996) Adaptive robust least squares estimate. J Surveying Mapp 25(3):206–211
7. Yang Y, He H, Xu G (2001) Adaptively robust filtering for kinematic geodetic positioning. J Geodesy 75:109–116
8. Yang Y (1999) Robust estimation of geodetic datum transformation. J Geodesy 73:268–274
9. Yang Y, Song L, Xu T (2002) Robust estimator for correlated observations based on bifactor equivalent weights. J Geodesy 76:353–358
10. Yang Y (1994) Equivalent weight principle–parameter adjustment model robust least squares solution. Bulletin of Surveying and Mapping, No 6, pp 33–35
11. Yang Y, FuMei W (2006) Critical value variable robust estimation equivalent weight function. J Surveying Mapp Sci Technol 23(5):317–320
12. Lijie S (2009) Program design of surveying adjust. National Defense Industry Press, Beijing, pp 116–117 (Ch)
13. Zhang C (2009) Research on astronomical measurement system and its application based on electronic theodolite. Zhengzhou institute of surveying and mapping (Ch)
14. Feng Y, Zhi X, Qiang Q (2011) Based on circulars intersection celestial positioning and integrated navigation method. J Aerosp 32(1):88–92
15. Yang Y (1991) Choose right least squares robust estimation. Surveying Mapp Technol, No 1, pp 1–6

Chapter 46
Experiment and Validation System for X-ray Pulsar-Based Navigation

Zhe Su, Yansong Meng, Qibing Xu, Xiaoliang Wang and Xingang Feng

Abstract Due to the huge costs, space flight experiment cannot be realized in the preliminary step of X-ray pulsar based navigation (XPNAV) research. So, a kind of XPNAV experiment and validation system is designed in this paper. This system is composed of two parts: the simulation of the pulsar signals and the calculation of navigation parameters. In the first part, the time at which X-ray photon arrive the solar system barycentre is modelled by non-homogeneous Poisson process, then the output pulse of X-ray detector while the observation of pulsars can be simulated by time transformation. In the second part, navigation information included in the pulsar signals which are simulated in the first part can be reached using the Delta-Correction method. This system can simulate four pulsar signals and the process of XPNAV at photo level. This system has the advantage of low costs and high simulation accuracy, and provides a reference for the design of prototype for space flight experiments.

Keywords Pulsar navigation · Experiment and validation system · Non-homogeneous poisson process · Time transfer

46.1 Introduction

X-ray pulsar-based navigation (XPNAV) is a kind of new spacecraft automatic navigation technology, which is suitable for near earth orbit, deep space and inter stars spacecraft [1]. Because of the absorbing of earth's atmosphere, we hardly can observe X-ray pulsar signal on the ground. Thus, the flight experiment of XPNAV should be implemented on the satellite out of earth's atmosphere [2]. But the flight

Z. Su (✉) · Y. Meng · Q. Xu · X. Wang · X. Feng
Academy of Space Information System, Xian 710100, China
e-mail: suzhe504@163.com

J. Sun et al. (eds.), *China Satellite Navigation Conference (CSNC) 2013 Proceedings*, Lecture Notes in Electrical Engineering 245,
DOI: 10.1007/978-3-642-37407-4_46,

experiment on the satellite costs hugely. Before the space experiment on the satellite, we firstly should develop the cheap and simple XPNAV experiment and validation system in the laboratory to evaluate the principle and precision of XPNAV [3, 4].

This paper designs an X-ray pulsar-based navigation experiment and validation system (XPNAV-EVS). This system is composed of pulsar signal simulator and navigation parameter calculator. In the pulsar signal simulator, the X-ray pulsar photon arrival satellite time is simulated through the follow steps: firstly, the photon arrival solar system barycenter (SSB) time is simulated by the non-homogeneous poisson process model, and the arrival time is then transferred to the arrival satellite time. In navigation parameter calculator, the position of satellite is calculated by the simulated arrival time of photons through the process of time transfer, period folding of photons and time delay measurement. This XPNAV-EVS can simulate the XPNAV algorithm on photons level, and is useful for the following flight experiment on the satellite.

46.2 The Structure and Principle of XPNAV-EVS

As shown in Fig. 46.1, the XPNAV-EVS is composed of pulsar signal simulator and navigation parameter calculator.

In pulsar signal simulator, the X-ray pulsar photon arrival satellite time is simulated through the follow steps: firstly, the phase of pulsar signal at SSB is calculated using pulsar phase prediction model; secondly, pulsar integrated pulse profile is simulated by the phase of pulsar signal and pulsar standard profile; thirdly, the photon arrival solar system barycenter (SSB) time is simulated by the

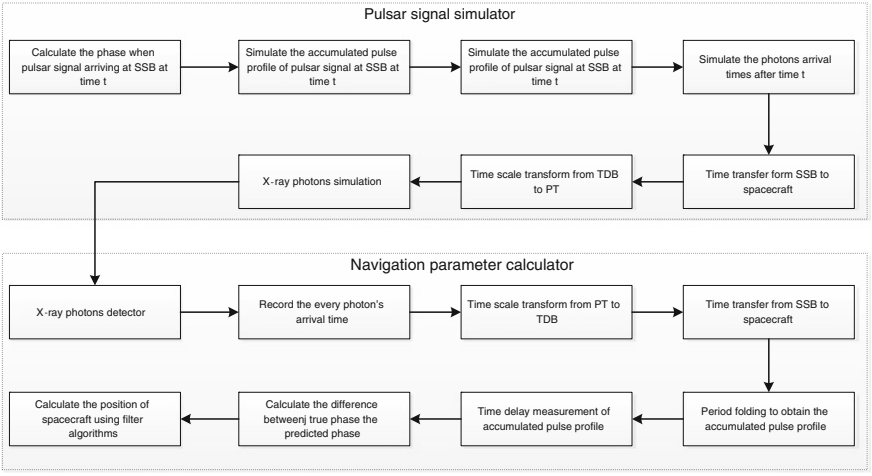

Fig. 46.1 The structure of XPNAV-EVS

non-homogeneous poisson process model based on pulsar integrated pulse profile; fourthly, the time that photons arrival SSB is transferred to the time that photons arrival spacecraft using the accurate position of spacecraft in the SSB reference frame; fifthly, the time scale is transferred from Terrestrial BabyCenter (TDB) to proper time (PT) of spacecraft, lastly the X-ray modulator generates the X-ray photons based on the photons arrival spacecraft time in PT.

In the navigation parameter calculator, the position of spacecraft is calculated through the follow steps: firstly, X-ray photons detector senses and records the arrival time of photons; secondly, the arrival time is the simulated photon arrival spacecraft time in PT, this time is then transferred to the photon arrival SSB time in TDB; thirdly, the integrated pulse profile is obtained through period folding process; fourthly, the time delay measurement is implemented between the integrated pulse profile and the standard profile; fifthly, the measured time delay and the predicated time delay is difference if the position of spacecraft, which is used in the time transfer, is not correct. The relationship between the time delay difference and position error is

$$\delta\phi = \phi_{\text{rea}} - \phi_{\text{mea}} = \frac{\delta t}{T_p} + \frac{\boldsymbol{n} \cdot \delta \boldsymbol{r}}{c \cdot T_p} \tag{46.1}$$

where ϕ_{rea} is predicated time delay, ϕ_{mea} is real time delay, δt is clock error, δr is the position error, T_p is the period of pulsar.

46.3 The Key Technologies of XPNAV-EVS

In this section, the key technologies of XPNAV-EVS are described in detail.

46.3.1 The Simulation of the Time that X-ray Photons Arrival SSB

We simulate the time that X-ray photons arrival SSB through the following steps:

1. **Calculate the phase of pulsar signal at SSB at time *t* using pulsar phase prediction model**

   Pulsar phase prediction model can be expressed as [5]

$$\phi(t) = \phi(t_0) + f(t - t_0) + \frac{\dot{f}}{2}(t - t_0)^2 + \frac{\ddot{f}}{6}(t - t_0)^3 \tag{46.2}$$

   Using the pulsar phase prediction model, we can calculate the phase of pulsar signal at SSB at any time t ($t \geq t_0$). In the above equation, the parameters $f, \dot{f}$ and $\ddot{f}$ refer to Princeton Pulsar Database. To simplify the design, set $\phi(t_0)$ zero.

Attention that t_0 and $\phi(t_0)$ should take the same value in the pulsar signal simulator and navigation parameter calculator.

2. **Simulate the pulsar integrated pulse profile at SSB at time *t***

After the $\phi(t)$ is computed from Eq. (46.3), we can calculate the number of phase bin between integrated pulse profile and standard profile. Then, the pulsar integrated pulse profile at time t can be obtained through Δn points shift of standard profile.

$$\Delta n = N \cdot \mathrm{frac}[\phi(t)] \tag{46.3}$$

In above equation, N represents the number of phase bin in one period, frac$[\cdot]$ is the decimal operator.

In most situations, Δn is not integer, and then the non-integral shift is needed. In this paper, we adopt the SINC interpolate method. The standard profile $s(t)$ can be expressed as the linear combination of SINC functions:

$$s(t) = \sum_{n=-\infty}^{\infty} s(n) \cdot sinc(t - nT_b) \tag{46.4}$$

where $sinc(x) = \sin(\pi x/T_b)/(\pi x/T_b)$, T_b is the length of phase bin.

The integrated pulse profile $p(t)$ is

$$p(t) = s(t + \Delta n \cdot T_b) = \sum_{n=-\infty}^{\infty} s(n) \cdot sinc(t - nT_b + \Delta n \cdot T_b) \tag{46.5}$$

We can see from above equation that SINC interpolate method obtain the shifted signal $p(t)$ through the weighted combination of the standard profile $s(t)$ and the SINC functions.

3. **Simulate the arrival time of photons at SSB after the time *t***

The integrated pulse profile at time t can only represents the phase of pulsar signal, and cannot accurately simulate the flow density of pulsar X-ray photons. In order to simulate the real flow density, we adopt the non-homogeneous Poisson process (NHPP) to model the arrival time of pulsar X-ray photons. In the time interval of (t_i, t_j), the probability of the event that the spacecraft receives k number of photons can be expressed as

$$p\left[k; (t_i, t_j)\right] = \frac{\left(\int_{t_i}^{t_j} \lambda(t)dt\right)^k}{k!} \exp\left(-\int_{t_i}^{t_j} \lambda(t)dt\right) \tag{46.6}$$

$\lambda(t) > 0$ is the flow of X-ray photons at time t, $\lambda(t)$ can be calculated through

$$\lambda(t) = B_x + (F_x - B_x) \cdot \tilde{p}(t) \tag{46.7}$$

F_x and B_x represent the average flow density of X-ray photons from pulsars and background respectively. $\tilde{p}(t)$ represents the unitary integrated pulse profile.

The arrival number of X-ray photons in the time interval (t_n, t_{n+1}) can be calculated through the above two equations.

46.3.2 Time Scale Transform

The time scale of pulsar phase prediction model is TDB at SSB, however the time scale of spacecraft is PT. In order to calculate the time difference of photon arrival at SSB and spacecraft, the time scale transform should be implemented.

In this paper we adopt the time scale transform method proposed in [6–8], the equation is

$$\left(1-\frac{W_0}{c^2}\right)\Delta t=\left(1+\frac{3\mu_E}{2c^2a}-\frac{W_0}{c^2}\right)\Delta\tau+2\frac{\boldsymbol{r}_{SC/E}\cdot\boldsymbol{v}_{SC/E}}{c^2} \tag{46.8}$$

Δt and $\Delta\tau$ represent the time interval of TDB and PT respectively, W_0 is the gravitation on the surface of the earth, c is the speed of the light, μ_E is the earth gravitation constant, $\boldsymbol{r}_{SC/E}$ and $\boldsymbol{v}_{SC/E}$ are the position and speed of spacecraft in earth center inertial frame.

In the process of navigation parameter calculation, the position and speed can be roughly deduced using the orbit dynamics model, and then the time scale transfer can be implement from PT to TDB using Eq. (46.8).

In the process of pulsar signal simulation, we need transform photons arrival time from TDB to PT. However, because the position and speed of spacecraft is measured in PT, if the TDB is known and PT is unknown, $\boldsymbol{r}_{SC/E}$ and $\boldsymbol{v}_{SC/E}$ cannot be calculated directly. In this paper, we use Newton iterative method to solve this problem. The $\Delta\tau$ can be obtained through the flowing steps:

(a) Set $\Delta\tau_1=\Delta t$;
(b) Calculate the $\boldsymbol{r}_{SC/E}$ and $\boldsymbol{v}_{SC/E}$ through the PT time $\tau_k=\tau_0+\Delta\tau_k$, $(k=1,2,\cdots)$;
(c) As Δt, $\boldsymbol{r}_{SC/E}$ and $\boldsymbol{v}_{SC/E}$ are known, calculate the $\Delta\tau_{k+1}$ through Eq. (46.8);
(d) If $|\Delta\tau_{k+1}-\Delta\tau_k|>\varepsilon=10^{-12}(\mathrm{s})$, set $k=k+1$ and jump to step (b); otherwise, stop the iteration.

46.4 Experiments and Results Analysis

In order to test the similarity of flow density and pulse profile between the simulated and real pulsar signal, take pulsar B0531+21 for example. The real experiment data is observed by the Rossi X-ray Timing Explorer (RXTE). The number of phase bin in each period is set 1,000. Figure 46.2 shows the real and

simulated X-ray pulsar signal in one period. Figure 46.3 shows the real and simulated pulsar integrated pulse profile, the start integrating time is 50849.000000544(MJD). Comparing Figs. 46.2 and 46.3, we can see that the simulated pulsar signals are similar to real pulsar signals.

In order to test the time delay measurement accuracy of the simulated pulsar integrated pulse profile, process the experiments in the following steps:

(a) Simulate the X-ray photons arrival times of pulsar B0531+21 in TDB at SSB;
(b) Transform the photons arrival times in TDB to PT by the accurate position of spacecraft;
(c) Using the estimated position of spacecraft, transform the photons arrival times in PT to TDB, and then implement the period folding to obtain the integrated pulse profile;
(d) Calculate the time delay between the integrated pulse profile and standard profile through Taylor FFT algorithm;
(e) Calculate the difference between the measured time delay and predicated time delay computed by pulsar phase model;
(f) Repeat the above steps for 20 times and calculate the squared variance of time delay difference;
(g) Set different simulation period and the experiment results are shown in the Table 46.1.

We can see from the above table that: (a) the time delay measurement accuracy reaches the order of microsecond, and this accuracy can satisfy the demand of the X-ray pulsar navigation experiment; (b) when the integrated time is less than 3,000 s, the extension of integrated time can enhance the signal-to-noise ratio (SNR) of integrated pulse profile, and also improve the time delay measurement accuracy; (c) when the integrated time is more than 3,000 s, the extension of integrated time cannot improve the time delay measurement accuracy obviously. This is because the main features that affect the time delay measurement accuracy is no more than SNR but the estimated error of spacecraft's position, when the

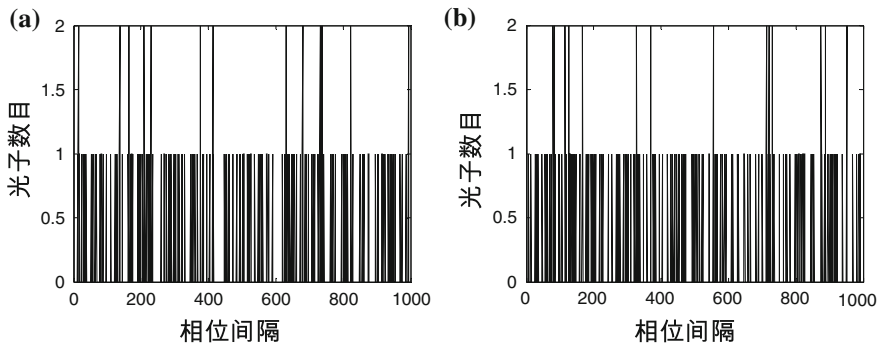

Fig. 46.2 Real and simulated pulsar signal in one period. **a** Real pulsar signal. **b** Simulated pulsar signal

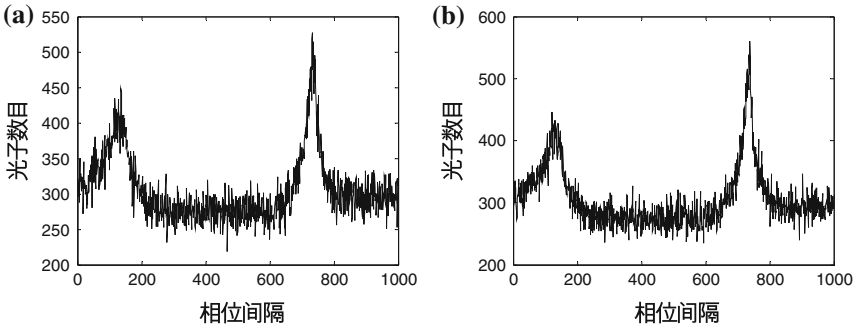

Fig. 46.3 Real and simulated pulsar integrated pulse profile. **a** Real pulsar integrated pulse profile. **b** Simulated pulsar integrated pulse profile

Table 46.1 The time delay measurement squared variance of simulated pulsar signal

Simulation period (s)	60	300	1,500	3,000	6,000
Squared variance (μs)	3.3	1.58	0.92	0.89	0.88

integrated time is long enough. So, the estimated error of spacecraft's position can be deduced from the time delay measurement error.

46.5 Results

In order to simulate the process of X-ray pulsar navigation in a laboratory, this paper has designed an X-ray pulsar-based navigation experiment and validation system. This system can simulate the X-ray pulsar signals received by the spacecraft, and then calculate the position and speed of spacecraft by the X-ray pulsar signals. This system can simulate the key process of XPNAV, such as time transform, time delay measurements and navigation filter algorithms. This system has the advantages of low costs and high simulation accuracy, and provides a reference for the design of prototypes in space flight experiments.

References

1. Sheikh SI, Pines DJ (2006) Spacecraft navigation using X-ray pulsars. J Guidance, Control, Dyn 29(1):49–63
2. Shuai P, Li Ming, Chen SL Huang Z (2009) The principle and method of X-ray pulsar based navigation system. China Astronautic Publishing House, Beijing

3. Xie Z, Yu H, Wang Z (2009) X-ray pulsar virtual observatory based on the HEASARC database. Res Explor Lab, vol 07
4. Zhenhua X, Songfeng P, Zhengyan W (2009) Development of the virtual experiment platform for X-ray pulsar-based astrospace navigation. Exp Technol Manage, vol 10
5. Zhen-Hua X, Lu-Ping X, Guang-Ren N (2008) Time offset measurement algorithm based on bispectrum for pulsar integrated pulse profiles. Acta Physica Sinica, vol 10
6. Mease KD, Bharadwaj S, Iravanchy S (2003) Time scale analysis for nonlinear dynamical systems. J Guidance, Control, Dyn 26(2):318–330
7. Chong-Xia Z, Ting-Gao Y (2007) Use of wiener filtration in wavelet domain in ensemble pulsar time algorithm. Acta Physica Sinica, vol 10
8. Theodore DM (2006) (Translated by Liu YC) Formulation for observed and computed values of deep space network data types for navigation. Tsinghua University Press, Beijing

Chapter 47
The Research on Indoor High Accuracy Frequency Source Based on Adaptive Loop Adjusting

Zhongliang Deng, Xu Li and Xie Yuan

Abstract China will establish the Xihe System based on Beidou/GNSS, Mobile Communication, Internet and Satellite Communication system to realize the Seamless Outdoor and Indoor Positioning in Wide Area (SOIPWA) on personal mobile terminals. Indoor Positioning System (IPS) is one of the main components and effective supplement for indoor positioning signal resource to resolve the positioning signal coverage of blind areas in complicated indoor environment based on current 2G/3G communication network and existing equipment. According to the requirement, the IPS adopted the unified time-frequency reference which affects the accuracy of indoor positioning directly. This paper provides an acquisition method of high accuracy frequency source used in the indoor positioning signal supplement. Positioning signals from outdoor base stations are acquired by RF front end and tracked by the carrier loop and code loop adjusting. After that, positioning signals are locked and synchronized to extract the high accuracy frequency source used for IPS, which can be built with low cost and precisely integrated with an outdoor positioning system. In practical test, the method satisfies the need of the accuracy and stability in time-frequency reference for IPS with high frequency accuracy, quick start and low drift rate through adjusting high accuracy Voltage Controlled Oscillator (VCO) by Digital to Analog Converter (DAC) with the frequency difference result from the adaptive loop.

Keywords Indoor positioning · Time-frequency reference · Adaptive loop adjusting

Z. Deng · X. Li (✉) · X. Yuan
Beijing University of Posts and Telecommunications, Xitucheng Road 10, Beijing 100876, China
e-mail: lixu@bupt.edu.cn

J. Sun et al. (eds.), *China Satellite Navigation Conference (CSNC) 2013 Proceedings*, Lecture Notes in Electrical Engineering 245,
DOI: 10.1007/978-3-642-37407-4_47,

47.1 Introduction

IPS adopts the unified time-frequency reference to ensure the high accuracy in indoor positioning. It is restricting development of indoor LBS that how to find a well-performance time-frequency reference with low cost. GPS, Beidou and other satellite navigation system could be applied to adjust local oscillator to promote accuracy and stability with time service in [1]. This method had some limitation in some places like canyon areas in downtown where satellite signal is too weak to be received and security problem exists additionally. To problems in [1], method in [2] provided another approach that combine the CAPS in space with Rubidium clock on ground to acquire high accuracy and well stable time-frequency reference, but obviously the cost is main obstacle to take into practice in large scale.

In this paper, an acquisition method of high accuracy frequency source applied in IPS was introduced where local Temperature Compensate X'tal (crystal) Oscillator (TCXO) was adjusted on the basis of Carrier Residual Frequency (CRF) with capturing and tracking the signal from outdoor base station based on current supplement network to realize combined calculation between indoor and outdoor.

47.2 The Principle and Model

Indoor Positioning Signal Generator (IPSG) in IPS turned into work condition including signal capturing, loop tracking and time adjusting when receiving outdoor positioning signal from ground base station.

47.2.1 Signal Capturing

I and Q two channel signals from RF front multiply with local code separately and then put results into integrator to acquire integrated signal power. If the code phase in receiving signal is similar with local, maxim power exists in integrated signal. If not, integrated power-like noise. The position of code head can be located by maxim and second maxim correlation peak from the approach mentioned above to synchronize toughly.

47.2.2 Loop Tracking

When succeed in signal capturing, IPSG steps into self-adaption adjustment to synchronize precisely in code phase.

In order to strip away IF carrier to acquire the phase difference $\varphi(n) - \varphi_o(n)$ between inputting carrier and local generating carrier, digital IF signal from RF front multiplies with sine and cosine carrier from local generating in separate. When the receiving carrier is same with the generating, the phase difference is zero. Considering the time-frequency reference of outdoor base station is Rubidium clock that error is regarded as zero, local frequency source can have incredible close to the clock through adjusting the local oscillator to make the code phase difference smaller and smaller and carrier residual frequency approach to zero. And CRF can be calculated more directly and precisely from two steps frequency research and loop adjustment.

Because of transitory in head capturing, the overturn of data code $D(t-\tau)$ can be ignored in integration time. So IF signal can be indicated as

$$s_{IF}(t) = A_{IF}DC(t-\tau)e^{\theta_{IF}}. \tag{47.1}$$

Imaging the local code is $C(t-\tau_L)$ from local GOLD code generator, the time difference in phase between local code and outer code is $\Delta\tau = \tau - \tau_L$. After captured, the effect of CRF to integration results is mainly considered when code heads are synchronized initially as $C(t-\tau) = C(t-\tau_L)$. So integration outputs of I and Q two signal channel are

$$\begin{aligned} I &= A_{IF}D\int_0^{T_s}\cos(2\pi f_d t + \theta_{IF})\mathrm{d}t \\ &= A_{IF}DT_s\mathrm{sinc}(f_dT_s)\cos(\pi f_dT_s + \theta_{IF}) \end{aligned} \tag{47.2}$$

and

$$\begin{aligned} Q &= A_{IF}D\int_0^{T_s}\sin(2\pi f_d t + \theta_{IF})\mathrm{d}t \\ &= A_{IF}DT_s\mathrm{sinc}(f_dT_s)\sin(\pi f_dT_s + \theta_{IF}), \end{aligned} \tag{47.3}$$

and power output is

$$\begin{aligned} P &= I^2 + Q^2 \\ &= A_{IF}^2T_s^2\mathrm{sinc}^2(f_dT_s). \end{aligned} \tag{47.4}$$

According to the character of sinc function, the power output P is maxim when $f_d = 0$ that is the difference between outer actual CRF f_a and local estimated CRF f_s that is the disperse matrix with interval value Δf as

$$f_s = \begin{bmatrix} -n\Delta f, -(n-1)\Delta f, \cdots, -2\Delta f, -\Delta f, 0, \\ \Delta f, 2\Delta f, \cdots, (n-1)\Delta f, n\Delta f \end{bmatrix}. \tag{47.5}$$

Disperse values in f_s are taken into integrated calculation and the maxim result is regarded as right value that is closest to f_s because of sinc function character.

And next, the more precise CRF is obtained based on carrier loop adjusting.

In the initial stage to lock condition, second order digital FLL is prior to bring in calculation which has wider noise bandwidth and better dynamics compared to PLL as Fig. 47.1 shows. Transfer function of loop filter is

$$F(s) = \frac{1}{K}\left(2\zeta\omega_{nf} + \frac{\omega_{nf}^2}{s}\right) \tag{47.6}$$

and system function in second order FLL is

$$H(s) = \frac{2\zeta\omega_{nf}s + \omega_{nf}^2}{s^2 + 2\zeta\omega_{nf}s + \omega_{nf}^2}. \tag{47.7}$$

More precise frequency difference can be obtained in discriminator in which the square of signal amplitude is quantified and discriminating result is put into second order DLF in which transfer function $F(z)$ is

$$F(z) = \frac{u_f(z)}{u_d(z)} = \frac{1}{K}\left(2\zeta\omega_{nf} + \frac{T_s}{2}\frac{1+z^{-1}}{1-z^{-1}}\omega_{nf}^2\right), \tag{47.8}$$

where T_s is signal sampling cycle that is also considered as data rate into DLF Fig. 47.2.

After several times of calculating in FLL, next stage to lock condition is another calculating in PLL that has tighter loop tracking and lower loop noise than FLL to completely match the CRF outside.

The principle and model of second order PLL is similar to FLL basically that has no need to introduce again here. Through self-adaption adjustment for times, loop reaches locked condition and CRF f_c is matched in local to actual precisely.

47.2.3 Time Adjusting

When actual CRF is precisely matched, local frequency source is approximating to outer Rubidium clock with adjusting TCXO controlled by DAC. Referring to the character of transient response in second order system, actual CRF is close to zero to reach steady condition with continuous adjustment and feedback. Simultaneously, characteristic frequency and damping factor are different in various

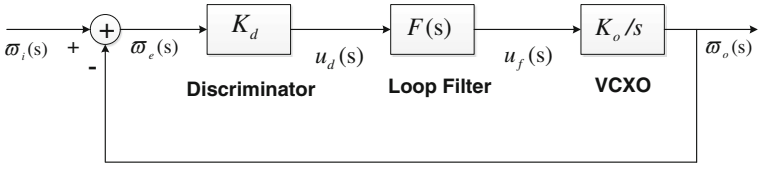

Fig. 47.1 Structure of Laplace transform in FLL

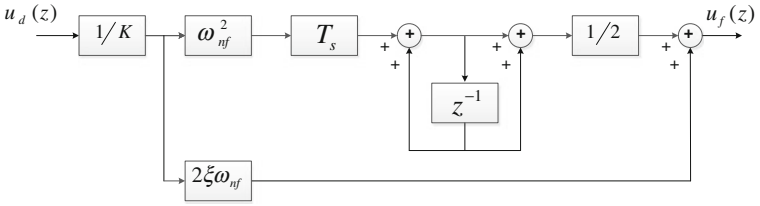

Fig. 47.2 Structure of digital filter with second order loop

stages, which led system to reach steady condition as soon as possible as Fig. 47.3 shows where local frequency source can be regarded Rubidium-like clock.

47.3 The Performance Analysis

Considering the TCXO with adjusting input voltage range from zero to *Vcc*, the output is central frequency when adjusting voltage input is middle of the range. If outer carrier frequency is f_c, the least matched carrier residual frequency in local Δf_a is

$$\Delta f_a = d \cdot f_c + d\sigma, \tag{47.9}$$

where d is frequency stability in magnitude of 10^{-6} and σ is system error per Hz including the Doppler frequency shift, circuit transfer delay, temperature drift and so on.

Assisted with the method that is introduced in this paper, the least matched carrier residual frequency $\Delta f_a'$ can reach the value as small as

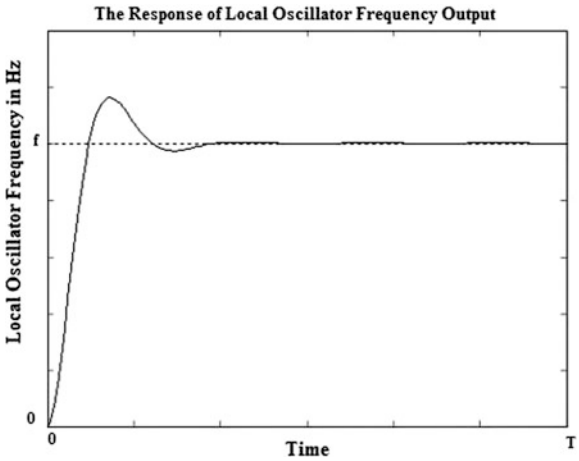

Fig. 47.3 The response *curve* of local oscillator frequency output

$$\Delta f_a' = \frac{p}{2^M} f_c + \frac{1}{2^N} f_c + \frac{p \cdot \sigma}{2^M}, \tag{47.10}$$

where M is quantifiable bit in Digit-Analog Converter, N is controlling bit for carrier residual frequency in loop tracking and p is value to judge the traction ability. To Eq. 47.10, the first formula refers to the least adjusting carrier residual frequency, the second refers to the least error for measuring in loop tracking and the last refers to system error in carrier residual frequency that mentioned in Eq. 47.9.

Comparing Δf_a to $\Delta f_a'$, it is obvious to see their relation in numerical as

$$n = \frac{\Delta f_a}{\Delta f_a'} = \frac{d \cdot f_c + d \cdot \sigma}{\frac{p}{2^M} f_c + \frac{1}{2^N} f_c + \frac{p \cdot \sigma}{2^M}}. \tag{47.11}$$

As $\frac{p}{2^M}$ goes further than $\frac{1}{2^N}$, $\Delta f_a'$ can be regarded as approximately as $\frac{p}{2^M} f_c + \frac{p \cdot \sigma}{2^M}$. So n is

$$n = \frac{\Delta f_a}{\Delta f_a'} = \frac{d \cdot f_c + d \cdot \sigma}{\frac{p}{2^M} f_c + \frac{p \cdot \sigma}{2^M}} = \frac{d \cdot 2^M}{p}. \tag{47.12}$$

To the given TCXO, the relation between ability of frequency traction and frequency stability is negative correlation which means that it raises the frequency stability at expense of decreasing frequency traction range. The ratio is 10 in normal and so n is

$$n = \frac{2^M}{10}. \tag{47.13}$$

From Eq. 47.13, the measuring accuracy of carrier residual frequency is promoted to $\frac{2^M}{10}$ times and also the frequency source.

The second order model can bring in the research on the specific character of indoor frequency resource and TCXO as both of them depend on basic model in loop tracking, adjusting and locking. Figure 47.4 tells transient response curve of two systems under step input where the dash line stands for TCXO and the other stands for indoor frequency source. Obviously, transient response curve of TCXO enters into adjusting condition earlier with lower accuracy in adjustment, but the curve of indoor frequency source turns into steady condition firstly and keeps a smaller vibrating around zero because of adjustable loop factor including characteristic frequency, damping factor and so on controlled by self-adaption loop in different state.

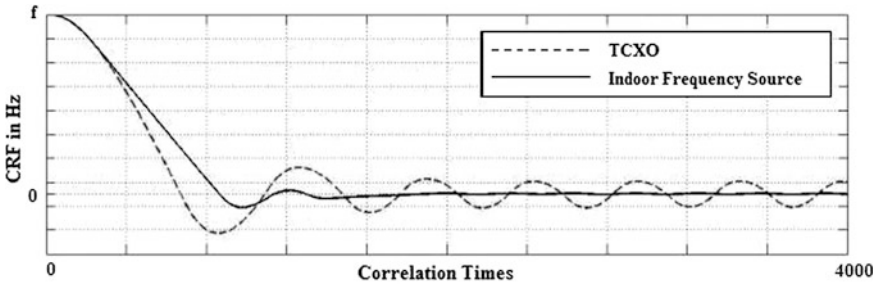

Fig. 47.4 Transient response *curve* of *indoor frequency source* and *TCXO* second-order system under step input

47.4 The Actual Test

Based on current indoor supplement network of Operators, actual test was accomplished recently to measure the performance.

47.4.1 Measurement in Carrier Residual Frequency

In self-adaption loop, carrier residual frequency was adjusting and reaches the steady condition finally around zero. Compared performance of TCXO and indoor frequency source in Fig. 47.5 where the upper refers to simulation test in indoor frequency source and the bottom refers to TCXO. It can reach a conclusion that indoor frequency source shows better performance both in dynamic and steady.

47.4.2 Technical Specification

Comparison test between indoor frequency source and Rubidium clock was brought into measure technical specifications with high accuracy frequency counter and frequency-spectrum analyzer.

47.4.2.1 Phase Noise

From Fig. 47.6, it visibly can see that phase noise in indoor frequency source is −121 dBc/Hz at 100 Hz and −127 dBc/Hz at 1 kHz that has no much difference to Rubidium clock in which phase noise is −121 dBc/Hz at 100 Hz and −130 dBc/Hz at 1 kHz which means local indoor frequency source can reach Rubidium-like clock with high accuracy to some extent.

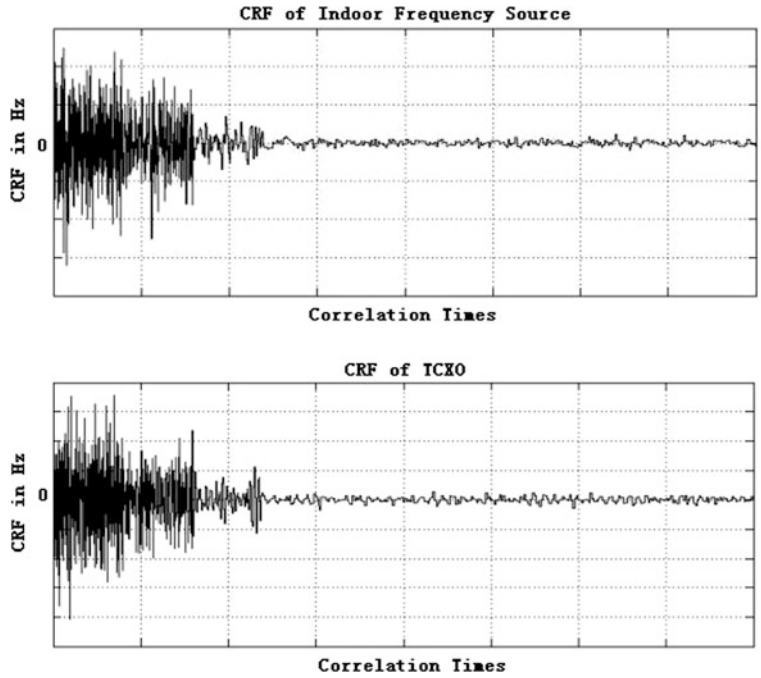

Fig. 47.5 *Curve* of CRF in simulation

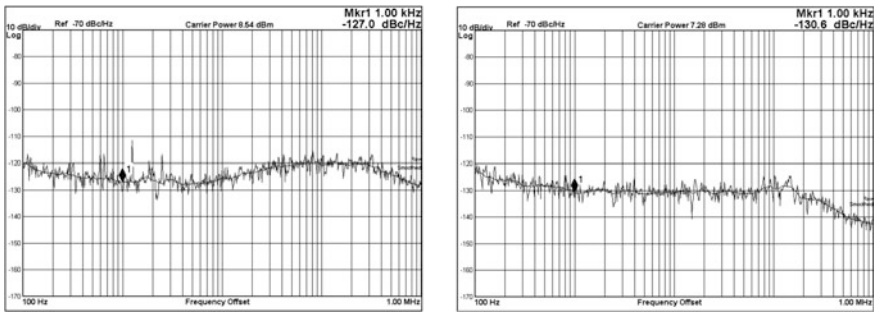

Fig. 47.6 *Curve* of phase noise test in indoor frequency source and Rubidium clock

47.4.2.2 Steady Curve

As Fig. 47.7 shows, indoor frequency source system turned into steady condition completely after 7 s with the vibrating error below 0.1 Hz. During the continuous 10 h test, the system kept working on steady with 0.002938303 Hz with a standard deviation of 0.08815 m in positioning error which fully met the need of stability and accuracy for positioning in indoor environment.

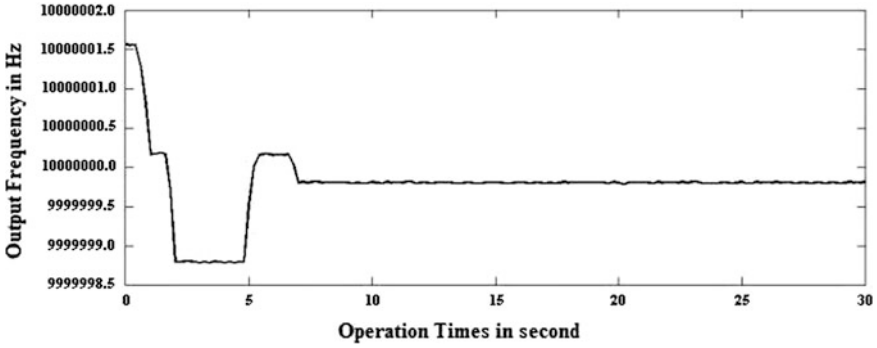

Fig. 47.7 *Curve* of steady level in indoor frequency source

47.5 Conclusion

The IPS adopts a unified frequency-time reference that affects the accuracy of indoor positioning and combined calculations between outdoor and indoor. Through performance analysis and actual test, the indoor frequency source based on self-adaption loop adjusting that has been introduced in this paper can provide Rubidium-like clock in high accuracy with low cost and better performance to contribute significantly the development of indoor positioning systems.

References

1. Shi M, Ye L, Gao S, Chen D et al (2008) A frequency calibration algorithm for single frequency GPS receivers. J Spacecraft TT&C Technol 27(5):27–29
2. Wu HT, Bian YJ, Lu XH et al (2009) Time synchronization and carrier frequency control of CAPS navigation signals generated on the ground. Sci China Ser G Phy Mech Astron 52(3):393–401
3. Shi HL, Jin G, Cui J et al (2011) The global positioning system in post GPS era. Science Press, Beijing
4. Xie G (2008) Principles of GPS and receiver design. Publishing House of Electronics Industry, Beijing
5. Kaplan ED, Hegarty CJ (2006) Understanding GPS: principles and applications. Artech House, Norwood
6. Huaming WU, Yanyong SU, Aijun LIU et al (2010) Application of PLL and FLL in the digital costas loop. Sci Technol Eng 10(19):4645–4650

Chapter 48
EMD De-Noising Theory Considering Static and Dynamic Conditions and Its Applications in INS

Yu Gan, Lifen Sui, Guorui Xiao and Yu Duan

Abstract De-noising IMU data is an important approach to improve the accuracy of INS. Wavelet threshold de-noising has many limitations under certain conditions, especially in processing inertial sensor errors. Based on Empirical Mode Decomposition (EMD), a novel systematic de-noising methodology for inertial sensor errors is established, including EMD compulsive de-noising, feasible in static conditions, and EMD threshold de-noising, feasible in dynamic conditions. For static data, EMD compulsive de-noising method first disposes IMFs of exceptional noise by 2sigma criterion and then the number of IMFs of high frequency noise is determined by correlation coefficient. The de-noising process is finally done by reconstructing the other IMFs. For dynamic data, EMD threshold de-noising method utilizes fractional Gaussian noise as the model of inertial sensor errors. The model parameter estimation method by power spectral density is given. Noise variance in IMFs is derived and noise thresholds of IMFs are estimated through the obtained variance.

Keywords INS · Empirical mode decomposition (EMD) · Compulsive de-noising · Threshold de-noising · Colored noise · Wavelet

48.1 Introduction

Inertial Navigation System (INS) suffers from time-dependent error accumulation, causing a drift in the solution. Random errors in inertial sensors can not be effectively eliminated even by GNSS (Global Navigation Satellite System) and INS integration [1]. Many researchers propose de-noising the inertial data to reduce the effects of random errors.

Y. Gan (✉) · L. Sui · G. Xiao · Y. Duan
Geospatial Information Institute, Information Engineering University,
Zhengzhou 450052, China
e-mail: ganyu099@163.com

J. Sun et al. (eds.), *China Satellite Navigation Conference (CSNC) 2013 Proceedings*, Lecture Notes in Electrical Engineering 245,
DOI: 10.1007/978-3-642-37407-4_48,

Wavelet thresholding is quite popular in INS signal de-noising applications [2–4]. However, wavelet threshold de-noising has many disadvantages in inertial data processing. Under static conditions, the amplitude of useful signal is low compared with noise, failing to be consistent with the thresholding principle. Classical wavelet threshold method operates well when the actual signal is affected by pure white noise. However, there are a large amount of colored noise components in inertial sensors, degrading the effects of wavelet threshold de-noising.

These years, many scholars use EMD (Empirical Mode Decomposition) to do de-noising, which directly use the thresholds of wavelet thresholding [5, 6], lacking comprehensive methodology and reliable fundament for EMD condition. A novel systematic de-noising methodology for inertial sensor is established, including EMD compulsive de-noising and EMD threshold de-noising. For static data, EMD compulsive de-noising method first disposes IMFs of exceptional noise by 2sigma criterion and then the number of IMFs of high frequency noise is determined by correlation coefficient. The de-noising process is finally done by reconstructing the other IMFs. For dynamic data, EMD threshold de-noising method utilizes fractional Gaussian noise as the model of inertial sensor errors. The model parameter estimation method by power spectral density is given. Noise variance in IMFs is derived and noise thresholds of IMFs are estimated through the obtained variance.

48.2 EMD Compulsive De-noising Method

48.2.1 Principle of EMD Compulsive De-noising

EMD process can be found in many references [7] which will not be given again here.

A gyro signal $x(t)$ can be decomposed into

$$x(t) = \sum_{i=1}^{n} imf_i + r_n \tag{48.1}$$

Eliminating a certain number of low order IMFs with relatively high frequencies naturally reduces the influence of noise since useful signal mainly corresponds to low frequency components.

Since there may be many abnormal variations in the outside environments, gyro signal may be contaminated by exceptional noise. The standard deviation of signal $x(t)$ is denoted by σ, we can carry out the following criterion on IMFs:

$$\begin{cases} A_i > 2\sigma & imf_i' = 0 \\ A_i \leq 2\sigma & imf_i' = imf_i \end{cases} \tag{48.2}$$

where A_i is the amplitude of imf_i.

After the exceptional noise is disposed, the subsequent de-noising process can be finished by eliminating m IMFs which is recognized as noise IMFs

$$x'_m(t) = x(t) - \sum_{i=1}^{m} imf_i \tag{48.3}$$

The difficulty is how to determine m properly. The correlation coefficient reflects the connection of two signals, we calculate the correlation of original signal $x(t)$ and de-noised signal $x'_m(t)$:

$$\rho_{xx'_m} = \frac{\sum_{k=1}^{N} x(k)x'_m(k)}{\sqrt{\sum_{k=1}^{N} x^2(k)}\sqrt{\sum_{k=1}^{N} {x'_m}^2(k)}} \quad (m = 1, 2, \ldots) \tag{48.4}$$

We calculate $\rho_{xx'_m}$ from $m = 1$ and continue. When it satisfies $\rho_{xx'_m} < c$ (c is an experience constant valued between 0.75 and 0.8) on the imf_m, then we have $M = m - 1$ as the number of noise IMFs. The de-noising is finished by

$$x'(t) = x(t) - \sum_{i=1}^{M} imf_i \tag{48.5}$$

EMD compulsive de-noising does not need prior parameter setting. The de-noising process is controlled by σ and $\rho_{xx'_m}$, which are all determined by the signal itself.

48.2.2 Calculation and Analysis

Three schemes are used in the INS calculation of static inertial data:

Scheme 1: IMU original gyro signal is used is INS mechanization.
Scheme 2: db8 wavelet soft threshold de-noised gyro signal is used.
Scheme 3: EMD compulsive de-noised gyro signal is used.

In static conditions, velocity is velocity error. The east errors of the schemes are showed in Figs. 48.1, 48.2, 48.3. The similar results in north are not showed here. RMS results are showed in Table 48.1.

The results above show that:

1. Scheme 2 outperforms scheme 1, since wavelet soft threshold shrinks all coefficients by the threshold value, reducing the noise level to some extent. However, the amplitude of actual useful signals in static conditions is relatively low and there may be some exceptional noise with quite high amplitude.

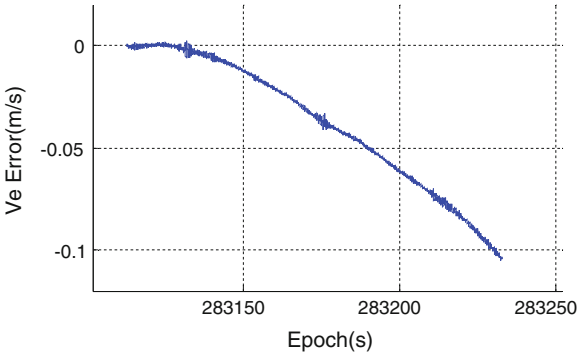

Fig. 48.1 Ve error of scheme 1

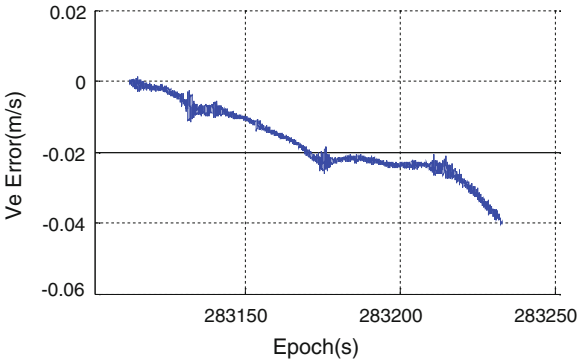

Fig. 48.2 Ve error of scheme 2

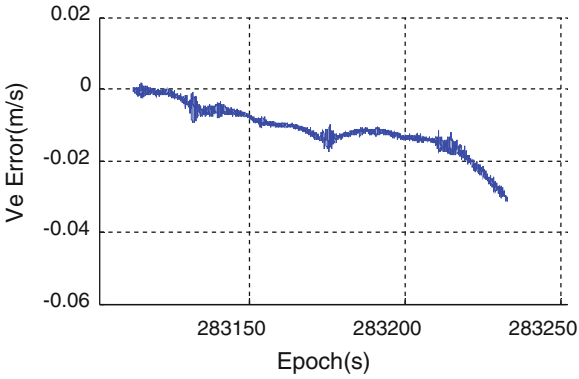

Fig. 48.3 Ve error of scheme 3

Threshold de-noising maintains high amplitude and retrains low amplitude basically, lacking effect in static conditions.

2. EMD compulsive de-noising reduces high frequency components as well as exceptional noise, resulting in higher accuracy than those of wavelet threshold de-noising.

Table 48.1 Comparison of RMS for three schemes

	RMS (m/s)	
	East velocity (Ve)	North velocity (Vn)
Scheme 1	0.050	0.156
Scheme 2	0.020	0.151
Scheme 3	0.013	0.040

48.3 EMD Threshold De-noising Method

The underlying basis of classical wavelet threshold de-noising, though ignored sometimes, is the assumption that the signal is contaminated by white Gaussian noise. Errors of inertial sensors contain many complicated components like bias instability, rate random walk and Markov process, resulting in colored property of the noise in inertial sensors. Fractional Gaussian noise model serves as the fundament of the proposed EMD threshold de-noising method in order to reduce the influence of colored noise.

48.3.1 Fractional Gaussian Noise Model for Random Inertial Sensor Errors

Fractional Gaussian noise (fGn) is a generalization of discrete white Gaussian noise. The statistical characteristic of fGn is determined merely by its second-order structure, which depends only upon a real-valued parameter H, termed Hurst parameter $(0 < H < 1)$. The concrete definition and property of fGn can be found in references [8, 9]. Especially, the case $H = 0.5$ reduces to white noise. As the core of fGn, Hurst parameter, reflecting the correlation degree of errors, should be estimated before the thresholding process.

Periodogram method is used to estimated Hurst parameter. If $H \neq 0.5$, the PSD of fGn is approximated by Huang and Shen [8]

$$S_H(f) \sim C\sigma^2 |f|^{1-2H}, \quad f \to 0 \tag{48.6}$$

where f denotes frequency and C denotes constant. The logarithmic style of Eq. (48.6) can be written as

$$\log S_H(f) \approx (1 - 2H) \log |f| + C, \quad f \to 0 \tag{48.7}$$

Therefore, a regression of the logarithm of the periodogram on the logarithm of the frequency should give a coefficient of $\hat{p} = 1 - 2H$, and the parameter H is calculated by

$$\hat{H} = (1 - p)/2 \tag{48.8}$$

48.3.2 Principle of EMD Threshold De-noising

To eliminate the noise and maintain the integrality of useful signal, thresholds applied on all the IMFs should be determined carefully. Inspired by wavelet threshold estimation, this paper seeks to derive the variance of the noise contained in each IMF, which will be further used to estimate the thresholds.

The PSD relation among the IMFs of fractional Gaussian noise decomposed by EMD is given by

$$S_{k'}(f) = \rho_H^{(2H-1)(k'-k)} S_k\left(\rho_H^{k'-k} f\right) \tag{48.9}$$

where $k' > k \geq 2$, ρ_H is approximated by

$$\rho_H \approx 2.01 + 0.2(H - 0.5) + 0.12(H - 0.5)^2 \tag{48.10}$$

Given that the integral of PSD over frequency results in variance, the variance relation among IMFs of fGn can be derived from (48.10):

$$\begin{aligned} V(k') &= \int_{-\infty}^{\infty} S_{k'}(f)df = \int_{-\infty}^{\infty} \rho_H^{(2H-1)(k'-k)} S_k\left(\rho_H^{k'-k} f\right)df \\ &= \rho_H^{(2H-1)(k'-k)} \int_{-\infty}^{\infty} S_k\left(\rho_H^{k'-k} f\right)df \\ &= \rho_H^{(2H-2)(k'-k)} V(k) \end{aligned} \tag{48.11}$$

The thresholds of EMD de-noising can be determined by Kopsinis and McLaughlin [10]

$$T_k = C\sqrt{V_k{}^* 2 \ \ln \ N} = C\sigma_k\sqrt{2 \ \ln \ N} \tag{48.12}$$

where N is the sample number and V_k is the variance of the noise in every IMF. C is a constant which can be easily set to 1.0 if the Hurst parameter is estimated accurately.

The empirical variance of imf_i can be estimated by

$$\mathrm{var}(imf_i) = \frac{1}{N}\sum_{j=1}^{N} [imf_i(j)]^2 \tag{48.13}$$

This variance contains the information of both signal of interest and noise, yet we need the variance of pure noise for the thresholding process. Considering that signal of interest is concentrated in a small subset of the IMF points, the standard deviations of noise in the first two IMFs can be estimated by a robust estimator:

$$\hat{\sigma}(k) = median(|imf_k(j)|)/0.6754, \quad k = 1, 2 \tag{48.14}$$

It is of dubious validity to use Eq. (48.14) to extract the noise variance for high order IMFs. The variances of the noise in high order IMFs are calculated by

$$\hat{V}(k) = \rho_H^{(2H-2)(k-2)}\hat{V}(2) = \rho_H^{(2H-2)(k-2)}[\hat{\sigma}(2)]^2, \quad k > 2 \tag{48.15}$$

The standard deviation or variance can be calculated by Eqs. (48.14) and (48.15) and the thresholds can be evaluated by (48.12).

Soft-thresholding and hard-thresholding are both commonly used schemes for threshold de-noising. It seems that soft-thresholding surpasses hard-thresholding in maintaining the continuity of signals. However, soft-thresholding generates biased outputs, which might result in additional error sources in certain conditions. Hence, hard-thresholding is preferred for the proposed EMD threshold de-noising method:

$$\tilde{imf_k}(j) = \begin{cases} imf_k(j), & |imf_k(j)| > T_k \\ 0, & |imf_k(j)| \le T_k \end{cases} \tag{48.16}$$

In fact, for de-noising it is not necessary to accomplish complete EMD when the residue r_n becomes a monotonic function or a function with only one extremum since noise mainly exits in low order IMFs. Thresholding on the first five or six IMFs is enough for real inertial data.

48.3.3 Calculation and Analysis

The dynamic inertial data used here are collected with a tactic-grade IMU mounted in a vehicle. This IMU consists of three gyroscopes and three accelerometers with the sample frequency of 100 Hz.

We implement INS mechanization algorithms to obtain position solutions. The following three schemes are designed in INS computations:

Scheme 1: Original inertial data is used in the mechanization;
Scheme 2: Wavelet threshold de-noised inertial data is used in the mechanization. The wavelet base function is db8;
Scheme 3: EMD threshold de-noised inertial data is used in the mechanization.

De-noising in Scheme 2 and Scheme 3 is implemented only in X-gyro data and Z-accelerometer data for explicitness. The estimated Hurst parameter of the gyro is 0.885 and that of accelerometer is 0.4474.

Longitude Errors of the three schemes are showed in Fig. 48.4. The Comparison of RMS and maximum values (MAX) of the errors is presented in Table 48.2.

From the above results, we can see that:

1. Wavelet threshold de-noising reduces the influence of white noise in inertial data, improving the positioning accuracy. However, this improvement is relatively tiny, since classical wavelet thresholding has underlying white noise assumption.
2. The proposed EMD threshold de-noising method outperforms wavelet threshold de-noising. EMD thresholding is based on fGn, which is utilized as the

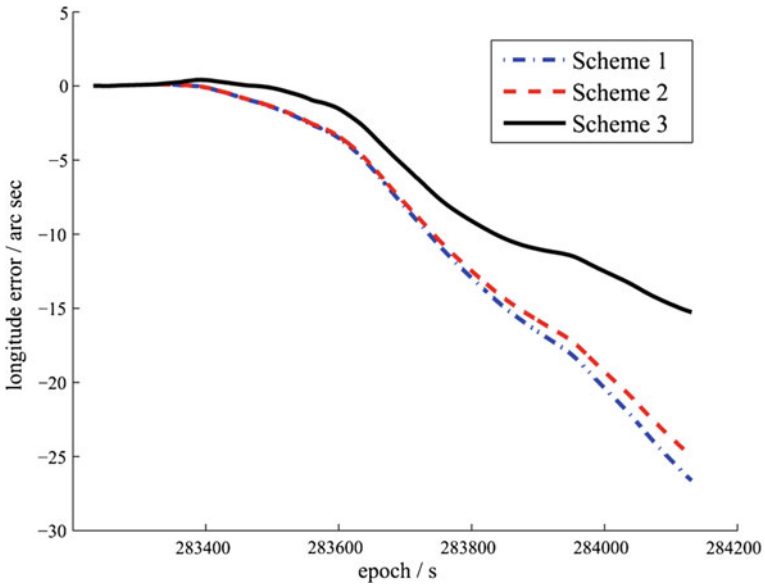

Fig. 48.4 Longitude errors

Table 48.2 Comparison of RMS for the de-noising results

	RMS(arc sec)		MAX(arc sec)	
	Longitude	Latitude	Longitude	Latitude
Scheme 1	43.901	12.661	99.418	26.623
Scheme 2	43.242	12.014	97.828	24.963
Scheme 3	36.987	7.924	81.623	15.265

model of sensor errors. By appropriate estimation of the Hurst parameter value, EMD thresholding can suppress the damage of time-correlated colored noise.

3. The corresponding position errors grow with time without outside assistance. Besides the remaining errors in *X*-gyro and *Z*-accelerometer after de-noising, errors in other unprocessed sensors and other error sources are also the causation.

48.4 Conclusions

The prevalent wavelet threshold de-noising has many disadvantages in de-noising inertial sensor errors. This paper has proposed the EMD compulsive de-noising method for static conditions and the EMD threshold de-noising method for dynamic conditions.

The EMD compulsive de-noising method can overcome the methodology unavailability of the wavelet threshold de-noising method in static situations and can effectively control the effects of exceptional noise.

Fractional Gaussian noise represents the correlation of noise and serves as the basis of the EMD threshold de-noising method. This new EMD threshold de-noising method estimates the threshold of every order of IMFs adaptively, reducing random inertial errors effectively and improving the accuracy of INS and GNSS/INS. As white noise is a special case of fGn, so the proposed EMD thresholding method can be used in de-noising both white noise and colored noise.

References

1. Abdel-Hamid W (2005) Accuracy enhancement of integrated MEMS-IMU/GPS systems for land vehicular navigation applications Department of Geomatics Engineering. University of Calgary, Canada
2. Yanhui W et al (2005) Application of wavelet analysis in gyro signal filtering. Piezoelectrics Acoustooptics 27(4):455–457
3. Xia D et al (2007) Application of wavelet's real-time filter in silicon micromachined gyroscope. J Chin Inertial Technol 15(1):92–95
4. Wu F, Yang Y (2007) GPS/INS integrated navigation by adaptive filtering based on wavelet threshold de-noising. Acta Geodaetica et Cartographica Sinica 36(2):124–128
5. Dai W et al (2006) EMD filter method and its application in GPS multipath. Acta Geodaetica et Cartographica Sinica 35(11):321–327
6. Boudraa AO, Cexus JC, Saidi Z (2004) EMD-based signal noise reduction. Int J Signal Process 1(1):33–37
7. Huang NE, Shen Z, Long SR et al (1998) The empirical mode decomposition and the Hilbert Spectrum for nonlinear and nonstationary time series analysis. Proc R Soc Lond Ser A 454:903–993
8. Huang NE, Shen SSP (2005) Hilbert-Huang transform and its applications. World Scientific, Singapore
9. Gan Y, Sui L, Wang B (2012) EMD Threshold De-noising and Its Applications in Processing INS Errors. Acta Geodaetica et Cartographica Sinica 41(4):504–509
10. Kopsinis Y, McLaughlin S (2009) Development of EMD-based De-noising methods inspired by wavelet thresholding. IEEE Trans Signal Process 57(4):1351–1362

Chapter 49
A Novel BD-2 RTK/Binocular Vision Navigation Solution for Automated Aerial Refueling

Yaqing Liu, Yulong Song and Baowang Lian

Abstract Automated Aerial Refueling (AAR) is a significant approach to improve sail distance, endurance and load of aircrafts, thus there is a wide range of needs in the military and civilian fields. The article presents a novel navigation solution for "Probe-and-drogue" air-refueling styles. Entire navigation process is divided into three steps. Firstly, tanker and receiver utilize BD-2 (Beidou-2 Navigation Satellite System) Real-Time Kinematics (RTK) to get closer at long-distance. Secondly, they utilize RTK/Binocular Vision Integrated Navigation to keep step with each other at mid-distance. Finally, at short-distance the Binocular Vision is used to keep tracking precisely. The RTK here is Dynamic to Dynamic Real time Differential Positioning. At last, this paper discusses the accuracy of the proposed AAR navigation solution, and simulation results are given.

Keywords Automated aerial refueling · RTK · Binocular vision · Integrated navigation

49.1 Introduction

The two main refueling systems are probe-and-drogue, which is simpler to adapt to existing aircraft, and the flying boom, which offers faster fuel transfer, but requires a dedicated operator station [1, 2]. For the flying boom refueling, simply by the oil machine can have the ability to maintain the relative position and tanker the hard pipe docking by the operator on the tanker manipulation to achieve. For plug drogue style refueling the receiver not only has the ability to formation flying, the need to find refueling drogue independent, real-time informed of the position and

Y. Liu (✉) · Y. Song · B. Lian
School of Electronics and Information of Northwest Polytechnical University,
Xi An, Shanxi Province, China
e-mail: tison.liu@126.com

J. Sun et al. (eds.), *China Satellite Navigation Conference (CSNC) 2013 Proceedings*, Lecture Notes in Electrical Engineering 245,
DOI: 10.1007/978-3-642-37407-4_49,

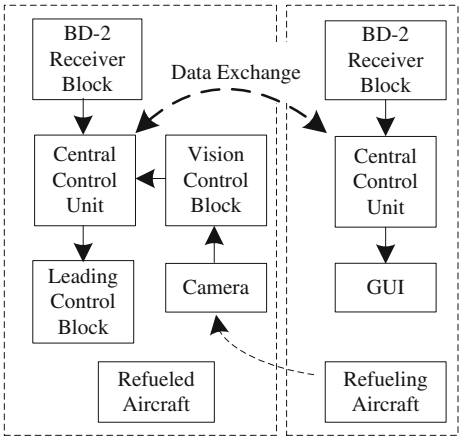

Fig. 49.1 AAR system structure

orientation of the drogue, in order to ensure the successful docking. Dong [3] presents a novel navigation solution for "Probe-and-drogue" air-refueling styles, automatic air refueling system structure shown in Fig. 49.1.

Automatic prediction accuracy of the relative position between the plug and drogue aerial refueling requirements needed to reach 10 cm level. RTK differential positioning satellite navigation signal carrier phase information, can achieve the required positioning accuracy, but only through the refueling Cone putting the receiving device can be installed directly in the terminal nearly into the docking stage to accurately capture Bushes movement state, which causes consolidated with security issues. Tanker wing, the tail will hamper the reception of satellite signals, at the same time there is multipath interference, the satellite signal loss, the electromagnetic interference. RTK is only suitable for work in the middle distance range [4].

Binocular visual system does not emit electromagnetic signal, does not get the interference of the electromagnetic environment, flexible measurement. The receiver can measure the position of the tanker, can measure the position and orientation of the drogue docking. However, by the limits of visibility, camera resolution, it is suitable for working in close range [5].

Two navigation techniques used in combination according to the distance between the tanker and the receiver, the disadvantage of the two can complement each other, play to their strengths, and to improve the reliability and availability of the entire automated aerial refueling navigation systems.

49.2 Dynamic to Dynamic RTK

The traditional RTK technique uses the known location of the fixed reference station, measuring and advertised receive pseudoranges and carrier phases of the satellite signals, the rover station uses the differential values of the measured

values of the local and measured values of the base station, satellite position and base station position obtaining satellite direction vector, and thereby obtain a precise relative position.

Since the fixed reference points are generally in the ground, for the aerial refueling purposes, the distance of the rover station and base station will become very long, thus will result in two problems: (1) With the growth of the baseline, Ambiguity time to grow, the accuracy will be reduced; (2) Data link will become very expensive, unreliable, even impossible to achieve.

In order to solve the relative positioning between the two moving targets require high precision, we present dynamic to dynamic RTK techniques, the base station is also set in motion vector, and the solution obtained the dynamic user with respect to the relative position of the dynamic reference station; and it is called the dynamic to dynamic RTK relative positioning.

The specific algorithm processes are as follows:

1. Use the pseudo-distance of rover station, make single-point positioning, $H * \vec{X} = P$ which $\vec{X}$ is the initial position, as P pseudorange, H is satellite vector, H_{DD} is double difference vector.
2. Use the base station and rover station pseudorange and carrier phase calculated double differential observation $\vec{D}$.
3. According to the formula $H * \vec{b} = \vec{D}$, the float solution baseline $\vec{b}$, and the covariance matrix Q.
4. Based on the covariance matrix Q, the integer ambiguity search.
5. Determine the integer ambiguity fixed solution calculated.

Compared with the traditional RTK technology, an increase of only a single point positioning, are a mature technology, feasibility good. Position due to the use of single-point positioning error will affect the results of the baseline solution. The Research Professor Zhou Zhongmo [6]:

1. Coordinate deviation of the starting point, the impact of the RNSS baseline vector with the orientation of the baseline, when the baseline change in orientation at 0°–360°, the relative change in amplitude of the above effects, a maximum of about 20 %.
2. Changes in the starting point coordinate, the RNSS baseline vector, and the geometric distribution of the satellites measured, for example, the largest value-added PDOP from 6.7 to 14.2, above the average impact of about 13 %.
3. The start point coordinate changes, the influence on the measured baseline, with baseline length are closely related, in the most unfavorable case, the impact of the size estimate, according to the following approximate relationship:

$$\delta S = 0.60 \times 10^{-7} \times b \times \Delta x \tag{49.1}$$

where δS in the relative positioning error, b is the baseline length, Δx is the deviation of the initial position. 10 km baseline, when the initial position deviation

of 10 m, relative positioning error of 0.6 cm. Visible, this deviation for aerial refueling boot is acceptable, when the baseline becomes short error will be further decreased.

49.3 Binocular Vision Navigation

Binocular vision guiding idea: in fuel taper pipe end surface placed red, yellow, green three LED, which constitute an equilateral triangle; install two cameras with filters in the receiver, to weaken the other environmental light interference; two cameras real-time recording LED image point and the image feature extraction, respectively, calculate the center of each color of the LED relative to the three-dimensional coordinates of the camera; calculated by the coordinates of the three points position and normal direction to arrive at the refueling the taper pipe position and posture.

49.3.1 Camera Model

49.3.1.1 Imaging Model

The camera lens is satisfy for the lens imaging formula $1/f = 1/m + 1/n$. Where f is the focal length of the lens, m is the image distance, n is the object distance. Actual case, n is often much larger than f, $m \approx f$, i.e. the image plane and the focal plane approximate coincidence. Such lens imaging model can be approximated with a shown in Fig. 49.2, apertures imaging model instead.

Figure 49.2, Oc is the optical center of the camera lens, the focal length f, for $P_1(x_1, y_1, z_1)$ an object point, to $P'_2(x_2, y_2, z_2)$ the equivalent image point. The image of the object compared with the original object, scaling and vertical and lateral direction opposite. The order of convenience, often in the inverted real image equivalent as a symmetry and lens, i.e. in the figure equivalent image plane.

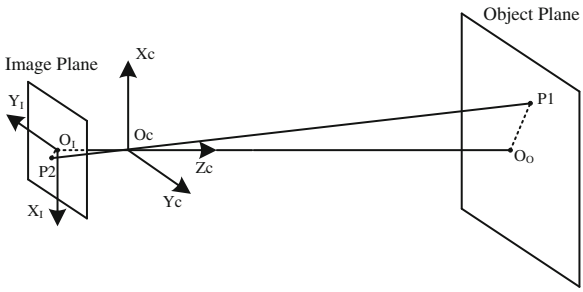

Fig. 49.2 Holes imaging model

49.3.1.2 Parameter Model

Image plane of the image obtained after the enlargement processing the digital image, the image point on the image plane (x, y) is converted into a digital image point (u, v) (pixel coordinates) of the optical axis in the image corresponding to the intersection of the plane of the image coordinates of markers (u0, v0), then

$$\begin{cases} u - u_0 = \alpha_x x_2 = \alpha_x f(x_1/z_1) \\ v - v_0 = \alpha_y y_2 = \alpha_y f(y_1/z_1) \end{cases} \tag{49.2}$$

Written in matrix form as:

$$\begin{bmatrix} u \\ v \\ 1 \end{bmatrix} = \begin{bmatrix} k_x & 0 & u_0 \\ 0 & k_y & v_0 \\ 0 & 0 & 1 \end{bmatrix} \begin{bmatrix} x_1/z_1 \\ y_1/z_1 \\ 1 \end{bmatrix} \tag{49.3}$$

α_x α_y is the imaging plane of the image plane in the X-axis and Y-axis direction amplification coefficient (x_1, y_1, z_1). The scene of the coordinates of the point in the camera coordinate system, $k_x = \alpha_x f$ is the X-axis direction of the amplification factor of the amplification factor $k_y = \alpha_y f$ is the Y-axis direction. Formula (49.3) within 4 parameters, called the four-parameter model of the camera, the more commonly used.

Seen by the photography geometric principles, the same image point may correspond to a number of different points in space. As shown below, all the points on the straight line OP with the same image coordinates.

When z = f, (x_{cf}, y_{cf}, f) point to the image point coordinates of the imaging spots on the imaging plane. When z = 1, the point $(x_{c1}, y_{c1}, 1)$ for the image point in the focal length normalization of the coordinates on the imaging plane of the imaging point. Using the intrinsic parameters of the camera, the imaging of the image point in the imaging plane focal length normalized coordinates can be obtained:

$$\begin{bmatrix} x_{c1} \\ y_{c1} \\ 1 \end{bmatrix} = \begin{bmatrix} k_x & 0 & u_0 \\ 0 & k_y & v_0 \\ 0 & 0 & 1 \end{bmatrix}^{-1} \begin{bmatrix} u \\ v \\ 1 \end{bmatrix} \tag{49.4}$$

The focal length normalized image point and the optical axis of the center point on the imaging plane can be determined scene point to the space where the straight (Fig. 49.3).

49.3.2 Position Measurement

Shown in Fig. 49.4, the binocular vision use the matching points on the images collected by the two cameras, and calculate the three-dimensional coordinates of

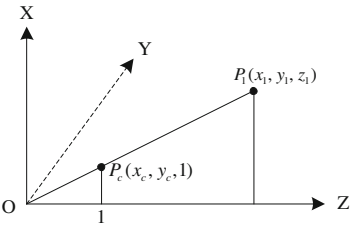

Fig. 49.3 Projection of image points in focal length normalized plane

the spatial points. The camera intrinsic parameters using a four-parameter model, respectively M_{in1}, and M_{in2} said. Relative outside the parameters of two cameras ${}^{c1}M_{c2}$ with C2 coordinate system is expressed as C1 coordinate system.

By spatial point P the point P in the focal length of the camera C1 of the normalized coordinates of the imaging plane of the imaging point in the image coordinates of the camera C1 (u1, v1), can be calculated $P_{1c_1}(x_{c1}, y_{c1}, 1)$ as:

$$\begin{bmatrix} x_{1c_1} \\ y_{1c_1} \\ 1 \end{bmatrix} = \begin{bmatrix} k_{x1} & 0 & u_{10} \\ 0 & k_{y1} & v_{10} \\ 0 & 0 & 1 \end{bmatrix}^{-1} \begin{bmatrix} u_1 \\ v_1 \\ 1 \end{bmatrix} \tag{49.5}$$

Space point P on the optical axis of the camera C1 of the center point $O_1(0, 0, 0)$ and $P_{1c_1}(x_{c1}, y_{c1}, 1)$ a line of the linear equation:

$$\frac{x-0}{x_{c1}-0} = \frac{y-0}{y_{c1}-0} = \frac{z-0}{1-0} = t_1 \Rightarrow \begin{cases} x = x_{c1}t_1 \\ y = y_{c1}t_1 \\ z = t_1 \end{cases}. \tag{49.6}$$

Similarly, from the spatial point P is a point P in the focal length of the camera C2 normalized coordinates of the imaging plane of the imaging point in the image coordinates of the camera C2 (u2, v2), can be calculated as:

$$\begin{bmatrix} x_{2c_1} \\ y_{2c_1} \\ 1 \end{bmatrix} = \begin{bmatrix} k_{x2} & 0 & u_{20} \\ 0 & k_{y2} & v_{20} \\ 0 & 0 & 1 \end{bmatrix}^{-1} \begin{bmatrix} u_2 \\ v_2 \\ 1 \end{bmatrix} \tag{49.7}$$

Camera P_{2c_1} C2 coordinate system conversion in the camera C1 coordinate system of coordinates:

$$\begin{bmatrix} x_{2c_1 1} & y_{2c_1 1} & z_{2c_1 1} & 1 \end{bmatrix}^T = {}^{c1}M_{c2} \begin{bmatrix} x_{2c_1} & y_{2c_1} & 1 & 1 \end{bmatrix}^T \tag{49.8}$$

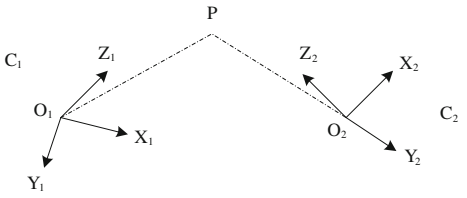

Fig. 49.4 Binocular vision measurement

On a straight line in the coordinate system of the camera C1, spatial point P at the center point $O_2(p_x, p_y, p_z)$ and $P_{2c_1}(x_{2c_1}1, y_{2c_1}1, z_{2c_1}1)$ the point of the optical axis of the camera C2 constituted p_x, p_y, p_z. Constituting the location of offset ${}^{c1}M_{c2}$.

$$\begin{cases} x = p_x + (x_{2c_1}1 - p_x)t_2 \\ y = p_y + (y_{2c_1}1 - p_y)t_2 \\ z = p_z + (z_{2c_1}1 - p_z)t_2 \end{cases} \tag{49.9}$$

Formula (49.6) and (49.9) associated Claim can be solved for the three-dimensional coordinates of a spatial point P in the coordinate system of the camera C1. Calibration error exists due to the internal and external parameters of the camera, the two straight lines and sometimes there is no intersection. Therefore in solving the three-dimensional coordinates of the point P in the coordinate system C1, it is usually the least squares method [7].

49.4 RTK/Binocular Vision Integrated Navigation

When the distance is far, by the limitations of binocular vision distance, we can not get the relative position, but with decreasing distance, the precision of binocular vision is improving, the RTK system is less influenced by the distance, but when close to the tanker, the signal will be blocked, RTK does not work, and therefore need integrated navigation of RTK and binocular vision.

As shown below, the article uses a simple weighted average algorithm to the result of the relative position of the two systems.

$$\begin{cases} \vec{b}_{final} = a_1 \times \vec{b}_{rtk} + a_2 \times \vec{b}_{bs} \\ a_1 = \dfrac{A_2}{A_1 + A_2};\ a_2 = \dfrac{A_1}{A_1 + A_2} \end{cases} \tag{49.10}$$

Which a_1, a_2 normalized weighting coefficient, A1 is RTK positioning error estimates, A2 is binocular vision positioning error estimates, $\vec{b}_{final}$ is integrate d positioning results, $\vec{b}_{rtk}$ is RTK positioning, $\vec{b}_{bs}$ is the positioning of the binocular vision results.

49.5 Simulation

Using Matlab to build simulation environment, designed tanker and receiver track simulation, Beidou-2 observational data and the acquisition of binocular vision data were used to calculate the relative position of RTK algorithms and Binocular Vision Ranging. The combination of binocular vision navigation algorithm and

RTK algorithms is for positioning results data fusion, the ultimate combination of navigation results.

49.5.1 Simulation Conditions

1. Itineraries

The relative distance is from 20 km to 20 m, uniform close relative velocity of 10 m/s, and the duration of 1998s. Then, at the relative speed of 1 m/s continues to approach until a distance of 0 m, the duration of 20 s.

2. Satellite system

BD-2 B1 frequency satellite signals, 5 GEO 2 IGSO, 2 MEO. RTK algorithm update rate of 1 Hz. Not consider electromagnetic interference, multipath interference, and satellite signal occlusion.

3. Visual system

The camera resolution is 512 × 512, binocular baseline distance of 0.4 m.

49.5.2 Simulation Results

Based BD-2, the RTK navigation system shown in Fig. 49.5, within the range of 0–20 km, positioning error remains within 7 cm, and with no linear relationship with the relative distance of the target.

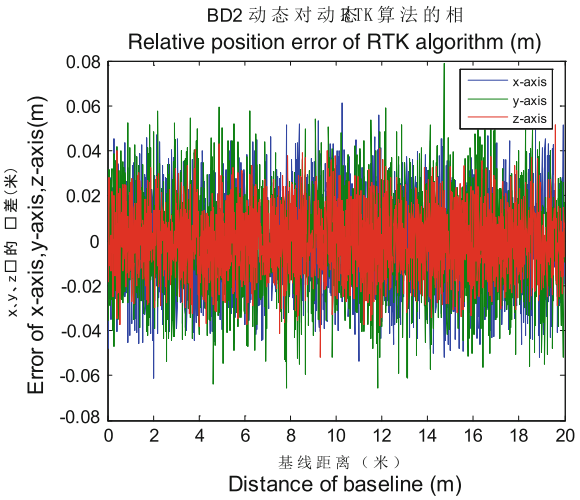

Fig. 49.5 RTK algorithm relative position error

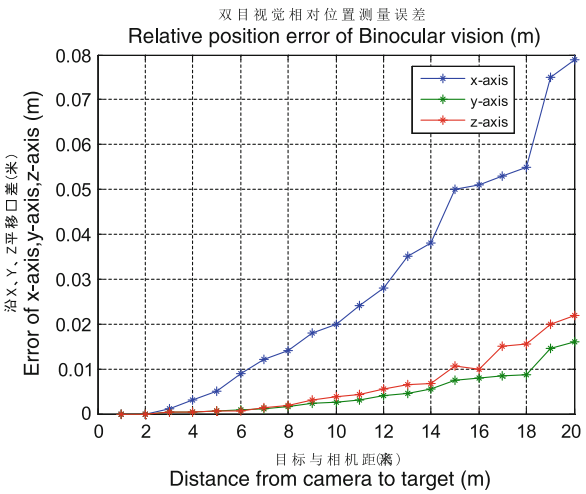

Fig. 49.6 Binocular vision relative position error

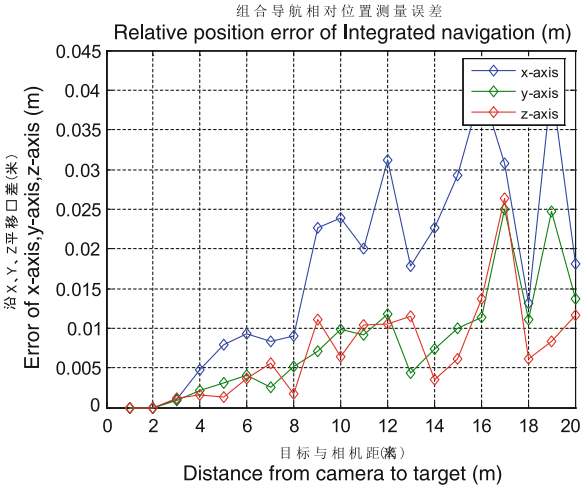

Fig. 49.7 Integrated navigation relative position error

As shown in Fig. 49.6, the binocular vision system in a distance of 18 m with the target range, the positioning error is less than 7 cm, and the error becomes large with the relative distance of the target increased.

As shown in Fig. 49.7, the integrated navigation system with a target distance of 20 m like the positioning accuracy with binocular vision and the RTK navigation systems.

49.6 Conclusion

The simulation results show that, in the range of 3–18 m away, the receiver use binocular vision to capture the target image, make feature extraction, and to obtain a three-dimensional position coordinates; at the same time get BD-2 navigation system relative positioning results based RTK technology; final positioning accuracy obtained by the combination of the two is similar to use separate one, but we can improve the reliability and availability of the system.

Close than 3 m, binocular vision measurement error is almost zero, when the satellite navigation system may be blocked or interfered by multipath interference and other factors.

Outside the range of 18 m, the positioning accuracy of binocular vision system decreased rapidly, because of camera resolution and aerial visibility limit, we used alone BD-2 navigation system based RTK technology for navigation at this time.

Acknowledgment The work was supported in part by the National Defense key Laboratory of Integrated Avionics System of China and by a grant from the Aviation Science Foundation under program No. 20110196004, and National Natural Science Foundation of China No. 61174194.

References

1. Nalepka JP, Hinchman JL (2005) Automated aerial refueling: extending the effectiveness of unmanned air vehicles. AIAA modeling and simulation technologies conference and exhibit., AIAA, San Francisco, USA, pp 2005–6005
2. Stepanyan V, Lavretsky E, Hovakimyan N (2004) Aerial refueling autopilot design methodology: application to F-16 aircraft model. AIAA guidance, navigation, and control conference, AIAA, Providence, RI, USA, pp 2004–5321
3. Dong X, Xu Y, Chen B (2008) Automatic aerial refueling technology research and development and the key problems. Air Force Eng Univ J (Science Edition) 9(6):1–5
4. Korbly R, Sensong L (1983) Relative attitudes for automatic docking. J Guidance, Control, Dyn 6(3):213–215
5. Honglun XHW (2011) Binocular vision-based short-range navigation method for autonomous aerial refueling. J Beijing Univ Aeronaut Astronaut 37(2):206–209
6. Liu L (2005) Dynamic of dynamic GPS precise positioning theory and its application research. Wuhan University, Wuhan
7. Xu D, Tan M, Li Y (2008) Robot vision measurement and control. National defence industry press, Beijing, p 2

Chapter 50
An Adaptive Dual Kalman Filtering Algorithm for Locata/GPS/INS Integrated Navigation

Zebo Zhou, Ling Yang and Yong Li

Abstract In modern navigation applications, Inertial Navigation System (INS) is attractive for integrating with Global Positioning System (GPS). Although traditional GPS/INS integrated systems can bridge the GPS gaps, the navigation capability is strongly dependent on the performances of standalone INS. As an important complementary, a new terrestrial, Radio-Frequency (RF) based, distance measurement technology "Locata" can provide continuously time-synchronised ranging signals even in many GPS challenged environments e.g. poor satellite geometry, signal blockage in suburban, tunnels, high rise buildings canyon. This paper investigates the integration of Locata, GPS, and INS with a focus on the loosely-coupled triple integration algorithm. Firstly, the Conventional Kalman Filtering (CKF) based triple integration of Locata/GPS/INS architecture is described and briefly discussed. Secondly, to overcome the pitfalls of conventional Locata/GPS/INS integration algorithm, an Adaptive Dual Kalman Filtering (ADKF) algorithm is proposed and developed in three stages: (1) To enhance the reliability of position and velocity (PV) quantities generated from Locata/GPS integrated sensors, the 1st KF is additionally constructed to reliably estimate the PV solution before fusing INS sensor. (2) Combining the 15-state INS error model and the measurements which are the differences between PV solution from the 1st KF and INS sensor, the 2nd KF is subsequently employed to correct the INS navigation errors. (3) The final integration solution is reversely used as the feedback for precisely estimating the stochastic model (i.e. variance of dynamic and observation model noise) of the 1st KF. Finally, the real flight experiment is carried out to demonstrate the efficiency and validity of Locata/GPS/INS integration algorithms. The results show that: (1) Conventional GPS/INS integration

Z. Zhou (✉)
School of Aeronautics and Astronautics, University
of Electronic Science Technology of China, Chengdu, People's Republic of China
e-mail: klinsmann.zhou@gmail.com

L. Yang · Y. Li
School of Surveying and Geospatial Engineering, University of New South Wales,
Sydney, Australia

J. Sun et al. (eds.), *China Satellite Navigation Conference (CSNC) 2013 Proceedings*, Lecture Notes in Electrical Engineering 245,
DOI: 10.1007/978-3-642-37407-4_50,

performs well but its accuracy dramatically decreases when GPS signals are unavailable for a short period. (2) Augmented by Locata, GPS/INS produces tolerable results in whole experiment even without aiding of GPS. (3) By additionally operation of the 1st KF and adaptively estimating its stochastic model with feedback of integration solution, ADKF achieves more accurate and reliable position, velocity and attitude (PVA) solution than CKF.

Keywords INS error · Locata/GPS/INS integration · Adaptive Kalman filtering · Stochastic model

50.1 Introduction

GPS provides the real-time precise position and velocity (PV) information suitable for most land, marine, and aircraft navigation applications [1]. However, it still faces challenges in ensuring continuity of service in urban areas due to, e.g., blockages of GPS signals, low carrier-to-noise density and multi-path including reflection and diffraction, which would limit GPS's ability to deliver the required level of availability, accuracy and reliability of positioning [2, 3]. The traditional means of overcoming the gaps in navigation coverage due to satellite signal blockages is to use other complementary navigation technologies. Integrating GPS with INS is implemented mainly to overcome the limitations of each navigation sensor and improve the overall system performance. However, there are still many problems for INS application, e.g., scale factor nonlinearities, misalignment, high noise and temperature varying biases. Therefore, regular calibration using external aiding sources is essential to control the growth of INS errors [4]. However, GPS signal interruptions frequently occur in canyons or tunnels. In such cases, the accuracy of INS without external correction will heavily be degraded with time, thus compromising integrated system accuracy and integrity [5]. Although the non-holonomic constraints can be applied, it only provides reliable solutions for longer periods in the absence of GPS [5, 6]. Another approach for preventing the errors from growing in adverse GPS condition is the use of backward smoothing techniques, e.g. the Rauch-Tung-Striebel (RTS) smoother [7, 8]. Nevertheless, it is an offline processing algorithm and hard to be applied in real-time navigation. Therefore, an auxiliary sensor system is required to substantially augmented GPS/INS navigation [5]. The Locata approach deploys a network of round-based transceivers that cover an area with strong time-synchronised ranging signals and provides the seamless and reliable navigation results by integrated with GPS/INS [9, 10].

Kalman filtering (KF) is extensively used for carrying out the solutions in integrated navigation systems. The operation of KF relies on the proper definition of a functional model and a stochastic model [11, 12]. Unfortunately, this is difficult in Locata/GPS/INS navigation, e.g. insufficient observation redundancy, time-variant noise, manoeuvrings, thus the un-modelled errors in either state or

observation model may cause the suboptimum even divergence of filter. A great of researches have been investigated to solve the problems with adaptive KF techniques [13–17], which are developed to estimate the optimal adaptive factors by innovations estimation to make the filter residuals covariance consistent with their theoretical covariance estimated with present information and residuals. Generally, adaptive factors are usually developed under a basic assumption that the current information should be reliable, which is not always true in real-time navigation.

To overcome the pitfalls of conventional Kalman filtering (CKF) in Locata/GPS/INS integration, a dual Kalman filtering integration architecture is designed to enhance the strength of integration model and the adaptive technique is further proposed in real time to reasonably adjust the covariances of dynamic and observation model noise. The paper is organised as follows: an overview of conventional Locata/GPS/INS integration algorithm is presented in Sect. 50.2. In Sect. 50.3, an adaptive DKF algorithm for triple integration of Locata/GPS/INS is proposed and developed in three stages. The real flight experiment is carried out to demonstrate the efficiency and validity of our proposed algorithm compared with the conventional algorithm in Sect. 50.4. Finally, conclusions are given in Sect. 50.5.

50.2 Conventional Locata/GPS/INS Loosely Coupled Integration Algorithm

50.2.1 Integration Architecture

The most common Locata/GPS/INS integration mode is known as loosely-coupled integration (see Fig. 50.1) in which the Locata/GPS derived PV solution is integrated with the INS derived navigation solution. GPS/Locata provides the PV for real-time correction of the inertial sensor errors as well as the navigation parameters of INS. In order to obtain the real-time navigation results in one KF, both dynamic model and observation model should be reasonably established beforehand.

50.2.2 Integration Estimation

A linear dynamic model and an observation model are involved in the KF,

$$\boldsymbol{x}_k = \boldsymbol{\Phi}_{k,k-1}\boldsymbol{x}_{k-1} + \boldsymbol{w}_k \tag{50.1}$$

$$\boldsymbol{l}_k = \boldsymbol{A}_k\boldsymbol{x}_k + \boldsymbol{\varepsilon}_k \tag{50.2}$$

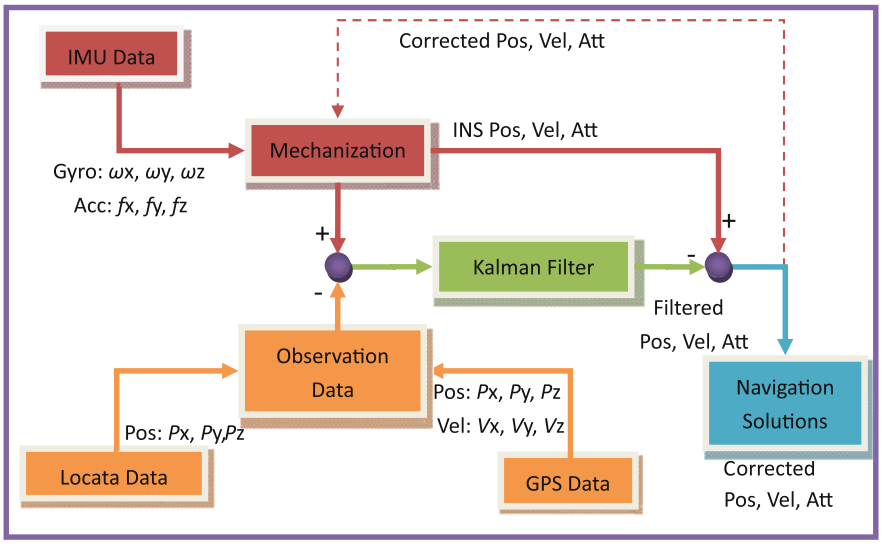

Fig. 50.1 The flowchart of conventional loosely-coupled Locata/GPS/INS integration architecture

where the subscripts denote the epoch number; $\boldsymbol{x}$ is the state vector to be estimated, $\boldsymbol{l}$ is the measurement vector; $\boldsymbol{w}$ and $\boldsymbol{\varepsilon}$ are the dynamic and observation model noise with the zero means and the covariance matrices of $\boldsymbol{\Sigma w}$ and $\boldsymbol{\Sigma}$, respectively; $\boldsymbol{\Phi}$ is the state transition matrix of the $(k-1)$th epoch to the kth epoch; $\boldsymbol{A}$ is the design matrix connecting the state vector with the observation vector. The sequential formulae in KF are given,

$$\bar{\boldsymbol{x}}_k = \boldsymbol{\Phi}_{k,k-1}\hat{\boldsymbol{x}}_{k-1} \tag{50.3}$$

$$\Sigma_{\bar{\boldsymbol{x}}_k} = \boldsymbol{\Phi}_{k,k-1}\Sigma_{\hat{\boldsymbol{x}}_{k-1}}\boldsymbol{\Phi}^T_{K,k-1} + \Sigma_{\boldsymbol{w}_k} \tag{50.4}$$

$$\boldsymbol{K}_k = \Sigma_{\bar{\boldsymbol{x}}_k}\boldsymbol{A}_k^T\left(\boldsymbol{A}_k\Sigma_{\bar{\boldsymbol{x}}_k}\boldsymbol{A}_k^T + \Sigma_k\right)^{-1} \tag{50.5}$$

$$\hat{\boldsymbol{x}}_k = \bar{\boldsymbol{x}}_k + \boldsymbol{K}_k(\boldsymbol{l}_k - \boldsymbol{A}_k\bar{\boldsymbol{x}}_k) \tag{50.6}$$

$$\Sigma_{\hat{\boldsymbol{x}}_k} = (\boldsymbol{I} - \boldsymbol{K}_k\boldsymbol{A}_k)\Sigma_{\bar{\boldsymbol{x}}_k} \tag{50.7}$$

where $\boldsymbol{I}$ is the identity matrix with same dimensions of $\Sigma_{\bar{\boldsymbol{x}}_k}$; $\bar{\boldsymbol{x}}_k$ and $\Sigma_{\bar{\boldsymbol{x}}_k}$ denote the predicted state vector and its covariance matrix, respectively; $\boldsymbol{K}_k$ is the gain matrix; $\hat{\boldsymbol{x}}_k$ and $\Sigma_{\hat{\boldsymbol{x}}_k}$ are the posterior KF estimate and its covariance matrix.

50.3 Adaptive DKF Algorithm for Locata/GPS/INS Integrated Navigation

50.3.1 Integration Architecture

Although the conventional Locata/GPS/INS integration algorithm is easy and convenient to implement, it still has two evident disadvantages:

1. No observation redundancy in either Locata or GPS, which significant decreases the reliability of PV solutions, which may lead to wrong corrections to INS.
2. The covariances of Locata/GPS are set as the experienced values, which degrades the accuracy and may lead to divergence of KF. Thus it is not suitable to be applied in the time-variant navigation environments.

In order to overcome the two disadvantages above, an adaptive dual Kalman filtering (ADKF) algorithm based Locata/GPS/INS architecture is proposed (see Fig. 50.2). The 1st KF is used to integrate the Locata and GPS outputs together with a dynamic model. Compared with Fig. 50.1, the dynamic model, to some extent, not only enhances the reliability of Locata/GPS with a prior dynamic assumption, but also improves the accuracy of PV if the dynamic model is

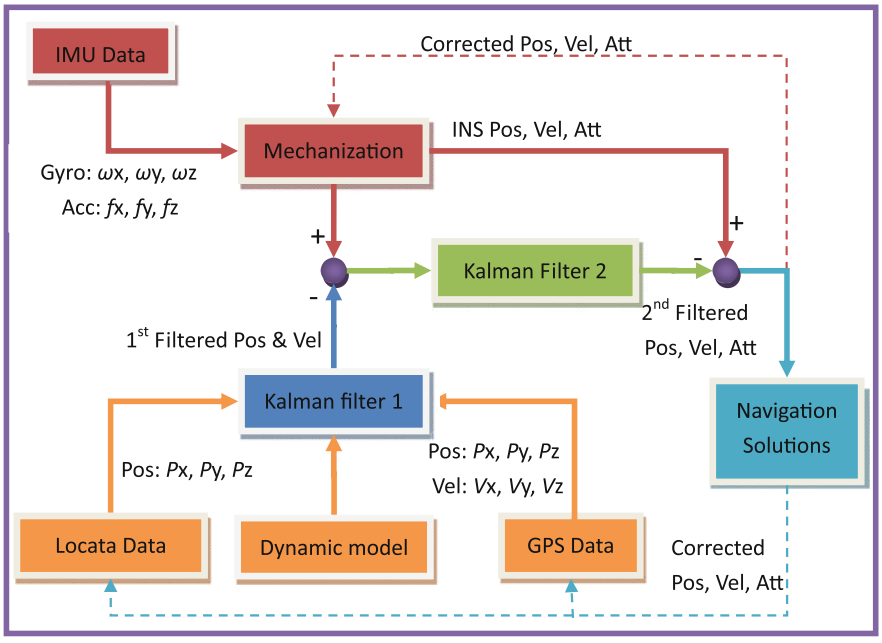

Fig. 50.2 The flowchart of ADKF based loosely-coupled Locata/GPS/INS integration architecture

adequately described the motion behaviours of moving objects. Using the PV solution from 1st KF, the 2nd KF is further employed to correct INS errors and obtain the final navigation solution. In the context of (2), the final integrated solution is used as feedback for estimating the variance of dynamic and observation model noise of the 1st KF. In the next subsection, the estimation procedure of ADKF algorithm for Locata/GPS/INS integration is conducted and discussed in details.

50.3.2 Estimation Procedure

According to the aforementioned ADKF architecture of Locata/GPS/INS integration, three stages are included in integration estimation procedure as follows.

Stage 1: 1st Kalman filtering based Locata/GPS integration

To enhance the model strength and improve the navigation accuracy, the dynamic model which describes the motion behaviours of moving objects is constructed for Locata/GPS integration as,

$$\boldsymbol{x}_k^1 = \boldsymbol{\Phi}_{k,k-1}^1 \boldsymbol{x}_{k-1}^1 + \boldsymbol{w}_k^1 \tag{50.8}$$

where the superscript "1" denotes the 1st Kalman filtering index; the PV state $\boldsymbol{x}_k^1 = \begin{bmatrix} \boldsymbol{r}_k^T & \boldsymbol{v}_k^T \end{bmatrix}^T$; $\boldsymbol{r}_k$ and $\boldsymbol{v}_k$ are three dimensional position and velocity column vectors respectively; $\boldsymbol{\Phi}_{k,k-1}^1 = \begin{bmatrix} 1 & \Delta t \\ 0 & 1 \end{bmatrix} \otimes \boldsymbol{I}_{3\times 3}$ and Δt denotes interval of two consecutive epochs; $\boldsymbol{w}_k^1 \sim \left(\boldsymbol{0}, \Sigma_{\boldsymbol{w}_k^1}\right)$.

The observation model of Locata/GPS integration is formed as,

$$\boldsymbol{l}_k^1 = \boldsymbol{A}_k^1 \boldsymbol{x}_k^1 + \boldsymbol{\varepsilon}_k^1 \tag{50.9}$$

where $\boldsymbol{l}_k^1 = \begin{bmatrix} \left(\boldsymbol{r}_k^{\text{gps}}\right)^T & \left(\boldsymbol{v}_k^{\text{gps}}\right)^T & \left(\boldsymbol{r}_k^{\text{loc}}\right)^T \end{bmatrix}^T$ and the superscript of PV state denotes the output source, i.e. GPS and Locata; $\boldsymbol{A}_k^1 = \begin{bmatrix} \boldsymbol{I}_{6\times 6} \\ \boldsymbol{I}_{3\times 3} \mid \boldsymbol{0}_{3\times 3} \end{bmatrix}$, $\boldsymbol{\varepsilon}_k^1 \sim \left(\boldsymbol{0}, \Sigma_k^1\right)$. Then the Locata/GPS integration state $\hat{\boldsymbol{x}}_k^1$ and its covariance $\Sigma_{\hat{\boldsymbol{x}}_k^1}$ are trivially estimated in the 1st KF with Eqs. (50.3)–(50.7).

Stage 2: 2nd Kalman filtering for INS integrated with GPS/Locata outputs

INS state error equation modelling

Error states vector with fifteen dimensions are involved in the 2nd KF, i.e. position, velocity and attitude (PVA), gyro drift and accelerator bias in three components respectively. For convenience in calculation, the WGS-84 coordinate

frame which is an Earth-Centred-Earth-Fixed (ECEF) coordinate frame (e-frame) is chosen and symbolized as 'e' for the superscript in the following content. Then the state error differential equations are established as [4],

$$\dot{\boldsymbol{x}}^2 = \boldsymbol{\Theta}\boldsymbol{x}^2 + \boldsymbol{w}^2 \tag{50.10}$$

where $\boldsymbol{x}^2 = \begin{bmatrix} \delta\boldsymbol{r}^T & \delta\boldsymbol{v}^T & \delta\theta^T & \boldsymbol{d}^T & \boldsymbol{b}^T \end{bmatrix}^T$ a δ denotes the error; $\boldsymbol{w}^2$ is the process noise; Define α and β as the time correlation parameters of gyro and accelerometer respectively, and then the coefficient matrix $\boldsymbol{\Theta}$ is,

$$\boldsymbol{\Theta} = \begin{bmatrix} \boldsymbol{0}_{3\times3} & \boldsymbol{I}_{3\times3} & \boldsymbol{0}_{3\times3} & \boldsymbol{0}_{3\times3} & \boldsymbol{0}_{3\times3} \\ \boldsymbol{N}^e & -2\boldsymbol{\Omega}^e_{ie} & -\boldsymbol{F}^e & \boldsymbol{0}_{3\times3} & \boldsymbol{R}^e_b \\ \boldsymbol{0}_{3\times3} & \boldsymbol{0}_{3\times3} & -\boldsymbol{\Omega}^e_{ie} & \boldsymbol{0}_{3\times3} & \boldsymbol{R}^e_b \\ \boldsymbol{0}_{3\times3} & \boldsymbol{0}_{3\times3} & \boldsymbol{0}_{3\times3} & -\alpha\boldsymbol{I}_{3\times3} & \boldsymbol{0}_{3\times3} \\ \boldsymbol{0}_{3\times3} & \boldsymbol{0}_{3\times3} & \boldsymbol{0}_{3\times3} & \boldsymbol{0}_{3\times3} & -\beta\boldsymbol{I}_{3\times3} \end{bmatrix} \tag{50.11}$$

where $\boldsymbol{N}^e$ relates to gravity parameters; $\boldsymbol{F}^e$ and $\boldsymbol{\Omega}^e_{ie}$ are the anti-symmetric matrices of stress and earth rotation respectively; $\boldsymbol{R}^e_b$ denotes the strapdown matrix from body frame to e frame. By expanding Eq. (50.10) to 1st order, we obtain the following discrete form of error state model,

$$\boldsymbol{x}^2_k = \boldsymbol{\Phi}^2_{k,k-1}\boldsymbol{x}^2_{k-1} + \boldsymbol{w}^2_k \tag{50.12}$$

where the superscript "2" denotes the 2nd Kalman filter index; the transition matrix $\boldsymbol{\Phi}^2_{k,k-1} \approx \boldsymbol{I}_{15\times15} + \boldsymbol{\Theta}\Delta t$ and the co-variance of process noise is $\Sigma_{\boldsymbol{w}^2_k} \approx \Delta t\boldsymbol{Q}_k$; $\boldsymbol{Q}_k$ denotes the spectrum density of process noise.

Observation model

If INS is aided by the outputs from 1st KF of GPS/Locata integration, the observation model relating to error state can be established based on the differences between GPS/Locata solution and INS only solution,

$$\boldsymbol{l}^2_k = \boldsymbol{A}^2_k\boldsymbol{x}^2_k + \boldsymbol{\varepsilon}^2_k \tag{50.13}$$

where $\boldsymbol{l}^2_k = \begin{bmatrix} \boldsymbol{B}_1\hat{\boldsymbol{x}}^1_k - \boldsymbol{r}^{\text{ins}}_k \\ \boldsymbol{B}_2\hat{\boldsymbol{x}}^1_k - \boldsymbol{v}^{\text{ins}}_k \end{bmatrix}$, $\boldsymbol{B}_1 = [\boldsymbol{I}_{3\times3} \quad \boldsymbol{0}_{3\times3}]$ and $\boldsymbol{B}_2 = [\boldsymbol{0}_{3\times3} \quad \boldsymbol{I}_{3\times3}]$; $\boldsymbol{A}^2_k = \begin{bmatrix} \boldsymbol{I}_{3\times3} & \boldsymbol{0}_{3\times3} & \boldsymbol{0}_{3\times9} \\ \boldsymbol{0}_{3\times3} & \boldsymbol{I}_{3\times3} & \boldsymbol{0}_{3\times9} \end{bmatrix}$; the observational noise $\boldsymbol{\varepsilon}^2_k \sim (\boldsymbol{0}, \Sigma^2_k)$, and $\Sigma^2_k = \Sigma_{\hat{\boldsymbol{x}}^1_k} + \begin{bmatrix} \Sigma_{\boldsymbol{r}^{\text{ins}}_k} & \boldsymbol{0}_{3\times3} \\ \boldsymbol{0}_{3\times3} & \Sigma_{\boldsymbol{v}^{\text{ins}}_k} \end{bmatrix}$. And then the Locata/GPS/INS integrated solution is calculated by Eqs. (50.3)–(50.7).

Stage 3: Feedback to local sensors
PVA correction for INS

With the INS error state estimated by the 2nd KF, the final navigation can be corrected and expressed by,

$$\boldsymbol{x}_k = \boldsymbol{x}_k^3 + \boldsymbol{B}\boldsymbol{x}_k^2 \tag{50.14}$$

where $\boldsymbol{x}_k^3 = \left[\left(\boldsymbol{r}_k^{\text{ins}}\right)^T \quad \left(\boldsymbol{v}_k^{\text{ins}}\right)^T \quad \left(\boldsymbol{\theta}_k^{\text{ins}}\right)^T \right]^T$ are computed according to INS mechanization in e-frame; $\boldsymbol{B} = \begin{bmatrix} \boldsymbol{I}_{9\times9} & \boldsymbol{0}_{9\times6} \\ \boldsymbol{0}_{6\times9} & \boldsymbol{I}_{6\times6} \end{bmatrix}$ and $\boldsymbol{x}_k$ are the final PVA solution at epoch k. Here the gyro and accelerometer measurements are not corrected in real time, because either the low-cost INS sensor or lack of sufficient Locata/GPS data will wrongly estimate errors of INS sensor, thus conversely degrade the accuracy of INS measurements.

Estimating the variance of GPS/Locata observation model noise

Since no observation redundancy for both GPS and Locata in the loosely-coupled integration mode, the variance of observation model noise should be reasonable to reflect the contribution of GPS and Locata data. Considering the independence of GPS and Locata observation, the variance matrix of observation model noise consists of,

$$\hat{\Sigma}_k = \begin{bmatrix} \hat{\Sigma}_k^{\text{gps}} & \boldsymbol{0}_{6\times3} \\ \boldsymbol{0}_{3\times6} & \hat{\Sigma}_k^{\text{loc}} \end{bmatrix} \tag{50.15}$$

where $\hat{\Sigma}_k^{\text{gps}}$ and $\hat{\Sigma}_k^{\text{loc}}$ are the estimated covariance matrices of GPS and Locata observation noise respectively. If we replace the true PV values with the final PV solution which is of course more accurate and reliable than 1st KF solution, the variance of GPS/Locata can be reliably estimated by further employing previous n epochs with following equations,

$$\hat{\Sigma}_k^{\text{gps}} = \begin{bmatrix} \dfrac{\sum_{i=k-n}^{k-1} \left[{}_1\left(\boldsymbol{l}_i^1 - \hat{\boldsymbol{x}}_i\right)\left(\boldsymbol{l}_i^1 - \hat{\boldsymbol{x}}_i\right)^T \boldsymbol{M}_1^T \right]}{n} & \boldsymbol{0}_{3\times3} \\ \boldsymbol{0}_{3\times3} & \dfrac{\sum_{i=k-n}^{k-1} \left[\boldsymbol{M}_2\left(\boldsymbol{l}_i^1 - \hat{\boldsymbol{x}}_i\right)\left(\boldsymbol{l}_i^1 - \hat{\boldsymbol{x}}_i\right)^T \boldsymbol{M}_2^T \right]}{n} \end{bmatrix} \tag{50.16}$$

$$\hat{\Sigma}_k^{\text{loc}} = \frac{\sum_{i=k-n}^{k-1} \left(\boldsymbol{M}_3\boldsymbol{l}_i^1 - \boldsymbol{M}_1\hat{\boldsymbol{x}}_i\right)\left(\boldsymbol{M}_3\boldsymbol{l}_i^1 - \boldsymbol{M}_1\hat{\boldsymbol{x}}_i\right)^T}{n} \tag{50.17}$$

where the design matrices are,

$$\boldsymbol{M}_1 = [\boldsymbol{I}_{3\times3} \quad \boldsymbol{0}_{6\times6}], \boldsymbol{M}_2 = [\boldsymbol{0}_{3\times3} \quad \boldsymbol{I}_{3\times3} \quad \boldsymbol{0}_{3\times3}], \boldsymbol{M}_3 = [\boldsymbol{0}_{6\times6} \quad \boldsymbol{I}_{3\times3}]$$

Estimating the variance of dynamic model noise

In real navigation applications, the dynamic model noise in 1st KF is time-variant with the dynamic characteristic, thus it is very essential to reliably estimate its covariance in real time as well. According to Eq. (50.4), it can be easily rewritten as,

$$\Sigma_{\boldsymbol{w}_k^1} = \Sigma_{\bar{\boldsymbol{x}}_k^1} - \boldsymbol{\Phi}_{k,k-1}^1 \Sigma_{\hat{\boldsymbol{x}}_{k-1}^1} {\boldsymbol{\Phi}_{k,k-1}^1}^T \tag{50.18}$$

and similar to observation noise variance estimation, $\Sigma_{\bar{\boldsymbol{x}}_k^1}$ can be approximately estimated by,

$$\Sigma_{\bar{\boldsymbol{x}}_k^1} = \left(\boldsymbol{M}_4 \hat{\boldsymbol{x}}_k - \bar{\boldsymbol{x}}_k^1\right)\left(\boldsymbol{M}_4 \hat{\boldsymbol{x}}_k - \bar{\boldsymbol{x}}_k^1\right)^T \tag{50.19}$$

where $\boldsymbol{M}_4 = [\boldsymbol{I}_{6\times 6} \quad \boldsymbol{0}_{6\times 3}]$, By further use of the time window, the variance of dynamic model noise is derived by,

$$\hat{\Sigma}_{\boldsymbol{w}_k^1} = \frac{\sum_{i=k-n}^{k-1} \left[\left(\boldsymbol{M}_4 \hat{\boldsymbol{x}}_i - \bar{\boldsymbol{x}}_i^1\right)\left(\boldsymbol{M}_4 \hat{\boldsymbol{x}}_i - \bar{\boldsymbol{x}}_i^1\right)^T - \boldsymbol{\Phi}_{i,i-1}^1 \Sigma_{\hat{\boldsymbol{x}}_{i-1}^1} {\boldsymbol{\Phi}_{i,i-1}^1}^T\right]}{n} \tag{50.20}$$

It should be noted that the right side of Eqs. (50.18) and (50.20) may result in a negative $\Sigma_{\boldsymbol{w}_k^1}$. To guarantee the positive definite property, an alternative way to estimate the $\hat{\Sigma}_{\boldsymbol{w}_k^1}$ is conducted as follows,

$$\boldsymbol{w}_k^1 = \boldsymbol{x}_k^1 - \boldsymbol{\Phi}_{k,k-1}^1 \boldsymbol{x}_{k-1}^1 \tag{50.21}$$

$$\Sigma_{\boldsymbol{w}_k^1} = \mathrm{E}\left[\boldsymbol{w}_k^1 \left(\boldsymbol{w}_k^1\right)^T\right] = \mathrm{E}\left[\left(\boldsymbol{x}_k^1 - \boldsymbol{\Phi}_{k,k-1}^1 \boldsymbol{x}_{k-1}^1\right)\left(\boldsymbol{x}_k^1 - \boldsymbol{\Phi}_{k,k-1}^1 \boldsymbol{x}_{k-1}^1\right)^T\right] \tag{50.22}$$

$\mathrm{E}(\bullet)$ denotes the expectation operator. By substituting $\boldsymbol{x}_k^1$ with $\boldsymbol{M}_4 \hat{\boldsymbol{x}}_k$, Eq. (50.22) is approximated as,

$$\hat{\Sigma}_{\boldsymbol{w}_k^1} \approx \left(\boldsymbol{M}_4 \hat{\boldsymbol{x}}_k - \boldsymbol{\Phi}_{k,k-1}^1 \boldsymbol{M}_4 \hat{\boldsymbol{x}}_{k-1}\right)\left(\boldsymbol{M}_4 \hat{\boldsymbol{x}}_k - \boldsymbol{\Phi}_{k,k-1}^1 \boldsymbol{M}_4 \hat{\boldsymbol{x}}_{k-1}\right)^T \tag{50.23}$$

and Eq. (50.23) in a time-window can be calculated by,

$$\hat{\Sigma}_{\boldsymbol{w}_k^1} = \frac{\sum_{i=k-n}^{k-1} \left(\hat{\Sigma}_{\boldsymbol{w}_i^1}\right)}{n} \tag{50.24}$$

50.4 Experiment and Analysis

The flight test was conducted on October 17, 2011 from Bankstown Airport, Sydney to Cooma Airport, which is located in the southern part of New South Wales, Australia. In order to test and evaluate our triple integration system

Fig. 50.3 LocataNet configuration in the Cooma area and flight trajectory

composed by GPS, Locata and INS, the flight trial in this paper was focused on the area around Cooma. The LocataNet consisting of six LocataLites was set up to cover the flight test within this area. The locataNet and analysed the trajectory are shown in Fig. 50.3. The aircraft used for the flight test was a Beech Duchess aircraft from the Department of Aviation, UNSW. The devices used in the test include one Leica dual-frequency GPS receiver, one NovAtel SPAN-CPT GPS/INS system, two meteorological measurement devices and two Locata rover units. In addition, data from three GPS reference stations was also collected. The GPS and Locata data sample rates were both 10 Hz. The IMU measurement rate was set to 100 Hz. The KVH's IMU is embedded in the SPAN-CPT, and the Design Quality Indicator (DQI) provided by the manufactures is listed in Table 50.1. All the measurements from Locata and INS are synchronised with GPS time. To correct the level arm effects among GPS, Locata and INS, we decide to compensate the antenna positions of Locata and GPS to the centre of INS by using the position and attitude solution of INS.

The pseudorange measurements of GPS and Locata are used to produce the PV solutions. The post-processing solutions resolved by Leica Geo Office (LGO) software with carrier phase measurements are chosen as the reference values. $\boldsymbol{\Sigma w}^1$ was selected as same as Ref. [18] and $\boldsymbol{\Sigma w}^2$ was chosen according to Table 50.1. The window length for variance estimation is set as 5. For intuitive expression, the

Table 50.1 Technical parameters of INS

Technical parameters	DQI of KVH's IMU
Acc bias	50 mg
Acc scale factor	4,000 ppm, 1σ
Acc random walk	55 μg/sqrt(Hz), 1σ
Gyro bias	20 degree/h
Gyro scale factor	1,500 ppm, 1σ
Gyro random walk	0.067 degree/sqrt(h), 1σ

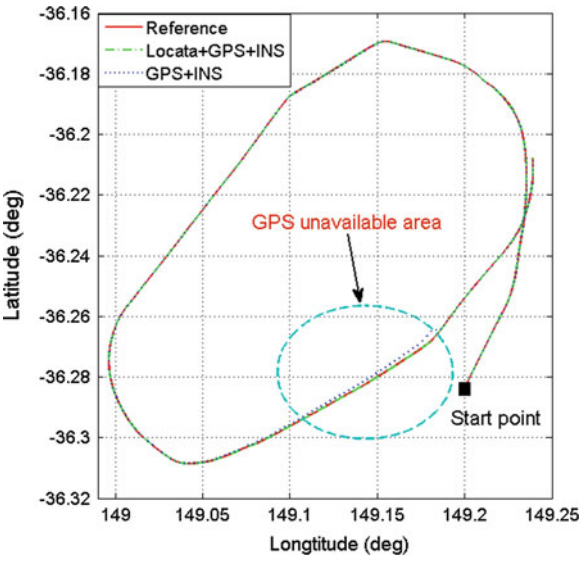

Fig. 50.4 Trajectories of reference, GPS/INS and Locata/GPS/INS

navigation results in e frame have been all transformed to local frame ENU (East-North-Up) for latter comparisons.

To demonstrate that Locata is an essential and efficient alternative when GPS signal is blocked or interfered, a short period (600–800 s) blockage of GPS signal is simulated in the experiment. Figure 50.4 shows the trajectories of reference, CKF based GPS/INS and CKF based Locata/GPS/INS. It can be seen that in most of the time, both trajectories of GPS/INS and Locata/GPS/INS are consistent with reference. However, in GPS blockage region (ellipse with dash line area), the trajectory of GPS/INS gradually deviates from reference as time elapsing (clearly shown in Fig. 50.5); while Locata/GPS/INS can resist the influences by GPS signal blockage and still continuously provide the reliable solutions which coincide with reference trajectory very closely in whole experiment.

In order to further demonstrate the performances of triple integration algorithms of Locata/GPS/INS, two schemes are employed and computed for comparison.

Scheme 1: CKF based GPS/Locata/INS integration in Sect. 50.2 (see Fig. 50.1).
Scheme 2: ADKF based GPS/Locata/INS integration in Sect. 50.3 (see Fig. 50.2).

The PVA differences between these two schemes and reference are shown in Figs. 50.6, 50.7, 50.8, where the blue dots are the results for CKF and the red dots are the results for ADKF. The Root Mean Squared Errors (RMSE) of Scheme 1 and 2 calculated by (50.25) are presented in Table 50.2.

$$\mathrm{RMSE}(\Lambda) = \sqrt{\frac{\sum_{i=1}^{q} (\Lambda_i - \Lambda_{i0})^2}{q}},\ \Lambda \in \{E, N, U, V_E, V_N, V_U, pitch, roll, yaw\} \tag{50.25}$$

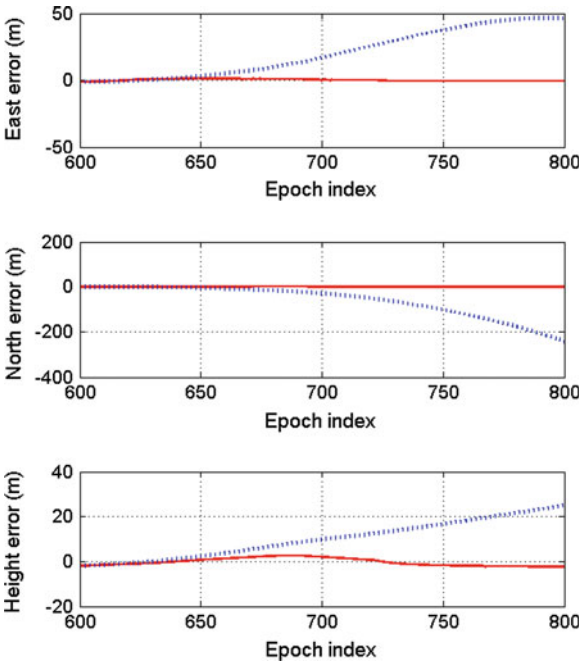

Fig. 50.5 The ENU errors of GPS/INS (*blue dot*) and Locata/GPS/INS (*red line*)

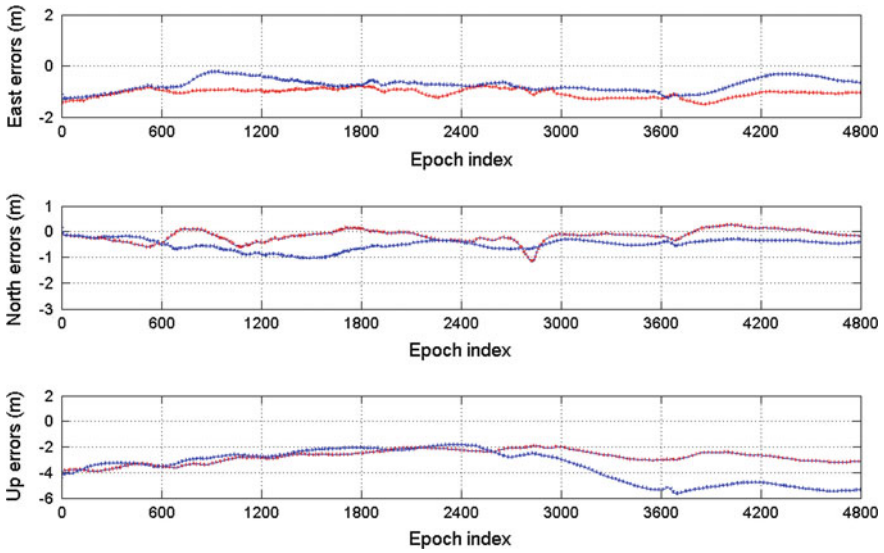

Fig. 50.6 Position errors of CKF (*blue dots*) and ADKF (*red dots*)

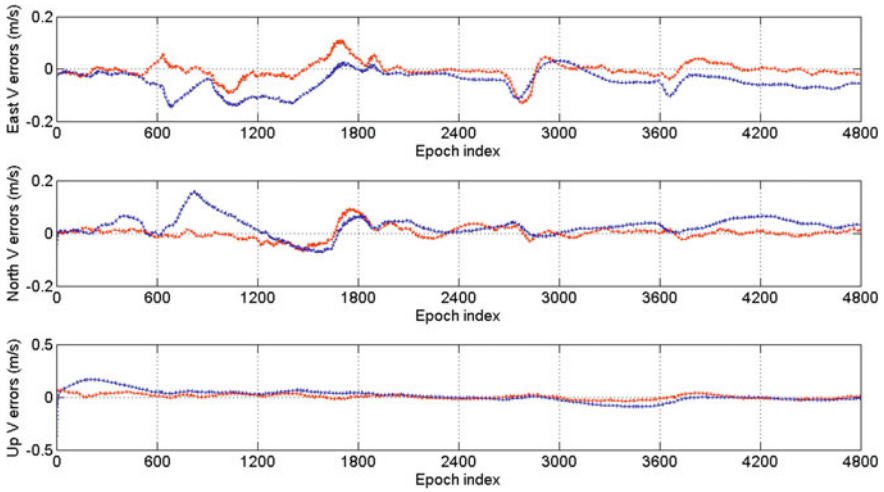

Fig. 50.7 Velocity errors of CKF (*blue dots*) and ADKF (*red dots*)

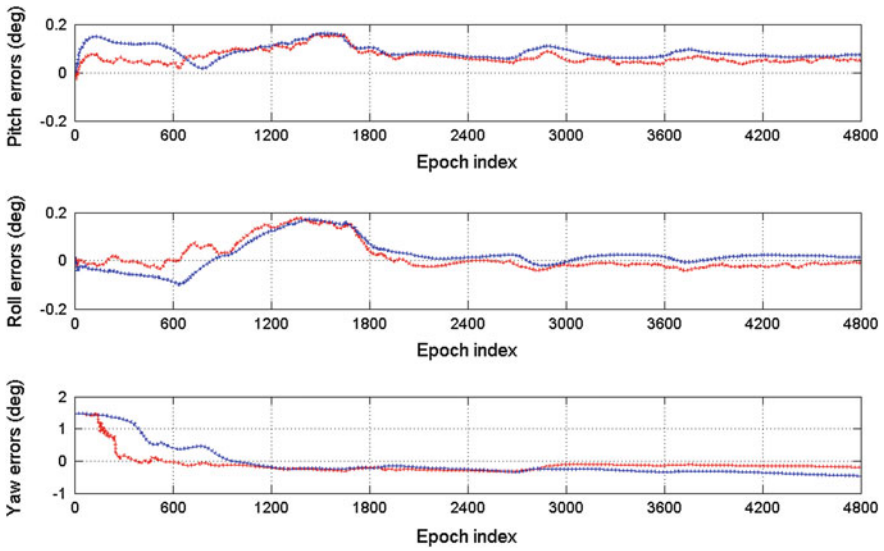

Fig. 50.8 Attitude angle errors of CKF (*blue dots*) and ADKF (*red dots*)

Table 50.2 RMSE of PVA for CKF and ADKF

Scheme	Position error (m)			Velocity error (m/s)			Attitude angle error (degree)		
	East	North	Up	East	North	Up	Pitch	Roll	Yaw
CKF	0.9918	0.5002	4.3883	0.0616	0.0457	0.0578	0.1220	0.0652	0.6903
ADKF	1.0729	0.2870	3.3366	0.0333	0.0241	0.0227	0.0800	0.0641	0.3670

where q is the number of all observed epochs; Λ_i and Λ_{i0} denote the estimated single element of PVA solution and reference value at epoch i.

It can be seen from the figures and the table that (1) in general, ADKF provides the more reliable and stable PVA solution than CKF. (2) Accuracy of the PVA solution computed by ADKF is significantly improved in comparison with CKF, with maximum in north position (42.6 %), up velocity (60.3 %), yaw (46.8 %). (3) Due to lack of direct observations related with attitude errors, roll, pitch and yaw angles are more probably affected by unreliable PV derived from Locata/GPS sensors. Evidently, the 1st adaptive KF in ADKF greatly enhances the reliability of the PV solution which is the input of 2nd KF. Thus more robust attitude angles are achieved by ADKF in comparison with that of CKF. (4) Position solution in vertical direction (i.e. up) is worse than that in horizontal direction (i.e. east and north) for both CKF and ADKF. This is because the LocataLites in the LocataNet are set up in a narrow range at the vertical direction, which leads to very week geometry constraint in this direction. It indicates that the configuration of the LocataNet is very crucial for the performances of the integrated system.

50.5 Concluding Remarks

In summary, an adaptive dual Kalman filtering (ADKF) algorithm is proposed and developed for Locata/GPS/INS integration in three stages: (1) The 1st KF is established to enhance the reliability of PV solution from Locata/GPS. (2) The 2nd KF corrects the INS errors with the outputs of the 1st KF. (3) The final integration solution is used as feedback for estimating variances of dynamic and observation model errors. The real flight experiment is carried out to demonstrate the efficiency and validity of our proposed algorithm against the conventional Kalman filtering (CKF) algorithm. The results show that: (1) GPS/INS integration performs well but its accuracy dramatically decreases when GPS signals are unavailable for a short period. (2) Augmented by Locata, CKF produces tolerable results in whole experiment even without aided by GPS. (3) By constructing the dynamic model and estimating the variances of Locata/GPS dynamic and observation model noise with feedback of navigation solutions, ADKF can achieve more accurate and reliable PVA solution than CKF.

Acknowledgments This work was substantially supported in part by the Fundamental Research Funds for the Central Universities under Grant ZYGX2010J114 and by the State Key Laboratory of Information Engineering in Surveying, Mapping and Remote Sensing, Wuhan University under Grant 10P01.

References

1. Leick A (1995) GPS satellite surveying, 2nd edn. Wiley, New York
2. Kuusniemi H, Lachapelle G, Takala JH (2004) Positioning and velocity reliability testing in degraded GPS signal environments. GPS Solutions 8(4):226–237
3. Zhou Z, Shen Y, Li B (2011) Moving time-window based real-time estimation algorithm for the stochastic model of GPS/Doppler navigation. Acta Geodaetica et Cartographica Sinica 40(2):220–225
4. Zhou Z, Li Y, Rizos C, Shen Y (2009) A robust integration of GPS and MEMS-INS through trajectory-constrained adaptive Kalman filtering. In: Proceedings of ION GNSS 2009, Savannah, Georgia, pp 995–1003, 22–25 Sept
5. Godha S, Cannon ME (2007) GPS/MEMS-INS integrated system for navigation in urban areas. GPS Solutions 11(3):193–203
6. Dissanayake G, Sukkarieh S, Nebot E, Durrant-Whyte H (2001) The aiding of a low cost, strapdown inertial unit using modeling constraints in land vehicle applications. IEEE Trans Rob Autom 17(5):731–747
7. Gelb A (1974) Applied optimal estimation. The Massachusetts Institute of Technology Press, Massachusetts
8. Nassar S, Niu X, El-Sheimy N (2007) Land-vehicle INS/GPS accurate positioning during GPS signal blockage periods. J Surv Eng 133(3):134–143
9. Rizos C, Grejner-Brzezinska DA, Toth CK, Dempster AG, Li Y, Politi N, Barnes J, Sun H, Li L (2010) Hybrid positioning—a prototype system for navigation in GPS-challenged environments. GPS World 21(3):42–47
10. Li Y, Rizos C (2010) Seamless navigation through a Locata-enhanced GPS and INS integrated system. International symposium on GPS/GNSS, Taipei, Taiwan, pp 40–45, 26–28 October
11. Brown R, Hwang PYC (1997) Introduction to random signals and applied Kalman filtering. Wiley, New York
12. Zhou Z, Shen Y, Li B (2010) A windowing-recursive approach for GPS real-time kinematic positioning. GPS Solutions 14(4):365–373
13. Geng Y, Wang J (2008) Adaptive estimation of multiple fading factors in Kalman filter for navigation applications. GPS Solutions 12(4):273–279
14. Yang Y, He H, Xu G (2001) A new adaptively robust filtering for kinematic geodetic positioning. J Geodesy 75(2):109–116
15. Yang Y, Xu T (2003) An adaptive Kalman filter based on sage windowing weights and variance components. J Navig 56(2):231–240
16. Yang Y, Gao W (2005) Comparison of adaptive factors in Kalman Filter on navigation results. J Navig 58(3):471–478
17. Yang Y, Gao W (2006) An optimal adaptive Kalman filter. J Geodesy 80(4):177–183
18. Zhou Z, Li B, Shen Y (2013) A window-recursive approach for GNSS kinematic navigation using pseudorange and Doppler measurements. J Navig 66(2):295–313

Chapter 51
The Timing Equation in X-Ray Pulsar Autonomous Navigation

Qingyong Zhou, Jianfeng Ji and Hongfei Ren

Abstract The timing equation is the basic theory of dealing with the observable data of pulsar. The pulse timing model is studied; With analyzing the existing conclusions about timing equations, the transformation equation of pulsar photon time of arrive in 1PN approximation is derived, and the classic transformation equations are compared with; the transformation of the proper time from the spacecraft to TCB is also obtained.

Keywords: SSB · Pulse timing model · Crab pulsar · Time delay of gravity

51.1 Foreword

X-ray pulsar, especially millisecond pulsar has strong flux density of radiation and extremely stable rotation frequency [1]. The autonomous navigation of spacecraft is achieved when receiving the signals from at least four pulsars in different direction so the X-ray pulsar autonomous navigation gets the great international

Project supported by the State Key Development Program for the National Natural Science Foundation of China (Grant Nos. 41004013, 41174025, 41204020).

Q. Zhou (✉) · J. Ji · H. Ren
State Key Laboratory of Geo-information Engineering, Xi'an 710054, China
e-mail: zjlzqy1986@163.com

J. Ji
e-mail: jjf117@126.com

H. Ren
e-mail: renhongfei@163.com

Q. Zhou · J. Ji · H. Ren
Xi'an Research Institute of Surveying and Mapping, Xi'an 710054, China

J. Sun et al. (eds.), *China Satellite Navigation Conference (CSNC) 2013 Proceedings*, Lecture Notes in Electrical Engineering 245,
DOI: 10.1007/978-3-642-37407-4_51,

attention. Since July 2004, the DARPA of USA has started to carry out "X-ray Source-based Navigation for Autonomous Position Determination (XNAV)", the other countries had the similar plans [2].

Timing equation is the basic theory of dealing with the observable data of pulsar, whose accuracy has the direct influence on the capacity of the autonomous navigation for spacecraft, and the refinement of pulsar's parameters in the XNAV [3]. For reaching the accurate solutions of pulsar navigation, the high precision timing equation is need to be established by analyzing all effects which can be modelled in timing data correctly [4]. The accuracy of timing equation improves with the development of the academic level and precision of observational equipments. Their researches of the early scientists mainly focused on the correction of the TOA of photons recorded by the ground-based telescope for getting higher precision observable data [1]. As the upgrade of observation equipment and the development of signal processing technology, the general relativity effects become to be a necessary considered factor, and establishing the timing equation in the relativistic framework is the precondition of high-precision dealing with observable data. For dealing the data of the radio telescope on the Earth and the x-ray data of satellites in space, some foreign experts analyzed all geometry and relativistic effects in the propagation of pulsar signal, derived and established the expression of the applied timing equation, developed the corresponding data processing software [5–9]. For achieving high-precision pulsar navigation, Dr. Sheikh derived the timing equation including higher relativistic effect, and compared with the other timing equation [10]. Meanwhile, the experts in our nation did a lot of studies on an astrometry parsing to the timing data of pulsar [4, 11], deriving the transformation equation of TOA (time of arrival) of pulsar signal including the higher relativistic effect [2, 3, 12, 13] In addition, most of millisecond pulsars belong to the binary systems, the timing equation for the pulsar in the binary system becomes more complicated by mainly considering the relativistic effects of the companion and using different theories of orbit dynamics to model the orbit of pulsar [14], this content about the pulsar in binary systems is not discussed in this paper. However, the timing equation, whose correctness is questioned [4, 12], used in research by most of the domestic scholars mainly refers to the equation derived by Dr. Sheikh, Meanwhile, the precision of difference timing equations is different, some can not meet with the desire of high-precision pulsar navigation. By analyzing the existing studied conclusions, we derived in detail the timing equation for pulsar navigation in 1PN approximation, developed the software which can deal with the timing data accurately.

51.2 The Timing Equation of X-ray Pulsar Navigation

The basic principle of x-ray pulsar autonomous navigation is similar to one of satellite navigation system. If the spacecraft can receive the signals from 4 pulsars in different direction, its position and clock error can be resolved. The process of

calculation is that TOA of photons received by spacecraft should transform to the origin defined by pulse timing model, the difference equation is made up with the TOA value predicted by this timing model. The process dealing with the timing data is the foundation of achieving the high-precision solution of pulsar navigation, obviously, the timing equation mainly includes three parts: pulse timing model, the transformation equation of TOA, the transformation from the proper time to TCB.

51.2.1 Pulse Timing Model

X-ray pulsar can be used to achieve autonomous navigation for spacecraft, these levels of performance require accurate pulse timing models that can predict the pulse phase over an extended time, so the fundamental premise is that pulsar has the extra stable rotation motion which can be predict with very high precision. Owing to the spinning motion of pulsar has high stable inherent law, the spinning mechanism of pulsar can be modeled. The timing model is often represented as the total phase of all photon accumulated during the observable time, the total phase $\Phi(t)$ can be described as the sum of fractional part $\phi(t)$ and integer cycle $N(t)$:

$$\Phi(t) = \phi(t) + N(t) \tag{51.1}$$

Based upon the characteristics of an individual pulsar, including its pulse frequency, f, and derivatives, a pulse timing model can be created based upon total phase as

$$\Phi(t) = \Phi(t_0) + f \cdot (t - t_0) + \frac{1}{2}\dot{f} \cdot (t - t_0)^2 + \frac{1}{6}\ddot{f} \cdot (t - t_0)^3 + o(\dddot{f}) \tag{51.2}$$

The pulse timing model of Eq. (51.2) is also known as the pulsar spin equation, or the pulsar spin down law. In this equation, the observation time, t, is the coordinate time of arrival of the signal phase, and t_0 is a chosen reference epoch for the model parameters, $\Phi(t_0)$ is the total phase at the initial epoch t_0. Higher order frequency derivatives may be required to accurately characterize some pulsars or pulsars within binary system have even further complicated pulse timing models that incorporate the pulsar orbital period. The great significance of pulse timing model is that can accurately predict the phase of a photon over an extended time, so in the pulsar navigation, the precision of pulse timing model directly affects the performance of navigation.

In order to initially create accurate pulse timing model as in Eq. (51.2), analytical methods must be defined that represent how to precisely note and deal with time of each photon arrival. Subsequent observations utilize these same methods to accurately achieve each TOA of photon. Meanwhile in order to reduce the complexity of these analytical methods, it is important to time the pulsar observations within an inertial reference frame that is stationary with respect to the

pulsar's frame. For many observations in solar system, the common frame utilized is the barycentric coordinate frame in solar system, the reference time scale for these observations is the barycentric Coordinate Time (TCB), the origin of this frame is SSB. For pulsar timing, these pulse timing models are often described to be valid at the origin of SSB frame, the process of pulsar navigation requires that time of photon arrival be transferred from the spacecraft to the SSB. According to the law of gravitation, the proper time should be converted to TCB.

51.2.2 TOA Transformation of Photon

For achieving autonomous navigation of spacecraft based on the X-ray pulsar, we should accurately transfer time of photon arrival from spacecraft to the SSB, geometric and relativistic effects must be included in this transfer. These effects account for the difference in light-ray path from a pulsar to the detector's and to the model's location. The light ray paths can be determined using the existing theory of general relativity and the known effects of the solar system. The equation from this theory relates the emission time of photons that emanate from a pulsar to their arrival time at a spacecraft and define the path of the photons traveling through curved space time. For a X-ray photon, its path has zero spacetime interval in traveling from the pulsar to the spacecraft and are referred to as null geodesics. From the theory of general relativity, the expression of the null geodesics can be expressed as:

$$ds^2 = -c^2 d\tau^2 = g_{00}c^2 dt^2 + 2\sum_{j=1}^{3} g_{0j} c dt dx^j + \sum_{i=1}^{3}\sum_{j=1}^{3} g_{ij} dx^i dx^j = 0 \qquad (51.3)$$

In a week—gravitational field and nearly flat space, which is appropriate for the solar system, a Post-Newtonian metric tensor is suitable and can be expressed to second order of the total gravitational potential within the system. The Post-Newtonian metric tensor that meets the linear superposition principle is recommended in the resolution of the 24th IAU [2, 15]:

$$\begin{aligned} g_{00} &= -1 + \frac{2U}{c^2} - \frac{2U^2}{c^4} \\ g_{0i} &= -\frac{4}{c^3} U^i \\ g_{ij} &= \delta_{ij}\left(1 + \frac{2}{c^2} U\right) \end{aligned} \qquad (51.4)$$

The total gravitational potential $U = \sum_{i=1}^{p} \frac{GM_i}{r_i}$, acting on the spacecraft clock is the sum of the gravitational potentials of all the bodies in the solar system. U, U^i

are the scalar potential and vector potential of gravitational field in solar system respectively, the vector potential is too small to be ignored [12].

The delay produced by interstellar gravitational field will be essentially constant over tens of years of data and need not be modeled, and the effects of unhomogeneous sphere of all bodies in solar system are not discussed. Along the null geodesic paths of photons the space time interval equals zero, the space-time interval, ds, has been shown in 1PN approximation to be:

$$ds^2 = -c^2 d\tau^2 = -\left(1 - \frac{2U}{c^2}\right)c^2 dt^2 + \left(1 + \frac{2U}{c^2}\right)\left(dx^2 + dy^2 + dz^2\right) = 0 \quad (51.5)$$

Using a binomial expansion, this relationship is valid to order (1/c2) as,

$$cdt = \left(1 + {}^{2U}/_{c^2}\right) \cdot \sqrt{dx^2 + dy^2 + dz^2} \quad (51.6)$$

By integrating Eq. (51.6) along the path of photons traveling, an algorithm can be developed to determine the relationship between the time of photons transmitted from pulsar and the time of these received by spacecraft. The Geometry of the path of a photon is shown in Fig. 51.1. We choose a reference frame that is at rest relative to the barycenter of solar system, the origin is the center of mass of the Sun. The coordinates are oriented that the pulsar, receiver, and Sun are in the x-y plane, the Z-axis is determined by right-hand rule. We let the coordinates of the pulsar be $\vec{D} = (D_X, d)$ at the instant when the photons are emitted.

The bending effects which produced by bodies other than the Sun is negligible, so the spatial trajectory may be determined by considering the effect of Sun alone. In the gravitational field of the Sun, light-like geodesics satisfy [7]:

$$\frac{d^2 y}{d^2 x} = 2\frac{GM_s}{c^2}\frac{\partial}{\partial y}\left(x^2 + y^2\right)^{-1/2} \quad (51.7)$$

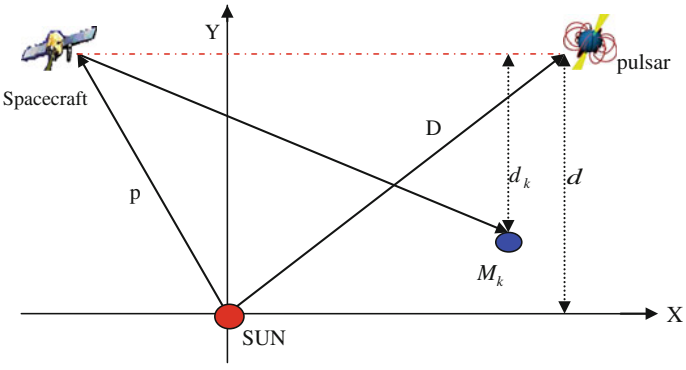

Fig. 51.1 Geometry of the path of photons originating at pulsar, passing through the *curved* space-time and arriving spacecraft

where GM_s is heliocentric gravitational constant, c is the speed of light in vacuum. The solution of this equation, to first order in the perturbation of the path from a straight line and subject to the initial condition $dy/dx = 0,\ y = d$ at $x = D_x$:

$$y = d + 2\frac{GM_s}{dc^2} \times \left[D - \left(x^2 + d^2\right)^{1/2} + (x - D_x)\frac{D_x}{D} \right] \tag{51.8}$$

where D_x is the component of D that projecting to the X-axis, D is the magnitude of $\vec{D}$. Differentiation of Eq. (51.8) gives:

$$\frac{dy}{dx} = \frac{2GM}{dc^2}\left[\frac{D_x}{D} - \frac{x}{\left(x^2 + d^2\right)^{1/2}} \right] \tag{51.9}$$

Because the travelling path of photons are in the XY plane, therefore, $z = 0$, the total coordinate time of flight of the photons can be calculated by integrating Eq. (51.6) along the path:

$$c\int_{t_{sc}}^{t_p} dt = \int_{P_x}^{D_x} \left(1 + \frac{2GM_s}{(x^2+y^2)^{1/2}\cdot c^2} + \sum_{k\neq S} \frac{2GM_k}{\left((x - x_{M_k})^2 + d_k^2\right)^{1/2}\cdot c^2} + \frac{2G^2M_S^2}{d^2c^4}\left[\frac{D_x}{D} - \frac{x}{(x^2+d^2)^{1/2}} \right]^2 \right) dx \tag{51.10}$$

where, t_p is the coordinate time of a photon emitted by pulsar, t_{sc} is the coordinate time of the same photon received by the spacecraft. GM_k is the gravitational constant of bodies in solar system, x_{M_k} is the X-axis component of distance from body M_k to the center of mass of the Sun, d_k is the vector of distance that body M_k is away from the travelling path of a photon, can be seen in Fig. (51.1). $\sqrt{(x_{Sc} - x_{M_K})^2 + d_k^2} = p_k$, is the position of spacecraft relative to the body M_k, and $|x_{SC} - x_{M_K}| = \vec{n} \cdot \vec{p}_k.\vec{n}$ is the unit vector of pulsar's position.

The time that photon passes through the curved space-time by Integrating each component in Eq. (51.10):

$$\begin{aligned} c(t_p - t_{sc}) = {} & \vec{n}\cdot(\vec{D} - \vec{p}) - 2\sum_{k=1}^{S} \frac{GM_k}{c^2} \ln\left(\frac{\vec{n}\cdot\vec{p}_k + p_k}{\vec{n}\cdot\vec{D}_k + D_k} \right) + \frac{2G^2M_s^2}{d^2c^4}\cdot \\ & \left[\left(\frac{\vec{n}\cdot\vec{D}}{D} \right)^2 \cdot \vec{n}\cdot(\vec{D} - \vec{p}) + 2(\vec{n}\cdot\vec{D})\left(\frac{p}{D} - 1\right) + \vec{n}\cdot(\vec{D} - \vec{p}) - d\cdot\left(\arctan\left(\frac{\vec{n}\cdot\vec{D}}{d} \right) - \arctan\left(\frac{\vec{n}\cdot\vec{p}}{d} \right) \right) \right] \end{aligned} \tag{51.11}$$

where $\vec{p}$ is the position of spacecraft relative to SSB at the instant that the photon arrives the detector. $\vec{D}_k$ is the position of body M_k relative to the pulsar, p, D_k is the magnitude of the corresponding vector. The Eq. (51.11) gives the relationship between the coordinate time of photons emitted by pulsar and their arrival coordinate time at spacecraft. The last term in this equation is the second-order effect of deflection of the path of photons due to the Sun, this term are typically small (<1 ns), can be considered negligible. SSB is the center of gravitation in solar system, the

small difference caused by transformation between the proper coordinate frame of pulsar and the solar system coordinate frame also can be ignored, and we suppose that the gravity field don't make any change in a few decade, so the total coordinate time of flight of the photons is the sum of the propagation time of the photons in vacuum and the Shapiro delay of all bodies in solar system. Some scaling factor must be included to insure the argument of the logarithmic term of Shapiro delay term is no units, the logarithmic arguments are scaled by dividing 1 AU.

$$c\left(t_p - t_{SSB}\right) = \vec{n} \cdot \vec{D} - 2\sum_{k=1}^{S} \frac{GM_k}{c^2} \ln\left(\frac{\vec{n} \cdot \vec{D}_k + D_k}{AU}\right) \tag{51.12}$$

The effects of deflection due to the Sun are considered negligible. The transformation between the TOA at spacecraft and TOA at SSB can be achieved by subtracting Eqs. (51.12) from (51.11).

$$c(t_{SSB} - t_{SC}) = -1 \cdot \vec{n} \cdot \vec{p} - 2\sum_{k=1}^{S} \frac{GM_k}{c^2} \ln\left(\frac{\vec{n} \cdot \vec{p}_k + p_k}{AU}\right) \tag{51.13}$$

In Eq. (51.13), to accurately transfer from t_{SC} to t_{SSB}, the geometric and relativistic effects must be included in this process, these effects account for the difference between the same photon arrival the spacecraft and the SSB. In practice, whether in the process that dealing with the data in radio observations at the ground-based station or the autonomous navigation of spacecraft, the described component included in the data are subtracted, the law is found in the residual and the appropriate model can be created, then the parameters of model are resolved. In other words, both the timing equations used in the observation of telescope and in the navigation of spacecraft are same in essence.

The further modification should include the knowledge of the change in position of the pulsar. Assuming a constant proper motion of pulsar, V, $\vec{D}_0$ is the position of pulsar at T_0, Δt is the time of reception elapsed since T_0

$$\begin{aligned} c(t_{SSB} - t_{SC}) = &-1 \cdot (\vec{n} \cdot \vec{p}) + \frac{1}{2D_0}|\vec{n} \times \vec{p}|^2 - \frac{1}{D_0}\left[\left(\vec{V} \cdot \vec{p}\right) - \left(\vec{V} \cdot \vec{n}\right) \cdot (\vec{n} \cdot \vec{p})\right]\Delta t \\ &- 2\sum_{k=1}^{S} \frac{GM_k}{c^2} \ln\left(\frac{\vec{n} \cdot \vec{p}_k + p_k}{AU}\right). \end{aligned} \tag{51.14}$$

A lot of transformation equations of TOA which are similar to the Eq. (51.14), are derived by a great many of scholars, whose main difference focuses on the Shapiro delay term in equation [1–12]. The equation of the Dr. Sheikh's thesis is in great dispute. Ignoring the effects of gravitational bending caused by solar system and proper motion of pulsar, the equation of sheikh is converted to the symbolic system of this paper:

$$c(t_{SSB} - t_{SC}) = -1 \cdot \vec{n} \cdot \vec{p} - 2\sum_{k=1}^{S} \frac{GM_k}{c^2} \ln\left(\frac{\vec{n} \cdot \vec{p}_k + p_k}{\vec{n} \cdot \vec{b}_k + b_k}\right) \tag{51.15}$$

where $\vec{b}_k$ is the position of bodies M_k in the solar system relative to SSB, b_k is the magnitude of $\vec{b}_k$. $\vec{p}_k = \vec{b}_k + \vec{r}$, $\vec{r}$ is the position of spacecraft relative to the SSB, r is the magnitude of $\vec{r}$. The equation is derived by Sheikh:

$$c(t_{SSB} - t_{SC}) = -1 \cdot \vec{n} \cdot \vec{p} - 2\sum_{k=1}^{S} \frac{GM_k}{c^2} \ln\left(\frac{\vec{n} \cdot \vec{r} + r}{\vec{n} \cdot \vec{b}_k + b_k} + 1\right) \tag{51.16}$$

In the process that Eq. (51.16) derived by Sheikh from Eq. (51.15), Sheikh uses the condition $p_k = b_k + r$ in error, while, in fact, $b_k + r > p_k$. the Eq.(51.15) is used in his later parper[10]. Compared with the Eqs. (51.13) and (51.15), the difference between them is the gravitational delay of SSB, SSB is the center of all mass in solar system, also is the center of gravity of the solar system. The TOA at SSB calculated by using Eq. (51.15) includes the effects of the gravitational delay of SSB, meanwhile, SSB is often in the Sun, the Shapiro delay at SSB is not a observed data. As discussed in previous section, the location of pulse timing model is SSB in vacuum, the equation of TOA transfer is not a concept of differentiation, the true process is that the geometric and relativistic effects of photons arrived at the Earth than SSB is considered, the corresponding model is built up and its effect is deducted from the origin data. In fact, either the tempo2 software dealing with the observational data on the ground or the Heasoft software dealing with the data of RXTE satellite is such.

51.2.3 Accurate Transformation from the Proper Time of Spacecraft to TCB

It should be remembered, however, that Eq. (51.14) only relates time coordinates to space coordinates, whereas the quantities that are actually observed are terrestrial proper times in X-ray pulsar autonomous navigation; so, we should derive the relationship that relates terrestrial proper time to coordinate time.

For the spacecraft around the Earth, the spacecraft's position $\left(\vec{r}_{OS}, \dot{\vec{r}}_{OS}\right)$ is the sum of position and velocity of the center of the Earth $\left(\vec{r}_{OE}, \dot{\vec{r}}_{OE}\right)$ and the position and velocity of the center of the spacecraft relative to the center of the Earth $\left(\dot{r}_{ES}, \dot{\vec{r}}_{ES}\right)$:

$$\begin{aligned} \vec{r}_{OS} &= \vec{r}_{OE} + \vec{r}_{ES} \\ \vec{v}_{OS} &= \dot{\vec{r}}_{OE} + \dot{\vec{r}}_{ES} \end{aligned} \tag{51.17}$$

At the same time, the gravitational potential $U(\vec{r})$ at the spacecraft is the sum of the potential of the Earth $U_E(\vec{r}_{OE})$ and the potential of the rest of the solar system $U_S(\vec{r}_{OS})$. We then expand $U_S(\vec{r}_{OS})$ in a Taylor series about the center of the Earth and keep only the leading term in the expansion, the neglected terms in the Sun's and Moon's gravitational fields will be less than 10^{-16} in the space around the Earth [7].

$$U(\vec{r}) = U_S(\vec{r}_{ES}) + \nabla U_S \cdot \vec{r}_{OE} + U_E(\vec{r}_{OE}). \tag{51.18}$$

The effect of the acceleration of the Sun is ignored, the gradient of U_S is equal to $\ddot{\vec{r}}_{ES}$. Can be seen in the equation of the null geodesics:

$$d\tau = \left(1 - \frac{U}{c^2} - \frac{v^2}{2c^2}\right)dt \tag{51.19}$$

We supposed that the corresponding coordinate time is t_0 while the proper time of spacecraft clock is τ_0. Considering the Eqs. (51.17) and (51.18), thus Eq. (51.19) becomes

$$\tau - \tau_0 = t - t_0 - \frac{1}{c^2}\int_{t_0}^{t}\left(U_S(\vec{r}_{ES}) + \ddot{\vec{r}}_{ES}\cdot\vec{r}_{OE} + \dot{\vec{r}}_{ES}\cdot\dot{\vec{r}}_{OE} + U_E(\vec{r}_{OE}) + \frac{v_{ES}^2 + v_{OE}^2}{2}\right)dt \tag{51.20}$$

The trajectory of the Earth around the Sun is elliptical orbit with the effect of conservative force only considered. The higher order inhomogeneity of the revolution of the Earth is considered negligible, the following equation can be derived by the energy integral equation:

$$v_{ES}^2 = \mu_S\left(\frac{2}{\vec{r}_{ES}} - \frac{1}{a_{ES}}\right) = 2U_S - \frac{\mu_S}{a_{ES}} \tag{51.21}$$

where $\mu_S = GM_S = U_S \cdot \vec{r}_{ES}$ the gravitational constant of the Sun is, a_{ES} is the semi-major axis of an ellipse that the Earth runs around the Sun.

Meanwhile,

$$\frac{d}{dt}(\vec{r}_{ES}\cdot\vec{v}_{ES}) = v_{ES}^2 - U_S(\vec{r}_{ES}) \tag{51.22}$$

so

$$U_S(\vec{r}_{ES}) + \frac{v_{ES}^2}{2} = \frac{3}{2}\frac{\mu_S}{a_{ES}} + 2\frac{d}{dt}(\vec{r}_{ES}\cdot\vec{v}_{ES}) \tag{51.23}$$

The trajectory of the spacecraft around the Earth is also elliptical orbit, the similar result can be achieved by the same method:

$$U_E(\vec{r}_{OE}) + \frac{v_{OE}^2}{2} = \frac{3}{2}\frac{\mu_E}{a_{OE}} + 2\frac{d}{dt}(\vec{r}_{OE} \cdot \vec{v}_{OE}) \tag{51.24}$$

where $\mu_E = GM_E$ the gravitational constant of the Earth is, a_{OE} is the semi-major axis of an ellipse that the spacecraft runs around the Earth.

Using the Eqs. (51.23) and (51.24) into (51.20), the integration of Eq. (51.20) gives:

$$\Delta\tau = \left(1 - \frac{3}{2c^2}\left(\frac{\mu_S}{a_{ES}} + \frac{\mu_E}{a_{OE}}\right)\right)\Delta t - \frac{1}{c^2}\left[\begin{pmatrix} \dot{\vec{r}}_{ES}(t_0+\Delta t)\cdot\vec{r}_{OE}(t_0+\Delta t) + 2(\vec{r}_{OE}(t_0+\Delta t)\cdot\vec{v}_{OE}(t_0+\Delta t) \\ + \vec{r}_{ES}(t_0+\Delta t)\cdot\vec{v}_{ES}(t_0+\Delta t) \end{pmatrix}\right]$$
$$+\frac{1}{c^2}\left[(\dot{\vec{r}}_{ES}(t_0)\cdot\vec{r}_{OE}(t_0) + 2(\vec{r}_{OE}(t_0)\cdot\vec{v}_{OE}(t_0) + \vec{r}_{ES}(t_0)\cdot\vec{v}_{ES}(t_0))\right] \tag{51.25}$$

where $\Delta\tau = \tau - \tau_0,\ \Delta t = t - t_0$.

The first term at the right of the equal in Eq. (51.25) is the secular effect, the second term is the periodic effects including the orbital motion of satellite and the orbital motion that the Earth run around the Sun. In the actual application of engineering, for avoiding the long-term drift of the spaceborne clock relative to the timescale of TCB, the frequencies of the spaceborne clock should be adjusted before the launch of spacecraft. We supposed that the reference frequency of the spaceborne clock is f_0, the adjustment of frequency is

$$f = (1-k)f_0 \tag{51.26}$$

If the non-linear change of the clock of spacecraft is considered negligible, so $k = \frac{3}{2c^2}\left(\frac{\mu_S}{a_{ES}} + \frac{\mu_E}{a_{OE}}\right)$, for the trajectory of GPS satellites, $k = 1.509788796367 \times 10^{-8}$ is adapted from using the astronomic constant of the criterion in IERS2003 [15]. We supposed that the reference frequency of spacebrone clock is 10.23 MHz, the adjustment of frequency before launch of spacecraft is 0.154451 Hz..

It should be noted that the gravity of the other bodies need to consider while the spacecraft is far away from the Earth and the effect of gravity of Earth is small. When the spacecraft comes into the radius of action of other planet, the effect of gravity of this body is mainly considered.

The trajectory of most spacecrafts in motion is the elliptic orbit, while the one of some satellites may be hyperboloidal and parabolic orbit for some purpose [16]. The timescale transformation equation for them will be given directly and not be deduced in detail.

For the clock in the hyperboloidal orbit, the transformation between the proper time and TCB timescale is:

$$\tau = \left(1 - \frac{3}{2c^2}\left(\frac{\mu_S}{a_{ES}} - \frac{\mu_E}{a_{OE}}\right)\right)t - \frac{1}{c^2}\left(\dot{\vec{r}}_{ES} \cdot \vec{r}_{OE} + 2(\vec{r}_{OE} \cdot \vec{v}_{OE} + \vec{r}_{ES} \cdot \vec{v}_{ES})\right) \tag{51.27}$$

For the clock in the parabolic orbit, the transformation between the proper time and TCB timescale is:

$$\tau = \left(1 - \frac{3}{2c^2}\frac{\mu_S}{a_{ES}}\right) \cdot t - \frac{1}{c^2}\left(\dot{\vec{r}}_{ES} \cdot \vec{r}_{OE} + 2\vec{r}_{ES} \cdot \vec{v}_{ES} - 22\sqrt{\mu_E \cdot \vec{p}}\left(\tan\frac{f}{2} - \tan\frac{f_0}{2}\right)\right) \tag{51.28}$$

where $\vec{p}$ is the semi-diameter of the parabolic orbit, f is the true anomaly of spacecraft at coordinate time t, f_0 is the true anomaly of spacecraft at initial time t_0.

51.3 Conclusion and Discussion

The X-ray pulsar autonomous navigation has the great value of the important academic studies and the applications of engineering. This paper mainly studies the timing equation of X-ray pulsar navigation. The purpose of the timing equation is that transforms the TOA of spacecraft to the time arrived at SSB, while SSB is not the center of dynamics in solar system, the position of SSB can not be measured by observing the big bodies. Meanwhile, SSB does not have the corresponding actual celestial body so that does not have the property of observability, only can be calculated by the heliocentric position and the mass distribution of each body, whereas, the space distribution of mass of bodies can not be determined accurately. In other words, the precision of SSB position is also a question need to consider in pulsar navigation. For the people on the Earth and the spacecraft near the Earth, we hope that the origin of pulse timing model is defined at the center of the mass of Earth for weakening the effect of position errors of pulsar. Is it very effective that the pulse timing model is built by such idea? The answer to this question is that such pulse timing model can predict very correctly and the standard pulse can keep steady or not for a long time.

References

1. Sheikh SI (2005) The use of variable celestial X-ray sources for spacecraft navigation. Department of Aerospace Engineering, University of Maryland, Maryland
2. Hongfei R (2009) The research on timing model of the pulsar navigation in the general theory of relativity. PLA information engineering university, zhengzhou
3. Hongfei R,Ziqing W,Zhehe Z,Fumei W (2012) The timing equation of pulsar navigation in 1PN Approximation and its accuracy analysis. Acta Geodaetica et Cartographica Sinca 41(1):41–47

4. M Zhao, TY Huang (2009) An astrometry parsing to the data of pulsar timing. Sci China: series G (11):1671–1677
5. Backer DC, Helling RW (1986) Pulsar timing and general relativity. Ann Rev Astron Astrophy 24:537–575
6. Lorimer DR, Kramer M ()2005 Handbook of pulsar astronomy. Cambridge University Press, Cambridge
7. Helling RW (1986) Relativistic effects in astronomical timing measurement. Astron J 91(3):650–659
8. Murry CA (1983) Vectorial Astrometry. Tsechno House of Adam Hilger, 1983
9. Edwards RT, Hobbs GB, Manchester RN (2006) Tempo2, a new pulsar timing package-II: The timing model and precision estimates. arXiv:astro-ph/0607664v1 31 Jul 2006
10. Sheikh SI, Hellings RW, Matzner RA (2007) High-order pulsar timing for navigation. ION 63th Annual Meeting, 23–25 April 2007, pp 432–443
11. Shuai P, Li M, Chen Z, Huang Z (2009) The principle and method the X-ray pulsar-Based navigation system. The china aerospace press, Beijing
12. Baojun F, Weijin S, Gaotian P, Chengxiang J (2010) Transformation of photon time of arrival in XNAV. Chin J Space Sci 30(1):85–90
13. Liu JQ, Xu CM ()1989 The high order relativistic effects in millisecond pulsar timing. ACTA Astron Sin 30(3):323–331
14. Blanford R, Teukolsky SA (1976) Arrival time analysis for a pulsar in a binary system. Ast rophsical J 205:580–590
15. Dennies DM, Petit G (2004) IERS Conventions (2003). http://www.iers.org/iers/publications/tn/tn32/
16. Liu L, Hou X (2012) The orbital mechanics of deep space probe. Pulishing house of electronics industry, Beijing

Chapter 52
X-Ray Pulsar Signal Detection Based on Time–Frequency Distributions and Shannon Entropy

Lu Wang and Luping Xu

Abstract A new algorithm based on time–frequency distribution and Shannon entropy in S transform domain is proposed for accurately and fast detecting pulsar signals in this paper. The bounds on the expected value of Shannon entropy of white Gaussian noise are derived. Based on these constant signatures, the optimum threshold detection algorithm based on the ROC curve is employed to detect pulsar signals. Finally, the experimental results show that the proposed method has high detection rate, fast processing speed and low requirement for temporal resolution.

Keywords Pulsar navigation detection · Shannon entropy · S-transform · Time–frequency distribution

52.1 Introduction

X-ray pulsar navigation (XPNAV) is a new astronomical autonomous navigation technology [1], which exploits portable X-ray detectors to receive the X-ray emission from pulsars. Because of the long distance from the earth and X-ray noise interference from the space background, most of the received X-ray pulsar signals are neglected [2]. Therefore, the detection of X-ray pulsar signal plays an important role in pulsar deep space autonomous navigation system.

L. Wang (✉) · L. Xu
School of Electronic Engineering, Xidian University, Xi'an 710071, China
e-mail: wanglu_xidian@163.com

L. Xu
e-mail: xd203@yahoo.com.cn

L. Wang · L. Xu
Institute of Astronautics and Aeronautics, Xidian University, Xi'an 710071, China

J. Sun et al. (eds.), *China Satellite Navigation Conference (CSNC) 2013 Proceedings*, Lecture Notes in Electrical Engineering 245,
DOI: 10.1007/978-3-642-37407-4_52,

At present, Taylor FFT algorithm is widely used for the detection of pulsar signal [3], which uses Fourier transform for noncumulative observed data directly and calculates its power spectrum also; then, harmonic power superimposition is conducted repeatedly, which intends to find out a frequency bin with higher energy. Finally, the frequency point is tested by time-domain energy accumulation method. The most important issue of this method is heavy calculation burden. By reducing the amount of the observation data, computational complexity can be reduced, meanwhile low signal-to-noise ratio (SNR) and the false detection [4] by harmonic interference can be caused also. Therefore, the pulsar search technique based on power spectrum estimation cannot provide a real-time pulsar search to the spacecraft space for navigation and positioning system. In order to overcome the problem in frequency-domain algorithm, we present a detection algorithm based on Shannon entropy for time–frequency distributions (TFDs) in this paper, the detected signal in the new method is the cumulative pulse profile rather than the noncumulative observed data.

The concept of entropy for TFDs is proposed by Williams et al. [4] and Aviyente et al. [5, 6] have extended it and proposed some detection algorithms based on entropy for Cohen's class TFDs of random signal, these algorithms construct a joint energy probability density function based on quadratic time–frequency transform, for the limitations on the result of time–frequency transform and the entropy's definition, only the Rayleigh entropy can be constructed from Cohen's class TFDs. However, bilinear time–frequency distributions for Cohen class are nonlinear, in which exists the cross-term for muti-component signals, some false signals may be produced by the cross-term, such as the Wigner-Ville distributions for complicated signals are meaningless [7]. Because the cumulative pulse profile of pulsar is constructed by a linear superposition of multiple Gaussian components [8], bilinear time–frequency transform for Cohen class cannot be used for analyzing the pulsar signal.

Compared with Cohen's class bilinear TFDs, S transform (ST) is a linear time–frequency transformed without the cross-term, which integrates the advantage of short-time window Fourier transform and wavelet transform, and possesses many good properties [9]. In this paper, we introduce a detection method based on Shannon entropy in S transform domain. The detection algorithm is based on the fact that Shannon entropy of a signal plus noise is always less than the entropy of the noise itself. First,we review the basic definition of Shannon entropy for TFDs. Then in Sect. 52.3, we derive the bounds on the expected value of the Shannon entropy of white Gaussian noise; combined with the experimental analysis, the optimum threshold detection algorithm based on a receiver operating characteristics (ROC) curve is proposed. In Sect. 52.4, we illustrate the performance of this detection algorithm and compare it to the Taylor FFT algorithm. Finally, a conclusion of the optimum threshold detection algorithm based on the ROC curve is summarized.

52.2 Shannon Entropy for Time-Frequency Distributions

S transform is proposed by the American geophysicist Stockwell et al. [9], which is a Fourier transform in time window, S transform for continuous function $u(t)$ can be expressed as:

$$S(\tau, f) = \int_{-\infty}^{\infty} u(t)\omega(\tau - t, f)\, \mathrm{e}^{-i2\pi ft}\, dt \tag{52.1}$$

$$\omega(\tau - t, f) = \frac{|f|}{\sqrt{2\pi}} \mathrm{e}^{(-f^2(\tau - t)^2/2)} \tag{52.2}$$

where $\omega(\tau, f)$ is a Gaussian window function, f is the frequency, τ and t are time variables and τ is the center of the Gaussian window function.

The expression for discrete S transform is:

$$\begin{aligned} S[m, n] &= \sum_{l=-N/2}^{N/2-1} U[l + n]\, \mathrm{e}^{-(2\pi^2 l^2/n^2)}\, \mathrm{e}^{(i2\pi lm/N)}, \quad n \neq 0 \\ S[m, 0] &= \frac{1}{N} \sum_{p=0}^{N-1} u[p] \end{aligned} \tag{52.3}$$

where m represents time, n represents frequency and $U[n]$ is the Fourier transform of $u(t)$. Formula (52.3) shows that discrete S transform can be calculated by means of FFT and convolution theorem, the calculated result is a complex time–frequency matrix. In addition, S transform is a linear operation, which meets the linear superposition principle and has many characteristics such as lossless invertibility, high time–frequency resolution and so on.

The essence of Cohen's class Bilinear TFDs is distributing the energy of signal in time–frequency plane, however, the essence of S transform is decomposing signal into the weighted sums of basic components which are concentrated in the time domain and frequency domain. Thus, in order to meet the form of the power spectrum, we define matrix P as the power spectrum of signal in S transform domain, its expression is:

$$\mathrm{P} = \mathrm{S} \circ \mathrm{S}^* \tag{52.4}$$

Where $\circ$ represents Hadamard product of two matrices.

All elements in power spectrum matrix P are nonnegative, so its normalized joint energy probability density function is defined as

$$P_{nor}(\tau, f) = \frac{S(\tau, f) \circ S^*(\tau, f)}{\int\int S(\tau, f) d\tau df \cdot \int\int S^*(\tau, f) d\tau df} \tag{52.5}$$

$$\begin{aligned} &\int\int P_{nor}(\tau, f)d\tau df = 1 \\ &P_{nor}(\tau, f) \in [0, 1], \quad \forall\ \tau, f \end{aligned} \tag{52.6}$$

Due to $P_{nor}(\tau, f)$ satisfying formula (52.6), Shannon entropy for TFDs can be calculated by $P_{nor}(\tau, f)$, the formula is defined as

$$H(P_{nor}) = -\int\int P_{nor}(\tau, f)\log_2 P_{nor}(\tau, f)d\tau df \tag{52.7}$$

52.3 Detection Algorithm

52.3.1 Bounds on Shannon Entropy

Shannon entropy for TFDs in discrete-time is defined as

$$\begin{aligned} H(P_{nor}) &= -\sum_{m=0}^{M-1}\sum_{n=0}^{N-1} P_{nor}(m, n)\log_2 P_{nor}(m, n) \\ P_{nor}(m, n) &= \frac{S(m, n)\cdot S^*(m, n)}{\sum_{m=0}^{M-1}\sum_{n=0}^{N-1} S(m, n)\cdot S^*(m, n)} \end{aligned} \tag{52.8}$$

where m and n represent discrete time and discrete frequency respectively.

In this section, bounds on the expected value of Shannon entropy for TFDs of white Gaussian noise will be derived, the bounds will be derived for general TFDs with arbitrary size.

It is known that uniform distribution has the maximum entropy value, similarly to the uniform distribution in time–frequency plane, therefore, Shannon entropy for the uniform distribution in time–frequency plane provides the upper bound on the expected value of Shannon entropy. For a uniformly distributed two dimensional random vector, its Shannon entropy is given as follows:

$$\begin{aligned} H(\mathrm{P}_{uni}) &= -\sum_{m=0}^{M-1}\sum_{n=0}^{N-1}\frac{1}{M\times N}\log_2\left(\frac{1}{M\times N}\right) \\ &= \log_2(M\times N) \end{aligned} \tag{52.9}$$

where P_{uni} is the uniform probability density function, M is the number of frequency points and N is the number of time points. Therefore, inequality (52.10) is true for all P_{uni}.

$$E[H(\mathrm{P}_{nor})] < \log_2(M\times N) \tag{52.10}$$

To derive the lower bound for the expected value, we have to make use of Jensen's inequality. It is well known that $-\log_2 x$ is a convex function, so that we can exchange the order of the exception operator and the logarithm function in $E[H(\mathrm{P}_{nor})]$ to obtain the following inequality.

$$\begin{aligned} E[H(\mathrm{P}_{nor})] &= -E[\sum_{m=0}^{M-1}\sum_{n=0}^{N-1} P_{nor}(m,n)\log_2 P_{nor}(m,n)] \\ &\geq -\sum_{m=0}^{M-1}\sum_{n=0}^{N-1} E[P_{nor}(m,n)]\log_2 E[P_{nor}(m,n)] \end{aligned} \tag{52.11}$$

Where $E[P_{nor}(m,n)]$ in inequality (52.11) can be expressed as

$$\begin{aligned} E[P_{nor}(m,n)] &= E\left[\frac{S(m,n)\cdot S^*(m,n)}{\sum_{m=0}^{M-1}\sum_{n=0}^{N-1} S(m,n)\cdot S^*(m,n)}\right] \\ &= \frac{E[S(m,n)\cdot S^*(m,n)]}{E[\sum_{m=0}^{M-1}\sum_{n=0}^{N-1} S(m,n)\cdot S^*(m,n)]} \end{aligned} \tag{52.12}$$

Inequality (52.11) indicates that the lower bound for the expected value is the right-hand side of inequality (52.11). For the lower bound's expression, $E[P_{nor}(m,n)]$ must be calculated out, the derivation process is described in the following details.

$$S(m,n) = \sum_{p=0}^{N-1} u(p)\frac{n}{N\sqrt{2\pi}} e^{-\frac{n^2(m-p)^2}{2N^2}} e^{-\frac{i2\pi pn}{N}} \tag{52.13}$$

$$E[u(i)u^*(j)] = \sigma^2\delta(i-j) \tag{52.14}$$

As is known, formula (52.13) is a kind of expression for discrete S transform, and formula (52.14) is the autocorrelation function of the white noise with mean zero and variance σ^2. Combining formulas (52.13) and (52.14), the power spectrum expectation of white Gaussian noise based on S transform can be derived as follow

$$\begin{aligned} &E[S(m,n)\cdot S^*(m,n)] \\ &= E[\sum_{p=0}^{N-1}\sum_{q=0}^{N-1} u(p)u^*(q)\frac{n^2}{2\pi N^2} e^{-\frac{n^2(m-p)^2+n^2(m-q)^2}{2N^2}} e^{-\frac{i2\pi n(p-q)}{N}}] \\ &= \frac{\delta^2}{2\pi N^2}\sum_{p=0}^{N-1} n^2 e^{-\frac{n^2(m-p)^2}{N^2}} \end{aligned} \tag{52.15}$$

It is well known that the distribution for the power spectrum expectation of white Gaussian noise based on S transform is $\frac{1}{2}P_{mean}\chi_2^2$ [10], where P_{mean} is a mean background spectrum of white Gaussian noise, which can be expressed as

$$P_{mean}(m,n) = \frac{\delta^2 n}{2\sqrt{\pi}N} \tag{52.16}$$

Then, the denominator of formula (52.12) is simplified as

$$\begin{aligned} & E[\sum_{m=0}^{M-1}\sum_{n=0}^{N-1} S(m,n)\cdot S^*(m,n)] \\ & = E[\sum_{m=0}^{M-1}\sum_{n=0}^{N-1}\frac{1}{2}P_{mean}(m,n)\chi_2^2] \\ & = \sum_{m=0}^{M-1}\sum_{n=0}^{N-1}\frac{1}{2}P_{mean}(m,n)E(\chi_2^2) \\ & = \frac{\delta^2}{2\sqrt{\pi}N}\sum_{m=0}^{M-1}\sum_{n=0}^{N-1} n \\ & = \frac{\delta^2 M(N-1)}{4\sqrt{\pi}} \end{aligned} \tag{52.17}$$

Formula (52.15) divided by formula (52.17) is $E[P_{nor}(m,n)]$, its expression is

$$\begin{aligned} E[P_{nor}(m,n)] &= \frac{\frac{\delta^2}{2\pi N^2}\sum_{p=0}^{N-1} n^2 e^{-\frac{n^2(m-p)^2}{N^2}}}{\frac{\delta^2 M(N-1)}{4\sqrt{\pi}}} \\ &= \frac{2\sum_{p=0}^{N-1} n^2 e^{-\frac{n^2(m-p)^2}{N^2}}}{\sqrt{\pi}MN^2(N-1)} \end{aligned} \tag{52.18}$$

In Eq. (52.19) can be obtained by substituting Eq. (52.18) into the right-hand side of inequality (52.11)

$$E[H(P_{nor})] \geq -\sum_{m=0}^{M-1}\sum_{n=0}^{N-1}\left[\frac{2\sum_{p=0}^{N-1} n^2 e^{-\frac{n^2(m-p)^2}{N^2}}}{\sqrt{\pi}MN^2(N-1)}\right]\log_2\left[\frac{2\sum_{p=0}^{N-1} n^2 e^{-\frac{n^2(m-p)^2}{N^2}}}{\sqrt{\pi}MN^2(N-1)}\right] \tag{52.19}$$

Then, the right-hand side of inequality (52.19) is the lower bound on the expected value of Shannon entropy of white Gaussian noise.

As it can be seen, the lower bound on the expected value is independent of the variance of the noise, but related to the size of time–frequency matrix only. This is an expected result since Shannon entropy is invariant under the random time shift frequency modulations and amplitude scaling in the signal.

52.3.2 Experimental Analysis of Shannon Entropy for TFDs

In this section, both white Gaussian noises and cumulative profiles of pulsar signal are analyzed through investigating the relationship between theirs Shannon entropy with theirs corresponding sampling point number in time domain, SNR, and the bounds on Shannon entropy, respectively. These analyses provide theoretical base for the detection algorithm in the next section.

The bounds on Shannon entropy for TFDs of white Gaussian noise are given for different sizes of TFDs in Table 52.1. Taking 100 white Gaussian noises as samples under the same conditions of sampling point number in time domain and SNR, calculating the average value of noise samples' Shannon entropy, the results shown in the left graph of Fig. 52.1. In a similar way, the average value of cumulative profiles of pulsar signal samples' Shannon entropy are shown in the right graph of Fig. 52.1. We consider a cumulative pulse profile of pulsar B0531+21 in our experiment. All pulsars used in this paper are from the ATNF EPN database.

From left graph of Fig. 52.1, we may know that the average value of noise samples' Shannon entropy is independent of SNR, but related to the size of time–frequency matrix only, the reason is that Shannon entropy is invariant under the scaling of amplitude. Right graph of Fig. 52.1 indicates that with a fixed size of time–frequency matrix, Shannon entropy of cumulative profiles of pulsar signal reduces as the SNR increases; under the same condition, the average Shannon entropy of noise is greater than the average Shannon entropy of cumulative sequence containing pulsar signal, this provides the theory basis for the detection algorithm; Left graph of Fig. 52.1 and Table 52.1 indicate that Shannon entropy of noise is closer to the upper bound, so that the upper bound can provide reference for decision threshold selection in the detection algorithm.

52.3.3 Detection Algorithm Based on Optimum Threshold

The detection of cumulative sequences is a binary detection, which involves the following hypothesis test

Table 52.1 Bounds on Shannon entropy for TFDs of Gaussian white noise in different size

M × N	Upper bound (bits)	Lower bound (bits)
32 × 17	9.087	5.459
64 × 33	11.044	6.324
128 × 65	13.022	7.255
256 × 129	15.011	8.231
512 × 257	17.006	9.233
1024 × 513	19.003	10.253

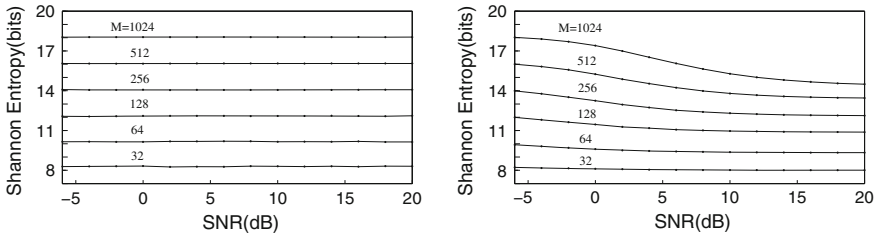

Fig. 52.1 SNR versus Shannon entropy of Gaussian white noise (*left*) and SNR versus Shannon entropy of cumulative pulse profile of pulsar B0531+21 (*right*)

$$\begin{aligned} H_0 &: x(m) = u(m), \qquad m = 0, 1, 2, \ldots, N-1 \\ H_1 &: x(m) = s(m) + u(m), \quad m = 0, 1, 2, \ldots, N-1. \end{aligned} \tag{52.20}$$

Where $x(m)$ represents a cumulative profile of pulsar signal, $s(m)$ represents a standard profile of pulsar, and $u(m)$ represents a white Gaussian noise.

Shannon entropy for TFDs of $x(m)$ is calculated according to formula (52.8), the result is denoted by $H(C_X)$. In line with the experimental results of Sect. 52.3.2, the decision rule of the detection algorithm is given as

$$H(C_x) \underset{H_1}{\overset{H_0}{\gtrless}} \gamma \tag{52.21}$$

Where γ is the decision threshold, let E_H and E_L are the upper bound and the lower bound respectively, while $\gamma \in [E_L, E_H]$.

The detection result of the present algorithm is related to γ only. Section 52.3.2 shows that although Shannon entropy of noise is irrelevant to SNR, Shannon entropy of cumulative sequence of pulsar signal reduces as the SNR increases; therefore while selecting the decision threshold, both the size of time–frequency matrix and the SNR of a signal need to be taken into account.

To get the optimum decision threshold, an optimum threshold detection algorithm based on ROC curve is proposed in this paper. First, 1,000 cumulative sequences containing pulsar signal and noise series are taken as the positive samples and the negative samples respectively. Shannon entropy for TFDs of every sample is calculated; Then all samples are detected by different decision thresholds from formula (52.22), meanwhile both *FPR* (false positive rate) and *TPR* (true positive rate) corresponding to each decision threshold are calculated. The higher the *TPR* and the lower the *FPR* in ROC curve are, the better the performance of corresponding detector will be, where higher *TPR* should be guaranteed firstly in the optimum decision threshold selection; Therefore, formula (52.23) is used as an index of the optimum decision threshold selection, when J is the maximum, the consideration to *TPR* and *FPR* will be the best; In addition, both *TPR* and *FPR* are considered as the function of γ. Finally, the optimum threshold γ_{opt} is worked out based on formula (24).

$$\gamma = \alpha E_H, \quad \alpha \in [E_L/E_H, 1] \tag{52.22}$$

$$J = TPR\sqrt{1 - FPR} \tag{52.23}$$

$$\gamma_{opt} = \underset{\gamma}{\text{argmax}} \left\{ TPR(\gamma)\sqrt{1 - FPR(\gamma)} \right\} \tag{52.24}$$

52.4 Experiment and Analysis

52.4.1 Experimental Analysis of the Optimum Decision Threshold

In this section, taking pulsar B0531+21 for example, under the condition of a given training sample set, the optimum threshold of the detection algorithm is worked out by Monte Carlo Simulation. Under the same conditions of sampling point number in time domain and SNR, 1,000 positive samples and negative samples are taken respectively as the training sample set in experiment, the bounds on Shannon entropy for the corresponding size of TFD are taken as the interval of decision threshold. The training sample set is detected by many decision thresholds from the interval, meanwhile both *FPR* and *TPR* corresponding to each decision threshold are calculated; the corresponding curves are shown in Fig. 52.2. The area under the ROC curve (AUC) is shown in Table 52.2, we can see from Table 52.2

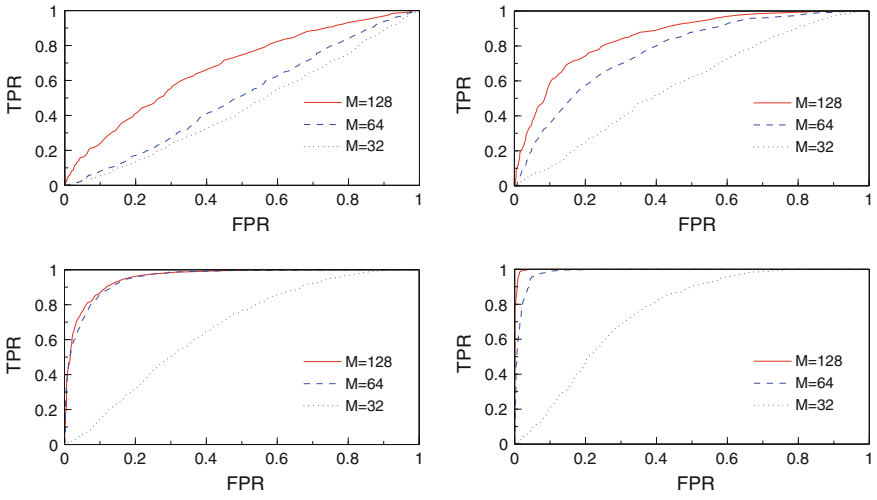

Fig. 52.2 ROC curves of training samples under different conditions of SNR and sampling number. SNR in *upper left graph* is −3 dB, SNR in *upper right graph* is 0 dB, SNR in *lower left graph* is 5 dB, SNR in *lower right graph* is 8 dB

Table 52.2 Each AUC of the curves in Fig. 52.2

M \ AUC \ SNR (dB)	-3	0	5	8
32	0.463	0.601	0.649	0.740
64	0.531	0.748	0.952	0.984
128	0.690	0.845	0.960	0.998

that every AUC is greater than 0.5, therefore the detection performance of every threshold is better than the random detection's. Besides, with the increment of sampling point number in time domain and SNR respectively, AUC increases, hence, the more the sampling point number and the higher the SNR respectively, the better the performance of the detection algorithm will be.

Values of J corresponding to different decision thresholds of γ in ROC curve are calculated according to formula (52.23), the results are shown in Fig. 52.3. The value of γ corresponding to the peak value of each curve in Fig. 3 is the optimum decision threshold γ_{opt} under a certain conditions of sampling point number in time domain and SNR. From top to bottom, the value of γ_{opt} corresponding to each curve in the two figures is 11.833, 11.999, 12.104 and 13.762, 13.932, 14.061 respectively; the peak value of J in Fig. 52.3 is 0.999,the detection performance of the corresponding threshold is very good. Comparing left graph of Fig. 52.3 with right graph of Fig. 52.3, it is shown that the peak value of J increases as SNR increases when the sampling point number in time domain remains the same, furthermore, the higher the peak value of J is, the better the detection performance will be, as a result, the higher the SNR is, the better the performance will be; When SNR is unchanged, the longer the sampling point number in time domain is, the higher the peak value of J will be, then the performance of the optimum decision detection algorithm improved also. In summary, the higher the SNR and the more the sampling point number in time domain are, the better the detection performance corresponding to the optimum threshold of γ_{opt} will be, meanwhile, under the same condition of the sampling point number in time domain, the optimum threshold of γ_{opt} decreases as SNR increases, when SNR is a constant, the optimum threshold of γ_{opt} increases as the sampling point number increases.

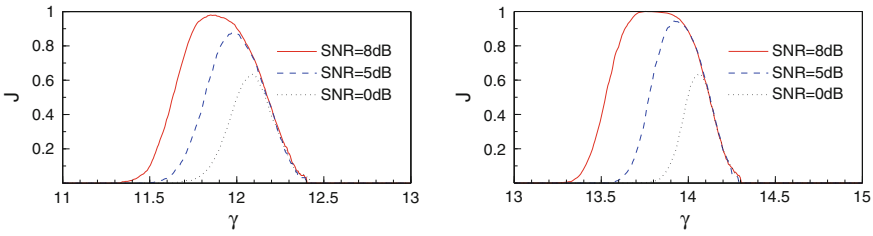

Fig. 52.3 γ versus J under different conditions of sampling number. Sampling number in *left* graph is 128 and sampling number in *right* graph is 256

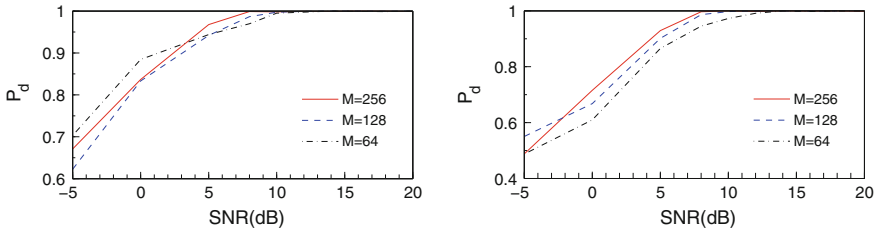

Fig. 52.4 Probability of detection of the average pulse profiles for PSR B0531+21 (*left*) and PSR J0437-4715 (*right*) at different signal-to-noise ratio

52.4.2 Experimental Analysis of the Detection Algorithm

Supposing that the optimum thresholds is given, we consider integrated pulse profiles of pulsar B0531+21 and pulsar J0437-4715 in our detection experiment, the corresponding results are shown in Fig. 52.4.

It can be seen from Fig. 52.4 that the detection results of the detection algorithm is rather good, moreover, the detection algorithm has a low requirement for temporal sampling, when the sampling point number in time domain is equal to 64, the detection result is still good. Both the noise power spectrum and the individual pulse power spectrum of pulsar J0437-4715 are shown in Fig. 52.5, it is clear that when SNR is -5 dB, the power spectrum of the individual pulse is buried in the power spectrum of noise, however under the same condition of SNR, the detection rate of the Shannon entropy algorithm in right graph of Fig. 52.4 is relatively good.

Under the same conditions of hardware and software, 1,000 positive samples and 1,000 negative samples are trained to obtain the optimum threshold by this algorithm, the optimum threshold training time of this algorithm is 29.2 s, the signal detection time of this algorithm is 14.8 ms; An observed data containing 2,000 periods is detected by Taylor FFT algorithm, the corresponding detection time is about 45 s. In comparison with Taylor FFT algorithm,under a certain condition, the optimum threshold training needs only once, on this basis it needs about 15 ms only for the detecting of any cumulative sequence under the same

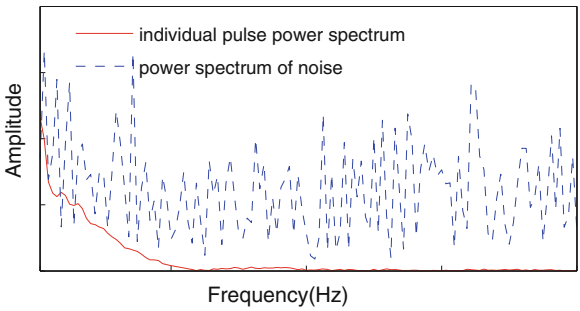

Fig. 52.5 Comparison of individual pulse power spectrum with noise power spectrum for PSR J0437-4715 (SNR $= -5$ dB)

condition, but for all observed data containing 2000 periods, the detection times of Taylor FFT algorithm are about 45 s, therefore the computing time of this detection algorithm is much shorter than Taylor FFT algorithm's.

52.5 Conclusion

Time–frequency analysis method is a powerful tool for nonstationary signal analysis, according to the cumulative profiles of pulsar signal with complex structure, the optimum decision threshold detection algorithm based on Shannon entropy for TFDs in S transform domain is proposed in this paper, theory analysis and experiment show that: (1) the cumulative profiles of pulsar signal with complex structure can be analyzed by Shannon entropy for TFDs in S transform domain; (2) on contrast against Taylor FFT algorithm, this detection algorithm has low requirements for temporal resolution and SNR; (3) the detection speed of this algorithm is faster than Taylor FFT algorithm's.

Acknowledgments This work is supported by National Science Foundation of China (61172138).

References

1. Sheikh SI (2005) The use of variable celestial X-ray sources for spacecraft navigation. PhD thesis, University of Maryland, Maryland
2. Hanson J, Sheikh SI, Graven P (2008) Noise analysis for X-ray navigation systems. In: IEEE/ION position, location and navigation symposium, USA (pp 704–713). Monterey, USA
3. Seward FD, Harnden FR, Helfand DJ (1984) Discovery of a 50 millisecond pulsar in the Large Magellanic Cloud. Astrophys J 287:19–22
4. Williams WJ, Brown ML, Hero AO (1991) Uncertainty information and time-frequency distributions. Proc SPIE 1556:144–156
5. Aviyente S, Williams WJ (2005) Minimum entropy time-frequency distributions. IEEE Signal Process Lett 12(1):37–40
6. Baraniuk RG, Flandrin P, Jansen AJ et al (2001) Measuring time-frequency information content using the Renyi entropies. IEEE Trans Inf Theory 47(4):1391–1409
7. Zou HX, Zhou XB, Li YD (2000) Which time-frequency analysis—a survey. Acta Electronica Sinica 28(9):78–84
8. Wu XJ, Xu W, Rankin JM (1992) At the separation of the components of the profiles of pulsar PSR 1451-68 and their spectral behavior. In: Proceeding of IAU Colloquium 128, Poland, p 172
9. Stockwell RG, Mansinha L, Lowe RP (1996) Localization of the complex spectrum: the S transform. IEEE Trans Signal Process 44(4):998–1001
10. Gao JH, Man WS, Chen SM (2004) Recognition of signals form colored noise background in generalized S-transformation domain. Chin J Geophys 47(5):869–875

Chapter 53
On the Agent Localizability of Hybrid GNSS-Terrestrial Cooperative Positioning

Shiwei Tian, Weiheng Dai, Jiang Chang and Guangxia Li

Abstract Cooperative positioning is a new paradigm around how devices can cooperate with each other to improve their abilities to compute position. The problem of whether or not a device can be localized is fundamental for cooperative positioning. Many efforts have been made to solve the problem of whether or not a network or a node in the network can be localized in wireless sensor networks. Nevertheless, existing studies mainly examine the network or node localizability in 2-dimension space, yet fundamental questions in 3-dimension space remain unaddressed. In this contribution, we study the agent localizability in hybrid cooperative positioning, where GNSS information is combined with terrestrial range measurements through sharing information with other agents in a small scale group. The results provide a characterization of availability of hybrid positioning schemes, and lead to a deep understanding of the reasons for why cooperation can improve the availability.

Keywords Cooperative positioning · GNSS · Localizability

53.1 Introduction

Nowadays, the most widely used positioning and navigation technology is Global Navigation Satellite System (GNSS). In GNSS, each device estimates its position individually based on pseudorange measurements taken with respect to multiple satellites with known positions. Unfortunately, because the received GNSS signal

S. Tian (✉) · W. Dai · J. Chang · G. Li
College of Communications Engineering, PLA University of Science and Technology, Nanjing 210007, China
e-mail: tianxwell@163.com

J. Sun et al. (eds.), *China Satellite Navigation Conference (CSNC) 2013 Proceedings*, Lecture Notes in Electrical Engineering 245,
DOI: 10.1007/978-3-642-37407-4_53,

is extremely low power, the satellite signals can be easily obstructed. For instance, GNSS-based techniques fail to provide satisfactory performance due to signal blockage in many scenarios such as urban terrain, forests, or jungles. At the same time, GNSS receivers are also susceptible to jamming and unintentional interference for this same reason [1]. Driven by the success of cooperative techniques in many research areas, cooperative techniques have been introduced in the research of positioning and navigation.

Cooperative positioning methods have been recognized as part of an effort to improve the performance of GNSS receivers in hostile environments, relying on information exchange and/or direct measurements among devices (also referred to as agents hereafter). They can be used not only when GNSS is unavailable, but also in combination with GNSS, in order to improve the performance of positioning, such as accuracy, availability, time to first fix (TTFF), integrity etc. Hybrid cooperative positioning is an emerging research topic [2].

In prior work, graph rigidity is found closely related to positioning problem. Based on rigidity theory, the necessary and sufficient condition for network positioning was proposed [3], and the concept of node localizability was proposed to answer the following two questions [4]: First, given a network configuration, whether or not a specific node is localizable? Second, how many nodes in a network can be located and which are them? Unfortunately, previous works on network localizability and node localizability are both in 2-dimension and its conclusion cannot be applied to the hybrid cooperative positioning.

In this paper, we attempt to answer the question of whether or not an agent can be localized and why cooperation among nodes can improve the availability. In contrast to prior works, this paper presents an analysis on the agent localizability in scenario for small scale cooperative GNSS positioning, under different cases depending on the measurements between agents. The measurements between nodes may include one or more of the following:

- Relative position between agents, including distance between agents and relative bearing between agents.
- Distance between agents. Considering the relative bearing may not be available in practice, distance between agents is usually considered, besides, IEEE 802.11v defines a protocol to obtain this measurement between two peer WiFi devices using time-of-flight or calibrated RSS measurements.
- Difference in clock bias between agents. IEEE 802.11v also defines a protocol to obtain this measurement.
- Difference in altitude between agents. When devices are equipped with altimeters, this measurement can be obtained to improve performance. Besides, equal altitudes can be assumed between agents in some scenarios.

53.2 Problem Formulation

53.2.1 Scenario Setting

Consider a hybrid GNSS-terrestrial cooperative network including satellite nodes with known clock bias and known position, anchor nodes with known position but unknown clock bias, and agents with unknown clock bias and unknown position. Generally, bias in range measurements from satellite to terrestrial devices is considered, resulting from imperfect synchronization of device clock with respect to satellites. Nevertheless, the above bias in terrestrial range measurements is usually not considered [2]. Figure 53.1 illustrates the scenario for hybrid GNSS-terrestrial cooperative positioning.

Let M be the set of agents, S the set of satellites, A the set of anchors; denote by S_m the set of satellites agent m can see, by A_m the set of anchors agent m can communicate with. Positional state of satellite $s \in S$, of anchor $a \in \mathrm{A}$, and of agent $m \in \mathrm{M}$, are indicated respectively by $\mathbf{x}_s = [x_s\ y_s\ z_s]$, $\mathbf{x}_a = [x_a\ y_a\ z_a]$, $\mathbf{x}_m = [x_m\ y_m\ z_m]$. The variable b_m represents the clock bias of agent m, expressed in distance units. The information agent m obtained from satellites (denoted by $\mathbf{P}_{sm}$) and terrestrial anchors (denoted by $\mathbf{R}_{am}$) and from useful neighboring agents (denoted by $\mathbf{P}_m$) is denoted by $\mathbf{M}_m = \mathbf{P}_{sm} \cup \mathbf{R}_{am} \cup \mathbf{P}_m$, a set of unknowns $\mathbf{U}_m = [\mathbf{x}_m\ b_m]$ for agent m are to be determined.

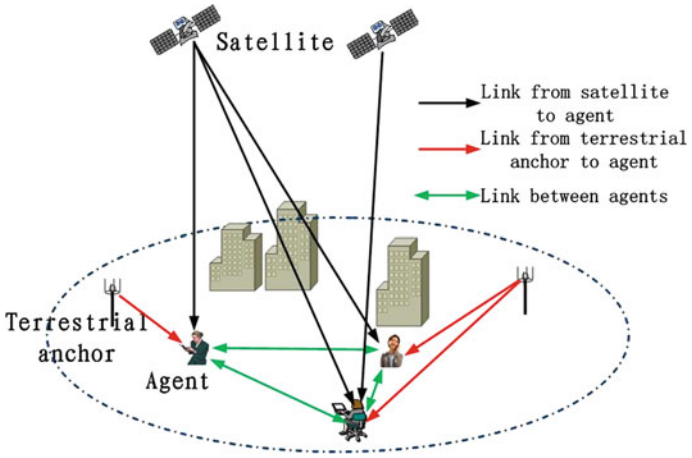

Fig. 53.1 Scenario for hybrid GNSS-terrestrial cooperative positioning

53.2.2 Different Models Between Agents

In this subsection, we describe the measurements models among agents in different cases. In all the cases, the following two types of measurements always exist:

1. Range measurements, i.e., distance between agents and anchors $r_{am} = \|\mathbf{x}_a - \mathbf{x}_m\| + v_{am}$.
2. Pseudorange measurements, i.e., distance between agents and satellites $\rho_{sm} = \|\mathbf{x}_s - \mathbf{x}_m\| + b_m + v_{sm}$.

where the symbol $\|\cdot\|$ denotes Euclidean distance, $m \in \mathrm{M}$, $a \in \mathrm{A}$, $s \in S$, v_{am}, v_{sm} are measurement noise. Without loss of generality, in the following of this paper, we only discuss on the situation when distance between agents and satellites is available, and the measurements between agents and anchors will not be considered.

Based on different intra- and inter-node measurement sensors that agents equipped, there are several measurement models in accordance with the description in Sect. 53.1.

Case 1: the relative position $\mathbf{p}_{mn}$ between agent n and a neighbour agent m can be measured, $\mathbf{p}_{mn} = \mathbf{x}_m - \mathbf{x}_n$.
Case 2: the distance between agent n and a neighbour agent m can be measured. $r_{nm} = \|\mathbf{x}_n - \mathbf{x}_m\| + v_{nm}$, where v_{nm} is measurement noise.
Case 3: the difference in clock bias between agent n and a neighbour agent m can be measured, $\Delta b_{mn} = b_m - b_n$.
Case 4: the difference in altitude between agent n and a neighbour agent m can be measured, $\Delta z_{mn} = z_m - z_n$. Besides, it can be supposed that all the agents work on the same altitude, $z_m = z_n$.

53.3 Conditions for Agent Localizability

To determine the solution of unknowns, a well-determined or preferably over-determined set of equations must be obtained, that is, the set of independent measurements $\mathbf{M}_m$ in the agent m must have greater cardinality than or equal to the set of unkowns $\mathbf{U}_m$ in the same agent.

53.3.1 Conventional GNSS Positioning Requirements

In order to determine agent position in the conventional satellite positioning as shown in Fig. 53.2, pseudorange measurements are made to at least four satellites resulting in the system of equations $\rho_{sm} = \|\mathbf{x}_s - \mathbf{x}_m\| + b_m + v_{sm}$.

There are three methods to solve the nonlinear equations, i.e., closed-form solutions, iterative techniques based on linearization and kalman filtering [5]. Given four measured pseudoranges, a position-bias pair almost always exists which exactly satisfies all four pseudorange equations. There are many previous works focusing on the exact solutions and the question of solution uniqueness. In the following of this paper, we discuss whether or not the unknowns can be resolved, and the uniqueness of the solutions will be our focal point in future works.

53.3.2 Cooperative Positioning Requirements for Two Agents

Using the conventional multilateration requirements as a starting point, the corresponding set of requirements for cooperative positioning between two agents can be established. Cooperative positioning between two agents represents the situation where one or both of the agents cannot see at least four satellites and then cannot obtain its position state individually. In this situation, the two agents can cooperate with each other, including the several cases in Sect. 53.2.2 to jointly solve the unknowns. In practice, the relative bearing may not be available, thus we only discuss on situations from the later three cases in the following.

Scenario 1, that case 2 and case 3 in Sect. 53.2.2 are satisfied. In this scenario, distance and difference in clock bias between the two agents can be measured, thus there are 7 parameters in the set of unknowns for the system. From this perspective, a condition for agent localizability in this scenario can be set.

Condition 1: To obtain the positional state of the two agents in this scenario, it is necessary that at least 7 measurements can be obtained in the system.

Unfortunately, this condition is necessary but not sufficient to guarantee that there is only one possible agent position estimate. Just as illustrated in Fig. 53.3c and d, both of the two cases have 7 measurements, but never of them can be localized. That is because each agent have 4 unknowns to be solved, only one of them can be shared by the two agents, still 3 unknowns are remaining and should be solved depend on its own measurements from satellites and the other agents. Actually, in the

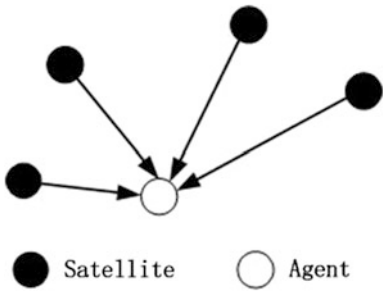

Fig. 53.2 Conventional positioning: an agent can be located by no less than four satellites

two cases, the measurements are not independent so that independent measurements are less than 7. To avoid the above problem, an additional condition is set.

Condition 2: To obtain the positional state of the two agents in this scenario, it is necessary that each agent can obtain at least 3 measurements.

Figure 53.3a and b satisfy both condition 1 and condition 2, and they can be localized. Condition 1 and condition 2 are individually necessary but jointly sufficient to guarantee that the two agents in scenario 1 can be localized. It is noted that the satellites observed by the two agents can be the same. Here is an example for Fig. 53.3a, when the two agents are in a canyon, they observe the same three satellites, and then they can cooperate to obtain their position state. The other example for Fig. 53.3b, one agent is outdoors with four satellite measurements to obtain its position, while the other agent who is nearby indoors can only observe two satellites, then the indoor agent can cooperate with the outdoor agent to compute its own position.

Scenario 2, that case 2, case 3 and case 4 in Sect. 1.2 are satisfied. In this scenario, distance, difference in clock bias and altitude between the two agents can be measured, thus there are 6 parameters in the set of unknowns for the system. Similar to scenario 1, two conditions agent localizability in this scenario can be set.

Condition 1: To obtain the positional state of the two agents in this scenario, it is necessary that at least 6 measurements can be obtained in the system.

Condition 2: To obtain the positional state of the two agents in this scenario, it is necessary that each agent can obtain at least 2 measurements.

Figure 53.4a and b satisfy both condition 1 and condition 2, and they can be localized while Fig. 53.4c cannot be localized since it doesn't satisfy condition 2. Condition 1 and condition 2 are individually necessary but jointly sufficient to guarantee that the two agents in scenario 2 can be localized.

53.3.3 Cooperative Positioning Requirements for Three Agents

Due to the generality between scenario 1 and scenario 2 in Sect. 3.2, we only focus on scenario 1 (distance and difference in clock bias between the two agents can be

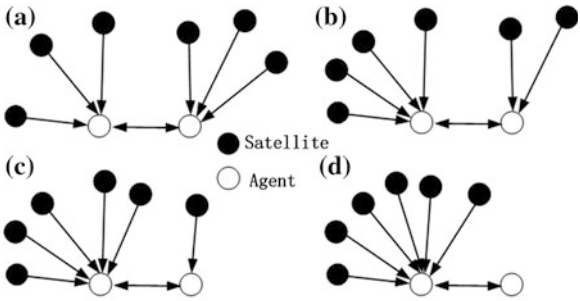

Fig. 53.3 Four basic cases (as shown in **a**, **b**, **c** and **d**) in scenario 1

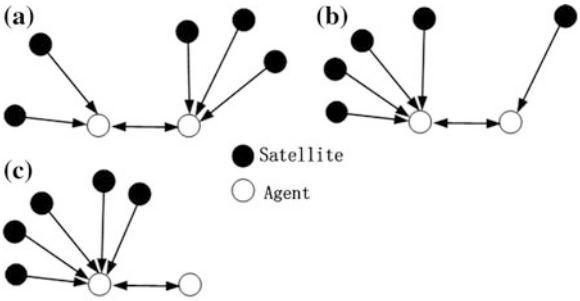

Fig. 53.4 Four basic cases (as shown in **a**, **b**, **c** and **d**) in scenario 2

measured) in this section. It is supposed that there are 3 agents in a group that participate in the cooperative positioning. In this case, there are 3 measurements among the 3 agents, and 10 unknowns in the system. Thus to solve the position of the agents, it is necessary that the cardinality of the set of independent measurements combining of the measurements among agents and from satellites is larger than 10. In the following cases, we only discuss the well-determined case, i.e. the cardinality of the set of independent measurements is 10.

Figure 53.5 illustrates the four cases that all the agents have no more than 4 satellites. We can declare that in the four cases, the positional state of the system in Fig. 53.5d cannot be solved, while the other three can be solved. However, like the two-agent case, the uniqueness of the solutions should be further discussed.

Besides, there are several cases that one agent can observe more than 4 satellites. For example, Fig. 53.6a illustrates one case that one agent observe 5 satellites while the other two agents both observe 1 satellites. In this case, the positional state cannot be solved, and the reason can be found in Fig. 53.6b, which is derived from Fig. 53.6a. In Fig. 53.6b, there are 6 unknowns to be solved, unfortunately, there are only 5 measurements in the system.

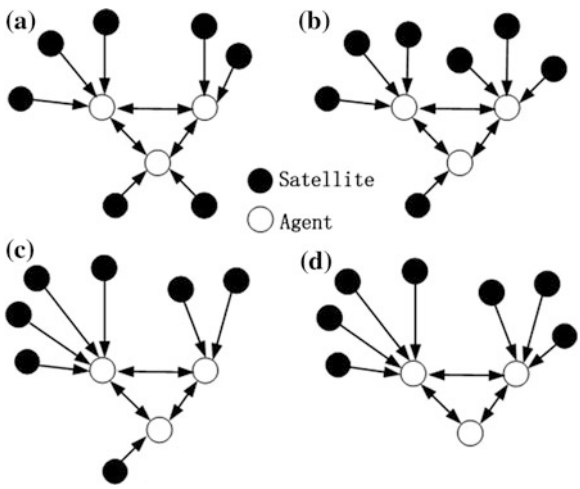

Fig. 53.5 Cases (as shown in **a**, **b**, **c** and **d**) that no agent can observe more than 4 satellites

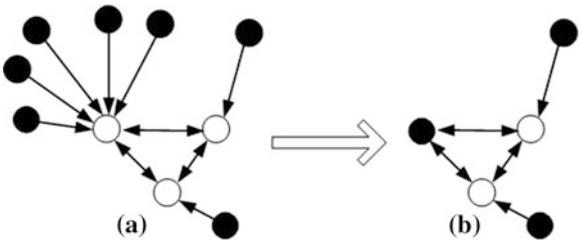

Fig. 53.6 Cases that one agent can observe more than 4 satellites: (a) can be converted to (b)

In a group consisting of m agents, there are $m(m-1)/2$ measurements among agents in total, and $3m+1$ unknowns in the system. Thus to solve the position of the agents, it is necessary that the cardinality of the set of independent measurements combining of the measurements among agents and from satellites is larger than $3m+1$. Then two fundamental questions must be addressed. First, are the $m(m-1)/2$ measurements referred above independent? Second, if the $m(m-1)/2$ measurements are not independent, then how many independent measurements can we get from them? To answer the first question, we propose Lemma l.

Lemma 1 In a group consisting of m agents, the $m(m-1)/2$ measurements among them are not independent when m is larger than some value.

Proof Since difference in clock bias between agents can be obtained, there are 3 m + 1 unknowns to be solved. Suppose the $m(m-1)/2$ measurements are independent, then when $m(m-1)/2 \geq 3m+1$, i.e., $m \geq 8$, the unknowns can be solved even there is no beacon. This is in conflict with the fact. Therefore, the $m(m-1)/2$ measurements among agents are not independent.

Inspired by Lemma 1, the answer to the second question should be further explored, and this will be our focal points in the future work.

53.4 Conclusion and Future Works

In this paper, we described the scenario setting and measurement model for the hybrid GNSS-terrestrial cooperative positioning. Cooperation enables agents that cannot compute positions on their own to compute their positions through sharing information with other agents. It also allows an agent that does not need cooperation to aid another agent that has insufficient measurements to compute its position alone. We analyzed agent localizability in small scale networks and explained the reason why cooperation can improve the performance of availability. Our results provide a characterization of availability of hybrid positioning schemes, and lead to a deep understanding of the reasons for why cooperation can improve the availability.

Several issues we plan to address in future mainly include the uniqueness of solutions, the localizability for a number of m agents, and simulations or experiments from live data.

References

1. Quebe S, Campbell J, DeVilbiss S et al (2010) Cooperative GPS navigation. IEEE/ION PLANS, pp 834–837
2. Penna F, Caceres MA, Wymeersch H (2010) Cramer-Rao Bound for hybrid GNSS-terrestrial cooperative positioning. IEEE Commun Lett 14(11):1005–1007
3. Jackson B, Jordan T (2005) Connected rigidity matroids and unique realizations of graphs. J Comb Theory B 94(1):1–29
4. Yang Z, Liu Y (2010) Understanding node localizability of wireless ad-hoc networks. In IEEE INFOCOM, pp 1–9
5. Kaplan E, Hegarty C (2006) Understanding GPS principles and applications, 2nd edn. Artech House, Norwood, p 55

Chapter 54
Precise Maritime Navigation with a Locata-Augmented Multi-Sensor System

Wei Jiang, Yong Li, Chris Rizos, Joel Barnes and Steve Hewitson

Abstract This paper investigates use of Locata—a ground signal-based navigation system—to augment a standard GNSS/INS integrated system for use in the marine environment. A loosely-coupled decentralized integration architecture based on a Kalman filter was implemented. The multi-sensor experiment was conducted on Sydney Harbour, Australia. The GNSS, INS and Locata measurements were collected and post-processed to evaluate the overall positioning performance of the integrated system. The test results indicate that the addition of the Locata measurements significantly improves the overall system performance. Moreover, accurate seamless navigation is achievable even when GNSS signals are unavailable.

Keywords Locata · INS · GPS · GNSS · Multi-sensor · Maritime applications

54.1 Introduction

Through innovative application of global navigation satellite system (GNSS) technology, mariners have access to more consistent and more accurate positioning capability than ever before. However, GNSS alone will be unable to meet emerging performance requirements for maritime applications with respect to service robustness, accuracy, integrity and availability. In particular, identified applications in port areas (for example, automated docking) and in constricted waterways, have very stringent performance requirements. Even when an integrated inertial navigation system (INS)/GNSS is used there will still be performance gaps. GNSS

W. Jiang (✉) · Y. Li · C. Rizos
School of Surveying and Geospatial Engineering, University of New South Wales, Sydney, Australia
e-mail: w.jiang@student.unsw.edu.au

J. Barnes · S. Hewitson
Locata Corporation Pty Ltd, Canberra, Australia

J. Sun et al. (eds.), *China Satellite Navigation Conference (CSNC) 2013 Proceedings*, Lecture Notes in Electrical Engineering 245,
DOI: 10.1007/978-3-642-37407-4_54,

signals can be blocked or interfered with, and sometimes the satellite geometry may not be good enough for high accuracy and high reliability applications. Furthermore, the INS accuracy degrades rapidly during GNSS outages. Therefore, the development of alternative, non-GNSS-based navigation solution has attracted increasing interest in situations where GNSS solution performance cannot be guaranteed.

Locata is a ground-based navigation system which transmits ranging signals at frequencies in the 2.4 GHz industrial, scientific and medical (ISM) radio band. Such ranging signals from transceivers—known as LocataLites—can be tracked by a Locata receiver. A Locata network—or LocataNet—contains at least four time-synchronized LocataLites that cover an area with strong transmitted ranging signals [1, 2].

Locata technology is able to operate independently of other navigation systems. The fundamentals of the Locata technology and some results of earlier testing have been reported in the literature [1, 3–5]. Such tests have verified that this technology can be used for a wide range of positioning applications, including precise indoor positioning [1, 2] and slow structural displacement monitoring [3]. More recently, researchers at University of New South Wales (UNSW) have studied Locata/GNSS/INS "triple integration" in order to derive the complete platform motion information with more reliable system performance. It has been demonstrated that a seamless high accuracy Locata-aiding system for vehicle navigation is possible [4].

This paper investigates a Locata-augmented hybrid navigation system, with an emphasis on its potential use in the marine environment. In October 2012, a field trial which was conducted by Locata Corporation, UNSW and New South Wales government agencies on Sydney Harbour. GNSS, Locata and INS data were recorded by a system installed on an inner harbour vessel. Locata and GNSS carrier phase measurements were post-processed, and combined with INS measurements to achieve a loosely-coupled integration system. In addition to describing the theoretical aspects of the hybrid system, this paper presents some results from this trial. The performance of a Locata standalone system, Locata/INS, GNSS precise point positioning (PPP)/INS and the triple integration system configurations were analysed.

This paper is organized as follows. An overview of the Locata technology and Locata measurement model is first presented. Then the hybrid system algorithm is introduced. Finally, the field test is described, and the data analysis and results presented.

54.2 Locata Technology and Measurements

54.2.1 Locata Technology

Locata is a terrestrial and radio frequency-based measurement technology which was developed by Locata Corporation, Canberra, Australia. The concept of a LocataNet is shown in Fig. 54.1. A Locata system is able to work together with GNSS, or operate independently. What is different from GNSS is that Locata

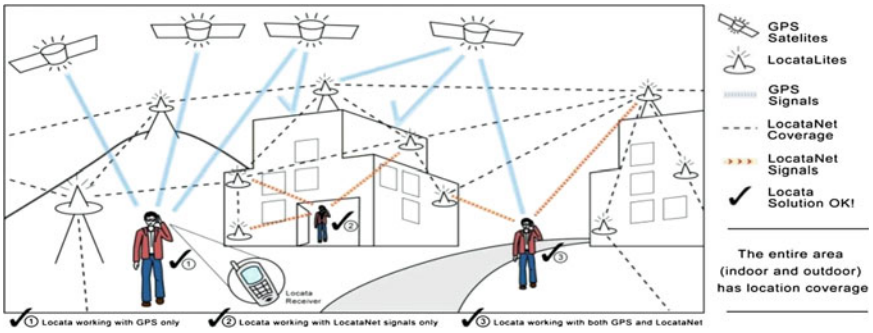

Fig. 54.1 LocataNet

signals are transmitted in the 2.4 GHz license-free ISM band, which permits output power of up to 1 W to be used—supporting line of sight distance tracking over tens of kilometers. In order to enable independent positioning capability, the LocataNet should consist of at least four LocataLites (LLs). To each LL transceiver two spatially separated antennas are connected, and from each antenna the signal is transmitted separately on two different frequencies at approximately 2.41428 and 2.46543 GHz—referred to as S1 and S6 respectively [6]. Hence a cluster of four distinct signals are transmitted by each LL. In this way, some problems associated with conventional pseudolite-based navigation techniques, such as "near-far" and multipath effects, can be mitigated.

Another significant character of Locata is the technique of time synchronization -also known as "Time-Loc" [6]. The use of this patented technique can realize time synchronization inside a LocataNet at the sub-nanosecond level, as well as enable good synchronization between the LocataNet and GNSS satellite constellations. The LLs within the LocataNet comprise one "master" and several "slave" LLs. Each LL, currently developed using Field Programmable Gate Array (FPGA) technology, contains both transmitter and receiver components. Thus, LLs transmit navigation signals to Locata user equipment, as well as transmitting and receiving tracking signals between each LL for purposes of time/signal synchronization. Normally, "slave" LLs are synchronized with the "master" LL, however, when the "master" LL cannot be received, a "slave" LL is able to be synchronized with other "slave" LLs in cascaded mode. This time synchronized characteristic makes Locata-based systems superior to conventional pseudolite-based systems.

54.2.2 Locata Measurement Approach

54.2.2.1 Locata Measurement

The range-like Locata measurements are of two types: pseudorange and carrier phase. As in the case of GNSS, the carrier phase measurements are more precise

than pseudorange measurements. The basic Locata carrier phase measurement model, between receiver and Locata transmit channel i is:

$$\varphi_r^i \lambda = \rho_r^i + \tau_{trop}^i + c \cdot dt_r + N_r^i \lambda + \varepsilon_\varphi^i \tag{54.1}$$

where φ_r^i is the carrier phase measurement; ρ_r^i is the geometric range from receiver to the LL transmitting antenna i; λ is the wavelength of the signal; τ_{trop}^i is the tropospheric delay; c is the speed constant of light; dt_r is the receiver clock bias, N_r^i is the carrier phase ambiguity, and ε_φ^i are unmodelled residual errors [7]. Note that there is no transmitter clock error in the observation equation because of the tight time synchronization of the LLs. At this time Locata's ambiguities are typically estimated to floating point values. Once the float ambiguities are estimated with a certain level of accuracy, they can be treated as known parameters in (1).

Similar to GNSS, Locata's Doppler measurements can be used to estimate the receiver's velocity:

$$D_r^i \cdot \lambda = \mathbf{H_r^i} \cdot \dot{\mathbf{r}}_\mathbf{r} + c \cdot \dot{dt}_r + \gamma_\varphi^i \tag{54.2}$$

where $\mathbf{H_r^i}$ is the direction cosine vector from the receiver to the LL; D_r^i is the receiver's Doppler measurements; $\dot{\mathbf{r}}_\mathbf{r}$ is the receiver's velocity vector; $\dot{dt}_r$ is the rate of receiver clock biases; and γ_φ^i is the combined error residuals.

54.2.2.2 Least Squares Estimation

Least square estimation (LSE) is a common approach for obtaining a position and velocity solution from an over-determined measurement system.

Applying the principles of LSE, the error equation $\mathbf{z} = \mathbf{Ax} + \mathbf{b}$ can be written as:

$$\mathbf{z} = \begin{bmatrix} \mathbf{H_r} & \mathbf{0} \\ \mathbf{0} & \mathbf{H_r} \end{bmatrix} \cdot \begin{bmatrix} \delta \mathbf{x_r} \\ \mathbf{v_r} \end{bmatrix} + \begin{bmatrix} \boldsymbol{\varphi}_\mathbf{r} \cdot \lambda - \boldsymbol{\rho}_\mathbf{r0} - \mathbf{N_r}\lambda \\ \mathbf{D_r} \cdot \lambda \end{bmatrix} \tag{54.3}$$

where

$\mathbf{H_r} = [\,\mathbf{e} \quad 1\,]$, $\mathbf{e}$, is the line of sight vector between receiver and the LL;

$\boldsymbol{\delta x_r} = [\,\boldsymbol{\delta r} \quad c \cdot dt_r\,]^{\mathrm{T}}$, combined position coordinate increments and receiver clock bias;

$\mathbf{v_r} = [\,\dot{\mathbf{r}}_\mathbf{r} \quad c \cdot \dot{dt}_r\,]^{\mathrm{T}}$, combined receiver velocity and receiver clock bias rate.

The solution for the vector $\mathbf{x}$ is:

$$\hat{\mathbf{x}} = \left(\mathbf{A^T P A}\right)^{-1} \mathbf{A^T P b} \tag{54.4}$$

where $\mathbf{P}$ is the weighted matrix which can be calculated from the inverse of the Locata measurements variance.

54.3 Locata/GNSS/INS Integration

Different navigation sensors or systems have their own advantages and disadvantages, and may make complementary contributions to an integrated system. INS is an autonomous navigation technology that operates independent of external signal sources. It can provide not only the complete motion information, but also does so at a high output rate. However, a good quality INS solution can only be obtained for a short period of time due to sensor error accumulation. The integration of INS with GNSS can calibrate INS sensor error and ensure acceptable navigation solution performance. However, GNSS has its own shortcomings. The signals become weak or even unavailable when the satellite signals are jammed or blocked. In addition, the quality of a GNSS solution is sensitive to satellite-receiver geometry. On the other hand, Locata is ground-based and the LLs can be installed anywhere they are needed—hence it has greater flexibility. However, Locata has the "hot spot" limitation, meaning its coverage area may be quite small. These different navigation sensor characteristics therefore motivate research into a so-called "triple integration" system, able to achieve a continuous good quality navigation solution.

The Locata/GNSS/INS sub-systems are loosely-coupled via an extended Kalman filter (EKF). The EKF first makes a prediction based on the dynamics of the platform, and later corrects this prediction using measurements [8]. The INS error mechanism is used as the system model, and the Locata position, velocity and GNSS position are used as the input measurements.

The system model describes how the true state of the system evolves over time:

$$\mathbf{x_k} = \mathbf{\Phi_{k-1}} \mathbf{x_{k-1}} + \mathbf{w_{k-1}} \tag{54.5}$$

The true state $\mathbf{x_k}$ of the system at epoch k depends on the state of the previous epoch k−1 and the system process noise. The matrix $\mathbf{\Phi}$ is the state transition matrix. The vector $\mathbf{w_{k-1}}$ models the white noise in the system. The INS mechanization errors can be modeled as:

$$\begin{bmatrix} \dot{\delta\mathbf{R}}^{\mathbf{n}} \\ \dot{\delta\mathbf{P}}^{\mathbf{n}} \\ \dot{\delta\mathbf{V}}^{\mathbf{n}} \\ \dot{\delta\mathbf{b}}_{\mathbf{g}} \\ \dot{\delta\mathbf{b}}_{\mathbf{a}} \\ \dot{\delta\mathbf{l}}_{\mathbf{L}} \\ \dot{\delta\mathbf{l}}_{\mathbf{G}} \end{bmatrix} = \begin{bmatrix} \mathbf{F_{RR}} & \mathbf{F_{RP}} & \mathbf{F_{RV}} & \mathbf{C_b^n} & \mathbf{0} & \mathbf{0} & \mathbf{0} \\ \mathbf{0} & \mathbf{F_{PP}} & \mathbf{F_{PV}} & \mathbf{0} & \mathbf{0} & \mathbf{0} & \mathbf{0} \\ \mathbf{F_{VR}} & \mathbf{F_{VP}} & \mathbf{F_{VV}} & \mathbf{0} & \mathbf{C_n^b} & \mathbf{0} & \mathbf{0} \\ \mathbf{0} & \mathbf{0} & \mathbf{0} & \mathbf{0} & \mathbf{0} & \mathbf{0} & \mathbf{0} \\ \mathbf{0} & \mathbf{0} & \mathbf{0} & \mathbf{0} & \mathbf{0} & \mathbf{0} & \mathbf{0} \\ \mathbf{0} & \mathbf{0} & \mathbf{0} & \mathbf{0} & \mathbf{0} & \mathbf{0} & \mathbf{0} \\ \mathbf{0} & \mathbf{0} & \mathbf{0} & \mathbf{0} & \mathbf{0} & \mathbf{0} & \mathbf{0} \end{bmatrix} \cdot \begin{bmatrix} \delta\mathbf{R}^{\mathbf{n}} \\ \delta\mathbf{P}^{\mathbf{n}} \\ \delta\mathbf{V}^{\mathbf{n}} \\ \delta\mathbf{b}_{\mathbf{g}} \\ \delta\mathbf{b}_{\mathbf{a}} \\ \delta\mathbf{l}_{\mathbf{L}} \\ \delta\mathbf{l}_{\mathbf{G}} \end{bmatrix} + \begin{bmatrix} \mathbf{c_b^n} & \mathbf{0} \\ \mathbf{0} & \mathbf{0} \\ \mathbf{0} & \mathbf{c_n^b} \\ \mathbf{0} & \mathbf{0} \\ \mathbf{0} & \mathbf{0} \\ \mathbf{0} & \mathbf{0} \\ \mathbf{0} & \mathbf{0} \end{bmatrix} \cdot \begin{bmatrix} \omega_{\mathbf{g}} \\ \omega_{\mathbf{a}} \end{bmatrix} \tag{54.6}$$

where $\delta\mathbf{R}^{\mathbf{n}} = [\,\delta\gamma \quad \delta\theta \quad \delta\psi\,]^T$ are the angular errors on the attitude; $\delta\mathbf{P}^{\mathbf{n}}$ and $\delta\mathbf{V}^{\mathbf{n}}$ are position and velocity errors in a local reference frame; $\delta\mathbf{b}_{\mathbf{g}}$ and $\delta\mathbf{b}_{\mathbf{a}}$ are the gyro and the accelerometer biases; $\delta\mathbf{l}_{\mathbf{L}}$ and $\delta\mathbf{l}_{\mathbf{G}}$ are level arm errors from Locata and GNSS to the INS centre respectively; $\omega_{\mathbf{g}}$ and $\omega_{\mathbf{a}}$ are the gyro and accelerometer

noises, which are assumed to be zero-mean Gaussian white noises; $\mathbf{C}_{\mathbf{b}}^{\mathbf{n}}$ is the attitude matrix, and $\mathbf{F}_*$ connects the sensor error sources and navigation solution errors. Details of the matrix components can be found in [9].

The measurement model describes how measurements are related to the states:

$$\mathbf{z_k} = \mathbf{H_k x_k} + \mathbf{v_k} \tag{54.7}$$

where $\mathbf{z_k}$ is the system input measurements, and the matrix $\mathbf{H_k}$ relates the current state $\mathbf{x_k}$ to the measurement $\mathbf{z_k}$. The vector $\mathbf{v_k}$ models the measurement noises. The Locata and GNSS estimated solutions are used as the measurements. Considering the lever arm effect, the measurements model can be written as:

$$\mathbf{z_k} = \begin{bmatrix} \mathbf{P}_{\mathbf{Locata}}^{\mathbf{n}} - \mathbf{P}_{\mathbf{INS}}^{\mathbf{n}} - \mathbf{C}_{\mathbf{b}}^{\mathbf{n}}\mathbf{L}_{\mathbf{Locata}}^{\mathbf{b}} \\ \mathbf{V}_{\mathbf{Locata}}^{\mathbf{n}} - \mathbf{V}_{\mathbf{INS}}^{\mathbf{n}} - \mathbf{A}\mathbf{C}_{\mathbf{b}}^{\mathbf{n}}(\boldsymbol{\omega}_{\mathbf{ib}}^{\mathbf{b}}\times)\mathbf{L}_{\mathbf{Locata}}^{\mathbf{b}} \\ \mathbf{P}_{\mathbf{GNSS}}^{\mathbf{n}} - \mathbf{P}_{\mathbf{INS}}^{\mathbf{n}} - \mathbf{C}_{\mathbf{b}}^{\mathbf{n}}\mathbf{L}_{\mathbf{GNSS}}^{\mathbf{b}} \end{bmatrix} = \mathbf{H_k x_k} + \mathbf{v_k} \tag{54.8}$$

where $\mathbf{A} = \begin{bmatrix} \frac{1}{R_E+h} & 0 & 0 \\ 0 & \frac{1}{(R_N+h)\cos L} & 0 \\ 0 & 0 & -1 \end{bmatrix}$

$$\mathbf{H_k} = \begin{bmatrix} -\mathbf{A}\left[\mathbf{C}_{\mathbf{b}}^{\mathbf{n}}\mathbf{L}_{\mathbf{Locata}}^{\mathbf{b}}\times\right] & \mathbf{I} & \mathbf{0} & \mathbf{0} & \mathbf{0} & \mathbf{AC}_{\mathbf{b}}^{\mathbf{n}} & \mathbf{0} \\ -\left[\left(\mathbf{C}_{\mathbf{b}}^{\mathbf{n}}(\omega_{\mathbf{ib}}^{\mathbf{b}}\times)\mathbf{L}_{\mathbf{Locata}}^{\mathbf{b}}\right)\times\right] & \mathbf{0} & \mathbf{I} & \mathbf{0} & \mathbf{0} & \mathbf{C}_{\mathbf{b}}^{\mathbf{n}}(\boldsymbol{\omega}_{\mathbf{ib}}^{\mathbf{b}}\times) & \mathbf{0} \\ -\mathbf{A}\left[\mathbf{C}_{\mathbf{b}}^{\mathbf{n}}\mathbf{L}_{\mathbf{GNSS}}^{\mathbf{b}}\times\right] & \mathbf{I} & \mathbf{0} & \mathbf{0} & \mathbf{0} & \mathbf{0} & \mathbf{AC}_{\mathbf{b}}^{\mathbf{n}} \end{bmatrix} \tag{54.9}$$

where $\mathbf{P}_*^{\mathbf{n}}$ and $\mathbf{V}_*^{\mathbf{n}}$ are the position and velocity of Locata, GNSS and INS respectively, with respect to the local reference system; $\mathbf{L}_*^{\mathbf{b}}$ represents the level arm errors from Locata and GNSS to INS centre in the body frame; $\boldsymbol{\omega}_{\mathbf{ib}}^{\mathbf{b}}$ is the body rotation angular velocity; R_E and R_N are the meridian and transverse radiuses of curvature respectively; h is the ellipsoidal height; L represent the latitude. $\mathbf{v_k}$ is characterized by measurement noises of the Locata and GNSS sub-systems.

54.4 Test and Result Analysis

The field test was conducted on October 2012 on Sydney Harbour. The LocataNet comprised 8 LLs, which were installed along the shore. They were time-synchronised in a cascaded mode with the master LL (LL3) configured for synchronisation with respect to GPS time. The trajectory and the location of the LLs are shown in Fig. 54.2.

The test vessel was provided by the Sydney Ports Authority, and was installed with two dual-frequency GPS receivers, two Locata user units and an Applanix INS system. The test vessel and installed receiver antennas are shown in Fig. 54.3. The right two antennas are the Locata and GNSS antennas used for processing in

Fig. 54.2 LocataNet configuration and rover trajectory

this paper. In this paper, Locata and GPS carrier phase measurements were post-processed. The GPS and Locata data output rates were both set to 10 Hz. The inertial measurement rate was set to 200 Hz and synchronized with GPS time. In addition, measurements from a GNSS reference station were collected during the trial. The RTK-GNSS solution, which was post-processed using Leica Geo Office (LGO) software, was used as the navigation system reference with accuracy at the few centimeter-level. No changes were made to the ground configuration during the trial.

By utilizing the algorithm introduced in Sect. 54.2, the error of the Locata standalone solutions for horizontal components (North and East in the local reference frame) are plotted in Fig. 54.4. The root mean square (RMS) of positioning solution errors are given in Table 54.1. It can be seen that the Locata stand alone

Fig. 54.3 Test vessel and installed Locata/GPS antennas

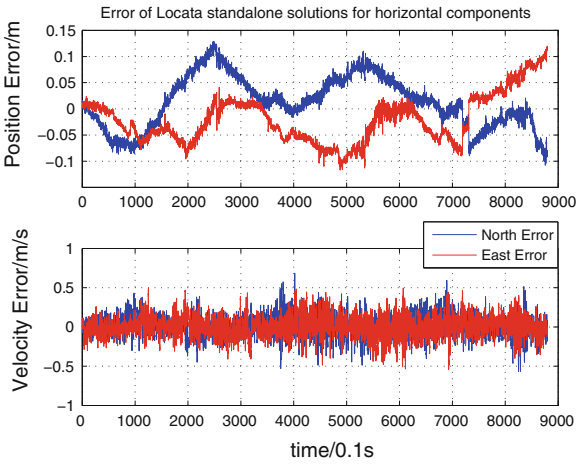

Fig. 54.4 Error of Locata standalone solutions for horizontal components

solution accuracy is better than 10 cm. Here the ambiguities were resolved by using known point initialization, however, it can also be resolved using geometry change [7]. In order to analyze the geometry and Locata signal tracking ability, the horizontal dilution of precision (HDOP) values and number of used LLs are shown in Fig. 54.5.

In order to compare the Locata standalone and GNSS system performance, a precise point positioning (PPP) GNSS solution was obtained using RTKLIB [10], using precise satellite orbit and clock data, as well as antenna corrections from the international GNSS service (IGS). The dual-frequency correction and the estimated zenith tropospheric delay correction were used to mitigate the ionosphere and troposphere delay respectively. The PPP-GNSS solutions for the horizontal direction components are compared with those obtained using Locata-only in Table 54.1.

A triple integration algorithm was then applied, combining the outputs of Locata, PPP-GNSS and INS, and compared with a conventional loosely-coupled GNSS/INS integration solution. The comparison of the two integrated systems is shown in Fig. 54.6. The RMS values of the two system solutions are compared in Table 54.2.

It can be seen that the Locata-augmented hybrid system can improve the system accuracy by almost an order of magnitude—from decimeter-level to centimeter-level. From Table 54.1 it can be seen that the improvement is mainly due to the high accuracy of the Locata standalone sub-system. Now consider a more accurate

Table 54.1 Comparison of Locata solution and PPP-GNSS solution

	RMS of solution		
	Locata position (m)	Locata velocity (m/s)	PPP-GNSS position (m)
North	0.0508	0.1407	0.4395
East	0.0497	0.1387	0.1457

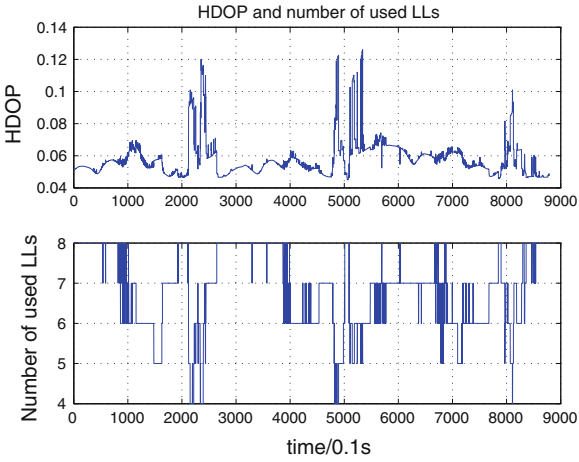

Fig. 54.5 HDOP and number of used LLs

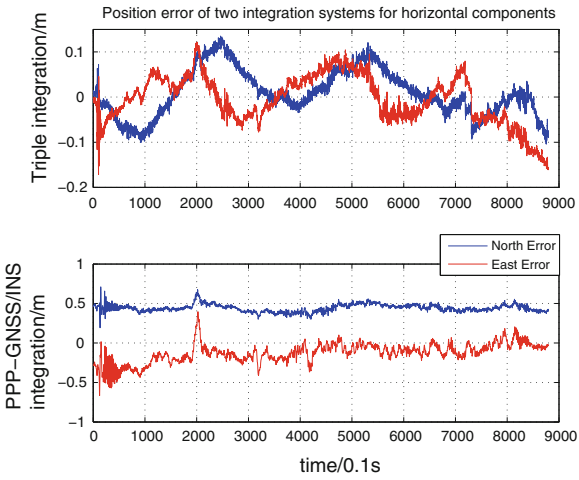

Fig. 54.6 Comparison of Locata/PPP-GNSS/INS and PPP-GNSS/INS integration systems

Table 54.2 Comparison of Locata/PPP-GNSS/INS solution and PPP-GNSS/INS solution

	RMS of position error	
	Locata/PPP GNSS/INS (m)	PPP-GNSS/INS (m)
North	0.0523	0.4448
East	0.0537	0.1776

hybrid system—the Locata/RTK-GNSS/INS triple integration system. The results are plotted in Fig. 54.7. The RMS values of horizontal components are given in Table 54.3. The results suggest that the triple integration solutions and the RTK-GNSS solutions are at a comparable level of accuracy.

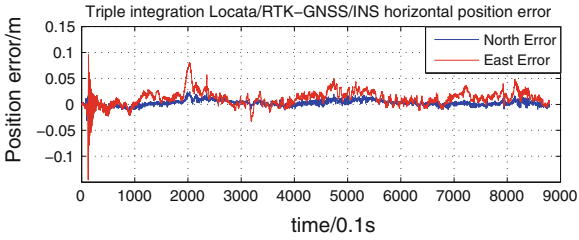

Fig. 54.7 Triple integration Locata/RTK-GNSS/INS horizontal position error

Table 54.3 Evaluation of triple integration system and system with GNSS signal obstruction

	RMS of position error	
	Precise hybrid system (m)	With GNSS obstruction (m)
North	0.0062	0.0512
East	0.0185	0.0561

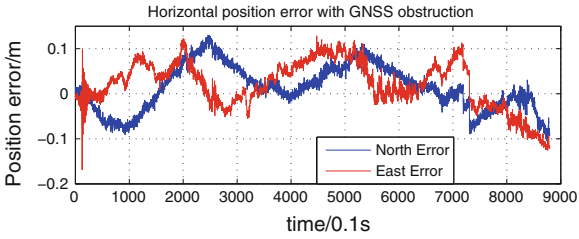

Fig. 54.8 Triple integration Locata/RTK-GNSS/INS position error with GNSS signal obstruction

The system performance assuming GNSS signal obstruction was also investigated. Figure 54.8 shows the Locata/INS integration without GNSS coverage, and the error RMS is compared with precise hybrid system in Table 54.3.

The accuracy of Locata/INS integration is better than 10 cm, and confirms that Locata is able to provide continuous and accurate navigation during GNSS outrages. Moreover the results also show that the Locata-augmented hybrid system can output an optimal navigation solution.

The Locata standalone solution is obtained from the point-based carrier phase measurements on an epoch-by-epoch basis, which is more accurate than the PPP GNSS solution. This further confirms that Locata can generate potentially better point positioning solutions than GNSS. Meanwhile, the accuracy of the Locata/INS integration system is better than a decimetre, which also confirms that Locata technology is able to provide continuous and accurate navigation during GNSS signal outages.

54.5 Concluding Remarks

A Locata-augmented hybrid multi-sensor maritime navigation system was developed and tested. The system can be configured first as carrier phase-based Locata and GNSS sub-systems to derive acceptable navigation solutions, which are then used as the pseudo-measurements in the triple integration algorithm, implemented within an extended Kalman Filter. The maritime trial was conducted on Sydney Harbour, and all data were collected and post-processed. In order to evaluate the performance of the hybrid system, Locata-only, PPP-GNSS/INS integration, triple integration and Locata/INS integration were investigated. The test results indicate that: (1) Locata standalone system is able to operate independently, and achieve better accuracy than PPP-GNSS; (2) Compared with conventional PPP-GNSS/INS integration, the hybrid Locata-augmented system can not only ensure high output rate and the provision of complete motion information, but obviously improve the solution accuracy; (3) When more precise GNSS solutions are used as measurements, solutions of triple integration become more accurate; (4) During periods of GNSS signal outage, Locata/INS integration solution is still accurate at the centimetre-level.

References

1. Barnes J, Rizos C, Kanli M (2004) Indoor industrial machine guidance using Locata: a pilot study at BlueScope steel. 60th Annual Meeting of the U.S. institute of navigation, Dayton, Ohio, 7–9 June 2004, 533–540
2. Rizos C, Roberts GW, Barnes J, Gambale N (2010) Locata: a new high accuracy indoor positioning system. 1st International Conference on indoor positioning and indoor navigation (IPIN), Mautz R, Kunz M, Ingensand H (eds) Zurich, Switzerland, 15–17 September 2010, 441–447
3. Choudhury M, Rizos C, Harvey BR (2009) A survey of techniques and algorithms in deformation monitoring applications and the use of the Locata technology for such applications. 22nd International Technology Meeting of the satellite division of the U.S. institute of navigation, Savannah, Georgia, 22–25 September 2009, 668–678
4. Li Y, Rizos C (2010) Seamless navigation through a Locata-enhanced GPS and INS integrated system. International Symposium on GPS/GNSS, Taipei, Taiwan, 26–28 October 2010, 40–45
5. Montillet J, Roberts G, Hancock C, Meng X, Ogundipe O, Barnes J (2009) Deploying a Locata network to enable precise positioning in urban canyons. J Geodesy 83(2):91–103
6. Barnes J, Rizos C, Wang J, Small D, Voight G, Gambale N (2003) Locatanet: the positioning technology of the future? 6th Int Symp on satellite navigation technology including mobile positioning and location services, Melbourne, Australia, 22–25 July 2003, CD-ROM proceedings paper 49
7. Jiang W, Li Y, Rizos C, Barnes J (2012) Using Locata and INS for indoor positioning. 3rd Int Conf on indoor positioning and indoor navigation (IPIN), Sydney, Australia, 13–15 Nov 2012
8. Hide C, Moore T, Smith M (2003) Adaptive Kalman filtering for low cost GPS/INS. J Navig 56(1):143–152
9. Angrisano A (2010) GNSS/INS integration method. Ph.D. thesis, Universita' Degli Studi Di Napoli "Parthenope"
10. RTKLIB: An open source program package for RTK-GPS, http://gpspp.sakura.ne.jp/rtklib/rtklib.htm

Chapter 55
Sub-Pixel Water-Sky-Line Detection Based on a Curve Fitting Method

Linyang Li, Chonghui Li, Yong Zheng and Chao Zhang

Abstract Celestial navigation is one essential means of the marine autonomous navigation, through taking photos of the Water-Sky-Line, natural horizontal plane can be provided for celestial navigation system, and the precision of Water-Sky-Line detection influences the precision of positioning. Traditional edge detection algorithms can only achieve pixel precision, as for more precise position of the Water-Sky-Line, those algorithms can't achieve. In order to achieve sub-pixel detection, first two processes on the original image are needed, including median filtering and resample, then the pixel sketch coordinates are detected by Kirsch operator, finally an algorithm based on a curve fitting method is introduced, and sub-pixel coordinates are detected. According to experimental analyses, it is effective to half of the pixels; after eliminating outliers, the precision is about 0.5 pixels.

Keywords Water-sky-line · Sub-pixel · Resample · Median filtering · The least square adjustment · Curve fitting

55.1 Introduction

Celestial navigation is a day and night navigation in the world, it only receives radiation of visible light or radio waves from sun, moon, stars and other natural objects. With simple equipments and a characteristic of disguise, it isn't easily detected and disturbed, and its positioning errors don't accumulate over time, these are its advantages [1, 2]. Although the development of the satellite navigation system is quicker and the positioning precision is better than celestial navigation,

L. Li (✉) · C. Li · Y. Zheng · C. Zhang
Zhengzhou Institute of Surveying and Mapping, Henan 450052, China
e-mail: Lilinyang810810@163.com

J. Sun et al. (eds.), *China Satellite Navigation Conference (CSNC) 2013 Proceedings*, Lecture Notes in Electrical Engineering 245,
DOI: 10.1007/978-3-642-37407-4_55,

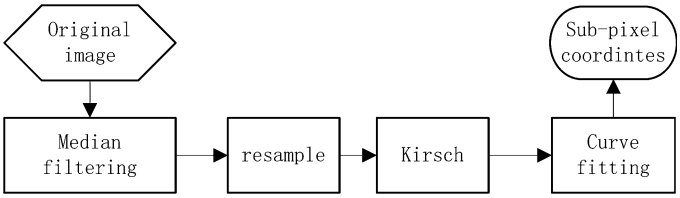

Fig. 55.1 The flow of detecting sub-pixel water-sky-line

celestial navigation is still one of the indispensable means of navigation technology, especially in the outbreak of war, the satellite signal is vulnerable to enemy's interferences, and celestial navigation doesn't exist such drawbacks. Furthermore, the International Maritime Organization (IMO) in "STCW78/95" Convention also explicitly provides that mariners must have the ability to use celestial bodies to determine the ship's position [3].

Water-Sky-Line is the dividing line to distinguish between the sea and sky, and it determines the natural horizontal plane perpendicular to each other with a plumb line. Based on this characteristic, even at sea, although the instruments swing with the ship and can't be leveled, the Water-Sky-Line can also determine the water level of ship navigation benchmark [4]. With the rapid development of digital image processing technology and the use of special camera, it allows simultaneous imaging of Water-Sky-Line with stars [5]; image processing to extract the edge of the Water-Sky-Line is a key technology of ship navigation. Traditional pixel-level edge extraction algorithms such as Sobel operator, Kirsch operator, which can only detect the pixel edge of the Water-Sky-Line. In order to achieve more precise celestial navigation at sea, a more precise edge extraction algorithm is needed, which is the sub-pixel Water-Sky-Line detection algorithm. In this paper, a sub-pixel algorithm based on a curve fitting method is introduced [6]; concrete steps are shown in Fig. 55.1.

55.2 Image Preprocessing

When we capture the image, due to optical system distortion, relative motion or other interferences of the weather conditions, besides the image of the original Water-Sky-Line inevitably contains the influence of noise of the waves, reefs, so the image will present low quality and it is low clear. In order to weaken the influence of the noise and improve the contrast of the sea and sky background, so the image should be preprocessed first, including median filtering and resample (Fig. 55.2).

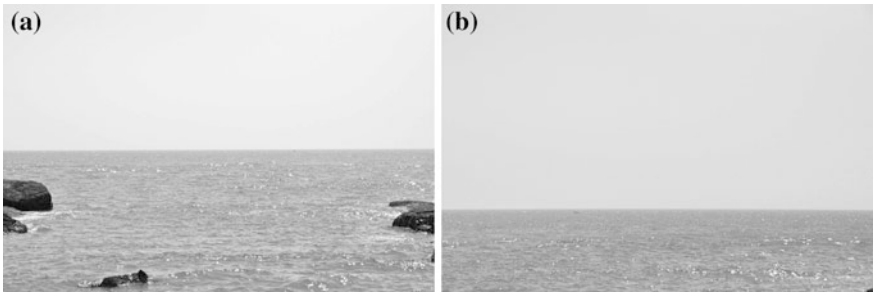

Fig. 55.2 The original water-sky-line image (**a**) and (**b**)

55.2.1 Median Filtering

The median filter is a signal processing method based on a kind of statistical theory which can effectively suppress noise nonlinear smoother; the basic principle is replacing one point's gray value with the point's surrounding gray values in the digital image, which is $med(a_1, a_2 \ldots a_n)$. Take into account the Water-Sky-Line's salt and pepper noise, 3×3 templates can eliminate noise and remain the edge information to some extent [7], so we use 3×3 templates.

The result of median filtering is shown in Fig. 55.3; the histogram is shown in Fig. 55.4.

55.2.2 Resample

According to the Fig. 55.4, the background gray value of the water and sky difference is obvious and concentrates in the two different gray zones. In order to enlarge the gradation differences of the sea and sky background and highlight the degree of gray-scale variation, we use the following methods: according to the gray histogram to set the minimum gradation value G_{Min} and the maximum

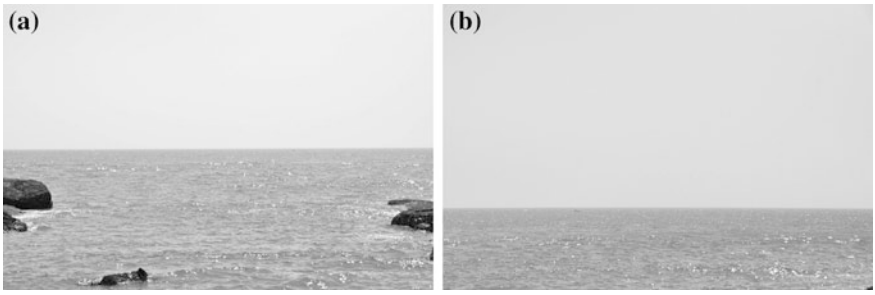

Fig. 55.3 The result of median filtering (**a**) and (**b**)

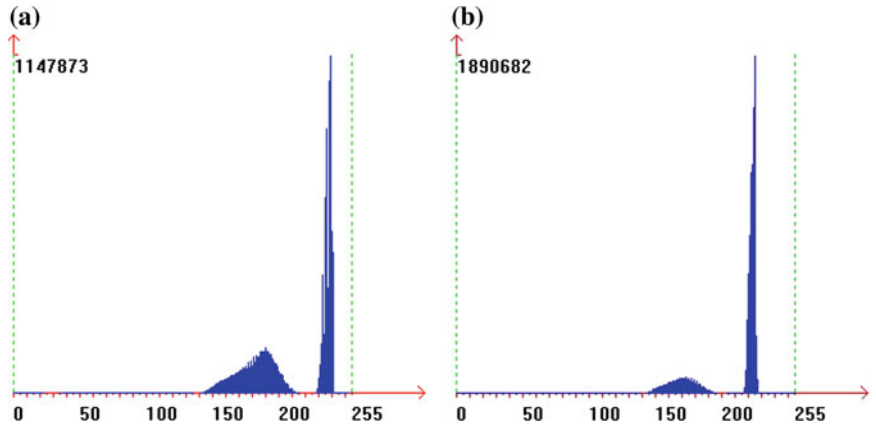

Fig. 55.4 The water-sky-line's gray histogram (**a**) and (**b**)

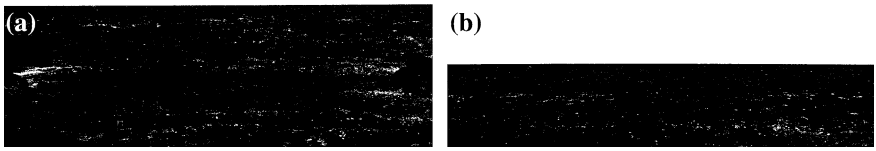

Fig. 55.5 The result of resample (**a**) and (**b**)

gradation value G_{Max} for re-sampling, then extract the gray value G of every point, reassignment in accordance with the formula (55.1), the result is shown in Fig. 55.5.

$$G = \begin{cases} 0 & G < G_{Min} \\ 256 \times \frac{G - G_{Min}}{G_{Max} - G_{Min}} & G_{Min} \leq G \leq G_{Max} \\ 255 & G > G_{Max} \end{cases} \tag{55.1}$$

55.3 Use Kirsch Operator to Detect Pixel Coordinates

Kirsch algorithm use eight templates to operate on every pixel, those eight templates stand for eight different detection directions [8–10], as is shown below.

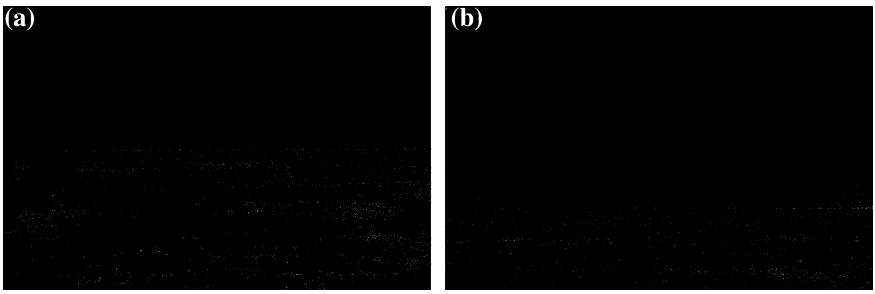

Fig. 55.6 The result of Kirsch operator (**a**) and (**b**)

$$\begin{bmatrix} -5 & 3 & 3 \\ -5 & 0 & 3 \\ -5 & 3 & 3 \end{bmatrix} \begin{bmatrix} 3 & 3 & 3 \\ -5 & 0 & 3 \\ -5 & -5 & 3 \end{bmatrix} \begin{bmatrix} 3 & 3 & 3 \\ 3 & 0 & 3 \\ -5 & -5 & -5 \end{bmatrix} \begin{bmatrix} 3 & 3 & 3 \\ 3 & 0 & -5 \\ 3 & -5 & -5 \end{bmatrix}$$
$$\begin{bmatrix} 3 & 3 & -5 \\ 3 & 0 & -5 \\ 3 & 3 & -5 \end{bmatrix} \begin{bmatrix} 3 & -5 & -5 \\ 3 & 0 & -5 \\ 3 & 3 & 3 \end{bmatrix} \begin{bmatrix} -5 & -5 & -5 \\ 3 & 0 & 3 \\ 3 & 3 & 3 \end{bmatrix} \begin{bmatrix} -5 & -5 & 3 \\ -5 & 0 & 3 \\ 3 & 3 & 3 \end{bmatrix}$$

Suppose the image as f, template as W_k, and then the gray value at point (x, y) is

$$E_{(x,y)} = \max_k \{W_k \cdot f\} \tag{55.2}$$

The result of Kirsch operator is shown in Fig. 55.6.

55.4 Sub-Pixel Algorithm Based on Curve Fitting

55.4.1 The Gray Value of the Edge

The edge of Water-Sky-Line is step edge, gray value of the step edge is shown in Fig. 55.7a, the equal gray value on both sides respectively symbolize the background and the object, of the gradient portion of the intermediate gray value of the edge is required to detect. Due to the convolution role of optical components and optical diffraction effects, object space's drastic changes in gray value are gradient changes in the form of optical imaging. The edge difference is shown in Fig. 55.7b, the edge's differential value is maximum, which is the principle of classical edge extraction. According to the central limit theorem, the edge of the gray value change should be exact position of the Gaussian distribution; the curve in Fig. 55.7b is the sampled value of the Gaussian curve, corresponding to the apex of the curve is the edge's precise point.

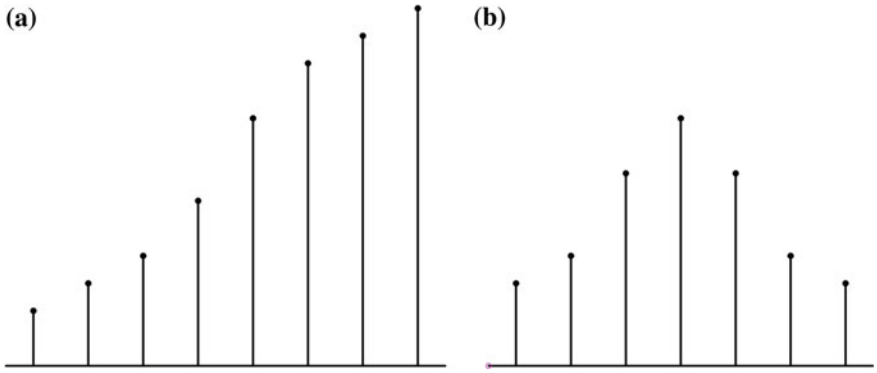

Fig. 55.7 **a** The gray value of the edge. **b** Its difference

55.4.2 The Deductive Process

The gray value should obey Gaussian distribution

$$y = \frac{1}{\sqrt{2\pi}\sigma} e^{-\frac{(x-\mu)^2}{2\sigma^2}} \tag{55.3}$$

The difference of the gray value takes logarithm for quadratic curve

$$y^* = \ln y = -\frac{(x-\mu)^2}{2\sigma^2} + \ln\frac{1}{\sqrt{2\pi}\sigma} \tag{55.4}$$

So according to the difference of the gray value to fit parabola coefficient

$$\ln y = ax^2 + bx + c \tag{55.5}$$

Just taking three pixels' gray values is enough to solve parabolic coefficient. This can directly acquire vertex position, and has a small amount of calculation, but it doesn't take advantage of the edge's information. As for Water-Sky-Line edge, the edge of the gray values' change may be slow, therefore we can extend to the edge more pixels on both sides, acquire more accurate parabolic coefficient and vertex position by the least square adjustment, five pixels (for example, on both sides and then upward selection is positive, the other side is negative) is suggested in this article, the output gradation value of each pixel can be obtained as follows:

$$\ln f = x^2 a + xb + c \tag{55.6}$$

Substitute the gray values of 11 pixels

$$\begin{aligned}
&\ln f_5 = 25\hat{a} + 5\hat{b} + \hat{c} \\
&\cdots \\
&\ln f_1 = \hat{a} + \hat{b} + \hat{c} \\
&\ln f_0 = \hat{c} \\
&\ln f_{-1} = \hat{a} - \hat{b} + \hat{c} \\
&\cdots \\
&\ln f_{-5} = 25\hat{a} - 5\hat{b} + \hat{c}
\end{aligned} \tag{55.7}$$

Use parameter adjustment, error equation is

$$v = A\hat{x} + l \tag{55.8}$$

$$A = \begin{bmatrix} 25 & 5 & 1 \\ 16 & 4 & 1 \\ \cdots & & \\ 16 & -4 & 1 \\ 25 & -5 & 1 \end{bmatrix} \hat{X} = \begin{bmatrix} \hat{a} \\ \hat{b} \\ \hat{c} \end{bmatrix} l = \begin{bmatrix} \ln f_5 \\ \ln f_4 \\ \cdots \\ \ln f_{-4} \\ \ln f_{-5} \end{bmatrix} \tag{55.9}$$

Solution

$$\hat{X} = -(A^T A)^{-1}(A^T l) \tag{55.10}$$

Sub-pixel position of the edge is the vertex position

$$x = -\frac{\hat{b}}{2\hat{a}} \tag{55.11}$$

Because the image inevitably contains noise, so that changes in the grayscale value don't meet the above rules, therefore, there should be two judgments to make.

First, if the difference value is less than or equal to zero, then the difference value's logarithm of this point is given as 0.

Second, if the absolute value of the sub-pixel correction value is bigger than 5, then the corrected value is not credible, compulsory to be assigned 0.

The result of curve fitting is shown in Fig. 55.8.

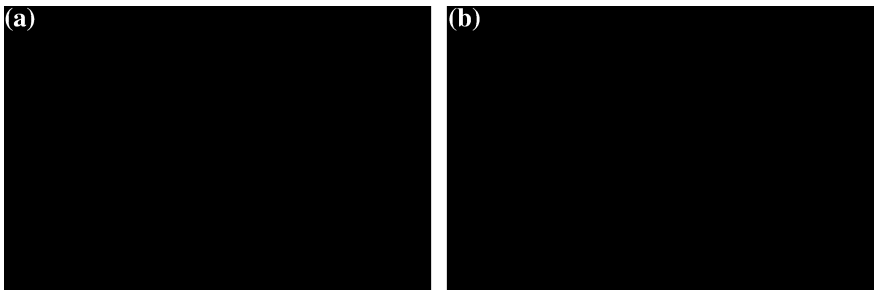

Fig. 55.8 The result of sub-pixel detection (**a**) and (**b**)

Table 55.1 The precision of the sub-pixel detection algorithm

	The number of Sub-pixel coordinates	The number of outliers	Standard deviation
a	2,142	102	0.5140
b	2,156	109	0.5020

According to the result of Fig. 55.8 and Table 55.1, we can conclude that in the original image of 4,288 pixels, as for the Fig. 55.8a, 2,142 pixels succeed in detecting sub-pixel coordinates; then filter 102 outliers and use the quadratic polynomial to fit the sub-pixel edge, and calculate the standard deviation. Analyze the edge without outliers, the precision is 0.5140 pixels. Then about the Fig. 55.8b, 2,156 pixels succeed in detecting sub-pixel coordinates, and the precision is 0.5020 pixels.

55.5 Conclusion

With the continuous improvement of the accuracy required by maritime celestial navigation, the original pixel-level Water-Sky-line extraction technologies can't meet the requirements of high-precision positioning and therefore more precise Water-Sky-line edge detection algorithm is needed, which is sub-pixel detection. First this paper describes two steps to extract the pixel-level Water-Sky-line edge from original image, including median filtering, image resample; and then use Kirsch operator to extract coordinates of the pixel level. Finally a curve fitting method is derived, least squares adjustment to solve unknown parameters is used, choose five pixel points near the former pixel coordinates, calculate the sub-pixel coordinates, and realize correction about half of the edge pixels, according to experimental analyses, the precision is about 0.5 pixels, it's meaningful to realize more precise marine celestial navigation.

Acknowledgments This study is funded by the National Natural Science Fund (41174025, 41174026), Space Navigation and Timing Technology Key Laboratory Open Fund in Shanghai (0901) and Chinese Academy of Sciences Precise Navigation Position and Timing Technology Key Laboratory Open Fund (2012PNTT07).

References

1. Bida J, Huilan F (1998) How to develop of astronomical navigation across to the 21st century. Navigation Technology Analecta of the Turn of Century. Chinese Institute of Electronics Navigation Branch, Xi'an, pp 30–38
2. Anguo W (2007) Modern celestial navigation and its key technologies. J Electron 12:2347–2348
3. Wencai H, Guanghua Huang L (2002) Research on marine electronics sextant angle sensor system. J Shanghai Maritime Univ 23(3):17–20

4. Zhao N, Weiting L, Zhiyu Z (2005) Research on digital image processing based on water-sky-line detection. J East China Shipbuilding Inst (Nat Sci) 19(1):54–58
5. Yulei Y (2012) Research on fish-eye camera stellar calibration technology. Zhengzhou Institute of Surveying and Mapping, p 6
6. Zhonghai H, Wang B, Yibai L, Lincai C (2004) Subpixel algorithm using a cueve fitting method. Chin J Sci Instrum 24(2):195–197
7. Kirsch RA (1974) Computer determination of the constituent structure of biological images. Computer boned Res 4:315–318
8. He B, Ma T, Wang YJ, Honglian Z (2001) VC++ digital image processing. People's Post and Telecommunication Publishing House, Beijing, pp 459–466
9. Duan R, Li Q, Li Y (2005) Studies review on edge detecting algorithm of image. J Opt Technol 31(3):415–419
10. Li J, Tang X, Jiang Y (2007) Research on the comparison of several edge detecting algorithm. J Inf Technol 9:106–108

Chapter 56
The Precision Assessment System of TT&C Equipment Based on Unmanned Aerial Vehicle

Wei Zhou and Jinming Hao

Abstract The precision assessment of the telemetry, track and command (TT&C) equipment are important to ensure they can work normally. A new method is proposed for precision assessment of the space TT&C equipment in this paper. In this method, an Unmanned Aerial Vehicle (UAV) equiped with global positioning system (GPS) receiver acts as the target, well the positioning information of target is obtained by DGPS technology and the Kalman Filtering is used to reduce the effects of disturbance to enhance the positioning accuracy. The precision of the space TT&C equipment is obtained through the comparison of the positioning data by DGPS and the observation by the space TT&Col equipment. The UAV flight adjusting system is built based on this method in this paper, and the result of flying experiment shows that this system can provide the high-precision standard data, which have many advantages such as strong mobility and wide application scope. This system provides a new efficient solution for precision assessment of space TT&C equipment, which lays the foundation for the application of BeiDou in the precision assessment field.The precision assessment of the telemetry, track and command (TT&C) equipment is important to make sure that the equipment can work normally. In this paper, a new method is proposed to assess the precision of the space TT&C equipment. In this method, an Unmanned Aerial Vehicle (UAV) equipped with a global positioning system (GPS) receiver acts as the target, the positioning information of target is obtained by DGPS technology and the Kalman Filtering is used to reduce the effects of disturbance to enhance the positioning accuracy. The precision of the space TT&Col equipment is obtained through comparing the positioning data of DGPS and the observation of the space TT&C equipment. An UAV flight adjusting system is built based on this method in this paper, and the result of flying experiment shows that this system gives high-precision standard data, which have many advantages such as strong mobility and wide application scope. This system provides a new efficient solution for the

W. Zhou (✉) · J. Hao
Information Engineering University, Zhengzhou, China
e-mail: zhouwei_0611@163.com

J. Sun et al. (eds.), *China Satellite Navigation Conference (CSNC) 2013 Proceedings*, Lecture Notes in Electrical Engineering 245,
DOI: 10.1007/978-3-642-37407-4_56,

precision assessment of space TT&C equipment, and lays the foundation for the application of BeiDou in the precision assessment field.

Keywords Unmanned aerial vehicle · Precision assessment · Space TT&C · GPS · Kinematic positioning · Flight adjusting

56.1 Introduction

The space tracking and control (TT&Col) system is an important information source of flight safety control and command display, therefore, it must maintain excellent performance and precision [1]. However, measurement error may be introduced into the space TT&C equipment due to manufacturing techniques, installation errors and aging of parts, which will affect the precision and reliability of equipments [2]. Therefore, it is required to verify precision of newly developed or reconstructed space TT&C equipment before usage, so as to evaluate whether it meets the technical index.

In early stage, trajectory camera and photoelectricity theodolite, which have disadvantages such as high requirement on meteorological condition, long data processing cycle and limited tracing capability, are adopt for the precision assessment of space TT&Col equipment. With the wide application of satellite navigation technology in economy, military, science research and social life, the flight adjusting method based on GPS positioning technology has provided a new solution for acquirement of space position standard data. But, there are also deficiencies such as complicated installation process and low performance/cost ratio in traditional flight adjusting method. The booming development of UAV(unmanned aerial vehicle) technology has provided strong technical support for the establishment of more efficient precision assessment method [3].

"UAV flight adjusting" uses UAV platform to carry target (responder and beacon) and small size GPS receiver, performing precision assessment through joint processing and analysing of tracing data of space TT&C equipment and measurement data of precision assessment system. This article discussed the construction, work mode and precision assessment method of UAV flight adjusting precision assessment system, realized the complete flow of precision assessment and analyzed the feasibility and effects of this program.

56.2 System Construction and Work Theory

56.2.1 System Construction

UAV flight adjusting precision assessment system consists of aerial subsystem and ground subsystem, as shown in Fig. 56.1.

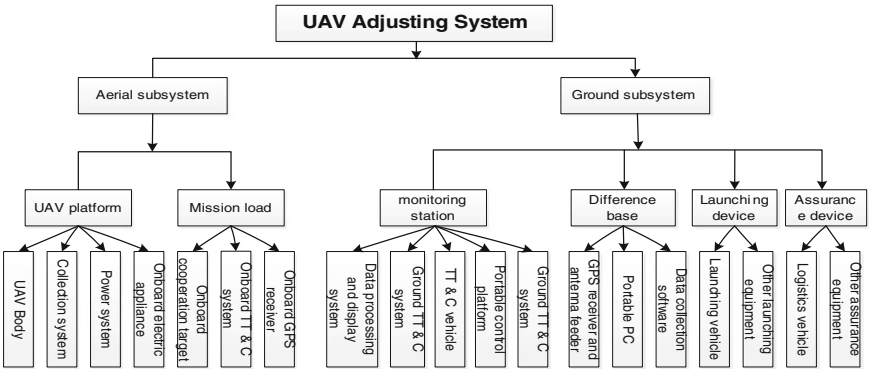

Fig. 56.1 System construction

56.2.1.1 Aerial Subsystem

Aerial subsystem is the aerial flight section of the entire system, mainly consisting of two sections: UAV platform and testing load. UAV platform is the aerial loading platform, which is responsible for carrying testing load to cruise along the preset route, and providing power supply to the testing load. Testing load consists of TT&C target, GPS receiver and communication system, of which the main function is to provide target which is in compliance with characteristics to on-ground TT&C equipment, so as to complete precise measurement of flight trace of UAV, and to complete collection, storage and transmission of TT&C target work condition parameter and onboard GPS measurement data.

Due to restriction of loading capacity and space availability of UAV, it is necessary to select small size GPS receiver, missile-borne or satellite-borne TT&C target and reasonable layout. The schematic diagram of onboard equipment installation is shown in Fig. 56.2.

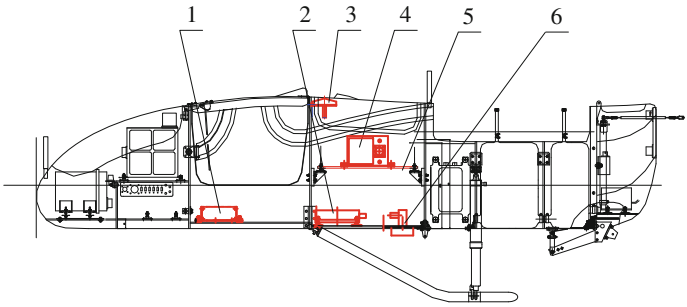

Fig. 56.2 Installation diagram of onboard equipment. *1* AC-DC power supply *2* GPS *3* GPS antenna *4* TT&C target *5* Equipment installation coupling board *6* TT&C target antenna

56.2.1.2 Ground Subsystem

Ground subsystem consists of four parts: UAV monitoring station, difference base, launching device and assurance device. UAV monitoring station is the control center of the entire system, which completes the control of UAV, meanwhile, completes receiving, demodulation and displaying testing load telemetering signal, and realizes post-processing and analysis of GPS measurement data after flight adjusting [3]. Difference base consists of GPS receiver, whose main function is to observe simultaneously with onboard GPS receiver, collects GPS original measurement data, and provides data element for post-processing. The main function of launching device is to complete the ground launching work of UAV [4]. Assurance device is responsible for completing storage, rotation and debugging of the aerial subsystem equipment, and providing relevant installation tools, instruments and meters and daily assurance appliance [5].

56.2.2 Working Theory of the System

Before flight, it is necessary to install space TT&C target and GPS measurement equipment on the UAV platform, and plan route according to the assessment demand.

After the UAV takes off, the operator uploads command to control the flight of UAV through monitoring station.UAV downloads status information in real time for decision made by the ground commander. Onboard GPS measurement equipment receives satellite signal, and performs positioning resolution in real time and stores original measurement data, meanwhile, downloads GPS resolution results and original measurement data to the UAV monitoring station for on-ground navigation display and GPS data processing. TT&C target transmits measurement signal and downloads work status parameter to the UAV monitoring station. Commanding/controlling center transmits digital guidance information to space TT&C equipment, which traces TT&C target, acquires and stores measurement data, meanwhile, transmits the work status parameter and measurement data in real time to commanding/controlling center for post-processing. Difference base receives pseudorange, L1/L2 carrier phase and Doppler of all visible GPS satellites, and makes records in real time. Provided that the network communication with the UAV monitoring station is available in difference base, GPS observation will be transmitted to the UAV monitoring station for GPS data post-processing.

Upon completion of flight, the UAV monitoring station transmits parachute-opening commands to the UAV, UAV is collected after response of UAV to the command.

After completion of flight, original measurement data of onboard GPS and ground difference base are collected, through post-resolution of carrier phase difference of GPS, precision assessment comparison standard data is provided, so

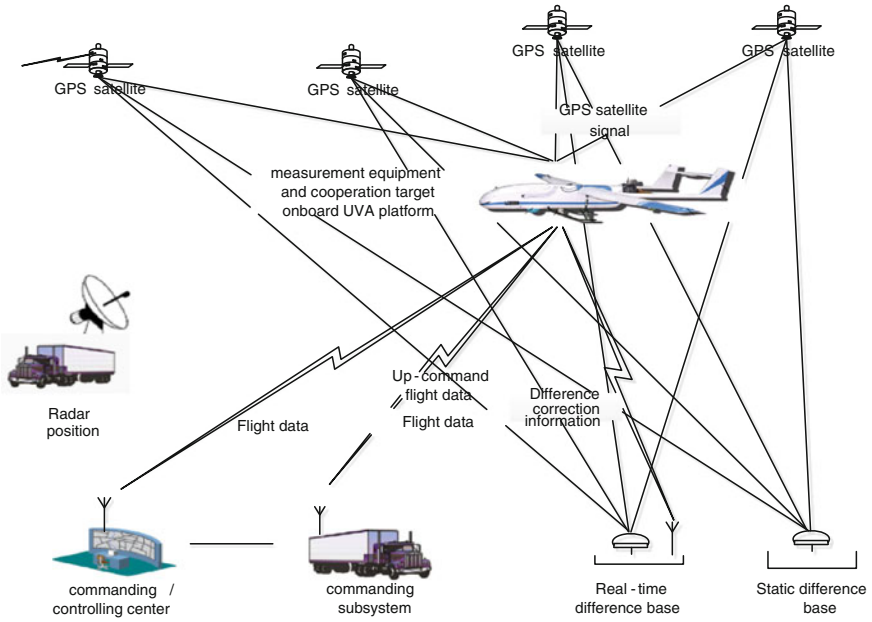

Fig. 56.3 System application mode

as to realize precision analysis and evaluation of space TT&C equipment, the typical system application mode is shown in Fig. 56.3.

56.3 Research of Precision Assessment Method

56.3.1 Theory of GPS Carrier Phase Kinematic Relative Positioning

High precision standard data is acquired through carrier phase relative positioning resolution of onboard GPS and ground base. Concurrent observation of GPS satellite j and n is performed by base i and onboard station k, so as to constitutes observables of double-difference carrier phase and linearization, as shown in formula (56.1) [6].

$$\nabla\Delta\varphi_{ik}^{jn} - \nabla\Delta N_{ik}^{jn} = \left(\frac{\partial\rho_{ik}^{jn}}{\partial X_k}\right)_0 \delta X_k + \left(\frac{\partial\rho_{ik}^{jn}}{\partial Y_k}\right)_0 \delta Y_k + \left(\frac{\partial\rho_{ik}^{jn}}{\partial Z_k}\right)_0 \delta Z_k + V_{ik}^{jn} \quad (56.1)$$

Expressed as matrix:

$$L_k = H_k \delta R_k + V_k \quad (56.2)$$

Kalman filtering data processing model is adopted, of which the status equation is:

$$X_k = \Phi_{k,k-1} X_{k-1} + \Gamma_{k-1} W_{k-1} \tag{56.3}$$

The corresponding equation is:

$$L_k = H_k X_k + V_k \tag{56.4}$$

In which, in formula (56.3) and (56.4):

$$X_k = \delta R_k \tag{56.5}$$

Recursion equation of Kalman filtering is:

$$\hat{X}_{k,k-1} = \Phi_{k,k-1} \hat{X}_{k-1,k-1} \tag{56.6}$$

$$P_{k,k-1} = \Phi_{k,k-1} P_{k-1,k-1} \Phi_{k,k-1}^T + \Gamma_{k-1} Q_{k-1} \Gamma_{k-1}^T \tag{56.7}$$

$$K_k = P_{k,k-1} H_k^T \left(H_k P_{k,k-1} H_k^T + R_k \right)^{-1} \tag{56.8}$$

$$P_{k,k} = (I - K_k H_k) P_{k,k-1} \tag{56.9}$$

56.3.2 Error Statistics Method

After GPS difference resolution, the target position information is expressed in launching coordinate system as follows: t_j, x_{gj}, y_{gj}, and z_{gj}; observation station site is expressed in launching coordinate system as follows: x_{0k}, y_{0k}, z_{0k} and $k = 1, 2, \ldots, m$; observation of space TT&C equipment is expressed as: t_j, R_j, E_j, A_j. Transformation between x_{gj}, y_{gj}, z_{gj} and R_j, E_j, A_j is as shown in formula (56.10–56.14) [7]:

$$\begin{bmatrix} \bar{x}_j \\ \bar{y}_j \\ \bar{z}_j \end{bmatrix} = \begin{bmatrix} x_{gj} - x_{0k} \\ y_{gj} - y_{0k} \\ z_{gj} - z_{0k} \end{bmatrix} \tag{56.10}$$

$$\bar{R}_j = \sqrt{\bar{x}_j^2 + \bar{y}_j^2 + \bar{z}_j^2} \tag{56.11}$$

$$\bar{E}_j = \sin^{-1}\left(\bar{y}_j / \bar{R}_j \right) \tag{56.12}$$

$$\bar{A}_j = tg^{-1}\left(\bar{z}_j / \bar{x}_j \right) + \begin{cases} 0 & \bar{x}_j > 0,\ \bar{z}_j \geq 0 \\ \pi & \bar{x}_j < 0 \\ 2\pi & \bar{x}_j > 0,\ \bar{z}_j < 0 \end{cases} \tag{56.13}$$

$$\bar{A}_j = \begin{cases} 0 & \bar{x}_j = 0,\ \bar{z}_j = 0 \\ \pi/2 & \bar{x}_j = 0,\ \bar{z}_j > 0 \\ 3\pi/2 & \bar{x}_j = 0,\ \bar{z}_j < 0 \end{cases} \tag{56.14}$$

The difference between observation data of space TT&C equipment and standard data, is shown in formula (56.15–56.17):

Range difference:

$$\Delta R_j = R_j - \bar{R}_j \tag{56.15}$$

Azimuth difference:

$$\Delta A_j = A_j - \bar{A}_j \tag{56.16}$$

Elevation angle difference:

$$\Delta E_j = E_j - \bar{E}_j \tag{56.17}$$

Error statistics formula is shown in (56.18–56.21):

Mean error:

$$\bar{X} = \frac{\sum_{j=1}^{N} X_j}{N+1} \tag{56.18}$$

In which, X_j is ΔR_j, ΔE_j and ΔA_j.

Total error:

$$\sigma = \sqrt{\frac{1}{N-1}\sum_{j=1}^{N} X_j^2} \tag{56.19}$$

Random error:

$$\sigma_R = \sqrt{\frac{1}{N-1}\sum_{j=1}^{N} (X_j - \bar{X}_j)^2} \tag{56.20}$$

System error:

$$\sigma_S = \sqrt{\sigma^2 - \sigma_R^2} \tag{56.21}$$

56.3.3 Evaluation Steps

The method of space TT&C equipment precision assessment can be summarized as following: firstly, take the positioning of UAV obtained by GPS as standard reference coordinate, then get performance and precision of space TT&C equipment through comparison, finally research the rule of error change. The evaluation method is divided into several steps as follows:

1. Acquire the positioning data through onboard and ground GPS receiver, and get the best assumption of UAV trace by data processing of carrier phase relative positioning;
2. Perform time calibration of space TT&C equipment and GPS equipment, so as to unify them under the same time system;
3. Transform target reference coordinate to azimuth α, elevation angle β and slant range R;
4. Compare space TT&C equipment data with reference data, so as to get error ΔR, ΔA and ΔE of all instances;
5. Analyze system error and random error, and research the error change rule of space TT&C equipment, so as to get precision assessment results.

56.4 Adjusting Analysis

56.4.1 Feasibility Analysis of UAV Platform Application

With the adoption of actual flight data of space TT&C equipment precision assessment system based on UAV platform, and the performance of UAV platform is analyzed regarding aviation direction stability, yaw stability and pitch stability, as shown in Figs. 56.4, 56.5 and 56.6, the mean value and mean square root error statistics are shown in Table 56.1, all indexes show that the UAV platform is capable to provide flight condition to testing load, and complete the acquirement of standard data in precision assessment of space TT&C equipment.

56.4.2 Analysis of Comparison Standard Data Precision

It is found out in actual flight data that work of GPS receiver is stable and is free from losing phenomena of satellite interlock, completed UAV flight trace has been acquired, as shown in Fig. 56.7, after resolution of carrier phase kinematic relative

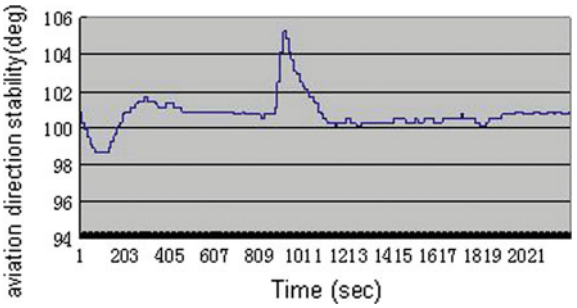

Fig. 56.4 Aviation direction stability curve

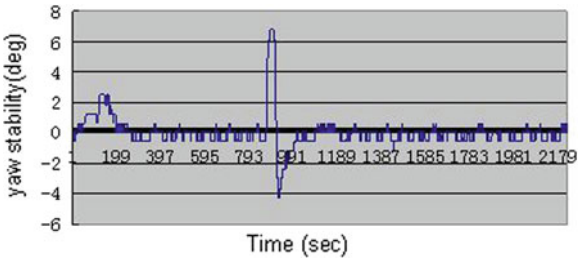

Fig. 56.5 Yaw stability curve

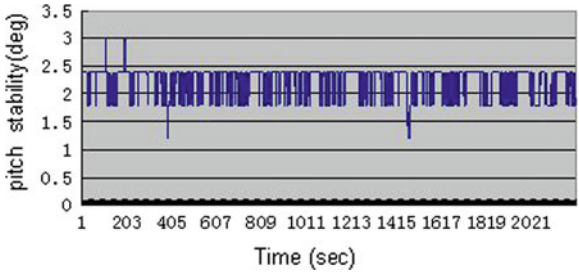

Fig. 56.6 Pitch stability curve

Table 56.1 Stability statistics

Stability	Mean (°)	RMS (°)
Aviation direction stability	100.752	0.905
Yaw stability	0.052	1.0567
Pitch stability	2.266	0.262

positioning, standard difference statistics of positioning results of all epochs are shown in Fig. 56.8 and Table 56.2, the results show that the system based on GPS carrier phase kinematic relative positioning technology can acquire kinematic positioning precision of centimeter level, which is higher than the positioning precision of space TT&C equipment by several times, it is completely feasible to use it as the standard reference value for evaluating whether space TT&C equipment is eligible.

56.4.3 Statistics and Analysis of Space TT&C Equipment Error

Precision assessment is performed for a radar, the resolution results in Sect. 56.4.2 are used as comparison standard, statistics of radar range error, elevation angle error and azimuth error are shown in Table 56.3 and Figs. 56.9, 56.10 and 56.11.

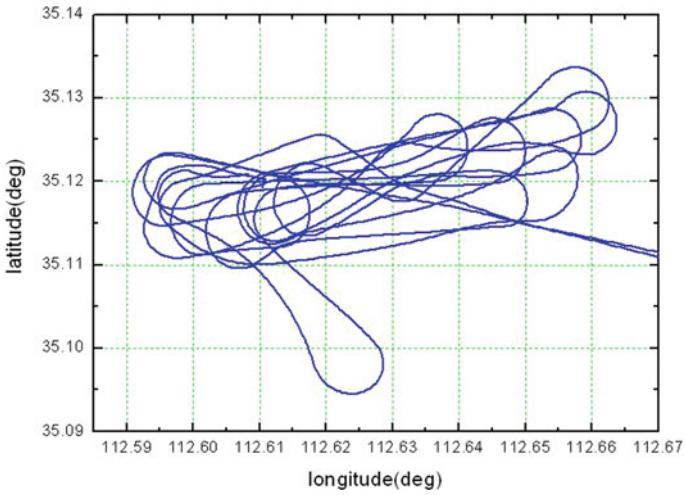

Fig. 56.7 Flight trace

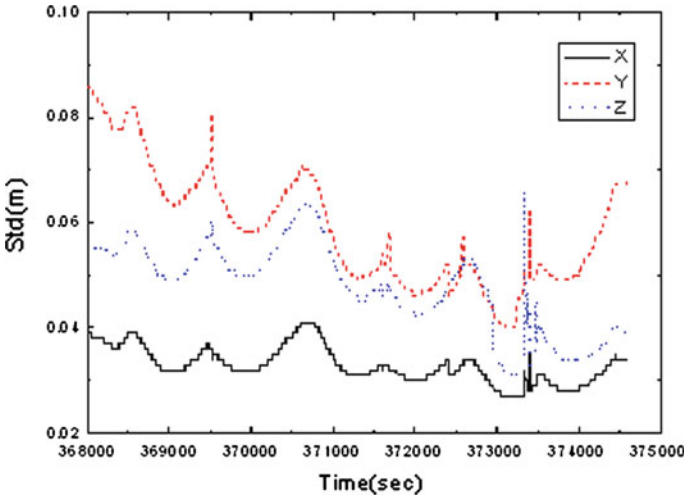

Fig. 56.8 Standard difference of positioning results

Table 56.2 Statics of positioning results standard deviation

Std	Mean (m)	Max (m)	Min (m)
X	0.033	0.041	0.027
Y	0.059	0.086	0.040
Z	0.048	0.066	0.031

Table 56.3 Results of precision assessment

	System error	Radom error
Range	45.32 m	2.60 m
Elevation angle	−2.00 s	1.69 s
Azimuth	17.58 s	12.46 s

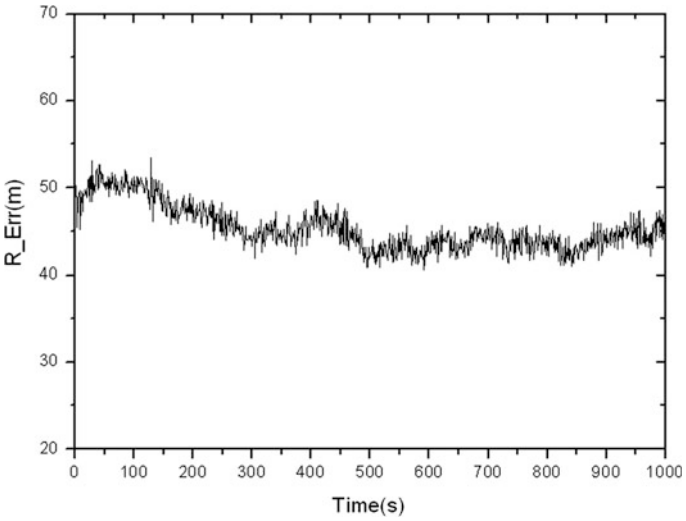

Fig. 56.9 Range error

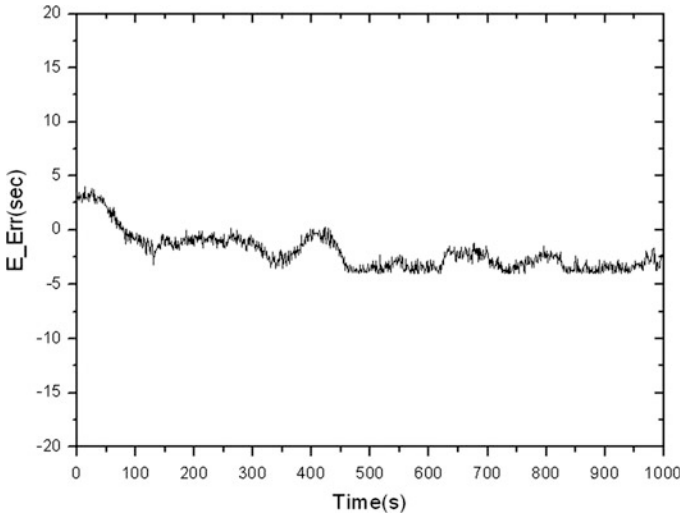

Fig. 56.10 Elevation angle error

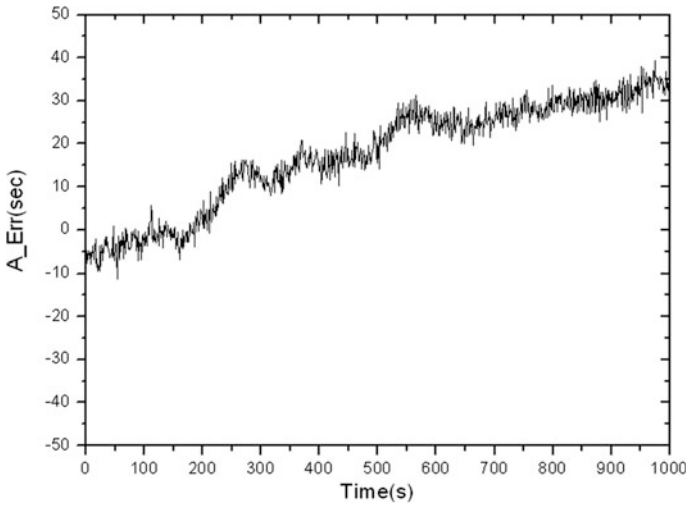

Fig. 56.11 Azimuth error

Statistical results show that the system error of the radar' range is distinct and the random error is stable; both the system and random error of radar's elevation angle are small; both of the system and random error of radar's azimuth are distinct and unstable.

56.5 Conclusion

This article has discussed the construction, work mode and assessment method of space TT&C equipment precision assessment system based on the UAV platform, has realized the complete testing flow procedure through actual flight adjusting and has analyzed the adjusting effect, as shown in the results:

1. UAV platform is capable to provide excellent flight conditions to testing load, features advantages such as cheap price, simple operation, strong mobility, short measurement cycle and wide application scope, etc., and has substantially reduced adjusting cost and expanded application scope;
2. the unmanned-aircraft -borne small size GPS receiver in the system features stable work, and availability of high-precision standard data, therefore, the UAV flight adjusting precision assessment system provides a new efficient and quick solution for realization of precision assessment of space TT&C equipment.

References

1. Jie H, Zhang S, Dong X (1999) Research on the precision appraisal of space tracking and control equipment in using GPS. J Inst Command Technol 10(3):30–34
2. Wu H (2008) Method of radar proof-adjusting of dynamic quality and appraisal of precision. Nanjing University of Science and Technology
3. Fahlstrom PG, Gleason TJ (2003) Introduction of the UAV system. Electronic Industry Press, Beijing
4. Jiang Y, Xue Y, Chen J (2009) Design and implementation of the UAV flight control system. Comput Measure Control 17(5):911–913
5. Li Y (2005) Research of air-ground datalink system for UAV. Northwestern Polytechnical University, Xi'an
6. Yang Y (2006) Adaptive navigation and kinematic positioning. Publishing House of Surveying and Mapping, Beijing
7. Jin Z, Lu W, Zhu J (2001) Radar precision assessment using GPS on an UAV. Tsinghua Univ (Sci & Tech) 41(9):40–43

Chapter 57
Shadow Matching: Improving Smartphone GNSS Positioning in Urban Environments

Lei Wang, Paul D. Groves and Marek K. Ziebart

Abstract Positioning using Global Navigation Satellite Systems (GNSS) is unreliable in dense urban areas. The accuracy in the across-street direction can degrade to a few tens of meters in deep urban canyons because the unobstructed satellite signals travel along the street, rather than across it, resulting in poor signal geometry. A new solution to this cross-street positioning problem is to use 3D city models to predict satellite visibility, and then compare with the measured satellite visibility to determine position. This concept is known as shadow matching. In this work, for the first time, the shadow-matching technique is demonstrated using GNSS data from a smartphone. The algorithm has been optimized for speed. The system is then verified with real-world GPS and GLONASS data from Samsung Galaxy S3 smartphones. The experimental data show that shadow matching outperforms the conventional GNSS positioning, improving cross-street positioning success rate for a 2 m accuracy from 18.5 to 86.9 % of the time at the selected test site. The system is also compatible with Beidou and Galileo, with potentially improved performance.

Keywords GNSS · Urban canyons · 3D city model · Shadow matching · Smartphone

57.1 Introduction

The poor performance of global navigation satellite systems (GNSS) user equipment in urban canyons in terms of both accuracy and solution availability is a well-known problem [1–3]. However, a great number of day-to-day navigation requests

L. Wang (✉) · P. D. Groves · M. K. Ziebart
Department of Civil, Environmental and Geomatic Engineering, University College London, Gower Street, London, WC1E 6BT UK
e-mail: lei.wang.10@ucl.ac.uk

J. Sun et al. (eds.), *China Satellite Navigation Conference (CSNC) 2013 Proceedings*, Lecture Notes in Electrical Engineering 245,
DOI: 10.1007/978-3-642-37407-4_57,

are made in urban areas by city residents. Location-based advertising, augmented-reality applications, and systematic guidance for visually impaired and tourists all require sufficient positioning accuracy [4, 5].

The problem of GNSS performance in urban canyons arises because where there are tall buildings or narrow streets, the direct line-of-sight (LOS) signals from many of the satellites are blocked. Sometimes, a degraded position solution may be obtained by making use of signals that can only be received by reflection of a building; these are known as non-line-of-sight (NLOS) signals [6, 7].

As well as affecting the number of available GNSS signals, an urban canyon also affects the geometry of positioning solutions. This is because signals with lines of sight going across the street are more likely to be blocked by buildings than those with lines of sight going along the street. This is illustrated by Fig. 57.1. As a result, the signal geometry, and hence the positioning accuracy, will be much better along the direction of the street than across it [2].

For improving navigation performance in highly built-up areas, navigation sensors have been used to enhance GNSS [8, 9]. However, these approaches improve the continuity and robustness of the position solution, while not the cross-street accuracy.

As 3D building models are becoming more accurate and widely available [10], they may be treated as a new data source for urban navigation and used to improve positioning accuracy in urban canyons. This can be implemented by predicting which satellites are visible from various locations and comparing this with the measurement to determine position. Satellite visibility predictions using a 3D city model have been validated with real-world observation, demonstrating the practical potential of shadow matching [3, 10–13].

A new approach, known as shadow matching, proposes to improve the cross-street accuracy using GNSS, assisted by information derived from 3D building models [2, 14]. In shadow matching, by determining whether a direct signal is

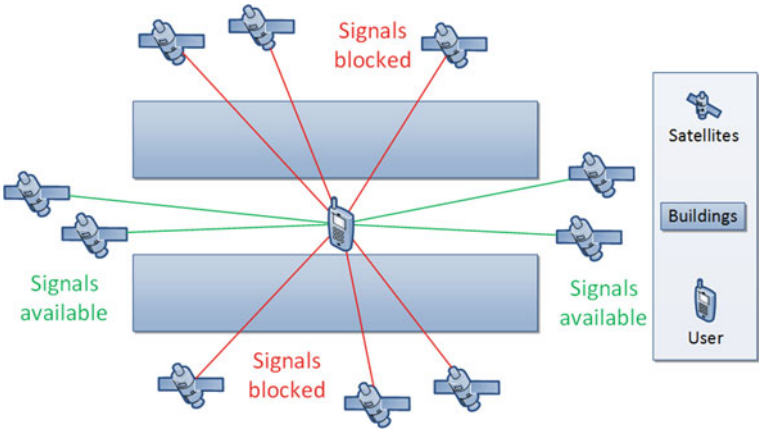

Fig. 57.1 A schematic diagram of shadow matching

being received from a given satellite, the user can localize their position to within one of two areas of the street. A preliminary shadow-matching algorithm has been developed and demonstrated the ability to distinguish pavement from vehicle lane, and identify the correct side of street using real-world GPS and GLONASS measurements [15, 16]. A new scheme has been proposed that considers the effects of satellite signal diffraction and reflection by weighting the scores based on diffraction modeling and signal-to-noise ratio (SNR) [17]. This work was conducted using geodetic GPS and GLONASS receivers.

However, most potential applications of shadow matching use consumer-grade GNSS user equipment, whereas previous test of shadow matching used geodetic GNSS receivers [17]. The consumer-grade GNSS receivers normally costs much less, but with worse signal reception, severer multipath reception and stronger non-line of sight (NLOS) reception due to the low gain and linear polarization of smartphone GNSS antennas. This difference can degrade shadow-matching performance. Thus, it is required to investigate shadow-matching performance using consumer-grade GNSS receivers with smartphone-grade antenna. This is the scope of this paper.

A modified shadow-matching positioning system compatible with GNSS data from smartphone has been developed. The system was then verified with GPS and GLONASS data from Samsung Galaxy S3 smartphone. The experimental data shows that the developed system outperforms the conventional GNSS positioning, reducing the cross-street positioning error. The system is also compatible with Beidou (Compass) and Galileo, with potentially improved performance.

A brief summary of the optimized shadow-matching algorithm is presented in Sect. 57.2. Section 57.3 then describes the test of the algorithm using real-world GPS and GLONASS measurements, and compares performance between the conventional GNSS navigation solution with the shadow-matching solution. Finally, in Sect. 57.4, conclusions are drawn and future work is discussed.

57.2 The Shadow-Matching Algorithm

The proposed shadow-matching algorithm has two phases—an offline phase (the preparation step) and an online phase, consists of a pre-processing step and five steps, illustrated in Fig. 57.2. An off-line phase is conducted to generate a grid of building boundaries from the 3D city model.

In the beginning of the online phase, the user position is first initialized, e.g. using conventional GNSS solution from the GNSS chip or Wi-Fi signals. The second step defines the search area—the potential user locations, for the shadow-matching position solution. For the third step, the satellite visibility at each grid position is predicted using the building boundaries generated from the 3D city model. After that, the similarity of satellite visibility between prediction and observation is evaluated using a scoring scheme, providing a score for each grid point in search area. Finally, the positioning solution is generated by a modified

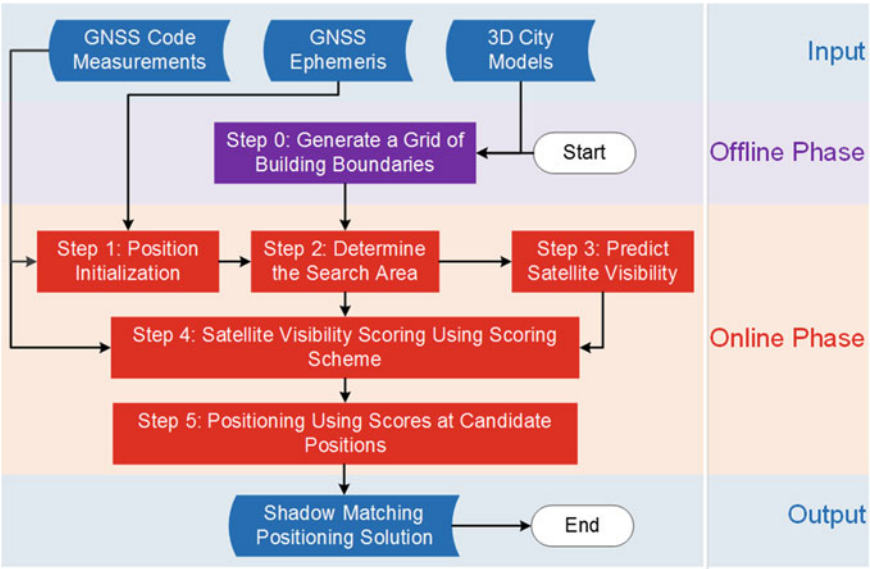

Fig. 57.2 A workflow of the improved shadow-matching algorithm (*Source* [17])

k-nearest neighbours algorithm, which averages the positions of the grid points with the highest scores. Details of the algorithm can be found in [17].

57.3 Experimental Verification Using Smartphone GPS and GLONASS Data

To evaluate the performance of shadow matching using smartphones, experiments were conducted in central London on 26th Oct. 2012. Section 57.3.1 introduces the 3D city model and test sites, and describes the configuration of the shadow matching algorithm. The scoring maps are shown in Sect. 57.3.2, with positioning results compared and analysed in Sect. 57.3.3.

57.3.1 Experiment Details

A 3D city model of the Aldgate area of central London, supplied by ZMapping Ltd, was used. The model has a high level of detail and deci-metre level accuracy.

An experimental site was selected on Fenchurch Street, a built-up urban area, standing on a footpath close to a traffic lane. Figure 57.3 shows an aerial view of the satellite image and city model used in this work, with a photo taken at the

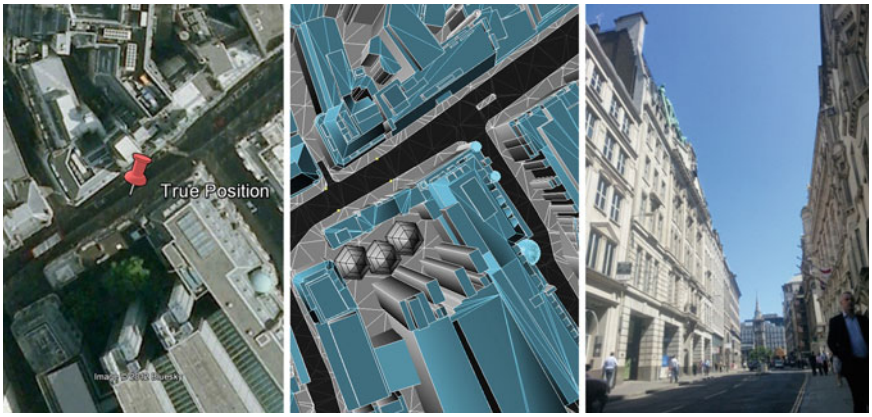

Fig. 57.3 An aerial view of the experimental site on Fenchurch street in the satellite image (*left*) and in 3D city model (*middle*); a photo taken at the experimental site (*right*)

experimental site. GPS and GLONASS observation data were recorded at a 1 Hz rate for 6 min using a Samsung Galaxy S3 smartphone.

In the offline phase of shadow matching, a 1 m by 1 m grid has been generated, and the building boundaries determined at each grid point as defined earlier in the paper. In the online phase, the search area for each epoch is centred at the output of conventional GNSS positioning solution. The search area for each site is defined as locations within a radius of 40 m, except for the indoor points. The modified k-nearest neighbours algorithm is used to determine the shadow-matching positioning solution.

57.3.2 Score Map at Candidate Positions

At each observation epoch, comparison is made between the predicted and observed satellite visibility. The score scheme is applied accordingly. To illustrate the distribution of scores at the grid points and its dynamic with respect to time, Fig. 57.4 shows the score maps at 1 min interval for the experimental site. The coloured dots represent the candidate positions. The more red a dot is, the higher score obtained at that candidate position using the matching algorithm. The true location of the experimental site is shown by a black dot in each colour map.

Figure 57.4 clearly demonstrated that the shadow matching algorithm is sensitive to changes in the across-street direction, but less sensitive in the along-street direction. This is in line with expectations and complements conventional GNSS positioning, which is generally more precise in the along-street direction in urban areas due to the signal geometry. There are some spaces that between buildings fall within the search area, but the highest scoring points are mostly in the correct street.

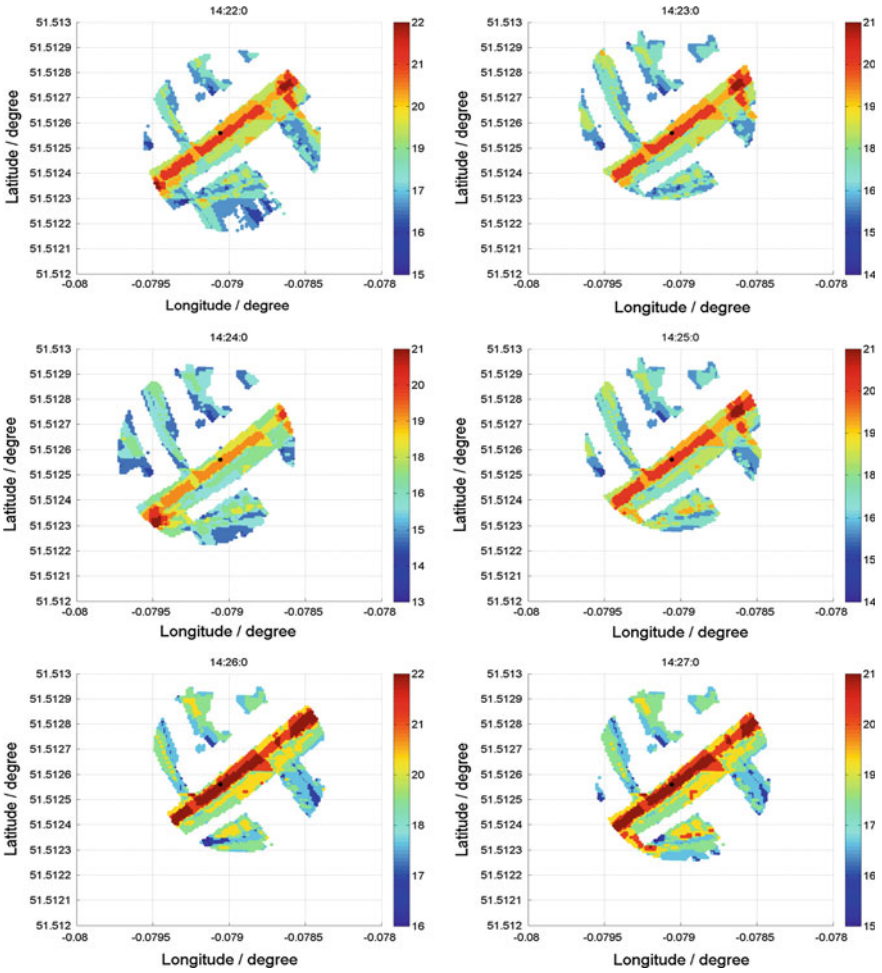

Fig. 57.4 Shadow-matching score map of the experimental site (from 14:22:00 to 14:27:30, 26 Oct. 2012)

57.3.3 Positioning Error Analysis

To assess performance, the position errors are transformed from local coordinates (Northing and Easting) to the along-street and across-street directions. Figure 57.5 shows the positioning results of conventional GNSS navigation solution from the smartphone GNSS chip, compared with shadow-matching positioning results, expressed as errors in across-street direction. It clearly shows that in most cases, shadow matching solution outperforms the conventional GNSS positioning solution. Shadow-matching solution has improved the conventional positioning error, at across-street direction, from 5 to 10 m to within 1 m accuracy in a major portion of epochs.

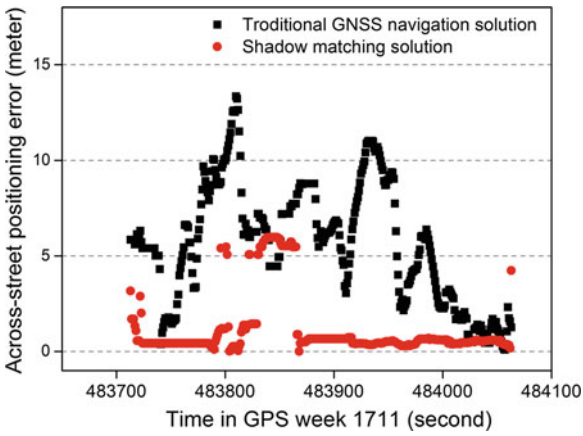

Fig. 57.5 Comparison of the across-street positioning error between conventional GNSS navigation solution and shadow matching solution

In order to evaluate the performance across all of the epochs, a statistical analysis was performed. The mean absolute deviation was used to evaluate the performance of shadow matching. In order to show the improvements of shadow-matching over conventional GNSS positioning, the mean absolute deviation at each site are compared in Fig. 57.6 (left). The bar shows the mean across-street positioning error using the conventional and shadow-matching algorithm,

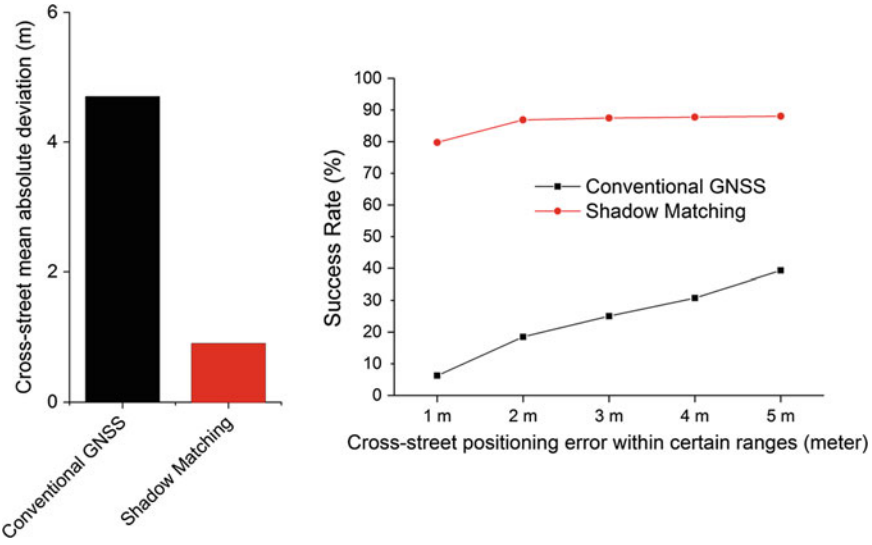

Fig. 57.6 Cross-street positioning error comparison between the conventional GNSS positioning solution and the shadow-matching solution. *Left* mean and RMS cross-street positioning errors; *right* success rate of cross-street positioning errors within certain ranges

respectively. It is shown in Fig. 57.6 (left) that the across-street positioning performance of shadow matching is significantly better than conventional GNSS. The shadow-matching algorithm improves the mean cross-street error from 4.7 to 0.9 m.

Further statistics have been computed to express the positioning performance as a success probability over a period of time (6 min), the results are shown in Fig. 57.6 (right). As the street is around 10 m wide, a positioning accuracy better than 5 m is considered good enough to determine the correct side of the street, while a positioning accuracy better than 2 m is considered good enough to distinguish the foot path from a traffic lane. At the best site, it shows that the success rate using shadow matching for determining the correct side of a street is 88.0 %, compared to 39.3 % of the conventional solution; The success rate of distinguishing the footpath from a traffic lane is 86.9 % for shadow matching, compared to 18.5 % for the conventional GNSS positioning.

As shadow matching improves the cross-street positioning significantly, it shows a high potential to be combined with conventional GNSS and other possible techniques.

57.4 Conclusions and Future Work

In this work, for the first time, the shadow-matching technique is demonstrated using consumer-grade GNSS receivers. A new shadow-matching positioning system compatible with GNSS data from smartphone is proposed and developed. Optimizations are implemented for improving efficiency in real-time. The system is then verified with real-world GPS and GLONASS data from Samsung Galaxy S3 smartphones. The experimental data show that the developed shadow-matching system performs better than conventional GNSS positioning solution, significantly reducing cross-street positioning error. The system is also compatible to work with Compass (Beidou) and Galileo, with potentially improved performance.

The results presented here are from a site well suited to shadow matching with a smartphone GNSS data. Performance with smartphone is normally poorer in area with highly reflective buildings because of the characteristics of the smartphone's antenna. Further research is therefore needed to improve the reliability of the shadow-matching solution in these areas and to develop a quality metric.

To obtain an accurate and reliable position solution in challenging urban environments, shadow matching must be combined with conventional GNSS positioning, NLOS signal detection and other techniques that exploit the 3D mapping, such as height aiding. This concept is known as intelligent urban positioning (IUP) and is introduced in [18]. IUP may also be extended to incorporate other techniques, such as Wi-Fi, Bluetooth Low Energy, and MEMS inertial sensors.

Acknowledgments The authors gratefully acknowledge Mr. Kimon Voutsis for his support with the experiments and Dr. Ziyi Jiang for his support on design of experiments. This work has been jointly funded by the University College London Engineering Faculty Scholarship Scheme and the Chinese Scholarship Council.

References

1. Jiang Z, Groves P, Ocheing WY, Feng S, Milner CD, Mattos PG (2011) Multi-constellation GNSS multipath mitigation using consistency checking. In: Proceedings of ION GNSS 2011
2. Groves PD (2011) Shadow matching: a new GNSS positioning technique for urban canyons. J Navig 64(03):417–430
3. Wang L, Groves PD, Ziebart M (2012) Multi-constellation GNSS performance evaluation for urban canyons using large virtual reality city models. J Navig 65:459–476. doi:10.1017/S0373463312000082
4. Omer R, Coulton P, Edwards R (2005) Implementing location based information/advertising for existing mobile phone users in indoor/urban environments. In: Mobile Business 2005. ICMB 2005. IEEE, pp 377–383
5. You Y, Chin TJ, Lim JH, Chevallet JP, Coutrix L, Nigay L (2008) Deploying and evaluating a mixed reality mobile treasure hunt: Snap2play. In: Proceedings of MobileHCI 2008
6. Ercek R, Doncker PD, Grenez F (2005) Study of Pseudo-range error due to non-line-of-sight-multipath in urban canyons. In: Proceedings of ION GNSS 2005
7. Viandier N, Nahimana DF, Marais J, Duflos E (2008) GNSS performance enhancement in urban environment based on pseudo-range error model. In: Proceedings of position, location and navigation symposium, IEEE/ION PLANS 2008
8. Farrell JA (2008) Aided navigation: GPS with high rate sensors. McGraw-Hill Professional, New York
9. Groves PD (2013) Principles of GNSS, inertial, and multi-sensor integrated navigation systems, 2nd edn. Artech House, London
10. Bradbury J, Ziebart M, Cross PA, Boulton P, Read A (2007) Code multipath modelling in the urban environment using large virtual reality city models: determining the local environment. J Navig 60:95–105
11. Suh Y, Shibasaki R (2007) Evaluation of satellite-based navigation services in complex urban environments using a three-dimensional GIS. IEICE Trans Commun 90(7):1816–1825
12. Kim HI, Park KD, Lee HS (2009) Development and validation of an integrated GNSS simulator using 3-D spatial information. J Korean Soc Surveying Geodesy Photogrammetry Cartography 27:659–667
13. Ji S, Chen W, Ding X, Chen Y, Zhao C, Hu C (2010) Potential benefits of GPS/GLONASS/GALILEO integration in an urban canyon—Hong Kong. J Navig 63:681–693
14. Tiberius C, Verbree E (2004) GNSS positioning accuracy and availability within location based services: the advantages of combined GPS-Galileo positioning. In: Proceedings of NAVITEC 2004
15. Wang L, Groves P, Ziebart M (2011) GNSS shadow matching using a 3-D model of London. In: Proceedings of European navigation conference 2011
16. Groves PD, Wang L, Ziebart M (2012a) Shadow matching: improved GNSS accuracy in urban canyons. GPS World, 23(2):14–18, 27–29
17. Wang L, Groves PD, Ziebart M (2012b) GNSS shadow matching: improving urban positioning accuracy using a 3D city model with optimized visibility prediction scoring. In: Proceedings of ION GNSS 2012
18. Groves PD, Jiang Z, Wang L, Ziebart M (2012b) Intelligent urban positioning using multi-constellation GNSS with 3D mapping and NLOS signal detection. ION GNSS 2012

Chapter 58
A Novel Three-Dimensional Indoor Localization Algorithm Based on Multi-Sensors

Zhifeng Li, Zhongliang Deng, Wenlong Liu and Lianming Xu

Abstract With the wildly application of the mobile internet, the market of location-based services is growing rapidly. At present, the main current method of indoor location is based on the finger point position technology of wireless local area network (WLAN), and combined with a fusion algorithm of pedestrian dead reckoning (PDR). Furthermore, due to the spread characteristics of Wi-Fi signal, there are some weak signal zones and even blind zones. This paper proposes a novel indoor localization algorithm. The algorithm combines the multi-finger point technology, geomagnetic navigation and inertial navigation, and uses the advantages of each technology to complement each other, to achieve the series, seamless, and three dimensions indoor location. Through the algorithm simulation and contrast analysis of experiment, the algorithm given in this paper has showed that the average positioning accuracy has improved nearly 37 %, the average positioning error can reach 2.72 m and the new algorithm has a 100 % coverage area rates in comparison with KNN\W-KNN\PDR and their fusion algorithm, which has proved the feasibility and effectiveness of this new fusion algorithm.

Keywords Multi-sensors · Fusion algorithm · High-precision

58.1 Introduction

As the rapid development of intelligent mobile phone, it drives the mobile Internet application innovation. Location Based Service is rising rapidly in china. It has become one of most popular application in the field of mobile Internet. According

Z. Li (✉)
Beijing University of Post and Telecommunication, Haidian District, Xitucheng Road. 10, Beijing 100876, China
e-mail: sky2852358@163.com

Z. Li · Z. Deng · W. Liu · L. Xu
Institute of EE, Beijing University of Post and Telecommunication, Beijing, China

J. Sun et al. (eds.), *China Satellite Navigation Conference (CSNC) 2013 Proceedings*, Lecture Notes in Electrical Engineering 245,
DOI: 10.1007/978-3-642-37407-4_58,

to a report released recently from the third data-research party—Enfodesk of the mobile Internet, the mobile Internet user scale will reach 606 million, the Mobile location services user scale will reach 510 million, and the Customer permeability will reach 84.2 % [1]. According to the development trend of intelligent mobile phone, the mobile phone will be integrated multi-functional sensor. It also shows the future development direction of intelligent mobile phone. How to make full use of these sensors, fuse the Wi-Fi location algorithm, to improve positioning accuracy, expand positioning range, increase location dimension. All these questions will become the focus of research in this paper.

58.1.1 The Wi-Fi Indoor Positioning

In the domestic and foreign countries, the new wireless network technologies, especially Wi-Fi based on 802.11 agreements are widely used. The intelligent terminal has contained basically Wi-Fi module. In the foreign, Ekaha system and Aero Scout system are representatives [2]. In domestic universities, Beijing University of posts and telecommunications, Wuhan University and Shanghai Jiaotong University are researching this technology [1]. It needs to meet two requirements; one is to receive three or more effective Wi-Fi signal at the same time, and the other is that the signal strength has obvious distinguishing degrees in different location areas [3].

58.1.2 The Magnetic Positioning

Magnetic field is a vector field. It is the earth inherent public resources. It also has all day, all weather, and all regional characteristics. Around earth space any point, the magnetic field intensity vector has uniqueness, it corresponds the latitude and longitude of this point. As long as accurately determine the point of magnetic field vector, we can realize global positioning.

58.1.3 The Inertial Navigation

Dead Reckoning is an assistive technology of Global navigation satellite system. In Pedestrian Dead Reckoning, the movement distance test by acceleration sensor [2], the movement Angle measured by compass sensor. The biggest malpractice of localization algorithm lies in error accumulation. Pedestrian navigation position prediction principle is shown in Fig. 58.1 [4].

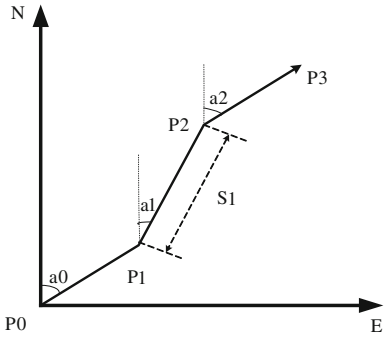

Fig. 58.1 The principle diagram of pedestrian dead reckoning

58.2 Algorithm Principles

58.2.1 Location Difficulty Analysis

K Nearest neighborhood matching algorithm is a kind of relatively mature and widely used technology. The first one is Wi-Fi signal cover shortage. The second one is that due to the Wi-Fi signal's penetrability, radioactive and multipath effect, especially strong signal APs, they can form the same fingerprint point even from long distance (in the same floor or in the different floors). The first positioning accuracy makes great challenge. The third one is about the human body to Wi-Fi interference. But if we take the average from four directions, that means we ignore the indoor walking directivity, and introduce the gross error artificially [1]. This article embarks from the reality, and puts forward a new algorithm which uses the Wi-Fi positioning system as the core, and makes full use of magnetic sensor and pressure sensor auxiliary and based on particle filter positioning output. It can further improve the positioning accuracy.

58.2.2 The Wi-Fi Localization Algorithm

Weighted K Nearest neighborhood is an improved algorithm in the matching algorithm from K Nearest neighborhood. This algorithm calculates the distance between the measurement of RSS during the online positioning and the data base of fingerprint library, and then selects recent K points. According to the weighted average, we can determine the initial estimate position.P.S: $K \geq 2$ for common.

58.2.3 The Geomagnetic Auxiliary Algorithm

Compared with outdoor environment, the magnetic field of indoor environment could be easily affected by architectural structure, strong-low electric field, electronic devices and human beings. But once the building is put into use, all of these influences are vanished. The magnetic field becomes stable. The indoor environment produced a relatively constant magnetic environment.

58.2.4 The Pneumatic Auxiliary Algorithm

At present most of the positioning technology mostly stay in 2-D plane. But the real positioning system should meet the 3-D demand (the floor positioning). The paper used the pressure sensor of intelligent mobile terminal. Through the comparison with the pressure fingerprint information and the comprehensive Wi-Fi positioning information, we make sure of the Initial location. And then use difference model determines the position of the third dimension.

58.3 A Novel Three-Dimensional Algorithm Based on Multi-Sensors

58.3.1 Fusion Positioning

The basic core thought of fusion algorithm is doing a data fusion processing of RSS of Wi-Fi, magnetic strength and the pressure value. Through the online matching and particle filtering, the output gets the best point. Fusion algorithm model is shown in Fig. 58.2.

The first step in the fusion algorithm is to deicide the height by Difference model. After determining the two-dimensional plane, we used the Weighted KNN. We suppose r_{ij} is signal strength of the No.j reference point and the No.i Wireless access point. R_i is signal strength of the No.i Wireless access point. "m" is the number of AP. "n" is the number of point. So distance formula can be expressed as: As the p = 2, it is the Euclidian Distance formula [5, 3]

$$d_j = \sqrt{\sum_{i=1}^{m} \left(R_i - r_{ij}\right)^p}, \quad j = 1, 2, \ldots, n \tag{58.1}$$

We can get the number K of the nearest matching points by the up formula. By calculating the mean of these points and giving the right value, we could get the weight KNN formula. W_i means the weight of No.i.

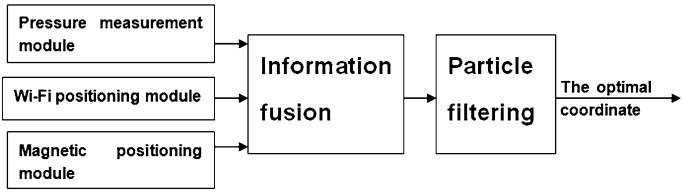

Fig. 58.2 The principle diagram of new algorithm

$$\begin{cases} (\bar{x}, \bar{y}) = \sum_{i=1}^{k} [w_i \times (x_i, y_i)] \\ w_i = \dfrac{1}{d_i + \varepsilon} \end{cases} \tag{58.2}$$

We calculated correlation coefficient between the four directions of above points and the magnetic field strength. At last we get the most matching point and the most matching direction.

$$\gamma_{Api,Apj} = \frac{Cov(rss_i, rss_j)}{\sigma_i, \sigma_j} = \frac{\frac{1}{n}\sum_{k=1}^{n}(rss_{ik} - u_i)(rss_{jk} - u_j)}{\sigma_i, \sigma_j} \tag{58.3}$$

58.3.2 Particle Filtering

For smoothing coordinate outputs, the paper chose the particle filter. To set up mobile model particle filter is the difficult and key point. Combined with characteristics of this paper we increased the forecast and analysis of the third dimension. According to the position of the Markova property, the system states transition equation of x, y, z direction is as shown:

$$\begin{cases} x(k) = a_x * x(k-1) + b_x * v_x(k-1) + Q_x \\ y(k) = a_y * y(k-1) + b_y * v_y(k-1) + Q_y \\ z(k) = a_z * z(k-1) + b_z * v_z(k-1) + Q_z \end{cases} \tag{58.4}$$

X means the coordinate figure on x, y, z coordinate at the k moment. V means the speed on x, y, z coordinate at the (k−1) moment. Q means the process noises. a_x, a_y, a_z and b_x, b_y, b_z mean the coordinate and their direction's state transfer coefficient. Observation equation on x, y, z directions are:

$$\begin{cases} Zx(k) = h_x * x(k) + R_x(k) \\ Zy(k) = h_y * y(k) + R_y(k) \\ Zz(k) = h_z * z(k) + R_z(k) \end{cases} \tag{58.5}$$

Z means observed value on x, y, z coordinate at the k moment. R means the noise on x, y, z coordinate. H means the measurement coefficient on x, y, z coordinate.

58.4 Test and Analysis

The paper selected the 2 terminal of Beijing airport for experiment place. We use Samsung mobile-i9300 phone as a standard test phone to complete offline training and online location.

58.4.1 Floor Location Test

Table 58.1 has shown us the pressure of the 2 terminal of Beijing airport including basement first, first floor, second floor, third floor. We can obviously find that different floors have different pressure values between 0.4 and 0.6 m Bars. We can calculate the value of location point in the third dimension by comparing with the reference pressure.

58.4.2 Magnetic Direction Matching Test

The paper chose three points from the data base of Offline training, and recorded their magnetic field intensity from each finger point of four directions. As shown in Table 58.2.

Through the contrast we can find that the adjacent fingerprint point magnetic field strength has obvious difference at least 7 μT, and the same fingerprint point in four direction of magnetic field strength also has the obvious difference at least 3 μT. They can be used in the fusion of matching algorithm as a set of characteristic values.

Table 58.1 Comparing with the reference pressure

	B1	F1	F2	F3
Pressure	1011.5	1010.9	1010.5	1009.9

Table 58.2 Magnetic field intensity from each finger point of four directions

	East (μT)	South (μT)	West (μT)	North (μT)
Point A	45	32	35	38
Point B	53	39	42	50
Point C	44	57	33	40

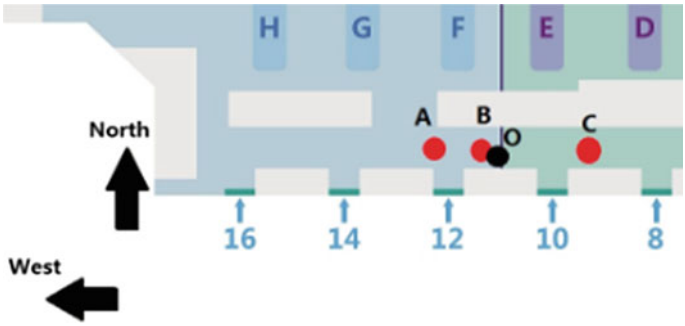

Fig. 58.3 Points map of experiment

Fig. 58.4 The calculation results about magnetic overall strength related

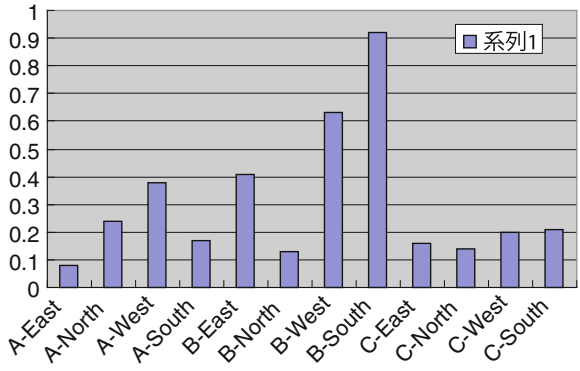

In order to validate the feasibility of the fusion algorithm, the paper first designated a method of fixing-point test. We chose point "O" which is toward the north, as shown in Fig. 58.3. Acquisition process lasted 10 s. First, we could know we are in the second floor according to the pressure value matching. Second, we get the most three matching points by K-NN algorithm. We calculate the coefficient of correlation between point "O" and each four directions of point "A", "B" and "C". The highest correlation coefficient with the test point is the point "B" with the direction of north almost 0.9. We get the results, as shown in Fig. 58.4.

Through the calculation results, we could obviously see that the matching results are very close to actual toward, also could effectively identify the direction.

58.4.3 Compare with Ekahua System

This paper used the Ekahua system to compare [2]. The paper validated the moving positioning results further. Walking direction is such as arrow shown in Fig. 58.5.

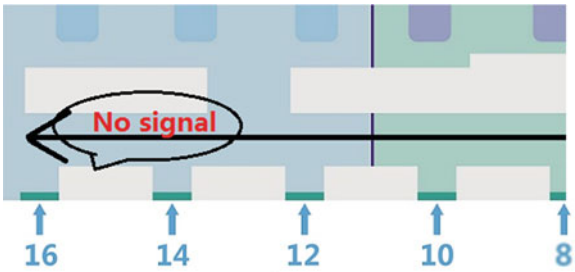

Fig. 58.5 Itinerary map of experiment

Table 58.3 System resulting data of standard experiment

	Maximum error (m)	Average error (m)	Floor accuracy (%)
Wi-Fi + particle filter	4.14	2.01	78
Wi-Fi/magnetic + particle filter	9.92	3.87	100

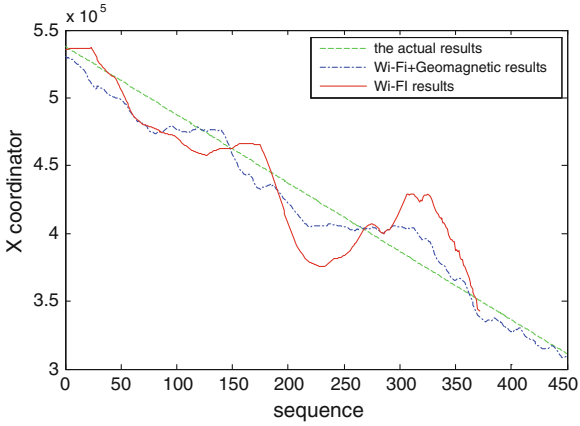

Fig. 58.6 Contrast diagram of matching results

In the outer part of the corridor Wi-Fi signal is difficult to distinguish from each other, so location accuracy is not accuracy in the original location system. In the gallery from gate 14 to gate 16 there cannot receive Wi-Fi signal, so it could not be located.

We used Samsung mobile-i9300 phone to compare the results from two different methods, Wi-Fi and magnetic fusion positioning and the sole Wi-Fi positioning. The sampling period is 600 MS. We get almost 500 location results during the test process. Two kinds of the performance of the system are shown in Table 58.3. We can see Wi-Fi/magnetic fusion positioning has greatly improved the positioning accuracy. At the same time by using the pressure difference comparison model, we could get 100 % correct floor.

We can easily find that the algorithm by this paper is better than Ekahua system. The maximum error, the average error, and the floor accuracy has promoted by 49.5, 37 and 28 %. And the paper has proved the effectiveness of the proposed algorithm.

In the Fig. 58.6 to show the advantages of the new algorithm more intuitive, the paper made three curves: the green one is actual route, the red one is the results from the Wi-Fi positioning system, and the blue one is the results from the Wi-Fi/magnetic fusion positioning system. We use the X coordinate to contrast each other. Because there is no Wi-Fi signal in the later of the process, the Ekahua system cannot locate [2]. But the new algorithm can also locate the position near the actual position. We can obviously find that the blue line is closer to the actual situation.

58.5 Conclusions

This paper puts forward a three dimensional positioning method which fuses Wi-Fi localization, magnetic field location and high barometric leveling. It outputs the smooth coordinates through the particle filter. The paper discusses the principle and realization. We tested in the 2 terminal of Beijing airport and proved the feasibility of the algorithm. By comparison with outputs of original Wi-Fi location particle system, it is easily found that positioning accuracy and positioning range has a wide improvement. The new method has solved the problem of unable to locate in the non-signal areas of Wi-Fi and also solved the problem of the orientation direction. A three dimensional orientation has realized. The next research goal is to perfect each module of this system, improve the robustness and efficiency, and further improve the positioning accuracy.

References

1. Zhuang P, Wang D, Shang Y (2010) SMART: simultaneous indoor localization and map construction using smart phones
2. Wang SC, Sun DW, Zhang JS, Chen LH (2010) Research on geomagnetism navigation and localization based on SLAM. Second artillery engineering college, vol. 35, No. 12
3. Golden SA, Bateman SS (2007) Sensor measurements for Wi-Fi location with emphasis on time-of-arrival ranging. IEEE Trans Mob Comput 6:1185–1198
4. Fang L, Antsaklis PJ, Montestruque LA (2005) Design of a wireless assisted pedestrian dead reckoning system-the navmote experience. IEEE Trans Instrum Measur 54(6):2342–2358
5. Cherri A, Fortier P, Tardif PM (2009) UWB-based sensor networks for localization in mining environments. Ad Hoc Netw 7(5):987–1000

Chapter 59
Particle Filtering in Collaborative Indoor Positioning

Hao Jing, Chris Hide, Chris Hill and Terry Moore

Abstract Satellite positioning accuracy cannot meet the required needs due to lack of GPS signals inside buildings. Wi-Fi fingerprinting has become a popular method of overcoming problems in indoor positioning and navigation. Yet the accuracy of fingerprinting is rather limited and the system is prone to the changes of the building structure and Wi-Fi networks. However, if mobile users can share their signal as well as ranging and positioning information collaboratively to form a local network, the information could be used to correct failures in the fingerprinting process and provide more signal and information to derive robust positioning results. This paper implements collaborative positioning using Particle Filters which give the potential of utilizing additional positioning information whenever possible. The filter takes into account the uncertainty of indoor positioning results. Therefore, it provides a series of possible solutions and outputs the most likely result. Simulation tests are carried out to evaluate the performance of the proposed algorithm. Results are analysed and improvement in accuracy could be seen in the results.

Keywords Particles filters · Collaborative · Indoor positioning · Wireless network

59.1 Introduction

Location-based services (LBS) and applications have been popular in everyday applications for both military and civil usage over the last decade as Global Navigation Satellite System (GNSS) technology matures. However, as both users and applications extend to a much broader scope [1] than what GPS was initially

H. Jing (✉) · C. Hide · C. Hill · T. Moore
Nottingham Geospatial Institute, University of Nottingham, Nottingham NG7 2TU, UK
e-mail: juliajing72@gmail.com

J. Sun et al. (eds.), *China Satellite Navigation Conference (CSNC) 2013 Proceedings*, Lecture Notes in Electrical Engineering 245,
DOI: 10.1007/978-3-642-37407-4_59,

designed for, researchers soon realized that satellite-based navigation system struggles to meet the required demands. Most LBS users actually spend most time of their day inside buildings or in urban areas where buildings, trees etc. tend to block satellite signals. Signals reflect and refract on walls and any other obstacles in their way causing multipath, which in effect lead to an inaccuracy of up to 200 m in urban areas [2]. As mobile social applications continue to gain popularity, an increasing problem is that a wrong location is attached when posting social events due to lack of positioning accuracy in such environment. Large international airports and shopping centres also tend to become bigger and more complicated. In emergency situations, this could be a huge problem if people are lost inside the complex maze of modern corridors and hallways.

Numerous sensor network based systems, such as wireless local area network (WLAN or Wi-Fi technology) and inertial navigation system (INS), have been proposed to overcome GNSS failures. Both methods are able to provide positioning information inside buildings, providing a promising solution for seamless outdoor-indoor positioning. Yet the problem is still not fully resolved as Wi-Fi relies on network architecture. Influences such as walls, furniture, electronics and moving pedestrians, as well as the nature of signal strength fluctuation, could lead to failure or sudden inaccuracies. On the other hand, most pedestrian navigation devices used for everyday applications are very low cost INS sensors. Thus, even with corrections, the inertial measurement drift will increase significantly after a period of time.

To overcome drawbacks of single sensor positioning system, research have been carried out to integrate sensors and positioning information into collaborative positioning systems. Chan et al. [3] proposed a collaborative system using ZigBee signals for museums. When users cluster together in a certain area, they help to correct nearby user positions by sharing their positions and how confident they are with that position. They have discovered that while the clustered users are able to help improve positioning accuracy, having a dense cluster could also lead to signal blockage or information overload. A collaborative localization algorithm based on Wi-Fi RSS is presented by Zhang et al. [4]. A group of mobile anchor nodes equipped with GPS remain relatively static to each other while moving and broadcasting messages to sensor nodes which helps estimate the position of the sensor node. Work done by Brzezinska et al. [5] provides a collaborative platform of integrating multi-sensors for both pedestrian and vehicle navigation. The algorithm was able to achieve 50 % improvement in positioning accuracy compared to stand-alone GPS positioning. Nevertheless, these systems still rely on GPS signals to some extent.

This paper proposes a collaborative multi-sensor multi-user positioning algorithm which takes advantages of sharing ranging information between nearby mobile users to form a local network. Particle Filtering (PF) is applied to integrate ranging and sensor information which helps to correct outages or bias in the received data. We will firstly discuss the integrated sensors which include Wi-Fi, Ultra-Wide Band (UWB) and pedestrian dead reckoning (PDR) performance. Then the PF approach to collaborative positioning will be discussed. In Sect. 59.4,

simulations are presented to evaluate the algorithm performance. Finally, results are concluded with an outline for future work.

59.2 Methodology

The proposed algorithm integrates all available location information to overcome the weakness of one single measurement. A short discussion of each integrated sensor measurement is outlined below.

59.2.1 Pedestrian Dead Reckoning

For a low-cost mobile user, PDR measurements usually consist of step length and heading. Measurement equation could be described as

$$\begin{bmatrix} \mathrm{E}_t \\ \mathrm{N}_t \end{bmatrix} = \begin{bmatrix} \mathrm{E}_{t-1} + \hat{\mathrm{s}}_{[t-1,t]} \sin \psi_{t-1} \\ \mathrm{N}_{t-1} + \hat{\mathrm{s}}_{[t-1,t]} \cos \psi_{t-1} \end{bmatrix} \tag{59.1}$$

where $[\mathrm{E}_t, \mathrm{N}_t]$ are coordinates of the positions, $\hat{\mathrm{s}}_{[\mathrm{t}-1,\mathrm{t}]}$ is the measured step length between time $(t-1)$ and t, ψ_{t-1} is the measured heading. These measurements could be obtained from accelerometers and gyroscopes on modern smart-phone. However, low-cost gyro sensor has a large drift bias up to 1°/s [6]. Therefore, it is only able to provide a very coarse measurement and becomes less reliable as time lengthens. Noisy PDR measurements provide the dynamic measurement parameters for the proposed PF algorithm.

59.2.2 Wi-Fi Received Signal Strength Patterns

Theoretically, wireless signals follow a propagation model where the received power, P_{RX}, is a function of the distance d, which is known as Friis' law [7]. It could be written in a simple form:

$$\mathrm{P}_{\mathrm{RX}}(d) = \mathrm{P}_{d0} - 10n \log_{10}(d) + a * \mathrm{WAF} \tag{59.2}$$

where P_{d0} is the RSS at a certain reference distance, normally 1 m away from the transmitter. n is the free space loss factor, WAF is the Wall Attenuation Factor, a is the number of walls between the transmitter and receiver.

To analyse signal patterns inside buildings, a series of Wi-Fi signals are collected in the corridor and roof of Nottingham Geospatial Building (NGB). A BT Voyager 2901 wireless ADSL router was setup as an AP which broadcasts Wi-Fi

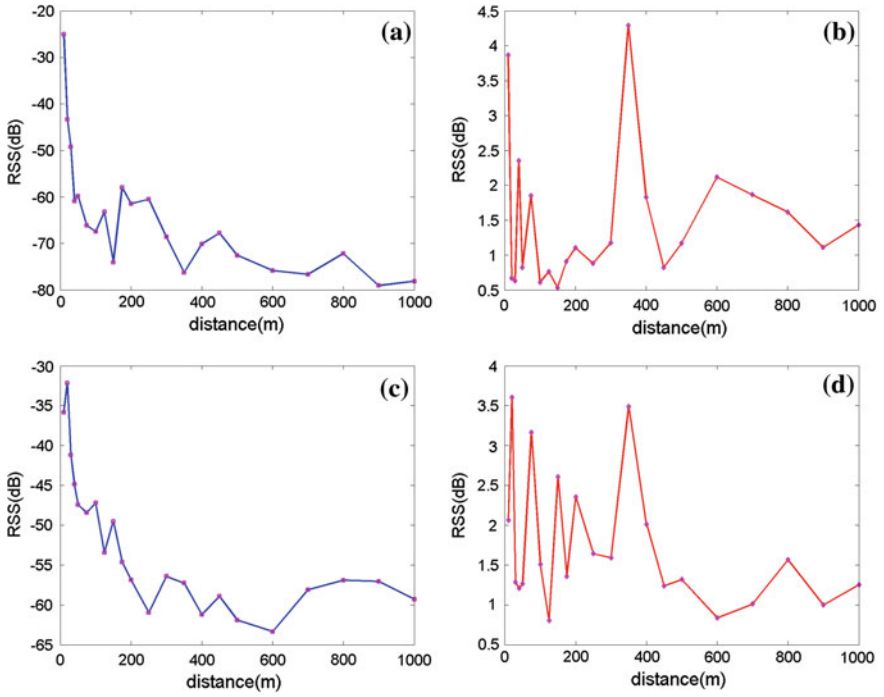

Fig. 59.1 Mean (**a**, **c**) and standard deviation (**b**, **d**) nSS in corridor and roof (10 cm–10 m)

signals, while a Samsung Galaxy Tab runs a program to collect RSS data at distances ranging from 10 cm to 10 m.

From the collected data, it could be seen that the RSS gradually drops as the distance between the receiver and transmitter grows (Fig. 59.1). However, due to the fluctuation of signals and surrounding environment, which is also shown in [8] and [9], the difference between the received maximum RSS and minimum RSS could vary from 4 dB up to 53 dB for a single position, with an average difference of 14.3 dB. According to the analysis results of collected data, we set $n = 3.0$. (Fig. 59.1).

59.2.3 Wi-Fi Fingerprinting

A simple propagation model is insufficient to provide an accurate range based on single RSS measurement as signals do not correlate well with the model due to fluctuation inside complicated environments where it is affected by changes in building structures and environmental factors. The first way to overcome this problem is the fingerprinting (FP) method. FP overcomes this problem by collecting and storing signal patterns that indicate certain areas of the building like a

"fingerprint" in a database. The approach consists of a training phase and positioning phase. During the training phase, "fingerprints" of RSS vectors are collected by walking around a designated area. Users could then go into the area and obtain positions by matching the RSS readings to the fingerprints in the database.

A fingerprint-mapping (FPM) method is proposed here for integrating RSS information into PF. The method searches through the RSS database for positions within $\pm n$ dB difference of the collected RSS separately for each AP. Intersections of all positions from the database are considered to be likely positions.

59.2.4 UWB Ranging

Another way to overcome Wi-Fi ranging imprecision is by using alternative wireless signals. UWB signals, as mentioned in [10], has strong penetration ability and could overcome multipath and signal reflection. It is able to provide very precise ranging solutions since it is based on the principle of detecting the TOA. By setting up an indoor network, accurate positions could be provided to users in its signal coverage area. Evaluation work discussed by Choliz et al. [11] and Meng et al. [12] suggests that a UWB network is able to achieve position precision up to sub-meter level. Tests also show that it is able to provide precise short distance ranging between nodes without having to setup a network, which can be used by mobile users.

59.2.5 Particle Filtering in Collaborative Positioning

The algorithm in this paper applies PF to integrate available sensors and user information mentioned above. PF is based on Monte-Carlo sampling, thus can deal with non-linear and non-Gaussian estimations. It is able to integrate a combination of data, including building maps. For non-linear filtering, states are described in the discrete-time stochastic model:

$$\mathrm{x}_k = \mathrm{f}_{k-1}(\mathrm{x}_{k-1}, \mathrm{v}_{k-1}) \tag{59.3}$$

where x_k is the state vector, k is the time index, f_{k-1} is a known function of the state x_{k-1} and noise v_{k-1}. Non-linear filtering recursively estimates x_k from measurements z_k,

$$\mathrm{z}_\mathrm{k} = \mathrm{h}_\mathrm{k}(\mathrm{x}_\mathrm{k}, \mathrm{w}_\mathrm{k}) \tag{59.4}$$

where h_k is a known non-linear function and w_k a noise measurement. To quantify the "truthfulness" of state measurements, a posterior probability density function (pdf) $\mathrm{p}(\mathrm{x}_k|\mathrm{Z}_k)$ is obtained recursively in prediction and update steps from previous observations using

$$p(x_k|Z_k) \approx \sum_{i=1}^{N} w_k^i \delta(x_k - x_k^i) \tag{59.5}$$

In this paper, we integrate DR measurement with other sensors using sampling importance resampling (SIR) filter [13]. The state dynamics and measurement functions need to be known, as well as the likelihood function $p(x_k|Z_k)$. Weights for particles are given by

$$w_k^i \propto w_{k-1}^i p(Z_k|x_k^i) \tag{59.6}$$

When resampling, number of new particles to generate depend on w_k^i. Once resampling is carried out, for each particle, previous importance weights are no longer passed on, thus

$$w_k^i \propto p(Z_k|x_k^i) \tag{59.7}$$

59.3 Simulations and Results

59.3.1 Simulation Settings

Simulations are carried out using Matlab R2011a to evaluate algorithm performance. In order to get a balance between program efficiency and effective positioning, 300 particles are generated. An indoor building map of NGB is used to provide building information, e.g. walls, doors. Details of implementing map information in PF is described in [14]. The true locations of the 6 APs in NGB Floor A and B were surveyed and a RSS database is simulated using Eq. (59.2) ($n = 3$, $WAF = 6$) for Floor A with a noise variance that follows the pattern identified in Sect. 59.2.2. The algorithm procedure is listed below:

1. Initialisation: initialise particles within 10 m around the initial position.
2. Prediction: Particles propagate forward according to DR measurements with a 0.5 m noise in velocity and a heading variance of $\pm 30^\circ$ as well as a heading drift bias of 0.5 /s.
3. Weighting: RSS and ranging measurements between users and APs are acquired. Particles are weighted according to Eq. (59.8).

$$weight = \begin{cases} 1/\Delta\, dist\left([x,y]_{particle}, [x,y]_{RSS}\right) \\ 1/\Delta\left(dist_{particle\_pairs}, dist_{ranging}\right), \ \text{(if other users available)} \\ 0, \qquad\qquad \text{(if crosses a all or outside building)} \end{cases} \tag{59.8}$$

4. Normalisation and re-sampling: weights are normalised. New particles are then re-sampled if the remaining effective particles fall below 50 % of the total number.

59.3.2 Result Assessment

59.3.2.1 Scenario 1

This scenario considers one mobile user moving along the corridor of Floor A in NGB according to a pre-defined true trajectory that starts off from the start point of the trajectory. The conventional FP method and FPM method is used for comparison.

Blue lines in Figs. 59.2 and 59.4 show the trajectory of PF performance based on DR measurements and conventional FP while using RSS collected from using 6APs and 1AP. Yellow lines illustrate the output of FP positions. Blue lines in Figs. 59.3 and 59.5 show the trajectory of PF performance based on DR measurements and FPM method using RSS collected from using 6AP and 1AP. Black circles highlight the doorways in the building.

Results are listed in Table 59.1. Error in the DR column is the average distance between the DR trajectory and true trajectory from independent DR measurements. PF columns show errors of the PF trajectory when using DR and RSS measurements integrated PF.

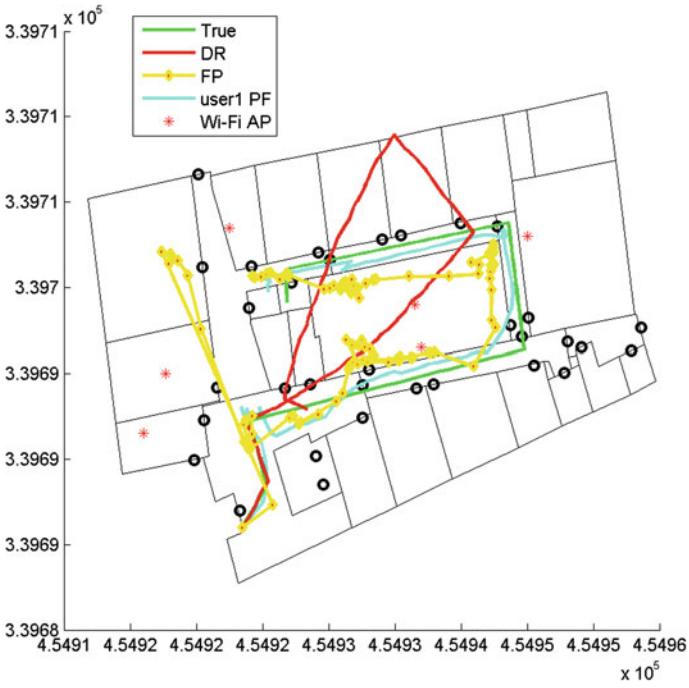

Fig. 59.2 DR and FP (6AP) based PF

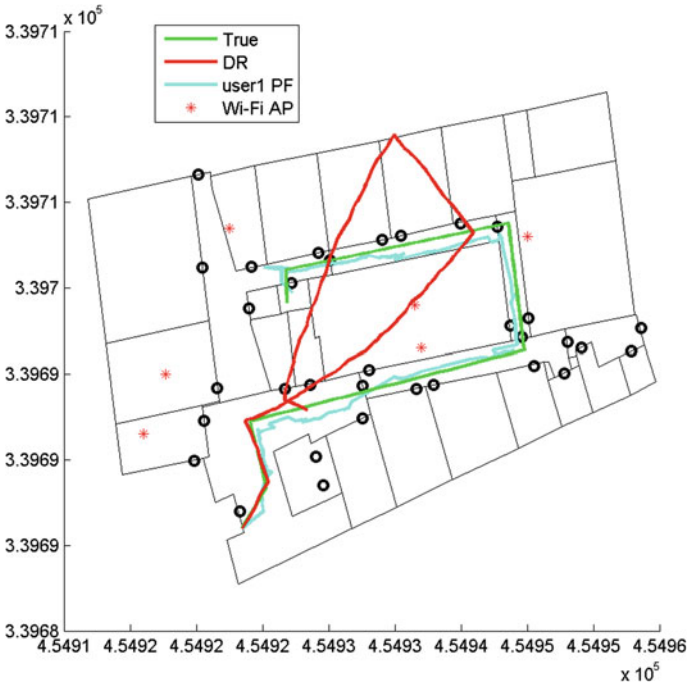

Fig. 59.3 DR and FPM (6AP) based PF

59.3.2.2 Scenario 2

This scenario is designed to identify how collaborative ranging could improve positioning results. In the model, two mobile users walk parallel to each other in a 50 × 50 area and ranging distance information between users as well as DR and Wi-Fi information (FPM method is used) is collected. Figure 59.6 is the trajectory of two users when not using ranging information. Figure 59.7 shows the trajectory when ranging is used between the two users.

Positioning results with ranging and without ranging are listed in Tables 59.2 and 59.3 respectively. Four sets of scenarios are simulated for this case. The first set is two users moving in the same direction; both 90° to the *x*-axis, their DR drift bias are in the same direction as well, either both left or right. The second set is two users both moving 90° to the *x*-axis, but with drifts the opposite direction, as shown in Figs. 59.6 and 59.7. In the third and fourth set, the left user moves −90° to the *x*-axis, thus moving in the opposite direction to the user on the right-hand side, respectively for each set their drift bias are in the same and opposite directions.

A model of two users moving perpendicular to each other with four cases was also simulated. In the first and second set, the first users moves 90° to the *x*-axis,

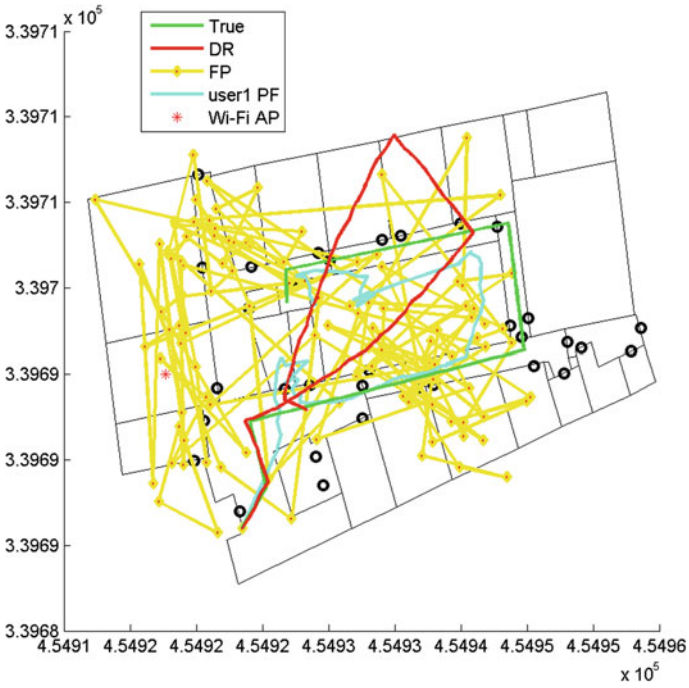

Fig. 59.4 DR and FP (1AP) based PF

while the second user moves 90° to the *y*-axis, drift bias are in the same and opposite direction for each set. For the third and fourth set, the first user moves 90° to the *x*-axis, while the second users moves −90° to the *y*-axis, with the same and opposite drift direction respectively. Figures 59.8 and 59.9 show the trajectory for case 2 when not including and including ranging information respectively. Results are listed in Tables 59.4 and 59.5.

59.3.2.3 Scenario 3

The ranging information is employed to two mobile users on Floor A of NGB. Respectively, results are listed below for using RSS from all APs in the building to using only ranging information and no Wi-Fi at all. In Figs. 59.10 and 59.11, blue and magenta lines plot the PF trajectory of two mobile users, DR trajectory is plotted in red lines and the true trajectory is plotted in green. Results are listed in Table 59.6.

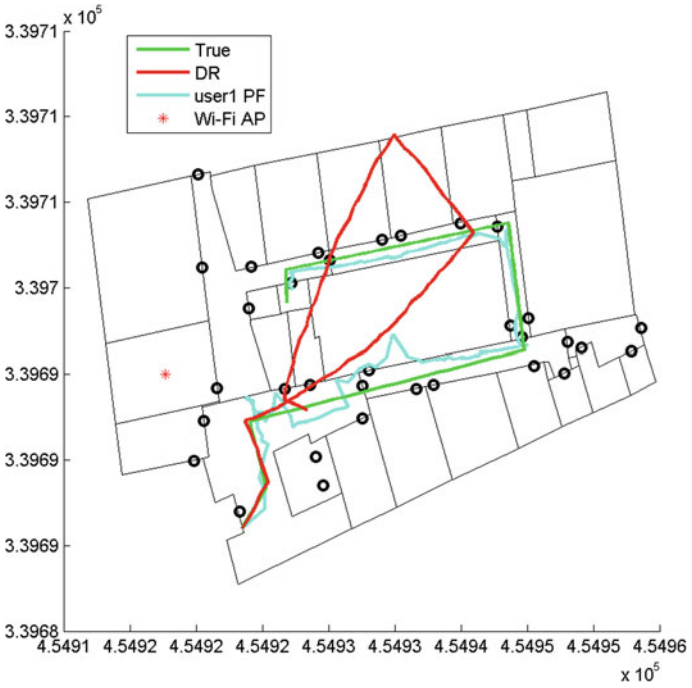

Fig. 59.5 DR and FPM (1AP) based PF

Table 59.1 Positioning errors (m)

	DR	PF (conv. FP)	PF (FPM)
6AP	4.80	2.12	1.72
3AP	4.80	1.50	1.77
2AP	4.80	2.56	1.59
1AP	4.80	2.79	1.52

59.4 Analysis and Conclusion

59.4.1 Result Analysis

From results obtained in Scenario 1, it could be recognized that the FPM method provides better positioning information. FPM keeps all possible positions from RSS matching and let particles decide which position matches best with the locations of the particles consequently keeping all possible solutions in the filter until some solutions come to a dead end and their weight drops to zero.

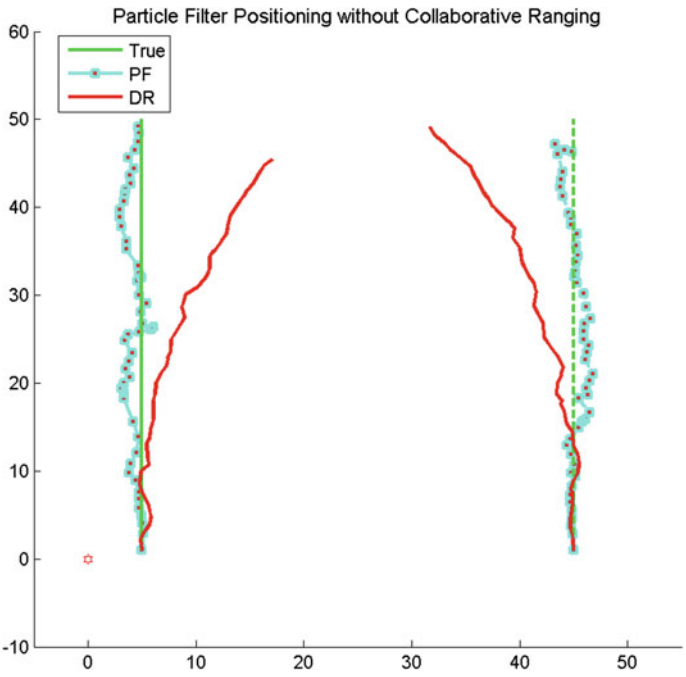

Fig. 59.6 PF trajectory without ranging

Scenario 2 helps to discover when collaborative ranging improves positioning. Ranging only constraint users to be at a relatively correct distance from each other, hence both users could still follow the wrong trajectory. From the results, we could see an overall 30 % improvement for the two users when moving parallel to each other and an overall 50 % improvement when moving perpendicular to each other. It could also be discovered that ranging improves positioning results greater when two users are walking in different directions. This could be due to effect of cancelling drift bias. In these situations, implementing ranging information could help to pull or push the two users into the right trajectory.

When implementing the ranging method to two users moving on Floor A in NGB, positioning accuracy showed to improve by an average of 70 % for both users when compared to DR positioning results, an improvement of 25 % when compared to non-ranging positioning for user 1, with a largest error of 3.91 m and smallest 0.08 m. What should also be noticed is that taking away Wi-Fi infrastructure will not break the system when either FPM method or ranging information is integrated. Therefore, the system has the potential of providing continuous navigation even if Wi-Fi AP infrastructure collapses or changes.

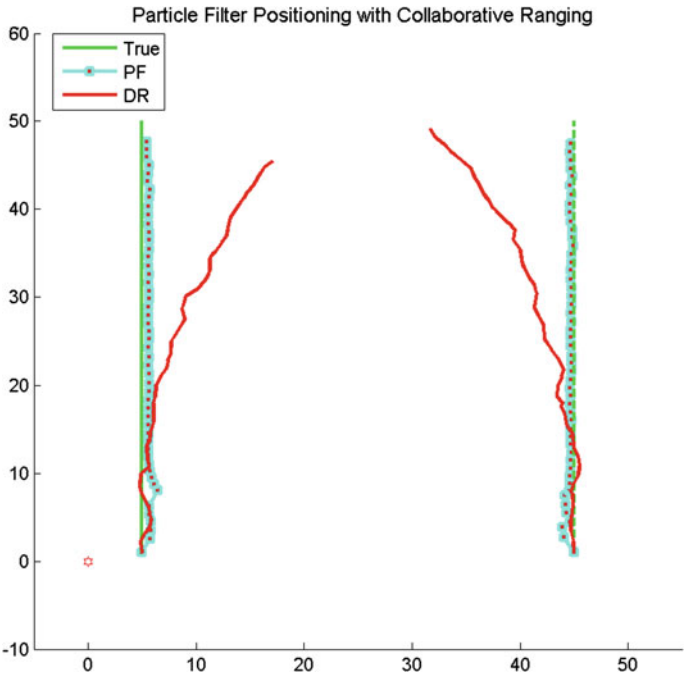

Fig. 59.7 PF trajectory with ranging

Table 59.2 Positioning errors with ranging (m)

	User 1		User 2	
	DR	PF (ranging)	DR	PF (ranging)
Case 1	4.71	1.48	3.88	1.61
Case 2	4.71	1.25	5.31	1.31
Case 3	4.29	0.87	5.31	0.95
Case 4	4.29	0.93	3.88	0.80

Table 59.3 Positioning errors without ranging (m)

	User 1		User 2	
	DR	PF (no ranging)	DR	PF (no ranging)
Case 1	4.71	1.71	3.88	1.83
Case 2	4.71	1.61	5.31	1.54
Case 3	4.29	1.85	5.31	1.42
Case 4	4.29	1.83	3.88	1.67

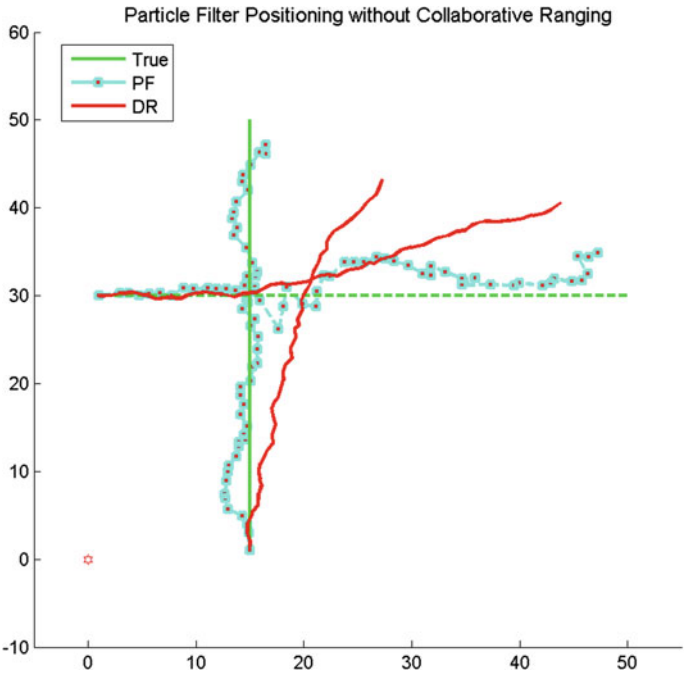

Fig. 59.8 PF trajectory without ranging

59.4.2 Conclusion and Future Work

In this paper, a collaborative indoor positioning and navigation algorithm using Particle Filtering is presented. We first discussed the sensors implemented in the collaborative system. The proposed system model was then introduced. Simulations using the proposed algorithm were presented.

The collaborative positioning algorithm employs several different positioning techniques to overcome the limitations of single sensor measurements. As DR drifts grow with time, adding Wi-Fi data and ranging constraint could help to correct the bias. Wi-Fi networks are unstable and RSS fingerprints do not always indicate the correct position, therefore, DR data and ranging constraint could help to eliminate positions that are far from possible positions. Collaborative ranging implemented PF has proven to be effective for indoor positioning and navigation. With the proposed method, the system becomes less reliant to Wi-Fi network.

However, real life situations are far more complicated. More users could appear in the designated area; users could be walking in random directions. When only

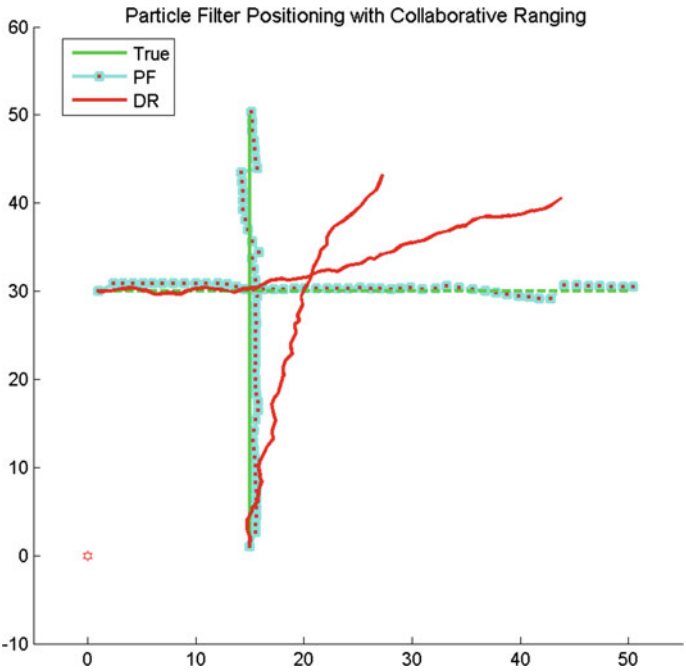

Fig. 59.9 PF trajectory with ranging

Table 59.4 Positioning errors without ranging (m)

	User 1		User 2	
	DR	PF (no ranging)	DR	PF (no ranging)
Case 1	4.77	2.15	4.77	2.48
Case 2	4.77	2.40	5.20	1.56
Case 3	5.20	1.55	5.20	1.70
Case 4	5.20	1.56	4.77	1.49

Table 59.5 Positioning errors with ranging (m)

	User 1		User 2	
	DR	PF (ranging)	DR	PF (ranging)
Case 1	4.77	0.66	4.77	1.01
Case 2	4.77	0.69	5.20	1.02
Case 3	5.20	0.88	5.20	0.74
Case 4	5.20	1.12	4.77	0.64

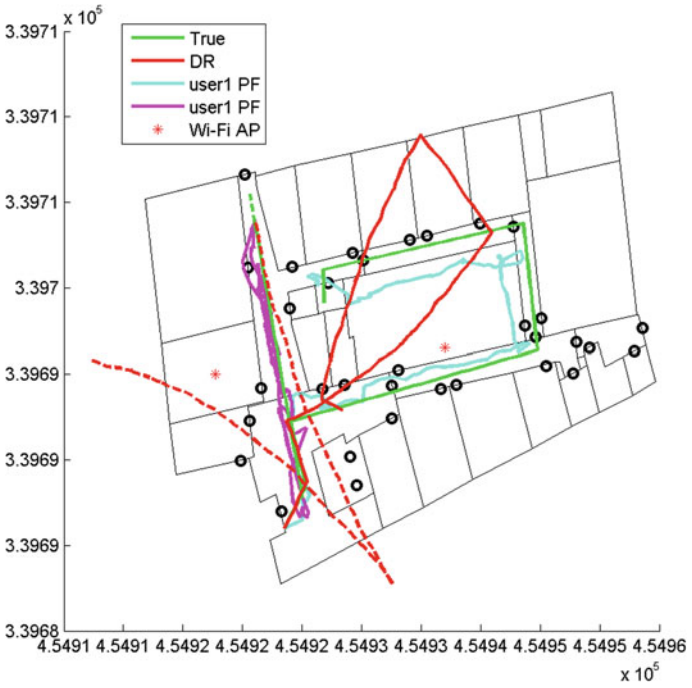

Fig. 59.10 PF trajectory without ranging

two users were simulated, ranging does not always improve results much. Failure could also occur when both DR and RSS information are dragging particles into the room on the other side of the wall where new particles would eventually be resampled in the wrong room.

Future work aims to test model robustness in real life scenarios and eliminate failure situations as much as possible by adding more users into the system. In the next stage, inertial measurements from a MicroStrain inertial measurement unit attached onto users and ranging measurements from UWB nodes carried by users will be implemented into the filter. Further research on taking out building map information and RSS database should also be investigated.

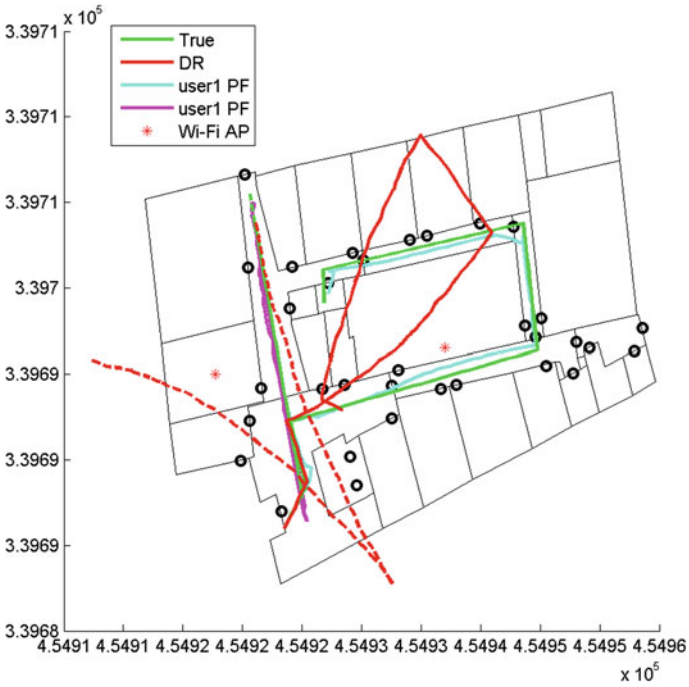

Fig. 59.11 PF trajectory with ranging

Table 59.6 Positioning Errors (m)

	User 1		User 2	
	DR	PF (ranging)	DR	PF (ranging)
6APs	4.80	1.22	6.69	1.67
2APs	4.80	1.16	6.69	1.51
1AP	4.80	1.27	6.69	1.75
No Wi-Fi	4.80	1.34	6.69	1.82

References

1. Benford S (2005) Future Location-Based Experiences. JISC Technology And Standards Watch, London, UK. Available at: http://www.jisc.ac.uk/techwatch.
2. Zandbergen PA (2009) Accuracy of iPhone locations: a comparison of assisted GPS, Wifi and cellular positioning. Trans GIS 13:5–25
3. Chan LW, Chiang JR, Chen YC, Ke CN, Hsu J, Chu HH (2006) Collaborative localization: enhancing Wifi-based position estimation with neighbourhood links in clusters. Pervasive Comput: Lect Notes Comput Sci 3968:50–66, Springer, Berlin/Heidelberg
4. Zhang B, Yu F, Zhang Z (2009) Collaborative Localization Algorithm For Wireless Sensor Networks Using Mobile Anchors. *Computational Intelligence And Industrial Applications*, Nov.,pp.309-312

5. Grejner-Brzezinska DA, Markiel JN, Toth CK, Zaydak A (2012) Collaborative navigation in transitional environments. GPS World, vol 23. pp. 43–49
6. Hide C (2003) Integration Of GPS and low cost INS measurements. P.h.D. Thesis, University Of Nottingham
7. Molisch AF (2011) Wireless communications. Wiley, UK
8. Bose A, Foh CH (2007) A practical path loss model for indoor Wifi positioning enhancement. In: Proceedings of 6th international conference on information, communications & signal processing, vol 1–4. pp. 876–880
9. Wang Y, Jia X, Lee HK (2003) An indoors wireless positioning system based on wireless local area network infrastructure. In: Proceedings of 6th international symposium on satellite navigation technology including mobile positioning & location services, Melbourne, Australia, 22–25 Jul
10. Ultra-Wideband (2012) http://en.wikipedia.org/Wiki/Ultra-Wideband
11. Choliz J, Hernandez-Solana A,Valdovinos A (2011) Evaluation of algorithms for UWB indoor tracking. 8th Workshop on Positioning Navigation and Communication (WPNC), 7-8 April 2011, Dresden, Germany, pp 143–148
12. Meng X, Gao Y, Kwok KH, Zhao H (2012) Assessment Of UWB for ubiquitous positioning and navigation, In: Proceedings on 2012 ubiquitous positioning indoor navigation and location based service (UPINLBS), Finland, 3–5 Oct
13. Ristic B, Arulampalam S, Gordon N (2004) Beyond the kalman filter: particle filters for tracking applications. Artech House, London, UK
14. Pinchin J, Hide C, Moore T (2012) A particle filter approach to indoor navigation using a foot mounted inertial navigation system and heuristic heading information. In: Proceedings of 2012 international conference on indoor positioning and indoor navigation, Sydney, Australia 13–15 Nov 2012

Chapter 60
A MEMS Multi-Sensors System for Pedestrian Navigation

Yuan Zhuang, Hsiu Wen Chang and Naser El-Sheimy

Abstract Micro-electro-mechanical system (MEMS) sensors are widely used in many applications due to their low cost, low power consumption, small size and light weight. Such MEMS sensors which are usually called multi-sensors include accelerometers, gyroscopes, magnetometers and barometers. In this research, Samsung Galaxy Note is used as the MEMS multi-sensors platform for pedestrian navigation. It contains a three-axis accelerometer, a three-axis gyroscope, a three-axis magnetometer and GPS receiver. Pedestrian Dead Reckoning (PDR) algorithms which include step detection, stride length estimation, heading estimation and PDR mechanization are carefully discussed in this paper. GPS solution is the major aiding source to reduce the MEMS IMU position, velocity and attitude errors when GPS signals are available. Magnetometers are also used to reduce the attitude errors of gyroscopes if there are no environment disturbances. A loosely-coupled extended Kalman Filter is implemented in the paper to fuse all the information to obtain the position result. Two typical scenarios are tested and analyzed in this paper: walking from outdoor to indoor and indoor walking. The MEMS multi-sensors system works well for both scenarios. To conclude, algorithms of MEMS multi-sensors system can provide an accurate, reliable and continuous result for pedestrian navigation on the platform of smart phone.

Keywords MEMS · Multi-sensors · Pedestrian navigation · Dead reckoning

Y. Zhuang (✉) · H. W. Chang · N. El-Sheimy
Department of Geomatics Engineering, The University of Calgary,
2500 Univerisy Dr. NW, Calgary, AB, Canada
e-mail: zhuangy@ucalgary.ca

J. Sun et al. (eds.), *China Satellite Navigation Conference (CSNC) 2013 Proceedings*, Lecture Notes in Electrical Engineering 245,
DOI: 10.1007/978-3-642-37407-4_60,

60.1 Introduction

Micro-electro-mechanical system (MEMS) sensors are widely used in many applications due to their low cost, low power consumption, small size and light weight. Such MEMS sensors include accelerometers, gyroscopes, magnetometer and barometer. On the current market, they can be found in various consumer products such as smart phones, personal digital assistants and gaming devices, etc. One important application of them is a pedestrian navigation system (PNS). The goal of PNS is to provide a continuous and reliable position for personal use in many different applications such as safety-of-life purpose and commercial utilization.

Low-cost MEMS inertial measurement unit (MEMS-IMU) has a main disadvantage: its in-run bias, scale factor and high level of noise accumulate as a function of time. Therefore, they cannot be used to provide relatively long term accurate solution. In order to limit the error accumulation over time, MEMS-IMU is usually combined with other sensors (such as magnetometer and barometer) and integrated with GPS to achieve desired accuracy by using fusion algorithms.

For pedestrian navigation application, MEMS-IMU data are used in two different ways to compute the navigation solution. The first way implements traditional Inertial Navigation System (INS) mechanization equation which computes user's relative position, velocity and attitude by using raw acceleration and angular rate data. Personal Dead Reckoning (PDR) is another approach for pedestrian navigation. PDR algorithms involve three critical procedures: detecting a step, finding heading and estimating step length. These parameters are then used to set up PDR mechanization equation in which user's horizontal position will be estimated. The main advantage of the first method is the ability to provide 3D position, velocity and attitude. However, it has the demerit that navigation solution errors grow up with time rapidly at this way. On the other hand, when using PDR, navigation solution errors are proportional to the traveled distance, and not to the time [1]. Both of these methods require additional sources and algorithms to maintain the required accuracy over time. GPS solution is the major aiding source to reduce the MEMS IMU position, velocity and attitude errors when GPS signal is available. Magnetometer is a complementary way to provide attitude besides the gyroscope.

Some of the studies related to pedestrian dead reckoning are based on MEMS-IMU mounted at foot to obtain the best results by utilizing zero velocity updates (ZUPT) [2]. Some of the studies are based on PNS mounted at waist belt [3]. However, it is not convenient to mount PNS systems at such parts of body. Currently, most smart phones contain multi-sensors. The widely use of smart phones makes it a good multi-sensors platform for pedestrian navigation. In this research, Samsung Galaxy Note is used as the platform for pedestrian navigation which contains 3-axis accelerometer, 3-axis gyroscope, 3-axis magnetometer, a barometer and GPS chip. The focus of this study is to develop an appropriate and robust PDR algorithm for multi-sensors in smart phones.

This paper is organized as follows. Section 60.2 introduces the step detection algorithm; Sect. 60.3 presents the methods to compute the stride length; the heading estimation algorithms are described in Sect. 60.4; PDR mechanization is discussed in Sect. 60.5 followed by the field tests and result' analyses given in Sect. 60.6.

60.2 Step Detection

Gait cycle is the basic to detect steps. A gait cycle for this study is defined as the time when the foot leaves the ground till the time when it hits the ground again. The detection algorithm contains four steps.

1. Compute the magnitude of the acceleration for each sample.

$$a_i = \sqrt{a_{xi}^2 + a_{yi}^2 + a_{zi}^2} \tag{60.1}$$

where a_{xi}, a_{yi} and a_{zi} are x-axis, y-axis and z-axis acceleration at i epoch. a_i is the magnitude of the accelerations at i epoch.

2. Choose the width of a window w to compute the local mean acceleration. This step is very important. The chosen window length affects the result significantly.
3. Compute the local mean acceleration value of each sample.

$$\bar{a}_i = \frac{1}{2w+1} \sum_{q=i-w}^{i+w} a_q \tag{60.2}$$

where $\bar{a}_i$ is the mean of accelerations at i window, a_q is the magnitude of the acceleration at q epoch.

4. Find the peak. The time between two peaks means a step period.

$$(\bar{a}_k - \bar{a}_{k-1}) \cdot (\bar{a}_{k+1} - \bar{a}_k) < 0 \tag{60.3}$$

where $\bar{a}_{k-1}$, $\bar{a}_k$ and $\bar{a}_{k+1}$ are means of accelerations at $k-1$, k and $k+1$ window.

60.3 Stride Length Estimation

The stride length is defined as the traveled distance between two heel impacts. It is necessary to estimate the stride length at each stride to compute the total forward moving distance of a person. Obviously, it cannot be assumed to be constant. Typically, different people's stride lengths are different. The stride lengths do not

stay the same even for the same person in different environments. Therefore, two methods to estimate stride length are used in this paper.

The first algorithm assumes the stride length is proportional to the vertical movement of the human hip [4]. The vertical movement is obtained from the largest acceleration difference in vertical direction at each step. The equation used to estimate the stride length is written as follows:

$$SL = \sqrt[4]{a_{z\max} - a_{z\min}} \cdot K \tag{60.4}$$

where $a_{z\max}$ is the maximum value of a_z, $a_{z\min}$ is the minimum value of a_z, and K is a constant need to be selected experimentally or calibrated.

The second algorithm estimates the average walking velocity of a person first. Then, the step length is calculated by Eq. (60.5)

$$SL = \bar{v} \cdot \Delta t_{stride} \tag{60.5}$$

where $\bar{v}$ is the average walking velocity. Δt_{stride} is the time spent to finish one stride. The average walking velocity comes from traditional INS mechanization equation [5]. It is reliable when GPS signal is available to reduce the errors of MEMS IMU. However, it is not reliable in indoor environment due to the unavailability of GPS signals. The two methods are combined to provide the estimation of stride length.

60.4 Heading Estimation

There are three main ways to estimate the heading of a person: using gyroscope, magnetometer or GPS. The first two methods are usually used to estimate the PDR heading while the third one is normally utilized to update the PDR heading in the GPS/PDR integration.

Gyroscope provides a relative heading. Therefore, an initial heading should be given by GPS or personally. It is accurate only at short term due to the accumulated error as a function of time. However, comparing to magnetometer which can be easily distributed by the environment, it will not suffer from sudden change in heading estimation.

The magnetometer provides long term accurate absolute azimuth. However, the main problem of this method is the affection of external disturbance. Gyroscopes can be used to detect external disturbance using Eq. (60.6) [6].

$$\begin{aligned} &|\omega_G - \omega_C| > th \\ &\omega_C = \frac{\psi(t_{k+1}) - \psi(t_k)}{t_{k+1} - t_k} \end{aligned} \tag{60.6}$$

where ω_G is the derived angle rate from magnetometer measurements, ω_C is the angle rate of the gyroscope, th is the threshold selected at the calibration process, and ψ is the magnetometer measurement which means the magnetic azimuth.

Another problem for the magnetometer is that it's not easy to calibrate. In this study, the algorithm in [7] is used to calibrate the magnetometer.

Heading estimation based on GPS is usually used as the PDR heading update. It also can be used to give an initial value for heading estimation based on gyroscopes. The accuracy of GPS heading depends on GPS velocity [8]. Typically, when GPS velocity is larger than 1 $m \cdot s^{-2}$, it can provide useful heading.

The integration of the complementary qualities of the gyroscope and magnetometer can provide a robust heading estimation for PDR. The magnetometer heading is incorporated in the navigation solution and used to reduce the gyroscope's errors. When magnetometer is disturbed by the environment the gyroscope is used to update the heading. When GPS signal is available, GPS heading is used to update the PDR heading. The details of three methods are shown at Table 60.1.

60.5 PDR Mechanization

PDR algorithm is the determination of current position using the information of previous position, travelled distance and heading. The pedestrian traveled distance needs step detection, stride length estimation and heading estimation which are discussed in Sects. 60.2 and 60.3. After getting all the information, the PDR algorithm will use the following equation to estimate the current position.

$$\begin{aligned} E_k &= E_{k-1} + \hat{s}_{(k-1,k)} \cdot \sin(\hat{H}_{k-1}) \\ N_k &= N_{k-1} + \hat{s}_{(k-1,k)} \cdot \cos(\hat{H}_{k-1}) \end{aligned} \tag{60.7}$$

where (E_{k-1}, N_{k-1}) and (E_k, N_k) are the previous and current positions in local level frame, $\hat{s}_{(k-1,k)}$ is the estimated stride length since step k−1 to k, and $\hat{H}_{k-1}$ is the estimated heading at step k−1.

Table 60.1 Summary of three methods for heading estimation

Heading	Mag-based	Gyro-based	GPS based
Theory	$H_M = \text{atan}_2\left(\frac{H_y}{H_x}\right)$	$H_{G(k+1)} = H_{G(k)} + \int_{t_k}^{t_{k+1}} \omega(t)dt$	$H_{gps} = \text{atan}_2\left(\frac{v_E}{v_N}\right)$
Pros	Absolute azimuth & long term accuracy	Less disturbance & short term accuracy	Absolute azimuth
Cons	Unpredictable external disturbance	Drift & relative azimuth	Accuracy depends on velocity
Calibration	Hard	Easy	No
Cost	Low	High	Low

60.6 Field Tests and Results

The data was collected at University of Calgary campus to evaluate the navigation performance of the proposed algorithm using Samsung Galaxy Note. As shown in Fig. 60.1, the smart phone is held in hands during the test. In Fig. 60.1, x-axis is in forward direction, y-axis is in right direction and z is in down direction.

60.6.1 Step Detection Algorithm Test

Three datasets are collected to test the step detection algorithm. The result is shown at Table 60.2 and Fig. 60.2. In Table 60.2, the average accuracy could achieve 96.53 %. It is acceptable due to the experimental situation. There was a lot of snow on the ground when the data was collected at outdoor environment. It affects the result of step detection because gait movements need caution to avoid slipping. If there was no snow, the result is expected to be better.

Figure 60.2 also shows the algorithm detects the steps successfully. It is worth mentioning that there is no green point at beginning because the algorithm starts after GPS signal is available.

60.6.2 Stride Length Estimation Algorithm Test

Two group data of walking at a line are used in the stride length estimation because the averages of the true stride length are easy to obtain. The result shows estimation error is about 2 %. It is accurate enough considering the affection of the snow on the group. Table 60.3 shows the result of stride length estimation.

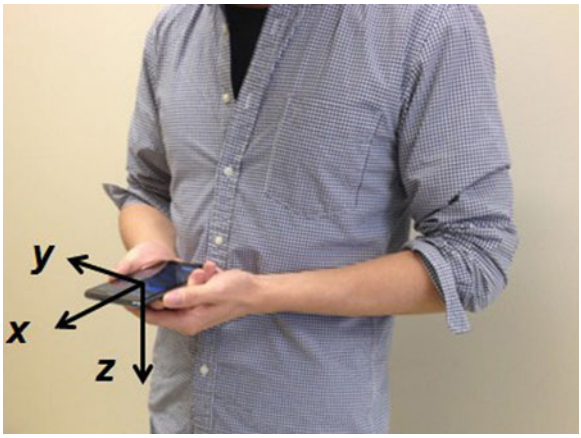

Fig. 60.1 Smart phone held in hand during the test

Table 60.2 Result of step detection algorithm

Detected steps	True steps	Accuracy (%)	Average (%)
770	787	97.84	96.53
223	230	96.96	
109	115	94.78	

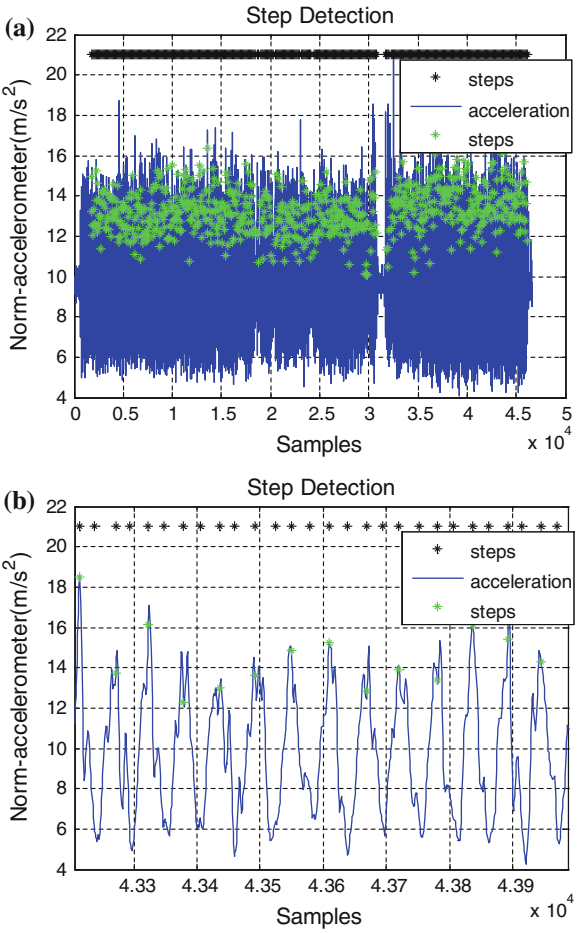

Fig. 60.2 Step detection result. **a** Result. **b** Enlarge view of result

60.6.3 Heading Estimation Algorithm Test

Two datasets are used to test the heading estimation algorithm. One dataset is collected in the environment includes indoor and outdoor. Another one is completely in indoor environment. The heading results are shown in Fig. 60.3. Because there is no reference system to provide accurate true heading, the reference heading is derived from the direction of walking shown on the Google map.

Table 60.3 Result of stride length (SL) estimation algorithm

Average estimated SL (m)	Average true SL (m)	Accuracy (%)	Average (%)
0.3797	0.3822	99.35	98.76
0.3892	0.3822	98.17	

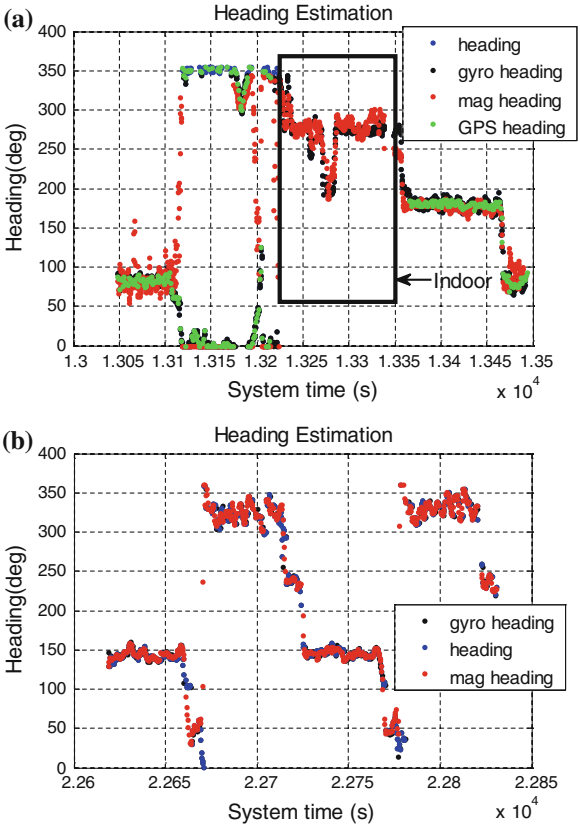

Fig. 60.3 Result of head estimation. **a** Dataset 1. **b** Dataset 2

Compare to the reference heading most of the results of PDR heading, gyro heading, magnetometer heading and GPS heading (if available) are less than 10°. They are acceptable.

60.6.4 Trajectory

Two trajectories of the two datasets are shown in Fig. 60.4. In Fig. 60.4a, the trajectory starts from outdoor to indoor, then outdoor again. The total time is about 7 min, while there is about 2 min indoor environment. The red, green and yellow

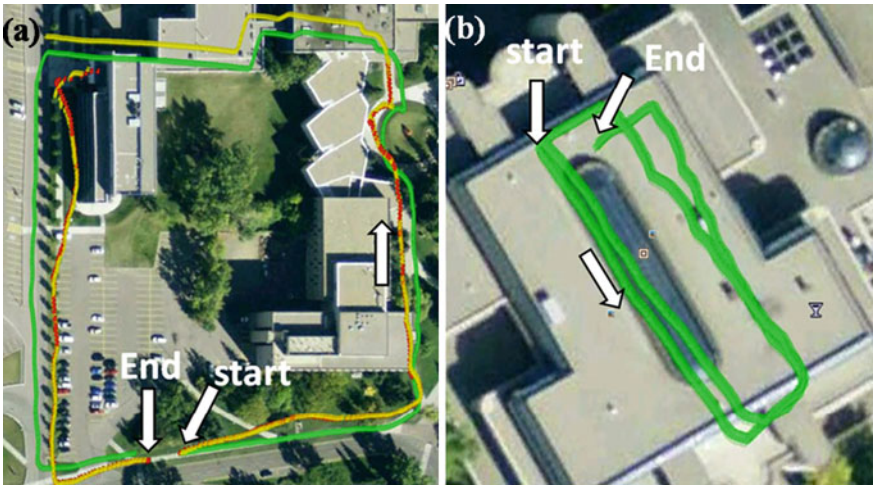

Fig. 60.4 Trajectories of two dataset. **a** Dataset 1. **b** Dataset 2

points represent results of GPS only, PDR only and GPS/PDR integration. After 2 min indoor walking, the accumulated position error shown in Fig. 60.4a (left-up corner) reaches 10 m and the maximum heading is about 10°. The initial heading and position for the PDR in indoor are obtained from the last available GPS signal. It is not accurate enough. Therefore, the indoor part of trajectory is not good in Fig. 60.4a. And after investigation, this is heavily caused by strong magnetic disturbance. Although gyroscope can detect magnetic interference, it is lack of heading update.

In Fig. 60.4b, the trajectory is the result of PDR only due to no available GPS signals in indoor environment. The total time is about 4 min. The maximum position error is about 8 m, and the maximum heading error is about 10°. Because the initial point is at indoor environment, so GPS signal is not available. The initial position and heading are given personally. Due the relatively accurate initial heading and position, the maximum position error is less than the indoor part of Fig. 60.4a.

60.7 Conclusions and Future Works

As shown in these experiments, the algorithms of MEMS multi-sensors system can provide accurate, reliable and continuous result for pedestrian navigation on the platform of smart phones. PDR algorithms are developed based on MEMS IMU, magnetometers and GPS. The field results have demonstrated the multi-sensors algorithm for pedestrian navigation works well during the test. Although the algorithms are implemented at Samsung Galaxy Note, they are also suitable for other smart phones. The future works will be threefold: (1) Better heading

estimation algorithm will be developed for the PDR to provide more accurate result. (2) Error of step detection will be reduced by new algorithm development. (3) Wi-Fi will be included at the algorithms for pedestrian navigation.

References

1. Mezentsev O (2005) Sensor aiding of HSGPS pedestrian navigation. PhD Thesis, Department of geomatics engineering, University of Calgary, Canada, UCGE Report No. 20212
2. Jimenez AR, Seco F, Priteo C, Guevara J (2009) A comparison of pedestrian dead-reckoning algorithms using a low-cost MEMS IMU. WISP 2009, Budapest Hungary
3. Zhao X, Syed Z, Wright DB, El-Sheimy N (2009) An economical and effective multi-sensor integration for portable navigation system. In: Proceeding of the institute of navigation GNSS 2009 conference, Savannah
4. Weinberg H (2002) Using the ADXL202 in Pdeometer and personal navigation applications. Analog devices AN-602 application note
5. El-Sheimy N (2012) Inertial techniques and INS/DGPS integration, ENGO 623-course notes. Department of Geomatics Engineering, University of Calgary, Canada
6. Ladetto Q, Gabaglio V, Merminod B (2001) Combining gyroscopes, magnetic compass and GPS for pedestrian navigation. International symposium on kinematic systems in geodesy, geomatics, and navigation, Banff, pp 205–212
7. Gebre-Egziabher D, Elkaim GH, Powell JD, Parkinson BW (2001) A non-linear, two-step estimation algorithm for calibrating solid-state strapdown magnetometers. In: Proceedings of the international conference on integrated navigation systems, St. Petersburg, pp 290–297
8. Li Q, Dempster A, Li B, Wang J, Rizos C (2006) A low-cost attitude heading reference system by combination of GPS and magnetometers and MEMS inertial sensors for mobile applications. Journal of Global Positioning System

Chapter 61
Fusion of Wi-Fi and WSN Using Enhanced-SIR Particle Filter for Hybrid Location Estimation

Dongjin Wu, Linyuan Xia and Jing Cheng

Abstract It is extremely important for pedestrian navigation and location-based services (LBS) that users of portable devices can quickly and accurately locate themselves wherever they might be. In this paper, we propose a novel hybrid approach for indoor and outdoor localization in urban area based on Enhanced Sequential Importance Resampling (Enhanced-SIR) Particle Filter (PF). The approach implements by gathering and processing signal strength information from Wi-Fi and other signals of opportunity, such as wireless sensor network (WSN). It combines WSN (2.4 GHz Zigbee) with Wi-Fi for hybrid location estimation, in which, Wi-Fi signal is used for the entire area, and WSN signal serves as the enhanced signal to assist the resampling of particles. The method of Enhanced SIR can not only solve the problem of degeneracy, but also improve the sampling accuracy of particles. Experimental results demonstrate that the proposed hybrid approach can provide more accurate location estimates in indoor and outdoor areas, and costs equivalent runtime, compared to conventional SIR PF.

Keywords Wi-Fi · Wireless sensor network · Hybrid location estimation · Enhanced-SIR particle filter

D. Wu · L. Xia (✉) · J. Cheng
Department of GIS, Geography and Planning School, SunYat-Sen University,
135# Xingangxi Road, Guangzhou 510275, China
e-mail: xialiny@mail.sysu.edu.cn

D. Wu
e-mail: wudj-no.15@163.com

D. Wu · L. Xia · J. Cheng
Guangdong Key Laboratory for Urbanization and Geo-simulation, Geography
and Planning School, Sun Yat-sen University, Guangzhou 510275, China

J. Sun et al. (eds.), *China Satellite Navigation Conference (CSNC) 2013 Proceedings*, Lecture Notes in Electrical Engineering 245,
DOI: 10.1007/978-3-642-37407-4_61,

61.1 Introduction

Following with the development of Global Navigation Satellite Systems (GNSS) and infrastructures of signals of opportunity, ubiquitous location for LBS and Smart City Project is proliferated. Conventional location technologies that depend on GNSS and cellular network are limited in urban canyons and indoor areas, because of weak signals and low location accuracy. Wi-Fi is recently regarded as one of the most potential technologies for indoor and outdoor location, since the hotspots are widespread, and it is easy to measure received signal strength indicator (RSSI) which is crucial for the application of mobile devices.

Individual technology, such as Wi-Fi based location may perform well in specific scenarios, but it cannot satisfy requirements of ubiquitous location. Existed researches have improved the coverage [1] and accuracy [2] of location services more or less, but research on hybrid model for multi-signals of opportunity based location estimation is still needed.

This paper presents a novel hybrid location technique employing Enhanced Sequential Importance Resampling (E-SIR) Particle Filter (PF). Depending on the characteristics of signals of Wi-Fi and wireless sensor network (WSN, 2.4 GHz Zigbee), we propose an E-SIR method assisted by multi-signals of opportunity based on conventional SIR [3]. E-SIR method combines the inherent characteristics of Wi-Fi and WSN to optimize the structure of particles, and further to improve tracking ability of PF. Experimental results demonstrate that our proposed hybrid location technique performs better, compared to individual signal based methods.

61.2 Signals of Opportunity Based Hybrid Location Estimation

The techniques applied by signals of opportunity based location estimation fall into the following three categories, proximity, intersection and scene analysis [4]. Location fingerprinting [5, 6] is a typical scene analysis method, and it is commonly used by RSSI based location systems. Location fingerprinting consists of two phases, offline and online. In the offline phase, we should construct a radio map, which is made up of RSSI vectors at each location covering the entire area. In the online phase, location of the mobile device is estimated using one or multi location fingerprints which are selected depending on the matching scores between online RSSI vector sampled by the mobile device and location fingerprints.

For ubiquitous localization, hybrid location estimation that combines different technologies and techniques is an alternative solution. For example, the PlaceLab [1] combines technologies, such as GPS, Wi-Fi, GSM and Bluetooth beacons for user localization. The coverage of this approach is nearly 100 %, but the accuracy is about 20–30 m. Kritzler and Muller [7] combine the UWB, RFID, keystroke

sensors and Wi-Fi technologies in an industrial environment to provide accurate location. They implement the hybrid location estimation by averaging all position estimates from available technologies. McGuire et al. [2] explore the data fusion of RSS and TDOA measurements at the estimate and measurement level in CDMA cellular network. The estimate level indicates that location estimate is a linearly weighted average between two individually outcomes according to the estimate's error covariance. And for the measurement level, location estimate is combined use both of the RSS and TDOA measurements. The WHERE project [8] investigates the performances of the fusion of TOA and RSS measurements under different implementations of Kalman Filter (KF). And it also describes the hybrid methods of TOA/AOA/angle of departure (AOD)/Doppler Shift and TOA/AOD/Doppler Shift. In addition, it also explores the performances of static positioning, as well as Extended Kalman Filter (EKF)-based dynamic tracking, combining the measurements of satellite and cellular networks. Moreover, it presents a Rao-Blackwellized PF implementation for hybrid of TOA and AOA measurements.

While the aforementioned research has focused on hybrid methods for different measurements or different technologies, less attention has been paid to the models about data fusion for different signals of opportunity.

61.3 Fusing Wi-Fi with WSN Using Enhanced-SIR Particle Filter for Hybrid Location Estimation

61.3.1 Fusion of Signals of Opportunity

Based on the analysis about the stability and dynamic environment, signals of opportunity, such as Wi-Fi, WSN, RFID, Bluetooth can be selected and fused for the implementation of E-SIR PF. In the following, we take Wi-Fi and WSN for example to present how to fuse signals for practical operation.

Since Wi-Fi and WSN (IEEE 802.15.4 based Zigbee) both operates over radio frequency (RF) signals in the 2.4 GHz band, which is a license-free RF band and saturate with various users, they are probable mutual interference. However, signal of Wi-Fi seems to be more probable to be influenced, compared to 2.4 GHz Zigbee, because Wi-Fi (IEEE 802.11b) signal has a wider channel bandwidth (22 MHz for IEEE 802.11b, and 2 MHz for 2.4 GHz Zigbee [9]), and thereby it is less stable. We conducted a comparative experiment to explore the performances of signals propagation of Wi-Fi and WSN. Figure 61.1 presents the RSSI sampling series of two signals, which are under the same environment. In the figure, we observe that the amplitude of WSN RSSI series is about 1 dBm, and for Wi-Fi, it is about 3 dBm. The experimental result proves our inference. Considering the widespread infrastructure of Wi-Fi and the above analytical results, we choose WSN as the enhanced signal to assist Wi-Fi for hybrid location estimation.

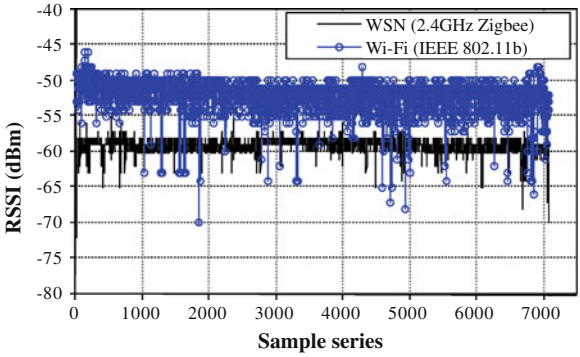

Fig. 61.1 RSSI sample series of Wi-Fi and 2.4 GHz Zigbee under the same environment

61.3.2 Enhanced-SIR Particle Filter for Hybrid Location Estimation

61.3.2.1 State Model

Let the state sequence denote as $\{X_k, k \in N\}$, considering the velocity of object indoors often stays small, the stationary state model is used, and can be formulated as

$$X_k = X_{k-1} + \omega_{k-1} \tag{61.1}$$

where $\omega_k \sim N(0, \sigma^2)$ is the state model noise.

Since the noisy observation of MS's location can't be measured directly and the estimation error can't be regarded as a Gaussian variable. The rational description of the relationship between the observations and states can be defined as

$$Z_k = h_k(X_k, \mu_k) \tag{61.2}$$

where h_k is a possibly nonlinear function, and μ_k is the observation noise.

Since PF can easily represent arbitrary probability density and converge to true posterior distribution even in non-Gaussian and non-linear systems [3, 10, 11], we choose PF for location estimation in this paper.

61.3.2.2 SIR Particle Filter

PFs are sequential Monte Carlo methods based on particles which can represent arbitrary probability densities, and can be applied to any state-space model [10]. Let $\{X^i_{0:k}, i = 1, \cdots, N_s\}$ denote a set of particles (N_s is the number of the particles), with the associated normalized weight w^i_k, and $X_{0:k} = \{X_j, j = 0, \cdots, k\}$ denote a set of states. Then the posterior density can be approximated as

$$p(X_{0:k}|Z_{1:k}) \approx \sum_{i=1}^{N_s} w_k^i \delta\left(X_{0:k} - X_{0:k}^i\right) \tag{61.3}$$

$\delta(\cdot)$ is Dirac delta function. The weight w_k^i is chosen using the principle of importance sampling [11]. Suppose $q(X_{0:k}|Z_{1:k})$ is the importance function, the weight can be

$$w_k^i \propto \frac{p\left(X_{0:k}^i|Z_{1:k}\right)}{q\left(X_{0:k}^i|Z_{1:k}\right)} \tag{61.4}$$

Since

$$q(X_{0:k}|Z_{1:k}) = q(X_k|X_{0:k-1}, Z_{1:k})q(X_{0:k-1}|Z_{1:k-1}) \tag{61.5}$$

and

$$p(X_{0:k}|Z_{1:k}) \propto p(Z_k|X_k)p(X_k|X_{k-1})p(X_{0:k-1}|Z_{1:k-1}) \tag{61.6}$$

With substitution of (61.5) and (61.6), (61.4) can be

$$w_k^i \propto \frac{p\left(Z_k|X_k^i\right)p\left(X_k^i|X_{k-1}^i\right)p\left(X_{0:k-1}^i|Z_{1:k-1}\right)}{q\left(X_k^i|X_{0:k-1}^i, Z_{1:k}\right)q\left(X_{0:k-1}^i|Z_{1:k-1}\right)} = w_{k-1}^i \frac{p\left(Z_k|X_k^i\right)p\left(X_k^i|X_{k-1}^i\right)}{q\left(X_k^i|X_{0:k-1}^i, Z_{1:k}\right)} \tag{61.7}$$

Equation (61.7) is the updating equation of weight. If $q(X_k|X_{0:k-1}, Z_{1:k}) = q(X_k|X_{k-1}, Z_k)$, the weight can be updated as

$$w_k^i \propto w_{k-1}^i \frac{p\left(Z_k|X_k^i\right)p(X_k^i|X_{k-1}^i)}{q(X_k^i|X_{k-1}^i, Z_k)} \tag{61.8}$$

Suppose the prior probability density $p\left(X_k^i|X_{k-1}^i\right)$ is regarded as the importance function $q(\cdot)$, the weight can be updated simply as

$$w_k^i \propto w_{k-1}^i p\left(Z_k|X_k^i\right) \tag{61.9}$$

Degeneracy problem can arise during the above phase, thus there are various schemes in literatures to limit the degeneracy, and the SIR algorithm [3] is an effective one. Since in every step the resampling is applied and the weight is set to N_s^{-1}, so the weight is computed as

$$w_k^i = p\left(Z_k|X_k^i\right) \tag{61.10}$$

Now, the $\widehat{X}_k$ can be recursively estimated using particles and associated normalized weights by

$$\widehat{X}_k = \sum\nolimits_{i=1}^{N_s} X_k^i w_k^i. \tag{61.11}$$

61.3.2.3 Enhanced SIR

Unfortunately, since RSSI measurements are easy to be distorted by dynamic environments, in the process of SIR the estimated probability density may be far away from true probability density. Depending on the knowledge about signal characteristics of WSN, we choose it as the assisting signal for the resampling of particles. First, RSSI measurements Z_k^0 of WSN signal is applied to determine a searching area around the reference node of WSN, with the searching radius R (as Fig. 61.2 depicts). Thanks to the development of Smart City, Wireless City, and Internet of Things (IOT), signals of opportunity will saturate our life in the future. Thus the searching radius R can be flexible from 0 to several meters. The particles in the searching area are selected, so we can get the a location set of selected particles Ψ_k,

$$D_i = \sqrt{\left(Loc_x^i - Loc_x^0\right)^2 + \left(Loc_y^i - Loc_y^0\right)^2},\ \Gamma_D = \{D_i < R\},\ i = 1, \ldots, N_s \tag{61.12}$$

$$\Psi_k = \left\{Loc_j = \left(Loc_x^j, Loc_y^j\right) : D_j \in \Gamma_D, j = 1, \cdots, N_k\right\} \tag{61.13}$$

where N_k is the number of selected particles. Now Ψ_k can be averaged to provide an initial location Loc_{new},

$$Loc_{new} = \left(Loc_x^{new}, Loc_y^{new}\right) = \frac{1}{N_k}\left(\sum_{j=1}^{N_k} Loc_x^j, \sum_{j=1}^{N_k} Loc_y^j\right) = \frac{1}{N_k}\sum_{j=1}^{N_k} Loc_j \tag{61.14}$$

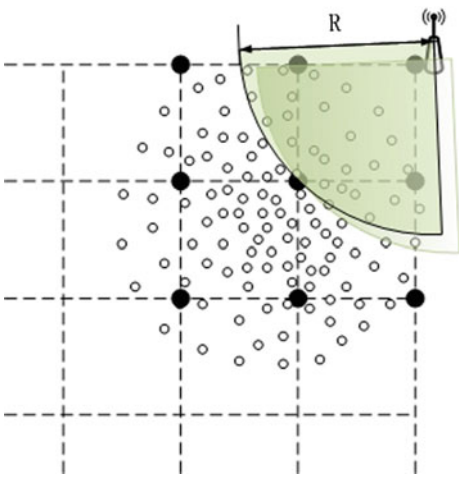

Fig. 61.2 Sketch map of E-SIR method

Finally, we can get a new set of particles $\{X_k^{i'}, i = 1, \cdots, N_s\}$ which is used to replace the resampling result of conventional SIR.

By the way, this paper employs the inverse Euclidean distance [as (61.15) presents] between Z_k and RSSI vectors in location fingerprints to estimate $p(Z_k|X_k^i)$.

$$w_k^i = \sqrt{\sum_{j=1}^{N} \left(RSSI_j - RSSI_{j'}\right)^2}. \tag{61.15}$$

61.4 Experimental Setup and Results

61.4.1 Experimental Setup

In order to evaluate the proposed hybrid location technique, we conducted extensive experiments on two different test beds: indoor and outdoor. The two test beds were both in Wi-Fi and WSN (2.4 GHz Zigbee) environments. Wi-Fi was the only signal applied to form offline location fingerprints, which were used for interpolating new location fingerprints according to the actual position of particles of PF. WSN acted as the enhanced signal. Thus, a laptop and a blind node (BN) of WSN served as the mobile device to receive two different signals. For comparison, K weighted nearest neighbors (KWNN, K equals 4) and SIR PF were used as baselines. By the way, the default number of particles is 1,000. However, the standard deviation of state model and searching radius R are correlated with dynamic environments, thus they are determined according to different environments, such as indoor and outdoor.

61.4.1.1 The Outdoor Test Bed

The outdoor test bed is close to the academic building, where the School of Geography and Planning, Sun Yat-Sen University is located. The test bed has dimension of 20 by 20 m, and the layout is shown in Fig. 61.3. In the test bed, seven Wi-Fi APs can be detected, in which five are existing resources in surroundings, and the other two are placed at two points marked by pentacles in the figure. We placed four WSN reference nodes (RN) at each corners of the area to simulate enhanced signals. The offline location fingerprints were collected at each grid with its size of 2 × 2 m. By the way, the standard deviation of state model is 2 m, and the default value of searching radius R is 1.5 m.

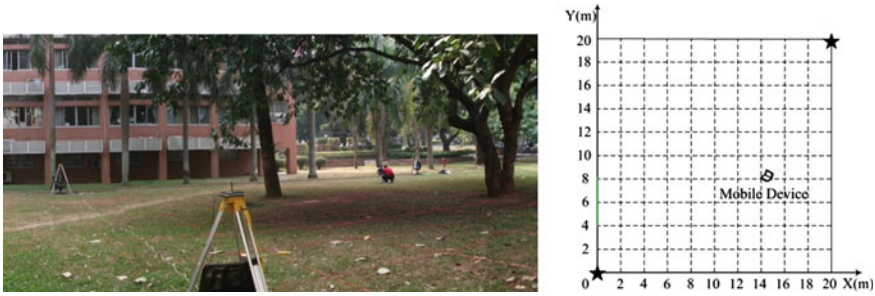

Fig. 61.3 Layout of the outdoor test bed

61.4.1.2 The Indoor Test Bed

To show the generality of the E-SIR PF algorithm, we also conducted a series of experiments on the indoor test bed. The test bed is in the corridor of fifth floor of our academic building. It measures 30 m, and the layout is shown in Fig. 61.4. In the test bed, eleven Wi-Fi APs can be detected, and all of them are existing resources in surroundings. Four WSN RNs were placed at four points marked by pentacles in the figure. The offline location fingerprints were collected at each point with the interval of 1 m. What's more, because of the complex and close environments of the indoor test bed, the default values of standard deviation of state model and the searching radius R are both 3 m, and larger than the counterparts on the outdoor test bed.

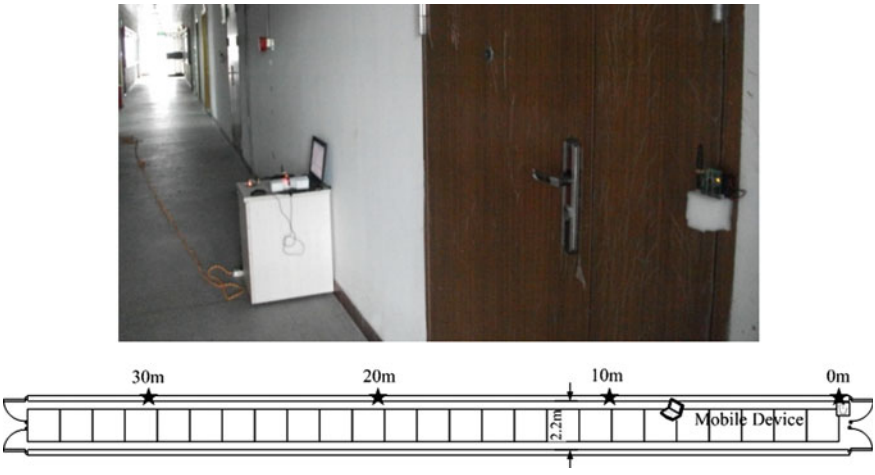

Fig. 61.4 Layout of the indoor test bed

61.4.2 Experimental Results

61.4.2.1 The Tracking Effects of Enhanced-SIR Particle Filter

Experiments were first performed to compare the three algorithms, E-SIR PF, SIR PF, and KWNN. Tables 61.1 and 61.2 contains the detailed comparative results of location errors with the three algorithms on the outdoor and indoor test beds respectively. We note that the average location error of E-SIR PF decreases 10 % and 30.8 % on the outdoor test bed, as well as 25 % and 18.2 % on the indoor test bed, compared to SIR PF and KWNN respectively.

Figure 61.5a presents a comparison of the tracking effects between E-SIR PF and SIR PF algorithm on the outdoor test bed. A mobile device is moving in the test bed, its motion trace measures 68 m, covering a half of the area. It should be noted that only a few portions of the trace locate in the range of enhanced signals, as marked by triangles in the figure. We observe from the figure that the tracking performance of E-SIR PF is improved remarkably with the assisting of enhanced signals, compared to conventional SIR PF.

A comparison of location errors between E-SIR PF and SIR PF on the indoor test bed is also presented in Fig. 61.5b. The whole trace of the mobile device measures 30 m. We can see from the figure that in the effective area of enhanced signals, the tracking performance of E-SIR PF is improved remarkably, compared to conventional SIR PF. Above all, we learn that it is important for location estimation to fuse signals of opportunity effectively.

Besides the tracking accuracy, runtime of the PF algorithm was also evaluated. For comparison, KWNN was used as the baseline. We calculate the runtime ratio, which demonstrates the ratio between runtime of PF algorithm and KWNN algorithm. Figure 61.6 depicts the average runtimes of E-SIR PF and SIR PF on the two test beds, considering different numbers of particles. We can see from the figure that, compared to SIR PF, the proposed E-SIR PF costs the equivalent runtime. However, compared to the KWNN algorithm, the PF algorithms cost several tens times of runtime, which increases linearly with the number of particles.

Table 61.1 Comparison of statistical results of location errors (m) on the outdoor test bed

Algorithm	Average	Standard deviation	90 %	Max
KWNN	5.2	3.2	9.5	15.0
SIR PF	4.0	2.1	6.9	7.9
E-SIR PF	3.6	2.1	6.6	7.8

Table 61.2 Comparison of statistical results of location errors (m) on the indoor test bed

Algorithm	Average	Standard deviation	90 %	Max
KWNN	1.1	0.8	2.4	3.9
SIR PF	1.2	0.7	2.1	2.7
E-SIR PF	0.9	0.6	1.7	2.4

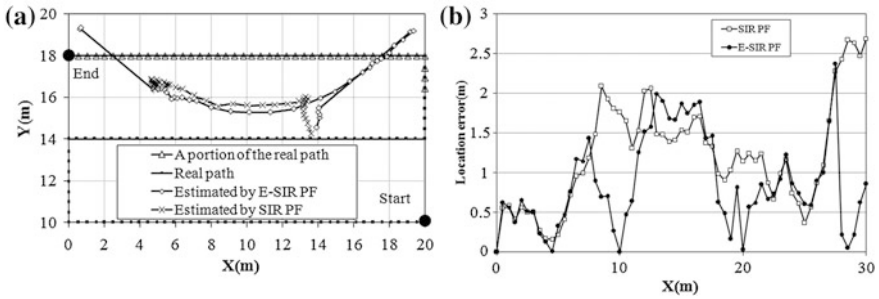

Fig. 61.5 Comparison of the tracking effects between E-SIR PF and SIR PF on the indoor (**b**) and outdoor (**a**) test beds

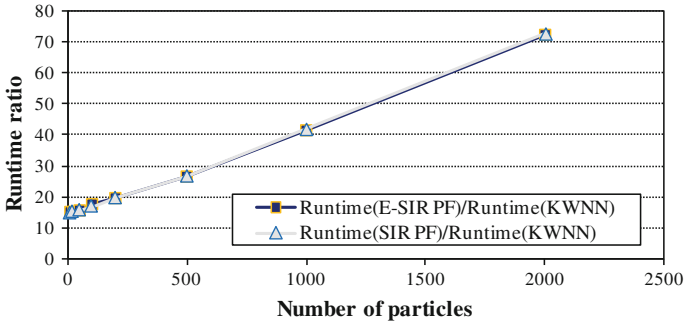

Fig. 61.6 Runtime ratios between the PF algorithms and KWNN

61.4.2.2 Impacts of the Parameters of Enhanced-SIR Particle Filter

Since the proposed technique is a PF algorithm, the performances of PF algorithm depends more or less on the number of particles. Experiments were also conducted to investigate the algorithm using different number of particles on the indoor and outdoor test beds. Figure 61.7 illustrates that with the increase of the number of particles, the average error and its standard deviation decrease gradually (the error bars represents the standard deviations).

For the method of Enhanced SIR, the performance is also correlated with the searching radius. We also carried out several experiments to study the effect of the searching radius on the location accuracy. Figure 61.8 presents the results on the two test beds. We can see that if the radius is too small or too large, the performance of the algorithm will be away from the best level. And when the radius equals 1.5 m, the algorithm performs the best on the outdoor test bed, but on the indoor test bed the best radius is 3 m. This is because, if the radius is too small, the method of Enhanced SIR will not be fully used, and if the radius is too large, the SIR process will be over corrected. In addition, we should increase the radius in blocked and complex environments.

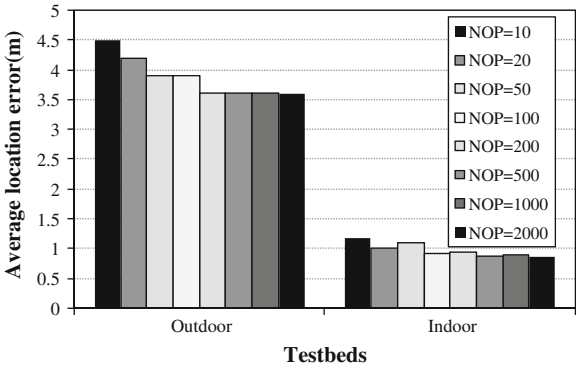

Fig. 61.7 Average location errors with different numbers of particles (NOP) on two different test beds

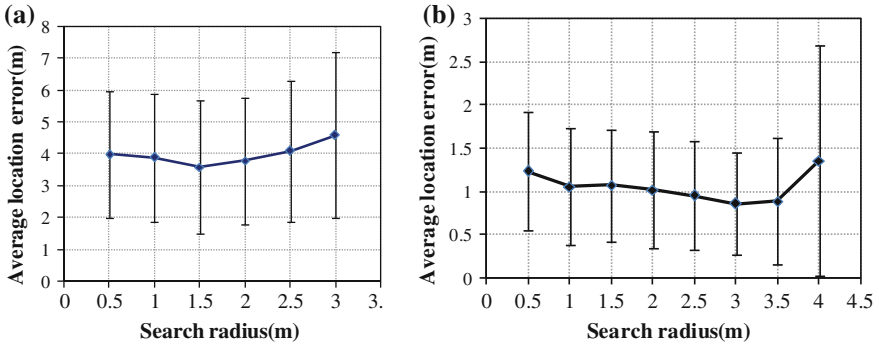

Fig. 61.8 Average location errors and standard deviations (represented by the error *bars*) with different searching radiuses of E-SIR PF on the indoor (**b**) and outdoor (**a**) test beds

61.5 Conclusion

In this paper, we proposed a novel hybrid location technique fusing Wi-Fi with WSN. We also explored the different characteristics of Wi-Fi and WSN signals, and then we proposed a method for the resampling of particles assisted by signals of opportunity based on conventional SIR to improve the tracking ability of PF-based system. Extensive experiments demonstrate that the proposed hybrid technique can provide more accurate location estimates and costs equivalent runtime, compared to SIR PF. Because of the heavy computation cost of the PF algorithm, it is best to process location estimation on a server.

Acknowledgments The project was supported by National Natural Science Foundation of China (41071284), Guangzhou Planning Project of Science and Technology (2010Y1-C711).

References

1. LaMarca A, Chawathe Y, Consolvo S, Hightower J, Smith I, Scott J, Sohn T, Howard J, Hughes J, Potter F et al (2005) Place lab: device positioning using radio beacons in the wild. In: Proceedings of the 3rd international conference on Pervasive Computing, pp 116–133
2. McGuire M, Plataniotis KN, Venetsanopoulos AN (2005) Data fusion of power and time measurements for mobile terminal location. IEEE Trans Mob Comput 4(2):142–153
3. Gordon N, Salmond D, Smith A (1993) Novel approach to nonlinear/non-Gaussian Bayesian state estimation. IEE Proc F Radar Sig Process 140(2):107–113
4. Hightower J, Borriello G (2001) A survey and taxonomy of location systems for ubiquitous computing. Technical report UW-CSE 01-08-03, University of Washington, Computer Science and Engineering, Seattle
5. Bahl P, Padmanabhan VN (2000) RADAR: an in-building RF-based user location and tracking system. In: Proceedings of the IEEE INFOCOM '00, pp 775–784
6. Fox D, Hightower J, Liao L, Schulz D (2002) Bayesian filtering for location estimation. IEEE Pervasive Comput 2(3):24–33
7. Kritzler M, Muller A (2010) From heterogeneous sensor sources to location-based information. In: Proceedings of UBICOMM2010, pp 367–372
8. Pedersen T, Mensing C, Papakonstantinou K et al (2010) Hybrid localization techniques. ICT-217033 WHERE D2.3 Version 1.0
9. IEEE Std 802.15.4™: Wireless medium access control (MAC) and physical layer (PHY) specifications for low-rate wireless personal area networks (LR-WPANs) [S]. IEEE, 2003, pp. 641
10. Arulampalam S, Maskell S, Gordon N, Clapp T (2002) A tutorial on particle filters for online nonlinear/non-Gaussian Bayesian tracking. IEEE Trans Sig Process 50(2):174–188
11. Doucet A, Godsill S, Andrieu C (2000) On sequential Monte Carlo sampling methods for Bayesian filtering. Stat Comput 10(3):197–208

Chapter 62
Efficient Quality Control Procedure for GNSS/INS Integrated Navigation System

Ling Yang, Yong Li and Youlong Wu

Abstract This paper proposed an efficient quality control algorithm for the GNSS/INS integrated navigation system, the system therefore can be efficiently and reliably applied in complex urban environment with shelters, multipath, reflections and data loss. The quality control algorithm consists of GNSS and INS modules. In order to reduce the adverse influence from abnormal GNSS data, a Kalman Filter with a Fault Detection and Exclusion (FDE) procedure is proposed to enhance the system reliability and stability. The stochastic model for Kalman Filter is determined by Allan Variance analysis to reduce the time dependent ramp error of INS data. In comparison with traditional GNSS/INS integrated system, the new system can detect and repair GNSS outliers in real-time and also can alleviate the INS ramp errors when GNSS signals are interfered with. In order to evaluate the performance of the proposed navigation system, a field test has been conducted in Sydney urban area. The performance of the proposed navigation system and the effectiveness of the FDE algorithm that was applied to the GNSS data with high fault rate and slight data loss were evaluated. The results show that the proposed algorithm with the optimal quality control design can give reliable navigation solution that is better than that with the normal quality control design.

Keywords Fault detection and exclusion · Allan variance · Abrupt error · Slowly growing error

L. Yang (✉) · Y. Li · Y. Wu
School of Surveying and Geospatial Engineering, University of New South Wales, Sydney, Australia
e-mail: ling.yang1@student.unsw.edu.au

Y. Wu
School of Mechanical Engineering, NUST, Nanjing 210094, China

J. Sun et al. (eds.), *China Satellite Navigation Conference (CSNC) 2013 Proceedings*, Lecture Notes in Electrical Engineering 245,
DOI: 10.1007/978-3-642-37407-4_62,

62.1 Introduction

Global Navigation Satellite Systems (GNSS) have been widely used to satisfy the position and navigation requirements in many fields such as geodesy, marine and aviation. Inertial Navigation System (INS) is a self-contained system with high short-term stability, immune to jamming as well as interference. Consequently, INS can be integrated synergistically with GNSS so that short-term and long-term stabilities of INS and GNSS, respectively, can be exploited.

When integrating measurements from GNSS and INS, Fault Detection and Exclusion (FDE) is an important and challenging problem, no matter which kind of integration algorithm is applied. Both abrupt and ramp errors contaminating in GNSS/INS measurements will disturb the accuracy of the mathematical model so as to ruin the optimality of the algorithm. It is for this reason FDE has being combined with various optimal estimation algorithm [1]. Some researchers are focusing on detecting and isolating faults within multiple sensors [2]. Other interests have been concentrated on developing efficient FDE methods for different types of errors according to the properties of various sensors ([3–7]).

The objective of this paper is to design an efficient quality control algorithm for integrity of a GNSS/INS integrated navigation system. The quality control algorithm consists of GNSS and INS modules. In order to reduce the adverse influence from abnormal GNSS data, a Kalman filter with a FDE procedure is proposed to enhance the system reliability and stability. The stochastic model for Kalman Filter is determined by Allan Variance analysis to reduce the time dependent ramp error of INS data, in comparison with traditional GPS/INS integrated system.

The paper is organized as follows. Introduction of the conventional Kalman Filter mathematical model applied in GNSS/INS integration is briefed in Sect. 62.2; The proposed fault detection and isolation method that deal with the abrupt error occurring in GPS measurements is presented in Sect. 62.3; The Allan Variance method is described briefly to monitor the random errors of IMU sensors in Sect. 62.4. Finally, the performance of the proposed algorithm is evaluated upon a field test that was performed in Sydney urban area.

62.2 GNSS/INS Integrated Algorithm

The Kalman filter estimates the navigation error and sensor error using the position and velocity measurements from the GNSS receiver. To construct the Kalman filter, an INS error model should be given. Many kinds of INS error models have been introduced in the literature [8, 9]. This paper utilises the Ψ angle error model [9]

$$\dot{\boldsymbol{x}}_k = \boldsymbol{F}\boldsymbol{x}_k + \boldsymbol{G}_k \quad \boldsymbol{w}_k \sim N(0, \boldsymbol{G}_k) \tag{62.1}$$

where

$$\dot{\boldsymbol{x}}_k = \begin{pmatrix} \dot{\boldsymbol{x}}_{\text{nav}} \\ \dot{\boldsymbol{x}}_{\text{sen}} \end{pmatrix} = \begin{pmatrix} \boldsymbol{F}_{9\times 9} & \boldsymbol{F}_{9\times 6} \\ \boldsymbol{0}_{6\times 9} & \boldsymbol{0}_{6\times 6} \end{pmatrix} \begin{pmatrix} \boldsymbol{x}_{\text{nav}} \\ \boldsymbol{x}_{\text{sen}} \end{pmatrix} + \begin{pmatrix} \boldsymbol{G}_{\text{nav}} \\ \boldsymbol{G}_{\text{sen}} \end{pmatrix} \tag{62.2}$$

The state vector $\boldsymbol{x}_{\text{nav}}$ and $\boldsymbol{x}_{\text{sen}}$ are the navigation error and sensor error, respectively. The sub-matrices $\boldsymbol{F}_{9\times 9}$ and $\boldsymbol{F}_{9\times 6}$ can be referred to literatures [10].

The discrete forms of (62.1) is

$$\hat{\boldsymbol{x}}_k = \Phi_{k/k-1}\hat{\boldsymbol{x}}_{k-1} + \boldsymbol{w}_{k/k-1}, \quad \boldsymbol{w}_{k/k-1} \sim N\left(0, \boldsymbol{Q}_{k/k-1}\right) \tag{62.3}$$

The measurement equation is described by

$$\boldsymbol{z}_k = \boldsymbol{H}_k\hat{\boldsymbol{x}}_k + \boldsymbol{v}_k, \boldsymbol{v}_k \sim N(0, \boldsymbol{R}_k) \tag{62.4}$$

The Kalman filter algorithm is composed of time and measurement updates. The prediction of the state, $\hat{\boldsymbol{x}}_k^-$, and it covariance matrix, $\boldsymbol{P}_k^-$, are obtained by the time-updating step.

$$\begin{cases} \hat{\boldsymbol{x}}_k^- = \Phi_{k/k-1}\hat{\boldsymbol{x}}_{k-1} \\ \boldsymbol{P}_k^- = \Phi_{k/k-1}\boldsymbol{P}_{k-1}\Phi_{k/k-1}^{\text{T}} + \boldsymbol{Q}_{k/k-1} \end{cases} \tag{62.5}$$

When the measurements are available, the state vector, $\widehat{\boldsymbol{x}}_k$, is updated as

$$\begin{cases} \boldsymbol{K}_k = \boldsymbol{P}_k^-\boldsymbol{H}_k^{\text{T}}\left(\boldsymbol{H}_k\boldsymbol{P}_k^-\boldsymbol{H}_k^{\text{T}} + \boldsymbol{R}_k\right)^{-1} \\ \hat{\boldsymbol{x}}_k = \hat{\boldsymbol{x}}_k^- + \boldsymbol{K}_k\left(\boldsymbol{z}_k - \boldsymbol{H}_k\hat{\boldsymbol{x}}_k^-\right) \\ \boldsymbol{P}_k = (\boldsymbol{I} - \boldsymbol{K}_k\boldsymbol{H}_k)\boldsymbol{P}_k^- \end{cases} \tag{62.6}$$

where $\boldsymbol{K}_k$ is the Kalman gain and $\boldsymbol{P}_k$ is the covariance matrix of the state.

62.3 FDE for GPS Abrupt Errors

The performance of the observation model in the Kalman filter relies on the GNSS output accuracy. In order to keep the optimality of the integration system, FDE for GNSS abrupt errors should be performed on the raw measurement. For the loosely-coupled algorithm, FDE should be tackled before the integration procedure within the GNSS solution stage. While for tightly-coupled algorithm, it can be finished simultaneously with the Kalman filter procedure. The conventional mathematical model is described in this section.

The measurement equation for both GNSS-only solution and GNSS/INS integrated solution is described by

$$\boldsymbol{z}_k = \boldsymbol{H}_k\widehat{\boldsymbol{x}}_k + \boldsymbol{v}_k \text{ and } E(\boldsymbol{z}_k) = \boldsymbol{H}_k\boldsymbol{x}_k, D(\boldsymbol{z}_k) = \boldsymbol{R}_k \tag{62.7}$$

where $\boldsymbol{v}_k$ is the residual vector, $\boldsymbol{H}_k$ is the n by t design matrix with rank t, $\boldsymbol{z}_k$ is the vector of n measurement, $\boldsymbol{x}_k$ is the vector of t unknown and its estimated value is $\hat{\boldsymbol{x}}_k$. The expectation and positive definite covariance matrix of the measurement vector are $E(\boldsymbol{z}_k)$ and $\boldsymbol{R}_k$ respectively.

In the case where it is assumed that there is an outlier in the ith observation, the functional model becomes [5, 11]

$$\boldsymbol{z}_k = \boldsymbol{H}_k \hat{\boldsymbol{x}}_k + \boldsymbol{c}_i \widehat{\nabla}_i + \boldsymbol{v}_k \tag{62.8}$$

where $\widehat{\nabla}_i$ is the fault in the ith pseudorange, and $\boldsymbol{c}_i = [0, \cdots, 0, 1, 0, \cdots, 0]^{\mathrm{T}}$ is a unit vector with the ith element equal to one, and the other symbols are the same as in the standard Gauss-Markov model. The outlier test statistic for the ith observation can then be formed as [5, 11]

$$w_i = \frac{\widehat{\nabla}_i}{\sigma_0 \sqrt{Q_{\widehat{\nabla}_i}}} = \frac{\boldsymbol{c}_i^T \boldsymbol{P} \boldsymbol{Q}_v \boldsymbol{P} \boldsymbol{l}}{\sigma_0 \sqrt{\boldsymbol{c}_i^T \boldsymbol{P} \boldsymbol{Q}_v \boldsymbol{P} \boldsymbol{c}_i}} \tag{62.9}$$

where $\boldsymbol{Q}_v$ is the cofactor matrix of the estimated residuals (from the standard Gauss-Markov model), and $Q_{\widehat{\nabla}_i}$ is the cofactor matrix of the estimated outlier. The outlier test statistic follows a standard normal distribution under the null hypothesis. The evidence on whether the model error specified by Eq. (62.8) did or did not occur, is then based on testing

$$|w_i| > c_\alpha = u_{1-\alpha_0/2} \tag{62.10}$$

where $u_{1-\alpha_0/2}$ is the lower percentage point of a standard normal distribution. By letting i run from one up to and including n, all of the pseudorange measurements can be screened for the presence of a fault. If one or more of the outlier tests fails then it is concluded that a fault exists.

62.4 Allan Variance Analyses for INS Slowly Growing Errors

The Allan Variance is a time domain analysis technique originally developed in the middle 1960s to study the frequency stability of oscillators [12]. It describes the variance of data as a function of averaging time.

For the IMU gyroscope or accelerometer outputs, the Allan variance is estimated as follows

$$\sigma^2(\tau) = \frac{1}{2\tau^2 (N - 2m)} \sum\nolimits_{k=1}^{N-2m} (\theta_{k+2m} - 2\theta_{k+m} + \theta_k)^2 \tag{62.11}$$

Table 62.1 Stochastic error sources in IMU

Noise type	Allan variance	Coefficients	Log–log model
Quantization noise	$3Q^2/\tau^2$	Q	$y = -x + b$
Angle/velocity random walk	N^2/τ	N	$y = -0.5x + b$
Bias instability	$(2\ln 2B^2)/\pi$	B	$y = b$
Angular/acceleration rate random walk	$K^2\ \tau/3$	K	$y = 0.5x + b$
Ramp noise	$R^2\ \tau^2/2$	R	$y = x + b$

where τ represent the cluster time, m is the length of each cluster, θ is the angular or velocity output and N is the number of data that will be analyzed, these measurements are made at discrete times from the inertial sensors.

$$\sigma^2_{\text{total}} = \sigma^2_Q + \sigma^2_N + \sigma^2_B + \sigma^2_K + \sigma^2_R = \sum\nolimits_{k=-2}^{2} A_k \tau^k \tag{62.12}$$

where the coefficients A_k are obtained in least squares.

According to Allan's definition and results, there are seven noise terms existing in inertial sensors [13]. The five basic noise terms are quantization noise, angular/velocity random walk, bias instability, angular/velocity rate random walk and drift rate ramp. The noises, their Allan Variance and coefficients are listed in Table 62.1. In most cases, different noise contribution appear in different regions of correlation time, thus, it is easy to identify the various stochastic errors that exist in the data, can be estimated directly from Eq. (62.12) using the least square. Finally, the noise coefficients can be obtained to compensate the stochastic error sources, which will be discussed in Sect. 62.5.

62.5 Test Analyses

62.5.1 Test Descriptions

The field test was implemented on July 23, 2012 from Beach Street to Barker Street, Sydney. The test last about 30 min, and the distance from the start to the end point is about 10 km. During the test, the IMU and GPS real data were collected. The IMU data consist of velocity and attitude increments; time tagged with GPS time. GPS data are in the form of the Receiver Independent Exchange Format (RINEX) file set. GPS data were captured by the Trimble's BD950 dual frequency receiver which sample rate was configured as 2 Hz in the test. The IMU is iMAR's iIMU-FSAS which sample rate was configured as 100 Hz. The iIMU-FSAS is tactical grade with the performance specifications shown in Table 62.2.

Figure 62.1 shows the position trajectory of the vehicle obtained from the raw GPS data from the RINEX files. The vehicle positions were computed from the pseudoranges by using the least squares algorithm. The start and end points are

Table 62.2 iIMU-FSAS performance specifications

Parameters	Values
Gyro bias	0.75°/h
Angular rate random walk	0.1°/sqrt (h)
Accelerometer bias	1 mg
Velocity rate random walk	0.05 mg/sqrt (Hz)

Fig. 62.1 The trajectory from the GPS data

marked by pink icons in Fig. 62.1. During the test, GPS signal is frequently sheltered by trees beside the road, which lead to large biases on estimated position. The green icons with labels 1–7 in Fig. 62.1 show the places where remarkable interference happened. The number of satellites in view of the vehicle mounted antenna is shown in Fig. 62.2. It can be seen that the minimum and maximum number of satellites available during the run are 1–10, respectively. It is also noted that between green icons 2–3, there is a 36 s GPS blockage when the vehicle was driven through the Sydney Airport Tunnel with the length of 0.56 km approximately.

After description of the test and the characteristics of the real data, the following sections assess the capability of the FDE method to detect the GPS abrupt errors and the performance of the Allan Variane method to compensate the inertial sensor errors in an integrated system.

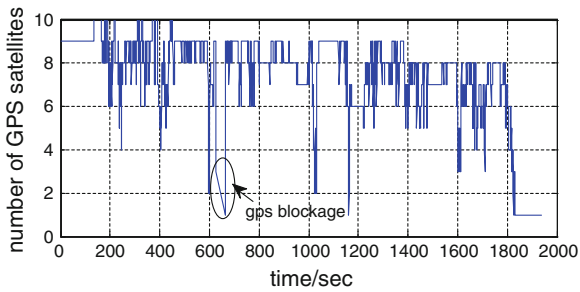

Fig. 62.2 Number of satellites in view

62.5.2 FDE for GPS Abrupt Errors

The current and proposed fault detection and isolation algorithm are applied to the loosely-coupled integrated system for the real data case. In the test, only the positions computed from the GPS pseudorange measurements are used for the integration procedure. The Kalman filtering time was chosen according to the GPS data rate. The FDE method is firstly used in the GPS-only solution, so as to provide much more reliable position measurements for the integration with INS. To compare the performance of the FDE method, results from three schemes are shown in Fig. 62.3a–c. The three schemes are designed as follows:

Scheme 1. GPS single point positioning using least squares algorithm;
Scheme 2. GPS single point positioning using least squares algorithm with FDE procedure;
Scheme 3. GPS and INS loosely-coupled integrated algorithm using the position solution from scheme 2.

In Fig. 62.3, points in red, blue and green are the results of schemes 1, 2 and 3, respectively. It is obvious that the least squares solutions from scheme 1 are remarkably swayed and even to be out of the road, while the solutions with FDE procedure can provide more robust results as the blue points show. After integrating the robust GPS solutions with INS, a much smoother trajectory in green points can be obtained. This is because the integration algorithm also takes account of the predict positions from INS measurements. Because of the particular

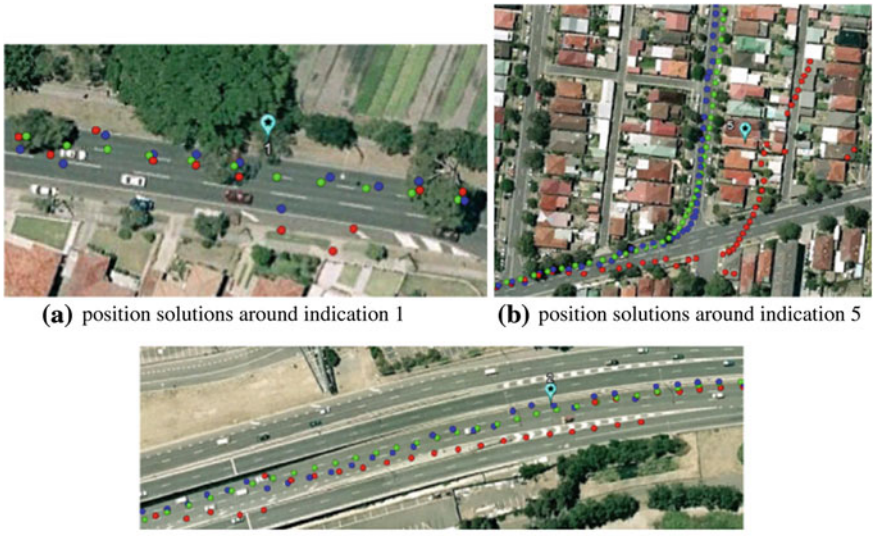

Fig. 62.3 Positions from GPS only and GPS/INS integration solutions

characteristics of INS sensor errors, the predicted position errors from INS measurements will not jump abruptly. Consequently, the large differences between GPS and the predicted INS positions can be considered as an indicator of GPS abrupt errors. The most remarkable example during the course of trajectory is shown in Fig. 62.3b. There are several ten meters' errors in the results of scheme 1. The results of scheme 2 and 3 are significant better than that of scheme 1. It shows a very good performance of the FDE method when dealing with remarkable abrupt errors.

To show the performance of the FDE method in a statistical view, the following analysis is based on simulating a gross error in one of the GPS pseudorange measurements during the first 800 epochs. To compare the positioning accuracy of least squares without and with FDE procedure, a reference trajectory should be obtained firstly. As we did not set up a base station during the test, a RTK solution with higher accuracy from the carrier phase measurements was not available. To solve the reference problem, we took the following steps:

1. Using the estimated solutions of least squares to correct the pseudorange measurements, so as to generate a clear data set without any errors. Also, a reference trajectory was obtained.
2. A group of random noises was added to the pseudorange measurements at each epoch.
3. An abrupt error of the size of 20 m which is slightly larger than the largest MDB ($\alpha = 1\ \%$, $\beta = 20\ \%$) is randomly added to one pseudorange.

The position errors of least squares without and with FDE procedure (Scheme 1 and 2, respectively) are shown in Fig. 62.4a–c, where blue and green lines correspond to the results of scheme 1 and 2, respectively. It is obvious that the FDE procedure performs well when there is an abrupt gross error.

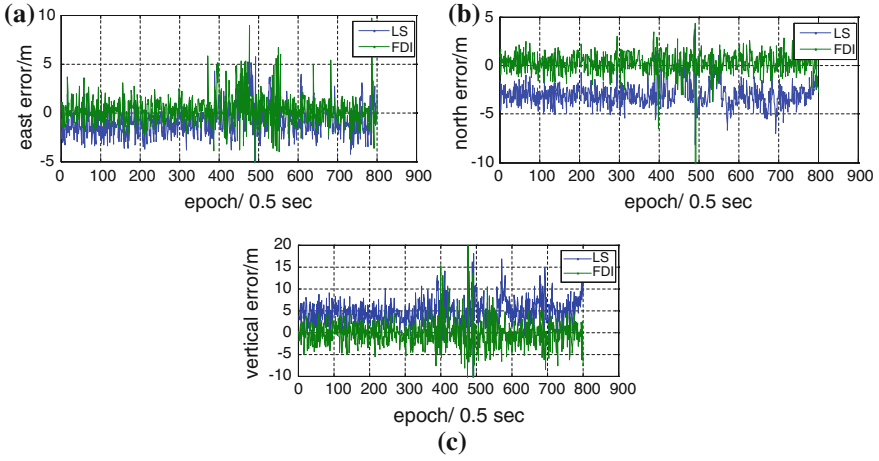

Fig. 62.4 **a** East position errors. **b** North position errors. **c** Vertical position errors

Table 62.3 RMS of the position errors (m)

Method	East	North	Vertical
LS	1.7793	3.2193	6.0612
FDE	1.6229	1.2261	4.9426

Table 62.4 RMS of the position errors (m)

Method	East	North	Vertical
LS	2.7568	3.8581	5.7023
FDE	2.3883	2.2238	1.9593

The Root Mean Square (RMS) values of the position errors are listed in Table 62.3. It shows that with the FDE procedure the position errors are reduced by 8.8, 61.9 and 18.5% in east, north and vertical direction, compared with the original least squares estimation.

To show the performance improvement in the integration procedure, the positions calculated by the least squares without and with the FDE procedure—are individually used to loosely-coupled integrate with INS data. To keep the stability of the Kalman filter, the data from epoch 400 to 800 is used for comparison. The estimated RMS values are listed in Table 62.4. It shows the improvement in east, north and vertical direction is 13.4, 42.4 and 65.6 %, respectively.

62.5.3 INS Error Compensation when GPS Data Loss

During the test, there were also several GPS signal blockages. The longest blockage occurred when the vehicle was drove through the Sydney Airport Tunnel which is 0.56 km long and the blockage last for 36 s. Figure 62.5 shows the location of the tunnel.

Having collected 10 h static IMU data with a sample rate of 100 Hz, the identification of the inertial sensors noise was carried out using Allan Variance. The log–log plot of Allan Variance results are shown in Fig. 62.6a and b for the gyroscope and accelerometer, respectively.

To show that the Allan Variance analysis method can provide a better compensation to the INS sensors errors, the INS-only solutions calculated with the prior parameters and the parameters from Allan Variance method were shown in

Fig. 62.5 The demonstration for Sydney airport tunnel

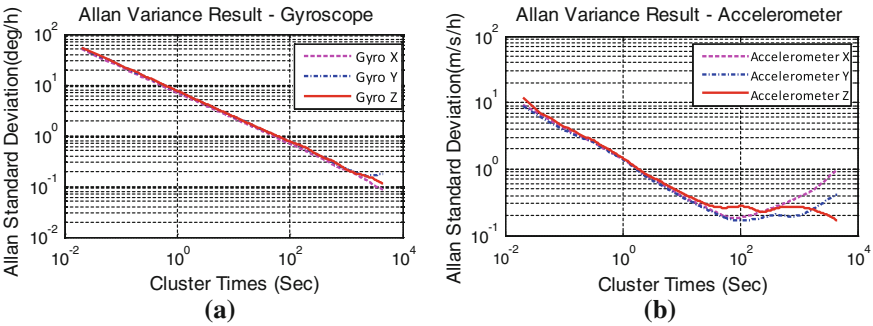

Fig. 62.6 **a** Allan variance result-Gyroscope. **b** Allan variance result-a ccelerometer

Fig. 62.7. The green line are results of prior parameters, blue line are results of parameters from Allan Variance Method, and red line are the trajectory calculated by GPS pseudorange measurements.

In Fig. 62.7, it is clear that the results with Allan Variance analysis can alleviate the bias of INS solution so as to provide a more reliable position when GPS signals are not available. However, due to the characteristics of INS sensors, the position bias from INS-only will drift increasingly along with the time no matter whether or not the Allan Variance method is used. From this point of view, the significance of Allan Variance method is to reduce this kind of slowly growing errors, so that INS can provide a relatively more reliable solution when GPS signals is interrupted for a short period of time.

Next, the GPS frequent signal blockages are monitored to show the differences on the position errors without or with Allan Variance analysis. From the 400 to 600th second, the GPS update rate is artificially changed from 2 to 0.2 Hz. The trajectories calculated without and with the parameters from Allan Variance analysis are shown in Fig. 62.8. Green line is the result when Allan Variance

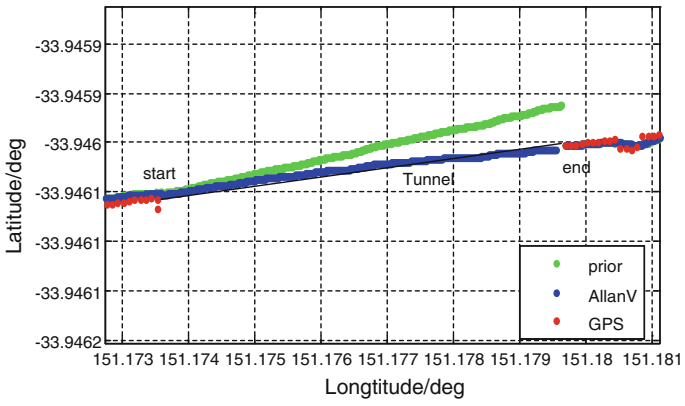

Fig. 62.7 The trajectory across the tunnel

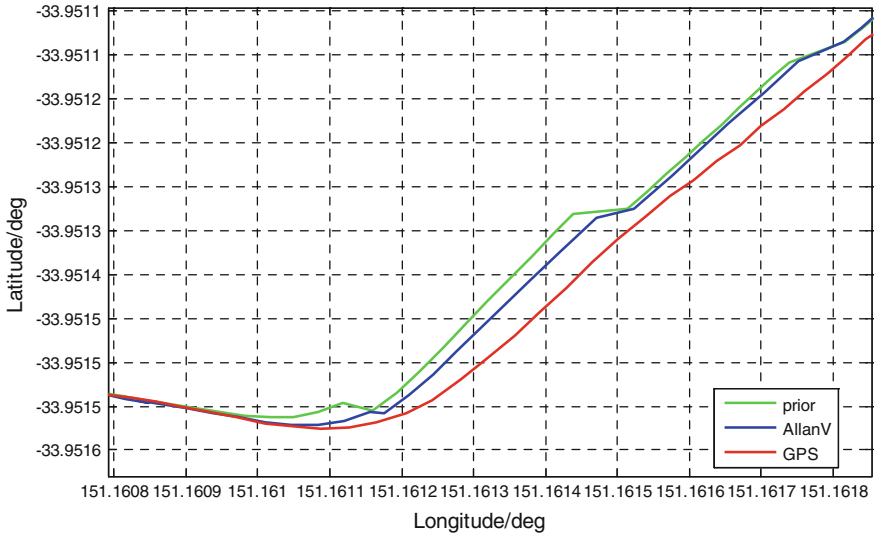

Fig. 62.8 The trajectory across the tunnel

method was not used, blue line is the result when Allan Variance method was used to estimate the INS sensors errors, and red line is the result from GPS single point positioning. It shows that the blue line is much closer to the red line compared with the green line. This indicates that using Allan Variance method can provide a much more accurate estimation to the INS sensors errors in comparison with the factory's specifications. Thus the position from INS only solution could be improved when GPS signals is frequently blocked for a short time. Especially as the sensors degrade gradually with time, the factory's specifications could gradually drift away from their real value. In this circumstance, it is of great importance to implement the Allan Variance analysis beforehand. Statistical results show that by using the parameters from Allan Variance analysis the position accuracy have an improvement of 8.25, 10.47, 5.51 % respectively in the east, north and vertical direction.

62.6 Conclusions

This paper presents an efficient quality control module for GPS/INS integrated navigation, from which the GPS abrupt errors can be detected and excluded firstly in GPS-only solution to provide much more reliable position measurements for the integration with INS. The slowly-growing INS errors can be reduced by the Allan Variance analysis. The performance of the system has been investigated and verified by a field test. In the test, the GPS suffered from frequent signal interference and blockages. It shows that the FDE procedure proposed in this paper can

detect the GPS abrupt errors with a high success rate and the adverse influence of INS slowly growing errors on the position accuracy could be alleviated by Allan Variance analysis.

Further research will implement the FDE procedure in GPS/INS tightly-coupled integration algorithm, to verify that the FDE procedure can be generally used in the integrated system with different algorithms.

References

1. Hwang I, Kim S, Kim Y, Seah CE (2010) A survey of fault detection, isolation, and reconfiguration methods. IEEE Trans Control Syst Technol 18(3):636–653
2. Guerrier S, Waegli A, Skaloud J, Victoria-Feser M (2012) Fault detection and isolation in multiple MEMS-IMUs configurations. IEEE Trans Aerosp Electron Syst 48(3):2015–2031
3. Bhatti UI, Ochieng WY, Feng S (2012) Performance of rate detector algorithms for an integrated GPS/INS system in the presence of slowly growing error. GPS Solutions 16:293–301
4. Bruggemann TS, Greer DG, Walker RA (2011) GPS fault detection with IMU and aircraft dynamics. IEEE Trans Aerosp Electron Syst 47(1):305–316
5. Kok JJ (1984) On data snooping and multiple outlier testing. NOAA Technical Report, NOS NGS. 30, U.S. Department of Commerce, Rockville, Maryland
6. Knight NL, Wang J, Rizos C (2010) Generalised measures of reliability for multiple outliers. J Geodesy 84:625–635
7. Yang L, Knight NL, Wang J (2012) Evaluating the probability of correctly identifying a fault in GNSS positioning. In: ION GNSS 2012, 17–21 September, Nashville, Tennessean, USA
8. Arshal G (1987) Error equations of inertial navigation. J Guid Control Dyn 10(4):351–358
9. Goshen-Meskin D, Bar-Itzhack IY (1992) Unified approach to inertial navigation system error modeling. J Guid Control Dyn 15(3):648–653
10. Hwang DH, Oh SH, Lee SJ, Park C, Rizos C (2005) Design of a low-cost attitude determination GPS. INS integrated navigation system. GPS Solutions 9:294–311
11. Baarda W (1968) A testing procedure for use in geodetic networks. Netherland Geodetic Commission, vol. 2, no. 5. ISBN-13: 9789061322092, ISBN-10: 906132209X
12. Allan DW (1966) Statistics of atomic frequency standards. Proc IEEE 54(2):222–230
13. IEEE Standard Specification format guide and test procedure for single-axis interferometric fiber optic Gyros, (1997), New York, USA

Chapter 63
Development and Evaluation of GNSS/INS Data Processing Software

Quan Zhang, Xiaoji Niu, Linlin Gong, Hongping Zhang, Chuang Shi, Chuanchuan Liu, Jun Wang and Matthew Coleman

Abstract Currently there is less mature and reliable commercial software for GNSS/INS data processing in China. Relevant users have to rely on foreign software, e.g., POSPac and Inertial Explorer (IE). This has become one of the bottle-neck of applying GNSS/INS technology to survey and mapping areas in China. This paper introduces newly developed GNSS/INS data processing software—Cinertial. In the design of the algorithm, the local level frame is chosen as the reference frame; and the rotation vector is applied for the attitude update. The GNSS and INS information are fused by a Kalman filtering based on 21-dimensional error states vector. Moreover, Rauch-Tung-Striebel (RTS) backward smoothing algorithm is applied in the software to help ensure the best possible accuracies. The correctness of the developed software is tested and evaluated by the airborne and terrestrial datasets compare to IE and POSPac. The results show that Cinertial can reach the same level of the navigation accuracy as foreign commercial software.

Keywords GNSS/INS · Kalman filtering · Position and Orientation System (POS) · Data processing software

Q. Zhang (✉) · X. Niu (✉) · L. Gong · H. Zhang · C. Shi
GNSS Research Center, Wuhan University, Wuhan 430079, China
e-mail: quanzhang@whu.edu.cn

X. Niu
e-mail: xjniu@whu.edu.cn

C. Liu
CSR, Shanghai 201206, China

J. Wang · M. Coleman
ROAMES Group, Ergon Energy Corp Ltd, Level 2, Waterfront Place, 1 Eagle St, Brisbane, QLD 4000, Australia

J. Sun et al. (eds.), *China Satellite Navigation Conference (CSNC) 2013 Proceedings*, Lecture Notes in Electrical Engineering 245,
DOI: 10.1007/978-3-642-37407-4_63,

63.1 Introduction

GPS/INS integrated systems can provide accurate and reliable navigation information (including position, velocity and attitude) using a Kalman filter, and significantly improve positioning continuity compared to the individual GPS or INS. However, the navigation accuracy of the real-time solution can not meet the requirement of some applications. Applications of mobile mapping and aerial photogrammetry require high accuracy navigation information in post-mission provided by Position and Orientation System (POS). GNSS/INS data processing software can provide the navigation results of high reliability and accuracy to meet the requirements. Post-processing methods (e.g., backward smoothing) can also be applied in the GNSS/INS data processing software to further improve the navigation accuracy [1, 2]. Currently there is less mature and reliable software for GNSS/INS data processing in China. Relevant users have to rely on foreign software, e.g., POSPac from Applanix Corp. and Inertial Explorer (IE) from NovAtel Inc. This has become one of the bottle-neck of applying GNSS/INS technology to survey and mapping areas in China.

This paper introduces a GNSS/INS data processing software that has been newly developed in the GNSS Research Center at Wuhan University—Cinertial. Software architecture and the navigation algorithm used in the software are firstly described. Then the correctness of the developed software is tested and evaluated by the airborne and terrestrial datasets compare to POSPac and IE.

63.2 Software Structure

Figure 63.1 is the flowchart of the loosely coupled GNSS/INS mode for Cinertial, including three main parts. The first part is the inertial navigation system (INS) such as the orange part of the flowchart. The main role the GNSS part (the green block) is to provide the initial position and velocity values and carry out the Kalman measurement update. The blue color of the flowchart represents the optimal estimation, including the Kalman filter and Rauch-Tung-Striebel (RTS) smoothing.

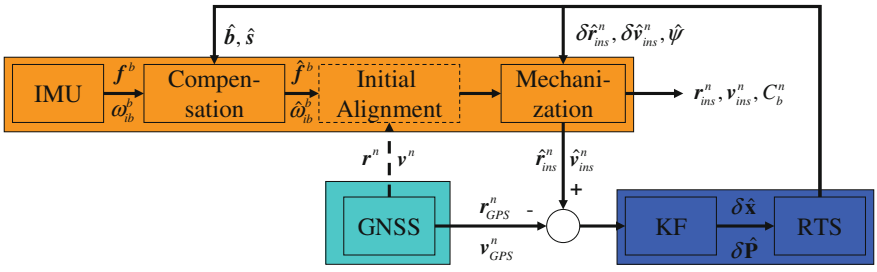

Fig. 63.1 The flowchart of the loosely coupled GNSS/INS mode for Cinertial

In Cinertial navigation process, the IMU delta-angle and delta-velocity measurements are compensated first by the estimated inertial sensor errors. The next step is the inertial alignment, which can provide the inertial attitude with different approaches (e.g., analytic coarse, in-motion, fine alignment and so on). This step is executed only once as shown in Fig. 63.1 by the dotted line. The initial position and velocity information can be obtained by GNSS or given by users. The compensated IMU delta-velocity measurements are integrated to update the INS velocity and position and the INS attitude is calculated by using the IMU delta-angle measurements. The process of getting the navigation results through integrating the IMU measurements is called INS mechanization. The loosely-coupled GNSS/INS mode is applied in Cinerrtial, the navigation application will pass a received position and/or velocity information to the Kalman filter for a loosely coupled Kalman measurement update. Precise time synchronization is needed because the GNSS and IMU sampling are usually made at different time. Here the position and velocity of IMU at the GNSS sampling time are obtained by the INS mechanization. The RTS backward smoothing algorithm is applied in the software to help ensure the best possible accuracies. The estimated gyros and accelerometers biases are fed back as compensation to the IMU raw data; and the estimated position, velocity and attitude errors of the INS are fed back correct the INS mechanization. The Final best estimated navigation solution of GNSS/INS is output and saved in files.

63.3 Navigation Algorithm

This section details the navigation algorithms implemented in Cinertial and gives a discussion of the loosely coupled methods of blending GPS and inertial information.

63.3.1 INS Mechanization

Strapdown IMUs work in discrete form and they usually output the delta-angle $\Delta\tilde{\theta}_{ib}^{b}$ and delta-velocity $\Delta\tilde{v}_{f}^{b}$. Therefore, discrete integration algorithms are applied to transform these measurements into navigation quantities [3, 4]. The digital algorithm for velocity update can be written generally as [3–5]

$$\boldsymbol{v}_{k}^{n} = \boldsymbol{v}_{k-1}^{n} + \triangle\boldsymbol{v}_{f,k}^{n} + \triangle\boldsymbol{v}_{g/cor,k}^{n} \tag{63.1}$$

where, n represents the navigation frame (n-frame), here the local level frame (North-East-Down frame) is used. A detailed description of the frames can be found in many references [3–5]. $\Delta\boldsymbol{v}_{g/cor,k}^{n}$ is the velocity increment due to the

gravity and Coriolis force and $\Delta \boldsymbol{v}_{f,k}^{n}$ is the velocity increment due to the specific force, which can be written respectively as follows:

$$\triangle \boldsymbol{v}_{g/cor,k}^{n} \approx \left[\boldsymbol{g}^{n} - \left(2\boldsymbol{\omega}_{ie}^{n} + \boldsymbol{\omega}_{en}^{n}\right) \times \boldsymbol{v}^{n}\right]_{k-0.5} \triangle t_k \tag{63.2}$$

$$\triangle \boldsymbol{v}_{f,k}^{n} = \frac{1}{2}\left[\boldsymbol{C}_{n(k-1)}^{n(k)} + I\right] \boldsymbol{C}_{b(k-1)}^{n(k-1)} \triangle \boldsymbol{v}_{f,k}^{b(k-1)} \tag{63.3}$$

$$\triangle \boldsymbol{v}_{f,k}^{b(k-1)} \approx \triangle \boldsymbol{v}_{f,k}^{b} + \frac{1}{2}\triangle \boldsymbol{\theta}_k \times \triangle \boldsymbol{v}_{f,k}^{b} + \frac{1}{12}\left(\triangle \boldsymbol{\theta}_{k-1} \times \triangle \boldsymbol{v}_{f,k}^{b} + \triangle \boldsymbol{v}_{f,k-1}^{b} \times \triangle \boldsymbol{\theta}_k\right) \tag{63.4}$$

where $\boldsymbol{\omega}_{ie}^{n}$ is the angular rate of the earth frame (e-frame) relative to the inertial frame (i-frame) in the navigation frame, $\boldsymbol{\omega}_{en}^{n}$ is the angular rate of n-frame relative to e-frame in n-frame. The second and third terms on the right hand side of (63.4) correspond to the rotational and sculling motion respectively.

For the position update, the quaternion form, expressed as (63.5), is used in the horizontal position (latitude and longitude) to avoid the induced error of numerical integral. The height can be update separately as (63.6).

$$\begin{aligned} \boldsymbol{q}_{n(k)}^{e(k-1)} &= \boldsymbol{q}_{n(k-1)}^{e(k-1)} * \boldsymbol{q}_{n(k)}^{n(k-1)} \\ \boldsymbol{q}_{n(k)}^{e(k)} &= \boldsymbol{q}_{e(k-1)}^{e(k)} * \boldsymbol{q}_{n(k)}^{e(k-1)} \end{aligned} \tag{63.5}$$

$$h_k = h_{k-1} - v_{D,k-1/2}\Delta t_k \tag{63.6}$$

The attitude quaternion update algorithm can be written as follows

$$\begin{aligned} \boldsymbol{q}_{b(k)}^{n(k-1)} &= \boldsymbol{q}_{b(k-1)}^{n(k-1)} * \boldsymbol{q}_{b(k)}^{b(k-1)} \\ \boldsymbol{q}_{b(k)}^{n(k)} &= \boldsymbol{q}_{n(k-1)}^{n(k)} * \boldsymbol{q}_{b(k)}^{n(k-1)} \end{aligned} \tag{63.7}$$

where $\boldsymbol{q}_{b(k)}^{b(k-1)} = \begin{bmatrix} \cos\|0.5\boldsymbol{\phi}_k\| \\ \frac{\sin\|0.5\boldsymbol{\phi}_k\|}{\|0.5\boldsymbol{\phi}_k\|} 0.5\boldsymbol{\phi}_k \end{bmatrix}$, and $\boldsymbol{\phi}_k$ is the b-frame rotation vector [6], and it can be obtained as

$$\boldsymbol{\phi}_k = \Delta\boldsymbol{\theta}_k + \frac{1}{12}(\Delta\boldsymbol{\theta}_{k-1} \times \Delta\boldsymbol{\theta}_k) \tag{63.8}$$

where $\frac{1}{12}(\Delta\boldsymbol{\theta}_{k-1} \times \Delta\boldsymbol{\theta}_k)$ is the second-order coning correction term.

63.3.2 Kalman Filter

Kalman filter (KF) is the most popular estimation technique for GNSS/INS integration systems, and a typical KF of 21-dimensional error states is chosen in this paper. Here the INS error analysis was done with respect to the computer frame

(c-frame) and results in the following error model, which is called the ψ-angle error model since the attitude errors are expressed in terms of the ψ-angles [5, 7]

$$\begin{aligned}\delta\dot{\boldsymbol{r}}^c &= -\boldsymbol{\omega}_{ec}^c \times \delta\boldsymbol{r}^c + \delta\boldsymbol{v}^c \\ \delta\dot{\boldsymbol{v}}^c &= \boldsymbol{f}^c \times \boldsymbol{\psi} - \left(2\boldsymbol{\omega}_{ie}^c + \boldsymbol{\omega}_{ec}^c\right) \times \delta\boldsymbol{v}^c + \delta\boldsymbol{g}^c + \boldsymbol{C}_b^p \delta f^b \\ \dot{\boldsymbol{\psi}} &= -\left(\boldsymbol{\omega}_{ie}^c + \boldsymbol{\omega}_{ec}^c\right) \times \boldsymbol{\psi} - \boldsymbol{C}_b^p \delta\boldsymbol{\omega}_{ib}^b\end{aligned} \tag{63.9}$$

where, $\delta\dot{\boldsymbol{r}}^c$, $\delta\dot{\boldsymbol{v}}^c$, $\dot{\boldsymbol{\psi}}$ are the rate of the position error, the velocity error and attitude error, respectively, $\boldsymbol{\omega}_{ie}^c$ is the angular rate of e-frame relative to i-frame, in c-frame; $\boldsymbol{\omega}_{ec}^c$ is the angular rate of c-frame relative to e-frame, in c-frame; $\delta\boldsymbol{g}^c$ is the gravity error in the c-frame; $\delta\boldsymbol{\omega}_{ib}^b$, $\delta\boldsymbol{f}^b$ are the inertial sensor errors, $\boldsymbol{C}_b^p$ is the rotation matrix from body frame (b-frame) to platform frame (p-frame).

Furthermore, the IMU errors, including gyros and accelerometer, are augmented into the KF states and estimated by the difference of GNSS and INS solutions. The inertial sensor error model is normally built as 1st-order Gaussian-Markov model in most KF implementation for GNSS/INS integration systems [8], which can be expressed as

$$\begin{pmatrix}\dot{\boldsymbol{b}} \\ \dot{\boldsymbol{s}}\end{pmatrix} = -\frac{1}{T}\begin{pmatrix}\boldsymbol{b} \\ \boldsymbol{s}\end{pmatrix} + \boldsymbol{w} \tag{63.10}$$

where $\boldsymbol{b}$, $\boldsymbol{s}$ represent the inertial sensors errors respectively, including the bias error ($\boldsymbol{b}_g$, $\boldsymbol{b}_a$) and scale factor error ($\boldsymbol{s}_g$, $\boldsymbol{s}_a$), and $\boldsymbol{w}$ is the driving white noise. Building up the ψ-angle error model and the IMU error model to yield the 21-dimensional error states equation,

$$\dot{\boldsymbol{x}} = \boldsymbol{F}\boldsymbol{x} + \boldsymbol{G}\boldsymbol{w} \tag{63.11}$$

where $\boldsymbol{F}$ is the dynamic matrix, $\boldsymbol{G}$ is the design matrix of the system noise, $\boldsymbol{x}$ is the state vector, and $\boldsymbol{x} = \begin{bmatrix}\delta\boldsymbol{r}^c & \delta\boldsymbol{v}^c & \boldsymbol{\psi} & \boldsymbol{b}_g & \boldsymbol{b}_a & \boldsymbol{s}_g & \boldsymbol{s}_a\end{bmatrix}^T$.

GPS position and/or velocity are used as the KF update measurement in the navigation algorithm. The concrete measurements vector of the KF is the position and/or velocity difference between the INS (derived from the mechanization equations) and the GPS information, i.e.

$$\mathbf{z} = \begin{pmatrix}\mathbf{r}_{\mathrm{INS}} - \mathbf{r}_{\mathrm{GPS}} \\ \mathbf{v}_{\mathrm{INS}} - \mathbf{v}_{\mathrm{GPS}}\end{pmatrix} \tag{63.12}$$

The information fusion is done through the loosely-coupled closed-loop implementation of GNSS/INS integration, as shown in Fig. 63.2. Here, the estimated IMU errors are fed back as compensation to the INS.

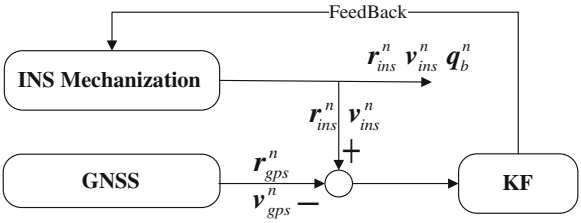

Fig. 63.2 Structure of Kalman filter for the GNSS/INS integration

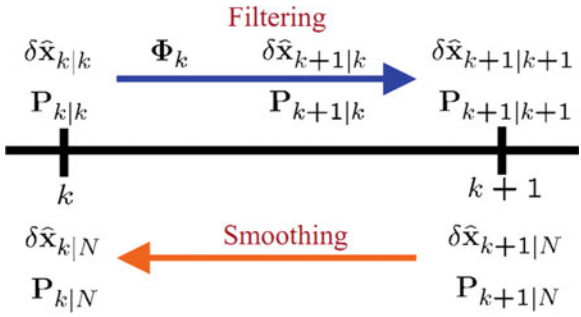

Fig. 63.3 RTS smoothing computation (After [4])

63.3.3 Optimal Smoothing

The purpose of the smoothing is to find an optimal estimate utilizing all past, current and future measurements. So it is a non-real-time data processing scheme. The smoothing algorithm can be applied in the GNSS/INS data processing software to help ensure the best possible accuracies. The Rauch-Tung-Striebel (RTS) algorithm is a well-known smoother for linear filters. The algorithm is written as follows [4, 9]

$$\begin{aligned} \hat{\boldsymbol{x}}_{k/N} &= \hat{\boldsymbol{x}}_k + \boldsymbol{A}_k\left(\hat{\boldsymbol{x}}_{k+1N} - \hat{\boldsymbol{x}}^-_{k+1}\right) \\ \boldsymbol{P}_{k/N} &= \boldsymbol{P}_k + \boldsymbol{A}_k\left(\boldsymbol{P}_{k/N} - \boldsymbol{P}^-_{k+1}\right)\boldsymbol{A}^T_k \\ \boldsymbol{A}_k &= \boldsymbol{P}_k\boldsymbol{\Phi}^T_{\boldsymbol{k}}\left(\boldsymbol{P}^-_{\boldsymbol{k+1}}\right)^{-1} \end{aligned} \tag{63.13}$$

where, $\boldsymbol{A}_k$ is the smoothing gain, Φ is the state transition matrix. $\boldsymbol{P}$ is the state error covariance, and subscript N is the total number of measurements. Figure 63.3 illustrates the computation procedure [4]. Here, all information of the filtering will be saved and used in the RTS algorithm to obtain the optimal estimations.

63.4 Test Results and Discussion

To demonstrate the correctness and usability of the developed software (Cinertial) in the airborne and land applications, real world data (including airborne and terrestrial datasets) was collected and post-processed for comparison with POSPac

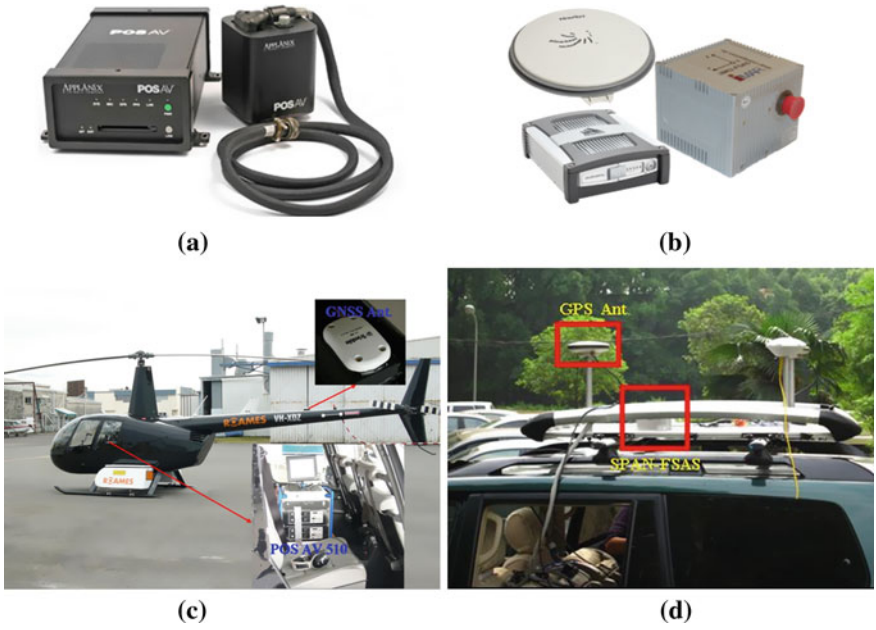

Fig. 63.4 Test vehicle and equipments setup. **a** POS AV 510, **b** SPAN-FSAS, **c** airborne test platform provided by ROAMES, **d** land test platform

and IE software. Two different GNSS/INS systems are used in our paper for airborne test and land vehicle test respectively. The first system is Applanix POS AV 510, as shown in Fig. 63.4a, which is an integrated "GNSS + Inertial" system built for airborne applications. It is available as a stand-alone product or as an OEM board set for systems integrators [10]. And POSPac is the corresponding post-processing software. The second one is NovAtel SPAN-FSAS tactical grade systems, as shown in Fig. 63.4b, which is integrated with NovAtel OEM4 GPS receiver and can be post-processed by IE [11, 12]. The key specifications of the IMUs applied in the two systems are listed in Table 63.1. The mounting of the tested devices was shown in Fig. 63.4c and d.

The navigation difference (including position, velocity and attitude) between Cinertial and POSPac/IE is the focus of our research in this article. The evaluation method is to compare the difference with the nominal accuracy of the used GNSS/

Table 63.1 Specifications of the used IMUs

	Test mode	Gyro bias (degree/h)	Gyro noise (degree/$\sqrt{h}$)	Accel. bias (mGal)	Accel. noise (m/s/$\sqrt{h}$)
POS AV 510	Airborne	0.1	0.02	300	0.03
SPAN-FSAS	Land	0.75	0.1	1,000	0.03

Table 63.2 Nominal accuracy of POS AV 510 and SPAN-FSAS (RMS)

	Position (m)	Velocity (m/s)	Roll and Pitch (deg)	True Heading (deg)
POS AV 510	0.05–0.30	0.005	0.005	0.008
SPAN-FSAS	0.01–0.015	0.02–0.01	0.008	0.012

INS systems themselves. It can prove the correctness and usability of the new developed software if the difference is significantly less than the nominal accuracy. Table 63.2 gives the nominal accuracy of POS AV 510 and SPAN-FSAS. The datasets collected by POS AV 510 and SPAN-FSAS are post processed by their respective software to show the reasonable analysis of the developed software. The following table gives the results of the two systems. Results of the airborne test will be presented first; then give the land vehicle test results.

63.4.1 Airborne Test

The airborne test, provided by Remote Observation Automated Modelling Economic Simulation (ROAMES) Group, was conducted in Australia on 1 June 2012. And the flight altitude is 600–1,400 m above ground. The test lasted for about 3 h. Figure 63.5 illustrates the flight path. The moving direction is indicated by the yellow arrows. The area covered by a red square is the mission field.

Figure 63.6 shows the difference of the processing results between Cinertial and POSPac of POS AV 510 systems. There are less than 5 cm difference in position

Fig. 63.5 Trajectory of airborne test in Jun 2012 (red highlighted mission field)

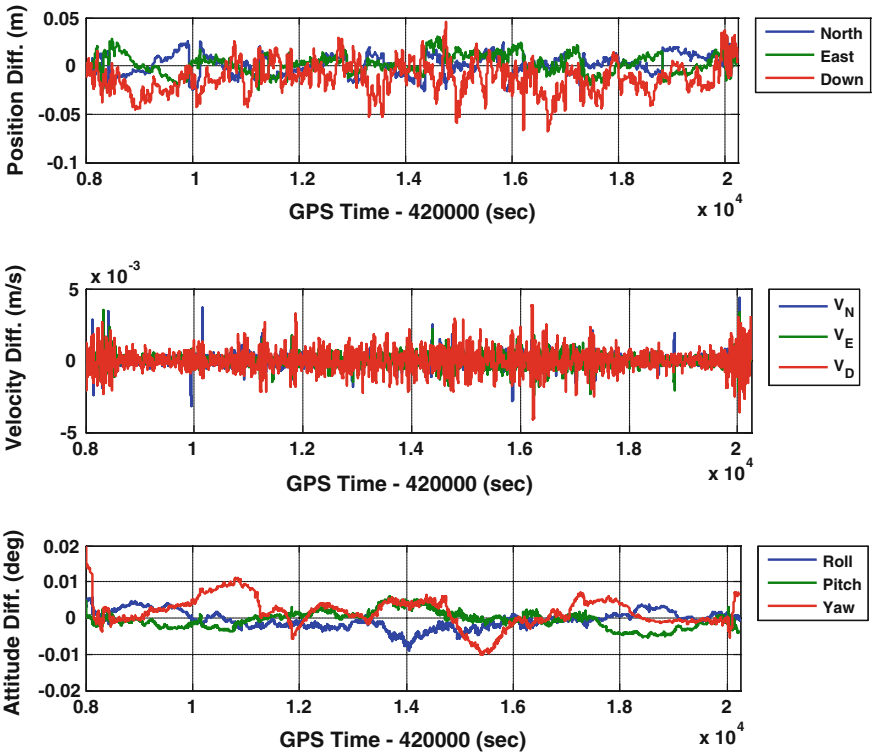

Fig. 63.6 Difference of POS AV 510 between Cinertial and POSPac

and less than 5 mm/s difference in velocity. The vertical difference is relatively low because GPS vertical positioning error is large. Additionally, there is less than 0.01° in attitude (roll, pitch and heading). Note that the heading difference has some drift behavior. This is because the heading estimation is under poor observability when the airplane flied without maneuver (e.g. move straight with constant speed).

Table 63.3 shows the corresponding statistic information. From Table 63.3 we can see that there are about 1 and 2 cm difference in horizontal and vertical position, less than 1 mm/s difference in velocity, 0.0025°, 0.0023° and 0.0044° difference in roll, pitch, and heading. Compare to the system nominal accuracy in

Table 63.3 Statistic summary of the difference between Cinertial and POSPac

	Position diff. (m)			Velocity diff. (m/s)			Attitude diff. (deg)		
	North	East	Height	North	East	Down	Roll	Pitch	Yaw
MEAN	0.0085	0.0081	0.0167	0.0003	0.0003	0.0005	0.0019	0.0018	0.0033
RMS	0.0103	0.0100	0.0206	0.0004	0.0004	0.0007	0.0025	0.0023	0.0044
MAX	0.0311	0.0308	0.0682	0.0044	0.0036	0.0041	0.0092	0.0061	0.0199

Fig. 63.7 Trajectory of land vehicle test in Jun 2011 (red highlighted urban area)

Table 63.2, the differences in position and velocity are far less than the nominal errors of POS AV 510. But the difference in attitude is only one half of the given absolute accuracy. The reason is that the mission part of this dataset has fewer maneuvers as shown in Fig. 63.5, which caused weaker observability of roll, pitch and heading. Therefore, the outputs of the two software have some difference even when processing the same dataset. However, the results can still show the level of the results of Cinertial can match the POSPac.

63.4.2 Land Vehicle Test

The land vehicle test was conducted using a sport utility vehicle (SUV) as the test platform (as shown in Fig. 63.4d). And it was conducted on slightly bumpy roads in the urban area of Wuhan on 21 June 2011, which contained various scenarios, as shown in Fig. 63.7. The moving direction is indicated by the yellow arrows. The test lasted for about 47 min with travel distance of more than 40 km. The area covered by a red square is the urban area.

Figure 63.8 shows the difference of navigation results between Cinertial and IE of SPAN-FSAS systems. It can be seen that there are obviously less than 5 cm difference in position, 5 mm/s difference in velocity and 0.02° in attitude. Compare to Fig. 63.6, the heading difference also has the drift behavior because of the poor observability. Table 63.4 is the statistic summary of the difference between the outputs of Cinertial and IE of SPAN-FSAS systems.

From Table 63.4 we can see there are less 1 cm difference in position results, less than 1 mm/s difference in velocity, 0.0033°, 0.0037° and 0.0139° difference in roll, pitch and heading. Compare to the system nominal accuracy in Table 63.2, the difference in position and velocity has far less than the absolute accuracy of SPAN-FSAS. But the difference in attitude is not obviously smaller than the nominal accuracy. The reason is that the attitude estimation is under poor observability when the land vehicle drove without maneuver (e.g. move straight with constant speed). Therefore, the attitude estimation is not under controlled and

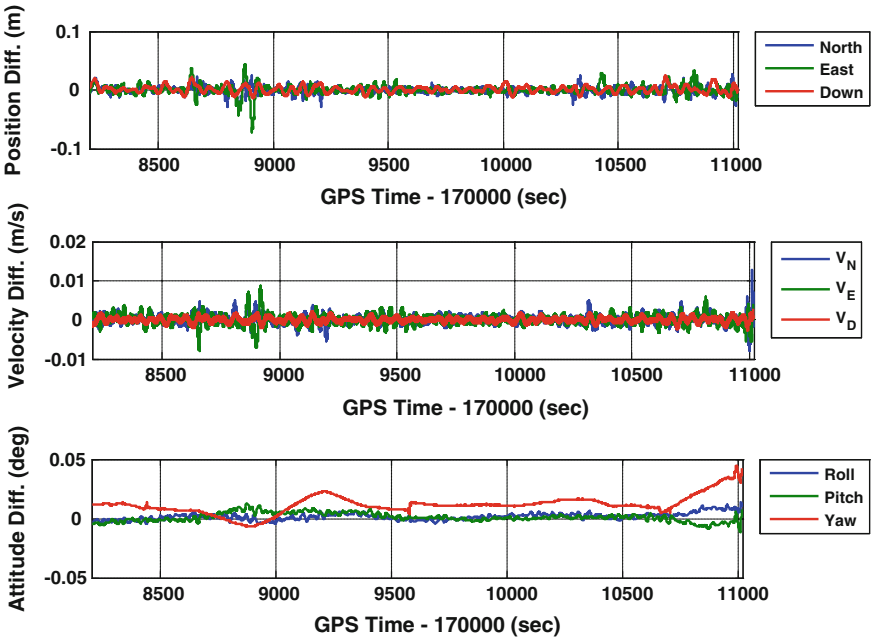

Fig. 63.8 Difference of SPAN-FSAS results from Cinertial and IE

Table 63.4 Statistic summary of the difference between Cinertial and IE

	Position diff. (m)			Velocity diff. (m/s)			Attitude diff. (degree)		
	North	East	Height	North	East	Down	Roll	Pitch	Yaw
MEAN	0.0042	0.0052	0.0048	0.0009	0.0010	0.0005	0.0026	0.0028	0.0121
RMS	0.0058	0.0083	0.0061	0.0012	0.0014	0.0007	0.0033	0.0037	0.0139
MAX	0.0289	0.0721	0.0240	0.0128	0.0087	0.0029	0.0140	0.0132	0.0443

can be easily affected by some random trivial factors, such as the minor differences between Cinertial and IE. It is possible that the concrete algorithm difference between the two software may introduce extra difference of the navigation solution. But the results still reflect that Cinertial and IE have about the same level of navigation results.

63.5 Conclusion

This paper introduces a GNSS/INS data processing software that has been newly developed—Cinertial, We simply describe the overall design of the software and detail the algorithms used in Cinertial. Field tests have been conducted to evaluate its correctness and usability by comparing to the well-known commercial software

including POSPac and IE. Results of the airborne and land vehicle tests using tactical grade INS/GNSS systems show that the difference of the data processing results between Cinertial and POSPac/IE is less than the given nominal accuracy. And it proved the correctness and usability of the new developed software. The next step of this work is to ensure the reliability and robustness of the new software by the processing of large amounts of datasets.

Acknowledgments Dr. Zhiqin Zhu from the School of Geodesy and Geomatics at Wuhan University is thanked for providing the reference system SPAN-FSAS with relevant cooperation. Qijin Chen is acknowledged for collecting the land test datasets used in our paper. This work was supported in part by the National Natural Science Foundation of China (41174028), the Key Laboratory Development Fund from the Ministry of Education of China (618-277176), the LIESMARS Special Research Fund, the Research Start-up Fund from Wuhan University (618-273438), and the Fundamental Research Funds for the Central Universities (201161802020002).

References

1. Inertial Explorer®. Available online:http://webone.novatel.ca/assets/Documents/Waypoint/InertialExplorer.pdf. Accessed 11 Dec 2012)
2. Gautier JD (2003) GPS/INS generalized evaluation tool (GIGET) for the design and testing of integrated navigation system. The dissertation for the degree of doctor of philosophy, Stanford University
3. Savage PG (2000) Strapdown analytics (part 1 and 2)
4. Shin EH (2005) Estimation techniques for low-cost inertial navigation. UCGE report. (20219)
5. Britting K (1971) Inertial navigation system analysis. Wiley Interscience, New York
6. Bortz JE (1971) A new mathematical formulation for strapdown inertial navigation. IEEE Trans Aerospace Electronic Systems AES-7(1):61–66
7. Benson DO (1975) A comparison of two approaches to pure-inertial and Doppler-inertial error analysis. Aerospace Electronic System IEEE Transactions 4:447–455
8. Park M (2004) Error analysis and stochastic modeling of MEMS based inertial sensors for land vehicle navigation applications. University of Calgary, Department of Geomatics Engineering
9. Brown RG, Hwang PYC (1992) Introduction to random signals and applied Kalman filtering, 2nd edn. Wiley, New York
10. POS AV specifications. Available online:http://www.applanix.com/media/downloads/products/specs/posav.pdf Accessed 11 Dec 2012)
11. IMU-FSAS User Guide. Available online: http://www.novatel.com/assets/Documents/Papers/FSAS.pdf Accessed 11 Dec 2012)
12. Kennedy S et al. (2007) GPS/INS Integration in real-time and post-processing with NovAtel's SPAN system. In: Proceedings of the international global navigation satellite systems society symposium, University of New South Wales, Sydney, Australia, pp 4–6

Chapter 64
Celestial Positioning with CCD Observing the Sun

Yinhu Zhan, Yong Zheng and Chao Zhang

Abstract Celestial navigation by observing the sun is a hot issue in recent years, and how to improve the positioning precision is a concerned problem to researchers in the world. The positioning principal by observing the height of the sun is adopted in this paper, and the gray centroid algorithm to extracting the sun's center is introduced. Processing the practical data, the CCD observing precision of the sun is analyzed. By simulative calculation, impact of the sun's position, observing precision, tracking time and CCD observing period on positioning precision is analyzed quantitatively. Then, the best observing scheme is put forward, which means that the best observing time is in transit around, and the tracking time should be as long as possible, and CCD sampling rate should be as high as possible. Practical observing data shows that positioning precision can be improved from 15″ to 5″ when tracking time extends from 30 to 90 min.

Keywords Celestial positioning · CCD · Sun · Error analysis · Precision

64.1 Introduction

Celestial navigation is a technology to determine the position and orientation of the observing station or carrier, which make use of the horizontal coordinate and time information of the stars, the sun, the moon, or the planets. As an independent, unconditional, and global navigation system, celestial navigation has such advantages as high autonomy, good concealment, and high precision. In time of war, it is a safe and reliable means of navigation [1].

Y. Zhan (✉) · Y. Zheng · C. Zhang
Zhengzhou institute of Surveying and Mapping, Zhengzhou 450052, China
e-mail: oscardad@163.com

J. Sun et al. (eds.), *China Satellite Navigation Conference (CSNC) 2013 Proceedings*, Lecture Notes in Electrical Engineering 245,
DOI: 10.1007/978-3-642-37407-4_64,

During the day time, the sun is the only-visible natural body in the sky. How to navigate by observing the sun has been a hot issue. At present, marine sextant has been used to observing the sun in a long tracking time to realize navigation on the boat, namely the sun line positioning. In order to get better spatial positioning structure, people usually choose the sun at transit nearby for continuous observation, and sun azimuth should change up to 30°. The sun line positioning needs about 2–3 h to achieve up to 2′ positioning accuracy. Wu Guanghua in Jimei University developed an improved astronomical positioning apparatus, called MGPES electronic sextant. While the electronic sextant is in the observation, navigation computer is calculating estimated position of the ship, and the predicted height of the sun. The combination of predicted height and observing height produces new information called intercept, then the combination of the intercept and the coefficient matrix selected by nonlinear Kalman filtering algorithm can produced position correction of optimal estimation. When the sun is at transit nearby, the positioning accuracy can achieve up to 1′, however the precision will dramatically reduce to 10′ when the sun is slightly deviated from the transit [2].

CCD-based celestial navigation technology is also a research hotspot. American Spirit and Opportunity Mars car equipped with a sun sensor, which was used for celestial navigation. Kruda and Geol proposed continuous observation of elevation and azimuth angles of the sun and the earth a celestial navigation and dead reckoning integrated navigation method to obtain the absolute position of the lunar rover on the moon, and the positioning accuracy is about 300 m., Yang Peng and Liu Jilin of Zhejiang University take use of the Cannon Eos 5D sun sensor on earth to achieve navigation, the positioning algorithm of which is similar to the sun line positioning principle in marine, while the best positioning accuracy is about 4 km in 30 min tracking [3, 4].

The positioning principal by observing the height of the sun is proposed in this paper, and the gray centroid algorithm to extracting the sun's center is introduced. By simulative calculation, impact of the sun's position, observing precision, tracking time and CCD observing period on positioning precision is analysed quantitatively, and the best observing scheme is put forward. Practical observing data shows that the positioning precision has been improved because of the research in this paper.

64.2 Positioning Principal by Observing the Sun

There are 2 key problems that should be solved in CCD-based celestial positioning. One is how to capture the sun's horizon coordinate information from the sun image; the other is how to calculate the position using the horizon coordinate information above.

64.2.1 Extraction Algorithm for the Center of the Sun

After obtaining images of the sun, it is necessary to accurately extract the center of the sun in the images before solving the zenith distance through the camera parameters. Therefore, higher-precision center extracted from the image of the sun is the prerequisite of high precision positioning. The following describes an extraction algorithm based on weighted gray-scale.

Figure 64.1 is a diagram of the image. Provided there is a small rectangular region completely containing the real sun image, then the rectangular region can be described by the pixel coordinates as follow [5]

$$i_1 \le u_p \le i_2 \quad j_1 \le v_p \le j_2 \tag{64.1}$$

$g(u_p, v_p)$ is the gray value of each pixel in the region, T_0 is the gray value of background of the image. Then the coordinate of the sun's center (u_c, v_c) can be described as [6]

$$\begin{cases} u_c = \dfrac{\sum_{u_p=i_1}^{i_2} \sum_{v_p=j_1}^{j_2} u_p[g(u_p, v_p) - T_0]}{\sum_{u_p=i_1}^{i_2} \sum_{v_p=j_1}^{j_2} [g(u_p, v_p) - T_0]} \\ v_c = \dfrac{\sum_{u_p=i_1}^{i_2} \sum_{v_p=j_1}^{j_2} v_p[g(u_p, v_p) - T_0]}{\sum_{u_p=i_1}^{i_2} \sum_{v_p=j_1}^{j_2} [g(u_p, v_p) - T_0]} \end{cases} \tag{64.2}$$

Obviously, T_0 does some impacts on the extracting. Observed on the earth, the apparent radius of the sun is 15–16′, which means dozens of pixels is occupied by the sun in the image. So there is an optimal T_0 to adjust the image radius of the sun to real size. In practice, it always costs some time to try for the optimal T_0.

64.2.2 Positioning Principal Based on the Zenith of the Sun

Under the measurement of the sun, the instantaneous UTC moment T_i is recorded. Z_i has been gotten from the images, and the apparent ascension α_i and declination δ_i have been calculated. According to the spherical triangle formula as follow

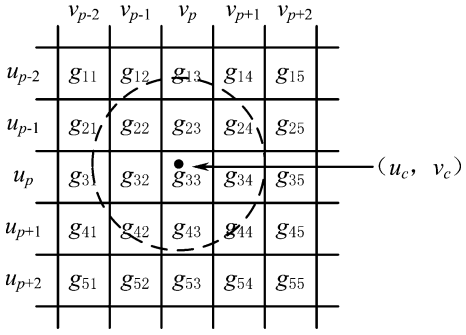

Fig. 64.1 Diagram map of extracting the *center* of the sun

$$\cos z_i = \sin\varphi \sin\delta_i + \cos\varphi \cos\delta_i \cos(S_i - \alpha_i + \lambda) \tag{64.3}$$

S_i is the side real time of Greenwich, which can be calculated according to T_i. Obviously, Eq. (64.3) contains only 2 unknown parameters, which is longitude λ and latitude φ. In theory, only the position of the station can be solved if the sun is observed twice. However, if the interval of two observations is too short, it is impossible to get a good result. In practice, it must take a considerable time to tracking and observing the sun to achieve a better positioning structure and high-frequency sampling data, only in this way can we get content results.

64.3 Simulative Positioning Experiments

The main factors affecting the positioning accuracy are as follows: the position of the sun, CCD observing precision, CCD sampling period, as well as tracking time. The followings are data simulation and calculation, respectively, to study the impact of the factors above, the purpose of which is to seek the best observing scheme. The data simulation scenarios are as follows:

According to the real astronomical position ($\lambda = 7^h30^m29.8^s$, $\varphi = 34°44'22.7''$), theoretical zenith distance of the sun is calculated. Symbol appointments are as follows:

σ variance of the simulative zenith distance
t track-observing time
T CCD sampling interval.

64.3.1 Impact of the Sun's Position on the Positioning Precision

Beijing time 8:00–16:00 is averagely divided into 16 periods. In other words, each period of observation is 0.5 h. The specific simulation conditions are $\sigma = 15.0''$, $t = 0.5$ h, and $T = 5$ s.

After processing the simulative data, mean square errors of longitude and latitude can be captured as m_λ and m_φ, and the positioning mean square error m can be represented by

$$m = \sqrt{m_\lambda^2 + m_\varphi^2}. \tag{64.4}$$

Figure 64.2 shows the sun position's impact on the positioning precision.

The sun goes through the transit at about 12:15 in the 9th period, and the Fig. 64.2 exactly reflects the highest positioning precision $\pm 21.0''$ in the 9th period.

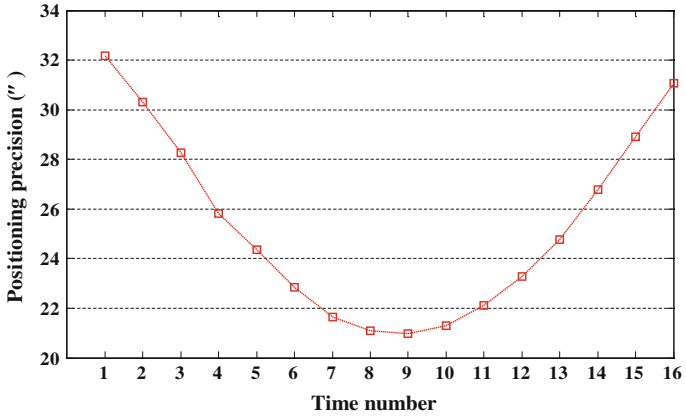

Fig. 64.2 Plot: Sun position's impact on the positioning precision

The positioning precision varies as regular as the position of the sun, which has a good symmetry. Obviously, observation of the sun should be chosen in transit near.

64.3.2 Impact of σ on Positioning Precision

Beijing time 8:00–16:00 is divided the same as the Sect. 64.3.1, and the specific simulation conditions are $t = 0.5$ h, $T = 5$ s, $\sigma = 10''$, $\sigma = 15''$, $\sigma = 20''$. Figure 64.3 shows the impact of zenith distance error on the positioning precision.

According to the Fig. 64.3, when the tracking time is 0.5 h, σ has a great impact on the positioning precision. The observations precision improves double

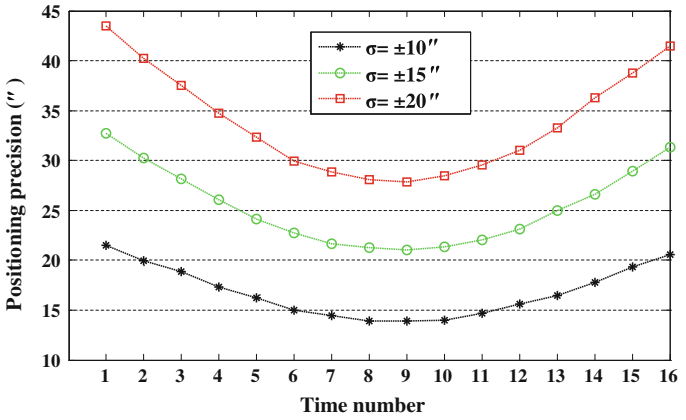

Fig. 64.3 Plot: Impact of zenith distance error on the positioning precision

as the σ is half of before. This demonstrates the importance of high-precision algorithm to extracting the center of the sun in the images.

64.3.3 Impact of t on Positioning Precision

The epoch 12:15 is the centric moment, and the step length is 10 min. So there are 12 periods as follow:

$$\begin{array}{ll} t_1 = 12{:}10{-}12{:}20 & t_2 = 12{:}05{-}12{:}25 \\ t_3 = 12{:}00{-}12{:}30 & t_4 = 11{:}55{-}12{:}35 \\ t_5 = 11{:}50{-}12{:}40 & t_6 = 11{:}45{-}12{:}45 \\ t_7 = 11{:}40{-}12{:}50 & t_8 = 11{:}35{-}12{:}55 \\ t_9 = 11{:}00{-}13{:}00 & t_{10} = 11{:}25{-}13{:}05 \\ t_{11} = 11{:}20{-}13{:}10 & t_{12} = 11{:}15{-}13{:}15 \end{array} \tag{64.5}$$

The other simulation conditions are $\sigma = 15.0''$ and $T = 5$ s. Figure 64.4 shows the relationship between the tracking time and positioning precision.

According to the Fig. 64.4, the longer tracking time is, the higher positioning precision achieves, because the larger the sun's position changes, the better the positioning structure improves. Obvious inflection point comes up at t_3 and t_5, and the tracking time are 30 and 50 min, which means the arc distances change of the sun are about 5.5° and 15° respectively. In practice, it is advised that the tracking time should not be less than 30 min to guarantee the arc distance change of the sun is larger than 5.5°.

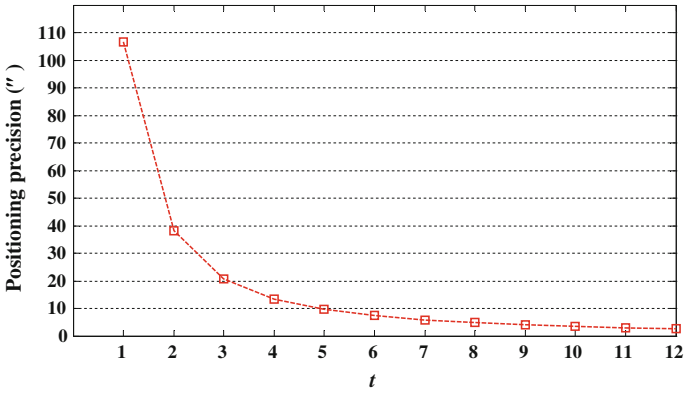

Fig. 64.4 Plot: Tracking time's impact on the positioning precision

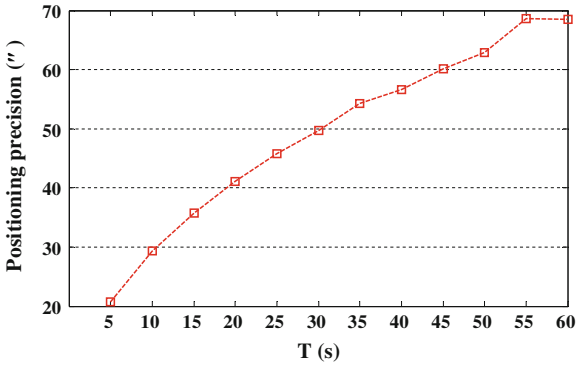

Fig. 64.5 Plot: Impact of CCD sampling interval on the positioning

64.3.4 Impact of T on Positioning Precision

The simulation conditions are t = 12:00–12:30, $\sigma = 15.0''$, and $T = 5-60$ s. Figure 64.5 shows the relationship between CCD sampling interval and positioning precision.

According to the Fig. 64.5, impact of CCD sampling interval on the positioning is significant. The shorter CCD sampling interval is, the higher. If the sampling rate doubled from 1/10 to 1/5 Hz, the positioning precision is improved from $30''$ to $20''$. In practical application, in the precondition of ensuring the stability of normal data transmission and timing, it should maximize the sampling rate of the CCD to improve the positioning accuracy.

64.3.5 The Optimal Scheme for Observing the Sun

Based on the study above, the optimal scheme for observing the sun is concluded as follow:

1. Try to observing the sun in the transit nearby;
2. Try to extend the observing time to guarantee the arc distance change of the sun is larger than 5.5°;
3. Maximize the sampling rate of the CCD.

64.4 Real Observing Data and Analysis

2012-11-11, a region in northern China, the sky has a small amount of thin cloud. When the sun was in transit nearby, the fish-eye camera took pictures continuously. The observing system adopted high-precision Rockle Spirit Level made in

German, and computer's internal clock time transferred by the GPS satellite kept the time system. Since the capacity of the single solar image reaches 20 M, because of the restrictions of the CCD and notebook computer, the image data transferred to the computer spent about 8 s. However, during the data transmission, computer crystal is unstable, which will affect the timing accuracy. Therefore, the sampling interval was set to 10 s, the total tracking time is 90 min, and 415 images were captured.

64.4.1 Observation Precision Analysis

According to the algorithm introduced in Sect. 64.2, center of the sun was extracted, and the zenith distance was solved, and the atmospheric refraction was corrected based on measured meteorological parameters. According to the accurate astronomical position of the station, the DE405 ephemeris was used to calculate true zenith distance of the sun. Figure 64.6 shows the deviation between observing zenith distance and theoretical zenith distance.

Error of the zenith distance overall is randomly distributed, but local trend term changes, due to the remnants of camera lens distortion correction. Absolute precision of zenith distance get to 0.5′, and the variance is about 13.0″; absolute precision of horizon get to 0.8′, and the variance is about 15.0″.

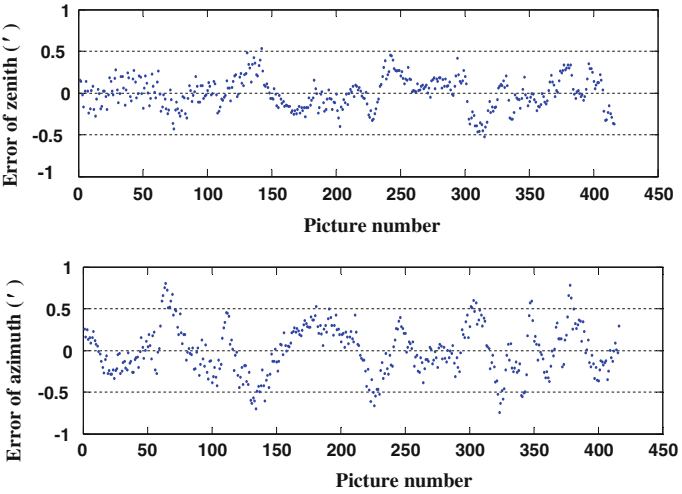

Fig. 64.6 Plot: Error of the observing zenith and azimuth

Table 64.1 Positioning results by observing the Sun

Picture number	Tracking time (min)	m_λ	m_φ	$\Delta\lambda$	$\Delta\varphi$
1–200	34	±15.1″	±1.2″	+9.2″	−0.2″
1–250	42	±11.2″	±1.2″	+0.2″	+0.3″
1–300	50	±8.1″	±1.0″	−8.0″	+0.9″
1–350	58	±6.8″	±1.0″	+4.5″	+0.1″
1–415	86	±5.2″	±0.9″	+6.5″	−0.1″

64.4.2 Positioning Results

Data was processed in classification of tracking time, and the results are shown in Table 64.1 where m_λ and m_φ represent the mean square errors of longitude and latitude, while $\Delta\lambda$ and $\Delta\varphi$ represent the deviations of longitude and latitude.

According to the Table 64.1, when the tracking time is 34 min, positioning precision can get to 15.1″. Furthermore, when the tracking time extends to 86 min, positioning precision can be improved to 5.2″. The positioning accuracy of the experiment is significantly better than the literature report in Sect. 64.1. At the same time, the experimental results demonstrate agreement with simulation.

64.5 Conclusions

1. The positioning principal and extracting algorithm proposed in this paper are correct and feasible, and good results have been achieved in practice.
2. Try to observing the sun in the transit nearby, extend the observing time to guarantee the arc distance change of the sun is larger than 5.5°, and maximize the sampling rate of the CCD.
3. Observing the sun by CCD can get high-precision positioning results. When the tracking time extends from 34 to 86 min, positioning precision varies from 15.1″ to 5.2″.

Acknowledgments Thank the Chinese National Natural Science Foundation (41174025, 41174026, 10878025) for subsidize for this paper.

References

1. Anguo W (2001) Celestial navigation technique in the background of navigation war. Progress Astron 19(2):326–330
2. Guanghua W (2003) An optimal estimating method for celestial navigation. J Navig 44(4):266–269

3. Kuroda Y, Kurosawa T, Tsuchiya A et al (1991) Accurate localization in combination with planet observation and dead reckoning for lunar rover. Proceeding of 2004 IEEE international conference on robotics and automation (ICRA2004), New Orleans, USA, 2004, pp 2092–2097
4. Furgale P, Enright J et al (2011) Sun sensor navigation for planetary rovers: theory and field testing. Aerosp Electron Syst 47(3):1631–1647
5. Rufmo G, Accardo D (2003) Enhancement of the centroiding algorithm for star tracker measure refinement (2) doi:10.1016/S0094-5765(02)00199-6
6. Hancock BR, Stirbl RC (2001) Cunning, ham T J CMOS active pixel sensor specific performance effects on star tracker/imager position accuracy

Chapter 65
Research on the Non-Cooperative Positioning Technologies for Combination of BeiDou and TD-LTE

Zhongliang Deng, Xiaofei Sun, Yannan Xiao, Xiaoguan Wang, Neng Wan and Zhongwei Zhan

Abstract Considering the urgent demand for related applications of BeiDou Navigation Satellite System and TD-LTE, this paper studies non-cooperative positioning technology combining the BeiDou and TD-LTE. It does not need or have a cooperation with network and mobile phones which not only reduced the cost of investment and broaden its application domain. The technology of this paper relies on the high-precision location and time service of BeiDou, efficient transmission bandwidth and Multiple Input Multiple Output (MIMO) of TD-LTE system. A complete scheme of real-time and high-precision non-cooperative positioning for mobile phones is proposed. It aims at the Sounding Reference Signal (SRS) of TD-LTE, utilizes a TDOA/AOA hybrid positioning method based on Fractional Fourier Transform (FRFT) and some related simulations are accomplished to verify its feasibility.

Keywords BeiDou · Navigation satellite system · TD-LTE · Non-cooperative positioning · FRFT

65.1 Introduction

Unlike the well-known satellite positioning technology, the non-cooperative positioning technology based on User Equipment (UE) is a kind of passive positioning technology without the cooperation of users. It accomplishes the estimation

X. Sun (✉)
Beijing University of Post and Telecommunication, Haidian District Xitucheng Road. 10, Beijing 100876, China
e-mail: 406931645@163.com

Z. Deng · Y. Xiao · X. Wang · N. Wan · Z. Zhan
Institute of EE, Beijing University of Post and Telecommunication, Beijing, China

J. Sun et al. (eds.), *China Satellite Navigation Conference (CSNC) 2013 Proceedings*, Lecture Notes in Electrical Engineering 245,
DOI: 10.1007/978-3-642-37407-4_65,

of users' location by capturing the signal from UE. Considering the properties, the non-cooperative positioning is applied to some special areas. For group users, it makes monitoring management and dispatch available by achieving identity and position information of employees. For relief department, it can effectively strengthen emergency rescue capability via swiftly positioning the mobile phones of trapped people on a large scale. For security sector, it can improve the ability to investigate and monitor crime through snugly positioning and tracking the abnormal phones.

In 1996, FCC proposed E911 services which requires that the location of an E911 caller be determined with an accuracy of 100 m in 67 % of the cases without modifying UEs. E911 is a typical application of non-cooperative positioning and urge many corporations and universities to do related research. Ian Paul Larsen briefly introduced their project about UE locator in Ref. [1]. Zhu Dali proposed a kind of induced scheme based on encoder to accomplish the UE non-cooperative positioning in Ref. [2]. XuBo do some research on non-cooperative positioning for CDMA2000 in Ref. [3].

The location parameter estimation, time synchronization, real-time acquisition and interaction of location information are the key of non-cooperative positioning technology. This paper combines BeiDou and TD-LTE to realize technologies above, the structure and principle of positioning system are proposed in the second chapter, the third chapter contains the key research on non-cooperative positioning technology, the fourth chapter and the fifth chapter are simulations and concluding remarks.

65.2 Combined Positioning System

65.2.1 System Structure and Operating Principle

The system combines the BeiDou navigation with TD-LTE to accomplish location calculation by estimating the parameters of UE's up-link signal. The system consists of BeiDou Navigation Satellite System, Positioning Equipment (PE) equipped with receiving TD-LTE up-link signal, the server providing related service and UEs. According to the application domain, the PE could be portable, vehicular or fixed. The structure of system is shown in Fig. 65.1.

Deploy the PEs on the scene when the service is launched. In order to establish the preparation for positioning UEs, the PEs receive and analysis the navigation messages from BeiDou Satellites to accomplish the accurate acquisition of three-dimensional location information and time synchronization information. Then, PE broadcast the TD-LTE Downlink Control Signal (DCS) to configure the UEs emit Positioning Reference Signal (PRS). PE estimates the location parameters (including AOA and TOA) of the PRS and completes location calculation of intra-regional UEs. In order to provide service for certain users, PE send the users' information (including location information and UE information, etc.) to the server

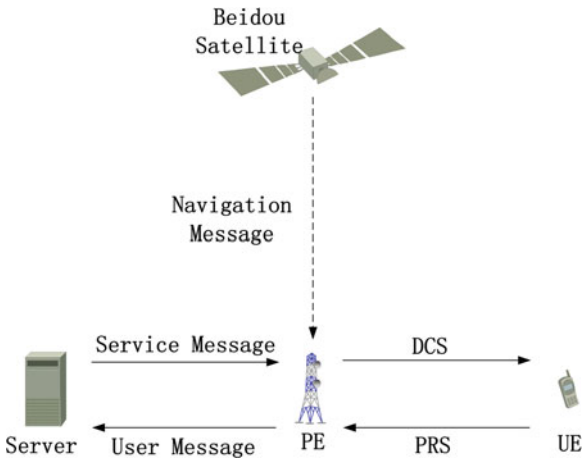

Fig. 65.1 The structure of system

65.2.2 System Analysis

To consider the whole system from PRS selection, system superiority, location method selection and time synchronization solution, etc.

1. Choosing Sound Reference signal (SRS) of TD-LTE as PRS. SRS modulated by ZC sequence and distinguished among MIMO antennas and UEs by frequency Division Multiplexing (FDM), Time Division Multiplexing (TDM), Code Division Multiplexing (CDM) or hybrid method. The Constant Amplitude Zero Autocorrelation (CAZAC) of ZC sequence makes it better for parallel detection. ZC sequence could be expressed [4]:

$$a_q = \exp\left[-\mathrm{j}2\pi q \frac{n(n+1)/2 + ln}{N_{ZC}}\right] \tag{65.1}$$

where $q \in \{1, \cdots, N_{ZC} - 1\}$ donating the root index of ZC sequence. $n = 0, 1, \cdots, N_{ZC} - 1$, $l \in N$, l could be any integer and $l = 0$ in TD-LTE.

2. The Cramer-Rao Lower Bound (CRLB) of delay estimation in single-path [5]:

$$\mathrm{var}(\widehat{\tau}) \geq \frac{1}{\frac{\varepsilon}{N_o/2}\overline{F^2}} \tag{65.2}$$

It can be shown that $\frac{\varepsilon}{N_o/2}$ is a SNR. Also, $\overline{F^2}$ is the bandwidth of signal. That means the performance of positioning could be promoted by increasing signal bandwidth. In TD-LTE, SRS is a kind of wideband reference signal and could be covered the whole system bandwidth by frequency hopping. The comparison of TD-LTE and 3G in system bandwidth is shown in Table 65.1.

Table 65.1 Comparing TD-LTE and 3G in system bandwidth

Typical mobile telecommunication system	Max system bandwith (MHz)
TD-SCDMA	1.6
CDMA 2000	1.25
WCDMA	5
TD-LTE	20

3. In TD-LTE, multi-antenna array is used for realizing MIMO. The addition of multi-antenna array enriches the location method and provides basic condition for TDOA/AOA hybrid location in this paper.
4. For the PEs, time synchronization, acquisition of real-time location information and interaction have a severe impact on location accuracy even feasibility. We choose BeiDou System to realize time synchronization and provide real-time coordinate for PEs. What's more, we consider using X2 interface of TD-LTE to accomplish the PEs' interaction. According to the different application areas, the requirement of TD-LTE. In order to location a client in a market, the accuracy of time service and horizontal location should better than 30 ns and 10 m.

65.3 Non-Cooperative Positioning Technologies

The key of non-cooperative positioning technology lies on receiver design. It aims at accomplish accurate estimation of location parameters (including AOA and TOA) in multi-path and multi-access condition.

65.3.1 Analysis of Location Parameters Estimation

By analyzing the Eq. (65.1), we could find SRS is a discrete form of Linear Frequency Modulation (LFM) signal. The normal expression of LFM:

$$x(t) = \exp(j2\pi f_0 t + j\pi\mu_0 t^2) \tag{65.3}$$

where f_0 is initial frequency and μ_0 is ratio of frequency modulate.

Considering the non-stationary of LFM signal, the performance of traditional algorithms for AOA estimation like Multiple Signal Classification (MUSIC) [6] and estimation of Signal Parameters via Rotational Techniques (ESPRIT) [7] will degrade. Meanwhile, parameter estimation based on correlation in frequency domain of TD-LTE protocol [4] may not be effective in eliminating the influence caused by multi-path, multi-access and noise.

In order to solve the problems above, we introduce an algorithm based on Fraction Fourier Transform (FRFT). The p order FRFT could be defined as follows [8]:

$$X_p(u) = F^p[x(t)] = \int_{-\infty}^{\infty} x(t)K_p(t,u)dt \tag{65.4}$$

$K_p(t,u)$ is the transforming kernel of FRFT and could be expressed by:

$$K_p(t,u) = \begin{cases} \sqrt{\frac{1-j\cot\alpha}{2\pi}}\exp(j\frac{t^2+u^2}{2}\cot\alpha - tu\csc\alpha), \alpha \neq n\pi \\ \delta(t-u), \alpha = 2n\pi \\ \delta(t+u), \alpha = (2n\pm 1)\pi \end{cases}$$

where $\alpha = p\pi/2$, $X_1(u)$ become general Fourier Transform with $p = 1$.

FRFT is a kind of linear operator. If we regard it as the $\pi/2$ counterclockwise rotation from the time axis to frequency axis and the operator is a rotation at any angle of α without cross-terms. LFM signal is characteristic of perfect aggregation in FRFT domain that an optimal transform order could be found out for separating interference and improving performance of parameter estimation.

65.3.2 Receiver Structure and Algorithms

Considering the receiver structure in Fig. 65.2:

Antenna array is uniform array with number of K elements and the interval is D. SRSs from number of M UEs radiate on antenna array. Analysis receiver signal of one branch:

$$r(t) = \sum_{m=1}^{M}\sum_{l=1}^{L} s_m^l(t-\tau_m^l) + n_o(t) \tag{65.5}$$

with τ_m^l donating the SRS from the l path of the m UE. L is the totals of path and $n_o(t)$ is gaussian noise which is not related to SRS and mutual independence.

Based on the physical structure of TD-LTE up-link, base-band signal is acquired after sampling, CP removal, FFT and subcarrier de-mapping:

$$r(n) = \sum_{m=1}^{M}\sum_{l=1}^{L} c_m^l(n-\tau_m^l) + n_o(n) \tag{65.6}$$

Then calculate multi-order FRFT of base sequence and root sequence. And select the optimal order p_{opt} by target function as follows:

$$p_{opt} = \arg_p \min\left(\frac{1}{N}\sum_{n=1}^{N}\left|\left|\frac{R_p(u)}{T_p(u)}\right| - 1\right|^2\right) \tag{65.7}$$

with $R_p(u)$ and $T_p(u)$ donating the p order FRFT of base-band sequence and root sequence. N is the total periods of root sequence. TOA could be obtained by searching the IFRFT of p_{opt} order transformed result in time domain.

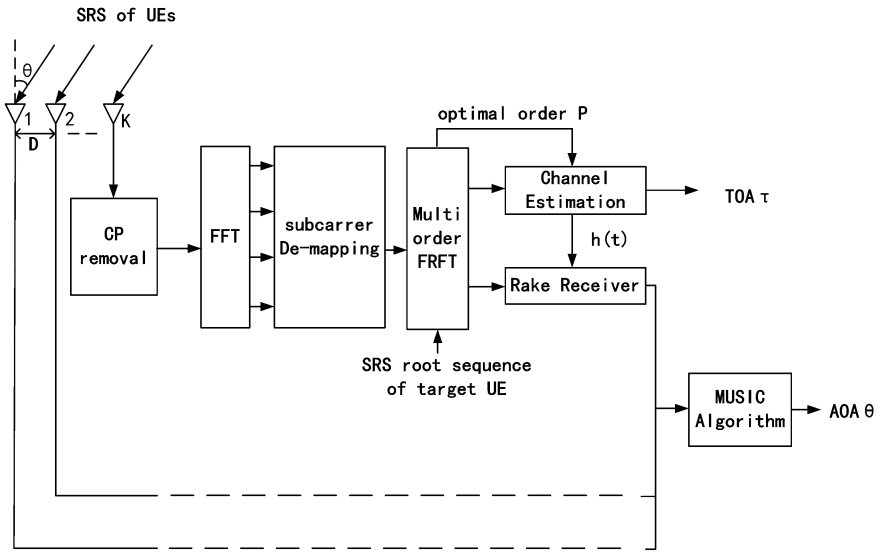

Fig. 65.2 The receiver structure of positioning system

$$\widehat{H}_{opt}(u) = \frac{1}{N}\sum_{n=1}^{N} \frac{R_{p_{opt}}(u)}{T_{p_{opt}}(u)e^{-j\frac{\cot\alpha}{2}u^2}} \tag{65.8}$$

$$\widehat{h}(n) = IDFRFT[\widehat{H}_{p_{opt}}(u)] \tag{65.9}$$

$$\tau = \arg_{\tau}\max[\widehat{h}(n)] \tag{65.10}$$

After time estimation accomplished, we could obtain the AOA reference signal by Rake diversity receiving on the base of $\widehat{h}(n)$:

$$S_k(n) = C_k(n) + N_k(n) \tag{65.11}$$

with $C_k(n)$ donating the base-band sequence of target UE. $N_k(n)$ is the interference including multi-path, multi-access and noise and in a low level due to the perfect aggregation of FRFT.

Then the MUSIC algorithm will be used. Express all AOA reference signals as vector form:

$$S = AC + N \tag{65.12}$$

$$S = [S_1(n)\ S_2(n)\ \ldots\ S_K(n)]^T$$

$C = C_0(n)$ base-band sequence of reference array element

$$A = \left[1\ e^{-jT_m}\ldots e^{-j(K-1)T_m}\right]^T \text{ where } T_m = \frac{2\pi D}{\lambda}\sin\theta_m$$

$$N = [N_1(n)\ N_2(n)\ \ldots\ N_K(n)]^T$$

Ignoring the correlation matrixes of independent components:

$$R_{SS} = E[SS^H] = AR_{CC}A^H + \sigma^2 I \tag{65.13}$$

Calculating eigenvalue decomposition of R_{CC}:

$$R_{CC} = U_C \sum_C U_C^H + U_N \sum_N U_N^H \tag{65.14}$$

with U_C and U_N respectively donating the signal space and noise space. The spatial spectrum of target UE could be expressed by:

$$P(\theta) = \frac{1}{\left\| U_N^H A(\theta) \right\|_2^2} \tag{65.15}$$

The value θ indexed by spectral peak is the AOA of target UE. Acquisition of location parameter from different UEs could be accomplished by changing root sequence of target UE.

65.4 Simulations and Analysis

The simulation system is configured on the index of 20 MHz TD-LTE: sample frequency $fs = 30.72$ MHz, the size of FFT is 2,048 and subcarrier interval is 15 kHz. The size of antenna array elements $K = 4$, the interval D is half wavelength. Other parameters configuration is listed in Table 65.2:

Select received signal from an array element. According to the object function in Eq. (65.6), observe the performance of estimation on multiple-order ($0 \leq p \leq 2$) FRFT domain in Fig. 65.3.

It could be found that the object function of $p_{opt} = 0.61$ smaller than the value of $p = 1$ (frequency domain) and $p = 0$ (time domain). It means that the performance of location parameters estimation could be promoted in the FRFT domain.

Accomplish the TOA and AOA estimation by algorithm above, comparing the performance with frequency domain correlation and smoothed MUSIC algorithm. The Figs. 65.4 and 65.5 show the compared results.

Table 65.2 Simulation parameters configuration

	SRS root index	AOA of direct-path (°)	AOA of reflect-path (°)	TOA of direct-path	TOA of reflect-path
UE1	29	40	45	55 samples	60 samples
UE2	61	60	67	58 samples	66 samples

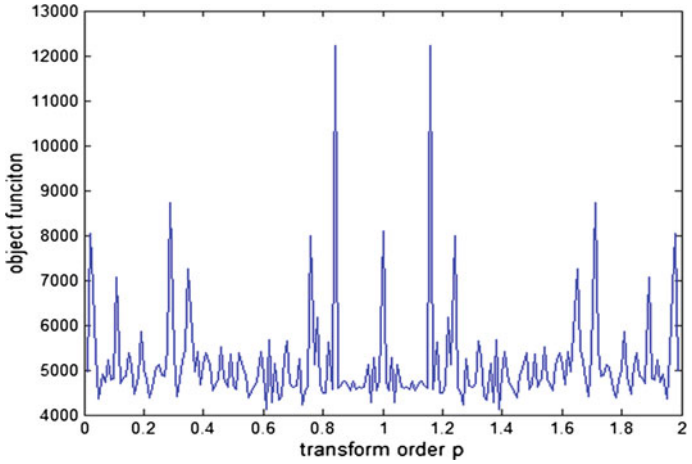

Fig. 65.3 The optimal transform order selection

Owing to the interference, in TOA estimation and there is a deviation in AOA estimation by smoothed MUSIC algorithm. What's more, MUSIC algorithm unable to separate the signals of different UEs in the same direction. The algorithm in this paper could solve the problems that can improve the accuracy of location.

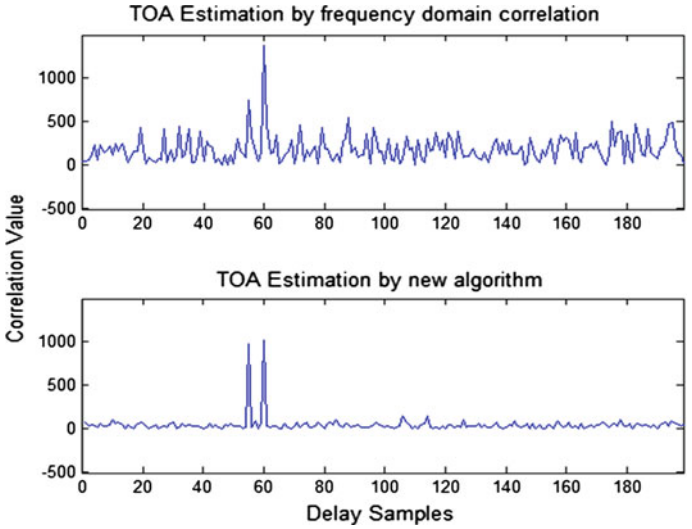

Fig. 65.4 Comparing performance of TOA estimation (SNR = 0 dB)

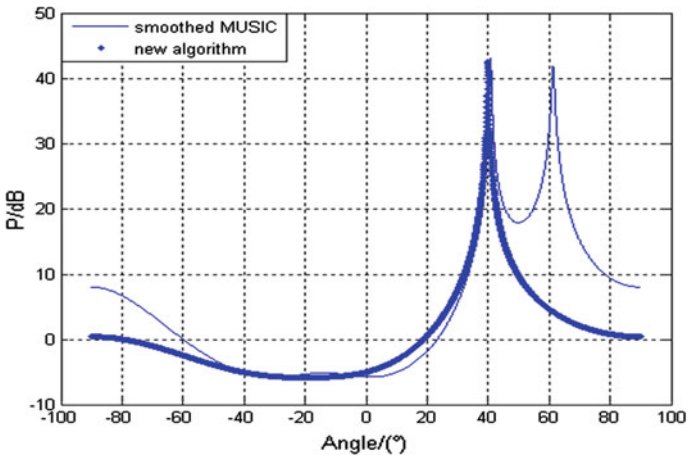

Fig. 65.5 Comparing performance of AOA estimation (SNR = 0 dB)

65.5 Conclusions

This paper proposed a non-cooperative positioning system by combining BeiDou and TD-LTE. It could be applied to security and relief, thus enrich the application of BeiDou and TD-LTE. An algorithm based on FRFT for location parameter estimation is proposed to improve the system. The simulation results show that its performance is better than existing algorithm in TDOA/AOA hybrid location based on the SRS of TD-LTE. It also provide a worthy location method for TD-LTE.

References

1. Ian Paul Larsen (2007) Design and implementation of a mobile phone locator using software defined radio. Naval Postgraduate School, Monterey
2. Dali Z (2006) An active mobile phone detection scheme based on induced technology. In: Mobile Communications, vol 1. pp 107–109
3. Xu BO (2011) Research on the key technologies of non-cooperative location for CDMA 2000 mobile station. Graduate School of National University of Defense Technology, Changsha
4. 3GPP (2012) Technical Specification 36.211 In: Physical channels and modulation (Release 11). www.3gpp.org. Accessed 17 Dec 2012
5. Kay SM (1993) Fundamentals of statistical signal processing Volume I: estimation theory. Cramer-Rao Lower Bound 3 (11):53–55
6. Schmidt RO (1986) Multiple emitter location and signal parameter estimation. IEEE Trans Antennas Propaggat 34(3):276–280
7. Roy R, Paulraj A, Kailath T ESPRIT (1986) A subspace rotation approach to estimation of parameter of Cissoids in noise. IEEE Trans ASSP 34 (5):1340–1342
8. Narayanan VA, Prabhu KMM (2003) The fractional Fourier transform. In: theory, implementation and error analysis. Microprocess Microsyst 27:511–521

Chapter 66
Research on the NLoS Mitigation Algorithm for Integrated Navigation of BeiDou and TD-LTE

Zhongliang Deng, Xiaofei Sun, Yannan Xiao, Xiaoguan Wang, Caihu Chen and Neng Wan

Abstract The Integrated Navigation of BeiDou and TD-LTE is a positioning technology which would be broad prospects in the application of the Intelligent Transportation Systems (ITS) and public security, etc. However, it also faces many challenges. In the positioning system based on the cellular network, the error caused by Non Line of Sight (NLoS) propagation can average between 500 and 700 m [1]. NLoS propagation will bias the measurements of location parameters including Time of Arrival (TOA), Angle of Arrival (AOA) even if there is no multi-path and multi-access interference and will seriously impacts on the calculation of location. This paper mainly studies on the NLoS mitigation algorithm for integrated navigation of BeiDou and TD-LTE, analyses the affection on 700 MHz and 2.6 GHz of TD-LTE caused by NLoS propagation. According to the problems, an NLoS mitigation algorithm based on dual-frequency detection is proposed and some related simulations are accomplished. The result shows that the algorithm doing better on mitigating NLoS affection than the traditional algorithm.

Keywords BeiDou · Navigation satellite system · TD-LTE · Non line of sight · Dual-frequency

66.1 Introduction

Integrated navigation overcomes the practical limitation of traditional single navigation by combining the Global Navigation Satellite System (GNSS), Inertial Navigation System (INS) or cellular network, etc. The Assisted-GPS (A-GPS)

X. Sun (✉)
Haidian District, Xitucheng Road.10 100876 Beijing, China
e-mail: 406931645@163.com

Z. Deng · Y. Xiao · X. Wang ·
C. Chen · N. Wan
Institute of EE, Beijing University of Post and Telecommunication, Beijing, China

J. Sun et al. (eds.), *China Satellite Navigation Conference (CSNC) 2013 Proceedings*, Lecture Notes in Electrical Engineering 245,
DOI: 10.1007/978-3-642-37407-4_66,

technology is a kind of integrated navigation combining GPS and the cellular network. In the situation of weak GPS signal, like urban, the GPS signal may be weakened by many buildings, walls or woods, it could accomplish the quick location by the signal of cellular network. Now, the A-GPS is widely used in the mobile phone with GPS function and its application has been involved in ITS, public security, etc. With the BeiDou and TD-LTE rapidly being commercial, the development of integrated navigation combining both has a broad application prospect, but faces many challenges from itself or other similar technology.

Location parameter estimation and location calculation are the key of positioning technology based on cellular network. The latter severely rely on the circumstance, especially the NLoS circumstance is urgent to be solved. Iterative Taylor-series algorithm [2] and Chan algorithm [3] are widely used at present. The former is heavy computation and need an approximate initial value. And the latter's performance will sharply degraded in NLoS circumstance. Chao-Lin Chen proposed a modified Chan algorithm by introducing geometry-constrain in [4] to obtain a good performance in NLoS but need prior information of circumstance. This paper proposed an NLoS mitigation algorithm based on dual-frequency detection for integrated navigation. The system for NLoS channel measurement and some analyses of data are proposed in the Chap. 2. The Chap. 3 contains the key research on NLoS mitigation algorithm. The Chaps. 4 and 5 are simulations and concluding remarks.

66.2 NLoS Channel Measurements

66.2.1 Overview of Measurement System

The integrated navigation system is shown in Fig. 66.1. The LTE User Equipment (UE) accomplished the active integrated location by receiving navigation message from BeiDou satellite and down-link signal from LTE Base Station (BS) which is similar to the A-GPS. Or the BS accomplished the passive integrated location by receiving navigation message from BeiDou satellite and up-link signal from UE. Whether it is active location or passive location, the propagation path between BS and UE may affected by NLoS.

Considering the restriction of current condition, measurements were accomplished using Universal Software Radio Peripheral (USRP) [5] and its clock synchronization system is improved by cable connection. The transmitter chose the Sounding Reference Signal (SRS) [6] of TD-LTE at 700 MHz and 2.6 GHz as Positioning Reference Signal (PRS) to emit. In order to determine the general propagation path, the receivers are equipped with antenna array for AOA measurement and accomplished channel estimation by correlation in frequency domain of LTE protocol [6]. Choosing a floor of teaching building as the test site and the details is shown in Fig. 66.2.

We deployed three receivers and one transmitter for the measuring system. The transmitter is at the center of the test site and the No. 1 receiver is in the left-most

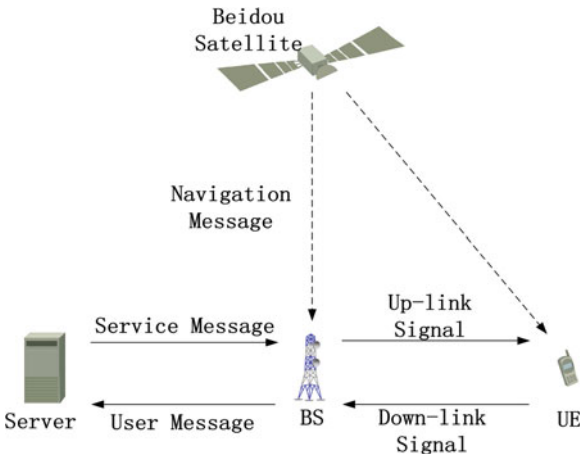

Fig. 66.1 The structure of integrated navigation system

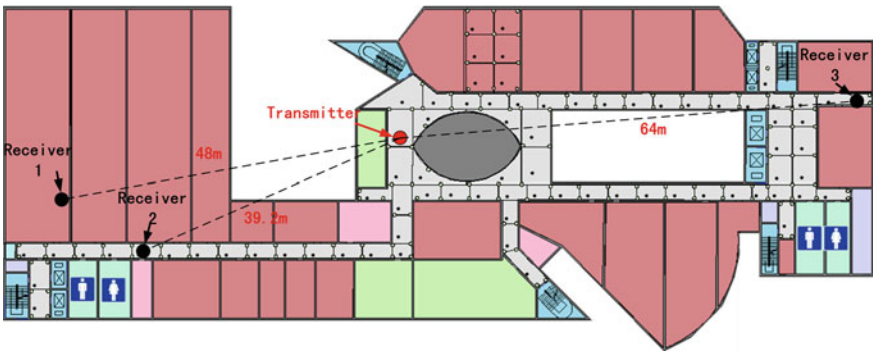

Fig. 66.2 The distribution of test site

room. The No. 2 and No. 3 receivers are respectively at the left corridor and right corridor. Respectively reckoning the three propagation paths between receivers and transmitter as No. 1 path, No. 2 path and No. 3 path, the measurement information of the three paths is shown in Table 66.1.

66.2.2 Measurement Analysis

Comparing the AOA measurement and the real angle in Table 66.1, we could find that No. 1 path is NLoS propagation path arrived from the front door by multiple reflections, No. 2 path is slightly disturbed by NLoS, while No. 3 path is approximate LoS path. Based on the Cumulative Distribution Function (CDF), obtain the NLoS error comparison between 700 MHz and 2.6 GHz by subtracting the measurement data and real data. As it has shown in Fig. 66.3, we could find the

Table 66.1 Parameters of each path

	Real distance (m)	Real angle (°)	700 MHz/2.6 GHz TOA (m)	700 MHz/2.6 GHz AOA (°)
No. 1 path	48	190	65.4/72.8	85/90
No. 2 path	39.2	204	48.3/50.4	198/192
No. 3 path	64	5	69.6/70.5	5/3

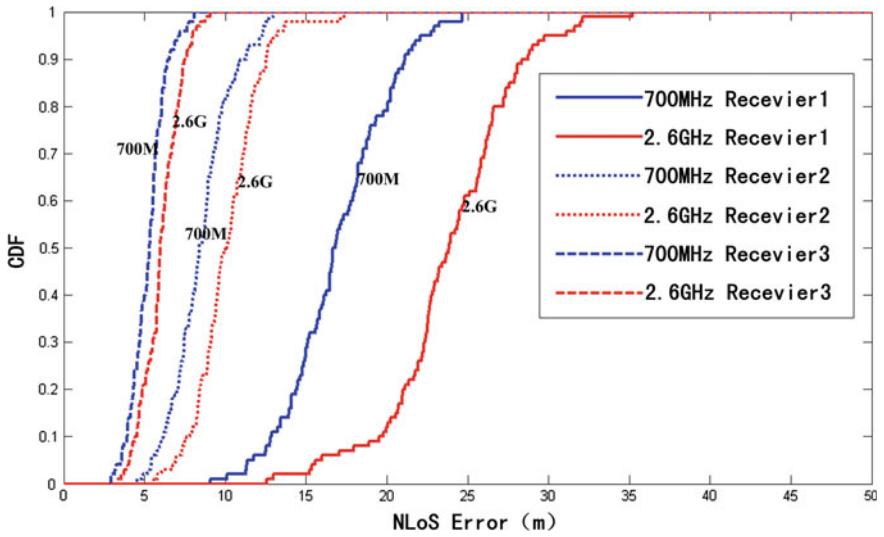

Fig. 66.3 The comparison of NLoS measurement at two frequencies

NLoS error of 700 MHz and 2.6 GHz are approximate and maintaining lower when the propagation path is well, like the No. 3 path. And the NLoS error in this circumstance is high spatial correlation and low frequency correlation. However, as the circumstance being more complex, NLoS error increase sharply while its spatial correlation decrease and frequency correlation increase. The reason is the absorptive capacity of obstacle increased as the frequency increasing. If we could effectively utilize the gradient relationship, the comparison between two frequencies may help us to determine the influence cause by NLoS and then mitigation the NLoS error. Based on this conclusion, we will propose an NLoS mitigation algorithm in the Chap. 67.

66.3 An NLoS Mitigation Algorithm Based on Dual-Frequency

Assuming the TOA measurements from transmitter to the *i*th receiver at 700 MHz and 2.6 GHz are

$$\begin{aligned} {}^{(1)}\tau i &= {}^{(1)}\tau_i^0 + {}^{(1)}ni + {}^{(1)}NLoSi \\ {}^{(2)}\tau i &= {}^{(2)}\tau_i^0 + {}^{(2)}ni + {}^{(2)}NLoSi \quad i = 1, 2 \cdots, M \end{aligned} \tag{66.1}$$

where (1) and (2) index the different frequencies, τ_i^0 donates the TOA without interferences. $NLoS_i$ is the TOA error caused by NLoS propagation and n_i is TOA error caused by Gaussian noise which is zero-mean and independent with $NLoS_i$.

Now, the Time Difference of Arrival (TDOA) could be expressed as follows:

$$\begin{aligned} {}^{(1)}\tau_{i,j} &= {}^{(1)}\ \tau_i - {}^{(1)}\ \tau_j = {}^{(1)}\ \tau_{i,j}^0 + {}^{(1)}\ n_{i,j} + {}^{(1)}\ NLoS_{i,j} \\ {}^{(2)}\tau_{i,j} &= {}^{(2)}\ \tau_i - {}^{(2)}\ \tau_j = {}^{(2)}\ \tau_{i,j}^0 + {}^{(2)}\ n_{i,j} + {}^{(2)}\ NLoS_{i,j} \end{aligned} \tag{66.2}$$

According to the Chan algorithm,

$$\begin{aligned} r_i^2 &= (x_i - x)^2 + (y_i - y)^2 \\ &= K_i - 2x_i x - 2y_i y + x^2 + y^2,\ i = 1, 2, \cdots M \end{aligned} \tag{66.3}$$

where $K_i = x_i^2 + y_i^2$, assuming c is the signal propagation speed, then

$$r_i, 1 = c\tau_i, 1 = r_i - r_1 \tag{66.4}$$

Let $z_a = [z_p^T, r_1]^T$ be unknown, where $z_a = [z_p^T, r_1]^T$. With noise and NLoS error the error vector derived from (66.3) is

$$\varphi = h - G_a z_a^0 \tag{66.5}$$

where

$$h = \frac{1}{2}\begin{bmatrix} r_{2,1}^2 - K_2 + K_1 \\ r_{3,1}^2 - K_3 + K_1 \\ \vdots \\ r_{M,1}^2 - K_M + K_1 \end{bmatrix}, Ga = -\begin{bmatrix} x_{2,1} & y_{2,1} & r_{2,1} \\ x_{3,1} & y_{3,1} & r_{3,1} \\ \cdot & \cdot & \cdot \\ x_{M,1} & y_{M,1} & r_{M,1} \end{bmatrix}$$

Assuming $cni, 1,\ cNLoS_{i,1} \ll r_i^0$, combined (66.2), (66.4) and (66.5) with measurement at two frequencies:

$${}^{(1)}\varphi = cB(n + {}^{(1)}NLoS) \tag{66.6}$$

$${}^{(2)}\varphi = cB(n + {}^{(2)}NLoS) \tag{66.7}$$

$$B = diag\left\{r_2^0, r_3^0, \cdots, r_M^0\right\} \tag{66.8}$$

According to the Chap. 2, the frequency correlation of NLoS error increase and spatial correlation decrease with the propagation circumstance becoming worse. Comparing the difference between the error vectors of two frequencies:

$$\begin{aligned} \psi &= E\left[{}^{(2)}\varphi \cdot {}^{(2)}\varphi^T - {}^{(1)}\varphi \cdot {}^{(1)}\varphi^T\right] \\ &= c^2[BQB + BPB] \end{aligned} \tag{66.9}$$

with Q donating the covariance matrix of noise. P represented the influence of NLoS error and impacted the weighted of Weighted Least Squares (WLS). When the NLoS is slight, ψ degraded which is equal to Chan algorithm.

Calculating WLS by ignoring the relationship between x, y and r_1 of z_a, we could obtain

$$z_a = (G_a^T \psi^{-1} G_a)^{-1} G_a^T \psi^{-1} h \tag{66.10}$$

Owing to the main application is array location, Chan algorithm could assume $B \approx r^0 I$ when the target is far away from the antenna array. But it's unreasonable to make the assumption in cellular network, because the distance between receiver and transmitter is differing a lot.

Expressing G_a, h where $G_a = G_a^0 + \Delta G_a$, $h = h^0 + \Delta h$ and considering $G_a^0 z_a^0 = h^0$, then (66.5) changed to

$$\varphi = \Delta h - \Delta G_a z_a^0. \tag{66.11}$$

Let $z_a = z_a^0 + \Delta z_a$ then (1.10) transform into

$$(G_a^{0T} + \Delta G_a^T)\psi^{-1}(G_a^0 + \Delta G_a)(z_a^0 + \Delta za) = (G_a^{0T} + \Delta G_a^T)\psi^{-1}(h^0 + \Delta h) \tag{66.12}$$

Ignoring the quadratic perturbation terms and then obtains estimation error of dual-frequency by using

$$\begin{aligned} {}^{(1)}\Delta z_a &= c(G_a^{0T}\psi^{-1}G_a^0)^{-1} G_a^{0T}\psi^{-1} B(n + {}^{(1)}NLoS) \\ {}^{(2)}\Delta z_a &= c(G_a^{0T}\psi^{-1}G_a^0)^{-1} G_a^{0T}\psi^{-1} B(n + {}^{(2)}NLoS) \\ E({}^{(1)}\Delta z_a \cdot {}^{(2)}\Delta z_a^T) &= (G_a^{0T}\psi^{-1}G_a^0)^{-1} \end{aligned} \tag{66.13}$$

According to $r_1^2 = (x - x_1)^2 + (y - y_1)^2$, construct a new error function:

$$\varphi' = h' - G_a' z_a'^0 \tag{66.14}$$

where

$$h' = \begin{bmatrix} (z_{a,1} - x1)^2 \\ (z_{a,2} - y1)^2 \\ z_{a,3}^2 \end{bmatrix}, \; G'_a = \begin{bmatrix} 1 & 0 \\ 0 & 1 \\ 1 & 1 \end{bmatrix},$$

$$z_a = \begin{bmatrix} z_{a,1} \\ z_{a,2} \\ z_{a,3} \end{bmatrix}, \; z'_a = \begin{bmatrix} (x - x_1)^2 \\ (y - y_1)^2 \end{bmatrix}$$

and its covariance matrix is

$$\psi' = E[\varphi' \varphi'^T] = 4B' E(^{(1)}\Delta z_a \cdot {}^{(2)}\Delta z_a^T) B' \tag{66.15}$$

$$B' = diag\{x^0 - x_1, y^0 - y_1, r_1^0\}$$

The final estimation with considering the relationship between x, y and r_1 is:

$$z'_a = (G_a'^T \psi'^{-1} G'_a)^{-1} G_a'^T \psi'^{-1} h' \tag{66.16}$$

The final position estimate is

$$z_p = \sqrt{z'_a} + \begin{bmatrix} x_1 \\ y_1 \end{bmatrix} \text{ or } z_p = -\sqrt{z'_a} + \begin{bmatrix} x_1 \\ y_1 \end{bmatrix} \tag{66.17}$$

The ambiguity of final position could be eliminated by treating the result of first WLS as verdiction. In general case, the NLoS error is not generalized zero-mean Gaussian distribution, so the location estimation is not Maximum Likehood (ML) estimation.

The computation of this algorithm is equal to Chan algorithm from the whole process by reason of just using dual-frequency data to obtain error vectors. However, it becomes more complex than the Chan algorithm of single-path by measuring at two frequencies.

66.4 Simulations and Analysis

According to the measurement in Chap. 2, we could decide the coordinates of three receivers and one transmitter are (−15, 85), (5, 80), (95, 100) and (30, 95). In order to accomplish the comparison with 4-sensors Chan algorithm, we choose (50, 100) as the LoS reference receiver. Using the dual-frequency detection and Chan algorithm to calculate the location and Chan algorithm is respectively completed at 700 MHz and 2.6 GHz. The comparison of performance is shown in Fig. 66.4.

By the comparison, we could find that the performance of 4-sensors Chan sharply degrade in NLoS circumstance. The accuracy is respectively 35 m at 700 MHz and 41 m at 2.6 GHz in 67 % of the cases. The algorithm of this paper

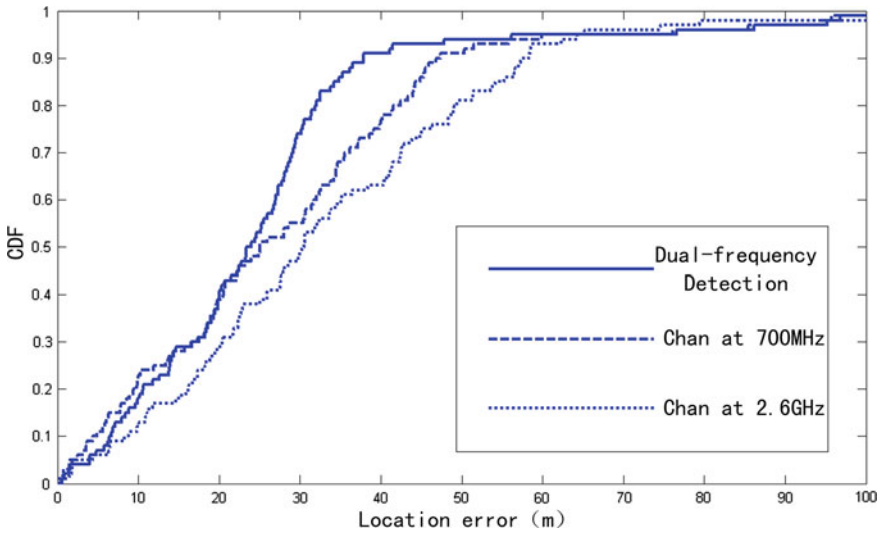

Fig. 66.4 Comparing the performance of algorithms (NLoS, SNR = 0 dB)

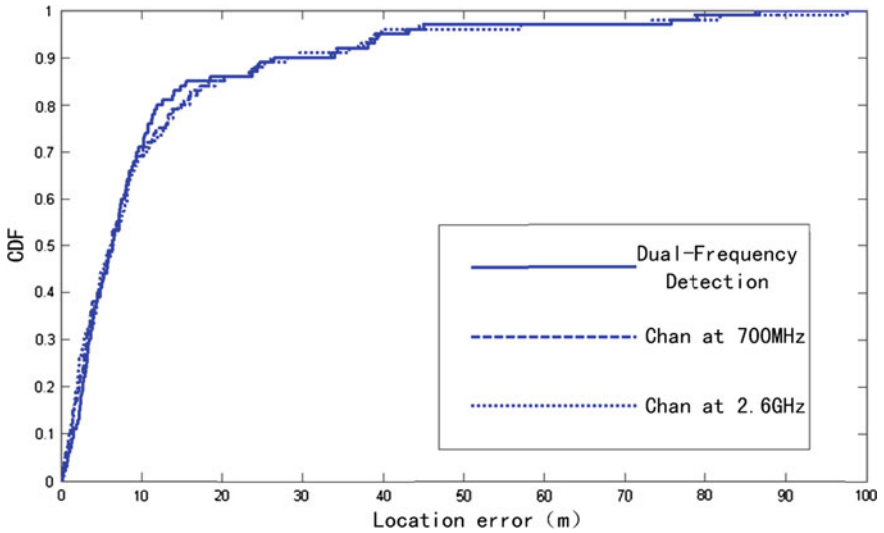

Fig. 66.5 Comparing the performance of algorithms (LoS, SNR = 0 dB)

mitigated the NLoS error by considering the difference of dual-frequency detection which could maintain the accuracy at 25 m. Although the NLoS error severely depend on the circumstance and a NLoS propagation model is hard to set up, the difference of dual-frequency is ever-present that ensure the universality of our algorithm.

In order to verify the performance of the algorithm in Line of Sight (LoS), we comparing it's performance and Chan algorithm's in the condition of LoS and SNR = 0 dB which is shown in Fig. 66.5.

From the Fig. 66.5, we could find that the performances of the algorithms in LoS are approximate which ensure the compatibility of this algorithm in LoS.

66.5 Conclusions

This paper measured and analyzed the relationship between NLoS influence at 700 MHz and 2.6 GHz on the basis of integrated navigation of BeiDou and TD-LTE. And a NLoS mitigation algorithm based on the dual-frequency detection is proposed. Comparing with the traditional algorithm, the algorithm preferably mitigating NLoS in positioning system based on the TD-LTE. What's more, it also provided a worthy method for the other system which is able to emit at multiple frequencies, for example the GSM900/DCS1800.

References

1. Silventoinen M, Rantalainen T (1996) Mobile station emergency locating in GSM. In: IEEE international conference on personal wireless communications, pp 232–238
2. Foy WH (1976) Position-location solutions by Taylor-series estimation. IEEE Trans Aerosp Electron Syst 12(2):187–194
3. Chan YT, Ho KC (1994) A simple and efficient estimator for hyperbolic location. IEEE Trans on Signal Process 42(8):1905–1915
4. Chen CL, Feng KT (2005) An efficient geometry-constrained location estimation algorithm for NLOS environments. In: Proceedings of IEEE international conference wireless networks, communication and mobile computing, Hawaii, USA, pp 244–249
5. www.ettus.com. Accessed 17 Dec 2012
6. 3GPP (2012) Technical specification 36.211. In: Physical channels and modulation (Release 11). www.3gpp.org. Accessed 17 Dec 2012

Chapter 67
An Adaptive Dynamic Kalman Filtering Algorithm Based on Cumulative Sums of Residuals

Long Zhao and Hongyu Yan

Abstract In order to overcome the drawbacks of the fault detection method based on χ^2 test that is insensitive to soft fault detection, an adaptive dynamic robust Kalman based on variance inflation model was developed, which can detect the soft fault of system. The proposed method cumulates the residuals in open windows. When the cumulant surpasses the threshold, the error covariance is enlarged to prevent abnormal Global Positioning System (GPS) observations. This method has been applied to integrated navigation system of Inertial Navigation System/ Global Navigation Satellite System (INS/GNSS). The simulation results show that the soft fault is detected by using adaptive dynamic robust Kalman, and the filtering precision is higher than the traditional Kalman filtering algorithm.

Keywords Integrated navigation · Fault detection · Robust filtering · Kalman filtering

67.1 Introduction

Integrated navigation technology is an effective way to improve the overall performance of the navigation system. Inertial navigation system (INS) is autonomous, anti-interference, hidden, reliable, real-time and accurate in the short term. However, the accuracy decreases as the time is evolving. Hence, the INS and GPS satellite navigation systems are combined into INS/GPS integrated navigation system, which can complement each other, and increase the redundancy. Thus,

L. Zhao (✉)
Science and Technology on Aircraft Control Laboratory, Beihang University, Beijing, China
e-mail: buaa_dnc@buaa.edu.cn

H. Yan
Digital Navigation Center, Beihang University, Beijing, China

J. Sun et al. (eds.), *China Satellite Navigation Conference (CSNC) 2013 Proceedings*, Lecture Notes in Electrical Engineering 245,
DOI: 10.1007/978-3-642-37407-4_67,

multidimensional navigation information of highly data update rate can be obtained, and estimation accuracy and reliability of the navigation system can also be improved. INS/GPS integrated navigation system has been widely applied to autonomous navigation and positioning system of aircraft [1, 2].

With the higher requirements of high accuracy and reliability for integrated navigation system, the higher demand is presented to the fault detection and isolation of navigation system. The fault of the system can be divided into three types: hard fault, abrupt fault and soft fault. The hard fault can be detected through build-in test for navigation system; abrupt fault can be detected by the traditional fault detection methods. However, the soft fault of navigation system are difficult to detect, such as the filtering divergence caused by the uncertainty of the system model, the uncertainty of positioning caused by the GPS signal is disturbed, et al. In order to improve the reliability and accuracy of navigation system, dynamic navigation positioning was completed after detecting and isolating wrong GPS observation [3]. Many fault detection algorithms has been applied to the navigation to detect satellite failures at present, such as the fault detection method based on fuzzy logic, neural network, and filtering. Yang et al. applied neural networks based on Adaptive Resonance Theory (ART) and Kohonen Network (KNN) to the fault detection [4]. The fault detection, identification and classification of the navigation systems has been completed by using Fuzzy ARTMAP neural Networks after bearing fault character obtaining based on state χ^2 test method [5]. Multiple model fault detection algorithm was applied to detect and isolate wrong GPS observation, and improve the positioning accuracy [6]. The above methods effects on the abrupt fault, but it is insensitive to soft fault in navigation system. The residual inhibition based on H_∞ estimator is sensitive to the fault [7]. When the navigation system has a soft fault, the performance of fault tolerance of navigation system is improved by using two levels of feedback structure, utilizing subfilter to detect the system fault timely, main filter to complete state fault tolerant and fusion estimation [8]. The traditional fault detection methods can detect the abrupt faults, but can not detect the soft fault. The soft fault increases slowly, and the fault statistic changes are small. The system states were corrected falsely by using the data of the soft fault. The fault statistic is not obvious because of small fault at first, the system state estimating value was affected by the soft fault, and then the system is difficult to detect soft fault even if the fault is large because of residuals accumulation with time.

In order to overcome these shortcomings of traditional fault detection methods, an adaptive dynamic robust Kalman filtering algorithm was developed, which can detect the soft fault by accumulating the residuals in data windows, and the failure restraint and dynamic robust filtering are realized by expanding error covariance based on robust Kalman filtering. Therefore, the system can avoid missing detection, and accurate filtering solution can be obtained.

67.2 Detection Method of Soft Fault in INS/GPS Integration Navigation

Consider the time-varying discrete systems,

$$X_k = \Phi_{k,k-1} X_{k-1} + W_k \tag{67.1}$$

$$L_k = A_k X_k + e_k \tag{67.2}$$

where $X_k \in R^n$ is the state variable at k time; $\Phi_{k|k-1} \in R^{n\times n}$ is the state transition matrix from $k-1$ to k time; $A_k \in R^{m\times n}$ is the measurement matrix of the system; $V_k \in R^m$ is the measurement noise vector; the covariance is Σ_k . $W_{k-1} \in R^r$ is the process noise vector of the system, and the covariance is Σ_{W_k}; $L_k \in R^m$ is the measurement value of the system at k time.

67.2.1 Traditional Fault Detection Method Based on Residual χ^2 Test

The fault of navigation system was detected by using information of filtering residual series, which includes fault information in traditional fault detection method based on residual χ^2 test. The one-step prediction residual is

$$\overline{V}_k = L_k - A_k \Phi_{k,k-1} X_{k-1} \tag{67.3}$$

The covariance matrix of prediction residual is

$$U_k = A_k \Sigma_{\overline{X}_k} A_k^T + \Sigma_k \tag{67.4}$$

$$\Sigma_{\overline{X}_k} = \Phi_{k,k-1} \Sigma_{\hat{X}_{k-1}} \Phi_{k,k-1}^T + \Sigma_{W_k} \tag{67.5}$$

where R_k is the covariance matrix of measurement noise.

Residual $\overline{V}_k$ is zero-mean Gaussian white noise when there is fault-free; $\overline{V}_k$ is not zero when there is fault. Therefore, fault can be detected by examining the mean of residual $\overline{V}_k$. The fault detection function $\lambda(k) = \overline{V}_k^T U_k \overline{V}_k$, $\lambda(k)$ obeys the χ^2 distribution in degrees of freedom m.

Setting a confidence factor α, and then the fractile value $z(\alpha)$ Based on χ^2 distribution graph is known. If $\lambda(k) \le z(\alpha)$, there is no fault; if $\lambda(k) > z(\alpha)$, there is fault.

According to the Eq. (67.3), when the system fault is large, the difference between the real observation L_k and prediction observation $A_k X_{k/k-1}$ was highlighted by one-step prediction residual $\overline{V}_k$. Hence, fault detection statistics was constructed by the difference, and the abrupt fault of navigation system can be detected effectively by using the fault detection method based on residual χ^2 test.

However, when the system fault is soft, the one step prediction residual $\overline{V}_k$ is small, and fault detection statistics is not sensitive. In this paper, a new method is proposed to increase the time interval of prediction residuals so that the soft fault can be accumulated to detect fault.

67.2.2 Soft Fault Detection Method Based on Cumulative Sums of Residuals

The difference is too small to detect because the soft fault is very small at first. In order to increase the difference of real observation and prediction observation, prediction observation is constructed by calculating the state beforehand for several times. Therefore, the soft fault is accumulated and the difference is obvious by subtracting w recursive prediction observation.

According to the Eqs. (67.1) and (67.2), we set a a step state recursive device, and the prediction observation is calculated by recursive state time beforehand, that is

$$A_k X_{k/k-a} = A_k \Phi_{k,k-1} X_{k-1/k-a} = A_k \Phi_{k,k-2} X_{k-2/k-a} = A_k \Phi_{k,k-a} X_{k-a/k-a} \tag{67.6}$$

Define the prediction observation of a one-step state recursive device

$$\begin{aligned} \overline{V}_k &= L_k - A_k X_{k/k-a} = A_k X_k - A_k X_{k/k-a} + e_k \\ &= A_k(\Phi_{k,k-1} X_{k-1} + W_k) - A_k \Phi_{k,k-1} X_{k-1/k-a} + e_k \\ &= A_k \Phi_{k,k-1}(\Phi_{k-1,k-2} X_{k-2} + W_{k-1}) - A_k \Phi_{k,k-2} X_{k-2/k-a} + A_k W_k + e_k \\ &= A_k \Phi_{k,k-a}(X_{k-a} - X_{k-a/k-a}) + A_k \Phi_{k,k-a+2} W_{k-a+2} \\ &\quad + A_k \Phi_{k,k-a+3} W_{k-a+3} + \ldots + A_k W_k + e_k \end{aligned} \tag{67.7}$$

where $\overline{V}_k$ obeys zero-mean normal distribution when W_k and V_k is Gaussian white noise and X_{k-a} is the unbiased estimation. The covariance matrix is

$$\begin{aligned} \Sigma_{\overline{V}_k} &= \overline{V}_k \overline{V}_k^T \\ &= A_k \Phi_{k,k-a} \Sigma_{\hat{X}_{k-a}} (A_k \Phi_{k,k-a})^T + A_k \Phi_{k,k-a+2} \Sigma_{W_{k-a+2}} (A_k \Phi_{k,k-a+2})^T + \ldots + A_k \Sigma_{W_k} (A_k)^T + \Sigma_k \end{aligned} \tag{67.8}$$

Normalize Eq. (67.8) as

$$\overline{V}_k = \frac{\overline{V}_k}{\sqrt{\Sigma_{\overline{V}_k}}} \sim N(0,1) \tag{67.9}$$

In the simulation experiment, $\overline{V}_k$ is unstable because prediction observation is computed by recursive state after a period of time. Hence, a new statistics was constructed by data windows (defined as window b) as follows,

$$T_k = \frac{1}{b}\sum_{j=0}^{j=b} \Sigma(\overline{V}_{k-j})^2 \tag{67.10}$$

Set threshold β, when $T_k > \beta$, GPS output is wrong. When $T_k \leq \beta$, GPS output is normal.

67.3 Robust Kalman Filtering Algorithm Based on Cumulative Sums of Residuals

The degree of dispersion should be reflected by the covariance matrix of observation vector. If the observation is accurate and reliable, the elements in a main diagonal of the covariance matrix should be small. Otherwise, the elements in a main diagonal of the covariance matrix should be enlarged to decrease the weight during the state estimation. When the satellite signal is abnormal and the fault occurs, which implies that the GPS observation is not reliable. The covariance matrix of observation vector is discrepancy with initial covariance matrix of observation vector. In order to overcome the problem, the elements in a main diagonal of the covariance matrix were enlarged, the navigation solution of high precision was obtained by using dynamic model information [9]. There are several ways to construct variance inflation factor. The equivalence of variance inflation model and equivalent weights model was proved [10]. Hence, variance inflation function is taken as reciprocal of equivalent weight function, such as reciprocal of Huber weight function and IGGIII weight function. When weight function is zero, the variance inflation factor should tend to infinity, where a relatively large positive number is replaced in the actual calculation.

According to IGGIII equivalent weight function model, the three sections function based on variance inflation model is taken as [10],

$$\lambda_i = \begin{cases} 1 & \left|\overline{V}_i\right| \leq k_0 \\ \frac{k_1 - k_0}{k_1 - \left|\overline{V}_i\right|} & k_0 < \left|\overline{V}_i\right| \leq k_1 \\ \infty & \left|\overline{V}_i\right| > k_1 \end{cases} \tag{67.11}$$

$$\left|\overline{V}_i\right| = T_k/\beta \tag{67.12}$$

where k_0 and k_1 are constant values. Generally $k_0 = 1.0 \sim 1.5$, and $k_1 = 2.5 \sim 8.0$.

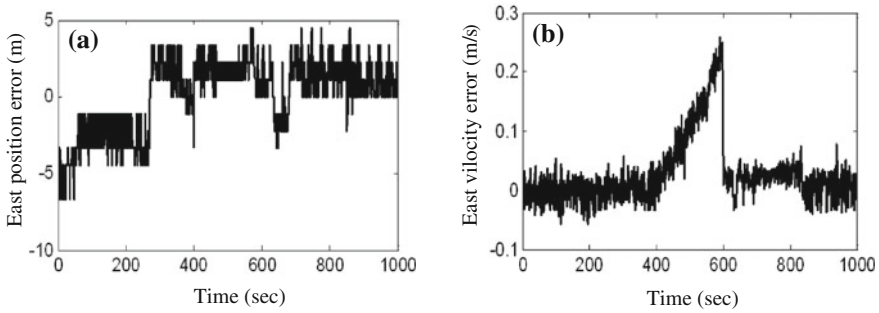

Fig. 67.1 The soft fault occurs in GPS east velocity, **a** east position error, **b** east velocity error

.4 Simulation Test

67.4.1 Experimental Conditions

In INS/GPS simulation test, locus is set by STR series GPS satellite constellation simulator of GSS corporation. The signal of constellation simulator is RF signal ephemeris. The real YP-4 GNSS receiver is used to collect data.

In this paper, gyro drift is 0.01°/h, accelerometer drift is 10^{-5} g, and the position error of GPS is 5 m in the normal state. The test data was generated by GPS satellite Constellation simulator, the data length is 1000 s. The soft fault was applied to the east velocity and north position of GPS in 400–600 s. When the soft fault was applied to the east velocity, the differences that are the east position error and east velocity error between GPS receiver output and the real trace are shown in Fig. 67.1. When the soft fault was applied to the north position, the differences that are the north position error and north velocity error between GPS receiver output and the real trace are shown in Fig. 67.2.

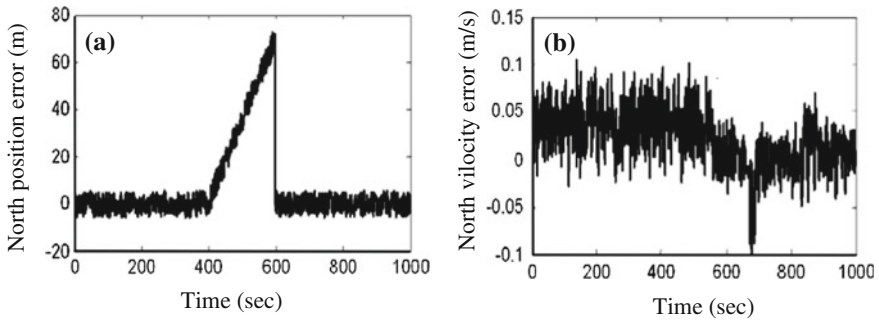

Fig. 67.2 soft fault occurs in GPS north position, **a** north position error, **b** north velocity error

67.4.2 Test of Integrated Navigation System Based on Fault Detection

Here, the fault detection method based on χ^2 test χ^2 (method 1) and the fault detection method based on cumulative sums of residuals (method 2) are applied to estimate errors of integrated navigation system. State recursive device is 50 steps, window length 10, and thresholds of GPS velocity and position fault 0.5 and 1, respectively. The results of navigation errors after the fault detection and isolation are as follows in Tables 67.1 and 67.2, Figs. 67.3 and 67.4.

As shown in Figs. 67.3a and 67.4a, when the soft fault accumulates gradually from 400 s to 600 s, the fault detection method based on χ^2 test could not detect the soft fault that is too small in the beginning. The state estimating values were influenced by the soft fault till big enough. The soft fault was detected by the fault detection method based on χ^2 test at the fault disappeared time 600 s, and has very high missing detection rate. The soft fault was detected at 420 s by using this paper's method based on cumulative sums of residuals. Because of the sensitivity the soft fault detection is improved by accumulating the soft fault within a steps.

From Tables 67.1 and 67.2, Figs. 67.3b, 67.3c and 67.4b, when the soft fault occurs, the fault detection method based on χ^2 test (method 1) has the missing detection. The state estimating values that were influenced by the soft fault lead to Kalman filtering accuracy reduce. The fault detection method based on cumulative sums of residuals (method 2) could detect the soft fault from 420 to 600 s, and as soon as the soft fault was detected, the system states were estimated by robust Kalman filter based on variance inflation model, where abnormal observed value is avoided by enlarging value of the covariance.

Table 67.1 The system error of the two methods when soft fault occurs in GPS east velocity

	East position (m)		North position (m)		East velocity (m/s)		North velocity (m/s)	
	Mean	Variance	Mean	Variance	Mean	Variance	Mean	Variance
Method 1	9.28	11.71	4.18	2.11	0.03	0.06	0.02	0.02
Method 2	1.18	3.57	2.68	1.77	0.01	0.01	0.02	0.02

Table 67.2 The system error of the two methods when soft fault occurs in GPS north position

	East position (m)		North position (m)		East velocity (m/s)		North velocity (m/s)	
	Mean	Variance	Mean	Variance	Mean	Variance	Mean	Variance
Method 1	1.69	4.64	9.34	6.33	0.01	0.01	0.02	0.02
Method 2	1.37	3.87	6.22	3.22	0.01	0.01	0.02	0.02

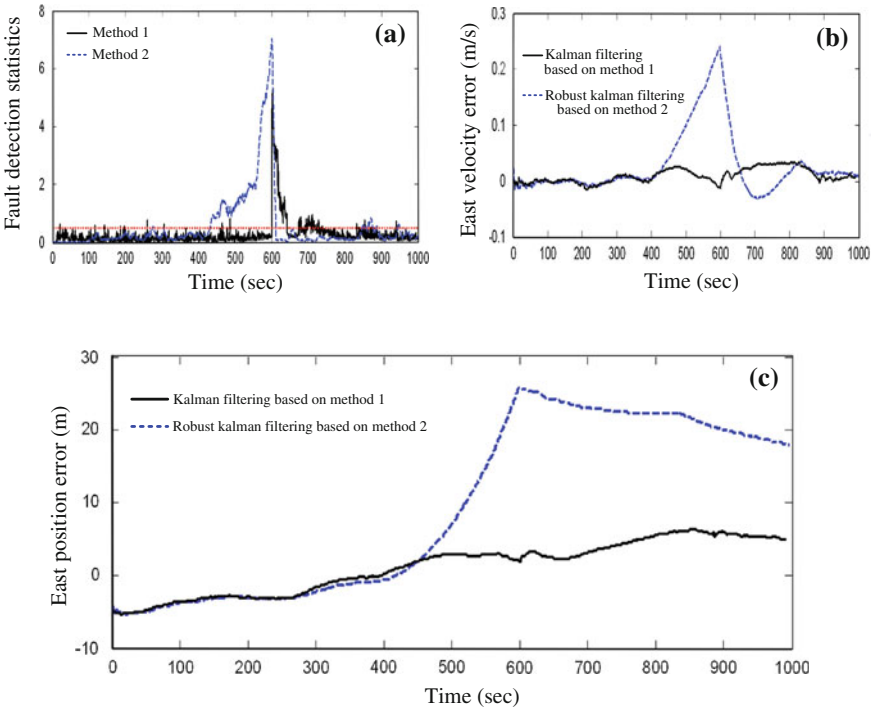

Fig. 67.3 soft fault occurs in GPS east velocity, **a** fault detection statistics, **b** east velocity error, **c** east position error

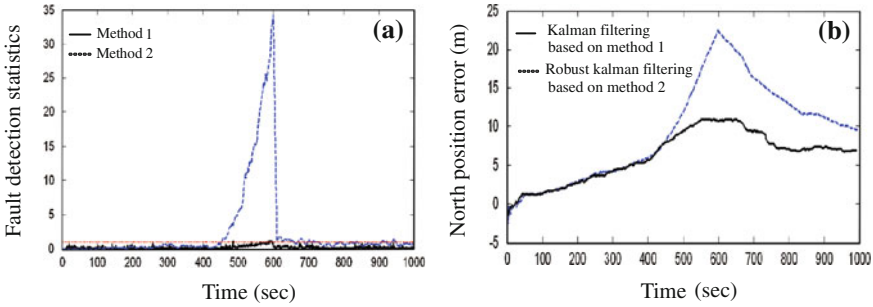

Fig. 67.4 soft fault occurs in GPS north position, **a** fault detection statistics, **b** north position error

67.5 Conclusions

In INS/GPS integrated navigation, when the soft fault occurs in satellite, filtering accuracy decreases because the traditional soft fault detection method based on χ^2 test (method 1) cannot detect the soft fault validly. In order to overcome the

problem, the fault detection method based on cumulative sums of residuals (method 2) were developed, a robust Kalman filter was obtained by using variance inflation model. The accuracy of navigation is improved.

Acknowledgments Project supported by the key program of the National Natural Science Foundation of China (Grant No. 61039003), the National Natural Science Foundation of China (Grant No. 41274038), the Aeronautical Science Foundation of China (Grant No. 20100851018)and the Aerospace Innovation Foundation of China(Grant No. CASC201102).

References

1. Ding WD, Wang JL, Rizos C (2007) Improving adaptive Kalman estimation in GPS/INS integration. J Navig 60:517–529
2. Jong KL, Christopher J (2012) Dual-IMU/GPS based geolocation system. J Navig 65:113–123
3. Jang CW, Juang JC, Kung FC (2000) Adaptive fault detection in real-time GPS positioning. IEE Radar, Sonar Navig 147(5):254–258
4. Yang BS, Han T, An JL (2004) Art-kohonen neural network for fault diagnosis of rotating machinery. Mech Syst Signal Process 18:645–657
5. Zhang HY, Chan CW, Cheung KC (2001) Fuzzy ARTMAP neural network and its application to fault diagnosis of navigation systems. Automatica 37:1065–1070
6. Faurie F, Giremus A, Grivel E (2009) Fault detection combining interacting multiple model and multiple solution separation for aviation satellite navigation system. IEEE Int Conf Acoust, Speech Signal Process 3273–3276
7. Shi J, Miao LJ, Ni ML (2011) Robust fault detection filter and its application in MEMS-based INS/GPS. J Syst Eng Electron 22(1):113–119
8. Cong L, Qin HL, Tan ZZ (2011) Robust fault detection filter and its application in MEMS-based INS/GPS. J Syst Eng Electron 22(2):274–282
9. Yang YX (2005) Comparison of adaptive factors in kalman filters on navigation results. J Navig 58:471–478
10. Yang YX (2006) Adaptive navigation and kinematic positioning. Surveying and mapping Press, Beijing

Chapter 68
Performance Evaluation of a Real-Time Integrated MEMS IMU/GNSS Deeply Coupled System

Tisheng Zhang, Hongping Zhang, Yalong Ban and Xiaoji Niu

Abstract Compared with loosely coupled system and tightly coupled system, deeply coupled system could enhance the accuracy and the robustness of the receiver and the whole system. The real-time integrated deeply coupled system based on MEMS IMU can provide technical support for navigation service. This paper proposes an integrated MEMS IMU/GNSS deeply coupled system framework whose processing core is DSP + FPGA. In this paper the IMU aided tracking loop is modeled first, and then the error of the tracking loop is analyzed, the design of system's real-time is optimized. Tests results show that the system can operate consecutively in real-time conditions, and the IMU auxiliary information latency is less than 0.5 ms; the error of the tracking loop is greatly reduced; the dynamic tests results preliminarily verify the feasibility of the real-time integrated deeply coupled system.

Keywords Deeply coupled · MEMS IMU · Real-time integrated · Tracking loop

68.1 Introduce

The supplementary characteristics of satellites navigation and inertial navigation facilitate the production and development of GNSS/INS coupled navigation system. GNSS/INS coupled navigation system includes three types which are loosely coupled system, tightly coupled system and deeply coupled system. There is no need to adjust the inner construction of the GNSS receiver in the rather matured

T. Zhang (✉) · H. Zhang · Y. Ban · X. Niu
GNSS Research Center of Wuhan University, Wuhan, China
e-mail: zts@whu.edu.cn

H. Zhang
e-mail: hpzhang@whu.edu.cn

J. Sun et al. (eds.), *China Satellite Navigation Conference (CSNC) 2013 Proceedings*, Lecture Notes in Electrical Engineering 245,
DOI: 10.1007/978-3-642-37407-4_68,

loosely coupled system and tightly coupled system, which is also helpless in the function improvement receiver. Currently, the deeply coupled system, which is still at an experimental stage, can transmit INS information to the receiver and improve the dynamic flexibility and accuracy of the receiver by helping acquiring and tracking the satellite signals [1].

MEMS IMU is expanding as it is low cost, small size and low power consumption [2, 3]. But it needs to be coupled with GNSS because of its low accuracy. Scholars have deeply carried out the algorithmic research and real-time integrated system design of loosely coupled system and tightly coupled system based on MEMS IMU [4–6]. The deeply couple research groups represented by MIT, Stanford University and Calgary University focus on algorithmic research based on software platforms [7–9]. Because the receiver's inner construction needs to be adjusted for the deep couple system, the current deeply coupled system are all produced by receivers manufacturers and INS manufacturers. The cited Ref. [10] records the deeply coupled system based on a vector structure, jointly produced by Honeywell and Rockwell. The cited Ref. [11] records a deeply coupled system of scalar structure, jointly produced by NovAtel and KVH. It is difficult to design deeply coupled products because of many technical problems, therefore there are few algorithm researches based on mature embedded integrated deeply-coupled systems on published literatures.

This paper designs a deeply coupled system based on an embedded platform to enhance the research and design of deeply coupled products. Firstly, it introduces the framework of an integrated MEMS IMU/GNSS deeply coupled system, in which the processing core is Digital Signal Processor (DSP) plus Field Programmable Gates Array (FPGA); and then it analyzes some key technology including IMU aided tracking loop model, loop tracking error and system's real-time, at last it test and evaluate the key characteristics of the system.

68.2 System Frameworks

DSP plus FPGA is the processing core of the platform. MEMS IMU data sampling unit and GNSS RF unit are two function units of the integrated platform. On the integrated embedded platform, GNSS and IMU information is highly fused, and the software and hardware of the system's function units work harmoniously. The framework of the deeply coupled system based on an integrated platform is as Fig. 68.1 [12].

On the platform based on a single clock, DSP with high computing and flexible controlling ability, as the main processor, is responsible for completing the software parts including the computing of complex floating point and matrix multiplication; FPGA with parallel processing mode, as an coprocessor, is used for completing the hardware parts including parallel signal processing and interface

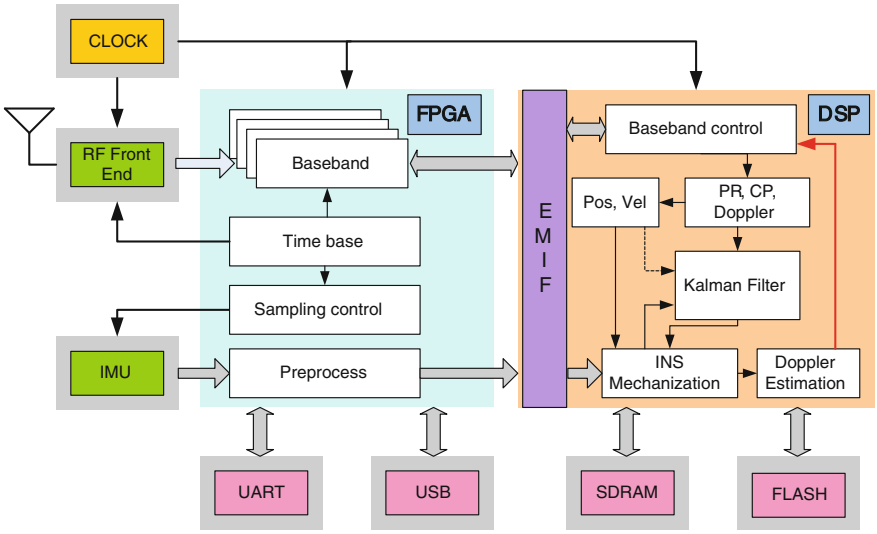

Fig. 68.1 Block diagram of integrated deeply coupled system

controlling; DSP accesses FPGA as an external memory via EMIF, thus the seamless communication could be realized between them. The data sampling units of MEMS IMU and the GNSS RF are connected to FPGA via I/O interface, and FPGA controls and receives their data. SDRAM, as the external memory of DSP, is used for storing the code block of lower process frequency.

Under the sampling clock produced by FPGA, the digitalized GNSS signal, which is adjusted to IF from RF unit, enters the digital signal processing part of the base band; the base band correlators of high speed and multi-channel (including carrier NCO, code NCO, code generator, mixer and coherent accumulator) must be completed in FPGA, and the time base managing unit is appropriate to be realized in FPGA; under interruption, the coherent accumulating results are passed to DSP via bus, and the satellites signals acquiring and tracking control of all channels are realized by flexible software. At the same time, bit and frame synchronization, observation measurement, ephemeris and PVT are all completed in DSP.

The sampling data of MEMS IMU are produced under the PPS, thus insuring the synchrony of IMU data sampling and GNSS time stamp. Firstly the sampled IMU data is preprocessed in FPGA including integration and adding time stamp, and then it is sent to DSP for information integrating process. After the initialization of INS, once the IMU data updates, an inertial navigation computing and coupled navigation calculating is performed; every time the GPS position updates, a coupled navigation updates; once an inertial navigation updates, a Doppler is estimated, thus realizing aiding the tracking loop [13].

68.3 Key Technologies

68.3.1 The Model of IMU Aided Tracking Loop

Carrier tracking loop (PLL) is easier to lose lock than code tracking loop (DLL). Therefore in our design of deep integration, the estimated Doppler is used to aid PLL while the DLL is aided by PLL then. In order to analyze the characteristics of INS aided tracking loop, mathematical models need to be built first. As INS and receiver's tracking loop are both used for computing the vehicle motion information, i.e. the vehicle dynamic is commonly experienced by both the IMU and the tracking loop, the IMU measurement branch could assist the GPS tracking loop based on the concept of feed-forward.

The Fig. 68.2 shows the working principle of IMU aided tracking loop [14, 15]: The phase error between the dynamic vehicle and satellites can be tracked by the carrier tracking loop of the receivers, and the discriminator can measure the difference between local oscillator and input signal phase, and convert the phase error to frequency information by a low pass filter, thus adjusting local signals to follow the input signal. The vehicle dynamic information in the navigation frame can be directly measured by IMU, then the measured velocity information is mapped to the LOS between satellite and vehicle, and now the Doppler information of relative motion of satellite and vehicle is estimated by INS. Finally, the INS estimated dynamic Doppler and receiver's clock drift form the feed-forward Doppler aiding information. With the aid of forward-feed branch, the tracking loop only needs to undertake the error of the Doppler estimation, which greatly reduces its working load. Figure 68.3 is the correspondent detailed mathematical model of the schematic diagram [16, 17].

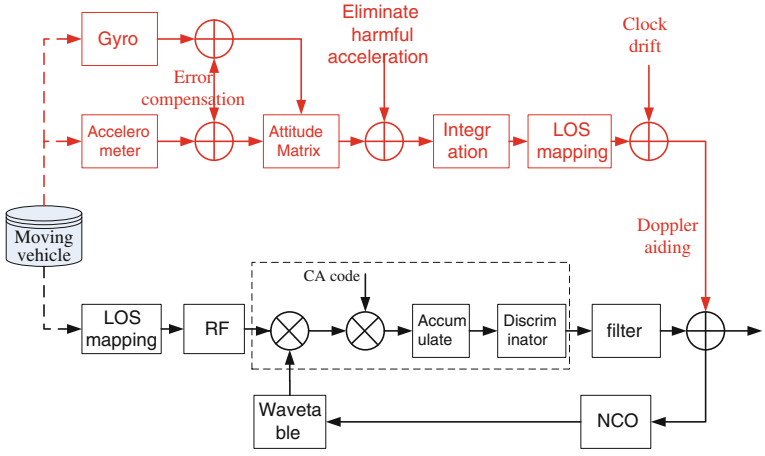

Fig. 68.2 Schematic of IMU aiding loop

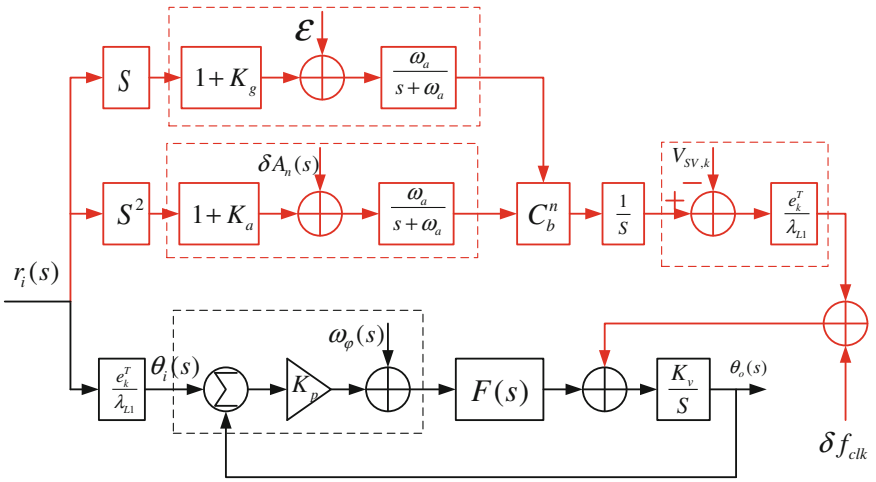

Fig. 68.3 Mathematical model of IMU aiding loop

68.3.2 Analysis of Loop Tracking Errors

In a traditional GNSS receiver, in order to keep the tracking loops locked under dynamic conditions, the bandwidth must be wide enough. However, when the bandwidth becomes wider, the loop noise will be higher. Obviously, to consider both the dynamic tracking and the noise, the bandwidth of traditional tracking loop must be compromised so as to balance the two sides. When the INS information is introduced, this contradiction will be mitigated or even eliminated.

Figure 68.4 shows the signal model of receiver's tracking loop with the aid of IMU [18]. Because the clock error of the receiver may transmit to the signals when local carrier is produced, and it can be ascribed to the part of signal input when analyzing signal transmission. The forward-feed branch can provide estimated dynamic information and receiver's clock drift information, and tracking loop only needs to track the residual part θ_r and thermal noise of input signals. The difference between θ_r and local carrier $\tilde{\theta}_r$ produced by the loop filter is the tracking error. According to the signal model, the input signal errors are composed of the INS estimated error and the clock error, which includes Allan deviation noise, vibration-induced noise and acceleration stress error; and the external error ω_φ is mainly environmental noise. Figure 68.5 is the correspondent error transmitting model of IMU aided loop. $1 - H(s)$ is the transfer function of $\delta\theta_r(s)$, and $H(s)$ is that of thermal noise. Therefore the tracking loop error can be demonstrated as [19]:

$$\sigma^2_{error} = \int_0^\infty \left(|H(j2\pi f)|^2 Sw(f) + |1 - H(j2\pi f)|^2 S_r(f) \right) df \qquad (68.1)$$

Tracking errors caused by all error sources on the basis of (68.1), and there is a detailed deduction in the cited Ref. [20]. Since all error sources are function of loop bandwidth, the INS aided PLL bandwidth can be optimal when $\partial\sigma_{error}/\partial B_L = 0$. Because INS aiding could isolate the receiver dynamics to create a quasi-stationary condition for the tracking loop, the receiver performance will be improved comprehensively including high-dynamics, dynamic tracking accuracy, dynamic tracking sensitivity. The deeply-coupled receiver will achieve better accuracy, availability, and robustness.

68.3.3 The Optimized Design of Real-Time

Deeply coupled system includes high speed signal process, complex navigation algorithm, frequent data exchange and so on, so the real-time deeply coupled system is a great challenge for the resource and computing capacity of an integrated platform. The system is optimized on three levels, which are software top-level structure, division of work of software and hardware and the algorithm efficiency, so as to realize real-time integrated deeply coupled system.

In a deeply coupled system, interrupt tasks can be divided into three types according to execution cycles: GNSS signal acquiring and tracking, the execution cycle of which is 0.8 ms, INS mechanization, Doppler estimating and integrated navigation calculating, the execution cycle of which is 50 ms, and GNSS observation extracting, GNSS navigation, integrated navigation updating and serial information output, the execution cycle of which is 1 s.

Generally when DSP enters an interrupt service routine, other interrupts are forbidden whatever their priority is. If the execution time of an interrupt surpasses 8 ms, then there is necessarily some loss in the 0.8 ms interrupt [21]. In order to avoid that an interrupt of higher priority is forbidden because of another interrupt is executing, the interrupt priority level and interrupt nesting design of the software is necessary.

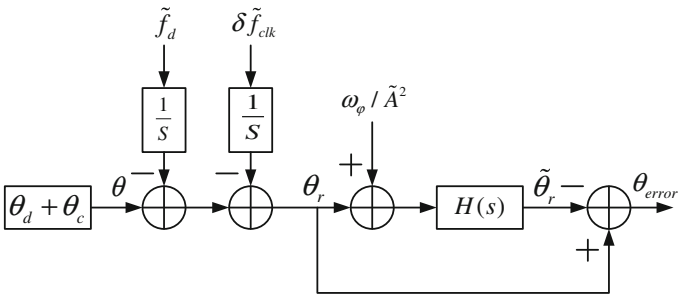

Fig. 68.4 Closed-loop signal transfer model with IMU aiding

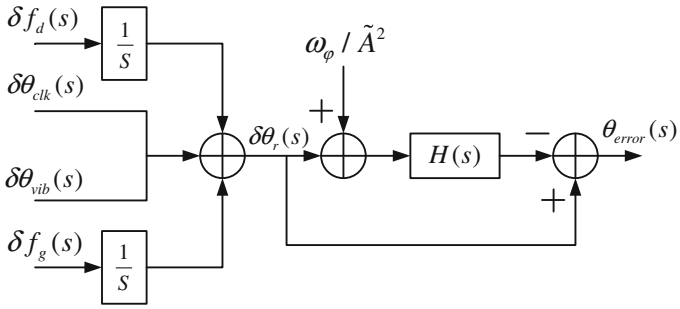

Fig. 68.5 Closed-loop error transfer model with IMU aiding

The top-level structure of the software is as Fig. 68.6, the priority of 0.8 ms external interrupt is the highest, the execution time of which is 0.2 ms, and the 50 ms external interrupt priority is in the second place, the execution time of which is 10 ms. The 1 s timing interrupt, the execution time of which is 18 ms, generates in the 50 ms external interrupt. At the same time, interrupt nesting is allowed in the two interrupts with low priority.

As the work division of software and hardware is described in the part of system framework, there is no more discussion in this part. Algorithm execution efficiency means shortening the execution cycle by simplifying algorithm and optimizing codes. When the system works overloaded, the overloaded DSP will not finish computing in given time, thus the system can not realize real-time performance. For the sake that the processor an finish all the requested tasks, measures are as follows: firstly, reduce calculating complexity by simplifying algorithm, such as split and simplify those matrix with many zero elements; secondly, complete complex matrix computing by assemble other than optimized principle of regular codes to reduce the computing complexity of deeply coupled system efficiently.

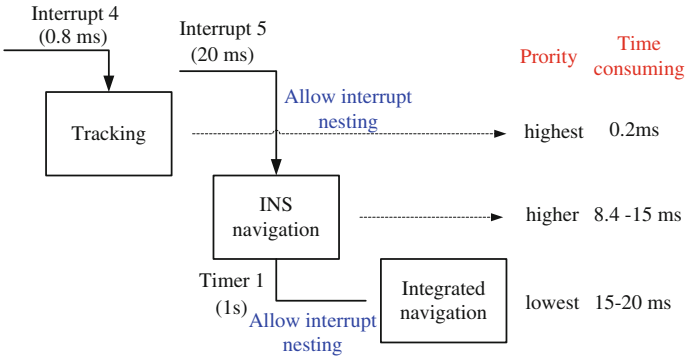

Fig. 68.6 Software top-level architecture

68.4 Performance Testing and Evaluation

The GPS/INS integrated navigation simulator produced by Navigation Laboratories is the signal source for system testing, and the MEMS IMU data exports in analog form through the SPI. The system test site is shown in Fig. 68.7, and the set trajectory is as screen shown. GPS RF signal and the IMU signal are exported simultaneously by the simulator, and the integrated system receives them respectively through GNSS RF module and IMU sampling unit.

68.4.1 Real-Time Testing of the System

Figure 68.8a shows the test results of loop controlling time consuming. The upper yellow wave is the INS estimated Doppler tests results. The consumed time each is about 600 us; the lower blue wave is the tests results of the loop circuit itself, the consumed time each is about 460 us. Under the condition that the carrier dynamic is 100 m/s^2, a real-time error of 0.46 ms may lead to a Doppler estimated error of 0.24 Hz. Compared to the error caused by INS Doppler estimation, the carrier wave loop circuit adding 0.24 Hz to delete the error is acceptable, thus no extra algorithmic is needed to reduce errors.

Figure 68.8b shows the real-time tests results of the system. The upper blue wave is the break execution results of 0.8 ms, and the lower yellow one is that of 50 ms. By observing the wave form before and after magnification, we found that the break execution of 50 ms does not lead to the break loss of 0.8 ms, which tells that the software structure design ensures all the break execution performs normally. By observing magnified wave, we found that the real execution time of every 0.8 ms break is 1 third of the total break time, and that of every 50 ms break

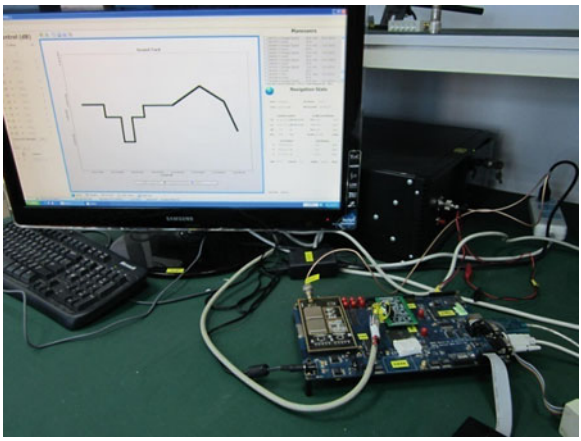

Fig. 68.7 Test site of deep couple

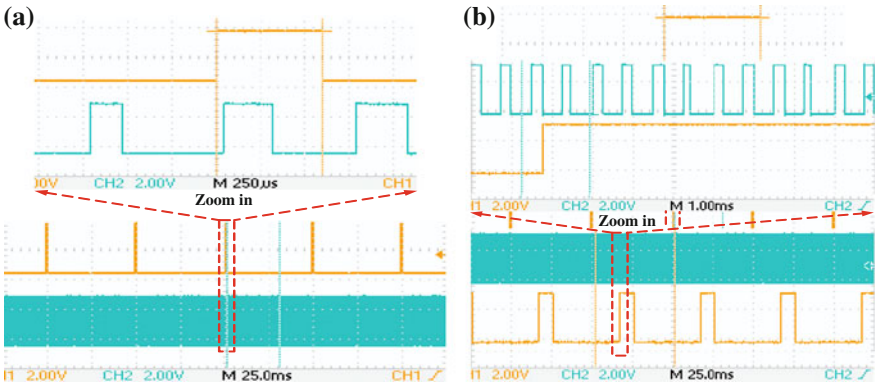

Fig. 68.8 **a** Time delay of loop control. **b** The results of interrupt operation

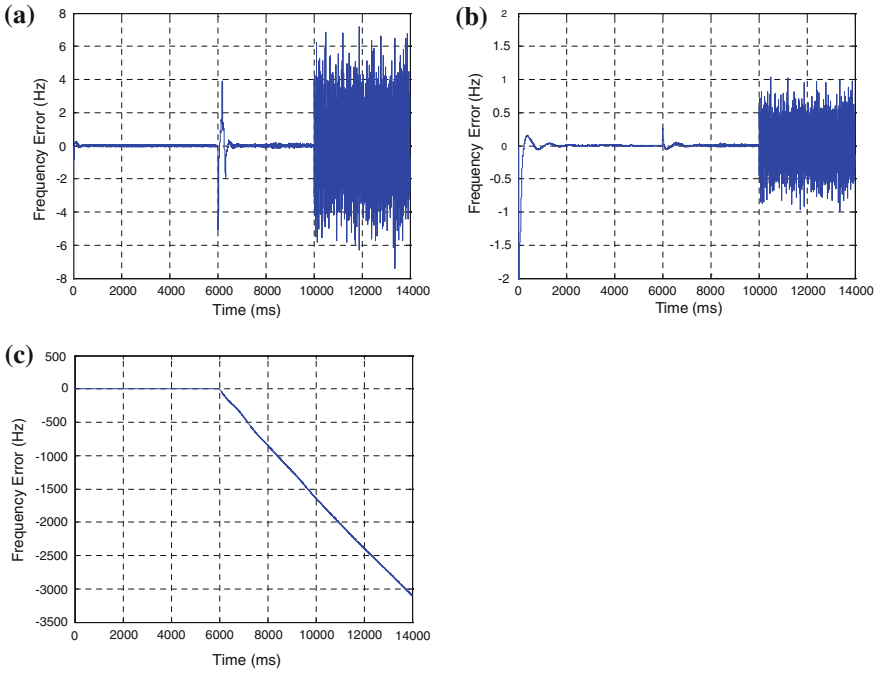

Fig. 68.9 **a** Frequency tracking error of 20 Hz traditional loop. **b** Frequency tracking error of 3 Hz IMU aiding loop. **c** Frequency tracking error of 3 Hz traditional loop

is 1 fifth of the total break time, which demonstrates that the real time that a processor needs to execute all break tasks are more than sufficient. Therefore, an integrated deeply coupled system is practical by the optimized design of real-time.

68.4.2 Loop Tracking Error Tests

Simulation data is used to verify the theory in Sect. 2.2, that with the aiding of the MEMS IMU, the tracking loop error would be decreased. The test scenario is stationary and noiseless in first 6000 ms, then 500 Hz/s ramp dynamic, and thermal noise added at 10000 ms. Three kinds of tracking loops are tested using this scenario including traditional PLL with 20 Hz bandwidth, IMU aided PLL with 3 Hz bandwidth and traditional PLL with 3 Hz bandwidth. Aiding information is modeled based on gyro's bias bigger than 36°/h, and Fig. 68.9a–c respectively show the three tracking loop's error. The comparative test results of Fig. 68.9a and b show that when the receiver dynamics changes, the tracking error amplitude is much less with IMU aided than traditional loop, meanwhile compressing loop bandwidth could reduce the frequency error. The comparative test results of Fig. 68.9b and c show that, narrow bandwidth loop is unable to withstand high dynamic without external Doppler aided, so the loop's bandwidth of traditional receivers could not be too narrow.

Based on theoretical analysis and simulation test conclusions, the IMU aided loop bandwidth of the real-time system is 3 Hz while traditional loop bandwidth is 20 Hz. Figure 68.10a and b are respectively two loops' real-time phase error. The phase error is significantly reduced with IMU aiding, and it further validates the excellence of the deeply coupled system.

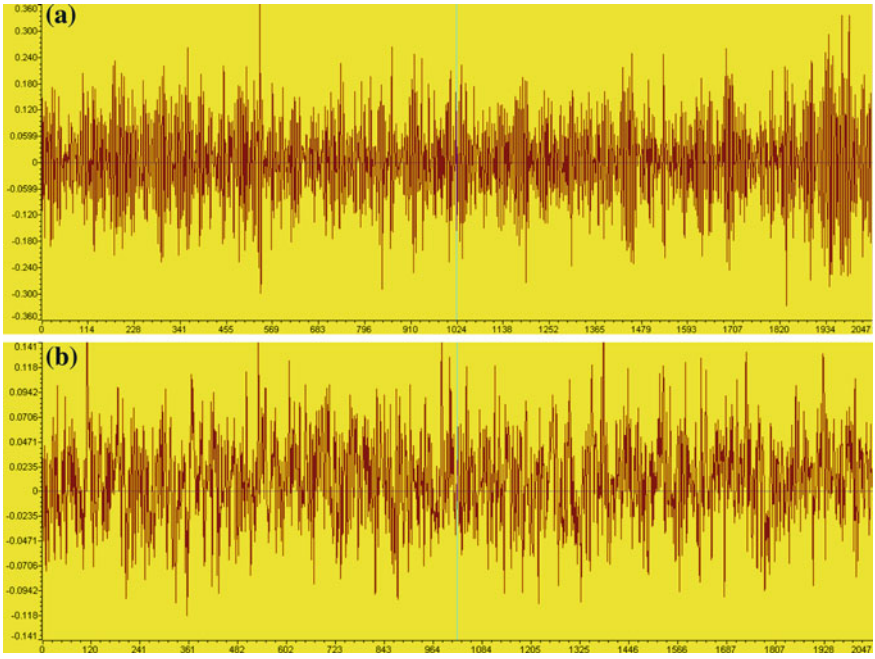

Fig. 68.10 **a** Real-time phase error of traditional loop. **b** Real-time phase error of IMU aiding loop

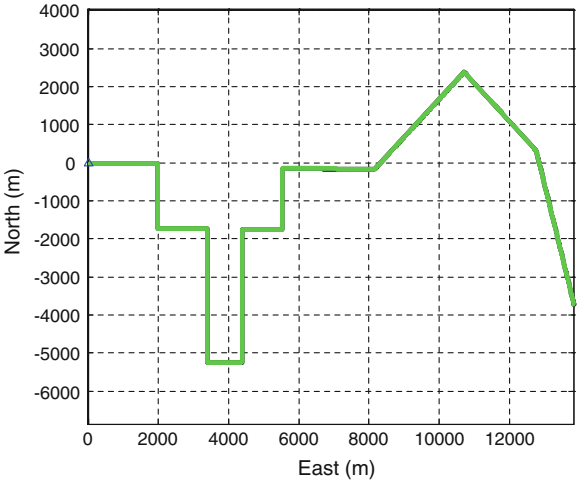

Fig. 68.11 Running track set for the simulator figure

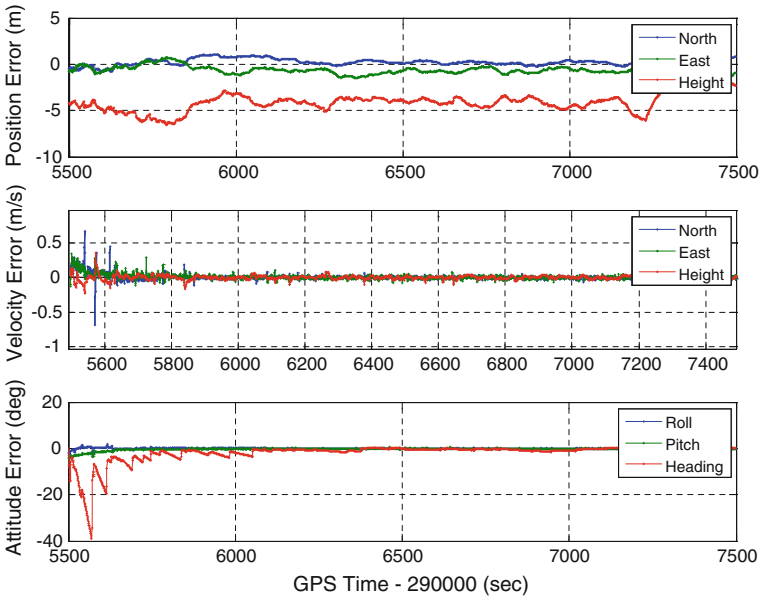

Fig. 68.12 Error curve of the real-time navigation results

68.4.3 Real-Time Dynamic Navigation Tests

To verify the feasibility of the integrated system solution, it is the most intuitive means to carry out the testing of real-time dynamic navigation. To facilitate the

testing and results analysis, the signal source of the system testing uses GPS/INS integrated navigation simulator. Figure 68.11 is the running track set for the simulator, including stationary, acceleration and deceleration, turning. And Fig. 68.12 is the error curve of the real-time navigation results by the integrated system. Once the MEMS IMU error is convergence through dynamic alignment, integrated navigation's horizontal position error is about 1 m, and the speed error is less than 5 cm/s. The test results not only illustrate that the integrated system scheme is feasible, but also show that a very small velocity error could provide precise Doppler aiding information for the tracking loop.

68.5 Conclusions

In order to promote the product process of MEMS IMU based deeply coupled system, this paper has proposed an embedded integrated system scheme. And it has focused on modeling the IMU aided tracking loop, analyzing the tracking error and optimizing the design of system's real-time. Tests and analysis showed that, in the integrated system, aiding information's delay was very little and each interrupt could perform real-time without missing. What's more, MEMS IMU aided loop could improve tracking accuracy by reducing bandwidth. The integrated deeply coupled system scheme is feasible, and it creates conditions for the in-depth study of real-time deeply coupled systems.

Acknowledgments The colleagues of the Navigation group from GNSS Research Center at Wuhan University who participated in the deep integration research and testing are thanked for their cooperation. And this work is supported by the National High Technology of China under contract 2012AA12A206, the National Natural Science Foundation of China under contract 41174028 and Opening project of Chinese Academy of Sciences under contract 2012PNTT10.

References

1. Alban S, Akos DM, Rock SM (2003) Performance analysis and architectures for INS-aided GPS tracking loops. In: Proceedings of ION NTM, Anaheim, CA, January 2003, pp 611–622
2. Barbour N, Hopkins R, Kourepenis A, Ward P (2010) Inertial MEMS system applications, NATO RTO-EN-SET-116, March 2010
3. Permutter M, Robin L (2012) High-performance, low cost inertial MEMS: a market in motion. In: Proceedings of IEEE/ION PLANS 2012, April 2012
4. Shin EH (2005) Estimation techniques for low-cost inertial navigation. PhD thesis, Department of Geomatics Engineering, University of Calgary, Canada
5. Godha S, Cannon ME (2007) GPS/MEMS INS integrated system for navigation in Urban areas, GPS solution
6. Guo M, Lin S (2011) MINS/GPS tightly-coupled integrated navigation system. J Chin Inert Technol 6:021
7. Gustafson D, Dowdle J (2003) Deeply integrated code tracking: comparative performance analysis. In: Proceedings of ION GPS 2003, September 2003

8. Chiou TY, Seo J (2008) Performance of a Doppler-aided GPS navigation system for aviation applications under ionospheric scintillation. In: Proceedings of ION GNSS 2008, September 2008
9. Lin T, Driscoll C, Lachapelle G (2011) Development of a context-aware vector-based high sensitivity GNSS software receiver. In: Proceedings of ITM 2011, January 2011
10. Timothy MB, Jason Wilmot, Michael JC (2006) A High G, MEMS based, deeply integrated, INS/GPS, guidance, navigation and control flight management unit. In: Proceedings of IEEE
11. Kennedy S, Rossi J (2008) Performance of a deeply coupled commercial grade GPS/INS system from KVH and NovAtel Inc. In: Proceedings IEEE
12. Zhang T, Niu X (2012) An integrated research platform for real-time deep integration. In: Proceedings of ION GNSS 2012, September 2012
13. Gao G, Lachapelle G (2006) INS-assisted high sensitivity GPS receivers for degraded signal navigation. In: Proceedings of ION GNSS 2006, September 2006
14. Kaplan E, Hegarty C (1996) Understanding GPS: principles and applications, 2nd edn. Artech House, Norwood, MA
15. Niu X, Nassar S, El-Sheimy N (2007) An accurate land-vehicle MEMS IMU/GPS navigation system using 3D auxiliary velocity updates. Navigation 54(3):177–188
16. Zhenglong Deng, Inertial Technology, Harbin Institute of Technology, 2006
17. Gardner FM (2005) Phaselock techniques, 3rd edn. Wiley, New York
18. Knight MF (2000) Ionospheric scintillation effects on global positioning system receivers. PhD Thesis, Department of Electrical and Electronic Engineering, University of Adelaide, South Australia
19. Parkinson B, Spilker J (1996) Global positioning system theory and applications. In: Proceedings of GPS receivers, the American Institute of Aeronautics and Astronautics, Inc.
20. Zhang T, Zheng T (2012) Oscillator effects on carrier phase measurements in GNSS receiver. In: Proceedings of gematics and information science of Wuhan University
21. Three Star Technology (2009) TM320C6713 DSP principles and application examples, Published by Electronics Industry